DTIC FILE COPY

AD-A

DISTRIBUTION STATEMENT A
Approved for public release;
Distribution Unlimited

The Physics and Chemistry of Carbides, Nitrides and Borides

Edited by

Robert Freer

90 12 18 028

NATO ASI Series

Series E: Applied Sciences - Vol. 185

The Physics and Chemistry of Carbides, Nitrides and Borides

NATO ASI Series

Advanced Science Institutes Series

A Series presenting the results of activities sponsored by the NATO Science Committee, which aims at the dissemination of advanced scientific and technological knowledge, with a view to strengthening links between scientific communities.

The Series is published by an international board of publishers in conjunction with the NATO Scientific Affairs Division

A Life Sciences **B Physics**	Plenum Publishing Corporation London and New York
C Mathematical and Physical Sciences **D Behavioural and Social Sciences** **E Applied Sciences**	Kluwer Academic Publishers Dordrecht, Boston and London
F Computer and Systems Sciences **G Ecological Sciences** **H Cell Biology**	Springer-Verlag Berlin, Heidelberg, New York, London, Paris and Tokyo

Series E: Applied Sciences - Vol. 185

The Physics and Chemistry of Carbides, Nitrides and Borides

edited by

Robert Freer
Materials Science Centre,
University of Manchester/UMIST,
U.K.

Accesion For
NTIS CRA&I ☑
DTIC TAB ☐
Unannounced ☐
Justification
By $195.00
Distribution /
Availability Codes
Dist | Avail and / or Special
A-1 | 21

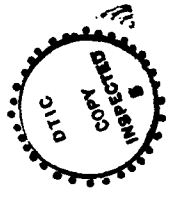

Available for $195 from Kluwer Academic Publishers. 101 Philip Drive. Norwell, MA 02061.

VHG 12/13/90

Kluwer Academic Publishers

Dordrecht / Boston / London

Published in cooperation with NATO Scientific Affairs Division

Proceedings of the NATO Advanced Research Workshop on
The Physics and Chemistry of Carbides; Nitrides and Borides
Manchester, U.K.
September 18–22, 1989

Library of Congress Cataloging-in-Publication Data

NATO Advanced Research Workshop on the Physics and Chemistry of Carbides, Nitrides, and Borides (1989 : Manchester, England)
The physics and chemistry of carbides, nitrides, and borides : proceedings of the NATO Advanced Research Workshop on the Physics and Chemistry of Carbides, Nitrides, and Borides, Manchester, U.K., 18-22 September, 1989 / edited by Robert Freer.
p. cm. -- (NATO ASI series. Series E, Applied sciences : vol. 185
Includes indexes.
ISBN 0-7923-0870-0
1. Refractory materials--Congresses. 2. Semiconductors--Materials--Congresses. 3. Carbides--Congresses. 4. Nitrides--Congresses. 5. Borides--Congresses. I. Freer, R. II. Title. III. Series: NATO ASI series. Series D, Behavioural and social sciences ; no. 58.
TA418.26.N38 1989
620.1'43--dc20 90-41853

ISBN 0–7923–0870–0

Published by Kluwer Academic Publishers,
P.O. Box 17, 3300 AA Dordrecht, The Netherlands.

Kluwer Academic Publishers incorporates the publishing programmes of
D. Reidel, Martinus Nijhoff, Dr W. Junk and MTP Press.

Sold and distributed in the U.S.A. and Canada
by Kluwer Academic Publishers,
101 Philip Drive, Norwell, MA 02061, U.S.A.

In all other countries, sold and distributed
by Kluwer Academic Publishers Group,
P.O. Box 322, 3300 AH Dordrecht, The Netherlands.

Printed on acid-free paper

All Rights Reserved
© 1990 by Kluwer Academic Publishers and copyright holders as specified on appropriate pages within
No part of the material protected by this copyright notice may be reproduced or utilized in any form or by any means, electronic or mechanical, including photocopying, recording or by any information storage and retrieval system, without written permission from the copyright owner.

Printed in the Netherlands

CONTENTS

Preface ix

List of Participants xi

I. **Powders, Ceramics and Single Crystals - Preparation and Characterisation** 1

Chemical Routes for the Preparation of Powders
D.L. Segal 3

Silicon Nitride: Relations Between Powder Characteristics and Sinterability
F. Cambier, A. Leriche, E. Gilbart, R.J. Brook and F.L. Riley 13

Kinetics of the Nitridation of Silicon
B. Myhre and K. Motzfeldt 29

Lanthanum Silicon Oxynitrides, Synthesis and X-Ray Diffraction and IR Studies
M. Kizilyalli and G. Gürbüz 45

Synthesis of Silicon Carbide of Different Morphologies and the Effect of Second Phase in Ceramic Composites
A. Leriche and F. Cambier 69

Laboratory Methods for the Preparation of Boron Carbides
F. Thevenot 87

Preparation and Properties of Icosahedral Borides
T.L. Aselage, D.R. Tallant, J.H. Gieske, S.B. Van Deusen and R.G. Tissot 97

Production, Fabrication and Uses of Borides
R. Thompson 113

Laser Ablation ICP-MS Analysis of Ceramic Materials
I.D. Abell, D. Gregson and S. Shuttleworth 121

II. **Synthetic Diamond - Preparation and Properties** 131

Metastable Synthesis of Diamond
T.R. Anthony 133

Selected-Area Deposition of Diamond Films
K. Kobashi, T. Inoue, H. Tachibana, K. Kumagai, K. Miyata, K. Nishimura and A. Nakaue 159

Surface Analysis of Diamond Nucleation on Silicon and Electron Microscopy of the Diamond/Silicon Interface
B.E. Williams, D.A. Asbury and J.T. Glass 169

Electrical Properties of B Doped CVD Grown Polycrystalline Diamond Films
K. Nishimura, K. Das, J.T. Glass, K. Kobashi and R.J. Nemanich 183

III. Structure, Crystal Chemistry, Phase Equilibria, Defects and Mass Transport 195

Silicon Carbide: Structure and Polytypic Transformations
T.F. Page 197

Crystal-Chemistry of Transition Metal Hemicarbides
T. Epicier 215

Structure and Properties of Si-Doped Boron Carbide
R. Telle 249

Actinoidmetal Boron Carbides
P. Rogl 269

Defects and Grain Boundaries in High Temperature Deformed α-SiC
J. Vicens, S.J. Lee, E. Laurent-Pinson, G. Nouet and J.L. Chermant 279

Application of Transmission Electron Microscopy to the Study of Transition Metal Carbides
T. Epicier 297

Defect Structures and Order-Disorder Transformations in Transition Metal Carbides and Nitrides
C.H. de Novion, B. Beuneu, T. Priem, N. Lorenzelli and A. Finel 329

Mass Transport in Carbides and Nitrides
Hj. Matzke 357

IV. Thermal, Chemical and Mechanical Stability 385

Thermal Shock and Corrosion of SiC - A Combustion Chamber Model Case Study
G.A. Schneider, K.G. Nickel and G. Petzow 387

High Temperature Corrosion of Silicon Nitrides (abstract only)
M.H. Van de Voorde 403

Corrosion and Mechanical Properties of Silicon Nitride Based Ceramics. Influence of Microstructural Changes
P. Goursat and J.L. Besson 405

The Role of Oxygen in Non-Oxide Engineering Ceramics
D.P. Thompson 423

Thermochemical Predictions of Metal-Metal Carbide Stabilities in Relation to WC and WC-Co Production
F.H. Hayes and F.R. Sale 435

Si_3N_4-SiC Composites
J.L. Baptista 447

Boride-Carbide Composites: TiB_2-TiC-SiC
F. de Mestral and F. Thevenot 457

V. Theoretical Studies 483

Electronic Structure of Stoichiometric and Non-Stoichiometric Titanium Carbides and Nitrides
A. Neckel 485

Further Electronic Structure Studies of Boron and Boron-Rich Borides
D.W. Bullett 513

The Electronic Structure of Crystalline Boron Carbide I: B_{12} Icosahedra and C-B-C Chains
A.C. Switendick 525

Electronic Structure of Lithium Boride Li_3B_{14}
D.W. Bullett 555

VI. Bulk Materials and Thin Films - Electrical, Optical and Thermal Properties 561

Optical and Electronic Properties of SiC
W.J. Choyke 563

Recent Advances Regarding the Definition of the Atomic Environment, Film Growth and Microelectronic Device Development in Silicon Carbide
R.F. Davis 589

Thermal Conductivity of Transition Metal Carbides
W. S. Williams 625

The Dielectric Properties of Nitrides
R. Freer and I.O. Owate 639

Current Status of the Research on III-V Mononitride Thin Films for Electronic and Optoelectronic Applications
R.F. Davis 653

Short Range Order in "Amorphous" Thin Films of Titanium Diboride
W.S. Williams 671

On the Electronic Transport Properties of Boron Carbide
H. Werheit 677

Theory of Electronic and Thermal Transport in Boron Carbides
D. Emin 691

Optical Properties of Boron-Rich Solids with Icosahedral Structure
H. Werheit 705

Subject Index 727

Compound and System Index 733

PREFACE

Carbides, nitrides and borides are families of related refractory materials. Traditionally they have been employed in applications associated with engineering ceramics where either high temperature strength or stability is of primary importance. In recent years there has been a growing awareness of the interesting electrical, thermal and optical properties exhibited by these materials, and the fact that many can be prepared as monolithic ceramics, single crystals and thin films. In practical terms carbides, nitrides and borides offer the prospect of a new generation of semiconductor materials, for example, which can function at very high temperatures in severe environmental conditions. However, as yet, we have only a limited understanding of the detailed physics and chemistry of the materials and how the preparation techniques influence the properties.

Under the auspices of the NATO Science Committee an Advanced Research Workshop (ARW) was held on the Physics and Chemistry of Carbides, Nitrides and Borides (University of Manchester, 18–22 September, 1989) in order to assess progress to date and identify the most promising themes and materials for future research. An international group of 38 scientists considered developments in 5 main areas:

The preparation of powders, monolithic ceramics, single crystals and thin films;
Phase transformations, microstructure, defect structure and mass transport;
Materials stability;
Theoretical studies;
Electrical, thermal and optical properties of bulk materials and thin films.

This volume contains the majority of the papers presented at the workshop and highlights current achievements, the importance of microstructure in controlling properties, and the benefit of linking experimental and theoretical studies. From discussions it was recognised that future progress in understanding and exploiting carbides, nitrides and borides, in the form of ceramics, single crystals and thin films, will only come through an interdisciplinary approach, with input from both experimentalists and theoreticians.

The organisers of the ARW gratefully acknowledge the financial and other support provided by:

The NATO Science Committee
US Air Force European Office of Aerospace Research and Development (EOARD)
European Office of the US Army
VG Elemental Ltd.
British Nuclear Fuels Ltd.
RTZ Chemicals Ltd.
Cookson Group plc
Instron Ltd.
BP International Ltd.
University of Manchester Institute of Science and Technology
Kratos Analytical Ltd.

Thanks are due to Professor G. Borchardt and all members of the Advisory Committee for their encouragement and guidance in the planning of the ARW, and to Mr. I. Easdon, Mr. J. Fan and staff of the Holly Royde Conference Centre for ensuring the smooth running of the workshop.

Finally I should like to thank Joan Colclough for her cheerful and efficient handling of the secretarial work involved in preparing the scientific programme and editing the proceedings.

Robert Freer

List of Participants

Dr. T.R. Anthony, Room IC30, Building K-1, GE Research and Development Center, 1 River Road, Schenectady, New York 12345, U.S.A.

Dr. D.R. Armstrong, Department of Pure and Applied Chemistry, University of Strathclyde, Glasgow, G1 1XL, U.K.

Dr. T.L. Aselage, Electronic Ceramics, Division 1842, Sandia National Laboratories, Alburquerque, New Mexico 87185, U.S.A.

Professor J.L. Baptista, Department Engenhario Ceramica E Do Vidro, Universidade de Aveiro, 3800 AVEIRO, Portugal.

Professor Dr. G. Borchardt, Institut für Allgemeine Metallurgie, Technische Universitat Clausthal, Robert Koch Strasse 42, D-3392 Clausthal-Zellerfeld, Federal Republic of Germany.

Professor D.W. Bullett, School of Physics, University of Bath, Claverton Down, Bath BA2 7AY, U.K.

Dr. F. Cambier, Research Manager, Centre de Recherches de l'Industrie Belge de la Ceramique, B-7000 MONS, Avenue Gouverneur Cornez, 4, BELGIUM.

Professor W.J. Choyke, Department of Physics and Astronomy, University of Pittsburgh, PITTSBURGH, PA 15260, U.S.A.

Professor R.F. Davis, Department of Materials Science and Engineering, North Carolina State University, Box 7907, Raleigh, NC 27695-7907, U.S.A.

Dr. C.H. de Novion, Laboratoire des Solides Irradies, S.E.S.I., Ecole Polytechnique, 91128 Palaiseau Cedex, FRANCE.

Dr. D. Emin, Division 1151, Sandia National Laboratories, Albuquerque, NM 87185-5800, U.S.A.

Dr. T. Epicier, INSA, GEMPPM, Bat. 502, 69621 Villeurbanne Cedex, FRANCE.

Dr. R. Freer, Materials Science Centre, University of Manchester/UMIST, Grosvenor Street, Manchester M1 7HS, U.K.

Professor J. Glass, Department of Materials Science and Engineering, North Carolina State University, Box 7907, RALEIGH, NC 27695-7907, U.S.A.

Dr. P. Goursat, Universite de Limoges, Laboratoire de Ceramique Nouvelles, 123 Ave. Albert Thomas, 87060 LIMOGES, France.

Dr. D. Gregson, VG Elemental Ltd., Ion Path, Road Three, Winsford, Cheshire, CW7 3BX, U.K.

Prof. M. Kizilyalli, Middle East Technical University, Department of Chemistry, 06531, Ankara, Turkey.

Dr. A. Leriche, Neoceram, Rue du Grand Peuplier, 1 Parc Industriel, B-7060 STREPY BRAQUEGNIES, BELGIUM.

Dr. Hj. Matzke, CEC Joint Research Centre, Karlsruhe Establishment, European Inst. for Transuranium Elements, Postfach 2340, Karlsruhe 7500, Federal Republic of Germany.

Professor K. Motzfeldt, Institutt for Uorganisk Kjemi, NTH/University of Trondheim, Norway.

Dr. A. Nakaue, Kobe Steel Ltd., Electronics Research Laboratory, I-5-5 Takatsukadai, Nishi-ku, Kobe 673-02, JAPAN.

Professor Dr. A. Neckel, Institut fur Physikalische Chemie, Universitat Wien, A-1090 VIENNA, AUSTRIA.

Dr. K.G. Nickel, Max-Planck-Institut fur Metallforschung, Institut fur Werkstoffwissenschaften, Pulvermetallurgisches Laboratorium, Heisenbergstr. 5, D-7000, Stuttgart 80, Federal Republic of Germany.

Professor T. Page, Department of Metallurgy and Engineering Materials, University of Newcastle, Newcastle upon Tyne, NEl 7RU, U.K.

Professor Dr. P. Rogl, Institut fur Physikalische Chemie, Universitat Wien, A-1090, AUSTRIA.

Professor F.R. Sale, Materials Science Centre, University of Manchester/UMIST, Grosvenor Street, Manchester Ml 7HS, U.K.

Dr. G. Schneider, Max-Planck-Institut fur Metallforschung, Institut fur Werkstoffwissenschaften, Pulvermetallurgisches Laboratorium, Heisenbergstr. 5, D-7000, Stuttgart 80, Federal Republic of Germany.

Dr. D. Segal, Applied Chemistry Group, Materials Development Division, B429 Harwell Laboratory, UKAEA, Oxfordshire, OXll ORA, U.K.

Dr. R. Telle, Max-Planck-Institut fur Metallforschung, Institut fur Werkstoffwissenschaften, Pulvermetallurgisches Laboratorium, Heisenbergerstrasse 5, 7000 STUTTGART 80, Federal Republic of Germany.

Dr. F. Thevenot, Ecole Nationale Superieure des Mines, Departement Materiaux et CRRACS, 158 cours Fauriel, 42043 Saint-Etienne Cedex 2, FRANCE

Dr. D.P. Thompson, Dept. of Metallurgy and Eng. Materials, University of Newcastle, Newcastle upon Tyne, NEl 7RU, U.K.

Professor R. Thompson, RTZ Chemicals Ltd., Advanced Ceramics Development Unit, Technical Centre, Cox Lane, Chessington, Surrey, KT9 lSJ, U.K.

Professor M. van de Voorde, CEC Joint Research Centre, Petten, Establishment, P.O. Box 2, 1755 ZG Petten, The Netherlands.

Dr. J. Vicens, LERMAT, ISMRA-Université, Boulevard Maréchal Juin, 14032 CAEN Cedex, France.

Professor H. Werheit, Universitat-Gesamthochschule-Duisburg, Fachbereich 10/Physik, D-4100 Duisburg 1, Federal Republic of Germany.

Professor W.S. Williams, Department of Materials Science and Engineering, Case Western Reserve University, Cleveland, Ohio 44106, U.S.A.

Dr. S. Witek, Cooksons Technology Centre, Sandy Lane, Yarnton, Oxfordshire, OX5 lAF, U.K.

Dr. L. Zuppiroli, Laboratoire de Solides Irradies, Ecole Polythechnique, 91128 Palaiseau Cedex, FRANCE.

I. POWDERS, CERAMICS and SINGLE CRYSTALS - PREPARATION and CHARACTERISATION

CHEMICAL ROUTES FOR THE PREPARATION OF POWDERS

D.L. SEGAL
Materials Development Division
Harwell Laboratory
Oxfordshire
OX11 ORA
United Kingdom

ABSTRACT. Chemical routes for the preparation of selected non-oxide ceramic powders, namely silicon carbide, silicon nitride, aluminium nitride, titanium diboride, boron carbide and boron nitride have been reviewed. Although these techniques include conventional ones such as powder mixing, this article is primarily concerned with non-conventional ceramic syntheses, that is, polymer pyrolysis, non-aqueous liquid phase reactions, gas phase reactions and sol-gel processing. Powder properties such as particle size, corresponding to different synthetic techniques are described. This review concludes that chemical synthesis can make a significant contribution to the development of ceramic precursors for non-oxide powders.

1. INTRODUCTION

Worldwide advanced ceramic activities during the last two decades have been characterised by an increasing use of chemical synthetic techniques for both non-oxide and oxide materials. These techniques are referred to as non-conventional when they exclude powder mixing, fusion and coprecipitation methods, that is, the three conventional synthetic routes to ceramic powders. Non-conventional techniques have the potential for preparation of powders with greater chemical purity and homogeneity than is attainable from conventional syntheses. They also allow fabrication of ceramic coatings and fibres, geometries which can be difficult to make by conventional syntheses. The non-conventional syntheses can often be assigned to one of six categories [1]. Thus, sol-gel processing involves either use of aqueous oxide colloids or hydrolysis of metal-organic compounds, usually alkoxide solutions. Publications on sol-gel have dominated the scientific literature on ceramic synthesis but these two techniques are applicable, almost exclusively, to oxide systems. Hydrothermal synthesis of ceramic powders has not attracted the attention, as measured by the output of publications, which has been afforded to sol-gel and it is also restricted to oxide systems. The remaining three

R. Freer (ed.), The Physics and Chemistry of Carbides; Nitrides and Borides, 3–11.
© 1990 *Kluwer Academic Publishers. Printed in the Netherlands.*

techniques, polymer pyrolysis, non-aqueous liquid phase reactions and gas phase reactions are appropriate for carbide, nitride and boride powders. This short review describes chemical preparative routes for selected carbide, nitride and boride powders with particular emphasis on recent developments in non-conventional syntheses.

2. BORIDE POWDERS

2.1. Use of Powder Reactants

Two of the three principal methods for production of titanium diboride involve powder reactants. The first method is carbothermic reduction of titanium dioxide and boron oxide at around 2273K while in the second conventional synthesis titanium dioxide is reduced by carbon at about 2273K in the presence of boron carbide. Both reactions have the same disadvantage, namely, considerable grinding of the titanium diboride product is required for particle size reduction.

2.2. Gas Phase Reactions

The third principal method for synthesis of titanium diboride involves hydrogen reduction of titanium tetrachloride and a boron halide at high-temperature, typically 1773K. Thus,

$$TiCl_4(g) + 2BCl_3(g) + 5H_2(g) \rightarrow TiB_2(s) + 10HCl(g) \qquad (1)$$

but the solid diboride product requires grinding for comminution.

2.3. Decomposition of Titanium (III) Borohydride

The synthesis of titanium (III) borohydride, $Ti(BH_4)_3$ is not new and was first achieved [2] by passing titanium tetrachloride vapour over lithium borohydride,

$$2TiCl_4 + 8LiBH_4 \rightarrow 2Ti(BH_4)_3 + 8LiCl + B_2H_6 + H_2 \qquad (2)$$

Later work [3] showed that $Ti(BH_4)_3$ could be prepared by bubbling diborane, B_2H_6, through a titanium butoxide solution in tetrahydrofuran. Recent studies [4] have shown that this solid borohydride decomposes at 413K when dissolved in xylene,

$$2Ti(BH_4)_3 \rightarrow 2TiB_2 + B_2H_6 + 9H_2 \qquad (3)$$

The resulting TiB_2 powder was agglomerated, of high chemical purity with a particle size 0.1-0.2 μm and had a nitrogen surface area of 42 $m^2\ g^{-1}$. The low temperature decomposition is an advantage in this synthesis as is the availability of a soluble ceramic precursor which had coating applications [4].

3. NITRIDE POWDERS

3.1. Use of Powder Reactants

Many methods have been used for production of hexagonal boron nitride powders on the laboratory scale and for manufacture [5]. Thus, reaction of ammonia with boron oxide,

$$B_2O_3 + 2NH_3 \rightarrow 2BN + 3H_2O \quad (4)$$

takes place between 1073-1473K but an inert filler such as calcium phosphate is necessary to present a large surface area of boron oxide, which is molten at the reaction temperature, to the gas. Although reactants are cheap it is necessary to leach out the filler from the boron nitride product, an operation which enhances the process costs. Boron oxide is reduced by molten sodium in nitrogen between 1073-1273K,

$$B_2O_3 + 6Na + N_2 \rightarrow 2BN + 3Na_2O \quad (5)$$

after which Na_2O is distilled off whereas alkali metal cyanides react with boron oxide at 1073-1773K. Thus,

$$3B_2O_3 + 2NaCN \rightarrow 2BN + 2CO + Na_2B_4O_7 \quad (6)$$

and sodium tetraborate, $Na_2B_4O_7$ is removed by raising the temperature to between 2173-2473K. Boron nitride has also been prepared by reacting calcium cyanamide, $Ca(CN_2)$, with boron oxide between 1673-1973K but the product contains calcium oxide which is dissolved in an acid-wash.

Silicon nitride is manufactured by direct nitridation, with controlled bed-depth, of chemically pure silicon powder (less than 10 μm diameter) between 1473-1723K in an atmosphere of NH_3, N_2/H_2 or N_2 [1]. Silica is more readily available than silicon metal and another manufacturing route involves carbothermic reduction of silica in a mixture containing fine silica and carbon powders followed by nitridation at 1473-1723K. The carbothermic pathway involves formation and reaction of gaseous silicon monoxide [1],

$$3SiO_2(s) + 3C(s) \rightarrow 3SiO(s) + 3CO(g) \quad (7)$$

$$3SiO(s) \rightleftharpoons 3SiO(g) \quad (8)$$

$$3SiO(g) + 3C(s) + 2N_2(g) \rightarrow Si_3N_4(s) + 3CO(g) \quad (9)$$

Both methods produce α-Si_3N_4 lumps that are comminuted and graded, operations which introduce impurities into the ceramic. Excess carbon has to be used in the carbothermic route which leaves a carbon residue. The latter is removed by air oxidation which partially oxidises Si_3N_4 to SiO_2.

3.2. Gas Phase Reactions

Boron nitride has also been prepared in the high-temperature gas phase reaction between ammonia and boron trichloride at 1873-2173K,

$$4NH_3(g) + BCl_3(g) \rightarrow BN(s) + 3NH_4Cl(s) \quad (10)$$

while a similar process has been used to manufacture α-Si_3N_4 powder,

$$4NH_3(g) + 3SiCl_4(g) \rightarrow Si_3N_4(s) + 12HCl(g) \quad (11)$$

The reaction takes place in an electrically-heated furnace at approximately 1200K although the α-phase crystallises at higher temperature. This gas phase reaction results in chlorine retention in nitride powders which can have adverse effects on the mechanical properties of sintered components [1].

3.3. Powders by Polymer Pyrolysis

Recent developments in the preparation of boron nitride ceramics involve polymer synthesis and pyrolysis in the B-N system. A major theme in the published literature has been identification of liquid or soluble ceramic precursors which can be fabricated into coatings, fibres and composites, the latter by impregnation and which can also be pyrolysed, to boron nitride powders. High ceramic yields on pyrolysis are essential for coatings in order to reduce shrinkage and cracking whereas low temperature routes to nitride powders are desirable for improvements in sintering properties.

It is instructive to distinguish between three types [6] of boron-nitrogen compounds when discussing polymer pyrolysis routes to boron nitride powders. Amineboranes such as $(C_2H_5)_3N.BH_3$ and $(C_2H_5)_3N.BCl_3$ are monomeric species in which the nitrogen atom supplies both electrons in the B-N bond. Aminoboranes include $((C_2H_5)_2N)_2BH$ and $((C_2H_5)_2N)_3B$. The electron distribution in the B-N bond of amino-boranes has contributions from each atom. Aminoboranes belong to the borazene class of compounds and the name refers specifically to monomeric species whereas borazenes are cyclic analogues of cyclohexane; these cylic trimers are also called cycloborazanes. Borazines, also called borazoles, are planar cyclic trimers with B-N bond distances intermediate between single and double bond values; they are isoelectronic with benzene. Although reports on the use of boron-nitrogen compounds as precursors for boron nitride have been made since the 1950s, only recent examples are described in this article.

A crosslinked diborazene solid was produced [7] by reacting B,B'-dimethyl B"-chloro N-trimethyl borazene with hexamethyldisilazane while a polymeric oil was obtained from the reaction of B-methyl B',B"-dichloro N-trimethyl borazene with heptamethyldisilazane. The reaction products which were soluble and stable in methylene chloride showed an approximately 50% weight loss on pyrolysis to 1273K although residues were not fully characterised. Pyrazabole polymers [8] are another class of ceramic precursors for boron nitride ceramics. They have been

prepared by reacting pyrazole with methylene bromide in an autoclave at 473K after which the resulting methylene dipyrazole was condensed with triethylborane to a polymeric pyrazabole solid. The latter exhibited a 50% weight loss on pyrolysis to 1073K but, as with the preceding example [7], products were not fully characterised. A recent review of polymeric ceramic precursors including those in the boron-nitrogen system is given in reference [9].

3.4. Non-Aqueous Liquid Phase Reactions

Non-aqueous liquid phase reactions are particularly associated with the preparation of α-Si_3N_4 in a process which has been taken to the manufacturing stage by Ube Industries [10]. Silicon tetrachloride liquid reacts with ammonia (liquid or gas) to form a solid polymer, silicon diimide $[Si(NH)_2]_x$ in association with ammonium chloride triammoniate, $NH_4Cl.3NH_3$. The diimide decomposes on heating through a series of polymeric intermediates and crystallises to α-Si_3N_4 between 1473-1673K. For the manufacturing process, silicon tetrachloride dissolved in a cyclohexane-benzene mixture undergoes an interfacial reaction with liquid ammonia at 233K. $NH_4Cl.3NH_3$ is extracted into $NH_3(l)$ and silicon diimide is collected by filtration, washed with $NH_3(l)$ and then calcined. α-Si_3N_4 powders are submicrometre and unaggregated with an equiaxial particle morphology. Metallic impurities (iron, calcium and aluminium) are present at less than $0.005^{W}/o$ while oxygen, carbon and chlorine concentrations are typically $1.3^{W}/o$, $< 0.1^{W}/o$ and $0.005^{W}/o$ [1]. This liquid phase reaction is not restricted to Si_3N_4 and has been used for synthesis of titanium nitride, boron nitride and vanadium nitride. For the latter, cubic VN was produced in high yield (> 94%) at 1773K as spherical particles, 0.01-0.1 μm diameter. As noted for the boron-nitrogen system (Section 3.3) increased effort is being applied to development of polymers, either liquids or soluble solids which can then be converted to coatings or fibres as well as powders. In the silicon nitride system these polymers include polysilazanes and they are described elsewhere [11,12].

3.5. Sol-Gel Processing

Although sol-gel processing is associated with synthesis of oxide ceramics [1] it has been applied to α-Si_3N_4 powders [13]. Thus, aqueous sols derived from flame-hydrolysed silica were doped with carbon powder and either spray-dried to spherical powders or tray-dried to fragments. For spray-dried gel, 100% submicrometre α-Si_3N_4 was produced at 1673-1773K in a N_2/H_2 atmosphere when the $C:SiO_2$ mole ratio was more than 2:1 whereas β-Si_3N_4 formed at 1837K. Oven-dried gel fragments gave α-Si_3N_4 between 1673-1773K for mole ratios of 2:1 because their water content, lower than for spray-dried gel, did not cause oxidation of carbon. Compared with the conventional synthesis of α-Si_3N_4 by carbothermic reduction (Section 3.1) which involves mixing dry powder this sol-gel process produces an intimate mixture of carbon and silica components.

3.6. Laser-Driven and Plasma-Heated Gas Phase Reactions

Although gas phase reactions have been used for production of α-Si_3N_4 and BN, experimental approaches in recent years have concentrated on developing heating sources which encourage homogeneous nucleation from supersaturated vapours and formation of unaggregated submicrometre powders [1]. Laser- and plasma-heated gases fulfil these requirements. For laser-heated reactions [14] a 150 W CO_2 laser was used as the heat source for decomposition, in a cross-flow cell, of a SiH_4/NH_3 mixture diluted by an argon stream. These laser-driven reactions which are characterised by rapid heating and cooling rates (10^6 Ks^{-1}, 10^5 Ks^{-1}) as well as fast reaction times, 10^{-3} s, yielded both stoichiometric and non-stoichiometric Si_3N_4 powders with particle diameters around 17 nm. Radio-frequency (r.f.) thermal plasmas have also been used [15] for synthesis of 8 nm diameter AlN powders from NH_3 and aluminium vapour generated by evaporation of metal powder. Plasma temperatures reached 6000K and residence time in the flame was 1.4×10^2 s. Silane and ammonia have been reacted in an r.f. plasma [16]. Amorphous Si_3N_4 was obtained for NH_3/SiH_4 mole ratios greater than 5.5 whereas a mixture of α- and β-Si_3N_4 containing unreacted silicon resulted when this ratio was between 1.6-3.8.

4. CARBIDE POWDERS

4.1. Powders by Polymer Pyrolysis

Lewis bases (:L) react with decaborane, $B_{10}H_{14}$, to yield $L.B_{10}H_{12}.L$ with loss of one mole of hydrogen but linear polymers are obtained when the base has two electron-pair donor sites (:L~~L:). Recent work [17] has shown that powders in the boron-carbon system result from pyrolysis of polymers which had been synthesized by reaction of $B_{10}H_{14}$ with diphosphine bases. Thus, suspensions of $B_{10}H_{12}.2((C_6H_5)_2PCl)$ and $B_{10}H_{12}.2((C_6H_5)_2POH)$ in benzene react at ambient temperature under nitrogen in the presence of triethylamine to yield the polymeric solid, $-[B_{10}H_{12}.(C_6H_5)_2POP(C_6H_5)_2]-_x$. This polymer (molecular weight 27,000) was soluble in polar organic solvents. It could be pyrolysed in Ar at 1273K to an amorphous powder which contained excess carbon. The product yield was high, 83%, and crystalline B_4C formed after adding boron powder and heating the mixture to 1773K. Polymers are also produced by reacting $B_{10}H_{14}$ with diammines [18] and they have been pyrolysed to ceramic materials. Hence $[B_{10}H_{12}.H_2NCH_2CH_2NH_2]_x$ (molecular weight 10^5) decomposed at 1273K to give an amorphous powder (83% yield) corresponding to the formula $(B_4C)_1(BN)_1C_{0.19}$. Boron carbide was identified after heating the latter in Ar at 1773K. The polymer $[B_{10}H_{12}.N(CH_2CH_2)_3N]_x$ decomposes in NH_3 at 1273K to a solid (70% yield) with a B:N ratio equal to 0.99:1.0 while fibres drawn from a polymer solution in acetone/dimethylsulphoxide remained intact after pyrolysis in NH_3 at 1273K.

Polymer pyrolysis is particularly associated with production of silicon carbide fibres from polycarbosilanes [1,19]. The ability to manufacture SiC fibres from these precursors has been a major

driving force in the search for polymeric precursors in other non-oxide ceramic systems.

4.2. Non-Aqueous Liquid Phase Reactions

Reductive dechlorination has been used to synthesize precursors for SiC powders [20]. Thus $SiCl_4$ and CCl_4 reacted with sodium in heptane at 403K,

$$SiCl_4 + CCl_4 + 8Na \rightarrow \text{'SiC' precursor} + 8NaCl \qquad (12)$$

A black amorphous precursor was produced in high yield ($90^{w}/o$) and crystallised between 1723-2023K in 5% H_2/Ar to SiC with particle size 1-5 μm. A possible mechanism involved initial generation of nucleophilic species, for example Cl_3Si^- which formed a complex with another halide molecule so that the product contained mixed metal bonds and the process continued until all Cl was eliminated leaving the matrix that constituted the precursor. This synthetic technique was also applicable to TiB_2 and B_4C.

4.3. Laser-Driven and Plasma-Heated Gas Phase Reactions

Laser-driven reactions (Section 3.6) have been used to prepare SiC powders (particle size 23 nm) from SiH_4 and C_2H_4,

$$2SiH_4(g) + C_2H_4(g) \rightarrow 2SiC(s) + 6H_2(g) \qquad (13)$$

Industrial silicon carbide powders are made in the Acheson process [1] by carbothermic reduction of SiO_2 using resistance furnaces at temperatures greater than 2073K in an endothermic reaction which generates gaseous SiO. The commercial powder has a large grain size and is contaminated with oxygen. Laser-driven reactions have the potential for producing SiC powders with smaller grain size and lower oxygen concentrations. A direct current argon-plasma jet reactor [21] has been used to prepare β-SiC. Gaseous silicon monoxide generated by hydrogen reduction of SiO_2 was reacted with CH_4 above 10^4K to produce β-SiC. Homogeneous nucleation was encouraged by cooling rates greater than 10^6 Ks^{-1} and powder was in the size range 2-40 nm with a 97%. conversion efficiency.

5. CONCLUSIONS

Conventional synthetic techniques for non-oxide ceramic powders often involve powder mixtures. Non-conventional ceramic syntheses include polymer pyrolysis, non-aqueous liquid phase reactions, sol-gel processing and gas-phase reactions. These techniques which have been applied increasingly to oxide ceramics in the last two decades have considerable potential for synthetic routes to non-oxide powders. In addition they can result in powders with improved properties compared with those obtainable from conventional syntheses.

6. REFERENCES

1. Segal, D. (1989) Chemical Synthesis of Advanced Ceramic Materials, Cambridge University Press, Cambridge.

2. Hoekstra, H.R. and Katz, J.J. (1949) 'The preparation and properties of the group IV-B metal borohydrides', J. American Chemical Society 71, 2488-2492.

3. Reid, W.E., Bish, J.M. and Brenner, A. (1957) 'Electrodeposition of metals from organic solutions. III. Preparation and electrolysis of titanium and zirconium compounds in non-aqueous media', J. Electrochemical Society 104, 21-29.

4. Gallagher, M.K., Rhine, W.E. and Bowen, H.K. (1988) 'Low-temperature route to high-purity titanium, zirconium and hafnium diboride powders and films', in J.D. Mackenzie and D.R. Ulrich (eds.), Ultrastructure Processing of Advanced Ceramics,Wiley-Interscience, New York, pp. 901-906.

5. Ingles, T.A. and Popper, P. (1960) 'The preparation and properties of boron nitride', in P. Popper (ed.), Special Ceramics, Heywood, London, pp. 144-167.

6. Smith, H.D. (1978) 'Organic boron-nitrogen compounds', in R.E. Kirk and D.F. Othmer (eds.), Encyclopaedia of Chemical Technology, Wiley-Interscience, New York, 3rd edition, vol. 4, pp. 188-201.

7. Narula, C.K., Paine, R.T. and Schaeffer, R. (1986) 'Precursors to boron-nitrogen macromolecules and ceramics', Materials Research Society Symposium Proceedings 73, 383-388.

8. Maya, L. (1988) 'Aminoborane polymers as precursors of ceramic materials', Materials Research Society Symposium Proceedings 121, 455-460.

9. Pouskouleli, G. (1989) 'Metallorganic compounds as preceramic materials. I. Non-oxide ceramics', Ceramics International 15, 213-229.

10. Iwai, T., Kawahito. T. and Yamada, T. (1980) 'Process for producing metallic nitride powder', United States Patent 4,196,178.

11. Seyferth, D. and Wiseman, G.H. (1984) 'Silazane precursors to silicon nitride', in L.L. Hench and D.R. Ulrich (eds.), Ultrastructure Processing of Ceramics, Glasses and Composites, Wiley-Interscience, New York, pp. 265-271.

12. Wynne, K.J. and Rice, R.W. (1984) 'Ceramics via polymer pyrolysis', Annual Reviews of Materials Science 14, 297-334.

13. Szweda, A., Hendry, A. and Jack, K.H. (1981) 'The preparation of silicon nitride from silica by sol-gel processing', Proceedings of the British Ceramic Society 31, 107-118.

14. Cannon, W.R., Danforth, S.C., Haggerty, J.S. and Marra, R.A. (1982) 'Sinterable ceramic powders from laser-driven reactions. II. Powder characteristics and process variables', J. American Ceramic Society 65, 330-335.

15. Canteloup, J. and Mocellin, A. (1975) 'Synthesis of ultrafine nitrides and oxynitrides in an rf plasma', Proceedings of the British Ceramic Society 6, 209-221.

16. Vogt, G.J., Hollabaugh, C.M., Hull, D.E., Newkirk, L.R. and Petrovic, J.J. (1984) 'Novel rf plasma system for the synthesis of ultrafine ultrapure SiC and Si_3N_4', United States Department of Energy Report DE 84-003774, Los Alamos.

17. Seyferth, D., Rees, W.S., Haggerty, J.S. and Lightfoot, A. (1989) 'Preparation of boron-containing ceramic materials by pyrolysis of the decaborane (14)-derived $[B_{10}H_{12}Ph_2POPPh_2]_x$ polymer', Chemistry of Materials 1, 45-52.

18. Seyferth, D. and Smith-Rees, W. (1988) 'The synthesis of boron-containing ceramics by pyrolysis of polymeric Lewis base adducts of decaborane (14)', Materials Research Society Symposium Proceedings 121, 449-454.

19. Seyferth, D. (1988) 'Polycarbosilanes. An overview', in M. Zeldin, K.J. Wynne and H.R. Allcock (eds.), Inorganic and Organometallic Polymers, American Chemical Society, Washington, pp. 23-42.

20. Ritter, J.J. (1986) 'A low temperature chemical route to precursors of boride and carbide ceramic powders', Materials Research Society Symposium Proceedings 73, 367-372.

21. Kong, P.C and Pfender, E. (1987) 'Formation of ultrafine β-silicon carbide powder in an argon thermal plasma jet', Langmuir 3, 259-265.

SILICON NITRIDE : RELATIONS BETWEEN POWDER CHARACTERISTICS AND SINTERABILITY

F.CAMBIER, A.LERICHE*

CRIBC-Belgian Ceramic Research Centre.
4, Avenue Gouverneur Cornez, 7000 Mons, Belgium.

E.GILBART, R.J. BROOK and F.L.RILEY.**

School of Materials, Division of Ceramics,
THE UNIVERSITY of LEEDS.
Leeds LS2 9JT, U.K.

ABSTRACT.

This paper describes the methods of synthesis of silicon nitride powders used today in industry, and the characteristics of such raw materials available for production of ceramics. The compaction behaviour and the sinterability of the various categories of powder are compared and discussed, taking into account their chemical purity, and their particle size and morphology. The mechanical properties of materials densified either by conventional sintering or by hot-pressing are assessed in terms of microstructural features.

1. INTRODUCTION.

Silicon nitride ceramics can be produced in several ways using silicon or silicon nitride as raw materials.

The use of silicon implies its nitridation during heat treatment to produce silicon nitride. Such a product, termed RBSN (reaction bonded silicon nitride) allows consolidation of the powder compact, without shrinkage, but also without complete pore removal. Further densification can be obtained by adding sintering aids to the starting mixture and heating it at higher temperature : the resulting

---

* present address : Neoceram S.A., Z.I.Strepy, 7060 La Louvière, Belgium.
** present address : Max Planck Institut für Metallforschung, Stuttgart, W.Germany.

R. Freer (ed.), The Physics and Chemistry of Carbides; Nitrides and Borides, 13–28.
© 1990 *Kluwer Academic Publishers. Printed in the Netherlands.*

material is called SRBSN (post-sintered reaction bonded silicon nitride).

The sintering of silicon nitride powders (SSN) proceeds through a solution-reprecipitation mechanism at temperatures, and under atmospheres carefully chosen to avoid as much as possible silicon nitride evaporation (dissociation with the formation of nitrogen) or the production of SiO by its reaction with the oxide additive.

Densification can be facilitated by additional uniaxial or isostatic pressure on the compact during thermal treatment leading to hot-pressed (HPSN) and hipped (HIPSN) materials, respectively.

The interest in high performance, high reliability, silicon nitride ceramics has increased over recent years, leading to the development of new raw materials. It is also now well established that the ultimate strength of sintered bodies is strongly linked to the achievement of a maximum density, fine-grained, microstructure. Moreover, to enter the market, the production costs have to be kept at the lowest level by the use of simple and cheap processing stages.

Such targets can be attained in SSN materials, the fabrication of which necessitates thermally active powders of specific characteristics : an extremely fine size of primary crystal, suitable morphology, high purity level.

Over the last five years, a large number of new silicon nitride powders have been developed, which can be supplied for SSN fabrication.

The aim of this paper is to describe comparative tests carried out on many of these powders in order to assess their performance in terms of the attainment of a high temperature, high strength, silicon nitride ceramic, and to establish the criteria for the selection of such powders.

2. MATERIALS AND METHODS.

2.1. Raw materials.

Forty different powders were obtained from 18 Japanese, US or European producers. The list of the producers and of the grades tested (presently produced, or produced at some time during the last five years) is given in Table 1.

2.2. Experimental methods.

The powder chemical data shown in Tables 4 and 5, are those given by the suppliers. However, some impurities were successfully checked using a wet chemical method (AAS) on randomly chosen samples. Moreover, the oxygen content, as it was considered to be a major characteristic of the silicon nitride powder, was analysed for each grade [1].

The following physical characteristics were determined : specific surface area (SA) by the dynamic BET method; beta phase content (BETA) by X-ray diffraction, using the Gazzara and Messier technique [2]; particle size distribution by sedimentation (Sedigraph) after ultrasonic treatment (Da being the equivalent spherical diameter value which corresponds to 50 % of the cumulative curve), and agglomeration and size of the primary crystals by scanning (SEM) and transmission (TEM) electron microscopy (Dc being the mean primary crystal size).

Powder compaction behaviour was evaluated using Rho t (the tap density), and Rho 0 (the green density achieved in the standard mixture conditions, measured by Archimedes method with mercury).

To assess their sinterability, most of the powders were mixed with a standard additive, 10 wt % of equimolar yttria-magnesia. Some selected powders were also evaluated with other classical systems : 1.5 wt % alumina-5.5 wt % yttria and 13.2 wt % yttria-2.6 wt % neodymia.

Table 1 : List of the main producers of silicon nitride powders.

Producer	Grades	Country
A.E.D.	AE200, AE325	U.K
A.M.E. (Matroc)	CP85, DP1, HP2	U.K
Aremco	AREMCO	U.S.A.
Cerac	S1068	U.S.A
Cookson	1001, 1002, 1002F	U.K
Denka	SN-9F, SN9-FW, SN-82	Japan
Elektroschmelzwerk	ESK	W. Germany
Hüls Troisdorf	SNA1, SNA2, SNA3	W. Germany
GTE Sylvania	SN-502	U.S.A.
Kemanord	P95M, P95	Sweden
Kyoritsu	KN9-5000H	Japan
Nippon Kokan	G3S3A7, G4S4A8	Japan
Shin Etsu	KSN-10SP	Japan
Starck	H1, H2, LC1, LC10, LC12, S, S1, LC10N, LC12N, LC12S, LC12SX	W. Germany
Sumitomo	TC2	Japan
Toshiba	A	Japan
Tosoh	TS-7, TS10	Japan
UBE	SNE-10	Japan

Two sintering techniques were used : conventional sintering of isostatically pressed cylinders (16 mm diameter, 40 mm length, pressed at 170 MPa) and hot pressing. Conven-

tional sintering was carried out in a powder bed (50 % silicon nitride, 50 % boron nitride, plus the additives of the samples to be sintered), between 1650 and 1800 °C. Hot-pressing was carried out in BN-coated graphite dies at 1650 °C with an applied pressure of 10 MPa. Hot-pressing was continued until the linear shrinkage rate became less than 60 nm s^{-1}. Continuous recording of the sample dimensions, together with measurements the final sample size and density, gave a record of sample density (Rho) as a function of time. Densification rate (Rho°) and the second derivative (Rho°°) were calculated by computer.

After sintering, bulk densities (Rho T) were measured by the Archimedes method in water.

The sintered bars were cut and polished to make 30 x 4 x 3 mm bars for mechanical tests. Those tests provided measurements of the Young modulus (E : natural vibration method - Grindosonic), bend strength (Sigma F by 3 point loading with a span of 15 mm and a load rate of 100 micron min^{-1}) and critical stress intensity factor (K_{1c} by single edge notched beam).

Densified materials were also examined by SEM after chemical etching to reveal their microstructure, and to determine the grain aspect ratio [3].

3. SYNTHESIS METHODS FOR SILICON NITRIDE POWDERS.

Four different routes, starting from three different precursors (silica, silicon and silicon halides) are used on the industrial scale for the production of commercial silicon nitride powders (Table 2).

Table 2 : Synthesis routes for silicon nitride.

$3\ Si + 2\ N_2 \rightarrow Si_3N_4$
Reaction 1 "Nitridation of silicon "
$3\ SiO_2 + 6\ C + 2\ N_2 \rightarrow Si_3N_4 + 6\ CO$
Reaction 2 "Carbothermal reduction of silica"
$3\ SiCl_4 + 16\ NH_3 \rightarrow Si_3N_4 + 12\ NH_4Cl$
Reaction 3 "Vapor phase reaction"
$SiCl_4 + 6\ NH_3 \rightarrow Si(NH)_2 + 4\ NH_4Cl$
$3\ Si(NH)_2 \rightarrow Si_3N_4 + 2\ NH_3$
Reaction 4 "Thermal decomposition of di-imides"

The nitridation of silicon is the most commonly used route. The nitridation of ultra pure silicon is quite impossible to complete due to the formation of protective nitride layer. Catalysts, mainly iron, are required during the thermal treatment carried out at temperatures below 1400 °C. Hard agglomerates form during the reaction that have to be ground to obtain the powder.

The carbothermal reduction of silica occurs in a nitrogen flow at temperatures ranging between 1400 and 1500 °C. One of the main characteristics of this route is the non-stoichiometry of the reactants by comparison with reaction 2 presented in Table 2, an excess of carbon always being used. Therefore, at temperatures close to or above 1500 °C, the competitive production of SiC can occur.

The two last methods (reactions 3 and 4) start from highly pure, but expensive, halides.

Table 3 shows the routes used for the production of the 40 different powders tested for this paper.

Table 3 : Silicon nitride powders classified by their synthesis route.

"Nitridation of silicon"
AE200, AE325, AREMCO, CP85, 1001, 1002, 1002F, DP1, ESK, 6393A7, 6494A8, H1, H2, HP2, KN9-5000H, KSN-10SP, LC1, LC10, LC10N, LC12, LC12N, LC12S, LC12SX, P95, P95M, S, S1, S1068, SNA1, SNA2, SNA3, SN9-F, SN9-FW, SN-82, TC2.
"Carbothermal reduction of silica"
A.
"Vapor phase reaction"
SN-502.
"Thermal decomposition of di-imides"
SNE-10, TS-7, TS-10.

Most of the commercial silicon nitride powders (35 of the 40 tested powders) are produced by nitridation of silicon. Because it is impossible to present, within the scope of this paper, all the data collected, the comparisons

given in the following use the most representative grades in order to illustrate the discussion.

4.CHARACTERISTICS OF THE POWDERS.

4.1 Chemical impurities.

Table 4 shows the most typical impurities for selected powders.

Table 4 : Chemical analysis of silicon nitride powders.

Grade	R	O_2	Si	C	Fe	Cl	Al	Ca
LC12		1.47	<0.1	0.17	0.06	-	0.02	0.05
LC12SX		1.98	0.1	0.08	0.003	0.001	0.001	0.001
SN-9F	1	2.0	<0.2	<0.20	0.19	-	0.23	0.15
SN-9FW		0.82	N.D.	0.22	0.03	-	0.15	0.13
63S3A7		2.0	<0.2	0.21	0.16	-	0.30	0.03
A	2	2.65	-	1.19	0.007	-	0.06	0.01
SN-502	3	1.0	<0.2	-	<0.05	<0.05	<0.01	0.001
TS-7	4	1.04	-	0.12	0.005	0.1	<0.001	<0.001
TS-10		1.7	-	0.06	<0.01	<0.03	<0.005	<0.005

(R : synthesis reaction, see Table 2 ; figures are in percent, Si is free silicon, N.D. : not determined.)

Direct nitridation of silicon involves the retention of other metals such as aluminium or calcium, alloyed in the reacting silicon. Carbon level is generally in the range 0.15-0.3 %. Iron, used as a catalyst in the nitridation reaction, is found at a relatively high level in some powders; unreacted silicon is detected in all the powders. It is clear that grades recently commercialised are much purer than the corresponding grades produced 2 or 3 years ago : for instance Hermann Starck (Germany) has recently introduced very pure LC12SX which replaces LC12; another example is Denka's SN-9FW for SN-9F (Japan). Such decrease of the metallic impurity content is obtained by using purer starting silicon as well as by washing the powder in acids. Very pure silicon nitride powder is therefore available but XPS analysis reveals the presence of surface fluorine species (in LC12SX for instance). Oxygen content is also

difficult to control in this synthesis route because of the post-milling of the hard agglomerates formed during the reaction at high temperature.

The A powder (synthesis reaction 2) is mainly characterised by the high levels of oxygen (2.65 %) and of carbon (0.90 %). XPS surface analysis shows that oxygen is linked as silica, one of the process reagents, and that part of carbon is as silicon carbide, probably due to competitive formation of this compound at temperatures close to or above 1500 °C.

The powders produced from silicon halides (reactions 3 and 4) are the purer ones when considering the metals content (excepted for the reaction 1 - LC12SX), but traces of chlorine are, however, found. For this series of powders, grades recently introduced (for instance TS10 for TS7), give also improved purity : lower carbon and chlorine levels.

4.2 Physical characteristics.

The physical characteristics of selected powders are given in Table 5, which shows powders with high surface area, small primary crystal size as well as low beta silicon nitride content (between 5 and 10 percent) are today largely available.

The compaction behaviour of the powders can be evaluated on the basis of the tap densities (Rho t) or of the green densities reached after uniaxial compression (Rho 0). Taking into account these two parameters, silicon nitride powders provided by the nitridation of silicon generally show a better behaviour than other series due to their wider size distribution (the tap density of LC12SX is an exception). SEM pictures (Figure 1) show that grains are usually irregular, as a result of the post-milling process.

Microscopic examination of the grains of SN-502 (Figure 2) reveals large-scale occurrence of whiskers, the presence of which can be probably attributed to growth through vapour transport. The presence of whiskers in this powder leads, as a consequence, to a very low tap density and to very bad compaction behaviour, which impeded the shaping of samples by uniaxial pressing under the standard conditions used in this study . Therefore, the sintering evaluation of this powder was carried out by hot-pressing only.

The powders formed by diimide decomposition as well as the A powder (silica carbothermal reduction) are more regularly shaped (Figures 3 and 4) but do not have high compacted densities, due to their narrow size distribution.

Figure 1 : SEM picture of LC12 powder.

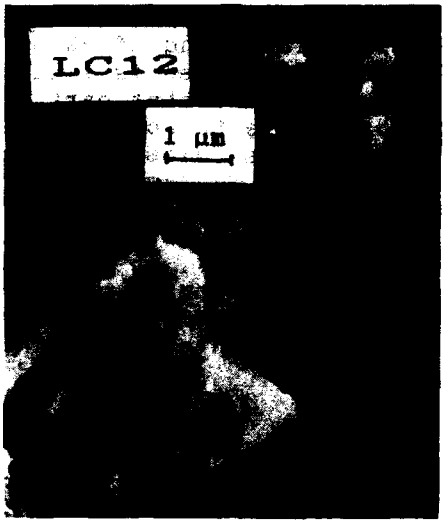

Figure 2 : SEM picture of A powder.

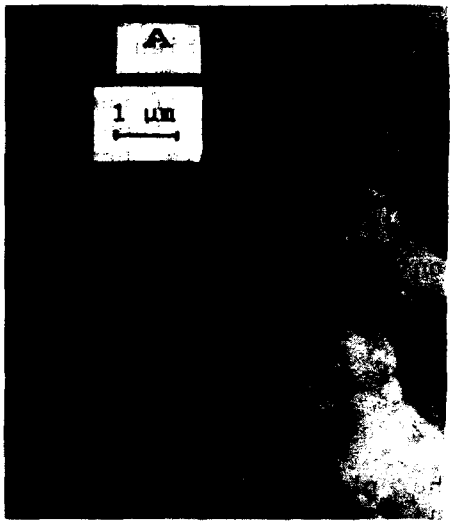

Figure 3 : SEM picture of SN-502 powder.

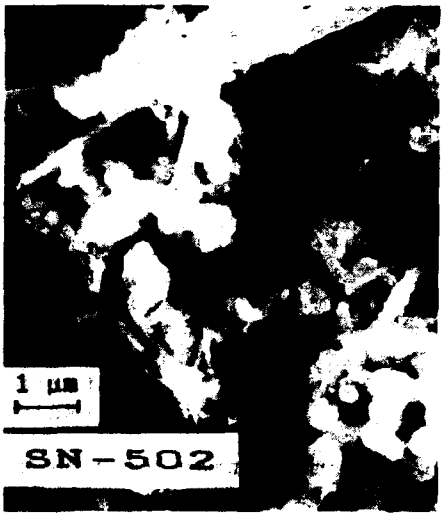

Figure 4 : SEM picture of TS7 powder.

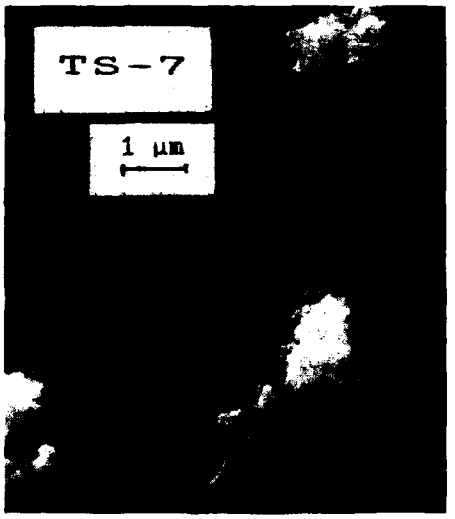

Table 5 : Physical characteristics of some silicon nitride powders.

Grade	R	SA	Da	Dc	BETA	Rho t	Rho 0	Whisk.
LC10		11.0	0.65	0.2	6	0.67	1.74	a few
LC12SX	1	22	0.4	0.15	8	0.45	2.03	none
1001		7.3	0.45	0.2	8	0.66	1.68	a few
SN-9FW		12	0.5	0.1	6.5	1.00	1.95	none
A	2	8.7	1.1	0.3	1	0.52	1.55	none
SN-502	3	4.9	1.6	0.5 4-10(*)	12	0.42	-	many
SNE-10	4	14.8	0.3	0.1	2	0.74	1.63	a few
TS-10		22.2	0.38	0.1	5	0.74	1.57	none

(R : synthesis reaction, see Table 2; Whisk. : occurrence of whiskers, (*) : length of whiskers)

4.3 Densification and mechanical properties.

Figure 5 shows densification levels (Rho T) as a function of specific surface area for the starting powders for pressureless sinterings carried out at 1650 °C with the three systems of additives. Under such experimental conditions, the maximum bulk densities reached after 2 hours are in the range 90-95 % of the theoretical density for most of powders of specific surface area higher than 7.5 $m^2 g^{-1}$. Such a figure seems to be the minimum acceptable value for raw materials to be used for conventional sintering.

Figure 6 shows the strengths of materials prepared by powder compaction followed by conventional sintering under different nitrogen over-pressure (0.1 MPa at 1700 °C, 0.2 and 1 MPa at 1750 °C), and by uniaxial hot-pressing at 10 MPa and 1650 °C.

The data presented in Figure 5 show that the heat treatment conditions used in these experiments do not allow high density to be reached, and therefore inhibit the attainment of good mechanical performance (see circles on Figure 6). However, such a procedure provides a good comparitive tool for assessing the sinterability of the powders. In these tests, the best behaviour is that of SNE-10 and other ex-diimide powders, which reach about 90 % of the theoretical density. The strengths can be satisfactorily correlated with the bulk densities (Figure 6), which means

that the most fully densified materials (around 2.8 to 2.9 Mg m^{-3}) : LC12 series, SN-9F, and A, powders coming from the diimide process, should be those of highest technological interest.

Figure 5 : Bulk densities of conventionally sintered compacts for the 3 systems of additives.

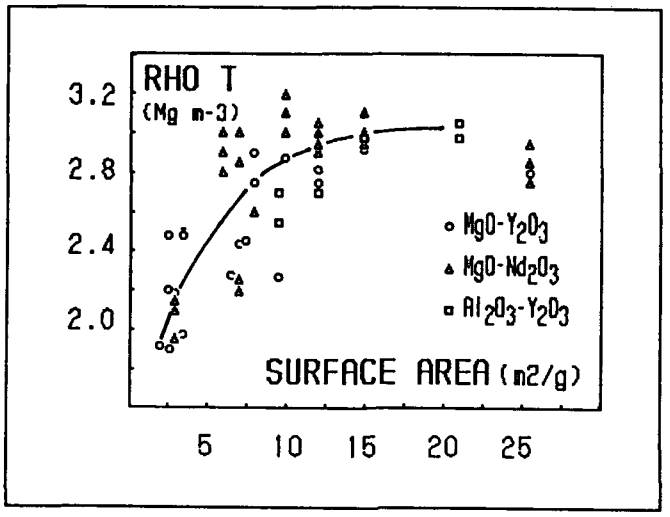

Some thermal treatments have been carried out at higher temperature and under pressure (0.2 and 1.0 MPa) to obtain the highest density possible. The results of the mechanical characterisation (bend strength) are also presented in Figure 6, together with corresponding data for hot-pressing experiments.

Sintering under 0.2 MPa allows the best raw materials (LC12SX, TS10) to reach a bulk density higher than 3.0 Mg m^{-3} which corresponds to strengths in the 475 MPa region, and toughnesses between 5.4 and 6.0 MPa $m^{½}$.

When processed under 1.0 MPa, bulk densities close to theoretical are achieved for SNE-10 and TS7, with sigma F close to or higher than 650 MPa, and K_{1c} higher than 6.0 MPa $m^{½}$.

It is, however, found that unexpectedly low values are obtained for some high bulk density compacts. One example is the hot pressed A powder, which strength reaches only 310 MPa, and K_{Ic} 3.6 MPa $m^{½}$, for a bulk density of 3.20 Mg m^{-3}. In this case, the alpha-Si_3N_4 to beta-Si_3N_4 crystallographic transformation did not occur to a large extent (only 14 % Si_3N_4) during the thermal treatment leading to the equiaxed microstructure shown in the SEM pic-

ture of Figure 7 which has to be compared with the elongated crosslinked grains of sintered LC12 (Figure 8). Other examples of a low bend strength is SNE-10 which sigma F is 473 MPa for a beta phase level of 53 %. An additional cause of decreasing strength is grain growth of beta-Si_3N_4 occurring in wide particle size distribution powders such as AE325 or AE200.

Figure 6 : Strength resistance of sintered compacts as a function of bulk density.

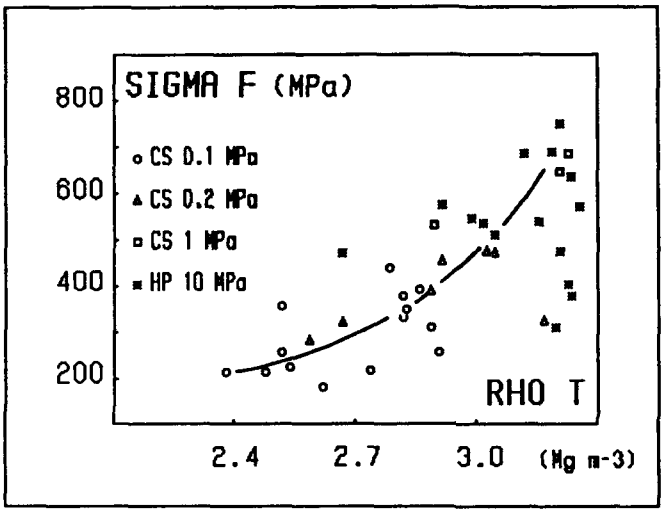

4.4 Densification by hot-pressing.

The hot-pressing curves of density as a function of log (time) provide an easy comparison of the powders at the initial stages of sintering. As in pressureless sintering, the starting density is dependent on the green density of the compact, and is increased by a wider particle size distribution in the starting powder, and the amount of sintering during heating and on application of pressure. Thereafter, densification will depend mainly on the inverse of the particle size, but if the particle size range is wide, coarsening of the particles may occur, leading to a loss of sinterability as densification proceeds.

Figure 7 : Microstructure of densified silicon nitride using A as starting powder.

Figure 8 : Microstructure of densified silicon nitride using LC12 as starting powder

The hot-pressing technique gives access to Gamma *, which is a figure of merit [4], related to the rate of grain growth, G°, and to the densification rate, Rho° :

$$\text{Gamma } * = \frac{G^\circ}{G} \times \frac{\text{Rho}}{\text{Rho}^\circ}$$

On the basis that a good structural material has a high density and a small grain size, a small value of Gamma * is beneficial. The major assumption made in the calculation of Gamma * is that the densification rate depends upon the grain size such that [5] :

$$\text{Rho}^\circ = k\, G^{-m}$$

where k and m are constants, m being characteristic of the densification mechanism. From this equation the value of Gamma * can be obtained :

$$\text{Gamma } * = -\frac{1}{m} \frac{\text{Rho}\ \text{Rho}^{\circ\circ}}{\text{Rho}^{\circ 2}}$$

Gamma * can be simply evaluated from the continuous record of the sample density as a function of time during hot-pressing, followed by computer calculation of Rho° and Rho°° for each value of Rho. Although the value of m is dependent on the mechanism of densification, change of mechanisms for powders processed under identical conditions are less likely to occur than changes in rate for a given mechanism.

A typical representation of Rho° and Gamma * as a function of density is given in Figure 9 for powder 1002F. It can be seen the densification rate (expressed in Mg m^{-3} s^{-1}) decreases with density, whereas Gamma * keeps almost constant up to a density of 2.6 Mg m^{-3} then dramatically increases for higher densities. Some data of Gamma * measured at three densities are also presented in Table 6, which confirms the better behaviour of the more recently commercialised powders (for instance LC12SX or TS10). Indeed value of the figure of merit is clearly smaller and does not increase with density.

Figure 9 : Rho° and Gamma *as a function of Rho for 1002F powder.

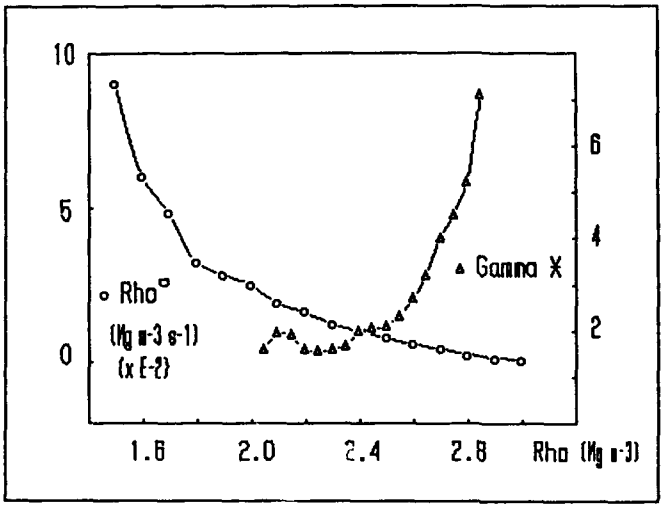

Table 6 : Densification of silicon nitride powders by hot pressing : Gamma * (G*) for various densities.

Grade	R	G* (2.1)	G* (2.4)	G* (2.7)
LC10		>10	7.0	9.2
LC12		-	6.2	7.0
LC12SX		2.0	2.1	2.2
1002F		1.9	2.0	4.0
SN-9F		11	6.0	4.9
SN-9FW		1.5	2.0	3.4
A	2	-	3.5	4.4
TS-7	4	6.3	6.6	3.5
TS-10		1.0	1.5	2.6

(R : synthesis reaction, see Table 2; figures under brackets correspond to bulk densities.)

5. CONCLUSION.

The ideal silicon nitride powder for the fabrication of high density components by the SSN process is the powder which will provide a high green density (to reduce the firing shrinkage and improve the precision of shape of the product), reach close to theoretical density (to eliminate porosity and improve the mechanical properties), in a reasonable time, with a controlled microstructure (complicated in the case of silicon nitride by the phase change from alpha to beta-Si_3N_4 and corresponding morphological changes), but avoiding abnormal grain growth and trapped porosity. This must be achieved without the presence of a large amount of low viscosity liquid, in addition to that intended as a result of the deliberate dopants. Oxide or cation impurities in the silicon nitride may increase the volume and decrease the viscosity of the liquid phase, promoting densification but degrading high temperature properties, further complicated by the presence of halogens or carbon from the synthesis or processing procedures used during the manufacture. From consideration of the data presented in this paper (though without the evaluation of high temperature behaviour) some recently introduced grades of silicon nitride powder show promise.

ACKNOWLEDGMENTS

The authors wish to acknowledge the support of the Commission of European Communities (DG XII). Many of the results presented in this paper have been obtained under CEC Contracts SUT 117 B, SUT 121 UK and Euram MA1E-0033-C (GDF). The authors wish also to acknowledge AERE Harwell for the measurements of oxygen contents.

REFERENCES.

1. Cambier, F., Leriche A. and Vandeneede V. (1986) : 'Powder characterisation and optimisation of fabrication and processing for sintered silicon nitride (Part 1)', Ceramic Material and Components for Engines, Ed. by W. Bunk and H. Hausner, Verlag DKG, 55-62.
2. Gazzara, C.P. and Messier, D.R. (1977) : 'Determination of phase content of Si_3N_4 by X-ray diffraction analysis', Am. Ceram. Soc. Bull., 56, 9.

3. Wötting, G. and Ziegler G. (1983) :'Microstructural development, microstructural characterization and relation to mechanical properties of dense Si_3N_4', Science of Ceramics, 12, 361-370.
4. Brook, R.J., Gilbart, E., Shaw, N.J. and Eisele, U. (1985) :'Solid solution additives and the sintering of ceramics', Powder Met. 28, 105-107.
5. Cannon, W.R. and Langdon, T.G. (1983) :'Creep of ceramics', J. Mat. Sci. 18, 1-50.

KINETICS OF THE NITRIDATION OF SILICON

Bjørn Myhre* and Ketil Motzfeldt
Institute of Inorganic Chemistry
The Technical University of Norway
N-7034 Trondheim, Norway

ABSTRACT. The nitridation of silicon powder (32-45μm) has been studied by thermogravimetry in the temperature range 1300 to 1340°C, using static pressures of pure nitrogen ranging from 25 to 200 torr (0.033 to 0.267 bar). The TG curves generally show a sigmoidal shape. It is a characteristic feature of the reaction that it comes to an almost complete stop when only a fraction of the original Si has reacted. The reaction is markedly dependent on the N_2 pressure; higher pressure gives higher initial rate but a lower final extent of reaction. SEM investigations show that the silicon surface is covered with nitride crystals already after a short time of reaction, and subsequent nitridation takes place on the outside of this initial nitride layer. The observations have been interpreted in terms of a model with nucleation and branching growth, coupled with a self-blocking channel model. The four parameters of the model show characteristic dependences on the nitrogen pressure. The temperature dependences are less clear because of the short temperature span used.

1. Introduction

Silicon nitride powders for ceramic applications may be produced by a number of methods, including both gas phase and solution reactions, see, e. g., Schwier [1] and Segal [2]. The direct reaction between silicon and nitrogen, however, appears as one of the simplest and most economical routes. This reaction is also of interest when silicon nitride articles are produced by first forming the article from silicon powder by pressing or slip casting, followed by treatment in nitrogen at a suitable temperature.

This communication does not, however, deal directly with the production of silicon nitride powder or ceramic articles. It is intended as a more fundamental study of the kinetics of the direct reaction, but silicon was used in the form of a fine powder in order to retain some similarity to processes of ceramic interest.

---

* Present address: Elkem Materials, P O Box 126, Vaagsbygd, N-4602 Kristiansand S.

R. Freer (ed.), The Physics and Chemistry of Carbides; Nitrides and Borides, 29–44.
© 1990 *Kluwer Academic Publishers. Printed in the Netherlands.*

2. Materials

The powder was prepared from electronic-grade silicon stock (Ventron-Alfa Products, Karlsruhe, Germany) by crushing in an iron mortar, followed by ball-milling in a polyethylene container using iron balls. Subsequently the silicon was wet-sieved using stainless steel sieves to a size fraction of 32-45 μm. The fraction was then washed in 3M HCl for 1 day, 1M HCl for 3 days and finaily in distilled water. Spectrometric analysis of the dried powder showed 15 ppm Fe as the only detectable contaminant. Assuming spherical particles, the specific surface area was calculated to 6.70×10^{-2} m^2/g.

In most of the thermogravimetric runs, this powder was used with addition of 1.7 wt% α-Si_3N_4 (H.C. Starck, Berlin, Germany) with particle size <5 μm, the two powders thoroughly mixed by shaking in a Spex mixer/mill.

Silicon discs, 0.5 mm thick, used for support of the powder, were cut from 25 mm dia. solid stock by means of a low-speed diamond saw and subjected to the same cleaning procedure as outlined above for the powder.

The nitrogen contained 99.99 % N_2 according to the manufacturer (Hydro Industrigasser, Herøya, Norway), the main impurity being argon. The gas was passed through a column of anhydrous magnesium perchlorate and then through copper turnings at 450°C to remove traces of water vapour and oxygen.

3. Equipment

The nitridation runs were carried out in a thermobalance, consisting essentially of a vertical tube furnace with an electronic balance mounted above it. The furnace is heated by a spiral-wound heating element (Type REH-B from Kanthal AB, Hallstahammar, Sweden). Inside this is a 60 mm I.D. mullite-type refractory tube (Pythagoras Brand, Haldenwanger, Berlin, Germany). This type of tube has been found to be vacuum tight to well above the temperatures used in the present investigation. It was found, however, that the use of a new tube resulted in atypical nitridation, possibly due to small amounts of volatile alkali species. The problem was solved by degassing the tube in a good vacuum at operation temperature for 24 h before nitridation runs.

Inside the tube, below and above the suspended sample, horizontal discs serve as radiation shields to reduce the heat losses towards the ends. The discs were made from alumina, except the first four discs directly above the sample which were made from sintered silicon powder in order to secure a low oxygen potential. Apart from acting as getters for oxygen, these discs will also become partially nitrided and thus may saturate the reaction atmosphere with respect to volatile Si-N species.

The balance is an old-fashioned knife-edge analytical balance, converted to electronic weighing by the addition of a position transducer (differential transformer) and force element (magnet bar in solenoid) acting in conjunction with an electronic unit (manufactured by SINTEF, Trondheim). The sensitivity of the balance (0.05 mg) and the drift rate (< 0.5 mg/24h) were better than required for the present work. The balance

proper is placed inside a glass bell jar, and the set-up is made vacuum tight by brass flanges with rubber gaskets. The system is evacuated by means of a 75 mm dia. oil diffusion pump and a rotary fore pump.

The equipment is in fact the same as used by Blegen [3] in her studies of silicon nitride fifteen years ago, although with another furnace and some improvements in signal conditioning and vacuum monitoring.

4. Procedure

The silicon powder, about 0.6 to 0.7 g for each run, was placed in a flat bed on a silicon disc resting in the bottom of a shallow alumina crucible with protruding "ears" for suspension. Fig. 1 shows the position of the sample in the furnace. Next the thermobalance was evacuated to about 10^{-5} mbar and heated at a rate of 600°C/h to reaction temperature (1300-1340°C) with continuous pumping. This heating in vacuum was done in order to remove the native silica film by the reaction $Si + SiO_2 = 2SiO(g)$, as evidenced by a weight loss in the temperature range 950 to 1100°C totaling about 0.1% of the weight of the powder charge. Approaching 1200°C a slow weight decrease was again observed, this time attributed to the slow evaporation of Si (vapour pressure 1 x 10^{-5} mbar at 1500K). After reaching the desired reaction temperature, this was held constant for 1/2 h before the system was closed and nitrogen admitted to the desired reaction pressure. This pressure was held constant within ± 1 torr during any one run, admitting more N_2 when necessary. Due to the relatively large volume of the gas-filled space (≈ 30 l), the pressure decreased only slowly as a result of the reaction.

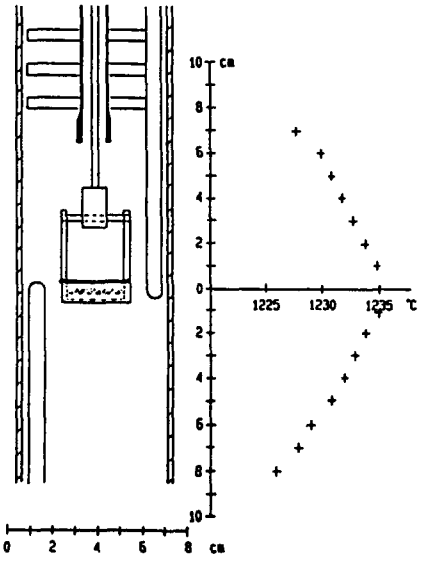

Fig. 1. Sample location and temperature distribution for the reaction zone

After reaction, the powder and silicon disc were removed form the crucible. The powder was subjected to X-ray diffraction analysis, using the method of Gazzarra and Messier [4] to determine the relative amounts of α- and β-Si_3N_4. Milling of the powder prior to X-ray diffraction was avoided in order to avoid exposed silicon surfaces. Selected samples of powders and of discs were also subjected to examination by SEM.

5. Results

A total of 43 thermogravimetric runs were performed on silicon powder with α-Si_3N_4 addition. A smaller number of runs were made with addition of β-Si_3N_4 and with no addition, but for brevity only the runs with α- addition will be discussed here. A few of the curves for various pressures at the same temperature are shown in Fig. 2 and 3, while curves for several temperatures at a common pressure are given in Fig. 4. It is immediately apparent that all of the curves have a more or less pronounced sigmoidal shape. It is interesting to note that while Atkinson et al. [5] interpreted their thermogravimetric curves in terms of a linear or monotonically decreasing rate, their actual experimental points indicate sigmoid behaviour for several of their runs.

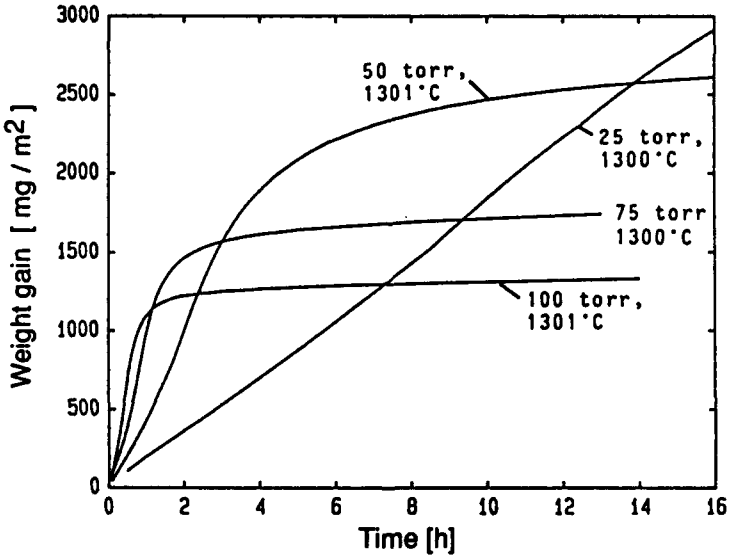

Fig. 2. Reaction between silicon powder with α-Si_3N_4 and nitrogen. Dependence of kinetics on N_2-pressure (25-100 torr).

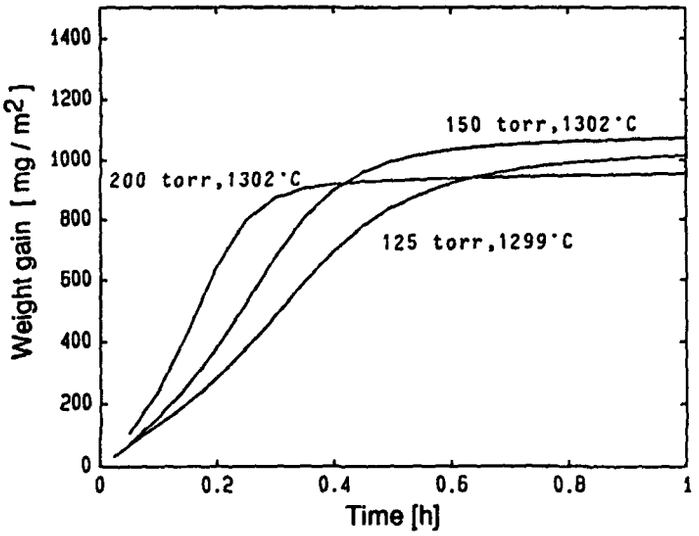

Fig. 3. Reaction between silicon powder with α-Si_3N_4 and nitrogen. Dependence of kinetics on N_2-pressure (125-200 torr).

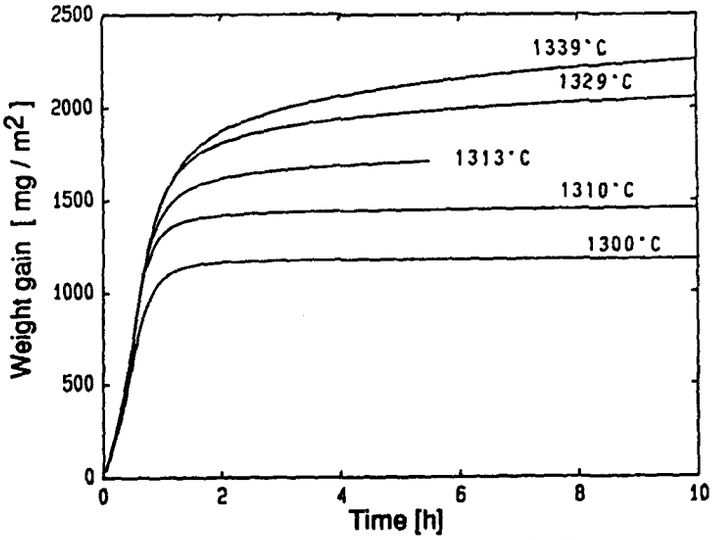

Fig. 4. Reaction between silicon powder with α-Si_3N_4 and nitrogen. Dependence of kinetics on temperature at 100 torr N_2-pressure.

Another feature of the curves is that the nitridation comes to an almost complete stop when only a fraction of the original silicon has reacted. For further elucidation it is noted that the complete nitridation of silicon corresponds to a weight increase of approximately 66.7 %, or 667 mg/g. In the present case we calculated a surface area of 0.067 m^2/g, from which it is found that approximately 100 mg/m^2 corresponds to an extent of reaction of 1%. Thus it is seen that the curves in Fig.s 2 and 3 show final extents of reaction in the range between 9 and 30 percent.

The curves furthermore show that while the initial rate increases with increasing nitrogen pressure, the final extent of reaction decreases. All of this is in general accord with previous observations of Atkinson et al. [5,6].

The X-ray investigations showed that α-Si_3N_4 was the dominating phase formed in all cases with α-addition to the Si powder, and also that the α/β ratio increased with increasing nitrogen pressure, see Fig. 5. In Fig. 6 are plotted the results of a series of interrupted nitridations, from which it appears that the initial nitridation yields the α-phase only, while the β-phase starts to appear when the degree of conversion has reached 2 to 3 percent.

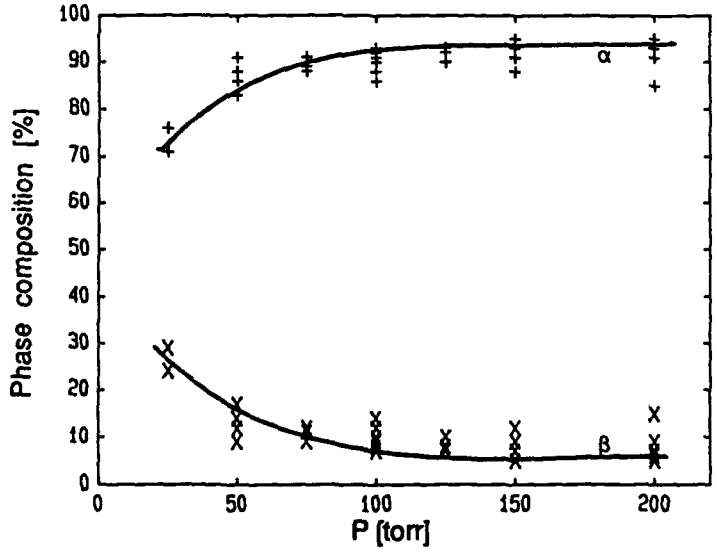

Fig. 5. Dependence of phase composition of nitrided product on N_2-pressure.

Scanning electron micrographs of the powders after the interrupted nitridations shown in Fig. 6 reveal that the silicon surfaces are covered with a layer of nitride crystals already after 0.25 h of nitridation (1304°C, 75 torr N_2 pressure). Further nitridation appears to take place not by any marked increase in size of these initial crystals, but rather by new crystals growing on top of those already formed.

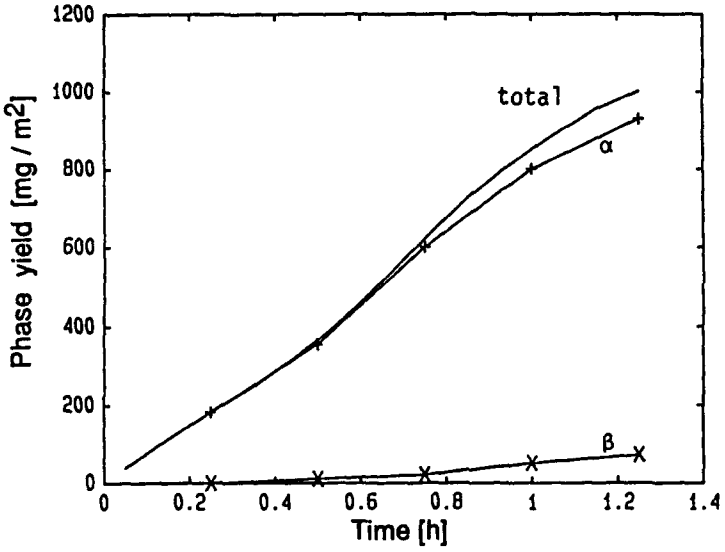

Fig 6. Nitridation of silicon powder with α-Si_3N_4. Development of the nitride phases. 1304°C, 75 torr N_2-pressure.

Micrographs of polished sections reveal that as the nitride grows, porosity is developed in the silicon substrate underneath. Little or no nitride appears inside the pores. Altogether these SEM investigations strongly suggest that the nitride grows not by reaction of N_2 molecules with the solid silicon surface, but rather by way of Si(g) which evaporates from the silicon surface and diffuses part-way through the pores in the nitride layer already formed, before it reacts with the nitrogen. Once again this is in general accord with the mechanism proposed by Atkinson et al. [6], but a quantitative kinetic model has been missing.

6. Development of a kinetic model

The general sigmoidal curve may be divided in three main parts as shown in Fig. 7. The initial part, region A, represents a short period of apparently constant rate of reaction. Next follows a period of increasing rate, region B, before the rate decreases and falls to nearly zero, region C. Our task is, not only to develop a mathematical model which may describe such a curve, but one that is also based on physically plausible assumptions.

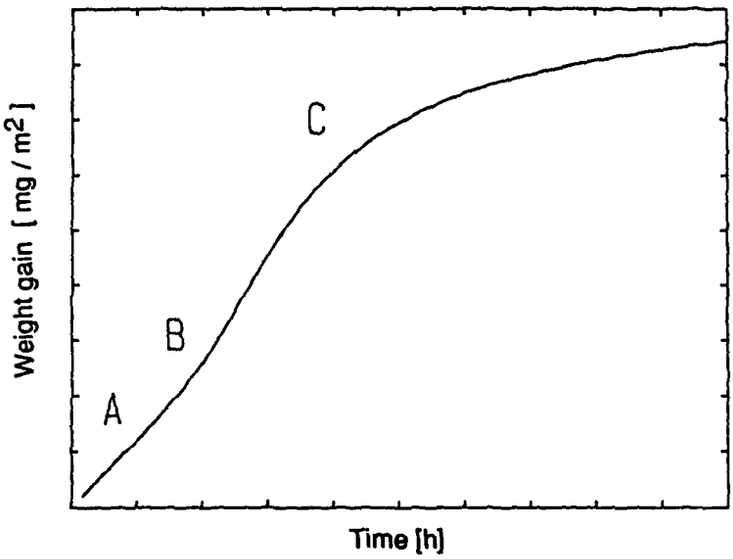

Fig. 7. Schematic representation of the thermogravimetric curves obtained when nitriding silicon powder.

Region A. As regards the first, linear part, no model was found into which this could be fitted without difficulty. Thus this part, which is of short duration in the actual experiments, is treated separately. With α denoting the extent of reaction and t time, region A is described by the simple equation

$$\alpha = kt$$

where k is a rate constant which in our case will have the dimension mg $m^{-2}h^{-1}$.

Region B is a period of increasing rate. We have chosen to interpret it in terms of chain nucleation, or "branching", a concept first introduced by Garner and Hailes [7], and further developed by Harrison [8]. The treatment is somewhat complex, however, and for reasons of space we will be content by giving only the final result of Harrison´s treatment, slightly rewritten for our purpose:

$$\alpha = \left(\frac{Bk_1}{k_2}\right)^3 \exp(k_2 t)$$

B: is a constant independent of temperature and pressure.

k_1: is the rate constant for linear growth of nuclei, and

k_2: is the rate constant for "branching".

The exponent 3 of the term in parenthesis presupposes that the nuclei grow in three dimensions, as is actually observed by the nearly equi-axed crystallites in the micrographs. In order to elucidate somewhat the underlying assumptions, we also give the meaning of the constant B.

$$B = \sqrt[3]{A_c K_g N_0 (3!)}$$

Here

A_c: is a factor to convert α from volume of product to mg/m^2

K_g: is a shape factor for crystallites.

N_0: is the number of initial nucleation sites, essentially an unknown number, but a constant for a given powder sample.

We will find it convenient to rewrite Eq. (2) so as to give the time explicitly:

$$t = \frac{1}{k_2} \ln\left(\alpha \left(\frac{k_2}{B k_1}\right)^3\right)$$

Region C represents a period of diminishing rate. We assume that the decreasing rate is caused by gradual blocking of the pores in the nitride layer, so that the silicon vapour finally cannot get through and react with the nitrogen. If the reaction rate is linearly dependent on the remaining pore area, and there exist a limiting or final extent of reaction α_f where the rate has fallen to zero, the following relation may be proposed:

$$\frac{d(\alpha/\alpha_f)}{dt} = k_a \left(1 - \alpha/\alpha_f\right)$$

where α is the extent of reaction in mg/m^2, α_f is the final extent of reaction in mg/m^2 and k_a is a constant giving the relative rate at which the pores are closing.

Integration with $\alpha=0$ for $t=0$ yields:

$$\ln\left(1 - \frac{\alpha}{\alpha_f}\right) = -k_a t$$

This is equivalent to the self-blocking channel model of Evans [9], which was used by Atkinson et al. [6].

Assuming that the two models describes consecutive events, the resultant thermogravimetric curve (regions B and C) should be described by the combination of Eq. (2a) and (3a), that is:

$$t = \frac{1}{k_2} \ln\left(\alpha \left(\frac{k_2}{B k_1}\right)^3\right) - \frac{1}{k_a} \ln\left(1 - \frac{\alpha}{\alpha_f}\right)$$

7. Comparison with the experiments

The slope of the initial, linear part of each thermogravimetric curve gives directly the value of the linear rate constant k of Eq. (1). In Fig. 8 the values of k for all runs with added α-phase, regardless of the reaction temperature, are plotted in dependence of the nitrogen pressure on a log-log scale. It is seen that this initial rate is found proportional to $P^{1.2}$, where P designates the nitrogen pressure. Within the limits of error this may be considered equivalent to the first power of the nitrogen pressure. This is taken to indicate that the rate determinings step in this very first part of the nitridation is the adsorption of N_2 molecules on the silicon surface.

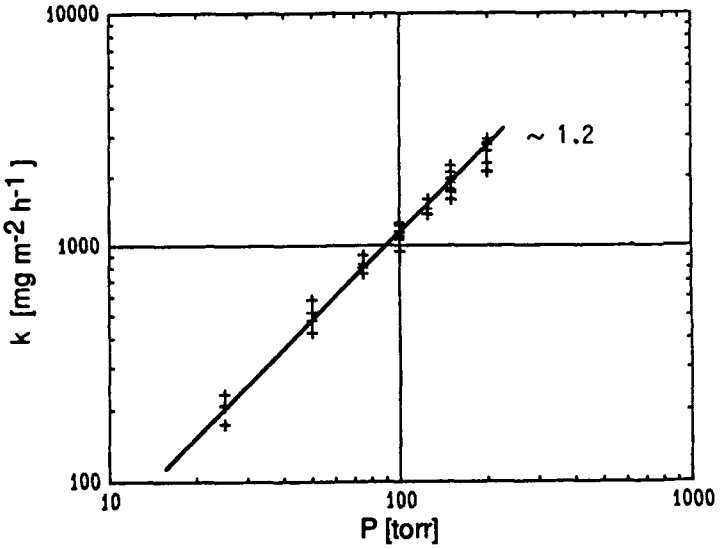

Fig. 8. Pressure dependence of the k value obtained for silicon powder with α-Si_3N_4 additions. The values for all temperatures are plotted. This explains the scatter, and gives an impression of the temperature dependence (≈1300 to ≈1340°C). Number refers to slope.

Next follows the fitting of Eq. (4) to the experimental curves. Parameters to be adjusted or evaluated are Bk_1, k_2, k_a, and α_f, the physical significance of which have been given above. The fit was performed using "Eureka - The Solver" on an Apple Macintosh SE computer. Without restraints on the parameters, a number of solutions may be found. Thus the initial values of the computer program were modified until the following criteria were met: The estimated parameters are all positive, they should have a reasonable temperature

dependence, they should have a reasonable pressure dependence, and the program should converge.

The model fitting was performed on the sigmoidal part of the curves with $\alpha = 0$ for $t = 0$, thus disregarding the brief linear part (region A). Fig. 9 shows one example of the calculated curve in comparison with the experimental one. Fig.s 10, 11, 12 and 13 show the resultant values of the four parameters found by model fitting of all experiments regardless of reaction temperature, plotted as functions of the nitrogen pressure on log-log scales.

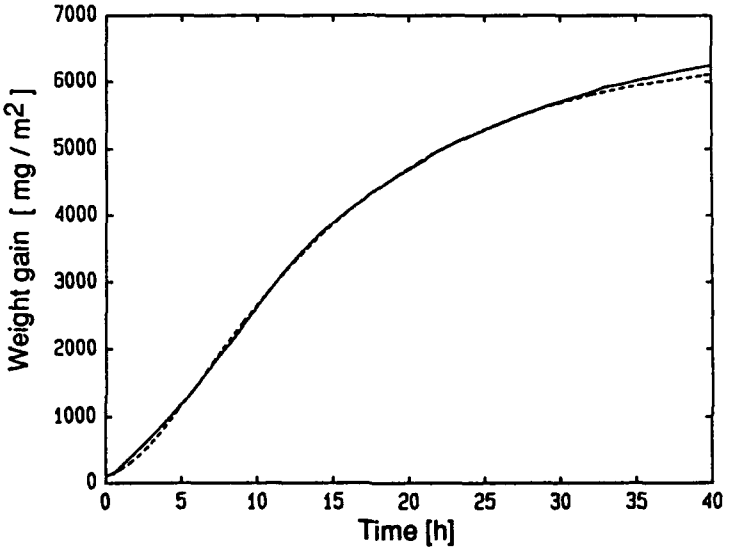

Fig. 9. Comparison between experimental and calculated (dashed) nitridation curves. Silicon powder with α-Si_3N_4, 1330°C, 25 torr N_2-pressure.

The rate constant of linear growth, k_1, is seen from Fig. 10 to be proportional to $P^{1.5}$, indicating that 3 N-atoms are necessary for the growth.

The rate constant of branching, k_2, is seen to vary proportional to P^2, indicating that 4 N-atoms are necessary for branching. These two observations may be rationalized with reference to the basic structural unit found in both α- and β-Si_3N_4, depicted in Fig.14. Adding another hexagonal ring next to one existing requires 3 N-atoms (and 3 Si-atoms), while the construction of an entirely new ring requires 4 N-atoms. It should be emphasized, however, that this is only a tentative picture, based on the results that came out of the model fitting.

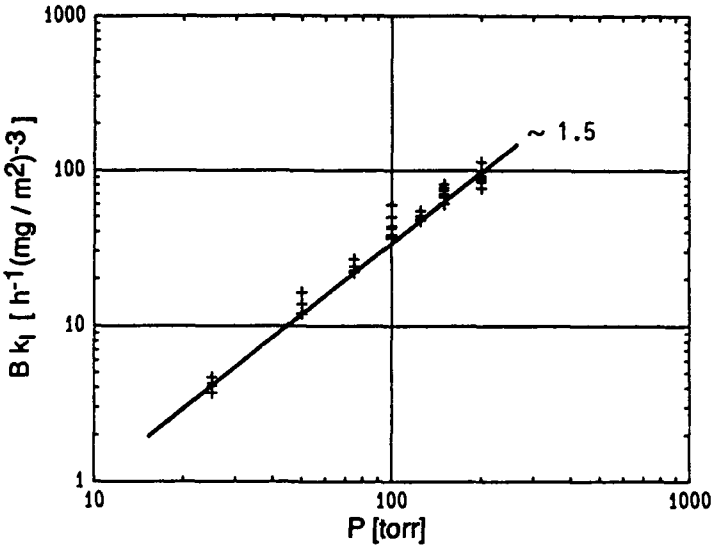

Fig. 10. Pressure dependence of the Bk_l value obtained for silicon powder with α-Si_3N_4 additions. The values for all temperatures are plotted. This explains the scatter, and gives an impression of the temperature dependence (≈1300 to ≈1340°C). Number refers to slope.

The rate constant of pore closure, k_a, is found to be proportional to $P^{2.5}$ as seen from Fig. 12. A tentative explanation goes as follows. We concluded above from the morphology that the growth of nitride appears to take place by means of silicon vapour diffusing through the pores of the nitride layer already formed. If the rate of diffusion of the silicon vapour is large, most of the growth will take place outside the pore, on top of the nitride layer. A low diffusion rate, on the other hand, means that more of the nitride growth will occur inside the pore, with gradual blocking as the result. Gas diffusivity is inversely proportional to the total pressure, which means that the time a silicon vapour atom spends inside a pore will be proportional to the nitrogen pressure. Furthermore it was found above that the rate constant for linear growth varied with $P^{1.5}$. Combining the two yields proportionality with $P^{2.5}$ as found for k_a.

The final extent of reaction, α_f, is found to be inversely proportional to the nitrogen pressure, that is, it varies with $1/P_{N_2}$. This is most probably related to the gas diffusivity as already related above; high pressure gives low diffusivity and hence a larger fraction of the total growth occurring inside the pores, with resultant blocking.

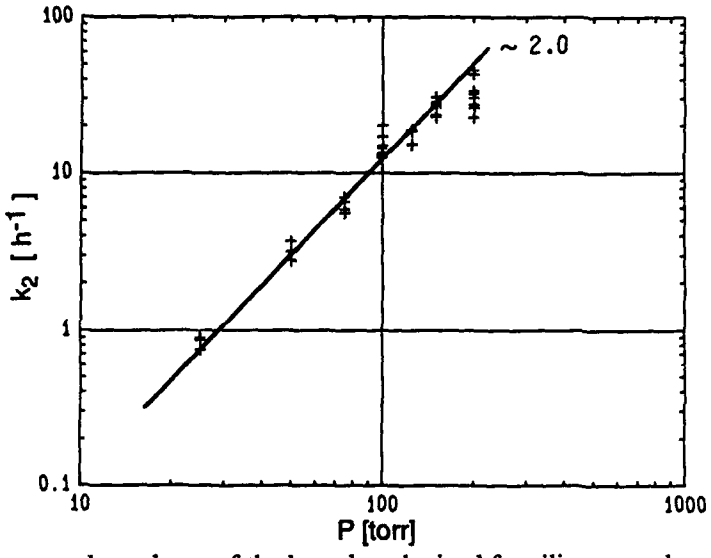

Fig. 11. Pressure dependence of the k_2 value obtained for silicon powder with α-Si_3N_4 additions. The values for all temperatures are plotted. (≈1300 to ≈1340°C). Number refers to slope.

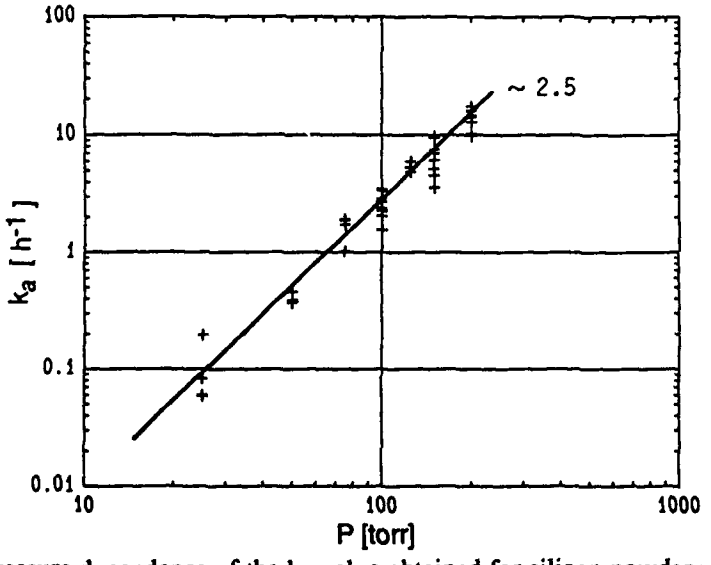

Fig. 12. Pressure dependence of the k_a value obtained for silicon powder with α-Si_3N_4 additions. The values for all temperatures are plotted. (≈1300 to ≈1340°C). Number refers to slope.

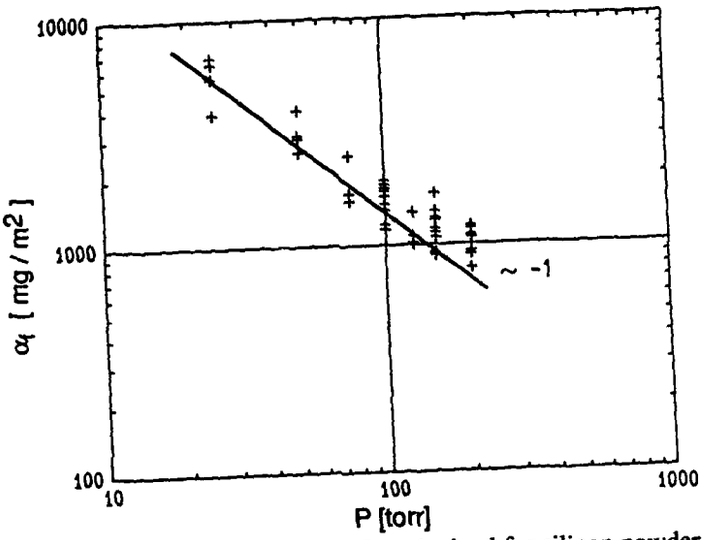

Fig. 13. Pressure dependence of the α_f value obtained for silicon powder with α-Si_3N_4 additions. The values for all temperatures are plotted. (≈1300 to ≈1340°C). Number refers to slope.

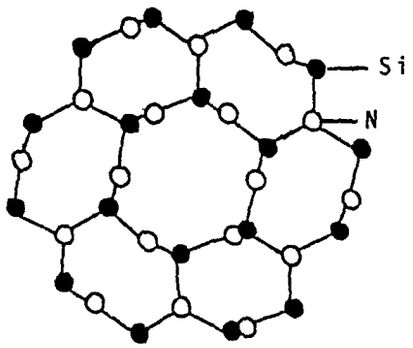

Fig. 14. The basal plane for constructing the α- and β-Si_3N_4 structure.

8. Discussion

In the above investigation of the pressure dependence of the parameters, all of the results were plotted in dependence of pressure regardless of the temperature of the runs. This resulted in some scatter of the points, but it could be done because the temperature span covered by the runs is fairly narrow, about 1300 to 1340°C, and also because it appears qualitatively already from the nitridation curves (Fig. 4) that the rates are not strongly dependent on temperature.

When investigating the temperature dependence, on the other hand, the runs for each pressure have to be plotted separately because of the marked pressure dependence of the rates. As a consequence, each Arrhenius plot comprises relatively few points. A further uncertainty comes from the narrow temperature span. Altogether the scatter in these plots is considerable, and they do not warrant the presentation of numerical results. Investigation of temperature dependences or apparent activation energies would have to be done with a fair number of runs at sufficiently different temperatures for each value of the nitrogen pressure.

It was noted above that α-Si_3N_4 is formed already in the very first stage of the reaction, while β-Si_3N_4 appears only after some time, see Fig. 6. This plot was based on observations with Si powder with α-Si_3N_4 added, but experiments with powder to which β-Si_3N_4 had been added, as well as with pure Si powder gave qualitatively the same results: The majority of the α-phase is formed in the initial reaction, while the β-phase becomes more pronounced with extended reaction time. This is in some contrast to the proposal by Moulson [10] that β-Si_3N_4 is preferentially formed on silicon surfaces. From the present work it appears likely that both phases are formed by the nitridation of Si(g). The observation that the α-phase is formed fist may be yet another example of Ostwald's old and qualitative "step rule", since the α-form thermodynamically is assumed to be slightly less stable than the β-form. Furthermore it has been shown that when either α- or β-nitride has been added as seeds to the silicon, the dominant phase in the product corresponds to that added. When nitriding pure silicon, the α/β ratio in the final product is found roughly to vary between 1.5 and 2. Generally speaking, both phases are formed in varying proportions in all of the present nitridation experiments, and the reasons for this remain unknown although nucleation of the phases by seeding may play a decisive role.

A fuller account of this work is found in the dr. ing. thesis by Bjørn Myhre, "Kinetics of the Nitridation of Silicon" Institute of Inorganic Chemistry, The Technical University of Norway, N-7034 Trondheim, Norway, Oct. 1989, 208 pp. Copies may be obtained from the Institute on request.

References

1. Schwier, G., (1983) in "Progress in nitrogen ceramics" ed. by F.L. Riley, Martinus Nijhoff Publ, p. 157-66.

2. Segal, D., (1989) "Chemical Synthesis of Advanced Ceramic Materials", Cambridge Univ. Press, 182 pp.

3. Blegen, K., (1975) in "Special Ceramics 6" ed. by P. Popper, Brit. Ceram Res. Ass., p. 233-44.

   Blegen, K., (1976) "Equilibria and kinetics in the systems Si-N, Si-O-N and Si-C-O-N". Dr.ing. thesis, Institutt for silikat og høgtemperaturkjemi, Norges tekniske høgskole, Trondheim.

4. Gazzarra, C.P. and Messier, D.R., (1977) Ceram. Bull 56, 777-80.

5. Atkinson, A., Moulson, A.J., and Roberts E.W., (1975) J. Mater. Sci. 10, 1242-43.

6. Atkinson, A., Moulson, A.J., and Roberts, E.W., (1976) J. Am. Ceram. Soc. 59, 285-89.

7. Garner, W.E. and Hailes, H.R., (1933) Proc. Roy. Soc. A139, 576-95.

8. Harrison, L.G., (1969) The Theory of Solid Phase Kinetics. In "Comprehensive Chemical Kinetics", Vol. 2, ed. by C.H. Banford. and C.H. Tipper, Elsevier Publ. Comp., p. 377-462.

9. Evans, U.R., (1960) "Corrosion and Oxidation of Metals", Edward Arnold Publ. Ltd., London.

10. Moulson, A.J., (1979) J. Mater. Sci. 14, 1017-51.

LANTHANUM SILICON OXYNITRIDES, SYNTHESIS AND X-RAY DIFFRACTION AND IR STUDIES

M. KIZILYALLI and G. GÜRBÜZ
Middle East Technical University
Chemistry Department
06531, ANKARA
Turkey

ABSTRACT. The previously unreported solid-gas reactions of La_2O_3+Si and LaF_3+Si under nitrogen flow were studied at around 1000-1200°C. According to the ratio of La/Si the expected products are $La_2Si_3N_4O_3$, $LaSiO_2N$, $La_5Si_3O_{12}N$ and $La_4Si_2O_7N_2$. However, $LaSiO_2N$ and $La_4Si_2O_7N_2$ were not obtained in these reactions at the temperatures studied. On the other hand, it was possible to prepare $La_2Si_3N_4O_3$ where 5% $CeCl_3$ was added to the reaction mixture with the composition of La_2O_3+3Si. The same compound was also prepared through the solid-gas reaction of $2LaF_3$+3Si reaction mixture with nitrogen at 1200°C. The structure of $La_2Si_3N_4O_3$ was found to be melilite type which is tetragonal but with the larger unit cell dimensions than reported before where a=10.67 and, c=15.647 A°. The powder pattern and unit cell dimensions of $La_5Si_3O_{12}N$ which were found to be a=9.69, c=7.15 Å (hexagonal) agreed very well with the reported data.

1. INTRODUCTION

Si_3N_4 type of materials are used instead of alloys in high temperature applications because of their high quality in mechanical strength, thermal resistivity, chemical resistivity to etching compounds and extreme hardness. Due to low electrical conductivity and dielectric properties, Si_3N_4 is also very important in microelectronic applications.

R. Freer (ed.), The Physics and Chemistry of Carbides; Nitrides and Borides, 45–67.
© 1990 *Kluwer Academic Publishers. Printed in the Netherlands.*

Actually thin dielectric films of SiO_2 could be used to insulate microelectronic devices in semiconductor industry but since alkali ions can easily penetrate through amorphous silicon oxide layers and destabilize them, amorphous Si_3N_4 films could be used for this purpose[1]. The quality of the silicon nitride material depends on the method of deposition. During the process some undesirable products may form, such as silicon oxynitrides.

Silicon nitride was also obtained by reaction sintering that is nitriding silicon powder with nitrogen at high temperatures. After reaction sintering β-silicon nitride which is a noncohesive white powder must be strongly compressed to have good mechanical properties [2]. This can be done by the employment of some high melting oxide additives as densification aids. Their effectiveness depend on the type of compounds formed when they are kept in contact with Si_3N_4 at high temperature[3]. If a small quantity of oxide was added, a liquid phase was obtained together with a vitreous phase on the grain boundaries. This lowers the resistance of Si_3N_4 deformation[4-5]. Oxynitride glass has higher strength, elastic modulus, hardness and lower thermal expansion than the corresponding oxide glass[6] and the properties of them are suitable for using them as bonding agent between Si_3N_4 ceramics[7].

Trivalent lanthanide oxides and Y_2O_3 were also used as sintering aids[3,8-9]. In the reaction of Si_3N_4 with Ln_2O_3 (where Ln stands for lanthanides) small amounts of SiO_2 was observed. It was found that the trivalent oxide rich liquid phase had no effect on the mechanical properties of Si_3N_4, but as the reaction proceeds, this phase gradually disappears and the edges are coated by high melting oxynitrides such as $M_2O_3.Si_3N_4$ [10]. If the reaction is incomplete some other oxynitrides may also be formed such as $M_4Si_2O_7N_2$. So it is very important to investigate the type of lanthanide silicon oxynitrides and their structures by x-ray powder diffraction and IR methods.

In metal oxynitrides [11-13] the fundamental unit is the $Si(O,N)_4$ group, so they are expected to be isomorphous with similar nitrides, silicates and phosphates depending on the coordination chemistry and

size of the metal ion. For example if the metal ion is larger than Si^{+4} ion (r=0.42 Å) than it cannot substitute Si^{+4} positions, so it resides outside the $Si(O,N)_4$ group. This is true for some lanthanide ions which are too large for the site of silicon. Replacement of nitrogen by oxygen is possible as long as the electroneutrality of the molecule is maintained. The type of oxynitrides that were reported in the literature are given on Table 1.

TABLE 1. The type of oxynitrides and their structures

Type of oxynitride	Structure	References
$2M_2O_3.Si_3N_4$	Tetragonal	14
$(M_4Si_3O_6N_4)$		
$M_2O_3.Si_3N_4$	Akermanite	14, 15, 16, 17, 30
$(M_2Si_3N_4O_3)$	$(Ca_2Mg\ Si_2O_7)$	32
	or melilite	33
$M_4Si_2O_7N_2$	Cuspidine	17, 19, 21-24, 10
	$Ca_4Si_2O_7F_2$	
$M_2O_3.2Si_3N_4$	Orthorhombic,	17, 19-21, 23, 24
$(M_2Si_6N_8O_3)$	Monoclinic	
$M_5Si_3O_{12}N$	Fluoroapatite	18-20, 25, 30
$M_5(SiO_4)_3N$	$Ca_5(PO_4)_3F$ (hex.)	
$MSiO_2N$	Wollastonite (hex)	26-27
	Pseudohexagonal	
	(Sr GeO_3 or α-$CaSiO_3$)	
$M_{10}(SiO_4)_6N_2$	Hexagonal	28, 29

All of the research workers prepared oxynitrides by the reaction of $Si_3N_4+M_2O_3$ or $Si_3N_4+SiO_2+M_2O_3$ [10]. Extensive investigations have been carried out in the system $Si_3N_4+La_2O_3$ at temperatures above 1600°C but there are some uncertainities in the compositions and structures of the phases obtained [17, 19, 23, 24, 26-31]. Mitomo et al[19] found two compounds $La_2Si_6N_8O_3=2Si_3N_4.La_2O_3$ and $La_5Si_3O_{12}N=La_5(SiO_4)_3N$ which have monoclinic and hexagonal structures above 1700°C respectively. An

orthorombic cell was also reported earlier for $2Si_3N_4.La_2O_3$ by Wills et al[19]. They used equimolar mixtures of Si_3N_4 and M_2O_3 (M= La, Sm, Dy, Er, and Yb, Y) to obtain $M_2Si_3N_4O_3$ compounds with tetragonal unit cell of melilite type. Rae et al[16] observed that the structure of $Si_3N_4.Y_2O_3$ is analog to that the structure of akermanite (a=7.846 Å, c= 5.020 Å, z=2, S.G. $P\bar{4}2_1m$). Then the unit cell parameters of Sm and Y were found to be a= 7.673, c=4.966 and a=7.598 Å, c=4.908 Å respectively which showed that these are also isostructural with akermanite. The transition from akermanite to oxynitride involves the replacement of Ca with M and Mg with Si and part of the oxygen with nitrogen. On the other hand the structures of $Dy_2Si_3N_4O_3$, $Er_2Si_3N_4O_3$ and $Yb_2Si_3N_4O_3$ are closely related to the akermanite structure since their unit cell dimensions are double for a and triple for c those of $Y_2Si_3N_4O_3$ unit cell[17]. Wills et al[17] gave a different structure for lanthanium oxynitride, $La_2Si_3N_4O_3$, with the unit cell parameters of a= 19.487, c= 13.489. Marchand et al[31] reported that Nd, Sm, Gd, Dy, Ho, Er, Yb and Y have melilite type of structures with the unit cell parameters observed by Wills[17], but $La_2Si_3N_4O_3$ had also similar cell parameters. Appendino et al [32] confirmed the results of Marchand et al and added $Tb_2O_3.Si_3N_4$ and $P_2O_3.Si_3N_4$ to the list. No x-ray powder diffraction data was reported for $La_2Si_3N_4O_3$ except by Wills et al[17]. Mitomo[19] suggested that there are no $La_2Si_3N_4O_3$ phases in the system $La_2O_3+Si_3N_4+SiO_2$ and $Ce_2O_3+Si_3N_4+SiO_2$ because of the large radius of La^{3+} and Ce^{3+} ions. The x-ray powder da of Wills et al for $La_2Si_3N_4O_3$ (J.C.P.D.S. Card No.31-667) was claimed to be due to $LaSiO_2N$ by Morgan [26] and Mitomo et al[19]. $LaSiO_2N$ was reported to be unstable around 1700°C and dissociates into $La_5(SiO_4)_3N$ and a glass when cooled 19 . $LaSiO_2N$ was reported to have pseudowollastonite structure [26] which is $SrGeO_3$ type. The x-ray data of the compounds with the formula $M_4Si_2O_7N_2$ were reported for $La_4Si_2O_7N_2$ [30], $Ce_4Si_2O_7N_2$ [10,23] $Nd_4Si_2O_7N_2$ [31] $Pr_4Si_2O_7N_2$ [10] and $Lu_4Si_2O_7N_2$ [34] by different research workers.

In this work the preparation of lanthanum silicon oxynitrides were attempted through solid-gas reactions of Si+ La_2O_3 or Si+LaF_3 mixtures under nitrogen flow, instead of Si_3N_4+La_2O_3 solid-solid reactions which were reported before. The reactions were carried out at lower temperatures to avoid melting and the formation of the glassy phase.

2. EXPERIMENTAL

La_2O_3 (99.9% from J.Mathey) and Si (99%, -325 mesh, from Aldridge) were dried before they were mixed and ground together in an agate mortar.

The mixed powders were sintered at around 900-1200°C in a tubular furnace under a nitrogen flow of 2-3 bubbles per second. The samples were kept at the desired temperatures for 6-12 hours and then cooled in nitrogen flow and weighed. In some experiments where excess oxygen was not needed, nitrogen gas was passed through a pyrogallol solution to eliminate it [10].

The procedures were repeated with compositions containing %5, %10 $CeCl_3$ or %10 Pd powder to see the effect of catalysis.

LaF_3 was also used instead of La_2O_3 to obtain oxynitrides since our previous experiments on rare earth phosphates proved that fluoride containing chemicals were good solid-state reaction promotors. On the other hand we avoided excess oxygen by using LaF_3.

The products were examined by x-ray poxder diffraction and IR spectroscopy to investigate the nitriding process.

Philips x-ray diffractometer (PW 1050/25 goniometer, AMR 3202 monochromator) with CuKα radiation and Perkin Elmer (Model 1430) IR spectrophotometer were used to identify the obtained products.

3. RESULTS AND DISCUSSIONS

Table 2. summarizes the compositions and conditions for La_2O_3+Si sintering reactions under nitrogen flow. In Table 3 the observed products together with weight changes in the sintering reactions are given.

TABLE 2. The compositions and conditions for La_2O_3+Si sintering reactions under nitrogen flow

No	Comp.	Additives	La:Si	Temperature, Time
1	La_2O_3+3Si	-	1:1.5	900°C, 15.5 hr.
2	" "	-	"	No.1 cont. 1100°C 19.5 hr.
3	" "	-	"	No.2 cont. 1300°C, 16 hr.
4	" "	5% $CeCl_3$	"	1200°C, 12 hr.
5	" "	10% $CeCl_3$	"	1200°C, 3 hr.
6	" "	" "	"	1200°C, 6 hr.
7	" "	" "	"	No.6 Cont. 1200°C, 9 hr.
8	" "	10% Pd	"	1200°C, 6 hr.
9	" "	"	"	No.8 Cont. 1200°C, 13 hr.

TABLE 3. The products observed in La_2O_3+Si reaction under nitrogen flow and weight changes

No.	La:Si	Initial Weight	Weight Change (gr)	Main Products observed*
1	1:1.5	1.98978	0.11091 loss	La_2O_3(s)+Si(s)+$La_5Si_3O_{12}N$(vw)+SiO_2
2	"	1.68051	0.03528 gain	$La_5Si_3O_{12}N$(m)+La_2O_3(s)+Si(s)
3	"	cont.	0.22311 gain	Melt, very hard ceramic material of mullite or sillimanite type +Si_3N_4
4	"	0.94060	0.07223 gain	two phase system, very hard (grey and white colour, α and β-Si_3N_4, $La_2Si_3N_4O_3$, but not a good fit to J.C.P.D.S card No. 31-667 +CeO_2+Si
5	"	-	-	$La_2Si_3N_4O_3$(s)+La_2O_3(w)+Si(w)+ SiO_2(w)+CeO_2(w)
6	"	1.10683	0.10627 gain	$La_5Si_3O_{12}N$(s)+$La_2Si_3N_4O_3$(s)+Si_3N_4(w), Si(w)
7	"	1.21188	0.00288 gain	$La_5Si_3O_{12}N$(s)+αSi_3N_4(m),$La_2Si_3N_4O_3$ (vw)

TABLE 3. Continued

No.	La:Si	Initial Weight	Weight Change (gr)	Main Products observed*
8	1:1.5	0.53700	0.02178 gain	La_2O_3+Si (Strong) $La_5Si_3O_{12}N$+Pd (weak)
9	"	0.44856	0.00355 gain	$La_5(SiO_4)_3N$(s)+La_2O_3(s)+ βSi_3N_4(w)

* s: Strong , m: Medium, w: Weak, vw: Very weak

For the composition La_2O_3+3Si the expected product is $La_2Si_3N_4O$ but in the x-ray powder diffraction pattern of the products obtained in reactions No. 1-9 the main observed compound was $La_5Si_3O_{12}N$ together with some unreacted La_2O_3+Si lines. On the other hand if 5% $CeCl_3$ was added to the previously heated La_2O_3+ 3Si mixture (under nitrogen flow at 1150°C) and then heated again under nitrogen flow for 12 hours a two phase system was obtained (No.4). The grey phase contains α and β Si_3N_4 and the white phase was predicted to be $La_2Si_3N_4O_3$. The x-ray diffraction data of this compound does not fit to the data of $La_2Si_3N_4O_3$ (J.C.P.D.S Card No. 31-667) which was given by Wills et al [17]. It was found out that it has a powder pattern which might be isostructural with melilite but with larger unit cell parameters.

It was observed that continuous heating and addition of Pd into the reaction mixture favored the formation of $La_5Si_3O_{12}N$.

In the second set of experiments nitrogen gas was cleaned by passing it through pyrogallol solution (Table 4-5) then the experiments were repeated. The main product was again found to be $La_5Si_3O_{12}N$ except in experiment 13, where $La_2Si_3N_4O_3$ was obtained together with $La_5Si_3O_{12}N$. The x-ray data of the product obtained in No.13 for $La_5Si_3O_{12}N$ agreed very well with the data of Mitomo et al [19] and was indexed in hexagonal system with the unit cell parameters of a= 9.698, c= 7.156 Å .

TABLE 4. The compositions and conditions for La_2O_3+Si sintering reactions under nitrogen flow.

No	Composition	La:Si	Temperature, Time
10	La_2O_3 + 3Si	1:1.5	1200°C, 9 hr.*
11	La_2O_3 + 2Si	1:1	1200°C, 9 hr.*
12	$5La_2O_3$ + 6Si	1:0.6	1200°C, 9 hr.
13	$5La_2O_3$ + 6Si	1:0.6	No.12 continued, 1200°C, 18 hr.
14	La_2O_3 + Si	1:0.5	1200°C, 9 hr.*

* Nitrogen was passed through pyrogallol solution and dried.

TABLE 5. The products observed in La_2O_3+Si reactions under nitrogen flow and weight changes

No	La:Si	Initial Weight	Weight Change (gr)	Product Observed
10	1:1.5	1.09685	0.06183 gain	La_2O_3(s)+$La_5Si_3O_{12}N$(w)+Si(s)
11	1:1	0.99413	0.01196 loss	$La_5Si_3O_{12}N$+La_2O_3(s)+Si(s)+SiO_2(w)
12	1:0.6	0.99244	0.02000 gain	$La_5Si_3O_{12}N$+La_2O_3(s)
13	1:0.6	0.76619	0.01000 gain	$La_5Si_3O_{12}N$+$La_2Si_3N_4O_3$(vw)
14	1:0.5	0.98922	0.09791 loss	$La_5Si_3O_{12}N$(s)+La_2O_3(s)

In the third set of experiments instead of La_2O_3+Si, LaF_3+Si was used in the nitriding reactions(Table 6). Table 7 summarizes the products obtained. Results of experiments No.15, 16, 17 and 18 showed that the main product is $La_2Si_3N_4O_3$. The x-ray powder diffraction data of No.16 was indexed in tetragonal system with the unit cell parameters of a=10.670 and C=15.647 Å which has a close resemblence to melilite structure where :

$^{c}_{melilite} \times 3 \sim {}^{c}La_2Si_3N_4O_3$

$^{a}_{melilite} \cdot \sqrt{2} \sim {}^{a}La_2Si_3N_4O_3$

As the Si content decreases (No. 18) the product again was $La_5Si_3O_{12}N$, which was also expected from the given La:Si ratio. The products were also analysed by IR spectroscopy. The results will be discussed in the next section.

TABLE 6. The compositions and conditions for LaF_3+Si sintering reactions under nitrogen flow

No.	Composition	La:Si	Temperature, Time
15	LaF_3+3Si	1:3	1200°C, 9 hr.
16	$2LaF_3$+3Si	1:1.5	1200°C, 9 hr.
17	$2LaF_3$+3Si	1:1.5	1200°C, 12 hr.
18	LaF_3+Si	1:1	1200°C, 9 hr.
19	$4LaF_3$+3Si	1:0.75	1000°C, 7 hr.
20	$5LaF_3$+3Si	1:0.6	1000°C, 9 hr.
21	$2LaF_3$+Si	1:0.5	1000°C, 9 hr.

3.1. IR Studies of Silicon Nitrides and Lanthanum Silicon Oxynitrides

In order to try to explain IR spectra for various lanthanum silicon oxynitrides, first of all it is necessary to assign the spectral bands to Si_3N_4 since oxynitride phases appear together with α and β-Si_3N_4.

The IR spectra of α and β Si_3N_4 and contaminated forms with oxygen have been reported in the literature [1,35-40].

Niihare et al.[35] examined the IR spectra of chemical vapor deposited (pyrolitic:Py)α-Si_3N_4 film on heated graphite substrate. The amorphous Py-Si_3N_4 indicated two broad absorption bands at approximately 500 and 900cm^{-1} showing the low crystallinity of the compound.

TABLE 7. The products observed in LaF_3+Si sintering reactions under nitrogen flow and weight changes

No.	La:Si	Initial Weight/gr	Weight Change (gr)	Product Observed
15	1:3	0.99255	0.15492 gain	$La_2Si_3N_4O_3(s)+SiO_2+Si_3N_4$
16	1:1.5	0.99561	0.015 gain	$La_2Si_3N_4O_3(s)+\beta Si_3N_4(w)+SiO_2(w)$
17	"	0.99903	0.02600 loss	$La_2Si_3N_4O_3+\beta Si_3N_4(w)+SiO_2(w)$
18	1:1	0.99730	0.03618 loss	$La_2Si_3N_4O_3(s)+\beta Si_3N_4(w)+La_5Si_3O_{12}N(w)$
19	1:0.75	1.09400	0.07786 loss	$La_5Si_3O_{12}N+La_2Si_3N_4O_3(w)$
20	1:0.6	0.97872	0.06981 loss	$La_5Si_3O_{12}N+La_2Si_3N_4O_3(w)$
21	1:0.5	0.99521	0.09759 loss	$La_5Si_3O_{12}N+La_2Si_3N_4O_3(w)$

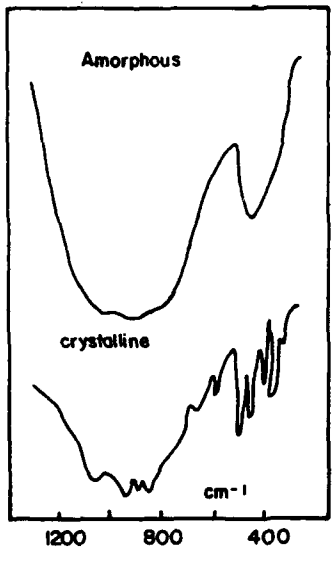

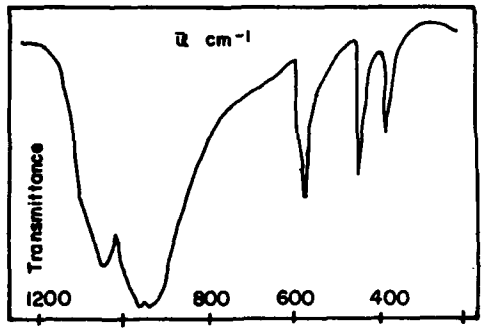

Figure 1. Infrared Spectra of α -Si_3N_4(35).

Figure 2. Infrared Spectra of β -Si_3N_4(37).

Increasing the pressure and lowering the nitriding temperature, these bands shift to lower frequencies, namely, to 480 and 860 cm^{-1}. On the other hand the absorption spectrum of crystalline Py-Si_3N_4 consisted of many sharp absorption bands, caused by the splitting of the broad ones. These are 1080, 920, 860-840, 690, 590, 480, 430, 400 and 380-370 cm^{-1} (Fig.1).

In the combined IR and x-ray studies of β -Si_3N_4 Wild et al[36] stated that only the presence of crystalline phases can be detected by x-ray diffraction. Undetectable glassy phase can lead to errors in the estimation of the composition of a crystalline phase. On the other hand changing the atoms in some crystallographic sites by other atoms have some effects on the absorption spectrum depending on the formation of ordered or random structures. Wild reported that [36] in the case of random distribution or ordering of atoms on nonequivalentsites, no new bands are observed but there may be frequency shifts. Ordering of atoms on equivalent sites cause the appearance of new bands together with frequency shifts.

The space group of β -Si_3N_4 is $P6_3/m$. Six principal absorption bands are observed in the spectra. If Si atoms are replaced by heavier atoms than Si, the wave numbers shift to lower values.

Luongo et al[1] suggested that the vibrational spectra of deposited films of amorphous Si_3N_4 had a strong broad absorption band at about 840 cm^{-1}. But in the presence of trace amounts of oxygen, the broadening of 840 cm^{-1} band was observed due to formation of structures such as Si-O, SiO_2, Si-O-N_x and Si-N which give bands between 800-1000 cm^{-1}.

Baraton et al and Volgin and Ukanov [37,38] also reported the IR data of β -Si_3N_4. Since each Si atom is at the center of slightly irregular Si_3N_4 tetrahedron and each nitrogen is common to three tetrahedra, the two nitrogens are at the center of an equilateral triangle formed by silicons. They reported two ranges a) 1100-850 cm^{-1} (1060, 920, 940 cm^{-1}) for the stretching vibrations of distorted Si_3N_4 tetrahedra which corresponds to degenerate F_2 vibration of a regular tetrahedron b) 600-350 cm^{-1} (590, 430 and 385 cm^{-1}) for bending vibrations of Si-N-Si and N-Si-N (Fig. 2) .

Ermer et al [39] studied the IR and Raman spectra of both α and β forms of Si_3N_4 and found out that α -Si_3N_4 indicated a more complicated structure. They investigated pure α-Si_3N_4 and α and β - Si_3N_4 mixtures which are also contaminated by oxynitrides (Fig. 3).

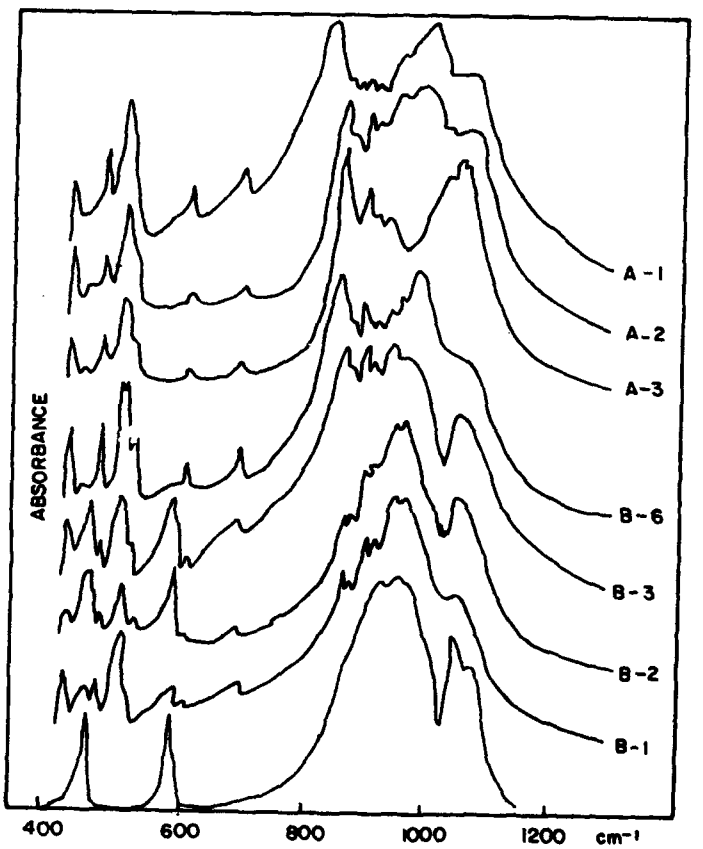

Figure 3. Infrared Spectra of Silicon Nitrides (39) A_1, A_2, A_3: α-Si_3N_4 from different sources, B_1, B_2, B_3, B_6 : Mixtures of α and β -Si_3N_4, B: β -Si_3N_4 from K.H.Jack

The characteristic frequencies of β -phase are given at 440-446 and 577-581 cm^{-1}. The position of other bands coincide with α-Si_3N_4. The spectrum of pure α-Si_3N_4 differs from sample to sample particularly in the range 880-1100cm^{-1}. The most significant difference is seen in the intensities of 930-950 cm^{-1} and 990 cm^{-1} bands. These have variable intensities in several spectra and are not observed in others.

Izhizaki et al.[40] reported the IR spectra of commercial α-Si_3N_4, air contaminated Si, nitrided at 1573°K and clean Si powder nitrided at 1473°K (Fig. 4). The air contaminated sample shows strong Si-O peaks (1020-1090 cm^{-1}).

The IR spectra of an oxynitride, Si_2ON_2, was reported by Baraton et al [41]. It consists of bands arising from Si-O-Si and Si-N networks. Three regions were distinguished in the spectra (Fig. 5).

a) 1400-800 cm^{-1} broad, intense
b) 600-200 cm^{-1} sharp, weak
c) 800-600 cm^{-1} only one significant band.

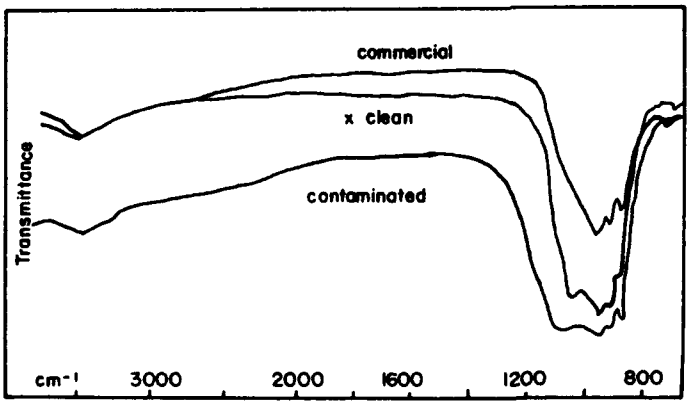

Figure 4. Infrared Spectra of Clean and Contaminated α-Si_3N_4 (40).

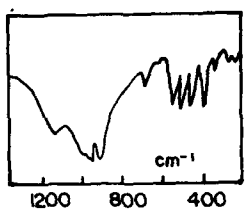

Figure 5. Infrared Spectra of Si_2ON_2 (41)

Factor group analysis yields for orthorombic S.G. Cmc2, or C_{2V}^{12}, $r_{opt.} = 7A_1 + 7A_2 + 6B_1 + 7B_2$ for reduced representations. Out of these $7A_1 + 6B_1 + 7B_2$ are IR active. In Table 8. the proposed assignments for Si_2ON_2(41) are given.

The bonding vibration, Si-O-Si of the pseudo-molecule $N_3Si-O-SiN_3$ would be expected in the range 300-340 cm^{-1}.

The IR spectra of oxynitrides prepared in this work are presented in Fig. 6. (No. 7, 11, 13) for $La_5Si_3O_{12}N$ and Figure 7. (No. 15, 16, 17 18) for $La_2Si_3N_4O_3$ respectively.

The x-ray powder diffraction data of $La_5Si_3O_{12}N$ showed that it can take large amounts of Si and O into solid-solution without any evidence of structural change. In the present work it has been shown that the only observable change in the x-ray diffraction pattern is the splitting of a line which has a "d" spacing of 2.90 Å. The results of numerous IR studies however indicated that structural changes are occurring. These which took place, and which would not be apparent in x-ray data, but produce changes in the IR spectra are related to the following reasons by Wild et al.[36]:

a) Small localized regions differing in both composition and structure from the bulk of the product.

b) Long range ordering of cations and anions on the available crystallographic sites.

TABLE 8. The proposed assignments for Si_2ON_2 (41)

Max. cm^{-1}	Assignment	Species
1314 w	-	-
1130 s (broad)	ν Si-O	B_1
1090 sh	ν Si-N	-
990 s	"	-
953 vs	"	-
906 vs	"	-
730 w	-	-
679 m	ν Si-O	B_2
648 w	-	-
542 s	δ Si-N	-
496 s	ν Si-O	A_1
448 s	δ Si-N	-
432 sh	"	-
376 s	"	-
327 m	δ Si-O	B_2
252 m	δ Si-O	A_1

The IR spectra (Fig. 6) of the product in experiment No.7 resembles β-Si_3N_4 which is contaminated by oxygen [39, 43]. In the x-ray powder diffraction data, the main product is $La_5Si_3O_{12}N$. The following changes are observed in the β-Si_3N_4 spectra. a) The band at 578-581 cm^{-1} shifts to 540 cm^{-1} showing the replacement of N with O b) Bands at 430 and 385 cm^{-1} broadens and disappears. Three new bands appear at 320, 250 and 690 cm^{-1} which correspond to δ Si-O (B_2+A_1) and ν Si-O (B_2) [41]. The bands at 270 and 730 cm^{-1} are attributed to Si-O_2 [44]. Symmetric and asymmetric vibrations of the Si-O-Si bonds which belong to $La_2Si_3N_4O_3$ compound are around 1050 (ν_{as}) and 503 cm^{-1} (ν_{as}) [45]. The bands between 1090-840 cm^{-1} correspond to ν Si-N and Si-O-N_x [1] and SiO_4^{4-} [46] showing the presence of Td symmetry.

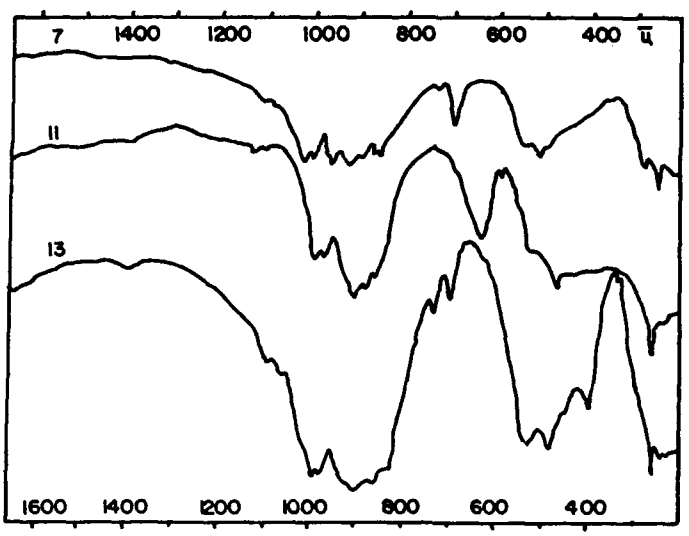

Figure 6. The IR Spectra of the products obtained in reactions No.7, 11 and 13 where La: Si are 1:1.5, 1:1 and 1:0.6 respectively.

The following absorption modes are present in SiO_4^{4-} ion: ν_1 at 872 cm^{-1}, ν_3 at 978, 934 and 905 cm^{-1} and ν_4 at 462, 396 and 380 cm^{-1}. ν_2 is Raman active.

Absorption spectrum due to CeO_2 should appear around 720 and 300-550 cm^{-1} which might be present in spectra No.7.

The IR spectra of the product obtained in experiment No.11 agrees with the x-ray diffraction data, showing the presence of La_2O_3 (630 cm^{-1}) [42]. Although the reaction is not complete, the presence of $La_5Si_3O_{12}N$ in the product and considerable amount of unexpected weight loss can be attributed to loss of SiO_2 via decomposition as SiO vapor [47].

Comparison of the IR spectra of product No.11 with No.7 in Fig.6 shows that increasing substitution of lanthanum with silicon cause further shift in the bands to lower wavenumber values and the band around 380 cm^{-1} has disappeared. Although there was no evidence of structural difference in the x-ray powder diffraction data of product No.7 and No.13,

the IR absorption bands between 380-545 cm^{-1} becomes sharper in the case of product No.13 which is found to be mainly $La_5Si_3O_{12}N$ depending on x-ray powder diffraction pattern. The IR data of the products of LaF_3+Si nitriding reactions (where no extra precautions are taken delibaretely for the purpose of allowing air into the system) are found to be quite complicated (Fig. 7).

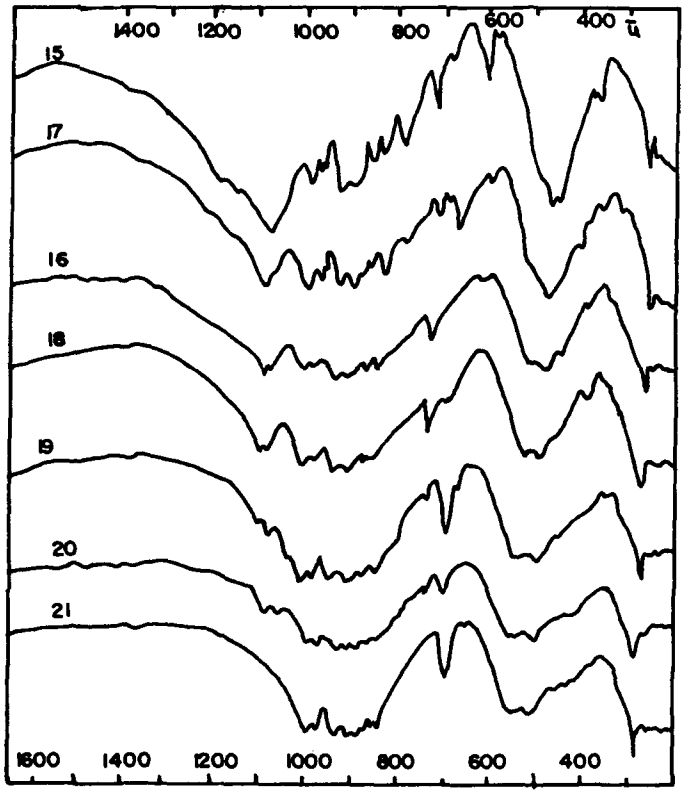

Figure 7. The IR Spectra of the products obtained through LaF_3+Si nitriding reactions of No. 15, 16, 17, 18, 19, 20, 21 where La:Si ratios are 1:3, 1:1.5, 1:1.5, 1:1, 1:0.75, 1:0.6, 1:0.5 respectively.

As the silicon content decreases in the original mixture, the SiO_2 absorption spectra (Fig. 8) around 1115-1190 and 800 cm^{-1} [48,49] and those reported by Mitsyuk et al. and Ross [50,51] at 620 and 475-450cm^{-1} disappears. The x-ray powder diffraction data of the products obtained

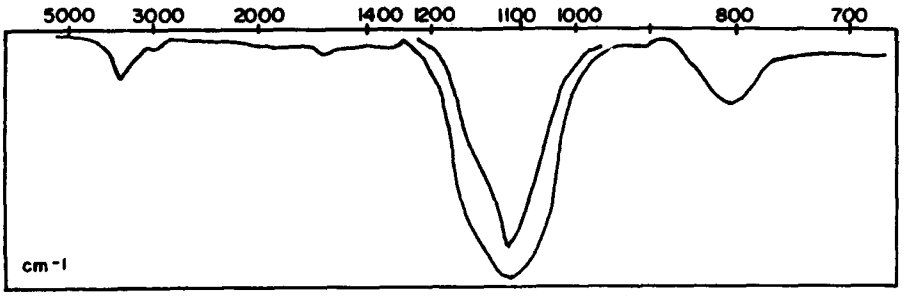

Figure 8. Infrared Spectra of silicon dioxide (47).

in experiments No. 15, 16, 17 and 18 showed the formation of $La_2Si_3N_4O_3$. On the other hand asymmetric stretching frequency, ν_{as} of Si-O-Si bonds at approximately 1050 cm^{-1} is used as a diagnostic frequency for compounds containing Si-O-Si bonds [52]. The symmetric stretching frequency, ν_s in the region 400-600 cm^{-1} has been established by Kriegsmann et al [53]. There appears to be a linear correlation between ν_s and $M^{1/2}$ where M is the mass of the atom or group attached to Si. On the other hand ν_{as} in compounds containing Si-O-Si group occurs at a relatively constant frequency which is determined mainly by the character of the Si-O bonds and not by the mass of group X.

The powder diffraction data of $La_2Si_3N_4O_3$ was indexed in tetragonal system as reported before, but in some cases there are some extra-lines in the x-ray diffraction pattern which can be covered using larger cell parameters and are due to superlattice reflections. It has been reported that [36] long range ordering would normally produce superlattice reflections since the difference in scattering power of Si and La is quite large. Because of the ordering of Si and La atoms in the structure, there might be a reduction in symmetry, and these would cause an increase in the number of predicted IR absorption bands. In experiments No.19, 20, 21 the compound $La_5Si_3O_{12}N$ was obtained. Prolonged heating of this

compound yields $La_{4.67}(SiO_4)_3O$ [54].

The following modes were assigned to the absorption peaks observed in numerous spectra.

Wavenumber cm^{-1}	Mode	Frequency cm^{-1}	Mode
255	δ Si-O(A_1)	730	ν Si-N
270	Si-O_2	800	SiO_2
327	δ Si-O(B_2)	840	Si-N
337	Si-O-Si(A_1)	872	$SiO_4(\nu_1)$
380	SiO_4 (ν_4)	909	ν Si-N vs
376-385	δ Si-N (sh)	930	Si-O-N_x
396	SiO_4 (ν_4)	940	ν Si-N vs
432	δ Si-N(sh)	960	
448	Si-N s or	905	
	O-Si-O bending	934	SiO_4(s) (ν_3)
462	SiO_4 (ν_4)	978	
475		980	ν Si-N (s)
490	ν Si-O (A_1)	1060	ν Si-O (ν_3)
600	ν SiO_2	1090	ν Si-N (sh)
648	ν Si-O (w)	1130	ν Si-O (B_1)
542	ν Si-N (s)		
679	ν Si-O m (B_2)		

CONCLUSION

Our studies concern the preparation of a series of lanthanum silicon oxynitrides by an alternative technique than reported previously. It consisted of nitridation of silicon by the addition of La_2O_3 or LaF_3 in a given stochiometric ratio. Using these two routes two oxynitrides namely $La_5Si_3O_{12}N$ and $La_2Si_3N_4O_3$ have been obtained. The results proved that the formation of particular structure are strongly influenced by the composition of the starting powder, temperature and duration of

reaction. No extra precaution was taken to avoid oxygen especially with the reactions performed by LaF_3.

The results of x-ray powder diffraction studies of $La_2Si_3N_4O_3$ indicated that there are some variations in the d-spacings and intensities depending on the conditions. It is most likely that these variations is closely related to the formation of superlattices with larger unit cell dimensions than reported previously for melilite structures. On the other hand the infrared absorption spectrum showed the presence of the bands due to Si-O-Si symmetric and asymmetric stretching vibrations together with $Si-O_2$ or Si-N bands which characterize melilite structure. Research is going on in our laboratory to clarify these complicated set of solid gas reaction products and the detailed x-ray powder diffraction data of $La_2Si_3N_4O_3$ will be published elsewhere later.

Acknowledgements :

M.Kızılyallı would like to thank NATO for providing fund to attend NATO ARW and to Dr.Robert Freer for inviting her to ARW in Manchester. The authors are also indebted to METU grant commission for supporting this research project under contract No. 88-01-03-16.

REFERENCES

1. Luongo, J.P. (1984) Appl. Spect. 38, 195.
2. Thompson, D.S. and Pratt, P.L. (1967) in G.H.Stewart (eds.), Science of Ceramics, vol.3, Acad. Press, New York, p.33.
3. Mazdiyasni, K.S. and Cooke, C.M. (1974) J.Amer.Chem.Soc. 57, 536.
4. Deelay, C.G., Herbert, J.M. and Moore, N.C. (1961) Powder Met. 8, 145.
5. Drew, P. and Lewis, M.H. (1974) J.Mater.Sci. 9, 261.
6. Roehman, R.H. (1979) J.Am.Cer. Soc., 62, 491.
7. Ibid (1981) in "Surfaces and Interfaces in Ceramics and Ceramic-Metal Systems" (eds.) J.A.Pask and A.G. Evans, Plenum, New York, p.701.
8. Gazza, G.E. (1973) J.Am.Cer.Soc., 56(12), 662.
9. Huseby, I.C. and Petrov, G. (1974) Powder Met.Int.,6(1), 17.
10. Montorsi, M. and Appendino, P. (1979) J.Less.Comm.Met., 68, 193.
11. Wild, S., Grieveson, P. and Jack, K.H. (1972) in P.Popper(eds.) "Special Ceramics, 5", Brit.Ceramic Research Asso. Stoke on Trent p.289.
12. Jack, K.H. (1973) Trans J.Brit.Ceram.Soc., 72, 376.
13. Wills, R.R. and Cunningham, J.A. (1977) J.Mater.Sci. 12, 208.
14. Tsuge, A., Kudo, H. and Komeya, K. (1974) J.Am.Ceram.Soc., 57, 269.
15. Wills, R.R. (1974) J.Am.Cer.Soc., Discussions, p.459.
16. Rae, A.W.J.M., Thompson, D.P., Pipkin, N.J. and Jack, K.H. (1975) in "Special Ceramics" vol.6, British Ceramic Research Asso. Stoke-on-Trent, England, p.347.
17. Wills, R.R., Stewart, R.W., Cunningham, J.A. and Wimmer, J.M. (1976) 11, 749.
18. Thompson, D.P. (1975) in Special Ceramics, 358.
19. Mitomo, M., Izumi, F., Haruichi, S. and Matsui, Y. (1982) J.Mater. Sci., 17, 2359.
20. Mitomo, N., Kuramoto, N. and Suzuki, H. (1978) J.Mater.Sci.Letters 2523.

21. Mah Tai, IL, Mazdiyasni, K.S. and Ruh, R. (1979) J.Am.Cer.Soc., 62(1-2) 12.
22. Rae, A.W.J.M., Buang, K.B., Thompson, D.P. (1980) J.Mater.Sci., 15, 264.
23. Morgan, P.E.D. (1979) J.Am.Ceram.Soc., 62(11-12)636.
24. Nisser, J.W., Johnson, G.G., Ruh, R. (1979) Ibid.
25. Lange, F.F. (1980) Cer.Bull. 59(2) 239.
26. Morgan, P.E.D., Carroll, P.J. (1977) J.Mater.Sci., 12, 2343.
27. Morgan, P.E.D., Carroll, P.J. and Lange, F.F. (1977) Mat.Res.Bull., 12, 251.
28. McCarthy, G.J. (1967) J.Inorg.Nucl.Chem. 29, 253.
29. Gaude, J., Guyader, J., and Lang, J. (1975) C.R.Acad.Sci.Ser C,280, 883.
30. Wills, R.R., Holmquist, S., Wimmer, J.M. and Cunningham, J.A. (1976) J.Mater.Sci. 11, 1305.
31. Marchand, R., Jayaweera, A., Verdier, D. and Lang, J. (1976) Compt. Rend.Acad.Sci.Ser C, 283, 675.
32. Appendino, P., Montorsi, M. (1979) J.Less Common Met., 64, 1303.
33. Wyckoff, R.W.G., Crystal Structures (1968) 2nd ed., vol.4, p.225.
34. Kockelhorn, J.H. (1979) Anorg.Allg.Chem. 456, 147.
35. Niihare, K., Hirac, T. (1977) J.Mat.Sci., 12, 1233.
36. Wild, S., Elliott, H., Thompson, D.P. (1978) J.Mat.Sci. 13, 1775.
37. Baraton, M.I., Marchand, R. and Quintard, P. (1986) J.Molec.Str., 143, 9.
38. Volgin, Yu.N. and Ukanov, Yu.I. (1975) Opt.Spec., 38, 412.
39. Ermer, E. and Ptak, W.S. (1986) J.Molec.Str. 143, 5.
40. Izhizaki, K., Yumoto, S. and Tanaka, K. (1988) 23, 1813.
41. Baraton, M.I., Labbe, J.C., Quintard, P. (1982) J.Molec.Str. 79, 333.
42. Baun, L.W. and McDewitt, N.T. (1963) J.Am.Ceram.Soc., 46, 1294.
43. Nyquist, R.A. and Kagel, R.O. (1971) Infrared Spectra of Inorganic Compound
44. Etchepare, J. (1970) Spectrochim. Acta, 26A, 2147.
45. Jezowska, B., Hanuza, J. and Wojchiechowski, W. (1967) Spectrochim Acta. 23A, 2631.

46. Tarte, P. (1963) Spectchim.Acta., 19, 25.
47. Lange, F.F., Singhal, S.C. and Kuznicki, R.C. (1977) J.Am.Ceram.Soc. 60(5-6), 249.
48. Mecke, R. and Langenbucher, F. (1965) Infrared Spectra of Selected Chemical Compounds, Heyden Ltd. London, Serial No. 1221.
49. Wood, D.L., Rabinovic, E.M. (1989) Appl.Spectr. 43(2) 263.
50. Mitsyuk, B.A. Gorogotskaya, L.I. and Rastrenko, A.I. (1976) Geakhimiya, 6, 803.
51. Ross, S.D. (1972) Inorganic, Infrared and Raman Spectra, McGraw Hill, U.K., p.104.
52. Gillespie, R.J. and Robinson, E.A. (1964) Can.J. of Chem., 42, 2496.
53. Kriegsmann, H., Schowta, K.H. (1958) Z.Phys.Chem.Leipzig, 209, 261.
54. Lange, F. (1980) Cer.Bull., 59(2), 239.

SYNTHESIS OF SILICON CARBIDE OF DIFFERENT MORPHOLOGIES AND THE EFFECT OF SECOND PHASE IN CERAMIC COMPOSITES.

A. LERICHE* and F. CAMBIER

C.R.I.B.C. - Belgian Ceramic Research Centre
4 Avenue Gouverneur Cornez, 7000 Mons, Belgium

ABSTRACT. This paper aims to review the current synthesis methods of SiC particles, platelets, fibers and whiskers which play a role of reinforcing phase in ceramic composites. A comparison of physical and chemical properties of various commercial grades such as purity, crystal phase, agglomerate and crystal size, dispersion behaviour, etc. is presented.

1. INTRODUCTION.

It is now well established that the mechanical properties of ceramic materials (fracture strength and toughness) are strongly enhanced by adding dispersed phases. This improvement is mainly explained by an increase of crack propagation energy owing to various mechanisms such as : crack bowing, crack branching, crack deviation, fibre pull out and bridging, etc. Among the various studied ceramic composites which have been studied up to now, a large number contain SiC as dispersed phase in the shape of particles, platelets, long or short fibres and whiskers. Many different toughening mechanisms are believed to be operative in SiC - reinforced ceramics.

The particulate reinforcing mechanisms are listed below :

The *microcracking* is associated with large expansion mismatches between SiC second phase particles and the matrix. It is clear that the efficiency of this reinforcement mechanism depends on the SiC particle size and on the bonding stresses developed within the matrix around the particles, as a function of the elastic modulus of the matrix.

The *crack pinning* requires a fine size of the dispersed particles, a high volume fraction of dispersed phase and a fracture energy of the particle much higher than that of the matrix.

---

* present address : Neoceram S.A., Z.I. Strepy -Bracquegnies, 7060 La Louvière, Belgium.

R. Freer (ed.), The Physics and Chemistry of Carbides; Nitrides and Borides, 69–85.
© 1990 Kluwer Academic Publishers. Printed in the Netherlands.

The *crack deflection* and the *crack branching* lengthen the crack path and therefore depend on the particle size and shape.

It has to be noted that such mechanisms like microcracking, crack deflection or branching can also play a significant role in fibre or whisker composites. For these composites, other toughening mechanisms can occur :

The *crack bridging* consists in bridging the crack behind the crack tip by unfractured whiskers or fibres. This phenomenon reduces the crack opening displacement and the stress intensity at the crack tip. It depends on the fibre strength and on its aspect ratio.

The *fibre or whisker pull out* has the potential for the greatest toughening effect and consists in a decohesion of fibre from the matrix consuming large energy. This mechanism depends strongly on the aspect ratio of the second phase and is favoured by weak interface bonds.

All the mechanisms mentioned above are strongly related to the characteristics of SiC dispersed phase, that is to say :

- the global purity and the surface composition which influence the nature of the second phase/matrix interfaces as well as the bond strength between the matrix and the reinforcing phase.
- the shape and size of the reinforcing phase
- the quality of the reinforcing phase dispersion, function of the behaviour of this phase in a suspension.

The selection of SiC second phase in ceramic composites has to take all these parameters into account and has to be oriented by a good knowledge of physical and chemical characteristics of commercial silicon carbide grades. Indeed a survey of literature, some representative data of which are listed in the Table 1, shows that the addition of SiC second phase generally induces an increase of the critical stress intensity factor (K_{Ic}) but not always of the flexural strength. The decrease of flexural strength in such composite materials can be attributed to the presence of defects like pores, second phase agglomerates, etc, which annihilate the improvement of behaviour due to reinforcing mechanisms.

2.SYNTHESIS METHODS AND CHARACTERISTICS OF SILICON CARBIDE SECOND PHASES.

2.1.Silicon carbide powders.

Many silicon carbide polytypes exist, which can be classified as two main allotropic phases. At room temperature, the stable phase is the cubic beta-SiC transforming into the hexagonal alpha-phase at approximately 2100°C. At normal pressure, SiC sublimes and dissociates at temperatures higher than 2500°C.

Table 1 : Mechanical properties of SiC reinforced ceramic composites (from literature data).

Material	Strength resistance (MPa)	Toughness (MPa√m)	References
Glass matrix			
LAS glass	200	2	
idem + fibre	830	17	[26]
Alumina matrix			
HP alumina		4.6	
id. + 10 v/o whiskers		8.0	
id. + 20 v/o whiskers		6.8	
id. + 30 v/o whiskers		9.0	[27]
HP alumina		4.8	
id. + 20 v/o particles		4.8	
id. + 20 v/o whiskers		5.1	[28]
HP alumina	150	4.5	
id. + 5 v/o whiskers	330		
id. + 10 v/o whiskers	450	6.8	
id. + 20 v/o whiskers	650	8.2	
id. + 30 v/o whiskers	700	9.2	[29]
Silicon nitride matrix			
HPSN	780	4.6	
id. + 10 v/o whiskers	720	4.4	
id. + 20 v/o whiskers	710	4.8	
id. + 30 v/o whiskers	980	6.4	[30]
HPSN	650	7.1	
id. + 10 v/o whiskers	550	9.5	
id. + 20 v/o whiskers	550	9.5	
id. + 30 v/o whiskers	480	10.5	[31]
SSN (a)	612	7.1	
id. + 10 v/o platelets	671	8.4	
id. + 20 v/o platelets	466	7.7	
SSN (b)	465	6.7	
id. + 10 v/o platelets	501	7.3	
id. + 20 v/o platelets	416	6.5	[32]

recent works [2] suggest the colour of SiC powders could be also attributed to different absorption ranges according to the polytype.
Table 2 presents the chemical and physical properties of three commercial silicon carbide powders synthesized by different routes.

Table 2 : Properties of silicon carbide powders from different synthesis routes.

Supplier	IBIDEN	LONZA	SUPERIOR GRAPHITE
Grade	Standard Betarundum	UF-10	HSC 059
Synthesis route	Vapor phase process	Acheson process	Direct reaction
Purity (%)	99.2	< 97.0	98.2
Si (Free)	-	< 0.2	0.03
C (Free)	0.4	< 0.4	0.85
Fe	0.05	< 0.1	0.02
Oz	0.1	< 0.7	0.8
Agglomerate size (microns)	0.32	1.3	0.6
Surface area (m^2/g)	11.5	10.0	15.0
Crystallographic phase	beta	alpha	beta

In general, silicon carbide powders prepared by vapour phase processes and the sol-gel process have very high purity (up to 99.99), submicronic size and are in the beta form opposite to the Acheson-type powders which are less pure (96 to 99%), have to be milled and are composed of alpha phase particles.
The oxygen content of SiC powders is a very important factor which determines the quality of the sintered bodies through the nature and amount of grain boundary phase. The total oxygen content is proportional to the specific surface area of the powder.
Both beta SiC and milled alpha SiC sinter at temperatures higher than 2000°C in the presence of small amounts of carbon, boron, aluminium, beryllium. The beta SiC grains are usually small and equiaxed, whereas alpha SiC are plate-like grains. Hence, when beta SiC is used as starting powders at temperature higher than 2000°C, special attention has to be paid to microstructure development because large plate-like crystals of alpha SiC can grow in a matrix of fine grains of beta SiC due to the beta to alpha transformation.
With regard to silicon carbide powders, the present researches are focused on the improvement of quality by an optimization of the alpha SiC after Acheson, and of beta SiC via gas phase deposition. The

2.1.1. Synthesis methods.

The silicon carbide powders are industrially produced by solid / solid reactions or gas / phase reactions :

i) Reaction between silicon and carbon

$$Si + C = \text{beta } SiC$$

The reaction occurs in solid phases at temperatures around the melting point of silicon (1408°C).

ii) Carboreduction of silica - Acheson's process

$$SiO_2 + 3\ C \xrightarrow{Fe} \text{alpha } SiC + 2\ CO$$

The reaction is still the most important production route of silicon carbide and consists in reducing silica at temperatures between 2000 and 2300°C to produce alpha SiC. The produced powders are crushed, milled and washed with hot hydrofluoric acid to remove the iron catalyst and melting contaminants. The Acheson's SiC powder purity is about 98 to 99 %, the main impurity being iron.

iii) Reaction between silicon chloride and methane.

$$SiCl_4 + CH_4 = \text{beta } SiC + 4\ HCl$$

The vapour phase reaction occurs in a plasma in which chloride is reacted with carbon or nitrogen containing gaseous species. This process produces a beta SiC powder of high purity and relatively uniform particle size.

iv)Thermal decomposition of organosilicon compounds carried out at 1600°C using argon as the carrier gas.

$$CH_3SiH_3 = \text{beta } SiC + 3\ H_2$$

For the last few years, several new vapour phase synthesis methods, the energy of which is provided by plasma burner, radio frequency or laser, have been studied [1]. Sol-gel processes (e.g. alkoxide process) have been also extensively studied. The resulting ultrafine and amorphous oxides are reacted with ammonia or methane at 600-1350°C to obtain very fine amorphous carbides. On heating the SiC powder to 1450°C in hydrogen, the powder crystallises as beta SiC.

2.1.2. Powder characteristics

Impurities include graphite, silicon and silica. The purity of SiC can be judged by the crystal colour. From black to green, yellow, colorless, the purity is increasing. Let us notice, however, that

development of these powders is dependent on the high production costs which should be reduced in the future. For instance, highly pure (five nine) silicon chloride has been produced from rice husks by Japanese researchers; in contact with methane, it enables the formation of ultra-fine spherical SiC particles at low production costs [3].

2.1.3.Dispersion behaviour.

The dispersion of silicon carbide particles as reinforcing phase in a ceramic matrix needs the preparation of a homogeneous suspension. According to the zeta potential evolution versus pH value illustrated at figure 1, it appears the best defloculation will be obtained at high basic value [4].

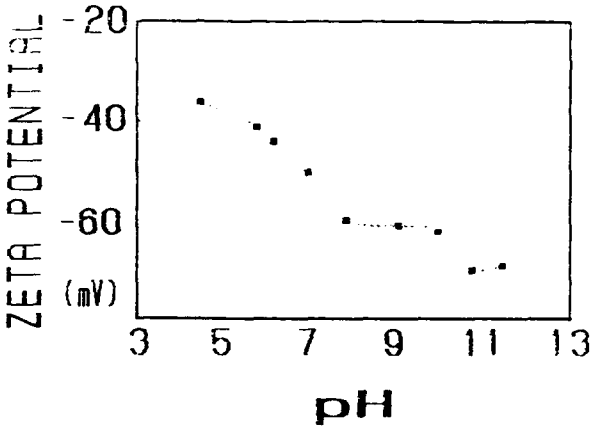

Figure 1 : Zeta potential of SiC particles versus pH.

2.2. Silicon carbide platelets.

For a few years, silicon carbide platelets have been commercially available. The synthesis of these platelets occurs probably through a chemical vapour method. The characteristics of platelets supplied up to now are presented in Table 3.

Table 3 : Characteristics of commercial SiC platelets.

Supplier	AMERICAN MATRIX -325 mesh	C-AXIS TECH.
Impurities	1000ppm	-
Diameter (microns)	20 - 70	30-60
Thickness (microns)	0.5- 5.0	2-5
Bulk density	1.30	-
True density	3.22	-
Crystallographic phase	alpha	-

The characterization results for the grade < 325 mesh from American Matrix show the main impurity is silicon, the particle size distribution is very wide (far below the 20 microns specified by the supplier) and the platelets present very variable shapes. These two last characteristics are illustrated in figure 2 which presents a scanning electron microscope image. According to the coarse size and non-uniform distribution of size and shape, post treatment of commercial platelets by milling, sieving,... is necessary in order to obtain high quality reinforced composites.
Coarser platelet grades are also available from American Matrix : <100 >200 mesh and <200 >325 mesh.

Figure 2 : SEM image of American Matrix platelets (1000*)

2.3.Silicon carbide fibres

2.3.1.Synthesis methods [5]

The fabrication of silicon carbide fibres is carried out through chemical processes:

- -The oldest used process has been the decomposition of organochlorosilanes carried by hydrogen gas in a furnace tube followed by the deposition onto hot carbon, tungsten or silicon carbide substrates. A modification of the chemical vapour deposition process is to deposit elemental silicon from the decomposition of tetrachlorosilane onto a carbon filament. This method presents some disadvantages : large diameter of the resulting fibres and high cost.
- - Another method discovered by Verbeek [6] and Yajima [7] consists in pyrolysis of polymeric fibres containing silicon.

The most commonly used precursors of silicon polymers are organohalosilanes especially organochlorosilanes. From these, polysilanes $(R_2Si)_n$ can be produced by dechlorination with alkali metals; polycarbosilanes (PCS) $(SiCH_2)_n$ by post treatment of polysilanes or polysiloxanes $(R_2SiO)_n$ by hydrolysis. These polymers are

suitable for spinning when dissolved in benzene or diethylether and silicon carbide fibres are obtained after evaporating the benzene and appropriate pyrolysis.
Commercial silicon carbide fibre "NICALON" are produced from organometallic polycarbosilane copolymers instead of classical PCS polymers which ensures a better thermal stability of fibres and an improved yield of fibre production.

2.3.2.Fibre characteristics

Table 4 presents the supplier's characteristics for 2 grades of SiC fibres

Continuous silicon carbide fibres are generally used as a reinforcing phase in glass ceramics or refractories. The processing methods consist of hot pressing of infiltrated unitape or slurry pressure casting or hot matrix transfer through a bi-dimensional or tri-dimensional fibre skeleton. This last method cannot be applied to production of dense ceramics because of the absence of shrinkage of the fiber skeleton. On the contrary, chopped silicon carbide fibres could be used as reinforcing phase and added to the matrix by classical mixing methods. Let us notice that such grades are today difficult to obtain from producers and certainly not available for large scale production.
The coating of fibers, for instance by carbon, allows a decrease in the interface bonding with the matrix, which increases the strength and the toughness by favouring pull out mechanisms [8]. As an example, an increase of flexural strength from 550 MPa to 1050 MPa has been noted for silicon carbide - pyrex composites by using (500 Å) carbon coated Nicalon fibres [9].

Table 4 : Characteristics of commercial SiC continuous fibres

Supplier	NIPPON CARBON Nicalon	UBE Tyranno
Fibre diameter (µm)	10 - 15	8.5 - 11.0
Density (g/cm3)	2.55	2.35
Tensile strength (GPa)	2.5 - 3.0	2.74
Elastic modulus (GPa)	180 - 200	206
Heat resistance	1250°C	1300°C (in N2 gas) 1000°C (in air)
Crystallographic phase	beta	-

2.4. Silicon carbide whiskers

Whiskers are single crystals as opposed to continuous filaments or fibres that are either polycrystalline or amorphous. They present, therefore, a higher thermal and chemical resistance.

2.4.1.Synthesis methods.

Silicon carbide whiskers can be produced by numerous methods which influence the purity and the morphology of whiskers. These synthesis methods differ from the raw materials and are summarized below.

Bulk SiC [10] : The bulk SiC is vaporized by heating under reduced pressure. Alpha-SiC whiskers form on nucleation sites containing catalyst.

Chlorosilanes : Beta-SiC whiskers grow through the hydrogen reduction of methyltrichlorosilane (CH_3SiCl_3) onto carbon substrate at 1500°C [11] or beta-SiC whiskers are synthesized by a controlled use of combinations of chlorosilane, carbon monoxide and methane as source gases [12].

Silicone oils : Beta-SiC whiskers result from thermal decomposition of sulfur-containing silicon oils at 1200°C - 1400°C. The whiskers are white and woolly with high aspect ratios (0.1 - 0.4 µm wide and 0.5 - 9 cm long) and a triangular rod form [13].

Silicon : Beta-SiC whiskers grow at about 1300°C by the reaction of silicon powder and propylene in a flowing hydrogen atmosphere containing a few percent of hydrogen sulphide. The whiskers produced are white and woolly having dimensions of a few millimeters in length and 0.1 to 1 microns diameter [14].

Rice hulls : Alpha and beta-SiC whiskers can be produced from the thermal decomposition of rice hulls containing a large amount of silica and carbon. The silicon carbide produced consists of particles and whiskers. The whiskers are 0.2 to 0.5 micron in diameter and up to 100 microns in length and present two basic types of morphologies. The whiskers of type I have a twinned beta structure and present a rounded cross section, a gradual decrease in thickness and conical tip with an angle of about 60°. The whiskers of type II are characterized by weak beta reflections and do not exhibit a gradually changing thickness. Their tips are usually flat or rounded. The cross section is usually rounded but in some cases hexagonal [15-17].

Silicon oxides : Silicon carbide whiskers are synthesized from SiO or SiO_2 and carbon through a VLS process (V stands for Vapour feed gases, L for Liquid catalyst and S for Solid crystalline whiskers growth) [18-22]. The presence of a liquid catalyst, such as a transition metal and iron alloy, distinguishes this last method

from all other whiskers growth techniques. The role of the catalyst is to form a liquid solution interface with the crystalline material which is to be grown and fed from the vapour through the liquid - vapour interface. Indeed, the catalyst solution is a preferred site for deposition of feed from the vapour. The liquid becomes supersaturated and a precipitation occurs at the solid-liquid interface. Figure 3 illustrates the sequence for VLS growth of SiC whiskers (adapted from [22]).

Figure 3. Illustration of the VLS process for SiC whisker growth [19]

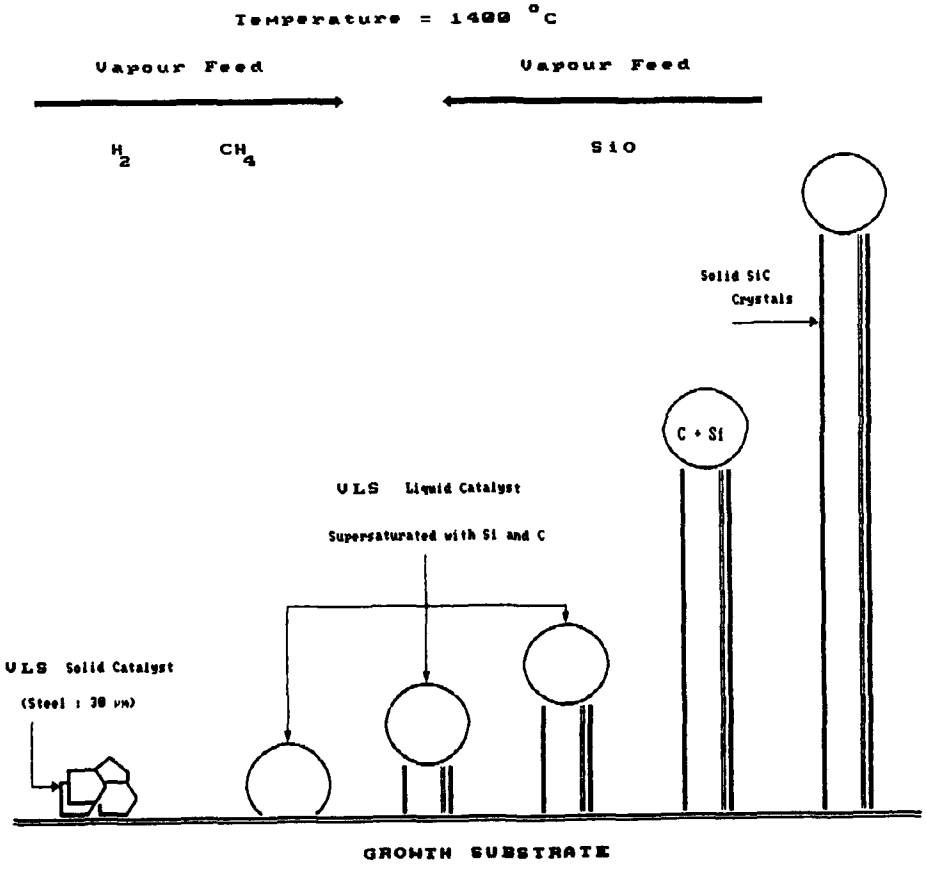

At 1400°C the solid catalyst melts and forms the liquid catalyst ball. Carbon and silicon atoms in the vapour feed are accreted to the surface by the liquid catalyst, which soon becomes supersaturated and solid SiC precipitates from the liquid catalyst onto the growth substrate. As precipitation continues, the whisker grows, lifting the catalyst ball from the substrate and forming a whisker which is proportional in size to the catalyst ball. To clearly identify the various types of whisker growth, a standard

identification code for SiC whisker growth has been developed by Petrovic et al [22]. Following these authors, the SiC whisker morphology changes according to the degree of gas phase supersaturation :

- At low supersaturation level, large diameter needles are formed. These whiskers are pure beta-SiC and present a smooth surface and a rounded-triangular cross section.
- For the next level of supersaturation, multiple growth sites are activated on the substrate and many smaller beta and alpha-SiC whiskers are grown.
- For higher supersaturation, the excess supersaturation is sufficient to activate secondary growth sites on the sides of the whisker causing very small (0.5 to 1 µm diameter) branches to occur.
- At the highest supersaturation level, all growth is the side branch type and gives small fibrous clusters.

The same analysis shows also that the carbon - silicon stoichiometry influences the SiC whiskers growth colour. The colour is black for carbon - rich stoichiometry due to excessive carbon deposits on the whisker. When the carbon amount decreases, the whisker becomes more and more colourless up to pure white for an ideal carbon - silicon stoichiometry. As the gases become more silicon rich, the SiC whiskers take on a light green colour possibly due to nitrogen doping up to a blue colour. Whiskers prepared by a VLS process generally present a morphology characterized by the presence of a sphere rich in iron and silicon at the whisker end furthest from the substrate surface. The whiskers will also present a smooth surface or a bamboo-like structure depending whether the growth temperature is lower or higher [21].

2.4.2.Whisker characteristics

The tensile mechanical properties of SiC whiskers and fibres have been tested by Petrovic et al. [22] for comparison purpose. These authors measured a mean fracture strength value of 8.40 GPa (1.66 to 23.74 GPa) and a Young modulus of 578 GPa (361 to 890 GPa) for whiskers produced by VLS process, presenting a diameter of 4 to 6 µm and a length of 10 µm. The mean fracture strength of long SiC whiskers presenting a diameter of 4 to 10 mm and a length of 13 to 20 microns was estimated to 9.45 GPa and their Young modulus to 581 GPa. In comparison, NICALON fibres of 17.3 microns present lower values : an average fracture stress of 2.40 GPa (0.52 to 3.53 GPa) and an elastic modulus of 180 GPa (21 to 318 GPa). The characteristics of commercial silicon carbide whiskers as claimed by producers and data from our laboratory [24] are presented in Tables 5 and 6. It can be noted that the five tested whisker grades show different colours. The lightest one is Tateho's product which presents a grey - blue colour which could come from the silicon - rich gaseous feed stock, whereas the darkest

one comes from Tokai Carbon's product (grey-green coloured); the colour could be due to excessive carbon deposits. The crystallographic structure was determined by X-Ray diffraction analysis, the physical characteristics such as diameter, length, crystal morphology and surface aspect was evaluated from scanning electron microscopy images.

For the microscopical observation, the whiskers were dispersed in water in proportions : 0.1 mg / 1 ml. Typical examples of whisker scanning electron micrographs are presented at figures 4 to 6. It has to be noted that all grades contain some whiskers with a diameter less than 1 micron which can be considered as carcinogenic [25] .So,the handling of presently available SiC whiskers requires specialized equipment.

Table 5 : Characteristics of commercial SiC whiskers.
(Supplier's data)

Supplier	Tokai Carbon	Tateho	Zirconia Sales	American Matrix	Shin Etsu	C-Axis Technol.
Phase	Beta	Beta	Beta	Beta	Beta	Beta
Length (µm)	20-50	5-200	50-200	30-200	3-20	
Diameter (µm)	0.3-1.0	0.05-1.5	1-3	1-3	0.15-0.25	0.3-1.0
Aspect Ratio		20-200			20-50	20-50
Density	3.2	3.18		3.21		3.21
Impurities				1000 ppm		
SiC (%)	> 99.0					
SiO2	< 0.5					
Cr	< 0.05		0.003			
Co	< 0.05					
Fe	< 0.05	0.1	0.003		0.03	
Mg		0.2			0.005	
Ca		0.5	0.018		0.05	
Al		0.6			0.01	
C			0.003			
O			1.14			
B			0.005			
Ni			0.002			
Si/O surf			0.44			
100 Å			0.65			
500 Å			3.17			

Table 6 : Characteristics of commercial SiC whiskers.
(Laboratory data)

Supplier	Tokai Carbon	Tateho	Zirconia Sales	American Matrix	Shin Etsu
Colour	grey-green	grey blue	green-yellow	green	grey
Phase	Beta			Beta	Beta
Dispersion behaviour	bad	good	good	good	bad
Length (μm)	a few 30	a few 60	2-100	5-100	10-70
Diameter (μm)	<< 1.0	<< 1.0	1-4	<< 1-2	<< 1.0
Surface	irregular	smooth	irregular		irregular
Morphology	(fibre, side branches	bamboo structure, some fine particles	2 aspects ratios (high & low) bamboo structure, side branches	2 families -smooth -bamboo structure and side branches	bamboo structure and side branches

Figure 4 : SEM image of Tokai Carbon SiC whiskers (2000 *).

Figure 5 : SEM image of Tateho SiC whiskers (1000 *).

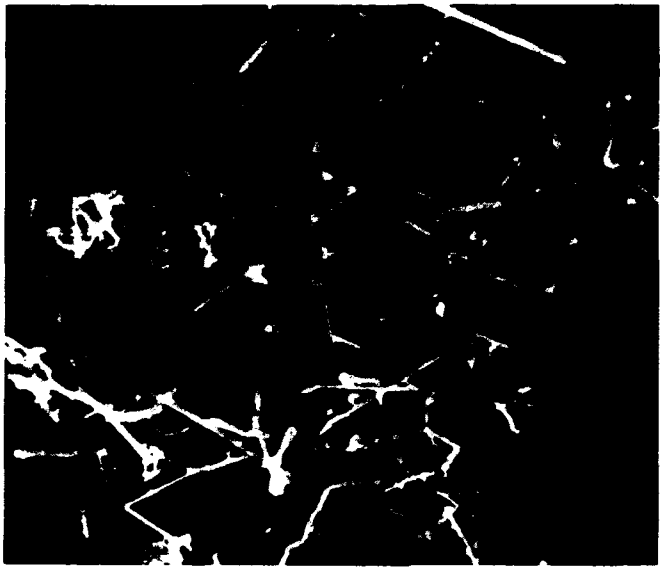

Figure 6 : SEM image of Zirconia Sales SiC whiskers (1000 *).

2.4.3. Dispersion behaviour

The whisker zeta potential evolution versus pH is quite similar to that for silicon carbide powders (figure 1). Dispersion at basic pH will give the best repulsion between SiC whiskers. Some difference in dispersion behaviour in water and alcohol was noted between the various whisker grades. For instance, the Tokai carbon and Shin Etsu whiskers were highly agglomerated even after ultrasonic treatment whereas other whisker grades were well dispersed.

3.CONCLUSION.

This paper has described the numerous methods used for synthesis of silicon carbide particles,fibres and whiskers. These methods start from different raw materials and catalysts which strongly influence the final product properties.
A literature survey of mechanical properties of silicon carbide reinforced composites shows that the addition of silicon carbide second phase generally induces an increase of toughness but more rarely of flexural strength. The decrease of strength resistance cannot always be attributed to microstructural defects due to unhomogeneous mixtures but it is linked to the silicon carbide phase characteristics, e.g. presence of impurities, too strong bond with matrix, presence of too large particles or fibres. Therefore, intensive effort is required on the part of the raw material suppliers to produce improved materials such as chopped silicon carbide fibres, uniform sized and shaped platelets...
Concerning silicon carbide whiskers, all the commercial grades contain submicron diameter whiskers which are suspected to be carcinogenic.

4. ACKNOWLEDGEMENTS

Part of this work has been performed within the frame of EEC contract n° MA1E/0033/C (B). The authors wish to thank EEC for allowing publication of these results.

REFERENCES

1. Suyama, Y, Marra, R.M., Haggerty, J.S., Bowen, H.K. (1985) Am. Ceram. Soc. Bull. 64 (10) 1356-59.
2. Choyke, W.J. (1989), ARW NATO, Manchester sept. 1989.
3. Hunold, K. and Reh, H.(1988) Interceram (1988), 37 (1), 35-39.
4. Moortgat, G. (1989) Silicates Industriels 5-6, 75.
5. Brook, R.J., Chen, L.F., Gilbart, E., Riley, F.L. 1988) The production of silicon carbide fibres. Report on EEC contract n° MA1E-0033-C (GDF).
6. Verbeek W (1974) Production of shaped articles of homogeneous mixtures of silicon carbide and nitride U.S. Patent 3, 853, 567
7. Yajima, S. et al. (1975) Chem. Lett. 931.

8. Rice, R.W., Spann J.R., Lewis D. and Coblenz W. (1984) Ceramic Eng. Sci. Proc. 5 (7-8) 614 - 24.
9. Jamet, J.F., Anquez, L., Parlier, M., Ritti, M.H., Peres, P., Grateau, L. (1987) Industrie Ceramique N° 819,9.
10. Knippenberg W.F. and Verspui G. "Silicon carbide 1972" edited by R.C. Marshall, J.W. Faust and C.E. Ryan University of South Carolina Press,(1973) 108.
11. Ryan, C.E.,Berman,I., Marshall, R.C., Considine, D.P. and Hawley, J.J.,j. Crystal Growth 1 (1967) 255.
12. Parrath, N.J."Fibre Reinforced Materials Technology" Van Nostrand Reinhold, London, (1972).
13. Katsuki, H., , Ushijima,H. Kanda,M.,Iwanaga, H. and Egashira, M. Yogyo-Kyokai-Shi, 95 (11) 1987, 1089.
14. Egashira,M. Katsuki, H. Mori, M.Kaneko, H. Kurahashi, W.and Kawasumi, S. Yogyo Kyokai Shi 93 (1985) 535.
15. Cutler, I.B. Production of Silicon Carbide from Rice Hulls. U.S. Patent 3 754 076, August 1973.
16. Sharma,N.K. Williams, W.S. and Zangvil, A. J.Am. Ceram Soc 67, ((11) 715-720 (1984).
17. Lee, G.J. and Cutler, I.B., Am. Ceram. Ceram. Soc. Bull 54 (2) 195-198 (1975).
18. Wagner, R.S. and Ellis, W.C.. Appl. Phys. Lett 4 (1964) 39.
19. Comer, J.J., Mater Res. Bull. 4, 279-88 (1969)
20. Bootsma, G.A. Knippenberg W.F. and Verspui, G. Journal of Crystal Growth 11 (1971) 297-309.
21. Shyne, J.J. and Milewski, J.V. Method of Growing Silicon Carbide Whiskers US Patent 3 622 272,(1971).
22. Petrovic, J.J. Milewski, J.V. Ohr, D.L. and Gac. F.D. J.Mater Sci 20 (1985) 1167.
23. De Jong, R Mc Cauley, R.A. and Tambuyser, P. Am Ceram Soc. Com 70 (11) C-338-341, 1987.
24. Leriche A., Cambier F. (1988) Silicon nitride ceramics and composites for high temperature applications Report on EEC contract n° MA1E/0033/C (B).
25. Birchall J.D., Stanley, D.R., Mockford, M.J., Pigott,G.H., Pinto, P.J. (1988) J. Mat. Sci.7, 350-352.
26. Brennan J.J., Prewo K.M. (1982) J. Mat. Sci. 17, 2371.
27. Wei G.C., Becher P.F. (1985) Am. Ceram. Soc. Bull. 64 [2] 298-304.
28. Wada S., Watanabe N., Tani T. (1988) Kyokai Shi 96 [2] 111-18.
29. Tiegs T.N., Becher P.F.(1987) Am. Ceram. Soc. Bull. 66 [2] 339-42.
30. Buljan S.T., Baldoni J.G., Huckabee (1987) Ceramic Bulletin 66, 2, 347-352.
31. Shalek P.D., Petrovic J.J., Hurley G.F., Gac F.D. (1986) Am. Ceram. Soc. Bull. 65 [2] 351-56.

32. Poorteman M., Cambier F. (1989) Silicon nitride ceramics and composites for high temperature applications. Report on EEC contract n° MA1E/0033/C (B).

LABORATORY METHODS FOR THE PREPARATION OF BORON CARBIDES

F. THEVENOT
Ecole Nationale Supérieure des Mines
158, cours Fauriel
42023 Saint-Etienne Cédex 2
France

ABSTRACT. Boron carbide has a wide phase homogeneity range : $B_{4.0}C$-$B_{10.5}C$. Direct synthesis from the elements is possible, but useless. Thin solid films are deposited by chemical vapor deposition (CVD), starting from mixtures of boron halides (BCl_3, BBr_3) - methane - hydrogen excess. Plasma assisted CVD, at low temperature (400-600°C), gives very hard amorphous films, with a variable carbon content (max. hardness 5000 kg/mm^2 for 38 at .C %) ; diborane may be used instead of boron halides. Boron carbide fibers are obtained i) by CVD on boron fibers or ii) by reaction of C.V. Deposited boron onto carbon fiber; fibers are used to reinforce light metallic matrices. Single crystals are obtained by CVD or by zone melting of a B_4C rod. Whiskers or platelets are prepared by CVD (starting from CCl_4-BCl_3-H_2 mixtures). Fine, pure, with a variable C content, narrow sized thus promising, powders are obtained by treating BCl_3/B_2H_6-CH_4-H_2 mixtures in a plasma or laser. Boron carbide is prepared at low temperature i) by carbothermal reduction of B_2O_3, ii) or by reaction of BCl_3-CCl_4 in an organic solvent in the presence of sodium. Cracking of boron containing organic precursors is possible, but still expensive.

1. Introduction

Boron carbide, which has a high melting point, outstanding hardness, good mechanical properties, low specific weight, great resistance to chemical agents and a high neutron absorption cross-section ($^{10}B_xC$, $x > 4$) is currently used in high technology industries [1-5] : nuclear energy [6], and high-temperature thermoelectric conversion [7].

Many proposed formulas are not confirmed. In the boron-carbon phase diagram, the rhombohedral boron carbide phase exists in the homogeneity range $B_{4.0}C$ (20 at % C) to $B_{10.4}C$ (8.8 at % C) [8,9] ; this phase is a complex solid solution [9-11]. "B_4C", commonly used as the boron carbide formula, is just a phase limit, not far from the more usual commercial powders composition. We will see later on, that stoechiometry may be widly varied.

Methods for the preparation of boron carbide allow to prepare either powders, or dense films or deposits. In order to elaborate dense species, powders may be densified by i pressureless sintering using diverse additives : metals, borides, silicon, carbon, polycarbosilane ... ii or hot pressing or high isostatic pressing, both being industrially used [12].

R. Freer (ed.), The Physics and Chemistry of Carbides; Nitrides and Borides, 87–96.
© 1990 *Kluwer Academic Publishers. Printed in the Netherlands.*

We are presenting : direct synthesis (§ 2) ; films, deposits and fibers (§ 3) ; crystal growth (single crystals, whiskers and platelets) (§ 4) ; different preparative routes of powders (§ 5).

2. Direct synthesis

Starting from fine and/or amorphous boron and carbon powders, the direct synthesis of stoechiometric boron carbide is possible and begins at 1600K [13-15], either under vacuum at 2300K in an electric furnace for 1h (the average particle size was 0.3-0.4 μm and sp. surface was 5.5-7.5 m^2/g)., or at 2273 K by hot pressing under Ar. This method is inefficient economically and finds no practical application. All the compositions in the phase homogeneity range $B_{10.4}C$-B_4C can be obtained by hot pressing mixtures of B_4C with boron [9,16,17].

Pressureless sintered mixtures of B_4C, B and C (C obtained by cracking of a precursor phenolic resin) give low densities (< 93 % d th) boron carbide species [18].

The diffusion diagram between B and C is established [9,16].

Implantation of C^+ ions into boron and subsequent annealing lead to boron carbide [19].

3. Preparation routes for films and solid deposits (using boron halides, oxides or hydrides)

3.1. BY REDUCTION OF BCl_3 BY H_2 IN THE PRESENCE OF CARBON (REACTIVE CVD)

Boron chloride can be reduced by hydrogen at 1300°C on a tungsten substrate with a recovery of approximately 85 % of elemental boron, without any reaction, whereas a deposit carried out on graphite at 1450°C gives adherent B_4C [20].

3.2. BY CHEMICAL VAPOR DEPOSITION (CVD)

A mixture of boron halides (eg BCl_3, BBr_3) and CH_4 or CCl_4 in the presence of H_2 is passed over a metallic filament (W, Ta, Mo, etc), electrically heated between 1273 and 2073K (thus giving a boron carbide filament or fiber), or boron nitride deposited on inductively hot graphite [22,23]; refractory metals, nickel or alumina [20,21] ; steel [24,25] ; tungsten carbide [25,26].

The reactions are :

$$4\,BX_3 + CH_4 + 4H_2 \longrightarrow B_4C + 12\,HCl \qquad (a)$$

with X = Cl [20,21,24-26] or Br [22,23,27,28]

$$BCl_3 + CCl_4 + 8H_2 \longrightarrow B_4C + 6\,HCl \qquad (b)$$

Calculations of the equilibrium conditions under which CVD of boron carbide from BCl_3-CH_4-H_2 mixtures take place consider the partial pressures of the gaseous species present and the temperature. The method minimizes the free energy and the theoretical diagrams are compared to experimental observations [29-31]. A deposition diagram for specific gas reactants ratios, under 10 mbar total pressure, by varying the substrate temperature (900-1450°C) describes a wide range of composition (0-18 at % C) with crystallized phases : β boron, "$B_{13}C_2$" rhombohedral type phase, tetragonal $B_{50}C_2$, graphite, either alone or codeposited [24,32]. Heat and mass transfers, and diffusion kinetics in the gas phase are related to the morphology and composition of the deposits [33-41]. A recent review is available [37].

The mixture BBr_3-CH_4-H_2 was studied into a microwave plasma (PACVD) at moderate temperature (400-600°C) ; very hard (5000 kg/mm^2) amorphous boron-carbon films, were deposited at 600°C, and the maximum microhardnes' as obtained for 38 at C % (outside of the phase homogeneity range) [42].

Depending on conditions, hot cracking of a mixture of iodides BI_3 and CI_4 gives the tetragonal boron phase $B_{48}B_2C_2$ or the orthorhombic carbide B_8C [23,43,44].

Using reaction (b), carbides in the range $B_{11}C$-$B_{13}C_2$ are obtained at 1020-1500°C [45]. Crystalline phases between B_2C and $B_{17}C$ were grown on graphite surfaces heated at 1000-1300°C (B_2C is a new carbon-rich, out of thermodynamic equilibrium CVD limit) [46,47].

Using the (dangerous) gaseous mixture (B_2H_6 (diborane), CH_4 and H_2) a plasma induced CVD [48] or a toroidal glow discharge [49], produce amorphous boron-carbon alloy films, with low hydrogen content, similar to those obtained by using BBr_3 [42]. This deposit is very promising as coating materials for fusion reactor walls [49].

3.3. PHYSICAL VAPOR DEPOSITION (PVD)

The vaporization-cold substrate condensation process of boron carbide melted by electron-gun heating [9,50,51] and plasma torch deposition [52] does not give a well-organized and crystalline B_4C-type structure deposit [9].

3.4. BORON CARBIDE FIBERS [2]

Boron fibers are used to reinforce different epoxy-or light metal matrices (Al,Ti ...). To hinder interactions with metals they should be protected by boron carbide deposits obtained by CVD, using BCl_3 or BBr_3 as boron source (cf. §3.2) [53-55]. Boron carbide fibers can be prepared directly by reaction of boron obtained by the H_2 reduction of BCl_3 on carbon fibers [56].

Complex fiber (e.g. C) structures should by consolidated by in-depth low pressure CVD [57] or by cracking of organic precursors, like carboranes [58].

4. Crystal growth

4.1. SINGLE CRYSTALS

All the CVD processes using boron halides, methane or carbon tetrachloride and hydrogen (reactions a) and b), § 3.2) are convenient to produce small single crystals used for crystallographic determinations.

B_4C single crystals, 3-4 mm long, are obtained by CVD (reaction b) [59], or by reduction of B_2O_3 by graphite in an electrical arc [1,60]. A 6 mm diameter sintered boron carbide rod can be zone melted under Ar [61].

4.2. WHISKERS AND PLATELETS

Using reaction (b), inlet gas ratio (BCl_3 : CCl_4) 0.2 to 9.3 with 10-70 times hydrogen excess, under 620 torr at 1050-1620°C, several deposit morphologies are obtained : granular, needles, whiskers (grey or yellow), nodular to smooth and even large crystals ; the stoechiometry is near B_4C and growth mechanisms are discussed [62]. i.e. vapor-liquid solid process for whiskers [63]. Single crystals needles up to 1 mm in length could have

also a high carbon content : $B_{2.0}C$-$B_{2.4}C$ whereas hexagonal plates (0.04-0.07 mm long) with another composition $B_{5.6}C$ may be obtained [46,47]. Mixtures of coarse platelets and whiskers are now industrially available [64].

The vaporization-condensation of B_4C at 2223K in vacuum allows the growth of whiskers, metallic impurities (W, Mo, Nb ...) catalyzing the growth [65-67].

5. Powders

Powders may be prepared i using reactants treated by physical technics (laser, plasma, electron beam) ii or by heating, cracking or reacting diverse inorganic or organic chemicals.

5.1. PLASMA AND LASER SYNTHESIS - ELECTRON BEAM EVAPORATION

Boron carbide can be prepared in a hydrogen - Ar plasma using : 1) amorphous boron and carbon powders [68] ; 2) an anode made of a mixture of graphite with boric anhydride (or borax) and a graphite cathode [69,70] ; 3) a mixture of B_2H_6-CH_4 [71], 4) a mixture of BCl_3-CH_4-H_2 [72-76]. In the latter, boron carbide is prepared in excellent yield, a wide stoechiometry range (B/C,15.8 - 3.9) and fine spherical granularity (20-30 nm) [73-76] and characterized by its infrared spectra [9-10] ; the sintering of such a powder should be promising.

Ultrafine (34 nm) powders were prepared by the CO_2 laser-driven pyrolysis of BCl_3-H_2-CH_4 (C_2H_4) mixtures. Powders of B_4C stoechiometry, free of excess B or C, were prepared through optimization of gas flow rates and laser intensity. The powders are loosely agglomerated, of high purity, consisting of equiaxed particles and exhibiting a narrow size distribution. The powders were classically hot-pressed (34-76 MPa, 1800-2230°C, Ar atmosphere), with theoretical density at 2050°C. Microstructure revealed examples of uniform and exaggerated grain growth. Mechanical properties were good [77-78].

Finally, B_4C powders, with a particle size of 6.3 nm, are prepared by evaporation of B_4C granules, melted by electron beam heating under vacuum, and condensed and collected on a water-cooled Ni cylinder [79]. These powders have a X-ray pattern characteristic of B_4C [79] ; using the same technic we obtained non-organized boron carbide deposits (cf. § 3.3, [9]).

5.2. - INORGANIC SYNTHESES

5.2.1. *Carbothermal reduction of boric anhydride.* A mixture of acetylene black, or sugar with ethylene glycol, is heated with boric acid at 1600-1800°C, in a stream of Ar ; the resulting B_4C powder is fine grained (1-5 μm) [80]. Similarly mixtures of boric acid with ethylene glycol [81] or glycerin [82] may be used. Fine carbide powder (0.7 μm) may be obtained by heating a mixture of boric acid-carbon black and dicyandiamide, giving a BN intermediate [83] ; ultra fine carbide powder (40 nm) are obtained by direct reaction at 1900-2200°C of hexagonal BN crystal powders with carbon [84].

5.2.2. - *Other syntheses.* Interaction of benzene with BCl_3 at 800°C yields a graphite like BC_3 [85].

Carbon tetrachloride and boron trichloride are mixed in anhydrous n-heptane in the presence of sodium ; an amorphous B-C-Cl precursor precipitates, which is then heated at 1980°C under vacuum. The resulting solid contains very fine (specific surface 215.6 m^2/g)

agglomerated, irregular particles of B_4C, characterized by XRD, with 10 % C excess [86,87]. Ceramic-ceramic multiphase compounds may be obtained by the same method [86]. This method of powder synthesis should be promising, but it is not well known.

5.2.3. - *Pyrolysis of boron-containing organic precursors.* The pyrolysis is generally carried out at high temperature (> 1300°C) under Ar flow. Boron carbide is ill-crystallized and may be mixed with SiC, BN ...

Single phase B_4C is obtained by the pyrolysis of boric acid/1,2,3 - propanetriol condensation product [88], , vinyl-pentaborane (> 90 % yield) [89], carboranes (obs. yield 2 %) [58], boronylpyridine (yield 22 %) [58].

Mixed phases may be produced :

- B_4C-BN by cracking of borate esters [82], an amine adduct of decaborane in a stream of Ar [90]
- B_4C-SiC-SiO_2 by cracking carborane-siloxane (yield = 60 %) [58,91], polyborodiphenylsiloxane [58].

6. Conclusions

In industry, and even in the laboratory, the boron carbide powder obtained by arc melting, with a boron rich stoechiometry ($B_{4.3}C$) is generally used for sintering [1,12].

Direct synthesis has no pratical use.

If a deposit is needed, CVD (with BCl_3 or BBr_3) is convenient. Plasma assisted CVD, producing amorphous very hard thin films seems to be very promising (§ 3.2).

Concerning powders for the future, laser or plasma, give very fine, narrow sized, pure powders, with different stoechiometries, and reactive powders, which should be of great interest for sintering. The method is still in the R.D. period and products are still expensive (§ 5.1), but it is worthy of interest.

Cracking of organic precursors does not seem to be appropriate for an economic preparation of powders : yields are low, sometimes the final product is polyphased, the precursors are difficult to synthesise and very expensive. But "the development of two-phase ceramic materials from single polymers blends as a method of tailoring desired ... properties is also expected to receive increasing attention" [91]. I think that boron organic precursors should be convenient as sintering additives for industrial, good quality, boron carbide powders ; we showed that boron carbide can be pressureless sintered with the addition of both carbon and silicon carbide organic (polycarbosilane) precursors. This method makes it possible to obtain ceramics with high relative density ($\geq$ 92 % dth) and without free carbon, and a low final SiC content ($\approx$ 5 wt %). It was necessary to introduce a minimal amount of carbon which could act in deoxidizing the boron carbide starting grains and to create a second phase which inhibits grain coarsening, thus improving mechanical properties [12]. An organic boron precursor should eliminate the residual SiC.

Another point. Whiskers and platelets of SiC are now used to reinforce ceramic matrices (Al_2O_3, Al_2O_3-ZrO_2, mullite ...). Ceramists need classified whiskers (mean diameter 1-3 µm) and narrow sized distributed platelets of boron carbide, which could be used to reinforce ceramics (borides, carbides ...) or metals (aluminum, Al- Ti alloys ...); the two latter may be a new generation of ceramic-ceramic and ceramic-metal composites.

REFERENCES

1. Lipp, A. (1965-1966) 'Boron carbide. Production, properties, application', Techn. Rundschau, 14, 28, 33 ; 7; 47 pp.
2. Beauvy, M. and Thévenot, F. (1979) 'Le carbure de bore : matériau industriel performant, 2ème partie : applications industrielles du carbure de bore', Ind. céramique, 734 (12), 811-814.
3. Schwetz, K.A., Reinmuth, K. and Lipp, A. (1981) 'Herstellung und industrielle Anwendung refraktâre Borverbindugen', Radex Rundschau, 3, 568-585.
4. Schwetz, K.A. and Lipp, A. (1985) 'Boron carbide, boron nitride, and metal borides', Ullmann's Encycl. Indust. Chem., A4, 295-307.
5. Thévenot F. (1986) 'Quelques applications actuelles des borures', Silicates indus. 51 (1-2), 17-22.
6. Reinmuth, K., Lipp, A., Knoch, H. and Schwetz, K.A. (1984) 'Borhaltige keramische neutronenabsorberwerkstoffe', J. Nucl. Mater., 124, 175-184.
7. Bouchacourt, M. and Thévenot, F. (1985) 'The correlation between the thermoelectric properties and stoechiometry in the boron carbide phase B_4C-$B_{10.5}C$', J. Mater. Sci., 20, 1237-1247.
8. Bouchacourt, M. and Thévenot, F. (1981) 'Analytical investigations in the B-C system', J. less comm. Met., 82, 219-226.
9. Bouchacourt, M. (1982) 'Etudes sur la phase carbure de bore - Corrélations propriétés-composition', Thèse d'état, INPG, Ecole des Mines de Saint-Etienne (F).
10. Bouchacourt, M. and Thévenot, F. (1981)'The properties and structure of the boron carbide phase', J. less comm. Met., 82, 227-235.
11. Conard, J., Bouchacourt, M., Thévenot, F. and Hermann, G. (1986) '^{13}C aand ^{11}B N.M.R. investigations in the boron carbide phase homogeneity range : a model of solid solution', J. less comm. Met., 117, 51-60.
12. Thévenot, F. (1988) 'Sintering of boron carbide and boron carbide-silicon carbide two-phase materials and their properties', J. nucl. Mater., 152, 154-162.
13. Cueilleron, J. and Thévenot, F. (1977) 'Chemical properties of Boron', in V.I. Matkovich (ed.), Boron and refractory borides, Springer Verlag, Berlin, Heidelberg, New York, pp. 203-213.
14. Benton, S.T. and Masters, D.R. (1975) 'Boron carbide articles', US Patent 3,914,371.
15. Lifshits, E.V. Ostapenko, I.T., Postogvard, G.I., Snezhko, I.A. and Shevyakova, E.P. (1986), 'Formation of finely dispersed powders of crystalline boron carbide during synthesis from elements', Izv. Akad. Nauk. SSSR, Neorg. Mater., 22 (11), 1835-1838.
16. Bouchacourt, M., Brodhag, C. and Thévenot, F. (1981) 'The hot pressing of boron and boron rich compounds : B_6O, $B_{10.5}C$-B_4C', Sci. Ceram, 11, 231-236.
17. Brodhag, C., Bouchacourt, M. and Thévenot, F. (1983) 'Comparison of the hot pressing kinetics of boron, boron suboxide B_6O and boron carbides', in P. Vincenzini (ed.), Materials Science Monographs, 16. Ceramic powders, Elsevier, Amsterdam, pp. 881-890.
18. Bougoin, M. (1985) 'Frittage sans charge du carbure de bore et de composites carbure de bore-carbure de silicium. Propriétés mécaniques', thesis, Ecole des Mines de Saint-Etienne (F).
19. Treutler, C.P.O., Dienel, G., and Hohmuth , K. (1981) 'The decrease of the electrical sheet resistance of boron and the formation of boron carbide by ion implantation of C^+ ions into boron and subsequent annealing', J. less comm. Met., 80, 1-5.

20. Cochran, A.A. and Stephenson J.B. (1970)'Boron and boron carbide coatings by vapor deposition', Metallurgical Trans., 1, 2875-2880.
21. ibid. J. Metals, 22, 37-42.
22. Ploog, K.. (1973) 'Preparation of a rhombohedral boron carbide with the composition $B_{13}C_2$', J. less comm. Met., 31, 177-180.
23. Ploog, K.. (1974) 'Composition and structure of boron carbides prepared by CVD', J. cryst. growth, 24-25, 197-204.
24. Lartigue, S. (1986), 'Elaboration par CVD et caractérisation de dépôts de carbure de bore. Application au revêtement de l'acier', thesis, INP Grenoble (F).
25. Lartigue, S., Cazajous, D. and Male, G. (1986)'Dépôts chimiques en phase vapeur de carbure de bore sur carbure de tungstène fritté et sur acier', J. Phys., Colloque C1, suppl. n° 2, 47, C1-197-202.
26. Rey, J. (1988) 'Dépôt par LPCVD de carbures de bore sur cermets WC-Co', thesis, Limoges (F).
27. Amberger, E., Druminski, M. and Ploog, K. (1971) 'Das B-C System im kinetischen Bildungsbereich : pyrolytische Bildung kohlenstoffreicher B-C Phasen', J. less comm. Met., 23, 43-52.
28. Ploog, K. (1974) 'Gasphasenabscheidung von binären Bor-Kohlenstoff -Phasen bei Substrattemperaturen von 900 bis 1800°C', J. less comm. Met., 35, 131-145.
29. Bernard, C., Deniel, Y., Jacquot, A., Vay, P. and Ducarroir, M. (1975) 'Détermination des équilibres chimiques complexes dans les systèmes polyphasés. I méthode de traitement', J. less comm. Met., 40, 165-171.
30. Ducarroir, M., and Bernard, C. (1975) ' Thermodynamic domains of the various solid deposits in the B-C-H-Cl vapor system', Proc. Chemical Vapor Deposition Fifth Intern. Conf'. pp. 72-83.
31. Ducarroir, M. and Bernard, C. (1976), 'Thermodynamic domains of the various solid deposits in the B-C-H-Cl vapor system', J. Electrochem. Soc., 123, 136-140.
32. Lartigue, S. and Male, G. (1988) 'Contribution to the study of tetragonal compounds in the boron carbon system', J. Mater. Sci. lett., 7, 153-156.
33. Vandenbulcke, L. (1977), 'Influence de la convection sur la solidification dirigée d'alliages binaires et sur les dépôts chimiques en phase vapeur du bore et du carbure de bore', Thesis, Orléans (F).
34. Vandenbulcke, L., Herbin, R. Basutcu, M. and Barrandon, J.N. (1981) 'Etude expérimentale du dépôt chimique du carbure de bore à partir de mélanges trichlorure de bore, méthane et hydrogène', J. less comm. Met., 80, 7-22.
35. Vandenbulcke, L., Vuillard, G. (1981) ,'Composition and structural changes of boron carbides deposited by chemical vapor deposition under various conditions of temperature and supersaturation', J. less comm. Met., 82, 49-56.
36. Vandenbulcke, L. (1983) "Theoretical influence of the deposition conditions on the uniformity of boron carbide coatings', Proc. 4th europ. Conf. on CVD, J. Bloem, G. Verspui and L.R. Wolff (eds.), Philips, Eindhoven, 44-50.
37. Vandenbulcke, L. (1985) 'Theoretical and experimental studies on the chemical vapor deposition of boron carbide', Ind. Eng. Chem. Prod. Res. Dev., 24, 568-575.
38. Jansson, U.and Carlsson, J.O. (1985) 'Chemical vapor deposition of boron carbides in the temperature range 1300-1500K and at a reduced pressure', Thin solid Films, 124, 101-107.
39. Rebenne, H. and Pollard, R. (1987) ' Theoretical analysis of chemical vapor deposition of ceramics in an impinging jet reactor', J. Am. Ceram. Soc., 70, 907-918.
40. Jansson, U., Carlsson, J.O., Stridh, B., Söderberg, S. and Olsson, M. 'CVD of boron carbides. 1. Phase and chemical composition', Thin solid films, in press.

41. Olsson, M. Söderberg, S., Stridh, B., Jansson, U. and Carlsson, J.O. 'CVD of boron carbides. 2. Morphology and unicrostructure', Thin solid films, in press.
42. Cholet, V., Herbin, P. and Vandenbulcke, L. (1987) 'CVD of boron carbide from BBr_3-CH_4-H_2 mixtures into a microwave plasma', Proc. 9th intern. symp. Boron, Borides and related Compounds, Duisburg (FRG), Sept. 21-25, pp. 423-424.
43. Ploog, K. (1974) 'Gasphasenabscheidung von binären Bor-Kohlenstoffphasen bei Substrattemperaturen von 900 bis 1900°C. I Tetragonales und orthorhombisches Borcarbid', J. less. comm. Met., 35, 115-130.
44. Ploog, K. and Druminski (1974) 'Strukturchemische Characterisierung eines durch Gasphasenabscheidung darstellbaren orthorhombischen Borcarbids der Zuzammensetzung B_8C', Kristall und Technik, 9, 25-31.
45. Campbell, A.N., Mullendore, A.W., Tallant, D.R. and Wood, C. (1987) 'Low-carbon carbides produced by CVD', Mater. Res. Soc. Symp. Proc., 97, 113-118.
46. Kevill, D.N., Rissmann, T.J., Brewe, D. and Wood, C. (1986) 'Growth of crystals of several boron carbon compositions by chemical vapor deposition', J. cryst. growth, 74, 210-216.
47. Kevill, D.N., Rissmann, T.J., Brewe, D. and Wood, C. (1986) 'Preparation of boron-carbon compounds, including crystalline B_2C material by chemical vapor deposition', J. less comm. Met., 117, 421-425.
48. Veprek, S. and Jurcik-Rajman, M. (1985) 'Plasma induced deposition of amorphous boron carbide', Symp. Proc.- Int. Symp. Plasma Chem. 7th, 1, 90-94.
49. Toyoda, H., Sugai, H., Isozumi, T. and Okuda, T. (1987) 'Formation of pure-boron and boron-carbon alloys by a toroidal glow discharge', in ibid [42], 409-410.
50. Bouchacourt, M. and Thévenot, F. (1978) 'Etudes sur le carbure de bore. III Domaine d'existence de la phase carbure de bore', J. less comm. Met., 59, 139-152.
51. Bouchacourt, M. and Thévenot, F. (1979) 'The melting of boron carbide and the homogeneity range of the boron carbide phase', J. less comm. Met., 67, 327-331.
52. Eschnauer, H. and Kilp, F. (1977) 'Harstoffe und ihre Eigenschaften zum Plasmaspritzen', D.V.S. , Ber. 47, 44-50.
53. Thébault, J., Pailler, R., Bontemps-Moley, G., Bourdeau, M. and Naslain, R. (1976) 'Chemical compatibility in boron fiber-titanium composite materials', J. less comm. Met., 47, 221-233.
54. Naslain, R. Pailler, R. and Hagenmuller, P. (1982) 'Solid-state reactions in the processing and use of advanced inorganic composite materials', Mater. Sci. Monogr., 10, 766-814.
55. Park, Y.H., Narayen, D., Schmerling, M. and Marcus, H.L. (1984) 'Fatigue crack growth behaviour of Ti-6Al-4V metal matrix/continuous SiC and B_4C/B fibre composites', J. Mater. Sci., 19, 2239-2245.
56. Smith, W.D. (1977) 'Boron carbide fibers from carbon fibers' in ibid [13], pp. 541-551.
57. Newkirk, L.R., Riley, R.E., Sheinberg, H., Valencia, F.A., Wallace, T.C. (1979) 'Preparation of fiber reinforced-titanium diboride and boron carbide composite bodies', Report, LA-UR-79-969, CONF-791017-3, 11 pp.
58. Walker, B.E.Jr, Rice, R.W., Becher, P.F., Bender, B.A. and Coblenz, W.S. (1983) 'Preparation and properties of monolithic and composite ceramics produced by polymer pyrolysis', Ceram. Bull., 62, 916-923.
59. Mierzejewska, S. and Niemyski, T. (1965) 'Preparation of crystalline boron carbide by vapour phase reaction', J. less comm. Met., 8, 368-374.
60. Sugaya, T. and Watanabe, O. (1972) 'Morphology of boron carbide single crystals', J. less comm. Met., 26, 25-31.

61. Borchert, W. and Born, E. (1969) 'Uber Eigenschaften von zonengeschmolzenem Borcarbid', Krist. und Tech., 4, 293-301.
62. Mullendore, A.W. (1986) 'Chemical vapor deposition of boron-based refractory solids', in D. Emin. T. Aselage, C.L. Beckel, I.A. Howard and C. Wood (eds), Boron-rich solids, AIP, Conf. Proc. 140, Am. Inst. Physics, New York, pp. 41-50.
63. Mackinnon, I.D.R. and Smith, K.L. (1987) 'Chemical vapor deposited boron carbide : growth by a vapor-liquid-solid process', Mater. Res. Soc. Symp. Proc., 97, 127-132.
64. Weaver, S.C., Nixdorf, R.D. and Vaughan, G. (1987) 'Silicon carbide and boron carbide platelets and fibers' in J.G. Morse (ed.), Ind.-Univ. Adv. Mater. Conf., Proc. Conf. TMS Annu. Meet., Metall. Soc. pub., Warrendale, Pa., pp. 305-315.
65. Gatti, A., Mancuso, C., Feingold, E. and Mehan, R., (1967) 'Growth and characterization of boron carbide whiskers', J. Phys. Chem. Sol., Suppl. N° 1, 317-323.
66. Ahmad, I. and Capsimalis, G.P. (1969) 'Formation of filamentary single crystals of B, CaB_6, B_4C and B_7O, in J.W. Mitchell (ed.), Reactivity of solids, Wiley, Interscience Pub., New York, pp. 477-485.
67. Motoc, C. and Constantinescu, F. (1973) 'Growth and thermal etching of boron carbide', J. cryst. growth, 18, 29-33.
68. Bosch, F.M. (1962) 'Essai de synthèse du carbure et du nitrure de bore', Silicates indus., 27, 587-590.
69. Wickens, A.J. (1976) 'Formation of boron carbide in a high-intensity plasma", Chem. Ind. (London), 7, 316-317.
70. Becherescu, D., Marx, F. and Lazau, I. (1985) 'Use of plasma in boron carbide synthesis', Mater. Constr. (Bucharest), 15 (2), 92-94.
71. Vogt, G.J., Hollabaugh, C.M., Hull, D.E., Newkirk, L.R. and Petrovic, J.J. (1984) 'Novel r.f. plasma system for the synthesis of ultrafine silicon carbide and silicon nitride (Si_3N_4)' Mater. Res. Soc. Symp. Proc., 30, 283-289.
72. Cruiziat, B. (1970) 'Réalisation de quelques réactions chimiques à l'aide d'un chalumeau à plasma inductif', Thesis, Univ. Lyon (F).
73. Mac Kinnon, I.M. and Wickens, A.J. (1973) 'The preparation of boron carbide using a radio frequency plasma', Chem. Ind. (London), 800.
74. Mac Kinnon, I.M. and Reuben, B.G. (1975) 'The synthesis of boron carbide in a r.f. plasma', J. Electrochem. Soc., 122, 806-811.
75. Mac Kinnon, I.M., Hamblyn, S.M.L. and Reuben, B.G. (1977) 'Mechanism of formation of boron and boron carbide by reduction of boron trichloride in an r.f. plasma', I.C.P. Inf. Newsl., 3, 311-312.
76. ibid in P. Fauchais (ed.), Comm. Symp. Int. Chim. Plasmas, 3rd, Paper S.4.3, Univ. Limoges (F), 8 pp.
77. Knudsen, A.K. and Langhoff, C.A. (1986) 'Submicron-sized boron carbide powders', PCT Int. Appl. WO 86 04,524, US Appl. 700, 841, 12 Feb 1985, 37 p.
78. Knudsen, A.K. (1987) 'Laser-driven synthesis and densification of ultrafine boron carbide powders', Adv. Ceram., 21, 237-247.
79. Ramsay, J.D.F. and Avery, R.G. (1977) 'Improvments in or relating to the preparation of carbide powders', Brit. Pat. 1, 479, 727, 2 p.
80. Dufek, G., Wruss, W., Vendl, A. and Kieffer, R. (1976) 'Ein Beitrag zur Herstellung von feinkörnigem Borkarbid', Plansee. Pulvermet., 24, 280-283.
81. Harris, G.L. and Parsons, D.S. (1975), 'Boron carbide from water-alcohol solution of carbon source', U.S. Pat. 3,885,022.
82. Wada, H., Kuroda, K. and Kato, C. (1986) 'Preparation of boron nitride/boron carbide ceramics by pyrolysis of boric acid-glycerin condensation product', Mater. Sci. Res., 20, 179-185.

83. Koshida, R., Kosakabashi, H. and Ogasawara T. (1987) 'Manufacture of highly pure boron carbide powders for sintered materials', Jpn. Kokai JP 62,202,811.
84. Tanemoto, H., and Kubo, H. (1987) 'Manufacture of boron carbide powder', Jpn. Kokai JP 62,182,110.
85. Kouvetakis, J., Kaner, R.B., Sattler, M.L. and Bartlett, N. (1986) 'A novel graphite-like material of composition BC_3 and nitrogen-carbon graphites', J. Chem. Soc., Chem. Commun., 24, 1758-1759.
86. Ritter, J.J. (1987) 'A low temperature chemical process for precursors to boride and carbide ceramic powders', Adv. Ceram., 21, 21-31.
87. Ritter, J.J. (1986) 'Refractory borides and carbides', USP 4,606,902.
88. Wada, H., Ito, S., Kuroda, K. and Kato, C. (1985) 'The synthesis of boron nitride and boron carbide by pyrolysis of a boric acid/1,2,3-propanetriol condensation product', Chem. Lett., 6, 691-692.
89. Mirabelli, M.G.L. and Sneddon, L.G. (1988) 'Synthesis of boron carbide via poly (vinylpentaborane) precursors', J. Am. Ceram. Soc., 110, 3305-3307.
90. Rees, W.S. Jr and Seyferth, D. (1988) 'High-yield synthesis of boron carbide (B_4C)/boron nitride ceramic materials by pyrolysis of polymeric Lewis base adducts of decaborane', J. Am. Ceram. Soc., 71, C194-C196.
91. Wynne, K.J. and Rice, R.W. (1984) 'Ceramics via polymer pyrolysis', Ann. Rev. Mater. Sci., 14, 297-334.

PREPARATION AND PROPERTIES OF ICOSAHEDRAL BORIDES

T. L. Aselage, D. R. Tallant, J. H. Gieske,
S. B. Van Deusen, and R. G. Tissot
Sandia National Laboratories
Albuquerque, NM 87185-5800
USA

ABSTRACT. The electronic and thermal transport properties of refractory icosahedral boron-rich solids suggest the utilization of these unique solids as high-temperature semiconductors. Such applications will require high-quality, well-characterized materials. A variety of techniques have been used to prepare powders, ceramics, and single crystals of boron carbides and the icosahedral boron pnictides. X-ray diffraction, Raman spectroscopy, and ultrasound measurements have been used to probe boron carbide sample quality. Each of these measurements supports the structural model of boron carbides developed from analysis of transport data. Initial electrical conductivity measurements on these samples show no thermal hysteresis. The thermally-activated conductivity ($E_a \approx 0.17$ eV) is consistent with a bipolaronic hopping mechanism.

1. INTRODUCTION

Icosahedral boron-rich solids such as α-rhombohedral boron, boron carbides, and the icosahedral boron-rich pnictides $B_{12}P_2$ and $B_{12}As_2$ are very hard, refractory solids. The boron-rich pnictides and α-boron are wide bandgap insulators, while boron carbides are hopping-type semiconductors with exceptional transport properties. These mechanical and electrical properties derive from the unusual structures and bonding arrangements in the solids. These structures, depicted in Figure 1, are based on boron-rich icosahedra [1,2]: twelve-atom, twenty-sided polyhedra, with each side an equilateral triangle. The simplest structure, that of α-boron, is shown in Figure 1a. Here, a B_{12} icosahedron is located at each vertex of the rhombohedral unit cell. The icosahedra are bonded to one another by very strong two-center bonds along the unit cell edges and by inter-icosahedral three-center bonds that lie along the long diagonal of the unit cell. These three-center bonds are represented by dark triangles in Figure 1a. The icosahedral boron-rich pnictides and the boron carbides are derived from this simple structure. In the pnictides, depicted in Figure 1b, the three-center bonds of α-boron are replaced by a two-atom "chain" containing two phosphorus or arsenic atoms. In the boron carbides, Figure 1c, a three-atom chain lies along the long cell diagonal. At

R. Freer (ed.), The Physics and Chemistry of Carbides; Nitrides and Borides, 97–111.
© 1990 *Kluwer Academic Publishers. Printed in the Netherlands.*

the idealized B_4C stoichiometry, each icosahedron contains a single carbon atom ($B_{11}C$), and each chain is C-B-C [1,2]. Boron carbides exist, however, as a single phase material over a wide range of compositions: from just less than 20 atomic % C to as low as 9 atomic % C [3]. In this paper, the use of "B_4C" will represent the carbon-rich single phase limit, near to but somewhat less than the 20 atomic % C composition of the idealized B_4C stoichiometry. Structural changes that accompany changes in carbon concentration will be discussed in detail below.

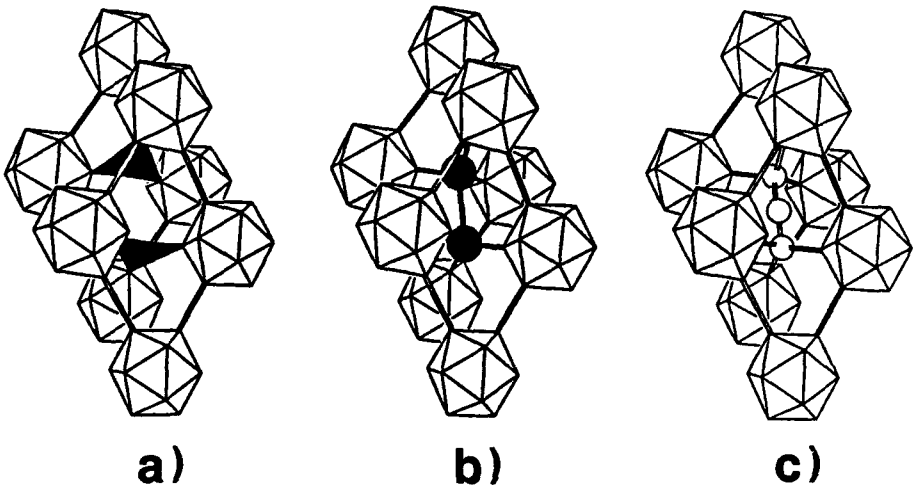

Fig. 1. Structures of icosahedral borides. a) α-rhombohedral boron. b) $B_{12}P_2$. c) boron carbide.

Despite the similarity of structure, the electronic properties of the boron carbides and the boron pnictides are quite different. The boron pnictides are wide-bandgap, transparent insulators [4] at room temperature. The electronic structure of the boron-rich pnictides is discussed elsewhere in this volume [5]. If doping can be controlled appropriately, these materials have the potential for utilization as high-temperature semiconductors [6]. Boron carbides, on the other hand, are p-type, bipolaron-hopping semiconductors with a large carrier density ($\approx 10^{21}/cm^3$) [7]. Several applications currently utilize the high-temperature electronic properties of boron carbides. Most of our work has focussed on the potential of boron carbides in very-high-temperature thermoelectric energy conversion [8], where boron carbides are the most efficient p-type material at high temperatures. Additionally, the thermally-activated electrical conductivity provides the basis for thermistors for use as automotive engine temperature sensors [9]. The B_4C/C thermocouple for very high temperatures (> 2000°C) [10] makes use of the large Seebeck coefficient of boron carbide.

Details of the theory of the bipolaronic conduction mechanism [11], the electronic and thermal transport measurements [12], and the

electronic structure of boron carbides [5] are presented elsewhere in this volume. Here, it is sufficient to note that one result of the transport analysis is a model for changes in the structure of boron carbides as carbon content is varied. As noted above, B_4C consists predominantly of $B_{11}C$ icosahedra and C-B-C chains. According to the transport-based model and a recent analysis of the change in free energy of boron carbides as boron substitutes for carbon [13], B-B-C chains first replace C-B-C chains as carbon content is reduced from B_4C. This substitution proceeds until the supply of C-B-C chains is exhausted, at the composition $B_{13}C_2$. Further reduction in carbon content is accomplished by replacing some of the icosahedral carbon atoms with boron. This model accounts for the p-type behavior of boron carbides over the entire single phase region. The replacement of C-B-C chains by C-B-B chains is also believed to be related to the transition in the thermal conductivity from crystal-like at high carbon concentration to glass-like at low carbon content [11,12,14]. Other structural models, based on x-ray diffraction data [15-17] or ^{13}C NMR results [18], differ with that proposed above. Our model, in particular, runs counter to the usual proposition that boron carbide with the composition $B_{13}C_2$ is comprised of B_{12} icosahedra and C-B-C chains [15,17].

Clearly, the use of boron-rich solids as electronic materials will place new demands on the quality of materials. In this paper, we shall describe the preparation of powders, ceramics, and single crystals of the icosahedral boron-rich solids. In addition, we will describe characterization techniques that we have employed to determine the sample quality. We will review the results of measurements [19-21] that provide evidence to support our structural model for the boron carbide solid solution. Finally, we shall comment on several areas for future work to enhance or expand the useful properties of these interesting materials.

2. EXPERIMENTAL PROCEDURES

2.1 Sample Preparation

Commercial boron carbide powder, typically with composition near B_4C, is frequently prepared by the carbothermal reduction of B_2O_3 [22]. In order to prepare small amounts of material with variable stoichiometry, we have used the solid-state reaction of a high purity, sub-micron amorphous boron powder (Callery Chemical Co.) with very high purity graphite powder (Ultra Carbon Corp.). These powders were primarily for use in precision lattice parameter determinations. The boron powder was first heated in a pyrolytic boron nitride (PBN) crucible (Union Carbide Corp.) under high vacuum (< 50 mTorr) to 1900°C. This removed surface contaminants (thought to be primarily oxygen) from the high surface area powder. The boron partially crystallized during this treatment, and some particle growth occurred. The desired boron carbide stoichiometry was obtained by mixing appropriate amounts of the treated boron with graphite. Powders were

prepared with B:C atomic ratios ranging from 4 to 12. These mixed powders were reacted in PBN crucibles with graphite lids at 1850°C for about 12 hours under Ar, reground, reheated at 1850°C for another 12 hours, and reground. Following this treatment, some amount of unreacted starting material was occasionally observed by x-ray diffraction. The powders were subsequently cold pressed into a pellet and reacted at 2000°C for 8 hours, with one intermittent regrind and pressing. The resulting powder patterns have very narrow diffraction peaks and, for sample compositions in the single phase region, show no evidence of second phases.

Powders of boron carbide are very difficult to sinter into dense ceramics. We have used uniaxial hot pressing to prepare dense ceramic samples. Boron powders, with either natural abundance or isotopically-enriched in ^{11}B or ^{10}B (Eagle-Picher Industries) were mixed (by shaking for several hours) with the high purity graphite powder. The use of ball mills in the mixing process was avoide as it leads to contamination of the sample. The powders were loaded into a graphite die with a high-purity BN die liner (Union Carbide Grade HBC) with inner diameter of 3/8" or 1/2". Graphite rams were used to apply pressure, and either graphite felt (graphoil) or tungsten foil was inserted between the boron carbide and the rams to prevent bonding (high purity BN crumbled when used between the rams and the sample). The system was heated at 15°C/min. under high vacuum and an applied load of 1500 psi to about 1650°C. Here, the atmosphere was switched to gettered argon and full pressure (5500-6000 psi) applied. Heating was resumed at 15°C/min. until the final die temperature of 2175°C was reached. After a 30 minute lag (for the interior of the die to reach the set temperature), the sample was held at temperature for 15 minutes. The system was then cooled to 1700°C at 5-10°C/min. (to avoid cracking), and finally cooled to room temperature by shutting off the furnace. Typically, the sample must be forced from the die liner, and the graphoil or tungsten foil bonds to the sample and must be removed by grinding. Small, shaped pieces of boron carbide were prepared by cutting with a low-speed diamond saw.

Boron carbide crystals are also of interest for structural and transport studies. Due to the refractory nature of boron carbide and problems associated with the incongruent melting [23] of the solid solution, growth of crystals from the melt is prohibitively difficult. Solution growth from metallic fluxes has, however, been used successfully to produce small (several mm) crystals of boron carbide [24]. Transition metals with filled or nearly-filled d shells (particularly Cu and Pd) have been used most successfully; these metals either do not form metal borides or they form less stable borides with no direct boron-boron bonding. Details of the growth conditions are given in Ref. 24. Briefly, about 10 w/o prereacted boron carbide powder was cold pressed with metal powder and melted at 1800°C. PBN crucibles and tubes were used to minimize contamination and to provide flat temperature profiles. The solution was slowly cooled (5-10°C/hr.) to ~ 1100°C. Crystals were recovered by dissolution of the metal matrix in aqua regia.

Considerably less work has been performed on the preparation of samples of the icosahedral boron-rich pnictides. Powders of these solids may be prepared by the thermal decomposition in vacuum of BP or BAs [24]. We have grown small single crystals of $B_{12}As_2$ using As vapor saturation of a molten Pd/B alloy at 1215°C [24]. These crystals exhibited a continuous range of opacity, from clear to black. These differences may be due to differences in Pd-rich inclusion density in the crystals. Because of the high vapor pressure of P or As at temperatures required for sintering or hot pressing, attempts to prepare dense ceramics of the boron-rich pnictides have not been successful.

2.2 Characterization

A variety of characterization techniques were routinely applied to ascertain the quality of our samples. Single crystal x-ray diffraction studies have been described elsewhere [1,2]. Powder x-ray diffraction of ceramics and powders was carried out using Cu Kα radiation on a Siemens D500 $\theta/2\theta$ automated diffractometer. Precision lattice parameter determinations employed a Si internal standard. Assignment of observed boron carbide reflections was based on the JCPDS B_4C standard [25], and lattice parameter refinement was performed using Siemens least squares software.

Raman spectra were obtained using a computer-controlled, scanning, double monochromator equipped with holographic gratings and a photon-counting photomultiplier tube [26]. Small single crystal samples were illuminated using a microscope accessory, while larger samples were illuminated with the laser beam focused to a 0.1 x 2 mm line. The 514.5 nm argon laser line was used for excitation. Background features (Rayleigh scattering, fluorescence) were removed by an empirical fitting procedure, and count axes have been scaled so as to normalize one of the more intense Raman bands in each spectrum.

Ultrasonic travel time data were obtained on thin boron carbide specimens with flat and parallel sides ranging from approximately 1.5 to 8 mm on a side. Both longitudinal and shear data were taken by the pulse-echo overlap method [27]. Longitudinal wave velocities were determined on all three faces of the specimen using 50 and 20 MHz transducers and the average was taken for moduli calculations. The measurements agreed to better than 1% from all faces of each specimen. The shear wave velocity could only be determined on the large face of the specimens using a 20 MHz transducer. Calculations of the elastic constants (Young's modulus E, shear modulus G, bulk modulus B, Poisson's ratio ν, and Lames' constants μ and λ) were made from the longitudinal velocity V_L, the shear velocity, V_S, and the sample density ρ using the following expressions:

$$\mu = \rho V_S^2 \qquad (1)$$

$$\lambda = \rho V_L^2 - 2\rho V_S^2 \qquad (2)$$

$$E = \mu(3\lambda + 2\mu)/(\lambda + \mu) \qquad (3)$$

$$G = \mu \qquad (4)$$

$$B = \lambda + (2/3)\mu \qquad (5)$$

$$\nu = \lambda/(2(\lambda + \mu)) \qquad (6)$$

Acoustic microscopy (f = 200 MHz to 1 GHz) was used to provide an image of boron carbide surfaces. This technique was particularly useful in identifying samples containing small cracks.

Four point electrical conductivity measurements were also made on the thin slabs of boron carbide described above. Gold wires were wrapped around the samples and were held in place at notches cut into the boron carbide with 1-2 mm spacings. Good electrical contact was assured by holding the sample between two flat, spring loaded PBN disks. The sample assembly and lead and thermocouple wires were contained within a quartz tube through which gettered Ar was passed. This tube was placed into the heated zone of a tube furnace equipped with a Na heat pipe. The programmable current source, digital voltmeter, and furnace controller were digitally-controlled using a minicomputer. Current levels were auto-selected (5-100mA) to provide voltage drops between 1 and 10 mV. The current during each measurement was precisely determined by measuring the voltage drop across a standard resistor in series with the sample. Forward and backward voltage drops were averaged to eliminate the effect of thermoelectric voltages. Measurements were made at intervals of 50°C. Steady state was assured by the criterion that conductivity values determined over ten minute intervals differ by no more than 1%. This criterion was usually met on heating. At low temperatures (< 400°C) during cooling, several attempts were usually required to meet this criterion due to the slow cooling rate of the furnace.

3. RESULTS AND DISCUSSION

3.1 Lattice Parameters

The high purity boron carbide powders described above were submitted for chemical analysis at two laboratories. Total boron was determined by titration of the mannitol complex [28] or by inductively-coupled plasma atomic emission spectroscopy [29], total carbon was determined by LECO analysis [28,29]. Boron to carbon ratios by analysis agreed with the batch ratios to within about 5% over all compositions. For the most B-rich compositions, the analyzed B:C ratios were uniformly low. This may indicate the loss of some boron due to evaporation during the high temperature reactions. The limiting composition of boron-rich boron carbide was determined by analysis of the free boron content (as nitric acid-soluble boron) [29] of samples with batch ratios of 10.5:1 and 12:1. This limiting value, about 9 a/o C (a ratio of 10:1), agrees very well with previous determinations [3].

The lattice parameters of these powder samples are plotted in Figure 2, along with values taken from the literature [1,2,15-17,30-35]. Our

results are seen to be in reasonably good agreement with the work of Bouchacourt and Thevenot [34] on hot-pressed samples. The point at which the increase in the a axis saturates at low carbon values is the lower phase boundary of boron carbide, again about 9 a/o carbon. Several factors may contribute to the large scatter in the rest of the data. First, the composition of boron carbides is frequently not well known. Thus, for compositions reported as B_4C, a values larger than 5.60 Å and c values larger than about 12.07 Å suggest that these samples were, in fact, of a more boron-rich composition. Second, small impurity concentrations can have a very large effect on the lattice parameter [2]. Also, internal stresses may affect lattice parameter values. Thus, boron carbide lattice parameters are indicative of carbon concentration for pure samples, but are sensitive to small impurity concentrations and internal stresses. We shall discuss another technique for verifying carbon content below.

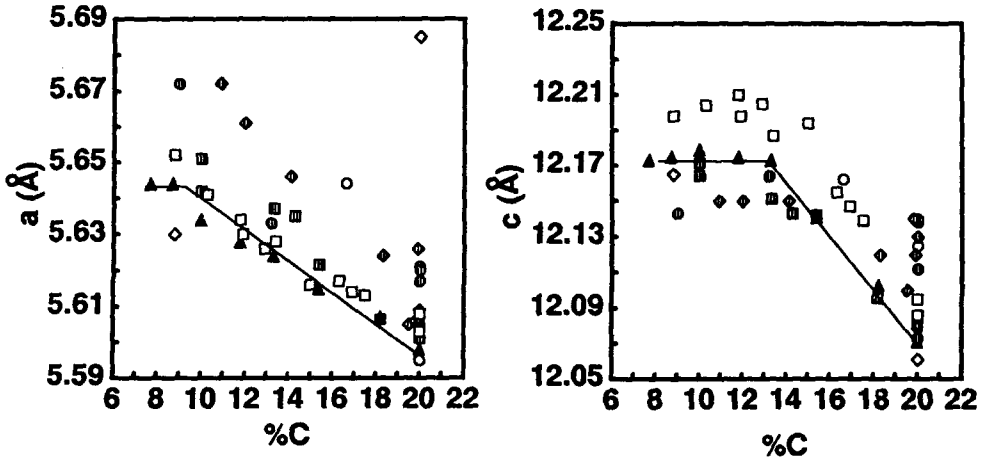

Fig. 2. Hexagonal lattice parameters of boron carbides vs. composition.—▲— this work, powder, ▥ this work, hot press, ◍ single crystals [1,2,15-17], □ hot press [34], ○ CVD [30,31], ◈ e-beam melted [32], and ◇ other preparations [33,35].

The variation of the lattice parameters with carbon concentration also supports our structural model of the boron carbide solid solution. The general increase in the size of the unit cell as carbon content decreases is consistent with the replacement of carbon atoms (covalent radius 0.77 Å) with somewhat larger boron atoms (0.82 Å). The a axis changes uniformly over the entire single phase region, with about 0.04 Å difference between the limiting compositions. The c axis, on the other hand, increases by 0.1 Å between B_4C and $B_{13}C_2$, then shows little further increase at lower carbon content. We can understand the c axis behavior in terms of the structural model. Figure 3 shows the hexagonal unit cell of boron carbides viewed along one of the basal plane unit vectors, say $\underline{a}_1$. The c axis is therefore in the vertical

direction on the page, and the three-atom chains are parallel to the c axis. The icosahedra in these solids are more compressible than the chains, so that the size of the unit cell is controlled by the size of the chains [1]. By replacing C-B-C chains with C-B-B chains, with a larger boron atom at one end and a B-B bond that is much weaker and softer than a C-B bond [14], we expect a longer chain unit and thus an increase in the c axis length. The break in the c axis increase at $B_{13}C_2$ occurs as the supply of C-B-C chains is exhausted; only C-B-B chains remain. Further substitution of B for C occurs within icosahedra, with a much smaller effect on the size of the unit cell.

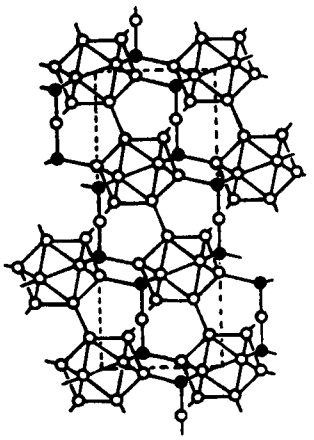

Fig. 3. Hexagonal unit cell of boron carbide, viewed along a basal plane unit vector. The c axis is vertical on the page, and the three-atom chains are parallel to c.

3.2 Raman Spectroscopy

Raman Spectroscopy has proven to be a very powerful tool in the analysis of boron-rich solids. In addition to local structural information, Raman spectra provide a semi-quantitative probe for carbon content in boron carbides and a check for the presence of amorphous carbon.

In an earlier study of the Raman spectra of hot-pressed boron carbides, Shelnutt et al. [36] observed two prominent broad bands centered at about 1365 and 1585 cm^{-1}. These Raman bands were clearly shown to be related to the presence of amorphous carbon in the samples. Indeed, they were absent from the spectra of chemical-vapor deposited material [36]. These carbon bands are also absent or vanishingly small in the Raman spectra of our hot-pressed boron carbide samples, indicating a substantial improvement in sample quality compared to the material used in the earlier studies. If a small amount of excess carbon is intentionally added during sample preparation, the amorphous carbon bands are readily observed. We do note, however, that infrared-active vibrational modes with frequencies near 1580 cm^{-1} <u>are</u> present in our samples. Thus, the IR mode comes from the boron carbide structure, and is most likely a chain-related vibration [37,38].

Figure 4 shows the Raman spectra obtained from hot-pressed samples with compositions between B_4C ($\leq$ 20 a/o C) and B_9C (10 a/o C) [19]. The broad bands with frequencies greater than 600 cm^{-1} are relatively insensitive to the carbon content. Two narrow bands, centered at 500 cm^{-1}, are most prominent at B_4C and gradually decrease in intensity as the carbon content decreases until, at $B_{13}C_2$ (13 a/o C), they have virtually disappeared. Below $B_{13}C_2$, a band near 380 cm^{-1} grows. These changes in the Raman spectra provide a semi-quantitative, non-destructive probe for carbon content in boron carbides. We have used this technique to identify the carbon content in boron carbide single

crystals (discussed below) and to study carbon gradients in hot-pressed samples due to contact with graphite or tungsten foil during the pressing. Carbon from the graphoil readily diffuses into boron-rich boron carbides. Typically, 500 μm must be removed from each end of a sample before the surface spectrum matches one taken from the interior side of the sample. Tungsten foil was used in an attempt to eliminate such diffusion. Here, we find that boron diffuses out of the boron-rich borides to form a tungsten boride interface, once again leaving a carbon-rich gradient of about 500 μm. Additionally, acoustic microscopy reveals cracking in samples pressed with a W foil interface, due to the lower thermal expansion coefficient of W compared to B_xC (43 x 10^{-7}/°C vs. 55-60 x 10^{-7}/°C). Other refractory metals with higher expansion coefficients (e.g. Ta) form eutectic liquids with boron at temperatures lower than the pressing temperatures. Thus, the best procedure seems to be the use of graphite felt with the subsequent removal of a 500 μm surface layer from each sample.

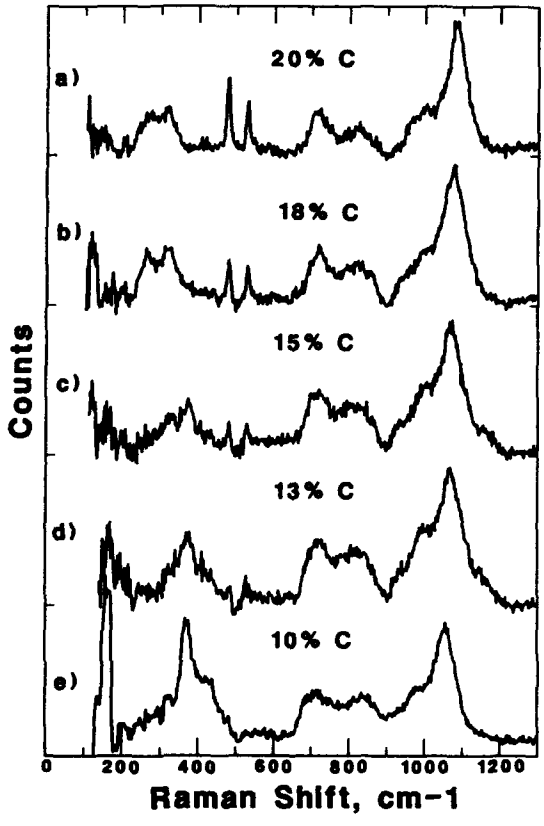

Fig. 4. Raman spectra of boron carbides with indicated compositions.

Based on an empirical comparison of the spectra of single crystals of α-boron, $B_{12}As_2$, and B_4C and of $B_{12}P_2$ powders [19], we have assigned Raman bands with frequency greater than 600 cm^{-1} to icosahedral vibrations, and bands with frequencies between 200 and 600 cm^{-1} to chain vibrations. These assignments are corroborated by normal coordinate calculations [39] and by the variation in intensity of the chain bands as the single crystals are rotated with respect to the polarization of the laser beam.

The Raman spectra shown in Figure 4 thus provide evidence of structural changes with composition in boron carbides. Consistent with the assignments described above, the narrow bands centered at 500 cm^{-1} are due to vibrations of the C-B-C chains [19]. These bands decrease in intensity between B_4C and $B_{13}C_2$, as C-B-C chains are replaced by C-B-B chains. The narrow Raman bands have virtually disappeared at

$B_{13}C_2$, the composition at which all of the C-B-C chains have been replaced.

The icosahedral bands of boron carbides are broad compared to the other icosahedral borides. Broad bands are more characteristic of a disordered solid or amorphous material than a well-ordered, crystalline material. We have interpreted this result [19] as being indicative of carbon atoms distributed among inequivalent sites in $B_{11}C$ icosahedra. Thus, in α-boron or the boron-rich pnictides, B_{12} icosahedra exist in a well-ordered environment and the Raman bands are narrow. In B_xC, $B_{11}C$ icosahedra are inherently disordered due to the distribution of carbon in inequivalent sites. This disorder is manifested in the broad icosahedral bands. Because the bands are broad over the entire single phase region, carbon must be present in the icosahedra at all compositions.

Thus, the Raman spectra of boron carbides support our structural model: 1) near B_4C, $B_{11}C$ icosahedra and C-B-C chains are the predominant structural units, 2) between B_4C and $B_{13}C_2$, boron replaces carbon in the chains, forming C-B-B chains, and 3) only for carbon concentrations below $B_{13}C_2$ does boron begin to replace carbon in icosahedral sites.

3.3 B_4C Single Crystals

Single crystal x-ray diffraction studies of our metal flux-grown crystals with composition near B_4C have been performed and confirm the presence of a single carbon atom in each icosahedron [2]. We have attempted to prepare single crystals with lower carbon content in order to perform additional structural studies. B:C ratios from 4:1 to 20:1 and a variety of metal solvents (Cu, Pd, Pt, Ni) have been employed in the solution growth procedure. We find that, regardless of B:C ratio and solvent choice, the resulting crystals have Raman spectra characteristic of B_4C. In addition, the lattice parameters of a number of individual crystals and of a powder generated from crushed crystals are very close to the values for B_4C. For the more boron-rich starting compositions, β-boron crystals are formed with the B_4C crystals. We conclude that, despite the wide single phase region of boron carbides, only B_4C crystals may be grown by the metal flux technique. This suggests that one reason for the width of the single phase region of boron carbides is the relative instability of β-boron. The free energy of boron is lowered by dissolution in the molten metal, and appears to be lowered even further by the presence of carbon in solution [40]. This lowering of the free energy of boron in solution drives the composition of boron carbide in equilibrium with the solution to its most energetically favorable value, near B_4C [13].

3.4 Sound Velocity and Elastic Constants

The thermal conductivity of boron carbides is surprisingly low, given the strong covalent bonding and light atoms that make up the solid [11,12]. In textbook formulations, the thermal conductivity of a solid is given by the formula

$$K = 1/3\ Cv\ell \qquad (7)$$

where K = thermal conductivity, C = phonon heat capacity, v = phonon velocity (speed of sound), and ℓ = phonon mean free path. In order to better understand the thermal transport behavior of boron carbides, we have measured the velocity of longitudinal and shear acoustic waves as a function of composition. The results of these measurements are shown in Figure 5. The longitudinal sound velocity in boron carbides, 1.2-1.4 x 10^6 cm/sec., is quite large, consistent with light atoms and stiff bonds. The cracking in samples pressed with W endcaps observed with acoustic microscopy was also reflected in the acoustic velocity measurements. Cracked samples exhibited badly distorted waveforms, large attenuation, and low values of the velocity (not shown in Fig. 5). Thus, the decrease in sound velocity below $B_{13}C_2$ observed in the data of Fig. 5 reflects changes in the boron carbide structure, not sample integrity.

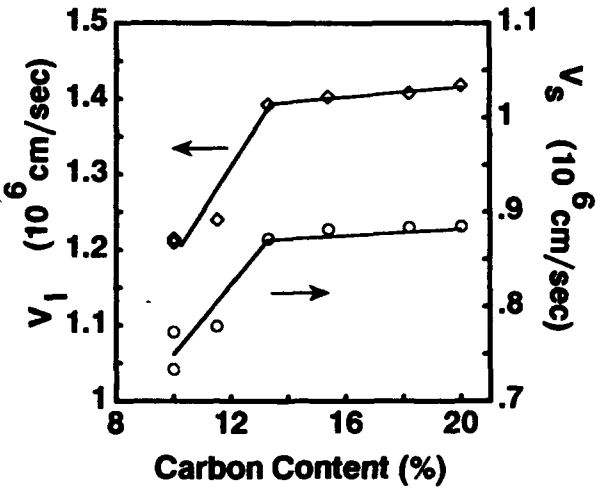

Fig. 5. Longitudinal and shear acoustic velocities (V_l and V_s) of boron carbides vs. composition.

The elastic constants derived from the sound velocity measurements using Equations (1) -(6) are listed in Table 1. The values for B_4C are in reasonable agreement with the literature [41]. We understand the large decrease in modulus below $B_{13}C_2$ to reflect a change in the stiffness of the most compressible structural unit, the icosahedron, as $B_{11}C$ icosahedra are replaced by B_{12} icosahedra [11]. Once again, the composition dependence of the sound velocities can be explained using the structural model.

Table 1: Elastic Properties of Boron Carbide

%Carbon	E(GPa)	G(Gpa)	ν	B(Gpa)
20.0	471	200	0.18	245
18.2	465	197	0.18	243
15.4	466	197	0.18	245
13.3	450	189	0.19	241
11.5	351	150	0.17	178
10.0	348	150	0.16	170
10.0	323	132	0.22	194

Using experimentally determined thermal conductivities, heat capacities, and sound velocities in equation (7), one derives phonon free mean paths as low as 2-3 Å at room temperature. Thus, the simple kinetic theory result (Equation (7)) for the thermal conductivity appears to be inadequate for boron carbides. An alternate formulation of the thermal transport is described elsewhere in this volume [11].

3.5 Electrical Conductivity

We have begun to measure the electrical transport properties of boron carbides using our well-characterized samples. The room temperature electrical conductivity was measured with a table-top version of the four point apparatus. The conductivity does not vary monotonically with carbon concentration; rather, the maximum conductivity is observed at $B_{13}C_2$ ($\approx$ 23 $(\Omega\text{-cm})^{-1}$). The lowest conductivity ($\approx$ 3 $(\Omega\text{-cm})^{-1}$) occurs at the most carbon-rich composition near B_4C. Once again, these observations are in agreement with the predicted composition dependence [6,7,11].

Previous measurements of the temperature dependence of the electrical transport properties of boron carbides always displayed some amount of thermal hysteresis [42]. This result has not been understood. We have measured the temperature dependence of the electrical conductivity of B_4C and $B_{13}C_2$ from room temperature to about 950°C. The results are plotted in Figure 5. Experimental difficulties (large background noise) were encountered during the initial heating of the B_4C sample. When this was corrected, the heating and cooling curves were quite reproducible and returned to the room temperature values determined in the table-top apparatus. The $B_{13}C_2$ conductivities were also reproducible with thermal cycling. Thus, no evidence for thermal hysteresis was found in our measurements.

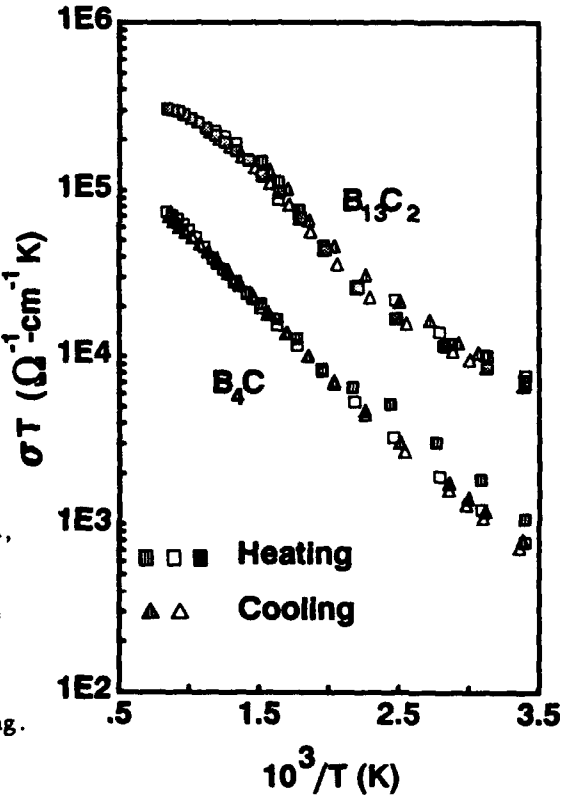

Fig. 6. Electrical conductivity vs. inverse temperature for B_4C and $B_{13}C_2$. Heating and cooling sequence as indicated.

Conduction in the boron carbides occurs by a bipolaronic hopping mechanism [6,7,11]. The temperature dependence of

the B_4C sample above about 350K is consistent with the adiabatic, semi-classical limit for such hopping, $\sigma \propto (1/T)\exp(-E_a/kT)$, with an activation energy of 0.17 eV. Interestingly, the conductivity of the $B_{13}C_2$ sample has more curvature than B_4C at both the low- and high-temperature ends. These differences may reflect the increasing disorder present in $B_{13}C_2$ compared to B_4C, as 1) the CBB chains have an orientation (up or down), whereas CBC chains are symmetrical, and 2) the chain-bonding sites within an icosahedron may be more accessible to icosahedral carbon when bonded to the boron end of a CBB chain. We shall continue these measurements on other low-carbon boron carbides to further explore such effects.

4. CONCLUDING REMARKS

The preparation and characterization of high quality materials is an essential step in the development of electronic applications of icosahedral borides. We have shown that high quality boron carbide powders, ceramics, and crystals can be made, and that x-ray diffraction, Raman spectroscopy, and ultrasonic measurements are useful probes of phase purity, composition, and sample quality. The structural model for the boron carbide solid solution is supported by a vast array of measurements, including the lattice parameters, Raman spectra, acoustic velocity, and electrical conductivity data described in this paper. The essential features of this model are 1) the presence of $B_{11}C$ icosahedra throughout the single phase region, and 2) the replacement of C-B-C chains with C-B-B chains as carbon content is reduced from B_4C.

Thus, many questions regarding the properties of boron carbides have been addressed. Our work in the future will address several remaining structural questions. In particular, we will try to understand the IR spectra of boron carbides in terms of our structural model, and we shall use ^{13}C MASS NMR to further study the location of carbon in the solid solution as a function of composition. In addition, we shall continue to measure the high-temperature electronic transport properties (conductivity and Seebeck coefficient) of our samples to study the effect of composition and disorder. Finally, we shall study the possibility of preparing n-type boron carbides by doping. These n-type boron carbides would then form the basis for an all boron carbide thermoelectric couple.

We foresee a growing effort in the preparation of large, pure icosahedral boron pnictide materials. We shall attempt to prepare ceramics by hot isostatic pressing and crystals by melt growth under pressure. Given suitable samples, we shall attempt to identify suitable n- and p-type dopants and try to control doping to appropriate levels for high temperature semiconductor applications.

ACKNOWLEDGEMENTS

Work performed at Sandia National Laboratories is supported by the US Department of Energy under contract #DE-AC-04-76DP00789.

REFERENCES

1. Morosin, B., Mullendore, A., Emin, D., and Slack, G., in Boron-Rich Solids, pp.70-86, D. Emin, T. Aselage, C. Beckel, I. Howard, and C. Wood, eds., American Institute of Physics, New York 1986.
2. Morosin, B., Aselage, T., and Feigelson, R., in Novel Refractory Semiconductors, MRS Symposium Proceedings Vol. 97, pp. 145-150, D. Emin, T. Aselage, and C. Wood, eds., Materials Research Society, Pittsburgh 1987.
3. Bouchacourt, M., and Thevenot, F., J. Less-Common Metals, 82, 219 (1981).
4. Slack, G., McNelly, T., and Taft, E., J. Phys. Chem. Solids, 44, 1009 (1983).
5. Switendick, A., this volume.
6. Emin, D., in Novel Refractory Semiconductors, Ref. 2, pp. 3-16.
7. Emin, D., in Boron-Rich Solids, Ref. 1, pp. 189-205.
8. Wood, C., in Boron-Rich Solids, Ref. 1, pp. 362-372.
9. See, for example, Ceramic Bulletin, 68, 1264 (1989).
10. Hunold, K., Chemie-Technik, 14, 82 (1985).
11. Emin, D., this volume.
12. Wood, C., this volume; Wood, C., and Emin, D., Phys. Rev. B 29, 4582 (1984); and Wood, C., Emin, D., and Gray, P., Phys. Rev. B 31, 6811 (1985).
13. Emin, D., Phys. Rev. B, 38, 6041 (1988).
14. Emin, D., Howard, I., Green, T., and Beckel, C., in Novel Refractory Semiconductors, Ref. 2, pp. 83-88.
15. Will, G., and Kirfel, A., in Boron-Rich Solids, Ref. 1, pp. 87-96; Kirfel, A., Gupta, A., and Will, G., Acta Cryst., B36, 1311 (1980); Kirfel, A., and Will, G., Acta Cryst., B36, 512 (1980); Kirfel, A., Gupta, A., and Will, G., Acta Cryst. B35, 2291 (1979); Kirfel, A., Gupta, A., and Will, G., Acta Cryst. B35, 1052 (1979).
16. Yakel, H., Acta Cryst., B31, 1797 (1975).
17. Larson, A., in Boron-Rich Solids, Ref. 1, pp. 109-113.
18. Duncan, T. in Boron-Rich Solids, Ref. 1, pp. 177-188; Duncan, T., J. Amer. Chem. Soc., 106, 2270 (1984).
19. Tallant, D., Aselage, T., Campbell, A., and Emin, D., J. Non-Cryst. Solids, 106, 370 (1988); Tallant, D., Aselage, T., Campbell, A., and Emin, D., Phys. Rev. B, accepted.
20. Aselage, T., and Tissot, R., manuscript in preparation.
21. Gieske, J., Emin, D., and Aselage, T., manuscript in preparation.
22. Bose, D., Nair, K., and Gupta, C., High Temp. Materials and Processes, 7, 133 (1986).
23. Bouchacourt, M., and Thevenot, F., J. Less-Common Metals, 67, 327 (1979).

24. Aselage, T., in Novel Refractory Semiconductors, Ref. 2, pp. 101-111.
25. Joint Committee on Powder Diffraction Standards File Card #35-798 (International Centre for Diffraction Data, Swarthmore, PA 1987).
26. Tallant, D. and Higgins, K., Proc. of the Scientific Applications of Lasers Symp., Laser Institute of America, 42, 12 (ICALEO 1983).
27. Papadakis, E., Rev. Sci. Instrum., 47, 806 (1976).
28. Galbraith Laboratories, Inc., Knoxville, TN.
29. Chambers, W. B., Sandia National Laboratories, Albuquerque, NM.
30. Kevill, D., Rissman, T., Brewe, D. and Wood, C., J. Cryst. Growth 74, 210 (1986).
31. Mierzejewski, S., and Niemyski, T., J. Less-Common Metals, 8, 368 (1965).
32. Bouchacourt, M., Thevenot, F., and Ruste, J., J. Less-Common Metals, 59, 139 (1978).
33. Matkovich, V. I., J. Less-Common Metals, 47, 39 (1976).
34. Bouchacourt, M., and Thevenot, F., J. Less-Common Metals, 82, 227 (1981).
35. Sugaya, T., and Watanabe, O., J. Less-Common Metals 26, 25 (1972).
36. Shelnutt, J., Morosin, B., Emin, D., Mullendore, A., Slack, G., and Wood, C., in Boron-Rich Solids, Ref. 1, pp. 312-324.
37. Becher, H., and Thevenot, F., Z. Anorg. Allg. Chem. 410, 274 (1974).
38. Werheit, H., and Haupt, H., Z. Naturforsch. 42a, 925 (1987).
39. Beckel, C. University of New Mexico, Albuquerque, NM, unpublished results.
40. Storms, E., and Szklarz, E., J. Less-Common Metals 135, 217 (1987).
41. Ramanamurthy, S., J. Mat. Sci. Lett., 4, 603 (1985).
42. Wood, C., in Boron-Rich Solids, Ref. 1, pp. 206-215.
43. Emin, D., in Electronic and Structural Properties of Amorphous Semiconductors, pp. 261-328, P. LeComber and J. Mort, eds., Academic Press, New York 1973.

PRODUCTION, FABRICATION AND USES OF BORIDES

R. THOMPSON
Advanced Ceramics Unit,
RTZ Chemicals Limited,
Cox Lane,
Chessington,
Surrey KT9 1SJ.

ABSTRACT. Industrial methods for the production of metal boride, boron carbide and boron nitride powders are reviewed, and reference made to the fabrication of artefacts by processes such as hot-pressing. Applications are indicated with special attention to the valuable properties displayed: very high hardness and the resistance to attack by molten metals. Special uses include the high added-value areas of the nuclear and electronics industries.

1. INTRODUCTION

Boron combines with most other elements. Compounds with metals, the true borides, display largely metallic properties except that brittleness rather than toughness categorises also as ceramic. The latter definition classifies more exactly two related binaries formed with non-metals: boron carbide and boron nitride. Like the metal borides they are produced as powder and fabricated by similar ceramic-type routes, while their refractoriness dictates uses on their own or as property modifiers for borides and other non-boron ceramics.

2. POWDER PRODUCTION METHODS

Industrial production processes for these materials are generally of a pyrometallurgical nature, with carbothermic reduction of the oxides to the fore in the cases of the metal borides and boron carbide. All of these products have melting points well in excess of 2000°C. The oxide reduction reactions are endothermic and proceed at above about 1400°C, but in order to achieve a practicable production rate they are mostly carried out at some 500°C higher. These reductions are typified by the following equations:

$$MO_2 + B_2O_3 + 5C = MB_2 + 5CO \qquad (1)$$

R. Freer (ed.), The Physics and Chemistry of Carbides; Nitrides and Borides, 113–120.
© 1990 Kluwer Academic Publishers. Printed in the Netherlands.

$$M_2O_3 + 6B_2O_3 + 21C = MB_6 + 21CO \quad (2)$$

$$2B_2O_3 + 7C = B_4C + 6CO \quad (3)$$

TiB_2 is the archetypal diboride, and produced on an industrial scale (possibly in the order of 100 tonnes per annum, world-wide) either by equation 1) or from boron carbide (see below). When made according to the route of the above equation, powdered boric oxide and carbon are mixed in the appropriate proportions with titanium dioxide, readily available in pure form as the pigment grade. The powder mixture is briquetted and heated in suitable graphite furnaces. The product from reaction at around 2000°C is a loose clinker of TiB_2 crystals, whose melting point is 1000°C higher. The reaction temperature needs to be reduced by several hundred degrees for the lower-melting CrB_2, but most other diborides (and the hexaborides, which are formed by rare-earth metals) can be made at 2000°C.

Producers who have low-cost boron carbide available can use this as a pre-reduced form of boron for boride production, for example:

$$B_4C + 2TiO_2 + 4C = 2TiB_2 + 5CO \quad (4)$$

Procedure may again be heating the powder mixture, or briquettes thereof, in graphite tube resistance or induction furnaces; or, alternatively, the carbon may be contributed along with the heat source in the form of a buried carbon resistor rod or use of the carbon arc principle.

What has been said for boride production can also apply to making boron carbide itself, according to equation 3). The product of commerce ranges from a fused clinker (boron carbide melts at around 2500°C), via an abrasive grit to a fine powder, the last two being made by comminution of the first. When made at lower temperatures, in resistance tube furnaces or similar, a fine powder results directly. Metal borides and boron carbide are extremely hard substances (harder than tungsten carbide and all oxides) and a balance needs to be struck between the time and energy consumption of making ab initio as a fine powder, and of grinding the more rapidly produced fused clinker. The hardness is such that unless resort is made to fluid-energy milling, contaminants (the materials of the grinding mill or media) are picked up during comminution and it may be necessary to remove subsequently by acid leaching.

Although other production methods have been evaluated, and employed on a development-quantity scale, little has changed in production principles in the past 20 years or so [1]. Other routes examined include plasma reduction of the chlorides with hydrogen, e.g.:

$$TiCl_4 + 2BCl_3 + 5H_2 = TiB_2 + 10HCl \quad (5)$$

$$CH_4 + 4BCl_3 + 4H_2 = B_4C + 12HCl \quad (6)$$

$$2BCl_3 + 3H_2 = 2B + 6HCl \quad (7)$$

During the early 1970's, RTZ Borax developed this technology at its Chessington, Surrey, Research Centre and entered production of high-purity, sub-micron "plasma boron" (equation 7) and offered borides made in the same way. Such processes are scale-dependent and demand then was insufficient to warrant a full production unit involving the recycle of chlorine species. For completeness it should be mentioned that elemental boron, which is very expensive to produce in pure form, has similar physical properties to boron carbide and the borides. It is occasionally used chemically for the direct combination with metals, or the wasteful borothermic reduction of metal oxides, to make small quantities of borides (usually of the rare-earths) for research purposes or the electronic industry [1].

More recently the "self-propagating" (exothermic) aluminothermic route has begun to be re-examined for borides production, notably in the Soviet Union, the U.S.A. [2] and Japan [3]. This is analogous to the early magnesiothermic method used to make so-called "Moissan boron", but all such metallothermic processes (with the exception for making low-melting chromium monoboride, which separates from the slag) demand post-treatment such as acid leaching to remove by-products.

Boron nitride is made by rather different methods. For commercial powder manufacture, most producers now prefer medium-to-high temperature reaction between boric acid or oxide and a nitrogenous organic such as urea or melamine in a nitrogen atmosphere. Many other routes have, however, been tried [1]. The product is the soft hexagonal crystal form, isostructural with graphite (and sometimes called "white graphite"). Just as graphite itself can be made in pyrolytic form, so also can BN. The method used is to react a stoichiometric mixture of boron trichloride and ammonia, the product being deposited on a heated substrate to provide a coating, or onto a removable mandrel to give a free-standing object (e.g., crucibles used for the melting of gallium arsenide are made in this way). Similarity between boron nitride and carbon is further maintained in the cubic structure type, obtained from the hexagonal by high-temperature, high-pressure transformation in equipment as used for synthetic diamond production. Cubic boron nitride, "Borazon" or "CBN", is thus similarly as expensive as diamond but is nevertheless widely used for the machining of ferrous metals.

3. FABRICATION

Most applications designed to exploit the unique properties of these boron binaries, or mixtures containing them, need items made at, or near, zero porosity. Unlike metals, none of these materials can be melted and cast. Not only are the melting points so high as to make

this impractical, but only carbon is sufficiently refractory to be used as a mould material; and even its use is precluded by chemical reaction with the molten borides. Casting of boron nitride is excluded by its not melting but decomposing into its elements at high temperature.

As with many other so-called advanced ceramic materials, when starting from the powders resort needs to be made to fabrication techniques similar to those evolved over the years in the powder metallurgy and clayware industries. A particular problem however is encountered with the boron binaries: they do not self-sinter satisfactorily without applied pressure, and no suitable sinter-aids (such as are used in the fabrication of the nitrides of aluminium or silicon) have been described in the literature. Thus, in order to achieve compactions of about 80% of theoretical (20% porosity) or better, the only successful technique is hot-pressing.

Boron carbide, boron nitride and most borides are fabricated routinely by hot-pressing in graphite dies at around 2000°C. Some items can be pressed to near net shape, such as small cylinders of boron carbide used as nuclear reactor control rod pellets (see below) or shot-blast nozzles; which is desirable in view of the extreme hardness of the material, necessitating diamond machining when further shaping is required. More refined press design enables large square plates to be compacted to high density, very necessary for the production of ceramic armour (see below) from boron carbide or titanium diboride. Boron nitride, on the other hand, is sufficiently soft to be machined to shape with woodworking tools. Most components made from hexagonal BN are carved from hot-pressed billets, and with care the swarf may be re-cycled. Similar considerations apply to the TiB_2-BN composite prepared for use in the vacuum metallising industry (see below). Hot isostatic pressing ("HIPing") of borides is now technically practicable, but not economically viable.

In the case of boron nitride it is not entirely accurate to say that sinter-aids have not been developed, for paradoxically this material cannot even be hot-pressed to high density without one. The usual "aid" is boric oxide, several per cent of which needs to be added to the BN powder (unless it is present already, as in the case of the lower commercial grades) to enable it to form a dense machinable ceramic. A very recent paper [4] epitomises the problems by attempting to produce items by the pressure-less sintering of a "mechanochemically activated powder", which is really nothing more than boron nitride powder subjected to excessive and prolonged grinding in air in order to hydrolyse the particle surfaces. All inter-particle bonding when BN is sintered on its own derives from the -B-O-N- boroxole linkages.

If heated to a sufficiently high temperature (and the finer the particle size, the lower this can be), boron carbide and all metal borides will, of course, self-sinter without applied pressure. But,

as is stated above, discontinuous porosity and the realisation of optimum mechanical properties can only be achieved by hot pressure compaction. If for any application a lower percentage of theoretical density can be tolerated, borides are amenable to the standard method of cold-pressing (including cold isostatic pressing), injection moulding and slip-casting (in all cases using a fugitive organic binder to improve "green" strength, followed by sintering. Porous coatings can be laid down by plasma spraying [1], and fully-dense ones by chemical vapour deposition ("CVD") using boron trichloride and methane (for B_4C) or the appropriate volatile metal halide.

The literature abounds with novel variations on the fabrication theme. An interesting more recent development is of reactive infiltration of the porous sintered item, in this case of aluminium into boron carbide followed by pressure-less re-heating to form a hard, glassy B-C-Al ternary compositon [5]. Unfortunately some of the hardness of the boron carbide is lost, but compensated for in reduced brittleness. As with all advanced ceramics, compromise is often necessary. Attempts have been made to develop titanium diboride as a cutting tool in substitution for the softer tungsten carbide (TiC and Ti(C,N) already being contenders), but the equivalent of cobalt as a reactive sinter aid has yet to be discovered.

4. APPLICATIONS

Uses for these materials are best summarised under the heading of the principal attractive attribute, although it is often a combination of properties which justifies these relatively expensive products; for example, the metallic electrical conductivity of TiB_2 plus its resistance to attack by molten (and even boiling) aluminium.

4.1. Applications Based on Extreme Hardness

Such uses fall into mainly two categories: as wear-resistance engineering components, and as abrasive or cutting materials. Boron carbide, which is harder than the free element or the metal borides, and is also much cheaper than either to produce, is used for both purposes. Its great hardness and the abrasion-resistance of its hot pressings are epitomised by the fact that shot-blast nozzles are the most commonly encountered form of this component. Hot pressings made from a finer grade of B_4C can take a mirror polish and have found use as virtually frictionless bearings for use in aircraft gyrocompasses. A military application has, however, accounted for by far the greatest use of hot-pressed boron carbide. Beginning with the Vietnam war, the U.S. forces began to use pressed tiles as lightweight ceramic armour for personnel jackets and in protection of helicopter gun-ships and the crew seats of fighter aircraft. As pressing technology devloped (encouraged by the requirement) it became possible to press monolithic breast plates. More recently it became realised that although titanium diboride pressings are almost twice as heavy for a given

plate thickness, they have an important place in the protection of ground-based military vehicles.

4.2. Applications Based on Resistance to Molten Metals

It was the total resistance of titanium diboride to attack by molten aluminium, coupled with the complete wetting of the surface, which more than any other factor stimulated the development of borides as industrial materials some thirty years ago [6]. The use for which it was intended, that of cathode leads in the Hall-Heroult electrolytic cell for the production of aluminium from a cryolite melt, has yet to be implemented on a commercial scale. Arising from the perceived need, much research was done in the early 1960's into the production of TiB_2 powder and hot-pressing it into bars of 98% theoretical density and of dimensions 21 inches long by 3 inches in diameter. Each of these bars could carry 5000 amps, and an assembly of them was arranged to connect the cathode bus-bars to the molten aluminium pool on the base of the cell. Thus the interface between the aluminium and the carbon base was by-passed, avoiding the electrical resistance (Al does not wet carbon) which accounts for much energy wastage in the production of the metal. The high cost of hot-pressing each bar individually, and the vast number required, militated against adoption. However, some quarter-century later, there is renewed interest and the concept is being re-engineered. It has long been realised [6] that if aluminium could constantly be drained off the cathode and just a thin film left (instead of a pool continuously rising and falling, as well as swirling in the electron-magnetic field), the anode could be brought much closer. This reduction of anode-cathode distance would further contribute to energy saving. In fact, it has been estimated that the combination of effects could save as much as 40% of the energy [7]. What was needed was a materials and design break-through, and this has possibly come about by a development described at a conference just a few years ago [7]. The notion is to disperse titanium diboride grains in a matrix of carbon and a special resin, which is then applied to the entire cell base. Tests showed that provided the concentration of TiB_2 particles is sufficiently high, the entire composite surface is wetted by aluminium.

Knowledge that TiB_2 is totally wetted by molten aluminium and not seriously affected by it even at the boiling point of the metal has transformed another industry: vacuum metallising of plastic film, used extensively in the packaging industry Resistance-heated evaporation crucibles ("evaporator boats") are now made in very large numbers from a hot-pressed composite of titanium diboride and boron nitride, sometimes with the addition of aluminium nitride. Compaction to high density of a mixture of electrially-conducting TiB_2 and the insulating nitrides enables a product of suitable resistivity for direct resistance heating, the boat then becoming the container and heating element in one. This outlet consumes at the present time a significant proportion of the total production of these compounds.

4.3. Metallurgical and Chemical Applications

Nickel-boron alloys and the lower boride of chromium have found use in the production of welding- and hard-facing alloys. The most important binary with iron is an alloy rather than true boride, containing about 15 wt.% B. It is used to introduce boron into steel (at about 0.002%) in order to improve hardenability, and in much higher concentrations for nuclear shielding. When an alloy approximating to $Fe_{80}B_{20}$ is quenched from the molten state at 1,000,000°C per second, a so-called glassy or amorphous metal results. Large tonnages of this are beginning to be used as laminates for electricity power transformers. Master-alloys for the grain refinement of commercial aluminium alloys contain very finely dispersed particles of TiB_2, precipitated in situ by the addition of fluoborates and fluotitanates to the molten metal. A chemical use for boron carbide is in the production of boron trichloride by the exothermic reaction with gaseous chlorine. Much of the BCl_3 made commercially is used in the production of boron filament for metal and plastics reinforcement purposes.

4.4. Nuclear Applications

The ^{10}B isotope, present to about 20% in natural boron, is a strong absorber of thermal neutrons and hence finds extensive use in the nuclear energy industry. Rather than employ the element itself, which is both costly and difficult to fabricate (hot-pressing in graphite dies is generally not possible because of reaction), it is normally preferred to use boron carbide which contains 78% B. An interesting and hopefully exceptional use of boron carbide for neutron absorption was the dropping of 45 tonnes onto the Chernobyl reactor within a day or two of the disaster. It is surprising that so much of this speciality material was so readily available, as such a major catastrophe could hardly have been foreseen. It is possible that the Soviet Union called from a stockpile intended for lightweight ceramic armour.

4.5. Electrical and Electronic Uses

Most boron nitride fabrications are destined for use in this sector. The product is the rare combination (AlN and BeO are others) of an electrical insulator while being a very good thermal conductor. Thus use is found in substrates and elsewhere in circuitry where heat dissipation is required. The only known use for the rare-earth hexaborides (which are all highly coloured in shades of red and blue, whereas other borides are metallic grey) until recently was as cathodic emitters, LaB_6 being a prime example and also having been studied as a cold cathode. However, in extension of work on the rapidly-quenched ferroboron alloys, materials of composition typified by $Fe_{14}Nd_2B$ have been developed for use as magnet alloys as a generation to succeed cobalt-samarium.

REFERENCES

1. Thompson, R. (1965), 'Borides: Their Chemistry and Applications" Royal Institute of Chemistry Lecture Series, No. 5.

2. Zavitsanos, P.D. and Morris, J.R. (1983), 'Synthesis of Titanium Diboride by a Self-Propagating Reaction' Ceram. Eng. Sci. Proc., 4, (7-8), 624-33.

3. Miyamoto, Y., Koizumi, M. and Yamada, O. (1984), 'High-Pressure Self-Combustion Sintering for Ceramics'. J. Amer. Ceram. Soc., 67, (11), C-224/5.

4. Hagio, T., Kobayashi, K., Yoshida, H., Yasunaga, H. and Nishikawa, H., (1989), 'Sintering of the Mechanochemically Activated Powders of Hexagonal Boron Nitride', J. Amer. Ceram. Soc., 72, (8), 1482-4.

5. Halverson, D.C., Pyzik, A.J. and Aksay, I.A. (1986), United States Patent No. 4,605,440.

6. Ransley, C.E. (1962), 'Refractory Carbides and Borides for Aluminium Reduction Cells'. Journal of Metals, 14, 129-35.

7. Cooke, A.V. and Buchta, W.M. (1985), 'Use of TiB_2 Cathode Material: Demonstrated Energy Conservation in VSS Cells'. Light Metals, TMS AIME, New York (Conference, February 1985).

LASER ABLATION ICP-MS ANALYSIS OF CERAMIC MATERIALS

I. D. Abell, D. Gregson, S. Shuttleworth,
VG Elemental Ltd,
Ion Path, Road Three,
Winsford, Cheshire,
CW7 3BX, UK

1. Abstract

The chemical analysis of ceramic materials is notoriously difficult, especially when looking for low levels of impurity. Yet the effects of contaminates, even at low levels, can have profound effects on the performance characteristic of the ceramic. LA-ICP-MS can overcome the difficulties normally associated with the analysis of ceramics by directly vaporising the solid sample, forming an aerosol which is injected into the plasma where it is ionised. Use of the technique will be illustrated by analysis of ceria, silicon nitride and silicon carbide.

2. Introduction

ICP-MS is an analytical technique which can yield information on the relative concentrations of the elements in a sample. To convert this information into absolute values, the instrument must be calibrated using standard reference materials which, in the case of solutions, is a fairly straightforward procedure. However ceramic materials are resistant to dissolution making this route to quantitative analysis inappropriate for these materials. Solid sampling can currently be achieved by two routes: slurry nebulisation or laser ablation (LA) of the sample. The former risks contamination of the sample during the grinding process and can be time-consuming, thus reducing sample throughput. The latter technique involves little or no sample preparation and little or no risk of contamination. The sample can be presented in virtually any form (powder, finished component, fragment, etc) and sample throughput is high. LA-ICP-MS is a technique which has been pioneered by VG Elemental and is already in use in many laboratories throughout the world. As the number of formulations and applications of ceramic materials continue to grow, the need for increased knowledge of trace and minor constituents of raw materials and finished products becomes more pressing. Fine ceramics cannot be effectively used in high temperature high stress environments until the effects and extent of impurities have been fully explored. LA-ICP-MS is now being developed for the analysis of ceramic materials so that bulk and point analyses yielding multi-element information will be routinely available.

There are some certified reference materials available and some scope does exist for quantification against these materials. The variety of ceramics already in use is so very wide that it is not realistic to expect standard materials to be generated to encompass all eventualities, so a reliable technique of standardless analysis would be of great value.

The VG PlasmaQuad and LaserLab solid sampling accessory allow the analyst to perform quantitative, matrix matched and standardless analysis of ceramics. The latter technique uses the instrument response at constant concentration as a function of atomic mass and a single internal standard to generate concentrations for other elements of interest. Typically, the internal standard would be a minor isotope of one of the matrix elements (e.g. ^{29}Si) which requires no knowledge of the sample other than its stoichiometry. The techniques are illustrated below for ceria, silicon nitride and silicon carbide.

R. Freer (ed.), The Physics and Chemistry of Carbides; Nitrides and Borides, 121–130.
© 1990 *Kluwer Academic Publishers. Printed in the Netherlands.*

3. Experimental Method

All samples were analysed by LA-ICP-MS.
The standard system consists of a pulsed Nd:YAG laser producing output at wavelength 1064nm [1]. The laser light is folded through 90 degrees by a mirror, and is brought to focus on the surface of the sample by a lens of focal length 75mm. The sample is mounted within a quartz cell [2] which has a controlled flow of argon carrier gas, transporting vaporised material to the inductively coupled plasma of the PlasmaQuad. The sample cell is mounted on precision stepper motor driven translation stages, which can be controlled manually by means of a joy-stick or automatically by the computer using a software module within the PlasmaQuad suite.

Sample viewing is by means of a binocular microscope head mounted co-linearly with the laser objective lens. The complete system is interlocked such that the operator is fully protected.

Ablated material is carried to the plasma via polyurethane tubing. Samples are introduced into the central channel of the plasma as a dry aerosol, which is rapidly atomised. Dissociation is virtually complete during transit through the plasma core and elements with a first ionisation energy of less than 10eV, are fully ionised. Ions are extracted from the central channel of the plasma through a sampling aperture into the quadrupole mass analyser, where they are separated on the basis of their charge to mass ratio prior to detection by an electron multiplier. These pulses are amplified and accumulated in a high capacity Multi-Channel Scalar. The raw data is transferred to a microcomputer for data manipulation.

3.1 QUANTITATIVE ANALYSIS

Where calibration standards are available accurate quantitation is achieved. Machine response calibration graphs can be drawn using the composition/ intensity relationships for each of the elements certified in the standards. Quantitative results can then be generated for these elements in samples whose matrices are closely matched to those of the standard material. Results accurate to within 5-10%.

3.2 SEMIQUANTITATIVE ANALYSIS

For those samples where calibration standards are not available, semiquantitative data can be generated using a general instrument response curve established by laser sampling of for example National Institute of Science and Technology (NIST) 612 glass. The mass/response relationship has been found to be applicable to a wide range of matrices and can therefore be used in conjunction with a single internal standard to generate effectively standardless analyses of the ceramics.

4. Results

4.1 THE ANALYSIS OF CERIA [3].

Ceria is a semiconductor whose conductivity changes linearly with oxygen pressure. It is oxygen selective and can thus be used to measure oxygen pressures in a mixture of gases. Further, its resistance to chemical attack means that it can be used in harsh environments, in monitoring combustion processes in internal combustion engines for example.

Samples of CeO_2 of nominal purity 98% (Merck) and 99.9% (Ventron) were subjected to multielement analysis by LA-ICP-MS. Full multi-element analyses of these materials takes approximately one minute. Our results show that the nominally lower purity material is in fact virtually free of impurities whilst the nominally higher purity material contains high levels of impurity, particularly in the rare earth region. Tables 1a and 1b give details of impurities in Merck ceria and Ventron ceria respectively.

Table 1a - Merck (sample A) Impurities in commercially available ceria (concentrations in ppm)

Mg	17	Ba	1
Al	21	Nd	1
Ca	(250)	Sm	4
Ti	11	Eu	0.2
V	0.4	Tb	3
Cr	0.5	Gd	0.7
Mn	3	Ag	0
Fe	37	Dy	0
Co	0.2	Er	0
Ni	3	Tm	0
Cu	0.6	Yb	0
Zn	0.4	Lu	0
Sr	0.5	Hf	0
Y	1	W	0
Zr	3	Pt	0
Nb	0.2	Hg	0
Mo	0.7	Pb	4
Sn	0.6	Bl	0
Sb	0.2	Th	0
		U	0

Total Impurities = 300 ppm

Table 1b - Ventron (sample B) Impurities in commercially available ceria (concentrations in ppm)

Mg	14	Pr	4
Al	22	Nd	9
Ca	(540)	Sm	450
Ti	114	Eu	19
V	1	Tb	87
Cr	0.5	Gb	422
Mn	1	Dy	361
Fe	13	Ho	39
Co	1	Er	69
Ni	3	Tm	6
Cu	0.7	Yb	27
Zn	0.5	Lu	2
Sr	2	Hf	0
Y	547	W	0.3
Zr	3	Pt	0
Nb	0.1	Hg	0
Mo	1	Pb	2
Sn	2	Bi	0.1
Sb	0.2	Th	8
Ba	2	U	3

Total impurities = 3000 ppm

FIGURE 1a

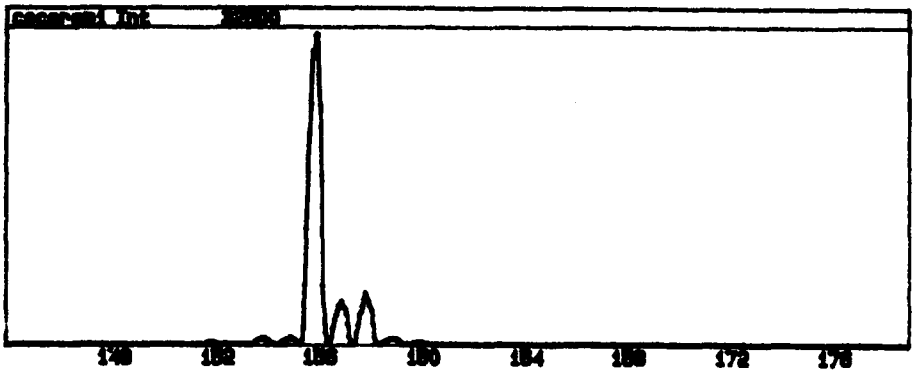

Detail from full multielement spectrum of Merck ceria, showing absence of rare earth impurities. The peaks are due to molecular species eg $(^{140}Ce\ ^{16}O)^+$

FIGURE 1b

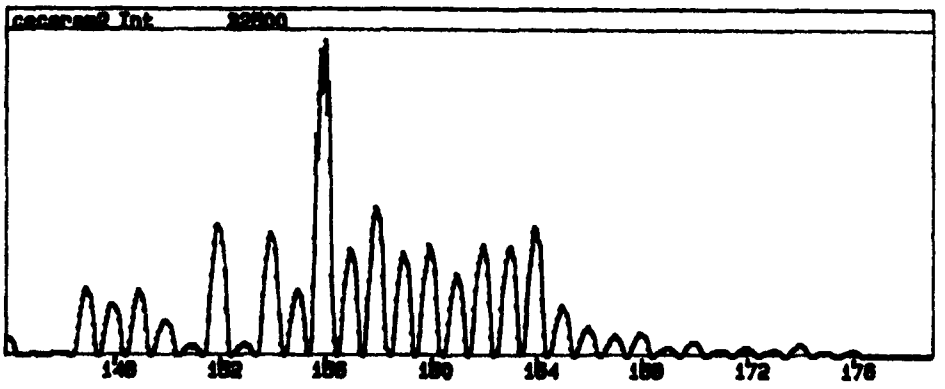

Detail from full multielement spectrum of Ventron ceria, showing high levels of rare earth impurities

The level of impurity in the ceria is critical to its behaviour as an oxygen sensor. Sample A (Merck) shows predictable, linear behaviour over a range of several orders of magnitude O_2 partial pressure (Figure 2); however, a ten fold increase in the total impurity content results in a reduced range for the sensor and significant deviation from linearity particularly at high pressures. The potential application for quality control by both supplier and buyer of such materials is evident.

FIGURE 2

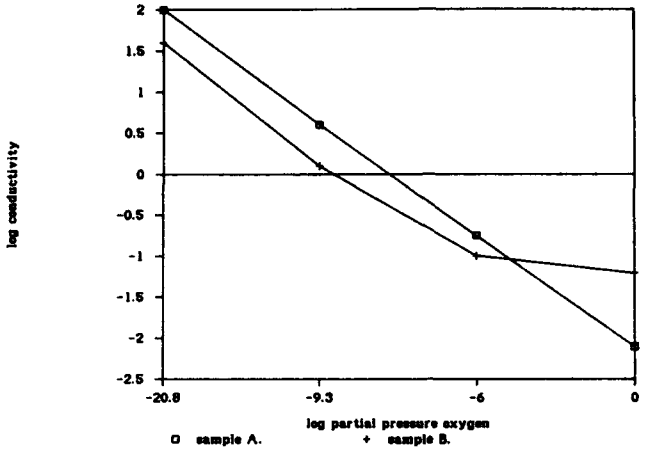

4.2 ANALYSIS OF SILICON NITRIDE AND SILICON CARBIDE.

Gravimetrically spiked samples of Si_3N_4 containing elements (Mg, Fe, Al, Y, Ti, Ce) at 10, 100, 1000 and 5000ppm and SiC containing elements (Fe, Al, Y, Ti, Ce) at 10, 1000, 5000 and 10000ppm were prepared from pure base materials (Ceramiques et Composites Bazet, France). The samples were analysed by LA-ICP-MS and the calibration graphs plotted. Examples are given in Figure 3 and show linear response to very high concentrations. Use of such calibrations allows quantitative analysis of samples for selected elements. Given the rarity of ceramic standards, a much more useful technique is standardless analysis. Table 2 shows the concentrations of various elements recovered using a single internal standard (^{29}Si) and a general instrument response curve and compares them with the known added concentrations. Figure 4 shows the logarithmic spectrum of the base material and compares it with that of the spiked material; note the differences in peak heights for the added elements and similar heights for others.

Table 2

Standardless analysis results compared with known concentrations for silicon carbide

Sample	Fe		Al		Y		Ce	
	Cert	Found	Cert	Found	Cert	Found	Cert	Found
1	1000	1380	1000	1390	1000	1260	1000	1180
2	5000	6520	5000	7990	5000	4950	5000	6240
3	10000	9690	10000	11700	10000	9040	10000	9610
4	1000	799	1000	1060	1000	1370	1000	860
5	5000	3490	5000	5230	5000	4560	5000	3690
6	10000	10100	10000	----*	10000	10200	10000	10900

All values ppm. * Flooded Multiplier

FIGURE 3

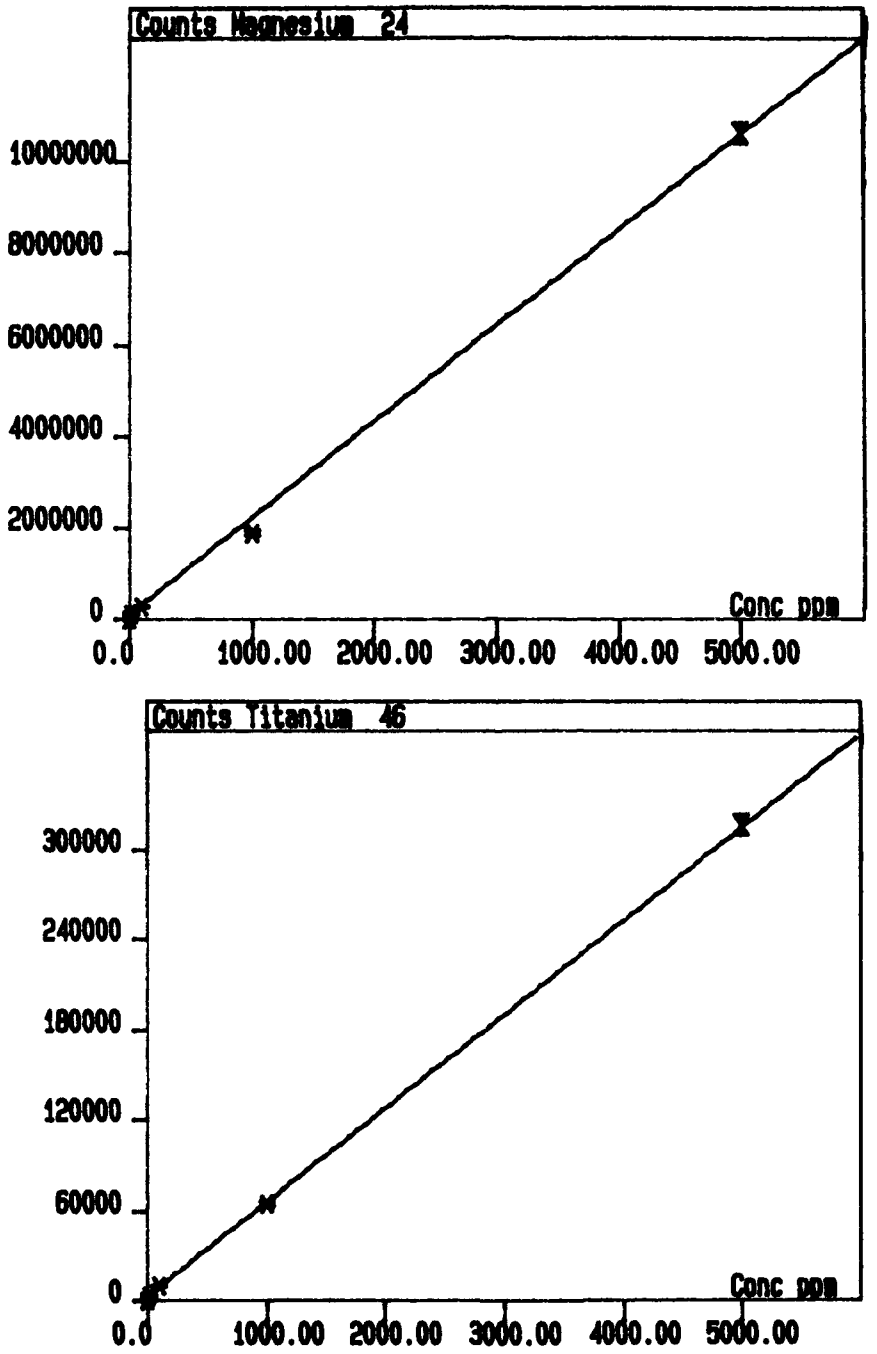
Counts Magnesium 24
10000000
8000000
6000000
4000000
2000000
0
Conc ppm
0.0
1000.00
2000.00
3000.00
4000.00
5000.00
Counts Titanium 46
300000
240000
180000
120000
60000
0
Conc ppm
0.0
1000.00
2000.00
3000.00
4000.00
5000.00

FIGURE 4

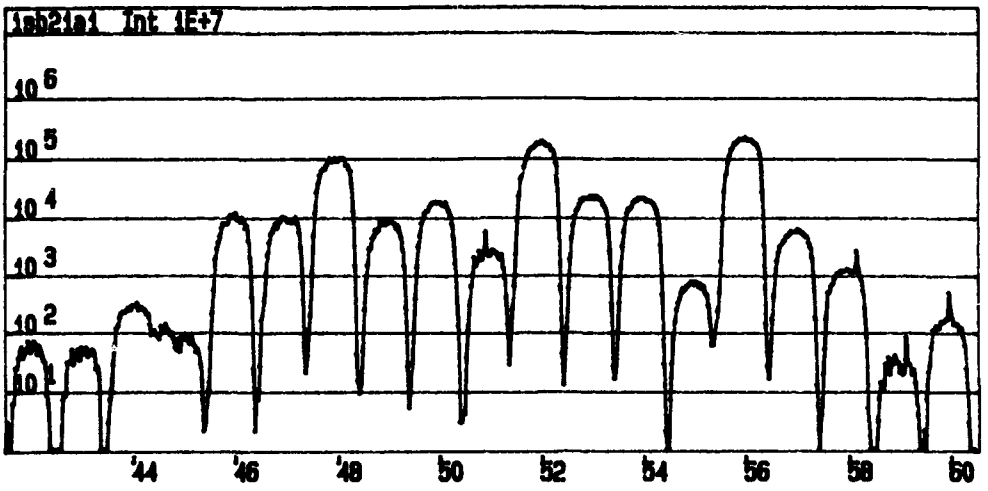
1mb2ia1 Int 1E+7
10 6
10 5
10 4
10 3
10 2
10 1
'44
'46
'48
'50
'52
'54
'56
'58
'60

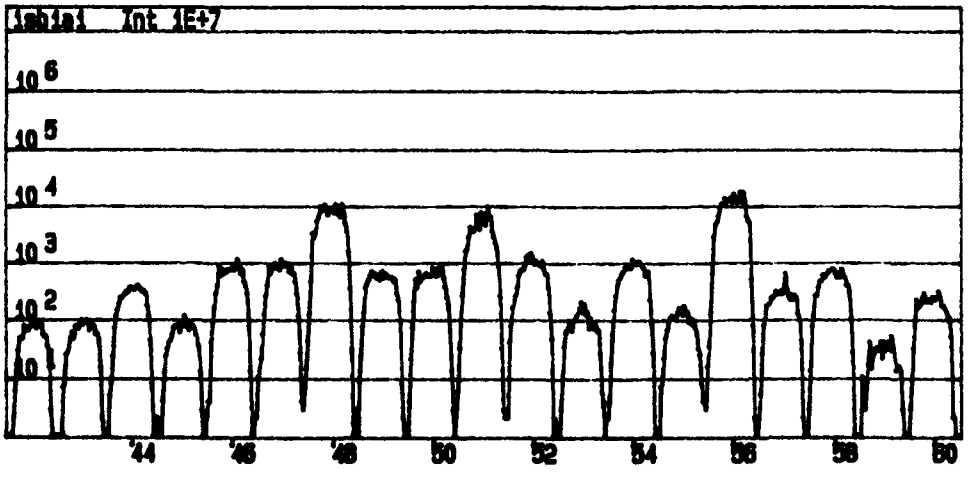
1mb1a1 Int 1E+7
10 6
10 5
10 4
10 3
10 2
10
'44
'46
'48
'50
'52
'54
'56
'58
'60

Moving on to a "real" sample, figure 5 shows the mass spectrum of the impurities. This sample had been prepared in a common processing route for this kind of ceramic, with yttria added as a sintering agent. The particularly striking rare earth impurities probably originated from the sintering agent, since rare earths are often associated in nature with yttrium. The standardless analysis of this sample gave the results in Table 3. As can be seen, the impurities are there at significant levels and may well effect the physical properties of the material.

FIGURE 5

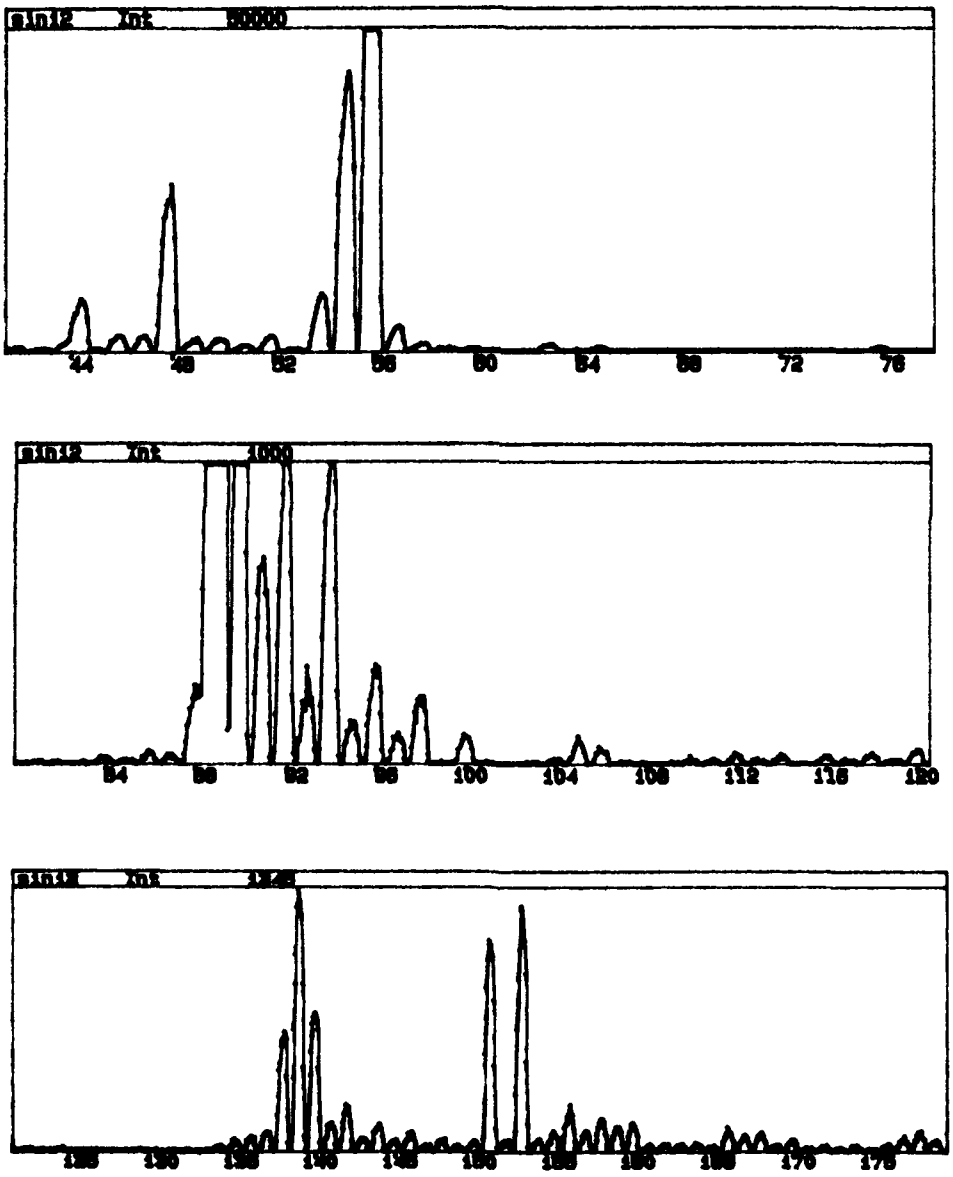

FIGURE 5 continued

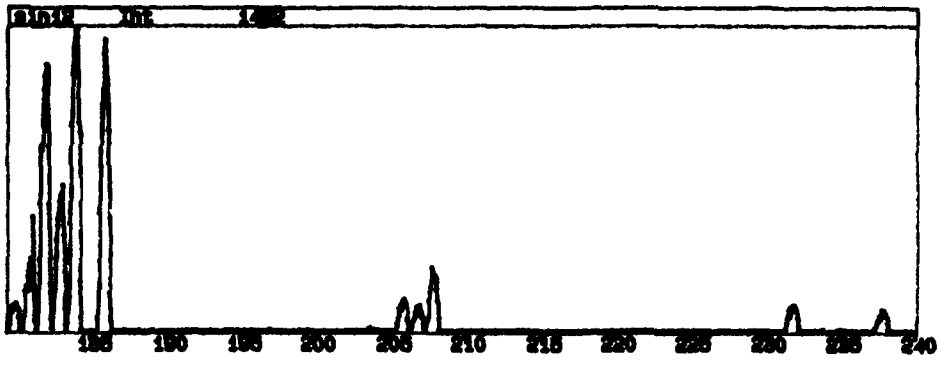

Table 3

Standardless analysis of unknown Si_3N_4

Element	Concentration	Element	Concentration
V	23.491	Ti	1054.840
Mn	1043.970	Cr	85.084
Co	12.840	Fe	4949.574
Sr	7.169	Ni	20.664
Zr	153.791	Cu	69.156
Mo	7.155	Zn	23.158
Cd	3.273	Nb	6.137
Sn	3.184	Ba	14.824
La	24.179	Ce	14.841
Pr	2.536	Nd	9.077
Sm	3.294	Eu	39.902
Dy	10.405	Tb	2.021
Er	4.844	Ho	0.276
Yb	1.144	Tm	0.398
Hf	4.994	Lu	0.107
W	69.727	Ta	4.944
Pb	7.060	U	1.150
Th	1.491		

5. Conclusions

LA-ICP-MS is probably the only technique which can provide simple spectra and yield meaningful results for virtually all elements within several minutes of receipt of ceramic samples. We have shown that certain physical parameters of the materials can be profoundly affected by high (total 0.3%) levels of impurity and that unwanted impurities in the ceramics are much more widespread than might commonly be expected. If non-oxide ceramics become widespread in the electronics industry, control of the level of impurity will become vital if high performance componants are required.

The desirable and undesirable effects of trace level impurities in Silicon Nitride are many and well documented [6,9]. Silicon Nitride is one of the promising candidates for high temperature structural materials; impurity content of a few hundred ppm was found to be sufficient to make densification easy but also to degrade high temperature strength [4,5].

The effects of the addition and presence of trace elements in Silicon Carbide are also well documented [6,7] and there is an obvious need for quality control for base materials as well as for additives a role which LA-ICP-MS is clearly well suited to carry out. It has been shown that high purity powder is a major factor for the production of good quality, high density, hot pressed Silicon Carbide [8]).

LA-ICP-MS as an analytical tool has the flexibility, sensitivity and dynamic range required for the analysis of impurities in ceramics. As more exacting applications are demanded of these materials, LA-ICP-MS will prove to be an invaluable tool in both research and quality control environments.

6. References

1 Spectron Laser Systems. 21 Paynes Lane, Rugby, Warwickshire.
See Spectron manual SL802.

2 Jowitt R.1984
Direct Analysis of Liquid Steel by Laser.
Proceedings of the BSC\BISPA Chemists Conference.

3 H.-J. Beie, A. Gnorich, E Ivers-Tiffee. 1989.
Influence Of Raw Materials On The Electrical Conductivity Of Ceria.

4 Crosby, Gary M. ;Nicholson John M. ;Stiles, Ernest D. 1989.
Sintering Factors For A Dry Milled Silicon Nitride-Yttria-Alumina Composition.
Am. Ceram. Soc. Bull. 68 [6]1202-6.

5 Brau, Wolfgang; Woetting, G ;Ziegler, Guenther. 1986.
Influence of Impurities in Different Processed Si_3N_4 Powders On High-Temp. Properties of Sintered Materials.
Br. Ceram. Proc. 37, pp. 71-80.

6 Shinroku Saito (Editor) President, The Technogical University of Nagaoka and Emeritus Professor,Tokyo Institute of Technology. 1985. Fine Ceramics

7 Takeda, Yukio ;Naamura, Kousuke; Maeda, Kunihiro; et Al. 1987. Effects of Additives On Thermal Conductivity and Electrical Resistivity of SiC Ceramics.
Yogyo Kyokaishi. 95 [9] 860-3 (Japanese).

8 Takeda, Yukio. 1988.
Development of High Thermal Conductive SiC Ceramics.
Am Ceram. Soc Bull. 67 [12] 1961-3.

9 Tanaka, Isao; Pezzotti, Guiseppe; Okamoto, Taira; et Al. 1989.
Hot Isostatic Press Sintering and Properties of Silicon Nitride Without Additives.
J. Am. Ceram. Soc. 72 [9] 1656-60.

ACKNOWLEDGEMENTS
The authors would like to extend their thanks to C.T.TYE for all of his help, Ceramiques et Composites, Ceraten and Siemens for the supply of samples and also to the EEC for their involvement in this venture [EEC contract No. SC1 -0067-C-(EDB)].

II. SYNTHETIC DIAMOND - PREPARATION and PROPERTIES

METASTABLE SYNTHESIS OF DIAMOND

Thomas R. Anthony
GE Research and Development Center
1 River Road
Schenectady, New York, 12309, USA

ABSTRACT. Diamond can be grown metastably at subatmospheric pressures and moderate temperatures from hydrocarbon gases in the presence of atomic hydrogen. Atomic hydrogen can be generated by various methods, each of which generally leads to new chemical vapor deposition (CVD) diamond growth processes. Atomic hydrogen serves several critical roles in CVD diamond growth, namely: 1) stabilization of the diamond surface; 2) reduction of the size of the critical nucleus; 3) "dissolution" of carbon in the gas; 4) production of carbon solubility minimum; 5) generation of condensable carbon radicals in the gas; 6) abstraction of hydrogen from hydrocarbons attached to surface; 7) production of vacant surface sites; and 8) etching of graphite. Atomic hydrogen can carry out these functions because of favorable relationships between energies for carbon-carbon, carbon-hydrogen and hydrogen-hydrogen bonds. A direct substitute for atomic hydrogen has not been found although potential substitutes have been used to increase diamond growth rates. Potential substitutes have also been used indirectly to develop new methods of CVD diamond growth.

1. Introduction

At first glance, it is surprising to find that diamond is rare since the energy difference of 453 cal/mole between metastable diamond and common graphite is less than RT (600 cal/mole) at room temperature [1]. There are several reasons diamond is uncommon. First, under ordinary circumstances, the kinetics of graphite formation are much faster than the kinetics of diamond formation. Thus competitive growth ensures that graphite nuclei grow and overcome any diamond nuclei that may form. Secondly, the entropy of diamond is less than the entropy of graphite by 0.78 cal/deg-mole. Thus, the fraction F of diamond particles in an aggregate of graphite particles in the absence of any activation barrier is:

$$F = \exp(\Delta S / k) \tag{1}$$

$$\Delta S = -0.78 - 453 / T(\text{cal / deg-mole}) \tag{2}$$

where ΔS is the total entropy change that occurs as a piece of graphite transforms into diamond and k is Boltzman's constant [1] Equation 2 assumes that the surface energies of small diamond and graphite particles are equal. At room temperature, the fraction of diamond particles in an aggregate of graphite particles is finite (1%) only if the particles have fewer than 10 atoms. Higher temperatures will slightly increase this fraction, while lower temperature will greatly decrease it. Finally, as shown

R. Freer (ed.), The Physics and Chemistry of Carbides; Nitrides and Borides, 133–158.
© 1990 *Thomas R. Anthony.*

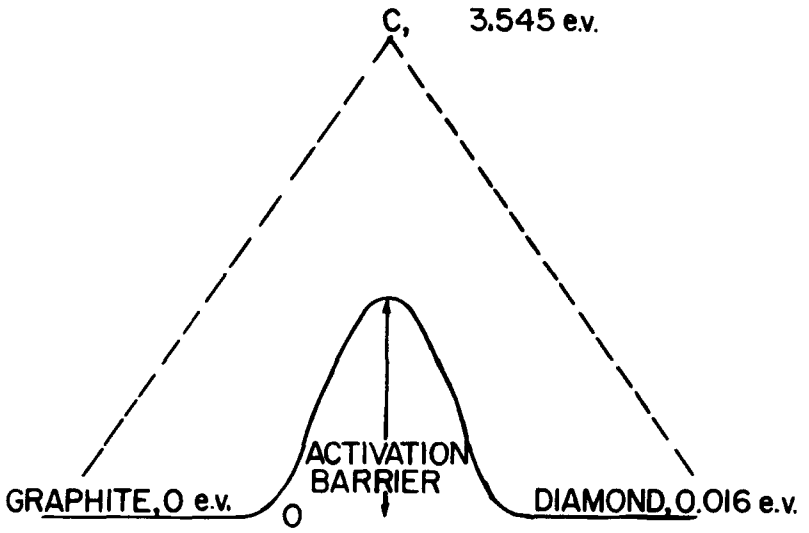

Figure 1. Atomic carbon, graphite and diamond energy diagram.

in Figure 1, a large activation energy barrier between graphite and diamond prevents even these small diamond particles from forming at room temperature.

Synthesis of diamond has been attempted for hundreds of years. In retrospect, most attempts were made under conditions where graphite was the stable phase of carbon and the lack of success was not surprising [2]. Because the density of diamond is greater than the density of graphite, diamond becomes the stable phase of carbon at high pressures In 1954, a reliable and repeatable process was invented for making diamonds at high pressures [3]. With the successful synthesis and industrial production of diamond at high pressure, most of the work on the metastable synthesis of diamond in the graphite stable region of the carbon diagram ceased.

2. Metastable Synthesis

A few researchers continued to work on the synthesis of diamond at low pressures with some reports of success [4]. However, the growth rate of diamond was so small that these results were not technologically important and in all cases, diamond substrates were required. Most methods utilized an alternating exposure of the diamond substrates to a hydrocarbon gas and then hydrogen at high temperatures [5–7]. Under these conditions, the hydrocarbon was pyrolysized to form diamond and graphite and then the hydrogen was used to etch the graphite away in a never-ending cycle (Reactions 3 and 4).

$$CH_4 \xrightarrow{\text{Heat}} \text{Deposit (Diamond \& Graphite)} + 2H_2 \qquad (3)$$

$$H_2 + \text{Deposit} \xrightarrow{\text{Heat}} \text{Diamond} + CH_4 \qquad (4)$$

In the late 1970s, an important invention changed this cyclic process to a continuous one, increased the diamond growth rate by orders of magnitude, and eliminated the need for diamond substrates [8]. This new process [9] is shown in Reaction 5.

$$CH_4 \xrightarrow{\text{Heat \& Atomic Hydrogen}} \text{Diamond} + 2H_2 \qquad (5)$$

The important invention was the addition of atomic hydrogen to the reaction. Let us look at some different methods of generating atomic hydrogen before examining the mechanisms by which it promotes metastable diamond growth.

3. Generation of Atomic Hydrogen

3.1. HOT FILAMENT

Atomic hydrogen can be generated using many techniques [10]. Chemical vapor deposition (CVD) diamond has been produced using many of these methods. Langmuir first reported the dissociation of molecular hydrogen on a hot tungsten filament in our laboratories in the early 1900s [11–14]. Coincidentally, this was the method that was first used extensively to make atomic hydrogen in CVD diamond growth (Figure 2a). Typically, a hot filament is heated to a temperature range of 1950 to 2300 °C in the presence of molecular hydrogen [15,16]. The molecular hydrogen adsorbs on the surface of the metal filament and dissociates into two atomic hydrogens that subsequently pass back into the surrounding gas (Figure 2).

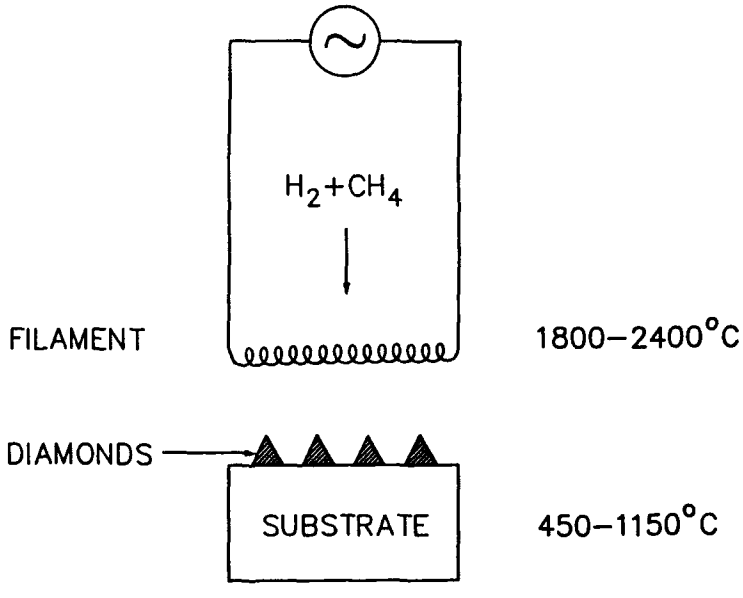

Figure 2a. Hot-filament diamond CVD.

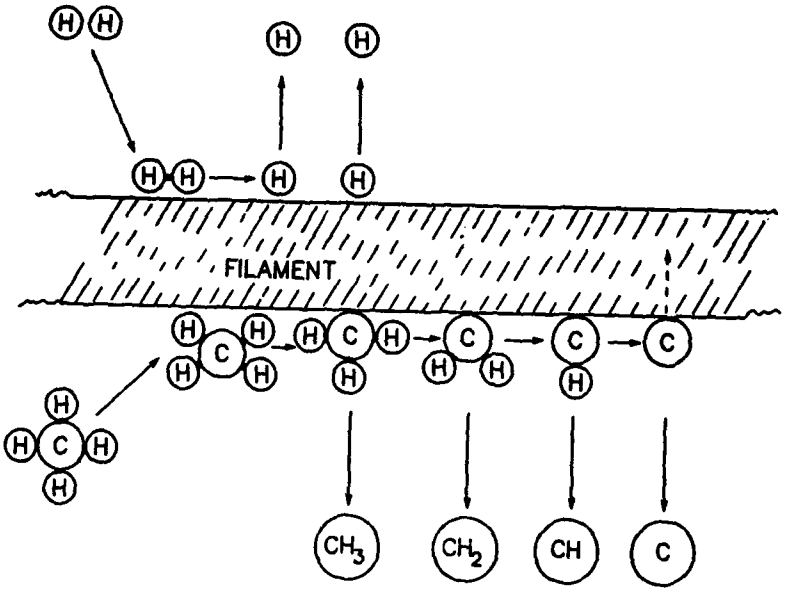

Figure 2b. Dissociation of hydrogen and methane on a hot filament.

TABLE 1
Reactions of Hydrogen and Methane On a Hot Filament

$CH_4(g)+\square = CH_4(ad)$	(1)
$CH_4(ad) = CH_3(ad) + H(ad)$	(2)
$CH_3(ad) = CH_2(ad) + H(ad)$	(3)
$CH_2(ad) = CH(ad) + H(ad)$	(4)
$CH(ad) = C(ad) + H(ad)$	(5)
$C(ad) = C(g) + \square$	(6)
$CH(ad) = CH(g) + \square)$	(7)
$CH_2(ad) = CH_2(g) + \square)$	(8)
$CH_3(ad) = CH_3(g) + \square)$	(9)
$C(ad) = \square + C$ (infilament)	(10)
$H_2(g) + 2\square = 2H(ad)$	(11)
$H(ad) = H(g) + \square$	(12)

□ = vacant surface site
(g) = gaseous species
(ad) = species absorbed on surface

$$H_2 \rightarrow 2\ H;\ \Delta H = +104{,}000\ \text{kcal/mole} \quad (6)$$

In addition, many other reactions [17,18] take place on the filament, as shown in Figure 2b and Table 1, involving the hydrocarbon that is in the hydrogen-hydrocarbon gas mixture used for CVD diamond growth.

Table 2 shows a number of possible filaments that can be used to make atomic hydrogen. Naturally, the melting points of all the materials must be higher than the operating temperature of the filament. Another constraint on the filament material is that its binary eutectic point with carbon must be higher than the filament operating temperature because the filament material is in contact with a hydrocarbon gas. This later requirement makes it hard to work with molybdenum filaments because a hot spot on a Mo filament may take it above the Mo-C eutectic temperature of 2200 °C and cause the filament to melt and fail.

TABLE 2
Possible Filaments for Hot-Filament CVD Diamond Growth

Material	Melting Point (°C)	Evaporation Rate (g/cm^2-s)	Carbon Eutectic Point (°C)
Tungsten	3387	10^{-9}	2475
Carbon	3727	6×10^{-8}	3727
Rhenium	3180	7×10^{-5}	2486
Tantalum	2996	10^{-8}	2800
Molybdenum	2610	4×10^{-7}	2200
Niobium	2468	8×10^{-9}	2335

While a carbon filament satisfies the melting-point and eutectic-point requirements, it does not produce CVD diamond because atomic hydrogen that forms on a carbon filament reacts with the carbon and releases a hydrocarbon species into the gas rather than atomic hydrogen. Without atomic hydrogen at the substrate, graphite is deposited instead of diamond. The failure of carbon filaments to produce diamond [19] implies that the atomic hydrogen does not form in the hot gas surrounding the filament but actually forms on the filament surface [11–14] where it can react with the filament material.

Of the remaining materials, tungsten, tantalum, and rhenium have been commonly used to produce CVD diamond. Both tantalum and tungsten react with the hydrocarbon in the gas to form carbides. Carburization is a two-stage process with M_2C forming first, followed by MC, where M is one of the refractory metals (Figure 3). Under typical hot-filament CVD diamond growth, M_2C forms in all cases. However, MC does not always form because the activity coefficient of carbon is too small [20] under some conditions of CVD diamond growth. Since the carbides of tantalum and tungsten occupy a larger volume than the metal from which they were formed, these filaments swell, crack, bend, distort, and embrittle as they carburize (Figure 4). Carburization and cracking increase the electrical resistance of the filament so the current and voltage must be monitored and changed to keep a constant filament temperature. Rhenium is attractive because it does not form a carbide [21,22]. However, rhenium dissolves large amounts of carbon that can react with dissolved impurities such as oxygen to form voids, which appear predominantly on grain boundaries. Also rhenium is two orders of magnitude more expensive than tantalum or tungsten.

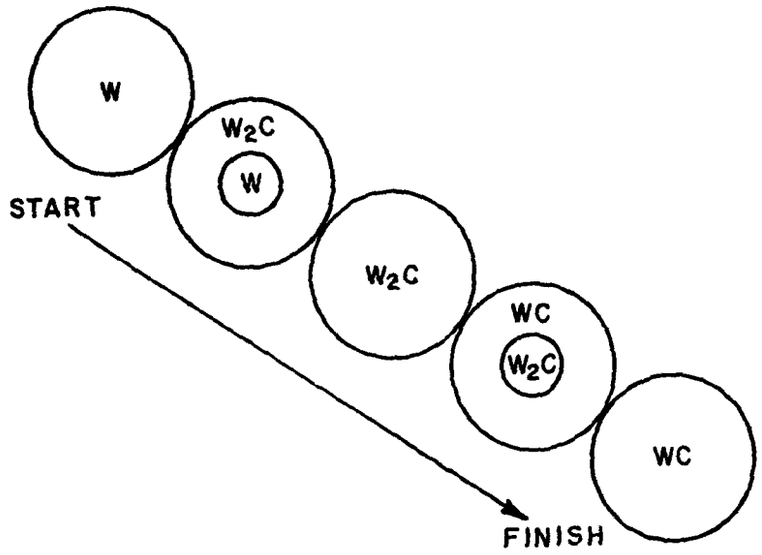

Figure 3. ***Stages of carburization of a tungsten filament during diamond CVD.***

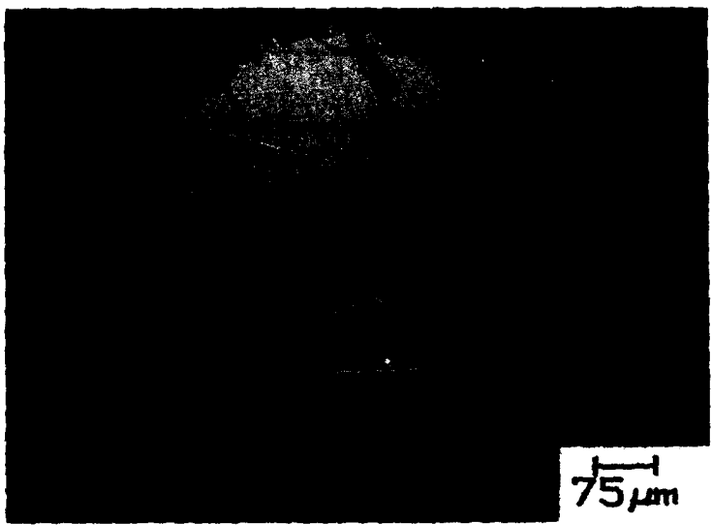

Figure 4. Metallographic cross section of a carburized tungsten filament.

In all cases, the filaments are embrittled during use. With carbide-forming refractory metals, a ductile metal is replaced by a brittle carbide that is extensively cracked. With rhenium, a fine-grain ductile wire anneals into a nonductile large-grain bamboo-structured wire with voids at the grain boundaries.

Finally, filaments represent a remote source of atomic hydrogen. During the transport of atomic hydrogen from the filament to the substrate, a considerable fraction is lost through trimolecular collision between two atomic hydrogens and a third gas molecule or the walls of the reactor [23]:

$$H + H + M \rightarrow H_2 + M \tag{7}$$

where H is atomic hydrogen and M represents a gas molecule or the walls of the reactor. This loss of atomic hydrogen during transport does not occur in processes where the substrate is immersed in the medium where the atomic hydrogen is being generated. Several such processes will be discussed below.

3.2. LOW-PRESSURE GLOW DISCHARGE

Another method of atomic hydrogen generation is based on the Wood's Tube method [24] where a stream of low-pressure molecular hydrogen is passed through a glow discharge between two metal electrodes (Figure 5). Over a pressure range of 0.1 to 20 torr, up to 25% atomic hydrogen can be generated by this method. The substrate is placed in this glow discharge or one electrode serves as the substrate so that atomic hydrogen is generated at the substrate surface. Although ac or dc can be used to form the discharge, dc is advantageous if an electrode is used as a susbtrate since diamond

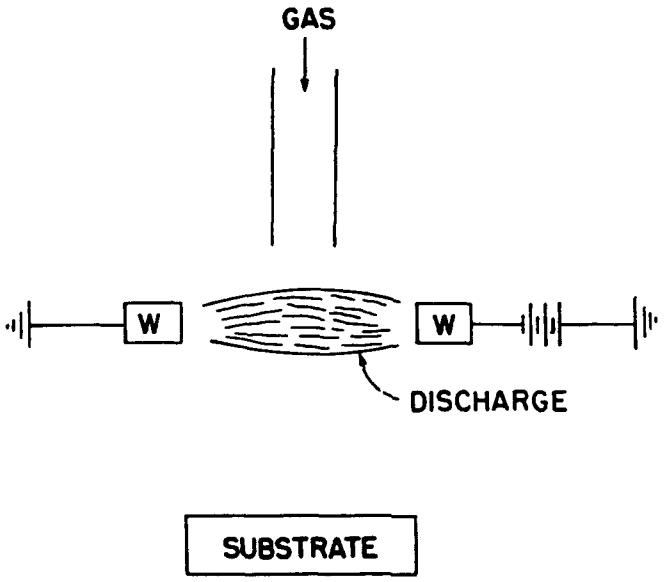

Figure 5. Low-pressure dc discharge for CVD diamond growth.

growth conditions are more favorable on the positive electrode. Crystallume of Menlo Park, California has used this method to produce very fine grain CVD diamond films. Disadvantages of this process include the limited pressure range of operation and the erosion of and contamination from the electrodes.

3.3. LOW-PRESSURE MICROWAVE DISCHARGE

Microwave discharges have been used extensively in CVD diamond synthesis (Figure 6) [25–32]. Microwave discharges are electrodeless and electrode and erosion problems are avoided. Microwave discharges are also very stable and provide up to 25% H atoms under typical CVD diamond growth conditions. Moreover, microwave sources are very economical because of the mass production of microwave ovens. Care must be taken that the plasma does not contact the walls of the reactor, which are usually made of quartz because diamond and/or graphite can deposit on them This carbon deposit will couple with the microwaves and heat up, causing more deposition, and the walls of the reactor will gradually become opaque to microwaves. Under other operating conditions, the plasma can seriously erode the walls by atomic hydrogen reduction of silicon dioxide. These problems can be avoided by magnetic confinement of the plasma.

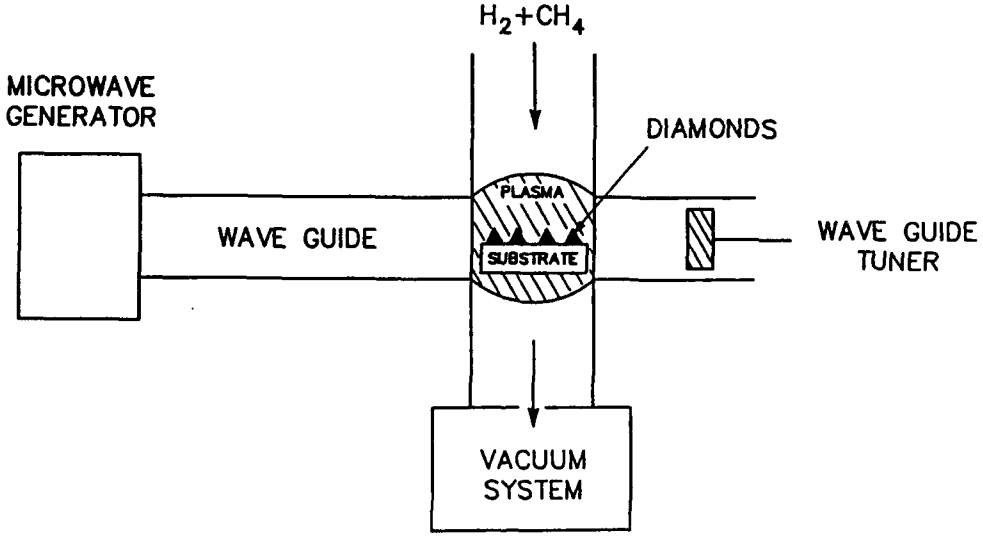

Figure 6. Low-pressure microwave discharge for CVD diamond growth.

One confinement method uses an axial magnetic field in a cylindrical cavity with a microwave window and substrate, respectively, on opposite ends of the cavity [25,29]. A gradient in the axial field is adjusted so ECR conditions exist near the substrate end of the cavity but not near the microwave window. Circularly polarized microwave electric fields drive free electrons in circular orbits around the axial field lines. Near the substrate, the ECR resonance conditions allow the electrons to receive resonance impulses during each orbit so these electrons acquire a higher energy than electrons

elsewhere in the cavity. Thus, the plasma forms preferentially in the region of these high-energy electrons adjacent to the substrate. No plasma forms at the microwave window at the opposite end of the cavity where ECR conditions do not exist. Hence, the microwave window is kept free of carbon deposits. CVD diamond machines based on microwave discharge are available from Astec of Cambridge, Mass and Wavemet of Plymouth, Michigan.

3.4. LOW-PRESSURE RF DISCHARGE

Electrodeless radiofrequency discharges have also been used to grow CVD diamond (Figure 7) [33]. Depending on the pressure, atomic hydrogen concentrations of 10 to 65% can be produced in a rf discharge. These discharges are less stable than microwave discharges and Ar sometimes has to be added to the hydrogen-hydrocarbon mixture to stabilize the discharge. Similar to the microwave discharge, deposits of carbon on the walls of the reactor can be a problem with an rf discharge. In addition, the rf can electromagnetically couple with any electrically conductive body in the reactor chamber and heat it. Finally, rf power sources are more expensive than microwave sources per watt of delivered power.

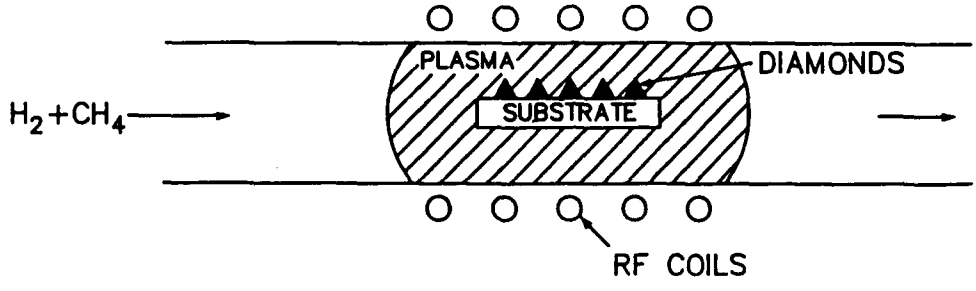

Figure 7. Low-pressure rf discharge for CVD diamond growth.

3.5. MERCURY PHOTOSENSITIZED DECOMPOSITION

Molecular hydrogen can be decomposed into atomic hydrogen by a mercury photosensitized reaction.

$$Hg(^1S_0) + h\nu \rightarrow Hg(^3P_1)$$

$$Hg(^3P_1) + H_2 \rightarrow Hg(^1S_0) + 2\,H \qquad (8)$$

Large amounts of atomic hydrogen can be produced at atmospheric pressure in this manner [34–37]. An experimental apparatus involves a pyrex tube containing hydrogen with a partial pressure of mecury from a small pool of liquid mercury in one end of the tube. A mercury or xenon arc lamp supplies the photons (Figure 8). A similar mercury photosensitized reaction can also produce hydrocarbon radicals.

Quantum yields increase with increasing gas temperature and exceed unity above 400 °C which indicates a chain reaction in a hydrogen-hydrocarbon mixture. Although work has been done in this

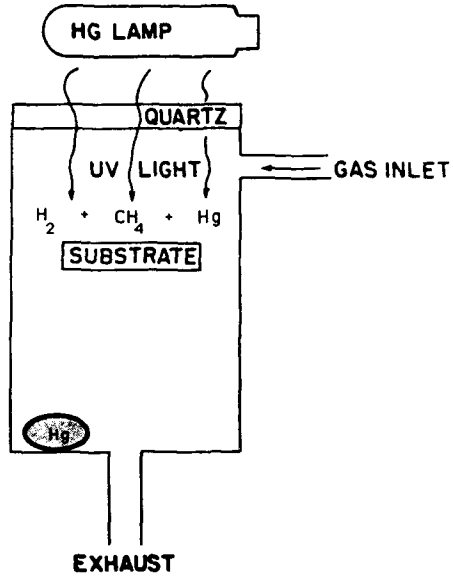

Figure 8. Mercury photosensitized CVD diamond growth.

area, there have been no published confirmations of mercury photosensitized decomposition being used to make CVD diamond. Disadvantages of the process include the use of mercury, which causes safety and environmental problems, and the low efficiency in converting electricity to light and converting light to atomic hydrogen.

3.6. PHOTOLYSIS AND RADIOLYSIS

Atomic hydrogen can be produced by exposing molecular hydrogen to vacuum ultraviolet or laser light. There have been scattered reports that CVD diamond has been made by such methods but these reports have not been confirmed or have later been retracted.

Atomic hydrogen can also be made by α, β or γ radiolysis of molecular hydrogen or hydrocarbons [38–40]. Consequently, it should be possible to grow CVD diamond in fission or fusion reactors in containers with a suitable hydrogen/hydrocarbon ratio.

3.7. HIGH-PRESSURE DC DISCHARGE

DC discharges between fixed electrodes at atmospheric pressure have been used to grow good-quality CVD diamond from hydrogen-hydrocarbon mixtures at very high rates (Figure 9) [41–44]. Because of technology developments over the years to make plasma torches, these dc discharges are now very stable. One disadvantage of this process is that because large amounts of power per unit of substrate area are used, the substrate must be directly cooled with running water to prevent it from melting. Other disadvantages include the high power consumption, the erosion of the electrodes, and the nonuniformity of the discharge.

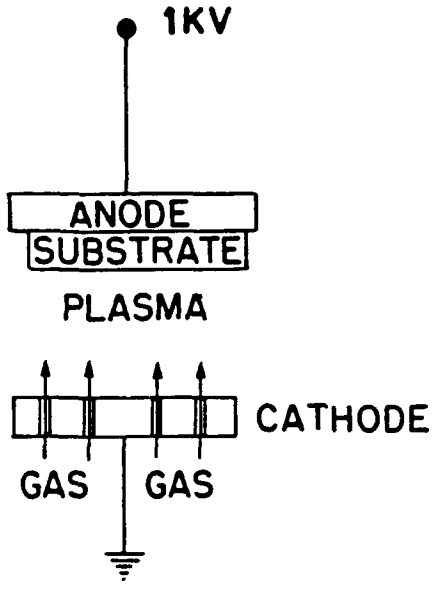

Figure 9. High-pressure dc discharge for CVD diamond growth.

3.8. HIGH-PRESSURE MICROWAVE DISCHARGE

High-power microwave discharges have also been used to grow CVD diamond at high rates at atmospheric pressure. Microwave discharges are electrodeless so electrode erosion problems are avoided. Once a conductive plasma is formed, the microwave radiation field falls off exponentially with distance into the plasma. The penetration depth of electromagnetic radiation is inversely proportional to the frequency of radiation [frequencies: a) dc = 0; b) rf = 13.56 MHz; c) Microwave = 2.45 GHz] and decreases with increasing pressure. The relatively small penetration distance of microwave radiation in a high-pressure plasma limits the potential size and uniformity of the discharge.

3.9. HIGH-PRESSURE RF DISCHARGE

High-pressure radiofrequency discharges have also been used to grow CVD diamond (Figure 10) [45]. These discharges are very unstable and large amounts of Ar are routinely added to the hydrogen-hydrocarbon mixture to increase the stability of the discharge. Nevertheless, the discharge must be monitored continuously and is typically only run for short periods of time. High rates of diamond deposition are possible during these short runs. As with other high-pressure discharges, the high power input requires that the substrates be cooled directly with running water.

3.10. HIGH AND LOW-PRESSURE FLAMES

Hydrogen atoms are created during the burning of hydrogen or hydrocarbons in an oxygen flame [46–48]. With a suitable ratio of carbon, hydrogen and oxygen, CVD diamonds can be grown with

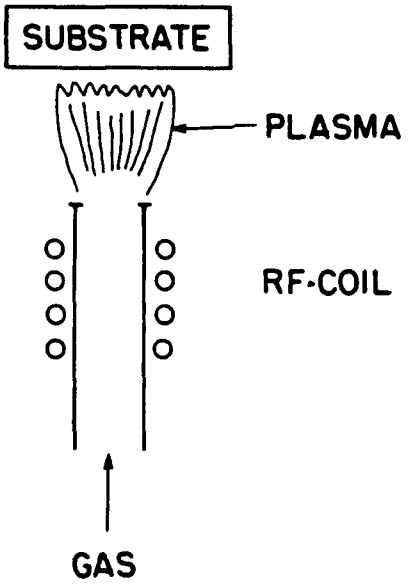

Figure 10. High-pressure rf discharge for CVD diamond growth.

a simple plumber's torch at atmospheric pressures in the "feather" of the flame just downstream of the flame front (Figure 11) [49–53]. Very high temperatures in common flames (Table 3) cause a plasma to form and atomic species to be generated at the flame front [54]. The flames are operated under fuel- rich conditions so atomic hydrogen and hydrocarbon radicals are abundant in the feather of the flame. Although this process has the potential to be an inexpensive way to make diamond, very low conversion rates of carbon to diamond have thwarted this goal. Because of the high heat input rate of this method, the substrate must be vigorously cooled.

Hydrogen atoms can also be generated in low-pressure hydrogen and hydrocarbon flames [47,48]. Advantages of low-pressure flames may be a higher carbon-to-diamond conversion rate, a wider spatial zone in the flame where diamond will grow and a much lower heat input to the substrate. Although work is underway at several laboratories, no successful CVD diamond growth has been reported yet in a low-pressure flame.

Work to date has been limited to hydrogen-hydrocarbon-oxygen flames. Flames with other chemical reactants may also generate CVD diamond growth. For example, hydrogen-hydrocarbon-fluorine, hydrogen-hydrocarbon-chlorine, hydrocarbon-fluorine, hydrocarbon-chlorine, halocarbon-fluorine and halocarbon-chlorine flames are promising candidates among many possibilities.

4. Atomic Hydrogen in CVD Diamond Synthesis

Various methods of generating atomic hydrogen have been discussed above. Now let us see why atomic hydrogen is important in CVD diamond growth.

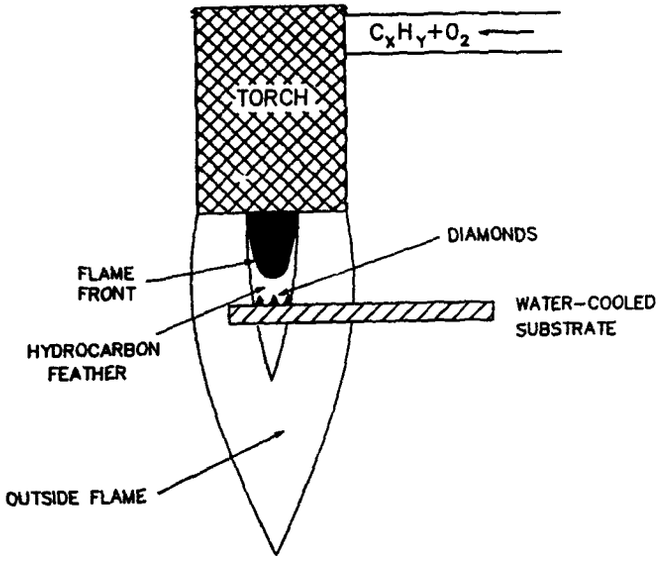

Figure 11. Atmospheric flame for CVD diamond growth.

TABLE 3
Temperature at Flame Fronts
In Various Fuel-Oxygen Mixtures (1 atm)

Fuel	Oxidizer	Temp (K)
Acetylene	O_2	3410
Carbon monoxide	O_2	3220
Heptane	O_2	3100
Hydrogen	O_2	3080
Methane	O_2	3030

4.1. STABILIZATION OF DIAMOND SURFACE

Figure 12 shows a schematic diagram of the structure of diamond and graphite. Diamond bonds are all single bonds while graphite contains both single and double bonds. Diamond will form if double and triple carbon bonds are prevented from forming.

Figure 13 shows a schematic diagram of a diamond crystal that has just been cleaved. The cleaved bottom surface shows dangling single bonds. These dangling bonds are energetically unstable and the cleaved surface will soon reconstruct to a "graphitic-like" surface containing a mixture of single and

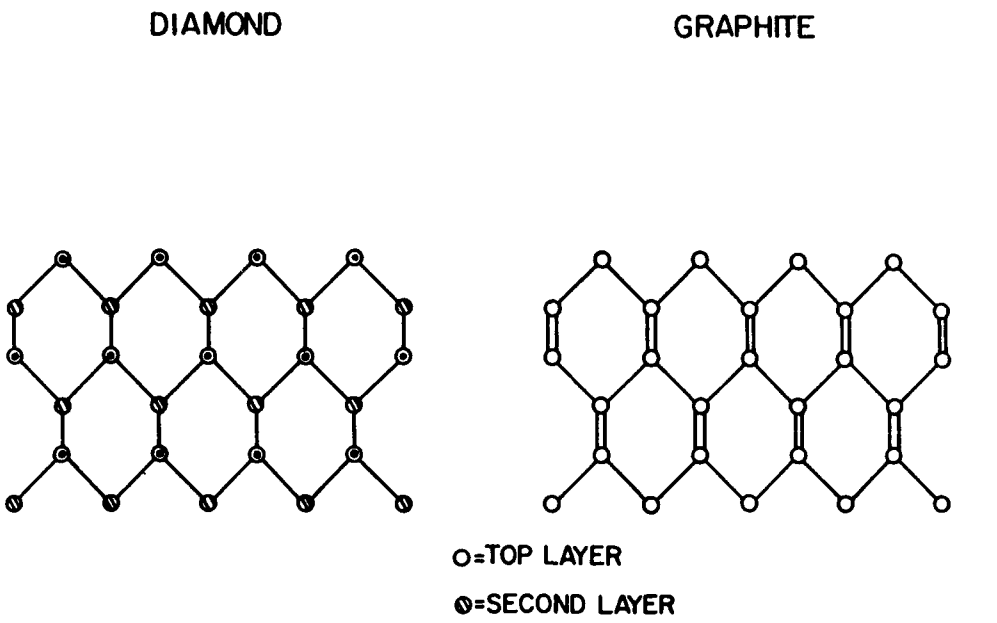

Figure 12. Schematic diagram of carbon-carbon bonding in diamond and graphite.

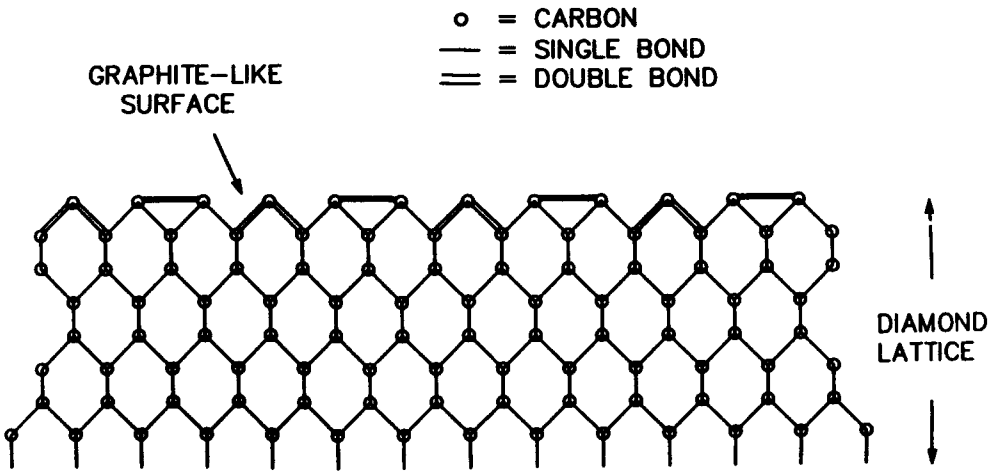

Figure 13. Reconstruction of the diamond surface.

double bonds to reduce the surface energy. The old top surface of the crystal has previously reconstructed. This reconstructed surface resembles graphite because of the mixture of single and double bonds. Consequently, carbon atoms depositing on this surface will form layers of graphite.

To prevent the reconstruction of the diamond surface, the surface can be exposed to atomic hydrogen, which reacts with carbon to form single bonds (Figure 14). The monolayer of reacted atomic hydrogen stabilizes the diamond surface [55]. However, because the hydrogen-carbon bond is stronger than a carbon-carbon bond, no diamond growth can occur since a carbon atom is not able to displace the bound hydrogen on the surface.

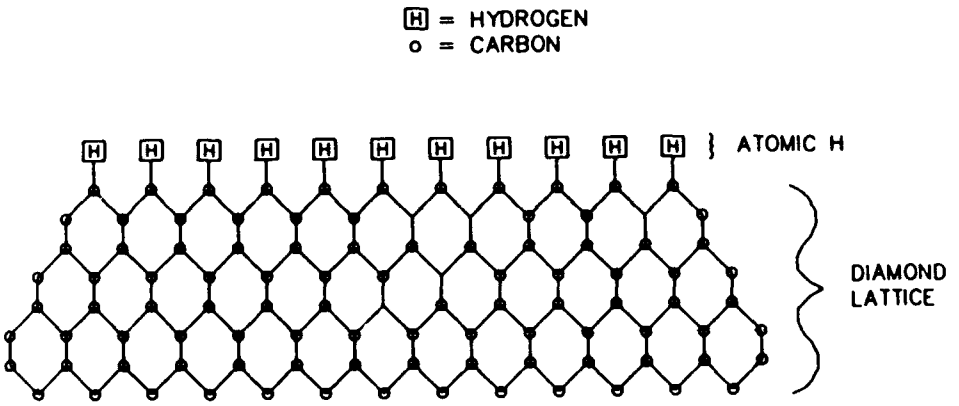

Figure 14. Diamond surface stabilized by atomic hydrogen.

4.2. GENERATION OF VACANT SURFACE SITES

A continuous rain of atomic hydrogen from the gas surrounding the diamond provides an escape from this no-growth situation by providing vacant surface sites through the mechanism [56] depicted schematically in Figure 15. An atomic hydrogen collides with a diamond surface and reacts with a surface hydrogen to form a hydrogen molecule and a vacant site (Figure 15b). Because the hydrogen-hydrogen bond is stronger than the hydrogen-carbon bond, this is an exothermic event.
In most CVD diamond growth [57], the ratio of hydrogen to carbon is approximately 50 to 1. Hence the most likely next event is that another atomic hydrogen will collide with the vacant site and fill it (Figure 15c). However, every now and then, a carbon radical will collide with the vacant site and attach to the diamond crystal, thereby generating diamond growth (Figure 15d).

From experimental data, it is estimated that 10,000 atomic hydrogens have to be produced for each carbon atom that attaches to the diamond lattice. Some atomic hydrogens are lost through trimolecular recombinations in the gas or bimolecular recombinations on the walls of the apparatus [58] but many are lost through the processes depicted in Figures 15a through 15c. This inefficient use of atomic hydrogen is a major factor in the cost of CVD diamond.

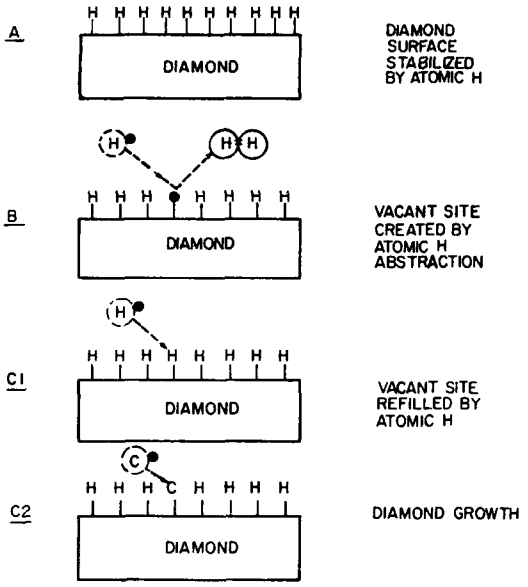

Figure 15. Generation of vacant surface sites by atomic hydrogen.

4.3. REDUCTION OF CRITICAL SIZE OF DIAMOND NUCLEUS

Before atomic hydrogen was introduced into metastable CVD diamond growth, diamond growth required a diamond substrate. The necessity of a diamond substrate suggests difficulty in nucleating diamond and a corresponding large critical nucleus size in the absence of atomic hydrogen.

In contrast, diamond crystals nucleate copiously in the presence of atomic hydrogen [59]. Atomic hydrogen reacts with and covers the surfaces of small diamond nuclei and drastically reduces their surface energy [55]. This reduction in surface energy, in turn, decreases the critical nucleus size to only a few atoms. The small size of the critical nucleus in an atomic hydrogen environment is suggested by adamantane, which is an organic compound that is stable well into the CVD diamond growing temperature range. The adamantane molecule is actually a small diamond crystal whose surface is covered with hydrogen (Figure 16).

4.4. SOLVENT FOR CARBON

Atomic hydrogen also serves a third role in CVD diamond growth in that it is a "solvent" for carbon. The word *solvent* is placed in quotation marks because atomic hydrogen does not really dissolve carbon but rather reacts with it to form a number of gaseous hydrocarbons [60,61].

4.5. PRODUCTION OF CARBON SOLUBILITY MINIMUM

With most solvents, the solubility of the solute increases monotonically with increasing temperature. However with atomic hydrogen as a "solvent," a solubility minimum for carbon is found at

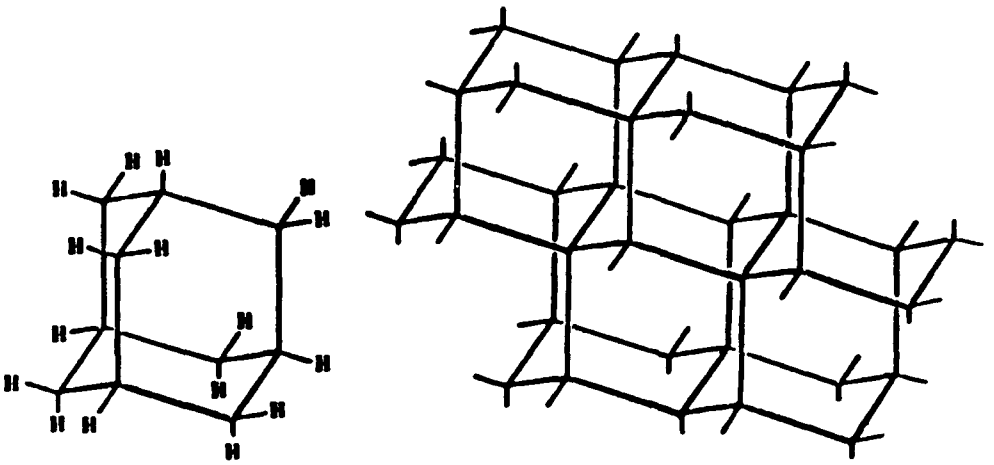

Figure 16. The lattice structure of adamantane and diamond.

approximately 1000 °C. (Figure 17) [60,61]. This minimum is generated by the decomposition of the exothermic compound CH_4 as the temperature is increased from room temperature to 1000 °C and by the reaction of carbon with hydrogen to form the endothermic compound C_2H_2 above 1000 °C. This solubility minimum is of great practical importance. If the substrate for diamond growth is placed at this solubility minimum, diamond will be deposited only on the substrate and not on the walls of the reaction chamber, which can be kept at room temperature where the solubility of carbon is higher.

Diamond could be grown on a substrate at the solubility minimum from gases with either a higher or lower temperature than the substrate. Figure 18 shows the gas temperature and electron temperatures of a plasma at different gas pressures. Because the mass of the electron is much smaller than the mass of a gas ion, the electron acquires most of the energy from the applied electric field in a plasma. At low pressures the mean free path of the electron is so large that the electron temperature and gas temperature do not equilibrate, with the result that the electron temperature is very hot while the gas temperature is relatively cool. Low-pressure dc, microwave, and rf discharges generally fit into this category. If the gas temperatures of these discharges are below the solubility minimum, they will only have the limited solubility drop available on the cool side of the minimum for CVD diamond growth. These processes are expected to have low growth rates, as observed.

At high gas pressures, the mean free path of the electron is short so equilibration between the gas temperature and the electron temperature makes both very hot. Here, a large solubility drop from the hot gas temperature to the solubility minimum will provide a large driving force for CVD diamond growth. High-pressure dc, rf, and microwave discharges fit this category and have high diamond growth rates, as expected.

The drop in solubility of carbon in hydrogen from the hot gas temperature to the substrate temperature is very large [60,61] and varies from a factor of about 200× for the low-pressure plasma CVD diamond method to a factor of 7,000 for high-pressure plasma CVD diamond methods

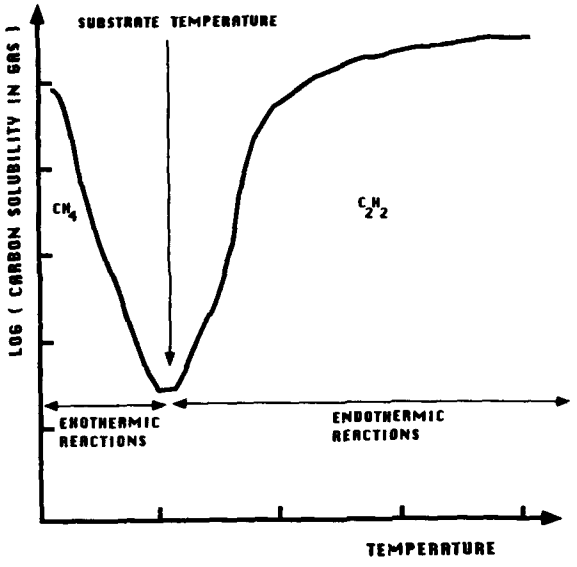

Figure 17. Solubility minimum of carbon in hydrogen.

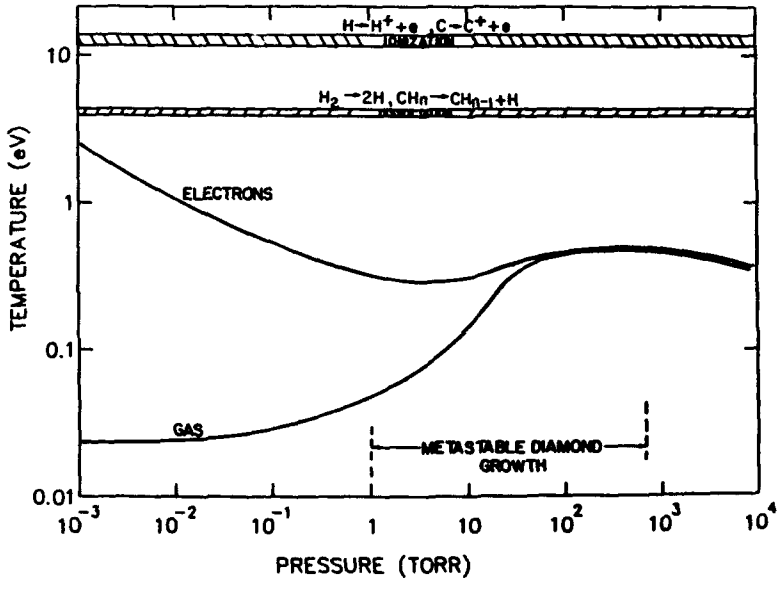

Figure 18. Electron and gas molecule temperatures in low- and high-pressure plasmas.

(Figure 19). The difference in growth rates between high- and low-pressure gas methods can largely be explained by this difference in carbon solubilities.

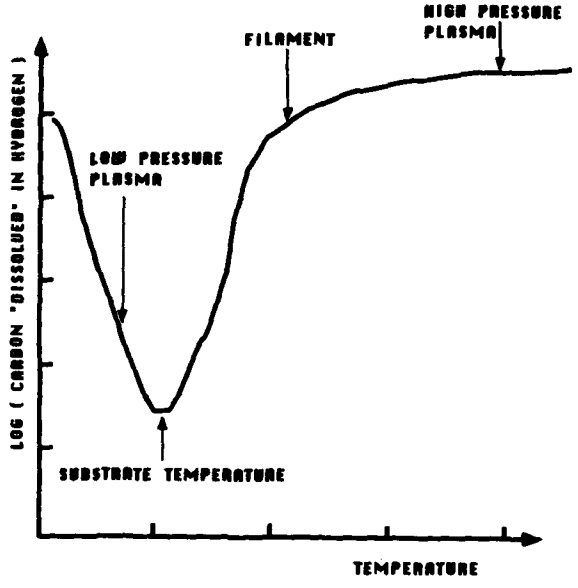

Figure 19. Differential solubility of carbon in hydrogen for different CVD diamond methods.

4.6. GENERATION OF CONDENSABLE CARBON RADICALS

Hydrocarbon molecules will not react with diamond to cause diamond growth. Only hydrocarbon radicals or ions can react at the diamond surface and form a carbon-carbon bond to propagate growth. Ions are very scarce even in a plasma and do not make a measurable contribution to CVD diamond growth. Consequently, CVD diamond growth is produced by hydrocarbon radicals and most of these are generated by a reaction of atomic hydrogen with hydrocarbon molecules [62] as shown schematically in Figure 20. Here an atomic hydrogen reacts with a methane molecule to produce a methyl radical and a hydrogen molecule. Which hydrocarbon radical is most important for diamond growth has not been proven experimentally [63]. However, theory indicates that the acetylene radical may be the principal actor in CVD diamond growth [64].

Hydrocarbon radicals that generate diamond growth can also be produced on the surface of diamond by reactions of atomic hydrogen with adsorbed hydrocarbon molecules.

4.7. ETCHING OF GRAPHITE

Atomic hydrogen etches both diamond and graphite [65,66]. However, if diamond is deposited faster than it is etched, diamond growth can occur. Conversely, if graphite is etched faster than it is deposited, graphite will not grow. Experiments show that atomic hydrogen etches graphite much more rapidly than diamond in the temperature range of CVD diamond growth [65,66]. Thus, the differential etching of atomic hydrogen favors diamond over graphite.

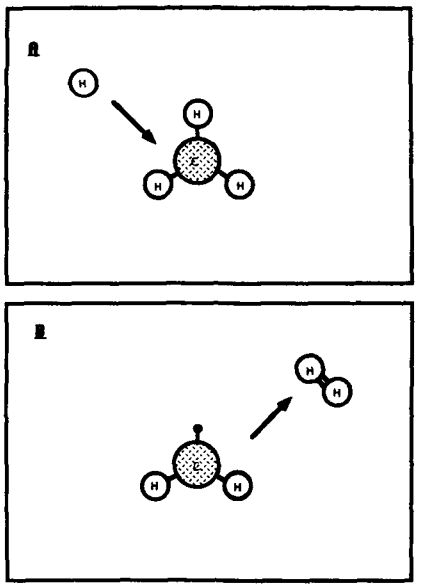

Figure 20. Generation of hydrocarbon radicals by atomic hydrogen abstraction.

4.8. PREVENTION OF GRAPHITE PRECURSORS

In the preceding paragraph, mention was made of the favorable etching characteristics of atomic hydrogen. However, it has not been proven that this differential etching is essential for CVD diamond growth or whether this property of atomic hydrogen is just an accidental correlation that appears logical. A recent proposal [67] suggests that the etching function of atomic hydrogen is not needed for CVD diamond growth. Instead, it is proposed that *molecular* hydrogen at high temperatures suppresses the formation of polycyclic aromatic hydrocarbon radicals that are graphite precursors and thus prevents graphite from forming in the first place by the following reaction:

$$PA\text{–} + H_2 \rightarrow PAH + H \qquad (9)$$

where PA– represents a polycyclic aromatic hydrocarbon *radical* and PAH represents a polycyclic aromatic hydrocarbon *molecule*. Polycyclic aromatic hydrocarbons are composed of benzene rings joined together in an array. These arrays have the same basic structure as graphite, that is, a resonance structure of alternating single and double carbon bonds. If a radical PA– forms from a PAH molecule, the radical can react and attach to another PAH molecule and extend the array. Eventually the array will evolve into a graphitic rather than a diamond structure. By suppressing the formation of radicals with excess molecular hydrogen, evolution of polycyclic aromatic hydrocarbon arrays is arrested.

5. Substitutes for Atomic Hydrogen

Potential substitutes for atomic hydrogen must meet a number of conditions so that they can carry out the various functions that have been discussed above. Potential substitutes for atomic hydrogen include any atoms or molecular groups that form a single bond with carbon. Examples of potential substitutes are F, Cl, Br, I, N, O, S, Si, OH, and OCH_3. Because of a lower bond energy in diatomic molecules of these substitutes than the bond energy of molecular hydrogen (see Table 4), these substitute atomic species will have a much higher concentration than atomic hydrogen under otherwise similar conditions.

TABLE 4
Diatomic Binding Energies
of Potential Atomic-Hydrogen Substitutes

Substitute	Diatomic Binding Energy (kcal/mole)
Hydrogen-Hydrogen	104
Sulfur-Sulfur	60
Chlorine-Chlorine	58
Silicon-Silicon	53
Oxygen-Oxygen	47
Bromine-Bromine	46
Fluorine-Fluorine	44
Nitrogen-Nitrogen	39
Iodine-Iodine	36

In addition to the requirement of forming a single bond with carbon, the product of the reaction between carbon and the atomic-hydrogen substitute must be gaseous. On this basis, Si can be dropped from consideration, for example, since SiC is a solid at CVD diamond growth temperatures. To produce a carbon solubility minimum, there must be exothermic gaseous reaction products at low temperatures and endothermic gaseous reaction products at high temperature between carbon and the substitute. Many of the substitutes meet this requirement.

Most potential atomic hydrogen substitutes etch graphite at much higher rates than atomic hydrogen [68,69]. If the graphite-etching hypothesis is true, then these substitutes would allow higher concentrations of carbon species to be used in the gas, which in turn would increase diamond deposition rates.

Once the list of substitutes has been reduced by the above conditions, some quantitative bond energy requirements must also be met. Let X represent the atomic-hydrogen substitute and C represent carbon and X-X, X-C, and C-C represent, respectively, the X-X, the X-C and the C-C bond energies. If X is to stabilize the diamond surface, then the X-C bond energy must be stronger than the C-C bond energy to prevent the surface reconstruction of diamond, shown in Figure 13. Consequently, stabilization of the diamond surface requires:

$$C\text{-}X > C\text{-}C \qquad (10)$$

Table 5 lists the carbon-carbon bond energy and the carbon-X bond energy for different potential atomic-hydrogen substitutes. Of the list of potential atomic-hydrogen substitutes given above, only F, O, OH and OCH_3 satisfy this condition.

The size of the critical diamond nucleus is also reduced if atomic X reacts with the surface of diamond and lowers its surface energy. Reactivity with the diamond will occur if:

$$C\text{-}X > C\text{-}C \tag{11}$$

Of the potential atomic-hydrogen substitutes given above, only F, O, OH, and OCH_3 satisfy this condition.

TABLE 5
Bond Energies Between Potential Atomic-Hydrogen Substitutes and Carbon

Substitute-Carbon	Bond Energy (kcal/mole)
Fluorine-Carbon	116
Hydrogen-Carbon	99
Oxygen-Carbon	86
Carbon-Carbon	83
Chlorine-Carbon	81
Nitrogen-Carbon	73
Silicon-Carbon	72
Bromine-Carbon	68
Sulfur-Carbon	65
Iodine-Carbon	52

In order for atomic X to generate vacant surface sites and hydrocarbon radicals in the gas or on the diamond surface, a carbon-X bond must be broken and replaced by an X-X bond as shown in Figure 15b. Hence, the X-X bond must be stronger than the C-X bond:

$$X\text{-}X > C\text{-}X \tag{12}$$

Tables 4 and 5 list the carbon-X and X-X bond energies. Unfortunately, no candidate in the above list of potential atomic-hydrogen substitutes satisfies this condition. However, this list is far from complete.

Instead of a straight substitution for atomic hydrogen, substitutes can be worked into a diamond-growing method in a number of ways. Recently, it was suggested [70] that diamond might be grown layer by layer by alternating exposures of diamond to CF_4 and CH_4:

$$CF_4 + \text{Diamond-H} \dashrightarrow \text{Diamond-C-F} + HF \tag{13a}$$

$$CH_4 + \text{Diamond-F} \dashrightarrow \text{Diamond-C-H} + HF \tag{13b}$$

where Diamond-F and Diamond-H represent, respectively, diamond covered with a monolayer of fluorine and hydrogen. This reaction works because the bond strength of H-F exceeds the bond strengths of C-F and C-H. Both reactions are exothermic with an enthalpy of reaction of about 8 kcal/mole.

One can generalize this type of reaction in a number of ways. One way is to use compounds of the type C_NX_M and C_LZ_P:

$$C_NX_M + \text{Diamond-Z} \rightarrow \text{Diamond-C-X} + ZX \tag{14a}$$

$$C_LZ_P + \text{Diamond-X} \rightarrow \text{Diamond-C-Z} + ZX \tag{14b}$$

where Diamond-Z and Diamond-X represent, respectively, diamond covered with a monolayer of Z and X. If the Z-X bond is stronger than the C-X and C-Z bonds, then alternate exposures of diamond to the respective gases will cause alternate exothermic chemical reactions where carbon is placed down during each exposure.

If C_NX_M and C_LZ_P do not react in the gas phase, then a gas mixture of them can be used to grow diamond instead of the alternating exposure of one and then the other depicted in Reaction 14. In this latter case, the reactions still alternate between (a) and (b) on a microscale but not on a macroscopic scale:

$$C_NX_M + C_LZ_P + \text{X-Diamond-Z} \rightarrow \text{Diamond} + ZX \tag{15}$$

where X-Diamond-Z is diamond covered with a monolayer of a mixture of X and Z.

Another way to utilize atomic hydrogen substitutes is to use them as "helpers" rather than as replacements for atomic hydrogen. Potential substitutes that meet many but not all of the above conditions have been found to accelerate diamond growth when used with hydrogen. For example, oxygen, alcohols, and acetone all accelerate diamond deposition when used in small concentrations with hydrogen [71–74].

6. Summary

Atomic hydrogen can be generated in numerous ways. Each method serves as a pathway to develop a new CVD diamond growth process. Atomic hydrogen serves several critical roles in CVD diamond growth, namely: 1) stabilization of the diamond surface; 2) reduction of the size of the critical nucleus; 3) "dissolution" of carbon in the gas; 4) production of carbon solubility minimum; 5) generation of condensable carbon radicals in the gas; 6) abstraction of hydrogen from hydrocarbons attached to surface; 7) production of vacant surface sites; and 8) etching of graphite. Atomic hydrogen can carry out these functions because of favorable relationships between energies for carbon-carbon, carbon-hydrogen and hydrogen-hydrogen bonds. Although no perfect substitute has been found for atomic hydrogen, some substitutes that partially meet the requirements accelerate diamond growth when used with hydrogen. Also some substitutes can be introduced in indirect ways to grow diamond successfully.

7. References

1. Bent, Henry A., (1965) "Second Law of Thermodynamics," Oxford University Press, New York.
2. Davies, Gordon, (1984) "Diamond," Adam Hilger Ltd, Bristol.
3. Bundy, F.P., H.T. Hall, H.M. Strong, and R.J. Wentorf Jr, (1955) *Nature 176*, 51-54.
4. Devries, R.C., (1987) *Ann Rev Mater Sci 17*, 161-187.
5. Eversole, W.G. (April 17, 1962) U.S. Patent No. 3030188,.
6. Angus, J.C., H.A. Will, and W.S. Stanko (1968) *J.Appl.Phys 39*, 2915.
7. Poferi, D.J., N.C. Gardner and J.C. Angus (1973) *J.Appl.Phys 44*, 1428.
8. Spear, K.E. (1989) *J. Am. Ceramic Soc 72*, 171.
9. Spitsyn, B.V., L.L.Bouilov and B.V. Deryagin (1981) *J.Cryst.Growth 52*, 219.
10. Jones, W.E., S.D. Macknight and L. Teng (1979) *Chemical Revs 73*, 407.
11. Langmuir, I. (1912) *J.Amer.Chem.Soc 34*, 860.
12. Langmuir. I (1912) *J.Amer.Chem.Soc 34*, 1310 .
13. Langmuir, I and G.M.J. Mackay (1914) *J.Amer.Chem.Soc 36*,1708.
14. Langmuir, I (1915) *J.Amer.Chem.Soc 37*, 417.
15. Kamo, M., Y. Sato, S. Matsumoto and N. Setaka (1983) *J. Crystal Growth 62*,642.
16. Matsumoto, S. Y. Sato, M. Kamo and N. Setaka (1982) *Japn.J.Appl.Phys 21*, L183.
17. Grabke, H.J. (1965) *Berichte der Bunsengesellschaft 69*, 409.
18. Grabke, H.J (1970) *Metallurgical Transactions 1*, 2972.
19. Anthony, T.R. (1987) MRS Fall Meeting, Nov30-Dec3, Boston.
20. Vakil, H.B.(March 1989) Am Chem Soc Meeting, Dallas.
21. Hughes, J.E. (1959) *J.Less Common Metals 1*, 377.
22. Gaines, G.B. C.T.Sims and R.I.Jaffe, (1959) *J.Electrochem Soc 106* ,881.
23. Lux, Benno and R. Haubner (1989) *Proceedings 12th Int Plansee Seminar C16*, 461.
24. Wood, R.W. (1923) *Proc Roy Soc, Ser A 102*, 1.
25. Suzuki, J., H. Kawarada, K.Mar, J.Wei, Y.Yokota and A. Hiraki (1989) *Jap Journ Appl Phys 28*, L281.
26. Watanabe, I. and K Sugata (1988) *Jap Journ.Appl.Phys. 27*, 1397.

27. Matsumoto, O, H.Toshima and Y.Kanzaki (1985) *Thin Solid Films 128*, 341.

28. Mitsuda,Y., Y.Kojima,T.Yoshida and K.Akashi. (1987) *Journ Mat Sci 22*, 1557.

29. Kawarda, H., K.S. Mar and A.Hiraki (1987) *Jap.Journ.App.Phys 26*, L1032.

30. Kamo, M., Y.Sato, S. Matsumoto and N. Setaka (1983) *J.Crystal Growth 62*, 642.

31. Saito, Y., S. Matsuda and S.Nogita (1986) *Journ.Mat.Sci.Letters 5*, 565.

32. Vandenbulke, L., P.Bou, R. Herbin, V.Cholet and C.Beny (1989) *Journ de Phys, Colloque C5*, Suppl 5, Tome 50, 177.

33. Matsumoto, S. (1985) *J.Mater.Sci.Letters 4*, 600.

34 . Taylor, H.S. (1926) *J.Amer.Chem.Soc.48*, 2840.

35. Taylor, H.S. and G.Marshall (1925) *J.Phys.Chem 29*, 842.

36. Melville, H.W. and J.C.Robb (1949) *Proc.Roy.Soc., Ser.A, 196*, 445.

37. Cvetanovic, R.J. and L.C.Doyle (1969) *J.Phys.Chem. 50*, 4705.

38. Yang, K.(1962) *J.Amer.Chem.Soc.84*, 719 .

39. Black, R.A. (1960) *J.Phys.Chem. 64*, 124.

40. Bishop, W.P. and L.M.Dorfman (1970) *J.Chem.Phys 52*, 3210.

41. Chonan, T., M.Uenura, S.Futaki and S.Nishi (1989) *Jap.Journ.Appl.Phys 28*, L1058.

42. Suziki, K., A.Sawabe, H.Yasuda and T.Inuzuka (1987) *Appl.Phys.Letters50*,728.

43. Akatsuka, F., Y.Hirose and K.Komaki (1988) *Jap.Journ.Appl.Phys 27*, L1600.

44. Kurihara, K., K.Sasaki, M.Kawarada and N.Koshima (1988) *Appl Phys Letters 52*, 437.

45. Matsumoto, S., T. Kobayshi, M. Hino, T. Ishigaki, and Y. Moriyoshi (1987) *8th International Symposium on Plasma Chemistry, ISPC 8*, Paper No. S7-03, p2458, Tokyo.

46. Baldwin, R.R., D.E. Hopkins and R.W. Walker (1970) *Trans Faraday Soc. 66*, 189.

47. Fenimore, C.P. and G.W.Jones (1961) *J.Phys.Chem 65*, 2200.

48. Fenimore, C.P and G.W.Jones (1963) *9th Symp. Int. Combust.Proc. 597.*

49. Hirose, Y. and N. Kondo (March 29, 1988) "Program and Book of Abstracts," Japan Applied Physics 1988 Spring Meeting, p434.

50. Yazu, S., S.Sato and N. Fujimori (August 16-20, 1988) *SPIE Proceedings*, San Diego.

51. Hanssen, L.M., W.A. Carrington, D.B. Oakes, J.E. Butler and K.A .Snail (July 11-13, 1989) *1989 Diamond Technology Initiative Symposium*, Paper T7.

52. Goodwin, D.G. (July 11-13, 1989) *1989 Diamond Technology Initiative Symposium,* Paper T15.

53. Cappelli, M.A. (July 11-13, 1989) *1989 Diamond Technology Initiative Symposium,* Paper W1.

54. Glassman, I. "Combustion," (1977) Academic Press, New York.

55. Pate, B.B. (1986) *Surf. Sci. 165*, 83 .

56. Angus, J.C. and C.C. Hayman (1988) *Science 241*, 913.

57. Bachman, P.K. and R. Messier (1989) *Chem & Eng News 67*, 24.

58. Litos, R., R. Haubner, and B. Lux (1989) *Proc 12th Int Plansee-Seminar C2*, 615.

59. Joffreau, P.O., R.Haubner and B. Lux (1988) *J.Ref Hard Metals 7*,186.

60. Lersmacher, B., H.Lydtin, W.F.Knippenberg and A.W. Moore (1967) *Carbon 5*, 205.

61. Van Den Hoek, W.J. and W. Klessens (1975) *Carbon 13*, 429.

62. Chen, Ian (1988) *J.Appl.Phys 64*, 3742.

63. Harris, S.J., A.M. Weiner and T.A. Perry (1988) *Appl.Phys.Letters 53*,1605.

64. Frenklach, M. and K.E. Spear (1988) *J.Mater.Res. 3*, 133.

65. Hsu, W.L. (Nov,1987) *34th Nat Symp AVS*, TF-WeA1,.

66. Deryagin, B.V. and D.V.Fedoseev (1977) "Growth of Diamond and Graphite from the Vapor Phase," *Izd Nauka.*, Moscow, USSR.

67. Frenklach, M. (1989) *J.Appl.Phys 65*, 5142.

68. Rosner, D.E. and J.P.Strakey (1973) *Jour.Phys.Chem 77*, 690.

69. Rosner, D.E. and H.D. Allendorf (1971) *Jour.Phys.Chem 75*, 308.

70. Rudder, R.A., J.B.Posthill, G.C.Hudson, M.J.Mantini and R.J.Markunas, (July 11-13, 1989) *1989 Diamond Technology Initiative Symposium*, Paper W16.

71. Kawato T. and K. Kondo (1987) *J.Appl.Phys. 26*, 1429.

72. Chang, C.P., D.L.Flamm, D.E.Ibbotson and J. Mucha (1988) *J.Appl.Phys 63*, 1744.

73. Saito, Y., K. Sato, H. Tanaka, K. Fujita and S. Matsuda (1986) *J.Mater.Sci 23*, 842.

74. Hirose, Y. and Y. Terasawa (1986) *Japan J. Appl. Phys 25*, L519.

SELECTED-AREA DEPOSITION OF DIAMOND FILMS

K. KOBASHI, T. INOUE, H. TACHIBANA, K. KUMAGAI,
K. MIYATA, K. NISHIMURA, AND A. NAKAUE
Kobe Steel Ltd., Electronics Research Laboratory,
1-5-5 Takatsukadai, Nishi-ku, Kobe 673-02,
Japan

ABSTRACT. Diamond film patterns with line/space dimensions of a few μm were accomplished on Si substrates prepared by reactive-ion etching (RIE) and amorphous-Si masking (ASM) methods, both including a photolithography process. A growth of diamond particles at selective sites was also attained using the RIE method.

1. INTRODUCTION

Diamond films synthesized by chemical vapour deposition (CVD) are a potential material for high-performance microelectronic devices [1-5] because diamond exhibits unique and excellent properties such as large band gap, low dielectric constant, high carrier mobility, high breakdown voltage, and high thermal conductivity. In Table 1, the characteristics of diamond are compared with those of Si, GaAs, SiC, and cBN.

Diamond itself is resistant to high temperatures. Furthermore, thermal diffusion of impurity atoms trapped in diamond is severely restricted because of the small lattice constant, and hence the p-n junction is not destroyed at high temperatures. Thus, it is expected that diamond semiconductor devices will be able to function at high temperatures, such as 400°C and higher. This is in strong contrast to the fact that Si and GaAs devices cannot work above temperatures of about 150°C and 200°C, respectively. Diamond is also superior to other materials in chemical inertness and resistance to radiations. For all the reasons stated above, diamond electronic devices are expected to be used in severe industrial environments such as automobiles, aerospace and nuclear reactors.

In order to visualize key technologies for diamond devices, Fig. 1 illustrates a possible process for fabricating a MISFET (Metal-Insulator-Semiconductor Field Effect Transistor). Some of the steps indicated by the arrows include a photolithography process shown in Fig. 2. From these figures, one may see that the following studies are necessary to establish the fabrication process technology:

R. Freer (ed.), The Physics and Chemistry of Carbides; Nitrides and Borides, 159–167.
© 1990 *Kluwer Academic Publishers. Printed in the Netherlands.*

TABLE 1. Properties of semiconducting materials

	Diamond	Si	GaAs	Beta-SiC	cBN
Crystal structure	Diamond	Diamond	Zincblend	Zincblend	Zincblend
Lattice constant (A)	3.567	5.431	5.653	4.360	3.615
Density (g/cm^3)	3.515	2.42	5.32	3.16	3.48
Melting point	~4000	1690	1511	3100	3000
Linear thermal expansion coeff. ($10^{-6}/K$)	4.5	2.6	6.6	4.8	4.3
Thermal conductivity (W/cm.K)	20	1.5	0.5	5.0	13
Refractive Index	2.41	3.43	3.75	2.48	2.11
Dielectric const.	5.5	11.8	12.8	9.7	-
Band gap (eV)	5.5	1.12	1.43	2.20	6.6-8.0
Mobility ($cm^2/V.s$)					
electron	1800	1500	8500	1000	-
hole	1600	600	420	70	-
Breakdown voltage ($x10^5V$)	100	3	4	40	-
Saturated electron velocity ($x10^7$ cm/s)	2.7	1.0	2.0	2.5	-

(1) morphology, crystal orientation and growth of diamond films
(2) characterisation of structural defects in the films
(3) synthesis of p- and n-type semiconducting films
(4) metal electrodes and metal/diamond interface structures
(5) MIS structures
(6) heterojunctions between diamond and other films
(7) planar technology
(8) selective deposition
(9) anisotropic etching
(10) device design
(11) heteroepitaxial growth
(12) large area, uniform and high rate deposition.

The purpose of the present paper is to demonstrate the possibility of selective deposition of diamond films on Si substrates which are prepared in two different ways: reactive-ion etching (RIE) and amorphous silicon masking (ASM). Deposition of both continuous diamond films on designated areas and nucleation of diamond particles at designated locations are possible using the methods presented here. The former will be hereafter referred to as Selected-Area Deposition (SAD) and the latter as Selective Nucleation.

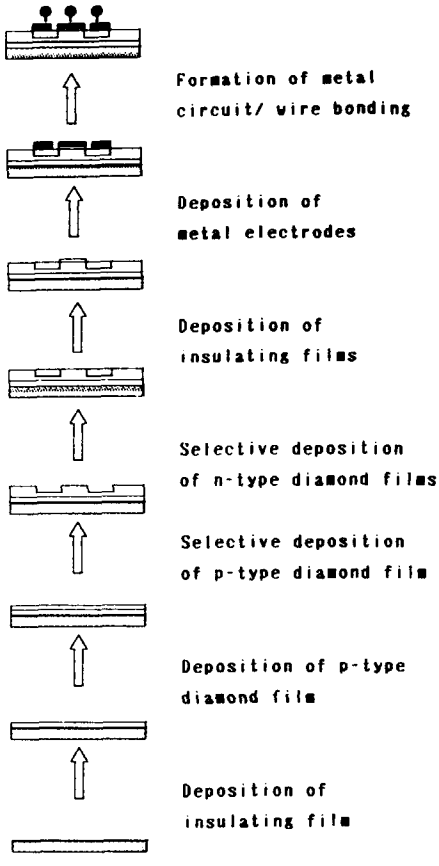

Figure 1. MISFET fabrication process.

2. EXPERIMENTAL

The selective deposition processes using the RIE and ASM methods are schematically shown in Figs. 3 and 4, respectively. First, a Si(111) wafer was polished by a diamond paste for 1h, and photoresist film patterns were formed on the substrate using a standard photolithography technique.

In the RIE method, the wafer was etched by a radio-frequency (rf) plasma using a gas mixture of carbon tetrafluoride, Ar and oxygen, followed by a complete removal of the photoresist films. The etching depth was less than 0.5 mm. In the ASM method, a hydrogenated amorphous silicon (a-Si:H) film was uniformly deposited by rf plasma CVD on the photolithographically patterned wafer. The thickness of the deposited a-Si:H was about 300 Å. The photoresist films were then lifted-off together with the overdeposited a-Si:H films in an organic solvent.

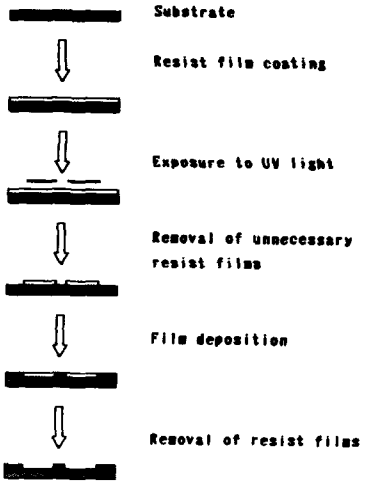

Figure 2. The photolithography process

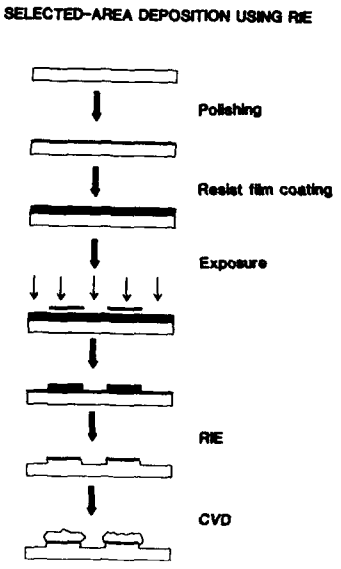

Figure 3. The RIE method.

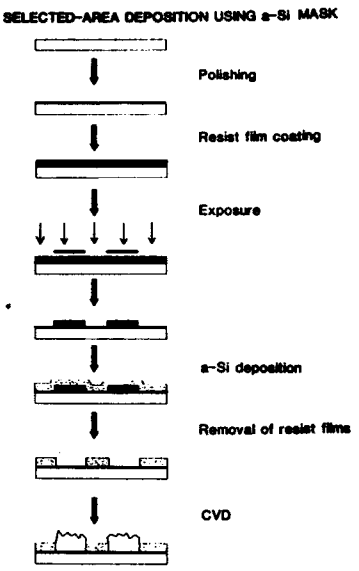

Figure 4. The ASM method.

The diamond deposition was made by Electron-Assisted CVD (EACVD) and microwave plasma CVD (MPCVD). The experimental conditions for EACVD were as follows: For the source gas, a methane gas diluted to 3 vol% by hydrogen was used. The gas pressure was 30 Torr and the gas flow rate was 100 sccm. The bias voltage and current were 90V and 1A, respectively. The substrate temperature, measured by a thermocouple attached to the back of the substrate, was 750°C during CVD. The filament temperature measured by a pyrometer was about 2000°C. The MPCVD apparatus used has been described in [6]. Here, a methane gas diluted to 0.5 vol% by hydrogen was used for the source gas, the gas pressure was 31.5 Torr and the flow rate was 100 sccm. The substrate temperature measured by an optical thermometer was 800°C and the microwave power input was about 300W.

3. RESULTS OF THE RIE METHOD

Figure 5 shows the SAD results for the case in which the Si substrate was RIE-treated for 15 min., and the diamond deposition was made for 70 min. by EACVD. In Fig. 5, the five groups of bars are polycrystalline diamond films deposited on the patterns of 5.0-1.5 μm line/spacing as indicated by the reversed numbers, which are also made by diamond films. In Fig. 6, which is a cross sectional view of a 4 μm line/space pattern after a 120 min. deposition, it is clear that diamonds started to grow from the plateau, which is the polished Si surface area, and finally occupied a considerably larger area beyond the plateau. The lateral growth of diamond resulted in a film width of about 8 μm, twice as large as the plateau width.

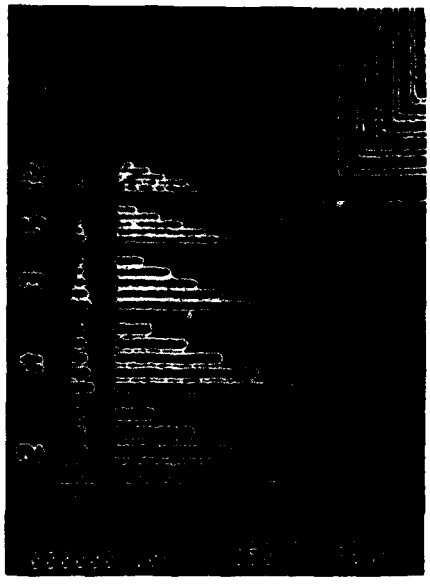

Figure 5. A SAD result using the RIE method.

Figure 6. A cross-sectional view of the film shown in Fig. 5.

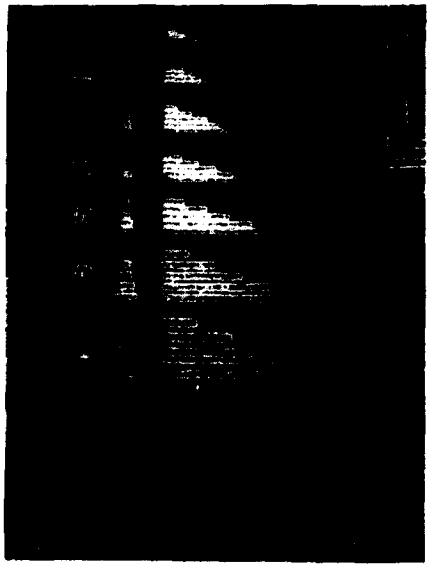

Figure 7. A SAD result using the ASM method.

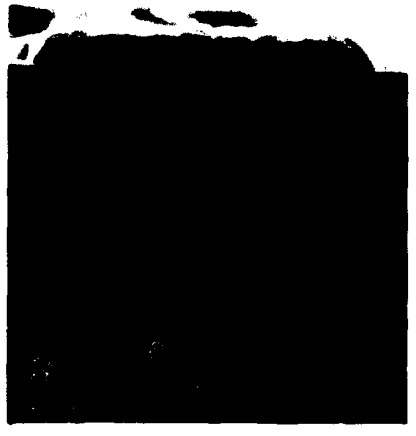

Figure 8. A cross-sectional view of the film shown in Fig. 7.

substrates prepared by the RIE method, diamond deposition was also made by MPCVD. However, only diamond particles grew and no continuous diamond film was formed even after a deposition for 7h.

4. RESULTS OF THE ASM METHOD

Figure 7 shows the SAD results of the ASM method, where the diamond films were deposited by MPCVD for 7h. It is seen that a highly selective deposition was attained according to the photomask pattern. An advantage of the ASM method is that the definition of the diamond film pattern is better than in the RIE method. This is because the diamond film thickness was only about 0.9 μm and no significant lateral growth has occurred, as seen in Fig. 8. By comparing Fig. 5 with Fig. 7, it is observed that in the latter case using the ASM method, nucleation of diamond particles occurred more frequently on the undesignated areas, i.e. on the a-Si:H film, so that the diamond deposition was less selective. However, in a similar experiment in which the a-Si film thickness was about 1 μm, the selectivity was greatly improved. The diamond film deposition was also carried out by EACVD, but in this case, diamonds grew almost non-selectively on the substrate.

5. RAMAN SPECTRA

Spectra (a) and (b) in Fig. 9 show the Raman spectra of diamond films deposited using the RIE and ASM methods, respectively. In both cases, there is a strong line at 1333 cm^{-1} due to diamond, and a broad band around 1550 cm^{-1} due to graphitic/amorphous carbon. In the spectrum (b) of Fig. 9, the intensity of the 1550 cm^{-1} band is very weak compared with the spectrum (a) of Fig. 9. The 1550 cm^{-1} band intensity relative to the 1333 cm^{-1} band intensity is even smaller than the corresponding relative intensity of the Raman bands of the diamond films deposited uniformly on Si substrates using the same experimental conditions. This means that in the film shown in Fig. 5, the density of grain boundaries, which is believed to be the major source of graphitic/amorphous carbon, is less than that in the uniformly deposited films.

6. RESULTS OF SELECTIVE NUCLEATION

An attempt to selectively nucleate diamond particles on Si was made using the RIE method. The result is shown in Fig. 10. In this case, polished square areas of 1.5 μm x 1.5 μm size were photolithographically left intact on a square lattice with a spacing of 10 μm. Both single crystalline and twinned particles were grown on each of the designated areas.

7. DISCUSSION

The major difference between the RIE method presented here and the methods used in [7,8] is that the former used a plasma etching whereas

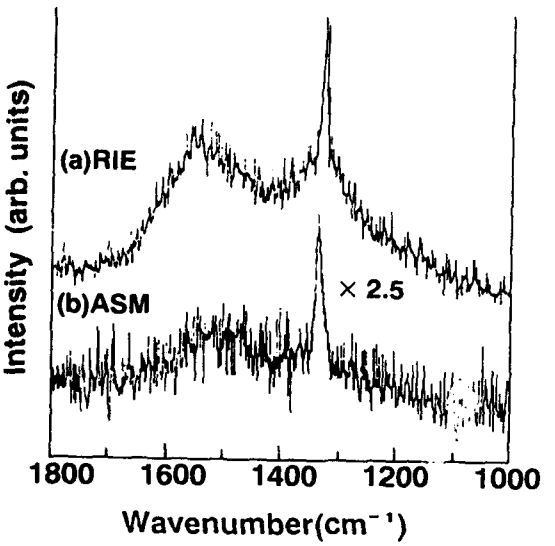

Figure 9. Raman spectra of diamond films (a) RIE, (b) ASM.

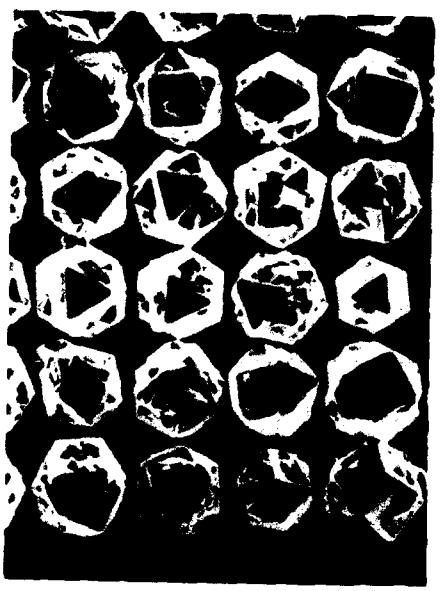

Figure 10. Selectivity nucleation of diamond particles on Si using the RIE method.

Thus, it was demonstrated that the RIE method can generate a highly selective deposition of polycrystalline diamond films on the designated areas when the deposition was made by EACVD. Using the

the latter two groups used an Ar ion beam to etch the polished Si substrate surface. It seems that there is no significant difference in selectivity between the two methods but the RIE method seems to be more advantageous because there are no problems associated with beam directionality and it is easier to control the etching process.

The ASM method is demonstrated here for the first time. Using ceramic films such as SiO_2, Si_3N_4 and metal films for masking, similar SAD will be attained. This method can be used for SAD and Selective Nucleation of CVD diamond not only on Si and other substrates but also on bulk diamond and CVD diamond films.

In conclusion, Selected-Area Deposition and Selective Nucleation were attained using the RIE and ASM methods. Both technologies will be used in future for the fabrication of diamond films for microelectronic devices.

ACKNOWLEDGEMENT

The authors would like to acknowledge Professor J.T. Glass and Professor R.F. Davis of North Carolina State University for fruitful discussion and collaboration.

REFERENCES

1. Davis, R.F., Sitar, Z., Williams, B.E., Kong, H.S., Kim, H.J., Palmour, J.W., Edmond, J.A., Ruy, J., Glass, J.T. and Carter, Jr., C.H. (1988) Mater. Sci. Eng. B1, 77.

2. Geis, M.W., Rathman, D.D. Ehrlich, D.J., Murphy, R.A., Lindley, W.T. (1987) IEEE Electron Device Lett., EDL-8, 341.

3. Geis, M.W., Efremow, N.N. and Rathman, D.D. (1988) J. Vac. Sci. Technol. A6, 1953.

4. Vavilov, V.S. and Konorova, E.A. (1976) Sov. Phys. Ups., 19, 301.

5. Bazhenov, V.K., Vikulin, I.M., and Gontar, G.A. (1985) Sov. Phys. Semicond., 19, 829.

6. Kobashi, K., Nishimura, K., Kawate, Y., and Horiuchi, T. (1988) Phys. Rev. B38, 3067.

7. Hirabayashi, K., Taniguchi, Y., Takamatsu, O., Ikeda, T., Ikoma, K., and Iwasaki-Kurihara, N. (1988) Appl. Phys. Lett., 53, 1815.

8. Hiraski, A. et al, J. Appl. Phys., to be published.

SURFACE ANALYSIS OF DIAMOND NUCLEATION ON SILICON AND ELECTRON MICROSCOPY OF THE DIAMOND/SILICON INTERFACE

B. E. WILLIAMS, D. A. ASBURY AND J. T. GLASS
Department of Materials Science and Engineering
North Carolina State University
Raleigh, NC 27695-7907

ABSTRACT. The nucleation of diamond films grown by microwave plasma chemical vapor deposition on silicon substrates has been examined by Auger electron spectroscopy (AES), x-ray photoelectron spectroscopy (XPS) and electron microscopy. Furthermore, cross sectional transmission electron microscopy (XTEM) was utilized to examine the diamond/silicon interface. The immediate (< 5 minutes) formation of a cubic SiC buffer layer was observed prior to the growth of a detectable diamond film. This SiC layer was too thin to be observed (< 10 monolayers) in XTEM when methane concentrations in the feedgas were relatively high (2.0%) but was observable via AES and XPS even at 3.0% CH_4. At low concentrations (0.3% CH_4) the SiC layer was relatively thick (~5OÅ) and easily observed in XTEM.

Introduction

Diamond is an excellent candidate material for use in both electronic and wear resistant coating applications due to its unique combination of exceptional properties.[1-3] Regarding electronic applications, these properties include high hole and electron mobilities (2000 and 1800 $cm^2 \cdot V^{-1} \cdot sec^{-1}$, respectively), a high breakdown voltage, high carrier drift velocities, and a much higher thermal conductivity (from 1000 to 10,000 W/m-K) than even copper, which is considered a good thermal conductor. Diamond films may thus be utilized as heat sinks on which to mount various electronic devices fabricated from more conventional semiconductors such as Si and GaAs or directly for the fabrication of microwave devices as well as devices to be employed in high power, high current density, high temperature and/or high radiation flux applications. Recent attempts to grow diamond films for such potential applications have been very encouraging. Researchers have deposited polycrystalline diamond films via RF-plasma CVD,[4] microwave plasma CVD,[5] and hot filament CVD[6] as well as various modifications of these techniques. However, in order to reach the true potential of diamond in many of the aforementioned electronic applications, high quality single crystal films will be necessary on economical non-diamond substrates. Therefore, it is important to develop an understanding of the nucleation of diamond on substrates of interest. The present paper investigates such nucleation on "scratched" single crystal Si substrates which have been the most extensively utilized substrates to date.

R. Freer (ed.), The Physics and Chemistry of Carbides; Nitrides and Borides, 169–181.
© 1990 *Kluwer Academic Publishers. Printed in the Netherlands.*

Experimental

The diamond films analyzed in this research were grown on 2 cm by 1 cm n-type Si (111) substrates immersed in a CH_4/H_2 plasma created by a 2.45 GHz microwave source. A schematic of the deposition system is shown in Figure 1. Details of the system have been given elsewhere.[7] The substrate temperature as measured by an optical pyrometer was maintained at approximately 800°C by controlling the microwave power (which was typically 300 - 350 watts). No corrections were made for emissivity changes or for the quartz window; therefore, this temperature is an approximation. The total pressure in the chamber was maintained at 30 Torr, and only the CH_4/H_2 ratio in the feedgas was varied for the films studied in this work (between 0.3 and 2.0% CH_4 in H_2). Raman spectroscopy was utilized to verify the presence of diamond.

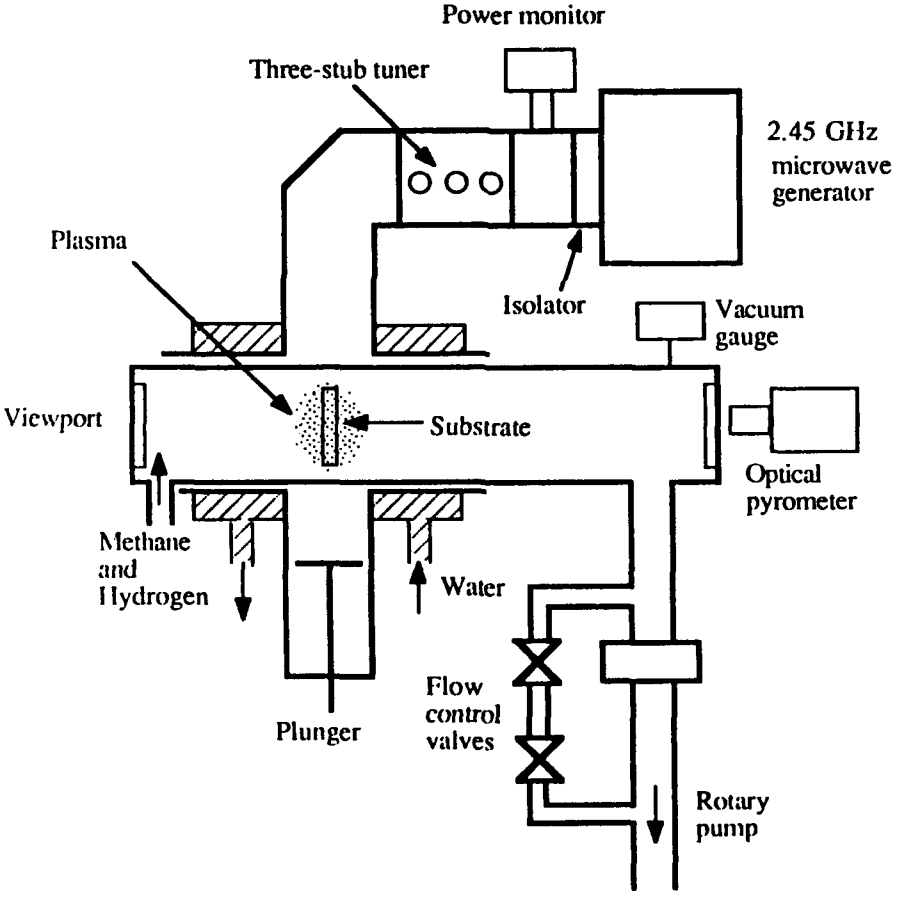

Fig. 1. Schematic diagram of microwave plasma CVD system used for the deposition of diamond films.

Prior to growth, the commercially polished silicon substrates were scratched with 0.25 μm diamond paste for one hour in order to increase the nucleation density of the diamond particles which make up the film. The substrates were then ultrasonically cleaned in acetone, ethanol, and distilled water. For the preparation of plan-view TEM specimens, 2.5 X 2.5 mm sections were cut from the as-grown sample with a diamond saw. The substrate was then thinned with 600 grit SiC paper to a thickness of 65 μm and subsequently polished with 0.3 μm Al_2O_3 suspended in water. This polished side was then dimpled with a steel ball coated with 1 μm diamond paste until the sample was less than 10 μm thick at the center of the crater. After affixing this sample to a 3 mm diameter Ta support ring, ion milling from the substrate side with 6 kV Ar^+ was used to thin the sample until perforation occurred. To remove as much ion milling damage as possible, the sample was then milled with 3 kV Ar^+ for an additional 15 minutes. Cross-sectional TEM (XTEM) samples were prepared in a similar manner. In this case, sections were obtained by cutting perpendicular to the plane of the film after gluing the substrate to silicon buffer layers to form a sandwich. Thinning of the sample was achieved as described for plan-view TEM samples, and the dimpling crater was carefully aligned to ensure that perforation of the specimen during ion milling occurred very near the diamond film. For the TEM reported in this research, a Hitachi H-800 operated at 200 kV and a Philips 430 operated at 300 kV were utilized.

The surface analysis was conducted in a custom built multi-technique analysis system containing Auger electron spectroscopy (AES), x-ray photoelectron spectroscopy (XPS), electron energy loss spectroscopy (EELS), reverse view low energy electron diffraction (RVLEED) and electron stimulated desorption (ESD) capabilities.

The Auger and XPS spectra were recorded using a Riber MAC 2 semidispersive electron energy analyzer which has a resolution of 0.3 eV to 4 eV. The resolution (ΔE) of the spectrometer is constant over the entire range of kinetic energies. For Auger spectroscopy, 3 KeV electrons were utilized and the analyzer was modulated at 8 kHz and differentiated spectra were obtained using a lock-in amplifier. The XPS was obtained using Mg Kα radiation, and spectra were recorded by pulse counting. The system is attached through ultrahigh vacuum (UHV) to a diamond microwave plasma CVD system and thus able to conduct in vacuo analysis of such films. However, the present results were obtained ex situ, thus samples were exposed to the atmosphere prior to analysis.

Results and Discussion

NUCLEATION OF DIAMOND ON SILICON

A transmission electron micrograph of diamond nucleation on Si is shown in Figure 2. In this case, the diamond growth was stopped after 45 minutes of growth using 1.0% CH_4 in H_2. Three interesting observations can be made from this data. First, the diamond is found to nucleate in a highly three dimensional, particulate manner. This is due to the very high surface energy of diamond which favors C-C as opposed to C-Si bonding, thus yielding 3-D nucleation and growth.[8] Next, the particles are also seen to vary in size indicating that nucleation probably does not occur all at one

time. Rather, new particles continue to nucleate while previously nucleated particles undergo significant growth. Another explanation for the observed results is that the growth rate of the particles varies substantially. However, given the broad range of particle sizes observed, this explanation seems unlikely. Finally, "scratches" can also be seen in these micrographs as bright lines. Some of the particles are seen to nucleate along these scratches; however, others appear to nucleate without the aid of any scratches. More research is necessary to understand the role of the scratches, but it appears from these results that they are an aid to nucleation density rather than a necessary condition.

Fig. 2. Plan-view TEM micrograph of diamond particles nucleated on (111) silicon.

To further evaluate the nucleation of diamond on Si, a series of samples grown for 5, 15, 30, 120 and 360 minutes with 3.0% CH_4 in H_2 were examined with XPS and AES. Scanning electron microscopy was also conducted and is shown for the 30 and 120 minute samples in Figure 3. The formation of a film is shown to occur by the intergrowth of discrete particles. C and Si concentrations from XPS correlate well with the observed particle coverage. XPS spectra for the 5 minute and 120 minute (2 hr.) growths are shown in Figure 4. The carbon film and silicon substrate are observed, as well as oxygen contamination. In addition to the XPS peaks of the elements, x-ray excited Auger peaks of the oxygen and carbon are visible. After 2 hours of growth the sample is seen to consist of mostly C with only small concentrations of Si and O remaining. The oxygen is believed to be due to the native oxide formed on the Si during atmospheric exposure prior to analysis.

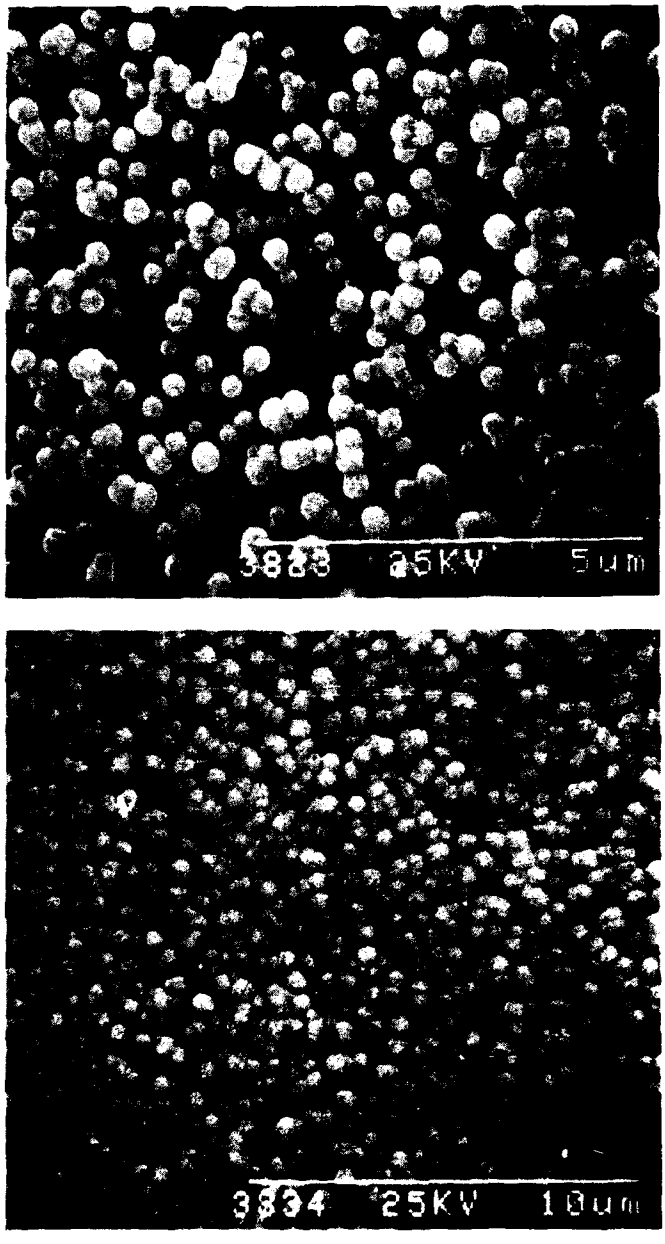

Fig. 3. SEM micrographs of diamond grown on silicon using 3.0% CH_4/H_2 for (a) 30 min. and (b) 120 min.

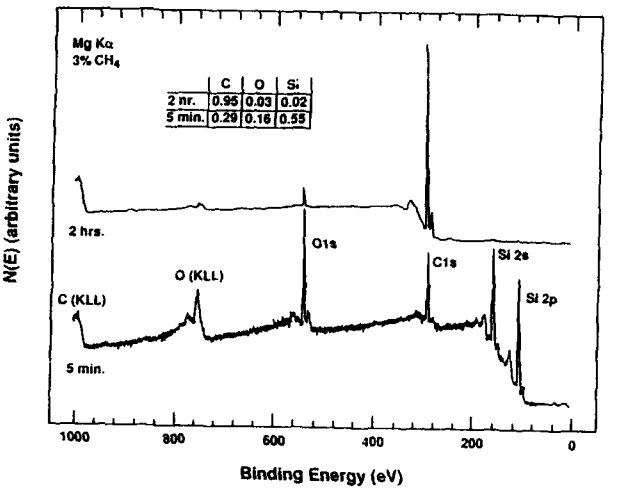

Fig. 4. XPS spectra obtained from diamond films grown with 3.0% CH_4/H_2 for 5 min. and 120 min.

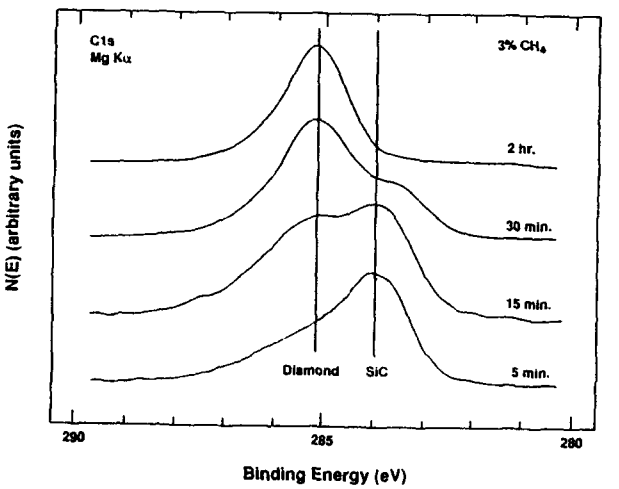

Fig. 5. XPS C1s spectra obtained after growth times of 5 min., 15 min., 30 min., and 2 hrs. using 3.0% CH_4/H_2.

Examining the carbon 1s, XPS peak more closely (Figure 5), an interesting observation is made. The first carbon peak to become visible is due to SiC.[9] This is followed by the slow increase in intensity of the diamond C 1s peak as growth proceeds. Although the formation of a SiC layer between the diamond film and the silicon substrate might be considered a somewhat obvious result, two major points make this observation interesting. First, formation of the SiC layer is extremely rapid relative to the formation of a discernable diamond layer. The plasma plays a critical role in this SiC formation since the growth temperature is much lower than generally used in the formation of such films by thermal CVD.[10] Second, the formation of a SiC layer has not been observed during XTEM of such films grown with relatively high methane concentrations as discussed later in this paper.

These results were verified by examining the fine structure of the carbon *KLL* Auger peak of these samples as shown in Figure 6. After 15 minutes of growth, this fine structure has the typical shape of a silicon carbide. After 2 hrs., the shape has become very similar to that obtained from bulk diamond.[11]

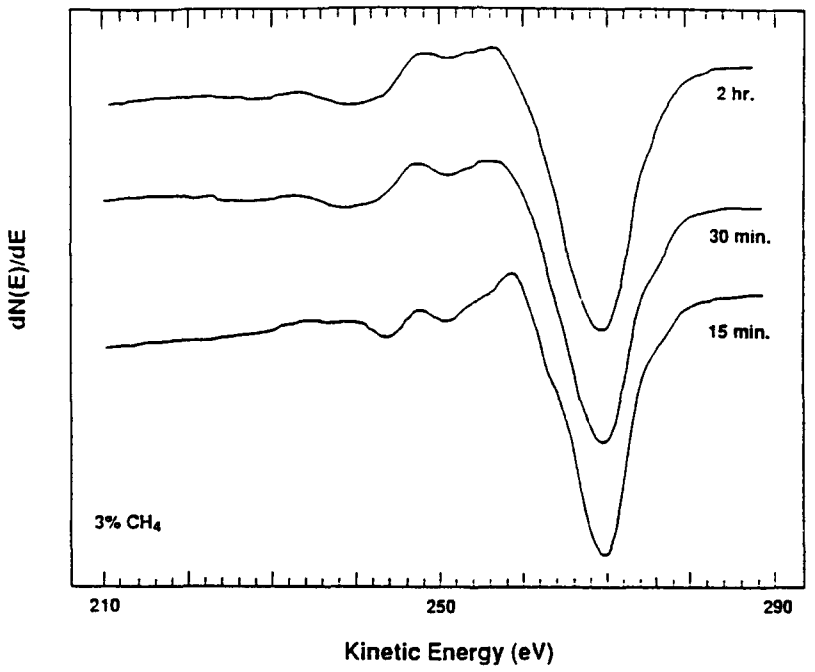

Fig. 6. AES C *KLL* spectra as a function of growth time. A characteristic SiC peak shape is present during the early stages of growth.

Thus, it appears that diamond is actually growing on a very thin layer of SiC rather than directly on the Si substrate. Unfortunately, it is not believed by the present authors that a similar statement can be made about the nucleation of the diamond. That is, it may still be possible that the initial nucleus of the diamond forms on Si but

due to the different growth modes for SiC and diamond, coupled with a rapid initial SiC growth rate, only the SiC is detectable. The SiC is nucleating as a true film, thereby rapidly covering the surface and yielding a strong initial XPS and AES signals. The diamond, however, is growing as small particles scattered over the surface, yielding a small signal due to the low areal coverage on the surface. As time continues, the SiC growth becomes diffusion limited since Si from the substrate is necessary. Thus the SiC growth begins to slow whereas the diamond continues to grow without limitations. After some period of time the diamond particles begin to grow up over the SiC layer, and thus yield the majority of the XPS and AES signal. It appears from the electron microscopy discussed in the following section that with high methane concentrations in the feedgas this overgrowth occurs relatively rapidly, thus yielding a thin SiC layer, whereas at lower concentrations a thicker SiC layer is able to form. Regarding the question of whether the diamond nucleates on Si or SiC, the authors believe that this question is still open and will remain so until further electron microscopy, field ion microscopy or scanning tunneling microscopy is performed during the initial stages of diamond nucleation.

THE DIAMOND-SILICON INTERFACE

To obtain more information about the nature of the diamond-silicon substrate interface, the samples were examined with cross-sectional transmission electron microscopy. Micrographs of films grown at 2.0% CH_4 and 0.3% CH_4 in H_2 are shown in Figures 7(a) and 7(b), respectively. The density of defects and/or the amount of

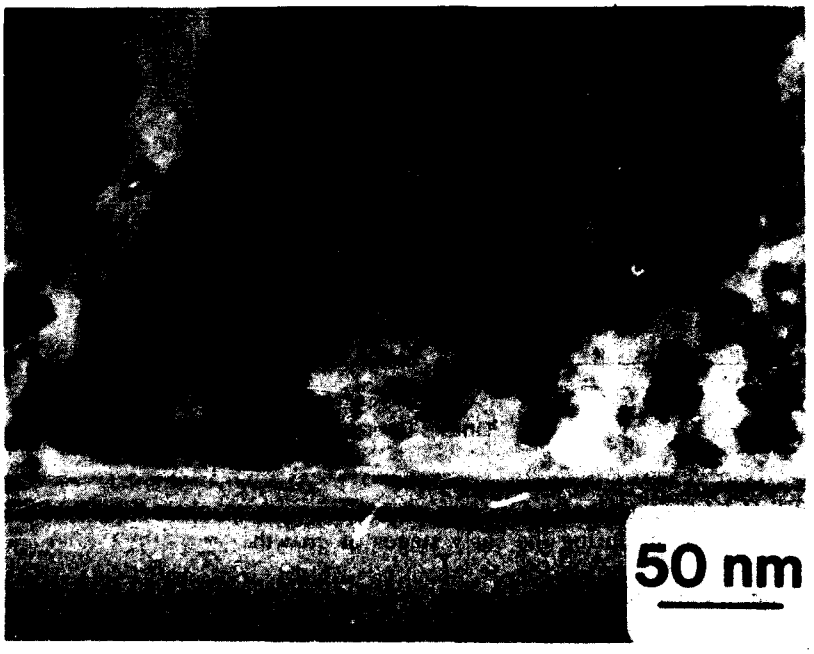

Fig. 7. (a) XTEM micrograph of diamond film grown in 2.0% CH_4/H_2, showing increased density of defects in the diamond film.

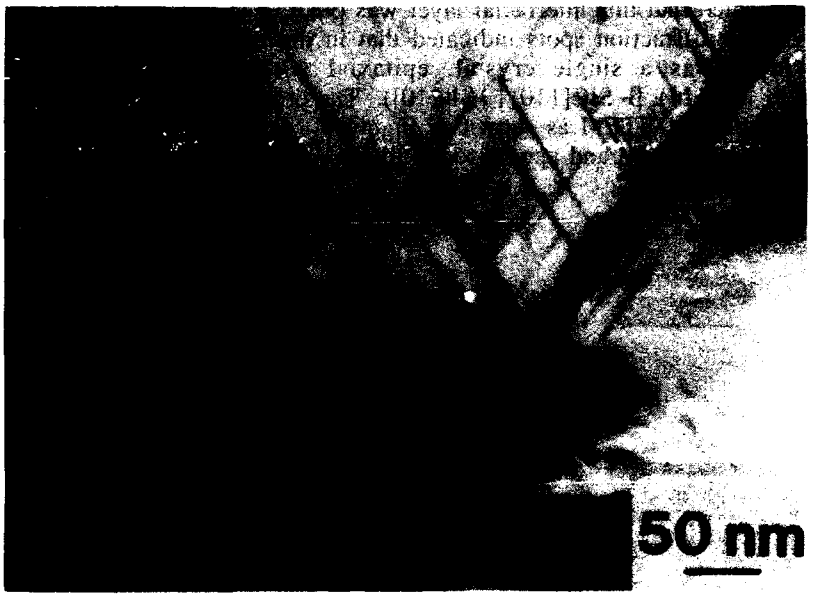

(b) XTEM micrograph of diamond film grown in 0.3% CH_4/H_2 showing lower defect density on the diamond film.

elastic strain (indicated by the dark regions in the micrograph) in the 2.0% CH_4 film [Figure 7(a)] is significantly higher than that observed in the XTEM micrograph of the 0.3% CH_4 film [Figure 7(b)], probably due to the lower growth rate at these lower methane concentrations which allows a less defective and/or less strained film to form. This observation may also be related to a decreased sp^2 bonding component which was observed during Raman spectroscopy,[12,13] but more research is necessary to confirm this hypothesis.

Closer examination of the diamond/silicon interface of films grown at 2.0% and 0.3% CH_4/H_2 reveals significant differences in the nature of this interface. In Figure 7(a), only an ion milling damage layer is observed, caused by the presence of the interface and the very different milling characteristics of the diamond film and the silicon substrate. This was confirmed by the absence of a second phase in this region during microdiffraction and the observation that no depth was apparent in this layer during TEM examination (i.e., this feature is confined to the surface of the TEM specimen). Therefore, it is believed to be an amorphous surface layer caused by interaction of the ion milling beam with the interface during sample preparation.[14] On the other hand, a sample grown at 0.3% CH_4 yields an obvious interfacial layer approximately 50 Å thick as shown in Figure 8. Due to the imaging contrast optimized to observe defects in the diamond, this layer was not visible in Figure 7(b); however, it can be observed readily in Figure 8. This is easily distinguished from an ion milling damage layer by the defect contrast observed as dark lines in the layer and the depth which was apparent parallel to the electron beam in this region.

indicating it is not simply a surface artifact. Furthermore, a SAD pattern from this region indicated that this interfacial layer was β-SiC. The alignment of the Si(111) and SiC(111) diffraction spots indicated that in the region of the SAD the β-SiC buffer layer was a single crystal, epitaxial with the Si substrate (i.e., β-SiC(111)||Si(111), β–SiC[110]||Si[110]). The presence of this layer is confirmed by high resolution XTEM as shown in Figure 9. Fringes for the Si and SiC(111) planes can be observed and appear to be aligned, indicating an epitaxial relationship between the Si and SiC.

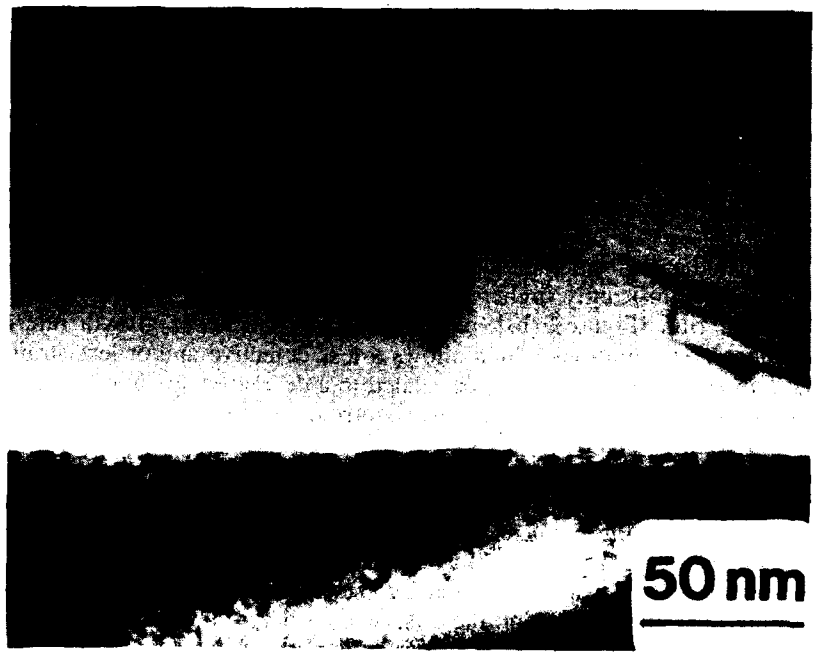

Fig. 8. XTEM micrograph of diamond film grown in 0.3% CH_4/H_2 showing 50Å layer of β-SiC at the interface.

The absence of the SiC layer in the sample grown with the higher concentration of CH_4 (i.e., 2% CH_4) may be due to the more rapid growth rate of the diamond in these samples. This may "cap" the Si before an SiC layer detectable in conventional TEM has time to form. After the diamond has covered the Si, the high bond strength and

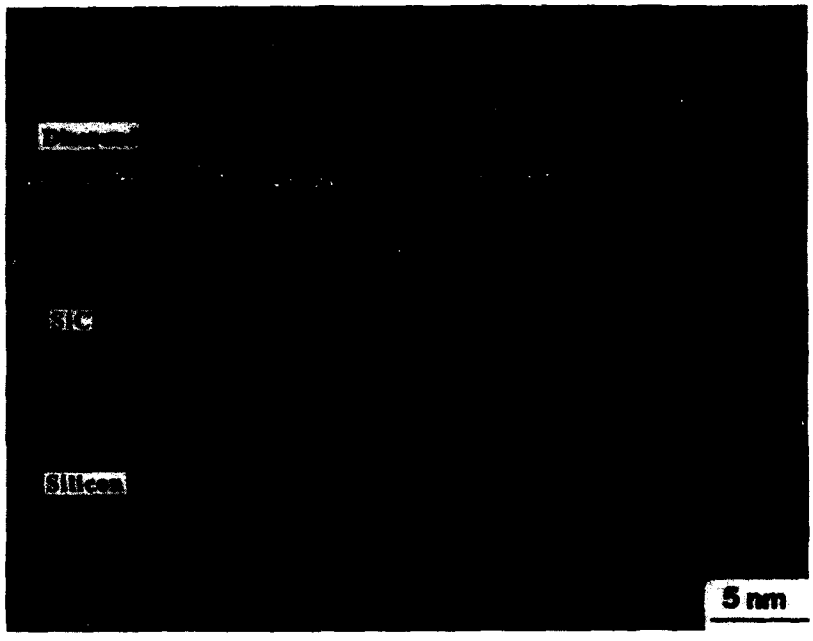

Fig. 9. High resolution XTEM micrograph of diamond film grown in 0.3% CH_4/H_2. Note the cross-fringes visible in both the silicon substrate and the β-SiC layer, indicative of the epitaxial nature of the β-SiC film.

"kinetic stability" (i.e. large activation energy required to transform the diamond) of the diamond prevents the inter-diffusion of the Si and C, thus limiting the SiC layer thickness. However, it should be remembered that an SiC layer was detected by XPS and AES in a sample grown with a high methane concentration (i.e., 3.0%). This is believed to be due to the increased surface sensitivity of these techniques and suggests that the layer is simply too thin to be detected in conventional and micro-diffraction TEM (i.e., less than 5 - 10 monolayers) for the reasons discussed above.

Summary

Diamond films grown by microwave plasma CVD have been examined by AES, XPS and TEM. The surface analysis of a series of samples grown for various times indicated that a detectable SiC layer forms within the first five minutes of growth. Then the diamond signal slowly increases until, after two hours of growth, the SiC is no longer observed. In cross sectional electron microscopy, the presence of an epitaxial SiC layer was observed for samples grown with a low CH_4 concentration. However, contrary to the surface analysis results, such a layer was not observed in the samples grown with higher CH_4 concentrations. This is believed to be due to the very thin nature of the SiC layer in this case, probably caused by the diamond film "capping" the substrate more quickly and thus preventing further carburization.

Acknowledgements

Kobe Steel, Ltd. is gratefully acknowledged for supplying samples (K. Kobashi, K. Nishimura, and K. Miyata) and partial financial support for this research. SDIO/IST through ONR is also gratefully acknowledged for partial financial support. Professor G. Hoflund and Custom Surface Technology are acknowledged for their help in the design and construction of the surface analysis system utilized for this study. The assistance of Karren More of ORNL in obtaining the cross-sectional HREM is gratefully acknowledged. Partial support for the TEM research was provided by the Division of Materials Sciences, United States Department of Energy under contract DE-AC05-840R21400 with Martin Marietta Energy Systems, Inc., and the SHaRE program under contract DE-AC05-76-ORO0033 with Oak Ridge Associated Universities.

References

1. Landolt and Börnstein (1987) Numerical Data and Functional Relationships in Science and Technology, Springer-Verlag.

2. Field, J. E. (1979) Properties of Diamond, Academic Press, London.

3. Bazhenov, V. K., Vikulin, I. M., and Gontar, A. G. (1985) 'Synthetic diamonds in electronics' (review), Sov. Phys. Semicond., **19** (8), 829.

4. Matsumoto, S. (1985) 'Chemical vapour deposition of diamond in RF glow discharge,' J. Mat. Sci. Lett.,**4**, 600.

5. Kamo, M., Sato, Y., Matsumoto, S., and Setaka, N. (1983) 'Diamond synthesis from gas phase in microwave plasma,' J. Cryst. Growth, **62**, 642.

6. Matsumoto, S., Sato, Y., Kamo, K., and Setaka, N. (1982) 'Growth of diamond particles from methane-hydrogen gas,' J. Appl. Phys., **21**, 483.

7. Kobashi, K., Nishimura, K., Kawate, Y., and Horiuchi, T. (1988) 'Synthesis of diamonds by use of microwave plasma chemical-vapor deposition: Morphology and growth of diamond films,' Phys. Rev. B, **38** (6), 4067.

8. Kern, R., LeLay, G., and Metois, J. J. (1979) Chapter 3, in E. Kaldis (eds.) Current Topics in Materials Science Volume 3, North Holland Publishing Co.

9. Wagner, C. D., Riggs, W. M., Davis, L. E., Moulder, J. F., and Muilenberg, G. E. (1979) Handbook of X-ray Photoelectron Spectroscopy, Perkin-Elmer, Eden Prairie, MN.

10. Liaw, P. and Davis, R. F. (1985) 'Epitaxial Growth and Characterization of β-SiC Thin Films,' J. Electrochem. Soc. 132, 642.

11. Williams, B. E. and Glass, J. T. (1989) 'Characterization of diamond thin films: Diamond phase identification, surface morphology, and defect structures,' J. Mater. Res, **4** (2), 373.

12. Nemanich, R. J., Shroder, R. E., Glass, J. T., and Lucovsky, G. 'Precursor Structures in the Formation of Diamond Films,' Proceedings of Physics of Semiconductors, Poland, Aug. 1988.

13. Kobashi, K., Nishimura, Kawate, Y., and Horiuchi, T. (1988) 'Synthesis of diamonds by use of microwave plasma chemical-vapor deposition: Morphology and growth of diamond films,' Phys. Rev. B **38** (6), 4067.

14. Carter, C. H., Davis, R. F., and Nutt, S. R., 'Transmission electron microscopy of process-induced defects in β-SiC thin films,' J. Mater. Res. **1** (6), 811.

Electrical Properties of B Doped CVD Grown Polycrystalline Diamond Films

K. Nishimura*, K. Das, J. T. Glass, K. Kobashi**, R. J. Nemanich***, Department of Materials Science and Engineering, North Carolina State University, Raleigh, NC, 27695-7907, USA
* Visiting scientist from Kobe Steel, Ltd., Japan
** Electronics Research Laboratory, Kobe Steel Ltd., Takatsukadai 1-chome, 5-5, Nishiku, Kobe, Japan, 652
***Department of Physics, North Carolina State University, Raleigh, NC, 27695-8202, USA

ABSTRACT. B doped diamond films were synthesized by microwave plasma CVD, and the crystal quality and the electrical properties were investigated. From SEM, clear facets were observed and X-ray diffraction data showed that only the diamond phase was present. Raman spectroscopy verified the presence of diamond and indicated that the crystal quality increased when B is incorporated in the films up to 400 ppm. SIMS analysis showed that on the order of $10^{20}/cm^3$ (564 ppm) of B was incorporated in the diamond film with a gas phase B/C ratio of 400 ppm. Electrode patterns of Pt were fabricated on the films and electrical properties were investigated. Undoped diamond films showed rectifying contacts with small leakage currents and B doped diamond films with a B concentration of 400 ppm showed ohmic behavior. The B in these films had small activation energies, which indicates that impurity band conduction plays an important role.

1 Introduction

Diamond can be considered a semiconductor with a very wide band gap (≈5.4 eV) and has a variety of useful properties [1]-[3], such as high: (a) thermal conductivity (2,000 W/K m), (b) carrier mobility, (c) breakdown voltage, (d) drift velocity, and (e) radiation hardness. Therefore, it is expected to be useful for power devices, high speed devices, and devices used at high temperature and in radiation intensive environments. As a consequence, many articles on the electrical properties of bulk semiconductive diamond have been published .[4]-[7] Unfortunately, the scarcity and expense of such diamond, as well as the necessity of utilizing thin films for many of the aforementioned devices, has limited the continued research and development of this area. Recently, however, renewed interest has been generated by the successful chemical vapor deposition (CVD) of diamond by various vapor phase methods.[8]-[10] In fact, it has been shown that semiconductive p type diamond films can be grown when B is introduced into the films.[11]-[13] These achievements are key technologies for the fabrication of devices and has further accelerated research in this area. However, although numerous studies of the electrical properties of bulk diamond have been conducted, the electrical properties of

R. Freer (ed.), The Physics and Chemistry of Carbides; Nitrides and Borides, 183–194.
© 1990 *Kluwer Academic Publishers. Printed in the Netherlands.*

B doped polycrystalline diamond films have not been investigated thoroughly. Thus, in the present research, B doped diamond films were grown by microwave CVD and investigated by scanning electron microscopy (SEM), X ray diffraction, Raman spectroscopy, Secondary Ion Mass Spectroscopy (SIMS), current-voltage characteristics (I-V characteristics), and resistivity measurements.

2 Experimental

B doped diamond films were grown on polycrystalline Al_2O_3 substrates with dimensions of 20 mm X 10 mm by microwave plasma CVD. Al_2O_3 substrates were employed due to their high resistivity which allowed electrical measurements to be made without influences from the substrates. The detailed features of this apparatus, experimental procedures and preparation of substrates are given in reference [14]. To grow B doped diamond films, CH_4, H_2 and B_2H_6 gases were employed. The concentration of CH_4 was 0.5 % and B_2H_6 concentrations ranged from 1 ppm to 0.1 ppm in the gas phase, which are equal to B/C ratios from 400 ppm to 40 ppm. For the remainder of this paper, B concentrations will be given as ppm of B relative to C in the gas phase as determined by mass flow measurements. The growth temperature was 800 ^oC and the gas pressure was 31.5 Torr. The films were deposited for 7 hours and the film thickness obtained was approximately 1.4 μm.

These specimens were cut into 5 mm X 5 mm samples using a diamond saw and then cleaned in H_2SO_4 at approximately 70^oC for 10 minutes, followed by a conventional RCA clean.[15] As a final cleaning step, specimens were dried in an oven at 120 ^oC for 5 minutes to eliminate moisture on the diamond films, otherwise, the Pt metal utilized for electrical contacts (see below) would sometimes separate from the diamond when an ultrasonic cleaning was performed.

Electrode patterns were fabricated on the diamond films by conventional photolithography and Pt electrodes were deposited on the films by RF sputtering. The RF power was 100 W and the gas pressure was 10 mTorr. The film thickness of the deposited Pt was about 2,000 Å. Lift-off was utilized to achieve the final pattern consisting of circular dots with diameters of 100 μm separated from the surrounding metal by an open annulus. Electrical ground was made on the same side of the specimen. There are several reasons for choosing Pt as the contact material; (a) Pt has a large work function (5.7 eV) [16], thus it should facilitate the achievement of ohmic contacts on p type diamond films [16], (b) Pt is inert in air, therefore, should yield stable contacts and, (c) perhaps most importantly, Pt yielded the minimum contact resistivity of the metals which were investigated for the present study, including as-deposited Ni, Al and $TaSi_2$.

To obtain atomic B concentration, B was implanted into undoped diamond films synthesized by the same growth conditions as B doped CVD grown films and they were used as standards during SIMS measurements.

3 Results and Discussions

3.1 MATERIAL CHARACTERIZATION

Surface morphology was observed via scanning electron microscopy (S-530, Hitachi Co.). Figure 1 shows the surface morphology of a B doped diamond film with a B/C ratio of 400 ppm. Clear (111) facets and five fold multiply twinned particles can be seen. It was found that, for B/C ratios from 0 to 400 ppm, no differences in this morphology could be observed. Furthermore, X-ray diffraction indicated that diamond was the only structure present in the films up to 400 ppm of B. However, when the B/C ratio was greater than 4,000 ppm, the shapes of particles became irregular and the size decreased. Additional X-ray diffraction peaks believed to be due to graphite were also observed as the B concentration was increased above 400 ppm. Details of the surface morphology of B doped diamond films are published in a separate article.[17] Similar research has been conducted by Y. Sato et. al..[12]

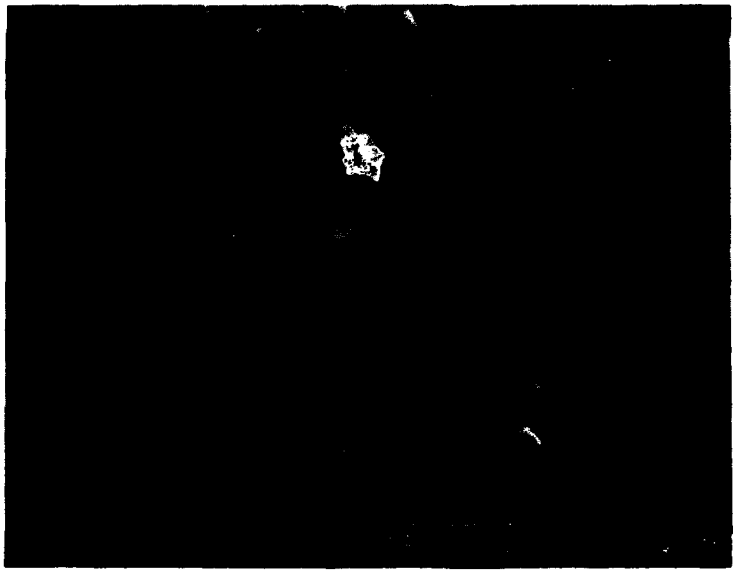

Figure 1. Surface Morphology of B doped diamond films on an Al_2O_3 substrate. The B/C ratio in gas phase was 400 ppm.

Laser Raman spectroscopy was used to investigate the crystal quality of the B doped diamond films. The diameter of the laser beam was 100 μm X 2 mm and the wave length used was 5145 A. Figure 2 shows Raman spectra obtained from B doped diamond films with different B concentrations. It can be seen that the Raman peak increased relative to the intensity of the sp^2 peak as the B concentration increased. Furthermore, the full width half maximum of the diamond sp^3 Raman peak decreased. This indicates that doping with B increases the quality of the diamond films. This may be a gas species effect due to the B_2H_6 or may be a surface effect during growth caused by B incorporation at the growth surface. Although speculation of the mechanism is possible, more experiments are necessary before any conclusions can be made.

The Raman peak position characteristic of diamond was located at 1,337 cm^{-1} for the undoped diamond films. This position is shifted by 5 cm^{-1} from the same peak in most natural diamonds which occurs at 1,332 cm^{-1}. This suggests that a residual compressive stress is present in the film.[18] When the films were doped with B, the peak position was shifted to even higher wave numbers (≈4 cm^{-1} at 400 ppm of B) than for undoped diamond films, implying that B doping increases the residual compressive stress or changes the domain size which can also affect the peak position.[19]

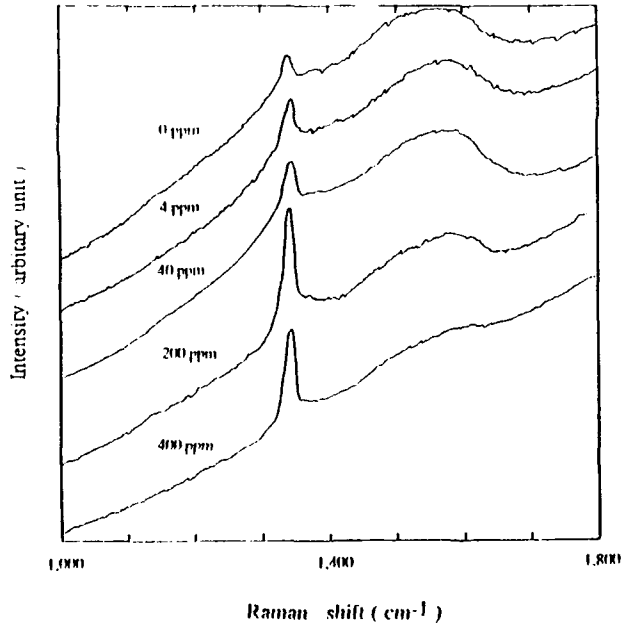

Figure 2. Raman spectra of undoped diamond and B doped diamond films. 1,332 cm^{-1} peak from diamond and a broad peak near 1,550 cm^{-1} caused by sp^2 components are observed. Crystal quality appears to increase with doping.

SIMS depth profiles (Fig.3) were obtained for diamond films containing different concentrations of boron. The apparatus used was a Cameca Co., IMS 3F instrument and an O^{2+} beam with 15 keV was used as the primary ion source. The sputtered area was about 180 μm X 180 μm and the sampled area was 60 μm in diameter. Figure 3 shows depth profiles of B doped and undoped diamond films. These profiles indicate that the interface between the Al_2O_3 substrates and the diamond films is sharp, thus, interdiffusion of C and B appears to be minimal at the growth conditions employed. It can be seen that the atomic concentration of B decreased when the B_2H_6 concentration in the gas phase was decreased.

Figure 4 shows the relationship between atomic concentration of B in the film and B concentration introduced into in the gas phase as measured by mass flow controllers. The atomic concentration of B decreases when the B_2H_6 concentration in the gas phase decreases. However, the B concentration in the film is greater than the B concentration in the gas phase. For example, the atomic concentration of B was on the order of $10^{20}/cm^3$ (i.e. B/C ratio of 564 ppm in the film) for a B concentration of 400 ppm in the gas phase. This actually means that the B/C ratios in the film are higher than the B/C ratios in the gas phase.

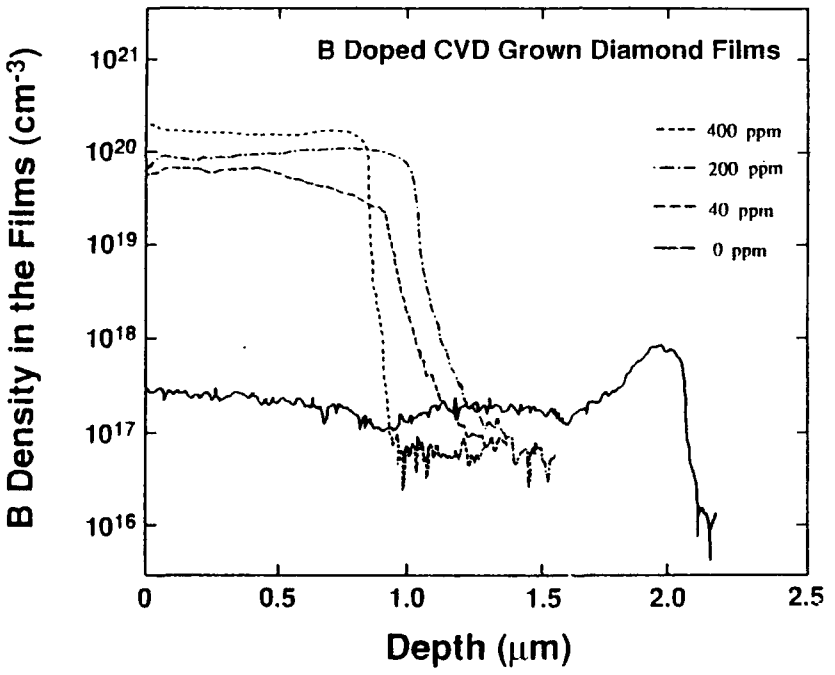

Figure 3. SIMS depth profile of undoped and B doped diamond films. It can be observed that B was distributed homogeneously in the films.

It can be speculated that this is caused by the difference between the sticking coefficients of carbon species and boron species, i.e., the sticking coefficient of boron is larger than the sticking coefficient of carbon at the growth conditions employed. (Note: The B concentration data presented in this manuscript is not corrected by this difference and thus refers to the gas phase B concentration.)

Finally, it should be noted that B was observed even in "undoped" diamond films at an approximate concentration of 5 X $10^{17}/cm^3$. This indicates that residual B in the growth chamber was incorporated into the undoped diamond films. Therefore, the expression " undoped diamond films " is not accurate in present case, but will be retained in this paper for convenience.

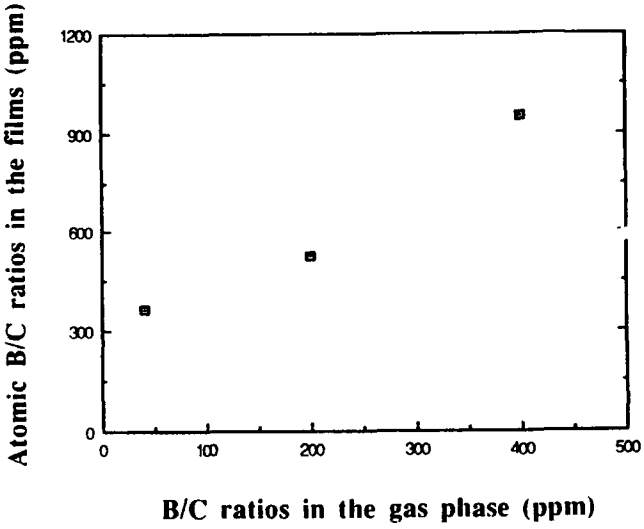

Figure 4. Atomic B concentrations obtained from SIMS data versus B concentrations in the gas phase obtained from SIMS data. B concentrations in the gas phase were obtained from C and B ratios controlled by mass flow meters during synthesis.

3.2 ELECTRICAL PROPERTIES OF DIAMOND FILMS

To obtain I-V characteristics of the films, a semiconductor parameter analyser (Hewlet Packard Co. 4145A) was used. Figure 5 shows I-V characteristics of an undoped diamond film with Pt electrodes. Clear rectifying contacts were obtained and leakage current was 40 nA at approximately 10 V. From the direction of the reverse current, the polarity of this film was determined to be p type. Some contacts had high breakdown voltages near 100 V, however, the current did not rise sharply as is expected for avalanche breakdown phenomena.[16] This "soft breakdown" may be caused by current flow through grain boundaries and defects and/or by generation current. It should be noted that photoconductivity was observed in this undoped sample (Figure 6) when it was illuminated with white light. The reverse and

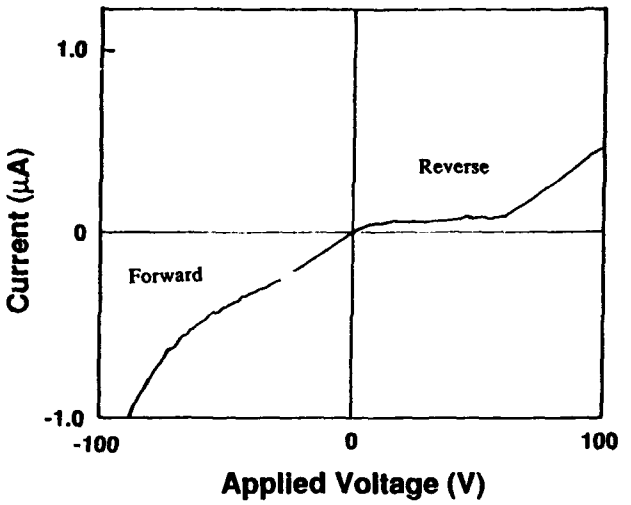

Figure 5. A typical I-V characteristic of an undoped diamond film with Pt electrodes at room temperature. Clear rectifying contacts were obtained and "soft breakdown" was observed.

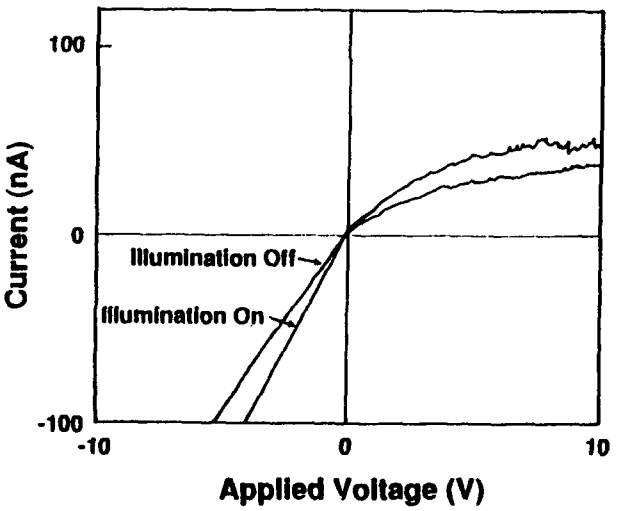

Figure 6. Photoconductivity was observed for the undoped diamond film in white light. Ratios of current gain of photocurrent to the dark current were 46 % and 32 % at 4 V for reverse and forward current, respectively.

forward current increased by ≈46 % and ≈32 % , respectively, at 4 V.

Figure 7 shows the temperature dependence of the I-V characteristics from room temperature to 473 K in air. When the temperature was increased, the leakage current increased and rectification disappeared at 473 K (i.e. ohmic behavior was obtained.). This effect is probably due to the presence of a high density of electrically active defects contributing to a large generation current at higher temperatures.

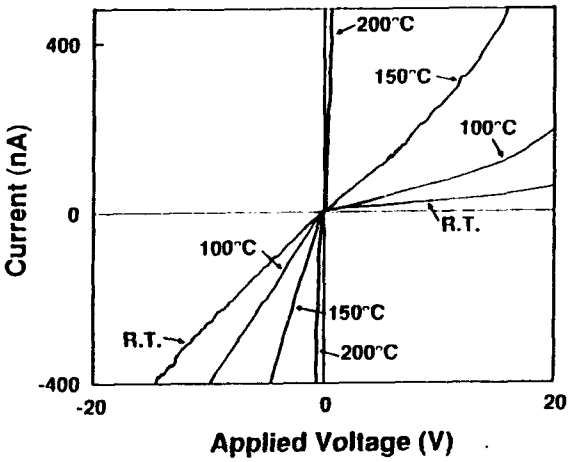

Figure 7. Temperature dependence of the I-V characteristic of the undoped diamond films with Pt electrodes. It can be observed that rectification disappeared at 200 °C and the contact showed an ohmic behavior.

Figure 8 shows the I-V characteristics of a 400 ppm B doped diamond film at various temperatures. In all cases, relatively straight lines are observed, indicating that ideal ohmic behavior is achieved between -5 V and 5 V. This ohmic behavior is believed to be due to tunneling through a thin depletion layer caused by heavy doping. When the absolute value of the applied voltage was over 5 V, the I-V characteristics deviated slightly from ideal ohmic behavior, however, a detailed study of this phenomenon has not been completed.

To obtain values of activation energy, resistivity was measured as a function of a temperature and is shown in Figure 9. The temperature ranged from room temperature to 673 K. The data shows that when temperature increased, resistivity decreased, which indicates that these films are behaving as semiconductors. However, from these data, it can be seen that a straight line was not obtained, thus, more than one activation energy is likely to be present for the charge carriers being measured. Although several activation energies may be present, for simplicity, only two slopes were assumed in this temperature regime as indicated in the figure. The activation energies obtained from this data are shown as a function of B/C ratios in Figure 10. When the B/C ratios increased, activation energies decreased. The maximum activation energy obtained was 0.16 eV for diamond films with the lowest B/C ratio of 40 ppm. These values are much smaller than the value of the acceptor

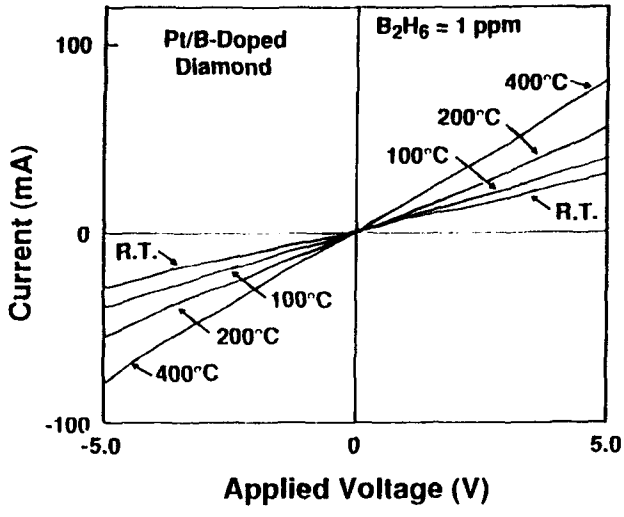

Figure 8. A typical I-V characteristic of a B doped diamond film with Pt electrodes at room temperature. Ohmic contacts were obtained.

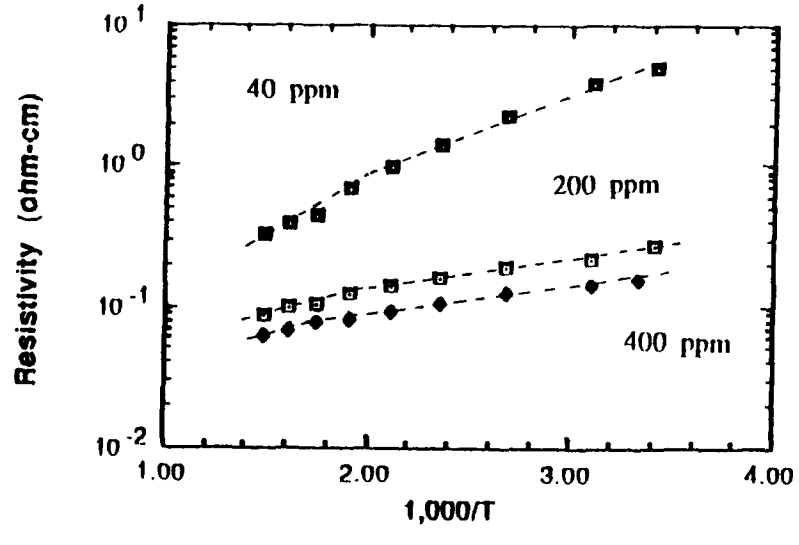

Figure 9. This shows the temperature dependence of resistivity for B doped diamond films from room temperature to 400 °C. B/C ratios were 400, 200, 40 ppm, respectively.

level of B impurities in bulk diamond as determined by photo-absorption (0.35 eV).[6] This suggests that impurity band conduction plays an important role in the films, causing them to behave as heavily doped semiconductors.[20] Such small activation energies due to heavy doping have also been observed in bulk B doped diamonds.[5], [21]. Photoconductivity was not observed in these films in white light which supports the conclusions that these films are heavily doped semiconductors.

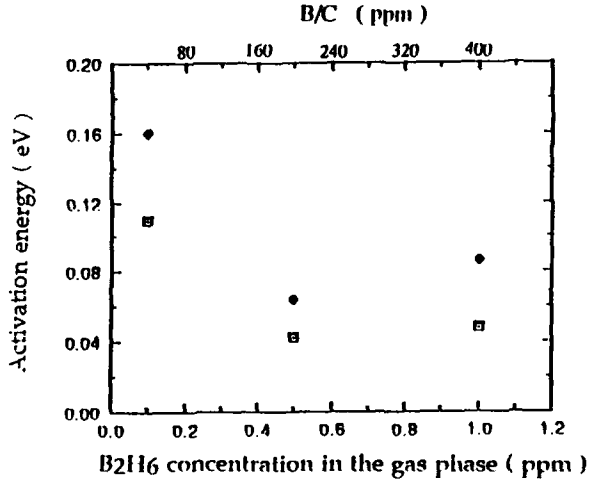

Figure 10. Activation energies versus reciprocal temperature for B doped diamond films were obtained from the higher temperature region (•) and from the lower temperature region (▫). Activation energies became larger when doping concentration decreased. This trend is observed for bulk B doped diamonds.[5], [21]

4 Summaries

B doped diamond films were synthesized by microwave plasma CVD, and the crystal quality and the electrical properties were investigated. From SEM, clear facets were observed and X-ray diffraction data showed that only the diamond phase was present. Raman spectroscopy verified the presence of diamond and indicated that the crystal quality increased when B is incorporated in the films up to 400 ppm. SIMS analysis showed that on the order of $10^{20}/cm^3$ (564 ppm) of B was incorporated in the diamond film with a gas phase B/C ratio of 400 ppm. Electrode patterns of Pt were fabricated on the films and electrical properties were investigated. Undoped diamond films showed rectifying contacts with small leakage currents and B doped diamond films with a B concentration of 400 ppm showed ohmic behavior. The B in these films had small activation energies, which indicates that impurity band conduction plays an important role.

5 Acknowledgments

Prof. R. F. Davis at North Carolina State University (NCSU) is gratefully acknowledged for the use of his experimental facilities and Dr. Griffis at NCSU for SIMS analysis. Sponsorship from Kobe Steel, Ltd. in Japan and SDIO/IST through ONR is also acknowledged.

References

[1] J. E. Field (1979) Properties of Diamond, Academic Press, London
[2] V. K. Bazhenov, I. M. Vikulin, and A. G. Gontar' (1985) " Synthetic diamonds in electronics ", **19**, (8), 829
[3] Landolt and Bornstein (1987) Numerical Data and Functional Relationships in Science and Technology, Springer-Verlag
[4] V. S. Vavilov (1975) " Semiconductive Diamond " Phys. Stat. Sol. (a), **31**, 11
[5] A. W. S. Williams, E. C. Lightowlers and A. T. Collins (1970) " Impurity conduction in synthetic semiconductive diamond ", J. Phys. C: Solid St. Phys., **3**, 1727
[6] A. T. Collins and A. W. S. Williams (1971) " The nature of the acceptor center in semiconductive diamond ", J. Phys. C: Solid St. Phys., **4**, 1789
[7] W. B. Wilson (1962) " Evidence for hoppimg transport in B-doped diamond", Phys. Rev., **127**, 5, 1549
[8] S. Matsumoto, Y. Sato, M. Tsutsumi, and N. Setaka (1982) " Growth of diamond particles from methane-hydrogen gas " J. Mater. Sci., **17**, 3106
[9] Y. Hirose and Y. Terasawa (1986) " Synthesis of diamond thin films by thermal CVD using organic compounds ", Jpn. J. Appl. Phys. **25**, L. 519
[10] A. Sawabe and T. Inuzuka (1985) " Growth of diamond films by electron assisted chemical vapor deposition " Appl. Phys. Lett. **46**, 146
[11] D. J. Proferl, N. C. Gardner, and J. C. Angus (1973) " Growth of boron -doped seed crystals by vapor deposition ", J. Appl. Phys., **44**, 4, 1428
[12] Y. Sato, M. Kamo, and N. Setaka (1987) " Growth of semiconductive diamond films by plasma-assisted vapor deposition ", High Tech Ceramics, edited by P. Vincenzini, 1719
[13] B. V. Spitsyn, L. L. Bovilov, and B. V. Derjaguin (1981) " Vapor growth of diamond on diamond and other surface " , J. Cryst. Growth, **52**, 219
[14] K. Kobashi, K. Nishimura, y. Kawate, and T. Horiuchi (1988) " Synthesis of diamonds by use of microwave plasma chemical vapor deposition: morphology and growth of diamond films ", Phys. Rev. B, **38**, 6, 4067
[15] W. Kern and D. A. Puotinen (1970) " Cleaning solution based on hydrogen peroxide for use in semiconductor technology ", RCA Review, June, 187
[16] S. M. Sze (1981) Physcis of Semiconductor Devices, 2nd Edition, John Wiley & Sons, Inc., New York
[17] K. Nishimura, K. Miyata, Y. Kawate, K. Kobashi (1988) " Surface morphology and defect structures in microwave CVD diamond films" '88 Proceeding of SPIE conference in San Diego

[18] D. S. Knight and W. B. White (1989) " Characterization of diamond films by Raman spectroscopy " J. Mater. Res. **4**, 2, 385
[19] Y.M. LeGrice and R. J. Nemanich, Submitted to Materials Research Socety, 1989 Fall meeting, Symposium F
[20] V. I. Fistul' (1969) Heavily doped semiconductors, Plenum press, New york
[21] J. C. Bougoin, J. Krynicki, and B. Blanchard (1979) " Boron concentration and impurity- to- band activation energy in diamond ", Phys. Stat. Sol. (a), **52**, 293

III. STRUCTURE, CRYSTAL CHEMISTRY, PHASE EQUILIBRIA, DEFECTS and MASS TRANSPORT

SILICON CARBIDE : STRUCTURE AND POLYTYPIC TRANSFORMATIONS

Trevor F Page
Materials Division
Department of Mechanical, Materials and
Manufacturing Engineering
The University
Newcastle upon Tyne NE1 7RU, U K

ABSTRACT. The polytypic nature of silicon carbide has been known for many years: that is that the crystal structure exhibits a number of different one-dimensional ordering sequences without any variation in stoichiometry. Although initially regarded as a scientific curiosity, the recent interest in SiC as a device material, as a structural ceramic for engineering applications and as a fibre or whisker reinforcement for composite materials has highlighted the importance of our both understanding and controlling this phenomenon.

This paper will briefly review our understanding of the polytypic structure and transformations in SiC including the possible reasons why some polytypes appear more stable than others.

INTRODUCTION

Silicon carbide is a man-made, very hard, very stiff, ceramic material of attractive low density. Its thermal conductivity is high leading to excellent thermal shock resistance and this, combined with its high hardness (it is one of the hardest substances known), outstanding properties per unit mass and the development of processing routes to form useful, and even complex, shapes of good quality material has led to considerable interest in its application as a structural ceramic for engineering applications, especially as wear-resistant or high-temperature components [e.g. 1]. Also, its wide band-gap (~3eV) suggests that it may have considerable potential as a semiconducting material for high temperature electronic devices [e.g. 2,3]. However, a central problem to the full exploitation and application of silicon carbide is that its crystal structure can exist in a number of simply-related stacking sequences. Not only can the growth of particular crystal structures be difficult to control, but unexpected transformations between stacking sequences can either change the band gap of device single crystals or be deleterious to the properties, microstructure and structural integrity of engineering components. For example, some polytypic changes can lead to the growth of tabular

R. Freer (ed.), The Physics and Chemistry of Carbides; Nitrides and Borides, 197–214.
© 1990 *Kluwer Academic Publishers. Printed in the Netherlands.*

grains during the sintering of originally-equiaxed powders with consequent difficulties in achieving a full-density, defect-free microstructure.

Recently, much interest has also centred on the use of silicon carbide whiskers and fibres as reinforcement in metal matrix and ceramic matrix composites. Commercial grades of whisker crystals are usually heavily faulted and impure while SiC fibres are generally fine-grained, faulted and also impure. In both cases, there is concern that any instability of crystal structure during exposure to high temperatures should not be deleterious to the integrity of the reinforcement either during fabrication or in-service.

The following sections briefly review our understanding of the polytypic nature of SiC, the nature and mechanisms of polytypic transformations and the apparent serendipity way in which different polytypes occur under different synthesis conditions. For a more detailed review, the reader is guided to Jepps and Page [4]

SiC POLYTYPES: STRUCTURE & NOMENCLATURE

The fundamental structural unit in all SiC polytypes is a covalently bonded primary co-ordination tetrahedron (either SiC_4 or CSi_4), the different structures having layers of these tetrahedra stacked to form polar frameworks in which all the tetrahedra have one apex out of the layer plane (see Fig 1). Four tetrahedra are linked through each corner to satisfy the four-fold coordination at any structure point. As with similar structures such as zinc sulphide, the tetrahedra then occupy an array of positions analogous to those occupied by spheres in close-packing (however, it must be remembered that these tetrahedral structures are far more open). Thus, one way of describing the stacking sequences is by the 'ABC' notation. While both cubic (..ABC..) and simple hexagonal (..ABAB..) stacking are found in SiC, these two stacking sequences can also occur in more complex, intermixed, forms yielding a wide range of ordered, larger period, stacked structures. Disordered (i.e. heavily faulted) structures are also well documented. Following the notation suggested by Jagodzinski [5], any one layer in these stacking sequences can be described as having a local cubic (k) or hexagonal (h) environment with respect to the positions of its immediate layer neighbours. However, the acentric nature of the tetrahedral unit requires that in sequences of the type ..CACA.. (hhhh), the A and C layers are not only offset, but rotated by π (see Fig 1). Thus, for SiC (and related structures such as ZnS etc) two stacking operations exist, namely:

(1) layer-translation only - yielding ..ABCABC.. (kkkkkk).
(2) layer-translation and rotation yielding ..ABAB.. etc (hhhh).

In order to indicate this rotation of π, dashes can be superposed to the layer notation, i.e. layers designated A and A' are in exact vertical registration in the stack but are rotated by π [e.g. 6].

Thus, the common high-temperature polytype has a hexagonal unit cell and a six-layer repeat in the c-direction (chosen perpendicular to the layers) and is described as ..C'ABCB'A'C'.. (the dashes clearly showing the crystallographic non-equivalence of the two A, B or layer-positions). The stacking sequence results in a zig-zag of three layers in one orientation followed by three rotated by π, resulting in a structure which may be derived from that of the cubic polytype by the insertion of <111> rotation twin boundaries every three layers (see Figure 1).

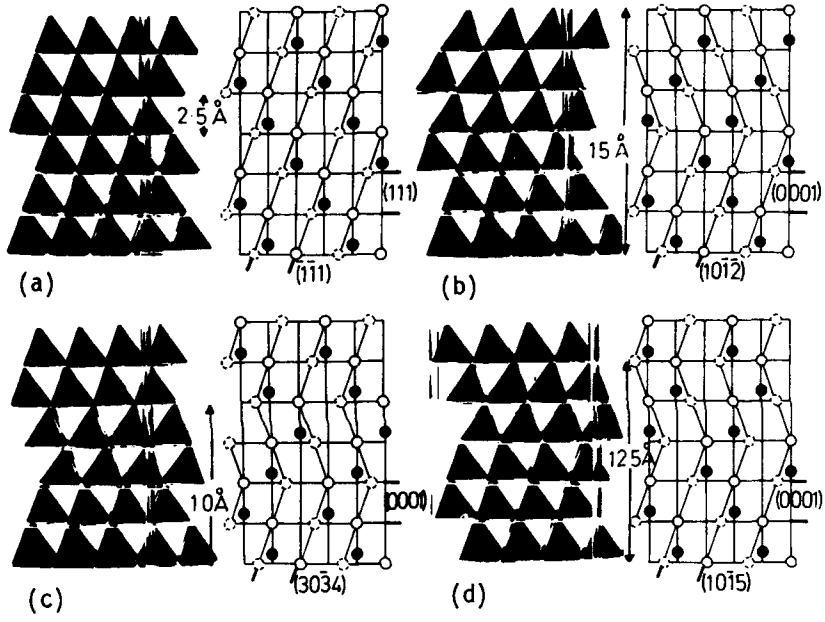

Figure 1. Models constructed from solid tetrahedra of the four most common SiC polytype structures together with 'tramline' structure diagrams. The stacking sequences may be visualised by considering the Zig-zag sequence of non-basal-plant tetrahedral faces. In addition to the 'ABC' notation, both Ramsdell and Zhadenov symbols for these stacking sequences are also given:

(a) 3C ABCABC - (∞)
(b) 6H ABCB'A'C'A (33)
(c) 4H ABA'C'A (22)
(d) 15R ABCB'A'BCAC'B'CABA'C'A $(32)_3$

An alternative description of this six-layer structures is 6H. This notation, due to Ramsdell [7], specifies both the number of layers in the repeat along the stacking direction, together with the Bravais

lattice type of the resultant structure (i.e. hexagonal (H), cubic (C) or rhombohedral (R)).

The sequence of tetrahedral layers may be visualised in models by considering the zig-zag sequence of non-basal tetrahedral planes (see Fig 1). In order to represent this zig-zag of layers, Zhadanov [8] devised a further notation which refers to the number of consecutive layers without rotation. Thus, the 6H structure is represented by the Zhadanov symbol (33), indicating that the cubic sequence is interrupted by rotation every three layers. Similarly, all other polytypes may be represented using this notation: the hexagonal polytype 2H (i.e. ..ABAB..), with two layers in the unit cell, has a structure represented by (11) i.e. each layer rotated by π with respect to the preceding layer, 15R becomes $(32)_3$ while 3C is represented by (∞) showing all layers to be stacked without rotation.

On a final point of nomenclature, it has become accepted practice to refer to the cubic polytype as β-SiC and to all other non-cubic structures collectively as α-SiC.

While, in principal, there are an infinite number of possible stacking variants, the structures of even the longest-period polytypes may be considered as sequences of one or more of what always appear to be the basic smaller-period units 4H(22), 6H(33), $15R(32)_3$ and $21R(34)_3$. For example, the sequence 39H may be represented $(33)_2 32 (33)_2 (32)_2$. Further, certain families of structures have been found to exist, for example $(33)_n 32$ sequences with n = 1,2,3,4,5,6,7,13,16,21 have been identified [e.g. 9]. The '2' in these Zhadanov symbols may be thought of as representing a single intrinsic stacking fault in otherwise unfaulted 6H(33) - the family of different structures then being seen to arise simply from a difference in the separation of the faults.

Because of the nature of the structures of SiC polytypes, differences in the internal energies are expected to be small. This is supported by the ease with which small changes in conditions can effect the growth or stability of particular polytypes. However, from measurements of bond lengths and band gaps it seems that they are not negligible. 2H is found to have the largest band gap (and hence largest binding energy) and measurements of lattice parameters suggest that it is the most dense structure with 3C the most open [10] (see Table 1): however, these differences are small. Conclusions from such measurements are that 2H is the most stable polytype with 3C the least stable [11]. If entropy is also taken into account, then the relative stabilities of the polytypes are expected to change away from 2H with increasing temperature [11]. This is generally observed [12,13]. A central problem in this otherwise gradual increase in the degree of cubic stacking from 2H through 4H to 6H etc with increasing temperature concerns the apparent stability of the cubic polytype at intermediate temperatures (1673-1873K). However, 3C often seems to be the polytype which grows most readily, probably because of the multiplicity of <111> rapid growth directions.

TABLE 1. Variation of the band-gap and lattice parameters for the four most common polytypes of SiC. The ratio (c/na) shows the variation of (c/a) per layer in an n-layer polytype. On passing down the sequence 2H→3C, the layers appear to become slightly more open (and thus closer together) while the volume per structural unit ($\propto a^2 c$) become slightly larger.

Polytype	Band gap [14]	Lattice constants [10]		
	eV	a	c	c/na
2H (11)	3.300	3.076	5.048	0.8205
4H (22)	3.263			
6H (33)	3.023	3.0806	15.1173	0.8179
3C (∞)	2.390	3.0827	7.5510	0.8165

Neither the actual process by which the regular separation of stacking faults is achieved nor the forces leading to structures with such very large unit cells are yet fully understood, although a number of theories have been put forward based on both kinetic (growth) and thermodynamic (energetic) considerations. These are briefly discussed in the next section.

However, Heine and co-workers [15,16] have recently developed interatomic force model calculations for SiC which, at last, promise an underlying explanation of the marginally differing stabilities of the polytypes.

POLYTYPIC TRANSFORMATIONS

Given that the polytype which grows may not be the most stable under given conditions, polytypic transformations are fairly common. Essentially, there are two radically different mechanisms by which transformations between polytypes might be accomplished.

At one extreme, a totally reconstructive transformation may be envisaged whereby progressive dissolution or sublimation is followed by regrowth of new crystals of different stacking sequence. These processes would probably be rapid but would only proceed at temperatures high enough either for sublimation (~3000K) or to promote dissolution in some fluid medium. While these mechanisms certainly exist, polytypes may also change from one to another, if more slowly, via solid state processes and these are the most important in terms of solid structural stability.

Comparison of the structural models in Fig 1 reveals that, in order to change one stacked sequence of layers to another, all that is apparently required is a re-arrangement of some layers with respect to others. This is more complex then it seems since it involves not only permutations of layer translations (i.e. k-operations) but also rotation of the coordination tetradhedra to give the h-operation. However, the problem is simplified by the realisation that, in order to preserve the primary bond array, any one layer (e.g. A) can only be followed in sequence by one of two others (e.g. either B or C').

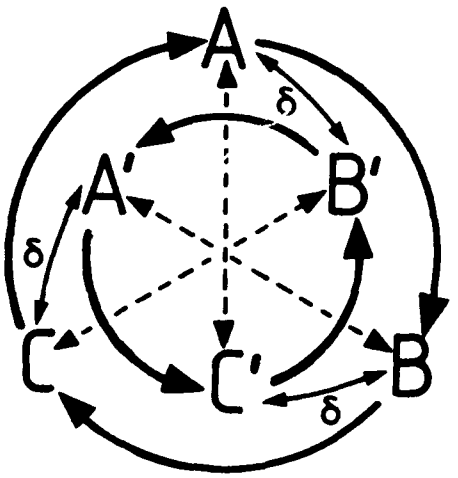

Figure 2

Figure 2 shows a useful nomogram for visualising this and indeed may be used for correctly specifying the stacking sequence of any SiC polytype.

The outer (clockwise) circuit ...ABC... shows the layer sequence when stacked with a translational offset only to produce 3C, i.e. successive k-operations. The inner (anticlockwise), circuit ...B'A'C'... shows the corresponding layer sequence if the whole stack is rotated by π to produce the structure twin-related to 3C, the layers still being stacked by translation only (but now translated in the opposite direction because of the π rotation). Crossing a diameter (eg A⟷C', B⟷A', C⟷B') shows the h-operated layer allowed to follow any given layer. Thus A can **only** be followed by eithe. B (k-operation) or C' (h-operation); C' can only be followed by B' or A. The 6H sequence can then easily be read as ...ABC B'A'C'A... etc, while 2H is ..AC'AC'. Further, since the only two layers which can be placed on A are either C' or B, B⟶C'(or C'⟶B) is the only stacking change allowable following A and this can be modelled in

terms of the passage of individual a/6 <112> (β) or a/3 <10$\bar{1}$0> (α) partial dislocations ($\pm\frac{1}{2}$) between the original A and B (or A and C') layers [4]. The vectors δ on the diagram are thus the Burgers vectors of the a/3 <10$\bar{1}$0> dislocations which must pass between the base and controid of a given tetrahedral layer in order to alter the stacking sequence (i.e. the necessary shear vectors). It can now readily be seen that the two sets of dislocations necessary to transform 2H to 6H (i.e. C→B and C→A') have opposite senses while the set necessary to transform 3C 6H (A→B', C→A', B→C') all have the same sense. These changes are shown schematically in Figures 3 and 4.

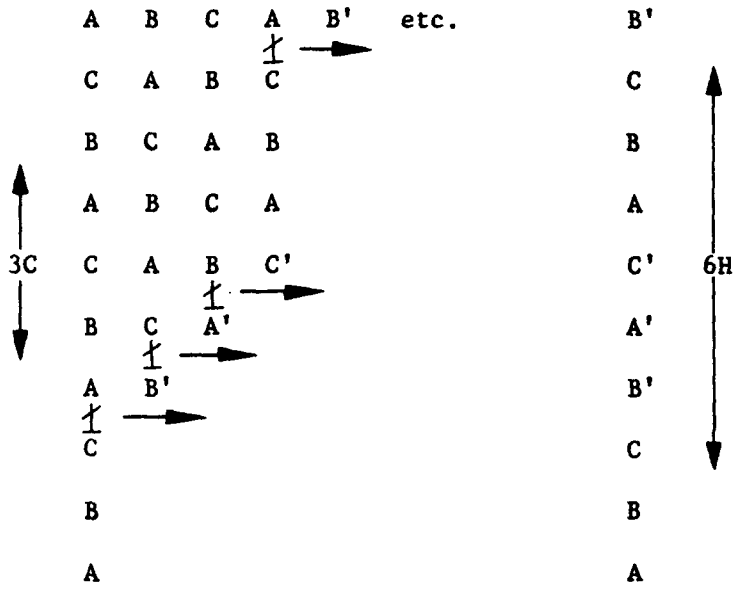

Figure 3 *Transforming* 3C to 6H: the same sense of shear passes over groups of 3 planes each group being 3 planes apart.

Thus a general transformation requires neither a homogeneous shear of every layer, nor the same sense of the shear each time. Such transformations could never be achieved by simple macroscopic stressing of the crystal though the dislocation descriptions remains a useful one and may be a viable mechanisms if the right periodic dislocation array could somehow be produced in the stack.

A diffusional rearrangement mechanism was proposed by Jagodinski [17,18] and requires the nucleation and expansion of stacking faults of the basal plane. The stacking faults are considered to expand by the thermally activated process of diffusional rearrangement of the

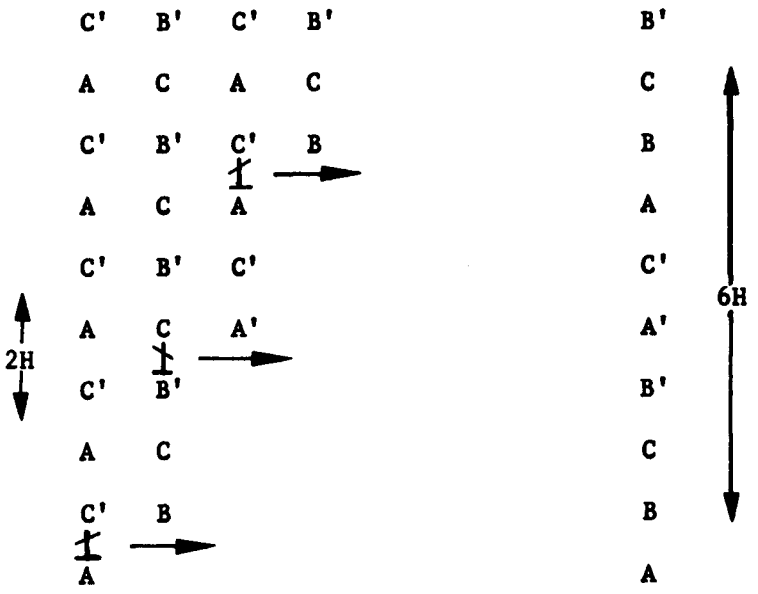

Figure 4 Transforming 2H to 6H: opposite senses of shear are required for every other layer.

atoms at the fault/matrix interface, leading to interchange or 'displacement' of layers. Originally the stacking faults are imagined to be introduced randomly but an (unspecified) ordering arrangement of faults can then result in a new polytype. For example, the proposed 'layer displacement' scheme for the 3C→6H transformation is shown in Figure 5.

In the extreme, these two solid state mechanisms may essentially be the same since, in directionally-bonded solids, dislocation motion usually requires rearrangement of the dislocation cores by diffusion [19]. In practice, it is impossible to distinguish the dislocation and layer-displacement mechanisms even when good high resolution transmission electron images of transformation interfaces are achieved [4,39].

As well as solid state mechanisms, a mechanism involving vapour and/or surface flow has been proposed by a number of workers in order to explain both the high rates of transformation and the habit changes occurring in bulk crystalline powders and compacts [e.g. 20-22]. This mechanism involves the detachment of atoms or groups of atoms from the crystal surface followed by their subsequent re-deposition as a crystal of different polytypic structure.

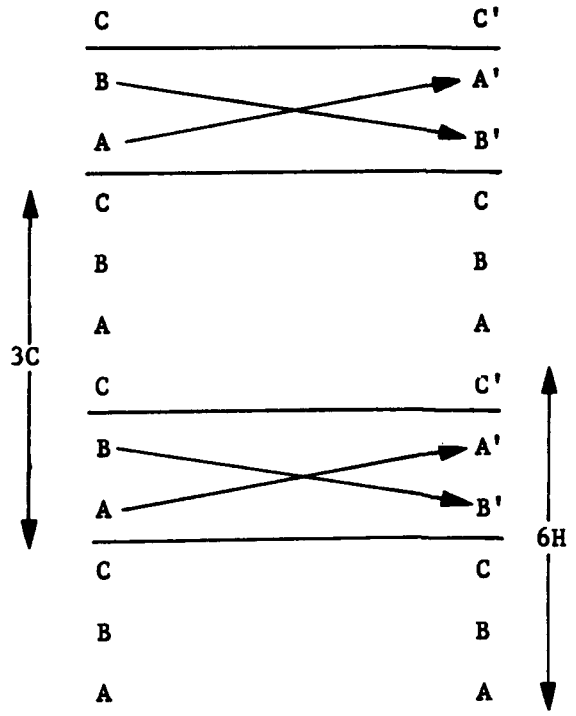

Figure 5 Transforming 3C to 6H by the diffusional rearrangement, or displacement, of A and B layers.

A combination of solid-state and fast grain boundary/surface materials transport mechanisms has been suggested by Jepps [9,23] in order to account for the kinetics of transformations experimentally observe to occur in polycrystalline compacts.

Finally, it is interesting to note how readily stacking defects such as twin boundaries in one polytype provide ready nuclei for other polytypes. For example Figure 6 shows incipient nuclei of 2H, 4H, 6H and 15R across a coherent twin boundary in 3C.

Thus, while the role of defects in propagating transformations is still questionable, there is no doubt that defects may well help to initiate transformations, perhaps by providing embryos of more stable polytypes. It is interesting to note that there are several reports of either defect-free crystals refusing to transform when other crystals have [eg 24], or, of fine twins proceeding various

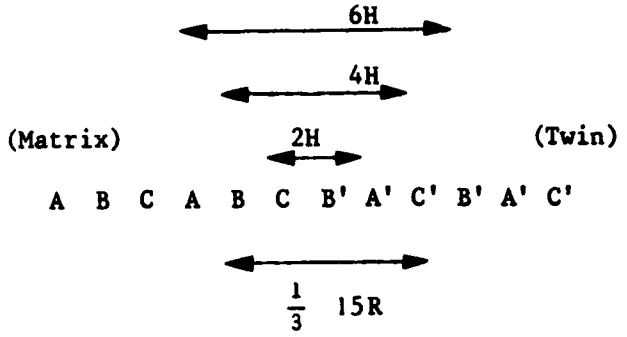

Figure 6 Incipient nuclei of various polytypes across a coherent twin boundary in 3C.

transformations [4], particularly 3C ⟶ 6H - see Figure 7(a). Once nucleated, polytype transformation usually proceed by the passage of unit-cell-high steps of the new polytype parallel to the stacking plane of the old (Figure 7(b)). If the original polytype was cubic, this may also involve the cooperative out-growth of transformations occurring on the different {111} stacking planes.

CONTROLLING THE OCCURRENCE OF POLYTYPES: GROWTH AND TRANSFORMATION

In practice, particular polytypes (including faulted structures) occur either due to the condition controlling **growth** or to **transformations** after growth. While there is a large literature discussing the multitude of experimental observations over the last 40 years or so [4], key issues appear to be the related topics of **epitaxy** and **seeding**. That is, given the almost negligible free energy differences between stacking sequences, it seems that almost any suitable stacking sequence 'template' will serve to determine the resultant crystal structure. Suitable templates are isostructural materials (silicon, diamond, graphite, AlN etc), existing SiC crystals or even defects within the crystals themselves, (e.g. grain and twin boundaries) [4].

There is general agreement that 3C often occurs preferentially perhaps as a result of the multiplicity of rapid growth directions. For example, 3C is observed to growth when SiC nucleates homogeneously from supersaturated solution of carbon in silicon [4,25,26]. However, 2H has been observed to grow on excess graphite in the solution [26] and 2H also appears stabilised if AlN (a 2H compound) is present in solid solution in SiC [27].

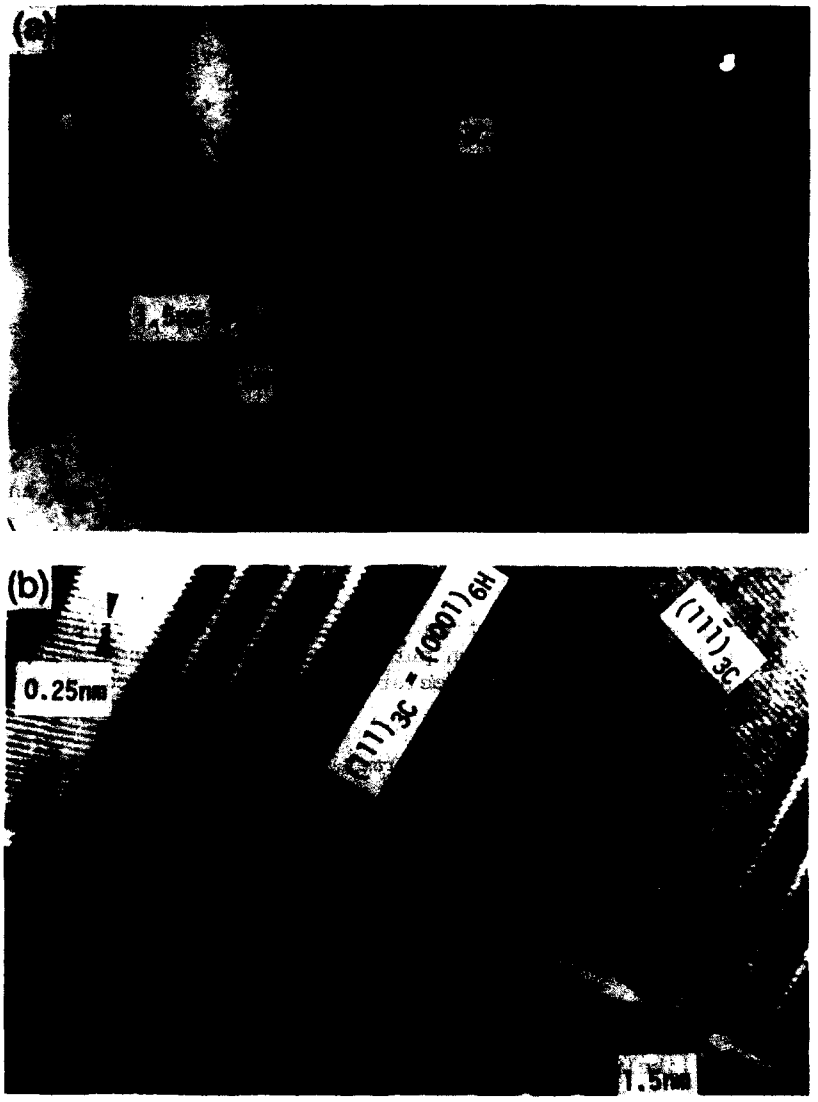

Figure 7 Transmission electron micrographs (tilted-beam, lattice images) showing various stages of the 3C⟶6H solid state transformation. (a) appearance of fine {111} twins which act as the precursors of the transformation. A region displaying 1.5nm ((0001) 6H) fringes can be seen. (b) a later stage of the transformation with unit-cell-high steps of 6H propagating along $(111)_{3C}$ and effecting the transformation [4].

If pre-existing SiC crystals are present during growth from supersaturated Si-C solutions, then the new SiC nucleates heterogeneously, grows epitaxially on the SiC crystals and takes on the exact stacking sequence of that part of each crystal it grows on (stacking faults included) [26]. However, it is now known that this process usually occurs by the nucleation and growth of 3C followed by subsequent solid state transformation seeded by the underlying SiC substrate acting as a template [28]. This implies that the resultant transformed stacking sequence (often 6H) is the most stable overall but cannot provide the rate of energy change on growth that the faster growing 3C can.

Transformations from 3C to other stacking sequences can often appear to result in a wide range of faulted structures (where the transformation starts from a series of uncoordinated sites simultaneously), regularly-faulted structures (which appear as long period polytypes) and well-defined short-period polytypes. Jepps and Page [4,29] clearly showed that this was all the result both of the way in which the nuclei of the new polytype formed and grew and the nature of the template controlling the nucleation.

THE EFFECTS OF IMPURITIES

An important result to emerge from studies of polytype transformations is their sensitivity to specimen purity and there are now a number of transformations proven to be associated with the presence of specific impurities, namely:

(a) 6H→3C ('reverse' transformation) - nitrogen
(b) 6H→4H→2H - either boron or aluminium
(c) 4H→6H - boron and nitrogen together.

All of these transformations support the theory that, relative to SiC, electronically p-type materials (e.g. B and Al) stabilise layers in hexagonal environments while electronically n-type materials (e.g. N and P) tend to stabilise layers in cubic environments [4].

While the solubility of these impurities in silicon carbide is reported to be very low (<0.3% [30,31]), little seems to be known regarding the likely atomic positions of such solute atoms in the SiC framework, that is whether the solutes are accommodated interstitially or substitutionally (on one or both of the Si and C site types) or whether, for example, local boron carbide or silicon nitride groups are formed. Thus, the actual mechanisms by which polytype stabilisation may occur is not understood but could include:

(i) band structure effects - Table 1 shows that the reported band gaps for different polytypes are significantly different and this could influence the energy levels available to p- or n-type solute atoms.

(ii) if the solute species are substitutional, then the introduction of a range of bond-strengths/lengths could influence the relative energy of different stacking sequences.

(iii) if the solutes are predominantly interstitial, then it is conceivable that more favourable site types are available in some structures rather than in others.

(iv) Although elemental purities are only soluble in small amounts in SiC [32,33] there is extensive solubility of compounds such as boron carbide, boron nitride and aluminium nitride in SiC [27,31,34]. Alloying with such compounds has been shown to effect the polytype, the structure of the resultant solid solution being influenced by the crystal structure of the alloying compound.

Finally, it must be borne in mind that trace impurities, including deviations from stoichiometry, could be responsible for some aspects of all reported transformations. Few workers, if any, have had the opportunity of working with very high purity materials and, for example, there is even some evidence that materials made from silicon-rich melts tend to show higher content of 3C than others [35]. This is obviously an area for future concern but will have to await parallel developments in techniques for accurately isolating and analysing trace levels of the (often low atomic number) impurities involved.

SiC WHISKERS AND FIBRES

SiC whiskers and fibres appear to present the greatest possibilities for transformation - they are impure, heavily faulted 3C and, in the case of fibres, very fine grained - but are being used in some of the most demanding applications. At least in the case of whiskers, recent work by Whitehead [36,37] has shown that forces driving recrystallisation (or spheroidisation of the whiskers to reduce their surface : volume ratio) act faster than those transforming the crystal structure. A surprising conclusion is that none of the structural features existing during recrystallisation (e.g. grain boundaries, twins, stacking faults) seem to act as templates for the expected 3C→6H transformation usually seen when faulted 3C is heated below ~2000°C. However, spheroidisation is expected to occur by creating grain boundaries across the width of the whiskers on planes parallel to the stacking plane (the whiskers are <0001> oriented) and thus there is little opportunity for stacking sequences to intersect each other. Observations such as those shown in Figure 8 allow time-temperature 'stability envelopes' to be defined (Figure 9) inside which little morphological change to whiskers etc will occur during either processing and/or service conditions.

It may be that the impurities present exert a controlling influence but the polytypic stability of whiskers and fibres is an area demanding urgent consideration.

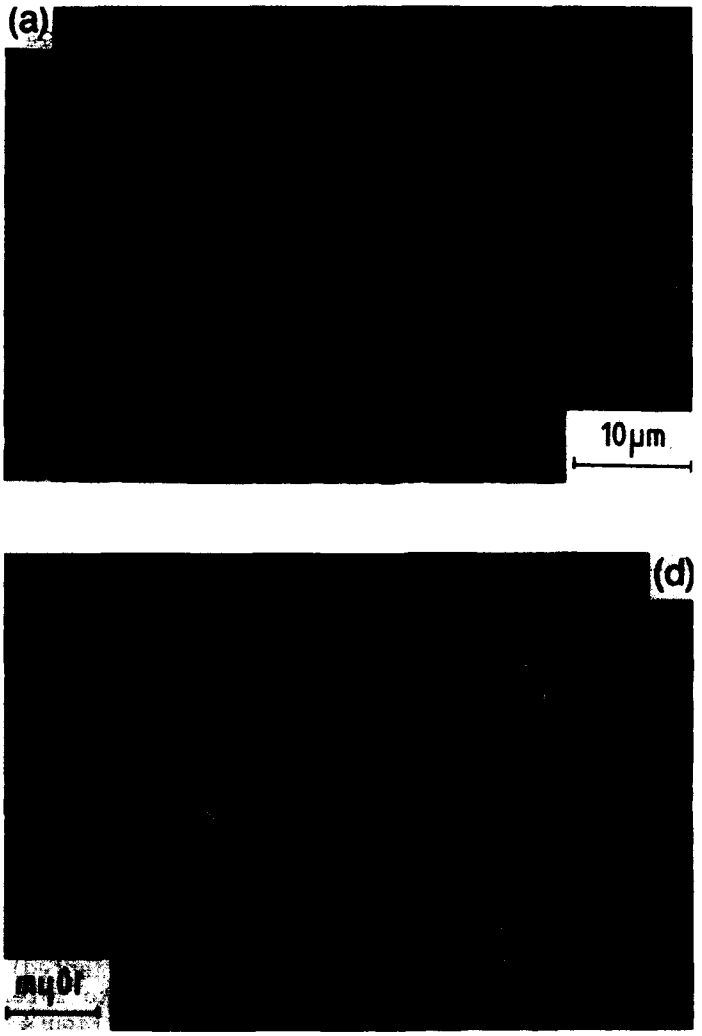

Figure 8 Scanning electron micrographs showing (a) the typical initial appearance of SiC whiskers ('Toka whiskers') and (b) the recrystallised/spheroidised appearance after heating in argon for 2 minutes at 2150°C [37].

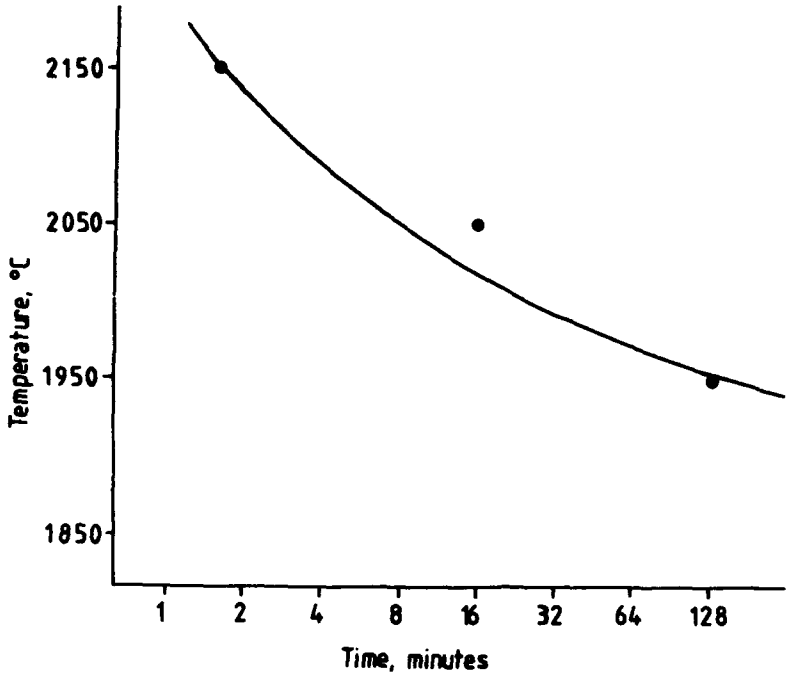

Figure 9 Suggested form of a stability envelope for SiC whiskers. To the left of the line, little change in either whisker morphology or structure can be expected to occur by virtue of heat treatment during processing. Stability decreases to the right of the line. The envelope position is expected to be sensitive to whisker purity and environment during heat treatment.

CONCLUSIONS

This paper has briefly reviewed the structure, nomenclature and polytypic transformation mechanisms in SiC. A number of conclusions can be drawn.

1. Despite there being clear conceptual models for polytypic transformations in SiC, careful microstructural and kinetic observations have to be made in order to unambiguously identify the exact combination of transformation mechanisms occurring [e.g. 4].

2. It is still often difficult to separate nucleation and growth effects in polytype transformations.

3. While 3C often occurs as the result of synthesis experiments at temperatures <2000°C, it appears that this will usually transform

to 6H which might be the most stable polytype in this temperature range.

4. Impurities have a strong influence on polytypic stability and transformations and it may be that variations in stoichiometry are important (but unknown) also. Thus, while various authors have tried to construct stability diagrams for polytypic structures either as a function of temperature [e.g. 12,13] or impurity tests [eg 38], these effects are almost certainly intimately connected [4].

5. Since the free energy difference between polytype is small, it appears that polytype growth or transformations are easily seeded by isomorphic structures, existing SiC stacking sequences or even the repeat distances on defects such as twin and (possibly) grain boundaries.

6. From the forgoing, it is clear that while we have sufficient practical knowledge to successfully influence the occurrence and stability of polytypes, a full understanding of polytype stability still awaits the refinement and application of detailed interatomic force calculations [e.g. 15,16].

ACKNOWLEDGEMENTS

It is a pleasure to acknowledge the work of my current and previous research students who have variously studied transformations in silicon carbide with respect to a number of applications: Nigel Jepps, Jeremy Ness, Graham Sawyer and Andrew Whitehead. Several of the figures regarding stacking sequences etc. appeared in the earlier extensive review by Jepps and Page [4] and Pergamon Press plc are kindly thanked for their permission to use them and quote from that earlier article. Ms Muriel Emery kindly typed the transcript.

REFERENCES

1. Burke, J. J., Lenoe, E. N. and Katz, R. N. (Eds) (1978). (Eds) Ceramics for High Performance Applications II (Brook-Hill, Chestnut Hill, Mass, USA).

2. Davis, R. F. (1990). This volume

3. Choyke, W. J. (1990). This volume

4. Jepps, N. W and Page, T F. (1983). Prog. Cryst. Growth and Characterisation, 7, 259-307.

5. Jagodzinski, H. (1949). Acta. Crystallog., 2, 201-207.

6. Smith, D. J., Jepps, N. W. and Page, T. F. (1978). J Microsc., 144, 1-18.

7. Ramsdell, R. S. (1947). Am. Min., 32, 64-82.

8. Zhadanov, G. R. (1945). Compte Rende Acad. Sci. URSS, 48, 39-42.

9. Jepps, N. W. (1979). Ph.D. Thesis, University of Cambridge.

10. Gomes de Mesquita, A. H. (1967). Acta Crystallog., 23, 610-617.

11. Inomata, Y. (1970). Yogo-Kyokai-Shi, 78, 365-369.

12. Inomata, Y., Inoue, A., Mitomo, M. and Suzuki, H. (1968). Yogyo-Kyokai-Shi, 76, 313-319.

13. Knippenberg, W. F. (1963). Philips Res. Rep., 18, 161-274.

14. Schneer, C. J. (1955). Acta Crystallog., 8, 279-285.

15. Cheng, C., Heine, V. and Jones, I. L. (1990). J. Phys. Condens. Matter (in press).

16. Cheng, C., Heine, V. and Needs, R. J. (1990). Phys. Rev. Lett., (in press).

17. Jagodzinski, H. (1954). N. J. Min. Monatsh., 3, 209-225.

18. Jagodzinski, H. (1954). Polytypism in SiC crystals. Acta Crystallog., 7, 300-305.

19. Kelly, A. (1966). Strong Solids (Clarendon Press, Oxford).

20. Bootsma, G. A., Knippenberg, W. F. and Verspui, C. (1971). J. Cryst. Growth, 8, 341-353.

21. Whitney, E. D. (1963). Nature, 199, 278-280.

22. Scace, R. E. and Slack, G. A. (1959). In: 'Silicon Carbide', Proc. Conf. Silicon Carbide, Boston Mass., Ed. O'Connor, J. R. and Smittens, J., Pergamon Press, New York (1960), p. 24.

23. Jepps, N. W. and Page, T. F. (1981). J. Am. Ceram. Soc. 64, C177-C178.

24. Powell, J. A. and Will, H. A. (1972). J. Appl. Phys., 43, 1400-1407.

25. Sawyer, G. R. and Page, T. F. (1978). J. Mater. Sci., 13, 885-904.

26. Ness, J. N. and Page, T. F. (1986). Bull. Mineral., 109, 151-161.

27. Ruh, R. and Zangvil, A. (1982). J. Am. Ceram. Soc., 65, 260-265.

28. Ness, J. N. and Page, T. F. (1986). J. Mater. Sci., 21, 1377-1397.

29. Jepps, N. W. and Page, T. F. (1980). J. Microsc., 119, 177-188.

30. Kieffer, A. R., Ettmayer, P., Gugel, E. and Schmidt, A. (1969). Mat. Res. Bull., 4, S153-S166.

31. Shaffer, P. T. B. (1969). Mat. Res. Bull., 4, 213-220.

32. Trefilov, V. I., Borisenko, V. A., Gnesin, G. G., Gridneva, I. V., Mill'man, Yu, V. and Chugunova, S. I. (1978). Sov. Phys. Dokl., 23, 207-208.

33. Drowart, J., de Maria, G. and Inghram, M. G. (1958). J. Chem Phys., 29, 1015-1021.

34. Shaffer, P. T. B. (1969). Mat. Res. Bull., 4, S13-S24.

35. Inomata, Y., Inoue, Z., Mitomo, M. and Tanaka, H. (1969). Yogyo-Kyokai-Shi., 77, 83-88.

36. Whitehead, A. J. (1990). PhD Thesis, University of Cambridge.

37. Whitehead, A. J., Page, T. F. and Higgins, I. (1989). Ceram. Eng. Sci. Proc., 10, 986-997.

38. Inomata, Y. Inoue, Z. and Kijuma, K. (1969). Yogyo-Kyokai-Shi., 77, 313-318.

39. Jepps, N. W. and Page, T.F. (1979). J. Microsc., 116, 159-171.

CRYSTAL-CHEMISTRY OF TRANSITION METAL HEMICARBIDES.

T. EPICIER
Institut des Sciences Appliquées de Lyon
Groupe d'Etudes de Métallurgie Physique et de Physique des Matériaux, Bât. 502,
u. a. CNRS 341
69621 Villeurbanne Cedex
France

ABSTRACT. Transition metal subcarbides near the composition M_2C_1 possess an hexagonal L'3 structure in which ordering of carbon atoms can occur, due to the presence of 50% of unoccupied sites in the interstitial sublattice. The crystal-chemistry of this "hemicarbide" phase is reviewed for compounds of the V^{th} (V, Nb, Ta) and VI^{th} (Mo, W) groups. Recent *in situ* powder neutron diffraction studies are presented, which allow the literature to be significantly corrected and updated. Structural refinements are considered, and the stability of ordered states is discussed in terms of effective-pair interactions.

1. Introduction

1.1 MOTIVATION OF THE STUDY

The phase "hemicarbide" M_2C_1 is based on a L'3-type structure which consists in a close-packed hexagonal (hcp) metallic sublattice, with half of the octahedral interstitial positions occupied by carbon atoms. Due to the presence of 50% of constitutional vacancies (e.g. unoccupied sites), ordering can take place on the metalloid sublattice. Hexagonal hemicarbides of the IV^{th} group (Ti_2C, Zr_2C, Hf_2C) are not stable ; subcarbides of the V^{th} and VI^{th} groups (respectively : V2C, Nb_2C, Ta_2C and Mo_2C, W_2C) exist over a narrow homogeneity range M_2C_{1-x}, as can be seen from the phase diagrams reported in figure 1.

It is the purpose of this paper to actualize the knowledge of the various (super)structures identified in metallic hemicarbides. Although a lot of general studies and reviews have already been devoted to these materials [4-9], it will be shown that the present *in situ* powder neutron diffraction experiments have noticeably modified the previous data concerning phases identification or temperatures and even type of structural transformations. These high temperature (up to 2200°C) experiments were conducted on the two-axis powder diffractometer with multi-detector D1B at the High Flux Reactor of the I.L.L. (Grenoble, F) [10]. General information about experimental procedures can be found in [11].

R. Freer (ed.), The Physics and Chemistry of Carbides; Nitrides and Borides, 215–248.
© 1990 *Kluwer Academic Publishers. Printed in the Netherlands.*

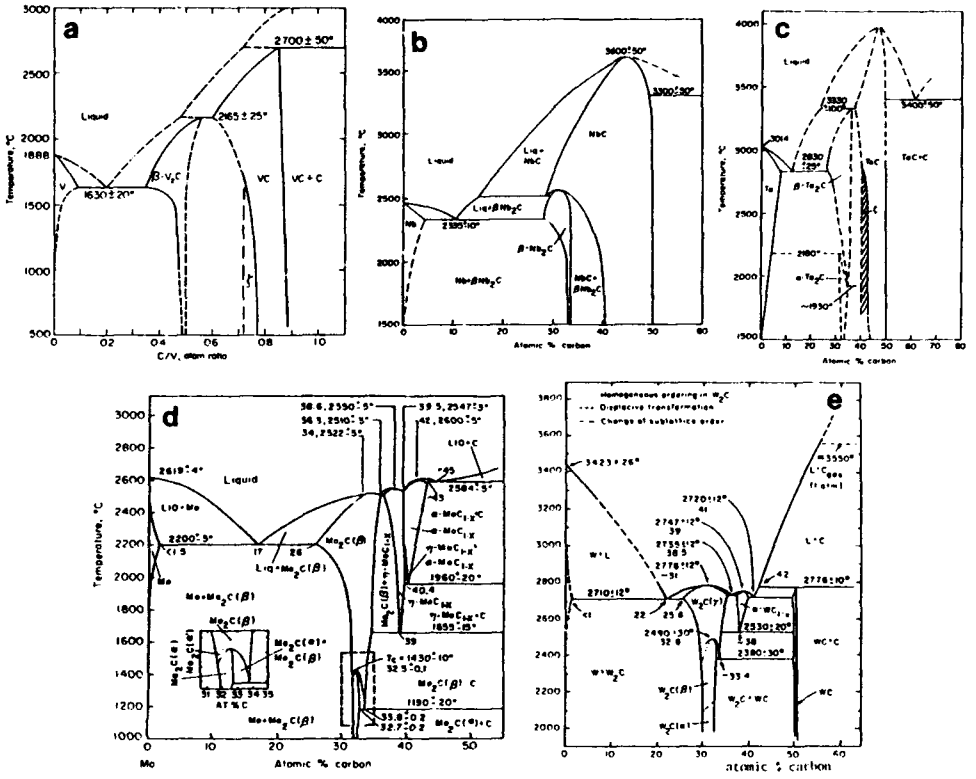

Figure 1. M-C systems showing the M_2C region. a) : V-C [1] ; b) : Nb-C [1] ; c) : Ta-C [1] ; d) : Mo-C [2] ; e) : W-C [3].

Reasons for the discrepancies which exist in literature are illustrated below through appropriate examples[1].

1.1.1. *Effects of the Chemical Composition.* The impurity concentration, or the presence of a second crystalline phase may influence the relative stability of various superstructures possible for a given hemicarbide. The case of Nb_2C is eloquent from this point of view :

.on the one hand, 2 at.% of oxygen seem to stabilize an ε-form rather than the ζ-form expected at low temperature [12] ; moreover, elaboration of thin films by heating above 1500°C in air produce the same ε-form [13].

.on the other hand, the ε - ζ transition is inhibited while cooling in compounds $Nb_2C + NbC_{1-x}$, but the ζ-form is preferentially observed when Nb is present as a crystalline phase [14].

These chemical effects are very embarrassing, since they make any comparison between data obtained by different authors, under different

[1] a description of the ordered structures evoked in these examples will be given in subsection 2.

conditions for elaboration or analysis, rather delicate and probably meaningless. They also lead to the conclusion that any published result should be accompanied by chemical analysis results, especially when long heat treatments have been conducted, which may modify the chemical composition of the compound in the course of the study.

1.1.2. *Influence of the Thermodynamical Conditions.* Transition metal hemicarbides are refractory compounds with very high melting points (2170, 2990, 3330, 2520 and 2780°C for V_2C, Nb_2C, Ta_2C, Mo_2C and W_2C respectively). The structural transitions affecting the ordered distribution of carbon atoms can reasonnably be identified only in temperature ranges where the carbon diffusion is efficient, above 0.4 T_m (e.g. ≈ 1000°C) nominally. Technical difficulties, due to the high temperatures involved, are encountered in direct (*in situ*) studies of these transformations.

Moreover, room temperature experiments may fail to reveal the low temperature stable state : as an example, it is proved that in W_2C, the "middle temperature" ε-form (thermodynamically stable between 1050 and 1800°C) can hardly be avoided at room temperature, although a transition ε - ζ occurs below 1050°C [15]. Also, it can be mentionned that the disordered state γ-W_2C cannot be completely frozen at 20°C even after severe quenching from 2200°C [16], on the contrary of V_2C, where the disordered form is easily quenched from above 1300°C [17].

These remarks emphasize the need for an *in situ* study of the structural modifications in most of the hemicarbides.

1.1.3. *Problems Associated with the Detection of Carbon Ordering.* Classical diffraction techniques involve 3 types of particles : X-rays, electrons and neutrons. Data reported in table 1 show that X-rays are generally not adequate to detect ordering of carbon in metal (hemi)carbides, due to their low ability to be scattered by light atoms.

In some cases however, carbon ordering produces a distorsion of the metallic sublattice, which can be detected through a splitting of X-ray diffraction lines (e.g. ζ-Mo_2C [21], ζ-V_2C [12, 22] or ξ-Nb_2C [12]). The example of Nb_2C shows that application of this technique remains delicate, since 3 different orthorhombic forms have been successively identified by room temperature X-ray diffraction work (i.e. β [23], ζ [22] and ξ [12]).

Although electrons can be employed, especially in a transmission microscope (which allows the ordered microstructure to be directly imaged), the nature of their dynamic interaction with matter does not allow precise atomic positions and occupancy factors to be refined. A typical example is an anomaly observed by electron micro-diffraction for the estimated intensity of the (0001) superlattice reflection of the ε-based structure in V_2C [8] and W_2C [16] : this feature, non-interpretable correctly by this technique, can be explained by a modification of the exact ε-form (labelled ε' hereafter) identified through careful structural refinements (see sections 1.2 and 3.2).

Neutrons overcome the previous difficulties ; moreover, their good penetration power allows to investigate bulk specimens, which reduces possible errors due to surface contamination. Also, it makes it easier to perform high temperature diffraction experiments, since the transmission mode can be employed, on the contrary of X-rays (see a general review in [24]).

element			V	Nb	Ta	Mo	W	C
atomic number Z			23	41	73	42	74	6
$r_{C/M}$[a]		X-rays	0.26	0.15	0.08	0.14	0.08	-
		electrons	0.41	0.28	0.20	0.28	0.20	-
		neutrons	17.4	0.94	0.96	0.96	1.39	-
"penetration power"[b]		X-rays	≈ 0.1 μm					
		electrons	≈ 0.5 μm					
		neutrons	≈ a few cms					
X-rays	f (10^{-12}cm)[c]	sinθ=0	6.6	11.5	20.5	11.8	20.8	1.69
		sinθ/λ=0.5[d]	2.8	5.7	11.3	5.9	11.4	0.48
electrons	f (Å)[e]	sinθ=0	5.9	8.6	12.3	8.7	12.4	2.45
		sinθ/λ=0.5[d]	1.2	1.9	3	1.95	3	0.41
neutrons	b (10^{-12}cm)[f]		-0.0382	0.7054	0.6910	0.6950	0.4770	0.6650

[a] $r_{C/M}$ is the ratio : $f_C(\sin\theta=0)/f_M(\sin\theta=0)$ for X-rays and electrons (f : atomic diffusion factor) ; b_C/b_M for neutrons (b : coherent diffusion length).
[b] typical thickness under classical diffracting conditions
[c] from [18]
[d] value corresponding to an interplanar distance of 1 Å.
[e] at 200 kV ; from [19].
[f] from [20] ; contrary to X-rays and electrons, this term does not vary with θ.

Table 1 : comparison between X-rays, electrons and neutrons for diffraction studies of transition metal carbides. Atomic diffusion factors are given for particles of usual wavelengths, e.g. 1.54 Å for X-rays and 1.08 Å for neutrons (from [18]).

1.2. DESCRIPTION OF THE SUPERSTRUCTURES

Known superstructures in pure transition metal hemicarbides are sketched in figure 2 ; note that the interstitial sites form a simple hexagonal lattice.

Complementary information about these structures is given in tables 2 ; results from structure refinements are also summarized. From such analyses, average interatomic distances can be deduced (see §4.2.2).

Furthermore, measurements of the Debye-Waller factors (B_M and B_C) allow the relative influence of thermal vibrations and atomic static dispacements to be estimated. For example, in compounds of the VIth group (for which several reliable refinements are available -see table 2-), B_M is equal to ≈ 0.56 Å^2 and 0.32 Å^2 respectively for Mo in ζ-Mo_2C and W in ε'-W_2C : these values are larger than the thermal contributions estimated to ≈ 0.24 and 0.17 Å^2 for Mo and W respectively (from comparison with pure metals or cubic monocarbides of metal of similar atomic weight -see details in [15]-). The same result is obtained for the carbon species, since B_C is equal to ≈ 0.58 and 0.48 Å^2 in Mo_2C and W_2C respectively ; these values are larger than a reasonnable estimation for the thermal contribution, i.e. ≈ 0.25 Å^2 [15]. Differences can be attributed to remaining incoherent displacements from the refined positions given in table 2 ; amplitudes of the average quadratic displacements ($|\Delta x|$ or $\sqrt{\langle u^2 \rangle_{static}}$)

can be deduced : $|\Delta x| \approx 0.11$ Å for Mo and C in ζ-Mo_2C ; 0.07 and 0.09 Å for W and C atoms in ε'-W_2C. These values (close to 0.1 Å) are similar to that estimated in cubic monocarbides (see in [32]).

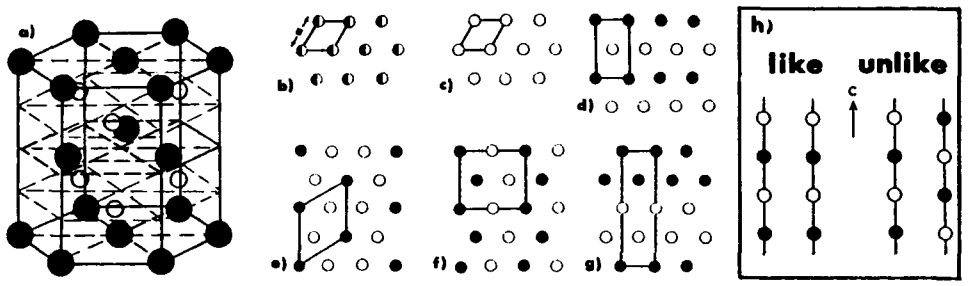

Figure 2. Distribution of the carbon atoms in the different M_2C structures. a) : host metallic hcp sublattice (solid circles ; the open ones indicate the octahedral interstitial sites). b) : disordered γ phase (L'3-type, hexagonal symmetry) projected onto the (0001) plane. c) : α-phase (C6-type or CdI_2-antitype, hexagonal symmetry). d) : β-phase (Co_2C-type or $CaCl_2$-antitype ; orthorhombic symmetry). e) : ε-phase (ε-fe_2N-type, hexagonal symmetry). f) : ζ-phase (ζ-Fe_2N-type, orthorhombic symmetry). g) : ξ-phase (ξ-Nb_2C-type, orthorhombic symmetry). In drawings b) to g), the solid and open circles correspond to carbon atoms respectively at z=0 and z=1/2 ; a distorsion of the metallic sublattice is expected within the structures of orthorhombic symmetry. h) : "like" and "unlike" pairs of carbon rows in M_2C structures.

structure description				neutron structure refinement[a]					
type	space group	Wyckoff positions Metal	Carbon[b]	compound[c]	atomic positions Metal	Carbon[b]	Debye-Waller factors (Å) M	C	ref.
α	P$\bar{3}$m1 n°164	2 (d)	1(a)	Ta_2C	x=1/3 y=2/3 z=0.2537	x=0 y=0 z=0	0.53		[17]
				Ta_2C	x=1/3 y=2/3 z=0.2550	x=0 y=0 z=0	0.32	0.41	[25]
β	Pnnm n°58	4 (g) x≈1/3 y≈1/4 z=0	2 (a) x=0 y=0 z=0						
γ	P6$_3$/mmc n°194	2 (c)	2 (a) τ=0.5	V_2C	x=1/4 y=2/3 z=1/4	x=0 y=0 z=0	0.97		[17]

Table 2.1. Crystallographic figures of M_2C structures (notations given in table 2.2).

structure description				neutron structure refinement[a]					
type	space group	Wyckoff positions Metal	Carbon[b]	compound[c]	atomic positions Metal	Carbon[b]	Debye-Waller factors (Å) M	C	ref.
ε	$P\bar{3}1m$	6 (k)	1 (a) 2 (d)	W_2C ($W_2C_{0.89}$)	x=0.335 y=0 z=0.2521	1(a) : τ=1 x=y=z=0 1(b) : τ=0 x=y=0, z=1/2 z=1/2 2(c) : τ=0.12 x=1/3, y=2/3, z=0 2(d) : τ=0.65 x=1/3, y=2/3, z=1/2	0.11	0.19	[26]
				W_2C ($W_2C_{0.84}$)	x=0.3270 y=0 z=0.2553	1(a) : τ=0.82 1(b) : τ=0 2(c) : τ=0.22 2(d) : τ=0.63	0.39	0.50	[25]
				W_2C ($W_2C_{0.86}$)	x=0.3335 y=0 z=0.2474	1(a) : τ=0.77 1(b) : τ=0 2(c) : τ=0.25 2(d) : τ=0.70	0.33	0.50	[16]
				W_2C ($W_2C_{0.92}$)	x=0.3337 y=0 z=0.2506	1(a) : τ=0.96 1(b) : τ=0 2(c) : τ=0.28 2(d) : τ=0.58	0.29	0.46	[16]
				W_2C (W_2C_1)	x=0.333 y=0 z=0.250	1(a) : τ=0.97 1(b) : τ=0.03 2(c) : τ=0.26 2(d) : τ=0.74	0.29	0.46	[27]
ξ	Pnma n°62	M_I : 4 (c) M_{II} : 4 (c)	4 (c)	Nb_2C	Nb_I : x=0.0417 y=1/4 z=0.75 Nb_{II} : x=0.2083 y=1/4 z=0.25	x=0.375 y=1/4 z=0			[12]

[a] *at room temperature ; references* [30, 31] correspond to X-ray determinations.
[b] τ represents the occupancy factor.
[c] chemical composition indicated between parenthesis.
[d] a slightly better agreement is proposed by the author assuming a carbon supercell described in the space group $P2_12_12_1$ (n°19).

Table 2.2

structure description				neutron structure refinement[a]					
type	space group	Wyckoff positions Metal	Carbon[b]	compound[c]	atomic positions Metal	Carbon[b]	Debye-Waller factors (Å) M	C	ref.
ζ	Pbcn n°60	8 (d)	4 (c)	V_2C	x=0.250 y=0.130 z≈0.078	x=0 y≈3/8 z=1/4			[12, 28]
				Mo_2C	x=1/4 y=1/8 z=1/12	x=0 y=3/8 z=1/4	0.5		[21]
				Mo_2C[d]	x=0.252 y=0.124 z=0.083	x=0 y=0.376 z=1/4	0.68	0.71	[29]
				Mo_2C (Mo_2C_1)	x=1/4 y=1/8 z=1/12	x=0 y=0.375 z=1/4	0.56	0.55	[27]
				Mo_2C ($Mo_2C_{0.95}$)	x=0.2438 y=0.1206 z=0.0789	x=0 y=0.3751 z=1/4	0.53	0.57	[16]
				W_2C	x=1/4 y≈1/8 z≈1/12	x=0 y≈3/8 z=1/4	0.5		[30]
				W_2C	x=1/4 y=1/8 z=0.071	x=0 y=3/8 z=1/4			[31]

Table 2.3 (notations as in table 2.2).

The ordered forms shown in figure 2 can be described as different combinations of a unique type of [0001] column, made of an alternative sequence C-Vac-C-Vac... (Vac = vacancy). When examining pairs of columns in first, second, ... neighbours positions, it is possible to discern the different structures by counting the number of like or unlike rows (figure 2h). This analysis (reported in table 3) allows the relative stability of phases to be discussed in terms of ground states [33] (see section 4.2).

structure-type	probability p_1	p_2	p_3
α	1	1	1
β	1/3	1/3	1
ε	1/3	1	1/3
ζ	1/3	2/3	1/3
ξ	2/3	1/3	1/3

Table 3. Probability of identical rows in positions of first, second and third neighbors (p_1, p_2 and p_3 respectively) in M_2C structures (from [33]).

In order to avoid confusion between the different structures, a unique labelling has been employed throughout this paper ; it consists in a single

greek letter, i.e. α, β, γ, ζ, ε, ξ, in agreement with some unambiguous notations (among all employed) from the literature[1] .

It can be seen that these various forms are easily discerned through the presence of specific superstructure peaks in neutron profiles (see figure 3).

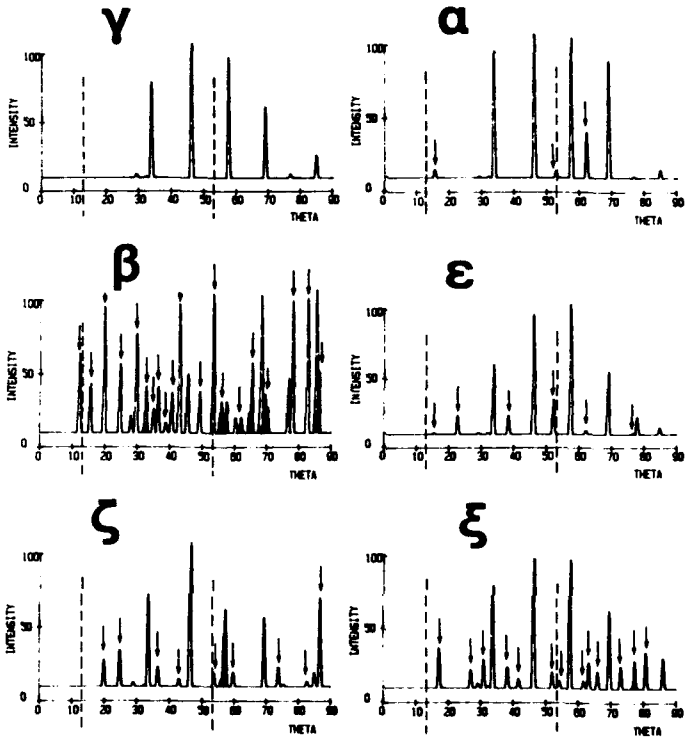

Figure 3. Calculated neutron diffraction profiles for possible M_2C structures (simulations are made for the case of W_2C, with a_{hcp} = 3 and c_{hcp} = 4.72 Å ; the wavelength λ is equal to 2.52 Å -D1B instrument, ILL-). Arrows indicate the superstructure peaks ; vertical dotted lines show the angular range explored in the high temperature experiments reported in this work.

2. Phase Transitions ; Updated Results

2.1. VANADIUM HEMICARBIDE V_2C

The most recent crystallographic studies of V_2C are reported in table 4. From these works, the following structural schema can be proposed :

$$\zeta\text{-}V_2C \rightarrow \gamma\text{-}V_2C$$
$$800 < T_c < 1250°C \quad (T_c : \text{transition temperature}) \qquad (1)$$

[1] see table III.2 of ref. [16] It can be mentionned that an alternative description, based on the Jagodzinski-Wyckoff symbols, was previously proposed [6].

An hexagonal modification ε-V_2C was also identified at low temperature ; this form appears to be stabilized by nitrogen for compositions near $VC_{0.32}N_{0.15}$ typically [38]. it was also claimed that oxygen stabilizes the β-form [23, 35] ; this last result appears however doubteful because of a possible mistake in the identification of the orthorhombic β-phase by X-ray diffraction work.

structure[a]	technique	temperature range[b]	impurities (wt %)	second phase[c]	elaboration conditions	ref.
γ a=2.902 c=4.577	X-ray diffraction	20 (1100-1950, rapid helium cooling)	O<0.95 N<0.15	V or VC (variable with y)	melting of V and graphite powders VC_y (under vacuum)	[34]
γ a=2.902 c=4.578	neutron diffraction	20 (1400)	O, N < 0.05	VC	repeated heat treatments of V+C powders	[17]
a=5.004 β b=4.577 c=2.897	X-ray diffraction	20	$VC_{0.458}O_{0.001}$ $VC_{0.508}O_{0.005}$ $VC_{0.507}O_{0.011}$	-	reaction $C+V_2O_5$ (15 hours at ≈1780°C)	[23, 35]
γ a=2.896 c=4.560			$VC_{0.579}$	VC		
a=4.555 ζ b=5.745 c=5.037	X-ray diffraction	20 (100 hours at 1350)	0.44<O<1.2	V		[36]
γ a=2.904 c=4.569			0.14<O<0.41	VC		
a=4.575 ζ b=5.760 c=5.020	X-ray diffraction	20 (1350-1450)	O ≈ N ≈ 0.8	V	heating of V+C or $V+VC_{1-x}$ powders at 1350°C (under vacuum or argon)	[28]
γ a=2.885 c=4.560				VC		
ε a=5.005 c=4.551	neutron diffraction	20 (7 days at 900)		-	*as above*	[12]
a=11.49 ζ b=10.06 c=4.55[d]	X-ray diffraction	20 (50 hours at 800-1400, rapid helium cooling)	O ≈ N < 0.02	VC	hot-pressing of V+C powders (annealed under vacuum)	[22]

[a] lattice parameters (in Å) correspond to the composition M_2C_1.

[b] the true temperature of determination is indicated first (in °C) ; value in parenthesis is the annealing or quenching temperature.

[c] possible minor phase in addition to the major M_2C phase.

[d] the cell parameters a and b are twice that of the exact ζ-phase.

[e] rough agreement : the (0001) superlattice reflection is weaker than predicted from the exact ε-form.

Table 4.1. Literature data on V_2C.

structure[a]	technique	temperature range[b]	impurities (wt %)	second phase[c]	elaboration conditions	ref.
γ a=2.900 c=4.574	X-ray diffraction	20 (1000-2000, cooling at ≈30°/s)	O + N ≈ 0.3	VC	pre-sintering of V+C powders (at 1300°C) and sintering at 1750°C (in helium)	[37]
ζ		20 (as above or <800, cool. ≤2°/s)				
ζ	electron diffraction	20 (< 950)				[8]
ε[e]		20 (>950)				
a=4.568$_8$ ζ b=5.756$_0$ c=5.033$_2$	X-ray diffraction	20 (14 days at 745) or 20-1125	O=0.5, N<0.01	V	arc melting of V+C powders (under argon)	[9]
γ a=2.887$_8$ c=4.574$_3$		20 (>2100?) ; meta -stable up to 723				
ζ	neutron diffraction	20 (≈500-1560)	O=0.1 $VC_{\approx 0.5}$ 0<0.1 VC_xN_y x≈0.11-0.46 y≈0.04-0.35		sintering of V+C+N powders (under vacuum)	[38]
ε		20 (>1400)				

Table 4.2.

Regarding the results concerning V_2C + V and V_2C + VC_{1-x} compounds, it can be said that the presence of the pure metal favours the ζ phase.

The present *in situ* neutron diffraction experiments allow a more general and consistent evolution to be identified in a V_2C (+ VC_{1-x} as a minor constituant) powder $VC_{0.455}\ O_{0.009}\ N_{0.002}$[1] :

$$\zeta\text{-}V_2C \rightarrow \varepsilon\text{-}V_2C \rightarrow \gamma\text{-}V_2C$$
$$T_{c1}=1087\pm12°C,\ T_{c2}=1278\pm5°C \qquad (2)$$

(see figures 4 and 5).

Both transitions occurs at relatively low temperatures, e.g. between ≈0.52 and 0.59 T_m) ; consequently, any of the 3 forms can be retained and detected at room temperature, depending upon the cooling rate. Moreover, since the ε and γ hexagonal appear to be almost indistinguishable by X-ray diffraction [38], it may explain why the transition ζ - ε was never mentioned in the previous literature.

Further comments about the present results are [16, 40] :

.the transition ζ - ε is very abrupt (see figure 5) and can then be considered of the first-order type ; it exhibits a small hysteresis (ΔT ≈ 20°).

[1] within ≈2% for the atomic ratio C/V before and after study.

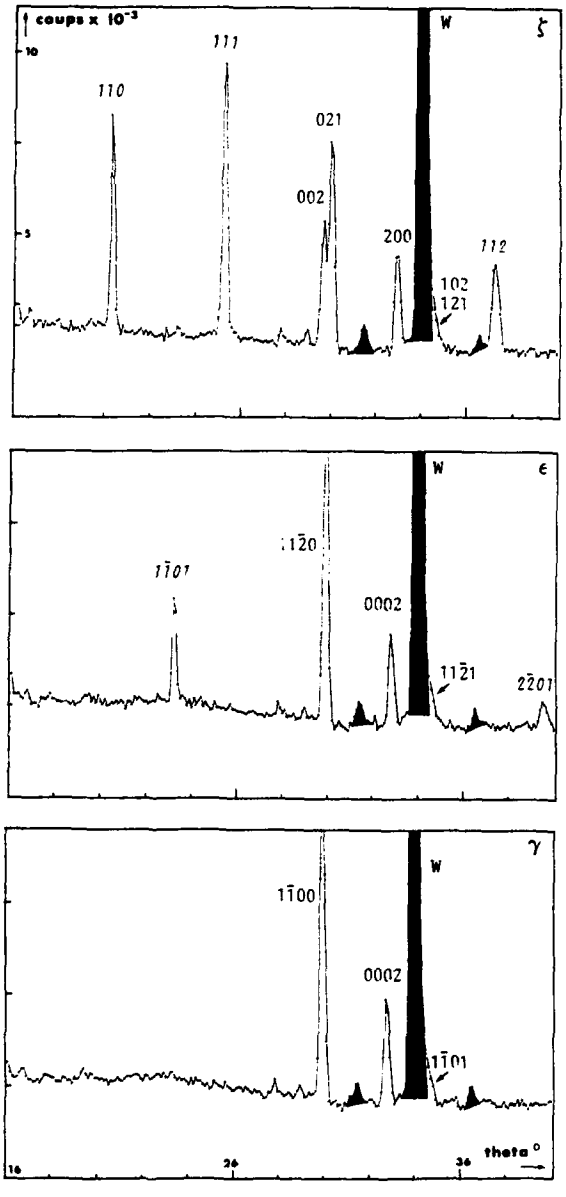

Figure 4. Structural evolution of V_2C at high temperatures : the neutron diffraction profiles show the successive phases ζ (*top*, T = 20°C), ε (*middle*, T = 1150°C) and γ (*bottom*, T = 1300°C) ; indexation of superstructure lines is written in italic letters. Extra diffraction lines are shaded ; the biggest one comes from the tungsten from the sample environment [11] ; the small ones are due to VC_{1-x} present as a minor phase.

.isothermal treatments performed between 1000 and 1125°C allow the kinetic of the transition to be described by a classical "Avrami" law :

$$n = 1 - \exp[-k\, t^n] \qquad (3)$$

(n : quantity of the growing phase ; t : growth time ; k : constant ; n : critical exponent, the value of which informs about the mechanism controlling the transformation).

In the present case (see figure 5), n is equal to 1.04 (i.e. very close to unity), which indicates that the transformation proceeds through the nucleation of bidimensional domains [41].
.the transition ε - γ appears to be continuous (see figure 4), and most probably of the second-order type. Fitting the experimental superstructure intensities I_s by the law :

$$I_s = A\,(T_c - T)^{2\beta} \qquad (4)$$

(A : constant)

leads to a value of 0.33±0.02 for the critical parameter β, which corresponds to the expected value (e.g. 0.31) for a three-dimensional second-order type transition in the Ising model [41].

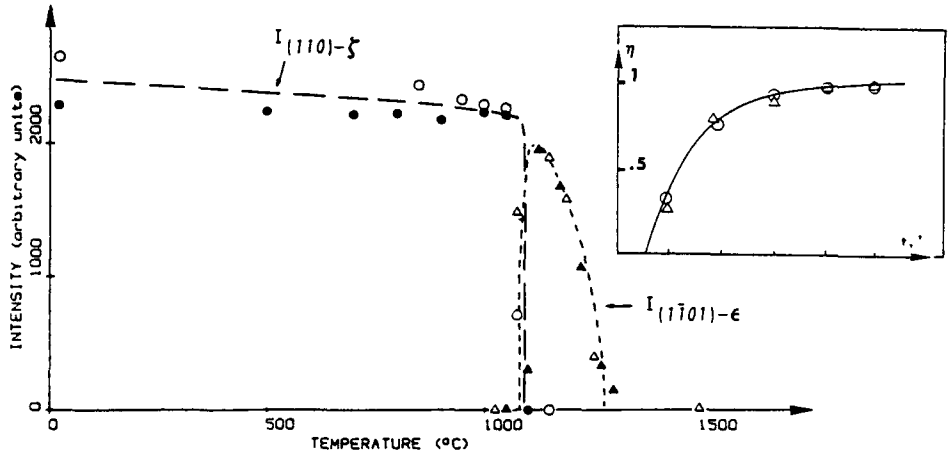

Figure 5. Intensity of superlattice reflections versus the temperature in V_2C (full and empty symbols correspond to measurements at heating and cooling respectively). The insert shows the analysis of the advancement of the reaction ε - ζ followed while cooling at 1075°C (the continuous line is the plot of equation (3)).

2.2. NIOBIUM HEMICARBIDE Nb_2C.

Although numerous results are in disagreement concerning the orthorhombic form observed at low temperature (see table 5), a consistent evolution for Nb_2C with temperature can be proposed [1, 14, 22] :

$$\xi\text{-}Nb_2C \rightarrow \varepsilon\text{-}Nb_2C \rightarrow \gamma\text{-}Nb_2C$$
$$T_{c1} \approx 1200°C \quad T_{c2} \approx 2500°C \qquad (5)$$

structure	technique	temperature range	impurities (wt %)	second phase	elaboration conditions	ref.
a=5.371 β b=4.956 c=3.129	X-ray diffraction	20 (occasional oxidation 7 hours at 300)	O≈0.04-0.61[a] N≈0.05-0.36		sintering of Nb + C powders at 1600-1800°C	[23]
ε a=5.407 c=4.960	X-ray and electron diffraction	20			heating of thin films Nb+C (in the air)	[13]
a=12.36 ζ b=10.895 c=4.968[b]	X-ray diffraction and thermal analysis[c]	20 (50 hours at 800-1200 ; helium cooling)	O≈N<0.02		hot-pressing of Nb + C powders	[22]
γ a=3.118 c=4.955		20 (as above at 1400)		Nb		
ε a=5.407 c=4.960	neutron diffraction	20	0≈0.16 N≈0	NbC_{1-x}	hot-pressing of Nb +C powders 10 hours at 2000°C (under vacuum)	[12]
a=10.92 ξ b=4.974 c=3.090		20 (20 hours at 2000)	0≈0.04			
a=10.910 ξ b=3.0954 c=4.9746	X-ray diffraction	20≈1195	O=0.16 ($NbC_{0.3}$)	Nb	arc melting of Nb + C powders (under argon) ; heat-treatment at 800°C during 14 days	[14]
ε		T > 1195				
ε a=5.4204 c=4.9698[d]		20≈1200	O=0.02 ($NbC_{0.68}$)	NbC		

[a] amount of oxygen determined by difference.
[b] the cell parameters a and b are twice that of the exact ζ-phase.
[c] *in situ* analysis ; the transitions ζ - ε and ε - γ are observed at ≈1200 and 2500°C respectively.
[d] the ε-phase is metastable down to room temperature.

Table 5. Literature data on Nb_2C.

As for V_2C, oxygen stabilizes probably some ordered structures. On the one hand, Alyamovskii et al [23] have reported an orthorhombic β form for $NbC_{0.43\text{-}0.52}N_{0.006\text{-}0.01}O_{0.002\text{-}0.04}$ powders. On the other hand, the ε-phase is clearly stabilized by oxygen : firstly, Terao identifies this structure after heating mixed Nb+C powders in air [13]. Secondly, Yvon et al [12] observe the

ε-form in compounds treated at 2000°C and containing 2 at.% of oxygen ; after long-term treatments, the ζ-phase appears simultaneously with a decrease of oxygen down to 0.5 at.%.

It has also been established that the orthorhombic ζ-form is more stable in Nb_2C + Nb powders [14] ; in Nb_2C+NbC_{1-x} compounds, the ε - ζ transformation is inhibited during cooling.

In the present neutron diffraction work, a new result has been obtained on a $NbC_{0.476\pm0.001}O_{<0.001}N_{0.003}$ powder (see figure 6) :

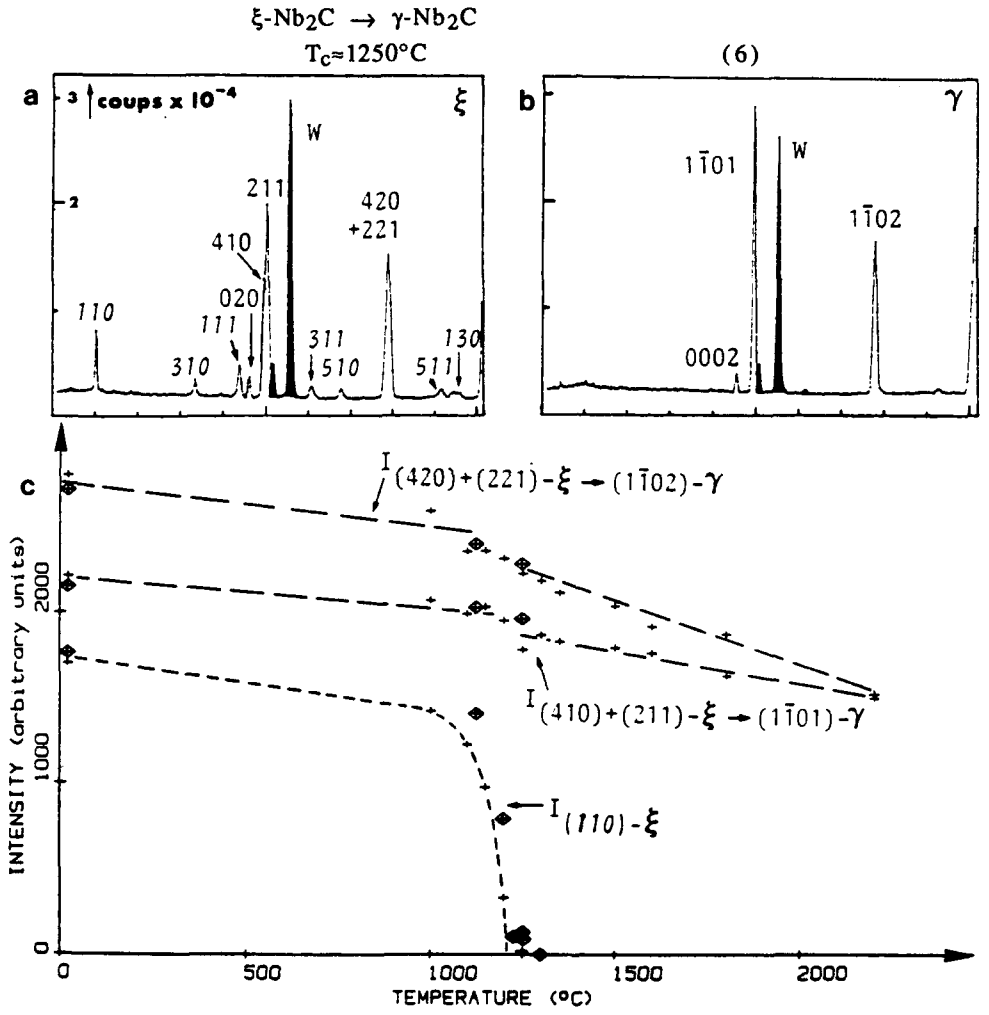

Figure 6. Structural evolution of Nb_2C with temperature. a) : neutron profile at 20°C : ζ-phase (presentation as in figure 4 ; the small dark peak is from pure niobium). b) : γ-phase at 1250°C. c) : plot of the intensity of characteristic peaks versus temperature (presentation as in figure 5 ; the highest intensities -divided by 20- are for matrix reflections).

The analysis of the thermal evolution of the superstructure $(110)_\xi$ peak (figure 6) seems to indicate that the transition is of the second order ; nevertheless, the value of the parameter β (see equation (4)) is relatively low (0.22±0.02), which could mean a transition slightly of the first order.

The evidence for a transition $\xi - \gamma$ at 1250°C is in clear disagreement with previous data (e.g. relation (5)). It can be argued that the chemical analysis of the powder indicates a sub-stoichiometric composition, which leads to the presence of a small quantity of pure niobium (see figure 6) ; this could stabilize the ξ-form. However, this stabilizing effect is doubtful since the expected ε-form still does not appear after more than 2 hours between 2000 and 2200°C. This point will be re-discussed later.

2.3. TANTALUM HEMICARBIDE Ta_2C

Main literature data concerning the system Ta-C are reported in table 6. The *in situ* neutron study conducted by Bowman et al [45] ascertains the accepted structural evolution with temperature :

$$\alpha\text{-}Ta_2C \rightarrow \gamma\text{-}Ta_2C$$
$$2035°< T_c < 2160°C \text{ (depending upon composition)} \quad (7)$$

This work establishes that this fully reversible transformation is non-isotherm for $TaC_{\simeq 0.96-1}$ compounds and isotherm outside this narrow compositional range.

The present *in situ* neutron investigation of $TaC_{0.497}O_{0.007}N_{0.001}$ powders confirms these general trends (see figure 7).

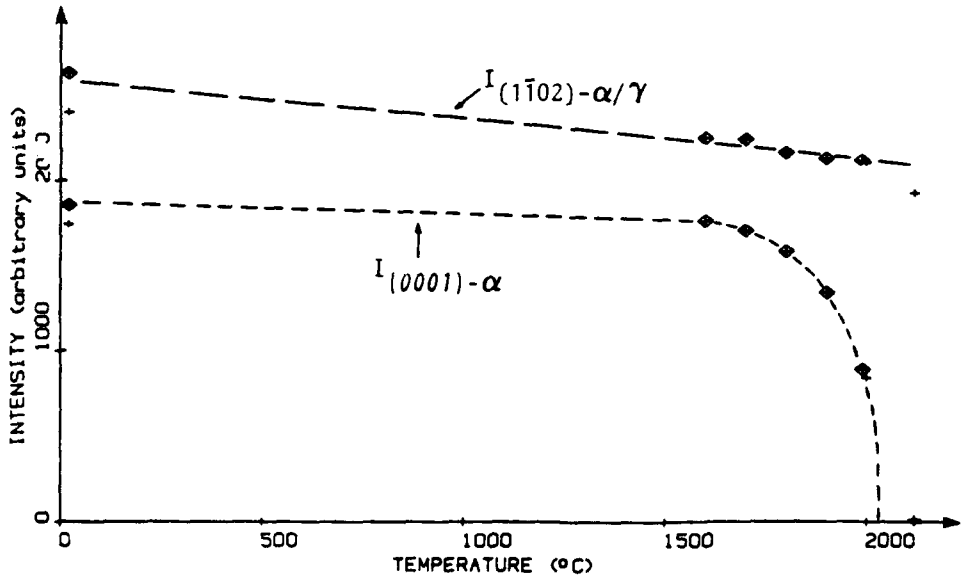

Figure 7. Same as figure 5 for Ta_2C.

structure	technique	temperature range	impurities (wt %)	second phase	elaboration conditions	ref.
γ a=3.106 c=4.945	X-ray diffraction	20	N=0.15	Ta,TaC or C depending on composit^n	sintering of Ta+C powders at 1800-2100°C under vacuum	[43]
α a=3.103 c=4.9378	X-ray and neutron diffraction	20	O≈N<0.05	Ta	heating of Ta+C powders at 1600°C (under vacuum)	[17]
α γ	thermal analysis	transition at ≈ 2000				[44]
α	neutron	20-1990/2160 depending on composition	O≈0.04 N<0.01	Ta	heating of Ta+C powders at 2100°C (under vacuum) ; annealings at 1800°C	[45]
γ		T>1990				
α a=3.1037 c=4.9394	X-ray diffraction	20-1023	0≈0.11 N<0.01	Ta, TaC	arc-melting of Ta+C powders (under argon)	[9]
	neutron diffraction	20			as above ; cooling at≈150°/s	[25]

Table 6. Literature data on Ta_2C.

However, the order-disorder transition (ODT) temperature appears to be 2020°C ; this value is lower than the previous one (the transition is significantly detected between 2070 and 2160°C in Ta_2C_1 [45], but with a thermal gradient of 60-80°C). This difference can be discussed as follows :

.the thermal gradient is estimated at less than 40°C in the latter study [11] ; thus, temperature values announced here are more reliable than those reported in [45].

.in the study of Bowman et al, the sample is enclosed in a graphite + TaC container which may react and carburize slightly the Ta_2C powder ; hence, initial compositions near $TaC_{0.9-0.95}$ (for which T_c is comparable with that obtained in our work) may correspond to actually richer compositions approaching the stoichiometric ratio Ta_2C_1. This discussion cannot be definitively concluded, since no chemical data is reported in the work of Bowman et al [45] ; in the present case, it can be indicated that the chemical analysis after the high temperature study reveals a minor compositional change, since the final composition is $TaC_{0.494\pm0.001}O_{0.002}N_{0.001}$.

.finally, it must be said that fitting techniques may influence the measure of T_c ; in the latter case, the indicated value was obtained after fitting by the law reported in equation (4), with $\beta = 0.14\pm0.03$.

As reported above, the critical parameter β is relatively low compared to that expected for a theoretical second-order transformation ; this could indicate a slight discontinuity in the transition.

2.4 MOLYBDENUM HEMICARBIDE Mo_2C.

structure	technique	temperature range	impurities (wt %)	second phase	elaboration conditions	ref.
a=4.724 ζ b=6.004 c=5.199	X-ray and neutron diffraction	20			commercial Mo_2C powder	[21]
γ a=3.103 c=4.9378	X-ray diffraction and thermal analysis	20 (1470-2300, cooling at ≈90-120°/s)	O=0.007 N<0.001	Mo or MoC depending on composit[n]	sintering of Mo+C powders (2 hours at 1600-1900°C under vacuum) ; various annealings	[2]
a=4.733 ζ b=6.042 c=5.202		20 (1000-1350)				
a=4.735 ζ b=6.038 c=5.208	X-ray diffraction	20 (1000)				[31]
ζ[a]	neutron diffraction	T<1200-1400 for $MoC_{0.41-0.56}$ compounds				[46]
γa		T>1200-1400				
a=4.73 ζ b=6.04 c=5.20	X-ray diffraction	20 (1/2 hour at 700-1000)		Mo	carburizing of Mo wires at 900-1600°C	[47]
γ a=3.00 c=4.78		20 (1 hour at 1600)		MoC		
a=4.732 ζ b=6.037 c=5.208[b]	X-ray and neutron diffraction	20			single crystal (zone-melting under helium)	[29]
γ a≈3.01 c≈4.73	X-ray diffraction	20 (>1700)			large grains extracted from ingots (annealings at 350-2300°C)	[48]
a=4.730 ζ b=6.027 c=5.198		20 (<1700)		Mo		
a=9.466 b=24.152 c=41.675[c]				MoC		

[a] isotherm transitions for $MoC_{0.41}$ and $MoC_{0.56}$ and non-isotherm for $MoC_{0.515}$.
[b] a modulation of this structure is proposed (see table 2).
[c] modification based on the ζ-phase.

Table 7. Literature data on Mo_2C.

Literature results on Mo_2C (see table 7) agree on the following evolution :

$$\zeta\text{-}Mo_2C \rightarrow \gamma\text{-}Mo_2C \qquad T_c \approx 2160°C \qquad (8)$$

This ODT has been observed by *in situ* neutron diffraction [46] ; the transformation is of the first order in Mo_2C_1 [2, 46].

Present results (detailed in [27]) show a different behavior for a $MoC_{0.496}O_{0.016}N_{0.001}$[1] powder :

$$\zeta\text{-}Mo_2C \rightarrow \varepsilon\text{-}Mo_2C \rightarrow \gamma\text{-}Mo_2C$$
$$T_{c1}=1350\pm15°C \quad T_{c2}=1960\pm5°C \qquad (9)$$

(see figure 8).

Similar results were obtained on a sub-stoichiometric powder $Mo_2C_{\simeq 0.95}$ (critical temperatures being lowered by about 150°C) [27]. Both transformations ζ - ε and ε - γ are similar to that observed in V_2C (see §2.1). The parameter β in equation (4) is respectively equal to 0.27±0.03 and 0.32±0.02 for the ODT in $Mo_2C_{\simeq 1}$ and $Mo_2C_{\simeq 0.95}$; these values suggest a transition of the second order.

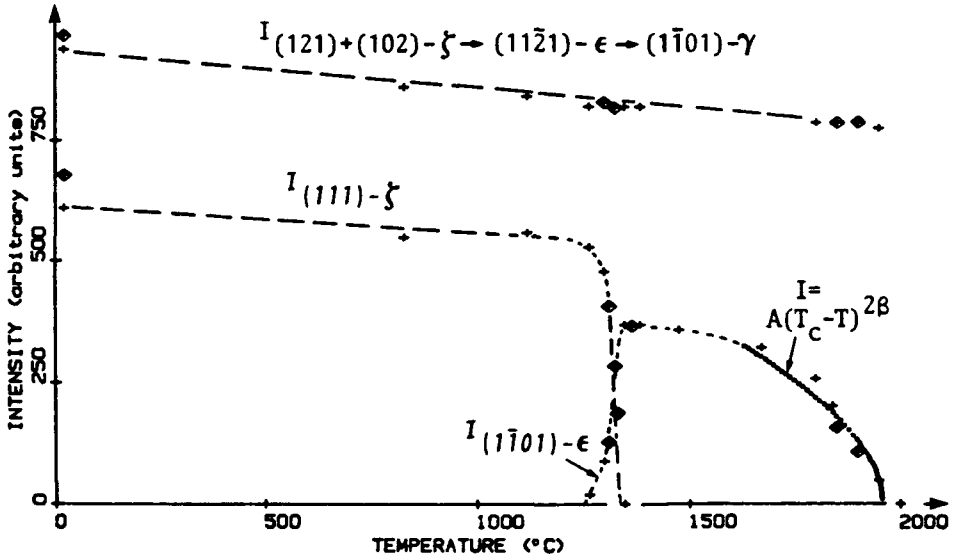

Figure 8. Same as figure 5 for Mo_2C (highest intensities -matrix reflections- are divided by ≈7) ; the fitting of the end of the ODT by equation (4) is shown).

The disagreement between present results (relation (9)) and previous literature data ((8)) will be commented later (§4.1.1).

2.5. TUNGSTEN HEMICARBIDE W_2C.

Tungsten hemicarbide is probably the most controversed compound regarding crystallography (see table 8) : 3 ordered forms, i.e. α, ζ and ε have been proposed at low temperature. Phase identifications performed after

[1] $MoC_{0.495}O_{0.018}N_{0.001}$ after the high temperature study.

long-term annealings (ζ [31] and ε [26]) suggest that the orthorhombic ζ-phase could be more stable at low temperatures ; no mention is made of any stabilizing chemical effect.

structure	technique	temperature range	impurities (wt %)	second phase	elaboration conditions	ref.
α a=2.98 c=4.71	electron diffraction	20			carburizing of W wires (≈5 minutes at T>1100°C)	[49]
a=4.728 ζ b=6.009 c=5.193	X-ray diffraction and thermal analysis	20 (quenching from 2000-2600)	O≈0.013, N≈0.006 in W_2C powders O≈0.072, N≈0.041 in W powders		hot-pressing of W and W_2C_1 powders	[30]
γ		20 (2650)				
α	X-ray diffraction	20 (600 hours at 1100-1200)	small excess carbon		hot-pressing of W+C powders (≈10 minutes at 2200°C) ; re-melting under He	[31]
a=4.721 ζ b=6.030 c=5.180		20 (600 hours at 600-1000)				
ε a=5.184 c=4.721	X-ray and neutron diffraction	20 (2100-2400, various cooling procedures)			hot-pressing of W+C powders (under vacuum)	[50]
ε	neutron diffraction	T<1750		WC		[46]
γ		T>1750				
a=4.72 ζ b=5.98 c=5.17	X-ray diffraction	20 (2300-2450 or 900-250 hours-)		WC	carburizing of W wires between 2000 and 2600°C	[47]
α a=2.98 c=4.71		20 (2150-2250)				
γ a=3.00 c=4.72		20 (2550-2600)				
ε a=5.1852 c=4.7232	X-ray and neutron diffraction	20 (1650)	0≈0.12		hot-pressing of W+C powders (30-50 hrs at 1650°C)	[26]
ε a=5.190 c=4.720	electron & neutron diffraction	20 (2100, slow cooling)	0≈0.003 N<0.001	WC, W	carburizing of W sheets embedded in graphite	[51]
ε a=5.1852 c=4.7232	X-ray and neutron diffraction	20 (rapid cooling at ≈150°/s)	0≈0.04 N<0.01 ($WC_{\approx 0.49}$)		melting of W+C powders (under argon)	[25]

Table 8. Literature data on W_2C.

Ignoring a possib ζ/ε transition at low temperature, the thermal evolution of W_2C can be described on the basis of *in situ* neutron experiments [46] :

$$\varepsilon\text{-}W_2C \rightarrow \gamma\text{-}W_2C \qquad T_c \approx 1750°C \qquad (10)$$

New results have been obtained here on 3 different powders, the compositions of which is detailed in table 9.

powder	chemical analysis	
	before study	after study
$W_2C_{\sim 1}$	$WC_{0.50<0.001}N_{<0.001}$	$WC_{0.46}O_{0.003}N_{<0.001}$[a]
$W_2C_{\sim 0.92}$	$WC_{0.460<0.001}N_{<0.001}$	$WC_{0.47}O_{<0.001}N_{0.001}$
$W_2C_{\sim 0.81}$	$WC_{0.4050<0.001}N_{<0.001}$	$WC_{0.415}O_{0.001}N_{0.001}$

[a]the significant decrease of the carbon content is caused by a carburization of the tungsten container during long annealings (more than 50 hours) at high temperatures.

Table 9. Chemical analysis of W_2C powders ([11]).

Details of the study have been published elsewhere [27]. In this work, no evidence was obtained for a ζ/ε transformation, although the ζ-phase was present in the $W_2C_{\sim 0.92}$ powder. Further investigation after annealing at 900°C during 550 hours reveals this transition [15] ; the complete structural schema in W_2C_1 is then :

$$\zeta\text{-}W_2C \rightarrow \varepsilon\text{-}W_2C \rightarrow \gamma\text{-}W_2C \qquad T_{c1}\approx 1050°C \quad T_{c2}=1800\pm 5°C \qquad (11)$$

(see figure 9).

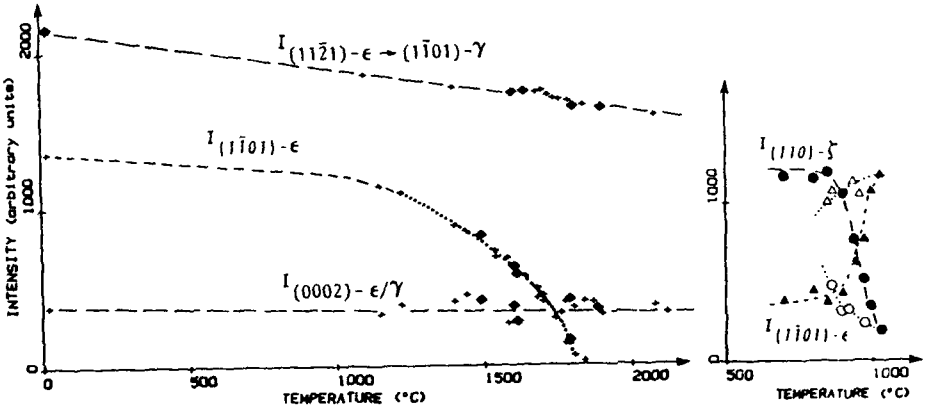

Figure 9. Same as figure 5 for $W_2C_{\sim 1}$. a) *(left)* : disordering of the metastable ε(')-phase (highest intensities -matrix reflections- are divided by 10). b) *(right)* : detail of the ζ - ε(') after stabilization of the ζ-phase.

This behavior is similar to that observed in V_2C (§2.1) and Mo_2C (§2.4). The same characteristics apply to both transitions ζ - ε (ε') and ε' - γ : the first one is of the first order (with a strong hysteresis, as shown in figure 9b)), the second one is of the second order, with β (equation (4)) respectively equal to

0.27 ± 0.02 and 0.25 ± 0.04 in $W_2C_{\sim1}$ and $W_2C_{\sim0.81}$ (the ODT temperature is 1625 ± 5°C in the latter case).

It can be noted that no evidence was obtained for the α-phase, even after various heat treatments and whatever the composition.

3. Transmission Electron Microscopy of Ordered Hemicarbides

This paragraph is devoted to applications of the Transmission Electron Microscopy (TEM) technique to the study of the microstructure of hemicarbides ; some results will be presented very briefly, since a detailed paper on TEM studies of metallic carbides is reported in the present proceedings [52]).

3.1. CONVENTIONAL TEM. DOMAIN STRUCTURES AND GEOMETRY OF ANTIPHASE BOUNDARIES.

3.1.1. *Example of Mo_2C.* Electron diffraction work confirms carbon ordering in Mo_2C_1 according to the ζ-form (see figure 10).

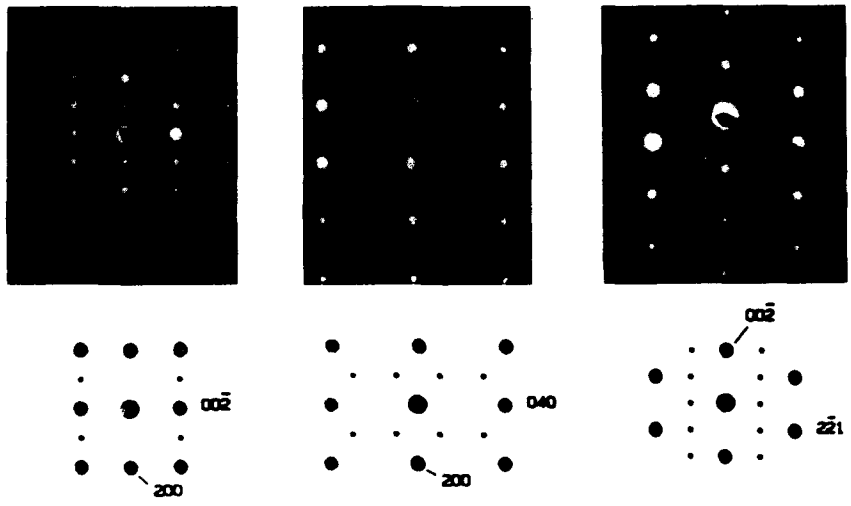

Figure 10. Electron diffraction patterns of ζ-Mo_2C *(from left to right)* : $[010]_\zeta$ $([1\bar{2}10]_{hcp})$, $[001]_\zeta$ $([10\bar{1}0]_{hcp})$ and $[110]_\zeta$ $([24\bar{2}\bar{3}]_{hcp})$.

Moreover, domain structures can be characterized. When variants exist for an ordered form, domains are present due to the growing of nuclei with different orientations. In Mo_2C, such domains have the 3 possible orientations depicted in figure 2a) of reference [51]. The orthorhombic distortion can be characterized by the parameter ρ defined as :

$$\rho = \frac{\sqrt{3}\, b_\zeta}{2\, c_\zeta} - 1 \qquad (12)$$

(ρ = 0 for a non-distorted crystal).

In Mo_2C_1 and $Mo_2C_{0.94}$, values respectively equal to 1.5 10^{-3} and 2 10^{-3} can be deduced from precise cell dimension measurements [16] ; these results indicate a compression along the c_ζ axis of the orthorhombic ζ-cell. This distortion is elastically accomodated at the interfaces of ordered domains for reasonably low domains sizes, and δ-fringes contrast are produced in TEM micrographs (figure 2b) in reference [52]). After subsequent annealing just below the ODT -70 hours at 1150°C in Mo_2C_1-, domain growth occurs, and the irregular shape of domains make it impossible to accomodate isotropically the orthorhombic distortion : interfacial $a/3<11\bar{2}0>_{hcp}$ dislocations are then produced, which relax the incompatible strains from each side of the domain boundaries. A typical example is reported in figure 11.

3.1.2. *Antiphase defects in ε'-W_2C.* A high density of antiphase boundaries (APBs) can be observed in the ε'-W_2C phase at room temperature (see figure 12). Typical dissociated APBs [52] are formed ; since the APBs are caused by basal $a/3<11\bar{2}0>_{hcp}$ dislocations [16], they can produce a perfect dislocation in the carbon sublattice by forming triplets as shown in figure 12 : the addition of three $a/3[11\bar{2}0]_{hcp}$ vectors gives a resulting displacement equal to $a[11\bar{2}0]_{hcp}$, which can be rewritten as a translation vector $a[1\bar{1}00]_\varepsilon$ in the ordered superlattice.

3.2. HIGH RESOLUTION ELECTRON MICROSCOPY (HREM). REFINEMENT OF ε'-W_2C.

As seen in table 2, neutron diffraction refinements of the ε-based ordered form in W_2C indicate that the actual occupancy factors for carbon sites differ from that of the exact ε-structure [16, 25-27]. This is clearly illustrated by the analysis of the neutron profile shown in figure 13. In this example, error factors R_1 and R_2 obtained from a classical "Rietveld-Hewat" refinement [54], and defined as :

$$R_1 = \frac{\sum |I_{exp}(hkl) - \rho I_{calc}(hkl)|}{\sum I_{exp}(hkl)}$$

$$R_2 = \frac{\sum |y_{exp}(\theta) - \rho y_{calc}(\theta)|}{\sum y_{exp}(\theta)} \qquad (13)$$

($I_{exp}(hkl)$ and $I_{calc}(hkl)$: respectively, experimental and calculated intensities of the (hkl) line ; $y_{exp}(\theta)$ and $y_{calc}(\theta)$: respectively, experimental and calculated counts at the angular position θ ; ρ : scale factor)

are respectively equal to 13.7 and 19.2% assuming the ε-structure, and 6.9 and 13.1% for the ε'-model.

A similar refinement can be attempted by HREM imaging [55]. Figure 14 shows a set of experimental $<11\bar{2}0>_{hcp}$ micrographs that are compared to image simulations from various models describing the following possible atomic arrangements (see figure caption).

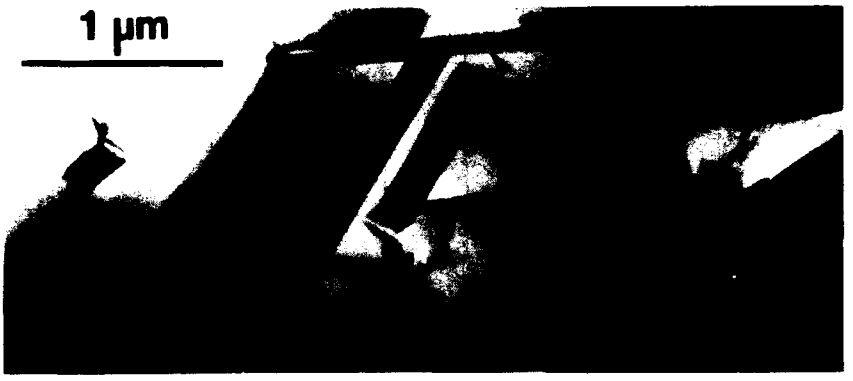

Figure 11. 200 kV bright field TEM image showing domain boundaries and interfacial dislocations (arrows) in annealed ζ-Mo_2C_1 (n-beam conditions).

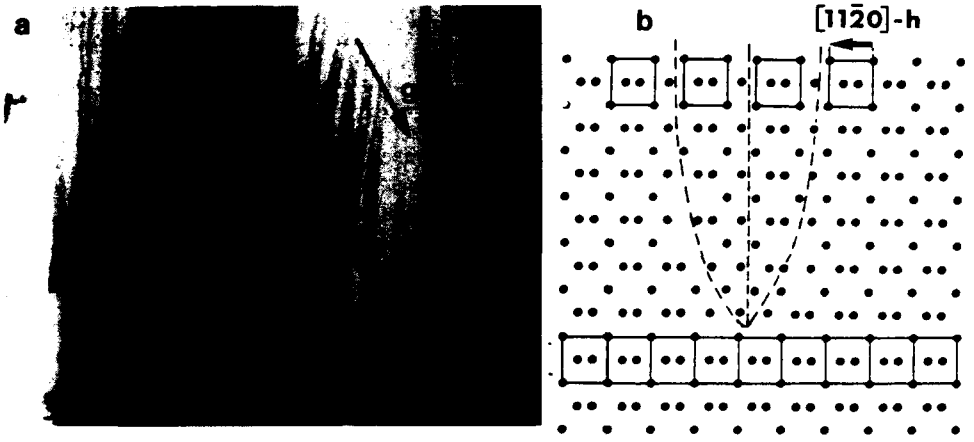

Figure 12. Typical triplets of APBs as observed by TEM in ε'-W_2C. a) : dark field image (diffracting vector $g=i0\bar{1}1_{\varepsilon'}$). b) : diagram showing the dislocation left in the carbon sublattice ($[1\bar{1}00]_{hcp}$ section of the ε-structure ; tungsten atoms are omitted for clarity).

The modified ε'-form consists of an atomic arrangement which equalizes the carbon repartition in interstitial basal planes at z=0 and z=1/2 (contrary to the ε-form, which leads to a distribution 1/3 - 2/3).

Unambiguously, the series of figures 14d) provide better matches than the other models. Various "random" distributions have been tested which lead to the same conclusion (in other words, the contrast is not significantly sensitive to the position of atoms along the viewing direction for the ε'-phase [56]). This simulation approach is realistic in the sense that integers are used for occupancy factors (contrary to the neutron refinement procedure, where average real values are iteratively determined). Consequently, these HREM observations confirm and complete the results of neutron refinements, and definitively indicate that the ε'-form is partially disordered.

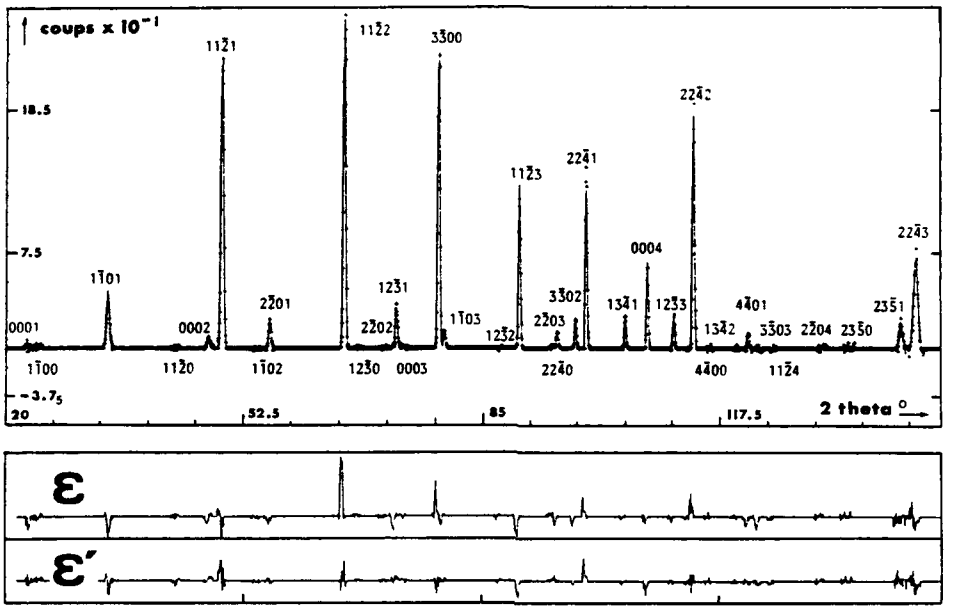

Figure 13. Neutron refinement of the ε-based form in $W_2C_{\sim 0.92}$ (high resolution spectrometer D1A at the ILL -λ=1.909 Å-). Difference profiles between experimental (dotted line) and calculated (full line) profiles are shown for the ε and ε' structures : they clearly show the better agreement for the latter model.

4. Discussion.

4.1. PHASE TRANSITIONS

4.1.1. *Transition* ζ - ε. This transition is observed in V_2C, Mo_2C and W_2C.

Evidence for this transformation in Mo_2C is in contradiction with previous litterature data (see table 7 and relation (8)). Reasons for this discrepancy are easy to explain :

.the transformation is perfectly reversible and almost instantaneous during cooling : this is why the ε-phase has never been reported previously at room temperature ;

.the only *in situ* structural study [46], which led to the conclusion of the direct disordering of the ζ-phase, is clearly in error because of inadequate experimental conditions (see complete discussion in [16, 27]). Other *in situ* experiments, performed by Differential Thermal Analysis (DTA), do not allow the symmetry of phases to be revealed [30].

In the W-C system, it has been shown that the ζ-phase cannot be observed without careful long-term annealings around 900°C [15, 31] ; thus, the transition ζ -ε can be missed very easily.

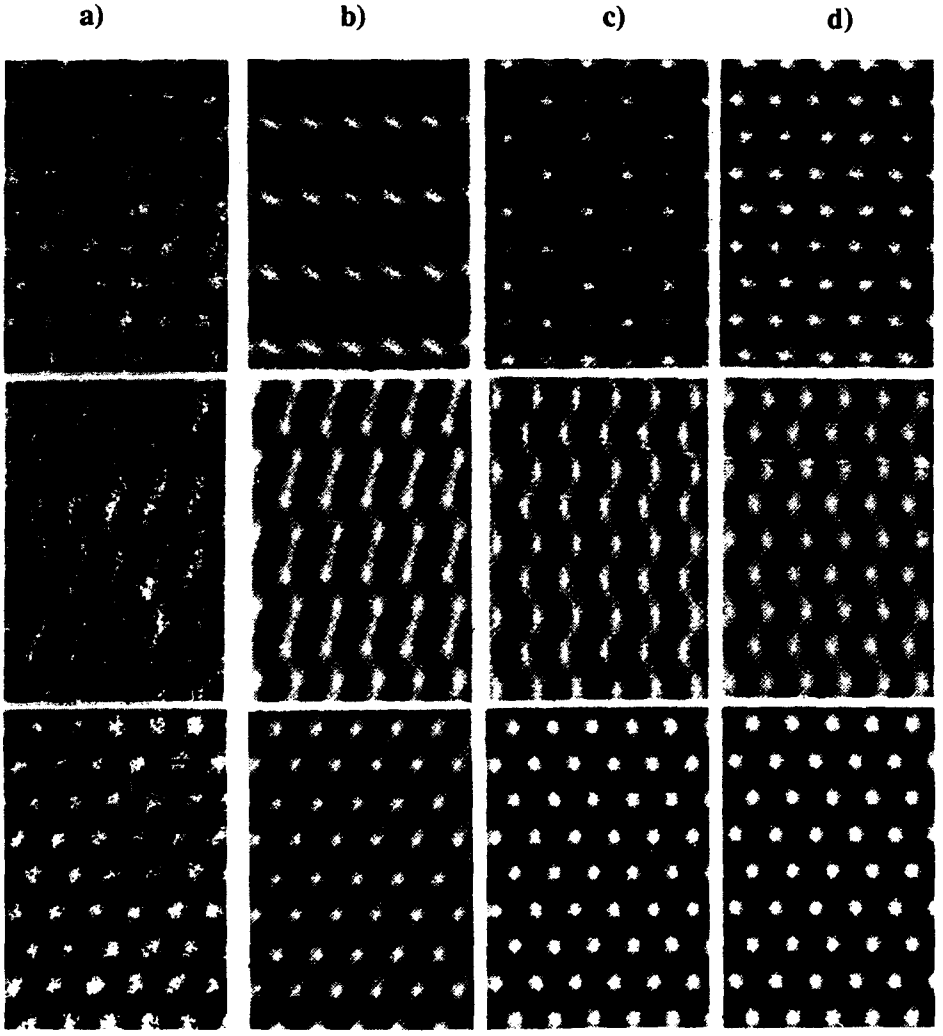

Figure 14. HREM analysis of the ε'-phase in W_2C (Jeol 200CX microscope). a) : experimental through-focus series ; defocus values are estimated from diffractograms to -79, -108 and -136±5 nm (respectively *from top to bottom*). b) : corresponding multislice simulations for the exact ε-cell (repartition 1/3-2/3 on interstitial planes). c) : idem for a "$\varepsilon^+/\varepsilon^-$" structure ; this model is based on a sequence of cells $\varepsilon^+/\varepsilon^-/\varepsilon^+/\varepsilon^-$.., where ε^+ and ε^- refer to ε-cells with c-axis oriented in opposite senses (this respects the equal repartition). d) : idem for ε', with a "random" distribution of carbon atoms in the thickness of the foil which respects the occupancies given in table 2 for W_2C_1. Calculated images in b) to d) have been obtained for a crystal thickness of 3 nm, and defoci respectively equal to -81, -95 and -137 nm.

In the case of V_2C, the present evidence for a ζ - ε transition was not mentioned in the previous literature (see table 4). Moreover, the credence of a direct disordering of the ζ-V_2C phase is only supported by X-ray experiments [9, 37] which are not adequate to discern the ε and γ phases. Endly, it appears that the temperature range of stability of the ε-V_2C phase is very narrow, since the ε-form gets disordered almost as soon as it appears. All things considered, the general thermal evolution ζ - ε - γ observed in this study is consistent with previous data, since each of these 3 forms were identified separately (see table 4).

From the present neutron diffraction investigation, the ζ - ε transition is quite abrupt for stoichiometric compositions M_2C_1, which leads to the hypothesis of a first-order transition. This result is confirmed by previous DTA analysis on Mo_2C [2] and W_2C [30] (first-order transformations can be revealed by this technique). Moreover, the theories of structural transitions predict a discontinuous transformation when the symmetry group of the first phase is not included in that of the second phase (obviously, this is the case for ζ and ε structures).

4.1.2. *Transition* ε - γ. This transformation was correctly announced in W_2C [46]. It occurs in V_2C, Mo_2C and W_2C. Temperatures involved in these transformations are sufficiently high to allow efficient diffusion processes ($T_c/T_m \approx 0.59$, 0.78 and 0.64 for V_2C, Mo_2C and W_2C respectively) : thus, the carbon diffusion does not limit the velocity of reaction, which is indeed very fast in the 3 compounds.

From experimental evidence, the ε - γ transition is of the second order. The simple Bragg-Williams (B-W) thermodynamical theory [57] has been applied to the case of ODT in metallic carbides $M_{n+1}C_n$ (V_6C_5 and V_8C_7 [58] and M_2C_{1-x} [16, 27]). In these compounds, the thermal evolution of the long-range order parameter η is predicted by the relation :

$$\frac{T}{T_c} = \frac{(n+2+1/n)\,\eta}{\ln\left[\frac{1+(n+1/n)\eta+\eta^2}{(1-\eta)^2}\right]} \qquad (14)$$

For n=5 or 7, the curves $\eta(T)$ show singularities which indicate a discontinuous transformation : this describes correctly the first-order transitions in V_6C_5 and V_8C_7 [58]. For n=1 (stoichiometric hemicarbides M_2C_1), no singularity occurs and the transformation is expected to be continuous as observed experimentally. These results are illustrated by figure 15.

4.1.3. *The ε'-phase*. Neutron and HREM analyses of the ε-based structure in W_2C have shown that this ordered form is more adequately described as a ε'-structure in which carbon atoms are equally distributed in both types of interstitial basal planes at z=0 and z=1/2. This structure can be considered as being partially disordered ; however, attempts to increase the order state by long-term annealings at 1200°C (0.48 T_m) were unsuccesful [27]. In fact, it can be noted that comparable repartitions (in terms of average occupancies in interstitial basal planes) exist in both ζ and γ-phases (see figure 2) ;

regarding the thermal evolution ζ - ε - γ identified in V_2C, Mo_2C and W_2C, it can be concluded that the ε'-modification is preferable, since it respects the "continuity" of the carbon distribution in interstitial basal layers, whatever the temperature. Thus, the ε'-form can also be assumed for the middle-temperature structure in V_2C and Mo_2C.

4.1.4. *Other Transitions (ξ - γ in Nb_2C and α - γ in Ta_2C).* Superstructures different from ε (ε') or ζ occur in Nb_2C and Ta_2C. The case of Ta_2C is easily discussed since all the investigators agree for the structural schema given by relation (7). The B-W formulation predicts a second-order transformation for the disordering of the α-phase ; however, the present experimental results suggest a slight discontinuity at the end of the transformation (β = 0.14 in equation (4)) ; however, a small amount of pure tantalum present in the powder might explain this singularity [45].

The situation is different in Nb_2C. The present investigation brings evidence for a direct disordering of the orthorhombic ξ-phase near 1250°C ; this result was indeed suggested by Bowman and Arnold [46]. In fact, previous authors have actually mentioned a transformation at similar temperatures (1200°C [22], 1230°C [37] and 1195±20°C [14]) : it can be assumed that the same transition was identified in all studies. There is no formal crystallogrpahic proof of the ε-form above 1200°C. It can be imagined that a ξ - ε transformation exists below 1250°C ; the ε-structure could be difficult to identify if the kinetics of the transformation are very slow (such as for the nucleation of the ζ-phase in W_2C) or if both assumed transformations ξ - ε and ε -γ are too close (e.g. even closer than in the case of ζ - ε and ε - γ reactions in V_2C). The unambiguous result obtained in the present *in situ* investigation leads to retain this hypothesis ; it would be useful to undertake long-term annealings near 1200°C to know if the ε-structure can be stabilized in temperature. Definitively, the ε-phase does exist from literature evidence (see table 5). It is certainly much more stable in carbon-rich compounds [14] : this could explain why it was easily observed at room temperature without any particular cooling conditions [12].

Endly, it can be mentionned that the ξ - γ transformation finishes probably as a first-order transition (β = 0.22±0.02 in equation (4), which is significantly smaller than the value expected for second-order reactions). This is consistent with the evidence of a discontinuous transformation near 1200°C obtained by thermal analysis [22].

4.2. STABILITY OF PHASES.

4.2.1. *General Ideas.* The large variety of ordered forms in hemicarbides raises the question of their relative stability. Clearly, a complete understanding of this problem would require a perfect knowledge of chemical bonding in these compounds. Although this field is relatively well covered in the case of cubic monocarbides through electronic structure calculations [59, 60], few works deal with hexagonal hemicarbides (see however [61]).

In the present work, the discussion will be restricted to the classification of superstructures based on the predictions of the Ising model. Ignoring metal atoms and assuming a rigid carbon (+vacancy) sublattice (i.e. without any atomic displacements from ideal positions), one can find the stable phases at

0°K by minimizing the free energy of the crystal (expressed as a configurational energy) :

$$E = \Sigma p_n V_n \qquad (15)$$

(p_n : probability of pairs of carbon atoms in n^{th} neighbor positions ; V_n : effective-pair interaction energy).
with respect to a limited number of V_n. In the case of cubic monocarbides, the diagram of ground states calculated with first and second neighbor pair interactions was confronted to experimental and theoretical determinations of V_n (n=1, 2) ; a reasonnable agreement was obtained [32].

The case of hemicarbides is discussed below on the basis of a pair-wise interaction model regarding pairs of interstitial atomic rows, rather than individual atoms [33].

4.2.2. *Stability of M_2C phases (model of Hiraga and Hirabayashi [33]).* Regions of existence of M_2C phases can be predicted in the space (V_1/V_3, V_2/V_3) on the basis of the Ising model applied to interstitial [0001] columns ; sets of p_n in equation (15) are listed in table 3 for the possible M_2C superstructures. Experimental values for ratios V_1/V_3 and V_2/V_3 can be estimated by fitting the diffuse intensity (due to short-range ordering -SRO-), observed in electron diffraction patterns of quenched hemicarbides, with the Clapp-Moss formula [62] :

$$I(\mathbf{q}) = \frac{C}{\left[1 - \frac{T_c}{T}\frac{V(\mathbf{q})}{V(\mathbf{q}_m)}\right]} \qquad (16)$$

(C : normalization constant ; T_c : ODT temperature)
$V(\mathbf{q})$ (with $\mathbf{q}_{hkl}$) is the Fourier transform of the pair-potentials :

$$\begin{aligned} V(\mathbf{q}) = {} & V_1 [\cos(2\pi h) + \cos(2\pi k) + \cos(2\pi(h+k))] \\ & + V_2 [\cos(2\pi(h-k)) + \cos(2\pi(2\eta+k)) + \cos(2\pi(h+2k))] \\ & + V_3 [\cos(4\pi h) + \cos(4\pi k) + \cos(4\pi(h+k))] \end{aligned} \qquad (17)$$

(as limited to the first 3 V_n ; $V(\mathbf{q}_m)$ is the absolute minimum of $V(\mathbf{q})$ in the reciprocal space).

Figure 16 shows the diagram deduced by Hiraga and Hirabayashi with $V_3 > 0$ (necessary condition for the existence of the ζ-phase, formally identified experimentally). Experimental points (V_1/V_3, V_2/V_3) corresponding to V_2C, Nb_2C and (Ta, V or Nb)$_2C$ crystals quenched from 1200-1600°C ($T/T_c \approx 1.05$ in equation (16)) are reported.

In the present study, W_2C polycrystals have been quenched from 2200°C ($T/T_c \leq 1.1$) with a dedicated installation [63]. The weaknesss of diffuse bands observed in diffraction patterns (see figure 17) does not allow a very precise estimation of ratios V_1/V_3 and V_2/V_3. However, it is definitively clear that this compound lies very close to the y-axis ($V_2 = 0$) as reported in figure 16.

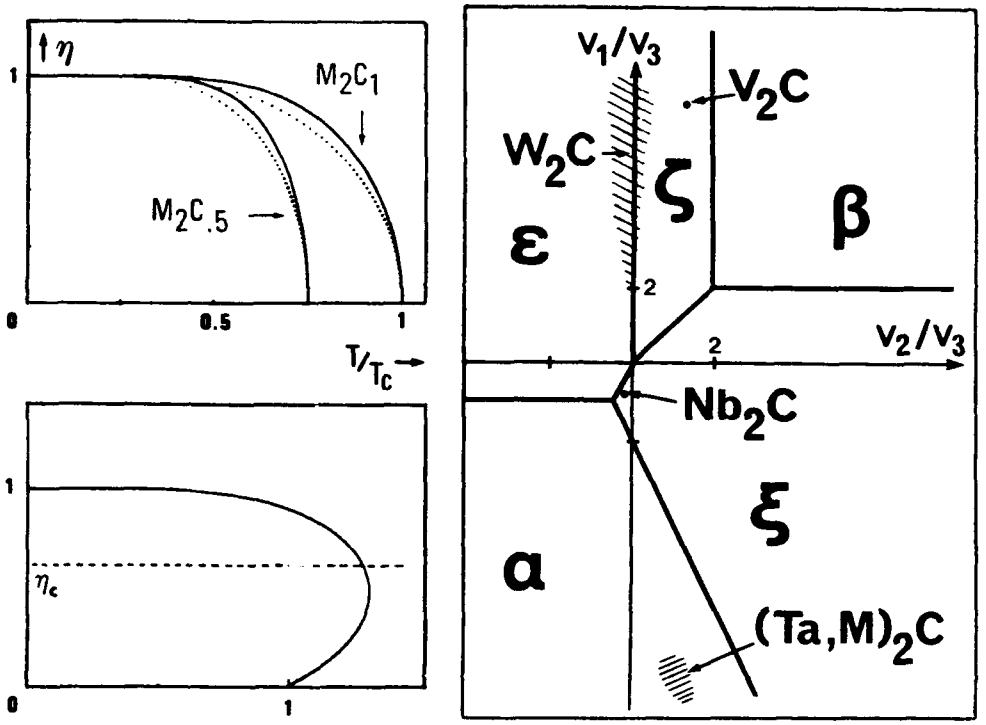

Figure 15 *(left)* . B-W analysis of ODT in : a) *(top)* : M_2C_{1-x} ; dotted and full lines correspond respectively to transitions ε - γ and ε' - γ [16, 27] ; the curves relative to the composition $M_2C_{0.5}$ illustrate that the transition remains continuous over the whole homogeneity range of the phase hemicarbide. b) *(bottom)* : V_6C_5 (η_c -0.63- corresponds to a singularity).
Figure 16 *(right)*. Regions of stability of M_2C superstructures [33] ; $(Ta,M)_2C$ represents estimations for $Ta_{\sim 1.5}V_{\sim 0.5}C$ and TaNbC alloys.

The application of the Ising model to the classification of M_2C superstructures appears to be successful : V_2C and Nb_2C lie respectively in the ζ and ξ-regions, which are the stable low-temperature phases observed experimentally ; pseudo-binary (Ta, V or Nb)$_2$C compounds, with compositions approaching that of pure tantalum hemicarbide, can be considered to lie in the α-region [33], which is the stable low-temperature form of Ta_2C. W_2C lies near the ε/ζ boundary and both structures are easily observed at room temperature. Furthermore, it is seen that ζ and ε-regions are close to each other ; in fact, both structures are geometrically similar, since they have the same first and third neighbor configurations (see table 3). In addition, it can be deduced, from the structure refinements reported in table 2, that ζ and ε-phases have similar bond lengths (see table 10). This is also confirmed by the determination of thermal expansion coefficients in the case of V_2C and Mo_2C compounds, which are not drastically affected by the transition ζ - ε [9].

These last remarks indicate that ordering in these compounds does not

modify significantly the building of M-M and M-C bonds ; such a conclusion supports a *posteriori* the hypothesis according to which the metallic sublattice can be neglected in the pair-interaction approach.

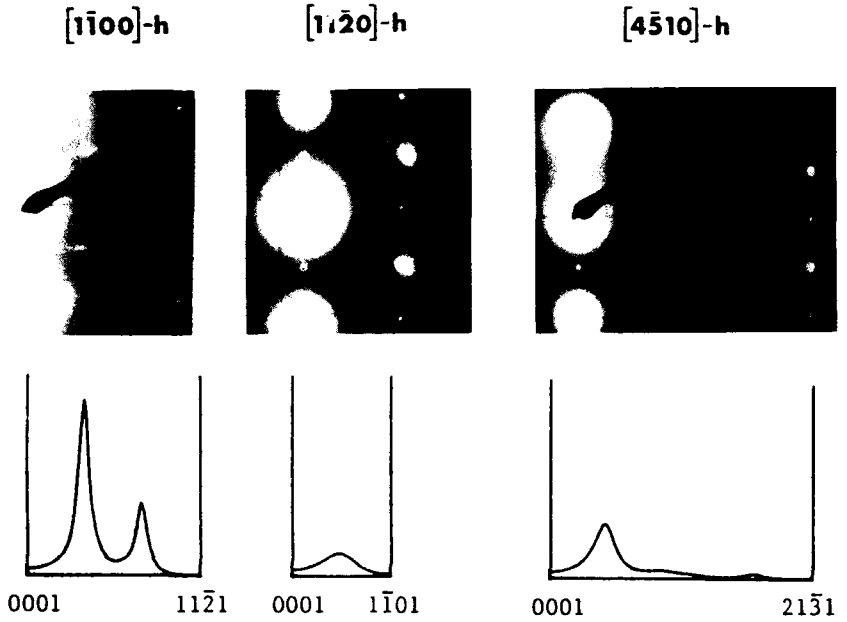

Figure 17. SRO evidence in W_2C polycrystals after quenching from 2200°C (TEM 200 kV). a) *(upper series)* : electron diffraction patterns showing diffuse bands perpendicular to the c-axis. b) *(lower series)* : calculated profiles with $V_1/V_3 = 7$, $V_2/V_3 = 0$ (intensity in arbitrary units) ; the damping due to the carbon diffusion factor $f_c(\sin[\theta/\lambda])$ is taken into account.

	ζ				ξ	ε'			α		γ
	V_2C	Mo_2C		W_2C	Nb_2C	W_2C			Ta_2C		V_2C
ref.	(12, 28)	(21)[a]	(16, 27)	(31)	(12)[a]	(26)[a]	(25)	(30, 31)	(17)	(25)	(17)
M-M	2.78 (2)	2.93 (4)	2.848	2.90 (4)	3.066 (4)	2.904 (1)	2.865 (2)	2.921	3.021 (3)	3.012 (3)	2.838 (3)
	2.84 (2)	3.00 (8)	2.915	3.00 (6)	3.081 (8)	2.920 (2)	2.925 (1)	2.924	3.080 (3)	3.091 (3)	2.904 (3)[a]
	2.865 (4)		2.944	3.015 (2)	3.137 (4)	2.937 (1)	2.934 (2)	2.931	3.103 (6)	3.104 (6)	
	2.87 (2)		2.951			2.952 (2)	2.946 (2)	2.934			
	2.92 (2)		2.980			2.986 (4)	3.004 (1)	2.995			
			3.009			3.009 (2)	3.020 (4)	2.999			
			3.011								
			3.033								
C-M	2.01	2.097	2.098	2.04[a]	2.182	2.085	2.079	2.092	2.186	2.190	2.030
	2.05		2.109	2.13	2.205	2.097	2.092	2.096			
			2.115			2.107	2.120	2.098			
C-C	2.91	3.00	3.004	3.00	3.137	2.367[b]	2.361[ab]	2.363[b]	3.103	3.104	2.290[ab]
						2.994	2.991	2.996			2.904[a]

[a]values recalculated from authors' data.
[b]distances between sites with occupancy factors less than 1.

Table 10. Interatomic distances in hemicarbides as deduced from structural refinements cited in table 2.

Regarding the proximity of ζ and ε-regions, it is reasonable to consider that chemical effects (presence of impurities and/or a secondary phase) might change the sign of V_2 and "stabilize" one of these two phases at the expense of the other : this can particularly explain the case of V_2C : the position determined for this compound is not far from the ζ/ε boundary [33], and it could even be closer (it was verified that calculated diffuse intensities with a lower value of V_2 might also fit the experimental diffraction patterns produced by these authors [16]). The same argument applies to the "stabilization" of ξ and ε-phases in Nb_2C, since this compound lies quite close to the ξ/ε boundary.

Conclusion

An updated presentation of known superstructures in metallic hemicarbides M_2C has been reported here.

New results have been obtained by an *in situ* high temperature neutron investigation ; a common structural schema ζ - ε(') - γ describes correctly the structural evolution of V_2C, Mo_2C and W_2C with temperature. Neutron refinements and High Resolution Electron Microscopy observations allow the modified ε-based ε' structure to be ascertained in W_2C ; regarding the carbon repartition in this structure, which is comparable to that of the ζ and γ-forms (in terms of average occupancy in interstitial basal planes), it is most probable that the same modification occurs in V_2C and Mo_2C, where the similar evolution ζ - ε - γ has been identified.

Some controversies exist for Nb_2C, where the possible ξ - ε transition remains unobserved.

Results on Ta_2C (i.e. transformation α - γ) are fully consistent.

The relative stability of the ordered forms ζ, ξ and ε (respectively in V_2C, Nb_2C and W_2C) is successfully discussed on the basis of Hiraga and Hirabayashi's pair-wise model ; further similar work would be appreciable on pure Ta_2C and Mo_2C.

Acknowledgements

The author extends sincere thanks to his colleagues Dr. J. Dubois, Pr. C. Esnouf and G. Fantozzi for their collaboration in the structural studies on Mo_2C_{1-x} and W_2C_{1-x}. P. Convert and J. Pannetier (ILL) are gratefully acknowledged for their respective help in the high temperature neutron investigation and the room temperature structural refinements.

References

[1] STORMS E.K, "The Refractory Carbides", New York : Academic Press (1967).

[2] RUDY E., WINDISCH St., STOSICK A.J., HOFFMAN J.R., "the constitution of binary molybdenum-carbon alloys", (1967), Trans. Met. Soc. AIME, vol. 239, pp. 1247-1267.

[3] RUDY E., "ternary phase equilibria in transition metal-boron-carbon-silicon systems. Part V", (1969), Techn. Rep. AFML, TR 65-2.

[4] NOWOTNY H., BENESOVSKY F., "Ordnungstrukturen bei Übergangsmetallcarbiden und -nitriden", (1968), Planseeber. Pulvermetall., Bd 16, pp.204-214.
[5] NAGAKURA S., OKETANI S., "structure of transition metal carbides", (1968), Trans. Iron Steel Inst. Japan, pp. 265-294.
[6] PARTHE E. , YVON K., "on the crystal chemistry of the close packed transition metal carbides (part II)", (1970), Acta Cryst., B26, pp. 153-163.
[7] BOWMAN A.L., "crystal chemistry of refractory carbides", (1972), N.B.S. Spec. Pub. n°364, Solid State Chem., pp. 561-566.
[8] LEWIS M.H., BILLINGHAM J., BELL P.S., "non-stoichiometry in ceramic compounds", pp. 1084-1115 in Electron Microscopy and Structure of Materials, ed. G. Thomas, R.M. Fulrath, R.M. Fischer, Berkeley : University of California Press, (1972).
[9] LÖNNBERG B. "thermal expansion studies of the subcarbides of group V and VI transition metals", (1986), J. less Com. Metals, 120, pp 135-146.
[10] I.L.L. REPORT "Neutron Research Facilities at the I.L.L. High Flux Reactor", Grenoble : Institut Laue-Langevin, (1983).
[11] DUBOIS J., EPICIER T., ESNOUF C., FANTOZZI G., CONVERT P., "neutron powder diffraction studies of transition metal hemicarbides M_2C_{1-x}. I", (1988), Acta Metall., vol.36, n°8, pp. 1891-1901.
[12] YVON K., NOWOTNY H., KIEFFER R., "Die Kristallstruktur der Subcarbide von Übergangsmetallen", (1967), Monatsch. Chem., vol. 98, pp. 34-44.
[13] TERAO N., "structure des carbures de niobium", (1964), Jap. J. of Appl. Phys., vol. 3, n° 2, pp. 104-111.
[14] LÖNNBERG B., LUNDSTRÖM T., "thermal expansion and phase analytical studies of Nb_2C", (1985), J. Less Com. Metals, vol. 113, pp. 261-268.
[15] EPICIER T., DUBOIS J., ESNOUF C., FANTOZZI G., CONVERT P., "high temperature powder neutron diffraction studies of structural transformations in transition metal hemicarbides M_2C_{1-x}. II : compounds of the VIth group (Mo_2C, W_2C)", (1989), Physica B, 156&157, pp. 44-46.
[16] EPICIER T., "contribution à l'étude des phénomènes d'ordre et des mécanismes de plasticité dans les carbures métalliques", (1988), thèse d'Etat, Lyon, n°88/SAL/0038.
[17] BOWMAN A.L., WALLACE T.C., YARNELL J.L., WENZEL R.G., STORMS E.K., "the crystal structures of V_2C and Ta_2C", (1965), Acta Cryst., 19, pp. 6-9.
[18] BACON G.E., "Neutron Diffraction", (1962), Oxford : Clarendon Press.
[19] HIRSCH P.B., HOWIE A., NICHOLSON R.B., WHELAN M.J., Electron microscopy of thin crystals, London : Butterworths, (1969).
[20] KOESTER L., RAUCH H., "Summary of Neutron Scattering Lengths", (198:), IAEA Contact 2517/RB.
[21] PARTHE E., SADAGOPAN V., "the structure of dimolybdenum carbide by neutron diffraction technique", (1963), Acta Cryst., 16, pp. 202-205.
[22] RUDY E., BRUKL C.E., "lower-temperature modifications of Nb_2C and V_2C", (1967), J. Am. Ceram. Soc., vol. 50, n° 5, pp. 265-268.
[23] ALYAMOVSKII S.I., SHVEIKIN G.P., GEL'D P.V., "oxydation of niobium and its lower carbide", (1963), Russian J. of Inorg. Chem., vol. 8, n°8, p.1042 *and* ALYAMOVSKII S.I., SHVEIKIN G.P., GEL'D P.V., VOLKOVA N.M., "orthorhombic β' phases of niobium an vanadium carbides", (1967), Russian J. of Inorg. Chem., vol. 12, n° 3, pp. 301-303.
[24] ALDEBERT P., "neutron and X-ray experiments at high temperature", (1984), Revue Phys. Appl., 19, pp. 649-662.
[25] LÖNNBERG B., LUNDSTRÖM T., TELLGREN R., "a neutron powder diffraction study of Ta_2C and W_2C", (1986), J. less Com. Metals, 120, pp 239-245.
[26] HÅRSTA A., RUNDQVIST S., THOMAS J.O., "a neutron powder diffraction study of W_2C", (1978), Acta Chem. Scand., Sect. A, 32, pp. 891-892.

[27] EPICIER T., DUBOIS J., ESNOUF C., FANTOZZI G., CONVERT P., "neutron powder diffraction studies of transition metal hemicarbides M_2C_{1-x}. II", (1988), Acta Metall., vol. 36, n°8, pp. 1903-1921.
[28] YVON K., RIEGER W., NOWOTNY H., "Die Kristallstruktur von V_2C", (1966), Monatsch. Chem., vol. 97, pp. 689-694.
[29] CHRISTENSEN A.N. "neutron diffraction investigation on a crystal of α-Mo_2C", (1977), Acta Chem. Scand. A31, pp. 509-511.
[30] RUDY E., WINDISCH St, "evidence for zeta Fe_2N-type sublattice order in W_2C at intermediate temperatures", (1967), J. Am. Ceram. Soc., vol. 50, n°5, pp. 272-273.
[31] TELEGUS V. S. ,GLADYSHEVSKII E. I. , KRIPYAKEVICH P. I. , "orthorhombic modifications of the compounds W_2C and Mo_2C", (1968), Sov. Phys. Cryst., vol. 12, n° 5, pp. 813-815.
[32] DE NOVION C.H., LANDESMANN J.P., "order and disorder in transition metal carbides and nitrides : experimental and theoretical aspects", (1985), Pure & AppL Chem., Vol. 57, n° 10, pp. 1391-1402 *and* "order-disorder and effective pair interactions in nonstoichiometric rocksalt-structure transition-metal carbides and nitrides", pp. 499-528 in "Nonstoichiometric Compounds", Adv. in Ceram. vol. 23, Westerville : Am. Ceram. Soc, (1987).
[33] HIRAGA K., HIRABAYASHI M., "long-range and short-range order in interstitial compounds M_2X with special reference to V_2C and Nb_2C", (1977), J. de Phys., colloque C7, t 38, pp. 224-226 *and* "the formation of varieties of carbon ordering in pseudobinary compounds of V_2C, Nb_2C and Ta_2C", (1980), J. Appl. Cryst., 13, pp. 17-23.
[34] STORMS E. K., Mc. NEAL R. J. , "the vanadium-vanadium carbide system", J. Phys. Chem., (1962), vol . 66, pp. 1401-1408.
[35] VOLKOVA N.M., GEL'D P.V., Izv. Vysshikh. Uchebnik. Zavedenii. Tsvetnaya Metallurgica, (1965), 3, pp. 77-81.
[36] RASSAERTS H., BENESOVSKY F., NOWOTNY H., "Beitrag zu den Systemen Vanadin-Kohlenstoff und Vanadin-Chrom-Kohlenstoff", (1966), Planseeber. für Pulvermet., Bd.14, n°3, pp. 178-183.
[37] RUDY E., WINDISCH St., BRUKL C.E., "revision of the vanadium-carbon and niobium-carbon systems", (1968), Planseeber. für Pulvermet., Bd. 16, pp. 3-33.
[38] ENAR^LIEV A., PATIEV M., FAIZULLAEV F., KARIMOV I., "structures of ordered modifications of vanadium carbide (V_2C) and vanadium carbonitride ($V_2(C,N)$) according to neutron diffraction data", (1986), Izv. Vyssh. Uchzebn. Zaved. Fiz., 29, 10, pp. 34-40.
[39] LÖNNBERG B., (1986), *private communication.*
[40] EPICIER T., CONVERT P., "high temperature pow neutron diffraction studies of structural transformations in transition metal hemicarbides M_2C_{1-x}. I : compounds of the V^{th} group (V_2C, Nb_2C, Ta_2C)", (1989), Physica B, 156&157, pp. 41-43.
[41] CHRISTIAN J.W. , § 58 in The Theory of Transformations in Metals and Alloys, Oxford : Pergamon Press (1965), pp. 481-489.
[42] GAUTIER F., "introduction to the study of phase transitions", (1978), pp. 223-336 in Solid State Transformations in Metals and Alloys, Ecole d'Eté d'Aussois, les Editions de Physique, (1980).
[43] LESSER R., BRAUER G., "Karbidphasen des Tantals", (1958), Z. Metallkde, Bd 49, H12, pp. 622-626.
[44] RUDY E., HARMON D.P., "ternary phase equilibria in transition metal-boron-carbon-silicon systems : part I", (1965), vol. 5, Techn. Rep., AFML TR 65-2.
[45] BOWMAN A.L., KRIKORIAN N.H., NERESON N.G., RUPERT G.N., "the order-disorder transformation of Ta_2C", pp. 193-197 in Colloque International du CNRS n°205 (Etude des Transformations Cristallines à Haute Température au-dessus de 2000 K), Paris : les Editions du CNRS, (1972).

[46] BOWMAN A.L., ARNOLD G.P., "high temperature neutron diffraction studies", dans Advances in High Temperature Chemistry, vol. 4, New York : Academic Press, (1971), pp. 243-264.
[47] MORTON N., JAMES B.W., WOSTENHOLM G.H., POMFRET D.G., DAVIES M.R., DYKINS J.L., "superconductivity of molybdenum and tungsten carbides", (1972), J. less Com. Metals, 25, pp. 97-106.
[48] KHAENKO B.V., VELIKANOVA T. Ya, KUBLII V.Z., "ordering in molybdenum carbide Mo_2C ", (1986), Dopov. Akad. Nauk. Ukr. RSR., Ser. A : Fiz. Mat. Tekh. Nauki, 10, pp. 78-82.
[49] BUTORINA L.N., PINSKER Z.G., "electron-diffraction study of W_2C", (1960), Kristallografiya, 5, 4, pp. 585-588.
[50] YVON K., NOWOTNY H., BENESOVSKY F., "Zur Kristallstruktur von W_2C", (1968), Monatsch. Chem., vol. 99, pp. 726-729.
[51] EPICIER T., DUBOIS J., ESNOUF C., FANTOZZI G., "identification de la phase β-W_2C, type ε-Fe_2N, dans l'hémicarbure de tungstène", (1983), C.R. Acad. Sci. Paris, t. 297, série II, pp. 215-218.
[52] EPICIER T., "application of transmission electron microscopy to the study of transition metal carbides", (1989), *these Proceedings.*
[53] RUEDL E, AMELINCKX S, "the observation of dissociated antiphase boundaries in Ni_3Mo", (1971), Cryst. Latt. Def., 2, pp. 247-249.
[54] RIETVELD H.M., "a profile refinement method for nuclear and magnetic structures", (1969), J. Appl. Cryst., 2, pp. 65-71 *and* HEWAT A.W., "the Rietveld Computer Program for the Profile Refinement of Neutron Diffraction Powder Patterns Modified for Anisotropic Thermal Vibrations", (1973), Harwell Report AERE-R 7350.
[55] EPICIER T., ESNOUF C., "high resolution electron microscopy in transition metal carbides. II : study of the hexagonal hemicarbide W_2C", pp. 323-324 in Inst. Phys. Conf. Ser. n°93, vol. 2, (1988).
[56] EPICIER T., ESNOUF C., (1989), *to be published.*
[57] BRAGG W.L., WILLIAMS E.J., "the effect of thermal agitation on atomic arrangement in alloys", (1934), Proc. Roy. Soc., 145, pp. 699-730, *and* (1935), Proc. Roy. Soc., A 151, pp. 540-566.
[58] EMMONS G.H., WILLIAMS W.S., "thermodynamics of order-disorder transformations in vanadium carbide", (1983), J. of Mat. Sci., 18, pp. 2589-2602.
[59] CALAIS J.L., "band structure of transition metal compounds", (1977), Advances in Phys., vol. 26, n° 6, pp. 847-885.
[60] NECKEL A., "recent investigations on the electronic structure of the fourth and fifth group transition metal monocarbides, mononitrides and monoxides", (1983), Int. J. Quant. Chem., vol. XXIII, pp 1317-1353.
[61] IVANOVSKII A.L., NOVIKOV D.L., GUBANOV V.A., "electronic properties of carbides, nitrides and oxides of subgroup VIa transition metals", (1987), Phys. Stat. Sol. (b), 141, pp. 9-33.
[62] CLAPP P.C., MOSS S.C., "correlation functions of disordered binary alloys. I", (1966), Phys. Rev., 142, 2, pp. 418-427 *and* MOSS S.C., CLAPP P.C., idem. III, (1968), Phys. Rev., 171, 3, pp. 764-777.
[63] DUBOIS J., RIVIERE R., "four de laboratoire à haute température pour frittage et trempe sous vide ou sous atmosphère", (1972), Rev. Int. Hautes Tempér. et Refract., t9, pp. 279-288.

STRUCTURE AND PROPERTIES OF SI-DOPED BORON CARBIDE

R. TELLE
Max-Planck-Institute for Metals Science
Institute for Materials Science
Powdermetallurgical Laboratory
Heisenbergstrasse 5
D-7000 Stuttgart 80, F.R. Germany

ABSTRACT. The extension of the homogeneity field of $B_{12}(B,C,Si)_3$ was established by sintering experiments in the B-rich corner of the B-C-Si system in the temperature range of 1000-2100° C. Below the ternary eutectic temperature of 1385° C the formation of $B_{12}(B,C,Si)_3$ is generated by a diffusion-controlled monomolecular phase boundary reaction. Above this temperature, a ternary liquid phase exists which promotes dissolution-reprecipitation reactions. The maximum solid solubility of Si in the boron carbide lattice is 2.5 ± 0.3 at.-% at 2050° C. The increase of the aspect ratio c_o/a_o of the unit cell with the Si-content indicates that Si occupies preferentially C-sites in the linear C-B-C chain and thereafter interstitial or icosahedral sites in prolongation of the chain.

As a result of the Si→C substitution, SiC-layers are precipitated around $B_{12}(B,C,Si)_3$ particles during liquid phase hot pressing which prevents an exaggerated grain growth and thus enhances strength and toughness. Pressureless sintering results in a high porosity because of unsuitable wetting conditions and evaporation-recondensation reactions.

1. Introduction

Boron carbide is an exceptional hard material with a high potential for the use in wear-resistant structural parts. Its poor sinterability, low toughness and oxidations resistance limit, however, a successful application. Usually, sintering additives such as 1-3 wt.-% C, 1-2 wt.-% AlN or 1-9 wt.-% SiC have been applied for a pressureless densification [1-2]. Boron as a sintering aid makes use of the wide binary homogeneity range of the (B_4C) solid solution and enhances sintering by introducing point defects and hence by decreasing the activation energy of bulk diffusion [3]. Although densities of approximately 95 % of the theoretical have been achieved by pressureless sintering the strong coarsening of the particles cannot be avoided since temperatures above 2100° C have to be applied. Furthermore, completely dense parts can still only be prepared by hot pressing or hot isostatic pressing.

Attempts to use Si as an additive for hot pressing of boron carbide because of its chemical relationship to B and C resulted in a significant reduction of the grain size and, therefore, in an enhanced fracture toughness of K_{Ic} = 2-6 $MPam^{1/2}$ and flexural strength of σ_b = 500-600 MPa [4,5]. Pressureless sintering of B_4C with Si,

R. Freer (ed.), The Physics and Chemistry of Carbides; Nitrides and Borides, 249–267.
© 1990 *Kluwer Academic Publishers. Printed in the Netherlands.*

however, was not studied before since there was no evidence for a stable equilibrium between a Si-melt and B_4C in which a liquid phase sintering would be possible. The only experimental data on the ternary B-C-Si system available at that time exhibited a ternary solid state equilibrium between $B_{12}(B,C,Si)_3$, (SiB_6) and SiC persisting up to temperatures exceeding 1900°C [6,7]. Thermodynamic calculations, however, clearly demonstrated the existence of a binary phase equilibrium of $B_{12}(B,C,Si)_3$ and a B-containing Si-melt above 1560°C [8]. The theoretical results were confirmed by hot pressing and pressureless sintering of powder mixtures as well as by model wetting experiments with Si-melt on (B_4C) substrates [5,9]. Thus, the B-C-Si system could be established up to 2100°C [10] yielding new opportunities for the development of B_4C- and SiC-based hard materials. An important factor for the densification kinetics of B_4C-Si- and SiC-B-mixtures is the formation of $B_{12}(B,C,Si)_3$ solid solutions since the involved reactions determine significantly the wetting behavior of the required liquid phase and hence influence the microstructure of the material. Furthermore, a Si-enriched $B_{12}(B,C,Si)_3$ may exhibit interesting oxidation properties compared to the binary solid solution series of (B_4C).

The crystal structure of boron carbide is rather well established and was subject to many refinements. The occupation of the particular sites in the unit cell by B and C is, however, especially for the C-rich solid solution still under a controverse discussion. Although the formation of ternary solid solutions with Al and Si is known for long time, systematic studies of the homogeneity ranges and the structural relationships have not been performed yet.

In this study, XRD investigations of the solid solution series are related to the phase equilibria in the B-C-Si system. The kinetics of the solid-liquid interactions are discussed in respect to the Si-C exchange in the boron carbide lattice and the implications for sintering of B_4C and SiC.

2. The Crystal Structure of Boron Carbide

Boron carbide, in the following referred to as (B_4C) or $B_{12}(B,C,Si)_3$ indicating the solid solution contrary to e.g. B_4C without brackets meaning the stoichiometry, crystallizes in the trigonal-rhombohedal space group $R\bar{3}m$. The unit cell is shown in Fig. 1. The structure may be described as a cubic primitive lattice elongated in the direction of the space diagonal with almost regular icosahedra at the corners. Parallel to the space diagonal, which becomes the c-axis in the hexagonal notation, a linear chain consisting of three atoms interconnects the adjacent icosahedra. Thus, a unit cell contains twelve icosahedral sites and three sites on the linear chain. If B-atoms are attributed to the icosahedral positions and C-atoms are considered to be situated in the linear chain, a stoichiometry of $B_{12}C_3$ - i.e. 4 x B_4C - results. The icosahedra exhibit two topologically different positions, first the B1 position (also denoted to $6h_1$) which consists of a planar array of three atoms perpendicular to the linear chain around the outer atoms. Thus, this position exists six times in the unit cell. The second distinguishable icosahedral site is the B2 (or $6h_2$) position which is situated in the middle of the edges of the rhombohedral unit cell and counts for further six atoms. A special position is the centrosymmetric B3 (or 1b) site in the linear chain which is considered to be preferentially occupied by solid solutions forming larger atoms such as Al and Si [11-14]. For the binary solid solution series, the question is, whether the linear chain is formed by a C-B-C or a C-C-C array throughout the homogeneity range, and, if it is not the case for the latter configuration, how the

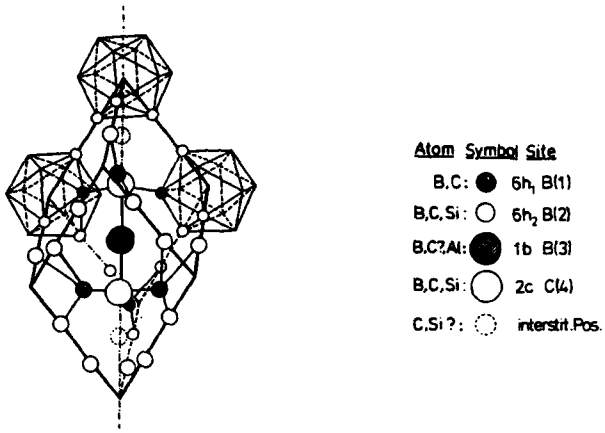

Figure 1. Crystal structure of boron carbide and probable sites for substitution.

stoichiometry of the C-richest composition B_4C could be explained [14-22]. The majority of the authors agree that the linear chain is of the C-B-C type and does not change with C-content which fits with the stoichiometry of the most stable compound in the system, $B_{13}C_2$.

The linear chain of $B_{13}C_2$ possesses a closed shell of ten valence electrons which is achieved by a charge transfer to the B_{12}-icosahedra. The charge difference between B and C within the chain results in even stronger electrostatic bonding forces [19]. Since there is a deficiency of one electron in the icosahedron, additional C as an electron donor preferentially replaces B in one of the icosahedral sites [23]. As the most favourable position thereof, the B2 site was established [22-27].

3. Materials and Methods

In the B-rich corner of the B-C-Si system 52 compositions with a Si-content up to 20 at.-% were studied. As starting materials B_4C powder (H.C. Starck, Berlin, F 1200/3, HCST 5090 average particle size 4.9 μm, 99.4 % purity, 0.25 % O, 0.15 % N, 0.09 % free C, 0.09 % metallic impurities), amorphous B powder (EGA Chemie, Steinheim, F.R.G., average particle size 0.5 μm, 95 % purity, 2.2 % O, 1.0 % Mg, 0.2 % Si, 0.16 % N, 1.4 % bonded water) and Si powder (Ventron, Karlsruhe, F.R.G., average particle size 2.0 μm, 98 % purity, 1.8 % SiO_2) were used. Cold isostatically pre-compacted powder mixtures prepared by pick-up free tumble mixing were packed in a desoxidised hexagonal boron nitride die and pressureless sintered in a graphite-tube furnace under argon atomosphere. Samples of the particular compositions were first subjected to dilatometric experiments by which sintering reactions were monitored with a differential dilatometer at heating rates of 5, 10, 33, and 50 K/min up to 2100°C. The first derivative of the $\Delta l/l_0$-curve was carefully evaluated in respect to the extend, temperature- and time-dependence and reproducibility of possible sintering reactions visible by a tendency to swell or to shrink. Significant reactions involving liquid phases were re-treated by DTA under same conditions. Isothermal annealing of unreacted

powder mixtures was carried out in the same furnace used for dilatometric measurements for 1–5 h at temperatures just below and above the observed sintering reactions, respectively. Within 1–5 h isothermal anneal, naturally, equilibrium conditions were not achieved completely but changes in the phase compositions during approaching equilibrium could be monitored. Prolonged annealing was found, however, to result in a strong evaporation of Si. Above 1900° C B evaporated significantly as well after two hours anneal. It was considered that both effects may influence strongly the overall composition of the sample and thus adulterate the results more severely than incomplete reactions. Additional model wetting experiments, the derivation of the phase diagram and the comparison with calculated thermodynamic data are published elsewhere [9,10].

Qualitative and quantitative XRD analysis were carried out on cut and ground or crushed samples with a Philips powder diffractometer PB 1011–01 using monochromatized Cu–Kα radiation scanning from $2\theta = 10°$ to 80° with a velocity of 0.05°/min. An external standard of polycrystalline high-purity Si was employed for the 2θ correction. Data of samples with free Si-content were evaluated by utilizing the diffraction patterns thereof as an internal standard. In this case, the lattice contraction of Si due to the dissolution of B was taken into account [28]. The diffraction patterns were indexed according to the JCPDS table 19–178 [12] basing on the hexagonal notation. The lattice parameters were calculated by the least-square method applying the Nelson–Rileigh-correction. Problems in the determination of the cell parameters arose from the low number of peaks visible and their strong broadening and decrease in intensity at higher 2θ angles. Moreover, the peak intensity of (B_4C) could not be measured appropriately because of strong coincidence with reflections of the silicon borides. The chemical composition of B_4C as well as of the residual Si if present was determined by electron energy loss spectroscopy (GATAN EELS M 607 attached to a 200 keV Jeol 200 CX TEM). Due to the high background level, the relative error for Si in (B_4C) was 15 % for B, however, only 0.9 %. In order to gain more date for the determination of the homogeneity field of $B_{12}(B,C,Si)_3$ and the lattice parameters, the equilibrium tie lines for the particular overall compositions investigated and the resulting phases were constructed according to the lever rule and Konovalov's rule. By this method the lack of analytical data and the scattering of XRD data can be compensated by the high number of samples treated.

4. Results

4.1 TEMPERATURE-DEPENDENT SINTERING REACTIONS

The temperature-dependence of the reactions between stoichiometric B_4C, B, and Si were analysed for particular overall compositions. In the following example, the result for a 30 wt.-% B_4C, 35 wt.-% B and 35 wt.-% Si (i.e. 72.2 at.-% B, 7.5 at.-% C, 17.3 at.-Si) composition situated in the binary equilibrium $B_{12}(B,C,Si)_3$–L (L = ternary liquid) will be presented.

Up to 1000° C, approximately, B_4C, amorphous B and Si do not react yet. At 1100° C, free carbon impurities if present, in the B_4C powder start to form ß-SiC. Moreover, stoichiometric B_4C tends to release C above 1000° C and to incorporate Si which also contributes to the formation of traces of ß-SiC [32]. Above 1220° C, (SiB_3) is generated by a solid state reaction of free Si and free B. Both, increasing amount of (SiB_3) and the crystallization of (SiB_6) at 1300° C are accompanied by a decrease in free Si. At 1380° C, a ternary liquid is formed which gives rise to an

enhanced formation of $B_{12}(B,C,Si)_3$ at the expenses of the initial stoichiometric B_4C. This reaction is accompanied by a five-fold increase of the SiC concentration between 1380° C and 1410° C. With higher temperatures, the (SiB_3)-content decreases to the credit of the peritectically formed (SiB_6).

At 1500° C, the formation of $B_{12}(B,C,Si)_3$ is completed after 1 h annealing. The solid solution remains associated with (SiB_6), ß-SiC, and liquid up to 1560° C. At higher temperatures, (SiB_6) and ß-SiC dissolve in the melt. Finally, above 1700° C, the sample consists of two phases only, namely $B_{12}(B,C,Si)_3$ and ternary Si-liquid, which crystallizes upon cooling as a Si(B,C)-solid solution with or without SiC and (SiB_6) precipitates. Annealing above 1700° C results in an enhanced evaporation of Si, whereas no significant change in the (B_4C) phase can be detected.

Figure 2. Fracture surfaces of pressureless sintered B_4C-B-Si ceramics.
a) Facetted $B_{12}(B,C,Si)_3$ crystals with SiC-layer in Si-melt
b) Facetted $B_{12}(B,C,Si)_3$ crystals in Si-B-melt

A microstructural study of reacted liquid Si/$B_{12}(B,C,Si)_3$ interfaces reveals the existence of a SiC interaction layer in sintered parts as well as in model experiments [9,29] which clearly demonstrates that the incorporation of Si into the B_4C-lattice is accompanied by the exsolution of C. If a B-rich liquid is present, the solubility of C in the melt increases. In this case, the interaction layer does not form and the original stoichiometric B_4C is partially dissolved in the melt followed by the epitactical growth of $B_{12}(B,C,Si)_3$-crystals on the residual B_4C particles [5,9].

In Fig. 2a-b, SEM micrographs of facetted crystals of $B_{12}(B,C,Si)_3$ are shown. In Fig 2a boron carbide is in contact with a pure Si-melt and hence is covered by a thin SiC-layer whereas in Fig. 2b the presence of a B-containing Si-melt obviously prevents the precipitation of such a coating.

4.2 THE HOMOGENEITY RANGE OF $B_{12}(B,C,Si)_3$ AT 2050° C

The homogeneity field of the Si-containing boron carbide solid solution was studied preferentially at 2050° C since this temperature is of technical interest and can be adequately adjusted by the melting point of high-purity alumina. Furthermore, equilibrium conditions are approached rather quickly due to liquid phase reactions.

The extension of the $B_{12}(B,C,Si)_3$ single phase field is shown in Fig. 3. Starting from the C-rich corner at 20.0 at.-% C it contacts the binary equilibrium (B_4C)-C which reaches to the ternary region for 0.5-1 at.-% Si (point 2 in Fig. 3).

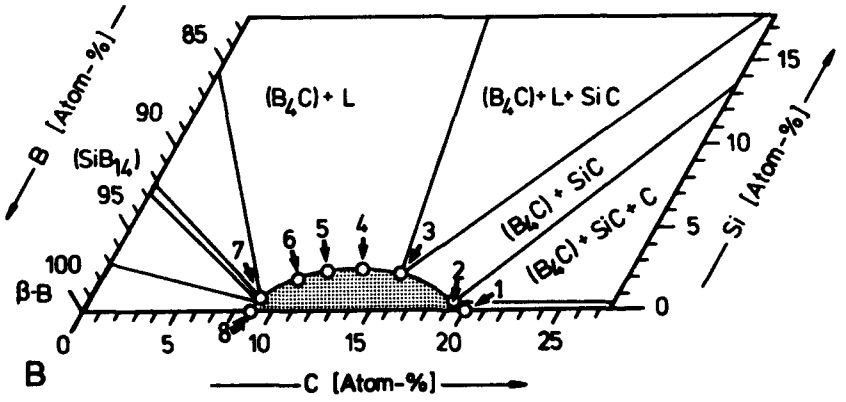

Figure 3. Homogeneity range of $B_{12}(B,C,Si)_3$ at 2050° C. The point numbers refer to Table 1.

At that point, other SiC-containing equilibria contact each other followed by equilibria involving the B-rich Si-liquid (point 3-7). In the B-rich corner only (SiB_{14}) and (ß-B) are the only associates of $B_{12}(B,C,Si)_3$ and liquid since all other Si-borides already decomposed peritectically at that temperature.

TABLE 1. Composition and lattice parameters of boron carbide solid solutions

Point in Fig. 3	Composition	Structural Formula Icosahedra	Chain	Lattice constants, hexag. notation a_o[nm]	c_o[nm]	c_o/a_o
1)	$B_{12.00}C_{3.00}$	$(B_{11.00}C_{1.00})$	(C-B-C)	0.5616(1)	1.2087(2)	2.152(2)
2)	$B_{12.04}C_{2.88}Si_{0.01}$	$(B_{11.04}C_{0.96})$	$(C-B-C_{0.93}Si_{0.07})$	0.5619(1)	1.2125(2)	2.158(1)
3)	$B_{12.33}C_{2.33}Si_{0.33}$	$(B_{11.33}C_{0.67})$	$(C-B-C_{0.67}Si_{0.33})$	0.5623(2)	1.2242(2)	2.177(2)
4)	$B_{12.61}C_{2.01}Si_{0.38}$	$(B_{11.61}C_{0.34}Si_{0.05})$	$(C-B-C_{0.67}Si_{0.33})$	0.5655(2)	1.2366(2)	2.187(1)
5)	$B_{12.89}C_{1.75}Si_{0.36}$	$(B_{11.89}C_{0.08}Si_{0.03})$	$(C-B-C_{0.67}Si_{0.33})$	0.5654(2)	1.2350(5)	2.185(2)
6)	$B_{13.15}C_{1.55}Si_{0.30}$	$(B_{12.00})$	$(C-B-C_{0.55}Si_{0.30}B_{0.15})$	0.5663(2)	1.2350(5)	2.181(2)
		or				
		$(B_{11.95}Si_{0.05})$	$(C-B-C_{0.55}Si_{0.25}B_{0.20})$			
7)	$B_{13.54}C_{1.34}Si_{0.12}$	$(B_{12.00})$	$(C-B-B_{0.54}C_{0.34}Si_{0.12})$	0.5667(2)	1.2260(2)	2.163(1)
8)	$B_{13.68}C_{1.32}$	$(B_{12.00})$	$(C-B-B_{0.68}C_{0.32})$	0.5672(2)	1.2204(2)	2.152(2)
[12]	$B_{12.9}C_{1.75}Si_{0.36}$			0.565	1.235	2.186
[5]	$B_{12.4}C_{2.31}Si_{0.29}$			0.563	1.230	2.185
[13]	$B_{12.0}C_{2.00}Al_{1.00}$	*theoretical*		0.5637	1.236	2.192
[13]		measured		0.5640	1.240	2.198

The maximum solubility for Si was established to be 2.5 ± 0.3at.-% within the border to the (B_4C)-L-equilibrium (point 4). The element concentrations of the described points 1-8 are listed in table 1. The particular stoichiometries correspond with the change of lattice parameters which will be discussed later in respect to the kinetics of the Si-incorporation.

It has to be noted that for thermodynamic reasons there is no solid solubility of SiC in stoichiometric B_4C at all but one for all other B-enriched compositions of the binary homogeneity range of boron carbide. As an example, SiC is soluble in "$B_{13}C_2$" to 5.4 ± 0.2 mol.-%.

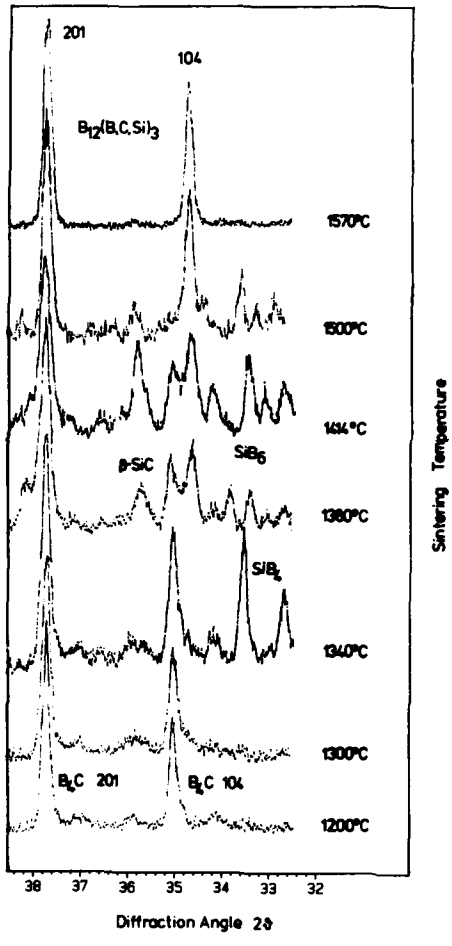

Figure 4. Diffraction patterns of B_4C-35 wt. % -Si-35 wt.-% B sintered at various temperatures. Note the evolution of the 104-peak.

4.3 THE FORMATION OF $B_{12}(B,C,Si)_3$

The sintering reactions show that a notable formation of $B_{12}(B,C,Si)_3$ takes place after 1 h anneal between 1340° C and 1500° C, approximately, whereas much longer sintering times have to be applied at lower temperatures. A sequence of diffraction patterns (Fig. 4) yields evidence for a discontinuous change in the crystal structure. Together with the formation and decomposition of ß-SiC, a shift of the diffraction patterns indexed with high l-numbers towards smaller 2θ angles appears (104 peak in Fig. 4), whereas the 201 peak does not move significantly in the whole temperature range. In spite of shifting continuously, a new 104 peak grows at a constant diffraction angle at the expenses of the original one. Thus, it can be concluded that below the eutectic temperature of 1385° C, a phase boundary reaction takes place, above 1385° C, a dissolution and reprecipitation reaction governs the crystallization of the solid solution. Both reactions are irreversible upon cooling.

The Si-saturated (B_4C) is precipitated in samples with an overall composition exceeding 4 at.-% Si. In comparison with the phase diagram (Fig. 3), this means that Si is required in excess to generate the dissolution-reprecipitation reaction. Furthermore, an excess of B has to be present in order to increase the solubility of C in the melt.

In table 1, the lattice parameter of solid solutions situated at the boundary of the homogeneity range are listed. For the maximum solubility for Si, the lattice constants are:

$$a_o = 0.5655(1)\ \text{nm},\ c_o = 1.2366(2)\ \text{nm},\ c_o/a_o = 2.187(1).$$

These data agree very well with the parameters measured by Lipp and Röder [31, JCPDS file no. 19-178] who prepared the solid solution by the reduction of a mixture of quartz and boric acid with C in an electric arc furnace.

Figure 5 shows a three-dimensional perspectivic viewgraph of the concentration dependency of the lattice parameter at 2050° C listed in table 1. The ordinate represents the elongation of the unit cell c_o and the aspect ratio c_o/a_o, respectively, basing on a detail sketch of the phase diagram. As it can be taken from this figure, c_o increases linearly with the amount of Si incorporated in the lattice. Contrary to the binary (B_4C), the aspect ratio c_o/a_o is not constant but increases up to a particular critical stoichiometry , then remains constant even at higher Si-contents. This fact is also outlined in Fig. 6 which is a projection of the border of the homogeneity range onto an imaginary plane parallel to binary line B-C ignoring the Si-content.

Unfortunately, no informations were gained for compositions within the homogeneity range as no reproducible conditions could be established due to the evaporation of Si.

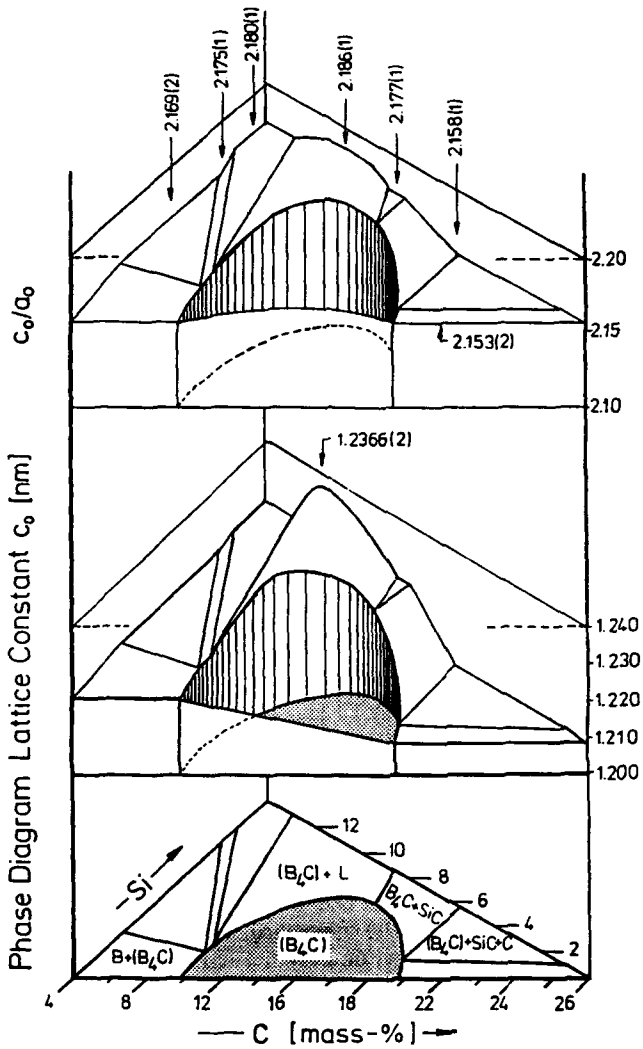

Figure 5. Schematic three-dimensional plot of the lattice parameters as a function of the phase composition. A detail of the isothermal section of the B-C-Si system at 2050° C is used as the basis.

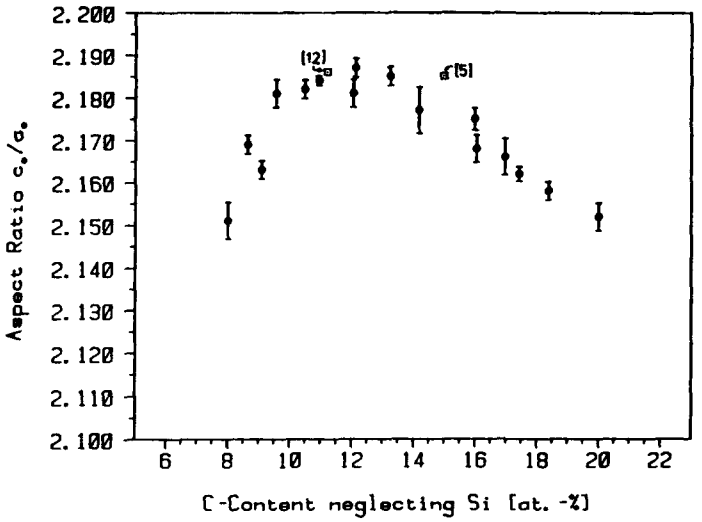

Figure 6. Projection of the c_0/a_0 ratios of $B_{12}(B,C,Si)_3$ on the B-C-edge of the phase diagram at 2050°C. The C-concentration is calculated from the overall composition neglecting the Si-content.

5. Discussion

5.1 REACTION KINETICS

The results of the microstructural and constitutional investigations clearly show that the formation of $B_{12}(B,C,Si)_3$ is accompanied by the exsolution of C which either reacts with Si forming SiC or, depending on the B-content, dissolves in the melt. This fact gives rise for the extension of the binary equilibrium B_4C-C into the ternary region for approximately 0.5-1 at.-% (Fig. 3). It is known from Auger-studies [30] that even single phase stoichiometric B_4C tends to set free C at temperatures above 1000°C. Ploog assumes [31] that $B_{13}C_3$, the C-richest phase prepared by CVD, is in reality a $B_{13}C_2$ with interstitial C enriched at twinning planes and grain boundaries. This statement is supported by the observation of lamellar SiC reaction layers forming pseudomorphs after B_4C crystals in model experiments [9].

Since in the presence of a melt there is no evidence for a Si-diffusion into B_4C but for its dissolution and the precipitation of $B_{12}(B,C,Si)_3$, the results are contradictionary to similar experiments performed with liquid Al [13]. The formation of the rather stoichiometric phase $B_{12}C_2Al$ was described to be a diffusion induced monomolecular phase boundary reaction. No details were discussed, however, on exsolution reactions which are expected to occur. A diffusion controlled phase boundary reaction is considered to take place in the Si-B_4C system in absence of a

melt, i.e. either below the ternary eutectic at 1380° C or in the case of compositions within the homogeneity field. This solid state reaction, however, will change to the benefit of the dissolution and reprecipitation mechanism above this temperature. An Arrhenius plot of the transformation velocity quantified by XRD peak area analysis reveals an 38% decrease in activation energy for the latter mechanism above 1380° C (Fig. 7).

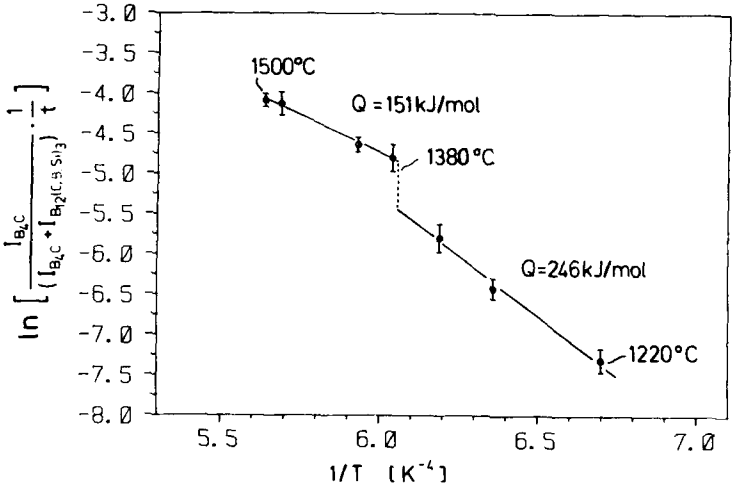

Figure 7. Arrhenius-plot of the formation velocity of $B_{12}(B,C,Si)_3$. Note the change in activation energy in presence of a liquid phase.

5.2 CRYSTAL STRUCTURE

The question of the Si-incorporation into the (B_4C) lattice is strongly related to the stability of the stoichiometric B_4C. According to refinements of the structure, it will be proposed in the following discussion that the structural unit of the linear chain remains unchanged of the C-B-C type all over the binary homogeneity range from 8.8 to 20.0 at.-% C. Thus, the C-rich composition is only reached if C substitutes B in one of the icosahedral positions, preferentially in the B2-site [22,23,25,26]. As another possibility C occupies an interstitial position, preferentially in the prolongation of the linear C-B-C-chain (Fig. 1) [21].

From the structure of the isotypic (SiB_3), a similar problem arises. The linear chain only consists of two Si-atoms which are situated in the C4-position (Fig. 1) whereas the B3 site is not occupied [14]. The residual Si which is required to explain the homogeneity range from $SiB_{2.89}$ to $SiB_{3.65}$ [32,33] replaces B in the icosahedra but contrary to B_4C in B1 position.

In spite of their topological similarity, the structures of (SiB_3) and B_4C differ so much in their electron structure that a continuous solid solution series between

these phases does not exist although it was proposed to in previous studies [34].

In case of ternary (B_4C), the crystal structure of the Al-containing solid solution was described in more detail [16]. Al replaces B in the centrosymmetric B3-position which results in the stoichiometry :

$$(B_{12-x}-C_x)(C_{2-y}B_y)(B_{1-z}Al_z).$$

As no data are available on the homogeneity range of this solid solution series, no numbers can be attributed to x, y and z. Since the covalent radius of Al (125 pm) is almost twice as much as that one of C, the central chain now consisting of a C-Al-B array exhibits a statistically oriented kink.

Similar relationships may be assumed for the Si-containing (B_4C). The small difference in atomic radii of Si, C, and B with 117 pm, 77 pm and 88 pm, respectively, furthermore enables the additional substitution of B in an icosahedral position by Si [35]. This corresponds to the formula:

$$(B_{12-x}C_{x_1}Si_{x_2})(C_{2-y}B_y)(B_{1-z}Si_z) \qquad \text{where } x_1 + x_2 = x$$

Lipp and Röder [12] already concluded from the chemical anlysis that both C as well as B might be replaced by Si.

The evaluation of lattice parameters of the binary solid solution series from 8.8 to 20.0 at.-% C reveals a constant aspect ratio of $c_o/a_o = 2.153(2)$ undependently from the stoichiometry or preparation method (Fig. 5 and 6). This fact can be explained by a statistical exchange of B and C in one of the icosahedral sites which yields a homogeneous expansion of the B_4C-lattice in [0001] as well as in [10$\bar{1}$0] direction, whereas the linear C-B-C chain is considered to remain unchanged. In contrary, the incorporation of Al or Si results in a relatively higher elongation of the c-axis (Table 1, Fig. 5 and 6) and, thus, in an increasing aspect ratio c_o/a_o. Consequently, it may be concluded in analogy to Al, that Si occupies preferentially sites within the linear chain itself or in the prolongation of the chain. As it was shown from the kinetics of the formation solid solution and the constitution of the B-C-Si system, the incorporation of Si results in the exsolution of C within a certain concentration range which corresponds to a strong increase of the aspect ratio at the C-rich side. Hence, the formation of a C-B-(C,Si) array of the linear chain is proposed. Situated in this position or in an interstitial site in the prolongation of this chain, Si would be a more efficient electron donor to the icosahedron than C because of its less electro-negativity. Similar considerations are valid for the substitution of C by Si in the icosahedron itself. As shown in Fig. 6, the incorporation of Si is associated with a linearly increasing aspect ratio only up to a value of $c_o/a_o = 2.182-2.186$. A further enrichment in Si results in a lattice expansion to the same extend in both a- and c-direction. As discussed before, this fact may be attributed to substitution mechanisms in icosahedral sites in which also B may be involved.

Neglecting the possibility of the occupation of interstitial spaces, the stoichiometries calculated for 15 sites per unit cell reveal values ranging from $B_{13.00}C_{1.67}Si_{0.33}$ on the B-rich corner of the homogeneity field to $B_{12.61}C_{2.01}Si_{0.38}$ (maximum solubility) and $B_{12.33}C_{2.33}Si_{0.33}$ on the C-rich side. According to the substitution mechanisms discussed before, it is concluded that on the B-rich as well as on the C-rich border Si replaces C in the linear chain at first until a saturation composition of $C-B-C_{0.67}Si_{0.33}$ is reached. Thereafter, with increasing

Si-content, Si is incorporated into icosahedral sites up to 0.05 Si per icosahedron. During this step, C is substituted preferentially on the C-rich side, whereas on the B-rich side B is replaced which is analogically the case for the C→B exchange in the binary solid solution series. Both mechanisms result in a constant c_o/a_o ratio. At the point of minimum C-concentration i.e. at the contact with the Si-B containing equilibria (point 7 in Fig. 3), an additional substitution of C by B in the linear chain has to be taken into account to fulfill the stoichiometric requirements. Thus, the structural formula may be written as follows:

Structural units:	Icosahedron	Linear Chain
Sites:	B1 + B2 B2	C4 B3
Occupation:	$(B_{12-x}C_{x1}Si_{x2})(C_{2-y-z}Si_yB_z)B$	
where:	$x_1 + x_2 = x$	
	$1 > x > 0$; $1 > x_1 > 0$; $0.05 > x_2 > 0$;	
	$0.33 > y > 0$;	
	$0.67 > z > 0$ if $x_1 = x_2 = 0$	
and	$z = 0$ if $x_1 > 0$ or $x_2 > 0$	

It should be noted again that these considerations are valid if no interstitial atoms are admitted. In the other case, the maximum solubility of 2.5 at.-% Si can be approximated even better. With increasing Si-content, the occupation of interstitial sites is believed to range between the favoured exchange in the linear chain and the energetically less priviledged incorporation in the icosahedron (Fig. 8). There is, however, no evidence for the necessity of interstitial atoms to be present.

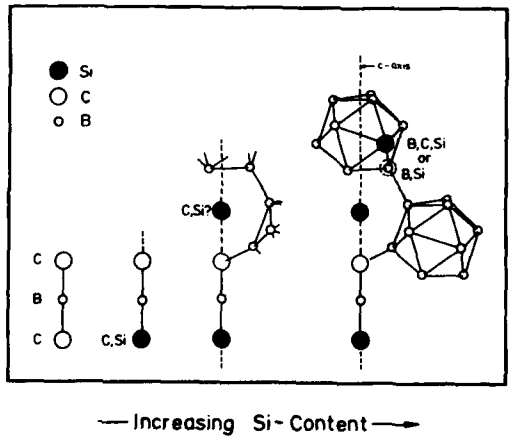

Figure 8. Model of the Si-incorporation in the crystal structure as a function of the Si-concentration.

The concept discussed before has been derived from relatively simple topological considerations and, of course, needs an experimental verification by e.g. more accurate XRD analysis of single crystals, nuclear magnetic spin resonance or phonon resonance spectroscopy. Experimental problems arise, however, because of the difficulties in the preparation of single crystals which are untwinned and large enough for XRD or polycrystalline single phase materials with particles sizes which are suitable for NMR or PRS. Since the B-containing liquid required for the growth of $B_{12}(B,C,Si)_3$ crystallizes upon cooling to either (SiB_6) or SiC and residual Si, these impurities are usually closely interconnected with the boron carbide phase and hence influence the measurements very strongly.

5.3 IMPLICATIONS FOR THE SINTERING OF B_4C WITH SI

According to the phase diagram liquid phase sintering of B_4C with Si or B-Si-alloys under reasonable conditions should be generally possible since the two phase equilibrium $B_{12}(B,C,Si)_3$-L is stable at temperatures as low as 1560° C (Fig. 9).

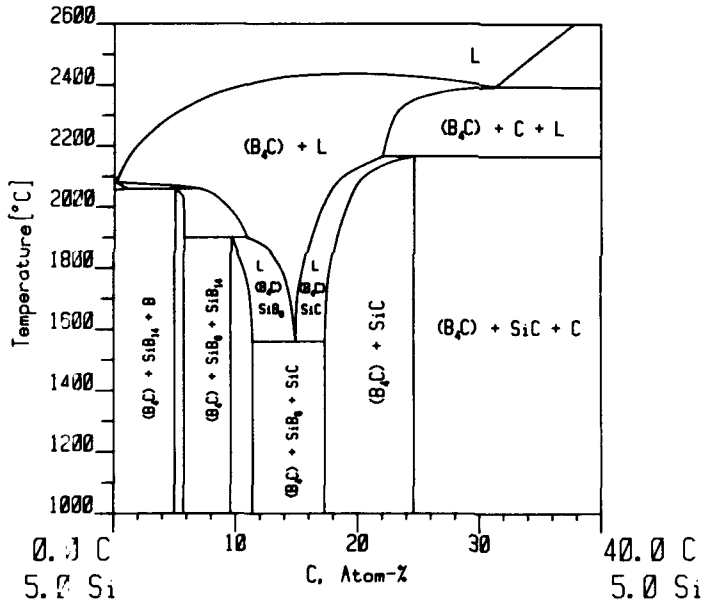

Figure 9. Isopleth of the B-C-Si phase diagram at 5 at.-% parallel to the B-C-edge.

One of the major problems of pressureless sintering is, however, that upon increasing temperature the first melt is generated at 1380° C. Contrary to the situation above 1560° C, this melt is in equilibrium with (SiB_6) and SiC which means that B_4C will decompose in the presence of that liquid. Approaching equilibrium conditions during annealing between 1380 and 1560° C, B_4C reacts at first forming $B_{12}(B,C,Si)_3$ + SiC which strongly influences the wetting behaviour of the melt [9]. Since thin SiC layers are precipitated onto the $B_{12}(B,C,Si)_3$ particles (Fig. 2a) but also close up the interspacings between the grains (Fig. 10) the melt cannot infil-

trate the open pores nor spread homogeneously in the powder compact. A similar effect occurs even above 1560° C if one has started with a mixture of stoichiometric B_4C and Si powder. Then SiC coatings form due to the dissolution of B_4C to the benefit of $B_{12}(B,C,Si)_3$ which is always accompanied by the release of C and hence by the precipitation of SiC. Consequently, during pressureless sintering either the Si-melt has to be saturated in B to increase the solubility for C and hence to prevent the precipitation of SiC as shown in Fig. 2b or the initial powder should be prereacted $B_{12}(B,C,Si)_3$ to suppress the release of free C.

Figure 10. Formation of SiC-layers during pressureless sintering of B_4C with Si and B.

In fact there is still another problem preventing a complete densification of $B_{12}(B,C,Si)_3$ with Si-melt. Above the melting point of 1414° C, Si evaporates which creates new porosity by forming degassing channels and initiates vapour phase reactions involving both silicon borides and $B_{12}(B,C,Si)_3$. Hence no densities exceeding 85 % have been achieved during pressureless sintering.

Contrary to pressureless sintering, Si was found to be a suitable additive for hot pressing of B_4C. Above 1380° C and - with an even better efficiency - above 1560° C the liquid phase aids the particle rearrangement by lubricating the grain boundary sliding. If only a small volume fraction of liquid was used it is consumed by the formation of $B_{12}(B,C,Si)_3$ and SiC or (SiB_6) which also is generated. The formation of SiC as an intergranular phase which is not desired for pressureless sintering was found to be beneficial for hot pressing since it retards the strong grain growth of boron carbide even at temperatures exceeding 2000° C [2,4,5,9]. That result initiated the development of a high-strength $B_4C-TiB_2-W_2B_5$-based material with Si-binder [36,37]. Moreover, boron carbide-based materials in which the (B_4C) particles are enveloped by SiC-layers have been proved to exhibit a higher oxidation resistance in comparison to composites with mechanically dispersed SiC-particles [38].

5.4 IMPLICATIONS FOR THE SINTERING OF SiC WITH B AND B_4C

B, C and B_4C are known to be suitable additives for pressureless sintering of SiC. The activation of sintering was mainly attributed to the decrease of the SiC grain boundary to surface energy ratio: B decreases the grain boundary energy and C increases the effective surface energy by removing oxidation layers on the SiC particles [39]. As a result, solid state sintering is promoted. There is, however, evidence that B and C if added as elements react in an early stage forming (B_4C) before B has dissolved in the SiC lattice and C has served as a desoxidising agent [40]. This may explain the similar efficiency of B_4C as a sintering aid. Contrary to these results, also a liquid phase sintering process was proposed in which a B-containing liquid was considered to generate dissolution-reprecipitation mechanisms which would be responsible for a rapid grain growth. In almost completely densified samples metallic precipitates were observed but could not be identified [41]. B_4C was also found as precipitates in B- and C-doped SiC samples which obviously were densified by an active liquid phase process [42].

Since the decomposition temperature of SiC-B_4C which was proposed to be a quasibinary eutectic at 2300°C, approximately, [43] but is in fact a transition reaction SiC + (B_4C) ≒ C + L at 2160°C (calculated in [8]), was never reached, this cannot be the reason for an existing liquid phase. If it is considered that C and B desoxidised most of the oxide impurities, that both B_2O_3 and SiO almost completely evaporated and that hence the residual amount of oxygen is too small to form an intergranular borosilica glass, the presence of a liquid phase can only be explained by the reaction of B with SiC. Since the diffusion path between B and SiC necessarily has to cross the euqilibria $B_{12}(B,C,Si)_3$ + (SiB_6) + L, $B_{12}(B,C,Si)_3$ + L, and $B_{12}(B,C,Si)_3$ + SiC + L, the simultaneous formation of a B-containing Si-liquid and $B_{12}(B,C,Si)_3$ seems to be reasonable (Fig. 3). Indeed, small $B_{12}(B,C,Si)_3$ precipitates have been identified by EELS and Auger measurements in B- and C-doped SiC [44]. Another explanation for the presence of a liquid phase considers the segregation of Si at the grain boundaries which is due to the recrystallization of stacking faults and point defects yielding 2% Si in excess [45].

As the ternary equilibrium $B_{12}(B,C,Si)_3$ + SiC + L even contacts the homogeneity range of SiC for B the formation of a melt preferentially occurs if solely B is added to an amount exceeding the solubility in SiC (0.3-0.5 at.-%). In fact, this always occurs locally in a powder mixture since neighbouring B and SiC particles usually are of similar size and thus yield a molar ratio of close to 50:50 which, of course, approaches the input ratio with prolonged annealing due to diffusion and the resulting homogenisation.

According to the afore-mentioned considerations, $B_{12}(B,C,Si)_3$-based ceramics already have been produced from SiC + B powder mixtures which consist of facetted $B_{12}(B,C,Si)_3$ crystals in a SiB_6-SiC-Si matrix. Depending on the overall concentration and the annealing conditions, the amount of matrix phase as well as the constituents SiC or SiB_6 can be adjusted in a defined way.

Acknowledgements

The author gratefully acknowledges the valuable support by H.-L. Lukas (thermodynamic calculations), E. Bischoff (TEM and EELS), both MPI/Metals Science, and E.-D. Franz, University of Stuttgart, Inst. f. Mineralogy, for discussion on the crystal chemistry.

REFERENCES

1. K.A. Schwetz and W. Grellner (1981), J. Less-Common Metals **82**, 37
2. K.A. Schwetz, K. Reinmuth and A. Lipp (1983), Sprechsaal **116** [12], 1063
3. P.S. Kislyi and B.L. Grabtchuk (1975), 4th Europ. Symp. Powder Metallurgy, Grenoble 1975
4. L.B. Ekbom and C.O. Amundin (1975), Science of Ceramics **10**, 237
5. D. Lange und H. Holleck (1985), Proc. 11th Plansee-Seminar, Reutte 1985, HM 50, 747
6. R. Kieffer, E. Gugel, G. Leimer und P. Ettmayer (1972), Berichte der Deutschen Keramischen Gesellschaft **49** [2], 44
7. E. Gugel, R. Kieffer, G. Leimer und P. Ettmayer (1972), Nat. Bur. Stand. Spec. Publ. 364, Solid State Chemistry, Proc. 5th Mat. Res. Symp. (1972)
8. P. Dörner (1982), Dr.-rer.nat.Thesis, University of Stuttgart
9. R. Telle and G. Petzow (1987), Proc. 6th CIMTEC, 24-28 June 1986, Milan, in: High Tech Ceramics, P. Vinzencini [Ed.], Elsevier Science Publ., Amsterdam 1987, 961-973
10. R. Telle, P. Dörner, H.-L. Lukas, and G. Petzow (1987), presented at the 89th Annual Meeting of the Am. Ceram. Soc., Pittsburgh 1987
11. S. La Placa and B. Post (1961), Planseeberichte für Pulvermetallurgie **9**, 109-112
12. A. Lipp und M. Röder (1966), Z. f. Anorgan. Allg. Chemie **344** [5-6], 225
13. A.R. Kerler (1974), Dr. rer. nat. Thesis, University of Munich, 1974, partially published in: W. Borchert und A.R. Kerler (1975), Metallwissenschaft und Technik, **29** [10] (1975), 993-1002
14. V.I. Matkovich and J. Economy (1977), in: Boron and Refractory Borides, V.I. Matkovich [Ed.], Springer, Berlin (1977), 96-106
15. R.D. Allen (1953), J. Am. Ceram. Soc. **75**, 3582
16. H. Neidhard, R. Mattes und H.J. Becher (1970), Acta Cryst. **326**, 215
17. K. Ploog (1974), J. Less-Common Metals **25**, 115
18. G. Will and K.H. Kossobutzki (1976), J. Less-Common Metals **47**, 43-48
19. A. Kirfel, A. Gupta, and G. Will (1979), Acta Cryst. **B35**, 2291-2300
20. H. Werheit and K. De Groot (1980), Phys. State Sol., **B97** [8], 571
21. J. Conard, M. Bouchacourt, F. Thevenot, and M. Hermann (1986) J. Less-Common Metals **117**, 51-60; Proc. 8th Int. Symp. Boron Borides, Carbides, Nitrides, and Related Compounds, Tbilisi, USSR, October 8-12, 1984
22. W.N. Lipscomb and D. Britton (1960), J. Chem. Phys. **33**, 275-280
23. D.R. Armstrong, J. Bolland, and P.G. Perkins (1983), Acta Cryst. **39**, 324
24. A.H. Silver and P.J. Bray (1959), J. Chem. Phys. **31**, 247
25. T.V. Hynes and M.N. Alexander (1974), J. Chem. Phys., **54**, 5296
26. H.J. Becher und F. Thevenot (1974), Z. Anorg. Allg. Chemie, **410**, 203
27. M. Bouchacourt and F. Thevenot (1981), J. Less-Common Metals **82** [2], 219
28. R.W. Olesinski and G.J. Abbaschian (1984), Bull. Alloy Phase Diagrams **5** [5], 478
29. U. Täffner, R. Telle, and U. Schäfer (1988), Z. Prakt. Metallographie **25** [1], 17-27
30. S. Fukuda, S. Kato, H. Mohri, and T. Yamashina (1982), J. Nuclear Materials **111-112**, 839

31. K. Ploog (1974), J. Less-Common Metals 35, 131
32. B. Magnusson and C. Brosset (1962), Acta Chem. Scand. 16, 449
33. P. Ettmayer, H.C. Horn und K.A. Schwetz (1970), Microchimica Acta, Suppl. IV, 87
34. G.A. Meerson, S.S. Kiparisov, M.A. Gurevich, and D. Feng-Siang (1966), Sov. Powder Metall. and Met. Ceram. 5 [3], 223
35. V.I. Matkovich and J. Economy (1970), Acta Cryst. B26, 616-621
36. H. Hofmann and G. Petzow (1986), J. Less-Common Metals, 117, 121-127
37. R. Telle (1988), Densification of Boron Carbide at Relatively Low Temperatures by Hot Pressing and Hot Isostatic Pressing, Final Report, Concerted Action of the Commission of the European Communities COST 503
38. R. Lörcher, K. Strecker, R. Riedel, R. Telle, and G. Petzow (1989), presented at the Int. Conf. Sintering of Multiphase Metal and Ceramic Systems, 31st Jan - 3rd Feb. 1989, New Delhi, to be published in: Sintering of Multiphase Metal and Ceramic Systems, G.S. Upadhyaya [Ed.], New Delhi 1989
39. S. Prochazka (1975), Special Ceramics 6, The Brit. Ceram. Res. Ass., Stoke-on-Trent, 171-181
40. H. Suzuki and T. Hase (1978), Proc. Int. Symp. Factors of Densification and Sintering of Oxide and Non-Oxide Ceramics, Hakone, Japan (1978) S. Somiya and S. Saito [Eds.], 345-365
41. F.F. Lange and T.K. Gupta (1976), J. Am. Ceram. Soc., 59, 537
42. W. Böcker and H. Hausner (1978), Powder Metallurgy Int., 10 [2], 87-89
43. D.R. Secrist (1964), J. Am. Ceram. Soc., 47 [3], 127-131
44. K.L. Moore, C.H. Carter, J. Bentley, W.H. Wadlin, L. La Vanier, and R.V. Davis (1986), J. Am. Ceram. Soc., 69 [9], 695-698
45. S. Prochazka (1989), Proc. Technische Keramik 2, Wiesbaden, F.R.G., 1989, M03, 71-96

ACTINOIDMETAL BORON CARBIDES

P. ROGL
Institut für Physikalische Chemie,
Universität Wien,
A-1090 Wien, Währingerstrasse 42
Austria

ABSTRACT. The constitution i.e. the phase equilibria of the ternary systems: actinoid metal (Th,U,Pu,Np) - boron - carbon has been investigated by X-ray diffraction and metallographic techniques as well as by melting point analysis, and phase relations have been established in isothermal sections. Phase equilibria are generally characterized by the formation of several high melting ternary compounds and by incompatibility of the actinoid carbides with boron or boroncarbide. Employing X-ray single crystal, powder X-ray and neutron diffraction techniques most of the ternary boroncarbide structures have been established. Classification of these structure types closely follows the general rules for metal borides and carbides. In some cases extended homogeneous regions have been observed with replacement of boron by carbon atoms. Sensitivity against moisture increases with increasing carbon content of the compound and carbon-rich boroncarbides are decomposing as fast as actinoid carbide materials.

Magnetism was particularly investigated in case of the uranium compounds revealing ferromagnetic and/or paramagnetic behavior in accordance to the distance dependent exchange interactions (Hill plot).

1. GENERAL REMARKS

The technological importance of transition metal borides, arising from novel high temperature, mechanical, electrical and magnetic properties has for a long time stimulated interest in structure, phase transitions and chemical bonding in binary and ternary metal-boron compounds (1). Besides an early interest in actinoid carbides and nitrides as socalled advanced nuclear fuel materials (2), actinoid metal compounds in general and compounds of the light actinoid elements in particular have recently attracted widespread attention with respect to their unusual electric and magnetic properties related to 5f-electron localization or delocalization and unusual bonding capabilities (heavy fermion

R. Freer (ed.), The Physics and Chemistry of Carbides; Nitrides and Borides, 269–277.
© 1990 *Kluwer Academic Publishers. Printed in the Netherlands.*

behavior etc.) (3,4).

2. PHASE RELATIONS IN THE TERNARY SYSTEMS ACTINOID METAL-BORON-CARBON

In an early exploration of the ternary systems (Th,U)-B-C Toth et al. (4,5) provided the basic information on phase formation and phase equilibria. Most of the ternary compounds have been corroborated since and many of the then unknown crystal structures have been determined meanwhile (6-9). Some more compounds have been revealed in a recent and detailed reinvestigation (10) of the Th-B-C and the U-B-C system (see Figs. 1,2). Phase equilibria in the U-B-C system (Fig. 2), determined in various isothermal sections, were found to remain practically unchanged in the temperature range from 1000°C to 1800°C (10). Phase equilibria in the Pu-B-C system have been recently investigated in part (11) and were found to essentially correspond to those observed for the uranium system. Except for the formation of two neptunium boroncarbides NpBC and NpB_2C (see section 3 and ref. (12)), there are yet no further informations available on the systems (Ac,Pa,Np, trans Pu)-B-C as far as the existence of ternary compounds or the equilibrium phase relations are concerned.

Thermodynamic phase equilibria An-B-C are basically characterized by the formation of at least two series of ternary compounds AnBC and AnB_2C (An= Th,U,Np and Pu; see also section 3, Tables 1,2), and by the existence of which no compatibility exists between the actinoid metal and boroncarbide 'B_4C' nor between elemental boron and the binary actinoidmetalcarbides. Mutual solid solubilities of borides and carbides appear to be small (10-12), and there is practically no solubility of the actinoid metals in boroncarbide. Homogeneity regions of the ternary compounds so far were found to be rather small except for an extended solid solution in $UB_{1-x}C_{1+x}$ (10).

3. STRUCTURAL CHEMISTRY OF TERNARY ACTINOID BORON CARBIDES

The comparison of the structure types for the various actinoid metal boroncarbides, as given in Figs. 3,5, directly reveals the close structural relation between the actinide monoboronmonocarbides and the structure types of the transition monoborides, typically characterized by the formation of boron chains. As pointed out earlier (6-9) the carbon atoms in ThBC and UBC occupy the interstices in a "UB" and "ThB"-sublattice corresponding to the CrB or the MoB-type structure - carbon atoms thus are considered to act as a stabilizer of a typical monoboride structure. Whereas the 'UBC'-type directly relates to the CrB-type, the close structural relation between the ThB-sublattice in ThBC and the ℓ-MoB-type exists via a theoretical crystallographic group-subgroup relation (8): $I4_1/a2/m2/d$ (ℓ-MoB)-$t_2 \longrightarrow I4_122$ - $k_2 \longrightarrow P4_122$ (ThBC).

Geometrical size restrictions exclude significant carbon solubility in the transitionmetal monoborides with much smaller unit

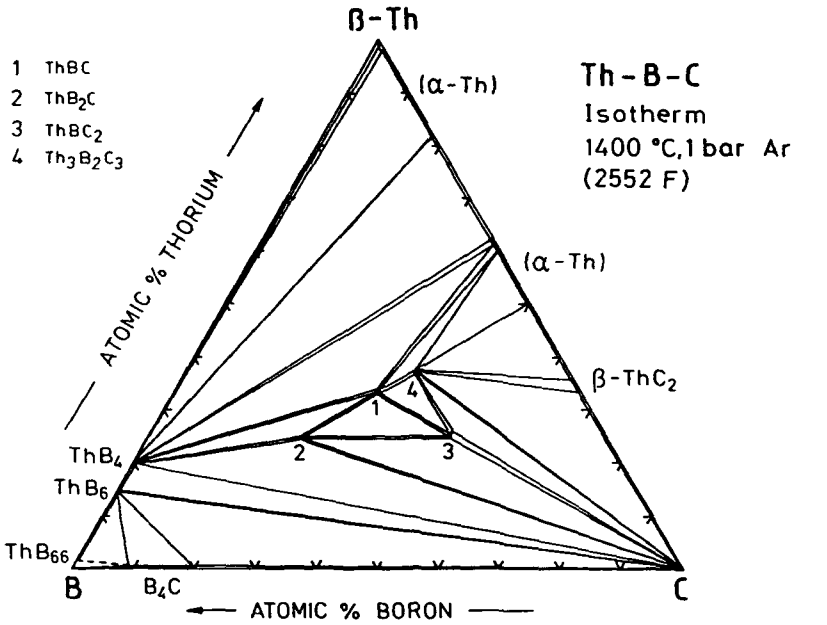

Figure 1. The ternary system Th-B-C, isothermal section at 1400°C (based on Tóth et al.(1), critically assessed by the author).

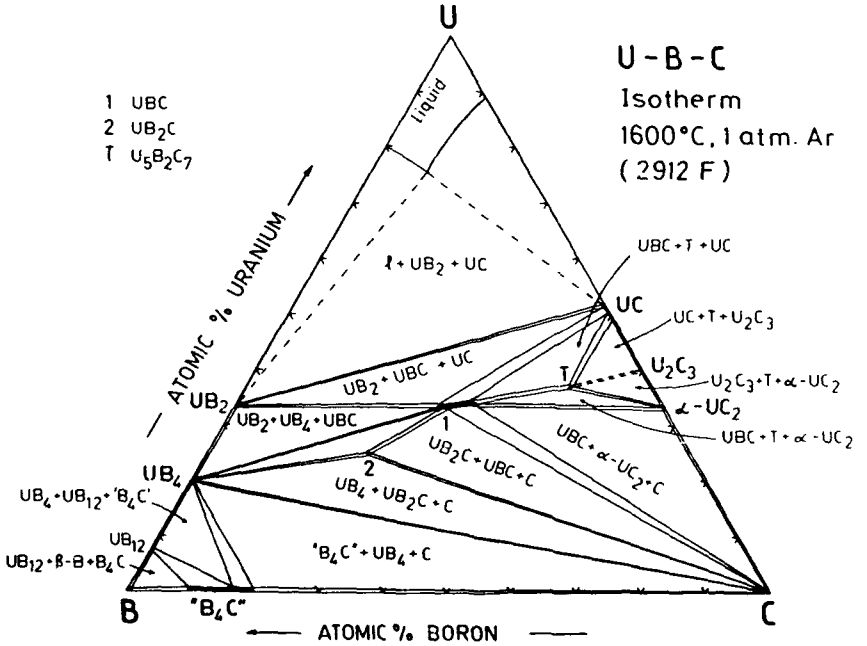

Figure 2. The ternary system U-B-C; isothermal section at 1600°C (ref.10).

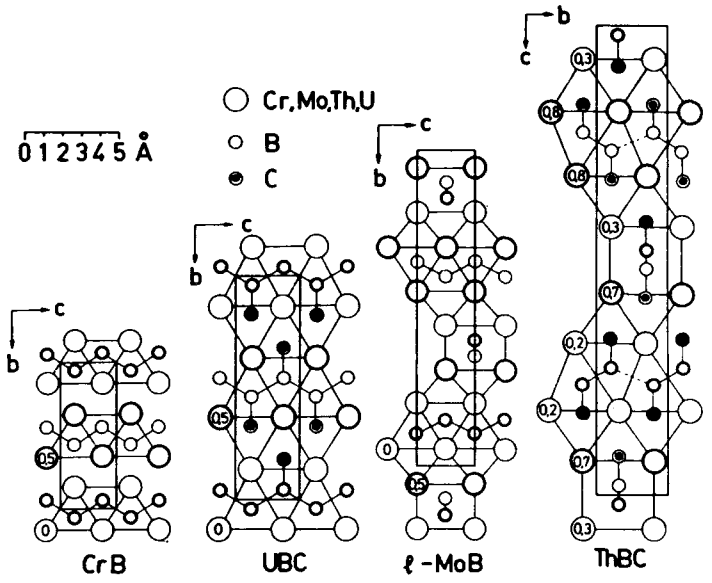

Figure 3. Comparison of the crystallographically related pairs of structure types CrB-UBC, ℓ-MoB-ThBC, as seen in projection along [100].

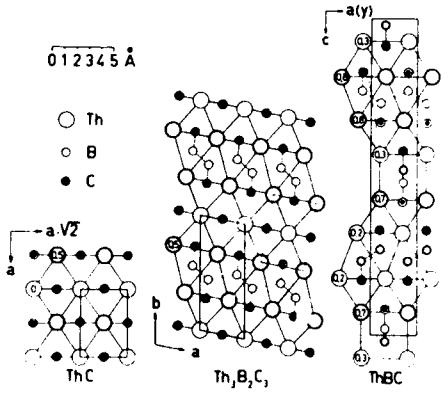

Figure 4. The crystal structure of $Th_3B_2C_3$ in projection along [001], and topochemical mode of formation: $Th_3B_2C_3$ = 2ThBC + ThC (ref.7). Numbers given indicate the height of the metal atoms along the axis of projection. Filled circles are carbon atoms in 1/2.

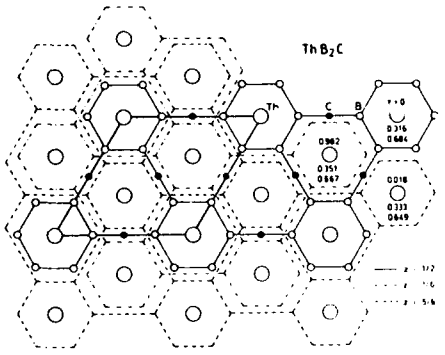

Figure 5. The crystal structure of ThB_2C in projection along [001]. The B-C nets and the heights of the Th-atoms along the axis of projection are outlined.

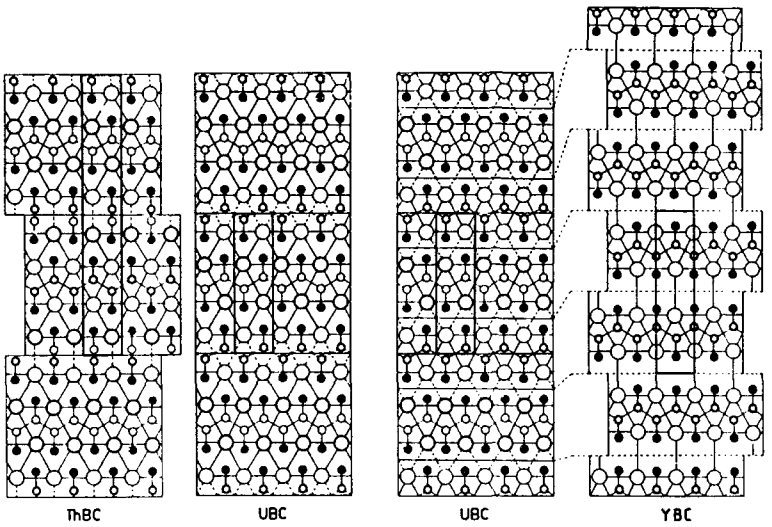

Figure 6. Comparison of the crystallographically related structure types of ThBC, UBC and YBC. The crystal structures of ThBC and YBC can be derived from UBC by shifting slabs common to each structural pair as indicated.

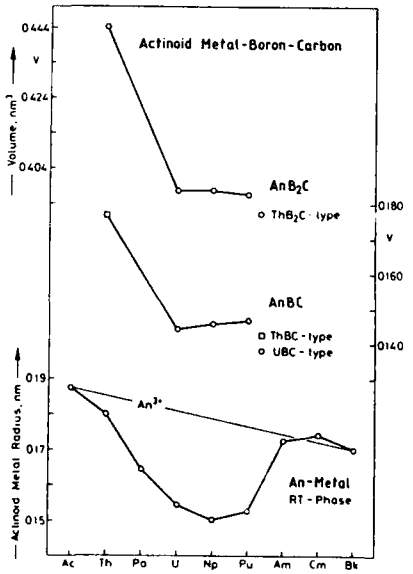

Figure 7. Unit cell volumes of the actinoid boroncarbides AnBC and AnB_2C in comparison with the An-metal radius (stable RT-phase) as a function of 5f-electron overlap.

cell dimensions such as (Nb,Ta,Mo,W)B etc. With respect to the correspondence of the metal boron sublattices for the pairs of structures ℓ-MoB-ThBC and CrB-UBC, the shift operation ThBC⟶UBC was found (8) to be an analogue of the transitionmetalboride transformation ℓ-MoB-hMoB. A similar shift operation may simply be used to generate the YBC-type from either UBC or ThBC, however, the slightly different stacking mode of the rows of triangular prisms in YBC results in an expansion of the unit cell which renders transitions of this type unfavorable (Fig. 6). The crystal structure of ThB_2C (Fig. 5) is a typical B,C-net type compound whose structure type derives from the $A\ell B_2$-type with carbon atoms entering the boron nets to form a $^2_\infty(6B).\ (6B(3C))^2$ kagomé layer (9). For the U,Np compounds the ThB_2C-type high temperature modification transforms to a low temperature phase of a hitherto unknown structure type ($h\text{-}UB_2C \xrightleftharpoons{1675°C} \ell\text{-}UB_2C$), whereas no phase transformation was observed for the Th,Pu-compounds. A listing of the crystallographic data for all actinoidboroncarbides investigated is found in Tables 1,2,3. The crystal structure of $ThBC_2$ is still unknown, whereas the structure of $U_5B_2C_7$ is likely to be isotypic with $Ho_5B_2C_7$ and thus is closely related to $\alpha\text{-}UC_2$. Based on the monoboroncarbide ThBC the crystal structure of $Th_3B_2C_3$ is easily understood as a formal topochemical sum of the structural units of ThBC and ThC according to the relation $Th_3B_2C_3 = 2ThBC + ThC$ (see also Fig. 4). As far as the boron aggregation is concerned, actinoid boroncarbides follow the general classification scheme of ternary boride structures (13). Bonding distances in B-B chain and B-C net type borides are within the common limit of covalent B-B bond distances (see Table 3); boron carbon distances range between 0.145 and 0.150 nm corresponding to a single boron-carbon bond, B-C distances, however, tend to smaller values when the total carbon concentration increases.

4. THERMODYNAMIC AND CHEMICAL STABILITY

Congruent melting behavior is reported for the boron-carbides investigated, and from Pirani-melting point analyses the points of fusion for ThB_2C (2040(15)), ThBC (2101 ± 22), UB_2C (2282 ± 30) and UBC (2144 ± 25°C) are all somewhat inferior to the melting temperatures of both the binary actinoid borides and the actinoid carbides (9), indicating no unusually strong carbon-boron bond formation. Thermal stabilities are in correspondence with an intermediate thermodynamic stability of the uraniumboroncarbides for which the free energy of formation data were estimated (10) from the phase equilibria by applying the clear cross principle in relation to the ternary phase reactions based on the thermodynamic data of the binaries (see Table 4).

All actinoid metal boroncarbides are remarkably stable in dry air, however tend to rapidly hydrolyse under moist conditions. Sensitivity against moisture increases with increasing carbon content of the compound and carbon-rich boroncarbides are decomposing as fast as binary actinoid metalcarbide materials.

TABLE 1. Actinoid Boroncarbides AnBC

Phase	Struct. Type	Space Group	a	b	c (nm)
ThBC	ThBC	$P4_122$	0.3762 (2)	-	2.5246 (5)
UBC	UBC	$Cm\bar{c}m$	0.35927(6)	1.19889(22)	0.33474(6)
PuBC	UBC	Cmcm	0.35872(5)	1.20122(21)	0.33999(5)
NpBC	UBC	Cmcm	0.35855(8)	1.20007(85)	0.33831(6)

TABLE 2. Actinoid Boroncarbides - ThB_2C-type

Phase	a	c (nm)	c/a
ThB_2C	0.66972(13)	1.14405(22)	1.708
UB_2C	0.65224(18)	1.07909(29)	1.654
PuB_2C	0.65104(3)	1.07966(6)	1.658
NpB_2C	0.65362(30)	1.07522(64)	1.645

Space Group: $R\bar{3}m$ - D_{3h}^5, No. 166; origin at $\bar{1}$

TABLE 3. B-B and B-C Distances (nm) in Actinoid Boroncarbides

UBC	B - 2 B	0.190		B - 1 C	0.152
ThBC	B - 1 B	0.177	(0.247)	B - 1 C	0.154
$Th_3B_2C_3$	B - 1 B	0.177	(0.230)	B - 1 C	0.155
ThB_2C	B - 2 B	0.185		B - 1 C	0.150

TABLE 4. Gibbs energy of formation of ternary uranium boroncarbides with respect to binary uraniumborides and uraniumcarbides; values correspond to the phase equilibria derived in Fig.2 (Rogl, 1989).

Compound	$f_{\Delta G^0_{298}}$(kJ/mol)	$f_{\Delta G^0_{1k,1}}$(kJ/mol)
UB_2	-160.7	-140.9
UB_4	-247.2	-218.2
UB_{12}	-430.4	-361.2
UC	-98.9	-107.9
U_2C_3		-222.2
UC_2	-87.5	-106.6
UBC	-179.3 to -127.4	-178.4 to -134.5
	Average: -153.0	Average: -156.0
	-172.4 to -127.6	-
	Average: -150.0	
UB_2C	-247.2 to -185.4	-218.2 to -185.2
	Average: -216.0	Average: -201.0
$U_3B_2C_7$	~620.0	~620.0

5. MAGNETIC BEHAVIOUR

Information on the electrical and magnetic behaviour of the actinoid boroncarbides is small and only the thorium and the uranium boroncarbides have been recently investigated (14). Whereas alloys $UB_{1-x}C_{1+x}$ ($0 < x < 0.22$) from magnetic susceptibilities in the range from 4.2 to 1000 K are characterized by a typical intermediate valence fluctuation behaviour ($T_{SF} \sim 350$ K). The high temperature modification of UB_2C is a ferromagnet with a rather high Curie temperature $T_M = 80(2)$ K. T_M as well as the saturation moment per U-atom ($\sigma = 0.64\ \mu_B$ for h-UB_2C) both sucessively decrease on substitution of U by Th,Sc,Lu until a temperature independent paramagnetism is obtained for ThB_2C, which interestingly is also observed for low temperature ℓ-UB_2C. The individual paramagnetic uranium moments are at a rather low value of 1.9 μ_B which probably arises from a relatively broad U-5f band at the Fermi-level. In both cases UBC and UB_2C, the U-U average distances are close to the socalled "Hill-limit" at $HL \sim 0.35$ nm, whereby the shorter average U-U separation of 0.35 nm in $UB_{0.78}C_{1.22}$ is a strong indication for strong direct U-U 5f overlap and thus 5f electron delocalization. With the progressive localization of the 5f-electrons in going from uranium to neptunium and plutonium, a future magnetic investigation of the pair of structures with the UBC- and the ThB_2C-type for the Np,Pu and Am compounds should thus reveal more insight in the interesting cross over regime.

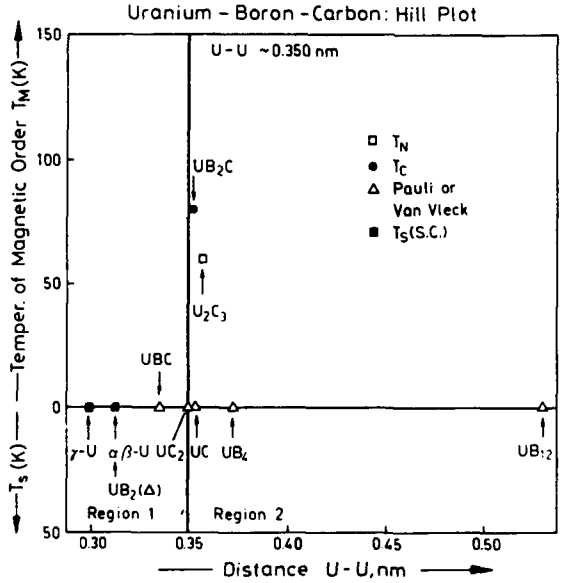

Figure 8. Hill-plot for uranium borides, carbides and boroncarbides.

6. REFERENCES

1. Schwetz, K. A., Reinmuth, K. and Lipp, A. (1981) 'Production and Industrial Use of Refractory Boron Compounds' (German), Radex-Rundschau 3, 569-585.
2. Potter, P. E., Spear, K. E. (1979) 'Advanced Fuels for Fast Breeder Reactors', in E. A. Beck (ed), Thermodynamics of Nucl. Materials, Vol.II, IAEA, Vienna, pp. 195-226.
3. Ott, H. R. and Fisk, Z. (1987) 'Heavy Electron Actinide Materials', in A.J. Freeman and G.H. Lander (eds.), Handbook on the Physics and Chemistry of the Actinides, Elsevier Science Publ., B.V., North Holland, Amsterdam, pp. 85-225.
4. Tôth, L. E., Benesovsky, F., Nowotny, H. and Rudy, E. (1961) 'The Ternary System: Thorium-Boron Carbon' (German), Monatsh. Chemie 92, 956-960.
5. Tôth, L. E., Nowotny, H., Benesovsky, F. and Rudy, E. (1961) 'The Ternary System: Uranium-Boron-Carbon' (in German), Monatsh. Chemie 92, 794-802.
6. Rogl, P. (1978) 'The Crystal Structure of ThBC', J. Nucl. Mater. 73, 198-203.
7. Rogl, P. (1979) 'The Crystal Structure of $Th_3B_2C_3$', J. Nucl. Mater. 79, 154-158.
8. Rogl, P. (1979) 'On the Crystallographic Relationship between Monoborides (CrB, -MoB) and Actinoid-Boroncarbides (UBC, ThBC)', J. Nucl. Mater. 80, 187-189.
9. Rogl, P. and Fischer, P. (1989) 'Single Crystal X-ray and Powder Neutron Diffraction of ThB_2C (ThB_2C-Type)', J. Solid State Chem. 78, 294-300.
10. Rogl, P., Bauer, J. and Debuigne, J. (1989) 'The Ternary System Uranium-Boron-Carbon', J. Nucl. Mater. 165, 74-82.
11. Rogl, P., and Potter, P. E. (1990) 'The Ternary System Plutonium-Boron-Carbon', research at Harwell, U.K., to be published
12. Rogl, P., Beauvy, M. and Larroque, J. (1989) 'The Ternary Neptunium Boroncarbides NpBC and NpB_2C', Proc. 19emes Journêes des Actinides, Madonna di Campiglio, Italy, paper P33, pp. 95-96.
13. Rogl, P. (1985) 'Structural Chemistry and Phase Equilibria of Ternary Rare Earth-Platinum Metal Borides', J. Less Common Metals 110, 283-294.
14. Rogl, P., Rupp, B. and Felner, I. (1990) 'Crystal Chemistry and Magnetism of Ternary Actinoid Boroncarbides $UB_{1-x}C_{1+x}$ and $U_{1-x}M_xB_2C$ with M = Sc,Lu and Th', J. Nucl. Mater., to be published.

DEFECTS AND GRAIN BOUNDARIES IN HIGH TEMPERATURE DEFORMED α-SiC

J. VICENS, S.J. LEE, E. LAURENT-PINSON, G. NOUET and J.L. CHERMANT
LERMAT - CNRS URA 1317 - ISMRa
Boulevard du Maréchal Juin
14032 CAEN CEDEX FRANCE

ABSTRACT. Transmission electron microscopy analyses of hot pressed SiC deformed at high temperature (1600°C) have been carried out to investigate the defects induced by the deformation inside the crystals and in carbide grain boundaries. They have shown the activation of the basal plane with glide dislocations dissociated into Shockley partials. Loop nucleations have been observed along the dislocation lines. Their formation has been explained by a climb mechanism. Grain boundary dislocations have been found in the deformed samples and considered as a result of a grain boundary sliding.

1. INTRODUCTION

Silicon carbide (SiC) is one of the most commercially important carbides. It is a complex material occuring in numerous polytypes. Moreover it frequently contains not only SiC but additional components and phases depending on the manufacturing process.

As a ceramic and in its polycrystalline form, its high value of hardness and mechanical strength make it a principal candidate for high temperature and high strength applications. The single crystal form is also used in semiconductor devices. So as a semiconductor with tetrahedral coordination it is a very interesting material to study the dislocation mechanisms already developed in well known semiconductors.

Because of the thermomechanical applications of SiC materials many studies have been performed usualy by three or four point bending or by compression in the high temperature range (T>1000°C) (FARNSWORTH and COBLE [1], FRANCIS and COBLE [2] , MARSHALL and JONES [3], KRISHNAMACHARI and NOTIS [4], GRATHWOHL et al. [5], DJEMEL et al. [6], CARRY and MOCELLIN [7], MOUSSA et al. [8]). Microstructure stu-

R. Freer (ed.), The Physics and Chemistry of Carbides; Nitrides and Borides, 279–296.
© 1990 Kluwer Academic Publishers. Printed in the Netherlands.

dies by SEM realized after creep experiments have shown the macroscopic aspects of the various mechanisms involved during the deformation at high temperature. It has been concluded that dislocation movement was not important in SiC materials. Diffusion mechanisms were mainly involved to explain the experimental results.

Direct observations of defects in SiC single crystals have been already made in TEM by STEVENS [9]. More recently microscopic defects of high temperature deformed SiC have been also observed and motion of partial dislocations after high temperature deformation in α-SiC (hexagonal form) was described by PILYANKEVICH and BRITUN [10]. Reaction bonded α-SiC (CARTER et al. [11]), α- and β-SiC prepared by CVD (CARTER et al. [12]) and α-SiC doped with boron (LANE et al. [13]) have been studied in TEM after creep experiments at about 1600°C. The creep mechanism was identified as a dislocation glide-climb controlled by climb both for reaction-bonded and chemically vapour deposited SiC. The most prominent features of the sintered material are the number of dislocation slip bands and the interactions between dislocations and B_4C precipitates.

A more recent investigation has described defects in plastically deformed 6H SiC single crystals in a temperature range from room temperature to 1650°C (FUJITA et al. [14], MAEDA et al. [15]). The high temperature deformation of SiC single crystals produces basal dislocations dissociated into Shockley partials on the (0001) basal plane. During the deformation of single crystals at high temperature the macroplasticity seems to be controlled by the most immobile partials. At low temperature the partials were only observed and a model was proposed to explain the change in the gliding behaviour of SiC crystals with temperature. The difference in mobility of partials were recently discussed by DEMENET et al. [16] from observations performed in sintered α-SiC deformed at 800°C under a confining pressure of 700 MPa.

JEPPS and PAGE have extensively studied by HREM polytype transformations occuring in silicon carbide [17]. On the contrary very few studies (ICHINOSE et al. [18], LANCIN [19], LANCIN et al. [20, 21]) have been made for characterizing the grain boundary structure in α-SiC. ICHINOSE et al. has obtained HREM images of α-SiC bicrystals formed by sublimation while LANCIN et al. have described transformation twins observed in the two 4H and 6H polytypes during the β (cubic) → α (hexagonal) transformation.

2. MATERIALS AND EXPERIMENTAL PROCEDURES

Hot-pressed α-SiC with 0.3% Al-based additives have been supplied by the Elektroschmelzwerk Company (F.R.

GERMANY). Some specimens have been deformed in the temperature range from 1300°C to 1760°C under vacuum by three-point bending. Slices of deformed specimens (1600°C) were mechanically ground and polished to a thickness of 80μm. Discs of 2.3mm in diameter were ion-milled (Ar^+, 6KV) for TEM observations (JEOL 120 CX and 200 CX).

3. STRUCTURAL CONSIDERATIONS

Silicon carbide exhibits a range of ordered structures (polytypism). All silicon carbide structures are made up by the single basic units of tetrahedra SiC_4 or C_4Si. Successive layers can arrange in different ways giving rise to cubic (c), hexagonal (H) or rhombohedral (R) unit cells. The most common polytypes observed are 4H, 6H (often reported as the hexagonal forms α-SiC) and 3C (β-SiC cubic form).

4. MICROSTRUCTURE

The hot-pressing process leads to a very dense state and a mean grain diameter $\bar{D}_{SiC} = 4\mu m$. An electron transmission micrograph (Fig. 1) reveals more precisely the shape of the carbide grains. Some of them tends to adopt an elongated shape developing large facets parallel to the (0001) basal plane of the hexagonal structure. Electron diffraction studies have shown that the carbide grains crystallized into the two main hexagonal polytypes 4H and 6H which have been indicated in some grains on the figure 1 with their corresponding crystallographic structure. Many defects can be seen inside the grains. They are due to either stresses induced during the preparation or to a modification in polytype structure inside a same grain. We note that the additive phase can be visible only inside some triple grain junctions. It is normally a glassy phase which can be observed as crystallized in annealed then deformed specimens.

Fig. 2 is an electron transmission micrograph of the deformed specimen at 1600°C. As a consequence of the deformation and the migration of grain boundaries, an important faceting of interfaces have been revealed in such specimens.

5. DISLOCATION CONFIGURATION IN THE DEFORMED SPECIMEN

TEM observations of high-temperature deformed α-SiC

Fig. 1 : Microstructure of the hot-pressed SiC - 0.3 % Al. The crystallographic nature of some grains have been indicated on the micrograph.

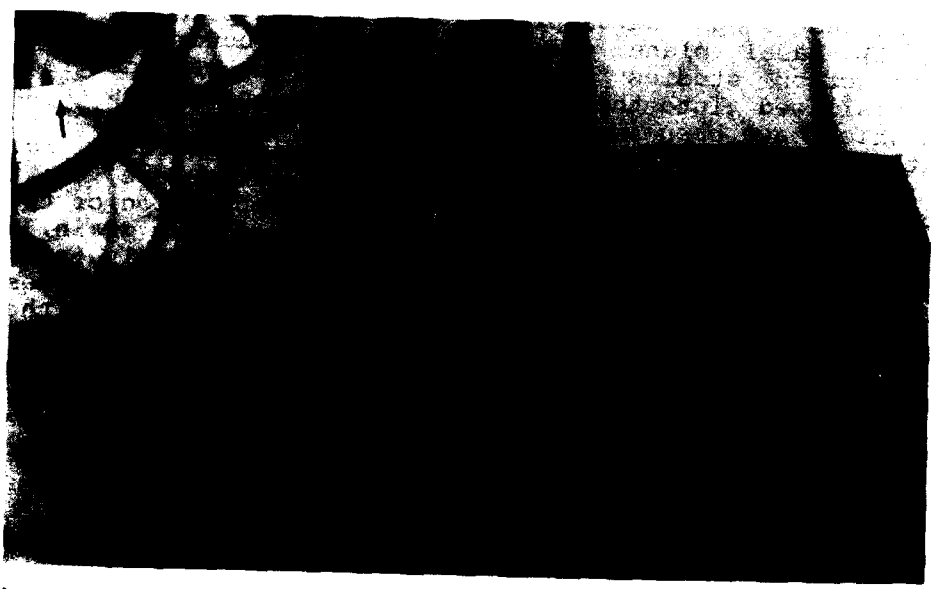

Fig. 2 : Microstructure of a specimen after deformation at 1600°C. Many grain boundaries are faceted and some facets have been indicated by an arrow on the micrograph.

show the activation of the basal (0001) glide plane. A number of dislocations have been analyzed as Shockley partials [a/3 < 10$\bar{1}$0>]. The dislocation lines are frequently straight and parallel to the <11$\bar{2}$0> or <10$\bar{1}$0> directions. No difference has been found between the 4H and 6H SiC dislocation configurations. Dissociated dislocations observed in the samples can be classified into 4 different types of Shockley partials according to their characters (30°-30°, 30°-90°, 60°-60° and 0°-60°).

Fig. 3 illustrates an example of partial dislocations in a 4H SiC grain. The two partials of the dissociatated dislocations have been imaged. The separation distance in this example is lower than the equilibrium width while has been proposed by MAEDA et al. [15] in a 6H single crystal deformed above 1500°C. Moreover dissociated dislocations can be viewed recombined along a part of their dislocation lines (partials denoted i in Fig. 3). Constricted nodes (marked j in Fig. 3) can also be found.

Two detailed analyses of dissociated dislocations are given in Fig. 4 and 5. On each micrograph the Burgers

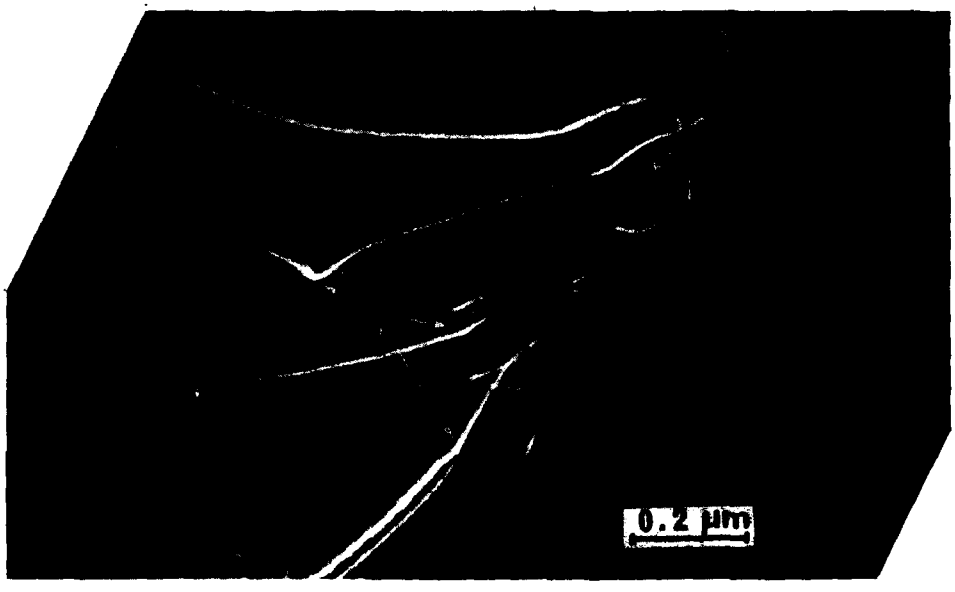

Fig. 3 : Weak beam images of Shockley partial dislocations observed in a 4H SiC crystal after a creep experiments at 1600°C. Some dissociated dislocations can be viewed recombined along a part of their dislocation lines (partials denoted i). Contricted jogs (marked j) can be also found.

vector of the different partials have been indicated. In the first example (Fig. 4) the two partials can be viewed recombined in some parts (marked i) of the dislocation lines. A redissociation of the perfect dislocation can occur also with an opposite sense as it is observed in a part of the dislocation line (marked k). The same mechanism appears in the second example shown in Fig. 5 where the two partials have been also inversed. In this case there is a strong interaction between the two partials and two precipitates (P) which character could not be clearly identified. A recombination of the partials and a redissociation has likely occurred between the two precipitates (P).

Both examples have revealed constrictions and inversions of Shockley partials. Only a climb mechanism taking place during the high temperature deformation can explain such configurations.

6. DISLOCATION-LOOP INTERACTIONS

Shockley partials with a smaller stacking fault width ($\simeq$ 0.03 μm) have also been observed in the same specimen. In this case TEM images reveal a strong interaction between dislocations and small loops (15 to 50 nm in size) nucleated along the dislocation lines. An example is shown in the dark field image (Fig. 6) with $g = 1\bar{2}14$. In this example six partial dislocations (denoted 1 to 6) can be seen. Their Burgers vectors have the following values $b = a/3\ [01\bar{1}0]$ for 1, 3 and 5 ; $b = (a/3)\ [\bar{1}100]$ for 4 and 6 ; $b = a/3\ [10\bar{1}0]$ for 2. The characters of these partials identified as 0°-60° for 1 and 2, 60°-60° for 3 and 4 and 90°-30° for 5 and 6 have been indicated in Fig. 6 except for partial 2 which is out of contrast with $g = 1\bar{2}14$. Loops are mainly found along the dislocation lines 1, 2, 3 and 4.

The precipitation of loops on Shockley partials have often been observed in our specimen after high temperature deformation. Another example is presented in Fig. 7. The two Shockley partials are imaged in bright field condition and contrast studies have given their Burgers vectors $b_1 = (a/3)\ [\bar{1}100]$; $b_2 = (a/3)\ [01\bar{1}0]$. In this case the dislocation line direction is not well defined as in the preceding case. But loop precipitations have occurred mainly on the dislocation lines when they tend to the 60° orientation for partials 1 and 2. The character of the two partials and the loop location are indicated on Fig. 7. This example and the precedent case reveal that loop nucleations are mainly observed on partials 0°-60° and 60°-60°.

If a climb motion of basal dislocation in SiC in the high temperature deformed specimen has been deduced from the observations described above (Fig. 4-5), the

Fig. 4 : Weak beam images (a and b) of two partials showing a recombination (marked i) and redissociated in an opposite sense (marked k). In b only one partial is in contrast.

Fig. 5 : Intersection between two partials and two precipitates (P). There is an inversion (marked k) in the part of the dislocation lines situated between the two precipitates.

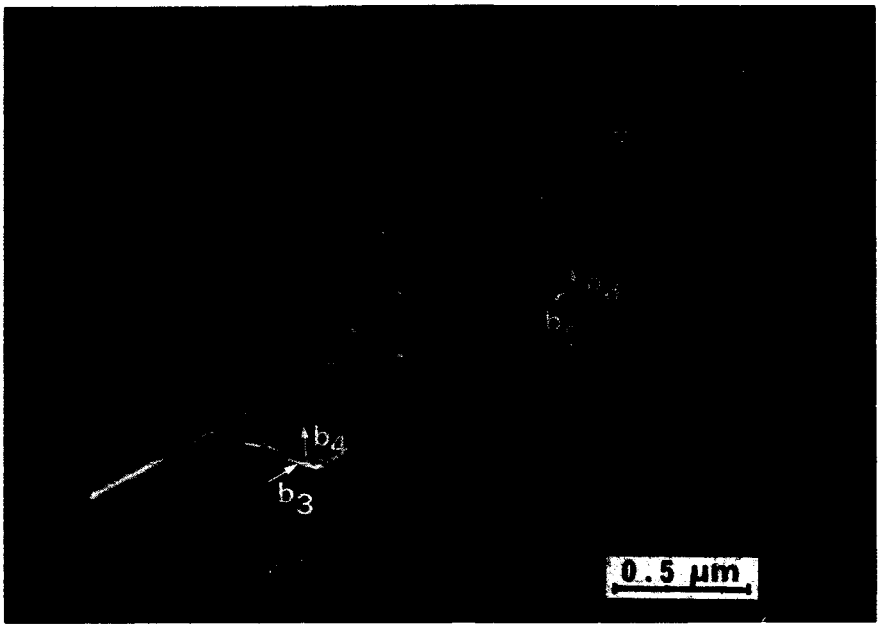

Fig. 6 : Dark field image with $g = 1\bar{2}14$ showing a high density of loops nucleated along Shockley partials. Six partials denoted 1 to 6 are indicated with their Burgers vector directions. The partial 2 ($b_2 = a/3\ [10\bar{1}0]$) is out of contrast.

Fig. 7 : Enlargement of a part of two Shockley partials denoted 1 and 2. loop nucleations are observed when the dislocation line directions tend to the 60° orientation for partials 1 and 2.

is based on the reaction between point defects and dislocations. In a first step we assume the nucleation of a perfect prismatic loop with a vacancy character on the dislocation line. CHERNS et al. [23] have first developed such a model which has already been applied to a large variety of cubic crystals such as Cu - 13.43% Al (DECAMPS et al. [24] Si and GaAs (OURMAZD et al. [25], Feuillet and CHERNS [26], CHERNS [27]).

This model has been applied to α-SiC. We assume that the prismatic loops have the three possible Burgers vector AB=(a/3) $[\bar{2}110]$, BC=(a/3) $[11\bar{2}0]$ and CA=(a/3)$[1\bar{2}10]$. The reactions between the prismatic loops and the four types of partials have been studied with the principle that the loop nucleation is only possible if it corresponds to a minimum activation energy (CHERNS et al. [22]). In these conditions the partials 0°-60° and 60°-60° are highly favoured for a loop nucleation.

Fig. 8 illustrates this model in four steps (a) nucleation of loops AB and CB on the partials Bσ and dissociation of the part of the loops situated in the basal plane (b) dipoles formation (c) reaction between the dipoles and the partial σC and (d) closed loop formation in the matrix. Consequently there is a climb movement of the two partials Bσ and σC. This model already applied to cubic crystals can explain in the present study the high density of loops observed around partial dislocations in high temperature deformed α-SiC.

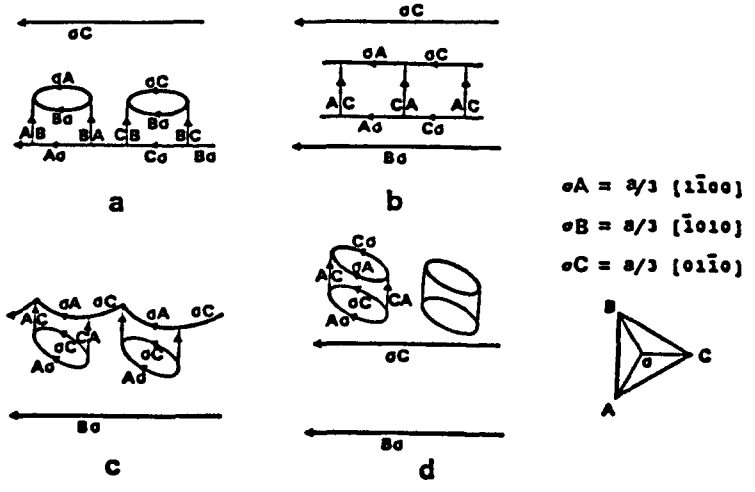

Fig. 8 : Schematic drawing of the climb mechanism and vacancy loop nucleation on the partials Bσ and σC. This mechanism has been already described in cubic crystals (OURMAZD et al. [25]).

7. GRAIN BOUNDARY ANALYSIS IN α-SiC

This part presents results concerning the grain boundary studies carried out in the as sintered material and in the high temperature deformed specimens. Before describing the defects in grain boundaries, a short introduction concerning the geometry of grain boundaries in such a material will be reported. This geometric description has been made by using the coincidence models developed by BOLLMANN [28, 29]. Since α-SiC polytypes are hexagonal, the coincidence models adapted to a hexagonal symmetry (WARRINGTON [24], BLERIS et al. [31], GRIMMER et al. [32]) have to be applied.

7.1. Coincidence descriptions in α-SiC

Two high angle misorientated grains are in a coincidence orientation if a coincidence site lattice (C.S.L.) is formed between the two interpenetrating lattices associated with the two crystals. For each coincidence orientation, a coincidence index Σ is defined as the ratio of the C.S.L. primitive cell volume to the crystal primitive cell volume.

Tridimensional coincidence orientations can be calculated theoretically in the hexagonal symmetry by assuming a $(c/a)^2 = \mu/\nu$ rational value. A real hexagonal crystal is always described by a c/a parametric ratio for which $(c/a)^2$ has not a rational value. Thus, on a first approximation, the three-dimentional coincidence orientations are calculated by using one or several μ/ν value close to the real $(c/a)^2$ value of the hexagonal crystal. This model has been previously applied to ceramic materials such as Al_2O_3 (MORRISSEY and CARTER [33], LARTIGUE [34], and WC (VICENS et al. [35]). The same approach has been carried out in the two α-SiC polytypes 4H and 6H firstly to obtain the lists of the theoretical coincidence orientations secondly to compare with experimental orientations between carbide grains.

At first the different μ/ν values close to the $(c/a)^2$ value have been calculated with a maximum deviation of 2% for the two 4H (c/a = 3.271) and 6H (c/a = 4.907) polytypes.

Results have shown that three ratios give a good description of coincidence orientations in the 4H polytype: μ/ν=21/2, 32/3 and 54/5, for the reason that they give rise to a high number of coincidence descriptions with low Σ values and are very close to the real c/a value (deviation < 1%). Only one ratio, μ/ν=24/1, has been used to obtain coincidence descriptions in the 6H polytype. The deviation with respect to the exact c/a ratio is only 0.2%. Moreover

this μ/ν ratio generates a high number of coincidence orientations. Furthermore a common cell between the 4H and 6H polytypes can be defined with $a=a_{4H}=a_{6H}$ and $c=3C_{4H}=2C_{6H}$. A list of coincidence orientations between the two different polytypes has also been obtained by using this new cell a and c. In this case the μ/ν ratio is equal to 96/1 [36].

7.2. Experimental orientations

Experimental orientations (about 60 cases) have been carried out in the α sintered specimen and in the high temperature deformed specimens. Table 1 gives some examples in both samples (" • " in table 1 denotes a deformed specimen) and reports only examples when a Σ value could be given even if the deviation is rather high in some cases. The corresponding Σ values as well as the deviation $\Delta\theta$ from the exact coincidence orientation have been indicated. The crystallographic nature of the grain boundary plane has been determined in both grains for each cases.

The results show that the experimental orientations deviate greatly from the exact coincidence orientations. However some special grain boundaries with low index Σ have been observed either with a common basal (0001) plane (Σ19) (#1, 2 in table 1) or with a common $(10\bar{1}4)$ plane (Σ6) (#12, 13 in table 1). The last case corresponds to a 70°53 rotation around the $[11\bar{2}0]$ common axis. This same orientation between two different 4H and 6H crystals has also been found (Σ12) (#19, 20 in table 1).

In many cases the boundary plane is parallel to the densest plane (0001). Consequently the most common observation consists of a boundary plane parallel to the basal plane for one crystal and parallel to high indices planes for the other crystal. However some dense plane have also been found parallel to the basal plane: $(10\bar{1}0)_{6H}$, $(10\bar{1}4)_{6H}$. Finally in the deformed specimen where a high faceting of grain boundaries has been observed, the most frequent facet which is formed is, parallel to the basal plane (Fig. 9). As a result these interfaces are also parallel to the glide plane of one crystal. Therefore an intergranular sliding is expected to occur for these boundaries when they are well oriented with respect to the stresses.

7.3. Grain boundary dislocations observed in the deformed specimen

Dislocations have been observed in some grain boundaries after the deformation at 1600°C.

Table 1 : Experimental orientations.

	#		Σ	$\Delta\theta_{exp}$	Grain boundary plane
Grains rotated around a common [0001] axis	1		19	4°	$(0001)_{4H}$ $(0001)_{4H}$
	2	•	19	4.5°	$(0001)_{4H}$ $(0001)_{6H}$
	3	•	7	12.5°	$(0001)_{6H}$ $(10\bar{1}4)_{6H}$
4H-4H μ/ν=21/2 or 32/3*	4		27	4.5°	$(0001)_1$ $(3\bar{4}11)_2$
	5		15	8.5°	$(0001)_1$ $(2\bar{2}01)_2$
	6		35	7°	
	7		21	8°	$(0001)_1$ $(12\bar{3}3)_2$
	8		25	11°	$(12\bar{3}6)_{1,2}$
	9		22*	8°	$(0001)_1$ $(1\bar{3}25)_2$
	10		76*	1°	$(0001)_1$ $(01\bar{1}8)_2$
6H-6H μ/ν=24/1	11		15	9°	$(10\bar{1}4)_{1,2}$
	12	•	6	11°	$(0001)_1$ $(2\bar{2}03)_2$
	13	•	6	8°	$(01\bar{1}4)_{1,2}$
	14		27	5°	$(3\ 2\ \bar{5}\ 16)_{1,2}$
	15		22	6°	$(0001)_1$ $(0\ \bar{1}1\ 11\ 2)_2$
	16		38	7°	$(0001)_1$ $(1\ \bar{1}\ 0\ 10)_2$
4H-6H μ/ν=96/1	17		30	5°	
	18		34	3°	$(0001)_{4H}$ $(10\bar{1}0)_{6H}$
	19	•	12	5°	
	20		12	9.5°	$(0001)_{4H}$ $(10\bar{1}3)_{6H}$
	21	•	22	9°	$(0001)_{4H}$ $(4\ 3\ \bar{7}\ 20)_{6H}$
	22		28	3°	$(0001)_{4H}$ $(10\bar{1}4)_{6H}$

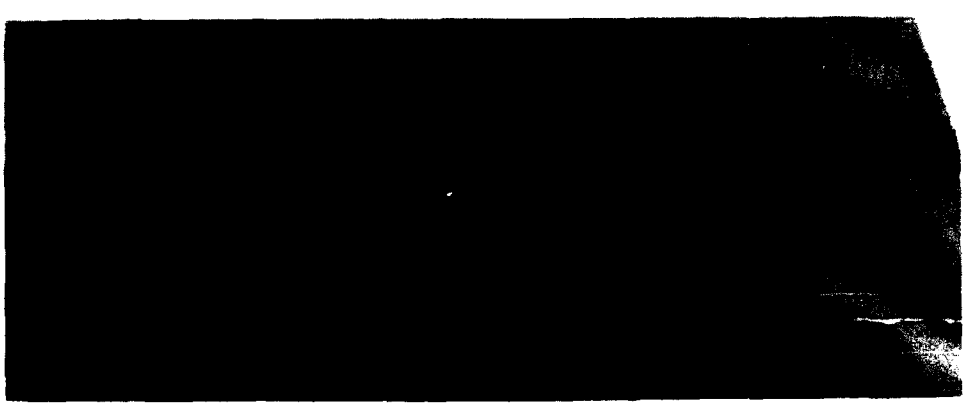

Fig. 9 : Faceted grain boundary between two 6H crystals observed in the deformed specimen.

Fig. 10 shows a grain boundary between two 4H crystals. In this orientation the grain boundary plane is parallel to the foil plane which is the basal plane of the crystal 1. The relationship between the two crystals has been determined showing that the two crystals are in a random orientation. Shockley dislocations (denoted L on the micrograph) can be seen in the crystal 1 and a dislocation pileup is imaged in the boundary plane. The dislocation configuration suggests an activation of a dislocation source likely situated near the triple junction denoted S on the micrograph. As a result of the activation of the glide plane in crystal 1, which is also the grain boundary plane, a grain boundary sliding has occured between the two crystals.

Fig. 11 (a to c) illustrates another example where dislocations have been imaged in the grain boundary between two 4H and 6H crystals. There is no tridimensional coincidence description between the two crystals as for the precedent case. The boundary viewed parallel to the electron beam in Fig. 10a is faceted, the two facets a and b are parallel to $(1\ 0\ \bar{1}\ 24)_{6H}$ and $(0\ 1\ \bar{1}\ \bar{15})_{6H}$ respectively (Fig. 11a). The angular deviations between these two high indices planes and the basal plane of the crystal 6H are small (~ 20°) and the two facets intersect the basal plane

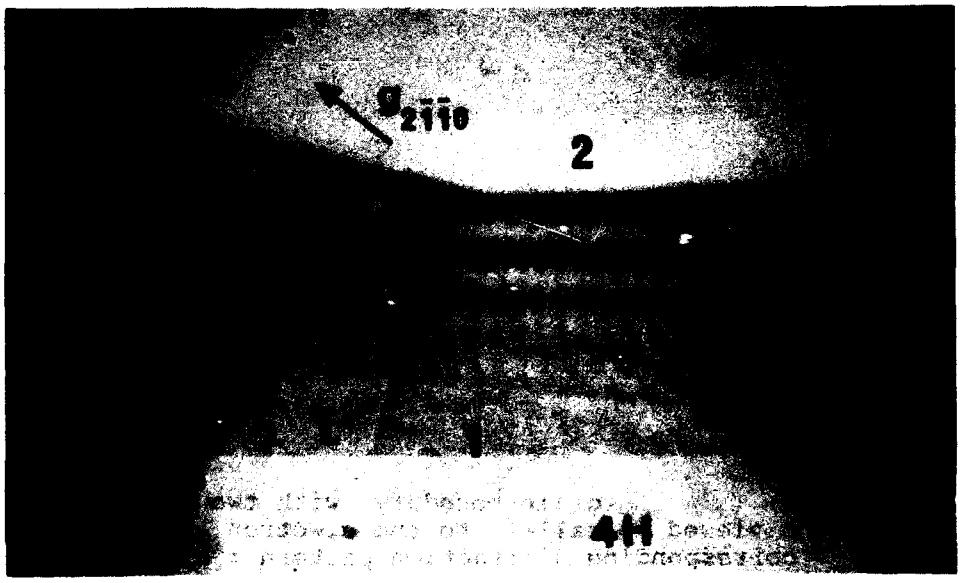

Fig. 10 : Pileup of glide dislocations imaged in a grain boundary between two 4H crystals. The grain boundary plane has been found parallel to the basal plane of crystal 1.

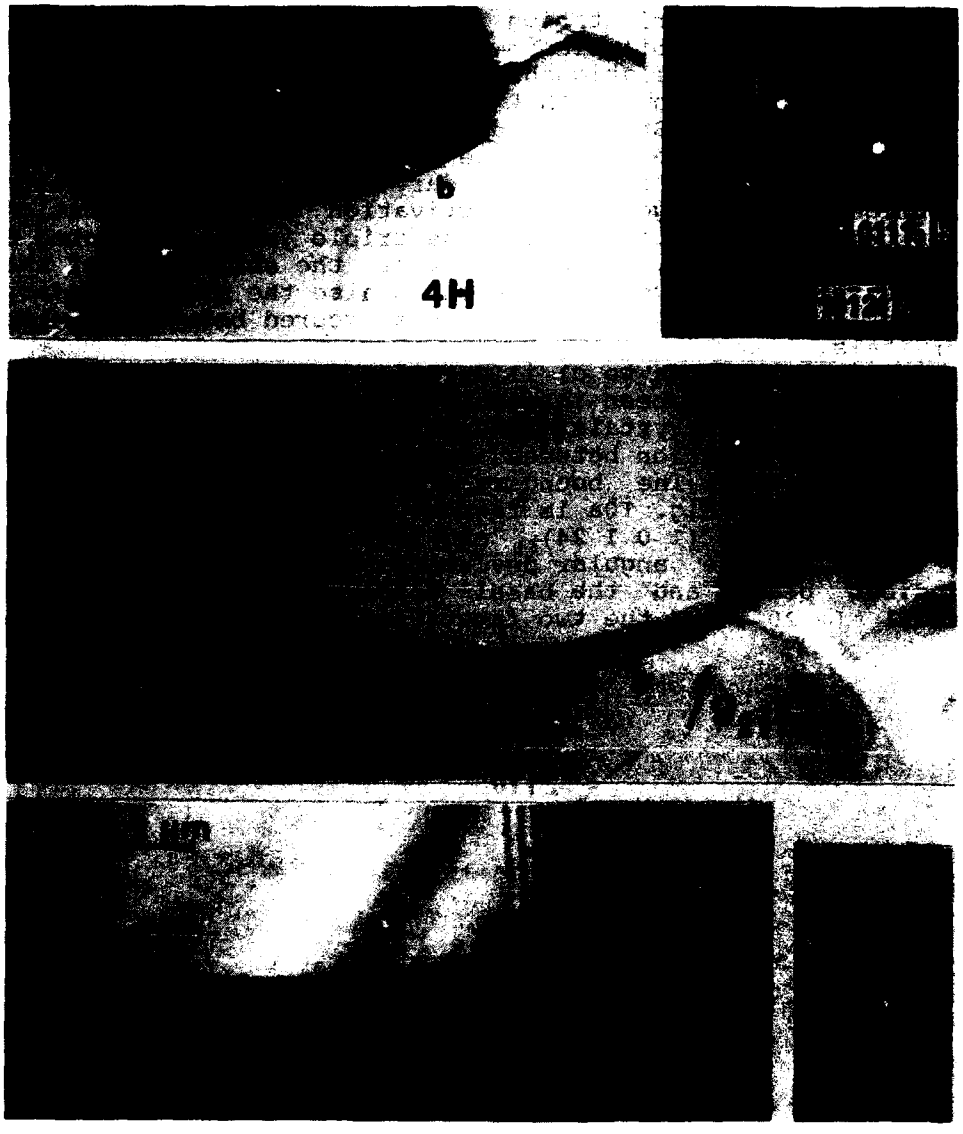

Fig. 11 : a) grain boundary with two facets a and b viewed parallel to the electron beam and the corresponding diffraction pattern ; b) Same boundary in another orientation. Dislocations are imaged in the two facets a and b ; c) The dislocations are out of contrast with g=0006. But another family of dislocations (denoted ℓ) is imaged.

along two equivalent <11$\bar{2}$0> directions. Fig. 11b shows the same boundary in another orientation and a dislocation pileup is imaged in the two facets. The dislocation line directions L_a and L_b have been denoted on the stereographic projection (Fig. 12) as well as the basal plane of the crystals 6H and 4H and the poles of the two facets a and b. These dislocations are out of contrast in Fig. 11c which is a dark field image with g=0006. These dislocations have likely a Burgers vector of the type 1/3 <11$\bar{2}$0>. From these observations a possible dislocation mechanism can be proposed.

For the reason that the two facets have a common <11$\bar{2}$0> direction with the basal plane, a cross slip mechanism can operate for screw glide dislocations with b = 1/3 <11$\bar{2}$0>. In the contrary of the preceding case a movement of these dislocations in the grain boundary plane involves also a climb mechanism. Additional work on deformation at grain boundaries are in progress in these high temperature deformed samples.

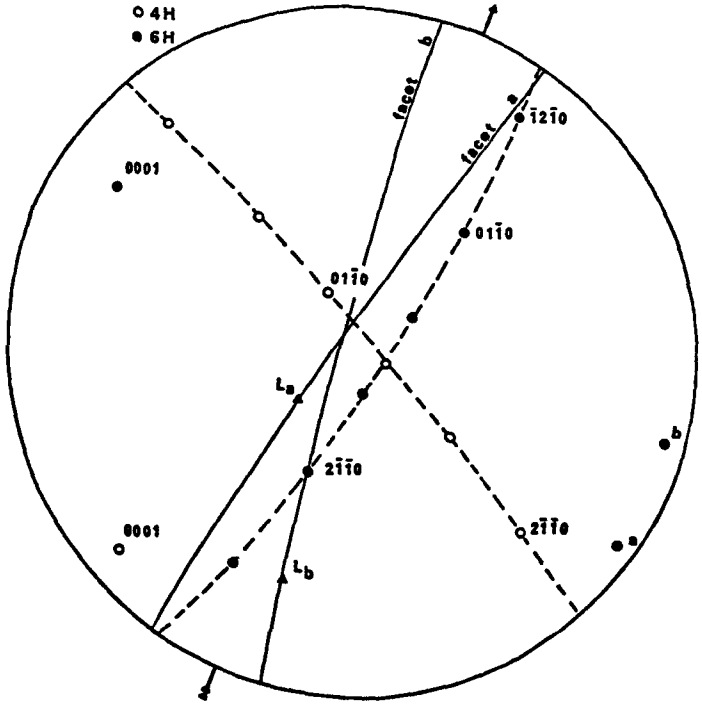

Fig. 12 : Stereographic projection of the example shown in figure 10.

8. CONCLUSION

TEM observations of high temperature deformed α-SiC (1600°C) indicate the activation of the basal glide plane. The glide dislocations are Shockley partials (0°-60°, 30°-30°, 30°-90° and 60°-60°). Evidence of climb motion of these dissociated dislocations have been found. The dissociated dislocations can act as loop sources and a possible mechanism, already applied for cubic crystals, is proposed to explain the loop formation in α-SiC (hexagonal crystal structure) after the high temperature deformation.

Accurate crystallographic studies of grain boundaries has been carried out in this material and have shown that the basal plane is the most favoured boundary. The basal plane is also the main facet observed in the deformed sample.

The tridimensional coincidence concept has been applied to α-SiC grain boundaries which deviate greatly from exact coincidence orientations.

Grain boundary dislocations have been observed in the deformed sample and considered as a result of a grain boundary sliding mechanism.

REFERENCES

[1] Farnsworth, P.L. and Coble, R.L. (1966) J. Am. Ceram. Soc., 49, 264.

[2] Francis, T.L. and Coble, R.L. (1968) J. Am. Ceram. Soc., 51, 115.

[3] Marshall, P. and Jones, R.B. (1969) Powd. Met., 12, 193.

[4] Krishnamachari, V. and Notis, M.R. (1977) Mater. Sci. Engng., 27, 83.

[5] Grathwohl, G., Reets, T.H. and Thummler, F. (1981) Sci. Ceram., 11, 425.

[6] Djemel, A., Cadoz, J. and Philibert, J. (1981) "Creep and fracture of engineering materials and structures", Eds Nilshire, B. and Owen, D.R.J., Swansea Pineridge Press, 381.

[7] Carry, C. and Mocellin, A. (1984) "High temperature creep of dense fine grained silicon carbides" in Materials Science Research, Eds Tressler, R.E. and Bradt, R.C., Plenum Press, New-York, 18, 391.

[8] Moussa, R., Chermant, J.L. and Osterstock, F. (1984) "High temperature creep of dense fine grained silicon carbides" in Materials Science Research, Eds Tressler, R.E. and Bradt, R.C., Plenum Press, New-York, 18, 617.

[9] Stevens, R. (1972) J. Mat. Sci., 7, 517.

[10] Pilyankevich, A.N. and Britun, V.F. (1984) Phys. Stat. Sol. (a), 82, 449.

[11] Carter, Jr C.H., Davis, C.H. and Bentley, J. (1984) J. Am. Ceram. Soc., 67, 409.
[12] Carter, Jr C.H., Davis, C.H. and Bentley, J. (1984) J. Am. Ceram. Soc., 67, 732.
[13] Lane, J.E., Carter, Jr C.H. and Davis, R.F. (1980) J. Am. Ceram. Soc., 71, 281.
[14] Fujita, S., Maeda, K. and Hyodo, S. (1987) Phil. Mag. A., 55, 203.
[15] Maeda, K., Suzuki, K., Fujita, S., Ichihara, M. and Hyodo, S. (1988) Phil. Mag. A., 57, 573.
[16] Demenet, J.L., Rabier, J. and Garem, H. (1986) 6th M.S.M. Oxford, England, 10-13 April 1989, to be published.
[17] Jeeps, N.W. and Page, T.F. (1983) "Polytypic Transformations in Silicon Carbide" ; Progress in Crystal Growth and Characterization, Vol. 7 - Crystal Growth and Characterization of Polytype Structures. Edited by Krishna, P., Pergamon, New-York, 259.
[18] Ichinose, H., Inomata, Y. and Ishida, Y. (1986) "Ceramic microstructure role of interfaces", Mat. Sci. Res., Eds Pask, J.A. and Evans, A.G., 21, 255.
[19] Lancin, M. (1984) J. Mat. Sci., 19, 4077.
[20] Lancin, M., Anxionnax, F., Thibault-Dessaux, J., STUTZ, D. and GRIEL, P. (1987) 22, 1150.
[21] Lancin, M. and Thibault-Dessaux, J. (1988) J. Phys., C5 N°10, (Lake Placid), 37.
[22] Lee, S.J., Nouet, G., Vicens, J. (1989) Phil. Mag. Letters, 60, N°2.
[23] Cherns, D., Hirsch, P.B. and Saka, H. (1980) Proc. R. Soc. Cond., 371, 213.
[24] Decamps, B., Cherns, D. and Condat, M. (1983) Phil. Mag. A., 48, 123.
[25] Ourmazd, A., Cherns, D. and Hirsch, P.B. (1981) Inst. Phys. Conf. Ser., 60, 39.
[26] Feuillet, G. and Cherns, D. (1983) Inst. Phys. Conf. Ser., 67, 27.
[27] Cherns, D. (1984) Dislocations 1984 (Paris Editions du CNRS) 215.
[28] Bollmann, W. (1970) Crystal defects and Crystalline interfaces, Springer-Verlag, Berlin.
[29] Bollmann, W. (1982) Crystals lattice, Interfaces, Matrices, Ed. Bollmann, Genève.
[30] Warrington, D.H. (1975) J. Phys., 36-C4, 87.
[31] Bleris, G.L., Nouet, G., Hagège, S. and Delavignette, P. (1982) Acta Cryst., A38, 550.
[32] Grimmer, H. and Warrington, D.H. (1987) Acta Cryst., A43, 232.
[33] Morrissey, K.J. and Carter, C.B. (1984) J. Am. Ceram. Soc., 67, 297.
[34] Lartigue S. (1988) Thesis, Orsay, Paris, France.

[35] Vicens, J., Lay, S., Laurent-Pinson, E. and Nouet, G. (1988) "Surfaces and Interfaces of Ceramic Materials" NATO ASI Oléron, France. To be published.
[36] Laurent-Pinson, E., Nouet, G. and Vicens, J. (1988) Inst. Phys. Conf., Série N°93, Vol. 2, EUREM 88, York, England, 543.

APPLICATION OF TRANSMISSION ELECTRON MICROSCOPY TO THE STUDY OF TRANSITION METAL CARBIDES.

T. EPICIER
Institut des Sciences Appliquées de Lyon
Groupe d'Etudes de Métallurgie Physique et de Physique des Matériaux, Bât. 502,
u. a. CNRS 341
69621 Villeurbanne Cedex
France

ABSTRACT. The importance and interest of Transmission Electron Microscopy for the microstructural characterization of transition metal carbides is illustrated through selected examples concerning ordering phenomena, irradiation studies and dislocation problems. Special attention is devoted to recent advances permitted by the application of High Resolution techniques.

1. General Introduction

The present work deals with carbides of the transition metals of the IVa (Ti, Zr, Hf), Va (V, Nb, Ta) and VIa (Mo, W) columns of the periodic classification. Cubic monocarbides MC_{1-x} (with Na-Cl type structure) and hexagonal hemicarbides M_2C_{1-x} (with L'3 -hcp- structure) will be considered in this paper. The case of hexagonal monocarbides, such as WC (frequently used under the form of cemented carbides) is not treated here : these compounds are very different from cubic monocarbides and hexagonal hemicarbides regarding crystallography and plasticity (see numerous contributions in [1]).

Transition metal carbides are refractory materials, which include compounds with the highest known melting point, e.g. ~4000°C for HfC/TaC alloys ; they have very interesting (thermo-)physical, mechanical, chemical or electrical properties which have been extensively described throughout the literature (see general reviews [2, 3, 4, 5] or compilation of data [6].

In any investigation program on materials, the microstructural characterization is a fundamental step for the understanding of their behaviour. The particular case of carbides do not escape from this rule, and their macroscopic properties depend directly upon microstructural features, as illustrated by the few examples reported below :

.the chemical ratio C/M influences most of the performances of monocarbides, such as their mechanical strength (for example, the critical resolved shear stress -which decreases from 150 to ~90 MPa for TiC single crystals from $TiC_{0.95}$ to $TiC_{0.79}$ at 1000°C [7]-), or their electrical

R. Freer (ed.), The Physics and Chemistry of Carbides; Nitrides and Borides, 297–327.
© 1990 Kluwer Academic Publishers. Printed in the Netherlands.

properties (the lower the carbon content, the higher the resistivity -about 50 μΩ.cm at room temperature in most carbides [8]-). These effects are due to the presence of vacancies on the carbon sublattice when departure from stoichiometry occurs ; ordering of these vacancies has also been proved to play a great role.

.a spectacular hardening (by a factor of several times) of titanium or vanadium carbides can be achieved by boron doping, which leads to the precipitation of metal borides at dislocations nodes [9, 10]. Generally, impurities such as oxygen or nitrogen may modify the stability of ordered phases as it seems to be the case in metallic hemicarbides (see [11]).

From these figures, it is easy to demonstrate the interest of the Transmission Electron Microscopy (TEM) technique in the microstructural characterization of carbides : ordered microstructures, organization of dislocations or precipitation phenomena can thought to be revealed by this technique. Since the latest paper reviewing essential TEM microstructural investigations of carbides [10], significant work has been performed ; furthermore, the recent development of new techniques, such as High Resolution Electron Microscopy and Micro-Chemical Analysis has allowed microstructural features to be studied in very deep details in adequate cases.

The present paper will then show representative results obtained by TEM concerning ordering phenomena (§2), irradiation processes (§3) and plasticity or dislocation problems (§4) in mono- and hemicarbides. In each case, the impact of the TEM observations on the metallurgical knowledge of these compounds will be emphasized. Unless specified otherwise, TEM micrographs shown below were taken on a 200CX Jeol microscope mounted in a side-entry configuration. In order to keep the text as clear as possible, other experimental details, which generally remain classical as for any TEM study, are not recalled ; the reader should then refer to the cited literature to learn further about the exact experimental procedure followed by the authors.

2. Ordering Phenomena

2.1. GENERAL IDEAS ABOUT CONVENTIONAL TEM (CTEM)

2.1.1. *Long-Range Order.* Basically, the establishment of long-range ordering (LRO) produces superstructure reflections which are easily detected in conventional selected-area diffraction work.

In the case of carbides, there is no major difficulty to reveal such additional spots in diffraction patterns (see figure 1). However, the intensity of superlattice reflections is considerably lower than that of the matrix reflections, since ordering only concerns the interstitial carbon sublattice.

Most of the known superstructures occuring in cubic monocarbides have already been observed by means of TEM ($TiC_{1/2}$ [12], $TiC_{1/2}$ in $TiC_{0.61}$ [13] and $TiC_{1/2}$ in $TiC_{0.93}$ after irradiation [14], Zr_2C in $ZrC_{0.64}$ [13] ; V_8C_7 [12, 15, 16] ; V_6C_5 and related long-period structure [17-23], Nb_6C_5 [24-26] ; ζ-phases in carbides of the Vth group -see review in [12, 27]- ; $Ta_{64}C$ [28][1]).

[1] a more recent TEM investigation has however shown that this solid solution gets ordered because of the presence of interstitial oxygen [29].

Information is still certainly lacking for the compounds of the IVth group ; the superstructures occuring near the composition $MC_{0.5}$ have mainly been studied by neutron diffraction, and the differences between proposed models (i.e. M_8C_5 or M_2C) are not definitively established (see review in [30]).

The case of hexagonal hemicarbides M_2C is discussed elsewhere [11].

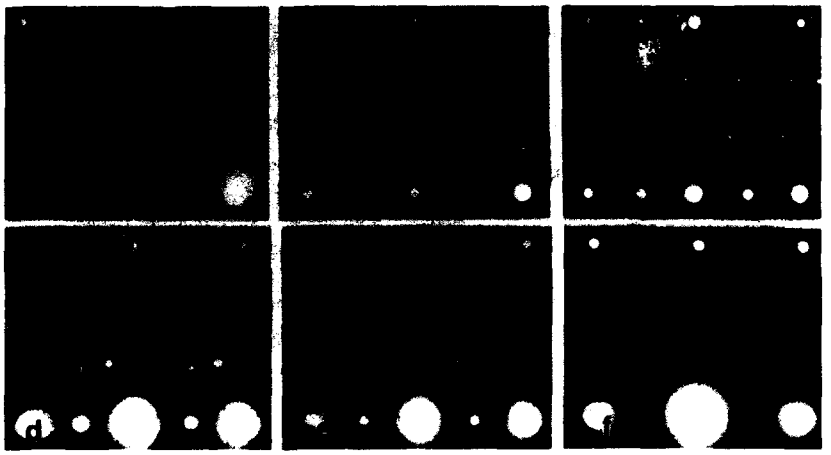

Figure 1. $<112>_{fcc}$ diffraction patterns of different states in VC_{1-x} : a) : disordered lattice ; b) : V_8C_7 superstructure in $VC_{\simeq 0.87}$; c) : V_6C_5 superstructure in $VC_{\simeq 0.84}$; d) : long-period structure based on V_6C_5 in $VC_{\simeq 0.85}$; e) : ζ-phase in $VC_{\simeq 0.7}$; f) : short-range ordering in $VC_{\simeq 0.75}$.

Among all these superstructures, a few have even been directly identified by TEM, especially in vanadium carbide near the composition V_6C_5 ; this particular case will be further discussed in §2.4 , since it clearly illustrates some of the difficulties encountered in identifying structures by TEM work.

2.1.2. *Short-Range Order*. Short-range ordering (SRO) has also been observed in TEM through the evidence of bands of diffuse intensity in diffraction patterns (VC_{1-x}, NbC_{1-x} and TaC_{1-x} -see reviews in [31, 32]- ; V_2C, Nb_2C, Ta_2C and related binary compounds [33] ; W_2C [16]). Recent diffuse scattering neutron and X-ray experiments have however shown that a major contribution to this diffuse intensity comes from metal atom displacements around carbon vacancies [13, 34].

2.2. STUDY OF ORDER DEFECTS

In addition to the basic identification of ordered states, the TEM technique is the adequate tool for studying the defective microstructure within grains, e.g. domains boundaries and antiphase defects. Application of contrast rules in the two-beam case allows the features of defects (type of planar imperfections, displacement vector) to be determined. In most cases, this directly brings information about the ordering processes. This point can be illustrated through two typical examples chosen in molybdenum and tungsten hemicarbides.

2.2.1. *δ-Fringes at Domain Boundaries in ζ-Mo_2C* (figure 2). In Mo_2C, the establishment of the orthorhombic ζ-Fe_2N type structure (see [11]) produces 3 variants sharing the same **a** axis, as seen from figure 2a).

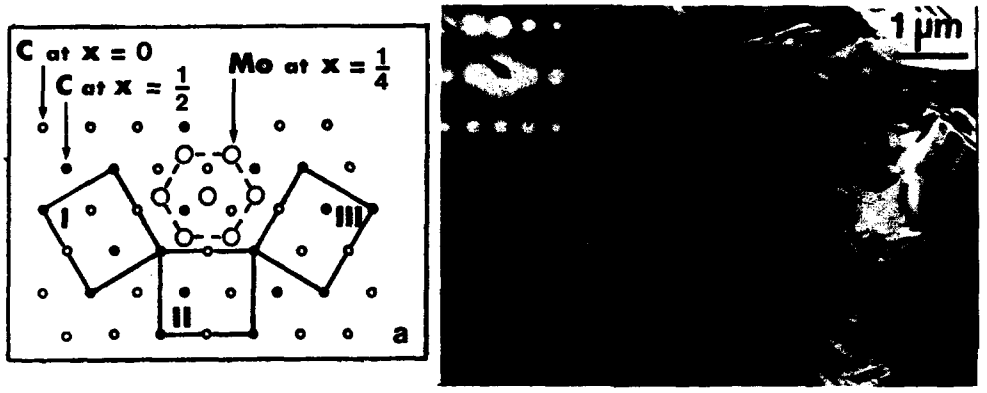

Figure 2. ordered microstructure in ζ-Mo_2C. a) : schema of the 3 variants I, II, III sharing the same a_ζ (c_{hcp}) axis -perpendicular to the plane of projection. b) : dark field image of domains in a single grain of Mo_2C (operating reflection $g = 102_\zeta$ as indicated by an arrow in the $[010]_\zeta$ diffraction pattern).

Intersection of domains growing with these 3 orientations are imaged by fringes (see figure 2b)), the contrast of which is characteristic of δ-fringes (i.e. pseudo-symmetric "black-white" contrast in dark field [35]). *δ-fringes* are due to a slight misfit in interatomic distances producing the diffracted beam used for imaging ; in the present case, this is due to a small elongation of the unit cell along the **b** axis (or compression along the **c** axis). Such observations bring a direct confirmation of this orthorhombic distortion, previously identified through X-ray diffraction experiments [36].

2.2.2. *Antiphase Boundaries in ε'-W_2C* (figure 3). The most common ordered form of W_2C at room temperature is based on the ε-Fe_2N type structure (see [11]). In this compound, basal $a/3<11\bar{2}0>_{hcp}$ dislocations are observed, which have to be considered as imperfect $a/3<1\bar{1}00>_\varepsilon$ defects in the ordered phase ; thus, they are systematically followed by a planar antiphase boundary (APB), as shown in figure 3a). The interesting feature is that these APBs, originally produced in the basal (glide) plane, deviate systematically to become parallel to the **c** axis. This particular behavior can be discussed in terms of pair interactions ; it can be stated that 'ideal' ordering in hexagonal hemicarbides involves 'pseudo-rigid" [0001] interstitial columns made of a regular sequence : carbon-vacancy-carbon-vacancy-....., with almost no carbon-carbon pairs (see [11]) ; in the diagram of figure 3b), it is easily seen that the basal configuration of the APB produces such undesirable carbon-carbon pairs (along the **c** axis), which are geometrically avoided if the APB is perpendicular to the (0001) plane. Thus, the TEM evidence for such an APB configuration brings an elegant confirmation of this fundamental property.

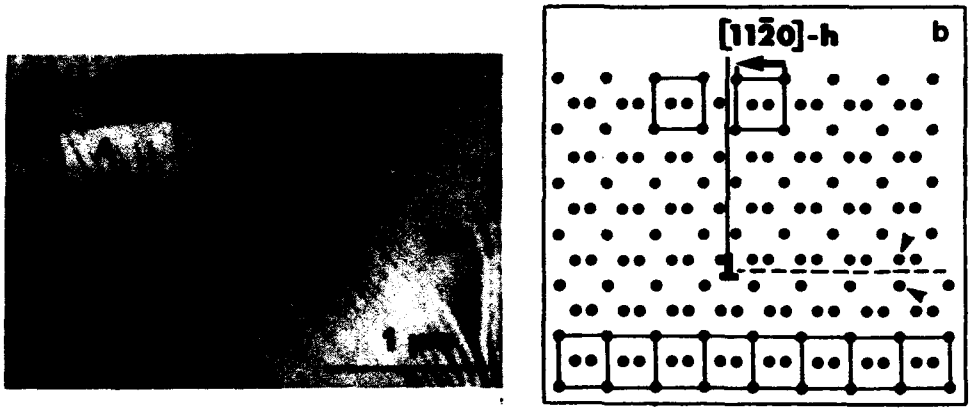

Figure 3. APBs in ordered ε'-W_2C. a) : basal edge dislocation (A) followed by an APB (arrows) ; the antiphase defect deviates out of the basal plane to become parallel to the c axis, as most of other APBs. b) : $[1100]_{hcp}$ section of the carbon sublattice (ε-structure) ; the shear $b=a/3[1120]_{hcp}$ produces an APB, which creates carbon-carbon pairs (arrows) in its basal configuration.

2.3. APPLICABILITY OF HREM

In any TEM study, one of the dreams of the investigators is to be able to see directly the atomic structure through observations at High Resolution. In case of carbides, this may be of a great help for confirming the ordered phases and for characterizing defective microstructures which cannot be completely understood by CTEM work.

Although modern microscopes allow now interatomic distances below 0.2 nm to be resolved, the resolution limit is not a drastic criterium from the point of view of ordering problems in carbides. In most cases, it is possible to produce "superstructure images" [37] by just including superlattice reflections in the objective aperture ; the distances to be resolved correspond to that between vacancy-containing carbon columns (VCCC), which can be imaged as white dots on a dark background. Interpretation of observed contrasts can be ascertained through simulation of images under exact experimental conditions of defocus, crystal thickness and aberation factors [38] ; such calculations can be conducted with adequate programs (in the examples reported here, SHRLI [39] and NCEMSS [40] packages), mainly based on the "multislice" formulation of the dynamical theory [41]. Figure 4 gives some examples in various carbides ; in some of these micrographs, no direct information can be obtained on the metallic sublattice which cannot be successfully revealed in this "superstructure imaging" mode.

Recent studies performed by HREM are :

.characterization of the V_6C_5 ordered monoclinic structure (see next subsection), the related long-period structure (identified by Hiraga [21]) and the defective microstructure in partially ordered compounds [38, 43]

.imaging of Nb_6C_5 ordered precipitates in $NbC_{\sim 0.9}$ single crystals [26]

.refinement of the ε'-W_2C form [11, 44].

Further details concerning the M_6C_5 surstructure(s) are given below.

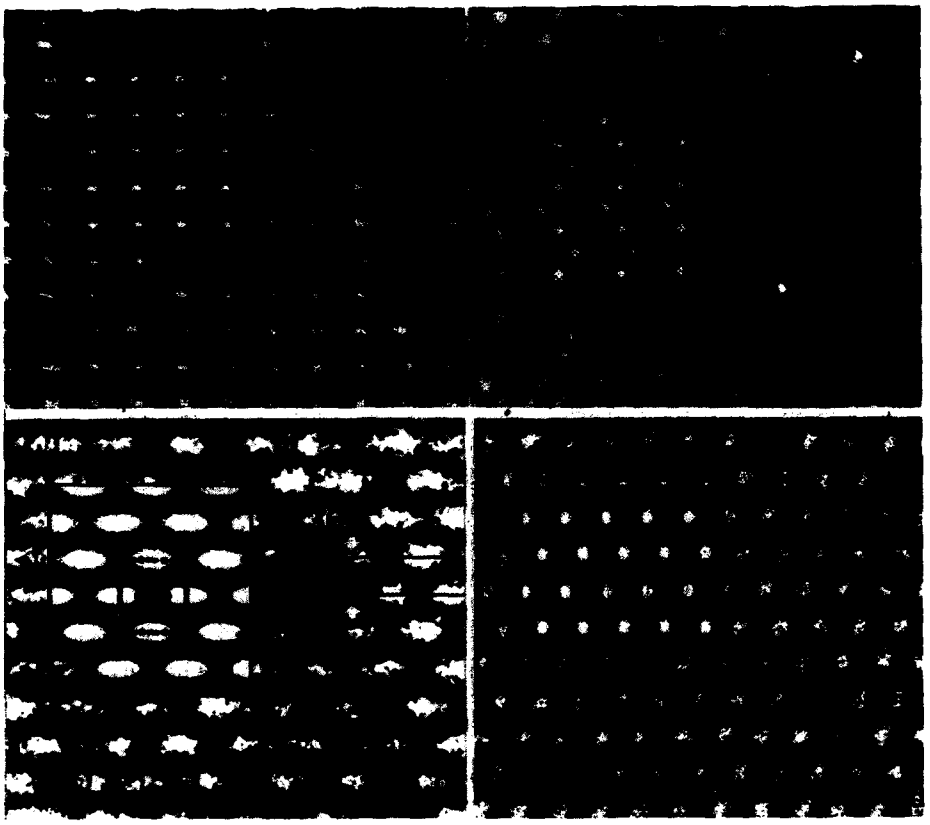

Figure 4. HREM imaging of ordered carbides (HR microscope Jeol 200 CX in a top-entry configuration). a) : V_8C_7 observed along a $[112]_{fcc}$ azimuth ; the superimposed multislice simulation has been calculated for a thickness t of 25 nm at a defocus Δf equal to -34 nm (≈Scherzer defocus) from the model of Guerin and De Novion [42]. This calculation provides a good match of the experimental micrograph, where white dots image VCCC (see the inset projected structure ; the bright spots correspond to a fraction of 1/4 of vacancies, the weak ones, 1/16). b) : same structure as viewed along a $[110]_{fcc}$ azimuth ; the superstructure is revealed through the imaging of VCCC as white dots (t = 15 nm, Δf = -40 nm). c) : ε'-W_2C observed along the $[1\bar{1}00]_{hcp}$ azimuth ; carbon columns are not fully resolved, but the experimental image is undoubtely related to the ε' structure (see inset simulation calculated from the ε' model -see [11]- with t = 5 nm and Δf = -50 nm -exact Scherzer defocus- [16]). d) : same structure as viewed along the $[11\bar{2}0]_{hcp}$ azimuth ; white dots image tungsten columns, and carbon columns do not produce any appreciable contrast (t = 3 nm, Δf = -130 nm).

2.4. THE M_6C_5-BASED SUPERSTRUCTURES

Figure 5 shows the 3 models that have been proposed for the M_6C_5 ordered structure in vanadium and niobium monocarbides. Although these cells are of different symmetry and appear to be easily discernable, it must be said that they are very similar. They all consist in regular stackings of $(111)_{fcc}$ carbon planes alternatively fully occupied and partially vacant (i.e. containing 1/3 of vacancies) ; consequently, they have very similar reciprocal lattices, and $<11\bar{2}>_{fcc}$ sections are the most differenciated. HR micrographs taken along these directions allow completely vacant carbon columns -shown in figure 5- to be easily resolved [38].

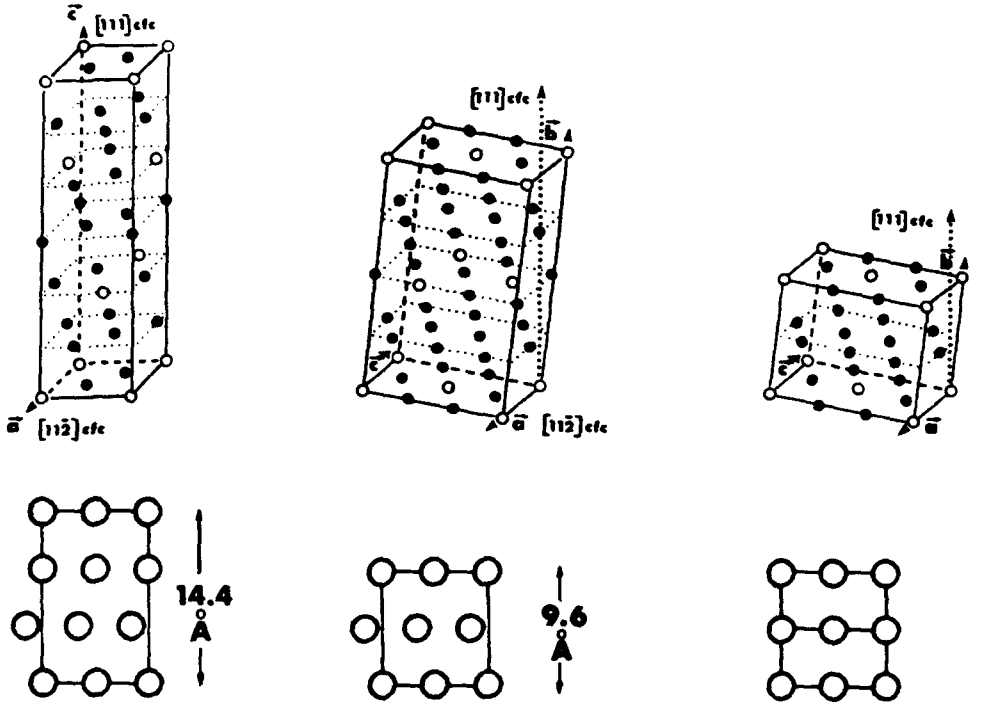

Figure 5. ordered M_6C_5 structures proposed throughout the literature (metallic atoms have been omitted for clarity). a) : hexagonal 'V' cell [17] (space group P31, a = 0.509, c = 1.44 nm in $VC_{\sim 0.84}$). b) : monoclinic 'B' cell [19] (space group B2/m, a = 0.509, b = 1.018, c = 0.882 nm, γ = 109.47° in $VC_{\sim 0.84}$). c) : monoclinic 'G' cell [45] (space group B2/m, a = b = 0.546, c = 0.946 nm, γ = 109.47° in $NbC_{\sim 0.83}$). Lower diagrams show the $[11\bar{2}]_{fcc} = [100]_{superstructure}$ projection of carbon vacancy columns.

Up to now, only the monoclinic 'B' form has been unambiguously identified by TEM in V_6C_5 [19, 21, 23] or Nb_6C_5 [16, 25]. When not sufficiently annealed, the ordered domains contain a very high density of stacking faults which divide the crystal into numerous slabs as shown in figure 6. The diffraction data obtained on such a microstructure, either by neutron

diffraction (Nb_6C_5 [45-47]) or by electron diffraction in the SAD mode (V_6C_5 [17, 18] and Nb_6C_5 [24]) cannot be considered as convincing for a correct identification of a unique superstructure.

High Resolution observations show that the 'B' form is the unique superstructure actually detectable in as-grown V_6C_5 single crystals (see figures 7 to 9). However, fluctuations in the positions of vacancies may produce diffraction patterns which suggest the 'G' or 'V' forms (figures 8 and 9 respectively), although these structures are confirmed by the HR micrographs (see figure captions for comments). These observations give evidence for a partially (dis)ordered structure based on a regular stacking of $(111)_{fcc}$ carbon planes, alternatively fully occupied and partly vacant (such as in perfectly ordered forms depicted in figure 5) ; this defective structure closely resembles that identified by X-ray diffraction in as-grown V_6C_5 single crystals by Hauck et al [48].

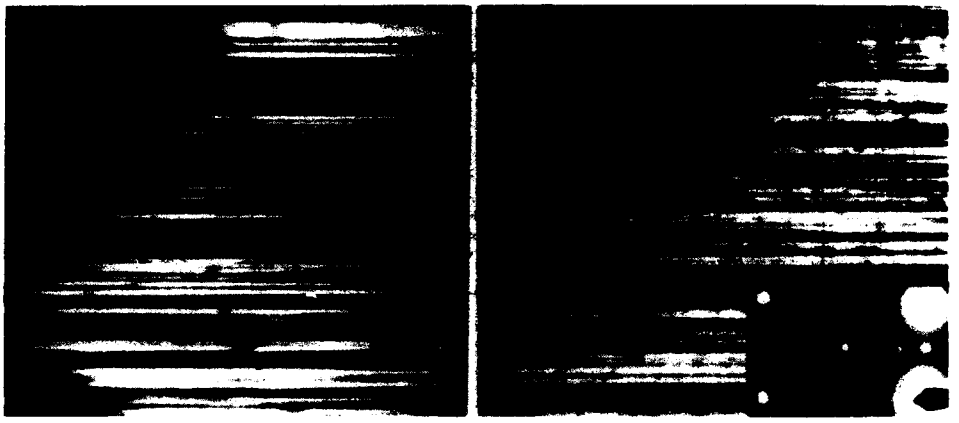

Figure 6. Faulted microstructure within a single domain of M_6C_5 ordered compounds. a) : V_6C_5 crystal annealed during 3 hours at 1150°C. b) : Nb_6C_5 crystal annealed during 15 days at 960°C.

In Nb_6C_5 (annealed just below the order-disorder transition and slowly cooled to room temperature), the prominent ordered form remains the 'B' one, but other sequences exist, which correspond to the 'V' form and to a new longer superstructure (see figure 10 and caption). It must be noticed that the partially ordered stacking of partially filled $(111)_{fcc}$ carbon planes leads to zig-zag sequences of $[112]_{fcc}$ VCCC (i.e. white dots in figure 10) which never correspond to the arrangements expected for the 'G' phase (see figure 5) ; this result is in disagreement with the conclusions drawn out by Gusev and Rempel [45], who claimed to identify the 'G' form in Nb_6C_5 single crystals annealed under similar conditions.

These contradicting results may justify further work on both V_6C_5 and Nb_6C_5, and it would be of the greatest interest to perform simultaneous neutron diffraction and HREM experiments for characterizing the same sample. Nevertheless, the neutron technique will average the information on

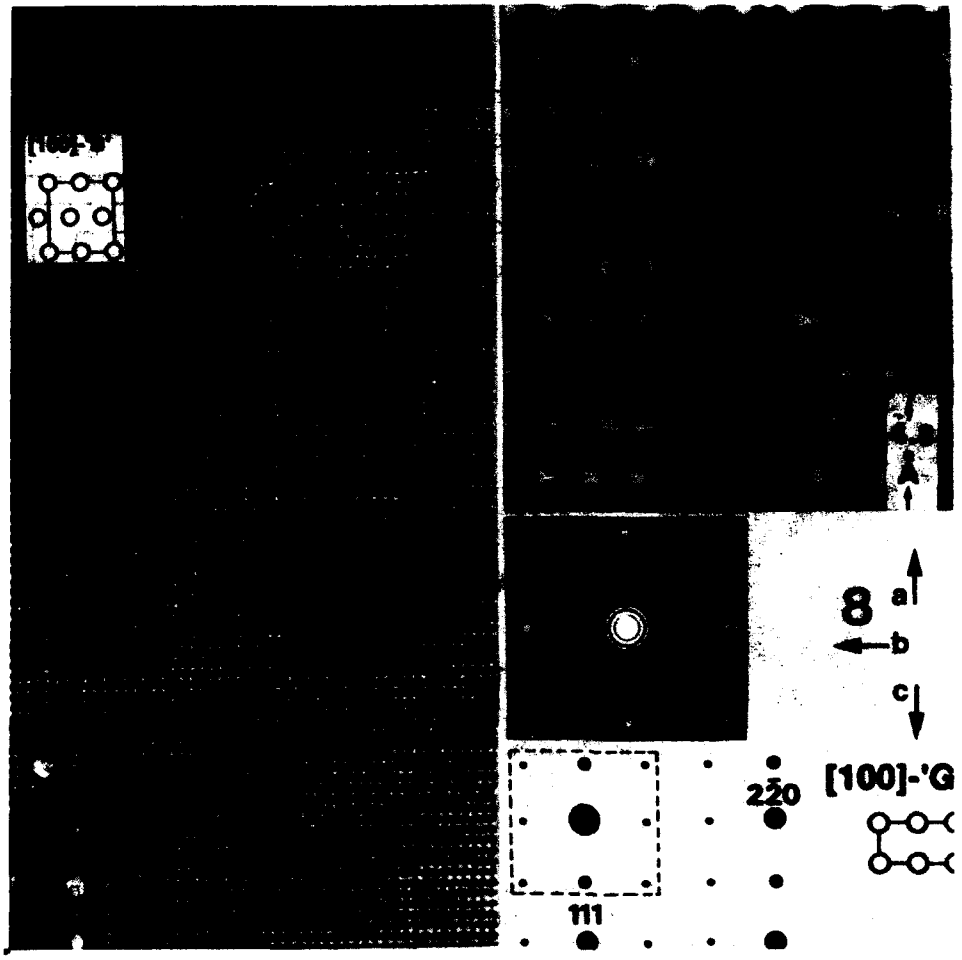

Figure 7 (left). HR $[112]_{fcc}$ micrograph of an as-grown V_6C_5 crystal. An ordered lamellae ($[100]_B$ as indicated) is seen at the top of the picture. Regions 1 and 2 are detailled in figures 8 and 9 respectively.

Figure 8 (right). Analysis of region 1 from figure 7. a) : enlargement showing VCCC (white dots) ; vertical dotted lines reveal that VCCC are not perfectly aligned. b) : diffractogram from a) ; the pattern is similar to the expected $[112]_{fcc}$ reciprocal lattice section of the 'G' phase (see in c)). c) : $[112]_{fcc}$ projections of the monoclinic 'G' structure ; although the diffraction pattern is like that shown in b) (compare the underline frame), there is no one-to-one correspondence between exact VCCC positions and white dots in a).

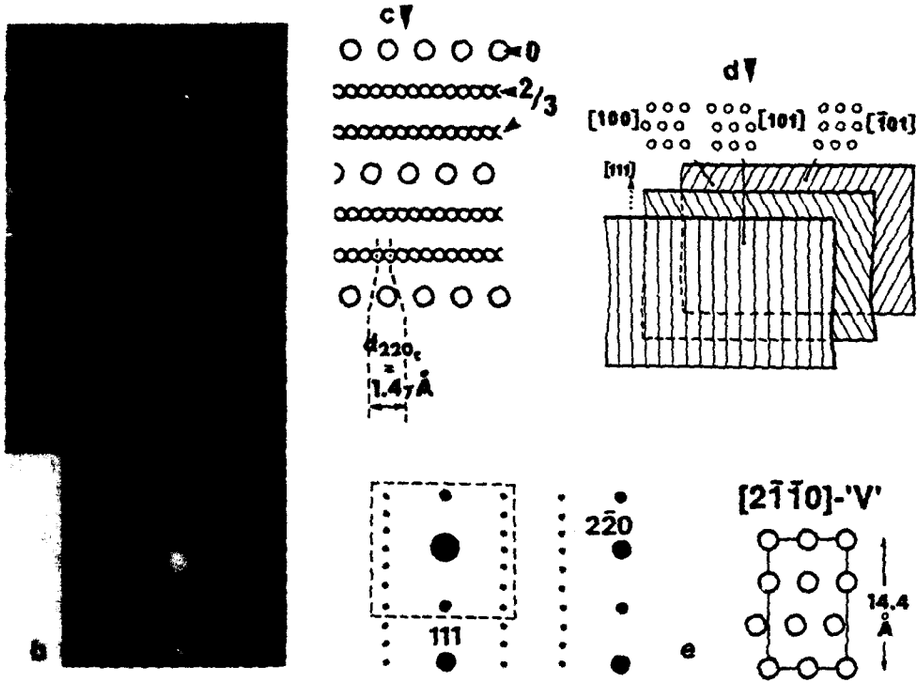

Figure 9. Analysis of region 2 from figure 7. a) : enlargement showing that white dots (i.e. VCCC) are sharply defined every three planes (arrows). b) : diffractogram produced by a). c) : diagram showing VCCC when the 3 variants $[100]_B$, $[101]_B$ and $[\bar{1}01]_B$ are superimposed as shown in d) (numbers refer to carbon occupancy factor) ; the periodicity revealed in a) is reproduced. d) : schema explaining the configuration shown in c). e) : expected $[11\bar{2}]_{fcc}$ projections of the hexagonal 'V' structure ; the diffraction pattern is similar to that reported in b) (compare the underline frame) ; however, the VCCC sublattice is not unambiguously resolved in the experimental image (a).

the whole specimen, contrary to the TEM technique, which is adapted for studying single ordered domains, several orders of magnitude smaller than the crystal itself.

3. Irradiation Processes

3.1. INTRODUCTION

Interest for irradiation studies in the case of metallic carbides arises from several reasons :

.transition metal carbides are binary compounds with constituents of very different atomic weights ; by choosing an incident beam of appropriate energy, it is then possible to study separately the different types of radiation-induced point defects.

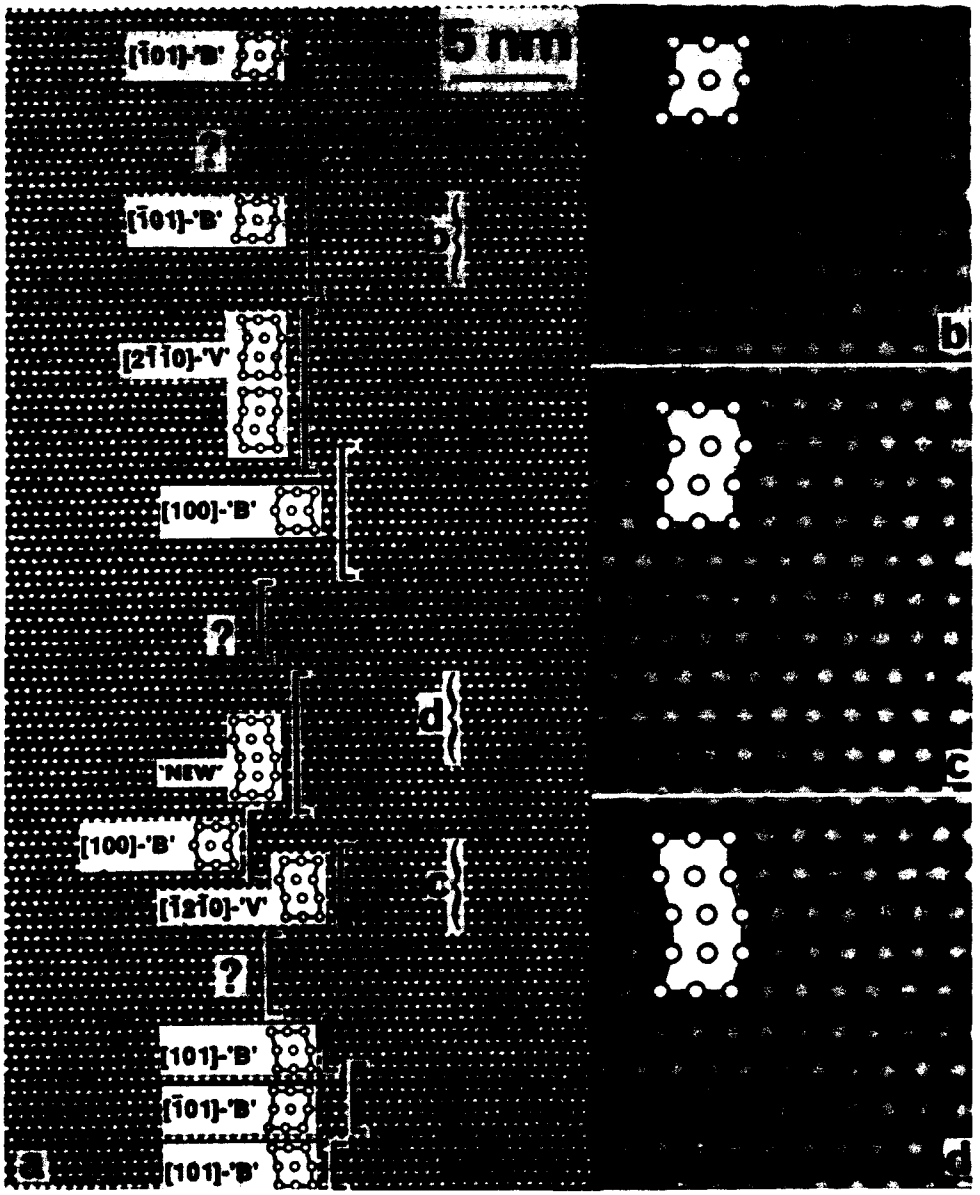

Figure 10. HR analysis of an imperfectly ordered Nb_6C_5 crystal observed along $[11\bar{2}]_{fcc}$; VCCC appear as white dots. a) : low magnification image showing a succession of lamellae with different orientations and structures (the symbol '?' designates severely faulted areas). Frames labelled b to d are enlarged in fig. 10b) to 10d) respectively. b) : detail showing the predominant 'B' form. c) : evidence for the hexagonal 'V' phase. d) : possible evidence for a 'new' stable stacking sequence of vacancy-containing $(111)_{fcc}$ carbon planes.

.due to their ability to accomodate a large number of pre-existing point defects under the form of carbon vacancies in substoichiometric compounds, metallic carbides are good candidates for fundamental studies where the concentration of one kind of point defects is externally varied and controlled.

.refractory carbides are of technological interest for application in the nuclear industry, since uranium carbide is a potential reactor fuel, and superconducting transition metal carbides, such as TaC or NbC (with $T_c \approx 10$ K), could be considered for use in the superconducting magnets of fusion reactors.

It is obviously not the purpose of the present paper to describe the complete literature concerning irradiation studies in metallic carbides (significant information can be found in ref. [49] -see also the bibliography cited by these authors for a survey of past works-). Nevertheless, the Transmission Electron Microscope is an adequate instrument for conducting irradiation experiments on most materials ; in particular, it allows the damage to be looked at in real time, and thus enabling created defects to be observed at a reasonnable resolution. Therefore, this elegant way has been frequently used for studying a variety of carbides as reviewed next.

3.2. SPECIFIC TEM IRRADIATION STUDIES OF TRANSITION METAL CARBIDES

When subjected to electronic bombardement of incident energy E_0 (in MeV), target atoms (of atomic weight M) receive a certain amount of energy through elastic collisions with electrons ; the maximal transferrable energy E_m is given (in eV) by the relation :

$$E_m = \frac{2148\, E_0\, (E_0+1.022)}{M} \qquad (1)$$

In the case of carbon atoms, E_m is respectively equal to 20 and 44 eV for 100 and 200 kV electrons.

Target atoms are displaced if E_m is greater that the threshold energy E_d. TEM determination of E_d for carbon in carbides was mainly accomplished following two different procedures : (1) : prediction of the disordering rate of the carbon superlattice in L.R.O. structures (V_6C_5 [50], W_2C [16]) ; (2) : occurence of some damage when varying the accelerating voltage (onset of disordering in V_6C_5 [50], detection of defect clusters -probably free carbon interstitial loops- in TaC [51]).

Values for E_d range between approximatively 25 and 50 eV for typical atomic species comprising carbon (as determined from irradiation experiments on graphite samples). Surprisingly, the threshold displacement energy for carbon appears to be considerably lower in V_6C_5 (5.4 eV [50]), W_2C (about 3 eV [16]) and probably TiC (much lower than 20 eV [14]). Such low values strongly support the hypothesis that they correspond to the transfer of carbon atoms into neighbouring vacant sites, owing to the presence of constitutional vacancies in non-stoichiometric carbides ; indeed, carbon migration energies are of the same order of magnitude as threshold energies for most carbides.

Controversial values were obtained on TaC_{1-x} compounds (12±4 eV in $TaC_{0.99}$ [52], 28±6 eV in $TaC_{\sim 1}$ and $TaC_{0.8}$ [53] -both previous studies were performed on a Van de Graff electron accelerator- and 23.2±1.1 eV in $TaC_{0.99}$ [51]. Comparison of these values with that previously mentioned suggest different damages in tantalum carbides : in fact, complex defects associated with carbon interstitials are suspected, although the stability of (clusters of) carbon interstitials remains somewhat puzzling in the case of the $TaC_{0.8}$ crystal where 20% of vacancies are present on the carbon sublattice [49].

Further fundamental and systematic irradiation studies would certainly be useful for most carbides. In this perspective, the use of TEM could allow crystallographic effects, untackled up to now, to be taken into account (for example, the variation of the threshold energy with the irradiation azimuth). Also, HVEM would be appreciated for studying defects affecting the metallic sublattice.

3.3. OTHER IRRADIATION EFFECTS DURING TEM OBSERVATIONS

Other interesting effects have been shown to occur during TEM irradiation experiments on metallic carbides ; they are briefly reviewed below :

.induced-disordering in ordered Mo_2C [16], V_8C_7 and $(Ti,Mo)C_x$ [54]

.void formation in deformed $TiC_{0.93}$ thin foils heated at 800°C and irradiated at the same time in a 100 kV microscope [55].

.decarburization of $TiC_{0.93}$ during electron irradiation at 100 kV [14]. This spectacular effect is the consequence of radiation-enhanced carbon diffusion ; carbon atoms apparently diffuse to the foil surface, thereby leaving an increasingly substoichiometric composition in the irradiated area : simultaneous radiation-induced ordering and disordering of the $TiC_{0.5}$ superstructure support this result.

As seen from the above experiments, radiation damage can be volontarly produced in carbides through controlled electron bombardment of thin foils during TEM observations. However, the facility for displacing carbon atoms at common low voltages may leads to undesirable effects which affect the quality of observations. A typical example concerns High Resolution studies of LRO structures (see §2.3 and 4). Resolution of VCCC in most orientations becomes impossible after a few minutes in both V_6C_5 [23] and W_2C, due to radiation-induced disordering ; in V_8C_7, the effect is more drastic, and the HR dots contrast vanishes after less than one minute.

A last effect worth being mentioned is the spectacular spreading of stacking faults in W_2C after prolonged exposures to a condensed electron beam [56]. In tungsten hemicarbide, basal dislocations $\mathbf{a}/3\langle 11\bar{2}0\rangle$ appear to be dissociated in a glissile way (see § 4.3 and 4). When irradiated at 200 kV with beam flux J of about 10^{19} $e^{-}cm^{-2}s^{-1}$, rather severe damage can be produced in the carbon sublattice, since the total number of displacements per atom (dpa) τ, given by :

$$\tau = \sigma_{tot} J t \qquad (2)$$

can be of the order of 10 for irradiation time t of about one hour, with σ_{tot} (total cross-section for carbon displacement) equal to 310 barns at 200 kV (extrapolated from an estimation at 1 MV [16]). Under such conditions, the

carbon sublattice is severely perturbed, and partial dislocations, initially closely spaced at equilibrium, become widely separated after irradiation (see figure 11). This effect has been discussed in terms of decarburization of the thin foil and segregation phenomena near the dislocation [16]. Since only carbon atoms are displaced at 200 kV (the maximal energy transferred by electrons to tungsten atoms is 2.8 eV -from eq. (1)- is much lower than the expected threshold energy $E_d \approx 48$ eV [16]), the role of carbon atoms in the motion of dislocations is clearly pointed out in W_2C. Moreover, it has been shown that undissociated dislocations remain unaffected during irradiation experiments [57] ; this has allowed jogs or recombined segments to be unambiguously visualized, as reported next (§ 4.3). Such features show that appreciable advantages can be taken from irradiation damage for a fine characterization of the dislocation structure.

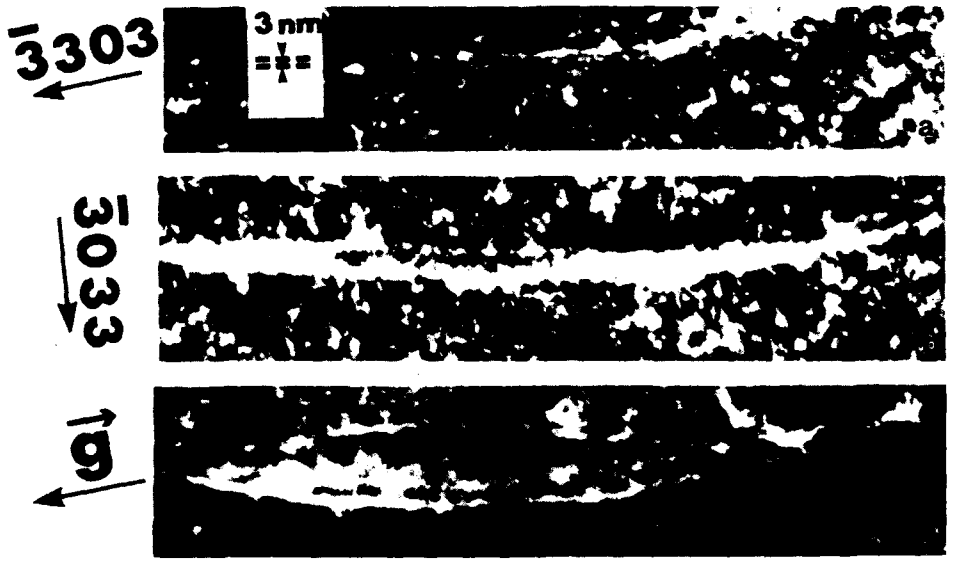

Figure 11. Irradiation sequence of a screw dislocation in W_2C. a) : before irradiation (note the partials separation, about 3 nm at equilibrium). b) : same defect irradiated during 0.5 hour. c) : idem, after 1 hour (from [56]).

4. Dislocation Problems

4.1. CHARACTERIZATION OF GENERAL DEFORMATION MICROSTRUCTURES

Mechanical properties of cubic monocarbides (TiC, ZrC, VC, NbC, TaC) and hexagonal hemicarbides (W_2C) have been extensively studied during the last three decades (see general works [3, 5, 6] plus dedicated reviews [58-61]).
Brittle at low temperatures, carbides show reasonable ductility above 0.3 T_m nominally. From this temperature, plasticity mechanisms resemble that of pure metals of comparable close-packed structure ; there is a fundamental interest to pursue research on carbides in this field, since it will be shown here that elementary dislocation processes, sometimes difficult to isolate in

classical materials (dissociation and motion -glide or climb- of dissociated defects) can be more easily identified in metallic carbides.

TEM appears to be the required complementary technique to mechanical testing, since it allows dislocations to be directly observed and characterized. Then, deformation processes, suggested by the results of the mechanical approach, can be confirmed or refined.

As a first step, general microstructures have to be observed. When well-organized dislocation arrangements are produced, e.g. after significant deformation (such as in creep experiments), alternative techniques can be employed : observation of slip traces (ZrC [62], TiC [63]), etch-pits methods (TiC [64], VC [65], NbC [66]) or X-ray topography for single crystals. Micro-indentation and hardness anisotropy measurements, combined with previous techniques and/or TEM, can also bring interesting information about dislocation motion and slip planes below the britlle-to-ductile transition (see general works [60, 67-69] and specific studies on TiC [6, 70], HfC and TaC [67], NbC [23], TaC [71], Mo_2C [72] and W_2C [73]) or even at elevated temperatures (TiC [74], ZrC and TaC [75], VC and NbC [76]). However, TEM remains the most powerful tool, since it allows an easiest geometrical characterization of Burgers vectors **b**, dislocation direction **u** and glide or climb planes to be made by stereographic analysis. Moreover, intermediate or High Voltage (HV) instruments make it possible to observe reasonnably thick foils, which gives a good idea of the bulk organization of dislocations. Figure 12 shows typical observations made at 200 and 1000 kV (a) and b) respectively).

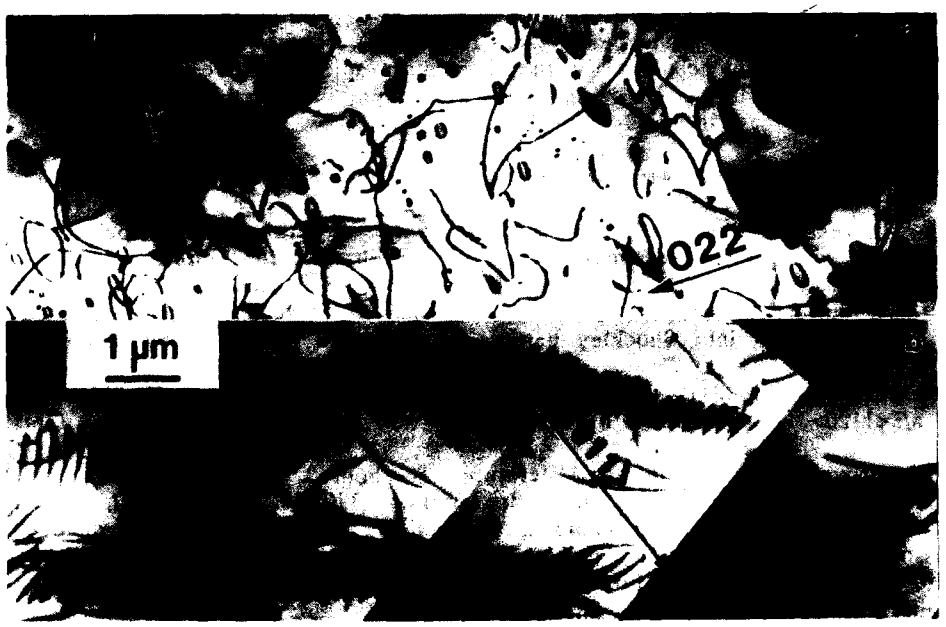

Figure 12. General deformation microstructures as revealed by TEM. a) : V_8C_7, after compression testing at 1150°C (0.49 T_m), ε = 1% (200 kV, from [16]). b) : W_2C, after plastic deformation of ≈ 1% by 3-point bending at 1750°C (1 MV - Cameca microscope, CEN Grenoble, F-, from [77]).

In the first case, the choice of the compression axis $[15\ 4\ 34]_{fcc}$ in a V_8C_7 single crystal has allowed a unique glide system, i. e. $[011](1\bar{1}1)$ to be activated. Consequently, all defects have the same Burgers vector, and no dislocation reactions are produced as can be seen on the representative 200 kV micrograph in figure 11a). Moreover, the presence of dislocation dipoles proves that local cross-slip has occured, which explains such dipolar configurations according to the mechanism proposed by Tetelman [78]. Finally, the presence of dislocation loops is a clear indication that pipe-diffusion has occured. TEM Evidence for similar dislocation mechanisms has been reported in TiC [63, 64, 79], ZrC [62], NbC [80] and TaC [81].

In the second case, i.e. W_2C, HVEM has allowed climb processes to be clearly proved through the identification of cell formation in polycrystals deformed less than 1% above 1750°C (0.66 T_m ; see [77] for further details). HVEM observations of creep microstructures have also been reported in NbC_{1-x} [80].

4.2. DISLOCATIONS IN LRO SURSTRUCTURES

Dealing with dislocations in ordered compounds raises questions about superdislocations and hardening or glide processes associated with ordering. As illustrated by figure 3, usual perfect dislocations in the hcp or fcc metallic sublattice of hemi- or monocarbides produce APBs in the ordered carbon sublattice. It must be accepted that the antiphase energy is very small, since no superdislocation has been observed in any of these compounds. Moreover, APBs trailed by perfect dislocations have a wavy form [12, 18] and rapidly deviate out of the glide plane (see figure 3a). These features indicate that APBs do not influence directly the dislocation microstructure. It will however be seen that ordering probably plays an important role in the deformation mechanism, at least in M_6C_5 compounds (cf. §4.4).

4.3. GLIDE MODELS IN CARBIDES

An interesting question concerns the core structure of dislocations in carbides with a close-packed structure such as the cubic mono- and hexagonal hemicarbides. As for pure metals with corresponding fcc or hcp lattices, perfect dislocations $a/2<1\bar{1}0>$ and $a/3<11\bar{2}0>$ respectively are thought to be dissociated into Shockley partials according to the following reactions :

$a/2<1\bar{1}0> \text{ --- } a/6<2\bar{1}\bar{1}> + a/6<1\bar{2}1>$ in Na-Cl type monocarbides (3)
$a/3<11\bar{2}0> \text{ --- } a/3<10\bar{1}0> + a/3<01\bar{1}0>$ in L'3 type hemicarbides (3bis)

Controversies exist in the literature about the motion of gliding dislocations: is it controlled by the lattice friction (TiC [82], NbC [61]), cross-slip (TiC [63]) or by a more complex mechanism involving a further dislocation dissociation and requiring the carbon diffusion (TiC [82, 83], ZrC [84], NbC [66], TaC [81], W_2C [85]) ; further discussions of these conflicting results can be found in reviews previously mentioned in §4.1.

In the latter model (so-called "synchroshear" mechanism), a zonal dissociation is proposed on the basis of geometrical considerations [86] : because of the insertion of close-packed carbon layers between metallic ones, each of the previous partial dislocations is re-dissociated on adjacent carbon and metal planes (see figure 13).

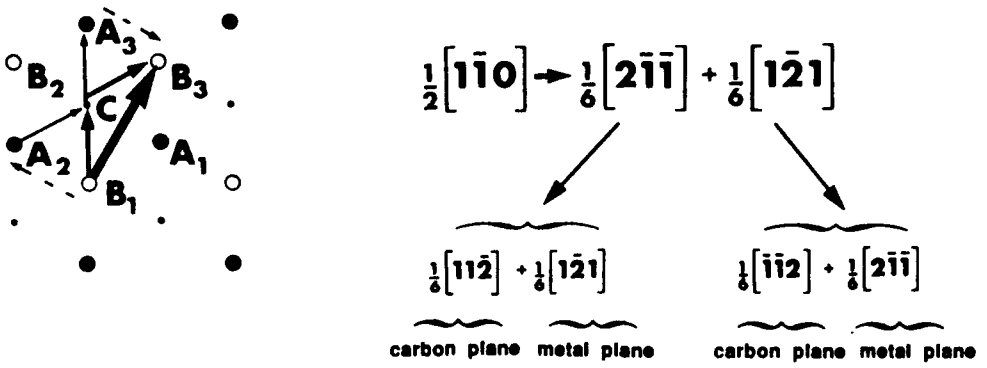

Figure 13 . Schematic representation of the "synchro-shear" mechanism in a cubic monocarbide (the model has also been adapted to hexagonal hemicarbides [85]) ; open and dark large circles represent metallic atoms respectively above and below the carbon plane (small circles show carbon atoms). The perfect dislocation B_1B_3 is dissociated into partials B_1C and CB_3 which are themselves splitted into B_1A_2 and A_2C, and CA_3 and A_3B_3 respectively (dashed arrows are for shears in the carbon plane).

Furthermore, an interesting description of this model has been given by Martin et al [81] in the case of $TaC_{\sim 1}$ polycrystals. From their thermodynamical analysis, these authors propose that the carbon concentration at the core of dislocations is less than that of the perfect crystal. Chemical analysis by Electron Energy Loss Spectroscopy (EELS) in $TaC_{0.78}$ brings an apparent credit to this result [87], as demonstrated in figure 14[1].
In such a sub-stoichiometric carbide, wide intrinsic stacking faults occur, which seem to be nucleation sites for further subcarbides, M_4C_3, M_3C_2 or M_2C

[1]Applications of EELS to carbides needs to be further documented, since this technique is well suited to the study of such a class of compounds, being sensitive to light elements ; from works by Williams and co-workers, the following major points can be emphasized :
. EELS can be made quantitative for estimation of carbon/metal ratio in individual crystallites of carbides (V_6C_5 [88], TiC [89]. However, such experiments are delicate to perform, since both experimental and theoretical difficulties have to be overcome for obtaining reliable results on such a light element (e.g., on the one hand, optimization of acquiring conditions -count rate, spatial or energy resolution-, control of contamination problems while analyzing, film thickness measurements ; on the other hand, theoretical frame for analysing the data -single or multiple-scattering assumption, sources for ionization cross-sections- and numerical procedures for profile treatment deconvolution, background estimation). Moreover, the need for a dedicated Scanning TE microscope has to be emphasized as well ; it may allow a reasonnably high spatial resolution to be attained, ~ 2 nm or better [90].
. other EELS techniques developped parallely to K/L edge identification, e.g. EXELFS, can also be used for microstructural characterization of carbides (see [91]).

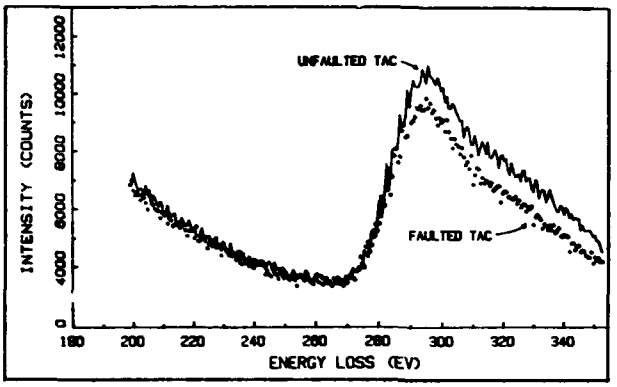

Figure 14. EELS profiles from unfaulted and faulted regions in a $TaC_{0.78}$ single crystal (from [87]) ; the lower carbon content in the stacking fault is revealed by the smaller carbon edge.

(see [92] and [93, 94] for V-C and Ta-C systems respectively). The stacking sequence of (111) planes :

$$A\,\gamma\,B\,\alpha\,C\,\beta\,A\,\gamma\,B\,\alpha\,C\,\beta\,A\,\gamma \qquad (4)$$

A, B, C : metallic planes ; α, β, γ : carbon (plus vacancy) planes)

is modified by the presence of a stacking fault in the following way :

$$A\,\gamma\,B\,\alpha\,C\,\beta\,A\,\gamma\,C\,\beta\,A\,\gamma\,B\,\alpha \qquad (5)$$

The sequence : A γ C correspond to tetrahedrally coordinated carbon atoms, which is unfavorable in transition metal carbides [4] ; an additional shear (corresponding to the situation described in figure 13) leads to :

$$A\,\gamma\,B\,\alpha\,C\,\beta\,A\,\beta\,C\,\beta\,A\,\gamma\,B\,\alpha \qquad (6)$$

It is seen here that the carbon sublattice adopts a simple hexagonal configuration $\beta\ \beta\ \beta$, which can easily be rearranged as the exact α-M_2C cell by condensing vacancies in the central carbon layer :

$$A\,\gamma\,B\,\alpha\,C\,\beta\,A\ \ C\,\beta\,A\,\gamma\,B\,\alpha \qquad (7)$$

α-M_2C is the stable low temperature form of Ta_2C (see [11]), and the proposed model is reasonnable ; moreover, it is supported by the work of Allison et al [87], who measured a carbon content consistent with the composition Ta_2C within stacking faults in $TaC_{0.78}$.

Since the stacking fault energy γ varies continuously with carbon content in TaC_{1-x} (i.e. γ increases when x decreases [81]), the mechanism under consideration in $TaC_{0.78}$ may occur at the core of narrowly dissociated dislocations in the nearly stoichiometric monocarbide [95]. However, a difference exists between substoichiometric and stoichiometric carbides : it is

easy to understand that the coalescence of vacancies on $(111)_{fcc}$ carbon planes in largely substoichiometric compounds such as $TaC_{0.78}$ decreases the free energy of the faulted crystal, since it leads to the nucleation of the stable Ta_2C phase ; this argument cannot be directly extended to the case of $TaC_{\sim 1}$ crystals, since the carbon content is too far from that of the M_2C composition to explain the spontaneous formation of a M_2C layer within the stacking fault in the stoichiometric carbide. The argument developed by Martin et al [81], i.e. the carbon sites are in compression at dislocation cores, might explain a depletion of carbon within defects in $TaC_{\sim 1}$.

Returning to the "synchroshear" mechanism (figure 13), it must be precised that shears in the carbon plane are more conveniently described in terms of a diffusion mechanism [58], since the activation energy for glide is frequently comparable to a diffusion energy (either bulk or pipe-diffusion) for carbon in the corresponding carbide (see, for example, table I.5 in [16]). Thus, figure 13 and equation (7) can be considered as two descriptions of the same mechanism that could be called a "shear-diffusion" mechanism.

4.4. DISLOCATION DISSOCIATION : WBDF AND HR TECHNIQUES

High Resolution observations are required in order to characterize the core of dislocations at the finest scale. Chemical analysis with a high spatial resolution (e.g. by the EELS method) have already been mentioned in the previous sub-section ; we will concentrate our attention on imaging techniques, i.e. Weak Beam Dark Field (WBDF) and High Resolution Lattice Imaging techniques.

4.4.1. *WBDF Observations*. The WBDF technique [96] allows dislocations to be observed at a resolution of about 1 nm. Results obtained by this technique are summarized below :

.a glissile dissociation between 3 and 5 nm has been resolved in $TaC_{\sim 1}$ polycrystals [97] ; this result has however been criticized by Davis [61].

.an apparent dissociation of a screw dislocation has been observed in TiC [98] ; this result needs however to be verified, since the observation remains unique and not ascertained from the point of view of the diffracting conditions.

.a systematic dissociation of basal dislocations occurs in the hexagonal hemicarbide W_2C [56, 85], as shown from figure 15. In samples deformed above 1750°C, viz. $0.66T_m$, advantage can be taken of the irradiation effect mentionned in §3.3 to reveal undissociated portions and jogs on extended dislocations, as shown in figure 16. Other typical configurations, such as an inversion of the partials sequence at jogs, have been reported previously [99] ; all these defects have been consistently interpreted as the evidence of deformation climb of dissociated basal dislocations [16].

.in crept NbC_{1-x} single crystals, Chevacharoenkul and Davis [80] claim to fail to reveal any dislocation splitting (however, no WB micrograph is reported in their work). The same conclusion has been actually established in similar but undeformed $NbC_{\sim 0.9}$ single crystals [26].

.in deformed ordered V_8C_7, no dislocation dissociation can be detected by WBDF work, but a lot of defects are unambiguously split in ordered V_6C_5 (see figure 17a) and b) respectively).

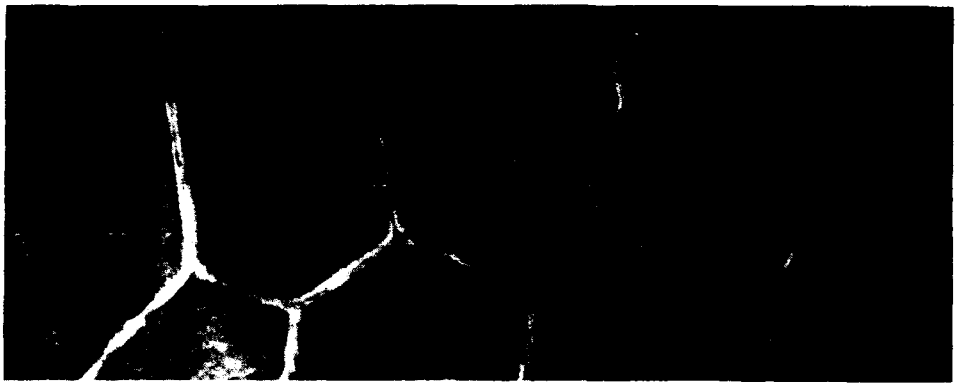

Figure 15. Network of dissociated dislocations in W_2C deformed at 2100°C [56].

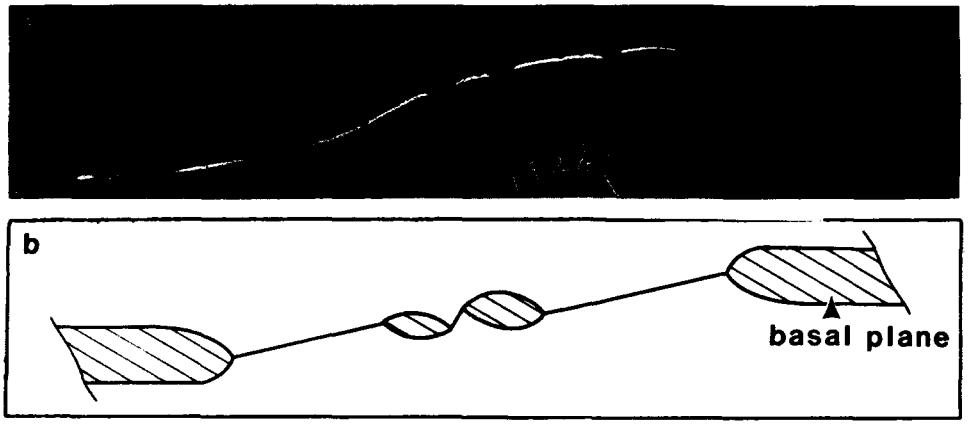

Figure 16. Near edge dislocation after climb in W_2C deformed 1% at 2000°C. a) : WBDF image after a short irradiation : note that small parts of the dislocation are still dissociated. b) : drawing showing the configuration of the defect imaged in a) ; undissociated portions are out of the basal plane.

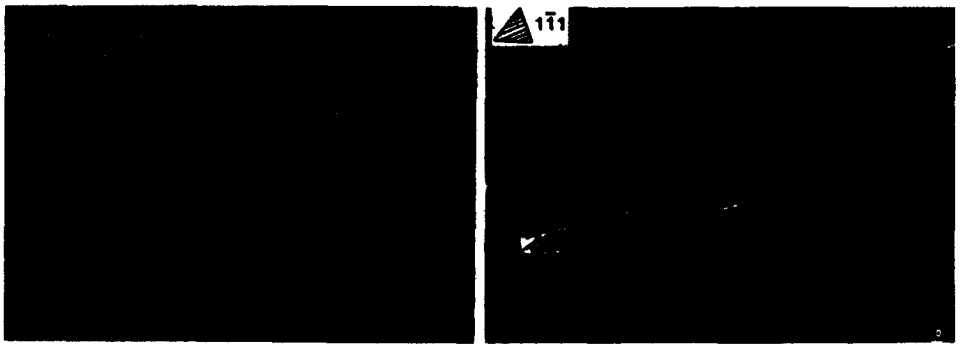

Figure 17. WBDF images of : a) : undissociated, b) : dissociated dislocations in ordered V_8C_7 and V_6C_5 single crystals respectively, deformed at 1150°C.

In the latter case, it can be emphasized that all the dislocations are not dissociated in the same way ; it is most probable that these differences are related to variations of the local carbon content in the glide plane due to the orientation of the ordered domains, as shown by figure 18. This behavior is consistent with the evolution of γ in TaC_{1-x} compounds [81], e.g. the higher the carbon content, more narrow the faulted ribbon. Moreover, it may explain why the yield stress in the V-C system passes through a maximum at $VC_{\sim 0.84}$ [58] : the crystallographic anisotropy of the dissociation state in V_6C_5 can be at the origin of various hardening processes, such as differences in dislocation mobility and velocity or preferred cross-slip paths. This analysis completes that of Hannink and Murray [100] who attempted to interprete the particular mechanical behavior of V_6C_5 in terms of dislocation pile-ups at domains boundaries. Further work is however necessary to precise and quantify these effects.

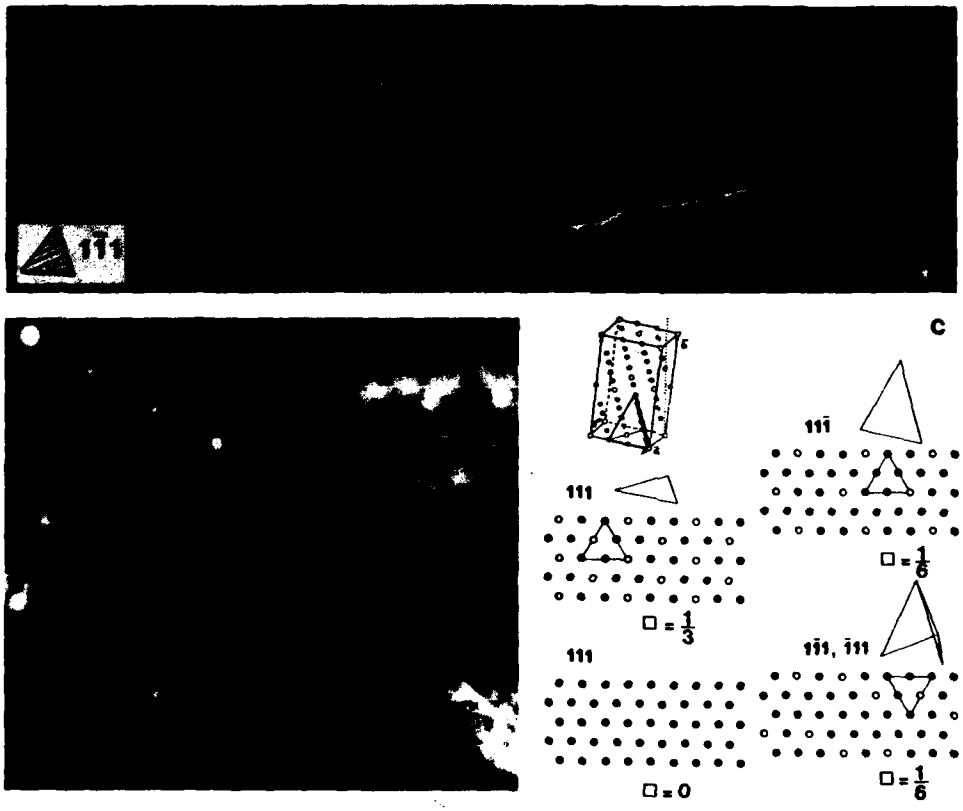

Figure 18. anisotropy of dislocation dissociation due to ordering in V_6C_5. a) and b) : WBDF image showing the change of dissociation width at the crossing of ordered domains (revealed by conventional dark field imaging in b)). c) : diagrams showing the differences of carbon content within the various $\{111\}_{fcc}$ planes of the monoclinic V_6C_5 superstructure (numbers indicate the vacancy fraction of each plane).

.in ZrC, no dissociation can be detected at a resolution of about 1.5 nm (see figure 19a)). however, stacking fault contrast is observed in $ZrC_{0.64}O_{0.26}$, as shown in figure 19b) (this chemical composition lies at the limit of the stability range of the zirconium oxycarbide phase -see [101]-). These results strongly suggest that oxygen segregation occurs at the core of dislocations, as previously mentioned in the similar case of iron-doped $NbC_{0.74}$ [101]. Comparable precipitation phenomena occur in boron-doped monocarbides, where metallic boride precipitates are formed at dislocation nodes [10].

Figure 19. Dissociation state in ZrC-based compounds (from [16]). a) : WBDF image of an undissociated defect in pure ZrC. b) : stacking fault contrasts (arrows) in $ZrC_{0.64}O_{0.26}$.

4.4.2. *High Resolution Observations.* Direct High Resolution Lattice Imaging of edge-on dislocations has also been applied to the case of compounds where the WBDF technique failed to reveal any dissociation. By this method, it is possible to appreciate narrow dissociations (a few Ångstroms in width) and to study the dislocation core.

A great care is however needed to interprete the micrographs, since no one-to-one correspondence can be established, without extensive multislice computations, between experimental dots and actual atomic positions near the core. Moreover, artefacts are still possible, such as a dislocation line not rigouresly parallel to the electron beam, which may produce an artificial dissociation. These precautions are well documented in the literature devoted to semi-conductors (see for example references quoted in [103]).

Recent HR observations are summarized below :

.the relatively large dissociation in W_2C (see § 4.3.1) is confirmed by direct lattice imaging, as shown by figure 20.

.a glissile dissociation of about 0.8 nm has been reported for a screw dislocation in an as-grown $NbC_{\sim 0.9}$ single crystal [26] ; this observation

confirms WBDF results which indicate a high stacking fault energy in this compound (see § 4.3.1). Further observations on deformed crystals will however be helpful to ascertain this result.

Figure 20. HR micrograph showing edge-on dislocations in W_2C (deformed at 1800°C) observed along the $[11\bar{2}0]_{hcp}$ axis (from [16]). a) : low magnification image of a dipole of dissociated 60° dislocations ; tungsten atoms appear as white dots. b) : enlargement of defect B ; the Burgers circuit exhibits a closure failure -arrow- equal to $1/2[1\bar{1}00]_{hcp}$, which corresponds to the projection of the Burgers vector $1/3[1\bar{2}10]$; the stacking fault (sequence of close-packed planes ABC inserted in the hcp sequence ABAB or ACAC) is clearly seen at grazing incidence.

.no dissociation can be detected in $VC_{0.87}$ single crystals deformed in compression up to a few % at 1100 and 1150°C. Figure 21 shows a perfect edge-on dislocation (fig.21a)) and a Lomer-Cottrell lock (fig.21b)) ; both defects clearly appear to be unsplit.

The above results definitively confirm the trends drawn out from the WBDF imaging of dislocations. Dissociation into partials remain narrow in $MC_{\geq 0.8}$ and M_2C compounds, which leads to values of ≈ 100 mJ/m^2 or more for the stacking fault energy.

However, lattice images do not allow precise information to be obtained concerning the core of such defects : although further modelisation would be necessary to ascertain this affirmation, the dots contrast revealed in figures 20 and 21 are not sensitive enough to the presence of carbon (ordering) to allow any conclusion to be established concerning the carbon content near the core of the dislocations.

Up to now, attempts to perform "superstructure imaging" of edge-on dislocations have been fruitless in deformed V_8C_7 or V_6C_5 crystals [104]. Since "superstructure imaging" of perfectly ordered domains and classical High Resolution observations of edge-on dislocations appear to be separately successful, the conjunction of both approaches would be a promising way to get definitive results ; further work is required on this still open subject.

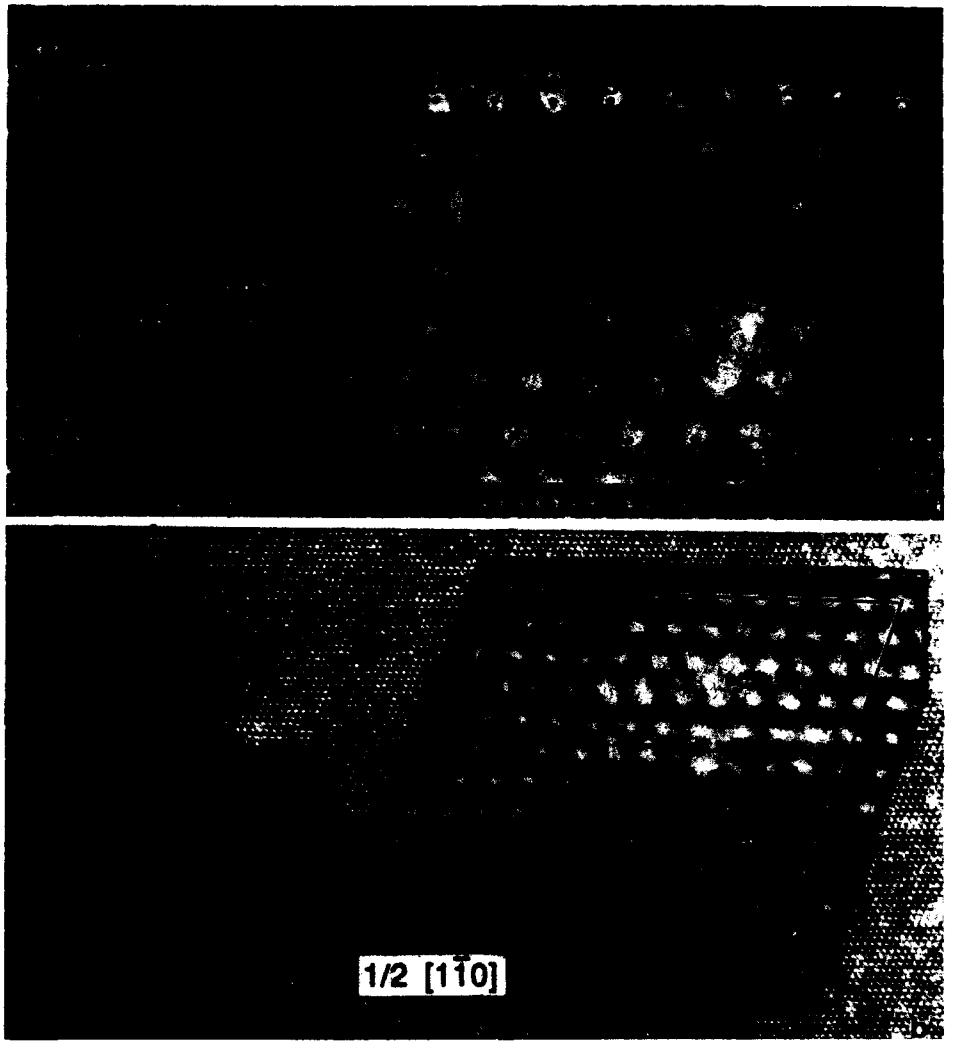

Figure 21. $[110]_{fcc}$ 7-beam images of edge-on dislocations in V_8C_7 single crystals deformed at 1100 (a) and 1150°C (b). a) : perfect unsplit $\approx 60°$ dislocation. An enlargement of the core region (extremity of the extra-half plane -arrow-) is superimposed on the low-magnification image ; the Burgers vector $\mathbf{a}/2[011]_{fcc}$ is deduced from the closure failure in the Burgers circuit). b) : Lomer-Cottrell lock $\mathbf{b} = \mathbf{a}/2[1\bar{1}0]_{fcc}$ (presentation as in a)).

4.5. CONCLUSION

From the above, it can be said that TEM observations bring convergent indices (i.e. evidence for dislocation dissociation, depletion of carbon within stacking faults, irradiation effects) favourable to the hypothesis of the "shear-diffusion" mechanism in TaC, V_6C_5 and W_2C.

A polemic discussion can be conducted to see if this model applies to other carbides, especially group IV compounds (see for example [61]). This analysis is beyond the scope of the present paper, but as far as TEM is concerned, it is pertinent to point out the following remarks :

1) the dislocation dissociation which is considered in the "shear-diffusion" model is not compulsory ; the mechanism can also apply if partials are very closely spaced (cf. ZrC in figure 18a) and even unresolvable by HREM work such as reported in figure 20a).

2) the "choice" of the controlling deformation process ("shear-diffusion", Peierls or cross-slip mechanism) is frequently guided by the comparison of the activation enthalpy with that of carbon diffusion ; unfortunately, there is still a large scatter in values reported from diffusion studies (see compilations in [16, 61, 105, 106]), and, more important, no data are available on pipe-diffusion. Regarding the "shear-diffusion" model, it is almost obvious that the diffusion process is a core process, and the comparison of the activation energy with that of a bulk diffusion is probably meaningless. As an example, the activation enthalpy for glide in polycrystalline W_2C, i.e. 2.1 eV [107], is closer to the carbon diffusion energy at grain boundary (2.9 eV [105]) than to that in the bulk (4±1 eV [105]) ; the former diffusion value can reasonably be compared to that of pipe-diffusion.

5. Summary and General Conclusions

Various Transmission Electron Microscopy studies on transition metal carbides have been reviewed in the previous sections. Irradiation processes, ordering phenomena and dislocation problems have been the most important fields covered by recent TEM works. Significant information has been obtained by a careful application of modern TEM techniques e.g. High Resolution and Micro-Chemical Analysis.

Nevertheless, obscure points remain, especially for the identification of deformation mechanisms. Regarding that concern, it would be of the greatest interest to attempt *in situ* deformation experiments in a microscope ; such studies will however be very delicate to undertake because of the elevated temperatures required for making dislocations mobile in most carbides. Finally, High Resolution studies of dislocations have definitively to be further developed.

Acknowledgements

The author is grateful to his colleagues, Dr. J. Dubois and Prs. C. Esnouf and G. Fantozzi for their collaboration to earlier studies partly reported in the present paper. Dr. Y. Kumashiro (Electrotechnical Laboratory, Ibaraki - Japan-), Drs. J.P. Landesman, N. Lorenzelli and C.H. De Novion (CEA/Ecole Polytechnique, Palaiseau -France-), Dr. P. Barnier and Pr. F. Thevenot (Ecole des Mines, St-Etienne -France-) are acknowledged for having provided some of the samples used in this investigation.

References

[1] "Science of Hard Materials", ed. R.K. Visvanadham, D.J. Rowcliffe, J. Gurland, New York : Plenum Press, (1983).
[2] STORMS E.K, "The Refractory Carbides", New York : Academic Press (1967), 285 p.
[3] KOSOLAPOVA T. Y., "Carbides : Properties, Production and Applications", (1971), New-York : Plenum Press.
[4] TOTH L.E., "Transition Metal Carbides and Nitrides", (1971), New York : Academic Press.
[5] WILLIAMS W. S. , "transition-metal carbides", (1971), Prog. Sol. State Chem. , 6, pp. 57-115
[6] "Engineering Property Data on Selected Ceramics : volume 2, Carbides", MCIC Report MCIC-HB-07, Battelle : Metals and Ceramics Information Center, (1979).
[7] WILLIAMS W.S., "influence of temperature, strain rate, surface condition and composition on the plasticity of transition-metal carbide crystals", (1964), J. Appl. Phys., vol. 35, n°4, pp. 1329-1338 and "brittle-ductile behavior of the transition metal carbides", pp. 181-190 in "Propriétés Thermodynamiques, Physiques et Structurales des Dérivés Semi-métalliques", Colloque International CNRS n°157, (1965), Paris : Editions du CNRS, (1967).
[8] DY L.C., WILLIAMS W.S., "resistivity, superconductivity and order-disorder transformations in transition metal carbides and hydrogen-doped carbides", (1982), J. Appl. Phys., 53, 12, pp. 8915-8927.
[9] WILLIAMS W.S., "dispersion-hardening of titanium carbide by boron-doping", (1966), Trans. Met. Soc. AIME, 236, pp. 211-216.
[10] VENABLES J.D., "the nature of precipitates in boron-doped TiC", (1967), Phil. Mag., 16, pp. 873-890.
[11] EPICIER T., "crystal chemistry of transition metal hemicarbides", (1989), these Proceedings.
[12] LEWIS M.H., BILLINGHAM J., BELL P.S., "non-stoichiometry in ceramic compounds", pp. 1084-1115 in "Electron Microscopy and Structure of Materials", ed. G. Thomas, R.M. Fulrath, R.M. Fischer, Berkeley : University of California Press, (1972).
[13] MOISY-MAURICE V, "structure atomique des carbures non-stoéchiométriques de métaux de transition", (1981), thèse d'Etat, Université de Strasbourg, rapport CEA-R-5127.
[14] DAS G., CHATTERJEE D.K., LIPSITT H.A., "electron irradiation damage in TiC", (1981), J. of Mat. Sci., vol. 16, pp. 3283-3291.
[15] ATHANASSIADIS T., LORENZELLI N., DE NOVION C.H., "diffraction studies of the order-disorder transformation in V_8C_7", (1987), Ann. Chem. Fr., 12, pp. 129-142.
[16] EPICIER T., "contribution à l'étude des phénomènes d'ordre et des mécanismes de plasticité dans les carbures métalliques", (1988), thèse d'Etat, Lyon, n° d'ordre 88/SAL/0038.
[17] VENABLES J.D., KAHN D., LYE R.G., "structure of the ordered compound V_6C_5", (1968), Phil. Mag., 18, pp 177-192.
[18] HANNINK R.H.J., MURRAY. M.J., PACKER M.E., "observations on the domain structures of V_6C_5", (1971), Phil. Mag., 191, pp 1179-1195.
[19] BILLINGHAM J., BELL P.S., LEWIS M.H., "a superlattice with monoclinic symmetry based on the compound V_6C_5", (1972), Phil. Mag., vol. 25, n° 3, pp. 661-671.
[20] THORNTON P.H., GOVILA R.K., "presence of coherent precipitate in $VC_{0.76}$ monocrystals", (1973), J. less Com. Metals, 30, pp. 343-349.
[21] HIRAGA K., "vacancy-ordering in vanadium carbides based on V_6C_5", (1973), Phil. Mag., vol. 27, n° 6, pp 1301-1312.

[22] LEWIS M.H., BILLINGHAM J., "long-period order in vanadium carbide", (1974), Phil. Mag., vol. 29, pp 241-252.
[23] EPICIER T. et KUMASHIRO Y., "a first HREM observation of the ordered carbon sublattice in a transition metal carbide (VC_{1-x})", (1987), PHil. Mag. Letters, vol. 55, n° 4 pp. 171-179.
[24] VENABLES J.D., MEYERHOFF M.H., "ordering effects in NbC and TaC", (1972), NBS Special Publ. 364, Solid State Chemistry, pp. 583-590.
[25] MORGAN G., LEWIS M.H., "hardness anisotropy in niobium carbide", (1974), J. Mater. Sci., 9, pp. 349-358.
[26] EPICIER T., KUMASHIRO Y., "conventional and high resolution electron microscopy of $NbC_{\sim 0.88}$ single crystals", (1989), J. Less Com. Metals, 146, pp. 17-32.
[27] YVON K., PARTHE E., "on the crystal chemistry of the close packed transition metal carbides. Part I", (1970), Acta Cryst., B26, pp. 149-153.
[28] Villagrana R.E., Thomas G., "interstitial ordering of carbon in tantalum", (1965), Phys. Stat. Sol., 9, p. 499.
[29] DAHMEN U., THOMAS G., "significance of oxygen on interstitial ordering in tantalum (the $Ta_{64}C$ artefact)", (1979), Scripta Met., 13, pp. 527-530.
[30] DE NOVION C.H., LANDESMANN J.P., "order and disorder in transition metal carbides and nitrides : experimental and theoretical aspects", (1985), Pure & AppL Chem., Vol. 57, n° 10, pp. 1391-1402, and "order-disorder and effective pair interactions in nonstoichiometric rocksalt-structure transition-metal carbides and nitrides", pp. 499-528 in "Nonstoichiometric Compounds", Adv. in Ceram. vol. 23, Westerville : Am. Ceram. Soc, (1987).
[31] BILLINGHAM J., BELL P.S. et LEWIS M.H., "vacancy short-range order in substoichiometric transition metal carbides and nitrides with the Na-Cl structure. I : electron diffraction studies of short-range ordered compounds", (1972), Acta Cryst., A28, pp. 602-606.
[32] SAUVAGE M., PARTHE E., "vacancy short-range order in substoichiometric transition metal carbides and nitrides with the Na-Cl structure. II : numerical calculations of vacancy arrangement", (1972), Acta Cryst., A28, pp. 607-616.
[33] HIRAGA K., HIRABAYASHI M., "long-range and short-range order in interstitial compounds M_2X with special reference to V_2C and Nb_2C", (1977), J. de Phys., colloque C7, t 38, pp. 224-226, and "the formation of varieties of carbon ordering in pseudobinary compounds of V_2C, Nb_2C and Ta_2C", (1980), J. Appl. Cryst., 13, pp. 17-23.
[34] OHSHIMA K., HARADA J., MORINAGA M., GEOGOPOULOS P., COHEN J.B., "distortion-induced scattering due to vacancies in $NbC_{0.72}$", (1988), Acta Cryst., A44, pp. 167-176.
[35] GEVERS R., "défauts plans", pp. 155-186 in "Méthodes et Techniques Nouvelles d'Observation en Métallurgie Physique", ed. B. Jouffrey, Paris : Soc. Fr. Microsc. Electr., (1972).
[36] PARTHE E., SADAGOPAN V., "the structure of dimolybdenum carbide by neutron diffraction technique", (1963), Acta Cryst., 16, pp. 202-205.
[37] HIRAGA K., SHINDO D., HIRABAYASHI M., "high voltage, high resolution electron microscopy of Au-Cd alloys: part I, II, III", (1981), J. Appl. Cryst., 14, pp 169-190.
[38] EPICIER T., BLANCHIN M.G., FERRET P., FUCHS G., "HREM imaging of the carbon vacancy superlattice in the ordered carbide VC_{1-x}", (1989), Phil. Mag. A, vol. 59, n°4, pp. 885-906.
[39] O'KEEFE M.A., BUSECK P.R., "computation of high resolution TEM images of minerals", (1979), Trans. Am. Crystallogr. Assoc., 15, pp. 27-46.
[40] KILAAS R., "interactive simulation of high resolution electron micrographs", pp. 66-69 in Proc. 45th Ann. Meeting EMSA, San Francisco : G.W. Bailey, (1987).

[41] COWLEY J.M., MOODIE A.F., "the scattering of electrons by atoms and crystals. I : a new theoretical approach", (1957), Acta Cryst., vol. 10, pp. 609-619.
[42] GUERIN Y., DE NOVION C.H., "structure cristalline de V_8C_7", Rev. Int. Hautes Tempér. et Refract., (1971), t.8, pp. 311-314.
[43] EPICIER T., KUMASHIRO Y., "an experimental study of crystallography and ordering phenomena in some transition metal carbides, part II : applicability of HREM to the study of order defects in vanadium carbide single crystals", pp.677-690 in "Nonstoichiometric Compounds", Adv. in Ceram. vol. 23, Westerville : Am. Ceram. Soc, (1987).
[44] EPICIER T., ESNOUF C., "high resolution electron microscopy in transition metal carbides. Part II : study of the hexagonal hemicarbide W_2C", pp. 323-324 in Inst. Phys. Conf. Ser. n°93, vol. 2, (1988).
[45] GUSEV A.I., REMPEL A.A., "order-disorder phase transition channel in niobium carbide", (1986), Phys. Stat. Sol. (a), 93, pp. 71-80.
[46] LANDESMAN J.P., CHRISTENSEN A.N., DE NOVION C.H., LORENZELLI N, CONVERT P., "order-disorder transition and structure of the ordered vacancy compound Nb_6C_5 : powder neutron diffraction studies", (1985), J. Phys. C, 18, pp 809-823.
[47] CHRISTENSEN A.N., "vacancy order in Nb_6C_5", (1985), Acta Chem. Scand., A39, pp. 803-804.
[48] HAUCK J., LARSON B.C., GRUZALSKI G.R., DARKEN L.S., BARHORST J.F., "ordering of carbon vacancies in VC_x", (1983), ORNL Report 5975, Solid State Division, p. 102.
[49] MORILLO J., DE NOVION C.H., DURAL J., "electron radiation defects in TaC_{1-x} and $TiC_{0.97}$", pp. 103-119 in "Science of Hard Materials", ed. R.K. Visvanadham, D.J. Rowcliffe, J. Gurland, New York : Plenum Press, (1983).
[51] VENABLES J.D., LYE R.G., "radiation damage of ordered V_6C_5 by electron microscope beam bombardment", (1969), Phil. Mag., vol. 19, pp. 565-582.
[52] ALLISON C.Y., STOLLER R.E., KENIK E.A., "electron microscopy of electron damage in tantalum carbide", (1988), J. Appl. Phys., 63, 5, pp. 1740-1743.
[53] GOSSET D., ALLISON C., MORILLO J., "défauts d'irradiation électronique dans le carbure de tantale", (1984), Ann. Chim. Fr., vol.9, pp. 99-102.
[54] GOSSET D., "Défauts d'Irradiation aux Electrons dans les Carbures de Tantale", Thèse D.I., Université d'Orsay, (1985).
[55] MURATA Y., YUKAWA N., MORI H., FUJITA H., "Electron irradiation induced disordering of short-range ordered $(Ti,Mo)C_X$ carbide", (1988), J. Less-Com. Met., 141, pp. 309-319.
[55] CHATTERJEE D.K., LIPSITT H.A., "electron irradiation damage in titanium carbide", (1980), J. of the less Com. Met., vol. 70, pp. 111-113.
[56] EPICIER T., ESNOUF C., "observations de l'hémicarbure de tungstène W_2C par microscopie électronique en transmission", (1984), J. Microsc. Spectrosc. Electron., vol. 9, pp. 17-28.
[57] EPICIER T., ESNOUF C., DUBOIS J., FANTOZZI G., "dislocation structures in pocycristalline tungsten hemicarbide W_2C deformed at high temperatures", pp. 73-86 in "Deformation of Ceramics II", Mat. Sci. Res., vol. 18, ed. R. E. Tressler, R.C. Bradt, New York : Plenum Press, (1984).
[58] HOLLOX G.E., "microstructure and mechanical behaviour of carbides", (1968/69), Mat. Sci. Eng., vol. 3, pp. 121-137.
[59] EPICIER T., DUBOIS J., ESNOUF C., FANTOZZI G., "mécanismes de déformation des carbures métalliques ; exemple de l'hémicarbure de tungstène", (1982), Rev. Int. Hautes Temp. Refract. Fr., 19, pp. 345-357.

[60] ROWCLIFFE D. J. , "plastic deformation of transition metal carbides", pp. 49-71 in "Deformation of Ceramic Materials II", Mat. Res. Sci. vol. 18, ed. R. E. Tressler, R. C. Bradt, New York : Plenum Press, (1984).
[61] DAVIS R.F., " nonstoichiometry and its effect on mass transport, order-disorder phenomena, and deformation behavior in transition-metal carbides", pp. 529-557 in "Nonstoichiometric Compounds", Adv. in Ceram. vol. 23, Westerville : Am. Ceram. Soc, (1987).
[62] LEE D.W., HAGGERTY J.S., "plasticity and creep in single crystals of zirconium carbide", (1969), J. Am. Ceram. Soc., vol. 52, n° 12, pp 641-647.
[63] DAS G., MAZDIYANSNI K.S., LIPSITT H.A., "mechanical properties of polycristalline TiC", (1982), J. Am. Ceram. Soc., vol. 65, n°2, pp. 104-110.
[64] CHATTERJEE D.K., Mendiratta M.G., LIPSITT H.A., "deformation behaviour of single crystals of titanium carbide", (1979), J. Mat. Sci., pp. 2151-2156.
[65] GOVILA R.K., "dislocation etch-pits in vanadium carbide monocrystals", (1970), Phil. Mag., 22, pp. 431-436.
[66] DEMENT'YEV L.N., ZUBAREV P.V., KRUGLOV V.N., TURCHIN V.N., KHARKHADIN Ye D., "high temperature creep of niobium carbide single crystal", (1978), Fiz. Met. Metalloved., vol. 46, N°3, pp. 620-624.
[67] ROWCLIFFE D.J., HOLLOX G.E., "plastic flow and fracture of tantalum carbide and hafnium carbide at low temperature", (1971), J. Mat. Sci., 6, pp. 1261-1269, and "hardness anisotropy, deformation mechanisms and brittle-to-ductile transition in carbides", (1971), J. Mat. Sci., 6, pp. 1270-1276.
[68] HANNINK R.H.J., KOHLSTEDT D.L., MURRAY M.J., "slip system detemination in cubic carbides by hardness anisotropy", (1972), Proc. Roy. Soc. Lond., A, 326, pp. 409-420.
[69] VAHLDIEK F.W., MERSOL S.A., "slip and microhardness of IVa to VIa refractory materials", (1977), J. less Com. Metals, 55, pp. 265-278.
[70] BREVAL E., "microplasticity at room temperature of single-crystal titanium carbide with different stoichiometry", (1981), J. Mat. Sci., 16, pp. 2781-2788.
[71] ROWCLIFFE D.J., WARREN W.J., "structure and properties of tantalum carbide crystals", (1970), J. Mat. Sci., 5, pp. 345-350.
[72] VAHLDIEK F.W., MERSOL S.A., LYNCH C.T., "microhardness anisotropy, slip and twinning in Mo_2C single crystals", (1966), Trans. Met. Soc. AIME, vol. 236, pp. 1490-1496.
[73] DUBOIS J., ORANGE G., MAI C., FANTOZZI G., "comportement plastique à température ambiante de l'hémicarbure de tungstène", (1978), C. R. Acad. Sc. Paris, série B, t. 287, pp. 53-56.
[74] KUMASHIRO Y., ITOH A., KINOSHITA T., SOBAJIMA M., "the microVickers hardness of TiC single crystals up to 1500°C", (1977), J. Mat. Sci., 12, pp. 595-601.
[75] KUMASHIRO Y., NAGAI Y., KATO H., SAKUMA E., WATANABE K., MISAWA S., "the preparation and characteristics of ZrC and TaC single crystals using an r.f. floating-zone process", (1981), J. Mat. Sci., 16, pp. 2930-2933.
[76] KUMASHIRO Y., SAKUMA E., "the Vickers microhardness of non-stoichiometric niobium carbide and vandium carbide single crystals up to 1500°C", (1980), J. Mat. Sci., 15, pp. 1321-1323.
[77] DUBOIS J., EPICIER T., ESNOUF C., FANTOZZI G., "mechanical behavior and electron microscopy analysis of W_2C", pp. 201-218 in "Science of Hard Materials", ed. R.K. Visvanadham, D.J. Rowcliffe, J. Gurland, New York : Plenum Press, (1983).
[78] TETELMAN A.S., "dislocation dipole formation in deformed crystals", (1962), Acta Met., vol. 10, pp. 813-820.
[79] HOLLOX G.E., SMALLMAN R.E., "plastic behavior of titanium carbide", (1966), J. Appl. Phys., vol. 37, n°2, pp. 818-823.

[80] CHEVACHAROENKUL S., DAVIS R.F., "dislocation mechanisms, diffusional processes and creep behavior in NbC_x", (1989), Acta Metall., vol. 37, n°2, pp. 417-427.
[81] MARTIN J.L., LACOUR-GAYET P., COSTA P., "plastic deformation of tantalum carbide up to 2200°C", pp. 1131-1140 in "Electron Microscopy and Structure of Materials", ed. G. Thomas, R.M. Fulrath, R.M. Fisher, Berkeley : University of California Press, (1972).
[82] KURISHITA H., NAKAJIMA K., YOSHINAGA H., "the high temperature deformation in titanium carbide single crystals", (1982), Mat. Sci. Eng., 54, pp. 177-190.
[83] CHERMANT J.L., LECLERC G., MORDIKE B.L., "deformation of titatnium carbide at high temperatures", (1980), Z. Metallkde, 71, 7, pp. 465-469.
[84] DARIOLA R., ARCHBOLD T.F., "plastic deformation of polycristalline zirconium carbide", (1976), J. Mat. Sci., vol. 11, pp. 283-290.
[85] EPICIER T., ESNOUF C., DUBOIS J., FANTOZZI G., "observations of dislocations in tungsten hemicarbide deformed at high temperatures", (1981), Scripta. Met., vol. 15, pp. 1279-1283.
[86] KELLY A., ROWCLIFFE D.J., "slip in titanium carbide", (1966), Phys. Stat. Sol., vol. 14, pp. K29-33.
[87] ALLISON C., HOFFMAN M., WILLIAMS W.S., "electron energy loss spectroscopy of carbon in dissociated dislocations in tantalum carbide", (1982), J. Appl. Phys., vol. 53, n°10, pp. 6757-6761.
[88] ALLISON C.,WILLIAMS W.S., HOFFMAN M., " quantitative electron energy loss spectroscopy of vanadium carbide", (1984), Ultramicroscopy, 13, pp. 253-264.
[89] ALLISON C., WILLIAMS W.S., "measurements of carbon/metal ratio in a single grain of non-stoichiometric titanium carbide", (1986), J. Am. Cer. Soc., vol. 69, n°1, pp. C2-C3.
[90] WILLIAMS W.S., (1989), *private communication.*
[91] WILLIAMS W.S., (1989), *these Proceedings.*
[92] BILLINGHAM J., LEWIS M.H., "dislocation mechanisms for the nucleation of transformations in vanadium carbide", (1971), Phil. Mag., vol. 24, n°188, pp. 231-240.
[93] MARTIN J.L., JOUFFREY B., "dislocations partielles dans un carbure de tantale", (1968), Le J. de Phys., t. 29, n°10, pp. 911-916.
[94] ROWCLIFFE D.J., THOMAS G., "structure of non-stoichiometric TaC", (1975), Mat. Sci. Eng., 18, pp. 231-238.
[95] HOFFMAN M., WILLIAMS W.S., "a simple model for the deformation behavior of tantalum carbide", (1986), J. Am. Ceram. Soc., vol. 69, n°8, pp. 612-614.
[96] COCKAYNE D.J.H., "the weak beam technique as applied to dissociation measurements", (1974), J. de Physique, C7, t. 35, pp. 141-148.
[97] MARTIN J.L., "evidence of dislocation dissociation in nearly stoichiometric tantalum carbide using the weak beam technique", (1973), J. of Microsc., vol. 98, pt 2, pp. 209-213.
[98] DAS G., "measurement of the stacking fault energy in TiC", (1982), J. less Com. Met., vol. 83, pp. L7-L10.
[99] EPICIER T., DUBOIS J., ESNOUF C., FANTOZZI G., "dissociation and non-dissociation of dislocations in W_2C deformed at high temperatures", pp. 525-528 in "Dislocations in Solids", ed. H. Suzuki, T. Ninomiya, K. Sumino, S. Takeuchi, Tokyo : University of Tokyo Press, (1985).
[100] HANNINK R.H.J., MURRAY M.J., "the effect of domain size on the hardness of ordered $VC_{0.84}$", (1972), Acta Metall., vol. 20, pp. 123-131.
[101] BARNIER P., "frittage et caracterisation de céramiques dans le système zirconium-carbone-oxygène", E.N.S. Mines de Saint-Etienne, (1986), Thèse (n° 54 C.I.).
[102] DAVIS R.F., (1986), *private communication.*
[103] SPENCE J.C.H., "Experimental High Resolution Electron Microscopy", Oxford : Clarendon Press, (1981) *(see p. 155).*

[104] EPICIER T., (1988), *unpublished results*.
[105] TREHEUX D., DUBOIS J., FANTOZZI G., "bulk and grain-boundary diffusion of ^{14}C in tungsten hemicarbide", (1981), Ceramics Int., vol. 7, n° 4, pp. 142-148.
[106] MATZKE Hj., "point defects and transport properties in carbides", (1984), Solid. State Ionics, 12, pp. 25-45.
[107] DUBOIS J., FANTOZZI G., EPICIER T., ESNOUF C., "deformation mechanisms of polycristalline tungsten hemicarbide W_2C", (1986), Inst. Phys. Conf. Ser., n°75, New York : Adam Hilger ltd., pp 265-278.

DEFECT STRUCTURES AND ORDER-DISORDER TRANSFORMATIONS IN TRANSITION METAL CARBIDES AND NITRIDES

C.H. de NOVION, B. BEUNEU, T. PRIEM, N. LORENZELLI, A. FINEL*
CEA/IRDI/DMECN/DTech, Laboratoire des Solides Irradiés,
École Polytechnique
91128 Palaiseau Cedex
France

ABSTRACT. This paper first reviews the long- and short-range ordered structures in metalloid deficient cubic transition metal carbides and nitrides. These structures can be simply classified in terms of effective interatomic ordering pair energies. Structural and kinetic studies of the long-range ordering of carbon vacancies in the TiC_x compound are presented. Elastic neutron diffuse scattering measurements were performed at high temperature in the short-range ordered state of TiC_x, NbC_x, $TiN_{0.82}$ single crystals ; they have allowed to separate chemical and topological disorder contributions, and to obtain effective interatomic ordering pair energies in qualitative agreement with those calculated "ab initio". *Preliminary f.c.c. coherent* phase diagrams have been calculated from these pair interactions.

1. Introduction

Transition metal carbides and nitrides MC_x and MN_x display many remarkable physical properties, which explain their use as hard materials and as coatings, as well as their theoretical interest : refractory character, metallic conductivity, occurrence of superconductivity, great hardness, simple crystal structure of NaCl type, complex bonding combining covalent, ionic and metallic characters. Many of these compounds have a large homogeneity range (i.e. $TiC_{0.50}$ to $TiC_{0.97}$, $TiN_{0.50}$ to $TiN_{1.15}$) ; for $x < 1$, vacancies on the metalloid sublattice accommodate the substoichiometry, while the metal sublattice remains fully occupied [1]. Thermodynamic properties, as well as atomic and electronic transport properties and high temperature plastic properties, are governed by the metalloid vacancy concentration 1-x [2,3], but also certainly by the detailed atomic distribution of metalloid atoms and vacancies, i.e. by short- or long-range ordering phenomena [4].

Depending on composition and temperature, one encounters :

---

* ONERA, B.P. 72, 92322 Chatillon Cedex, France

R. Freer (ed.), The Physics and Chemistry of Carbides, Nitrides and Borides, 329–355.
© 1990 *Kluwer Academic Publishers. Printed in the Netherlands.*

(i) either compounds where vacancies □ long-range order (LRO), forming a superlattice (i.e. $V_8C_7□$, $Nb_6C_5□$,...) ; in fact, because of the very high self-diffusion enthalpy of metalloid (~ 4 eV for carbides) and metal (~ 7 eV) atoms [3], atomic mobility is very low and thermodynamic equilibrium unattainable below ~ 700°C for carbides (500°C for nitrides) ; phase diagrams are unknown below this temperature ;

(ii) or cubic disordered compounds with remaining short-range order (SRO) between metalloid atoms and vacancies ; these are a good example of "disordered crystalline solids" : a large chemical disorder affecting the metalloid sublattice is superposed to a small topological disorder affecting both sublattices, metalloid and metal (see figure 1). Depending on its chemical environment (4C-2□, 3C-3□,...), the bond lengths affecting a metal atom are modified, and the latter is slightly shifted from the sites defined by the average f.c.c. lattice.

In this paper, we shall show how :

(i) sophisticated physical techniques such as elastic diffuse neutron scattering, which can analyse separately chemical and topological disorders,

(ii) recent theoretical progress in the electronic structure theory of disordered systems, and in that of statistical mechanical description of solid solutions,

have allowed to get a much deeper description and understanding of the detailed atomic structure of the non-stoichiometric compounds.

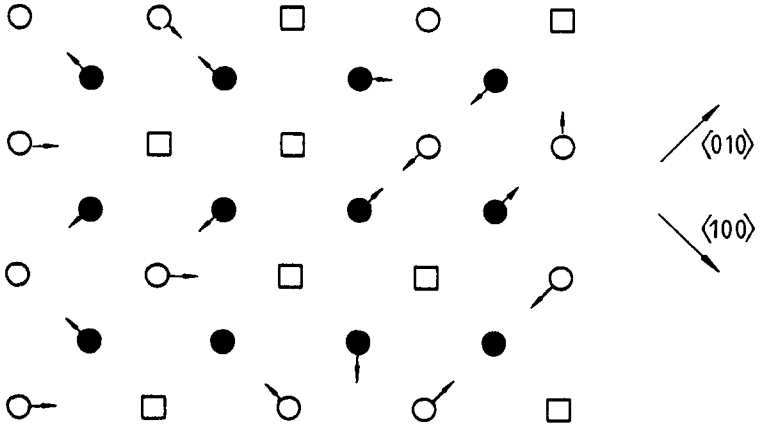

Figure 1. Typical disordered non-stoichiometric crystalline solid $MX_x□$: (001) lattice plane of the rocksalt structure. • : M. ○ : X. □ : vacancies. Chemical disorder in the ○-□ sublattice. Topological disorder in the two sublattices (• and ○-□). The arrows represent atomic static displacements : each vacancy pushes away its first neighbours M and attracts its first neighbours X ; additivity of the displacement fields due to the vacancies is assumed.

2. Classification And Characteristics Of Ordered Defect Structures

2.1. THE LONG-RANGE ORDERED STRUCTURES

Carbide and nitride superstructures form two well distinct groups ; a detailed review is presented in [4].

In carbides, the main superlattice reflexions are of the type (½ ½ ½), which corresponds to a (carbon-vacancy) concentration wave of wavelength $(2\sqrt{3}/3)\ a_{fcc}$ in the <111> direction, a_{fcc} being the lattice parameter of the disordered compound : the superstructures can be described as stacking of (111) carbon planes alternately full and partially vacant [5]. In fact, transition metal carbides of groups III and IV (Sc, Y, rare earths, Ti, Zr) order for $x \simeq 0.5$ in two possible superstructures $M_2C\square$ I and II represented in figure 2. These structures are intimely related, as will be discussed in section 4. Group V carbides (VC_x, NbC_x and probably TaC_x) form very stable M_6C_5 superstructures which present many polytypes [6,7,8,9]. An extra cubic superstructure is found for vanadium carbide, V_8C_7 [10] : as for M_6C_5, vacancies are third neighbours on the f.c.c. metalloid sublattice. Ordering leaves the lattice cubic, or in some cases induces a weak trigonal distortion ; the metal atomic positions are found displaced by $\simeq 0.1$ Å from the sites of the average f.c.c. lattice (away from their vacancies first neighbours).

In nitrides, the main superlattice reflexions are of the type (1 ½ 0), corresponding to a (nitrogen-vacancy) concentration wave of wavelength $(4\sqrt{5}/5)\ a_{fcc}$ in the <021> direction. The superstructures (Ti_2N displayed on figure 2, $V_{32}N_{26}$, Nb_4N_3) are body-centered tetragonal ; the tetragonal distortion is relatively large for Ti_2N.

All these superstructures can be described by a cluster model [11], where the metalloid octahedra surrounding a metal atom have a single configuration (i.e. 3C and 3□ for Ti_2C and Ti_2N, 5C and 1□ for M_6C_5), or at most two configurations (when x is not a multiple of 1/6, i.e. for V_8C_7).

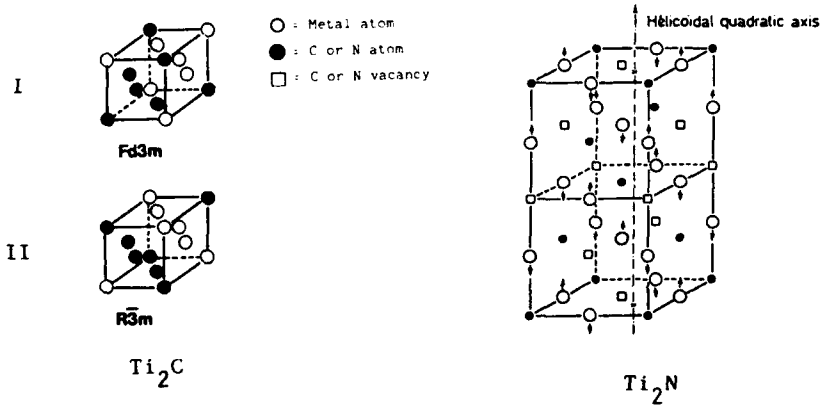

Figure 2. Superstructures observed in cubic transition metal carbides and nitrides.

2.2. THEORETICAL STUDIES OF THE LRO PHASE STABILITY

For a given compound MC_x or MN_x, the most stable superstructure is given by a minimization of the free enthalpy of the system.

The simplest model for the order-disorder problem in a solid solution is the rigid Ising hamiltonian, limited to pair atomic interactions, i.e. where triplet and larger multiplet interactions are neglected, and where lattice distortions and static displacements are ignored [12]. The non-stoichiometric compound $MX_x\square_{1-x}$ is considered analogous to a substitutional f.c.c. binary alloy $A_{1-x}B_x$, the metal atoms acting only on the values of the effective interactions between metalloid sites [13].

The (Ising) hamiltonian which describes the order of vacancies (configuration energy contribution to the total energy) is written in the canonical system (composition x fixed) as :

$$H = V_1 \sum_{i,j}{}_1 C_i C_j + V_2 \sum_{i,j}{}_2 C_i C_j + \ldots \qquad (1)$$

The sums $\sum_1$, $\sum_2$, ..., $\sum_n$ run respectively through the first, second,..., n-th neighbours in the f.c.c. metalloid sublattice. V_n is the effective ordering pair energy between metalloid sites i and j distant by $\vec{R}_n = \vec{R}_i - \vec{R}_j$: $V_n = (V_n^{AA} + V_n^{BB} - 2\,V_n^{AB})/2$, and C_i is the occupation number (= 1 if site i is occupied by B, 0 if it is occupied by A). V_n depends of the nature of constituants A and B, of x, but not of the atomic distribution of A and B atoms in the solid.

Figure 3 shows the stability diagram at 0 K of the different f.c.c. ordered phases versus V_1 and V_2 (assuming $V_n = 0$ for $n \geqslant 3$) ; the carbide superstructures M_2C are stable in regions I and IV, M_6C_5 in region I ; the nitride superstructures are stable in region II. This pattern suggests that in carbides $V_2 > 0$ is the predominant pair interaction energy, and that in nitrides $V_1 > 2\,V_2 > 0$. No interstitial compound is found in regions III (which corresponds to many intermetallic alloys) and V (A-B phase separation).

Relative phase stabilities were calculated by Landesman et al [13] for different possible M_2C and M_2N superstructures assuming that, as in transition metals, the energy difference between two ordered phases depends only on the band energies (summed over the occupied states). The electronic densities of states were calculated by the "recursion method" [14], starting from a tight-binding interpolation scheme for the band structure of the stoichiometric compounds. All bonds were cut between a vacancy and its neighbours (i.e. transfer integrals $\beta_{\square-i} = 0$).

The calculations for carbides showed that the Ti_2C (I and II) ordered phases are the stablest in a large electron concentration range ($0.22 < N_e < 0.50$, N_e = fractional occupation of the metalloid 2p-metal d hybrid bands). This is in agreement with experiment as $N_e = 0.31$ for Sc_2C and Y_2C, 0.38 for Ti_2C and Zr_2C. But for nitrides, Ti_2N could not be obtained as stable phase for the right N_e ($\simeq 0.42$), although the change of input parameters between carbides and nitrides (2p metalloid

level energy, metalloid-metalloid transfer integrals, crystal-field splitting of the metal d states) gave qualitatively the good trends [13].

2.3. THE SHORT-RANGE ORDERED STRUCTURES

Short-range ordering of metalloid vacancies in a transition metal carbide was first shown by a ^{51}V NMR study on VC_x [15]. It was afterwards suggested by the observation of a diffuse scattering surface in the electron diffraction patterns of several non-stoichiometric MC_x and MN_x compounds [16,17]. But a recent X-ray study on quenched $NbC_{0.72}$ [18] showed that this diffuse scattering is dominated by the static displacement contribution due to heavy metal atoms (see section 3.1).

Because the neutron scattering lengths of C, N and metal atoms are comparable, the study of chemical SRO must be made by diffuse neutron scattering. A quantitative study in the $(1\bar{1}0)$ reciprocal lattice planes of $NbC_{0.73}$ and $TiC_{0.76}$ single crystals cooled down to room temperature, showed two contributions of comparable importance [19] :

(i) the topological disorder due to static displacements, the main of which is a shift of metal atoms away of their vacancies first neighbours by $\simeq 0.05$ Å. This topological disorder was confirmed by channeling studies on NbC_x and $TiC_{0.9}$ [20,21], and by the strong damping of the titanium K EXAFS in TiC_x [22] ;

(ii) the chemical SRO between metalloid atoms and vacancies, the main contribution being a large second neighbour α_{002} Cowley-Warren coefficient (defined in section 3.1), indicating that vacancies avoid f.c.c. second neighbour positions. Concerning the mentioned experiment [19], one cannot exclude for samples cooled down to room temperature, the existence of very small LRO microdomains : more quantitative studies (i.e. at high temperature in thermodynamic equilibrium, and with a larger data set in the reciprocal space) were therefore necessary.

An interesting result was obtained recently on titanium mononitride [23] : the diffuse neutron scattering of $TiN_{0.82}$ showed maxima in (½ ½ ½) type reciprocal points, when the superstructure peaks of Ti_2N are in (1 ½ 0) ; this confirmed experimentally the strong dependence of pair interactions V_i with non-stoichiometry 1-x.

2.4. THEORETICAL EVALUATION OF EFFECTIVE INTERATOMIC ORDERING PAIR ENERGIES

The V_n pair interactions entering in the Ising hamiltonian (1) were calculated "ab initio" using the "generalized perturbation method" [13]. In this method, developed by Ducastelle and Gautier [24], the completely disordered alloy is described by the tight-binding coherent potential average medium approximation ; the V_n are obtained from a perturbation development when replacing average atoms by specific A or B atoms.

Figure 4 shows the V_1, V_2, V_3, V_4 pair interactions versus N_e, for the compositions M_2C and M_6C_5 [13,25]. One can see that these pair interactions depend strongly on N_e and x, and that for $0.3 < N_e < 0.5$,

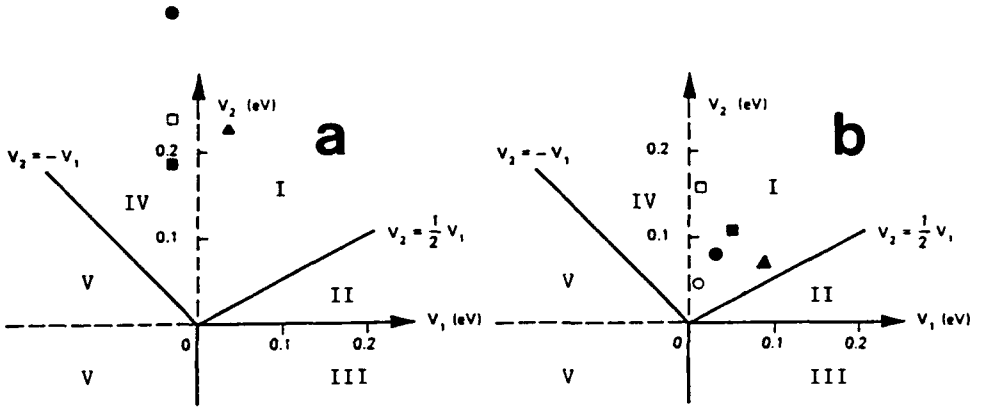

Figure 3. First and second neighbour pair interactions V_1 and V_2 for the f.c.c. metalloid sublattice in non-stoichiometric carbides and nitrides.
a) Calculated by the generalized perturbation method [25],
b) obtained by Inverse C.V.M. from the elastic neutron diffuse scattering measurements (Table 3).
• : $TiC_{0.64}$, ○ : $TiC_{0.76}$, ■ : $NbC_{0.73}$, □ : $NbC_{0.83}$, ▲ : $TiN_{0.82}$.
In the mean-field approximation of SRO, regions I and IV correspond to (½ ½ ½) type diffuse maxima, II to (1 ½ 0), III to (100) and V to (000) (segregation). These regions correspond also to different LRO stable phases at 0 K (*I and IV : Cu-Pt and* $Ti_2C\square$, II : $Ti_2N\square$, III : CuAu, V : phase separation).

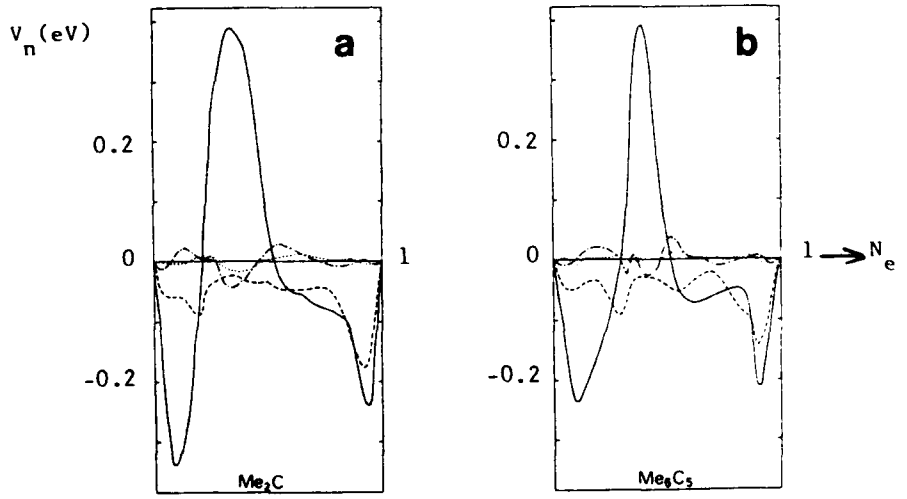

Figure 4. Pair interactions calculated for carbides [25]. (a) composition M_2C and (b) composition M_6C_5.
---- = V_1, ——— = V_2, ... = V_3, —·—·— = V_4. N_e = relative filling of the p-d bands = 0.31 for Sc_2C, 0.38 for Ti_2C, 0.44 for V_6C_5 and Nb_6C_5.

V_2 is positive and largely dominates ; this confirms the deduction made from the classification of LRO structures. The (V_1,V_2) sets calculated theoretically for several compositions are reported on the stability diagram of figure 3a. One can see that the V_2/V_1 ratio is much larger for carbides than for nitrides, as predicted from the LRO structures. These (V_1,V_2) values will be compared to those deduced from elastic neutron diffuse scattering experiments in section 3.

3. Elastic Diffuse Neutron Scattering Study Of Short-Range Order

3.1. THE ELASTIC DIFFUSE SCATTERED INTENSITY

Disordered crystalline solids show in their X-ray, neutron or electron diffraction patterns, a diffuse intensity between the Bragg peaks ; the elastic part (i.e. with no energy change of the incident particles) of this diffuse scattering is characteristic of the time-averaged disorder.

Let us consider a static non-stoichiometric f.c.c. rocksalt structure crystal $MX_x\square_{1-x}$ ($0 < x < 1$, M = metal, X = carbon or nitrogen, $\square$ = vacancy). The topological disorder displaces each atom i by $\vec{u_i}$ from the average lattice site $\vec{R_i}$. If $|\vec{u_i}| \ll a_{fcc}$, the elastic diffuse scattered intensity may be developed to 2nd order in $|u|/a_{fcc}$ and expressed as :

$$I(\vec{Q}) \simeq I^0(\vec{Q}) + I^1(\vec{Q}) + I^2(\vec{Q})$$

The detailed formalism is given in [19,26,27].

$I^0(\vec{Q})$ depends only of the chemical short-range order between occupied sites and vacancies on the metalloid sublattice :

$$I^0(\vec{Q}) = x(1-x)\ b_x^2 \left[1 + \sum_{\substack{\vec{R}_{\ell mn} \neq 0 \\ \ell+m+n \text{ even}}} \alpha\,(\vec{R}_{\ell mn})\ e^{i\vec{Q}.\vec{R}_{\ell mn}}\right]$$

where $\vec{Q}$ is the scattering vector ($|\vec{Q}| = 4\pi \sin\theta/\lambda$, θ = scattering angle), b_x the neutron scattering amplitude of metalloid atoms, $\alpha(\vec{R}_{\ell mn}) = \alpha_{\ell mn}$ the Cowley-Warren SRO coefficient between metalloid sites distant by $\vec{R}_{\ell mn}$: $\alpha(\vec{R}_{\ell mn}) = 1 - P^{\square x}(\vec{R}_{\ell mn})/x$, $P^{\square x}(\vec{R}_{\ell mn})$ being the conditional probability to have an atom X distant by $\vec{R}_{\ell mn}$ from a vacancy placed at the origin ($\vec{R}_{\ell mn} = \ell\vec{a}/2 + m\vec{b}/2 + n\vec{c}/2$, $\vec{a}$, $\vec{b}$, $\vec{c}$, unit vectors of the f.c.c. cell). $I^0(\vec{Q})$ appears as a modulation, periodic in the reciprocal space, of the constant Laue scattering $x(1-x)\ b_x^2$ of a completely chemically disordered solid ($\alpha_{\ell mn} = 0$).

$I^1(\vec{Q})$ is linearly related to the average components $\langle L_{\ell mn}\rangle$, $\langle M_{\ell mn}\rangle$, $\langle N_{\ell mn}\rangle$ of the relative static displacement $\vec{u}_{\ell mn}$ between atoms distant

of $\vec{R}_{\ell mn}$; it contains two contributions : metal-metalloid M-X (for $\ell + m + n$ odd) and metalloid-metalloid X-X (for $\ell + m + n$ even).

$$I^1(\vec{Q}) = x(1-x)\, b_x^2 \sum_{\ell,m,n} \gamma_{\ell mn} \left[h_1 \sin(\pi h_1 \ell) \cos(\pi h_2 m) \cos(\pi h_3 n)\right.$$

$$\left. + h_2 \sin(\pi h_2 \ell) \cos(\pi h_3 m) \cos(\pi h_1 n) + h_3 \sin(\pi h_3 \ell) \cos(\pi h_1 m) \cos(\pi h_2 n)\right]$$

where h_1, h_2, h_3 are coordinates in the reciprocal space, and $\gamma_{\ell mn}$ is proportional to $\langle L_{\ell mn} \rangle$.

$I^2(\vec{Q})$ is linearly related to mean correlations between the displacements of atoms distant by $\vec{R}_{\ell mn}$. In X-ray scattering, $I^2(\vec{Q})$ is largely contaminated by dynamic contributions which cannot be experimentally discriminated.

$I^1(\vec{Q})$ and $I^2(\vec{Q})$ are not periodic in the reciprocal space.

3.2. EXPERIMENTAL

The samples were five single crystals of dimensions $\simeq 1$ cm^3, prepared in Aarhus University (Denmark) by Dr. A.N. Christensen : $TiC_{0.64}$, $TiC_{0.76}$, $NbC_{0.73}$, $NbC_{0.83}$, $TiN_{0.82}$.

The experiments were made on the diffuse neutron scattering spectrometer G4-4 of Laboratoire Léon Brillouin*, CEN-Saclay, France [28]. This is a two-axis spectrometer, with a focussing pyrolytic graphite monochromator, a vacuum chamber (10^{-6} torr) with a niobium heater surrounding the sample, a rotation movement of the single crystal sample, 48 He^3 detectors, and a 12 cm thick shielding made of polyethylene and B_4C. The incident wavelength was $\lambda = 2.59$ Å (2.56 Å for $TiN_{0.82}$). The measurements were made at high temperatures (between 700 and 1200°C) in the disordered state (above the Ti_2C and Nb_6C_5 order-disorder transition temperatures). It was therefore necessary to discriminate the inelastic scattering due to interactions with the phonons : this was made by time-of-flight analysis of the scattered neutrons.

For each single crystal, the elastic diffuse scattering was measured in the (001) and (1$\bar{1}$0) reciprocal planes, in the scattering vector domain $|\vec{Q}| \leq 4.5$ Å^{-1}. The results were corrected for background, absorption and Debye-Waller factors. They were calibrated with a vanadium standard, and are given in Laue units (1 Laue = $x(1-x)\, b_x^2$) after subtraction of the nuclear incoherent scattering. Details are given in [27,29,30].

3.3. RESULTS

They were obtained at 900°C for TiC_x, 1200°C for NbC_x, 700, 800 and 900°C for $TiN_{0.82}$. The detailed results for $TiN_{0.82}$ are given in [27]. The elastic neutron diffuse scattering cross-sections are shown on figure 5 for $NbC_{0.73}$, $TiC_{0.64}$ and $TiC_{0.76}$.

For all samples, the diffuse intensity in (001) reciprocal planes is

---

* Laboratoire Commun CEA-CNRS.

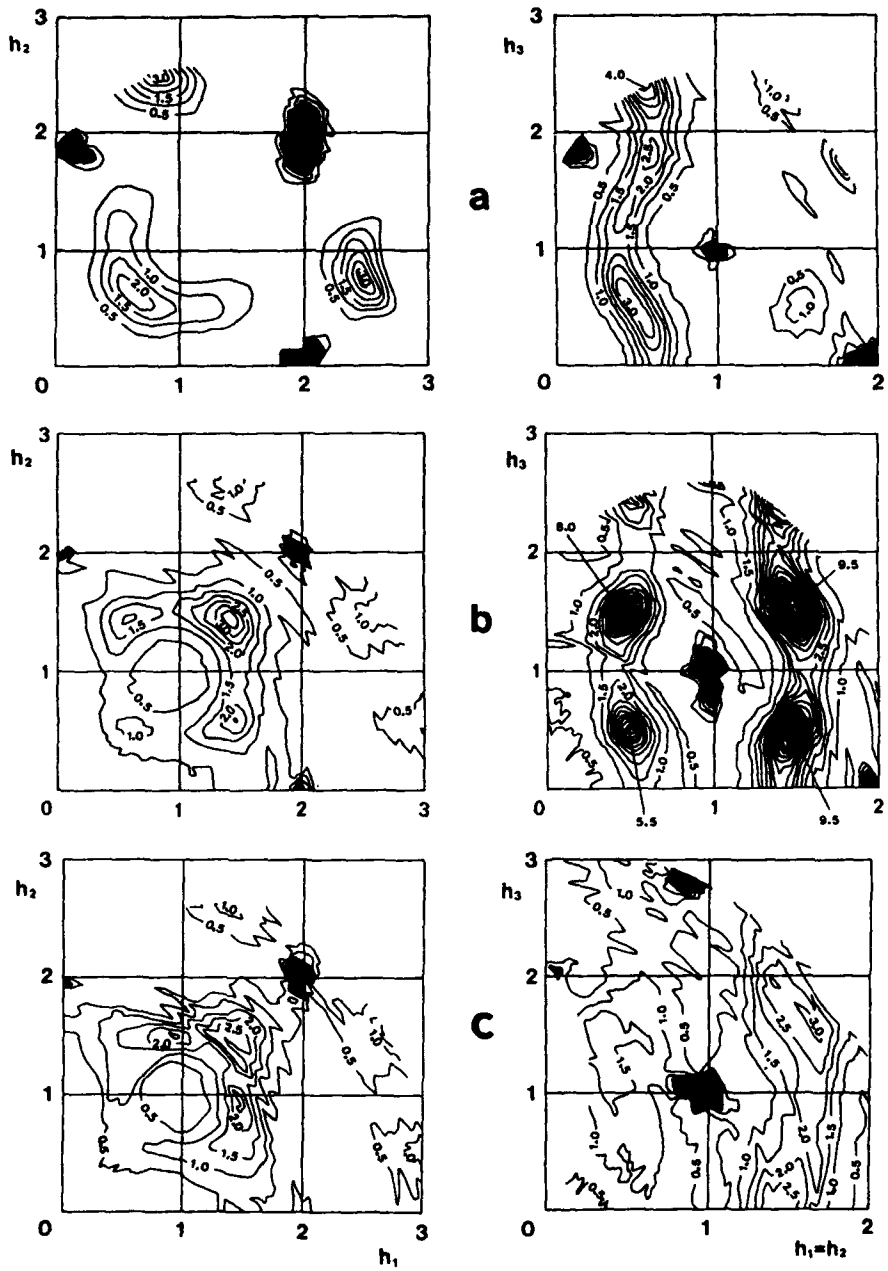

Figure 5. Elastic diffuse neutron scattering cross-sections (in Laue units) corrected for incoherent scattering, of (a) $NbC_{0.73}$ at 1200°C, (b) $TiC_{0.64}$ at 900°C, (c) $TiC_{0.76}$ at 900°C. Left-hand side : (001) reciprocal plane. Right-hand side : $(1\bar{1}0)$ reciprocal plane.

concentrated near circles surrounding the (110) type points. In the ($1\bar{1}0$) reciprocal planes, it forms diffuse bands roughly parallel to <001>. The neutron diffuse scattering is therefore concentrated near the surfaces observed by Billingham et al [16] on electron diffraction patterns, but the intensity is far from constant along these surfaces. All compounds, including $TiN_{0.82}$ (but with the exception of $TiC_{0.76}$) show diffuse intensity maxima at the (½ ½ ½) type reciprocal lattice points. The diffuse intensity is not periodic in the reciprocal space : this shows that static atomic displacements give an important contribution ; in the case of NbC_x, it is such as to nearly cancel the short-range order contribution in (3/2 3/2 1/2) and (3/2 3/2 3/2) (see figure 5a).

3.4. ANALYSIS OF THE RESULTS. SHORT-RANGE ORDER COEFFICIENTS

The elastic diffuse neutron scattering cross-sections were analysed by least-squares fit, according to the formalism presented in section 3.1 and developed in [19,27]. A separate detailed study on $NbC_{0.73}$ at room temperature (in a SRO state similar but not identical to that measured at 1200°C) has shown that the results obtained by this technique are in very good agreement with those obtained from the data taken in a 3-dimensional volume of the reciprocal space by the classical Sparks-Borie method with Fourier transform type of analysis [30].

The influence of various errors or approximations such as :

- number of neighbour shells introduced in the fit,
- size of the suppressed zone around the Bragg peaks, and diffuse intensity value taken in these zones,
- calibration errors,

is discussed in detail elsewhere for $TiN_{0.82}$ [27] and $NbC_{0.83}$ [29]. They introduce a total uncertainty of typically 0.01 to 0.02 on the three first $\alpha_{\ell mn}$ coefficients.

The short-range order coefficients $\alpha_{\ell mn}$ obtained for the first neighbour shells are given in Table 1. On figure 6 are displayed the SRO intensities $I^0(\vec{Q})$ for $TiC_{0.76}$ and $NbC_{0.73}$, reconstructed from the obtained $\alpha_{\ell mn}$. For $TiC_{0.76}$, the maxima of $I^0(\vec{Q})$ are at the (2/3 2/3 0) type reciprocal lattice points, rather than at (½ ½ ½) as for all the other samples ; but, for this compound, the diffuse intensity is very shallow and the α coefficients very weak (except α_{002}).

The following statements can be made :

- The α coefficients decrease (in absolute value) with increasing temperature (increasing disorder) as shown by $TiN_{0.82}$.
- For the same compound, large changes are observed with vacancy concentration ; this is the case, in particular, for TiC_x : the spatial range of α is much larger in $TiC_{0.64}$ than in $TiC_{0.76}$, as may be inferred directly from figure 5. In $TiC_{0.64}$, the diffuse peaks around (½ ½ ½) are consistent with Ti_2C microdomains of size $\simeq$ 25 Å, while for $TiC_{0.76}$ the correlations are limited to the first neighbour shells.
- For all the studied samples, one has : $\alpha_{011} < 0$, $\alpha_{002} < 0$, $\alpha_{112} > 0$. Vacancies avoid the f.c.c. first and second neighbour positions, and prefer third neighbour positions (and even more 4th neighbour positions in $TiC_{0.64}$). The α signs for $NbC_{0.83}$ and $TiN_{0.82}$

TABLE 1. Short-range order coefficients $\alpha_{\ell mn}$ for the ten first neighbour shells of the metalloid sublattice, deduced from elastic diffuse neutron scattering measurements. Statistical errors are placed into brackets. The theoretical values for the LRO superstructure M_6C_5 are indicated for comparison. α_{000} was included as a fit parameter : the departure from the theoretical value 1 is characteristic of the quality of the fit ; it is mainly due to the uncertainty on calibration [27,29,30].

ℓmn	$TiN_{0.82}$ 700°C	$TiC_{0.64}$ 900°C	$TiC_{0.76}$ 900°C	$NbC_{0.73}$ 1200°C	$NbC_{0.83}$ 1200°C	M_6C_5
000	1.127(20)	1.202(78)	0.934(72)	0.831(14)	1.063(34)	1
011	- 0.105(4)	- 0.058(12)	- 0.047(10)	- 0.075(16)	- 0.066(24)	- 0.2
002	- 0.118(10)	- 0.291(10)	- 0.122(8)	- 0.170(12)	- 0.174(18)	- 0.2
112	0.047(4)	0.039(6)	0.035(8)	0.062(8)	0.098(14)	0.2
022	0.019(6)	0.093(12)	0.018(8)	0.016(6)	0.005(10)	0
013	0.020(2)	0.022(4)	- 0.003(2)	0.025(2)	0.027(2)	0
222	- 0.029(2)	- 0.041(8)	0.008(4)	- 0.025(6)	- 0.020(8)	- 0.2
123	- 0.019(2)	- 0.020(2)	- 0.001(2)	- 0.021(2)	- 0.031(2)	- 0.1
004	0.003(6)	0.076(12)	0.009(4)	0.009(6)	0.009(10)	0.2
033	- 0.002(2)	0.001(2)	0.010(2)	- 0.003(4)	0.005(10)	0.4
114	- 0.010(2)	- 0.015(8)	- 0.007(8)	- 0.024(2)	- 0.037(6)	0

TABLE 2. Average static displacements $\langle L^{\square-A}_{\ell mn} \rangle$ (in units of 10^{-4} $a_{fcc}/2$) around a metalloid vacancy, deduced from elastic diffuse neutron scattering measurements. Comparison with the displacements $u^{\square-A}_{\ell mn}$ around a single vacancy calculated by lattice statics (a_{fcc} = 4.228 Å for $TiN_{0.82}$, 4.322 Å for $TiC_{0.64}$, 4.330 Å for $TiC_{0.76}$, 4.442 Å for $NbC_{0.73}$, 4.453 Å for $NbC_{0.83}$).

$\langle L^{\square-A}_{\ell mn} \rangle$ A = X or M	<L> $TiN_{0.82}$	u TiN_x	<L> $TiC_{0.64}$	<L> $TiC_{0.76}$	u TiC_x	<L> $NbC_{0.73}$	<L> $NbC_{0.83}$	u NbC_x
□-M 100	206	141	253	232	262	164	255	276
□-M 111	- 83		- 48	- 40		- 69	- 84	
□-X 110	- 36	- 65	- 45	- 38	- 61	1	7	- 121
□-X 200	31	69	42	- 13	101	- 28	- 38	153

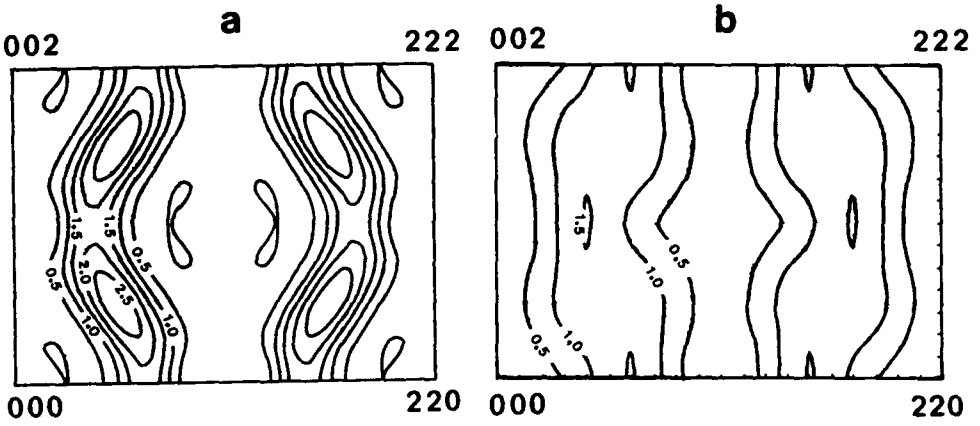

Figure 6. Short-range order diffuse intensities $I^0(\vec{Q})$ (in Laue units) reconstructed from the $\alpha_{\ell mn}$ parameters for (a) $NbC_{0.73}$ at 1200°C and (b) $TiC_{0.76}$ at 900°C. ($(1\bar{1}0)$ reciprocal plane).

are the same as those of the superstructure M_6C_5 (see Table 1) : the SRO state of $TiN_{0.82}$ is very different of the Ti_2N superstructure for which $\alpha_{002} = + 0.33$.

- The first α coefficients do not follow well the sum rule predicted by the cluster model, where the crystal is described as a stacking of octahedra of a single or two compositions, the closest possible to the nominal composition, and where the diffuse scattering is restricted to a surface in the reciprocal space [11,17,31] (for $NbC_{0.83}$, the predicted sum rule is $1 + 4\,\alpha_{011} + \alpha_{002} = 0$, when the measured value of this sum is + 0.58).

3.5. STATIC DISPLACEMENTS AND LOCAL DISTORSIONS

The average static displacements around a metalloid vacancy are directly deduced from the $\gamma_{\ell mn}$ coefficients in the expression of $I^1(\vec{Q})$:

$$\left\langle L^{\square\text{-}M}_{\ell mn} \right\rangle = (x b_x / 2\pi b_M)\ \gamma_{\ell mn}, \qquad \text{for } \ell + m + n \text{ odd},$$

$$\left\langle L^{\square\text{-}X}_{\ell mn} \right\rangle = (2\pi\ (1-\alpha_{\ell mn}))^{-1}\ \gamma_{\ell mn}, \quad \text{for } \ell + m + n \text{ even}.$$

A positive value of $\left\langle L^{\square\text{-}A}_{\ell mn} \right\rangle$ corresponds to a repulsion by the vacancy, a negative value to an attraction.

The values obtained for the five studied samples are given in Table 2 ; the displacement field around a vacancy is represented on figure 7 for $TiC_{0.64}$. For all samples, the main displacement is a shift of first neighbour metal atoms away from a vacancy ($\left\langle L^{\square\text{-}M}_{100} \right\rangle$) by typically 0.05 Å.

It is important to note that the displacements found are averaged on all configurations of a compound containing a large concentration of

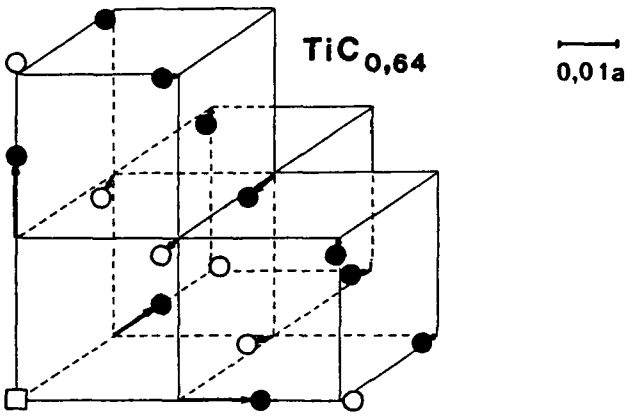

Figure 7. Static atomic displacement field around a carbon vacancy in $TiC_{0,64}$, deduced from elastic diffuse neutron scattering measurements at 900°C. The displacements are amplified (displacement scale : upper right). □ : vacancy, • : Ti, ○ : carbon.

vacancies ; for vacancy-metal first neighbour displacements, assuming additivity of displacement fields around different vacancies, <L> is related to the displacement u around an isolated vacancy by :

$$\left\langle L_{100}^{\square-M} \right\rangle = x\ (1 - \alpha_{002})\ u_{100}^{\square-M}$$

For TiC_x, the $u_{100}^{\square-M}$ values found (0.081 Å for x = 0.64 and 0.063 Å for x = 0.76) are in good agreement with those deduced from X-ray Bragg diffraction on a $TiC_{0,94}$ single crystal (0.097(2) Å [32]) and EXAFS (0.081(1) Å [22]), but somewhat larger than measured by channeling (0.044(10) Å [21]). One must emphasize that the three latter techniques gave only the absolute value $|u_{100}^{\square-M}|$, but that diffuse scattering gives the sign of the displacements.

For $NbC_{0,83}$, the $u_{100}^{\square-M}$ value is somewhat smaller than found by channeling [20] (0.063 instead of 0.090 Å). For $NbC_{0,73}$, the displacement values deduced from X-ray diffuse scattering at room temperature [18] are in reasonable agreement with the present results for □-M displacements, but show large differences for □-C displacements (for example $\left\langle L_{011}^{\square-C} \right\rangle$ = + 0.074 Å by X-rays and − 0.002 Å by neutrons) : this is certainly due to the weak sensitivity of X-rays for light carbon atoms.

Lattice statics calculations were performed to determine theoretically the displacements around an isolated metalloid vacancy, from the force constants deduced from the phonon dispersion curves, using the formalism developed previously for uranium carbide UC [33]. We took the M-M and M-X first neighbours force constants given by Kress et al. for TiN_x [34], Pintschovius for TiC_x (fit with 8 force constants) [35], Weber for NbC_x [36], and a X-X first neighbour force constant (δ_3') deduced from the composition variation of lattice parameter a(x) [37].

The calculated displacements are given in Table 2 : they are in qualitative agreement with the experimental values, except for metalloid displacements in NbC_x. Summarizing, lattice statics calculations give reasonable results, if one knows the force constants (even if very weak) between the pair of atoms whose relative displacement is being calculated.

3.6. EFFECTIVE ORDERING INTERATOMIC PAIR ENERGIES

Assuming the short-range order in these compounds is described correctly by an Ising hamiltonian on a f.c.c. lattice, the effective ordering interatomic pair energies V_i defined in section 2 may be deduced from the experimental $\alpha_{\ell mn}$. Three different approximations have been used in the present work.

(i) Mean-field Clapp-Moss-Krivoglaz formula [38], where the Fourier transforms of the pair interactions, $V(\vec{Q})$, and of the SRO coefficients, $\alpha(\vec{Q})$ (≡ the SRO diffuse intensity), are related by :

$$\alpha(\vec{Q}) = C \left[1 + 2x(1-x)V(\vec{Q})/k_B T\right]^{-1},$$

where C is a normalization constant, and k_B the Boltzmann constant. The V_i, limited to 4 or 8 neighbour shells, were fitted by a least-squares technique [39].

(ii) Inverse Monte-Carlo simulation, allowing to obtain the four first V_i from the four first experimental $\alpha_{\ell mn}$ [40]. The theoretical crystal used contained 20808 atomic sites, with helicoïdal boundary conditions along x and y, and periodical boundary conditions along z.

(iii) Inverse CVM (Cluster Variation Method). In principle, CVM approximates the exact entropy of the system by a linear combination of the entropies of the clusters contained in a basic cluster [41]. In the present case, the basic cluster consists in the f.c.c. cube (14 points) associated to the 13 points cluster formed by a metalloid atom surrounded by its 12 first neighbours. This 13-14 cluster includes interactions up to 4th neighbours. The inverse CVM algorithm, allowing to calculate the four first V_i from the four first $\alpha_{\ell mn}$, is described in [42].

In Table 3 are given the four first V_i calculated by the above methods. The following comments can be made :

- the interactions V_i were found practically temperature independent (case of $TiN_{0.82}$ [27]) ;
- the inclusion of interactions V_5 to V_8 (Clapp-Moss formula) modifies somewhat V_3 and V_4, but not much V_1 and V_2 (less than 10 %) ;
- in most cases (i.e. except for $NbC_{0.83}$), the $I^0(\vec{Q})$ SRO diffuse intensity maps recalculed from the interactions of Table 3, are in good agreement with the experimental maps ; in particular, they display the correct maxima ;
- the interactions calculated by Inverse Monte-Carlo and Inverse CVM are in excellent agreement ;
- the Clapp-Moss approximation gives systematically lower values for V_1 and V_2. This is due to frustration phenomena in the f.c.c. lattice :

the conditions $\alpha_1 < 0$ and $\alpha_2 < 0$ cannot be verified simultaneously in the triangles defined by first and second neighbours [27]. These frustrations are accounted for by the Monte-Carlo and CVM calculations, but not by the mean-field approximation.

- The V_1 and V_2 values obtained by the CVM approximation have been reported on the stability diagram of figure 3b : in all cases, a SRO of type (½ ½ ½) is predicted. This is in agreement with experiment, except for $TiC_{0.76}$ where $I^0(\vec{Q})$ (recalculated from the $\alpha_{\ell mn}$ or from the Clapp-Moss V_i) is maximum in (2/3 2/3 0).
- There is qualitative agreement with the "theoretical" V_i obtained by the generalized perturbation method (section 2.4), although the latter gives much larger V_2 values, and does not explain the strong V_3 observed for NbC_x. The SRO is reasonably described by V_1 and V_2 only for $TiN_{0.82}$ and $TiC_{0.64}$, but not for $TiC_{0.76}$ and NbC_x.
- The V_2/V_1 ratio is much larger for carbides than for nitrides, as predicted theoretically [13].

TABLE 3. Effective ordering interatomic pair energies V_i (in meV) for the metalloid sublattice deduced from elastic diffuse neutron scattering measurements ($V_1 \equiv V_{110}$, $V_2 \equiv V_{200}$, $V_3 \equiv V_{211}$, $V_4 \equiv V_{220}$). V_2/V_1 ratio deduced from the C.V.M. interactions.

		$TiN_{0.82}$ 700°C	$TiN_{0.82}$ 900°C	$TiC_{0.64}$ 900°C	$TiC_{0.76}$ 900°C	$NbC_{0.73}$ 1200°C	$NbC_{0.83}$ 1200°C
	V_1	55	59	15	18	39	- 4
Mean	V_2	39	42	48	37	54	71
-field	V_3	1	2	- 4	- 7	- 11	- 34
	V_4	2	3	8	9	6	14
	V_1	85	82	34	17	51	14
Monte	V_2	64	62	85	51	108	185
Carlo	V_3	3	4	- 7	- 10	- 32	- 74
	V_4	4	4	13	13	12	20
	V_1	90(6)	87(6)	35(8)	16(4)	50(2)	14(6)
	V_2	67(4)	66(4)	84(6)	54(4)	110(2)	160(30)
C.V.M.	V_3	4(2)	6(2)	- 6(4)	- 10(2)	- 32(2)	- 74(10)
	V_4	5(1)	6(1)	14(2)	14(2)	14(2)	16(10)
	V_2/V_1	0.74	0.76	2.40	3.37	2.20	11.40

4. Order-Disorder Transformation And Phase Diagram : The TiC_x System

4.1. THE SUPERSTRUCTURE PROBLEM IN TiC_x

Titanium monocarbide forms at high temperature a single phase f.c.c. solid solution TiC_x, with $0.50 \lesssim x \lesssim 0.97$ [37]. At low carbon content, i.e. $0.50 \lesssim x \lesssim 0.70$, long-range ordering of the carbon vacancies accommodating non-stoichiometry is obtained on samples annealed below 800°C. From the first neutron and electron diffraction studies [43,16], (½ ½ ½), (½ ½ 3/2),... type superlattice reflexions were observed, and two superstructures based on formula Ti_2C were proposed :

- a cubic Ti_2C I superstructure of space group Fd3m, and lattice parameter $b = 2\ a_{fcc}$, with titanium and carbon atoms occupying respectively the 32(a) and the 16(c) positions in the cell, and vacancies in the 16(d) positions ;
- a trigonal Ti_2C II superstructure of space group $R\bar{3}m$, with alternate empty and full {111} carbon planes ; the trigonal lattice distortion of this structure was assumed too small to be experimentally detected.

In the absence of trigonal distortion for Ti_2C II, both structures, which have identical atomic pair correlations up to infinity [44], present also identical powder diffraction spectra [5]. The elementary basis are represented on figure 2 : in both structures, each Ti atom has 3 carbons and 3 vacancies first neighbours, with vacancies in -x, -y, -z, if the carbons are in +x, +y, +z. The order-disorder transition was studied by high temperature neutron diffraction by Moisy-Maurice et al [45] who found it (nearly) of second-order type, with the following critical temperatures T_c : 765 ± 5°C for $TiC_{0.58}$, 785 ± 5°C for $TiC_{0.63}$, 770 ± 5°C for $TiC_{0.67}$. For $TiC_{0.71}$, $350 < T_c < 600$°C [46].

More recently, Khaenko et al [47] detected by X-ray diffraction on a single crystal $TiC_{0.60}$ new superlattice reflexions such as (001) and (110), and proposed another superstructure of composition Ti_8C_5, space group $R\bar{3}m$, consisting of {111} carbon planes alternately 1/4 and completely full. However, this Ti_8C_5 superstructure has been suspected to be stabilized by oxygen [48].

In fact, long duration anneals (i.e. much longer than required to observe Ti_2C I or II) suggest a more complex situation :

- annealing of a $TiC_{0.625}$ sample for 10 days between 780 and 750°C led to a trigonal distortion of the lattice [49] ;
- new superlattice reflexions near the positions (2/3 2/3 0) were observed by elastic diffuse neutron scattering on a $TiC_{0.61}$ single crystal annealed 7 days at 600°C [50] : these new reflexions are unexplained by any of the three previous superstructures (Ti_2C I, Ti_2C II, Ti_8C_5) ; they should be due to (i) either another superstructure, or (ii) a supplementary ordering of the carbon excess relative to the ideal composition Ti_2C.

In conclusion, the exact structure(s) of the long-range ordered TiC_x is (are) not fully understood. The ordering is always very partial ($S \simeq 0.6$ at 600°C [50]). Nevertheless, it was shown to decrease the residual resistivity of $TiC_{0.625}$ [49], and might play a role on the superconductive properties of $TiC_{0.45-0.60}$ observed below 3 K [51].

4.2. EXISTENCE OF A TRIGONAL ORDERED SUPERSTRUCTURE Ti_2C_{1+y}

4.2.1. *Experimental.* Systematic X-ray diffraction experiments were performed on TiC_x samples after long duration thermal treatments (up to one month). Three compositions were studied : $TiC_{0.58}$, $TiC_{0.63}$ and $TiC_{0.67}$. The method of preparation and the characteristics of samples, which were already studied by neutron diffraction, are given in [45].

The thermal treatments were made under vacuum (10^{-6} torr) in a vertical furnace, and followed by quenching. For long duration treatments ($\geq$ 8 days), the samples were in a sealed quartz tube under vacuum ; a Ti sponge getter was left in the tube to avoid any sample oxidation.

The X-ray diffraction measurements were made with the Cu $K\beta_1$ radiation in order to study more easily the profiles and the line splittings due to the trigonal distortion ; a graphite monochromator between sample and detector eliminated the $K\alpha_1$ and $K\alpha_2$ radiations, as well as a great part of the fluorescence.

4.2.2. *Results : $TiC_{0.67}$.* On figure 8 is shown the evolution of the (420) f.c.c. diffraction line of $TiC_{0.67}$ after isothermal anneals at 730°C. One observes a progressive broadening and splitting of the line ; then, after one month, the two components have narrowed again and are well resolved. Figure 9 shows the shape of several diffraction lines of $TiC_{0.67}$ after one month anneal at 730°C : the (422) f.c.c. line splits into 3 lines, (420) in 2 lines, (331) in 3 lines, and (400) does not split. This is typical of a trigonal distortion of the f.c.c. cell.

In Table 4 are given the multiplicity, as well as the corresponding d spacing for each component of the lines. The least squares refinement of data led to the following trigonal lattice parameters of the distorted metal sublattice : $a_{rh} = 4.320$ Å, $\alpha_{rh} = 90°24(1)$, compared to $a_{fcc} = 4.322$ Å in the disordered state ; ordering leads to a slight compression along the <111> axis.

During the same isothermal anneal at 730°C, weak superstructure lines of the type (½ ½ ½), (½ ½ 3/2), (½ 3/2 3/2),..., previously observed by neutron diffraction [43,45], and characteristic of the Ti_2C I and II superlattices, appear and grow. Their integrated intensity reaches its maximum after less than 24 hours, and then remains constant ($I_{3/2\ 3/2\ 3/2}/I_{220} = 0.020(2)$). These superstructure lines narrow continuously during the anneal. On figure 10 is reported the time dependence of the average ordered domain size $\bar{D}$, deduced from the integral width of the (3/2 3/2 3/2) superlattice reflexion, after correction for instrumental broadening and use of the Scherrer formula (for details, see [52]). $\bar{D}$ varies with annealing time t according to the law :

$$\bar{D}^{1/n} - \bar{D}_0^{1/n} = Ct \quad (2), \quad \text{i.e. } \bar{D} \simeq C't^n \quad \text{for } \bar{D} > \bar{D}_0 \ (= 45 \text{ Å}),$$

with $n = 0.316$. This n value is practically identical to that obtained by neutron diffraction for $TiC_{0.63}$ ($n = 0.308$) [45], and is characteristic of a growth model of antiphase ordered domains separated by a disordered layer ($n = 1/3$ [53]).

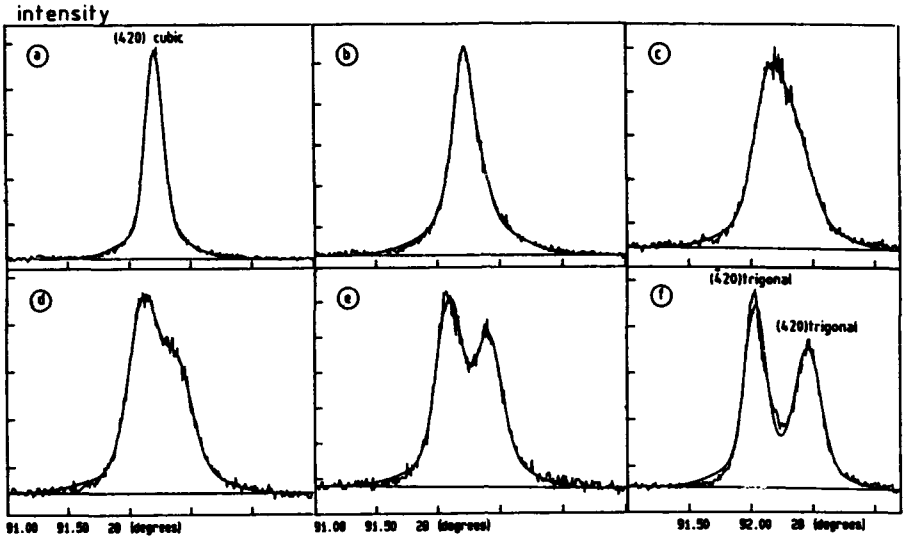

Figure 8. Evolution of the profile of the (420) f.c.c reflexion of $TiC_{0.67}$ during isothermal anneals at 730°C (X-ray Cu $K\beta_1$ radiation). a) Quenched from 1500°C (disordered) ; b) annealed for 5 hours ; c) annealed for 1 day ; d) annealed for 3 days ; e) annealed for 7 days ; f) annealed for 1 month.

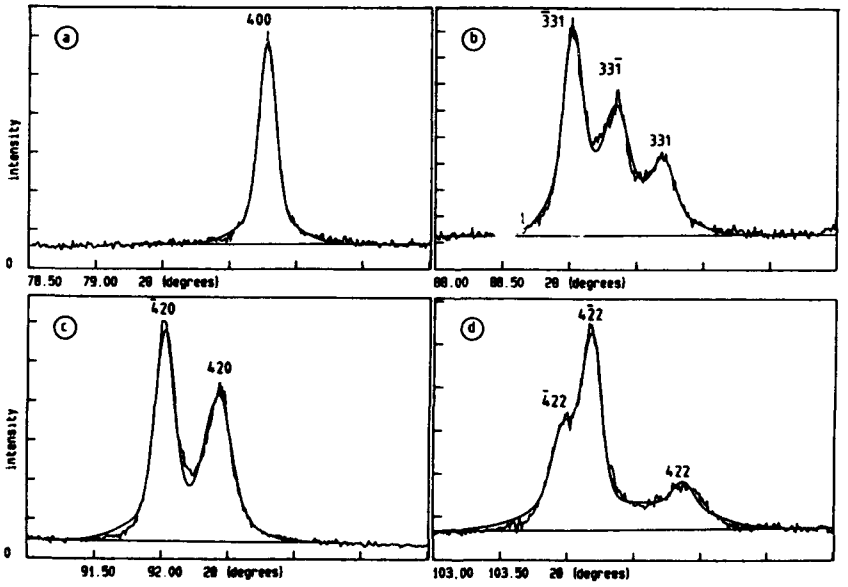

Figure 9. Profiles of several f.c.c. X-ray diffraction lines for $TiC_{0.67}$ annealed 1 month at 730°C (Cu $K\beta_1$ radiation). a) (400) reflexion, b) (331), c) (420), d) (422).

TABLE 4. Trigonal splitting of f.c.c. diffraction lines displayed in figure 9, for $TiC_{0.67}$ annealed 1 month at 730°C (X-ray Cu $K\beta_1$ radiation, $\lambda = 1.39217$ Å). The observed intensity ratio $I(\bar{4}20)/I(420) \simeq 1.4$ (see figure 9c) can be explained by static displacements $(\epsilon,\epsilon,\epsilon)$ of Ti atoms along the <111> axis, with $\epsilon \simeq 0.07$ Å.

f.c.c. indices	trigonal indices	d(Å) observed	d(Å) calculated	multiplicity
400	400	1.0801	1.0800	6
331	$\bar{3}31$	0.9930	0.9931	12
	$33\bar{1}$	0.9904	0.9904	6
	331	0.9876	0.9878	6
420	$\bar{4}20$	0.9675	0.9676	12
	420	0.9643	0.9644	12
422	$\bar{4}22$	0.8836	0.8837	6
	$4\bar{2}2$	0.8824	0.8824	12
	422	0.8788	0.8787	6

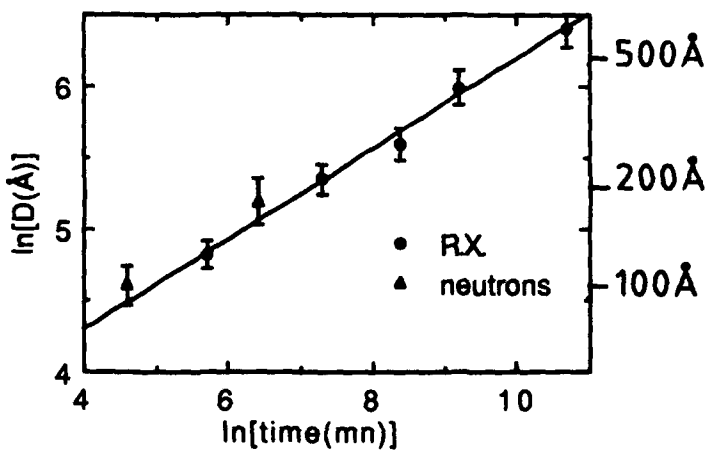

Figure 10. Isothermal evolution at 730°C of the average ordered domain size of $TiC_{0.67}$ initially quenched from 1500°C, deduced from the width of the (3/2 3/2 3/2) superstructure reflexion. The continuous line represents the fit by expression (2). Δ : data from neutron diffraction at 735°C [45].

All these results suggest strongly that the Ti_2C_{1+x} II trigonal superstructure is the stable LRO state for $TiC_{0.67}$ at 730°C. The hexagonal lattice parameters of this phase are a_{hex} ($\simeq a_{fcc}\sqrt{2}/2$) = 3.062 Å, c_{hex} ($\simeq 2a_{fcc}\sqrt{3}$) = 14.91 Å.

The disordering of this superstructure was followed by 24 hours duration isochronal anneals. Figure 11 shows the isochronal evolution of the (420) f.c.c. line : the splitting decreases with increasing temperature, and the order → disorder transition occurs at T_c = 780 ± 5°C, i.e. 10°C higher than for the undistorted ordered $TiC_{0.67}$ studied by neutron diffraction [45]. No hysteresis between heating and cooling across the transition was observed within the error bars.

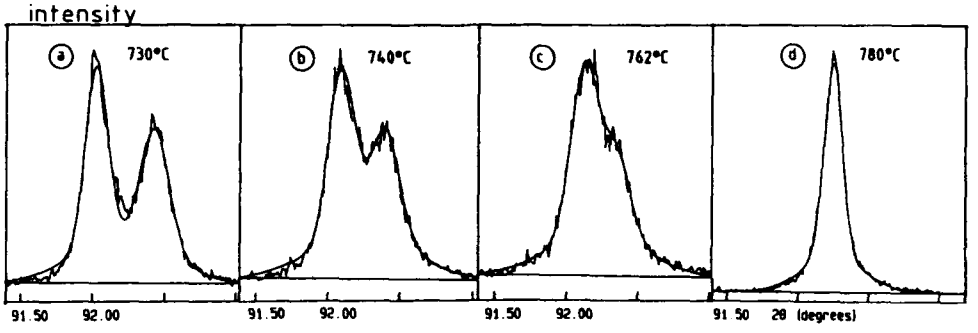

Figure 11. Isochronal evolution of the (420) f.c.c. X-ray diffraction line (Cu $K\beta_1$ radiation) of $TiC_{0.67}$ across the order (trigonal) → disorder (cubic) transition.
a) 1 month anneal at 730°C (trigonally ordered) ; b) a + 24 h anneal at 740°C ; c) a + 24 h at 762°C ; d) a + 24 h at 780°C (disordered).

4.2.3. *Results : $TiC_{0.63}$ and $TiC_{0.58}$.* In these two samples, one observes an heterogeneous behaviour during ordering : the progressive appearance of a well-defined trigonally distorted phase, coexisting with the cubic phase (see figure 12). The kinetic of phase transformation is very slow, and complete transformation to the trigonal phase difficult (or impossible) to obtain. For example, in the condition where $TiC_{0.67}$ transforms completely (5 weeks anneal at 730°C), one observes only 30 % trigonal phase in $TiC_{0.63}$. The largest proportion of trigonal phase was observed when cooling very slowly (< 0.2°C/hour) from 800°C (just above T_c) and following by long anneals : for $TiC_{0.58}$, with 15 days at 750°C + 15 days at 740°C, the transformation was practically complete.

Several remarks can be made :

- Below 700°C, for $TiC_{0.58}$ and $TiC_{0.63}$ as well as for $TiC_{0.67}$, even after one month anneal, it was practically impossible to obtain the trigonal phase, although superlattice reflexions appeared.

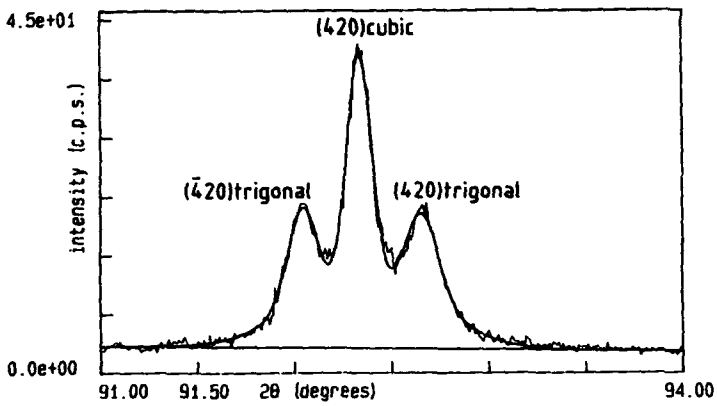

Figure 12. Profile of the (420) f.c.c. X-ray diffraction line (Cu $K\beta_1$ radiation) of $TiC_{0.63}$ after the following ordering thermal treatment : 3 h at 800°C (*in the disordered state*) + slow cooling (0.2 °C/h) from 800 to 750°C + 15 days at 750°C + 15 days at 740°C. This profile shows a central line belonging to the cubic phase and two side lines corresponding to the trigonal phase.

- During the isothermal cubic → trigonal phase transformation process, the (½ ½ ½) type superlattice reflexions intensities remain constant : the cubic phase is then very probably $Ti_2C_{1+y}I$. The f.c.c. cubic lines remained narrow, contrary to the trigonal phase lines which showed some broadening.
- For $TiC_{0.58}$, it was observed, in agreement with previous studies [45], that titanium metal precipitates during the long anneal at 730°C. The increase of lattice parameter was consistent with a final composition $TiC_{0.61}$ (i.e. 5 % Ti precipitated).
- The order-disorder transition temperature is maximum (795°C) for $TiC_{0.63}$.
- The trigonal distortion is larger for $TiC_{0.63}$ (α_{rh} = 90°37 at 740°C) than for $TiC_{0.67}$.

4.3. THE TiC_x PHASE DIAGRAM

The above results, together with literature data, lead to the following conclusions for the TiC_x phase diagram in the composition range $0.5 < x < 0.8$:

- the stable ordered phase above 700°C for $0.60 \lesssim x \lesssim 0.67$ is (trigonal) $Ti_2C_{1+y}II$;
- cubic $Ti_2C_{1+y}I$ appears as a metastable superstructure (its T_c value is $\simeq$ 10°C lower than for $Ti_2C_{1+y}II$) formed in the first period of isothermal treatments ;
- the order-disorder transition is nearly second order : the existence of an ordered + disordered two-phase domain just below T_c is possible but not proved on the basis of diffraction experiments (figure 11).

The resulting experimental phase diagram is summarized in figure 13.

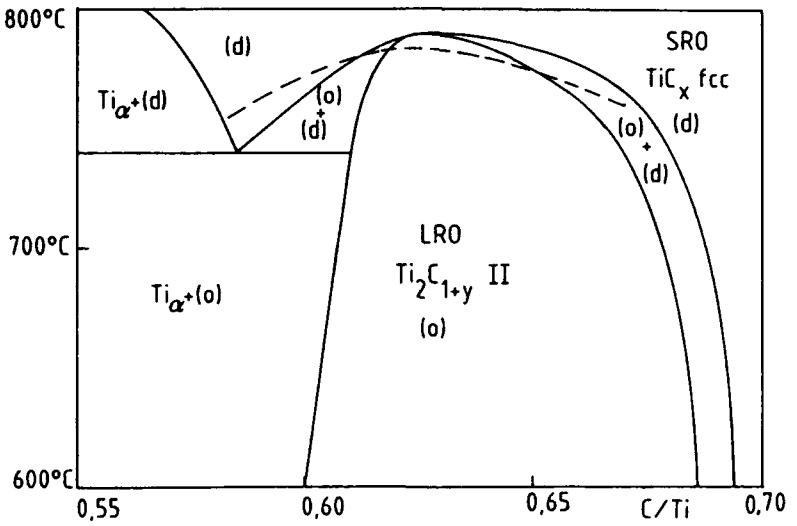

Figure 13. Ti-C experimental phase diagram for $0.5 < x = C/Ti < 0.7$ and $600 < T < 800°C$. Dashed line : upper limit of (metastable) Ti_2C_{1+y} I.

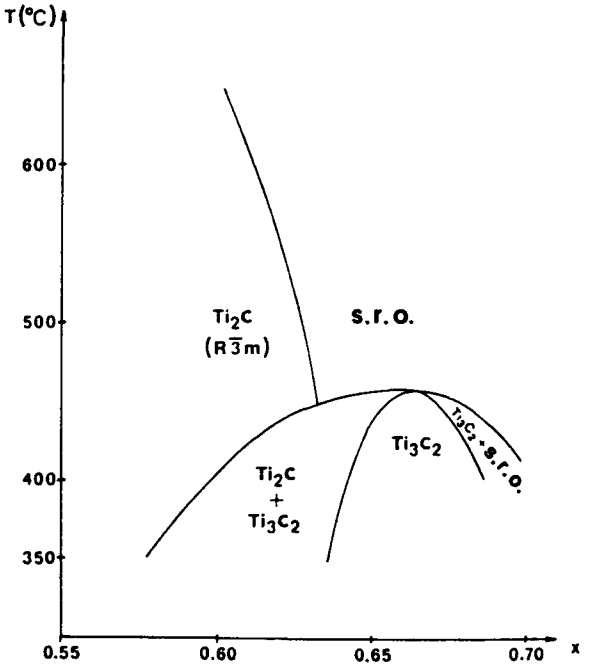

Figure 14. (Coherent f.c.c.) Ti-C phase diagram calculated by Monte-Carlo simulation from the C.V.M. V_i pair interactions in $TiC_{0.64}$.

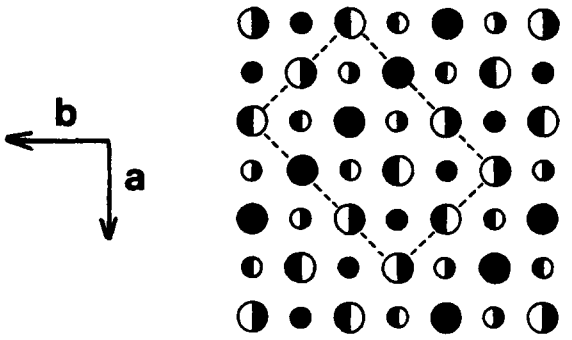

Figure 15. $Ti_3C_2\square$ crystal structure calculated by Monte-Carlo simulation from the C.V.M. pair interactions in $TiC_{0.64}$, projected on the f.c.c. (001) plane. The metal atoms are not represented. • : C atoms. ○ : vacancies. The large (resp. small) circles represent the metalloid sites on (00n) planes with n integer (resp. half-integer) ; the half-filled circles correspond to a C-vacancy alternance along the (001) axis.

In order to evaluate the ability of pair interactions deduced of elastic diffuse neutron scattering experiments to predict f.c.c. coherent phase diagrams, a Monte-Carlo simulation was performed for $0.55 < x < 0.70$, from the CVM energies V_i of $TiC_{0.64}$ (see Table 3). The calculated phase diagram is shown on figure 14.

Two different LRO phases are obtained :

(i) the ordered $R\bar{3}m$ Ti_2C II,

(ii) and a Ti_3C_2 phase for larger carbon concentrations. This Ti_3C_2 phase (A_2B in the carbon sublattice) predicted by Monte-Carlo is orthorhombic of space group $C222_1$, with unit cell vectors $\vec{a} + \vec{b}$, $3(\vec{a}-\vec{b})$ and $2\vec{c}$ (if $\vec{a}$, $\vec{b}$, $\vec{c}$ are the primitive f.c.c. cell vectors) (see figure 15). Ti_3C_2 shows (2/3 2/3 0) superstructure peaks in the reciprocal lattice.

All transformations in this Monte-Carlo phase diagram are first order, except Ti_2C II $\longleftrightarrow$ f.c.c. disordered, which is second order.

The experimental arguments for the existence of the Ti_3C_2 superstructure are the following :

- the (2/3 2/3 0) and (½ ½ ½) type superlattice reflexions observed on the diffuse neutron scattering spectrum of $TiC_{0.61}$ annealed one week at 600°C [50] are consistent with a $Ti_2C + Ti_3C_2$ phase mixture ;
- the SRO diffuse maxima of $TiC_{0.76}$ (figure 6b) are of the type (2/3 2/3 0) ;
- the $\alpha_{\ell m n}$ parameters measured for $TiC_{0.64}$ at 900°C (Table 1) are consistent with a Ti_2C or Ti_3C_2 superstructure, but not with Ti_8C_5 proposed in [47] (for the latter : $\alpha_{112} = -0.067$, when the experimental value is + 0.037, and the calculated values 0 for Ti_2C and -0.125 for Ti_3C_2).

In conclusion, the Monte-Carlo calculated phase diagram is in qualitative agreement with experiment, if one displaces the calculated phase boundaries towards richer carbon concentrations.

5. Conclusion

In this paper, we have shown that :

(i) topological disorder and chemical SRO in non-stoichiometric compounds can be precisely separated and studied by single crystal diffuse neutron scattering,

(ii) reasonable coherent phase diagrams can be calculated from the ordering pair interactions deduced from the chemical SRO. It is important to recall that high temperature studies are necessary to obtain equilibrium thermodynamic informations, and that neutrons have great advantages on X-rays in this case, as they allow to discriminate experimentally the scattering by phonons, and are more sensitive to light metalloid atoms.

The success in the case of transition metal carbides and nitrides is largely due to the fact that topological disorder is weak. The calculation of "incoherent" phase diagrams with lattice reconstruction will of course require an evaluation of the distance dependence of the V_i.

Future important progress in this field of ordering in non-stoichiometric compounds should be made with the use of high-resolution electron microscopy and analytical techniques, in order to complement the bulk "statistically averaged" information given by diffuse neutron scattering [9]. For this, very homogeneous non-stoichiometric crystals will be required.

6. Acknowledgements

We wish to thank Dr. A.N. Christensen (Aarhus University, Denmark) who elaborated the single crystals used in the diffuse neutron scattering experiments, and Dr. G. Treglia (Orsay University, France) who calculated the pair interactions displayed in figure 4.

7. References

1. de Novion, C.H. and Landesman, J.P. (1985) 'Order and disorder in transition metal carbides and nitrides : experimental and theoretical aspects', Pure Appl. Chem. 57, 1391-1402.
2. Toth, L.E. (1971) Transition metal carbides and nitrides, Academic Press, New-York and London.
3. Davis, R.F. (1987) 'Non-stoichiometry and its effect on mass transport, order-disorder phenomena, and deformation behavior in transition-metal carbides' in C.R.A. Catlow and W.C. Mackrodt (eds.), Non-stoichiometric compounds, Advances in Ceramics Vol. 23, The Amer. Ceram. Soc., Westerville, Ohio, pp. 529-557.
4. de Novion, C.H. and Landesman, J.P. (1987) 'Order-disorder and effective pair interactions in non-stoichiometric rocksalt-structure transition-metal carbides and nitrides', in C.R.A. Catlow and W.C. Mackrodt (eds.), Non-stoichiometric compounds, Advances

in Ceramics Vol. 23, The Amer. Ceram. Soc., Westerville, Ohio, pp. 499-528.
5. Parthé, E. and Yvon, K. (1970) 'On the crystal chemistry of the close-packed transition metal carbides. II - A proposal for the notations of the different crystal structures', Acta Crystallogr. Sect. B 26, 153-163.
6. Venables, J.D., Kahn, D. and Lye, R.G. (1968) 'Structure of the ordered compound V_6C_5', Phil. Mag. 18, 171-192.
7. Lewis, M.H., Billingham, J. and Bell, P.S. (1972) 'Non-stoichiometry in ceramic compounds' in E. Thomas, R.M. Fulrath and R.M. Fisher (eds.), Electron Microscopy and Structure of Materials, Univ. of California Press, Berkeley, CA, pp. 1084-1115.
8. Gusev, A.I. and Rempel, A.A. (1986) 'Order-disorder phase transition channel in niobium carbide', Phys. Stat. Sol.(a) 93, 71-80.
9. Epicier, T. and Kumashiro, Y. (1987), 'A first HREM observation of the ordered carbon sublattice in a transition metal carbide (VC_{1-x})', Phil. Mag. Lett. 55, 171-179.
10. de Novion, C.H., Lorenzelli, R. and Costa, P. (1966) 'Existence d'une surstructure dans le carbure de vanadium VC_{1-x}', Comptes Rendus Acad. Sc. Paris Ser. B 263, 775-778.
11. Sauvage, M. and Parthé, E. (1972) 'Vacancy short-range order in substoichiometric transition metal carbides and nitrides with the NaCl structure. II - Numerical calculations of vacancy arrangement', Acta Crystallogr. Sect. A 28, 607-616.
12. de Fontaine, D. (1979) 'Configurational thermodynamics of solid solutions', Solid State Phys. 34, 73-274.
13. Landesman, J.P., Treglia, G., Turchi, P. and Ducastelle, F. (1985) 'Electronic structure and pairwise interactions in substoichiometric transition metal carbides and nitrides', J. Phys. France 46, 1001-1015.
14. Haydock, R. (1980) 'The recursive solution of the Schrödinger equation', Solid State Phys. 35, 215-294.
15. Froidevaux, C. and Rossier, D. (1967) 'NMR investigation of the atomic and electronic structure of vanadium and niobium carbides', J. Phys. Chem. Solids 28, 1197-1209.
16. Billingham, J., Bell, P.S. and Lewis, M.H. (1972) 'Vacancy short-range order in substoichiometric transition metal carbides and nitrides with the NaCl structure. I - Electron diffraction study of the short-range ordered compounds', Acta Crystallogr. Sect. A 28, 602-606.
17. Sauvage, M. and Parthé, E. (1974) 'Prediction of diffuse intensity surfaces in short-range ordered ternary derivative structures based on ZnS, NaCl, CsCl and other structures', Acta Crystallogr. Sect. A 30, 239-246.
18. Ohshima, K., Harada, J., Morinaga, M., Georgopoulos, P. and Cohen, J.B. (1988) 'Distortion-induced scattering due to vacancies in $NbC_{0.72}$', Acta Crystallogr. Sect. A 44, 167-176.
19. Moisy-Maurice, V., de Novion, C.H., Christensen, A.N. and Just, W. (1981) 'Elastic diffuse neutron scattering study of the defect structure of $TiC_{0.76}$ and $NbC_{0.73}$', Solid State Commun. 39,

661-665.
20. Kaufmann, R. and Meyer, O. (1983) 'Ion channeling in NbC_{1-c} : determination of local atomic displacements around carbon vacancies', Phys. Rev. B 28, 6216-6226.
21. Kaufmann, R. and Meyer, O. (1984) 'Determination of static displacements around non-metal vacancies in NbN_{1-c} and TiC_{1-c}', Solid State Commun. 51, 539-543.
22. Moisy-Maurice, V. and de Novion, C.H. (1988) 'An application of Ti-K X-ray absorption edges and fine structures to the study of substoichiometric titanium carbide TiC_{1-x}', J. Phys. France 49, 1737-1751.
23. Priem, T., Beuneu, B., de Novion, C.H., Caudron, R., Solal, F. and Christensen, A.N. (1987) '(½ ½ ½) versus (1 ½ 0) type ordering of nitrogen vacancies in TiN_x', Solid State Commun. 63, 929-932.
24. Ducastelle, F. and Gautier, F. (1976) 'Generalized perturbation theory of disordered transition alloys : application to the calculation of ordering energies', J. Phys. F : Metal Phys. 6, 2039-2062.
25. Treglia, G. unpublished.
26. Hayakawa, M., Bardhan, P. and Cohen, J.B. (1975) 'Experimental considerations in measurements of diffuse scattering', J. Appl. Crystallogr. 8, 87-95.
27. Priem, T., Beuneu, B., de Novion, C.H., Finel, A. and Livet, F. (1989) 'Short-range order, atomic displacements and effective interatomic ordering energies in $TiN_{0.82}$', J. Phys. France 50, 2217-2242.
28. Caudron, R. and Finel, A. (1983) 'Application de la diffusion diffuse des neutrons aux études de thermodynamique des alliages', Technical Report n°11/1221M, ONERA, Chatillon, France.
29. Priem, T. (1988) 'Etude de l'ordre à courte distance dans les carbures et nitrures non-stoechiometriques de métaux de transition par diffusion diffuse de neutrons', PhD Thesis, Univ. Paris-Sud, Orsay, France.
30. Beuneu, B, Priem, T., de Novion, C.H., Lefebvre, S., Chevrier, J. and Christensen, A.N., 'Short-range order determination in quenched $NbC_{0.73}$ by elastic diffuse neutron scattering', to be published.
31. de Ridder, R., Van Tendeloo, G., Van Dyck, D. and Amelinckx, S. (1976) 'A cluster model for the transition state and its study by means of electron diffraction', Phys. Stat. Sol.(a) 38, 663-674.
32. Dunand, A., Flack, H.D. and Yvon, K. (1985) 'Bonding study in TiC and TiN. I. High precision X-ray diffraction determination of the valence-electron density distribution, Debye-Waller temperature factors, and atomic static displacements in $TiC_{0.94}$ and $TiN_{0.99}$' Phys. Rev. B 31, 2299-2315.
33. Lesueur, D. (1981) 'Deplacements atomiques autour d'une lacune de carbone dans UC', J. Nucl. Mater. 102, 87-96.
34. Kress, W., Roedhammer, P., Bilz, H., Teuchert, W.D., and Christensen, A.N., (1978) 'Phonon anomalies in transition metal

nitrides : TiN', Phys. Rev. B 17, 111-113.
35. Pintschovius, L., Reichardt, W. and Scheerer, B. (1978) 'Lattice dynamics of TiC', J. Phys. C : Solid State Phys. 11, 1557-1562.
36. Weber, W. (1973) 'Lattice dynamics of transition metal carbides', Phys. Rev. B 8, 5082-5092.
37. Storms, E.K. (1967) 'The refractory carbides', Academic Press, New-York and London.
38. Clapp, P.C. and Moss, S.C. (1966) 'Correlation functions of disordered binary alloys', Phys. Rev. 142, 418-427.
39. Fletcher, R. and Powell, M.J.D. (1963) 'A rapidly convergent descent method for minimization', The Computer Journal 6, 163-168.
40. Livet, F. (1987) 'Linearized inverse Monte-Carlo method applied to Ni_3Fe', Acta Metall. 35, 2915-2919.
41. Kikuchi, R. (1977) 'The Cluster-variation method', J. Phys. France Coll. C7, 38, 307-313.
42. Finel, A. (1987) 'Contribution à l'étude des effets d'ordre dans le cadre du modèle d'Ising : états de base et diagrammes de phase', PhD Thesis, Univ. Pierre et Marie Curie, Paris.
43. Goretzki, H. (1987) 'Neutron diffraction studies on titanium-carbon and zirconium-carbon alloys', Phys. Stat. Sol. 20, K141-143.
44. Richards, M.J. and Cahn, J.W. (1971) 'Pairwise interactions and the ground state of ordered binary alloys', Acta Metall. 19, 1263-1277.
45. Moisy-Maurice, V., Lorenzelli, N., de Novion, C.H. and Convert, P. (1982) 'High temperature neutron diffraction study of the order-disorder transition in TiC_{1-x}', Acta Metall. 30, 1769-1779.
46. Em, V.T., Karimov, I., Petrunin, V.F., Khidirov, I., Latergaus, I.S., Merzhanov, A.G., Borovinskaya, I.P. and Prokudina, V.K. (1975) 'Neutron diffraction study of ordering in titanium carbides', Sov. Phys. Crystallogr. 20, 198-199.
47. Khaenko, B.V., Galab, S.Y. and Arbuzov, M.P. (1980) 'The order structure of titanium carbide', Sov. Phys. Crystallogr. 25, 63-67.
48. Hauck, J., Larson, B.C., Gruzalski, G.R., Darken, L.S. and Barhorst, J.F. (1984), Report ORNL-6128, Oak-Ridge, Tennessee, p. 109.
49. Lorenzelli, N., Caudron, R., Landesman, J.P. and de Novion, C.H. (1986) 'Influence of the ordering of carbon vacancies on the electronic properties of $TiC_{0.625}$', Solid State Commun. 59, 765-769.
50. Moisy-Maurice, V. (1981) 'Structure atomique des carbures non-stoechiometriques de métaux de transition', Commissariat à l'Énergie Atomique (France), Rept N° CEA-R-5127.
51. Utkima, T.G., Karimov, Yu. S. and Rogachev, A.S. (1984) 'The possibility of a high-temperature superconducting phase of titanium carbide near the lower bound of the region of homogeneity', Sov. Phys. Solid State 26, 172-173.
52. Athanassiadis, T., Lorenzelli, N. and de Novion, C.H. (1987) 'Diffraction studies of the order-disorder transformation in V_8C_7', Ann. Chim. Fr. 12, 129-142.
53. Krzanowski, J.E. and Allen, S.M. (1983) 'The migration kinetics of antiphase boundaries wetted by a second phase', Acta Metall. 31, 213-222.

MASS TRANSPORT IN CARBIDES AND NITRIDES

Hj. Matzke

Commission of the European Communities
Joint Research Centre
European Institute for Transuranium Elements
Postfach 2340, D-7500 Karlsruhe
Federal Republic of Germany

ABSTRACT

The existing knowledge on diffusion processes, on point defect behaviour and on radiation damage in carbides and nitrides is discussed. Most data exist for transition metal carbides and for actinide carbides and nitrides, and some data exist for SiC. Very little information is available for other carbides and, in particular, for many interesting nitrides.

The diffusion activation enthalpies are generally high, and the entropy values are generally consistent with Zener's theory of volume diffusion. However, the mechanisms of diffusion usually differ for the metal and the non-metal sublattice. They may even change with composition for different parts of the often very wide region of existence of the monocarbides.

Recent work on the actinide compounds UC and UN including self-diffusion and quenching studies as well as work on radiation damage produced by ion or electron bombardment with subsequent damage recovery followed by measurements of electrical resistivity or with the aid of the Rutherford backscattering-channeling technique has provided further insight in defect formation, and in instantaneous and thermally activated recovery. Supporting electron microscopy helped to better define the defect behaviour. Though in the carbides and nitrides considered, the metal atoms are generally the less mobile species - and are therefore rate-controlling for high-temperature kinetic processes and matter transport - important metal atom mobility at and below room temperature has recently been seen in UN.

Finally, some high-temperature diffusion-related processes (e.g. sintering, creep, grain growth, etc.) are also treated to some extent.

R. Freer (ed.), The Physics and Chemistry of Carbides; Nitrides and Borides, 357–383.
© 1990 *Kluwer Academic Publishers. Printed in the Netherlands.*

1. Introduction

This article has the aim of reviewing existing diffusion data for the materials treated in the NATO Advanced Research Workshop on the Physics and Chemistry of Carbides, Nitrides and Borides held at Manchester, September 18 - 22, 1989. Since very little is known on mass transport in borides, the article is restricted to carbides and nitrides, and, more specifically, it is restricted to those carbides and nitrides, for which reliable diffusion data exist. These are mainly transition metal carbides of groups IV and V, and to a much smaller extent the corresponding nitrides, the actinide carbides and nitrides of U and the corresponding mixed compounds of (U, Pu), as well as the "light high-tec advanced ceramics" SiC and Si_3N_4.

These carbides and nitrides are of considerable technological and scientific interest, as is explained in more detail in other contributions to these proceedings and as is described in a contribution of the author to a previous NATO Advanced Study Institute held in Aussois, France, in March 1989 [1]. The present article is therefore rather brief in a description of the technological and scientific interest in the carbides and nitrides, as well as in giving a characterization of this class of materials. Rather, besides reviewing the existing data on diffusion, it concentrates on new unpublished results from the laboratories of the author on diffusion and point defect behaviour of a specific nitride, UN, and it describes some of the relations between diffusion and other technologically interesting high temperature mass transport processes such as grain growth, sintering, creep, densification and restructuring in a temperature gradient etc.

Most of the materials treated here are of the NaCl structure. The materials for which reliable diffusion data exist are summarized in Table 1, which gives melting points and the widths of the phase fields of the monocarbides and mononitrides, many of which show a very wide single phase field and large degrees of nonstoichiometry (see Fig. 1). A particularly impressive example is $ThC_{1\pm x}$ for which the single phase field extends practically from the fcc Th metal to the dicarbide ThC_2. First, the octahedral sites of the Th structure are filled with single carbon atoms and subsequently carbon pairs replace these single carbon atoms. The lattice parameter increases from 0.508 nm (Th) over 0.534 nm (ThC) to 0.580 nm (ThC_2). At such large degrees of nonstoichiometry and consequently large defect concentrations, defect interactions, cluster formation and ordering phenomena are expected to occur. These ordering phenomena are treated in the contribution of de Novion to these proceedings [2]. Because of the high temperatures necessary for diffusion studies no significant effects of order - disorder phenomena on diffusion measurements are expected since the transition temperatures from order to disorder for most carbides and nitrides are $\leq$ 1000 °C. This is in striking contrast to phase changes which occur in materials like $UC_{1\pm x}$ where the single phase field is wide only at very high

temperatures, and where the substoichiometric monocarbide UC_{1-x} can decompose into UC+U, and the hyperstoichiometric monocarbide UC_{1+x} into $UC+U_2C_3$ or $UC+UC_2$. In such a two-phased material, the effective diffusion coefficient will not be that for any of the two phases, but will rather be a complex quantity, e.g. for $UC+UC_2$ in a needle-shaped so-called Widmanstätten structure, it will be

$$D_{eff} = (1-g)D_{UC} + gD_{UC_2} + D_{pb}$$

where g is the fraction of UC_2 and D_{pb} is the coefficient describing diffusion along the phase boundaries. Such a D_{eff} should not be mistaken as the intrinsic D of a single-phased non-stoichiometric compound.

Table 1: Carbides and nitrides of transition metals, of actinides and of Si for which reliable diffusion data exist together with the melting points, T_m and the phase fields of the monocarbides MC and the mononitrides MN

	carbides		nitrides	
	phase field, MC	T_m (°C), MC	phase field, MN	T_m (°C), MN
Ti	0.47 - 0.95	3067	0.6 - 1.0	2949
Zr	0.55 - 0.98	3420	~ 0.5 -1 .0	2982
Hf	0.52 - 0.98	3928	0.74 - 1.13	3387
V	0.75 - 0.90	2648	0.74 - 1.00[a)]	2177
Nb	0.70 - 0.99	3600	0.75 - 1.06[a)]	2204
Ta	0.72 - 0.99	3983	-	3093
U	0.9 - 1.95 (T<1100 °C, l.c.)	2525	narrow	2830
Si	narrow	2760	l.c.	1900 (Si_3N_4)[d)]

The width of phase field of the MX (X = C or N) phase depends on temperature. Often, disagreeing results exist depending on whether or not equilibrium in dissolution of metal or non-metal atoms in the MX-phase was achieved.
a) For high temperature cubic δ-phase, d = decomposes, l.c. = line compound

A number of *specific difficulties exist in measuring diffusion* in carbides and nitrides. To start with, good specimens (high purity, preferable single crystals) of the hard materials with extremely high melting points are difficult to produce. Because of the high melting points (T_m), diffusion experiments have to be performed at very high temperatures as well. To exceed temperatures of 0.7 T_m, furnaces achieving temperatures in excess of

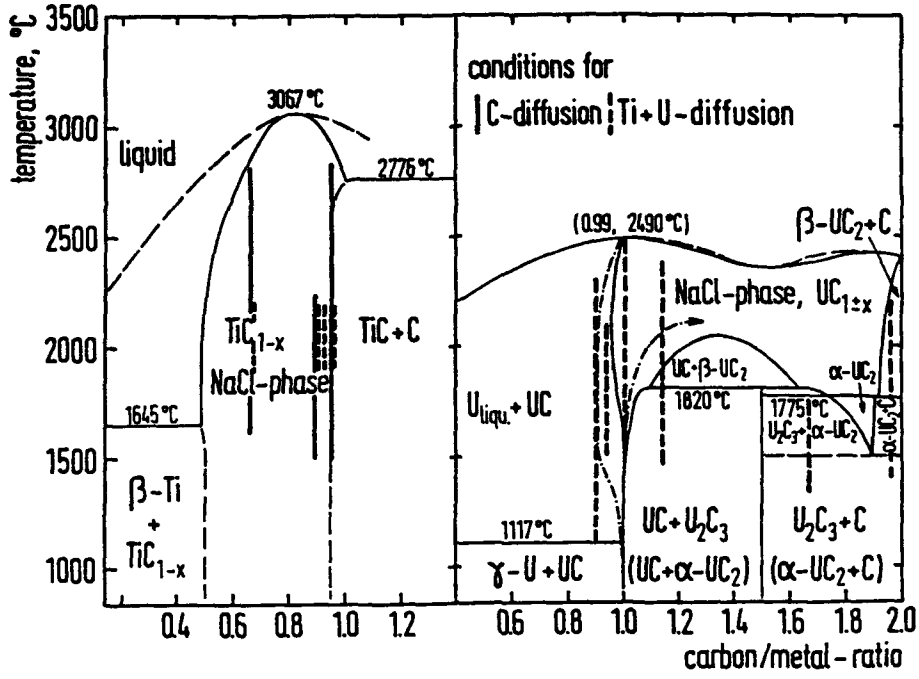

Fig. 1: Phase diagrams of the Ti-C and the U-C systems around the field of the NaCl-type nonstoichiometric monocarbides TiC_{1-x} and $UC_{1\pm x}$, as suggested in [9, 10]. Thick vertical lines indicate the compositions used for diffusion work (C and Ti in TiC_{1-x}, U in $UC_{1\pm x}$; very many data exist for C diffusion in $UC_{1\pm x}$ [10]; the corresponding vertical lines are not included in Fig. 1.

1700°C are needed. In fact, diffusion measurements have been performed up to ~ 3000°C (see Fig. 2), and, e.g. for the case of U diffusion in UC up to a few degrees below the melting point [3].

For some interesting nitrides, Si_3N_4 and BN, no suitable radioactive tracer exists. To measure nitrogen diffusion, either mass spectrometric analysis of N-15 (analysis of gas phase or SIMS on specimen) or a suitable nuclear reaction induced in the specimen following a diffusion anneal in, e.g., an N_2 atmosphere enriched in N-15 are needed to determine nitrogen diffusion profiles. The problem is similar to that of measuring oxygen diffusion with O-18, but the abundance of N-15 in natural N_2 is about twice that of O-18 in natural O_2 (0.37 vs 0.20 %), thus yielding a higher background. The readily available radioactive isotope for silicon, Si-31, has an inconveniently short half-life of only 2.6 h, and Si-32 with a suitable half-life (~ 300 yrs) is very difficult to produce (e.g. by spallation of heavier nuclides in a cyclotron) and has only a very weak β-radiation. Therefore,

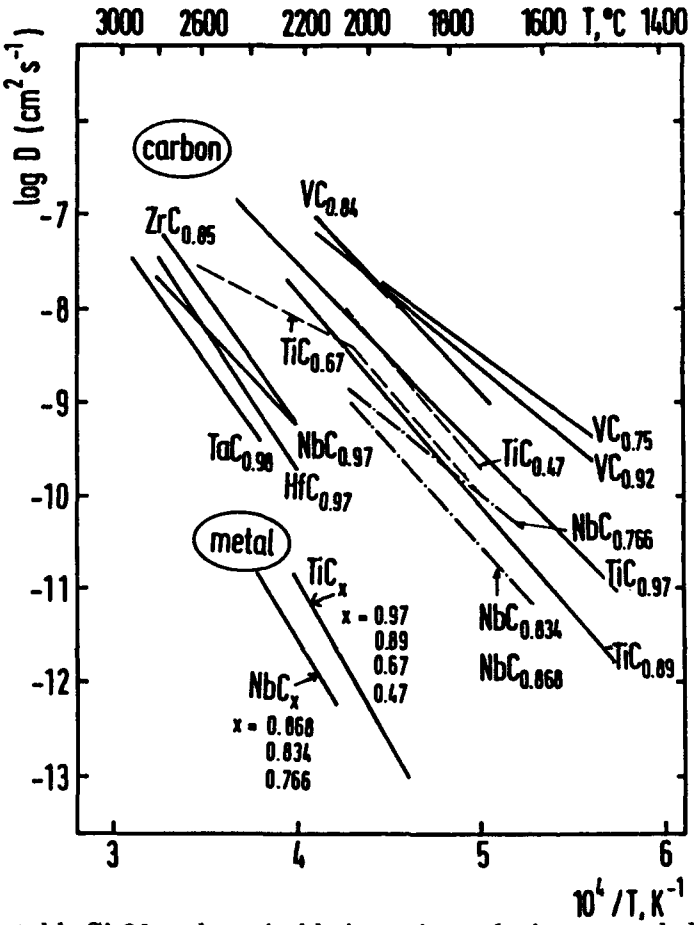

Fig. 2:
Typical data for carbon and metal diffusion in transition metal carbides of different C/M-ratios [11-18].

stable Si-30 and a suitable isotopic analysis are needed. Isotopic analysis is, of course, a great problem in the absence of radioactive radiation and the presence of complete interference of mass numbers: Si-28, Si-29, Si-30, $(N\text{-}14)_2$, (N-14/N-15), $(N\text{-}15)_2$.

For carbon diffusion, C-14 is used as radioactive tracer. It has a low specific activity, since it has a long half-life (5700 yrs) and is often not available in carrier-free form. Therefore, tracer layers are often thick. If they are identical in composition and purity with the diffusion sample, the only additional difficulty is trivial and consists in applying the appropriate solution of the diffusion equation (not always done in the existing literature!). If a thick carbon layer is used, the data (at least for short diffusion distances) are representing chemical rather than self-diffusion of the tracer.

The most frequently used *experimental technique* to determine diffusion profiles of carbon is sectioning and counting of the activity of

removed layers and/or of the remaining sample. The same technique is used to measure metal diffusion (e.g. Ti, Ta, Zr, etc.) in transition metal carbides and nitrides. For the actinides, besides applying sectioning, use can be made of the specific properties of the (largely) monoenergetic α-particles emitted in the decay of most actinides. With special spectrometers and adequate mathematical treatment, the α-energy spectra can be unfolded to yield diffusion profiles. Very small diffusion coefficients can be measured reliably, down to about 10^{-18} cm^2s^{-1}, and the time dependence of diffusion can easily be followed since the method is non-destructive. This allows separation of surface effects, grain boundary diffusion, etc. (if existant) from volume diffusion. This method has been described in detail in a previous review of the author on diffusion in ceramic nitrides [4].

A number of supporting measurements yielding additional information on point defect formation and migration exists and has been applied to a few carbides and nitrides (mostly UC and UN, but also TiC and TaC). The techniques used are, briefly

i) *quenching* with subsequent isochronal or isothermal anneals which, in principle, yields formation and migration energies of point defects. Unfortunately, the results are usually affected by incomplete quenching, often by the possible presence of at least four types of defects (vacancies and interstitials of metal and metalloid atoms) and by impurity-vacancy interactions, though sometimes the formation energies are different enough to largely obtain defects in one sublattice only in a certain temperature range;

ii) *recovery of radiation damage*. As in quenching, changes in electrical resistivity or lattice parameter can be used to study damage ingrowth and recovery upon annealing. Again, the attribution of recovery stages to defects in different sublattices is often arbitrary. Examples of such work for damage production by fission or by bombardment in accelerators are refs. [5, 6].

iii) *channeling and Rutherford backscattering*: These methods involve energetic beams of e.g. 2 MeV He-ions from a van de Graaff accelerator and make use of the largely different scattering cross sections of (heavy) metal atoms and (light) metalloid atoms to selectively study one sublattice. The above ambiguity of attributing the observed defect ingrowth or thermal recovery to one of the two different sublattices does thus not exist. Use is made of the crystal structure to amplify the signal from displaced atoms by the channeling effect. This technique, developed in the 1960's is now widely used [7] and has also recently been applied to a nitride, UN [8].

Recent results for the carbides and nitrides mentioned above (UC, TiC, TaC, UN) for all these techniques will be discussed in Chapter 3, following a discussion of the diffusion results in Chapter 2. Finally, diffusion-related kinetic processes will be treated in Chapter 4.

2. Results for Diffusion

2.1 TRANSITION METAL CARBIDES

Many data have been published on self-diffusion, and some results exist on impurity diffusion, in transition metal carbides of the NaCl-structure, often for widely differing C/M-ratios, as e.g. indicated in Fig. 1 by vertical lines. Representative results for self-diffusion of both carbon and of metal atoms in transition metal carbides are shown in Fig. 2. The impressive feature are the unusually high diffusion temperatures. Early work was done in Russia [e.g. 11, 12], and more recent data are due to Sarian [13-16] and Davis et al. [17, 18] which include a rather systematic variation of C/M-ratio in order to cover some or most of the single phase fields of the monocarbides (see Fig. 1 and Table 2). The experimental temperatures were high enough so that any residual order and hence non-random vacancy contribution, can safely be assumed to have no influence on matter transport processes. In contrast to SiC (see below), there is no report on antisite defects in NaCl-type carbides. Changes in concentration of defects in one sublattice may therefore be expected to affect the other sublattice mainly by changes in the bonding conditions.

More than 50 % vacancies can exist in the carbon sublattice, as shown in Table 1. This percentage is fixed by the C/M-ratio and equals (1-x) if the carbide is referred to as MC_x. The normal diffusion equation $D = D_0 \exp(-Q/RT)$ can thus be written for carbon diffusion, D_C, as

$$D_C = f_C a_o^2 \nu_C^o (1-x) [\exp \Delta S_C^m/k][\exp - (\Delta H_c^m / kT)] \qquad (1)$$

where f_C is the correlation factor ($0.78 \leq f_C \leq 1$, depending on x), a_o is the lattice parameter, ν_C the fundamental frequency, (1-x) the fraction of C-vacancies, and ΔS_C^m and ΔH_C^m the activation entropy and enthalpy for C-migration, respectively, a formation term not being needed because of the high C-vacancy concentration due to the non-stoichiometry.

The situation is different for the actinide carbides which may be overstoichiometric as well (e.g. UC_{1-x} and UC_{1+x} exist both, see Fig. 1). Equ. (1) has to be rewritten for the hyperstoichiometric side by replacing the term (1-x) by a factor $F = (1-x)(2-x)/x$.

In contrast to C-diffusion, formation and migration terms are needed in the diffusion equation for metal atom diffusion. In the metal sublattice, vacancies are formed thermally by Schottky disorder, and these concentrations may be assumed to be independent of the C/M-ratio, as is confirmed by the experimental data. Thus

$$D_M = f_M a_o^2 \nu_M^o \exp[(\Delta S_M^f + \Delta S_M^m)/k] \exp[-(\Delta H_M^f + \Delta H_M^m)/kT] \qquad (2)$$

where f_M = 0,78 and the other terms are as above, with ΔS_M^f and ΔH_M^f being the entropy and enthalpy, respectively, for vacancy formation.

Fig. 2 shows the existing metal diffusion data for TiC_x, ZrC_x and NbC_x with widely varying x-values indicating no dependence on x ($TiC_{0.971}$, $TiC_{0.95}$, $TiC_{0.89}$, $TiC_{0.67}$, or $NbC_{0.868}$, $NbC_{0.834}$, $NbC_{0.766}$ etc. were used to establish Arrhenius diagrams for both C and M diffusion). The activation enthalpies are high (see Table 2) and an evaluation of D_o-values, applying the well-known Zener model [32], yields ΔS values in the range 5 to 15 R, pointing to a single vacancy mechanism for metal atom diffusion, and, also, for carbon diffusion.

Carbon diffusion shows ΔH's for VC, NbC, TaC, TiC, ZrC and HfC in the range of 2.8 to 5.7 eV (see Table 2), scaling well with the melting points, T_m (ΔH_C / T_m = (1.30 ± 0.12) x 10^3 eV K^{-1}), and - but with different dependences for group V and group VI metal carbides - with the heats of formation [e.g. 33]. The available results are in agreement with a random migration of C-vacancies, the rather high ΔH_C values being the migration energy. There are some changes in D_C and ΔH_C with C/M-ratio. Although the data for TiC (and UC, see below) point to a common mechanism at all C/M-ratios investigated, Yu and Davis [17] have argued that, at least for NbC_x, the exact diffusion path for C may change as a function of C/M-ratio. From the rigid-sphere NaCl structure, they considered three atomic paths as most probable:

- O-O mechanism: the C atom jumps along the <110> direction directly to the nearest C octahedral site (O), with a jump distance $\sqrt{2}\,a_o$
- O-T-O mechanism: the C atom jumps via <111> directions to the nearest vacant C octahedral site via an unoccupied tetrahedral site (T) formed by the metal sublattice (effective jump distance again $\sqrt{2}\,a_o$)
- C-M transient divacancy mechanism (D mechanism): the C atom jumps to a vacant C octahedral site via a normally occupied metal vacancy that momentarily became associated with the C vacancy.

A large lattice strain and the movement of 2 M atoms are necessary for the O-O mechanism to be operative; the O-T-O mechanism involving two jumps into and from the T site requires less strain energy. The smallest migration energy is involved in the D mechanism, the total ΔH being essentially that of forming an M vacancy, ΔH_M^f. For NbC_x, this value is reported as being 2.6 eV; therefore, Yu and Davis attributed the D-mechanism to strongly substoichiometric $NbC_{0.76}$ (ΔH = 3.3 eV), and the O-T-O mechanism to the carbon-richer Nb $C_{0.834}$ (ΔH = 4.5 eV) and $NbC_{0.868}$ (ΔH = 4.3 eV). Thus, the increase in carbon diffusion rates with higher carbon deficiency would be due to a change from the O-T-O to the D mechanism. For Nb-diffusion, in contrast, the direct O-O mechanism is favored [17], just as for a pure fcc metal. This proposed behavior is consistent with the results of calculations invoking the model of Zener [32].

Table 2: Typical diffusion results for monocarbides and mononitrides of the NaCl-structure

Substance	Diffusing Atom	T-range °C	D_0 cm^2s^{-1}	ΔH eV	log D at 0.6 T_m, cm^2s^{-1}	Remark	Refs.
$TiC_{0.97}$	C	1475-2720	7.0	4.15	- 9.6	a.c	13
"	Si	1800-2227	$4.4x10^4$	7.65	- 14.5	a.c	13
$TiC_{0.87}$	C	1780-2110	45.4	4.6	-9.9	a.c	16
$ZrC_{0.97}$	C	1350-2150	132	5.6	- 9.0	p.c.,s.c	15
"	Zr	2325-2830	1030	7.5	1 .1	h.p.	12
$HfC_{0.97}$	C	2250-2800	63	5.7	-9.6	h.p	11
$VC_{0.84}$	C	1700-2200	2.65	3.7	- 10.2		14
$NbC_{0.87}$	C	1625-2050	2.60	4.3	- 9.0	s.c.	17
"	Nb	2100-2390	4.5	6.1	-12.5	s.c.	17
$NbC_{0.77}$	C	1625-2050	0.022	3.3	-8.8	s.c.	17
"	Nb	2100-2390	4.5	6.1	-12.5	s.c.	17
$TaC_{0.98}$	C	2360-2960	3.9	5.2	-9.6	h.p.	11
$UC_{1.0}$	C	1500-1800	24.0	3.7	-9.7	a.c.	19
"	U	1500-2485	11.7	6.2	-17.5	s.c.	3
UN	N	1200-2000	$2.3x10^{-4}$	2.7	--10.8	a.c.,p.	20-22
"	U	1640-1850	$1.2x10^{-3}$	5.0	-16.5	s.c.	23
(U,Pu)N	Pu	1400-1810	0.25	5.1	-14.4	sint.	24

s.c. = single crystal, a.c. = arc cast, sint. = sintered specimens, h.p. = hot pressed, p = powder

* constant N_2-pressure, hence not necessarily constant composition

Table 3: Diffusion results for Si_3N_4, SiC, and for another non-NaCl type carbide

Substance	Diffusing Atom	T-range °C	D_0 cm^2s^{-1}	ΔH eV	log D at 0.6 T_m, cm^2s^{-1}	Remark	Refs.
β-SiC	C	1855-2200	$4.4x10^7$	8.7	- 16.4	-	25
"	Si	2010-2275	$8.4x10^7$	9.5	- 18.3	-	26
α-SiC	C	1850-2180	$8.6x10^5$	7.4	- 14.5	pure 6H	27
"	C	1850-2180	$3.3x10^7$	8.2	- 15.1	6H, N-doped	27
α-SiC	Si	2000-2300	$5x10^2$	7.2	-17.2	pure 6H	28
"	Si	2000-2300	$1.5x10^5$	8.2	-15.1	6H, N-doped	28
α-SiC	Kr	1300-1900	0.3	4.4	- 12.6	6H,ion implant.	29
WC	C	1965-2370	$1.9x10^{-6}$	3.8	- 16.1	-	30
α-Si_3N_4 *	N	1200-1410	$1.2x10^{-12}$	2.4	- 20.1	isot.exchange	31
β-Si_3N_4	N	1300-1390	$6x10^6$	8.1	- 20.8	"	31

* Si_3N_4 decomposes at 1900° C. The log D-value in column 6 is, somewhat arbitrarily, chosen for 1200° C

2.2 TRANSITION METAL NITRIDES

Such nitrides are often used as thin layers or coatings on tools to reduce wear and to improve high temperature corrosion resistance, in miniature resistive and capacitive electronic components, or in solar energy technology. Chemical and reactive physical -vapor deposition, sputtering or ion implantation with nitrogen are used to produce these layers. Such layers are also often used as diffusion barriers between different metals, or between metals and silicon. Examples are 100 nm TiN layers between Si and various metals (e.g. Ag, Au, Pd, Cu etc.) to prevent interdiffusion in solar cells during heat treatments (800° C, 15 min) or multilayers such as a sequence of TaC, TiC, Al_2O_3, TiN on Co-bonded WC cutting tools, ZrN layers for tribological applications, or TiN or ZrN layers to provide thermal stability of high-conductivity silicides in large-scale integrated circuits against Al etc. [e.g. 34]. The purpose of such layers is to *prevent* diffusion. Therefore, the *absence* of diffusion at the temperatures of application (usually ≤ 600° C) is usually confirmed.

Some diffusion measurements exist for transition metal nitrides: N-15 exchange between the gas phase and ZrN and TiN was measured [35, 36] at rather low temperatures yielding low ΔH's of 1.0 to 1.6 eV/atom and D-values of the order of 10^{-14} cm^2s^{-1} at 0.5 T_m which might seem low for a material with 7, 18 or 29 % substitutional vacancies (these were the compositions used). However, as shown above for the isostructural nonstoichiometric carbides, such D-values are found there as well (though the ΔH-values are sigificantly higher). Whereas for the transition metal carbides, different diffusion mechanisms can be attributed to different degrees of nonstoichiometry (see above), it is still premature to suggest mechanisms for nitrogen diffusion. Data for metal atom diffusion in transition metal nitrides are still missing.

2.3 SiC, Si_3N_4 AND OTHER NON-NaCl TYPE CARBIDES AND NITRIDES

As mentioned above, no suitable radioactive tracer exists for Si_3N_4. Despite the importance of Si_3N_4 as high-tech light ceramic, very little is known on its diffusion behavior. The situation is better for *silicon carbide* though many of the earlier measurements were affected by decomposition of the specimens. In more recent work, the specimens were embedded in SiC powder in closed crucibles to give a saturated environment [27, 28] . The results for pure and N-doped single crystalline 6H α-SiC are shown in Fig. 3, and summarized in Table 3. In a compound semiconductor as SiC, electronic compensation occurs if donors or acceptors are added. The concentration of (charged) vacancies *on both sublattices* will be affected by adding impurities.

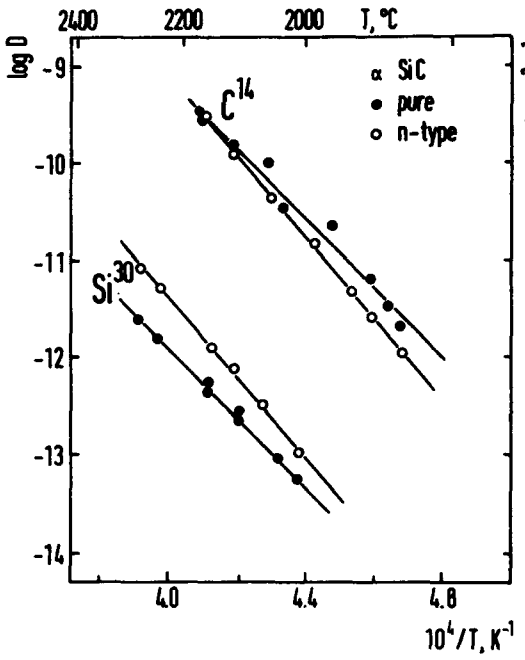

Fig. 3: Silicon and carbon self-diffusion in pure and N-doped 6 H α-SiC [27, 28]

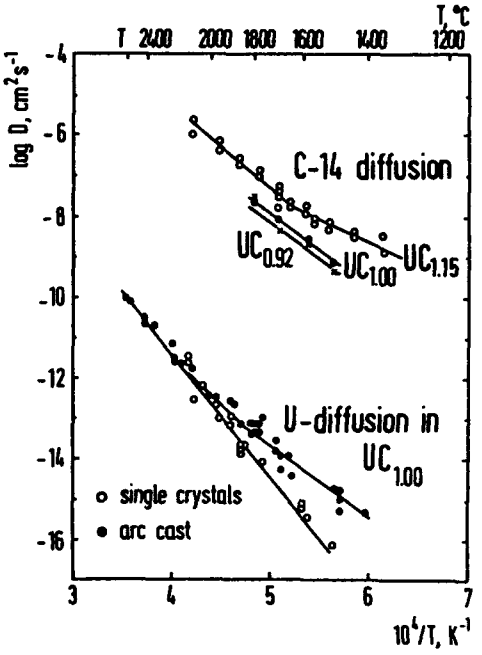

Fig. 5: Diffusion of C and U in $UC_{1\pm x}$. For U-diffusion, the open symbols are for zone-refined single crystals, the other data are for arc-cast polycrystals [3, 19]

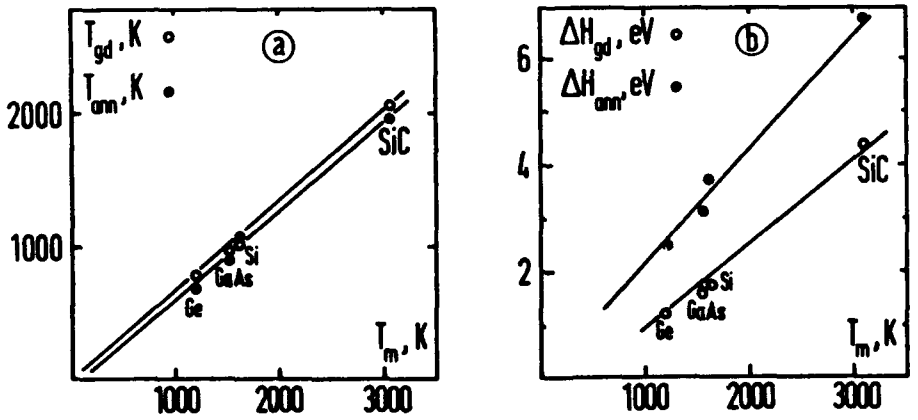

Fig. 4: Rare gas diffusion and annealing of radiation damage produced by ion implantation in the semi-conductor 6H α-SiC compared with data for Ge, Si and GaAs [29, 41]
The figures show: a) temperatures for 50 % gas release (T_{gd}) and for damage annealing (T_{ann}) as a function of the melting point, T_m, b) corresponding activation energies for gas diffusion and for damage annealing.

It is believed that C-vacancies in SiC are donors (positively charged), and that Si-vacancies can be assumed to be acceptors (negatively charged). Therefore, N-doped n-type α-SiC (700 ppm) should show a decreased number of C-vacancies, and an increased number of Si-vacancies, if essentially complete ionization of donor N-impurities occurs and interaction with the (postulated) donor-type C and acceptor-type Si-vacancies takes place. This would explain the reverse trend on C- and on Si-diffusion of N-impurities in SiC as compared to very pure 6H α-SiC single crystals in Fig. 3, as well as earlier results [e.g. 37] on the effect of doping with N or Al on the diffusion of Be and B.

As is obvious from Fig. 3 and from Table 3, the activation energies for C- and Si-self-diffusion are very similar (and very high), the pre-exponentials D_0 are also high, pointing to a vacancy mechanism, but making both a large concentration of C-vacancies and the existance of Si-interstitials in SiC with the (previously) reported non-stoichiometry and C/Si ratios < 1 unlikely. If carbon vacancies were responsible for nonstoichiometry, C-diffusion should be much faster than Si-diffusion and should have a lower activation enthalpy ΔH. If non-stoichiometry were accomodated by silicon interstitials, Si diffusion would be expected to be faster than C diffusion. As a solution, the interesting concept of Si-diffusion being coupled to and controlled by the presence of C-vancancies, Si-atoms occupying C-vacancies and thus creating *antisite defects* was introduced [38]. This concept can explain diffusion data, non-stoichiometry of SiC, and the effect of sintering aids (e.g. of B). However, subsequent calculations coauthored by the same scientist [39] yielded a very high value of the formation energy of antisite defects, thus that neither C- nor Si-antisites would likely explain the diffusion results (or contribute to nonstoichiometry). The most recent ab initio calculations by Davis et al. [40], on the other hand, do confirm the Si_C-antisite as the dominant defect in n-type SiC, whereas carbon vacancies (double donors) are predicted to dominate in p-type crystals; finally, C_{Si}-antisites (electrically inactive) are favored as dominant defect in C-rich SiC. This shows convincingly that the seemingly simple carbide SiC is in reality a very complex material. Some further questions for this technologically important substance await also a final answer: why periodic stackings lead to polytypes, which polytypes are stable as function of temperature, pressure, impurity content etc., the exact width of the single phase field of SiC, the relative importance of antisites, etc.

Results on both C and Si self-diffusion exist also for β-SiC (3 C-type, dense polycrystals) due to Davis et al. (25, 26). The reported ΔH's and D_0's are again high (see Table 3), C diffuses faster than Si, the diffusion coefficients are also low as for α-SiC and are, in fact, rather similar to those shown in Fig. 3 for α-SiC. Since SiC is widely used as semiconductor, many studies have been performed on diffusion doping, in particular in the USSR. Results on the diffusion of B, Ba, Al, Ga, Li, etc. exist. These results cannot

be reviewed here in detail. Rather, an example of relevance for application of SiC as a (high temperature) semiconductor and for its use in nuclear applications involving radiation damage and its recovery will be given. Controlled ion implantation with mass-separated heavy ions (here 0.5 MeV Kr-85 ions) as frequently used to produce tailor-made properties in semiconductors, introduces also radiation damage. For the above case of Kr-ions, amorphization of SiC occurs at high ion doses ($\geq 10^{14}$ ions/cm^2) leading to a fast release not compatible with volume diffusion, but rather caused by recrystallization of the amorphous surface layer on the crystalline substrate [29]. Trapping of gas atoms at radiation-induced defects and gas bubble formation are also affecting release, though at low enough doses, volume diffusion of rare gases can be measured (see Table 3 and Fig. 4). Both ΔH-values and temperatures of gas release for volume diffusion as well as for recrystallization of the amorphous state (which is formed in Si, Ge and GaAs as well) scale well with the melting points of these four semiconductors [29, 41] pointing to a behavior more closely related to the bonding conditions than to the crystal structure.

Silicon nitride, Si_3N_4: The available knowledge on diffusion in Si_3N_4 is very limited and far from being adequate for a material of such a prominent importance as Si_3N_4. The lack of suitable radioactive tracers, the hardness, the decomposition at 1900°C, the existence of glassy phases at the grain boundaries and the near to complete interference of mass numbers of different Si-isotopes and nitrogen molecules (see above) are some of the reasons for this unsatisfactory situation. An early attempt [42] to measure self-diffusion in α- and β-Si_3N_4 and in SIALON's, using Si-29 and N-15 as tracers, led to the successful development of procedures for coating with tracer layers and isotopic analysis. However, glassy grain-boundary phases, first evident in this study, made the interpretation of the limited data difficult. Later work [31] using gas-solid exchange of N-15 in a very limited temperature range (1200 - 1400° C) yielded data (see Table 3) which are also difficult to understand: Unexpected combinations of D_0's and ΔH's, and unexpectedly low D-values of 10^{-18} to 10^{-19} cm^{2}s^{-1} at 1400°C were reported. The plausible aspect of the data is that at the temperatures measured, nitrogen diffusion in β-Si_3N_4 with its hexagonal channels is faster than in α-Si_3N_4 whose structure does not show such channels. However, due to the extreme difference in the reported ΔH's (Table 3), this (expected) trend becomes opposite below 1200° C.

Other non-NaCl type carbides and nitrides: Hardly anything is known on diffusion in other non-cubic nitrides. For non-cubic carbides, extensive work has been done rather early on chemical diffusion, e.g. for carbides of metals of group VI B, hence WC, W_2C, MoC, Mo_2C, different Cr-carbides [e.g. 44, 45]. Usually, growth rates of carbide layers on the metals were measured. These were often rate-controlled by carbon diffusion in the different carbides. The ΔH-values of the corresponding diffusion processes in

chemical gradients were usually high; most of them fall in the range 4 ± 0.5 eV. This extensive literature as well as that on similar experiments with NaCl-structured carbides and nitrides is not treated here in more detail because of lack of space. Self-diffusion data exist also for UC_2 and U_2C_3 [10].

2.4 ACTINIDE CARBIDES

The actinide monocarbides UC and $(U_{0.8}\ Pu_{0.2})C$ are so-called advanced nuclear fuels. Much diffusion work has been done on these two substances. UC can be both hypo-and hyperstoichiometric (see Table 1 and Fig. 1). The NaCl-type single phase field extends from about $UC_{0.95}$ to $UC_{1.9}$ at 2300°C. For practical applications in nuclear reactors with relatively low operating temperatures, non-stoichiometric MC will be two-phased. MC_{1-x} will consist of the monocarbide and the metal and can therefore not be used as nuclear fuel because of compatibility problems with the metal clad containing the fuel and because of its very high swelling rate. MC_{1+x} will consist of the monocarbide and precipitates of higher carbides (M_2C_3, MC_2). Diffusion in UC_{1-x} was nevertheless studied because of the basic interest and in order to understand the diffusion mechanisms. Carbon and metal atom bulk diffusion [3, 19, 46], impurity diffusion [47, 48], grain boundary diffusion [49], diffusion in U_2C_3 and UC_2 [50] and radiation enhanced diffusion during fission [51] have all been measured. UC and (U,Pu)C are thus the most studied carbides for diffusion properties.

Carbon diffusion has been investigated for many C/U-ratios in wide temperature ranges by many authors [see e.g. 10, 33]. However, much of the early work disregarded the U-C phase diagram. The reported ΔH_C-values showed a wide scatter since often phase boundaries were passed within the experimental temperature range without correction for the enhanced diffusion in the two-phased material ($UC+U$, $UC+U_2C_3$, $UC+UC_2$, see introduction. Diffusion mechanisms via C vacancies, C interstitials, C_2 pairs and an interstitialcy mechanism were all suggested. The most recent data [19] are included in Fig. 5. They yield ΔH_C-values of 4.0, 3.7 and again 4.0 eV/atom for three sets of either clearly hypostoichiometric $UC_{0.92}$, fully stoichiometric $UC_{1.0}$ or clearly hyperstoichiometric $UC_{1.15}$, with an only very slight variation of D_C with x. A critical review of previous data [33] shows similarly high ΔH_C-values for experiments performed in the single phase field or, if the experiments were done below and above the temperature of the phase boundary, for those evaluations allowing for a knee in the Arrhenius diagram. Previous lower ΔH_C-values of about 2.5 eV represent two-phased material and cannot be accepted as reliable anymore. The most probable diffusion mechanism [33] consists in dissociation of C_2-pairs with jumps of single carbon atoms to other single carbon atoms to form a new pair. Calculations [52] predict that such pairs exist not only in UC_2 and UC_{1+x},

but also in stoichiometric UC (e.g. 2 % at 2400 K) and even in the hypostoichiometric $UC_{0.92}$ of Fig. 5 (about 0.1 % at 2000 K).

Many results have also been reported on *metal (U and Pu) diffusion* in $UC_{1\pm x}$ and $(U_{0.8}Pu_{0.2})C_{1+x}$. Fig. 5 shows that D_U is much smaller than D_C. A straight line is obtained in the Arrhenius diagram for pure zone-refined UC single crystals (< 30 ppm metallic impurities) whereas a pronounced curvature is observed in less pure arc-cast UC with ≤ 120 ppm metallic impurities. The most likely reason for this curvature and for the lower ΔH below about 2100°C are influences by these impurities. Extrinsic diffusion is thus operative with vacancy-impurity interactions enhancing diffusion, as also shown in detailed studies [47, 48] on UC doped with different concentrations of V, W, Ta, Zr, La, Ce, Fe or Ni. Intrinsic diffusion is only operative above 2100° C in the arc-cast UC, whereas it is still observed at 1500°C in the zone-refined single crystals. As with transition metal monocarbides, the D_0 and ΔH-values are compatible with a single vacancy mechanism. The resulting Arrhenius equations are (D in $cm^2\,s^{-1}$)

U in $UC_{1.0}$	$D = 11.7 \exp(-6.2\ eV/kT)$	single crystals
U in $UC_{1.0}$	$D = 6.9 \exp(-6.2\ eV/kT) +$	arc cast, T > 2100° C
	$+ 3.6 \times 10^{-5} \exp(-4.2\ eV/kT)$	arc cast, T < 2100° C
Pu in $(U_{0.8}Pu_{0.2})C$	$D = 0.013 \exp(-4.65\ eV/kT)$	sintered.

Since sintered technological grade specimens are less pure than the arc-cast UC, and since fission products grow in at a high rate during reactor operation (up to 500 ppm/d in a metal cooled fast neutron breeder reactor), extrinsic diffusion and impurity effects will control the in-pile kinetics of carbide fuels.

D_{Pu} in (U, Pu)C is larger than D_U in UC at any given temperature. The cause is a combination of a faster diffusion of the smaller Pu-atom ($D_{Pu}/D_U \sim 3$ to 5 in UC) and the slightly larger lattice spacing in (U,Pu)C as compared with UC. The above Arrhenius equation is for a typical technological carbide (composition $(U_{0.8}\ Pu_{0.2})\ C_{0.98}\ N_{0.02}\ O_{0.06}$, with lower density, smaller grain size and smaller purity than UC) [43].

Deviations from stoichiometry strongly affect metal self-diffusion rates in $MC_{1\pm x}$, in contrast to transition metal monocarbides: D_M decreases and ΔH_M increases with x in $MC_{1\pm x}$ (M = U or U/Pu). This can be explained by carbon atoms donating electrons to the metal-metal bond thus increasing the binding energy and hence also ΔH_M [46, 55].

For the important effect of impurities on D_M in MC, no obvious relation between the enhancement (e.g. by V, W, Ta, Fe, Ni) or diminution factor (e.g. by large impurities such as Ce and La, but also by Zr), and the atomic size of the impurity or the lattice parameter of the doped carbide could be found. The integral effect of all fission products is to *enhance* metal atom diffusion

significantly, in particular at low temperatures. As expected, the effect of added impurities decreases with increasing temperature [47, 48].

The diffusion of rare gases, formed by fission and causing the carbide to swell due to gas bubble formation, has also been studied. The interested reader is referred to ref. [10].

2.5 ACTINIDE MONONITRIDES

The actinide mononitrides UN and $(U_{0.8}\ Pu_{0.2})N$ of the NaCl structure are also investigated as advanced nuclear fuels for space reactors or for fast breeder reactors. Results on both N, U and Pu diffusion exist [e.g. 10, 20-24, 53, 54]. Both nitrogen and metal atom diffusion show a pronounced dependence on nitrogen pressure, $p(N_2)$, as indicated by the arrow at 1946° C for D_N and the two N_2-pressures in Fig. 6 for D_U, and as also indicated by the dependence of D_{Pu} and of ΔH_{Pu} on X/M ratio for Pu diffusion in (U,Pu)N (X = N+O+C) [24]. Both the U-N and the Pu-N phase diagrams show a single phase field of the mononitrides that is very narrow if expressed in terms of X/M-ratio [10] but which is very wide if presented in a plot of $p(N_2)$ versus T (see Fig. 7). The decomposition pressures of sesquinitride in equilibrium with the mononitride are, e.g. at 1400°C, higher by a factor $\sim 10^9$ than the decomposition pressure of the mononitrides in equilibrium with liquid, nitrogen-saturated metals. No fundamental significance should therefore be attributed to reported activation energies measured at constant $p(N_2)$ (see horizontal lines in Fig. 7) since the phase field is traversed from high to low N/M ratios (even if the changes are too small to be detected by conventional chemical analysis). Such data do *not* represent constant composition. However, a number of important conclusions can be drawn nevertheless

i) nitrogen diffusion in UN and (U,Pu)N (or briefly MN) is slow compared with carbon diffusion in UC, but it is much faster than metal diffusion in the nitrides. The dependence on $p(N_2)$ indicates an interstitial mechanism. The reported ΔH's vary from 2.4 to 4.2 eV but these numbers should be taken as apparent values (see above).

ii) metal atom diffusion rates (D_U in UN, D_{Pu} in (U,Pu)N) increase also with $p(N_2)$, and the dependence is compatible with a vacancy mechanism for U in UN and for Pu in (U,Pu)N, at least up to 1650°C [23, 24].

iii) Arrhenius diagrams constructed for different N/M-ratios show a trend in D_0 and ΔH that is different from that observed in carbides. Whereas D_M increases and ΔH_M decreases in carbides with decreasing C/M-ratio, the opposite trend is indicated for nitrides: D_M decreases and ΔH_M increases with decreasing N/M-ratio. This indicates that the bonding conditions are different in actinide monocarbides and mononitrides [24, 55].

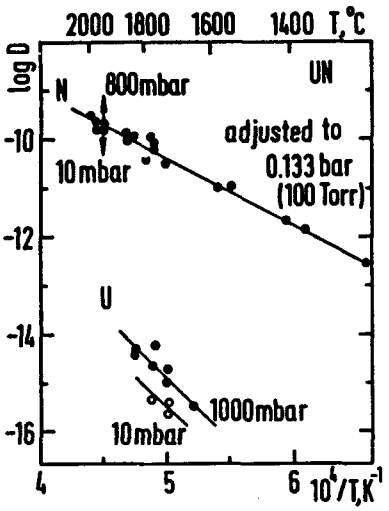

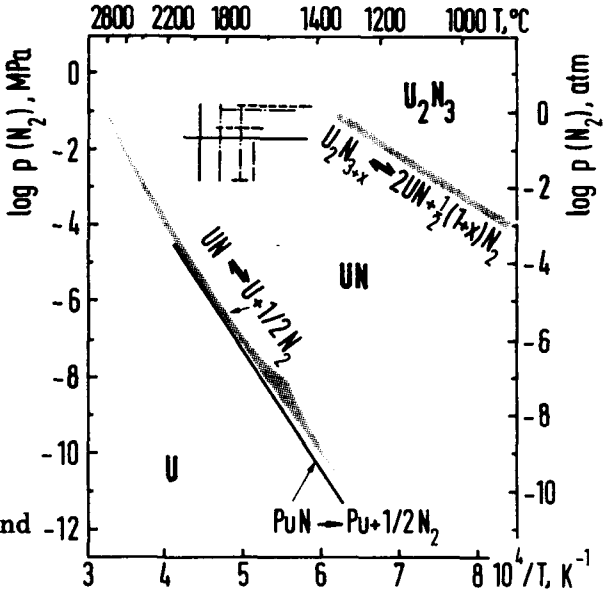

Fig. 6: Diffusion of nitrogen and uranium in UN at different nitrogen pressures [20-23]

Fig. 7: Decomposition pressures of U_2N_3 in equilibrium with UN, and of UN in equil. with N-saturated U, showing the single phase UN field. The lines show the parameters (T, $p(N_2)$) selected for diffusion measurements in UN and U_2N_3.

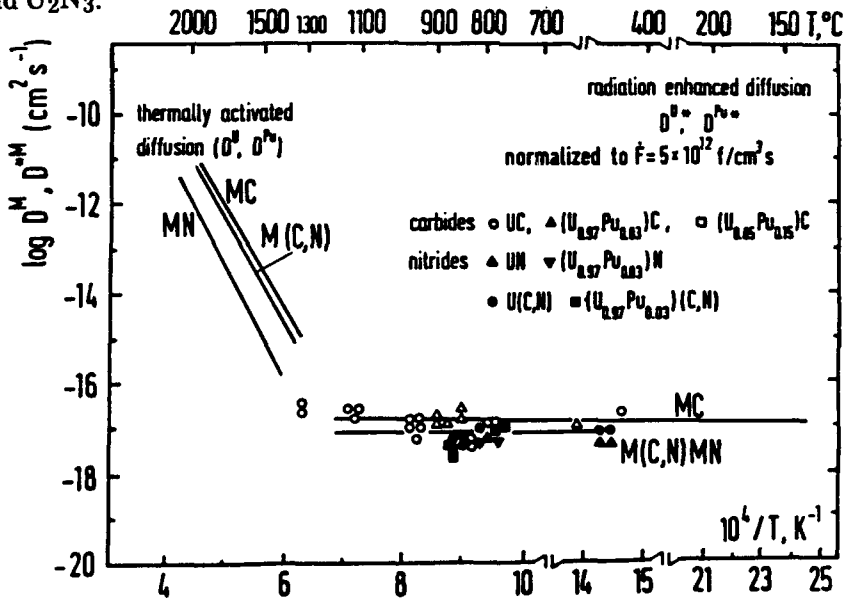

Fig. 8: Radiation-enhanced diffusion of U and Pu in UC, (U,Pu)C, UN, (U,Pu)N and in carbonitrides U(C,N) and (U,Pu) (C, N) during fission in a nuclear reactor, compared with thermally activated diffusion [51].

iv) Impurities and the accumulation of fission products affect U and Pu diffusion. Whereas in carbides D_M increases to a saturation value, a maximum of D_{Pu} is found in MN at intermediate burn-up (or fission product concentration) followed by a decrease towards the original value. The explanation for this different behaviour is the action of rare earths which retard diffusion. These are soluble in MN and compensate the enhancing effect of the other impurities [24].

v) Finally, for both actinide carbides and nitrides, radiation and fission enhance D_U and D_{Pu} in UC, MC, UN, MN and in U-Pu carbonitrides [4, 51]. The radiation enhanced diffusion coefficient D* is completely temperature independent (athermal) below about 1000 °C (see Fig. 8) and is proportional to the fission rate. The enhancement factors D*/D can easily be larger than 10^{10} in operating fuels. Enhancement is probably caused by a combination of displacement, temperature, and pressure effects during the slowing-down of the fission fragments [51].

2.6 ACTINIDE CARBONITRIDES

The third type (besides the mononitrides and the monocarbides of U and Pu) of potential advanced nuclear fuel are the carbonitrides M(C, N) (M = U and/or Pu). As mentioned above, the diffusion results indicate different bonding conditions in MC and MN. Diffusion measurements (C, U, Pu) have also been performed on carbonitrides of different C-content [10, 24, 53]. The results clearly show carbide-like behavior for N/(C+N) values up to about 0.3, and nitride-like behavior for N/(C+N) ≥ 0.8. For intermediate N-contents, diffusion rates, as well as rates of diffusion-related processes such as grain growth and fission gas release decrease significantly, such that the temperatures needed for nitrides MN to achieve the same rates as for carbides MC increase by about 250° C (see Fig. 9).

2.7 GRAIN BOUNDARY AND SURFACE DIFFUSION OF METAL ATOMS

Grain boundary diffusion: Nothing is known for nitrides, but extensive data exist for pure and impurity doped $UC_{1.0}$, $UC_{0.93}$ and $UC_{1.15}$ as well as for UC_2 [49]. As usual, the product of the grain boundary diffusion coefficient, D_{gb}, and the grain boundary width, δ, was measured. Though recently progress was achieved in understanding, observing and calculating grain boundaries in oxides, little information exists for the atomistic structure of the grain boundaries and their effective width δ in carbides. δ may depend on temperature, deviation from stoichiometry and presence of additives. Applying the simplifying assumption that δ is 0.4 nm for all the

above carbides and all temperatures, ratios of D_{gb}/D_v (D_v = volume diffusion coefficient) of 10^3 to 10^5 and ΔH-values in the range

$$0.5\,\Delta H_v \leq \Delta H_{gb} \leq 0.8\,\Delta H_v$$

were obtained, e.g. ΔH_{gb} for uranium in $UC_{1.0}$ = 3.3 eV/atom (or 55 % of ΔH_v). D_{gb} increased as the C/U-ratio decreased, just as D_v. Impurities tended to impede grain boundary diffusion (including those which enhance volume diffusion).

These studies served also to increase the knowledge about the effects of phase changes on D_{gb} about which few results exist. For the phase change of α-$UC_2 \rightarrow \beta$ - UC_2, at which D_v changes by about a factor of ~ 2 (see above), D_{gb} changes by a factor 50.

Surface diffusion: has been measured on UC and UN (see review [40]). The main experimental difficulties in obtaining D_s for these compounds are their high vapour pressures and the anisotropy of the surface energies.

Fig. 10 summarizes D_s-values for UC and UN and compares them to D_v-values. For both materials, an interesting techniques of obtaining D_s was used, i.e. the mobility of rare-gas filled bubbles was measured. The indicated ΔH_s-values are surprisingly low, possibly due to changes in X/M-ratios at different temperatures.

3. Supporting Measurements: Quenching and Radiation Damage Studies

In this section, recent studies to better understand the point defect behavior in UC and UN will be discussed, and some results for TiC and TaC will be mentioned. Quenching from high temperature or bombardment with electrons or heavy ions are used to produce defects, and electrical resistivity is measured or the Rutherford channeling technique is applied to detect defect formation and defect anneling. In particular the latter technique is valuable since it yields unequivocally results for metal defects, in contrast to measurements of electrical resistivity or lattice parameter which react on both metal and non-metal atom defects. The interested reader is referred to ref. [59] for details on the Rutherford backscattering-channeling technique.

In principle, defect formation energies can be obtained by measuring the dependence of a suitable physical property (e.g. electrical resistivity, ρ, or the lattice parameter, a_o) on the quenching temperature. This physical property should show changes proportional to the defect concentration. Following (or during) an isothermal or isochronal recovery anneal, recovery stages and, again in principle, defect migration energies can be measured. In a compound with two sublattices, it is not a priori obvious which type of defect is formed or is mobile, if Δa_o or $\Delta\rho$ are followed: metal vacancies,

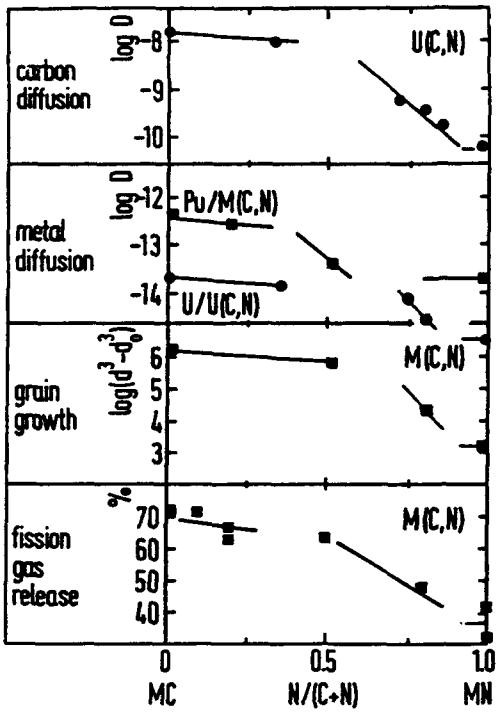

Fig. 9: Typical trend in high-temperature kinetic processes in the series MC-M(C,N)-MN (M = U and/or Pu). Diffusion of C, U and Pu (D in cm^2s^{-1} at 1700°C), grain growth (1700°C) [56] and fission gas release from a fast flux irradiation at ~ 1.2 at.% burn-up are shown [57].

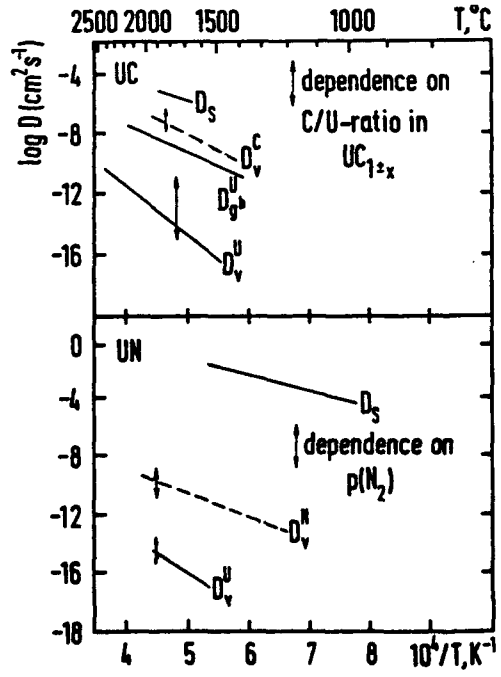

Fig. 10: Arrhenius diagrams for diffusion processes in UC and UN, including surface diffusion and grain boundary diffusion (for UC) as well as the dependence of volume diffusion (coefficients D_v) of nonmetal and metal atoms on deviations from stoichiometry. Such measurements are still missing for D_s (see [49] for D_{gb} and [58] for D_s).

metal interstitials, metalloid vacancies, metalloid interstitials (and their clusters) may all contribute. With the channeling technique, in contrast, displaced atoms in different sublattices can be measured individually.

A few examples follow from recent work on UN. Single crystals from the same batch as the one used for the uranium self-diffusion measurements (see Fig. 6) were employed for quenching, channeling and ion bombardment to produce defects. The quenching work measuring $\Delta\rho$ yielded two recovery stages (see Fig. 11), tentatively attributed to N-defects (stage at ~ 370 K) and U-defects (stage at ~ 770 K). Channeling studies of ion-implanted UN yield less arbitrary results, since the signal from U-defects is well separated from any disturbance by N defects. Fig. 12 shows Rutherford-backscattering-channeling energy spectra for UN before and following implantation with different doses of Kr-ions at 77 K. In contrast to single crystals of semiconductors and insulators (as SiC, see above), no typical *damage peaks* due to direct scattering of channeled ions from displaced U-atoms within the range of the implanted ions are seen. From such damage peaks, the total number of displaced atoms can be directly deduced. For UN, rather, two characteristic portions of the spectra are obvious: the first one begins just behind the *surface peak* (s.p.) and shows a large dechanneling rate, extending to a depth where the dechanneling rate levels off. Such features are known as *dechanneling knees* in metals. They are due to extended defects (clusters, dislocations, dislocation loops, stacking faults, etc.). A further peak is located at the interface between damaged and undamaged regions. It may therefore be referred to as *interface peak*. The aspects of interest for the present context are the following: i) at room temperature, and even at 77 K as in Fig. 12, some U-defects migrate away from the place where they are formed, and penetrate into the undamaged crystal, the driving force being the large compressive stress gradient produced by ion implantation near the crystal surface. This process is similar to that causing U-atoms (probably interstitials) to migrate away from the path of a fission fragment in reactor irradiated UN, because of the large pressures being set up along the axis of the fission spike, thus contributing to the enhanced diffusion coefficient D* (see Section 2.5 and Fig. 8). Warming up the 77 K crystals to room temperature, causes some of the U-defects which are immobile at 77 K, to migrate below room temperature. Following isochronal anneal steps, two recovery stages are seen (Fig. 11), a first one at ~ 870 K and a second one between about 1250 and 1500 K. Since in radiation damage work *all* possible point defects are formed (and not preferentially those with a low formation energy, as is the case in thermal anneals), it is now clear that the recovery stage at ~ 370 K of Fig. 11 is *not* due to U-defect mobility. It is also clear that some U-defects are mobile at and below room temperature (probably interstitials) and that another type of U-defects (probably vacancies and annealing or dissociation of clusters) becomes mobile at 770 - 870 K. The stage at 1200 to 1500 K is due to cluster dissociation giving rise

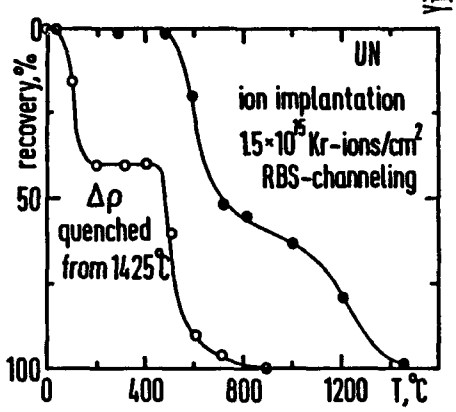

Fig. 11: Defect annealing (damage recovery) of quenched or ion implanted UN, as a function of annealing temperature [8, 23]

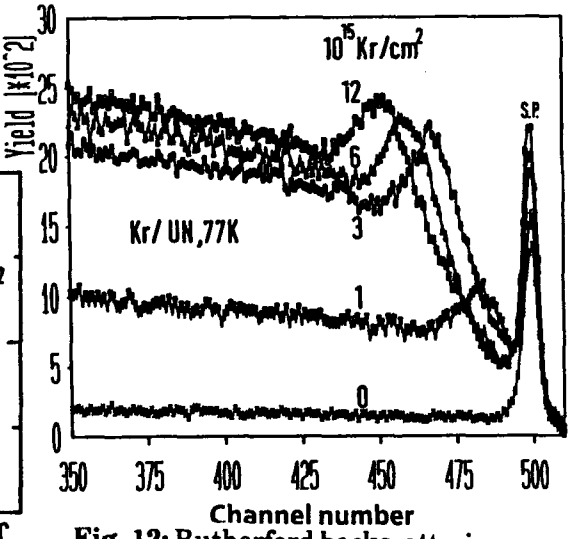

Fig. 12: Rutherford backscattering spectra in the channeling mode of ion implanted UN single crystals (implantation at 77 K with increasing doses of Kr-ions) [8, 63]

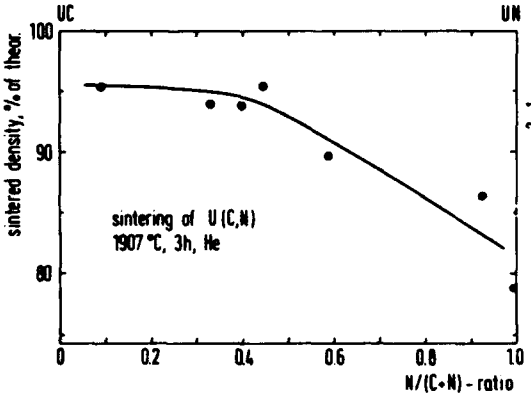

Fig. 13: Sintering of U(C,N): as-sintered density of different carbonitrides (1907 °C, 3h , He) [67]

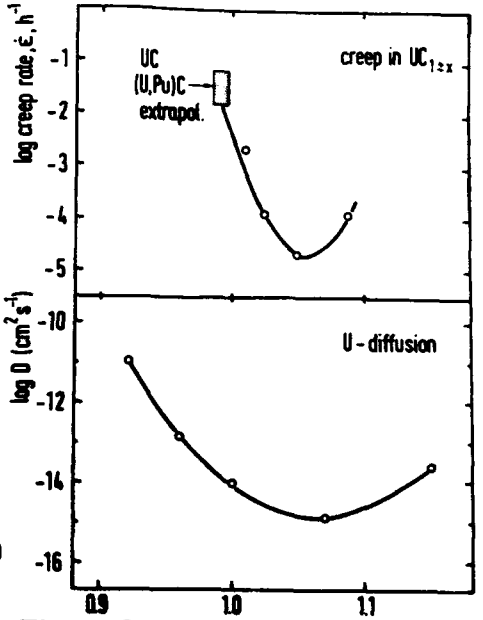

Fig. 14: Dependence of creep at 1400°C (see [10] for refs.) and of uranium diffusion at 1800°C on C/U-ratio in $UC_{1\pm x}$ [46, 55]

to the formation of dislocations and dislocation loops as they were observed in transmission electron microscopy [60] on parallel specimens.

For UC, quenching studies on arc-cast [61] and single crystalline specimens [62] yielded results consistent with the diffusion data, i.e. thermal formation of U vacancies either by dissociating vacancy-impurity complexes or as Schottky defects, with a migration energy for U vacancies in the range of 2.4 ± 0.5 eV, and a formation energy of 3.7 ± 0.4 eV, hence a sum of 6.1 eV identical with the directly measured value for self-diffusion (see Section 2.4).

Electrical resistivity changes were also measured on reactor irradiated UN [5] and UC [64] to deduce recovery stages with the difficulties mentioned above to attribute mechanisms and specific defects to the observed stages. Electron irradiation at low temperatures of TiC and TaC [6] showed that 50 to 75 % of the defects formed anneal before room temperature is reached. This is in agreement with the channeling data on UN described above. These defects will never be observed in room temperature work since they annihilate during the irradiation and thus before the measurement is done. Better knowledge of these low temperature anneal stages is necessary before a unique assignment of stages above room temperature to specific defects can be achieved, an important field for future work.

4. Kinetic processes related to diffusion

The diffusion properties are also reflected in the *kinetics* of a number of *high-temperature processes:* In all the above carbides and nitrides, the metal atoms are the slower species which is therefore rate-controlling for diffusion-related high temperature processes such as grain growth, creep, to some extent sintering, restructuring of nuclear fuels, or total release of fission products. The relations together with the trend in actinide carbides and nitrides towards reduced rates with increasing nitrogen content were already shown in Fig. 9. Diffusion coefficients, grain growth and release of fission gases follow all the same trend, i.e. they decrease with increasing N-content. The same is true for sintering rates (see Fig. 13) and restructuring of nuclear fuels in the temperature gradients existing during reactor operation [10].

Fig. 14, finally, shows the parallel trend for creep and metal atom diffusion for actinide carbides. Another example is the use of Ni as sintering aid (and also to increase creep rates) in UC and (U, Pu)C. Though liquid Ni may contribute to increased sintering, the trend of sintering, creep, and diffusion rates is again parallel. For instance, at 1250°C, the creep rates of UC and (U, Pu)C are increased by about a factor of 2500 by adding 0.1 wt.% Ni [65], and the rates of uranium diffusion increased by about a factor of 500 at (the higher temperature of) 1400°C [66]; (the increase in D for C/U > 1.07

is most likely due to the formation of UC_2-needles in the UC_{1+x} matrix). Given the complex mechanism of sintering from its initial to its final stage and the low temperatures for most creep experiments, numerical agreement between measured and deduced D-values should not be expected (though it is sometimes obtained, e.g. for shrinkage of UC [e.g. 3]).

5. Summary

Today's knowledge on diffusion processes and on point defect behavior of carbides and nitrides is summarized. For some interesting materials, notably for actinide carbides and nitrides but also for the transition metal carbides TiC and NbC and to some extent for SiC, this knowledge is rather complete. Much less is known for transition metal nitrides, and for the second "advanced light hi-tec ceramic", i.e. Si_3N_4 (as well as for the class of SIALONs).

The majority defects in NaCl-type carbides and nitrides are vacancies in the metalloid sublattice. The mobilities in the metal sublattice are significantly slower and are therefore rate-controlling for diffusion-related matter transport. The activation energies are generally high. Due to the often large degree of substoichiometry in the NaCl-type monocarbides and mononitrides, different types of ordering have been observed. Information about the effect of these phenomena on diffusion rates is still missing.

In the transition metal monocarbides, vacancy mechanisms are indicated for both carbon and metal diffusion, with the possibility of different diffusion paths for C-diffusion at different deviations from stoichiometry. The activation energies are generally high. For actinide monocarbides, a different mechanism for carbon diffusion is suggested, i.e. dissociation of C_2-pairs (existing also in substoichiometric MC_{1-x}) and jumps of single carbon atoms to form new pairs with other single carbon atoms. Metal atom diffusion in the actinide monocarbides UC and (U, Pu)C depends on C/M-ratio, in contrast to that in transition metal monocarbides. The explanation is an increase in migration energy with increasing C-content due to C-atoms donating electrons to the metal-metal bonds. For the mononitrides UN and (U, Pu)N, an interstitial mechanism for N-diffusion and a vacancy mechanism for U and Pu diffusion are suggested, based on the measured dependence of diffusion rates on nitrogen pressure. Diffusion and matter transport rates are slowed down in actinide carbonitrides by replacing C by N atoms.

The diffusion data can frequently be related to other technologically important kinetic properties, such as final stage sintering, grain growth, fission gas release from nuclear fuels and their restructuring in temperature gradients thus providing the fundamental basis to understand and predict the behavior under operating conditions.

Some progress has also been made on calculations of defect parameters, and a certain amount of data on defect properties exists based on studies of radiation damage or quenched-in defects and their recovery. However, much work remains to be done before a general understanding of point defects and atomic transport properties in carbides and nitrides is achieved, in particular for such interesting and important materials as Si_3N_4. Also, no relevant knowledge exists on the important class of borides.

REFERENCES

1. Matzke, Hj., March 1989, Proc. NATO ASI "Diffusion in Materials", Aussois, France, Eds. A.L. Laskar and G. Brebec, Kluwer Acad. Publ. Dordrecht, The Netherlands
2. De Novion, C.H., these proceedings
3. Matzke, Hj., Routbort, J.L. and Tasman, H.A., (1974) J. Appl. Phys. **45**, 5187
4. Matzke, Hj., (1987) Advances in Ceramics **23**, 617
5. Tamaki, M., Matsumoto, S., Ishimura, K., Matsumoto G. and Kirihara,T., (1980) J. Nucl. Mater. **108/109**, 258, and Tamaki, M., PhD Thesis, (1984) Univ. Nagoya
6. Morillo, J., de Novion, C.H. and Duval, J., (1981) Rad. Effects **55**, 67
7. Matzke, Hj., (1988) in Non-Stoichiometric Compounds, Grain Boundaries and Structural Defects, Nato Proceedings, ASI Rottach-Egern, Eds. Nowotny, J. and Weppner, W., (1989) Kluwer Acad. Publ., Dordrecht, The Netherlands, 321
8. Turos, A., Fritz, S. and Matzke, Hj., Phys. Rev. B, submitted
9. Storms, E.K., (1967) The Refractory Carbides, Monogr. Ser. Refract. Mater., Vol. 2, Academic Press, New York, 278 p.
10. Matzke, Hj., (1986) Science of Advanced LMFBR Fuels: A Monograph on Solid State Physics, Chemistry and Technology of Carbides, Nitrides and Carbonitrides of Uranium and Plutonium, North-Holland, Amsterdam, 740 p.
11. Andriyevskij, R.A., Klimenko, V.V., and Khromov, Yu.F., (1969) Fiz. Met. Metalloved. **28**, 298
12. Andriyevskiy, R.A., Kromov, Yu. F. and Alekseyva, I.S., (1971) ibid. **32**, 664
13. Sarian, S., (1968) J. Appl. Phys. **39**, 3305, 5036; **40** (1969) 3515
14. Sarian, S., (1972) J. Phys. Chem. Solids **33**, 1637
15. Sarian, S. and Criscione, J.M., (1967) J. Appl. Phys. **38**, 1794
16. Sarian, S., (1974) in Recent Advanc. Sci. Technol. Mater. **3**, 247
17. Yu, B.B. and Davis, R.F., (1979) J. Phys. Chem. Solids **40**, 979; **42** (1981) 83
18. Yu, B.B. and Davis, R.F., (1979) Phys. Stat. Solidi **51a**, 261
19. Matsui, H. and Matzke, Hj., (1980) J. Nucl. Mater. **88**, 317
20. Droege, J.W. and Alexander, C.A., (1978) Battelle Mem. Institute, Reports BMI-1882, 1883 and 1918 (1971)
21. Sturiale, T.J. and DeCrescente, M.A., (1965) US Report PWAC-477, 1

22. Holt, J.B. and Almassy, M.Y., (1961) J. Am. Ceram. Soc. 52, 631
23. Fritz, S., (1988) Ph.D Thesis, Univ. Strasbourg, and Fritz, S. and Matzke, Hj., to be published
24. Bradbury, M.H. and Matzke, Hj., (1978) J. Nucl. Mater. 75, 68 and 91 (1980)13
25. Hon, M.H. and Davis, R.F., (1979) J. Mater. Sci. 14, 2411
26. Hon, M.H., Davis, R.F. and Newbury, D.E., (1980) J. Mater. Sci 15, 2073
27. Hong, J.D. and Davis, R.F., (1980) J. Am. Ceram. Soc. 63, 546
28. Hong, J.D., Davis, R.F. and Newbury, D.E., (1981) J. Mater. Sci. 16, 2485
29. Matzke, Hj. and Königer, M., (1970) Phys. Stat. Sol. (a) 1, 469
30. Bushmer, C.P. and Crayton, P.H., (1971) J. Mater. Sci. 6, 981
31. Kijiama, K. and Shirasaki, S., (1976) J. Chem. Phys. 65, 2668
32. Zener, C., (1952) in Imperfections in Nearly Perfect Crystals, Eds. Shockley, W. et al., Wiley, New York, pp 289
33. Matzke, Hj., (1984) Solid State Ionics 12, 25
34. Murarka, S.P., (1988) Defect and Diffusion Forum 59, 99
35. Desmaison, J.G. and Smeltzer, W.W., (1977) J. Electrochem. Soc. 124, 152
36. Abauret, F. and Eveno, P., March 1989, presented at Nato-ASI, Diffusion in Materials, Aussois, France,
37. Vodakov, Yu. A. and Mokhov, E.N., (1974) in Silicon Carbide 1973, Eds. Marshall, R.C., Faust, J.W., Jr. and Ryan, C.E., Univ. South Carolina Press, Columbia, S.C., 508
38. Birnie III, D.P., (1986) J. Am. Ceram. Soc. 69, C-33
39. Birnie III, D.P., Mackrodt, W.C. and Kingery, W.D., (1987) Advances in Ceramics 23, 571
40. Wang, C. Bernholc and Davis, R.F., (1988) J. Phys. Rev. B38, 12752
41. Matzke, Hj., (1970) Radiation Effects 3, 93
42. Wuensch, B.J. and Vasilos, T., (1975) US Report Avco Corp., Lowell Mass Systems Div., Rep. A 0211175
43. Nitzki, V. and Matzke, Hj., (1975) Proc. Reaktortagung Nürnberg, German Atomforum, p. 399
44. Fries, R.J., Cummings, J.E., Hoffman, C.G. and Daily, S.A., (1968) Report Los Alamos, USA, LA-3795-MS
45. Vil'k, Yu. N., Nikolskii, S.S. and Averbe, R.G., (1967) Teplofiz. Vys. Temp. 5, 607
46. Matzke, Hj. and Routbort, J.L., (1975) in Thermodynamics of Nuclear Materials 1974, IAEA, Vienna, pp. 397
47. Routbort, J.L. and Matzke, Hj., (1974) J. Nucl. Mater. 54, 1
48. Inoue, T. and Matzke, Hj., (1980) J. Nucl. Mater. 91, 1
49. Routbort, J. L. and Matzke, Hj., (1975) J. Am. Ceram. Soc. 58, 81
50. Matzke, Hj. and Politis, C., (1973) Sol. State Comm. 12, 401
51. Matzke, Hj., (1985) in Transport in Nonstoichiometric Compounds, Eds. G. Simkovich and V.S. Stubican, Plenum, 331
52. Jeanne, F., (1972) PhD Thesis, Grenoble
53. Matsui, H., Bradbury, M.H. and Matzke, Hj., (1978) Nucl. Sci. Eng. 66, 406
54. Reimann, D.K., Kroeger, D.M. and Lundy, T.S., (1971) J. Nucl. Mater. 38, 191

55. Matzke, Hj., (1979) J. Physique (France) 40, C4, 24
56. Sari, C., (1978) CEC, Euratom Report EUR 5812 EN
57. Coquerelle, M. and Walker, C.T., (1980) Nucl. Technol. 48, 43
58. Matzke Hj., (1989) in "Surfaces and Interfaces of Ceramic Materials", Eds. Dufour, L.-C., Monty, C. and Petot-Ervas, G., NATO ASI Series E: Applied Sciences, 173, 241
59. Feldmann, L.C., Mayer, J.W. and Picraux, S.T., 1982 Materials Analysis by Ion Channeling, Academic Press. N.Y.,
60. Ray I., Thiele H. and Matzke, Hj., unpublished results
61. Matsui, H. and Matzke, Hj., 1980 J. Nucl. Mater., 89, 41
62. Matsui, H., Kato, T., Yagi, K., Okitsui, S. and Horiki, M., 1989 Rad. Eff. Def. Sol., 108, 115
63. Matzke, Hj. and Turos, A., 1989 Proc. Int. Conf. Radiation Effects in Insulators, Hamilton, Canada, Nucl. Instrum. Meth. B, in print
64. Dienst, W. and Brucklacher, D., 1969 Proc. Int. Symp. Ceramic Nucl. Fuels. Amer. Ceram. Soc., p. 82; Dienst, W., (1970) German Report KfK-1215
65. Hall, A.R., (1973) UK Report AERE-R 7326
66. Matzke, Hj., (1974) J. Nucl. Mater. 52, 85
67. Wolters, R.A.M., (1979) Dutch Report ECN-49

IV. THERMAL, CHEMICAL and MECHANICAL STABILITY

Thermal Shock and Corrosion of SiC - a combustion chamber model case study

G.A. SCHNEIDER, K.G. NICKEL and G. PETZOW
Max-Planck-Institut for metals research
Institut for materials science
Powdermetallurgical Laboratory
Heisenbergstr. 5
D-7000 Stuttgart 80

Abstract

The behaviour of SiC tiles in a combustion chamber under thermal stresses is investigated. Based on an analysis of temperature distributions during start/stop and operation of the engine thermal shock and corrosion are identified as most serious problems.

Thermal shock is modelled using experimentally determined physical and fracture mechanical data. The importance of Weibull analysis for the modelling of such problems is demonstrated. Lateral thermal gradients are shown to be significantly more dangerous than those through the component.

Based on experiments, thermodynamical analysis and kinetic modelling it is shown that a critical temperature of app. 1700°C exists above which problems concerning corrosion resistance are expected to be serious.

Introduction

SiC is a prime candidate for currently developed applications such as heat engine linings, because of known good strength retainment and oxidation resistance to at least about 1600°C in air.

The applications mentioned impose the problem of thermal shock resistance because temperature gradients both during working conditions and during starting or switching off may be severe. The often very high gas temperatures and extremely fast gas flow imply corrosion resistance to be a second major testing bench mark for the applicability of the material. The prevailing atmosphere in such engines is fuel-controlled and may vary from oxidative to reducing.

The problem of thermal shock resistance is treated by model calculations using experimentally derived material parameters for SiC and simulating the conditions of a gas turbine. The evaluation of corrosion behaviour is performed by application and extrapolation of thermodynamic-kinetic calculations based on experiments and simple models.

R. Freer (ed.), The Physics and Chemistry of Carbides; Nitrides and Borides, 387–401.
© 1990 *Kluwer Academic Publishers. Printed in the Netherlands.*

Combustion chamber environment

The modelled combustion chamber was designed by MTU[1*] company and consists of a segmented SiC tube supported by metallic components. The tube has a wall thickness of 3 mm and a radius of 4.7 cm. To minimize thermal stresses the ceramic torch is divided into two axial parts which are in turn segmented into four parts each (Fig. 1).

The calculated wall temperatures of SiC tiles and metallic supports is shown in Fig. 2, indicating maximum steady state temperatures of 1800 K and a rapid lateral temperature decrease of 250 K within a few mm. Metallic supports can be chosen to sustain calculated temperatures of 1200 K.

Two types of transient temperature situations are assumed:

a) Start and stop of the engine with an instantaneous temperature change of the burning gas ($T_{gas}^{max} \approx 2200$ K) inducing temperature gradients through the tiles;
b) Temperature fluctuations during combustion ($\Delta T = 200$ K) inducing lateral temperature gradients.

The model fuel is diesel-air.

Material

The material investigated was made by MTU company from α-SiC powder using boron and phenolic resin as sintering additives (0.5 and 3.8 wt% respectively). After spray drying from aqueous suspension of 1% polyvinyl alcohol the powder was cold isostatically pressed and pressureless sintered at 2370°C.

We have measured the fractural strength σ_b and Weibull modulus m up to 1400°C by four-point bending using a Schenk "hydropuls" apparatus with a 20/40 mm span and a loading rate of 10^4 MPa/s. Fracture toughness K_{IC} measurements were carried out by the single edge notch beam test in three-point bending with identical loading rate. Thermal expansion coefficients α were measured by a Netzsch differential dilatometer. Thermal diffusivity κ was determined by a Theta laser flash apparatus and used to calculate the heat conductivity k. The heat capacity data for the calculation were taken from [1]. The data are listed in table 1.

Experimental set-up

Oxidation experiments in air and oxygen to 1550°C have been done in a differential thermal apparatus (Netzsch STA 429).

For oxidation tests at higher temperature we have used a thermal shock apparatus [2] shown in Fig. 3. The treatment results in a steady state thermal gradient with temperatures of 1720 ±60°C in the center of the specimen. This temperature was not measured but is deduced from a heat balance between black body radiation of the specimen and the lamp irradiation [2].

The samples used were parts of disks with a thickness of 600 μm.

[1*]Motoren- und Turbinen Union, München, F.R.G.

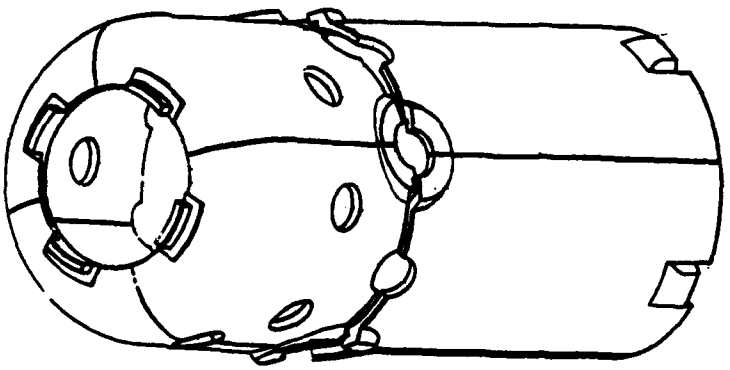

Fig. 1: Sketch map of SiC components for the model combustion chamber. Total length: 20 cm, axial diameter: 9.5 cm, thickness of tiles: 3 mm

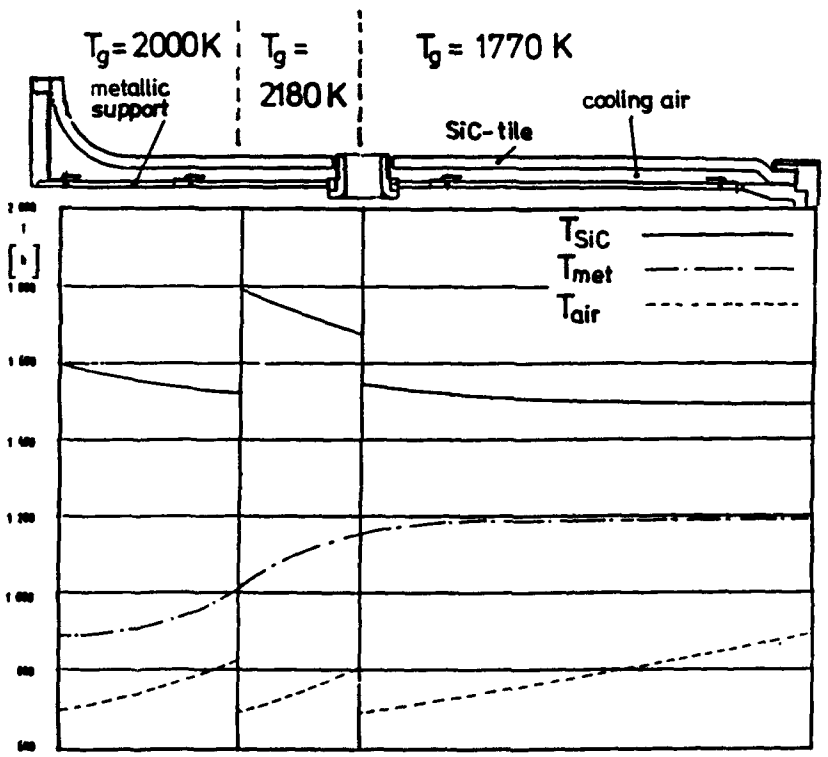

Fig. 2: Cross section of the SiC- tube and temperature profiles of the burning gas (T_g), the SiC tiles (T_s), the metallic support (T_{met}) and the cooling air (T_{air})

Table 1: physical and mechanical properties of investigated SiC (density ρ= 3.14 g/cm^3, Poisson ratio ν= 0.16 at RT), T: Temperature [°C], σ_b: bending strength [MPa], m: Weibull modulus, K_{IC}: fracture toughness [MPAm$^{0.5}$], α: thermal expansion coefficient [$10^{-6}K^{-1}$], E: elastic modulus [GPa], κ: thermal diffusivity [cm^2/s], k: thermal conductivity [W/(m·K)], C_p: heat capacity [J/(kg·K)]

T °C	σ_b MPa	m	K_{IC} Mpa$\sqrt{m}$	α $10^{-6}K^{-1}$	E GPa	κ cm^2/s	k W/mK	C_p* J/kg·K
20	390	9	4.0	3.0	433	0.38	83	700
1000	350	7	3.8	5.1	414	0.10	42	1200
1400	375	10	4.4	5.9	407	0.096	40	1300

*: C_p data from Barin & Knacke [1]

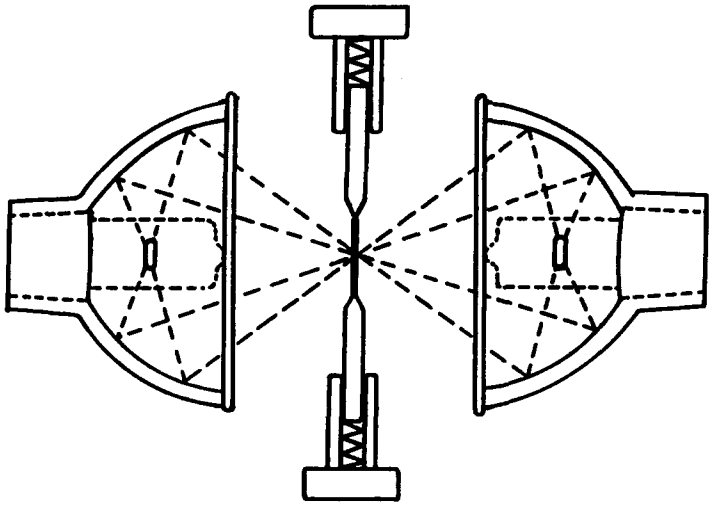

Fig. 3: Schematic cross section of the thermal shock apparatus with two lamps focused on the central specimen, which is supported by spring-loaded Al_2O_3 holders.

Experimental results

At temperatures up to 1550°C and run times up to 60 hrs the growth rate of oxide scale was too small to be quantitatively followed by the DTA apparatus. No bubble formation comparable to those reported by Mieskowski et al. [3] has been observed.

The result of the oxidation treatment in the thermal shock apparatus is shown in Fig. 4. Large blisters (up to 5 mm) develop within the hot central zone. The time to develop the blisters is dependent on the size of the specimen, small samples show blister formation after seconds, larger samples may need a few minutes.

Upon cooling a partial crystallisation of the blister skin in spherulitic manner is observed. This feature is similar to small-scale spherulitic growth of cristobalite in the (bubble-free) oxide scale of pure SiC at high temperatures [4].

Fig. 4: A ≈ 5 mm large blister formed on SiC after 3 min at 1720±60° C. During quench-cooling spherulitic crystallisation of cristobalite occurs.

Discussion

a) TEMPERATURE GRADIENTS THROUGH THE SiC TILES:

Under conditions of Newtonian heat transfer the heat flux $\dot{q}$ is proportional to the temperature difference between the surface temperature T_s and the temperature of the surrounding medium T_g

$$\dot{q} = h\ (T_g - T_s) \qquad (1)$$

where h is the heat transfer coefficient (Fig. 5a). An infinite strong thermal shock happens when the heat transfer coefficient equals infinity, i.e. the surface temperature of the material decreases instantaneously by ΔT whereas the rest of the material is still at the original temperature T_0. In this case the tensile thermal stresses produced at the cooled surface

$$\sigma_{th}^{max} = \frac{\alpha E \Delta T}{1 - \nu} \tag{2}$$

have their maximum value and are identical for different shapes of components (plate, cylinder, hollow cylinder, sphere and hollow sphere). σ_{th}^{max} is also independent of wall thickness and radii of curvature.

An infinite plate of thickness d, which is cooled from the outside has a Temperature profile T(x) perpendicular to the surface according to [5]

$$T(x) = T_m + \beta \sum_{n=1}^{\infty} \frac{\cos(2\alpha_n x/d)\ \sec(\alpha_n)}{0.5\ \beta\ ((0.5\beta+1) + \alpha_n}\ \exp(-\alpha_n^2\ (t/\tau)) \tag{3}$$

where α_n are the positive roots of

$$\alpha_n \tan \alpha_n = \beta \tag{4}$$

and β denotes the Biot number

$$\beta = (dh/k) \tag{5}$$

and τ has the form

$$\tau = 0.25\ d^2/\kappa \tag{6}.$$

The Biot number β relates the heat in- or output (h) to the capacity of the material to transport the heat (k) weighted by the dimension of the plate. This dimensionless number is used to characterize the severity of the thermal shock. The worst case thus corresponds to $\beta = \infty$. τ describes the relaxation of the temperature field to steady state conditions (Fig. 5b) and is a measure of the transient time of the thermal shock loading.

In general the maximum thermal stresses during thermal shock loading can be expressed by

$$\sigma_{th} = \frac{\alpha E \Delta T}{1 - \nu}\ f(\beta)\ g(t/\tau) \tag{7}$$

with

$$f(\beta) = \begin{cases} 1 \text{ for } \beta = \infty \\ \propto \beta \text{ for } \beta > 1 \end{cases} \tag{8}$$

and

$$g(t/\tau) = \begin{cases} 1 \text{ for } t=0 \\ 0 \text{ for } t=\infty \end{cases} \qquad (9)$$

Using the given tile thickness of 3 mm and an assumed heat transfer coefficient in the combustion chamber of 2000 W/(m² K) we get the small Biot number $\beta \cong 0.12$. The corresponding maximal thermal stresses shown in Fig. 6 are calculated according to [6]

$$\sigma_{th} = 0.02\ \alpha E \Delta T/(1-\nu) \qquad (10).$$

Even for a very improbable temperature difference of 2200 K the stresses would reach only 100 MPa, which is below the bending strength of the

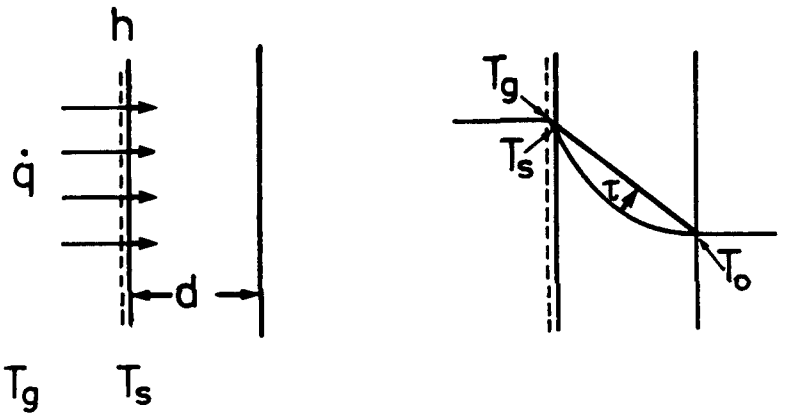

Fig. 5: a) heat flux $\dot{q} = k\ (T_g - T_s)$ with heat transfer coefficient h from the burning gas at T_g to the SiC tile at T_s. d= thickness of tile. The severity of the thermal shock is characterized by $\beta = (h \cdot d)/k$, where k is the thermal conductivity. b) relaxation of the non-linear transient temperature profile to the linear steady state profile; relaxation time $\tau = d^2/(4\kappa)$

material. Using the values of table 1 the relaxation time is ≈ 0.3 s. Therefore the wall temperature will be in a steady state regime already at less then 1 s after the start or stop of the engine. Steady state conditions always lead to a linear temperature profile in the thickness direction of the plate and if the plate is unconstrained the thermal stresses are zero.

The situation changes if we calculate the thermal stresses for a hollow sphere or a hollow cylinder with linear radial temperature profiles of temperature difference ΔT. If the SiC components were constructed out of a single hollow sphere and a single hollow cylinder both would have the very small thickness/radius ratio d/R = 0.07. The maximal thermal stresses are calculated applying equation (7), so that [6]

$$\sigma_{th} = 0.5 \frac{\alpha E \Delta T}{1 - \nu} \qquad (11).$$

The result is illustrated in Fig. 6. It shows that already for a temperature difference of 300 K tensile stresses of 350 MPa occur and it is evident that such shapes with small d/R ratios have to be avoided.

If a cylinder is cut into pieces the magnitude of the thermal stresses can be estimated by the theory for curved beams. For the combustion chamber with a d/R ratio of 0.07 this results[6] in stresses, which are smaller than $0.005 * \sigma_{th}^{max}$ (Fig. 6), i.e. they reach only about 1% of the magnitude of the closed structure and can be neglected.

b) TEMPERATURE GRADIENTS IN LATERAL DIRECTION:

Two cases of thermal stresses arising from lateral temperature gradients are modelled:
1) axial symmetric temperature field in a disk of radius R

$$T(r) = \begin{cases} \Delta T \text{ for } r \leq r_o \\ 0 \text{ for } r > r_o \end{cases} \qquad (12)$$

2) periodic temperature field with wavelength l in an infinite plate

$$T(x) = \Delta T \sin (2\pi/l)x \qquad (13).$$

In the first case the corresponding tangential stresses are [6]

$$\sigma_{th} = 0.5\ \alpha\ E\ \Delta T \begin{cases} (r_0/R)^2 - 2 & \text{for } r \leq r_0 \\ (r_0/R)^2 + (r_0/r)^2 & \text{for } r > r_0 \end{cases} \qquad (14)$$

The tangential stresses are compressive and constant and the highest values of $-\alpha E \Delta T$ occur if the plate is infinite ($R=\infty$). Outside the heated zone the maximum tensile stresses are at the edge ($r=r_0$) and they reach the highest value of $\alpha E \Delta T$ if R approaches r_0.

In the case of the periodic temperature field the solution [7] also gives maximal tensile stresses with a magnitude of $\alpha E \Delta T$ which is correct for wavelength to plate ratios $l/d < 1/8$. The results illustrated in Fig. 6 signify that temperature gradients in lateral direction produce much higher stresses than gradients in thickness direction of the tiles.

c) LIFE TIME PREDICTION AND THERMAL SHOCK

The brittle fracture of ceramics has to be treated by statistical methods because of the randomly distributed and orientated defects in the material. A useful tool to describe the failure probability P_f of ceramics is the Weibull distribution [8]

$$P_f = 1 - \exp\left[-\frac{V}{V_0}\left[\frac{\sigma}{\sigma_0}\right]^m\right] \qquad (15).$$

V_0 is the characteristic volume (typically 1 mm³), σ_0 the characteristic strength and m is the Weibull modulus. For $V=V_0$, a Weibull modulus of 10 and a characteristic strength of 400 MPa the failure probabilities of SiC have been calculated and illustrated in Fig. 7. The result shows that a still relatively high failure probability of 10^{-2} allows tensile stresses of 250 MPa only, a required failure probability of 10^{-4} decreases the tolerable stresses to 160 MPa. Fig. 7 shows that this corresponds to lateral temperature differences of 250 K and 150 K respectively. Through the thickness temperature differences are not dangerous.

A more rigorous application of the Weibull theory has to take into account the different effective volume of the bending bar V_{bend} and the burning chamber V_{burn} according to equation

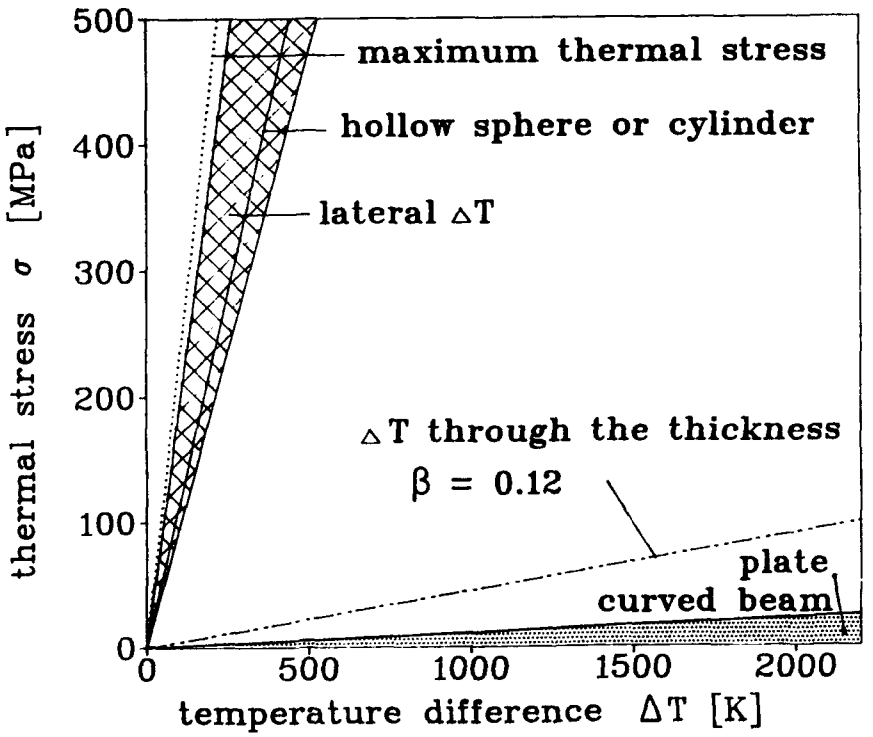

Fig. 6: Tensile stresses produced by lateral and through the thickness temperature gradients for different geometries (transient and steady state). Parameters used: E=420 GPa, $\alpha=4.5\cdot10^{-6}$ K^{-1}, $\nu=0.16$.

$$\frac{\sigma_{burn}}{\sigma_{bend}} = \left[\frac{V_{bend}}{V_{burn}}\right]^{\frac{1}{m}} \qquad (16).$$

In a 4-point bending test a bar with a 20/40 mm span and dimensions of 3.5*4.5*45 mm^3 has an effective volume of 16 mm^3. Assuming only 0.1% of the real volume of $1.7*10^5$ mm^3 for V_{burn} the tolerable strengths and temperature differences are further reduced and shown in Fig. 8.

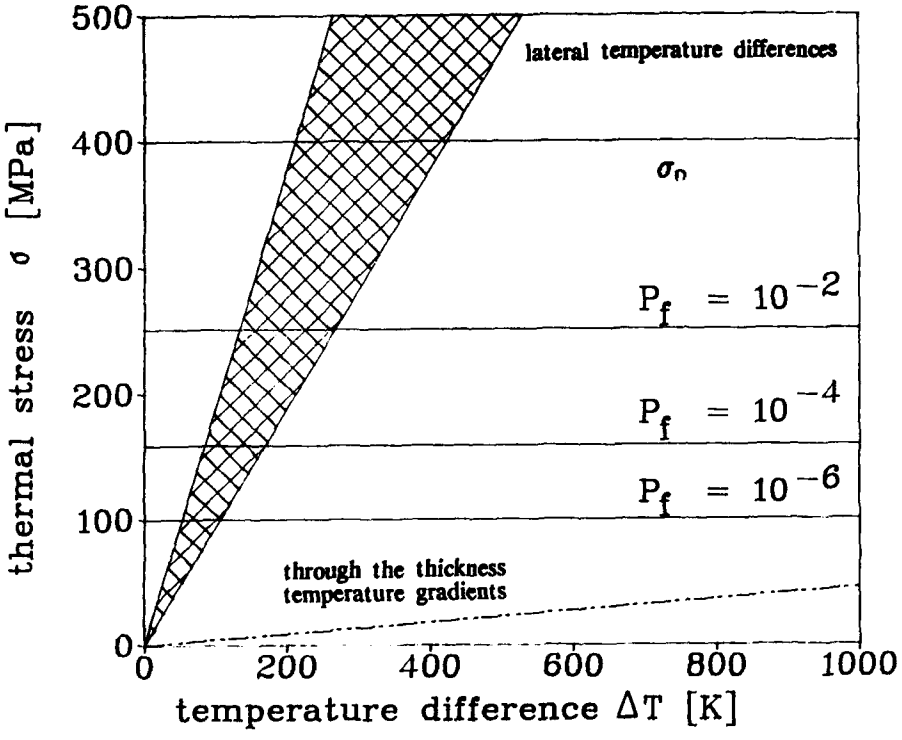

Fig. 7: Maximum tolerable stresses for different failure probabilities P_f with $V_{burn} = V_0$ and m = 10.

d) CORROSION

Diesel-air mixtures are strongly dominated by air and it can be shown that equilibrium compositions and measured values for those gas mixtures are characterized by a few percent CO, 1 to 15% CO_2 and a few ppm C_xH_y and NO_x and variable amounts of H_2O. Before and after combustion these mixtures have free O_2 contents between 5 to 20% and thus have to be considered to be highly oxidizing.

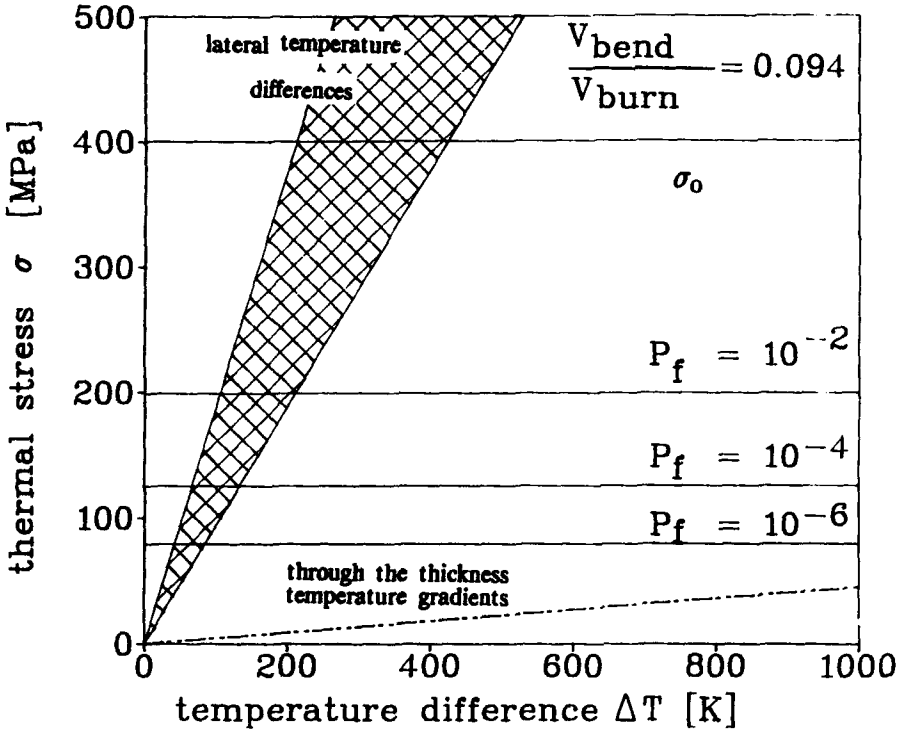

Fig. 8: Maximum tolerable stresses for different failure probabilities P_f with $V_{bend} = V_0$, $V_{bend}/V_{burn} = 0.094$ and m = 10.

The passivation type of oxidation of SiC is due to

$$SiC + 1\tfrac{1}{2}\ O_2 \rightleftharpoons SiO_2 + CO \qquad (17)$$

while experiments [9] indicate that active oxidation is probably due to instability of SiO_2 coexisting with SiC:

$$SiC + 2\ SiO_2 \rightleftharpoons 3\ SiO + CO \qquad (18).$$

The development of bubbles in oxide scales on SiC at lower temperatures ($\leq$ 1400°C) was only observed on polycrystalline SiC and lacking on single crystals [3]. Thus Mieskowski et al. [3] argued that the CO-production from free carbon according to

$$C + \tfrac{1}{2}\ O_2 \rightleftharpoons CO \qquad (19)$$

should be the main reason for bubble formation. Experiments for up to 60 hrs on the SiC used in this study showed no blister formation to 1550°C. We cannot exclude this effect to be decisive. However, using the data of Chase et al [10] reaction (2) is calculated to be in equilibrium at ≈1800°C, which means SiO + CO total 1 bar. According to Wagners [11] theory the active-passive transition is defined by the condition ($P_{SiO}+P_{CO} = P_{O2}$). Lowering the oxygen pressure thus lowers the active-passive transition temperature.

As described elsewhere [12] an analysis of the Si-C-H-O system shows that SiC in steam would be incompatible with SiO_2 at temperatures above ≈1710°C.

Thus depending on the composition of the atmosphere the transition from passive to active oxidation is expected to occur in diesel-air combustion atmospheres between 1650 to 1800°C. In crevaces, where soot collects and is re-ignited, we may have local reducing atmospheres. Here active oxidation will take place at lower temperatures.

At temperatures somewhat below passivation may occur in moderately flowing air. However, if extensive blister formation occurs the adhesion of SiO_2 layers to the SiC cannot be firm. Thus in the conditions of a fast gas flow SiO_2 will continuously be removed from the SiC surface. Therefore the growth mode (or rather removal mode) is not parabolic and may be equated with the speed of passive oxidation in the initial period of oxidation under steady state conditions. This type of model is shown in Fig. 9. The times required to destroy a component are accordingly very different.

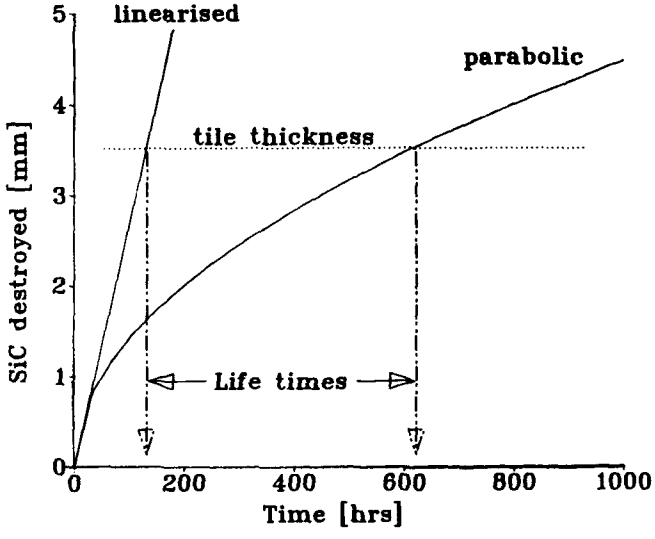

Fig. 9: SiC tile life times predicted from the assumption of parabolic growth of an oxide scale with a $K_p = 10^{-4}$ cm/h$^{-0.5}$ (experimental value for 1600°C[9]) and linearised using the initial slope of the oxidation rate as rate controlling.

At higher temperatures we have the conditions of active oxidation, which may be treated as a special case of hot-gas corrosion. Hot gas corrosion is controlled by the emission of gaseous particles from a material and thus strongly dependent on the boundary conditions of the system. Two types of situations involving flowing and extremely fast flowing atmosphere have been modeled and presented earlier [13], yielding

$$J = \dot{X}_l \cdot \varrho = \frac{M \cdot P_i \cdot \dot{V}}{a \cdot u \cdot R \cdot T} \qquad (20)$$

and

$$J = \frac{P_i}{\sqrt{2 \pi R T M}} \qquad (21).$$

(J: mass flux, $\dot{X}_l$: corrosion rate [depth/time], ϱ: density, M: molecular weight, P: partial pressure of species i, $\dot{V}$: flow rate of atmosphere, T: temperature, R: gas constant, u: ratio of gas species:reacting species, a: exposed surface).

Equation (20) is an equilibrium type of calculation, which necessitates the (experimental) verification of an effective gas flow rate $\dot{V}$, while (21) is a formulation neglecting all kinetic hindrances and as such a "worst case" calculation to evaluate extreme conditions.

Thermodynamic calculation of *reaction equation (18)* yields partial pressures of SiO and CO approaching 1 bar in the vicinity of 1700-1800°C. This is confirmed by model calculations in more complex systems using more sophisticated thermodynamic calculation methods [14].

Applying equations (20) and (21) to such high partial pressures yields corrosion rates in the order of μm to mm/min even under the assumption of an effective gas flow of only 1 m^3/sec.

Thus if the temperatures of the SiC tiles can be kept at the limits shown in Fig. 2, i.e. below 1600°C, we do not expect serious corrosion problems at all spots fully exposed to the gas. If however fluctuations of gas temperatures make the material to cross the active-passive transition temperature (≈ 1700°C) these components are likely to be destroyed very rapidly by corrosion.

Summary

For the modelled SiC combustion chamber thermal shocks as large as $\Delta T = 2000$ K cause stresses *through the thickness* of the componenet, which are not dangerous. The reason for this is the high thermal conductivity of SiC and the small wall thickness of the design.

However, *lateral* temperature differences of only $\Delta T = 200$ K induce stresses of 250 MPa. Application of Weibull theory shows that even for a high failure probability (10^{-2}) such stresses and hence such temperature differences are not tolerable.

The diesel- air fuel should be sufficiently oxidizing to guarantee a passivation type of oxidation to at least 1600° C. Oxide scale growth rates up to this temperature are sufficiently low to predict a manageable life time. Temperatures above 1700° C are either within or very close to the active- - passive oxidation transition in the environment of a combustion chamber. The expected very rapid decay of material under those boundary conditions make SiC for the combustion chamber application useless, if these temperatures are exceeded for any longer period of time.

Thus, both for the reason of controlling thermal shock behaviour and corrosion, a main goal for the design of the combustion chamber has to be the proper control of combustion in axial direction to minimize temperature fluctuations.

Acknowledgements

We gratefully acknowledge support from the projects 03 M 2028 I and 03 M 2012 organised by the German Ministry of Research and Technology. We also would thank Dr. Eßlinger and Mr. Andrees of MTU company for fruitful cooperation.

References

1. Barin, I. and Knacke, O. (1973) "Thermochemical Properties of Inorganic Substances", Springer Verlag, Berlin

2. Schneider,G.A. (1989) "Thermoschockverhalten von Hochleistungskeramik", *Ph.D. Thesis*, Unversität Stuttgart

3. Mieskowski, D.M., Mitchell, T.E. and Heuer, A.H. (1984), "Bubble Formation in Oxide Scales on SiC", *J.Am.Ceram.Soc.* 67, C- 17- 18

4. Ogbuji, L.U. (1981), "Development of oxide scale microstructure on single- crystal SiC", *J.Mat.Sci.* 16, 2753- 2759

5. Carslaw, H.S., Jaeger, J.C. (1986) "Conduction of Heat in Solids", Clarendon Press, Oxford

6. Boley, B.A., Weiner J.H. (1985) "Theory of Thermal Stress", Robert E. Krieger Publishing Company, Malabar, Florida

7. Timoshenko, S.P., Godier, J.N. (1985) "Theory of elasticity", McGraw Hill Book Company, New York

8. Danzer, R. (1989) "Bruch Spröder Werkstoffe - Grenzen und Möglichkeiten der Bruchstatistik" in *Proceedings of the 12th Int. Plansee-Seminar*, pp. 183 - 198

9. Gmelins Handbuch d. anorganischen Chemie (1986) "Silizium", B3, p.349- 351, Verlag Chemie, Weinheim

10. Chase, M.W., Davis, C.A., Downey, J.R., Fridup, D.J., McDonald, R.A. and Syverud, A.N. (1985) "JANAF Thermochemical Tables", 3rd ed., *J.Phys.Chem.Ref.Data* **14** (1985)

11. Wagner, C. (1958) "Passivity during the Oxidation of Silicon at Elevated Temperatures", *J.Appl.Phys.* **29**, 1295- 1297

12. Nickel, K.G., Lukas, H.L. and Petzow, G. (submitted) "High- temperature corrosion of SiC in hydrogen- oxygen environments", submitted to: Hack, K. (Ed) "Computer assisted thermochemistry - an introduction and application to practical problems", Springer Verlag, Berlin

13. Nickel, K.G., Danzer, R., Schneider, G.A. and Petzow, G. (1989) "Corrosion and Oxidation of Advanced Ceramics", *Powdermetallurgy International*, **21**, 29- 34,

14. Eriksson, G. (1975) "Thermodynamic studies of high- temperature equilibria", *Chem.Scripta*, **8**, 100- 103

HIGH TEMPERATURE CORROSION OF SILICON NITRIDES

M.H. VAN DE VOORDE
European Communities Joint Research Centre
1755 ZG PETTEN
The Netherlands

ABSTRACT. Silicon nitride based ceramics have potential use in high temperature application, e.g. aeronautics and space, petrochemistry, automobiles, energy generation and utilization. The severe operating conditions are very demanding on properties: reliable mechanical properties, extreme temperature capabilities and good resistance against oxidative and corrosive attack.

Newly developed silicon nitrides, with controlled composition, and traditionally processed materials are being studied and a relationship between processing, microstructure and corrosive behaviour searched for. The experimental data cover a temperature range from 1000°C to 1500°C.

The high temperature oxidation phenomena will be reviewed and the oxidation determining parameters highlighted; the results coincide with published data. Silicon nitrides generally show a satisfactory resistance against oxidation.

The gaseous corrosion 'carburisation and sulphidation' have been studied. Silicon nitrides are severely damaged in relatively short times when exposed to reducing environments at temperatures up to 1300°C. The sulphidation/oxidation behaviour of these ceramics is consistent with pure oxidation behaviour; the corrosion products being predominantly silicates from oxidation reactions and sulphates from sulphidation reactions.

The molten salt degradation of Si_3N_4 ceramics is being investigated, particularly the corrosion by Na_2SO_4 and V_2O_5 in SO_2/SO_3 and oxygen environments respectively.

The effects of corrosion on mechanical strength and the strength degradation by gaseous corrosion and molten salt is investigated. Although high temperature oxidation improves mechanical property behaviour, hot corrosive species cause serious damage.

R. Freer (ed.), The Physics and Chemistry of Carbides, Nitrides and Borides, 403–404.
© 1990 Kluwer Academic Publishers. Printed in the Netherlands.

The purpose of the exercise is to understand the corrosion mode of attack in a qualitative and quantitative way and to propose corrosion degradation mechanisms. It will help to determine the boundary conditions for industrially safe operation and to fix the ultimate limits of usage.

Guidelines will be given for the development of silicon nitride materials and selection criteria for silicon nitrides provided . The paper will pinpoint the research and development needs for high temperature corrosion of silicon nitrides. Hints will be given for cooperation on an international scale and the need for international agreement on test methodologies will be stressed.

CORROSION AND MECHANICAL PROPERTIES OF SILICON NITRIDE BASED CERAMICS. INFLUENCE OF MICROSTRUCTURAL CHANGES.

P. GOURSAT* and J.L. BESSON**
* Laboratoire de Céramiques Nouvelles - UA CNRS 320
Université - 123, Av. A. Thomas - 87060 LIMOGES Cedex
** Laboratoire de Matériaux Céramiques - UA CNRS 320
ENSCI - 47-73 Av. A. Thomas - 87065 LMOGES Cedex
FRANCE

ABSTRACT. Silicon nitride ceramics contain vitreous intergranular phase resulting from sintering additives. The rheological properties, the microstructural transformations and the oxidation resistance of nitrogen glasses with compositions close to the amorphous phase are studied. The results, compared with those for the ceramics, allow a better understanding of the change in the mechanical properties at high temperature in oxidizing environments.

1. INTRODUCTION

Due to its intrinsic properties silicon nitride has emerged as the most promising candidate for high temperature applications [1,2]. However nitrogen ceramics are densified with the aid of a liquid-sintering medium which leads to a vitreous intergranular phase on cooling. The materials have not reached their equilibrium state at the end of fabrication.

In the working temperature range, the mechanical properties of this secondary phase are controlled by its viscosity. But, in addition, its structure may change by crystallization and its chemical composition may be affected by reactions with the environment. Detailed studies of these interdependent phenomena are essential to explain the oxidation behaviour and the changes in the mechanical properties of ceramic parts.

2. SILICON NITRIDE CERAMICS

Pure silicon nitride cannot be densified, due to its dissociation at high temperature and the very high diffusion energy of silicon, resulting from the covalent nature of Si-N bonds. Unfortunately, the silica always present on the surface of the grains is not efficient in promoting sintering through a liquid phase. Metallic oxides such as CaO, MgO, BeO, Al_2O_3, Y_2O_3 must be added to form an nitrogen eutectic (SiMON). With this liquid, capillary forces appear which induce rearrangements of grains and dissolution-diffusion-precipitation processes [3]. The refractoriness of this phase varies with the nitrogen content and with the nature and the quantity of metallic cations. On cooling, crystallization is slow and usually thermodynamic equilibrium is not reached at room temperature. Depending on initial

R. Freer (ed.), The Physics and Chemistry of Carbides; Nitrides and Borides, 405–421.
© 1990 *Kluwer Academic Publishers. Printed in the Netherlands.*

composition and on the processing routes, the materials are composed of one or more cristalline phases and of an intergranular glassy phase [4]. The microstructure studied by transmission electron microscopy consists of silicon nitride grains with a mean size of about 1-2 μm. However, exaggerated growth of grains which could reached several microns is observed. Their aspect ratio varies from grade to grade, but the acicular form of ß Si_3N_4 is favored by a large quantity of liquid phase.

Usually the grain boundary structure may be classified into four types [5], namely :

- Thick intergranular vitreous phase
- Thick intergranular crystalline phase
- Thick intergranular crystalline phase between thin glassy films
- Thin intergranular glassy films.

In the material, heterogeneities are observed (fig. 1) : areas where nitride grains are embedded in an abundant vitreous phase, contrasting with regions where the vitreous phase is restricted to thin intergranular films and pockets at triple junctions. These structural inhomogeneities can be eliminated by hot isostatic pressing [6].

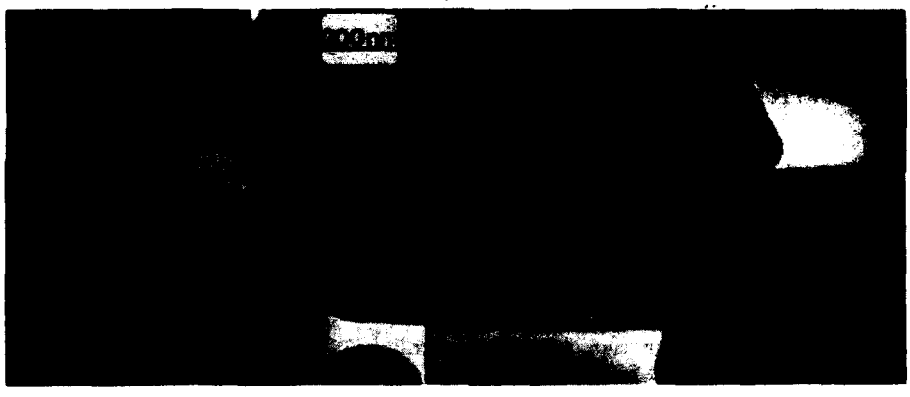

Figure 1. a : Microstructure of a silicon nitride ceramic (ß $Si_{5.6}Al_{0.4}O_{0.4}N_{7.6}$) dark film, b: Selected diffraction area.

3. SILICON OXYNITRIDE GLASSES

Whereas the glass forming regions in the different systems are well documented [7,8], very little information is available on their rheology [9]. By using classical techniques (dilatometry-DTA), it is possible to determine the glass transition temperature (T_G). However only creep measurements provide the changes in viscosity over a wide temperature range. Moreover, the creep techniques [10] allow comparison with the behaviour of the ceramics.

Nitrogen glasses are obtained usually by melting mixtures of oxides and nitrides and quenching. For the different systems the transition temperature depends on the nature of the modifying cations and on the quantity of dissolved nitrogen (Table 1).

Table 1. Glass transition temperature for various glasses.

Glass	Composition (wt%)							T_G (°C)
	Si	Ca	Al	Y	Mn	O	N	
G_1	30		8,6	15		46		890
G_2	34,2		9,8	17,1		34,7	4,2	940
G_3	34,7		9,9	17,3		31,9	6,2	965
G_4 (11)	27,7	19,4	8,7			40,1	4,1	778
G_5 (11)	21		5,90		35,16	35,70	2,24	701

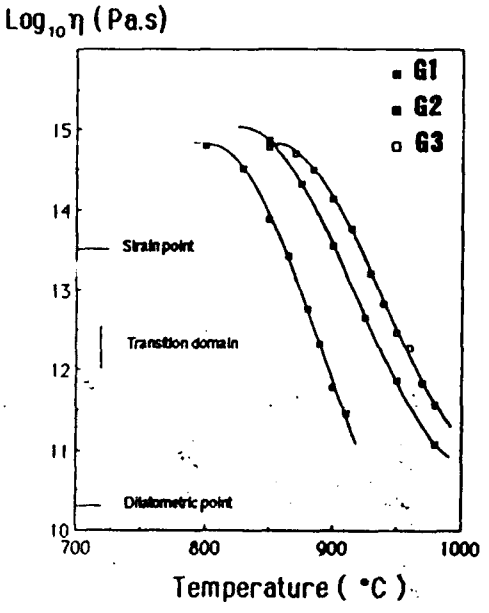

Figure 2. Evolution of viscosity versus temperature.

The higher the nitrogen content the higher the transition temperature. Replacing divalent oxygen by trivalent nitrogen increases the degree of crosslinking of the network, which explains the enhanced rigidity. The viscosity (η) curves (fig. 2) show a decrease of η by 4 orders of magnitude in a 100°C interval centered on T_g.

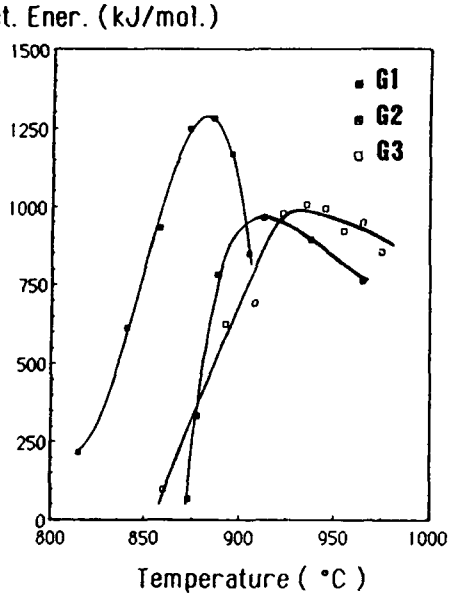

Figure 3. Activation energy for viscosity.

Calcium [11], manganese [11], magnesium [9] give eutectics with the lower melting points and lower glass transition temperatures, whereas yttrium, neodymium [12] formed glasses with higher refractoriness. Activation free energy for viscous flow can be calculated from the viscosity curves, by assuming an Arrhenius approximation between two successive temperature steps (fig. 3). The energy rises with temperature up to a maximum corresponding to the strain point, then diminishes slowly.

The crystallization ranges are usually determined by DTA and the compounds by XRD (Table 2).

The changes in Young's modulus with temperature gives additional informations. Young's modulus is a mechanical property sensitive to structural modifications : glass transition, formation of new phases. In addition, as for creep, it allows the comparison between the thermomechanical behaviour of glasses and ceramics. Young's modulus is obtained by using an ultrasonic technique [13]. On the curves (fig. 4) departures from linearity appear in the temperature ranges corresponding to the glass transition region.

Table 2. Crystalline phases after heat treatment at various temperature for G_2.

Temps °C	1050	1100	1150	1200	1250	1300
Time (hrs)	90	20	15	7	7	1
Compounds	$\alpha Y_2Si_2O_7$ traces	$\alpha Y_2Si_2O_7$	$\alpha Y_2Si_2O_7$ + $\delta Y_2Si_2O_7$	$\delta Y_2Si_2O_7$ + $\beta Y_2Si_2O_7$	$\beta Y_2Si_2O_7$ + Si_2N_2O traces	$\beta Y_2Si_2O_7$ + Si_2N_2O

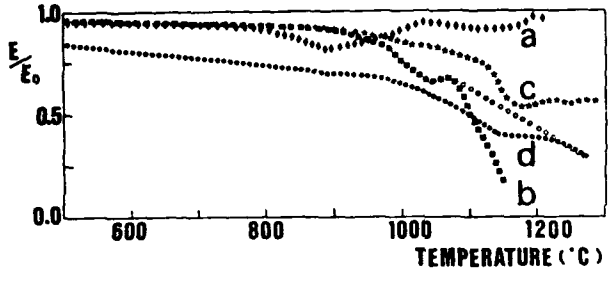

Figure 4. Young's modulus evolution versus temperature
a : G_1, b : G_2, c : G_3 and d : $\beta'Si_{5.6}Al_{0.4}O_{0.4}N_{7.6}$ densified with 9% Y_2O_3.

Above this temperature the change is complex and results from the competition between the rapid decrease of the viscosity and the consolidation due to the successive sequences of crystallization. For the oxide glass, crystallization is fast and Young's modulus increases. For the nitrogen glasses, viscosity is higher and crystallization slower. The modulus keeps decreasing until the crystallization of $\alpha Y_2Si_2O_7$ has proceeded sufficiently to compensate the loss in rigidity, that leads to a plateau at about 1050°C. For higher temperatures the modulus decreases again up to 1150°C, where $\beta Y_2Si_2O_7$ and Si_2N_2O precipitate. Isothermal experiments permit the transformation kinetics to be followed in situ. For instance, the crystallization of $\alpha Y_2Si_2O_7$, is fast at the beginning and slows down after 15 hours.

4. OXIDATION

4.1. Nitrogen glasses

Though the knowledge of their oxidation resistance is essential in understanding the degradation of ceramic parts, only a few systems have been investigated : CaSiAlON [11], Mn SiAlON [11], YSiAlON [14]. The behaviour depends on the starting composition, the viscosity, the glass transition temperature and the crystallization temperatures. Oxidation starts above T_G.

$$\text{SiAlYON glass} + O_2 \longrightarrow x\ SiO_2 + y\ Y_2Si_2O_7 + z\ Y_2SiO_5 + \overrightarrow{N_2}$$

For high nitrogen content, it is generally associated with a decomposition (fig. 5). The release of nitrogen results in a swelling of the specimen.

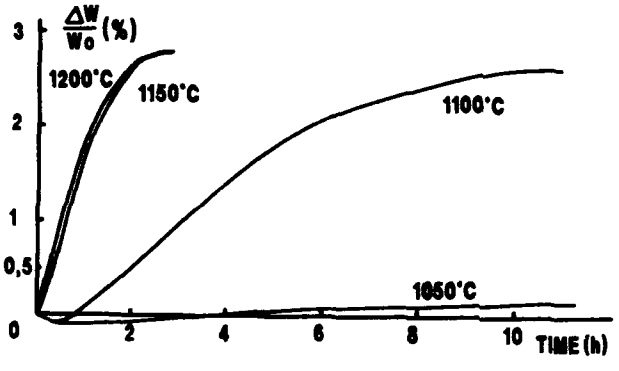

Figure 5. Isothermal oxidation in air of glass G_2.

An outward migration of modifying cations takes place during the reaction. At temperature above T_c, a competition occurs between oxidation and crystallization, which hinders the migration of the species. In the meantime the dissociation creates porosity. A transient improvement is observed. For higher temperatures the reaction becomes faster. The oxidation is completed in a few hours.

4.2. Powdered silicon nitride

Powdered silicon nitride exhibits two oxidation mechanisms depending upon the ambient oxygen potential.

Active oxidation is observed for low pressures according to :

$$2\ Si_3N_4 + 3O_2 \longrightarrow 6\ \overrightarrow{SiO} + 4\overrightarrow{N_2}$$

$$Si_3N_4 + 3\ SiO_2 \longrightarrow 6\ \overrightarrow{SiO} + 2\overrightarrow{N_2}$$

Due to the lack of a protective scale, the reactions proceed up to the complete destruction of the substrate.

For high oxygen pressures, a protective silica layer forms above 950-1000°C through the reaction :

$$Si_3N_4 + 3O_2 \longrightarrow 3\ SiO_2 + 2N_2 \qquad (IV)$$

The weight gain curves have a parabolic shape.

ß'$Si_{3,87}\ Al_{2,12}\ O_{2,15}\ N_{5,85}$ powder undergoes a similar behaviour [15]. Oxygen migrates towards the substrate across the oxide scale while nitrogen moves outwards. In most cases from Arrhenius plots of parabolic rate constants three regions are determined (fig. 6). At low temperature (T < 1100°C) the oxide coating is dense and protective. The reaction is controlled by the permeation of oxygen through the surface layer. In the 1050-1250°C interval, the crystallization of silica and mullite induces pores which facilitate the access of oxygen to the bulk.

Above 1200°C, due to the decreasing viscosity, the coating becomes more protective. The reaction is controlled again by the diffusion of oxygen.

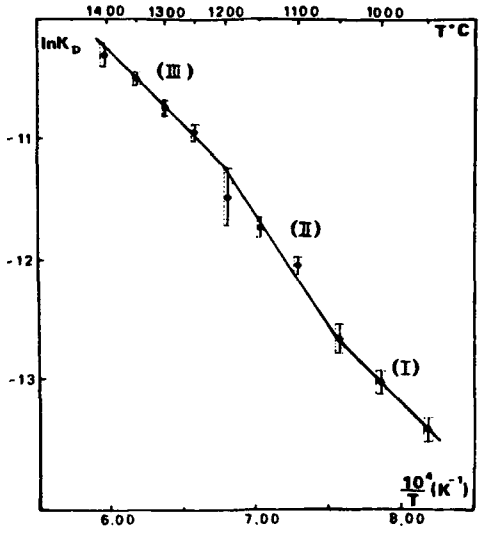

Figure 6. Arrhenius plots of parabolic rate constants :
I : 105±20 KJ.mol^{-1} ; II : 150±15 KJ.mol^{-1} ; III : 135±15 KJ.mol^{-1}.

4.3. Sintered silicon nitride

4.3.1. Crystalline intergranular phases

It is in the Si_3N_4 - SiO_2 - Y_2O_3 system that the influence of the crystalline phases is the more obvious [16] (fig. 7). The oxidation of samples in the Si_3N_4 - $YSiO_2$ N - $Y_2Si_3O_3N_4$ triangle occurs in two

intervals (800-1100°C) and (1400-1600°C), whereas the material is unaffected in the intermediate domain (fig. 8).

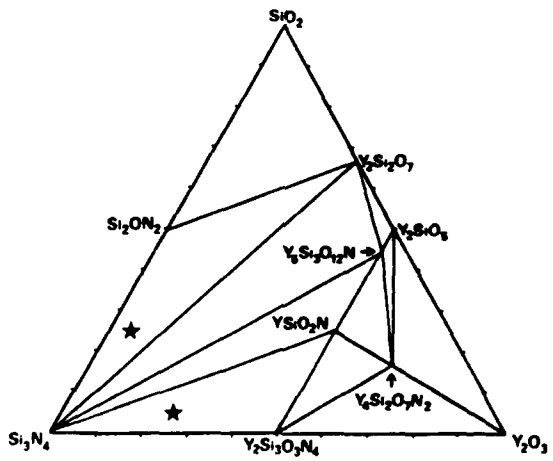

Figure 7. The Si_3N_4 - SiO_2 - Y_2O_3 system.

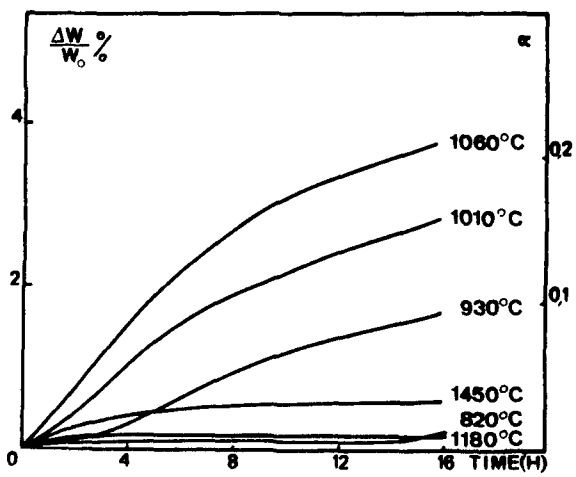

Figure 8. Isothermal oxidation in air.
Composition Si_3N_4 - SiO_2 - Y_2O_3 = 70 - 5 - 25 mole %.

In the 800-1100°C range, the oxynitride phases are very sensitive to oxygen and react preferentially to form an yttrium silicate (Y_2SiO_5) and silica (tridymite). At these temperatures the volume expansion due to the formation of oxides induces stresses in the substrate. The adherence and the mechanical properties of the coating are poor. Cracks appear at the internal interface and in the scale, which favours the access of oxygen to the bulk (fig. 9).

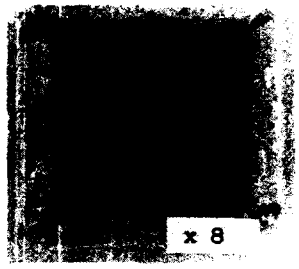

Figure 9. Optic cross section of a sample oxidized at 1020°C.

In the case of $YSiO_2N$, it is possible to develop a model for the oxidation mechanism [17]. With increasing temperature the scale becomes more plastic, and the stresses are relieved. The oxide film protects the sample and the oxidation is stopped. It becomes active again above 1450°C when the viscosity of silicates is low enough to allow nitrogen to be released.

4.3.2. Glassy intergranular phases

For different silicon nitride alloys, isothermal kinetics curves have parabolic to paralinear shapes depending on the composition [18], the ambient atmosphere [19] and the temperature (fig. 10). At the beginning the curves are parabolic, then the rate decreases leading to a linear regime at low temperature or an arrest of the weight gain. At high temperature the reaction goes on to completion.

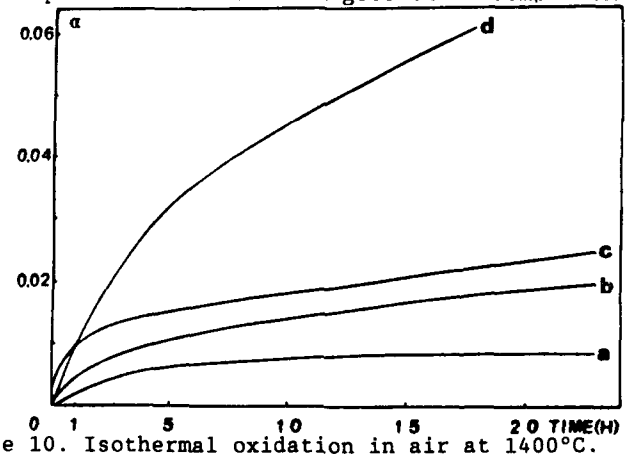

Figure 10. Isothermal oxidation in air at 1400°C.
a) Si_3N_4 - SiO_2 - Y_2O_3 (70 - 25 - 5 mole %) ; b) Si_3N_4 [20]
c) ß'$Si_{3.82}Al_{2.18}O_{2.18}N_{5.82}$; d) ß'$Si_{5.6}Al_{0.4}O_{0.4}N_{7.6}$ - 9% Y_2O_3.

An increasing fraction of silica and silicates produced by the oxidation is in an amorphous state as temperature rises. At low oxidation temperature the scale consists of crystals embedded in dense glaze. Above 1450°C bubbles of molecular nitrogen formed at the internal interface migrate through the fluid scale, creating an interconnected porosity (fig. 11).

Figure 11. SEM oxidation layer of ß'$Si_{3.20}Al_{2.66}O_{3.20}N_{4.80}$ at 1600°C.

It is well established that the cationic impurities accumulate in the oxide layer. From concentration profiles obtained by EDX [20-21-22] 3 regions are observed (fig. 12).

- the unaffected bulk
- a zone depleted with metallic impurities (Ca, Fe, Ti, Y)
- the external oxide layer with the impurities.

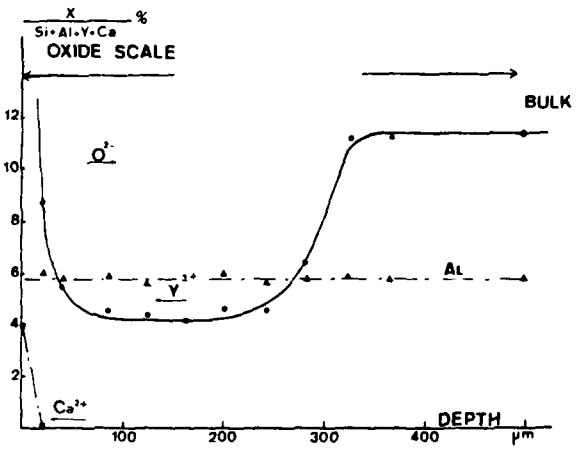

Figure 12. Concentration profiles of metallic elements.
ß'$Si_{5.6}Al_{0.04}O_{0.4}N_{7.6}$ - 9% Y_2O_3 oxidized in air.

The smaller the ionic radius the faster the diffusion rate. As a consequence calcium migrates at a rather low temperature [23]. The driving force for the migration arises from the chemical potential gradient between the silica layer and the intergranular phase.

These general trends are illustrated by a composition (Si_3N_4, SiO_2, Y_2O_3 = 70 ; 25 ; 5 mole%) chosen in the compatibility triangle Si_3N_4, Si_2N_2O, $Y_2Si_2O_7$. The duration of the parabolic regime

$(\Delta W/Wo)^2 = K_D t$ depends on the temperature [24]. The Arrhenius law is verified over two seperate ranges (fig. 13). The behaviour is complex because of viscosity variations, and crystallization taking place in the scale and in the bulk. The rate and the extent of the different processes (impurities migration, nitrogen release), change with temperature.

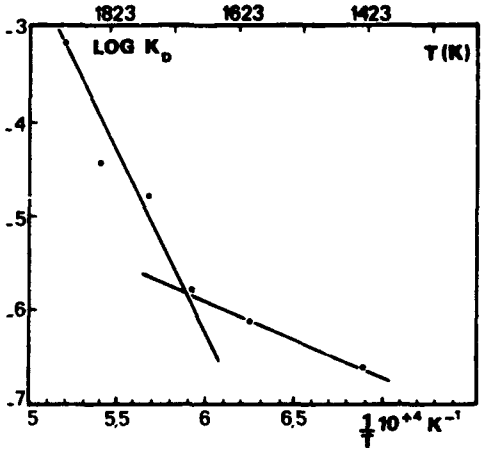

Figure 13. Arrhenius plot of parabolic rate constants for oxidation.

In the temperature range 1150-1400°C the oxide film is dense. On a cross section the depth of the affected region is emphasized by a colour change. After removing the film, X-ray patterns of this region did not reveal any change in the silicon oxynitride content, which may result from a limited oxidation of silicon nitride. So the microstructural changes are due to the oxidation of the intergranular phase. TEM observations reveal microcrystallites, in triple junctions (fig. 14). During the oxidation, the devitrification of the boundary phase is not complete. Absence of cavities or loosenings at grain boundaries suggests an ionic intergranular diffusion. Oxidation results from an inward diffusion of oxygen coupled with an outward diffusion of nitrogen and metallic cations. The diffusion of oxygen could be the limiting step.

Figure 14. Microcrystallized triple junction (dark field).

In the second interval (1400-1600°C) the scale behaves as a viscous liquid. Its stirring by the release of nitrogen facilitates the supply of oxygen at the internal interface. Several mechanisms are active due to the concentration gradients and the high temperature ($T > T_E$). The nitride grains dissolve in the eutectic and the liquid is enriched in nitrogen, which exchanges with oxygen. The released nitrogen recombines to form molecular nitrogen. The overall reaction proceeds in a way similar to a zone refining process : there is a reaction front at the internal interface which shifts to the centre. Moreover, at these temperatures, silicon nitride and silica begin to decompose which favours the formation of porosity in the scale.

5. MECHANICAL PROPERTIES

5.1. Young's modulus

Young's modulus of the ceramics is higher than those of the glasses [25], but its variation with temperature shows the same features (fig. 4). For silicon nitride densified with Y_2O_3 and Al_2O_3 aids, the departure from linearity is observed at 950°C, that is the glass transition for the G_3-SiYAlON glass (table I). The plateau in the 1150-1250°C interval corresponds to the beginning of the crystallization of yttrium silicates. The change due to crystallization is irreversible and the room temperature modulus is increased.

5.2. Modulus of rupture

The rupture strength remains roughly constant up to 900-1200°C (fig. 15) and the fracture is transgranular. Above this range, the strength decreases rapidly and the rupture becomes mainly intergranular. The temperature for the beginning of the degradation is of the same order as the transition temperature of the nitrogen glasses.

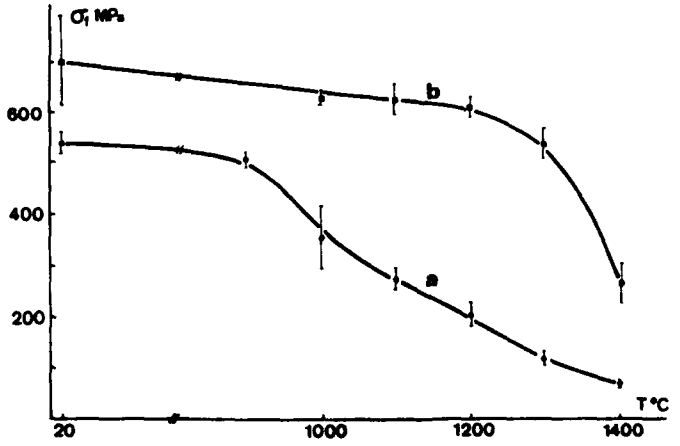

Figure 15. 3 Point bending strength versus temperature for ß'$Si_{5.6}Al_{0.4}N_{7.6}$ densified with 9% Y_2O_3 ; Ca : a = 0.14 W% ; b = 0.07 W%.

The onset of the weakening depends on the quantity and the nature of the sintering aids and on the impurity (Ca, Fe, Ti) levels in the raw materials. This is illustrated for materials with the same gross composition but with different calcium contents (fig. 15). When the yttria addition is reduced, the decrease commences at a lower temperature. The quantity of yttria determines the volume fraction of vitreous phase. At a given temperature, the higher the Ca/Y ratio the lower the viscosity [26].

Alumina plays a specific role by facilitating densification and then forming a solid solution with the nitride. The temperature at which strength decreases is independent of alumina content. No aluminium migration is observed during oxidation for usual compositions.

5.3. Influence of oxidation on mechanical strength

5.3.1. Room temperature strength

The modulus of rupture may be strongly affected by the presence of certain secondary crystalline phases (fig. 16.b). For instance the oxynitride phases in the Si_3N_4 - SiO_2 - Y_2O_3 system are readily oxidized between 800 to 1000°C [16]. Their preferential oxidation is associated with a strong volume expansion (see 4-3-1). Flaws appear to release the internal stresses, which cannot be accomodated by plastic flow at these temperatures. The new population of defects accounts for the decrease in strength. Above 1000°C the reaction products are viscous enough to relax the growth stresses, while ensuring an efficient protection. The room temperature strength is not affected.

When the oxidation starts above the transition temperature of the glassy phase, the reaction products coat the surface and blunt the defects. The room temperature strength increases (fig. 16.a).

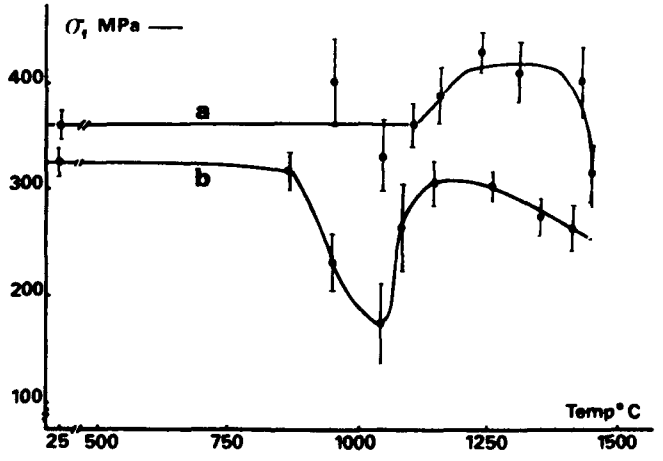

Figure 16. Room temperature bend strength after 48 h oxidation in air at various temperatures.
a = Si_3N_4 - SiO_2 - Y_2O_3 = 70 - 25 - 5 mole % ;
b = Si_3N_4 - SiO_2 - Y_2O_3 = 70 - 5 - 25 mole %.

At very high temperatures (T > 1450°C) the coating becomes too fluid and allows the release of nitrogen gas. The coarse porosity created by the nitrogen bubbles explains the drastic drop in modulus of rupture at room temperature.

5.3.2. High temperature strength

At high temperature the strength is controlled by the viscoelastic response of the glassy phase. A preoxidizing treatment induces the migration of metallic cations and a partial crystallization.

The viscosity of the intergranular phase is enhanced and as a consequence the high temperature strength is improved, provided that the oxide scale is removed before testing [27].

5.4. Creep

Creep deformation becomes detectable above 1000-1100°C [24,28,29]. Typical creep curves are reported in figure 17. The creep rate decreases rapidly during the primary stage, then very slowly (pseudo-stationary stage)and the true steady state is reached only after several hundred hours. During the first few hours, a large fraction of the vitreous phase is exuded at the surface [30] which results in a better grains packing, which are, at the most, separated by a thin vitreous film, and in a decrease in size of the triple points. Due to this microstructural evolution, a slight oxidation occurs on the surface but diffusion of oxygen into the bulk is very slow. Crystallization of the vitreous phase remains limited.

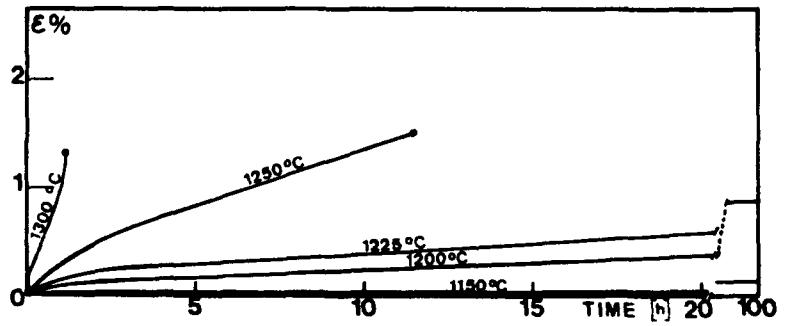

Figure 17. Creep curves at various temperatures at a stress of 240 MPa (Si_3N_4 - SiO_2 - Y_2O_3 = 70 - 25 - 5 mole %).

After this stage, which lasts a few tens of hours, the contribution due to the viscoelastic response of the vitreous phase itself vanishes and the deformation results from grain boundary sliding. Buttressings appear at irregularities on adjacent grains (ledges-precipitates). The induced stress fields increase as the thickness of the vitreous films diminishes. They give rise to chemical potential gradients which act as the driving forces for a solution-migration-precipitation process.

The mass transport through the glass is rate controlling for both the viscoelastic creep component and the diffusional creep. It derives from the fact, that the main controlling parameter is the viscosity of the glass. Thus, a decrease in the calcium content improves the creep resistance, as does an increase in yttrium content. The apparent activation enthalpy for creep ($\tilde{}$ 800 kj.mole^{-1}) is similar to that for plastic flow in nitrogen glasses above T_G (fig. 3).

For preoxidized samples it is noted that the steady state stage is reached more rapidly, but the steady state creep rate is faster [26]. Heat treatments in an oxidizing atmosphere promote crystallization and the lower quantity of remaining glassy phase explains why the steady state is reached in a shorter time. The solution-migration-precipitation mechanism induced along grain boundary defects take place at contact points between microprecipitates in triple junctions. As a consequence the mass transport is increased and the diffusional creep rate is higher.

6. CONCLUSION

A number of metallic oxides can be used as sintering aids for silicon nitride in order to achieve full densification. Out of these additives the Al_2O_3-Y_2O_3 couple has been selected for it forms with silica a nitrogen containing eutectic with a high melting point. However some impurities in the raw materials, especially calcium, lower the viscosity of the intergranular phase. As a consequence, particular attention must be paid to the control of the purity of the starting powders.

The study of the rheological properties and of the structural transformations of oxynitride glasses with compositions similar to the intergranular glasses seems to be essential in order to understand the behaviour of materials to operate at higher temperatures. The deleterious effect of the amorphous state of the secondary phase may be reduced by post-sintering heat treatments inducing their crystallization.

Although these materials exhibit a high modulus of rupture and a good oxidation resistance, they remain brittle. Two methode are in progress to improve the toughness. The first one concerns the reasearch of additives promoting the formation of an acicular microstructure. The second one consists in the introduction of short fibres to develop interfacial effects increasing the work of rupture.

7. REFERENCES

1. Ceramics for High Performance Applications II, eds Burke J.J., Lenoe E.M. ; Katz R.N..
   Brook Hill Publishing Co, Chestnut Hill, 1978.
2. Progress in Nitrogen Ceramics, ed. F.L. Riley, Nato ASI Series, Nijhoff Publishers, La Hague, 1983.
3. Popper P., Sintering of silicon nitride, a review, Progress in Nitrogen Ceramics, ed. F.L. Riley, Nijhoff Publishers, La Hague, 1983, 187-210.
4. Clarke D.R., Thomas G. ; Grain boundary phases in hot pressed MgO fluxed silicon nitride, J. of Amer. Cer. Soc. 60, 1977, 491-495.

5. Laval J.Y., Delamarre C., Amaura M.C., Broussaud D. ; Influence of the intergranular microstructure of substituted nitrides on high temperature strength, J. of Mater. Sci. 20, 1985, 381-390.
6. Thorel A., Laval J.Y., Broussaud D. ; High temperature mechanical properties and intergranular structure of sialons, Journal de Physique 47, C1, 1986, 353-357.
7. Loehman R.E. ; Preparation and properties of oxynitride glasses, Journal of non-cristalline solids, 56, 1983, 123-134.
8. Pastuszak R., Verdier P. ; Verres azotés contenant du manganèse (II). Preparation et propriétés. Revue de Chimie Minérale, 19, 1982, 107-115.
9. Drew R.A.L., Hampshire S., Jack K.H. ; The preparation and properties of oxynitride glasses, 323-336, ibid ref. 2.
10. Rouxel T., Besson J.L., Gault C., Goursat P. ; Elastic properties and crystallization in SiYAlON glasses and ceramics, Proceedings of the 1st ECers Conference, 18-23 June 1989, Maastricht (Netherlands), Elsevier Publishers (To be published).
11. Desmaison-Brut M., Desmaison J.G., Verdier P. ; The reactivity in oxygen of two MSiAlON oxynitride glasses (M = Ca, Mn), Solid State Ionics, 32/33, 1989, 843-851.
12. Hampshire S., Drew R.A.L., Jack K.H. ; Oxynitride glasses, Physics and chemistry of glasses, 26, 1985, 182-186.
13. Gault G. ; Ultrasonic non destructive evaluation of microstructural changes and degradation of ceramics at high temperature, M.R.S.
Fall Meeting Symposium U, Boston, 1988 (To be published).
14. Anger J.F. ; Internal report ENSCI, Limoges, France.
15. Brossard M. ; Solution solide sialon ß' : Préparation, résistance à l'oxydation, évolution structurale sous contrainte, Thèse, 1986, Limoges, France.
16. Bouarroudj A. ; Influence de l'environnement et de la microstructure sur les propriétés mécaniques de céramiques du system SiYON, thèse, 1982, Limoges, France.
17. Goursat P., Dumazeau C., Billy M. ; Oxidation of hot pressed silicon oxynitride yttria ceramics, Environmental degradation of high temp. materials, Inst. Metallurgists N°13, Vol 2, Chameleon, London, 1980.
18. Billy M. ; Reactivity in nitrogen ceramics.
SC 14, ed. D. Taylor, The Institute of Ceramics, 1988, Stoke on Trent, Staffs UK, 45-60.
19. Desmaison J., Brossard M., Desmaison-Brut M., Goursat P. ; Oxidation behaviour of ß'Sialons in oxygen and carbon dioxide, ibid ref. 2.
20. Cubicciotti D., Laue K.H. ; Kinetics of oxidation of hot pressed silicon nitride containing magnesia.
J. Amer Cer. Soc. 61, 1978, 512-517.
21. Clarke D.R. and Lange F.F. ; Oxidation fo Si_3N_4 alloys : relation to phase equilibria in the system Si_3N_4 - SiO_2 - MgO.
J. Amer. Cer. Soc. 63, 1980, 586-593.
22. Babini G.N., Bellosi A., Vincenzini P. ; A diffusion model for the oxidation of hot pressed Si_3N_4 - Y_2O_3 - SiO_2 materials.
J. of Mater. Sci. 19, 1984, 1029-1042.
23. Chartier T., Besson J.L., Goursat P. ; Microstructure, oxidation and creep behaviour of a ß'Sialon ceramic, Int. J. High. Tech. Ceram., 2, 1986, 33-45.

24. Bouarroudj A., Goursat P., Besson J.L. ; Oxidation resistance and creep behaviour of a silicon nitride ceramic densified with Y_2O_3, J. of Mater. Sci. 20, 1985, 1150-1159.
25. Rouxel T., Besson J.L., Gault C., Goursat P., Leilgh M., Hampshire S. ; Viscosity and Young's modulus of an oxynitride glass. J. of Mater Sci. Letters (To be published oct. 89).
26. Besson J.L., Goursat P. ; Optimization of SiAlYON ceramics. Relations : processing-microstructure-properties, in Technical ceramics, ed. Nosbusch H. and Mitchell I.V. ; Elsevier Applied Science Publishers, London, 1988, 127-135.
27. Chartier T. ; Céramiques de type SiAlYON : relations élaboration microstructure-propriétés, thèse, 1985, Limoges, France.
28. Lange F.F., Davis B.I., Clarke D.R. ; Compressive creep of Si_3N_4/MgO alloys. J. of Mater. Sci. 15, 1980, 601-618.
29. Karunaratne B.S.B., Lewis M.H. ; High temperature fracture and diffusional deformation mechanism in SiAlON Ceramics. J. of Mater. Sci. 15, 1980, 449-462.
30. Besson J.L., Streicher E., Chartier T., Goursat P. ; Viscoelastic creep of nitrogen ceramics. J. of Mater. Sci. letters 5, 1986, 803-805.

THE ROLE OF OXYGEN IN NON-OXIDE ENGINEERING CERAMICS

D.P.THOMPSON
Wolfson Laboratory, Materials Division,
Department of Mechanical, Materials and Manufacturing Engineering,
University of Newcastle upon Tyne, U.K.

ABSTRACT. Non-oxide ceramics (borides, nitrides, carbides and silicides) are important engineering materials because in comparison with oxides they offer increased refractoriness, higher strength and stiffness and often improved thermal shock resistance at elevated temperatures. Unless elaborate precautions are taken, oxygen is present at every stage of production from the processing of the raw materials to the firing of the final product, in some cases helping, but more often hindering the success of each step of the process. Most non-oxide starting powders contain up to 8 w/o of oxides and larger amounts may be introduced during powder handling and processing. In the case of nitrogen ceramics the oxygen is indispensible if a fully dense product is to be achieved but the resulting glassy phase degrades the properties of the final product. Current technology therefore aims to minimize the levels of oxygen required for densification and techniques such as HIPing are useful for this purpose. Preparation of non-oxide fibres and whiskers, often carried out via organic routes, can result in residual oxygen, especially on the fibre surface. This causes problems during the firing of composite materials containing these fibres, and of course the quality of the fibre-matrix interface is critical in controlling the subsequent mechanical performance of the material.

The role of oxygen in the final product depends to some extent on its location. Thus, for example, oxygen dissolved in the lattice of aluminium nitride significantly reduces the thermal conductivity. Oxygen present as a grain-boundary glass in silicon nitride-based ceramics is helpful as regards fracture toughness and room temperature strength but detrimental as far as high-temperature mechanical properties are concerned. Residual oxygen on the surface on many non-oxide ceramics is helpful in forming a passivating film which protects against oxidation at both room and elevated temperatures.

1. INTRODUCTION

Oxygen plays a fundamental role in all aspects of the behaviour of non-oxide ceramics because in the form of atmospheric gases (O_2, CO_2, H_2O), it is active during the handling of starting powders and during the

R. Freer (ed.), The Physics and Chemistry of Carbides; Nitrides and Borides, 423–433.
© 1990 *Kluwer Academic Publishers. Printed in the Netherlands.*

fabrication and furnacing procedures used for the production of solid components. Furthermore, there is some (albeit very small) solubility of oxygen in the crystal lattices of most non-oxide ceramics and this affects properties, especially electrical and thermal conductivity. Its presence as a surface layer on the finished product is essential for good high-temperature oxidation resistance, whereas its occurrence dissolved in small amounts in the crystal lattice may in some cases be detrimental to properties. Its presence in grain boundaries gives both advantages and disadvantages, but as a general rule, oxygen is detrimental to material properties at high temperatures. This paper discusses the various ways in which oxygen plays a part in the behaviour of non-oxide ceramics, using illustrations chosen mainly from the field of nitrogen ceramics.

2. POWDER HANDLING

All powders readily pick up moisture from the atmosphere; for oxides this is often an adsorption phenomenon, but for non-oxides, hydrolysis occurs giving a gaseous hydride plus a metal oxide, the latter forming a more or less passivating layer on the grain surface. The amount of oxide can be estimated either chemically [1] or by a combination of chemical and physical techniques [2]. If the powders are handled in an atmosphere of controlled humidity [3], hydrolysis can be prevented, but under normal laboratory conditions, further hydrolysis occurs, either because of exposure to atmospheric moisture or because of other factors associated with processing. Thus for example, when powders are milled, fresh surfaces are exposed, and even if non-aqueous solvents are used, the trace levels of water present combined with water pick-up during drying can initiate significant amounts of further hydrolysis. The real oxygen content of a powder is more reliably estimated from analysis after processing rather than from a chemical analysis of the starting powders themselves.

Many non-oxide powders also contain oxygen in solid solution in the crystal lattice. Thus, for example, interstitial transition metal nitrides and carbides are often isostructural with one another and also with the related oxides. In the case of titanium, TiC, TiN and TiO all form an extensive Ti(N,C,O) solid solution, and a precise knowledge of the C : N : O ratio is difficult to obtain. In covalently bonded nitrides and carbides, ranges of solid solubility are far less. Thus in the case of aluminium nitride, it has been estimated that 2.7% O [4] can be accommodated in the lattice. Generally a valency difference of one between the solute and solvent non-metal atom species allows some solubility, whereas a difference of two (e.g. oxygen in carbides) permits negligible solubility. Thus nitrogen has an appreciable solubility in silicon carbide [5] but oxygen has not.

The question of oxygen solubility in silicon nitride has still not been entirely resolved. α-Si_3N_4 does not incorporate oxygen [6] but the original data of Jack and co-workers [6,7,8] giving convincing evidence that α-Si_3N_4 is an oxynitride has been moderated but not refuted. The current position is that when α-Si_3N_4 is prepared under conditions of low oxygen partial pressures (for example by CVD methods), there is a

negligible oxygen content in the lattice and an equally small amount on the surface of the grains. When α-Si_3N_4 is prepared by routes involving higher partial pressures of oxygen, some oxygen is incorporated into the lattice and some of the silicon may be present in a lower valency state [9]. At least two variables (the concentrations of O and Si^{2+}) are needed to account for the published lattice parameter variations of α-silicon nitride [9]. Recent work by Peuckert and Greil [2] using chemical analysis to measure total oxygen and ESCA to measure surface oxygen, has provided the most accurate evidence to date to show that different amounts of lattice and surface oxygen are present in different α-silicon nitride powders.

Two areas in nitrogen ceramics where the amount of surface oxide is critical are (a) in the preparation of high-nitrogen compositions (e.g. α'-sialons) and (b) in the preparation of samples in regions where a large number of tie lines occur close together on the phase diagram. The problems of preparing α'-sialons have been discussed by Slasor and Thompson [10] and in the Y-Si-Al-O-N system, the range of compositions accessible using Si_3N_4/AlN/Y_2O_3 starting mixtures, assuming that the silicon nitride powder contains 4 w/o SiO_2 and the aluminium nitride powder 6 w/o alumina, corresponds to a very small fraction of the total α' region. Fortunately it includes the area of greatest commercial interest. Further discussion of this point has been given by Bartek et al. [11]. Large numbers of tie lines occur close together at the Si_3N_4 corner of the Y-Si-O-N and related M-Si-O-N systems, where M = La, Ce, Nd... . Depending on the oxygen content of the starting silicon nitride powder, additions of the same amount of metal oxide can result in different second phases being observed in quite different amounts [12]. This has a corresponding effect on the properties of the final material.

3. DENSIFICATION

Non-oxide ceramics cannot be densified by simple metallurgical processes (casting, forging, pressing etc.) because the covalent bonding in these refractory solids results in high self-diffusivities and decomposition often precedes melting. Complete densification is important if the best properties are to be achieved and this has been studied by numerous researchers and an in-depth discussion will not be given here. Different routes are required for different materials. Interstitial nitrides, carbides and borides can generally be densified by adding small amounts of a metallic species in which the matrix phase has some solubility. Covalent nitrides can only be densified by liquid phase sintering using small amounts of metal oxides or nitrides which promote the formation of oxynitride liquids and in which the parent nitride has some solubility [13,14]. The oxide layer on the surface of the starting nitride not only provides the oxygen necessary for the liquid phase but also locates it in the best place (i.e. around the grain) for achieving optimum surface area contact between nitride and liquid. SiC on the other hand cannot be densified if the oxide layer is still present and additions of carbon are a prerequisite for successful sintering. Small grain

size and high (2000-2200°C) temperatures are additional requirements, whilst additions of boron improve the kinetics by facilitating surface diffusion. Other effects (e.g. liquid phase sintering) may also contribute but a complete understanding of the densification behaviour of silicon carbide is still needed [15,16,17]. In the case of silicon nitride it is easy to see that a phase transformation involving a reconstructive process [18] allows redistribution of material and hence a filling up of pores with the newly created material. In silicon carbide, a similar situation applies when aluminium-containing compounds are used for densification and the starting 6H or β-SiC is substantially converted to 4H and the phase transformation can in principle assist densification; however, transformation proceeds by shear [19] and very little redistribution of material occurs compared with the complete reconstruction characteristic of the $\alpha \rightarrow \beta$-Si_3N_4 transformation.

4. THE RESIDUAL GLASS PROBLEM

As mentioned above, covalent nitrides are densified by additions of metal oxides (or nitrides) which form oxynitride liquids and promote densification by a liquid phase sintering process. In the absence of such additives, even if the silica layer is removed, no densification occurs [20]. Pressure, either uniaxial (i.e. hot-pressing) or isostatic (i.e. HIPing) can acheive substantial reductions in additive levels whilst still achieving densification, but a certain level of intergranular glass is necessary for the final material to display good room temperature properties. More importantly, the liquid phase plays a role in improving the final toughness of the material and the K_{1c} of 7.7 quoted for β'-sialon 101 ceramics [21] arises because the large volume of liquid phase allows large aspect ratios to be developed [22,23]. High-temperature properties fall off at temperatures determined by the T_g of the residual glass (typically 850-

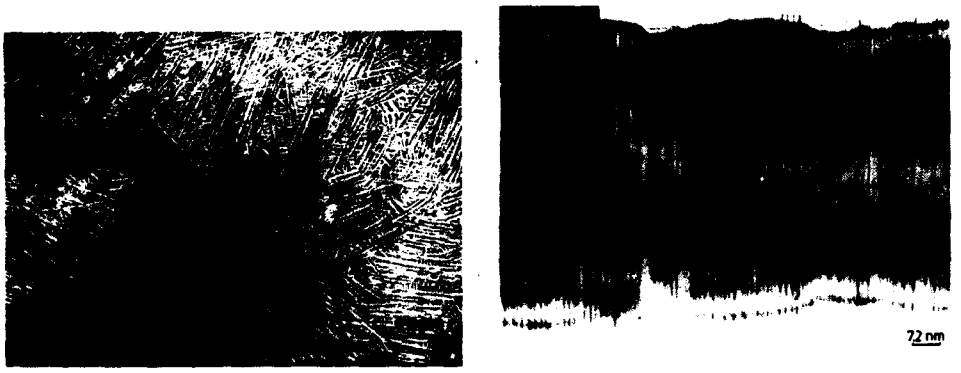

Figure 1. (a) optical micrograph of sialon X-phase (after [33] prepared at a 'high-X' composition, and (b) heavily faulted needle of a 2H SiC-AlN alloy of composition 25% AlN, 75% SiC.

1000°C) but this can be raised by ~300°C if all the glass is converted into appropriate crystalline phases [24]. This is often accompanied by associated disadvantages, notably in the case of β'-YAG ceramics by a deterioration in oxidation resistance [25] and by the development of porosity (due to reduction in specific volume [26]) which results in lower room-temperature strength. Alternatively in yttria-densified Si_3N_4 ceramics, the choice of crystalline phases is limited because $Y_2Si_2O_7$ exhibits numerous phase transformations [27] and the melilite phase, $Y_2Si_3O_3N_4$ (which occurs in some α' sialon and β-Si_3N_4 ceramics densified with yttria) results in low temperature oxidation problems [28,29,30]. An interesting observation in AlN ceramics densified with small amounts of CaO is that the intergranular Ca-Al-O-N liquid phase which aids densification can be almost entirely removed by post-sintering in a reducing atmosphere, leaving a glass-free final ceramic [31]. At the same time, oxygen in the AlN lattice is removed.

It is difficult to estimate the amount of residual glass in non-oxide ceramics. When present in large amounts (>5%), this can be determined (albeit rather slowly) from creep measurements [32]. In smaller amounts, TEM is an accepted technique, and this gives relatively easy qualitative identification but accurate quantification is still difficult because of the tortuous location of the glass within the microstructure. Two examples which illustrate these points are shown in Figure 1. Figure 1(a) shows an optical micrograph of sialon X-phase [33] prepared at a high-X starting composition on the SiO_2-rich side of the true X composition. At first glance the micrograph appears fully crystalline, but in fact the glassy regions in between the high aspect ratio X-phase grains account for some 30-40% of the total microstructure. Figure 1(b) shows a grain of SiC-AlN alloy of composition 25% SiC-75% AlN, which is heavily faulted and contains amorphous regions [5]. The glassy globules arise because lime was added to the starting mix to form a Ca-Si-Al-O-N liquid to aid reaction, and clearly some of this liquid

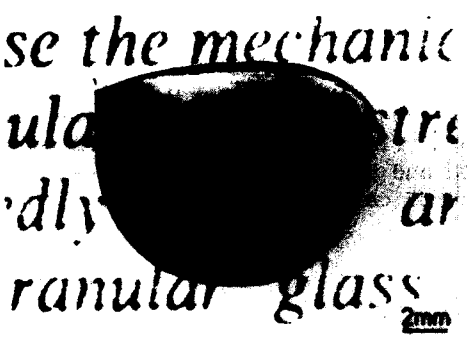

Figure 2. Magnesium sialon glass melt containing 10 equivalent % of nitrogen.

Figure 3. Transmission optical micrograph of a yttrium sialon glass containing 10 equivalent % of nitrogen.

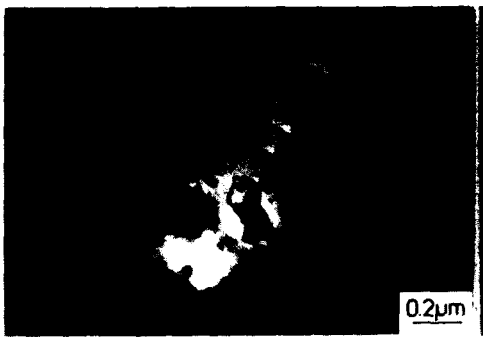

Figure 4. TEM micrograph of a precipitate in a magnesium sialon glass containing 10 equivalent % of nitrogen.

Figure 5. Crystallization in a Mg-Si-Al-O-N glass initated at a silicide precipitate.

was trapped in the growing crystals.

An additional feature of the residual glassy phase which has not been commented on by previous workers is illustrated in Figures 2,3 and 4. The residual glassy phase is black (Figure 2) because of the concentration of metallic precipitates (Figure 3) consisting principally of Si and $FeSi_2$ (Figure 4). These arise because of the trace metal impurities present in the starting Si_3N_4, which, above 1250°C react with the silicon nitride to form silicides. At these temperatures, the silicides are molten and catalyse further decomposition of the silicon nitride, the silicon thus produced dissolving in the existing molten metallic globules. As the temperature is further increased, the M-Si-O-N or M-Si-Al-O-N liquid forms and for long glass melting times and low liquid viscosities, the heavier molten metallic globules sink through the oxynitride liquid giving a more transparent upper layer and a darker lower region (Figure 2). On cooling, the metallic globules provide sites where crystallization of the glass can readily occur (see Figure 5,[34]). Obviously starting with nitride powders containing minimal levels of metallic impurities minimizes the resulting blackness but it should be noted that the glass shown in Figure 2 was prepared from a starting mix containing less than 0.02 % total metal impurities. Exceedingly pure powders are therefore required. However the challenge of making a transparent glass (or when incorporated into a silicon nitride-based matrix, a white ceramic product) is worth the effort involved and in some applications (e.g. optical properties of glasses and use of ceramics for dental fillings) offers important advantages.

5. OXIDATION RESISTANCE

There have been numerous studies of the oxidation resistance of silicon nitride and silicon carbide-based ceramics (see for example [35-37]). The aim of this paper is only to summarize the main principles and to

emphasize points which have not received sufficient attention in previous studies. SiC, Si_3N_4 and sialon ceramics have the advantage of forming a substantially silica or silicate-based surface layer which, above its softening temperature, spreads over the surface and protects against further oxidation. With a passivating surface layer, oxidation behaviour can be divided into three regimes. At low temperature (i.e. below the softening point of the glassy surface film), oxidation proceeds slowly and essentially linearly because the solid oxide layer is not protective. Passivation is the desirable state and occurs when the surface glass has sufficient fluidity to spread over the surface, but at some higher temperature, the surface layer becomes so fluid that the transport of oxygen ions through it is rapid and continuous oxidation results. In the best oxidation-resistant materials, the onset of this third regime is delayed until the highest possible temperatures and in the case of silicon-based ceramics, this is below 1720°C (the melting point of pure SiO_2) but with silicon carbide it is possible to get reasonable lifetimes at temperatures up to 1650°C. SiC ceramics exhibit better oxidation resistance than silicon nitride-based materials because no ionic metal oxides are used for densification. If they are, the lower eutectic temperature of the silicate allows surface oxide layers to form which melt (and give low viscosity liquids) at temperatures much lower than 1700°C. In many sialon ceramics this temperature is typically ~1300°C [24]. In nitrogen-based ceramics, minimizing the level of additive (consistent with achieving densification) and using trivalent additives in preference to divalent (because they exhibit higher eutectics) and ensuring that any residual glass is removed by devitrification (because the glass offers an easy path for ion transport) are the accepted ways of optimizing oxidation resistance. In non-silicon based nitrides and carbides, passivating oxide layers are not as easily formed and oxidation becomes a problem at much lower temperatures. In the case of AlN, crystalline alumina platelets grow perpendicular to the surface giving very poor oxidation protection at

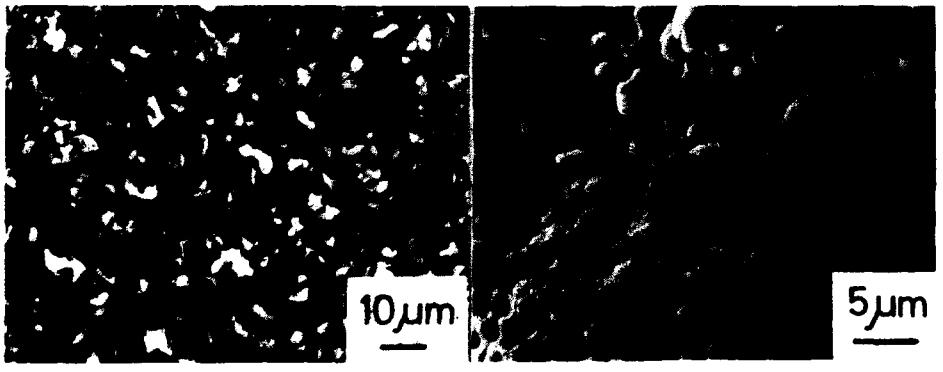

Figure 6. Crystalline mullite on the surface of $Al_5Si_2C_6$ oxidized for 24 hours in air at (a) 1400°C and (b) 1600°C.

quite low temperatures [38]. Similarly, the formation of mullite on for example Al-Si-C alloys (Figure 6), is not protective but slow diffusion rates give acceptable oxidation behaviour up to ~1400°C. Much more rapid oxidation occurs above this temperature [39].

Ultimately the most reliable answer to oxidation problems is the development of oxidation-resistant coatings. The requirements of such coatings are severe, namely, lack of reaction with the substrate, minimal grain growth at the maximum temperature of operation, compatibility in thermal expansion coefficient with the substrate and of course good oxidation resistance itself. If these properties are not available in a single coating, the development of multiple coatings (as for example in the case of cemented carbides) may be necessary, but there are then more incompatibilities to be balanced. A considerable wealth of experience has been gained on carbon-based materials where this problem is much more severe; this may be transferable to present carbide, nitride and boride systems [40]. Good oxidation resistance for extended periods still remains the main reason why most non-oxide ceramics are not used in engineering applications at temperatures above 1700°C.

6. EFFECT OF RESIDUAL OXYGEN ON PROPERTIES

Room temperature mechanical properties of non-oxide ceramics are affected only to a secondary extent by the oxygen present either in the lattice or as part of the grain-boundary phase assemblage. High-temperature properties are a different story, and mechanical properties are dominated entirely by grain-boundary phases. Lattice oxygen has very little effect on mechanical properties; indeed, in most non-oxide

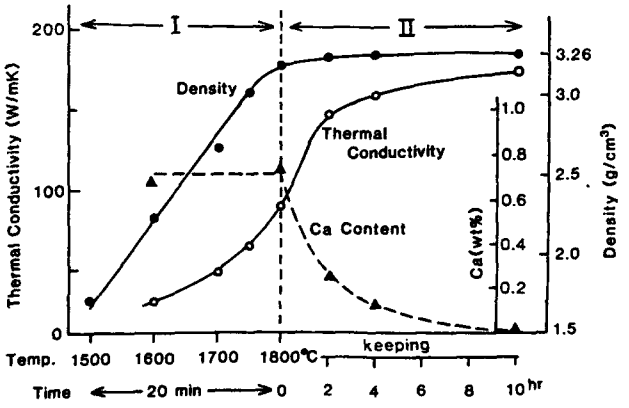

Figure 7. The development of high thermal conductivity in a lime-densified sample of AlN sintered for increasing times at 1800°C (after [41]).

ceramics, residual oxygen in the lattice is removed entirely during firing in inert or reducing atmosphere at 1500-2000°C.

Other properties affected to a much greater extent by oxygen include those involving diffusional transport. A striking example is the role of oxygen in modifying the thermal conductivity of aluminium nitride ceramics. Whereas the calculated thermal conductivity of either single crystal or polycrystalline AlN is in the range 270-300 W/mK [4], typical commercial materials in recent years have shown values of 100-150 W/mK. For many years it has been known that the root cause of the low thermal conductivity is oxygen, especially oxygen dissolved in the lattice rather than in grain-boundary phases. AlN can be densified either with or without additives by sintering withour pressure at temperatures up to 2200°C. In the first case a metal aluminate grain boundary phase is present, whereas in the second case the $Al_2O_3.9AlN$ polytypoid phase (27R) is formed which drastically reduces thermal conductivity. Recent Japanese studies [31] have shown that longer sintering treatments at high temperatures "sweep away" oxygen from the grain boundaries (and from within the grains) resulting in higher conductivities with values of up to 270 W/mK (see for example Figure 7 from [41]). Such materials are proving extremely useful as electronic substrates.

7. CONCLUSIONS

Oxygen is the most important and yet the most difficult element to control in the preparation, characterization and property assessment of non-oxide engineering ceramics. The level of oxygen present initially in the starting powders and introduced during processing should be kept to a minimum and reproducibly controlled to achieve consistency in performance of the final product. Oxygen occasionally benefits room temperature behaviour but is almost invariably undesirable for achieving good high-temperature material performance. A surface layer of oxide is generally essential for protection against oxidation at both room and elevated temperatures.

REFERENCES

1. Thompson, D.P. (1985) 'Chemical analysis of nitrogen ceramics', in the 7th Ceramic Chemists Conference, BCRA Special Publication No. 110, 108-119.
2. Peuckert, M. and Greil, P., (1987), J. Mater. Sci. 22, 3717-3722.
3. Schwier, G. (1988), private communication with H.C.Starck-Berlin.
4. Slack, G.A. (1973), J. Phys. Chem. Solids, 34, 321-335.
5. Patience, M.M., England, P.J. and Thompson, D.P. (1984) 'Ceramic alloys of silicon carbide with aluminium nitride and nitrogen', in S.Somiya, E.Kanai and K.Ando (Eds.) Ceramic Components for Engines, KTK Scientific, Tokyo, 473-479.
6. Wild, S., Grieveson, P. and Jack, K.H.(1972),Special Ceramics 5,

271-287.
7. Wild, S., Grieveson, P. and Jack, K.H. (1972), ibid, 385-395.
8. Colquhoun, I., Wild, S., Grieveson, P. and Jack, K.H. (1973), Proc. Brit. Ceram. Soc., 22, 207-227.
9. Jack, K.H. (1983), 'The characterization of α'-sialons and the α→β relationships in sialons and silicon nitrides' in F.L.Riley (Ed.) Progress in Nitrogen Ceramics, Nijhoff (The Hague), 45-60.
10. Slasor, S. and Thompson, D.P. (1986), 'Preparation and characterization of yttrium α' sialons', in S Hampshire (Ed.) Non-Oxide Technical and Engineering Ceramics, Elsevier Applied Science, 223-230.
11. Bartek, A., Ekstrom, T. and Herbertsson, H. (1990), 'Single phase yttrium α'-sialon ceramics by hot isostatic pressing', accepted for publication in J. Amer. Ceram. Soc.
12. Rae, A.W.J.M., (1976), Ph.D. thesis, University of Newcastle upon Tyne.
13. Hampshire, S. (1980), Ph.D. thesis, University of Newcastle upon Tyne.
14. Hampshire, S. and Jack, K.H. (1983) 'The kinetics of densification and phase transformation of nitrogen ceramics', Special Ceramics 7, 37-49.
15. Prochazka, S. (1974), 'Sintering of silicon carbide' in J.J.Burke, A.E.Gorum and R.N.Katz (Eds.) Ceramics for High-Performance Applications, 239-249.
16. Suzuki, H. and Hase,T. (1979), 'Some experimental considerations on the mechanism of pressureless sintering of silicon carbide' in S.Somiya and S.Saito (Eds.) Factors in Densification and Sintering of Oxide and Non-Oxide Ceramics, Tokyo Institute of Technology, 345-365.
17. Mizrah, T., Hoffman, M. and Gauckler, L.J. (1986), 'Pressureless sintering of silicon carbide' in H.Hausner (Ed.) Ceramic Materials and Components for Engines, Deutsche Keramische Gesellschaft, 347-352.
18. Wild, S., Grieveson, P., Jack, K.H. and Latimer, M.J., (1972), Special Ceramics 5, 377-384.
19. Jepps, N.W. and Page, T.F. (1983), J. Cryst. Growth and Characterization, 259-271.
20. Peitzsch, R. and Hausner, H. (1984), 'Sintering of silicon nitride with non-oxide additives' in S.Somiya, E.Kanai and K.Ando (Eds.) Ceramic Components for Engines, KTK Scientific (Tokyo), 208-217.
21. 'Syalon 101', Technical data sheet produced by Lucas Cookson Syalon (now Vesuvius Zyalons (Midlands)), Solihull, West Midlands.
22. Lewis, M.H. (1986), 'Microstructural engineering of ceramics for high-temperature application', in R.E.Tressler, G.L.Messing, C.G. Pantano and R.E.Newnham (Eds.) Tailoring Multiphase and Composite Ceramics, Materials Science Research Vol. 20, 713-730.
23. Lewis, M.H. (1987), 'Microstructural design of high-temperature ceramics', in R.Freer, S.Newsham and G.Syers (Eds.) Engineering with Ceramics 2, Brit. Ceram. Proc. 39, 1-13.
24. Thompson, D.P. (1990), 'Alternative grain-boundary phases for heat-treated Si_3N_4 and β'-sialon ceramics', in R.W.Davidge and D.P. Thompson (Eds.) Fabrication Technology, Brit. Ceram. Proc. 45, in publication.

25. Lewis, M.H., Mason, S. and Szweda, A. (1986), 'Syalon ceramic for application at high temperature and stress' in S. Hampshire (Ed.) Non-Oxide Technical and Engineering Ceramics, Elsevier Applied Science, 175-190.
26. Lumby, R.J. (1989), private communication.
27. Liddell, K. and Thompson, D.P. (1986), Brit. Ceram. Trans. & J. 85, 17-22.
28. Lange, F.F. (1980), Int. Met. Rev., 1, 1-20.
29. Patel, J.K. and Thompson, D.P. (1989), 'Further studies of the low-temperature oxidation problem in yttria-densified silicon nitride ceramics' in V.J.Tennery (Ed.) Ceramic Materials and Components for Engines, The American Ceramic Society, 987-996.
30. Govila, R.K. (1987), J. Mater. Sci. 22, 1193-1199.
31. Kuramoto, N, Taniguchi, H. and Aso, I. (1989), Amer. Ceram. Soc. Bull., 68, 883-887.
32. Lumby, R.J., North, B. and Taylor, A.J. (1975), Special Ceramics 6, 283-298.
33. Thompson, D.P. and Korgul, P. (1983), 'Sialon X-phase', in F.L.Riley (Ed.) Progress in Nitrogen Ceramics, Nijhoff(The Hague), 375-380.
34. Korgul, P. and Thompson, D.P. (1987), 'Transparent Nitrogen Glasses' paper presented at the Institute of Ceramics Annual Convention.
35. Singhal, S.C. (1976), J. Mater. Sci., 11, 500-509.
36. Clarke, D.R. and Lange, F.F. (1980), J. Amer. Ceram. Soc. 63,586-594.
37. Singhal, S.C. (1976), J. Mater. Sci., 11, 1246-1253.
38. Roebuck, P.H.A. (1976), Ph.D. thesis, University of Newcastle upon Tyne.
39. Oscroft, R.J. and Thompson, D.P. (1990), 'Carbonitride Ceramics for high temperature applications', poster presented at the Institute of Ceramics Christmas Conference 'Advanced Engineering with Ceramics', London 1989, paper submitted for publication.
40. Jamet, J.F. (1987), 'Ceramic-ceramic composites for use at high temperature' in S.G.Burnay (Ed.) New Materials and their Applications, Inst. Phys. Conf. Ser. 89, 63-75.
41. Kuramoto, N., Tanaguchi, H. and Aso, I. (1986),'Translucent AlN ceramic substrates' in IEEE Trans. Compon. Hybrids. Manuf. Tech. 9, 386-390.

THERMOCHEMICAL PREDICTIONS OF METAL-METAL CARBIDE STABILITIES IN RELATION TO WC AND WC-Co PRODUCTION

F.H. HAYES and **F.R. SALE**
Manchester Materials Science Centre
University of Manchester and UMIST
Grosvenor Street
MANCHESTER M1 7HS
UK

ABSTRACT. Thermochemical data are used to predict and examine possible production routes for WC powders by the reduction/carburisation of tungsten oxides. It is shown that the reduction route chosen may control the particle morphology of the carbide phase obtained. Further data are then used used to examine the conditions under which WC-Co composite powders may be obtained directly from $CoWO_4$ by a similar reduction/carburisation process. The evolution of carbide phases during such processing is related to predictions of phase stabilities in the W-Co-O system at 1400 K. Experimentally, the extent of reduction/carburisation is shown to be dependent upon time, temperature and carbon activity in the gas phase.

1. INTRODUCTION

Thermochemical predictions of phase stability have advanced the understanding of many phase systems over recent years, as evidenced by the many publications and meetings associated with CALPHAD. Nevertheless, the use of such predictions, and their immediate relation to materials production, have been less intensively reported. The aim of the present paper in this NATO workshop proceedings is to demonstrate the methodology and application of such predictions in the study of metal carbide-metal equilibria and in the assessment of alternative manufacturing routes. The examples selected are based on the experience and publications of the present authors. These relate specifically to the W-C-O and W-C-Co systems and thus deal with the industrial production of WC and WC-Co composite materials. Nevertheless, the methodology may be used for other carbides and for the other compounds, borides and nitrides, which form the basis materials for study in this workshop.

2. THE W-C-O SYSTEM AND WC PRODUCTION

Figure 1 shows a section of the predominance area diagram for the W-C-O system at 1200 K as calculated by Morris (1) using data

R. Freer (ed.), The Physics and Chemistry of Carbides; Nitrides and Borides, 435–445.
© 1990 *Kluwer Academic Publishers. Printed in the Netherlands.*

collected and assessed by Worrall (2). This figure can be used to assess present and alternative processes for the production of tungsten carbide. The present industrial method consists of the manufacture of tungsten powder followed by extensive ball milling and mixing with carbon black with a subsequent reaction at temperatures of the order of 1800 K to yield tungsten carbide. With reference to Figure 1 the process can be seen to be one in which the oxygen potential is reduced in the first stage so that a solid oxide feedstock is converted from WO_3 or $W_{20}O_{58}$ (or "blue" oxide, a mixture of these two oxides) to metallic tungsten. The reduction in oxygen potential is achieved using hydrogen. The second stage of the process is effectively a simple increase in carbon potential of the system such that tungsten carbide is formed. It is clear from Figure 1 that this route for the manufacture of tungsten carbide is probably the most indirect method possible. Over the years modern developments have introduced rotary kilns into both metal and carbide production stages and a wide variety of sophisticated gas control systems have been used. Nevertheless, the process chemistry is still essentially:

$$WO_3(s)+3H_2(g)\rightarrow W(s)+3H_2O(g)$$

followed by:

$$W(s)+C(gr)\rightarrow WC(s)$$

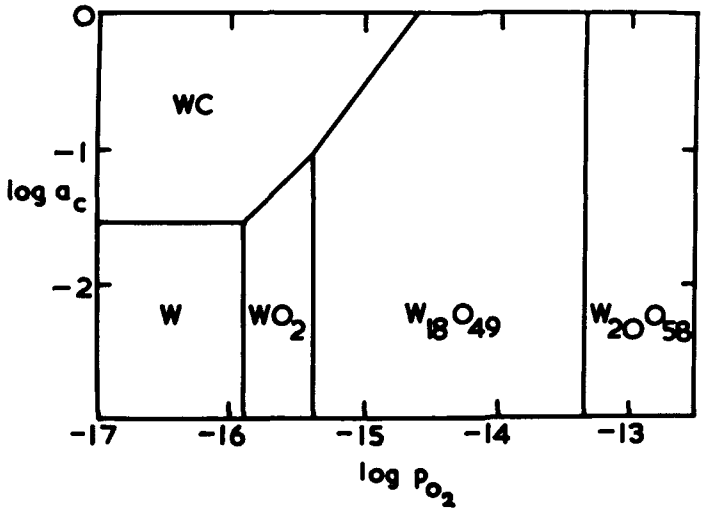

Fig. 1: W-C-O predominance area diagram at 1200 K (after Morris [1]).

The first stage of reduction proceeds through the sub-oxides $W_{20}O_{58}$, $W_{18}O_{49}$ and WO_2 before tungsten metal is obtained (3-6). (At low temperatures, of less than 860 K, β-W is obtained as a non-equilibrium product rather than the equilibrium product of α-W.) Whilst there may be a number of industrial reasons and 'folklore' for operating such a two-stage process, a more direct route would offer tremendous benefits particularly in terms of energy efficiency. It is apparent from Figure 1 that if the reduction of the oxide phases is carried out with a gas phase of sufficiently high carbon potential then it is possible to reduce/carburise the oxides to yield WC directly. In addition it is evident that the WC field on Figure 1 may be accessed across either the WO_2-WC boundary or the $W_{18}O_{49}$-WC boundary. This possibility offers interesting morphological control as the two oxides have been shown to possess quite different morphologies when produced from the same feedstock (3-6) and these morphologies may be retained in a WC product under certain conditions(7). Figures 2 and 3 show examples of the quite different morphologies of WC that may be obtained from WO_2 and $W_{19}O_{49}$ respectively. The control of carbon content is achieved by control of the gas phase used for the direct reduction/carburisation process. Either CO/CO_2 or H_2/CH_4 mixtures may be used.

Fig. 2: WC produced from W_02 by reduction/ carburisation with CO.

Fig. 3: WC produced from $W_{18}O_{49}$ by reduction/ carburisation with CO.

Such direct reduction/carburisation processes using gaseous reactants have been investigated by a number of workers. Newkirk and Aliferis (8) studied the carburisation of tungsten, tungstic acid, tungsten trioxide, ammonium paratungstate and blue oxide mixtures in H_2/CH_4 mixtures. It was found that at 1273K WC was obtained from all the different feedstocks although the carbon content was close to the theoretical level only in the carburisation of tungsten. The carburisation of tungstic acid and tungsten oxides has been shown to occur in two stages when H_2/CH_4 mixtures are used (8, 9). Initially a rapid reduction to tungsten metal occurs and this is followed by a slower carburisation process to give WC. Accordingly, morphological control using H_2/CH_4 is extremely difficult, if not impossible. In contrast it has been shown that the use of CO/CO_2 mixtures allows the morphology of the last oxide reduced to be retained in the WC product (7). Kim and Chang (10) indicate that the reduction/carburisation of WO_3 using CO/CO_2 mixtures is more rapid than the carburisation of metallic tungsten and hence show the necessity of control of both carbon and oxygen potentials in the reducing gas to obviate both the production of tungsten and the deposition of free carbon. Interesting electron microscopy observations of the in-situ carburisation of WO_3 with CO have been reported by Fornwalt et al (11) who have shown that platelets of WO_3 obtained from freeze-dried ammonium metatungstate converted directly to WC in pure CO without the production of any lower oxides. This observation of an apparently sharp interface between WO_3 and WC in partially-carburised material is in conflict with the reports of many other workers and must be explained by differences in the rate-controlling steps in the reactors used by different investigators. It is not unexpected that the observations made on a single platelet in the environmental cell of an electron microscope are different to those made on materials produced in gram or kilogram quantities.

The direct reduction/carburisation of WO_3 with carbon in a continuous rotary kiln has been described by Miyake et al (12), who heated stoichiometric quantities at 1273 K in nitrogen to reduce the oxygen content and then heated the reduced mixture at 1673 K in hydrogen to allow carburisation to occur. Carbon control in this system is difficult and can only be achieved on the basis of reaction stoichiometry and mass balance of the reactants.

3. COBALT - CONTAINING TERNARY SYSTEMS AND THE PRODUCTION OF WC-Co MIXTURES

Based upon the predictions and observations made on the direct production of tungsten carbide, a possible alternative route for the production of WC-Co composite material is the direct reduction/carburisation of cobalt tungstate ($CoWO_4$) or mixtures of WO_3 and $CoWO_4$, to allow for variations in the Co-WC ratio in the resultant product. Such a method would possess the advantages outlined for the direct production of WC and would also have the advantages that the separate production of Co powder by the hydrogen

reduction of cobalt oxide and the subsequent mixing of Co powder with WC powder would both be obviated. Data for the Co-W-C system by Uhrenius and Johansson (13) and Akesson (14) along with the measurements of Rezukhina and Kashina (15) on Co-W alloys and $CoWO_4$ allow a thermochemical assessment of a direct reduction/carburisation route to be made.

Using the section of the ternary diagram for the W-Co-O system shown in Figure 4 and standard Gibbs energy of formation data for CoO, $CoWO_4$, Co_7W_6 and H_2O it has been shown that the equilibrium reduction of stoichiometric $CoWO_4$ at temperature of 1073 K and above will traverse two three-phase fields to yield a mixture of Co_7W_6 and α-W (16). The three phase fields are $CoWO_4$+WO_2+Co_7W_6 and Co_7W_6+WO_2+α-W. The stability of $CoWO_4$ is such that a two-phase equilibrium can exist between it and WO_2. As a result of this direct formation of WO_2 from $CoWO_4$ potential morphological control by the production of $W_{18}O_{49}$ is not possible in this system. Such predictions are in agreement with the experimental data of Bracconi and Dufour (17) and French and Sale (18), although the reduction of $CoWO_4$ at lower temperatures in non-equilibrium and proceeds via the formation of an amorphous W-Co-O containing phase.

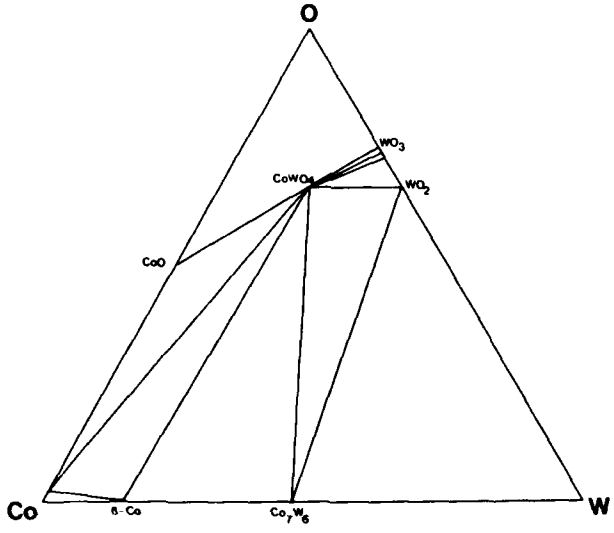

Fig. 4: W-Co-O system at 1400 K.

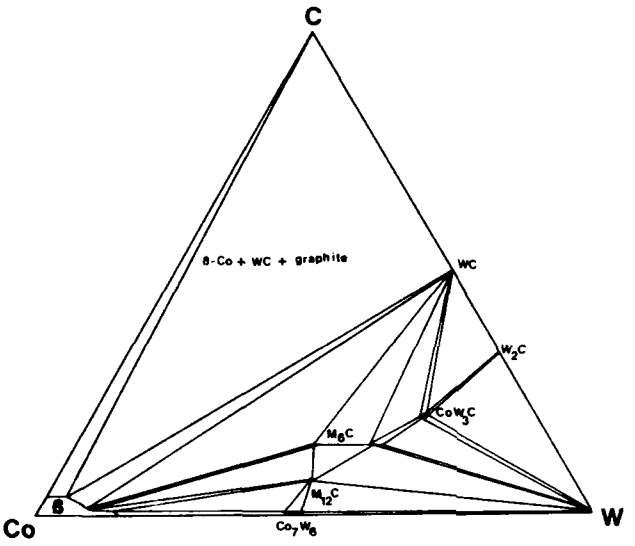

Fig. 5: W-Co-C system at 1400 K.

The reduction/carburisation of $CoWO_4$ using either CO/CO_2 or CH_4/H_2 mixtures relies upon the gas phase having a sufficiently high carbon potential for the production of the required carbide phase (or carbide phase/metal mixture) whilst simultaneously having an oxygen potential which is lower than that of WO_2 at the temperature considered. Figure 5 shows an isothermal section at 1400 K of the W-Co-C system. The β-Co+WC field can be seen to be bordered by two three-phase fields, namely β-Co+WC + graphite and β-Co+WC+M_6C. At temperatures below 1373 K the latter phase field becomes metastable relative to a β-Co+WC+$M_{12}C$ mixture (14). To produce the composite WC+β-Co it is apparent that the carbon activity must be controlled at a value below unity so that free carbon is not formed (sooting reaction), but the activity must be greater than that at which the brittle M_6C phase (η phase) is produced. These values may be calculated from available data for a range of temperatures to give the relationships shown in Figures 6 and 7, where it can be seen that the deposition of free carbon in an industrial reactor should be easier to avoid with CH_4/H_2 mixtures rather than CO/CO_2 mixtures because of the manner in which the equilibrium gas ratios vary with temperature.

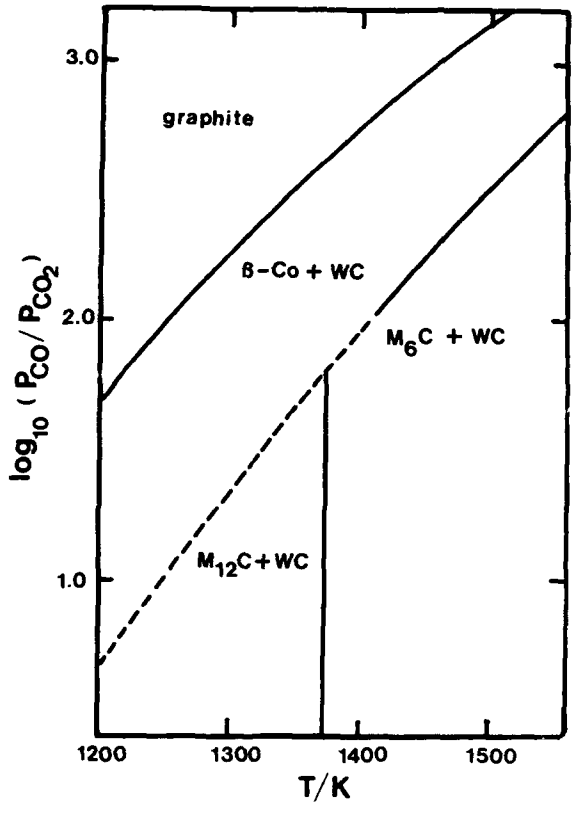

Fig. 6: Stability regions for W-Co-C system as a function of CO/CO_2 ratio and temperature.

The production of WC+β-Co powders from WO_3-$CoWO_4$ mixtures using CH_4-H_2 mixtures in a rotary kiln has been studied by Takatsu (19). Gortsema and Kotval (20) have used by CO-CO_2 and CH_4-H_2 mixtures on a laboratory scale to reduce/carburise WO_3-$CoWO_4$ mixtures and French and Sale (9) have used a combination of thermogravimetry, X-ray diffraction analysis and scanning electron microscopy to follow the sequences of phases and particle morphologies during reduction/carburisation with CH_4/H_2 mixtures.

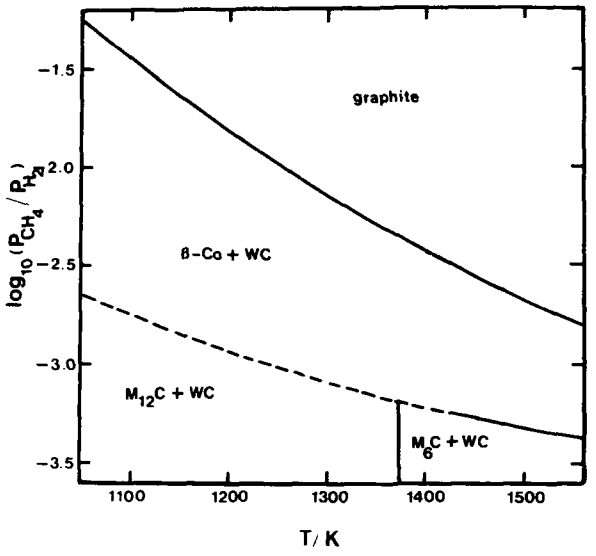

Fig. 7: Stability regions for W-Co-C system as a function of CH_4/H_2 ratio and temperature.

French and Sale (9) showed the process to occur via the formation of the intermetallic compounds Co_7W_6 and Co_3W along with metallic tungsten all of which were subsequently carburised through a sequence of carbides, as shown on Figure 8, to yield the end products of β-Co and WC. Gortsema and Kotval (20) comment that carbon control was found to be more difficult with CH_4-H_2 mixtures rather than CO-CO_2 mixtures, in direct opposition to thermodynamic reasoning. However, it is interesting to note that the ratios used by Gortsema and Kotval (20) fall wihin those predicted for the three-phase β-Co+WC+graphite field whereas the CO/CO_2 ratios used fall within the predicted range for β-Co+WC production. As a result it is to be expected that free carbon would be found in the products from the CH_4/H_2 reduction/carburisation. Gortsema and Kotval (20) observed W_2C in the sequence of phases produced before WC and β-Co were obtained, whereas this phase was not observed by either French and Sale (9) in the reduction/carburisation of $CoWO_4$ alone or by Takatsu (19) in the reduction/carburisation of $CoWO_4$-WO_3 mixtures. French (21) does report the observation of W_2C as a metastable transient phase during the reduction/carburisation of $CoWO_4$-WO_3 mixtures and so the observation of Gortsema and Kotval (20) may simply indicate that insufficient time was available for complete carburisation to occur during the residence period of the solid phases in the reactor used.

Apart from these observations of W_2C in WO_3-rich mixtures all the phases observed by the various workers (9, 19, 20) agree with predictions based on the isothermal section of the W-Co-C system given by Uhrenius and Johansson (13), Figure 5.

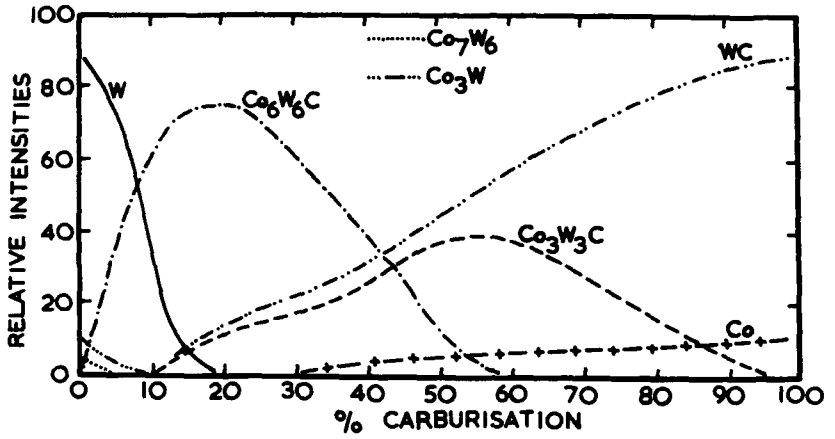

Fig. 8: Relationship between relative intensities of phases detected by XRD and % carburisation of reduced $CoWO_4$, using CH_4/H_2 at 1273 K (after French and Sale [9]).

4. CONCLUDING COMMENTS

Although this paper has dealt exclusively with WC and WC-Co mixtures it is evident that the use of predominance area diagrams and other thermodynamic predictions of phase stabilities can be extremely useful in determining conditions required for the formation of carbide, boride and nitride phases. The methodology demonstrated briefly in this paper is limited in its application to other systems only by the paucity of available data. Even today, in the systems considered in the present paper, difficulties are encountered in obtaining a self-consistent set of data for all the phases of interest (22). Problems still exist in the thermodynamic description of the W–WO_2 equilibrium. Whilst the extensive use of various national and international thermodynamic data banks may make it easier and quicker to carry-out the calculations required for the prediction of phase stabilities, such computer-based calculations can only be performed with confidence when the basic experimental data (or good estimates based on other data) are also known with confidence. Accordingly, the vital role of the experimentalist must

not be forgotten. Unfortunately today, as the materials of interest become more complex, and as the experimental difficulties associated with the determination of relevant thermodynamic data increase, activity in the experimental aspects of the subject have decreased. It is to be hoped that the undoubted value of such data will lead to more funding for experimental determinations of thermochemical data for use in the prediction of phase stabilities. There is little doubt that future advances in the manufacture, understanding and use of a range of high technology ceramics and ceramic-containing composite materials will need information on phase stabilities and the compatibilities of various phases under a variety of service conditions.

5. ACKNOWLEDGEMENTS

The authors would like to acknowledge the SERC for the provision of funding for much of the work described. One of the authors (FRS) would like to thank a number of his past research students all whom have worked in the general subject area of this brief paper. In particular thanks are due to Drs. A.K. Basu, G.J. French, T.D. Halliday, P. Walkden and J.N. Albiston for their efforts in gaining an understanding of the reduction and carburisation of tungsten oxides and metal tungstates.

6. REFERENCES

1. Morris, A.E., (1975), "Application of thermodynamics to metallurgical processes", Proc. 104th AIME Annu. Meet., New York, Amer. Inst. Mech. Engrs., New York, p.8.

2. Worrell, W.L., (1965), Trans. Metall. Soc. AIME, 233, 1173.

3. Basu, A.K. and Sale, F.R., (1977), Trans. Inst. Min. Metall., Sect. C, 86, 134 and 169.

4. Taskinen, P. and Tikkanen, M.H., (1977), Scand. J. Metall., 6, 228.

5. Basu, A.K. and Sale, F.R., (1976), in H.H. Hausner and P.V. Taubenblat (eds.), "Modern developments in powder metallurgy, Proc. Int. Powder Metall. Conf., Chicago, Volume 9, Metall. Powder Industry Federation and American Powder Metall. Inst., N.J., p. 171.

6. Wilken, T.R., Morcom, W.R., Wert, C.A. and Woodhouse, J.B., (1976), ibid, p. 161.

7. Basu, A.K. and Sale, F.R., (1978), Metall. Trans. B., 9, 603.

8. Newkirk, A.E. and Aliferis, (1957), J. Am. Chem. Soc., 79, 4629.

9. French, G.J. and Sale, F.R., (1985), Proc. 2nd Congress on cobalt, metallurgy and uses", Venice, Cobalt Development Inst., London, p. 370.

10. Kim, J.W. and Chang, H.G., (1968), J. Korean Inst. Met., 6, 73.

11. Fornwalt, D.E., Felten, E.J. and Stonehart, P., (1975), Micron, 6, 147.

12. Miyake, M., Hara, A., Sho, T. and Kawakata, Y., (1978), Proc. 5th Eur. Powder Metall. Symp., Stockholm, Jernkontoret, Stockholm, p. 93.

13. Uhrenius, B. and Johansson, T., (1978), Met. Sci., 12, 83.

14. Akesson, L., (1978), Jernkontorets Forskn., D223, 1.

15. Rezukhina, T.N. and Kashina, T.A., (1976), J.Chem. Thermodyn., 8, 513.

16. Halliday, T.D., Hayes, F.H. and Sale, F.R., (1980), in T.I. Barry (ed.), "The industrial use of thermochemical data", Sp. Publ. 34, Chemical Society, London, p. 291.

17. Bracconi, P. and Dufour, L.C., (1976), Metall. Trans. B., 7, 321 and 329.

18. French, G.J. and Sale, F.R., (1985), J. Mater. Sci., 20, 1291.

19. Takatsu, S., (1978), Powder Metall. Int., 10, 13.

20. Gortsema, F.P. and Kotval, P.S., (1976), Planseeber. Pulvermetall., 24, 254.

21. French, G.J., (1983), PhD Thesis, Victoria University of Manchester.

22. Sale, F.R., (1984), J. Less Common Metals, 100, 277.

Si_3N_4 - SiC COMPOSITES

J.L.Baptista
Departament of Ceramics and Glass Engineering
University of Aveiro, 3800 AVEIRO, Portugal

ABSTRACT. Silicon nitride and silicon carbide are excellent materials for high temperature applications. Their combination in composites obtained by dispersing SiC inclusions in a Si_3N_4 matrix should produce superior materials. The availability of SiC whiskers prompted their use as a reinforcing phase in Si_3N_4 composites. Toughening increments were expected due to energy dissipating mechanisms related to the fibrous nature of the whiskers. This paper describes results of work concerning the obtention of homogeneous dispersions of SiC inclusions in Si_3N_4, a necessary condition to obtain uniform green bodies. Results showing the influence of the non sintering inclusions on the densification of the composites will be analyzed and possible solutions for the obtention of dense composites will be discussed. The mechanical properties of the composites obtained will be presented and possible ways of improving the fracture toughness will be discussed in relation to the particle-matrix interfaces developed during the sintering process.

1. INTRODUCTION

Silicon nitride has several properties, namely corrosion resistance and retention of mechanical strength up to high temperatures, which make it an adequate choice for structural applications at temperatures and environments where other materials can not be used. Limitations to its application come from the brittle nature of Si_3N_4 ceramics and therefore its successful use relies on improving its fracture toughness which would then make possible the fabrication of reliable components.

Although great improvements in toughness have been obtained by the production of ceramic matrix composites reinforced with continuous fibers, this has been achieved by very elaborate fabrication procedures, at a considerable cost.

Recently attention has been focused on the use of short fibers or whiskers as a means of reinforcement, which allows the utilization of more conventional ceramic fabrication processes. High strength single crystal SiC whiskers were an obvious choice to try to improve the mechanical characteristics of Si_3N_4, in order to obtain a suitable

R. Freer (ed.), The Physics and Chemistry of Carbides; Nitrides and Borides, 447–456.
© 1990 *Kluwer Academic Publishers. Printed in the Netherlands.*

material for medium and high temperature applications. Whiskers of SiC are already available from several producers with market costs decreasing steadily. Recently SiC platelets have also been available in the market. Although adequate handling of this type of materials, namely the SiC whiskers, is necessary because of safety reasons, it seems that Si_3N_4 ceramic composites reinforced with SiC whiskers or platelets could became good candidates for the applications envisaged. Al_2O_3 reinforced with SiC whiskers is already available commercially for industrial applications in high speed cutting tools.

The problems associated with the obtention of such composites, the solutions tried and the results obtained will be outlined in this work.

2. Si_3N_4 - SiC Whiskers Composite Fabrication

2.1. Processing of the Green Body

The first problem to be overcome in processing a Si_3N_4-SiC whisker composite is obtaining a homogeneous green microstructure. The difficulty in mixing homogeneously batches of particles with two different sizes is enhanced due to the tendency of the whiskers to agglomerate together, which could lead to inhomogeneous density in the green state. pH control has been used to achieve good dispersion and subsequent homogeneous packing of Si_3N_4 powders with SiC whiskers [1,2, 3].

Particles in aqueous suspensions develop surface charges. These charges can be detected and the values of electrophoretic mobility or the zeta potential as a function of pH can be used to determine the best dispersing conditions. Good deflocculation conditions are usually obtained for zeta potential values of 50-60 mV. Figure 1 shows such graphs for Si_3N_4 particles and SiC whiskers. Different values have been reported for the isoelectric point (iep) of different kinds of SiC whiskers [4], and attributed to different oxygen content at the whiskers surface. X-ray photoelectron spectra (XPS) shows that high contents of surface oxygen are associated with strong Si-O bond signals and low surface oxygen contents with high SiC and C-C bond signals [5].

High pH values (9-10) are usually used to obtain good dispersing conditions due to high values of the zeta potentials both of Si_3N_4 and SiC. A different approach was simultaneously presented by two research groups to achieve homogeneous green packing of Si_3N_4 powders with SiC whiskers [1,2]. This approach relied on obtaining uniform dispersion mixing by using low pH values (~4), where opposite charges were present at the surface of each kind of particle. Good uniform dispersions were obtained, although a slightly higher green density was achieved by consolidating the dispersions obtained at higher pH as can be seen in Table 1 [1]. Organic molecules in solution can also act as good dispersants leading also to good packing characteristics of the green body. This was achieved using triethanolamine as shown also in Table 1. Up to 65-66% green density has also been obtained by slip casting of similar mixtures with a commercial polyacrilate dispersant although non uniformity of the casts was reported [6]. Slip casting or pressure

TABLE 1: Variation of relative green density with the type of suspension media, for samples of Si_3N_4-SiC whisker composites. [1]

Dispersion Conditions	%Rel. Density
pH 4	58
pH 11	61
Triethanolamine	62

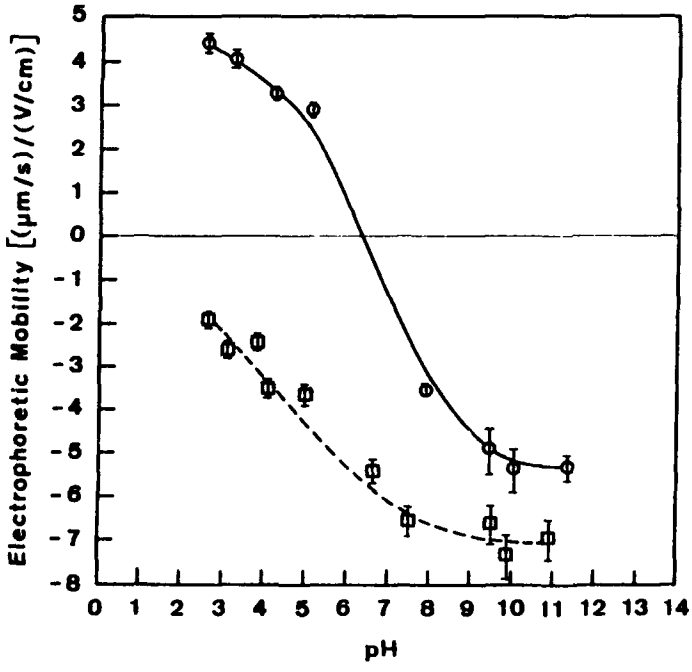

Figure 1. Electrophoretic mobility of Si_3N_4 particles and SiC whiskers. ○= Si_3N_4; □= W-SiC. [1]

casting are important techniques for forming green bodies of these materials, since they allow complicated shapes to be obtained.

2.2. Sintering.

Hot pressing has been the most used method to sinter Si_3N_4-SiC whiskers composites [7,8,9]. Although this method of densification limits the production to simple shapes it is a way of obtaining dense composites with a limited amount of sintering aids. The sintering difficulties associated with the covalent character of Si_3N_4, usually overcome by the use of oxide sintering aids like Al_2O_3, Y_2O_3, SiO_2, MgO, Li_2O and rare earth oxides, are enhanced in Si_3N_4-SiC whiskers composites due to the presence of the whiskers. The densification of the ceramic matrix is prevented by the presence of the hard, non sinterable crystals of the second phase. Sintering rates are considerably decreased due to the development of tensile stresses at the matrix-whisker interface and shear stresses in the matrix itself. The decrease in densification rate caused by increasing amounts of SiC whiskers in the mixture is clearly seen in Figure 2 with values calculated from the work of S. Buljan et al. [7]. Although in this case the substitution of SiC whiskers by the premixed Si_3N_4+additives (7.5 wt.% Y_2O_3+Al_2O_3), would result in a decrease in sintering aids content, the overall effect is the one expected and generally observed.

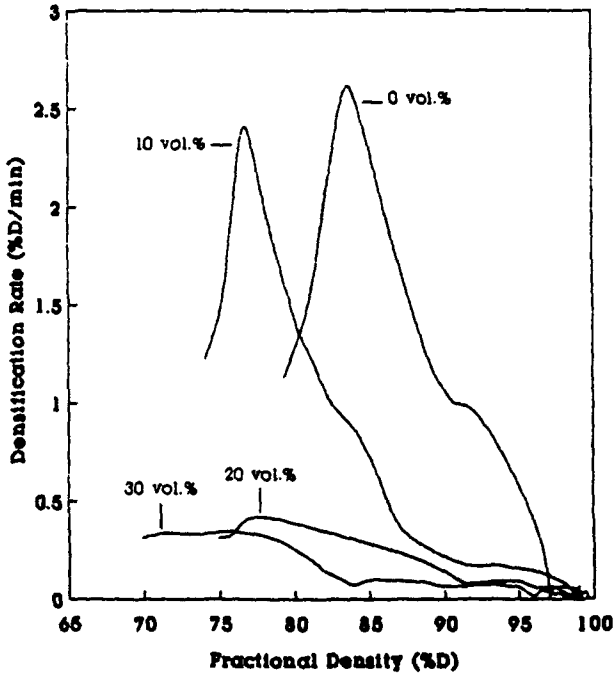

Figure 2. Densification rate decrease caused by whisker addition [7].

Pressureless sintering has not the shape limitations of hot pressing and can therefore be used to obtain complicated shapes, but requires a higher amount of additives to achieve complete densification. The high content of glassy phase present after pressureless sintering is detrimental to the high temperature performance of the sintered composites. Possible solutions to solve this problem, which have also been tried to Si_3N_4 itself, require either the solid solution of some of the components of a transient liquid phase in the silicon nitride matrix of the composite, or the recrystallization of the residual glass to more refractory phases, by an annealing process after sintering. Heterogeneous shrinkage due to the presence of the whiskers is also present, decreasing the densification rate for increasing contents of the whiskers, as well as the maximum density attained for the same sintering conditions with fixed amount of the liquid phase.

High sintering temperatures are usually necessary for pressureless sintering. A low viscosity liquid phase present during sintering will increase the creep of the matrix around the whiskers allowing densification at lower temperatures. The use of several additive compositions chosen in the system Li_2O-Al_2O_3-SiO_2 (LAS) has shown that high sintering densities could be obtained for Si_3N_4 at moderate temperatures [10]. The results of Figure 3 show that pressureless sintering at moderate temperature (1550°C) of a Si_3N_4-SiC whiskers composite containing 16 vol.% of whiskers required a high content of glass forming additives.

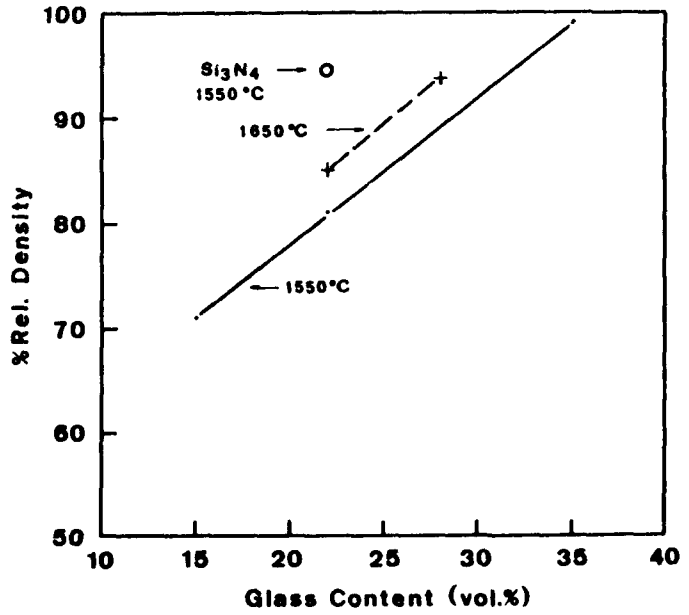

Figure 3. Relative sintered density versus LAS glass content, for samples sintered for 1 hour at 1550 and 1650°C. [1]

To avoid the development of stresses due to the presence of non sinterable second phases a different approach was tried by H. Jong et al. [11]. They tried to create a free space around the non sinterable particle where the sintering matrix could shrink into. The free space was obtained by burning a polymeric coat, previously adsorbed at the surface of the SiC particles. Densification rates and final shrinkages were found to be approximately proportional to the amount of polymer adsorbed. The workability of this concept was not tried for Si_3N_4-SiC whiskers composites but it is worthwhile keeping it in mind, for future use, either alone (by itself) or in conjunction with other approaches.

3. Mechanical Properties.

Reinforcement of Si_3N_4 with SiC whiskers aims at obtaining tough and strong materials. Although increases in toughness and flexural strength have been reported they are, however, smaller than those obtained with similar reinforcement in other matrices [5]. Also, the results reported for similar types of composites show some undesirable variations, as can be seen in Table 2. An increase in flexural strength concomitant with increased toughness has been found [7], but a decrease in flexural strength has also been reported [8] and even a decrease in toughness, with increasing amounts of whiskers [12].

Several reasons can be at the origin of this diversity of experimental results, the most probable being difficulties arising from the fabrication procedure. Processing flaws, caused by the addition of the whiskers, will act as crack initiators, reducing the overall strength of the composite. Such flaws were indeed observed in some cases [12]. Another possible and concomitant reason could come from the use, by the different research groups, of whiskers furnished by various suppliers and therefore with different quality.

The most probable mechanisms by which the toughness of a composite containing whiskers can be increased are whisker pullout and bridging, due to its fibrous nature, or crack deflection as for any other second phase particles. In long fiber-reinforced composites the first two mechanisms are considered to be responsible for the great increase in toughness experimentally observed, with particular relevance for fiber pullout. Although there have been indications of some whiskers protruding from the fracture surfaces of Si_3N_4-SiC composites and of craters, previously occupied by whiskers [7], it is doubtful that whisker pullout has been an important toughening mechanism in the increases in toughness reported to date. There is also no experimental evidence for crack bridging in Si_3N_4-SiC whiskers systems. On the other hand, for hot pressed Si_3N_4-SiC whiskers composites a toughening mechanism based on crack deflection has been used to fit experimental results with the predictions of a theoretical model, which takes into account the alignment of the whiskers into planes parallel to the hot pressing direction [13].

Although the experimental evidence, points to crack deflection as the main process of interaction between the whiskers and the progressing crack in Si_3N_4-SiC whiskers composites, it is considered that conditions

promoting the appearance of the other two mechanisms would lead to composites with high toughening increments. Indeed, Si_3N_4 sintered ceramics, which show intergranular fracture, have usually a high proportion of ß Si_3N_4 interlocked elongated grains and therefore intergranular crack deflection is already present in them. Any increments in toughness, due to this type of mechanism of interaction of the crack front with the whiskers, would be less marked than for matrices with equiaxed grains. Besides, crack bridging has been reported for other composites containing SiC whiskers, like Al_2O_3-SiC whiskers [5], which showed higher toughness values (up to ~9 $MPa.m^{1/2}$).

In contrast with the oxide matrix composites, covalent ceramics like Si_3N_4 require the presence of a liquid oxide phase to sinter. Densification is achieved by a solution-diffusion-precipitation mechanism of the Si_3N_4 grains. Very likely some reaction will also take place between the liquid phase and the whiskers surface. The nature of the interface between the matrix and the whiskers resulting from this reaction will certainly determine which toughening mechanism is operative. It would seem that, up to now, a too strong bond has been formed, making whisker pullout or bridging not possible (Figure 4).

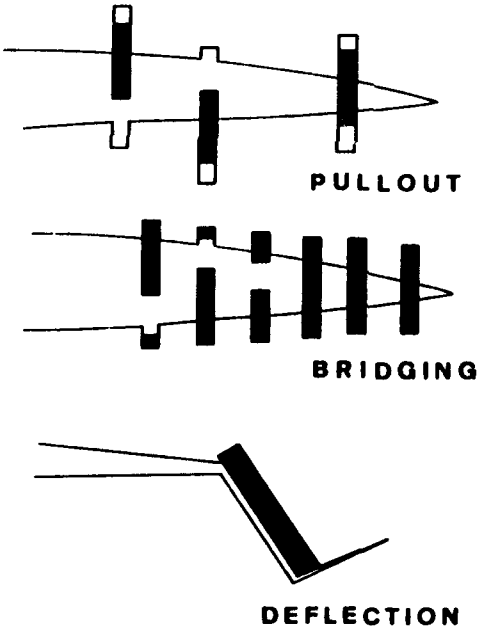

Figure 4. Toughening mechanisms present in whisker reinforced ceramic composites.

TABLE 2. Some results obtained for Si_3N_4-SiC whisker composites.

Ref.	Si_3N_4	whiskers	Composition (wt.%)	Sintering Conditions	whiskers vol.%	σ (MPa)	K_{Ic} (MPa.$m^{1/2}$)
1	SN 502 GTE	Silar SC-9 Arco Chem.	92.5 Si_3N_4 6 Y_2O_3 1.5 Al_2O_3	Hot Press ~1800°C	0	770	4.7
					10	720	4.4
					20	710	4.8
					30	980	6.4
2	LC-12 H.C.Starck	Tokawhisker Tokai Co.	89 Si_3N_4 8 Y_2O_3 3 Al_2O_3	Hot Press 1750°C/1h vaccum 30 MPa	0	895	4.8
					20	735	4.9
					30	621	5.3
3	LC-12 H.C.Starck	VLS Los Alamos Nat.Lab.	95 Si_3N_4 5 MgO	Hot Press 1700°C	0	660	7.2
					10	540	9.7
					20	530	10
					30	450	10.5
4	LC-12 H.C.Starck	Tokawhisker Tokai Co.	37 Si_3N_4 6 Y_2O_3 2 Al_2O_3 55 Si	Nitridation + HIP 1700°C 200 MPa	0	900	6
					10	620	5.5
					20	580	5

References: (1) Segej Buljan et al., Am.Ceram.Soc.Bull., 66, 2, 1987, 347-52.
(2) A.Bellosi and G de Portu, Mater.Sci.Eng., A109, 1989, 357-62.
(3) Peter D. Shalek et al., Am.Ceram.Soc.Bull., 65, 2, 1986, 351-56.
(4) Robert Lundberg et al., Am.Ceram.Soc.Bull., 66, 2, 1987, 330-33.

Either modifications of the glass composition or/and of the physical and chemical nature of the whiskers surface (roughness, impurity content) will be necessary to modify the character of the interface. Whiskers covered by films of different chemical nature (C, BN, etc.) are already being developed but it is not known yet how effective they will be in contributing to solve the remaining problems concerning the fabrication of tougher and stronger Si_3N_4-SiC whiskers composites.

REFERENCES.

1. Almeida, J.C., Sacramento, J.M., Correia, R.N., Fonseca, A.T., and Baptista, J.L. (1989) "Dispersion and Packing of mixtures of Si_3N_4 powders with SiC whiskers", presented at Fabrication Technology, The Institute of Ceramics, Swansea, to be published in the conference proceedings.

2. Crimp, M.J. and Preston, R.F. (1989) "Evaluation of Sedimentation as a technique for the separation of sub-micron diameter silicon carbide whiskers", ibid Ref. 1.

3. Hoffmann, M.J., Greil, P., and Petzow, G. (1988) "Pressureless sintering of SiC-whisker reinforced Si_3N_4", in Science of Ceramics 14, D. Taylor (ed.), The Institute of Ceramics, Stoke-on-Trent, pp. 151-156.

4. Adair, J.H., Mutsuddy, B.C., and Drauglis, E.J. (1988) "Stabilization of silicon carbide whisker suspensions: I, the influence of surface oxidation in aqueous suspensions", Adv. Ceram. Mater., 3, 231-234.

5. Becher, P.F., Hsuem, C., Angelini, P., and Tiegs, T.N. (1988) "Toughening behaviour in whisker-reinforced ceramic matrix composites", J. Am. Ceram. Soc., 71, 1050-1061.

6. Hoffmann, M.J., Nagel, A., Greil, P., and Petzow, G. (1989) "Slip casting of SiC-whisker-reinforced Si_3N_4", J. Am. Ceram. Soc., 72, 765-769.

7. Buljan, S.T., Baldoni, J.G., and Huckabee, M.L. (1987) "Si_3N_4-SiC composites", Am. Ceram. Soc. Bull., 66, 347-352.

8. Bellosi, A. and De Portu, G. (1989) "Hot pressed Si_3N_4-SiC whisker composites", Mater. Sci. Eng., A109, 357-362.

9. Shalek, P.D., Petrovic, J.J., Hurley, G.F., and Gac, F.D. (1986) "Hot-pressed SiC whisker/Si_3N_4 matrix composites", Am. Ceram. Soc. Bull., 65, 351-356.

10. Sacramento, J.M., Correia, R.N., Fonseca, A.T., and Baptista, J.L. (1989) "Sintering of silicon nitride with lithium-aluminium silicates", presented in The 1st European Ceramic Society Conference, Maastricht, to be published in the conference proceedings.

11. Jang, H.M., Rhine, W.E., and Bowen, H.K. (1989) "Densification of alumina-silicon carbide powder composited: I, effects of a polymer coating on silicon carbide particles", J. Am. Ceram. Soc., 72, 948-953.

12. Lundberg, R., Kahlman, L., Pompe, R., Carlsson, R., and Warren, R. (1987) "SiC-whisker-reinforced Si_3N_4 composites", Am. Ceram. Soc. Bull., 66, 330-333.

13. Liu, H., Weisskopf, K., and Petzow, G. (1989) "Crack deflection process for hot-pressed whisker-reinforced ceramic composites", J. Am. Ceram. Soc., 72, 559-563.

BORIDE-CARBIDE COMPOSITES : TiB_2-TiC-SiC.

F.de MESTRAL and F. THEVENOT
Ecole Nationale Supérieure des Mines de Saint-Etienne
158 cours Fauriel, 42023 St. Etienne cedex
France

ABSTRACT. In the ternary system TiB_2-TiC-SiC, the different two-phase composites, TiC-TiB_2, SiC-TiB_2 and SiC-TiC exhibit remarkable mechanical properties in regard with the single phase ceramics. The evolution of those mechanical properties, i.e. modulus of rupture σ_f, fracture toughness K_{1c}, hardness Hv and electrical resistivity ρ, over the complete ternary diagram was investigated.

A methodology of research using optimal design was used to minimize the number of composites to be elaborated. In this study, 16 samples were sufficient to empirically determine a provisional mathematical model for each property. A model, then, enables the plot of isoresponse curves in the ternary diagram. The samples were hot pressed and the optimal hot-pressing cycles were determined using densification rates versus temperature curves. The concordence between computed and experimental values is excellent, e.g. a sample containing 20 mol % of TiB_2, 55 mol % of TiC and 25 mol % of SiC has $\sigma_{f\ exp}$ = 1080 MPa, $\sigma_{f\ comp}$ = 1070 MPa ; $K_{1c\ exp}$ = 6.7 MPa $m^{1/2}$, $K_{1c\ comp}$ = 6 MPa $m^{1/2}$; Hv_{exp} = 16.6 GPa , Hv_{comp} = 17.3 GPa ; and ρ_{exp} =57.4 $\mu\Omega$ cm , ρ_{comp} = 55 $\mu\Omega$ cm

Although titanium diboride does not react with silicon carbide, a strong interface bond is developed between titanium diboride and titanium carbide, and between titanium carbide and silicon carbide. This explains the bend strength evolution in the ternary system, and more particularly the fact that, in the area $\sigma_f > 1000$ MPa and $K_{1c} > 6$ MPa $m^{1/2}$, to high SiC contents correspond low TiB_2 contents and conversely. The relevant microstructures will be discussed.

R. Freer (ed.), The Physics and Chemistry of Carbides; Nitrides and Borides, 457–481.
© 1990 *Kluwer Academic Publishers. Printed in the Netherlands.*

1. Introduction

Carbide and boride ceramics have intrinsic characteristics, i.e. high melting point, high hardness, good chemical inertness, high wear resistance, good strength, that make them suitable candidates for thermomechanical applications. However, the use of those single phase ceramics, even fully densified, in structural or wear applications is limited by the variability of their mechanical strength and their poor fracture toughness. The scatter of the strength measurements is usually attributed to microstructural defects such as pores, inclusions, exaggerated grain growth or nonuniform sintering. The number of those defects, and hence their influence, could be seriously reduced by a careful mastery of each step of the elaboration process.

Second phase additions can improve the strength and the fracture toughness of single phase ceramics. This second phase can act as a particle phase transforming toughening, e.g. zirconia toughened alumina, or as an intergranular binder, either glassy, e.g. SIALONs, or metallic, e.g. WC-Co. Although these methods are quite efficient at room temperature, the toughening mechanisms do not hold with increasing temperatures. This is due either to inappropriate phase transformation, or to binder softening or recrystallization. However, the use of a second phase that is both thermodynamically and chemically stable with the host matrix will allow the retention of the matrix-second phase intrinsic properties, even at elevated temperatures. Depending on the physical characteristics and the shape of the second discrete phase, i.e. fibres, whiskers or particles, the toughening mechanisms can be fibres pullout or shearing, crack tip deflection or pinning, and/or crack tip stress redistribution.

The good electrical conductivity of titanium diboride as well as its chemical inertness at high temperatures make it a good candidate for special electrical applications [1], e.g. cathodes used in aluminium electrosmelting or vaporizing elements for vacuum metal deposition installations. However these applications are mainly limited by TiB_2 poor fracture toughness and its sensitivity to slow subcritical crack growth. Titanium carbide was found to be an efficient toughening second phase [1,2].

High density silicon carbide is an extremely hard and wear resistant material which has, furthermore, excellent corrosion, thermal shock and oxidation resistance. All these properties together with its good high temperature strength allow the use of SiC for numerous structural and wear applications, e.g. heat exchanger, metal working parts, nozzles... However, once more, SiC moderate fracture toughness limits its use under severe conditions. Additions of TiB_2 [3,4] or TiC [5] particles were found to be effective in terms of increasing fracture toughness. Titanium carbide has a further advantage since it possess five independent slip systems which allow the material to be ductile above $\approx$ 800°C [6]. Such plasticity may result in a stress redistribution at the crack tip and, hence, toughens the composite at high temperatures.

Composites based on the three ceramics, TiB_2-TiC-SiC, could be tailored with very different characteristics, depending on which phase is the major constituent. A predominance of SiC would lead to a composite for structural and corrosion applications, and a composite based on TiC or TiB_2 could be used for electrical applications. The knowledge of the composites properties for every composition over the complete ternary diagram would be paramount for the selection of an optimized composite for a determined application. The present paper discusses the methodology of research used to elaborate the isoresponse plots for the flexural strength σ_f, the fracture toughness K_{1c}, hardness Hv and the electrical resistivity ρ, as well as the microstructural properties of the TiB_2-TiC-SiC composites.

2. Methodology of Research

It has been shown that the different two-phase composites TiB_2-TiC, SiC-TiB_2, SiC-TiC, exhibit much better mechanical properties than the single phase ceramic, TiB_2, TiC and SiC [1,3,5]. Would the addition of the third phase in the composites further improve those mechanical characteristics ? One classical way of answering this question could be to take a well-known two-phase ceramic, e.g. SiC-TiB_2, and study the effect of the substitution of some TiB_2 by TiC. Although this technique may lead to good results, it does not allow to find the optimum composition of the ternary system. This last point would require the knowledge of a property value for an infinite number of compositions, which is obviously non-applicable. Even if the study is limited to

compositions taken every 10 or 5 percents, it would require the manufacture of 66 and, respectively, 231 samples, which is still prohibitive. A methodology of research using a statistical approach is hence necessary.

R. Phan-Tan-Luu developed a methodology of research using optimal design [7,8] and applied it to the problems of mixtures [9]. The aim of the methodology consists in describing, predicting or explaining the studied phenomenon, i.e. finding the relations between the factors (in this study, the composition of the composites] and the responses (here,the mechanical properties). This can usually be done by modeling the phenomenon. Mathematical models of any sorts can be used depending on the type of the problem : linear, non-linear, exponential, differential,... Polynoms are often used since they allow a sequential application. In a three phase system, three points are sufficient to develop a linear model; adding three other points and a second order polynom can be calculated; with one more point a reduced cubic model can be generated and so on, until the model fits the experimental data. Therefore, it is possible, with a very limited number of points, e.g. 13 pts, 10 for the coefficients of a cubic model and 3 as test points, to develop a mathematical model giving a good estimation of a mechanical property for every composition of the ternary diagram. A mathematical model is purely empirical and, hence, the explanation of why such behaviour occurs cannot be drawn from the model's coefficients, but must be generated from what is known about the system.

A complete third order polynom contains 20 coefficients which can be reduced to 10 since, in mixtures problems, the constraint: sum of every constituent is always equal to 1 ($\Sigma X_i = 1$), allows the simplification of numerous terms (equation 1).

$$\begin{aligned} Y = {} & b_1 X_1 + b_2 X_2 + b_3 X_3 \\ & + b_{12} X_1X_2 + b_{13} X_1X_3 + b_{23} X_2X_3 \\ & + g_{12} X_1X_2 (X_1-X_2) + g_{13} X_1X_3 (X_1-X_3) + g_{23} X_2X_3 (X_2-X_3) \\ & + b_{123} X_1X_2X_3 \end{aligned} \qquad (1)$$

where Y is the mechanical property studied, e.g. modulus of rupture, or fracture toughness; X_1 the molar fraction of TiB_2, X_2 the molar fraction of TiC, X_3 the molar fraction of SiC, and b_{ijk}, g_{ij} the coefficients of the model.

If the number of experiments taken into account is equal to the number of coefficients, these can be estimated by :

$$b_i = Y_i$$
$$b_{ij} = 9/4\,[Y_{iij} + Y_{ijj} - (Y_i + Y_j)]$$
$$g_{ij} = 9/4\,[3\,Y_{iij} - 3\,Y_{ijj} - (Y_i - Y_j)]$$
$$b_{123} = 27\,Y_{123} - 27/4\,(Y_{112} + Y_{122} + Y_{113} + Y_{133} + Y_{223} + Y_{233}) + 9/2\,(Y_1 + Y_2 + Y_3)$$

where Y_i is the value measured for 100 % of i, Y_{ij} is the value measured for a sample containing 50 molar percent of i and 50 molar percent of j, Y_{iij} is the value measured for a sample containing 67 molar percent of i and 33 molar percent of j,and Y_{123} is the value measured for a sample composed by 33.3 molar percent of each phase i,j,k.

TABLE 1: Points necessary to develop polynomial models up to the third order. A star * represents the points that are at least necessary for the particular degree. The test points can indefferently be used for the coefficients calculation or as test points.

	TiB2	TiC	SiC	Order of the Polynomial Model			
	molar %			1 rst	2 nd	red. cub.	3 rd
1	100	0	0	*	*	*	*
2	0	100	0	*	*	*	*
3	0	0	100	*	*	*	*
4	50	50	0	Test	*	*	Test
5	50	0	50	Test	*	*	Test
6	0	50	50	Test	*	*	Test
7	33	33	33	Test	Test	*	*
8	67	33	0	Test	Test	Test	*
9	33	67	0	Test	Test	Test	*
10	67	0	33	Test	Test	Test	*
11	33	0	67	Test	Test	Test	*
12	0	67	33	Test	Test	Test	*
13	0	33	67	Test	Test	Test	*
14	67	16,5	16,5	Test	Test	Test	Test
15	16,5	67	16,5	Test	Test	Test	Test
16	16,5	16,5	67	Test	Test	Test	Test

These simple rules to calculate the model's coefficients force the polynom exactly through the experimental data, and hence will exaggerate the significance of a possible drift of an experimental point by concentrating it on a single coefficient. This drawback can be of real

importance with ceramics characterization, since their mechanical properties are usually only accurate to 10%. It is therefore desirable to make the coefficients' calculation with more data than theoretically necessary so that an eventual inaccuracy on a experimental measurement will be distributed on several coefficients. But in this case, the use of an appropriate software (e.g. NEMROD [10]) is necessary to make the polynom fitting using the least square method.

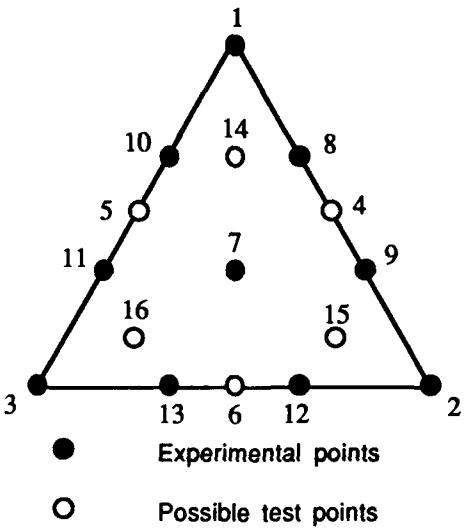

Figure 1: Position of the points at least necessary to develop polynomial model up to the third order.

In this study, polynomial models up to the third degree were developed. Table 1 lists the compositions necessary to develop such a model. The positions of those points are shown in Figure 1. The time required to optimize the complete processing route of every composite was estimated to be prohibitive. Therefore, the arbitrary choice was made, first to determine the best composition on non-optimized samples and, only then to optimize its whole elaboration process. However, the validity of a composite for its use in the model's calculation still has to be assessed. Two criteria are used: density and microstructure. The density has to be higher than 98% of theoretical density (computed using the mixture rule) and a visual check has to make sure the microstructure is fine and homogeneous.

3. Experimental Procedures

The starting powders were : Titanium Diboride, grade A from Starck (Berlin), mean particle size $\approx$ 4 μm; Titanium Carbide ceramic grade C.A.S. from Starck, mean particle size $\approx$ 3 μm and a Silicon Carbide from ESK (Germany) mean particle size $\approx$ 1 μm. The powders were

desagglomerated in ethanol with an ultrasonic desintegrator, and then mixed for three days in a small ballmill. The mixture was vacuum dried and sieved at 200 μm. The powders were then hot-pressed in graphite dies under 40 MPa in argon atmosphere in tablets with 20 mm in diameter and 15 mm in height. The resulting ceramic cylinders were cut in four bars of dimensions 3x4x18 mm^3. One face of these bars was carefully polished down to 3 μm with diamond paste and its edges were beveled. The flexural strength was measured under 3 point bending (15 mm outer span), the fracture toughness was determined using the Vickers indentation technique (measurements made at l'Ecole Nationale Supérieure des Mines de Paris) and the electrical resistivity was measured with the four linear points method.

3. 1. HOT-PRESSING TECHNIQUE

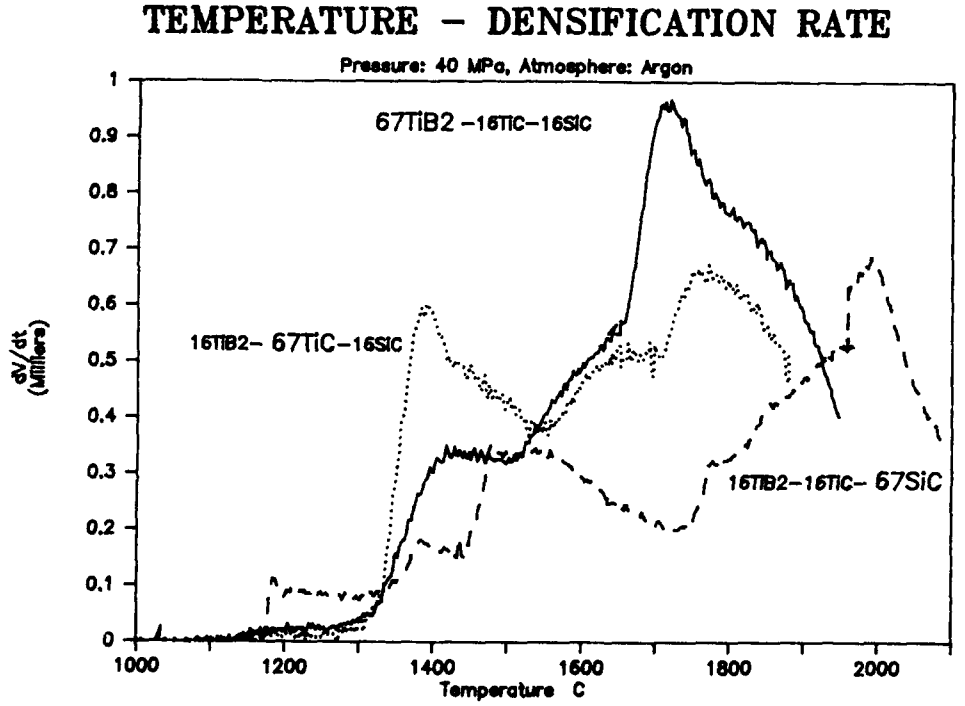

Figure 2 : Densification rate versus temperature curves for three different composites.

The material used is a laboratory press, type VS Pgr 7/10 from Degussa [11,12]. The temperature limit of the graphite resistor is 2500°C. A double-action pneumatic jack can develop forces up to 20 KN. Since the inner diameter of the die is 20 mm, a pressure of 60 MPa can be reached. It is, however, limited to 40 MPa due to the graphite resistance. The working atmosphere is either vacuum or inert gas.

The special feature about this press is that, both, the measure and the control of the temperature, pressure and displacement are completely computerized. This allows a very close control of the phenomenon occurring during sintering. The selected mixtures were hot-pressed a first time and the related densification rate versus

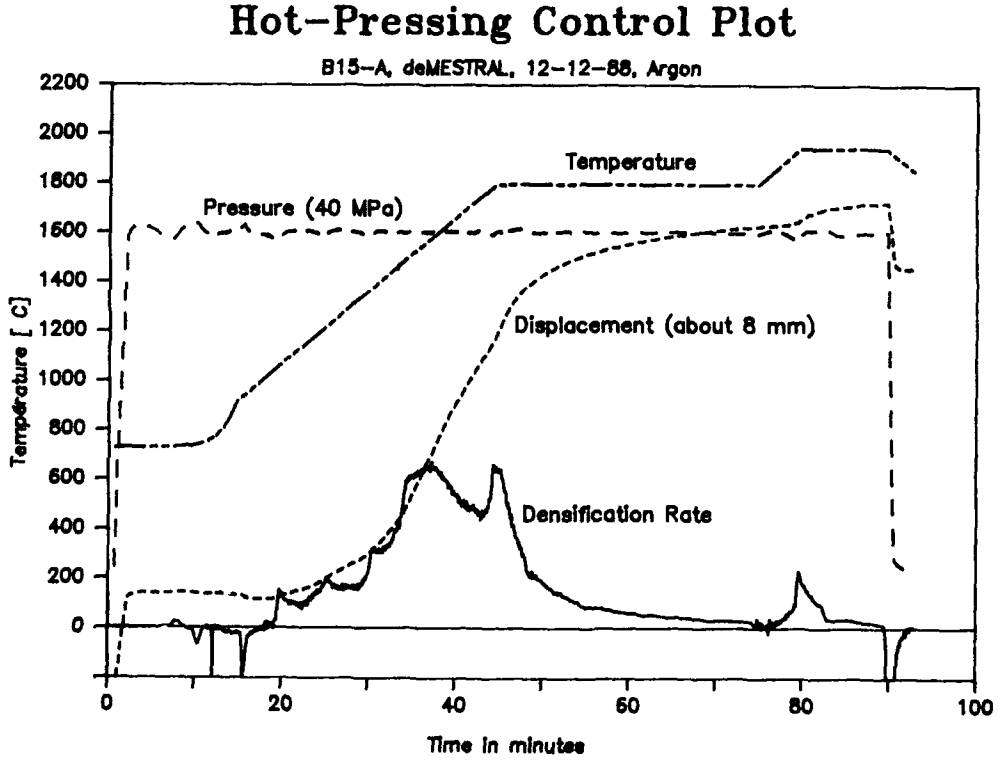

Figure 3: Typical hot-press control plot showing the temprature, the plungers displacement, the pressure and the densification rate as a function of time .

temperature curves were plotted (Fig. 2). The overall dilatation of the system press plus carbon die and plungers was found to be linear from 800°C to 2100°C. Therefore, it is possible to neglect it since it will only influence the height of the densification rate peak but will not cause any shifting of its actual position.

From these plots, the optimum hot-pressing cycles were determined. A 1/2 hr stage at the temperature of maximum densification rate was found to result in samples having approximately 95% theoretical density. A second stage about 150°C above is necessary to achieve full densification. A typical hot-pressing cycle plot is given for a composite with 33.3 molar percent of each phase (Fig. 3). It consists in a first stage at 1800°C for 30 min. and a second one at 1950°C for 10 min; the heating and cooling rates are of 30°C/min; the applied pressure was 40 MPa. The advantage of such a cycle is that most of the densification occurs at a rather low temperature and that the higher temperature stage is short. Therefore, there is no time for grain growth to occur, and the resulting microstructure is fine and homogeneous (Fig. 4).

Figure 4: Microstructure of composite N° 7, i.e. 33.3 mol. % of each phase TiB_2 (grey),TiC (white) and SiC (black), etched with Murakami.

4. Results and Discussion

4.1. INTERACTIONS IN THE SYSTEM

Dense cylinders of TiB_2, TiC and SiC, polished down to 6 μm, were hold together at 2100°C for 2 hrs under 40 MPa. The first evidence is that no reaction at all occurred between TiB_2 and SiC since the two tablets fall apart once pushed out of the die. This is consistent with the observations of Mc Murtry et al., [3]. However, the two other diffusion couples were found to be firmly bonded. Figure 5 shows the TiB_2-TiC interface. TiC diffused in TiB_2 on an average distance of 50 μm. Ordon'yan [13] found a very small solubility of TiB_2 in TiC at temperatures equal or higher than 2100°C. Since both materials exhibit a very similar coefficient of thermal expansion (CTE) ($\approx 8\ 10^{-6}\ K^{-1}$), no interface stresses are generated during cooling. It is therefore possible to assume a very strong cohesion between TiB_2 and TiC particles.

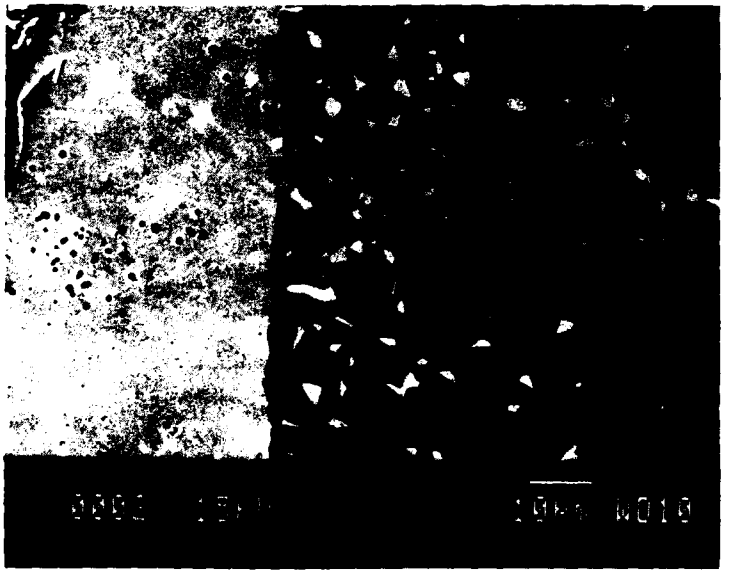

Figure 5: TiB_2 (black) - TiC (white) interface. TiC diffuses on about 50 μm

The interface between TiC and SiC (Fig. 6) exhibits a marked degradation of the TiC region. This is due to the large CTE mismatch, i.e. 8 10^{-6} K^{-1} for TiC and 4,8 10^{-6} K^{-1} for SiC. However, this degradation proves that both materials develop very strong bonds even at 2100°C. Wei and Becher [5] also concluded to strong TiC-SiC bonds since they found no evidence of interfacial debonding in their composite, and Jiang [14] proved it with a TEM study of a TiC-SiC composite. TiC diffused in SiC on an average distance of 20 μm. This diffusion seems to be favoured by the presence of Fe and Co (Fig.6).

Figure 6: SiC (black) - TiC (white) interface. TiC diffuses on about 20 μm.

4.2. BEND STRENGTH

The bend strength of eigthteen different composites are listed in Table 2. The flexural strength of pure TiC and pure SiC are rather low in regard of the values obtained for the other composites, i.e. 550 ± 10% MPa and 500 MPa respectively. Of the three 50-50% composites, it is normal for

the TiB_2-SiC combination to exhibit the lower flexural strength (630 ± 7% MPa) since there is no or little interaction between SiC and TiB_2 particles. The other two-phase composites, TiC-TiB_2 and TiC-SiC, have satisfactory modulus of rupture, i.e. 950 ± 10% MPa and 910 ± 8% respectively. This is consistent with the interaction observations since TiC was found to develop strong bonds with both TiB_2 and SiC. It is interesting to notice that the higher flexural strengths (σ_f > 1000 MPa) are located in an area located "far away" from the TiB_2-SiC axis. The maximum SiC content of these compositions, i.e. point 8,9,12,15 and 17, never gets over 33 mol. %. The average standard deviation is around 10%, and since we are dealing with strength up to nearly 1100 MPa, the precision of the mathematical model cannot be better than ± 100 MPa.

TABLE 2: Values of the experimental bend strength and their difference with the theoretical values computed with different models of degree 1,2,reduced cubic and 3.

	TiB2	TiC	SiC	Experimental Strength	Difference with the Polynomial Models			
	molar %			[MPa]	1 rst	2 nd	red. cub.	3 rd
1	100	0	0	890 ± 24	84	23	20	13
2	0	100	0	550 ± 54	**388**	63	60	9
3	0	0	100	500	**122**	-46	-49	10
4	50	50	0	950 ± 98	6	84	88	90
5	50	0	50	628 ± 43	**170**	**110**	**113**	**111**
6	0	50	50	907 ± 70	**-127**	45	48	48
7	33	33	33	970 ± 77	**-126**	20	0	0
8	67	33	0	1030 ± 140	-67	24	27	51
9	33	67	0	1083 ± 164	**-133**	**-129**	**-126**	-51
10	67	0	33	973 ± 75	**-117**	**-165**	**-162**	-63
11	33	0	67	624 ± 15	**115**	31	34	-63
12	0	67	33	1040 ± 75	**-208**	**-109**	**-105**	-27
13	0	33	67	831 ± 130	**-104**	48	51	-27
					Test points			
14	67	16,5	16,5	980 ± 107	-70	-3	-12	5
15	16,5	67	16,5	1074 ± 24	**-183**	**-127**	**-136**	-17
16	16,5	16,5	67	716 ± 48	**135**	79	69	-67
17	32	55	13	1073 ± 131	**-165**	-65	77	13
18	20	55	25	1075±106	**-209**	-82	-96	-11

Therefore the validity criterion for a model is that both the polynomial fitting and the test points fall within 100 MPa of the experimental data.

The mathematical model developed for the description of a property being purely empirical, it has to remain as simple as possible. To illustrate this point, the difference between the theoretical values, computed with linear, quadratic, reduced cubic and cubic polynoms, and the experimental data are reported in Table 2. The four models are determined using points 1 to 13. Since there are more points than theoretically necessary, a polynomial fitting is made which explains the discrepancy between the experimental measurements and calculated values. Points 14 to 18 are test points only used to assess the validity of the models The first degree model is of really poor quality since both the polynomial fitting and the test points exhibit differences Δ with the measured values much higher than 100 MPa (13 Δ > 100 MPa and Δ max. = 388 MPa). The quadratic and the reduced cubic models are already more accurate since the regression generates four values with Δ > 100 MPa (Δ max. = 165 MPa) and only one test point has a difference higher than 100 MPa. However it is still not satisfactory. On the other hand, with the complete cubic model only one point has Δ > 100 MPa and the three test points 14,15 and 16 have accurate predicted values.(Δ < 67 MPa). It is therefore concluded that the cubic model (equation 2) satisfactorily describes the evolution of the bend strength over the complete ternary diagram.

$$\begin{aligned} Y = {} & 903\,X_1 + 559\,X_2 + 510\,X_3 \\ & + 1238\,X_1X_2 + 133\,X_1X_3 + 1683\,X_2X_3 \\ & - 1132\,X_1X_2\,(X_1-X_2) + 1472\,X_1X_3\,(X_1-X_3) + 1301\,X_2X_3\,(X_2-X_3) \\ & - 714\,X_1X_2X_3 \end{aligned} \qquad (2)$$

where Y is the flexural strength and X_i the molar fraction of i, with
1 : TiB_2, 2 : TiC, 3 : SiC.

Once the polynomial model is determined it is possible to plot isoresponse curves. Figure 7 shows the predicted isoflexural strength curves in the complete ternary diagram. The experimental measurements are also reported to allow direct comparison with the predicted values.

This third degree polynomial model predicts a maximum bend strength value of 1087 MPa for the composition 32 mol.% TiB_2, 55 mol.% TiC, 13 mol.% SiC. This is an obvious point to check to assess the validity of the model. The experimental strength is found to be 1073 ± 12 % MPa (point 17). The correspondence between the experimental and

the predicted values is excellent. A backscattered electron image of this optimum composite microstructure is given in Figure 8. Nearly every grains of both discrete phases TiB_2 and SiC are surrounded by the TiC matrix. Therefore, the number of weak TiB_2-SiC contact points is of minor importance in regard with the strong TiC-SiC and TiC-TiB_2 interaction. This is consistent with the fact that, in the large area

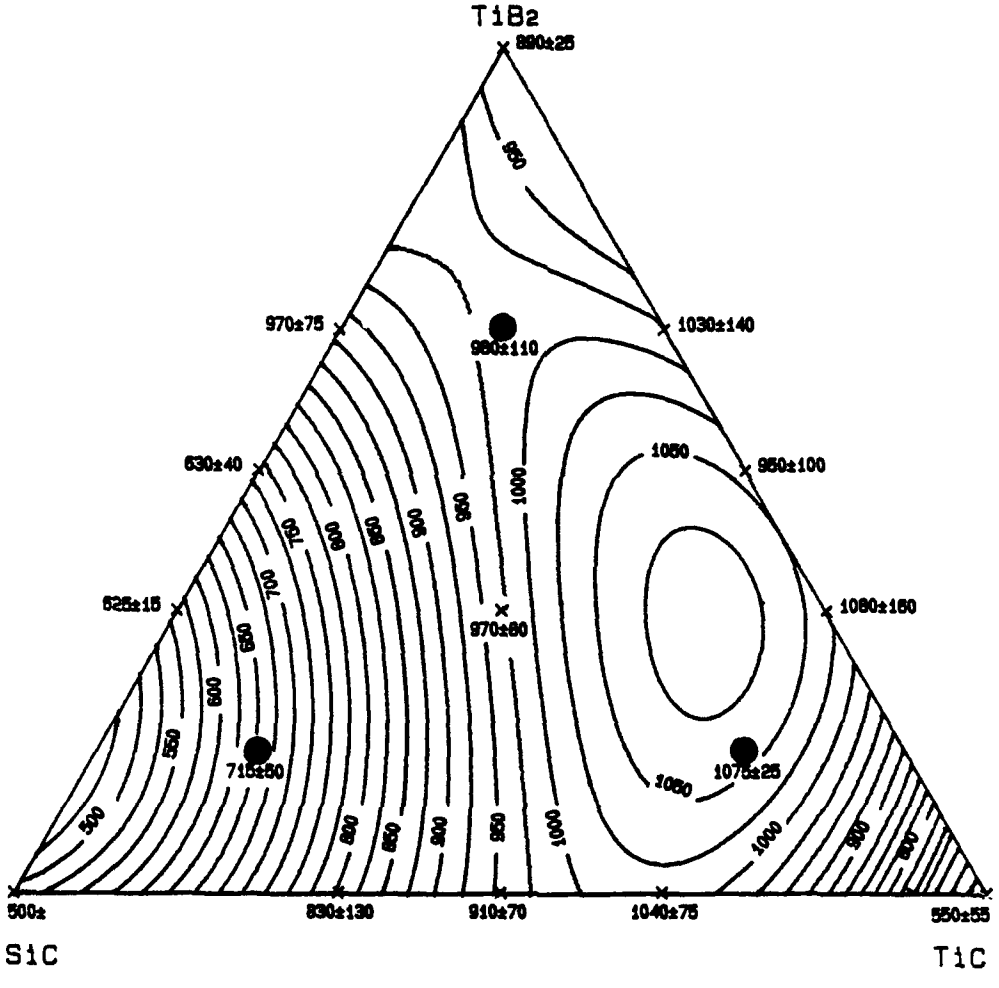

Figure 7: Iso-bend strength.curves ploted using a third order polynomial model. The incrementation step between two curves is 25 MPa. The circled points are test points.

σ_f>1000 MPa, to high SiC content corresponds low TiB_2 content and inversely, i.e. large SiC amounts are never found together with large TiB_2 amounts.

Figure 8: Microstructure of the optimum composite N° 17, i.e. 32 mol. % TiB_2 (grey) ,55 mol.% TiC (white) and 13 mol.% SiC (black)

4.3. FRACTURE TOUGHNESS

The fracture toughness of the single phase ceramics are relatively low, i.e. 5 MPa $m^{1/2}$ for TiB_2, 4.4 MPa $m^{1/2}$ for TiC and 2.9 MPa $m^{1/2}$ for SiC (see Table 3). The two phase composites exhibit already a higher K_{1c}, i.e. 5.2 MPa $m^{1/2}$ for TiB_2-TiC, 6.3 MPa $m^{1/2}$ for SiC-TiC and 5.1 MPa $m^{1/2}$ for SiC-TiB_2. However, the best fracture toughness values were measured for the three phase composites, i.e. the four of them (points 7,14,15, and 16) have an average value of 6.1 ± 0.2 MPa $m^{1/2}$.

A second order polynomial model (equation 3) is sufficient to describe the evolution of the fracture toughness over the complete ternary diagram.

$$Y = 5.1\,X_1 + 4.4\,X_2 + 3\,X_3 + 2.7\,X_1X_2 + 5.4\,X_1X_3 + 11.2\,X_2X_3 \qquad (3)$$

where Y is the computed fracture toughness and X_i the molar fraction of i, with 1 : TiB_2, 2 : TiC, 3 : SiC.

The maximum difference between the predicted and the measured values is equal to 0.7 MPa $m^{1/2}$, which is relatively large. However, it is not possible to expect the mathematical model to issue values with more precision than the experimental accuracy. Considering the confidence it is possible to have in fracture toughness measurements using the Vickers indentation technique as well as their standard deviation, the accuracy of the predicted values is thought to be within ± 1 MPa $m^{1/2}$.

The isofracture toughness curves plot is given in Figure 9. It is particularly interesting to study the fracture toughness evolution at the

TABLE 3: Values of the experimental fracture toughness , values computed with a quadratic model and their difference.

Difference	TiB2	TiC	SiC	Fracture Toughness [MPa m1/2]		
	molar %			Experimental	Computed	
1	100	0	0	5,0 ± 0,8	5,1	0,1
2	0	100	0	4,4 ± 0,6	4,4	0
3	0	0	100	2,9 ± 0,5	3	0,1
4	50	50	0	5,2 ± 0,4	5,4	0,2
5	50	0	50	5,1 ± 0,8	5,4	0,3
6	0	50	50	6,3 ± 0,9	6,5	0,2
7	33	33	33	5,9 ± 0,8	6,3	0,4
14	67	16,5	16,5	6,4 ± 0,5	5,8	-0,6
15	16,5	67	16,5	6,2 ± 0,4	6	-0,2
16	16,5	16,5	67	5,9 ± 0,5	5,5	-0,4
					Test points	
8	67	33	0	4,9 ± 0,4	5,5	0,6
9	33	67	0	5,2 ± 0,5	5,2	0
10	67	0	33	6,3 ± 0,4	5,6	-0,7
11	33	0	67	4,2 ± 0,2	4,9	0,7
12	0	67	33	6,4 ± 0,2	6,4	0
13	0	33	67	5,6 ± 0,3	5,9	0,3
17	32	55	13	6,7 ± 0,5	6	-0,7
18	20	55	25	6,4±0,7	6,3	-0,1

experimental field boundaries. On the TiB_2-TiC axis, major reinforcement effects are not expected since the CTE of both materials are similar. However, their good cohesion allows for a steady stage of about 5 MPa $m^{1/2}$ to be reached (composites N° 4,8,9).

On the TiB_2-SiC axis, the situation is more differentiated. The large CTE mismatch allows for reinforcement effects to be expected, however, the lack of cohesion between both materials will be a limiting factor. On the TiB_2 side, the bonding problem has no importance since the SiC discrete particles are put under compression by the surrounding TiB_2 matrix. This may cause microcracking and, hence, increase the

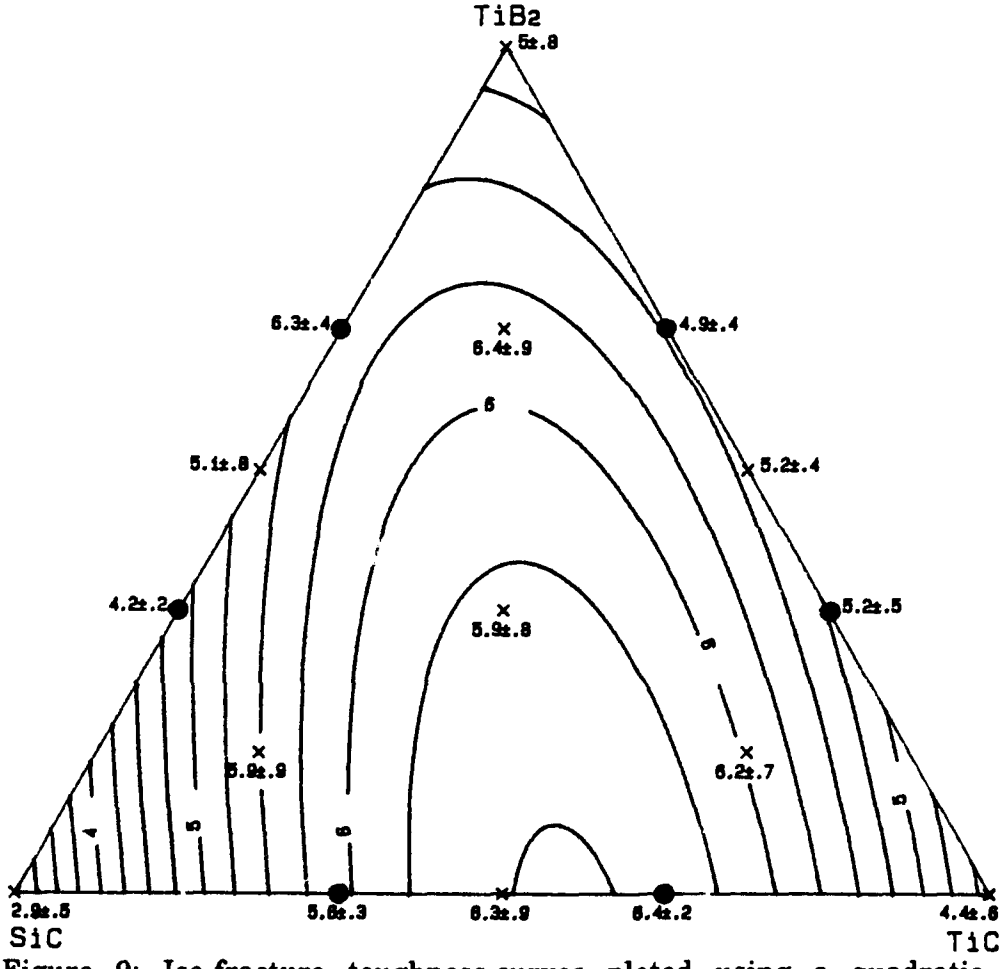

Figure 9: Iso-fracture toughness.curves ploted using a quadratic polynomial model. The incrementation step between two curves is 0.25 MPa $m^{1/2}$. The circled points are test points.

fracture toughness, i.e. 6.4 MPa $m^{1/2}$ for composite N° 10. On the SiC side, the large TiB_2 CTE causes this second phase to shrink from the SiC matrix, since there are only weak bonds between these phases, decohesion of the TiB_2 particles may occur. This explains the moderate fracture toughness of composite N° 11, i.e. 4.2 MPa $m^{1/2}$.

On the TiC-SiC axis, both the large CTE mismatch and the strong bonds developed between the materials are favourable in terms of reinforcement effects. On the TiC side, microcracking may occur in the TiC matrix around the SiC particles, with its propitious consequences already described, i.e. 6.4 MPa $m^{1/2}$ for composite N° 12. On the SiC side, the TiC discrete particles will again tend to shrink away from the SiC matrix. However, this time, the strong bonds developed between the materials, will avoid decohesion and, furthermore, will cause the SiC matrix to come into compression. This is an efficient toughening mechanism, i.e. 5.6 MPa $m^{1/2}$ for composite N° 13. The steady stage of the fracture toughness values for the three phase composites (N° 7,14,15,16) around 6 MPa $m^{1/2}$ seems to indicate, that whatever the toughening mechanisms are, their benefit is similar. This is confirmed by the crack observation for, crack deflection and crack pinning were mainly observed for every composite.

4.4. HARDNESS

The Vickers hardness (1 kg. load) of the different composites are listed in Table 4. The hardness values range form 17,5 GPa for pure TiB_2 to 32,3 GPa for pure SiC. In Table 4, the differences Δ between the experimental hardness and the values computed with polynomial models of different orders are also reported.

With the linear model, the Δ values ranges from 0 to 3,1 GPa. Since the confidence it is possible to have in hardness measurments is estimated to be ±2 GPa, this model is discarded.With the quadratic model, the Δ values are smaller than 1 GPa for the points used for the polynomial fitting and Δ reaches 1,4 GPa for the test points. Considering the hardness measurments precision, this model is in good agreement with the experimental values. The cubic model matches the experimental points even better, i.e. $\Delta_{fitting} < 0,4$ GPa and $\Delta_{test} < 1$ GPa. However, there is no point in having a polynomial model predicting hardness values with a better precision than the physical measurments. And since we are looking for an empirical model as simple as possible, we conclude that the quadratic polynomial model (equation 4) is

TABLE 4: Values of the experimental hardness, values computed with polynomial models of first, second and third order and their differences.

	TiB2	TiC	SiC	Experimental Hardness	Difference with the Polynomial Models		
	molar %			[GPa]	1 rst	2 nd	3 rd
1	100	0	0	17,5±0,6	3,1	0,5	0
2	0	100	0	26,7±1,9	0	-0,1	-0,1
3	0	0	100	32,3±1,5	0	0	0
4	50	50	0	25,3±1,1	-1,7	-0,6	-0,4
5	50	0	50	28,1±2,6	-1,6	-0,6	-0,4
6	0	50	50	29,0±2,4	0,5	-0,6	-0,4
7	33	33	33	26,3±0,7	0,3	1	0
8	67	33	0	23,9±2,0	-1,3	-0,9	0,2
9	33	67	0	24,8±1,4	-0,1	1	0,2
10	67	0	33	24,9±2,1	-0,4	0	0,2
11	33	0	67	29,5±2,5	-1,1	0,1	0,2
12	0	67	33	27,9±2,2	0,7	-0,3	0,2
13	0	33	67	29,0±2,9	1,5	0,5	0,2
					Test points		
14	67	16,5	16,5	25,2±1,1	-1,7	-1,4	-1,1
15	16,5	67	16,5	26,4±1,4	0,2	0,6	-0,3
16	16,5	16,5	67	28,8±1,7	0,7	1	0,2
18	20	55	25	26,6±1,0	0,3	0,7	-0,4

sufficient to satisfactorily describe and predict (Fig. 10) the evolution of the hardness in the ternary system TiB_2-TiC-SiC.

$$Y = 17.95\,X_1 + 26.6\,X_2 + 32.2\,X_3 + 9.7\,X_1X_2 + 9.8\,X_1X_3 - 4\,X_2X_3 \qquad (4)$$

where Y is the computed hardness and X_i the molar fraction of i, with 1 : TiB_2, 2 : TiC, 3 : SiC.

4.5. ELECTRICAL RESISTIVITY

The electrical resistivity ρ of pure TiB_2, given in Table 5, is rather low, i.e. 13 μΩ cm; it is equivalent to that of steel and tin. TiC resistivity is somewhat higher, i.e. 64 μΩ cm. This corresponds to constantan or

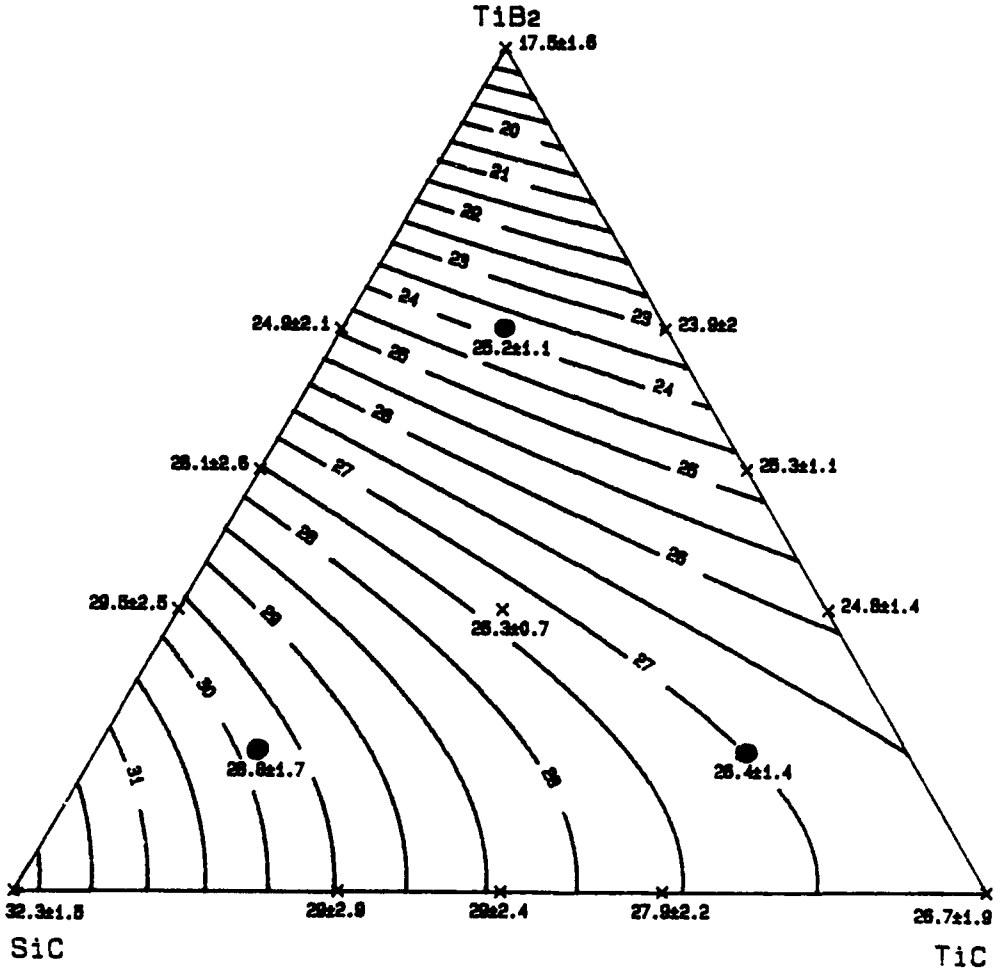

Figure 10: Iso-curves of the harness ploted using a second order polynomial model. The incrementation step between two curves is 0.5 GPa. The experimental values are also reported in the plot. The circled points are test points.

mercury. Although SiC is a semi-conductor, processed under the present conditions, it is non-conductor, i.e. 10^{13} μΩ cm.

As can be seen, the ρ values of pure SiC is about 10^{10} times larger than the highest value measured for the other composites (point 13). It

TABLE 5: Values of the experimental electrical resistivity, values computed with a third order polynomial model, their difference and their logarithm.

	TiB2	TiC	SiC	Experimental Resistivity	Logarithm Resistivity		Comp. Resist.	Diff.
	molar %			[μΩ cm]	exp.	Comp.	[μΩ cm]	
1	100	0	0	13,1 ± 0,1	1,117	1,118	13,2	0,1
2	0	100	0	64,0 ± 1,3	1,806	1,809	64,4	0,4
3	0	0	100	1 E 13	-	-	-	-
4	50	50	0	21,1 ± 0,1	1,324	1,351	22,4	1,3
5	50	0	50	46,1 ± 0,3	1,664	1,665	46,2	0,1
6	0	50	50	220 ± 1,0	2,342	2,359	228,6	8,6
7	33	33	33	50,6 ± 1,0	1,704	1,704	50,6	0
8	67	33	0	18,7 ± 0,2	1,272	1,257	18,1	-0,6
9	33	67	0	30,6 ± 0,3	1,486	1,471	29,6	-1
10	67	0	33	26,6 ± 0,9	1,425	1,425	26,6	0
11	33	0	67	127 ± 1,6	2,103	2,103	126,9	0
12	0	67	33	114 ± 1,0	2,057	2,048	111,7	-2,2
13	0	33	67	632 ± 6,0	2,801	2,792	619,4	-12,6
					Test points			
14	67	16,5	16,5	21,2 ± 0,1	1,326	1,357	22,8	1,6
15	16,5	67	16,5	49,7 ± 0,7	1,696	1,699	50	0,3
16	16,5	16,5	67	313 ± 2,6	2,496	2,455	285,1	-2,8
17	32	55	13	36,9 ± 0,2	1,567	1,549	35,4	-1,5
18	20	55	25	57,4±0,6	1,759	1,741	55	-2,4

is impossible for a polynomial model to accommodate such a huge difference. By taking the logarithm of the resistivity, the difference factor is reduced to 5, i.e. form 13 for point 3 to 2.8 for point 13. It may be possible for a polynom to fit these new data, however, its degree will have to be superior or equal to 4. In this study we decided to limit the polynomial models to the third order to stay within the limit of 20 different compositions and since our only pretension is to find an empirical model describing the evolution of the electrical resistivity, we tried to find a value for the logarithm of SiC resistivity that would allow for an accurate second or third order polynomial fitting on every other points. A third order polynomial model (equation 5) with a value log. $\rho_{SiC} = 4$ is perfectly satisfactory.

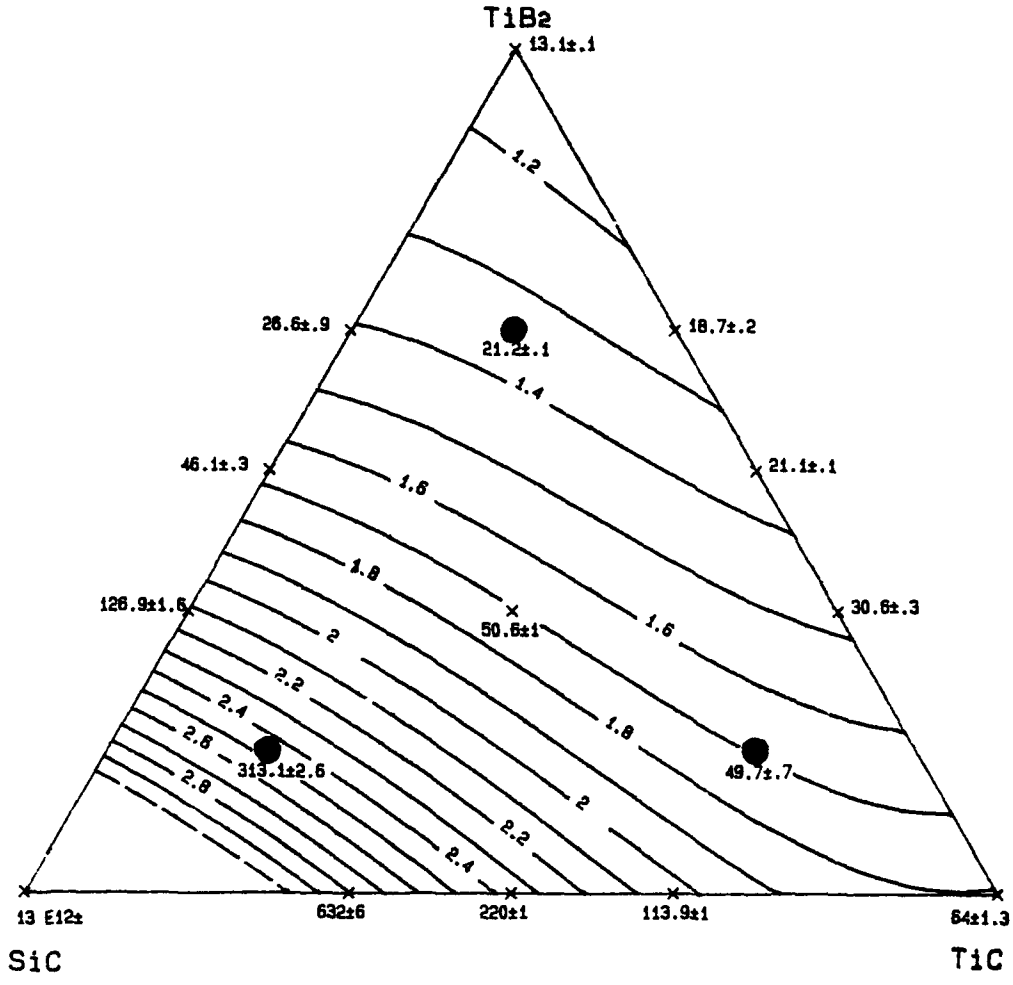

Figure 11: Iso-curves of the logarithm of the electrical resistivity.ploted using a third order polynomial model. The incrementation step between two curves is 0.1 (log.ρ). The experimental values are also reported in the plot. The circled points are test points.

The differences Δ between the computed and the experimental resistivity are given in Table 5. They are very satisfactory since $\Delta_{fitting} < 12.6$ μΩ cm and $\Delta_{test} < 2.8$ μΩ cm. The isoresistivity curves are shown in Figure 11. Obviously, this model with the logarithm of the resistivity

is only valid up to the last real measured point (point 13). Therefore, no prediction can be made in the SiC corner.

$$Y = 1.119\,X_1 + 1.809\,X_2 + 4.001\,X_3 - 0.45\,X_1X_2 - 3.581\,X_1X_3 - 2.184\,X_2X_3 + 0.108\,X_1X_2\,(X_1-X_2) + 1.902X_1X_3\,(X_1-X_3) - 0.089\,(X_2-X_3) + 2.297\,X_1X_2X_3 \quad (5)$$

where Y is the logarithm of the electrical resistivity and X_i the molar fraction of i, with 1 : TiB_2, 2 : TiC, 3 : SiC.

5. Conclusions

The use of a methodology of research using optimal design allows to drastically reduce the number of samples, i.e. 16 compositions, necessary to describe and predict the evolution of mechanical and electrical properties, i.e. modulus of rupture σ_f, fracture toughness K_{1c}, hardness Hv and electrical resistivity ρ over the complete ternary system TiB_2-TiC-SiC. Third order polynomial models are perfectly satisfactory to describe the flexural strength and the electrical resistivity; for the fracture toughness and the hardness quadratic models are already sufficient.

The mathematical model predicts a maximum bend strength for the composition 32 mol% TiB_2 - 55 mol% TiC - 13 mol% SiC, i.e. 1083, in excellent agreement with the experimental measure, i.e. 1073 ± 131 MPa. The location of this maximum can be explained by the fact that strong bonds are able to develop between TiC and TiB_2 and between TiC and SiC particles. Therefore every TiB_2 and SiC reinforcement particles are firmly bonded to the TiC matrix. A fracture toughness of ≈ 6 MPa $m^{1/2}$ is found for every three phase composites. The fracture toughness evolution is explained by the coefficient of thermal expansion mismatch between SiC on one side and TiC, TiB_2 on the other, and by their cohesion differences. The main toughening mechanisms observed are crack deflection and crack pinning.

We may imagine to use such a composite as structural ceramics (dies, cutting tools ...), crucibles , electrodes for molten metals or resistors. In function of this latter application, one composition with good characteristics, e.g. $\sigma_f > 1000$ MPa, $K_{1c} > 6$ MPa $m^{1/2}$ and $\rho > 50$ $\mu\Omega$ cm, was selected., i.e. 20% TiB_2 - 55% TiC - 25% SiC. The elaboration

process of this composite will be optimized, its pressureless sinterability assessed and its mechanical properties studied in deeper details, i.e. thermal shock resistance, CTE, ··· . This will be reported in a further paper.

References

1. R.E. Murashko, V.N. Sumarokov et al., (1978),"Hydrostatic Pressing of a Mixture of Titanium Diboride and Titanium Carbide Powders", Poroshkovaya Metallurgya (Eng.), **4** [184], 85-89.

2. W.A. Zdaniewski, (1986),"Degradation of Hot-Pressed TiB_2-TiC Composite in Liquid Aluminium", Am. Ceram. Soc. Bull., **65** [10], 1408-14.

3. C.H. McMurtry , W.D.G. Boecker, et al., (1987),"Microstructure and Material Properties of SiC-TiB_2 Particulate Composites", Am. Ceram. Soc.Bull., **66** [2], 325-329.

4. M.A. Janney,(1987), "Mechanical Properties and Oxidation Behavior of a Hot-Pressed SiC-15-vol%-TiB_2 composite", Am. Ceram. Soc. Bull.,**66** [2], 322-324.

5. G.C. Wei and P.F. Becher,(1984), "Improvement in Mechanical Properties in SiC by Addition of TiC Particles", J. Am. Ceram. Soc., **67** [8], 571-574.

6. G.Das, K.S. Mazdiyasni et al., (1982),"Mechanical Properties of Polycrystalline TiC", J. Am. Ceram. Soc., **65** [2] 104-110 .

7. E. Fargin, M. Sergent et al., (1985).,"Approche méthodologique de la recherche expérimentale", Bio-Sciences, 4 [4] , 77-88

8. R. Phan-Tan-Luu, D. Mathieu and D.Feneuille, (1983), Méthodologie de la recherche expérimentale, Fascicules de cours, L.P.R.A.I., Université d'Aix-Marseille.

9. M. Sergent, D. Mathieu and R. Phan-Tan-Luu, (1985), "Méthodologie de la recherche expérimentale appliquée aux

mélanges de vins provenant de différents cépages", R.F. OE., **98**, 36-43.

10 D. Mathieu and R. Phan-Tan-Luu, (1988),Logiciel NEMROD, L.P.R.A.I., Université d'Aix-Marseille.

11. C. Brodhag, M. Bouchacourt and F. Thevenot, (1981),"La cinétique de compression à chaud de céramiques spéciales", Silicates Industriels, **4-5**, 91-101.

12 C. Brodhag, (1983), Thesis N° 83-27, Limoges.

13. S.S. Ordon'yan, V.I. Unrod and A.I Avgustinik, (1975),"Reactions in the systemTiC_x-TiB_2", Poroshkovaya Metallurgya (Eng.), **9** [153], 40-43.

14. D.L. Jiang, J.H. Wang, Y.L. Li and and L.T. Ma, (1989), "Studies of the Strengthening of Silicon Carbide-based Multiphase Ceramics, I: The TiC-SiC System", Materials Science and Engineering, A109, 401-406.

V. THEORETICAL STUDIES

ELECTRONIC STRUCTURE OF STOICHIOMETRIC AND NON-STOICHIOMETRIC TITANIUM CARBIDES AND NITRIDES

A. Neckel
University of Vienna
Institute for Physical Chemistry
Währingerstraße 42
A-1090 Vienna
Austria

ABSTRACT. In the present article a brief overview is given on the electronic structure and the nature of the chemical bonds in stoichiometric and substoichiometric titanium carbides and nitrides crystallizing in the sodium chloride structure. On the basis of APW band structure calculations it is shown that metallic, ionic, and covalent bonding occurs in the stoichiometric compounds. Three main types of covalent bonds can be distinguished: X 2p - Ti 3d σ bonds, X 2p - Ti 3d π bonds, and Ti 3d - Ti 3d σ bonds (X = C,N). The influence of vacancies at the non-metal sublattice sites on the electronic structure of the substoichiometric cubic phases TiX_x was studied by two different approaches: (i) APW band structure calculations, assuming a hypothetical model structure with an ordered arrangement of vacancies, corresponding to the composition $TiX_{0.75}$. (ii) KKR-CPA calculations, assuming a random distribution of vacancies and non-metal atoms over the non-metal sublattice sites. Both calculations lead to additional peaks ("vacancy peaks") in the density of states, induced by the vacancies. The changes in the covalent bonds, compared with the stoichiometric compounds, are discussed on the basis of local partial densities of states and electron densities.

1. INTRODUCTION

Refractory transition metal carbides and nitrides crystallizing in the sodium chloride structure continue to be of considerable practical and theoretical interest. This class of substances exhibits, on the one hand, high melting points and ultrahardness - properties typical of covalent compounds - and, on the other hand, metallic properties, such as good electrical and thermal conductivity. Furthermore, these substances crystallize in the sodium chloride structure, which is generally found with ionic compounds. This unusual combination of properties has attracted an early and continuing interest in the electronic structure and nature of the chemical bonds in these substances.

The electronic structure of the refractory transition metal

R. Freer (ed.), The Physics and Chemistry of Carbides; Nitrides and Borides, 485–511.
© 1990 *Kluwer Academic Publishers. Printed in the Netherlands.*

carbides and nitrides has been studied theoretically by various authors, using different methods of calculation. Several review articles on these investigations are available in literature [1,2,3,4].

Titanium carbide and titanium nitride have been chosen as representative examples of this class of compounds. In the first chapter of this article, the electronic structure and the chemical bonding of the stoichiometric compounds TiC and TiN will be discussed, whereas, in the second chapter, the influence of vacancies at the non-metal lattice sites on the electronic structure will be dealt with.

2. THE ELECTRONIC STRUCTURE OF THE STOICHIOMETRIC COMPOUNDS TiC AND TiN

The discussion of the electronic structure of the stoichiometric compounds TiC and TiN presented in this article is based on the results of band structure calculations obtained by means of the self-consistent Augmented Plane Wave (APW) method [5] and by the linearised version of this method (LAPW method) [6].

In the APW method, the so-called muffin-tin approximation for the crystal potential is commonly used, whereby it is assumed that the crystal potential is spherically symmetric within non-overlapping spheres around the atomic sites and constant in the region between the atomic spheres. Figure 1 shows on the left side the actual potential and on the right side the corresponding muffin-tin potential for a hypothetical, two-dimensional lattice.

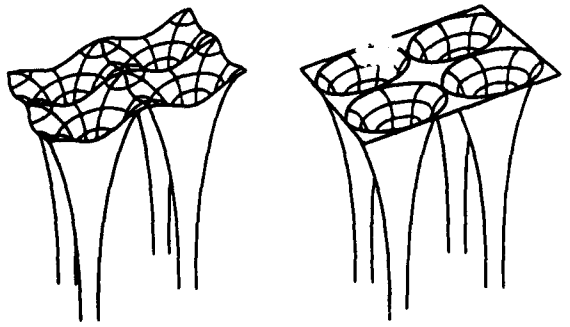

Figure 1. Crystal potential of a square two-dimensional lattice: actual potential (left); muffin-tin potential (right). (According to [7].)

The calculations yield the band structure, the corresponding density of states (DOS), charges, and electron densities. These quantities provide valuable information on the chemical binding.

2.1. Band Structure and Density of States (DOS)

The graph of the energy eigenvalues corresponding to $\vec{k}$ vectors along a certain path through the first Brillouin zone represents the "band structure".

The band structure of TiN, calculated by Neckel et al.[8], is displayed in Figure 1 as an example.

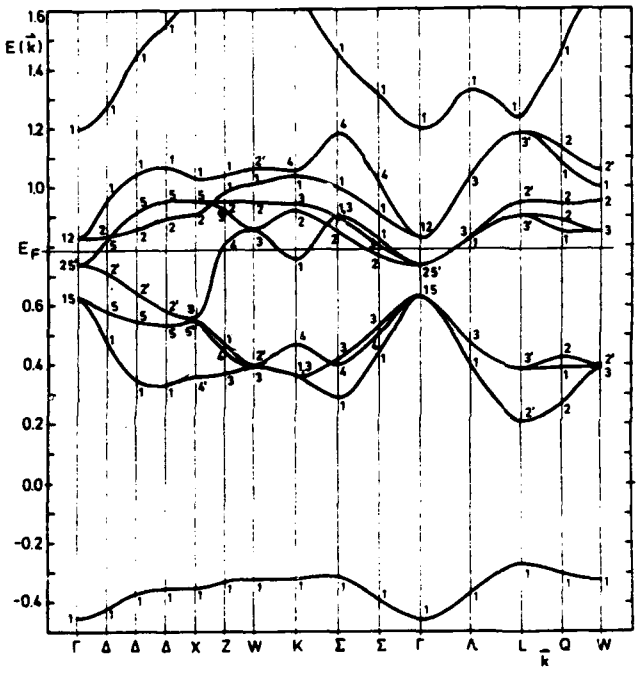

Figure 2. Band structure of TiN. Energy $E(\vec{k})$ in Rydberg with respect to the constant muffin-tin potential between the atomic spheres. (From Neckel et al.[8]. With permission.)

The DOS is defined as the number of electronic energy states per unit energy range (Rydberg) and unit cell. The total DOS can be divided into partial ℓ-like densities of state, $g_\ell^t(E)$, using additional information derived from the corresponding wave functions. The partial ℓ-like DOS is defined as the number of electronic states corresponding to the angular momentum quantum number ℓ per Rydberg and unit cell.

Figure 3 shows the partial ℓ-like DOS of TiC and TiN plotted versus the energy. The partial ℓ-like DOS shown in this figure have been obtained by means of a Linear Combination of Atomic Orbitals (LCAO) interpolation scheme [8,9,10]. (The superscript t in $g_\ell^t(E)$ refers to the atom t on which the corresponding orbital is centred.)

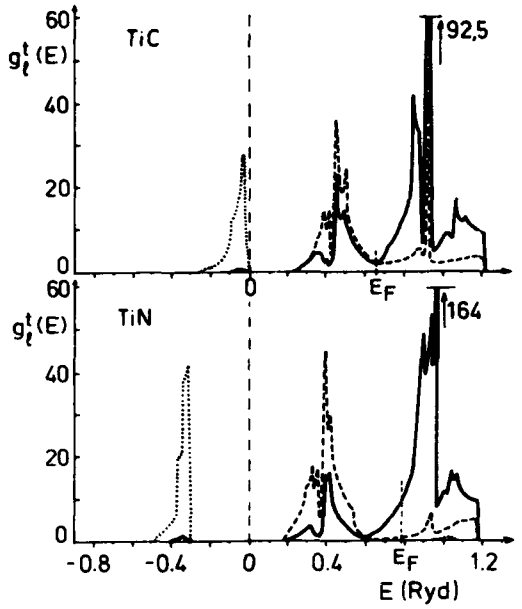

Figure 3. LCAO partial ℓ-like DOS, $g_\ell^t(E)$, in units of electronic states with both spins per Rydberg and unit cell for TiC and TiN. ..... non-metal 2s DOS; ---- non-metal 2p DOS; —— Ti 3d DOS. (From Neckel et al. [8]. With permission.)

Both compounds possess a low lying energy band which exhibits almost exclusively s character. This band is derived from the 2s state of the non-metal atom and will be called "s band". In passing from the carbide to the nitride this band is energetically lowered and becomes narrower, corresponding to an increased localization of the wave functions of these states at the non-metal atom sites.

Three overlapping bands, separated from the "s band" by an energy gap and extending to the minimum of the DOS follow in the energy scale. These three bands will be called the "p band", because it can be derived basically from the 2p states of the non-metal atom. The crystal wave functions of these states, however, possess not only p symmetry, but also d symmetry, particularly in the region of the Ti sphere. This leads to the appearance of partial Ti 3d DOS in the "p band". The strong interaction between non-metal 2p states and titanium 3d states is characteristic for these compounds and represents the main covalent binding component, as will be discussed later.

Five overlapping bands which possess mainly d character are found above the "p band". They are derived from the 3d states of the titanium atom, and will therefore be called "d band". The partial p-like DOS in the "d band" decreases in passing from the carbide to the nitride.

There is a sharp minimum in the DOS between the "p" and the

"d band" which corresponds to a filling of the valence bands with 8 electrons. Therefore, the Fermi level E_F for TiC, which has 8 valence electrons, lies in the minimum of the DOS. The additional valence electron of TiN causes the Fermi level to shift into the "d band".

At higher energies, a band (including the energy state Γ_1 at 1.194 Ryd.) follows which originates from the Ti 4s state. It is characterized by highly delocalized states with prevailing Ti 4s and Ti 4p symmetry. Whereas in the pure metal the broad 4s band overlaps with the narrow Ti 3d bands, it is shifted in TiC and TiN to higher energies above the Fermi energy, due to the repulsive interaction with the non-metal 2s band. The partial DOS of the 4s band are not included in Figure 3.

2.2. Binding Mechanisms

The electronic structure calculations show that all three main types of chemical bonding occur in TiC and TiN.

2.2.1. Metallic Bonding

There is a non-vanishing DOS at the Fermi energy in both compounds TiC and TiN, and - as will be shown later (see Fig.9) - a relatively high electron density in the region between the atomic spheres. The occurrence of metallic properties can be deduced from both findings.

2.2.2. Ionic Bonding

An ionic contribution to the binding mechanism is caused by the transfer of electronic charge from the Ti atom to the non-metal atom, leading to an electrostatic contribution to the binding energy. In order to determine the charge transfer a reference state must be defined. For the present discussion the reference state used is the spherically averaged radial electron density $\sigma^t_{superposed}(r)$ ($\sigma(r) = 4\pi r^2\rho(r)$, r: distance from the centre of the atomic sphere t; $\rho(r)$: spherically averaged electron density) in the atomic sphere t, obtained by the superposition of the atomic electron densities of the corresponding neutral atoms, placed on the positions of the TiX crystal (X = C, N). The charge transfer $\Delta\sigma^t(r)$ is given by the difference between the radial electron density, $\sigma^t_{crystal}(r)$, obtained from the band structure calculation after it reaches self-consistency, and the radial electron density, $\sigma^t_{superposed}(r)$, of the superposed atomic electron densities:

$$\Delta\sigma^t(r) = \sigma^t_{crystal}(r) - \sigma^t_{superposed}(r)$$

In Figure 4, the difference $\Delta\sigma^t(r)$ is plotted versus the distance r from the centre of the atomic sphere t. R_{Ti} and R_X are the radii of the respective atomic spheres around the Ti site and the non-metal atom X site.

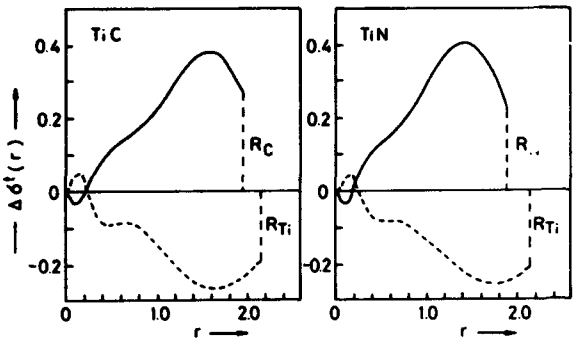

Figure 4. Difference $\Delta\sigma^t(r)$ (in units of electrons / a.u.) between the crystal and the superposed atomic radial electron density, plotted versus the distance (in atomic units; a.u.) from the centre of the atomic sphere t; in the non-metal sphere: —— ; in the Ti sphere: ----. (From Neckel et al. [9]. With permission.)

$\Delta\sigma^t(r)$ is positive (except for a very small region near the atomic nucleus) in the non-metal sphere, indicating an increase of electronic charge in the crystal compared with the electronic charge of the hypothetical crystal of non-interacting neutral atoms, and negative in the Ti sphere. The total amount of transferred electronic charge ΔQ_t, obtained by integrating $\Delta\sigma^t(r)$ over the respective atomic sphere t, depends on the atomic sphere radius R_t, which is not unequivocally defined. However, also for a different choice of the atomic sphere radii R_t there will always be an increase of electronic charge inside the non-metal sphere and a decrease in the Ti sphere, compared with the hypothetical crystal of non-interacting neutral atoms.

The values of the atomic sphere radii, used by Neckel et al. [8,9], lead to the following amounts of transferred electronic charge (in electrons per atomic sphere t):

$$\text{TiC: } \Delta Q_{Ti} = -0.36; \quad \Delta Q_C = 0.43;$$
$$\text{TiN: } \Delta Q_{Ti} = -0.32; \quad \Delta Q_N = 0.46.$$

2.2.3. Covalent Bonding

In the simple "Molecular Orbital" (MO) theory of diatomic molecules, atomic orbitals of appropriate symmetry can be combined to form bonding and antibonding molecular orbitals. Applying the same description to the case of crystals, three main types of covalent bonds can be distinguished in TiC and TiN. The Ti atoms in these compounds are octahedrally surrounded by six non-metal atoms. Therefore, the five 3d orbitals of a Ti atom are split by the octahedral ligand field generated by the non-metal neighbours into three orbitals of t_{2g}

symmetry (d_{xy}, d_{xz}, d_{yz}) and two orbitals of e_g symmetry (d_{x2-y2}, d_{z2}). In the same way, the partial 3d DOS can be split into a t_{2g} and an e_g component.

The orbital lobes of the Ti e_g orbitals extend towards the neighbouring non-metal atoms. These orbitals can form pd_σ bonds with the 2p orbitals on neighbouring non-metal atoms, as it is shown schematically for the (100) plane in Figure 5.

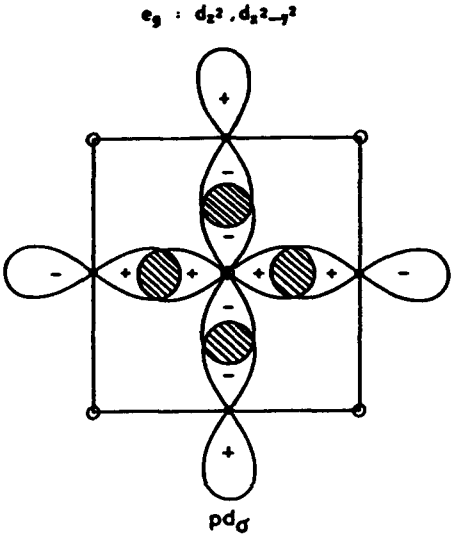

Figure 5. Schematic representation of the pd_σ bonds between a Ti e_g orbital and non-metal 2p orbitals in the (100) plane of the sodium chloride structure. ○ : Ti atom; ● : non-metal atom. (According to Neckel et al. [11]. With permission.)

From the fact that the partial X 2p DOS and the partial Ti e_g DOS are both relatively high in the energy range of the "p band" [8,9], the existence of bonding X-Ti pd_σ interactions can be expected in this energy region. The corresponding antibonding X-Ti pd_σ* interactions are found in the unoccupied range of the "d band".

The orbital lobes of the Ti t_{2g} functions extend towards the neighbouring Ti atoms. These orbitals are capable of forming pd_π bonds with 2p orbitals of adjacent non-metal atoms, as shown on the left side of Figure 6. The bonding pd_π interactions occur mainly in the "p band". The Ti t_{2g} orbitals, however, can also form metal-metal dd_σ bonds with the t_{2g} orbitals of adjacent Ti atoms, as depicted on the right side of Figure 6. This type of bonding is expected to occur primarily in the lower range of the "d band", since the Ti t_{2g} DOS is high in this energy range. However, a small number of dd_σ bonds appears in the upper range of the "p band". The antibonding dd_σ* interactions are mainly found in the central part of the "d band".

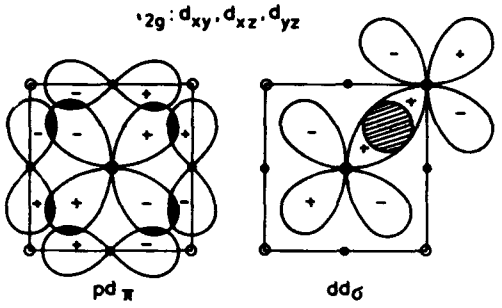

Figure 6. Schematic representation of the pd_π bonds between a Ti t_{2g} orbital and non-metal 2p orbitals (left) and of the dd_σ bonds between the Ti t_{2g} orbitals of adjacent Ti atoms (right) in the (100) plane of the sodium chloride structure. ○ : Ti atom; ● : non-metal atom. (According to Neckel et al. [11]. With permission.)

These three types of covalent bonds can be visualized by calculating the electron density in the (100) plane for special energy states from the corresponding crystal wave functions. The upper part of Figure 7 shows the electron densities of three occupied states (just below the Fermi energy) at $\vec{k} = \Delta$ of TiC, calculated by Schwarz and Blaha [12]. The lower part of Figure 7 shows schematically the corresponding bond types, which are realized in these energy states.

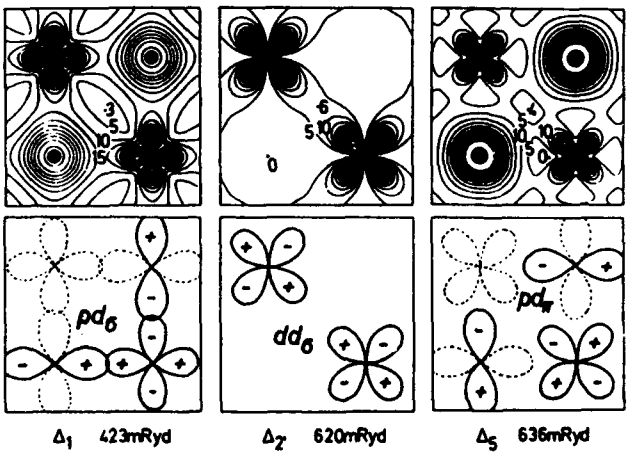

Figure 7. Electron density in the (100) plane of three occupied band states for $\vec{k} = \Delta = \pi/a(1,0,0)$ of TiC. (From Schwarz and Blaha [12]. With permission.)

2.3. Valence Electron Density

The valence electron density can be computed from the crystal wave functions. The valence electron densities of the stoichiometric compounds TiC, TiN, and TiO were calculated by Blaha and Schwarz [13].

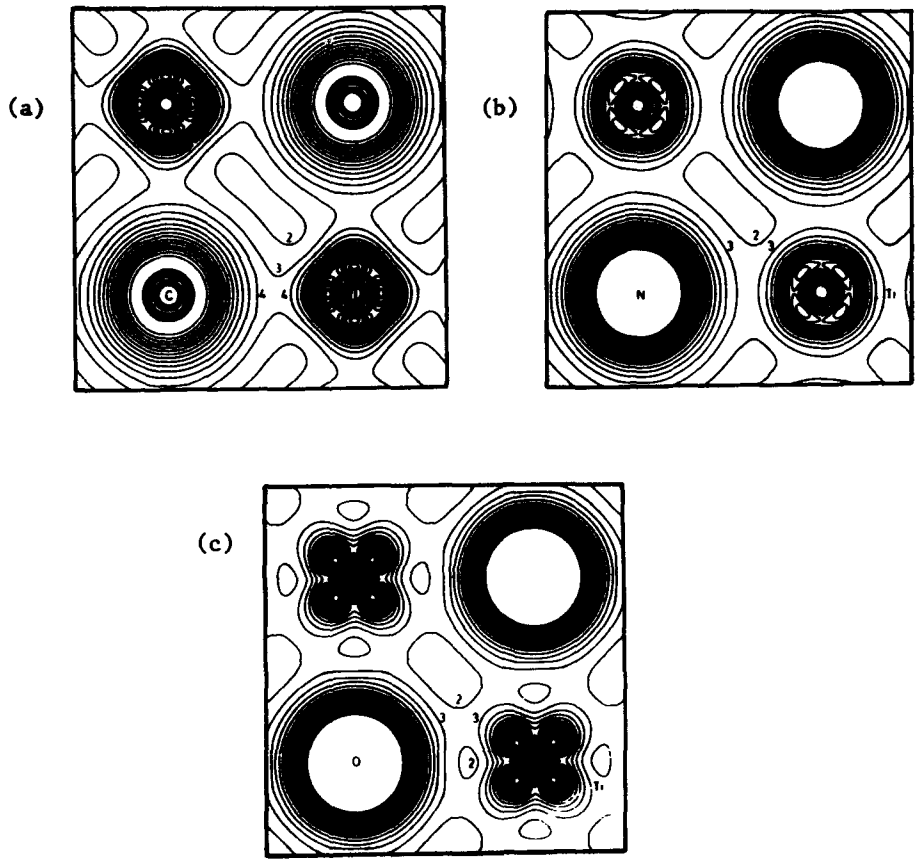

Figure 8. Valence electron density in the (100) plane of (a) TiC, (b) TiN, and (c) TiO. Contour intervals 0.1 electrons/$Å^3$; indicated figures are in these units; cutoff at 1.7 electrons/$Å^3$. (From Blaha and Schwarz [13]. With permission.)

In TiC, the valence electron density around a Ti site clearly exhibits e_g character. The maxima of the valence electron density lie in the directions towards neighbouring C atoms, indicating that pd_σ bonds are the most dominant.

From the valence electron density distribution in TiN it can be

concluded that in addition to pd_σ bonds, pd_π bonds and dd_σ bonds take part in the covalent binding mechanism as well. Because the formation of pd_π bonds requires N 2p orbitals, this bond type will occur in the energy range of the "p band". In the occupied range of the "d band", where the number of 2p states is rather low, the occurrence of dd_σ bonds is to be expected.

In TiO, the valence electron density distribution around a Ti site exhibits almost exclusively t_{2g} character, indicating the predominance of dd_σ bonds.

The valence electron density distribution around the non-metal atom sites is almost spherically symmetric. This fact is due to the equal occupancy of the three 2p orbitals (p_x, p_y, p_z) of the non-metal atom in a crystal field of cubic symmetry. The sum of the electron densities of the three equivalent 2p orbitals is spherically symmetric.

The valence electron density between the atomic spheres remains relatively high, as can be seen from Figure 9, in which the valence electron density $\rho(\vec{r})$ of TiC [12] and TiN [14] is plotted in the [100] direction from the non-metal atom to the Ti atom.

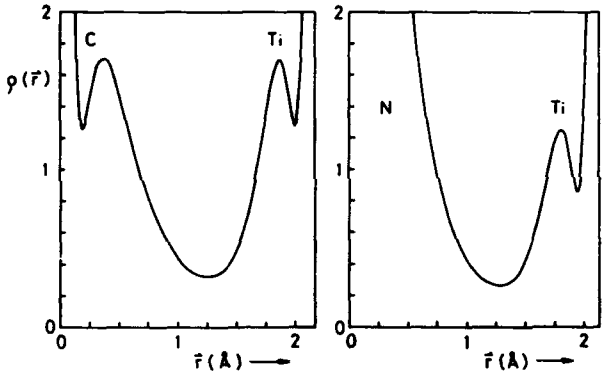

Figure 9. Valence electron density $\rho(\vec{r})$ in units of electrons/Å^3 in the [100] direction from the non-metal atom to the Ti atom in TiC [12] and TiN [14]. (From [12] and [14]. With permission.)

3. SUBSTOICHIOMETRIC COMPOUNDS TiC_x AND TiN_x.

The cubic phases in the systems Ti-C and Ti-N exhibit wide homogeneity ranges, corresponding to the compositions $TiX_x (x < 1)$. The sub-stoichiometry of these phases is caused by vacancies at the non-metal sublattice sites. The vacancies may be randomly distributed over the non-metal sublattice sites of the sodium chloride structure. However, they may exhibit also short or long-range order. A general overview of the experimental data concerning long and short-range order of the non-metal atom vacancies in transition metal carbides and nitrides with

sodium chloride structure has been given by de Novion and Landesman [15]. In the Ti-C system the TiC_x phase exists in the composition range between x = 0.5 and x = 0.97 [16]. Goretzki [17] showed that in the composition range between x = 0.5 and x = 0.71 a long-range ordered superstructure, corresponding to the crystal structure of $TiC_{0.5}$ can be obtained after long annealing at 600°C. Short-range order has also been observed, particularly in the composition range between x = 0.5 and x = 0.7 [18,19]. It should be mentioned that the vacancies avoid occupying second neighbour positions of the sublattice of the carbon atoms.

In the Ti-N system [20] the cubic phase TiN_x extends from about x = 0.42 (depending on the temperature) to about x = 1. A long-range ordered vacancy structure, (δ'-Ti_2N), was found for x ≈ 0.61. Short-range ordering of the vacancies seems to exist at all compositions TiN_x [15]. Furthermore, a shortening of the first neighbour Ti-C or Ti-N distance has been observed for the Ti atoms adjacent to a vacancy, where the Ti atom is shifted away from the vacancy.

The physical and chemical properties of the TiX_x phases depend strongly on the concentration of vacancies. We have implemented two different approaches to study the influence of vacancies on the electronic structure of titanium carbide and nitride.

3.1. APW Band Structure Calculations

Conventional band structure calculations using the APW method were performed for a hypothetical model structure with an ordered arrangement of vacancies, corresponding to the composition $TiX_{0.75}$. The model structure used (Figure 10) is derived from the cubic unit cell of the sodium chloride structure, containing four formula units, by replacing the non-metal atom at the centre of the unit cell by a

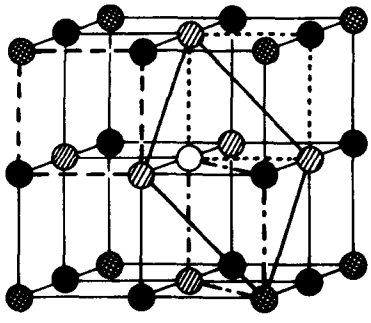

Figure 10. Cubic unit cell for the hypothetical, ordered model compound $Ti^{[6]}Ti^{[4]}X_3\square_X$. ● : X atom; ○ : vacancy; ◍ : $Ti^{[4]}$ atom; ◍ : $Ti^{[6]}$ atom; ---: (100) plane, cut 1; ...: (100) plane, cut 2; -.-.: (110) plane; ——: (111) plane.

vacancy $\square_X$. Due to the existence of the vacancy, two different types of Ti atoms can now be distinguished in the unit cell. The two different types are designated by their respective number of coordinating non-metal atoms. The $Ti^{[6]}$ atoms at the corners of the unit cell are octahedrally coordinated by six non-metal atoms, as in the stoichiometric compounds TiX. The Ti atoms occupying the centres of the cube faces possess four non-metal atoms and two vacancies as nearest neighbours. They are designated $Ti^{[4]}$. Therefore, the model structure can be described by the formula $Ti^{[6]}Ti^{[4]}_3X_3\square_X$.

Because the translational symmetry is preserved in this long-range ordered structure, the self-consistent APW method can be applied to calculate the electronic structure of the model compound.

3.1.1. Band Structures of the Model Compounds

Figures 11(a) and (b) display the band structures of stoichiometric TiC [8] and of the model compound $Ti^{[6]}Ti^{[4]}_3C_3\square_C$ [21] for some symmetry directions in the first Brillouin zone. The band structure of TiC shown in Figure 11 is entirely equivalent to the band structure in [8]. However, in order to facilitate the comparison with the band

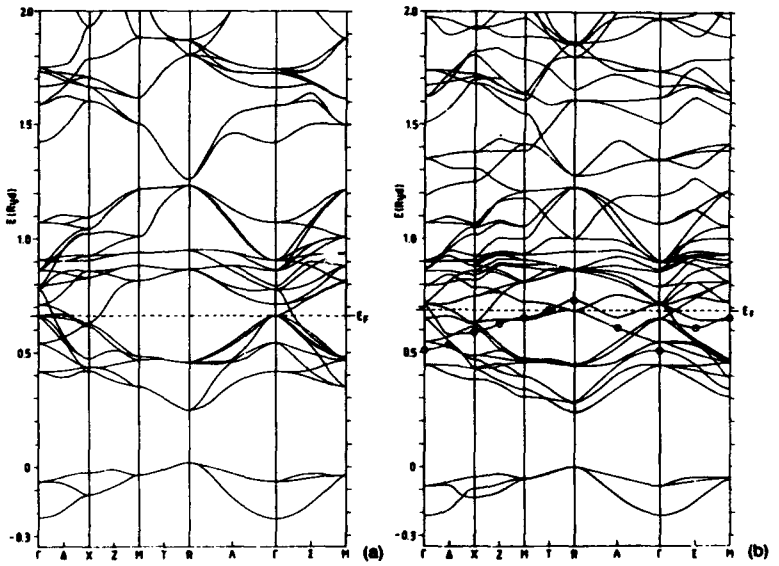

Figure 11. Band structure of stoichiometric TiC(a) and ordered $TiC_{0.75}$ (b). Energy (Ryd) with respect to the constant muffin-tin potential between the atomic spheres. The band structure of TiC [8] has been backfolded into the Brillouin zone corresponding to the cubic unit cell of the sodium chloride structure. So-called "vacancy states" are encircled in Figure 11(b). (From Redinger et al. [21]. With permission.)

structure of ordered $TiC_{0.75}$, it is represented for a cubic unit cell containing four formula units.

Due to the lowered symmetry of $Ti^{[6]}Ti^{[4]}_3X_3\square_X$ compared with stoichiometric TiX, some degeneracies of the energy bands of TiX are removed. Three X 2s bands, nine X 2p bands and twenty Ti 3d bands are expected to appear in the model compounds. However, an additional energy band in the region between the "p" and the "d band" of stoichiometric TiX occurs as well, which will be called "vacancy band". A charge analysis of the energy states of the vacancy band reveals that the so-called "vacancy states" contain a substantial amount of electronic charge (about 20%) in the vacancy sphere. Such vacancy states also follow from the cluster calculations by Schwarz and Rösch [22] for substoichiometric niobium carbide and by Ries and Winter [23] for substoichiometric vanadium nitride and niobium carbide. The appearance of vacancy states in substoichiometric titanium oxide and carbide has been predicted by Huisman et al. [24]. A vacancy band has also been found for the NbO structure, which is derived from the sodium chloride structure and exhibits a long-range ordered arrangement of vacancies at the niobium and the oxygen sublattice sites [25].

3.2. KKR-CPA Electronic Structure Calculations

The Korringa-Kohn-Rostoker Coherent Potential Approximation (KKR-CPA) was used to calculate the electronic structure of TiC_x and TiN_x, assuming a random distribution of vacancies and non-metal atoms over the non-metal sublattice sites of the sodium chloride structure. These calculations [26,27] were performed for various concentrations x.

3.3. Density of States and Local Partial Densities of States

The DOS curves (Figures 12 and 13) of the model compounds $Ti^{[6]}Ti^{[4]}_3X_3\square_X$ show two additional peaks in the region of the minimum of the DOS between the "p" and the "d band" of stoichiometric TiX. These peaks will be referred to as "vacancy peaks", because they are induced by the vacancies. In $Ti^{[6]}Ti^{[4]}_3C_3\square_C$ only the energetically lower ("first") vacancy peak is occupied, whereas in $Ti^{[6]}Ti^{[4]}_3N_3\square_N$ the Fermi level coincides with the maximum of the energetically higher ("second") vacancy peak. This position of the Fermi level may be an artifact, caused by the assumed highly symmetric long-range order of the model structure.

The DOS can be divided into *local* partial ℓ-like DOS, $g^t_\ell(E)$. The *local* partial DOS is defined as the number of electronic states corresponding to the angular momentum quantum number ℓ in specified atomic spheres of type t per unit energy range (Ryd) and unit cell. It is to be distinguished from the LCAO partial ℓ-like DOS, used in chapter 2. The latter refers to the entire unit cell, whereas the former only applies to the atomic spheres of type t. A discussion of the difference of these two concepts can be found in the review article by Schwarz [4].

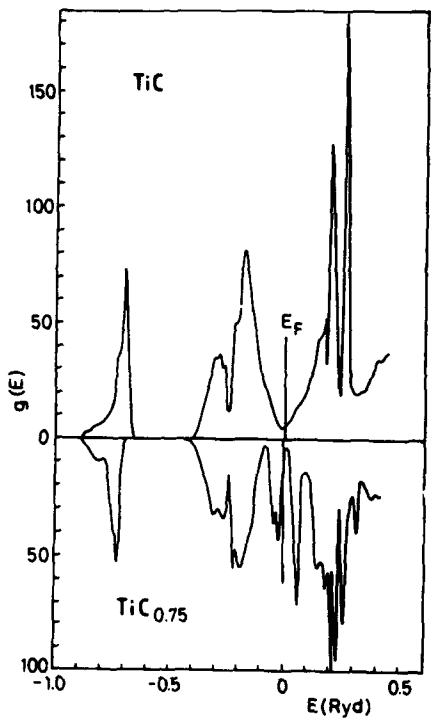

Figure 12. Total DOS of TiC and ordered $TiC_{0.75}$ in number of electronic states per Rydberg, spin, and cubic unit cell. The cubic unit cell contains four formula units. The curves are adjusted to coincide in the bottom of the C 2s band. The Fermi level of $TiC_{0.75}$ is chosen as energy zero. (From Redinger et al. [21]. With permission.)

The local partial d-like DOS within the atomic sphere of the $Ti^{[6]}$ atom is split by the octahedral ligand field into the components with t_{2g} and e_g symmetry, as it is the case with the stoichiometric compounds.

To describe the orbitals of the $Ti^{[4]}$ atom a local coordinate system is used, in which the z axis points from the $Ti^{[4]}$ atom to the vacancy, whereas the x and y axes point to the non-metal atoms.

The four non-metal atoms surrounding a $Ti^{[4]}$ atom in a square planar arrangement generate a ligand field of D_{4h} symmetry. This ligand field causes the five d orbitals to split into four components with a_{1g} (d_{z2}), e_g (d_{xz}, d_{yz}), b_{2g} (d_{xy}), and b_{1g} (d_{x2-y2}) symmetry (Figure 14). Accordingly, the $Ti^{[4]}$ 3d DOS can be split into four components corresponding to these four groups of orbitals.

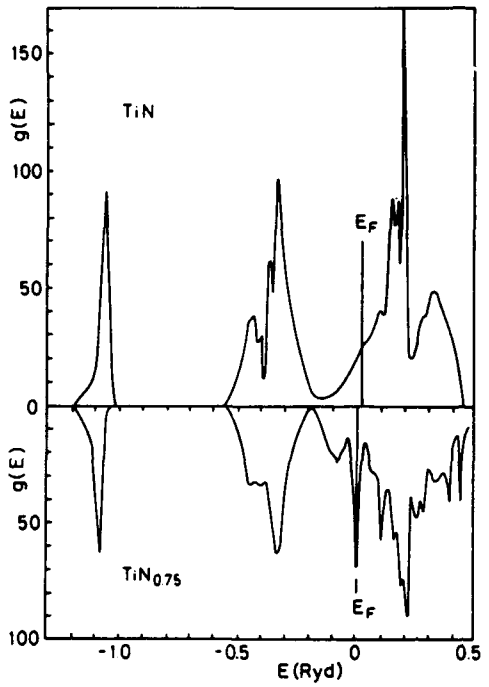

Figure 13. Total DOS of TiN and ordered $TiN_{0.75}$ in number of electronic states per Rydberg, spin, and cubic unit cell. The cubic unit cell contains four formula units. The curves are adjusted to coincide in the bottom of the N 2s band. The Fermi level of $TiN_{0.75}$ is chosen as energy zero. (From Herzig et al. [28]. With permission.)

Figure 15 presents the main local partial DOS components, $g_\ell^t(E)$, of ordered $TiC_{0.75}$ and TiC. The reduced number of C atoms in substoichiometric $TiC_{0.75}$ leads to a reduction of the C 2s and the C 2p DOS in the "s" and "p band".

The C 2p - Ti $^{[4]}$3d interaction is reduced in the substoichiometric compound, because only the Ti $^{[4]}d_{x^2-y^2}$ orbitals can form pd_σ bonds with the 2p orbitals of the adjacent carbon atoms, whereas the Ti $^{[4]}d_{z^2}$ orbitals which extend towards the vacancy are unable to form pd_σ bonds. This causes also the Ti $^{[4]}$3d DOS to decrease in the range of the "p band", where this type of bonding mainly occurs. A large amount of Ti $^{[4]}$3d DOS is found in the range of two vacancy peaks. In the energy range above the vacancy peaks, in the "d band", the Ti 3d DOS prevails. A similar situation is found for ordered $TiN_{0.75}$.

Of special interest is the local partial DOS in the vacancy sphere, which is high only in the region of the vacancy peaks. In the first vacancy peak the local partial DOS exhibits almost exclusively s character, whereas in the second vacancy peak the local partial

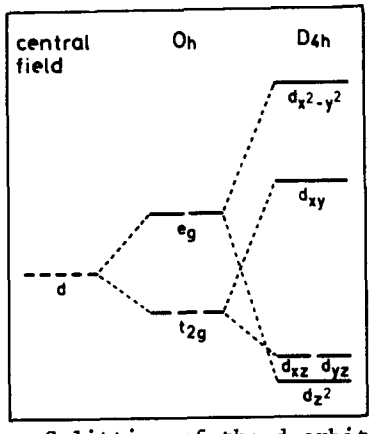

Figure 14. Splitting of the d orbitals in ligand fields of O_h and D_{4h} symmetry.

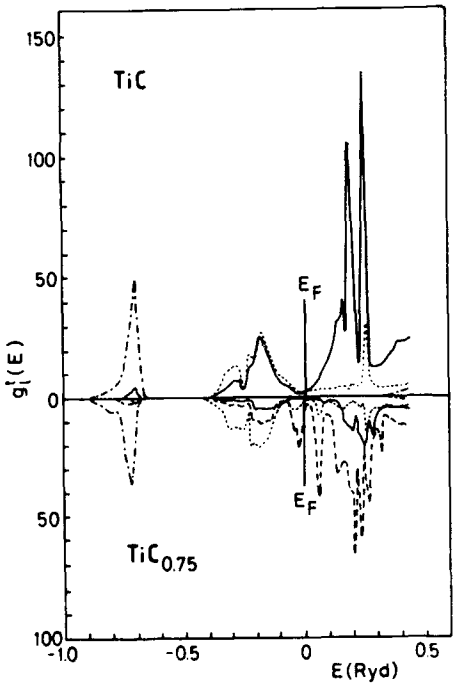

Figure 15. Main local partial DOS components, $g_\ell^t(E)$, of TiC and ordered $TiC_{0.75}$ in units of electronic states per Rydberg, spin, and atomic spheres t in the cubic unit cell. -.-.-: C 2s DOS; ....: C 2p DOS; ——: Ti ($Ti^{[6]}$) 3d DOS; ---: $Ti^{[4]}$ 3d DOS. The cubic unit cell contains four formula units. The curves are adjusted to coincide in the bottom of the C 2s band. The Fermi level of $TiC_{0.75}$ is chosen as energy zero. (From Redinger et al. [21]. With permission.)

p-like DOS dominates. (See Figure 16)

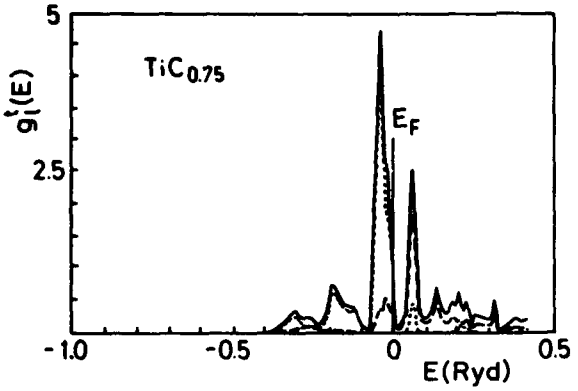

Figure 16. Local total and local partial DOS in the vacancy sphere of ordered $TiC_{0.75}$. The same units and conventions as for Figure 15 are used. ——: total vacancy DOS; ....: vacancy s DOS; ---: vacancy p DOS. (From Redinger et al. [21]. With permission.)

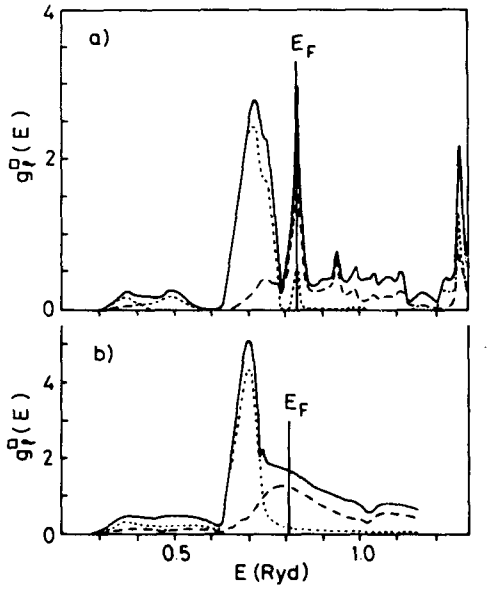

Figure 17. Local total and local partial DOS in the vacancy sphere of ordered $TiN_{0.75}$ (a) and according to the KKR-CPA calculation (b). The same units and conventions as for Figure 15 are used. ——: total vacancy DOS; ....: vacancy s DOS; ---: vacancy p DOS. (From Herzig et al. [28]. With permission.)

Figure 17 shows a comparison of the local partial DOS in the vacancy sphere for $Ti^{[6]}Ti^{[4]}_3N_3\square_N$, (upper part of Figure 17) with the results of the KKR-CPA calculation [26,27] (lower part of Figure 17) for disordered $TiN_{0.75}$. For both calculations the first vacancy peak contains almost exclusively states with s symmetry in the vacancy sphere. The second peak contains according to the KKR-CPA calculation a smaller number of states with p symmetry and is not as pronounced as for the model structure.

Experimental evidence for the existence of a vacancy peak in the DOS has recently been given by photoemission [29,30,31], K [32] and L [33,34] X-ray emission spectroscopy. Changes in the density of the unoccupied states caused by non-metal atom vacancies were observed by energy loss spectroscopy [35].

For the discussion of the covalent bonds, in which the $Ti^{[4]}$ atoms participate, the subdivision of the $Ti^{[4]}$3d DOS into its components is of importance.

Figure 18 shows the subdivision of the $Ti^{[4]}$3d DOS into its components for the titanium nitride model structure.

The $Ti^{[4]}d_{x^2-y^2}$ DOS can be found in the "p band" and in the "d band" at higher energies, indicating that $Ti^{[4]}d_{x^2-y^2}$ orbitals take

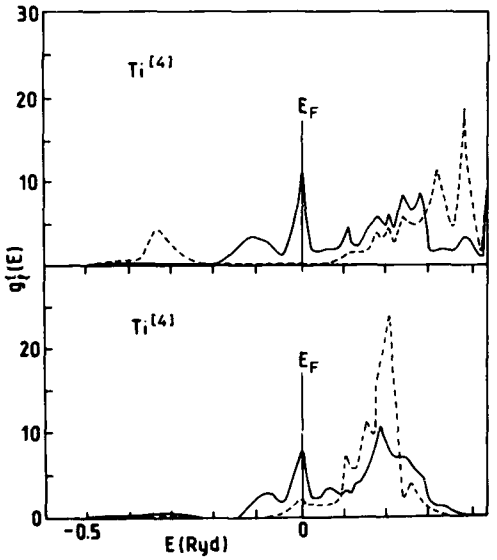

Figure 18. Subdivision of the local partial $Ti^{[4]}$3d DOS in ordered $TiN_{0.75}$. The same units and conventions as for Figure 15 are used. Top: $Ti^{[4]}d_{z^2}$ (——) and $Ti^{[4]}d_{x^2-y^2}$ (---) DOS. Bottom: $Ti^{[4]}$ (d_{xz}, d_{yz}) (——) and $Ti^{[4]}$ d_{xy} (---) DOS. (From Herzig et al. [28]. With permission.)

part in bonding and antibonding pd_σ interactions. The $Ti^{[4]}d_{z^2}$ and the $Ti^{[4]}(d_{xz}, d_{yz})$ components are found mainly in the energy range of the vacancy peaks. The $Ti^{[4]}d_{xy}$ states occur mostly in the unoccupied region of the "d band". The DOS derived from the KKR-CPA calculations [27] correspond well to the DOS obtained by the APW calculations [21, 28]. As an example the KKR-CPA DOS for TiC_x (x = 1.00; 0.94; 0.875; 0.76) are displayed in Figure 19.

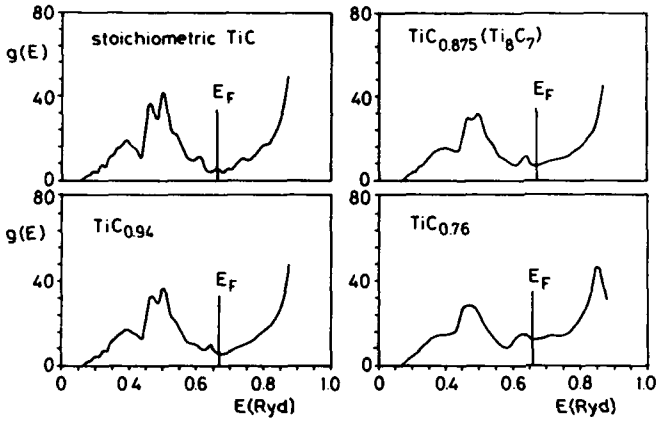

Figure 19. Total DOS of TiC_x phases according to the KKR-CPA calculations in units of electronic states per Rydberg and unit cell. (From Marksteiner [36]. With permission.)

The KKR-CPA results for the DOS of TiC_x and TiN_x can be summarized as follows:

1. All sharp peaks are smoothed with increasing vacancy concentration.
2. The peaks originating chiefly from the non-metal 2s and 2p states decrease.
3. Additional peaks ("vacancy peaks") appear near the minimum of the DOS of the stoichiometric compounds.
4. The DOS at the Fermi level increases with increasing vacancy concentration.
5. The peaks of the DOS with mainly Ti 3d character ("d band") are minimally affected by the introduction of vacancies.

3.4. Covalent Bonding

All three main types of covalent bonds (pd_σ, pd_π, dd_σ) discussed in conjunction with the stoichiometric compounds also occur in the model compounds, although modifications can be observed which may differ for carbide and nitride. In addition a new type of covalent interaction is encountered in the substoichiometric compounds.

The bonding situacion can be evaluated on the basis of electron density and difference electron density plots.

As previously mentioned, the d_{z^2} and $d_{x^2-y^2}$ orbitals on the $Ti^{[4]}$ atoms are no longer equivalent in the square ligand field of the four non-metal atom neighbours. Because the $Ti^{[4]}$ d_{z^2} orbitals extend towards the vacancy, they cannot form pd_σ bonds with the non-metal 2p orbitals. The number of pd_σ bonds is therefore reduced in relation to the stoichiometric compounds. The reduction of the Ti d_{z^2} DOS can be seen from Tables 1 and 2, which list the local partial Ti 3d charges inside the atomic spheres for ordered $TiC_{0.75}$ and $TiN_{0.75}$, respectively [21,28]. We find that the partial $Ti^{[4]}$ d_{z^2} charge in the "p band" is significantly lower than the $Ti^{[4]}$ $d_{x^2-y^2}$ charge.

TABLE 1. Split of the partial Ti 3d charge in TiC [8] and in ordered $TiC_{0.75}$. All charges are given in number of electrons per atomic sphere

	$TiC_{0.75}$						TiC	
	$Ti^{[4]}$				$Ti^{[6]}$		Ti	
Band	d_{z^2}	$d_{x^2-y^2}$	d_{xy}	(d_{xz},d_{yz})	e_g	t_{2g}	e_g	t_{2g}
p	0.09	0.39	0.21	0.26	0.80	0.69	0.84	0.78
vacancy	0.22	0.01	0.03	0.31	-	0.07		
occupied valence	0.33	0.44	0.24	0.57	0.89	0.76	0.94	0.78

TABLE 2. Split of the partial Ti 3d charge in ordered $TiN_{0.75}$ and in TiN. All charges are given in number of electrons per atomic sphere.

	$TiN_{0.75}$						TiN	
	$Ti^{[4]}$				$Ti^{[6]}$		Ti	
Band	d_{z^2}	$d_{x^2-y^2}$	d_{xy}	(d_{xz},d_{yz})	e_g	t_{2g}	e_g	t_{2g}
p	0.04	0.24	0.10	0.13	0.55	0.38	0.58	0.46
vacancy	0.33	0.01	0.09	0.51	0.01	0.41	0.01	0.58
occupied valence	0.38	0.27	0.19	0.64	0.61	0.79	0.65	1.05

A similar situation to that with the pd_σ bonds is observed with the pd_π bonds. The number of $Ti^{[4]}$ d_{xy} states in the "p band" is slightly reduced in passing from the stoichiometric to the substoichio-

metric compound, whereas the number of (d_{xz}, d_{yz}) states in the "p band" is greatly reduced. From these figures, it can be concluded that the number of pd_π bonds decreases as well.

However, the pd_σ and pd_π bonds in which $Ti^{[6]}$ atoms take part, are not significantly altered by the introduction of vacancies.

Whereas the number of titanium - non-metal bonds is reduced in the substoichiometric compounds, the Ti-Ti d-d bonds increase in importance.

Three types of Ti 3d - Ti 3d bonds can be distinguished in the model compounds $Ti^{[6]}Ti^{[4]}_3X_3\square_X$:

(i) The $Ti^{[4]}d_{xy}$ orbitals can form dd_σ bonds with $Ti^{[6]}t_{2g}$ orbitals, entirely analogous to the dd_σ bonds in the stoichiometric compounds. Calculation of the difference of the valence electron density between the ordered substoichiometric compound $TiX_{0.75}$ and the stoichiometric compound shows that the valence electron density in the $Ti^{[6]}$- $Ti^{[4]}$ direction increases in the carbide and decreases in the nitride with respect to the stoichiometric compound. This effect indicates a strengthening of the covalent bond between these two atoms in the carbide and a weakening in the nitride.

(ii) A new bond type is created by the introduction of vacancies. Examination of the valence electron density in the (100) plane of three typical vacancy states, displayed in Figure 20 for the model nitride [28], reveals that there is a distortion of the electron density around the $Ti^{[4]}$ atoms towards the vacancy. The appreciable amount of electronic charge in the vacancy sphere, found with these states, proves the occurrence of an interaction of the $Ti^{[4]}d_{z2}$ orbitals of the $Ti^{[4]}$ atoms across the vacancy, leading to a weak $Ti^{[4]}d_{z2}$ - $\square_X$ - $Ti^{[4]}d_{z2}$ σ bond. The bonding

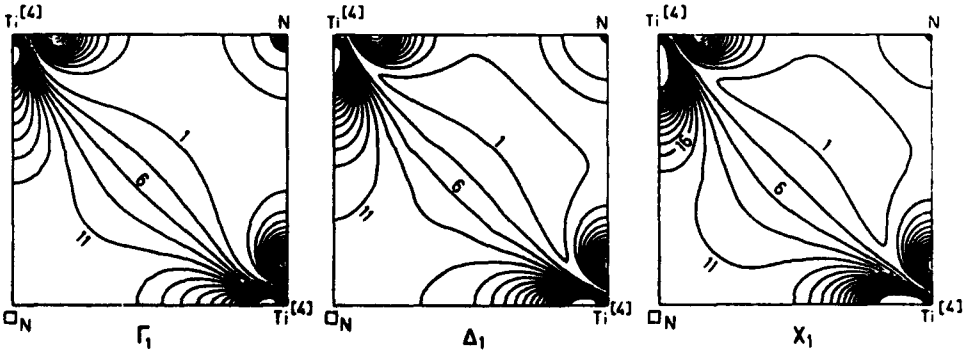

Figure 20. Valence electron densities for the "vacancy states" Γ_1, Δ_1, and X_1 of ordered $TiN_{0.75}$ in the (100) plane (cut 2) in units of 10^{-2} e/Å^3. (From Herzig et al. [28]. With permission.)

vacancy states involved in this type of a covalent bond are found in the energy range of the first vacancy peak in the DOS, as can be deduced from the local partial $Ti^{[4]}d_{z^2}$ DOS (Figure 18) and from the s character of the electronic charge in the vacancy sphere. The corresponding antibonding states with p-like electronic charge - i.e. a node in the vacancy sphere - are found in the second vacancy peak. Whereas in $TiC_{0.75}$ only the bonding $Ti^{[4]}d_{z^2} - \square_X - Ti^{[4]}d_{z^2}$ states in the first vacancy peak are occupied, in the nitride some of the antibonding counterparts are already situated below the Fermi level.

(iii) The third type of a covalent Ti-Ti bond is represented by the $Ti^{[4]}(d_{xz}, d_{yz}) - Ti^{[4]}(d_{xz}, d_{yz})$ interaction. Because the number of pd_π bonds is reduced in the substoichiometric compounds, the $Ti^{[4]}d_{xz}$ and $Ti^{[4]}d_{yz}$ orbitals can form better overlapping dd_σ bonds. These bonds are oriented along the edges of the octahedra formed by the $Ti^{[4]}$ atoms surrounding a vacancy. This type of bonding can be recognized from the electron density plot in the (111) plane of a special state (X_3) of the model nitride (Figure 21).

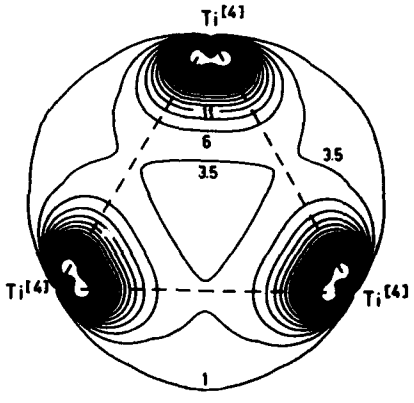

Figure 21. Valence electron density for the state X_3 of ordered $TiN_{0.75}$ in the (111) plane in units of 10^{-2} e/Å^3. (From Herzig et al. [28]. With permission.)

The strengthening of the $Ti^{[4]}(d_{xz}, d_{yz}) - Ti^{[4]}(d_{xz}, d_{yz})$ σ bonds in the model carbide compared to the Ti t_{2g} – Ti t_{2g} σ bonds in stoichiometric TiC can be gathered from Figure 22, which shows the difference between the valence electron density of the substoichiometric and the stoichiometric carbide in the (111) plane [37]. The solid lines indicate an increase, the dashed lines a decrease in electron density. It should be noted that the negative spherical difference between the triangular arrangement of the $Ti^{[4]}$ atoms is caused by the carbon atom which lies below or above the center of the triangle in stoichiometric TiC and which is missing in the

substoichiometric compound.

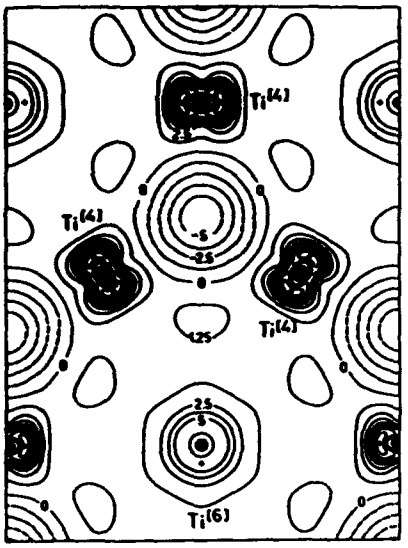

Figure 22. Difference between the valence electron densities of ordered $TiC_{0.75}$ and TiC (omitting the electron density of the "s band") in the (111) plane in units of 10^{-2} e/Å^3. (From Redinger *et al.* [37]. With permission.)

Because in the substoichiometric nitride a larger number of $Ti^{[4]}(d_{xz}, d_{yz})$ states is occupied than in the corresponding carbide, a greater stabilization of the $Ti^{[4]}$ octahedra is to be expected.

Although the conclusions regarding the chemical bonding are based on a hypothetical model structure, it can be assumed that they retain their principal validity even in the case of randomly distributed vacancies. From the fact that both the long range order and the random distribution of vacancies yield a similar DOS, it can be concluded that the present description of the electronic structure of the substoichiometric compounds is essentially correct.

ACKNOWLEDGEMENTS

The support obtained by the "Hochschuljubiläumsstiftung der Stadt Wien" is greatly acknowledged. The author appreciates valuable discussions with Dr.R.Eibler and Prof.P.Herzig.

REFERENCES

[1] Calais, J.-L. (1977) 'Band structure of transition metal compounds', Adv. Phys. 26, 847-885.

[2] Neckel, A. (1983) 'Recent investigations on the electronic structure of the fourth and fifth group transition metal monocarbides, mononitrides, and monoxides', Int. J. Quantum Chem. 23, 1317-1353.

[3] Schwarz, K. and Neckel, A. (1986) 'Chemical bonding in refractory transition metal compounds', in E. A. Almond, C. A. Brooks, and R. Warren (eds.), Proc. 2nd. Int. Conf. Hard Materials, Inst. Phys. Conf. Ser. No 75, 45-60.

[4] Schwarz, K. (1987) 'Band structure and chemical bonding in transition metal carbides and nitrides', in CRC Critical Reviews in Solid State and Materials Science 13, issue 3, 211-257.

[5] Slater, J. C. (1937) 'Wave Functions in a Periodic Potential', Phys. Rev. 51, 846-851.

[6] Koelling, D. D. and Arbman, G. O. (1977) 'Use of energy derivative of the radial solution in an augmented plane wave method: application to copper', J. Phys. F. 5, 2041-2053.

[7] Slater, J. C. (1968) 'Quantum Theory of Matter', McGraw-Hill, New York.

[8] Neckel, A., Rastl, P., Eibler, R., Weinberger, P., and Schwarz, K. (1976) 'Results of self-consistent band structure calculations for ScN, ScO, TiC, TiN, TiO, VC, VN and VO', J. Phys. C. 9, 579-592.

[9] Neckel, A., Rastl, P., Eibler, R., Weinberger, P., and Schwarz, K. (1976) 'Results of self-consistent band structure calculations for ScN, ScO, TiC, TiN, TiO, VC, VN, and VO', report obtainable from the British Library under the Supplementary Publication Scheme, Ref. No. SUP 700 17.

[10] Eibler, R., Dorrer, M., and Neckel, A. (1983) 'Partial LCAO densities of states for ScN, TiN, ZrN, and ScP', Theoret. Chim. Acta 63, 133-141.

[11] Neckel, A., Schwarz, K., Eibler, R., Weinberger, P., and Rastl, P. (1975) 'Bandstruktur des Festkörpers - Interpretation der chemischen Bindung in einigen Übergangsmetallverbindungen aufgrund von Bandstrukturrechnungen', Ber. Bunsenges. Phys. Chem. 79, 1053-1063.

[12] Schwarz, K. and Blaha, P. (1983) 'Electron densities in solid compounds' in J. P. Dahl and J. Avery (eds.), Local density approximations in Quantum Chemistry and Solid State Physics, Plenum Press, New York, pp. 605-616.

[13] Blaha, P. and Schwarz, K. (1983) 'Electron densities and chemical bonding in TiC, TiN, and TiO derived from energy band calculations', Int. J. Quantum Chem. 23, 1535-1552.

[14] Redinger, J. (1983), private communication.

[15] de Novion, C. H. and Landesman, J. (1985) 'Order and disorder in transition metal carbides and nitrides: experimental and theoretical aspects', Pure a. Appl. Chem. 10, 1391-1402.

[16] Storms, E. K. (1967) The Refractory Carbides, Academic Press, New York,

[17] Goretzki, H. (1967) 'Neutron diffraction studies on titanium-carbon and zirconium-carbon alloys', phys. stat. sol. 20, K141-K143.

[18] Moisy-Maurice, V., de Novion, C. H., Christensen, A. N., and Just, W. (1981) 'Elastic diffuse neutron scattering study of the defect structure of $TiC_{0.76}$ and $NbC_{0.73}$', Solid State Comm. 39, 661-665.

[19] Moisy-Maurice, V., Lorenzelli, N., de Novion, C. H., and Convert, P. (1982) 'High temperature neutron diffraction study of the order-disorder transition in TiC_{1-x}', Acta Met. 30, 1769-1779.

[20] Wriedt, H. A. and Murray, J. L. (1987) 'The N-Ti system', Bulletin of alloy phase diagrams 8, 378-412.

[21] Redinger, J., Eibler, R., Herzig, P., Neckel, A., Podloucky, R., and Wimmer, E. (1985) 'Vacancy induced changes in the electronic structure of titanium carbide - I. Band structure and density of states', J. Phys. Chem. Solids 46, 383-398.

[22] Schwarz, K. and Rösch, N. (1976) 'Effects of carbon vacancies in NbC on superconductivity', J. Phys. C. 9, L433-L437.

[23] Ries, G. and Winter, H. (1980) 'Electronic structure of vacancies in refractory compounds and its influence on T_c', J. Phys. F. 10, 1-7.

[24] Huisman, L. M., Carlson, A. E., Gelat, C. D., and Ehrenreich, H. (1980) 'Mechanisms for energetic-vacancy stabilization: TiO and TiC', Phys. Rev. B22, 991-1006.

[25] Wimmer, E., Schwarz, K., Podloucky, R., Herzig, P., and Neckel, A. (1982) 'The effect of vacancies on the electronic structure of NbO', J. Phys. Chem. Solids 43, 439-447.

[26] Klima, J., Schadler, G., Weinberger, P., and Neckel, A. (1985) 'On the electronic structure of TiN_x', J. Phys. F: Met. Phys. 15, 1307-1320.

[27] Marksteiner, P., Weinberger, P., Neckel, A., Zeller, R., and Dederichs, P. H. (1986) 'Electronic structure of substoichiometric carbides and nitrides of titanium and vanadium', Phys. Rev. B33, 812-822.

[28] Herzig, P., Redinger, J., Eibler, R., and Neckel, A. (1987) 'Vacancy induced changes in the electronic structure of titanium nitride', J. Solid State Chem. 70, 281-294.

[29] Höchst, H., Bringans, R. D., Steiner, P., and Wolf, T. (1982) 'Photoemission study of the electronic structure of stoichiometric and substoichiometric TiN and ZrN', Phys. Rev. B25, 7183-7191.

[30] Porte, L., Roux, L., and Hanus, J. (1983) 'Vacancy effects in the x-ray photoelectron spectra of TiN_x', Phys. Rev. B28, 3214-3224.

[31] Bringans, R. D. and Höchst, H. (1984) 'Photoemission resonance effects in the nitrides of titanium and zirconium, Phys. Rev. B30, 5416-5420.

[32] Beauprez, E., Hague, C. F., Mariot, J.-M., Teyssandier, F., Redinger, J., Marksteiner, P., and Weinberger, P. (1986) 'X-ray emission spectroscopy study of vacancy-induced electronic states in substoichiometric TiN_x', Phys. Rev. B34, 886-890.

[33] Gubanov, V. A., Kurmaev, E. Z., and Ellis, D. E. (1981) 'Valence states of titanium atoms in non-stoichiometric carbides: x-ray emission spectra and cluster calculations', J. Phys. C: Solid State Phys. 14, 5567-5574.

[34] Kucherenko, Yu. N., Sheludchenko, L. M., Khrinovsky, V. Z., and Nemoshkalenko, V. V. (1984) 'Study of the electron states in nonstoichiometric titanium nitrides by the X_α-scattered-wave method', J. Phys. Chem. Solids 45, 319-322.

[35] Pflüger, J., Fink, J., Crecelius, G., Bohnen, K. P., and Winter, H. (1982) 'Electronic structure of unoccupied states of TiC, TiN, and VN by electron-energy-loss-spectroscopy', Solid State Comm. 44, 489-492.

[36] Marksteiner, P. (1987) 'Elektronische Struktur nichtstöchiometrischer Verbindungen: Hartstoffe und Hochtemperaturlegierungen. Theorie der winkelintegrierten Photoemission im Röntgenbereich: Hartstoffe und heavy Fermiions',thesis, Technical University, Vienna.

[37] Redinger, J., Eibler, R., Herzig, P., Neckel, A., Podloucky, R., and Wimmer, E. (1986) 'Vacancy induced changes in the electronic structure of titanium carbide - II. Electron densities and chemical bonding', J. Phys. Chem. Solids 47, 387-393.

FURTHER ELECTRONIC STRUCTURE STUDIES OF BORON AND BORON-RICH BORIDES

D.W. BULLETT
School of Physics
University of Bath
Claverton Down
Bath, BA2 7AY, UK

ABSTRACT. Calculations of electronic structure are reported for a range of boron–rich solids: α– and β– rhombohedral boron, tetragonal boron, and compounds of boron with carbon, silicon, phosphorus, and arsenic.

1. Introduction

This paper forms part of a continuing study of the electronic structure of boron and boron-rich compounds. Since our earlier reports [1,2] there have been considerable developments, both in crystal structure determinations for this class of materials, some of which contain very complex networks of boron-boron bonds, and in the computational power that makes such electronic structure calculations possible. As before, we use an atomic basis of 2s and 2p orbitals on each boron site and a local approximation to the potential, in a non–empirical calculation of the electron states in each crystallographic arrangement.

Boron continues to present to us, in its elemental forms and in the structures of the higher borides, the richest variety of crystal structures of any of the elements. Common to many of these structures is the tendency to form relatively large polyatomic groups – the B_6 octahedron, the B_{12} cuboctahedron, and above all the B_{12} icosahedron, as well as larger units such as M_{15} (in BeB_3 [3] and SiB_6 [4], B_{19} (in AlB_{12} [5,6] and β–tetragonal boron [7]) and B_{28} (in β–rhombohedral boron [8]); compared to some of these, other boride structures containing infinite chains, multiple chains, and planar networks appear relatively mundane. The distribution of molecular orbitals within these polyhedra can make them quite stable, and provided their outward–pointing valence orbitals can be saturated, for example with hydrogen, stable molecular clusters can form in isolation. Extra constraints in the solid state are imposed by the need to pack these polyhedra into a three–dimensional network which will allow full valence satisfaction of the outward–pointing orbitals (or "dangling bonds") of every cluster; in the boron–rich borides the way in which

R. Freer (ed.), The Physics and Chemistry of Carbides, Nitrides and Borides, 513–524.
© 1990 *Kluwer Academic Publishers. Printed in the Netherlands.*

B_n polyhedra bond together can depend more on the size and valence of the other constituent atoms than on their electronegativity.

In all these compounds the driving force for chemical bonding is the covalent interaction between s and p orbitals on neighbouring boron atoms, but the conventional two–electron pair–bond picture does not generally apply. Boron shares with its neighbour in the periodic table, carbon, an s–p excitation energy which is in some sense anomalously small (because there is no pseudopotential cancellation for its p–orbital), inducing a strong desire to form covalently bonded networks. However, unlike carbon, boron is intrinsically electron deficient: it simply does not have enough electrons to create three–dimensional networks of two–centre electron–pair bonds. Instead, boron chemistry is dominated by the tendency of B atoms to form covalently bonded clusters, and in the solid state these are most often comprised of 12 atoms.

2. Rhombohedral crystal structures containing boron–rich icosahedra

The compounds α–boron, boron carbide, boron phosphide, boron arsenide, and $B_{2.89}Si$ [9] all have the same underlying structure [10]: icosahedral units are bonded together with direct intercluster B–B bonds, as well as other linkage units. All these materials crystallise in the space group $R\bar{3}m$, and either a primitive rhombohedral unit cell (with $a_R \approx 5$ Åand $\alpha \approx 65°$) or a hexagonal unit cell of three times larger volume (with $a_h \approx 6$ Åand $c_h \approx 12$ Å) may be assigned. Table 1 summarises some of the crystallographic data. In the case of boron carbide, at least beyond the $B_{13}C_2$ composition, and in the boron silicide structure which is reported to have a composition near $B_{2.89}Si$, there is substantial substitution of non–boron atoms within the icosahedra.

Table 1. Structural data for crystals related to α–rhombohedral boron [10]

	α–boron	$B_{12}P_2$	$B_{12}As_2$	$B_{13}C_2$
a_h (Å)	4.927	6.000	6.156	5.617
c_h (Å)	12.564	11.857	11.929	12.137
B_1 x	-.1368	-.1770	-.1823	-.1629
z	.3576	.3619	.3619	.3585
B_2 x	-.1187	-.1046	-.1030	-.1076
z	.1088	.1175	.1190	.1139
P/As/C/Si x		0	0	0
z		.4054	.3998	.3817
B_3 x				0
z				$\frac{1}{2}$
(y=−x)				

The molecular orbital structure of the B_{12} icosahedral unit has already been discussed in detail elsewhere [1,2]. The stability of the unit requires saturation of the outward pointing "dangling bond" at each vertex – the relatively weak interactions between these 12 sp radial hybrids within the icosahedron generate the 12 molecular orbitals of s_g, t_{1u}, t_{2u} and v_g representations labelled *non-bonding* in Table 2. The remaining three orbitals at each vertex interact much more strongly with orbitals on their five nearest-neighbour atomic sites within the cluster, to produce 13 bonding and 23 antibonding molecular orbitals. Thus in an ideal closed-shell environment the B_{12} icosahedral cluster would require not 36 but 38 electrons: 26 to satisfy the bonding requirements within the cluster and 12 to establish external two-centre bonds from each vertex. The occupied charge configuration of each boron atom turns out to be near s^1p^2, compared to the s^2p^1 configuration of the isolated atom.

Table 2. Molecular orbitals for the B_{12} icosahedral cluster. Orbitals in italics are non-bonding within the cluster but are ready to bond to neighbouring clusters. (Isolated atom energy levels are $E_s = -11.1$eV, $E_p = -5.7$eV.)

	Energy, eV	degeneracy	symmetry
	13.9	3	t_{2u}
	12.7	5	v_g
unfilled	9.5	3	t_{1u}
states	5.8	3	t_{1g}
	3.5	5	v_u
	1.1	4	u_g
	−3.8	*5*	v_g
	−4.7	*3*	t_{2u}
	−4.8	*3*	t_{1u}
occupied	−6.6	4	u_u
states	*−8.1*	*1*	s_g
	−10.4	5	v_g
	−14.9	3	t_{1u}
	−23.2	1	s_g

Elemental boron would not have sufficient electrons to bond a three-dimensional lattice of icosahedra in such a way that conventional bonds between icosahedra are established at every atom, even if this arrangement were geometrically possible. (We note in passing that the B_{156} unit, comprising an icosahedron completely surrounded by 12 icosahedra, does occur in phases such as YB_{66}.) The simplest structure which comes close to satisfying this criterion is the α-rhombohedral structure

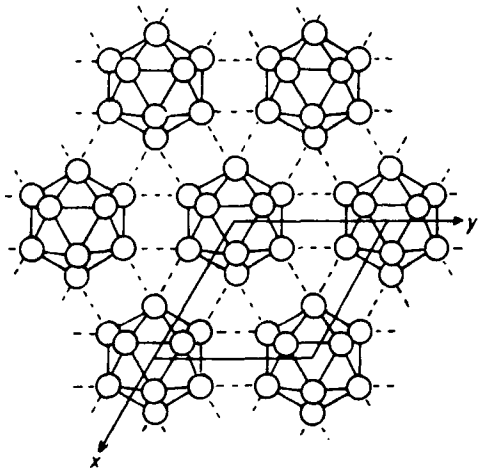

Figure 1. The α–rhombohedral structure viewed down the 3–fold axis. Broken lines symbolise the three–centre bonds linking adjacent icosahedra in the basal plane.

(Figure 1), which contains just one (distorted) icosahedron in the unit cell oriented with a 3–fold axis along the rhombohedral [111] direction. The icosahedra pack together in close–packed layers in such a way that six of the atoms in each cluster (the B(2) sites in Table 1) do establish nearly ideal external pair–bonds to clusters in adjacent layers, while the remaining four electrons per B_{12} unit must be assigned to 3–centre bonds linking icosahedra within the same layer. The calculated density of states for electrons in the α–rhombohedral structure, and the relative contributions to these states from the B(1) and B(2) sites, are shown in Figure 2. Within the approximations of this calculation, minimum indirect and direct gaps were found to be 1.7 and 2.3 eV respectively, while over most of reciprocal space the direct gap was $\approx$ 3–4eV. It is interesting to note in this spectrum that the states right at the top of the valence band (between -4 and -6eV in the energy scale of figure 2) originate almost entirely from B(1) atoms, and can be identified as the signature of the "three-centre" bonds. The weakness of these bonds is also evident from the abnormally long B–B distances involved: 0.202 nm compared to 0.175–0.180 nm within the icosahedron and 0.167 nm in the "two–centre" inter–cluster links.

One way to stabilise the structure, by replacing the weak three–centre bonds by strong, radial pair–bonds, is to introduce additional atoms in the octahedral interstices between the layers of icosahedra. This is precisely what happens in the remaining compounds of this section. In $B_{12}P_2$ and $B_{12}As_2$, P_2 or As_2 pairs oc-

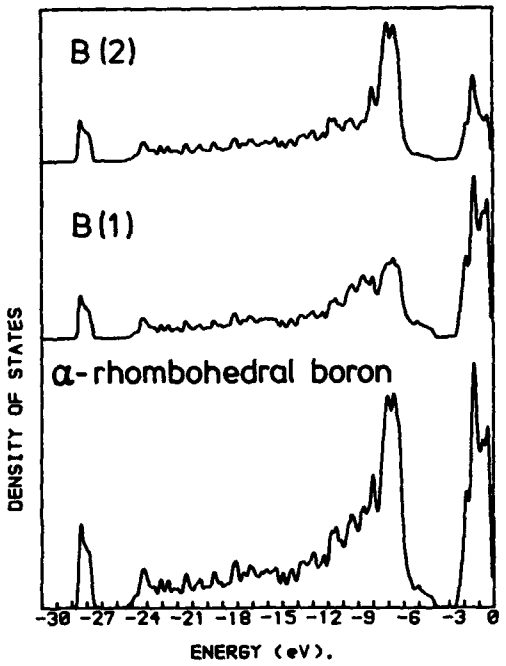

Figure 2. Calculated density of states for electrons in α–rhombohedral boron, showing the contributions from B(1) and B(2) sites.

cupy these sites, and the electron count is just right for each interstitial atom to establish conventional pair–bonds to B atoms in three neighbouring icosahedra as well as with the other atom of the interstitial pair. The associated bond lengths are 0.191 nm for the P–B and 0.224 nm for P–P linkages (and 0.199nm for As–B, 0.239nm for As–As). With the removal of the three–centre bonds, the occupied band of electron states now cuts off much more sharply at its maximum energy (figure 3). The gap between valence and conduction band edges increases to about 4 (3.5) eV, although within this gap there is a single localized peak arising from the antibonding P–P (or As–As) molecular orbital about 1.7 (or 1.5) eV above the valence band edge. Correlation effects which we have neglected here mean that transitions into this localized state will actually require a somewhat larger energy, and we should therefore expect the crystals to be transparent and colourless at perfect stoichiometry. In practice, grown crystals can show both colourless and blue–black regions, even in adjacent regions of the same single–crystal boule [10], presumably arising from slight changes in stoichiometry and disordering effects.

The case of boron carbide appears to be rather more complicated. Here a three–

atom chain occupies the octahedral interlayer site, and the structure forms over a range of stoichiometries containing 9 – 20 at% carbon, ending at the carbon–rich composition B_4C. Crystallographic studies suggest that the central atom of the chain is always boron, and that in the carbon–rich crystals C is statistically substituted for B within the icosahedron: B_4C occurs as a $(B_{11}C)(CBC)$ configuration. Experimental C–B linkages to icosahedra are 0.161 nm, and 0.144 nm within the chain. The distribution of electron states in figure 4 was calculated for an ideal $B_{13}C_2$=$(B_{12})(CBC)$ configuration of atomic sites within the unit cell.

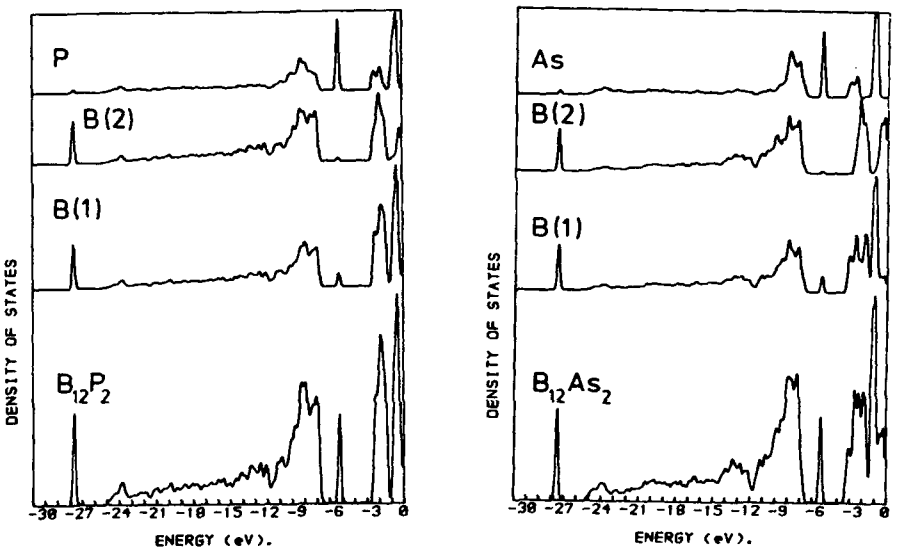

Figure 3. Calculated electronic structures of $B_{12}P_2$ and $B_{12}As_2$.

The upper edge of the valence band again shows a sharp cut–off (just above –6eV on the energy scale of the figure), and complete filling of this valence band requires 24 electron pairs per unit cell, i.e. the composition $B_{12}C_3$. All electrons can thus be assigned to pair bonds. The main gap to conduction band states of the boron network has now expanded to almost 5eV, although 1eV below this conduction band edge we can see a band of states associated with the two B–C antibonds within the chain, and consequently strongly localised on the intrachain boron atom. Electron transfer from this central B atom to the icosahedra, as well as to the outer C atoms of the CBC chain, leave this atom with an electron deficit which is clearly visible in the occupied part of its projected density of states of figure 4. Formally this B atom has only two bonds giving a B^+ configuration; the more electronegative nature of

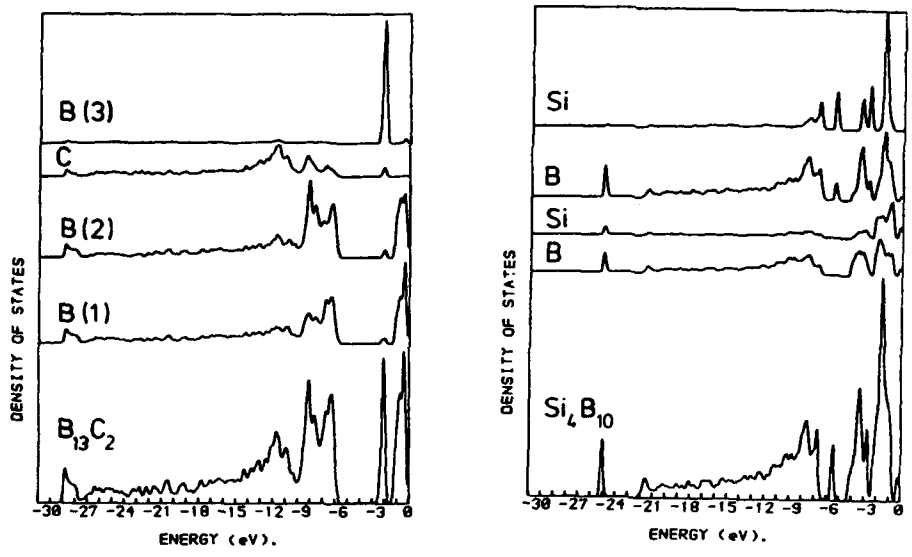

Figure 4. Densities of states in boron carbide and boron silicide, modelled by the idealised structures $B_{13}C_2$ and $B_{10}Si_4$ respectively. For the silicide, projections are shown on silicon atoms in both icosahedral and paired sites.

the two atoms to which it is bonded increase this charge further. It is immediately clear on electonegativity grounds that carbon compositions between $B_{13}C_2$ and $B_{12}C_3$ are likely to lead to C substitution by carbon within the icosahedron, rather than at the central site of the three-atom chain.

Substitution within the icosahedron appears to proceed much further in the case of the boron silicide phase of low boron content, said to have a composition near $B_{2.89}Si$ [9]. Silicon being so much larger than carbon, the structure is able to accommodate only a pair of Si atoms in the sites between icosahedra, and additional substitution within the B_{12} unit is required in order to supply the structure with a sufficient number of electrons. In calculating the density of states in figure 4 the "ideal" composition $B_{10}Si_4 = (B_{10}Si_2)(Si_2)$ was assumed, with Si substituting for two of the B atoms within the icosahedron.

At this composition, i.e. $B_{2.5}Si$, the valence band would be completely filled. In reality it may be that the competition between the bonding energy gained by silicon substitution in (and electron donation to) the lattice and the strain energy introduced by the substitutional atoms, causes the stable composition to occur at $B_{2.89}Si$, leaving just a few holes at the top of the valence band. The resulting density of states does not seem to be sensitive to the particular choice of substitutional

sites. The projected density of states on the Si atoms appears very similar to that of the B atoms which they are replacing, and very different from the projections on the Si atoms of the interstitial Si_2 pairs.

2. The β–rhombohedral boron structure

The stable high-temperature structure of boron, that is in equilibrium with the melt at atmospheric pressure, is the much more complex β-rhombohedral form. A full analysis of the location of all atoms in this structure has taken many years. While the observed density was reported to correspond to 324 atoms per hexagonal unit cell, only 315 could be located in the first x–ray studies. Several studies attributed the discrepancy to disorder and partial occupation of sites. The most recent reinvestigation concluded that there are 320 atoms occupying 20 different symmetry–equivalent atomic positions within the unit cell, and six of the 20 are partially occupied [8]. The basic structural component is again the icosahedron.

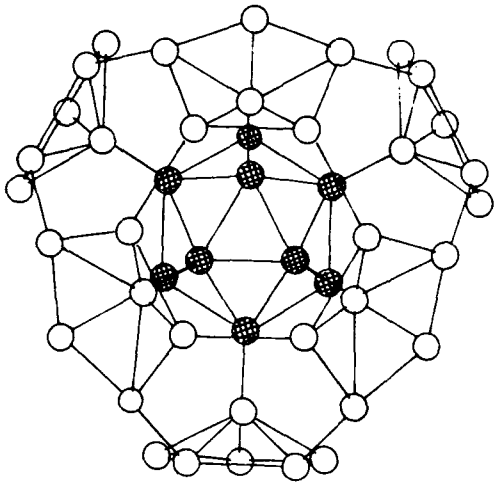

Figure 5. Part of the 84–atom unit from the β–rhombohedral structure. Six of the 12 half–icosahedra surrounding the central (shaded) icosahedron link directly together along the rhombohedral cell edges.

In each rhombohedral cell 84 boron atoms take up positions B(1) – B(10) forming a central icosahedron linked at each vertex to a half icosahedron. Six of these 12 half–icosahedra join with their neighbours to form complete icosahedra along the rhombohedral axes; the others are each connected to half–icosahedra from two

neighbouring B_{84} units by a B_{10} unit (B(11) – B(14)), itself consisting of a condensate of three half–icosahedra. The two primary clusters are thus the B_{12} icosahedron and a more complex B_{28} unit. Of the 320 atoms per hexagonal cell, 312 form a rigid three–dimensional boron network in which the local environment resembles part of an icosahedron. In addition there are non-icosahedral boron positions: three atoms per hexagonal cell in the fully occupied, octahedrally coordinated B(15) site and five partially occupied sites, one of which, B(16), appears to induce vacancies in some of the B(13) sites.

Figure 6 shows the resulting spectrum of electron states for an ordered model of the crystal in which sites (1) – (15) are fully occupied by boron atoms, and sites (16) – (20) are empty, i.e. a model with 315 atoms in the hexagonal unit cell. This network of boron bonds again induces a substantial gap (≈3eV) in the energy spectrum, but the valence band is capable of holding 3x320 electrons per hexagonal cell, slightly more than there are available in this idealised model. We see immediately the driving force that induces the true β–rhombohedral structure to contain a further 5 boron atoms per hexagonal cell, in disordered interstitial sites: it is tempting to conclude that the role of these extra atoms is to donate electrons to the covalent bonding states of the boron framework.

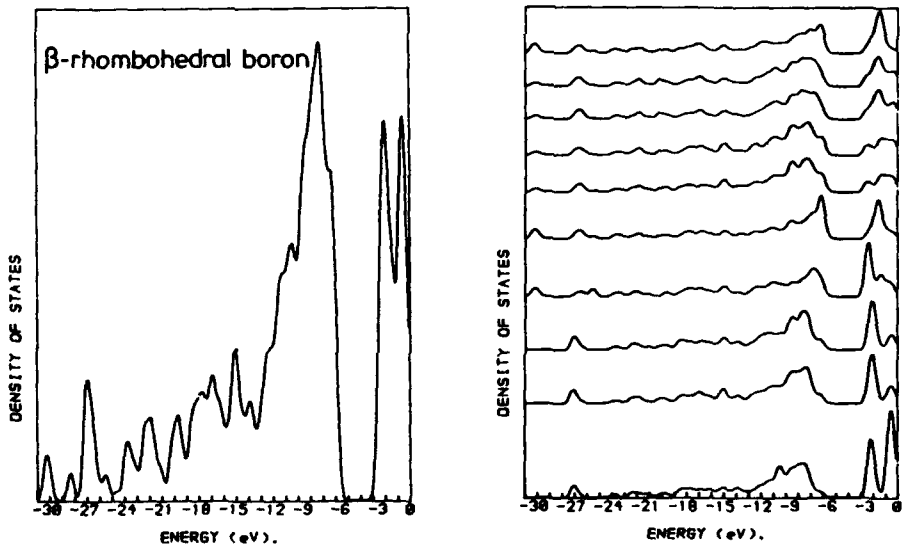

Figure 6. The calculated density of states in β–rhombohedral boron, and its projection on different sites within the structure.

The space filling of the network in β–rhombohedral boron is about 36%, and leaves plenty of opportunity for alternative dopant atoms to enter the structure. Detailed x–ray studies of the atomic positions of various transition–metal dopants have recently been reported [11-14], and the associated modifications to the local electronic structure will be recorded elsewhere.

3. The α–AlB_{12} structure and β–tetragonal boron

Two tetragonal forms of boron have been reported in the past. The alpha form is now known to correspond, in fact, to tetragonal boron–rich phases in which a three–dimensional network of B_{12} icosahedra is stabilised by foreign atoms such as C or N; the necessity for the presence of such atoms to donate electrons to the boron network has been discussed previously [1,2].

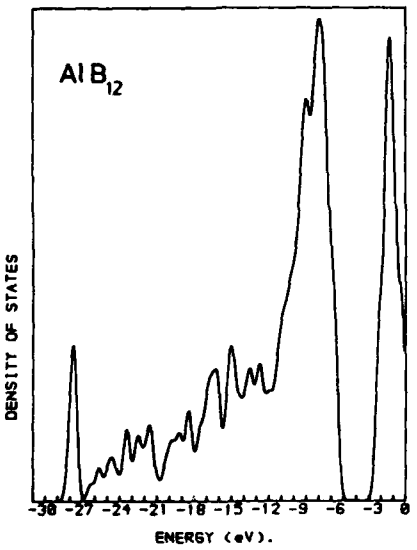

Figure 7. Calculated density of states for an idealised model of the α–AlB_{12} structure, with 192 atoms in the tetragonal unit cell.

The second tetragonal form, referred to variously as β–tetragonal, tetragonal II or tetragonal III, is a true modification of pure elemental boron, with a structure closely related to that of α–AlB_{12}. The three-dimensional framework contains B_{12} icosahedra, B_{19} units, and single B atoms; the B_{19} unit is formed by a pair of icosahedra sharing one triangular face and losing an apex atom on each side.

The unit cell is large: in the case of AlB_{12} it is reported to contain $8B_{12}$ icosahedra, $4B_{19}$ units, 4 single B atoms, and 13.0 Al atoms statistically distributed over five interstitial sites in the boron framework. In order to model the structure in an ordered lattice, we assumed that two of the Al sites were fully occupied by Al, and the others were empty. The resulting density of states is shown in figure 7. Space precludes any detailed discussion of the bonding in this arrangement; we merely note that once again this framework induces a separation of about 2eV between valence and conduction bands. The valence band is calculated to accommodate 284 electron pairs per tetragonal unit cell. For this model of the structure, with 16 Al atoms per unit cell, the lattice would be left with an excess of 4 electron pairs after filling all valence band states; if the Al atoms can be considered as donating electrons directly into the electron-deficient boron framework (just like the interstitial atoms in the β-rhombohedral boron structure), complete valence satisfaction would occur at an Al concentration of $13\frac{1}{3}$ Al atoms per unit cell, very close to the experimentally observed value.

References

1. Bullett, D.W. (1982) "Structure and bonding in crystalline boron and $B_{12}C_3$" J. Phys. C. **15** 415.

2. Bullett, D.W. (1985) "Electronic structure studies of boron and boron-rich borides" AIP Conf. Proceedings 140, "Boron-Rich Solids" eds. D. Emin, T. Aselage, C.L. Beckel, I.A. Howard and C. Wood, 249.

3. Mattes, R., Tebbe, K.-F., Neidhard, H. and Rethfeld, H. J. (1976) "The Crystal Structure of BeB_3" J. Less Common Metals **47**, 29.

4. Vlasse, M., Slack, G.A., Garbauskas, M. and Viala, J.C. (1986) "The Crystal Structure of SiB_6" J. Solid St. Chem. **63**, 31.

5. Higashi, I., Sakurai, T. and Atoda, T. (1977) "Crystal Structure of α-AlB_{12}" J. Solid St. Chem. **20**, 67.

6. Kasper, J.S., Vlasse, M. and Naslain, R. (1977) "The α-AlB_{12} structure" J. Solid St. Chem. **20**, 281.

7. Vlasse, M., Naslain, R., Kasper, J.S. and Ploog, K. (1978) "Crystal Structure of Tetragonal Boron Related to α-AlB_{12}" J. Solid St. Chem. , 289.

8. Slack, G.A., Hejna, C.I., Garbauskas, M.F. and Kasper, J.S. (1988) "The Crystal Structure and Density of β-Rhombohedral Boron" J. Solid St. Chem. **76** 52.

9. Magnusson, B. and Brosset, C. (1962) "The Crystal Structure of $B_{2.89}Si$" Acta Chemica Scandinavica **16**, 449.

10. Morosin, B., Mullendore, A.W., Emin, D. and Slack G.A. (1985) "Rhombohedral Crystal Structure of Compounds Containing Boron-Rich Icosahedra" AIP

Conf. Proceedings 140, "Boron–Rich Solids" ed. D. Emin, T. Aselage, C.L. Beckel, I.A. Howard and C. Wood, 70.

11. Lundström, T. (1985) "The Structure and Bonding of Solid Solutions of Transition and p–Elements in β–Rhombohedral Boron" AIP Conf. Proceedings **140**, "Boron–Rich Solids" ed. D. Emin, T. Aselage, C.L. Beckel, I.A. Howard and C. Wood, 19.

12. Wong, J. and Slack, G.A. (1986) "EXAFS and XANES Study of Vanadium in β–Rhombohedral Boron" J. Solid St. Chem. **61**, 203.

13. Garbauskas, M.F., Kasper, J.S. and Slack, G.A. (1986) "The Incorporation of Vanadium in β–Rhombohedral Boron as Determined by Single–Crystal Diffractometry" J. Solid St. Chem. **63**, 424.

14. Slack, G.A., Hejna, C.I., Garbauskas, M. and Kasper, J.S. (1988) "X–ray Study of Transition–Metal Dopants in β–Boron" J. Solid St. Chem. **76**, 64.

THE ELECTRONIC STRUCTURE OF CRYSTALLINE BORON CARBIDE I: B_{12} ICOSAHEDRA AND C-B-C CHAINS

A. C. SWITENDICK
Solid State Theory, 1151
Sandia National Laboratories
Albuquerque, New Mexico 87185
U. S. A.

ABSTRACT. The one-electron energy levels of boron carbide, $B_{12}C_2$, consisting of B_{12} icosahedra and C-B-C chains have been calculated self-consistently. Calculations for B_{12} icosahedra without the chains and for C-B-C chains without the icosahedra were performed using the same crystal geometry for comparison. Charge density plots of the total charge densities and individual orbital densities are given to elucidate the nature of the interactions between the atoms of the icosahedra and chains.

1. Introduction

I have calculated the one-electron energy levels of crystalline boron carbide, $B_{12}C_2$ using the linearized augmented plane wave (LAPW) method[1]. The Hedin-Lundqvist[2] form of the exchange-correlation potential was used. The calculations were iterated to self-consistency. Although the muffin tin approximation[3] was used for the crystalline potential, charge density plots show that the wave function and charge density solutions are not restricted to this form. Calculations[4] for α-boron and related systems showed little influence of the muffin-tin approximation on the eigenvalues, their ordering, or the charge distributions. Full potential (FLAPW)[5] calculations are probably needed to get accurate total energies; although an evaluation using final total charge density and related potential may be adequate[6].

The concern of this paper is the nature of the interaction between the atoms; of the icosahedron, of the chain, and of the icosahedra with the chains. To this end I have also performed calculations for: $B_{12}Z$-Z-Z, boron icosahedra with the chain replaced by spheres of zero charge; Z_{12}C-B-C, a C-B-C chain in the crystalline arrangement with the icosahedral boron atoms replaced by spheres of zero nuclear charge. From comparisons of the energy levels and charge distributions for these structures, one can attempt to sort out the relevant interactions and the underlying electronic structure.

R. Freer (ed.), The Physics and Chemistry of Carbides; Nitrides and Borides, 525–553.
© 1990 *Kluwer Academic Publishers. Printed in the Netherlands.*

The crystal structure parameters of Morosin[7] were used. The structure is shown in Figure 1. For this calculation only boron atoms are located on the icosahedra, with no carbon substitutions, as presumably occurs for boron carbide of composition B_4C[7]. The unit cell contains six polar borons, B2, forming triangular planes at the top and bottom of the icosahedra. Each of these polar atoms is bonded[8] to two other polar atoms in its plane and to a polar atom in the icosahedron above or below it. It is also bonded to three of the six atoms, B1, which form a puckered hexagon around the middle of the icosahedra. Each of these equatorial atoms is bonded to three polar atoms, two other equatorial atoms and one of the carbons, C, forming the end of a C-B-C chain. Thus each icosahedral atom forms five bonds with other atoms of the icosahedra and one external bond. Each chain end(carbon) is bonded to three equatorial B1s (in different icosahedra) and the central boron, B3. A three fold axis passes through the center of the polar triangles and the C-B-C chains located halfway up the rhombohedral axis. The space group is $R\bar{3}m(D_{3d}^5)$. The relevant distances are given in Table 1.

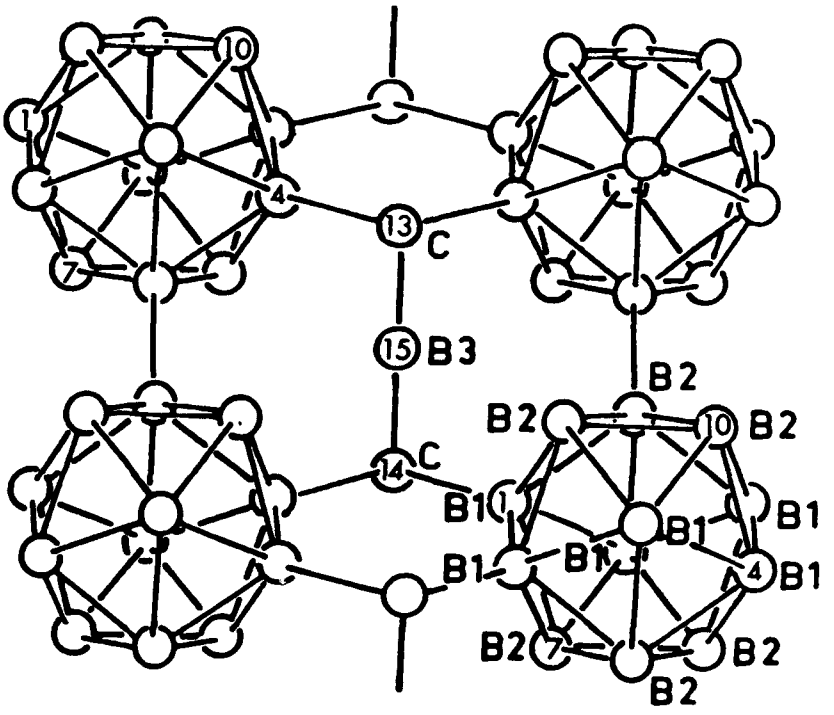

Figure 1. Structure of $B_{12}C$-B-C: four icosahedra, a C-B-C chain, the top and bottom carbon of other chains, the equatorial borons, B1, and the polar borons, B2. The atoms labeled 1, 7, 10, 4, 13, 15, 14, and their counterparts in the lower righthand icosahedra establish our x-plane.

TABLE 1. Distances, angles and muffin tin radii

BOND (neighbors)		DISTANCE(Å)	
		B_{12}C-B-C	α-Boron
		Intra-icosahedral	
B1-B1 (2)		1.767	1.782
B1-B2 (1)		1.795	1.801
	B2-B1 (1)	"	"
B1-B2 (2)		1.808	1.806
	B2-B1 (2)	"	"
B2-B2 (2)		1.814	1.751
		External	
B3-C (2)		1.436	
	C-B3 (1)	"	
B1-C (1)		1.610	
	C-B1 (3)	"	
B2-B2 (1)		1.721	1.670
B1-B1 (2)		2.747	2.019
angle			
B1-C-B3	100.1°		
tetrahedral	109.5°		
Muffin tin radius			
R(B1)	0.88		
R(B2)	0.86		
R(B3)	0.71		
R(C)	0.72		

Earlier calculations for boron carbide have been made by Yamazaki[9], Bullett[10] and Armstrong[11]. Studies of boron icosahedra have been made by Longuet-Higgins and de Roberts[12], Lipscomb and coworkers[13] and for boron icosahedra with hydrogen atoms to study borohydrides per se or to simulate a crystalline environment[14-16].

2. Results

2.1 B_{12}C-B-C

Table 2 gives the results for the $\vec{k}$=0 point in the Brillouin zone. The point group is D_{3d} and the wave function repeats itself in every unit cell. The symmetry notation is that of Bouckaert et. al. [17]. The zero of energy is the muffin-tin value and positive energies do not indicate unbound states. The charge decomposition headings give the 2s(2p) charge in the muffin tin spheres of each of the atom types, e.g. p(6B1) means the 2p-like charge in the six B1 spheres. The charge is normalized to one; any unaccounted for charge is in the interstitial region outside the muffin-tin spheres. These eigenvalues fall into four ranges: band 1, bands 2-15, 16-24, 25-, with separations of from approximately 0.2-0.4 Ryd. between. The lowest band is primarily associated with s-like states on the icosahedra. Band two is largely associated with the C-B-C chain, particularly when considered on a per atom basis. The first fifteen bands correspond (in symmetry) to the 13 internal bonding orbitals of Longuet-Higgins[12] plus the totally symmetric external state(band 3) and a chain state(band 13). Using a criteria of greater than 0.1 for any one component one can make an association of the bands. Bands 4-12, 14,15, 18, 19, 23 and 24 are largely associated with the icosahedra. Bands 1, 3, 16, 17, 21 and 22 are hybridized between the icosahedra and the chains. Bands 2, 13, and 20 are largely associated with the chains. Band 18 is quite unique for although considered an the external orbital, it allows no s or p-character on the chain atoms. Each band is capable of holding one electron of each spin, so on average 23.5 bands are needed to accomodate the 47 valence electrons of B_{12}C-B-C. There is a gap between bands 24 and 25 at $\vec{k}$=0 and this gap persists throughout the Brillouin zone.

In addition to $\vec{k}$=0 we have calculated the energy eigenvalues(bands) at the equivalent of 32 points in the full Brillouin zone(eight $\vec{k}$ values). The results of these calculations are given in the form of total and component densities of states in Figures 2a and 2b. The top portion of each figure gives the total density of states(spin included) while the separate panels show the component densities of states. The normalization is on a formula unit(total) or per atom basis(component). The bands are broadened and band 1 is no longer split-off from the others. There is a slight separation after the first four bands(eight electrons). The dashed line indicates the Fermi energy, E_F, separating filled from empty states. This defines the zero of energy for these plots. Since there are empty states (one hole per unit cell) immediately above the Fermi energy, this one-electron calculation would predict metallic behavior for B_{12}C-B-C. The approximately 2.5 eV gap between the 24th and 25 band is considerably less than the value at $\vec{k}$=0 in Table 2. The highest state of band 24 is at $\vec{k}=(\pi/a,\pi/a\sqrt{3},\pi/c)$ and the lowest state of band 25 is at the same point, making the gap direct in our calculation. The overall occupied bandwidth of approximately 13.5 eV agrees well with the photoemission result of 15.2eV[18].

TABLE 2. Energy eigenvalues and charge decomposition for $B_{12}C$-B3-C at k=0, L. The largest component is underlined(solid) and those greater than 0.10 are dashed

Band symm.		$\epsilon(\vec{k})$ (Ry)	s(B3)	p(B3)	s(2C)	p(2C)	s(6B1)	p(6B1)	s(6B2)	p(6B2)
1	L1	-0.5182	0.020	0.000	0.120	0.000	0.249	0.000	0.127	0.005
2	L2'	-0.2825	0.000	0.045	0.374	0.001	0.094	0.074	0.007	0.003
3	L1	-0.2507	0.036	0.000	0.186	0.002	0.021	0.189	0.137	0.034
4 5	L3'	-0.1303	0.000	0.004	0.000	0.021	0.384	0.052	0.074	0.093
6	L2'	-0.0283	0.000	0.000	0.016	0.003	0.006	0.142	0.347	0.114
7 8	L3	-0.0220	0.000	0.000	0.000	0.059	0.134	0.188	0.110	0.033
9	L1	0.0615	0.018	0.000	0.009	0.027	0.109	0.044	0.139	0.170
10 11	L3	0.0905	0.000	0.000	0.000	0.041	0.111	0.105	0.215	0.104
12	L2'	0.1534	0.000	0.027	0.001	0.078	0.004	0.085	0.005	0.209
13	L1	0.1674	0.110	0.000	0.002	0.152	0.000	0.082	0.011	0.103
14 15	L3	0.1827	0.000	0.032	0.000	0.082	0.001	0.236	0.015	0.111
16 17	L3'	0.3691	0.000	0.003	0.000	0.150	0.020	0.239	0.012	0.169
18	L1'	0.4242	0.000	0.000	0.000	0.000	0.000	0.543	0.000	0.093
19	L1	0.4626	0.013	0.000	0.058	0.035	0.023	0.042	0.008	0.431
20	L2'	0.4898	0.000	0.125	0.000	0.282	0.035	0.032	0.003	0.129
21 22	L3	0.5300	0.000	0.000	0.000	0.176	0.001	0.379	0.001	0.122
23 24	L3	0.5366	0.000	0.000	0.000	0.011	0.005	0.202	0.027	0.421
E_F		0.5435								
25 26	L3	0.9285	0.000	0.000	0.000	0.002	0.094	0.168	0.016	0.169
27	L1	0.9641	0.060	0.000	0.021	0.027	0.042	0.366	0.001	0.006
28 29	L3'	0.9670	0.000	0.264	0.000	0.015	0.038	0.071	0.000	0.101
30	L1	1.0873	0.013	0.000	0.183	0.001	0.011	0.048	0.052	0.144

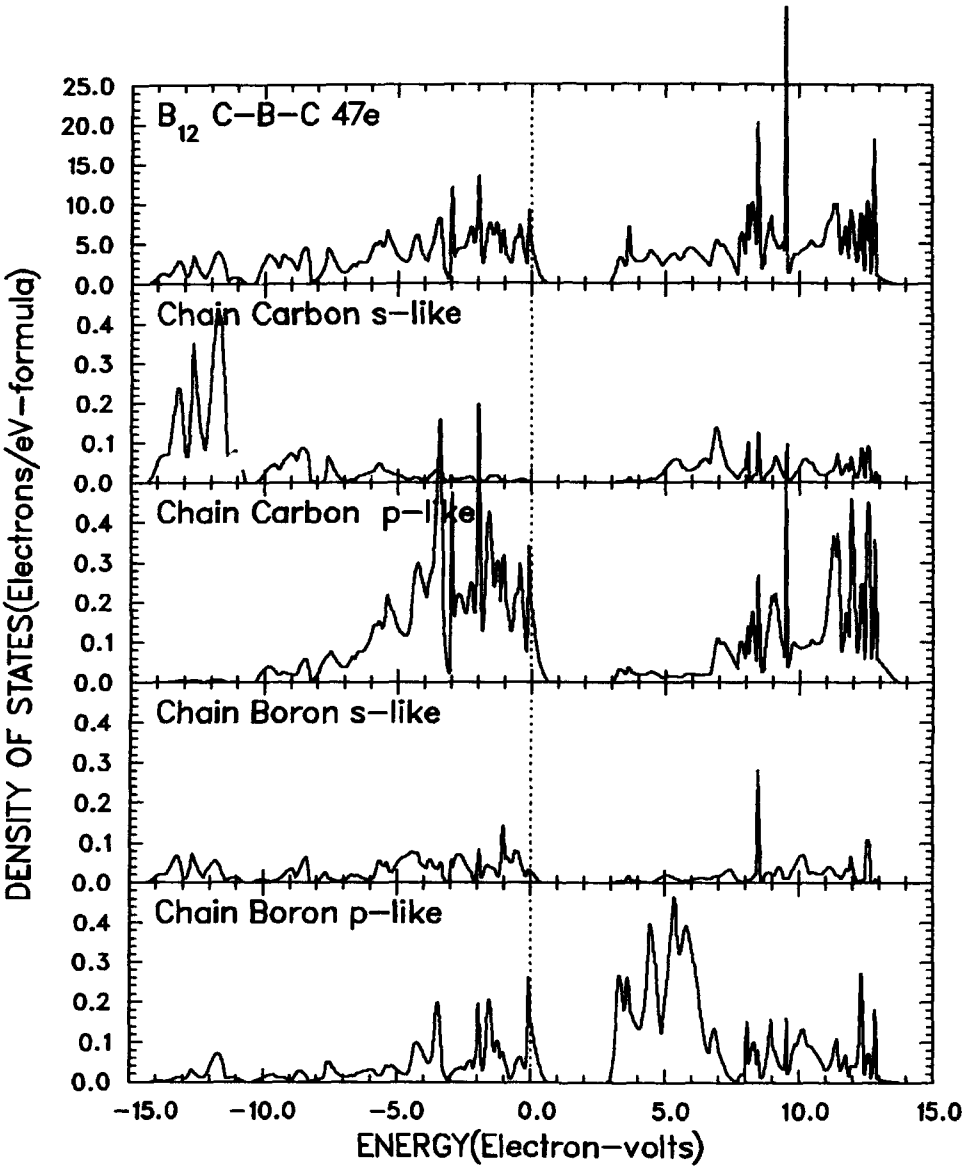

Figure 2a. Total and component densities of states for $B_{12}C$-B-C. Top panel: total density of states per unit cell; lower panels: component densities of states per atom. Fermi energy is shown dashed at 0.0 eV.

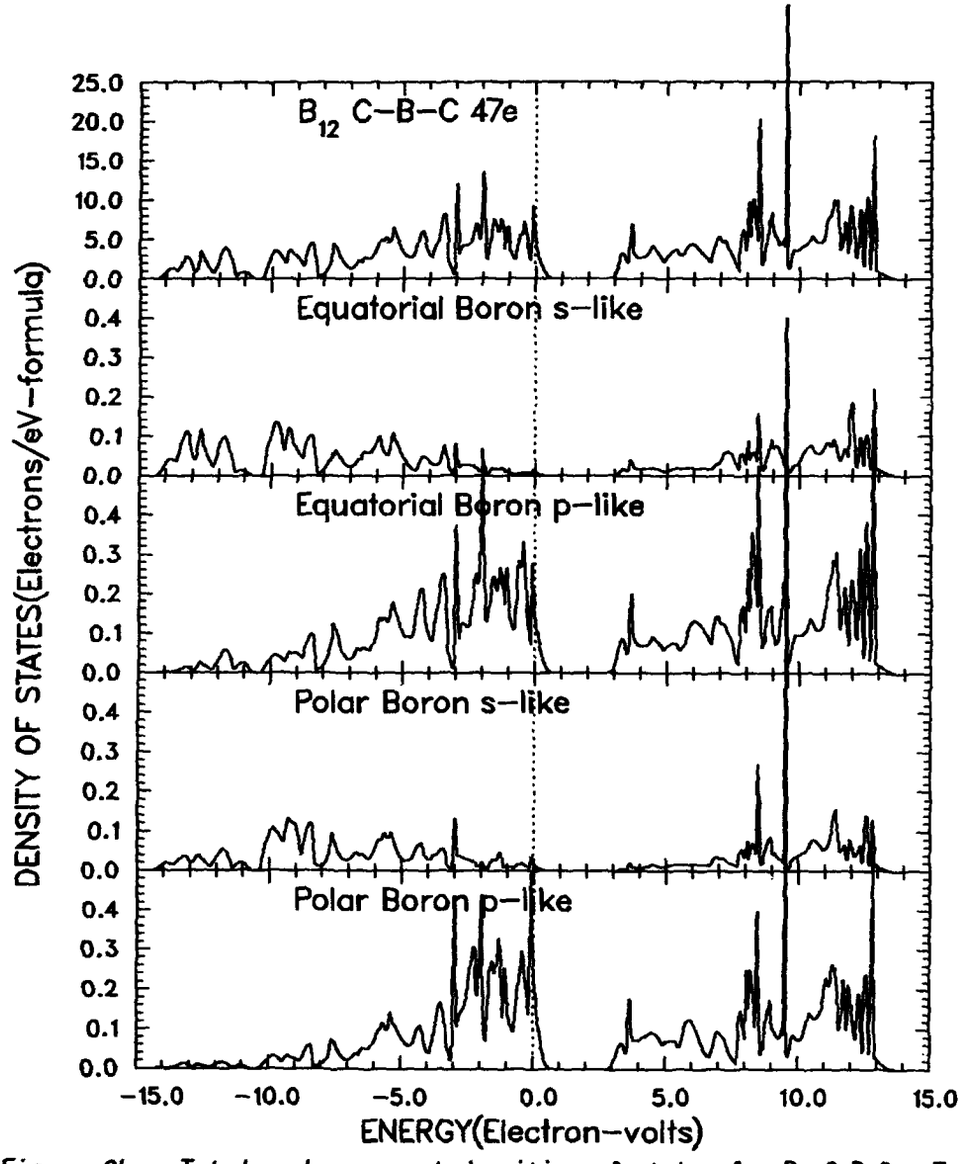

Figure 2b. Total and component densities of states for B_{12}C-B-C. Top panel: total density of states per unit cell; lower panels: component densities of states per atom. Fermi energy is shown dashed at 0.0 eV.

The component densities of states show the expected association of s-states with lower energies and p-states with the higher occupied states. The plots show a sizeable chain carbon contribution over the entire occupied energy range. The smaller chain boron contribution is real in view of the less than 2.5% difference in chain sphere radii (the icosahedral boron spheres are over 75% larger).

2.2 Z_{12}C-B-C

Table 3 gives our results for the $\vec{k}$=0 point for Z_{12}C-B-C: repeating C-B-C chains. This gives a 3.5Å distance from a carbon in the end of one chain to the end carbon in the nearest other chain, almost 2.5 times the C-B intrachain distance. With the correspondence L1 → σ_g, L2' → σ_u, L3' → π_u, and L3 → π_g, the results agree with chemical intuition and an unpublished Gaussian[9]86 isolated molecular calculation for C-B-C [19] as to ordering and occupation of levels. The charge is largely localized on the chain atoms, a small contribution from the equatorial Z1 s, and very little contribution from the Z2 s. Any missing charge is outside the muffin-tin spheres. Charge density plots show this missing charge on and near the chains. The eleven electrons fill 5.5 bands on average to determine the Fermi energy, E_F.

TABLE 3. Energy eigenvalues and charge decomposition for Z_{12}C-B3-C

Band	symm.	$\epsilon(\vec{k})$ (Ry)	s(B3)	p(B3)	s(2C)	p(2C)	s(6Z1)	p(6Z1)	s(6Z2)	p(6Z2)
1	L1	-0.5980	0.126	0.000	0.386	0.022	0.028	0.013	0.002	0.000
2	L2'	-0.5525	0.000	0.112	0.479	0.024	0.020	0.017	0.000	0.000
3	L1	-0.0592	0.130	0.000	0.077	0.297	0.034	0.012	0.002	0.000
4	L2'	0.0406	0.000	0.108	0.060	0.396	0.012	0.014	0.000	0.001
5 6	L3'	0.1173	0.000	0.126	0.000	0.312	0.052	0.015	0.001	0.004
	E_F	0.1064								
7 8	L3	0.2022	0.000	0.000	0.000	0.440	0.063	0.037	0.001	0.001
9	L1	0.3464	0.001	0.000	0.104	0.000	0.085	0.021	0.155	0.000
10 11	L3	0.6058	0.000	0.198	0.000	0.230	0.036	0.015	0.000	0.008

Figure 3 shows the density of states for this calculation. The "molecular" levels are only slightly broadened by the crystalline repeat. The lowest L1 is 2s-like on the carbon and boron. The second band(L2') is s-like on the carbon and p-like on the boron. Band 3: C-pσ, B-s; band 4: C-pσ, B-pπ; bands 5 and 6, L3': C-pπ and B-pπ. The unoccupied bands 7 and 8, L3, contain only C-pπ_u; there is no boron p contribution. One does not see remnants of the molecular states of Figure 3 in Figure 2.

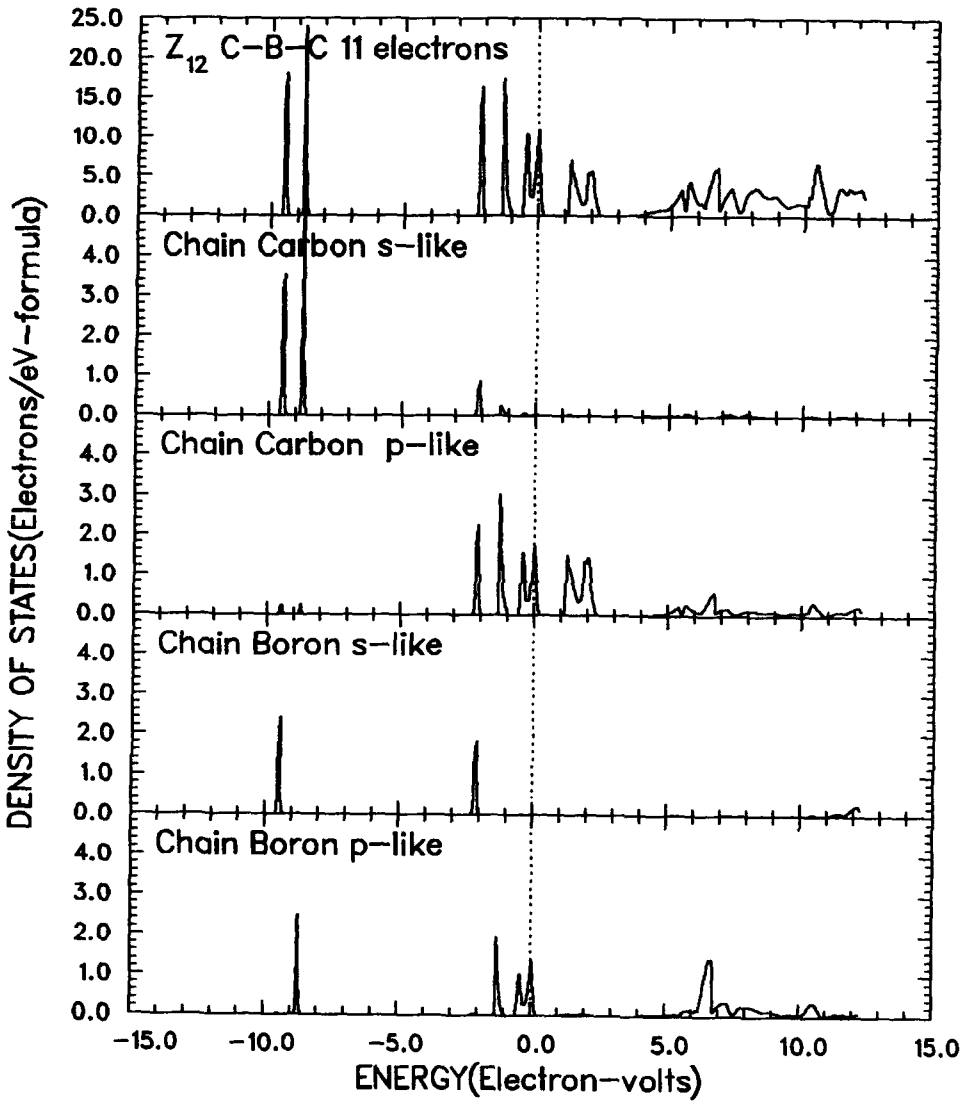

Figure 3. Total and component densities of states for Z_{12}C-B-C. Top panel: total density of states per unit cell; lower panels: component densities of states per atom. Fermi energy is shown dashed at 0.0 eV.

2.3 $B_{12}Z$-Z-Z

In order to see how the molecular states are accomodated with the icosahedral states we have calculated the eigenvalue spectra without the chains. The results should fall somewhere between a calculation for an isolated icosahedra and the structurally related α-boron. Table 1 shows the intericosahedral B1-B1 distance is over 35% longer than in α-boron to accomodate the chains, whilst the intericosahedral B2-B2 distance is only 3% longer and still shorter than any of the internal distances. The chain carbon-B1 bond is second shortest and replaces the so-called delta bond of α-boron (2.019Å). Our $\vec{k}$=0 results for $B_{12}Z$-Z-Z are given in Table 4. Again the first band is well separated from the others. There is significant interaction between the polar atoms of different icosahedra. States L2' and L3' cannot form a polar bond by symmetry. There is a gap between bands 18 and 19. These 18 filled states are the same ones found for α-boron. This gap persists throughout $\vec{k}$-space and this system with 36 electrons would be insulating since there is a gap above the last filled state at E_F. This gap is found theoretically [18,21,22] and experimentally [23] for rhombohedral α-boron. This gap is shown in Figure 4 and is about 1.0eV. The states immediately above the gap are largely associated with the equatorial atoms. This time, band one is only slightly broadened and maintains a gap to band two. Similarly bands 2-4 are split off from the rest, reflecting the lack of interaction with other icosahedra or chains.

3. *Charge Distribution*

Table 5 shows a summary of the muffin tin charges associated with each muffin-tin sphere in the various calculations. For comparison we give the results "xtal"; the amounts associated with superposed atoms calculated with the same exchange and correlation approximation and "bands": the results derived from our eight $\vec{k}$-point bandstructure charge density. Since the xtal superposition is linear the atomic sums for Z_{12}C-B-C and $B_{12}Z$-Z-Z equal the results for B_{12}C-B-C. Comparing xtal and bands one concludes: 1)for the isolated C-B-C chain both the boron and the carbon pick up about one-third of an electron which represents additional bonding between these atoms. 2)similarly for the chainless icosahedra the B1 atoms pick up 0.14 electrons while the B2 atoms pickup over 0.30 electrons with slight losses from the chain region. 3) For B_{12}C-B-C the carbon atoms pick up no more charge in bonding than they did in the isolated chain. The chain boron atoms lose charge with respect to the isolated chain(0.33) and with respect to the superposed atoms(0.05). The equatorial boron atoms, B1, gains charge both with respect to the xtal superposition and the bands summation. The polar, B2, atoms lose some of the charge they had in $B_{12}Z$-Z-Z but there is an increase over the xtal superposition of atoms. With the formation of the bonds with the chains, charge has flowed from the polar borons to the equatorial borons.

TABLE 4. Energy eigenvalues and charge decomposition for B_{12} Z-Z3-Z

Band	symm.	$\epsilon(\vec{k})$ (Ry)	s(Z3)	p(Z3)	s(2Z)	p(2Z)	s(6B1)	p(6B1)	s(6B2)	p(6B2)
1	L1	-0.6179	0.000	0.000	0.002	0.000	0.257	0.038	0.278	0.018
2 3	L3'	-0.2990	0.000	0.000	0.000	0.001	0.362	0.092	0.099	0.112
4	L2'	-0.2711	0.000	0.000	0.001	0.000	0.030	0.102	0.377	0.139
5 6	L3	-0.1702	0.000	0.000	0.000	0.001	0.016	0.162	0.334	0.070
7	L1	-0.1234	0.001	0.000	0.001	0.000	0.061	0.098	0.107	0.282
8	L1	-0.0310	0.002	0.000	0.029	0.001	0.128	0.122	0.082	0.174
9 10	L3	-0.0269	0.000	0.000	0.000	0.004	0.251	0.173	0.036	0.148
11	L2'	0.0500	0.000	0.000	0.001	0.001	0.004	0.142	0.001	0.334
12 13	L3'	0.1009	0.000	0.001	0.000	0.001	0.000	0.200	0.001	0.312
14	L1'	0.2445	0.000	0.000	0.000	0.000	0.000	0.552	0.000	0.110
15	L2'	0.2786	0.000	0.003	0.086	0.022	0.275	0.179	0.009	0.022
16 17	L3	0.2964	0.000	0.000	0.000	0.000	0.002	0.221	0.019	0.455
18	L1	0.3394	0.007	0.000	0.035	0.000	0.006	0.213	0.015	0.368
	E_F	0.3877								
19 20	L3'	0.5071	0.000	0.002	0.000	0.021	0.093	0.430	0.028	0.048
21	L1	0.5702	0.018	0.000	0.000	0.010	0.001	0.259	0.002	0.079
22 23	L3	0.6414	0.000	0.000	0.000	0.020	0.037	0.369	0.004	0.184
24 25	L3	0.7808	0.000	0.000	0.000	0.002	0.101	0.315	0.006	0.165
26	L2	0.9097	0.000	0.000	0.000	0.000	0.000	0.207	0.000	0.439
27	L2'	0.9333	0.000	0.001	0.000	0.004	0.017	0.077	0.011	0.370
28	L1'	0.9379	0.000	0.000	0.000	0.000	0.000	0.150	0.000	0.460

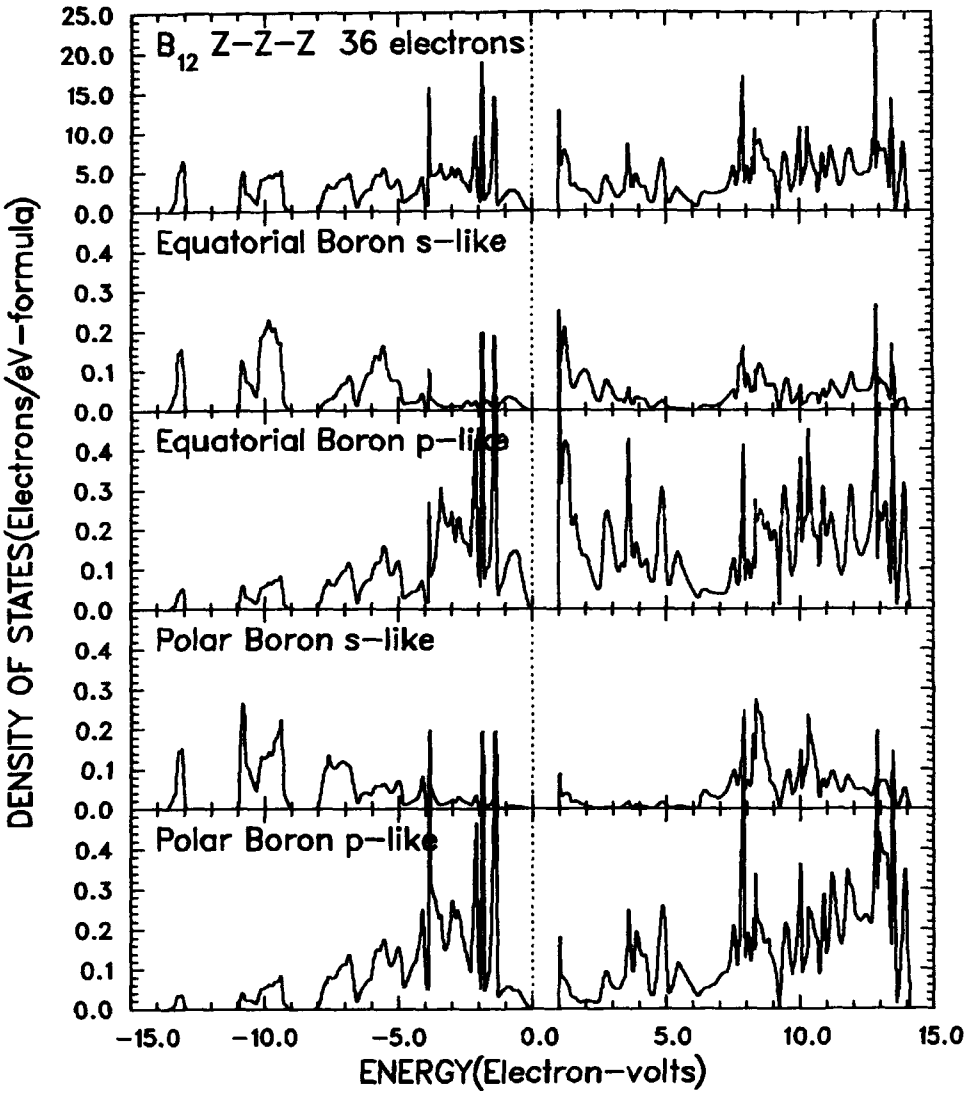

Figure 4. Total and component densities of states for B_{12}Z-Z-Z. Top panel: total density of states per unit cell; lower panels: component densities of states per atom. Fermi energy is shown dashed at 0.0 eV.

TABLE 5. Muffin-tin decomposition of charge distributions

	Z_{12}C-B-C				B_{12}Z-Z3-Z				B_{12}C-B-C			
	Z1	Z2	C	B	B1	B2	Z	Z3	B1	B2	C	B3
xtal	0.14	0.01	3.79	2.93	3.61	3.57	0.21	0.05	3.76	3.58	4.00	2.98
bands	0.10	0.01	4.15	3.26	3.75	3.88	0.17	0.03	4.00	3.70	4.33	2.93

Figure 5 shows a charge density plot derived from our calculation for Z_{12}C-B-C. The plane is an x-z plane with y=0. The numbering system and spheres will be the same for all x-z plots. The contours in the lower half of the figure are at 0.025e/(a.u.)^3 and twice that in the top half for readability. Spheres 1,4,7,10 surrounding the origin are in one icosahedron. One and four are equatorial, Z1s, and seven and ten are polar, Z2s. The spheres are drawn to scale and represent the muffin-tin spheres. The first thing to notice is that although the potential is spherically symmetric in each sphere, the charge density is far from so. The second thing to notice is the continuity of the charge from inside the muffin-tins to outside. One sees very little charge in the chain boron (#15) midplane and a charge distribution which is quite highly polarized towards the carbon atoms (13 and 14) at the ends of the chain. The charge on the carbon atoms rises to a higher value away from the boron than towards it. The charge between the carbons and the boron has a two peaked structure with the higher peak near the carbons.

Figure 6 shows a charge density plot for B_{12} C-B-C. One can clearly see the formation of a intericosahedral polar bond between atoms seven and ten. There is some charge build up between an equatorial boron(1) and a polar boron(7) on the same icosahedron. There are also equatorial borons at the same z as atoms one and four in front of and behind the plane at a distance 2.87 Å from the one at the same z and 1.795Å from the one above or below. Similarly there are also polar atoms at the same z-value as atoms ten and four, in front of and behind the plane, at a distance of 1.814Å from the other polar atom at this level and 1.808Å from equatorial boron below or above them; only slightly longer than 1.798Å for the in plane B2-B1 shown. These B1-polar bonds gives rise to the seagull like contour in this projection. The bonding between the equatorial borons is not shown in this section. Again there is very little charge in the chain boron midplane. The chain carbons (13 and 14) show strongly polarized bonds, both with the chain boron(15) and the equatorial borons (four and one). From the equatorial borons point of view the charge build up going towards the chain carbon starts out and resembles the polar-polar bond but increases to a higher level as it approaches a carbon rather than another boron. The chain carbon's interaction with the chain boron is greater than with the equatorial borons(of which there are three, two not shown). The two peaked structure observed for the isolated chain has been lost in boron carbide reflecting loss of charge on the chain boron.

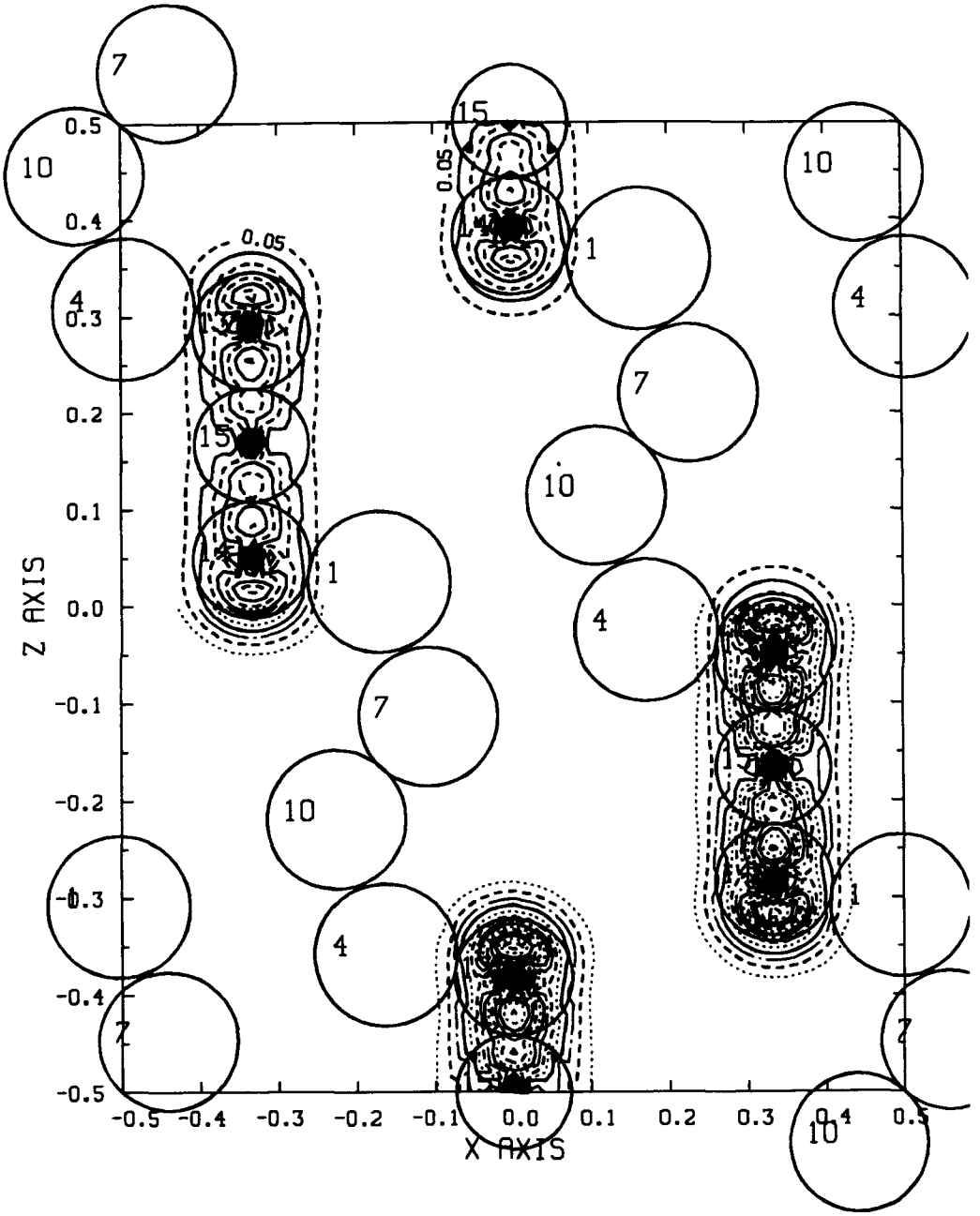

Figure 5. Total valence charge density for $Z_{12}C\text{-}B\text{-}C$ in the plane described in Figure 1. Contour interval 0.025 electron/(au)^3 in the lower half and 0.05 electron/(au)^3 in the upper half.

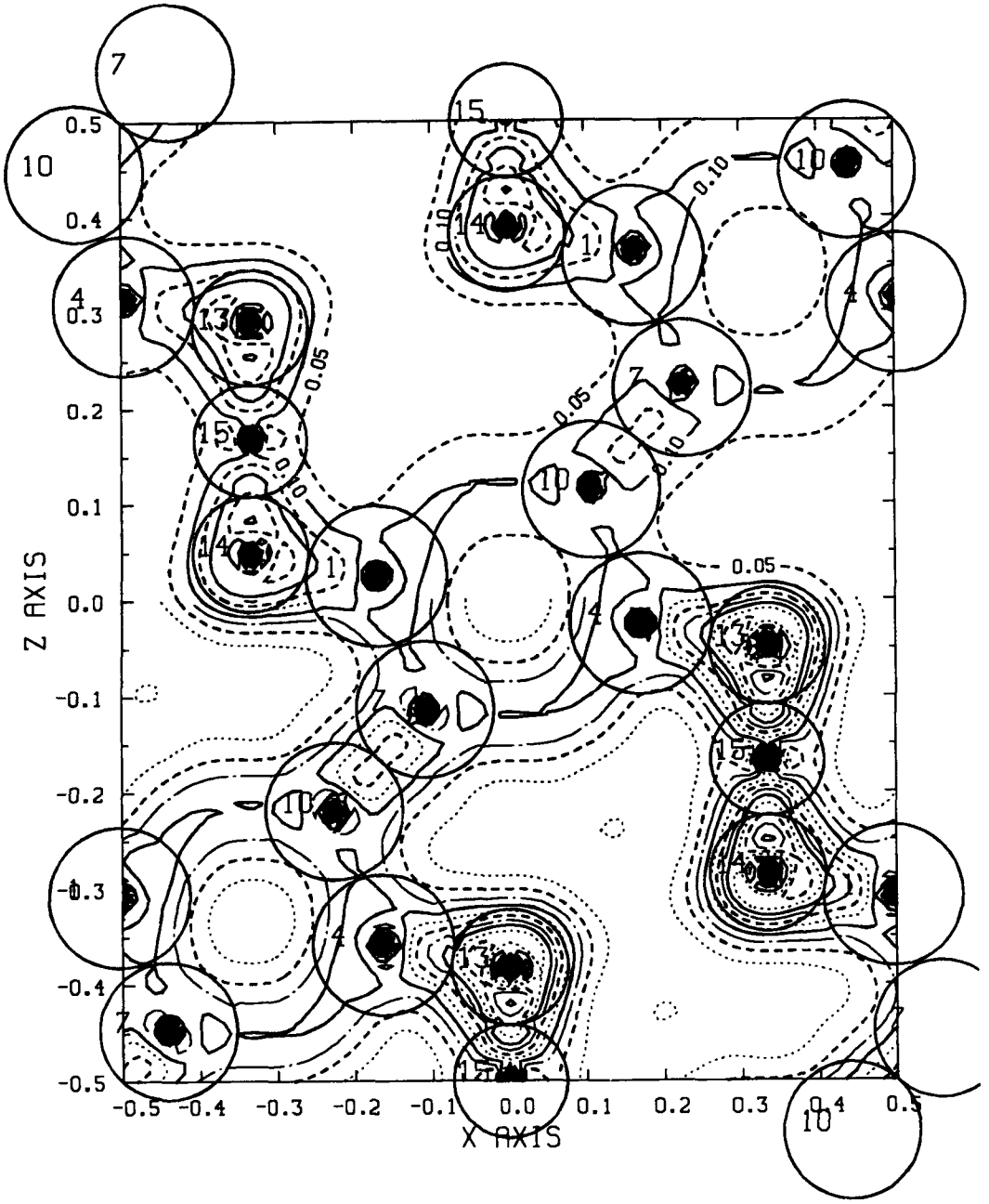

Figure 6. Total valence charge density for boron carbide $B_{12}C$-B-C as in Fig. 5.

4. Discussion

The question of interest is, what states of the chain and what states of the chainless icosahedra combine to form the states of boron carbide, $B_{12}C$-B-C? From a comparison of Tables 2, 3, and 4 on a level by level basis and individual band charge density plots, I have tried to sort out the various interactions involved. They are summarized in Figure 7, where a solid line indicates a more(or less) direct association and dashed lines indicate bonding and dotted lines, antibonding combinations of icosahedral states and chain states. Some icosahedral (chain) states have a direct counterpart in the carbide. In some cases bonding-antibonding combinations of the icosahedral and chain states are formed. If the antibonding combination is low in energy and can be occupied, then the corresponding states of both the icosahedron and the chain are occupied in the carbide. In other cases the antibonding combination is above the new Fermi level and electrons have to be accomodated in new states which were originally above the Fermi level in the original systems and may have been lowered by the interaction. These features are examined in some detail below.

To the 18 states below the gap at 36 electrons of the icosahedra, B_{12}Z-Z-Z in Table 4, the states L2', L1, L3' and L3 have been added to to form the 24 states capable of holding 48 electrons in $B_{12}C$-B-C in Table 2. Of these, the states L1, L2' and L3' correspond to occupied states of a C-B-C chain. The remaining occupied states L1 and L2' of the chain hybridize with their icosahedral counterparts. The added state L3, corresponds to states which are empty(excited) in both the icosahedra and in the chain. The picture is significantly modified over that of an icosahedron plus a chain. There are sizeable interactions. In Figure 7 our eigenvalue results for $\vec{k}$=0 are shifted to a common Fermi level. On this scale the correspondence between the levels for the icosahedron on the left and the chain on the right is clearer.

We shall start from the bottom of the chain states and try to keep track of these states. The low energy L1's hybridize and form bonding, antibonding combinations (bands 1 and 3) of $B_{12}C$-B-C. This is almost quantitatively true for these L1 states. There is some loss of chain s-character and equatorial p- character.

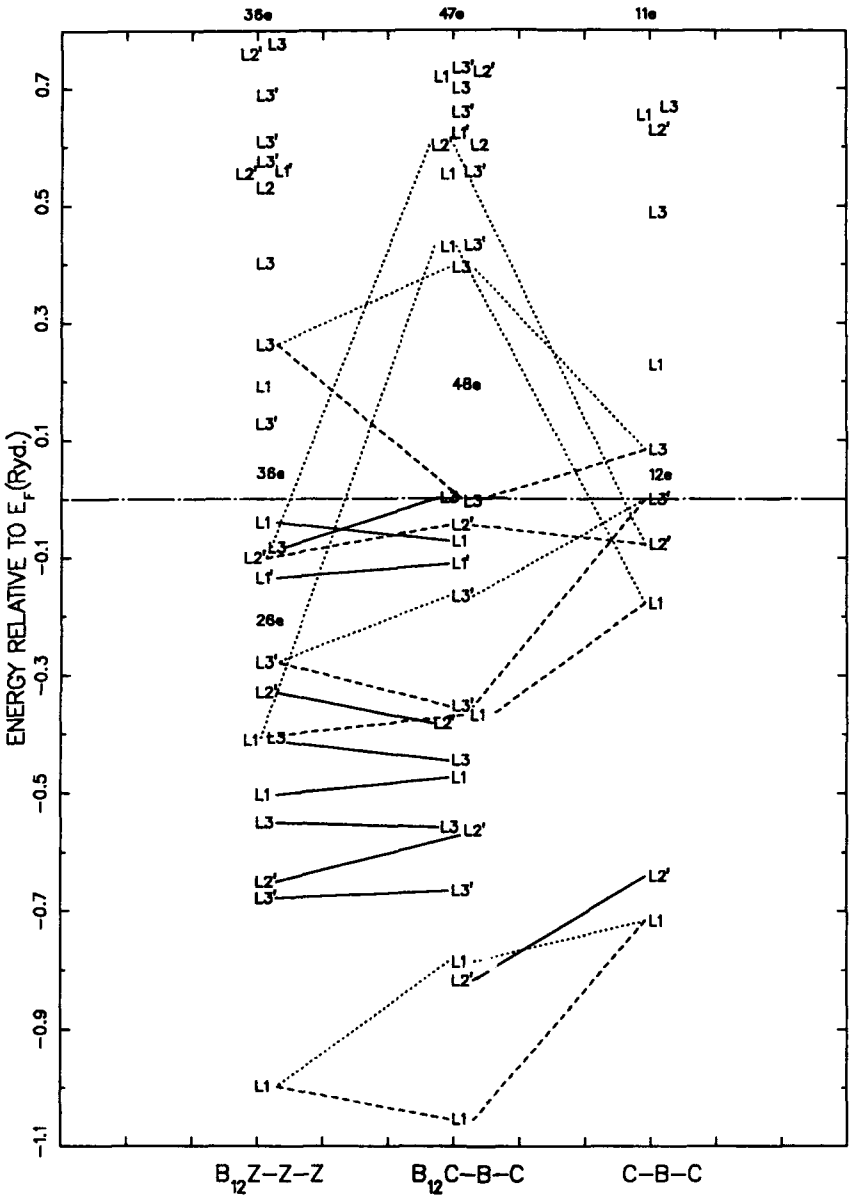

Figure 7. Correlation diagram between the states of B_{12} Z-Z-Z on the left and Z_{12}C-B-C on the right to form B_{12}C-B-C in the center. Solid lines indicate a strong transferrence, dashed (dotted) lines indicate a bonding (antibonding) combination.

Figure 8 and Table 3 give the charge distribution for the lowest L1 for $B_{12}C$-B-C, an "isolated" chain. There is sizeable boron s-character as well as chain carbon 2s-character (the table value is for two carbons). The charge associated with the equatorial borons, Z1, (atoms 1 and 4) is merely an extension of the chain carbon charge inside these spheres.

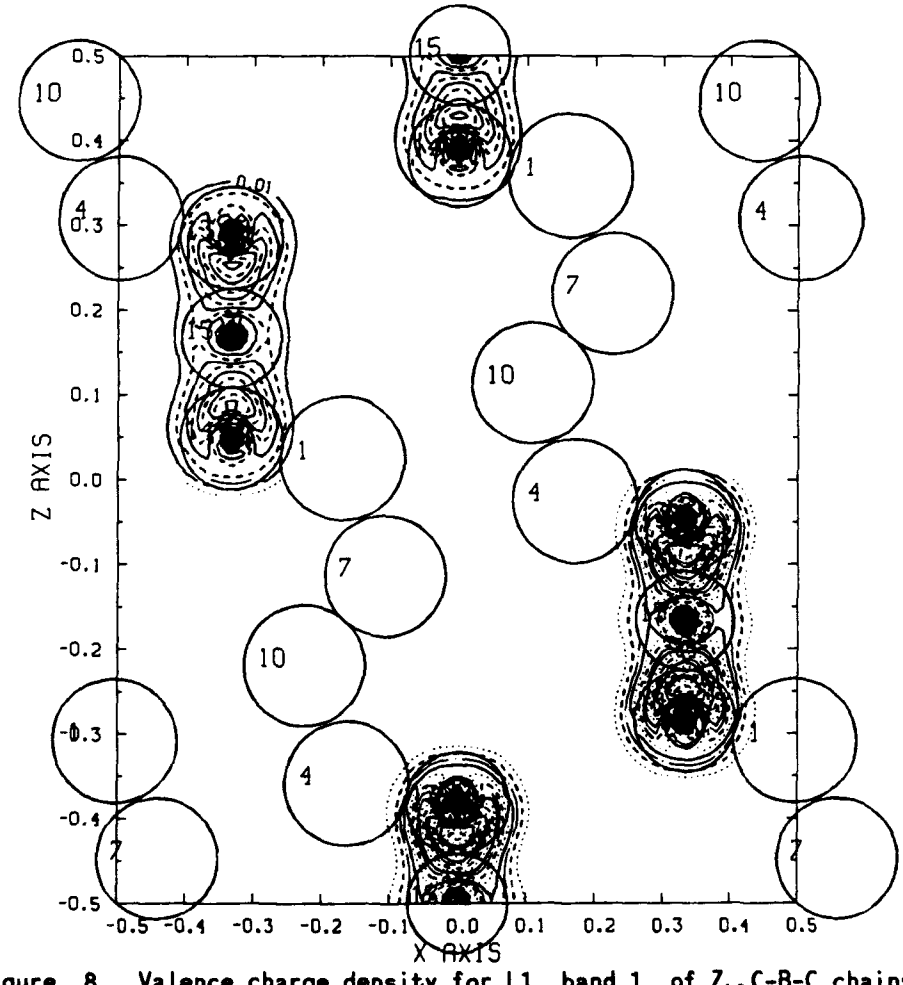

Figure 8. Valence charge density for L1, band 1, of Z_{12}C-B-C chains in the x-z plane of figure 1. Contour interval: lower half, 0.005 e/(au)^3; upper half, 0.01 e/(au)^3.

Figures 9 and 10 (and Table 2) show the results for L1, bands 1 and 3, respectively, for boron carbide, $B_{12}C$-B-C. The loss of the chain boron charge is apparent. From a comparison of Tables 2 and 3, the chain boron s-charge is halved while the chain carbon falls only 25%.

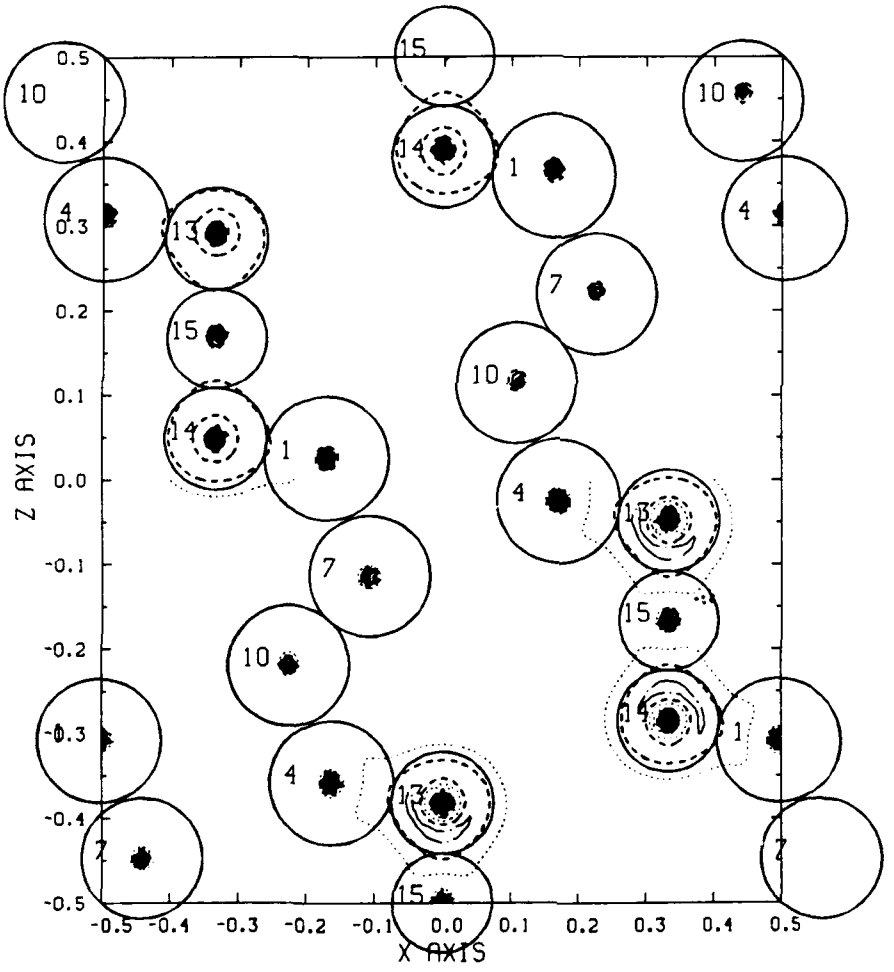

Figure 9. Valence charge density for L1, band 1, of boron carbide, $B_{12}C$-B-C. Contour interval: lower half, 0.005 e/(au)^3; upper half, 0.01 e/(au)^3.

A clear indication of the formation of an interaction with the icosahedra is seen, both in the tables and in the figures. Recall that the sharp spectrum of the chain is lost and that lowest state is spread out over 4eV in energy, further indicative of the bonding-antibonding hybridization in boron carbide.

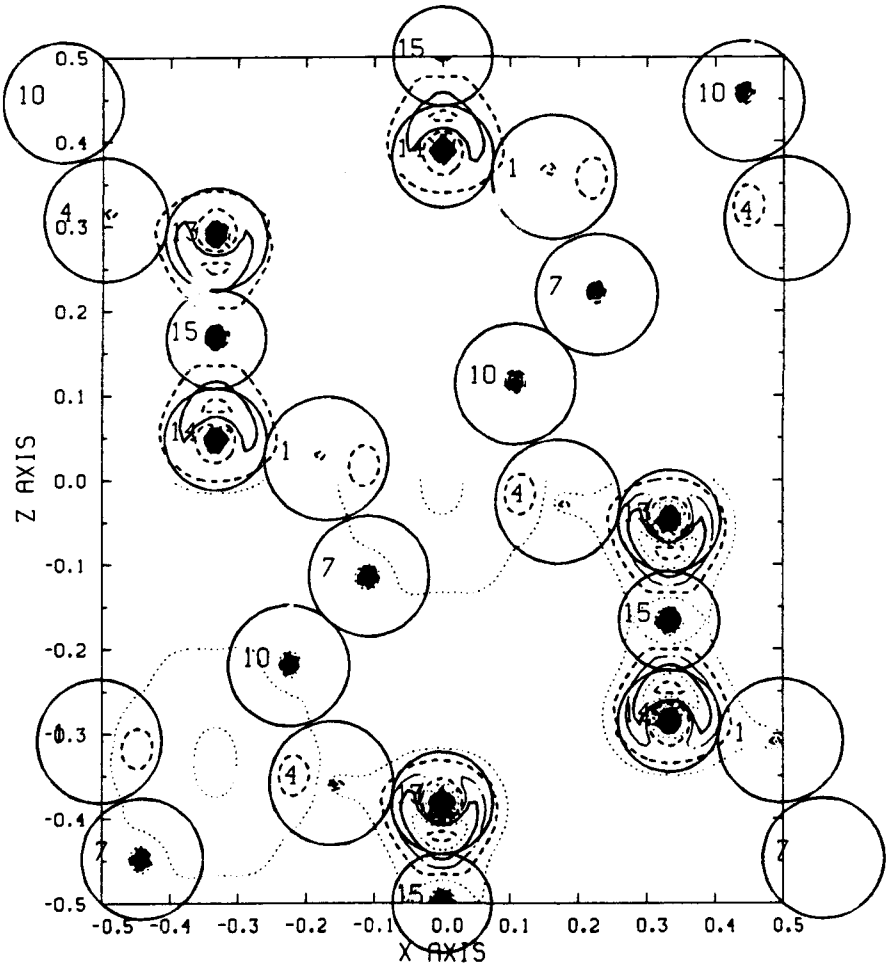

Figure 10. Valence charge density for L1, band 3, for $B_{12}C$-B-C: the other half of the bonding-antibonding pair(Fig. 9). Contour interval: lower half, 0.005 e/(au)^3; upper half, 0.01 e/(au)^3.

The low energy L2' of the chain and the low energy L2'(band 4) of the icosahedra hybridize very little to form bands 2 and 6 of the joint system. There again is some loss of chain character and a gain of equatorial boron character with distortion of the charge density into the boron spheres. This is shown in Figure 11 for band 2 of the carbide and in Tables 2-4.

The second L1 of the chain hybridizes with the third L1 of the icosahedra to form a bonding (band 13) and antibonding combination. The antibonding combination is well above the Fermi energy. Two electrons of the joint system have to be accomodated in new states.

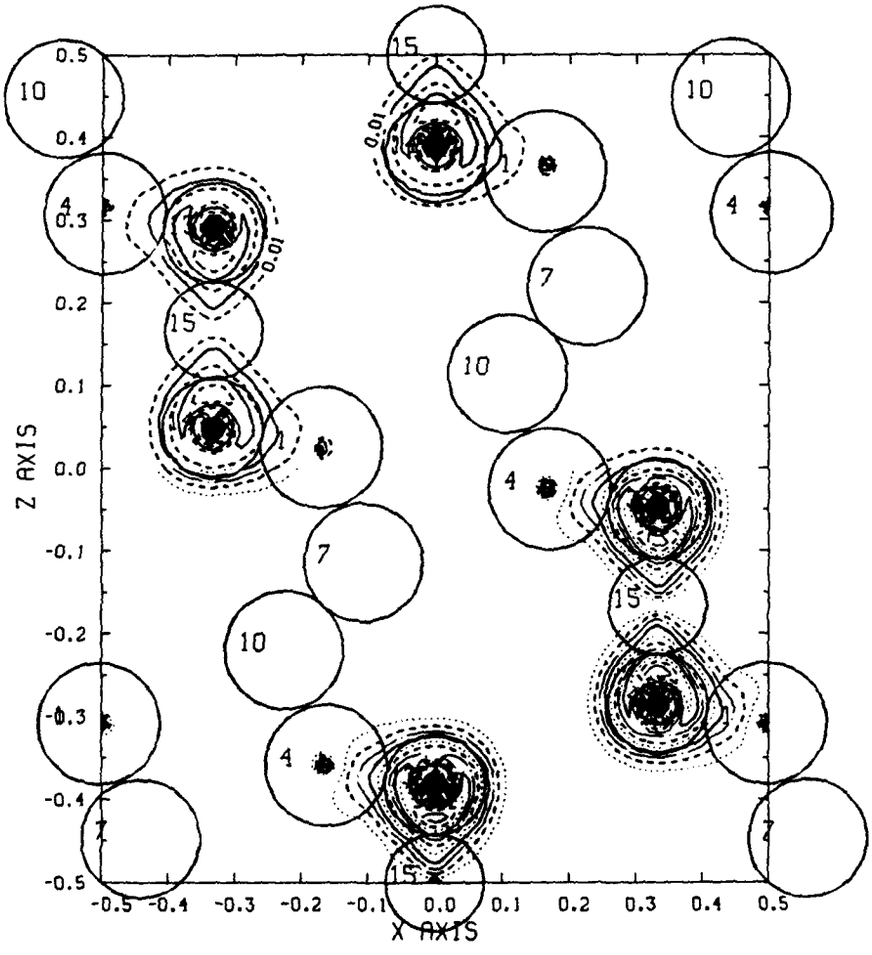

Figure 11. Valence charge density for L2', band 2, for $B_{12}C$-B-C. Contour interval: lower half, 0.005 e/(au)^3; upper half, 0.01 e/(au)^3.

Band 4, L2', of the chain largely dominates band 20 of the carbide to the detriment of band 15 of the icosahedra as Fig. 12 shows. Charge which was associated with the equatorial boron in the icosahedra is significantly reduced in this state.

In both of these hybridizations (bands 13 and band 20), the chain character is predominant over the icosahedra. The charge in these states which is lost from the icosahedron.

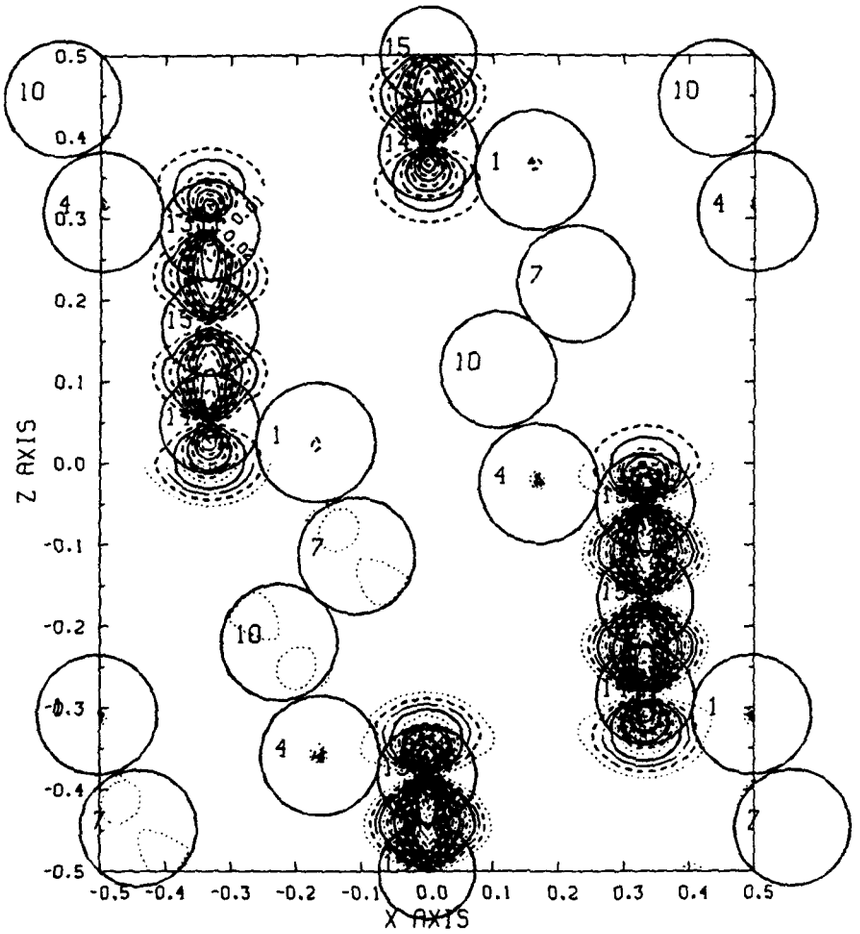

Figure 12. Valence Charge density for L2', band 20, of $B_{12}C$-B-C. Contour interval: lower half, 0.005 e/(au)^3; upper half, 0.01 e/(au)^3.

The partially occupied states L3'(5,6) of the chain hybridize with the states L3'(12,13) of the icosahedra to form (14,15 and 16,17) of the carbide which are fully occupied. The states of the icosahedra L3'(2,3), L2'(4), L3(5,6), L1(7), L3(9,10), L2'(11), L1'(14), L3(16,17), L1(18) correspond to states (4,5), (6), (7,8) and (9), (10,11), (12), (18), (23,24) and (19) respectively, of boron carbide and have little chain character. This connection is indicated by the heavy solid lines of Figigure 7. Figure 13 shows this type in charge density plots for L3', bands 4 and 5. The internal nature of the icosahedral bonding is clearly evident.

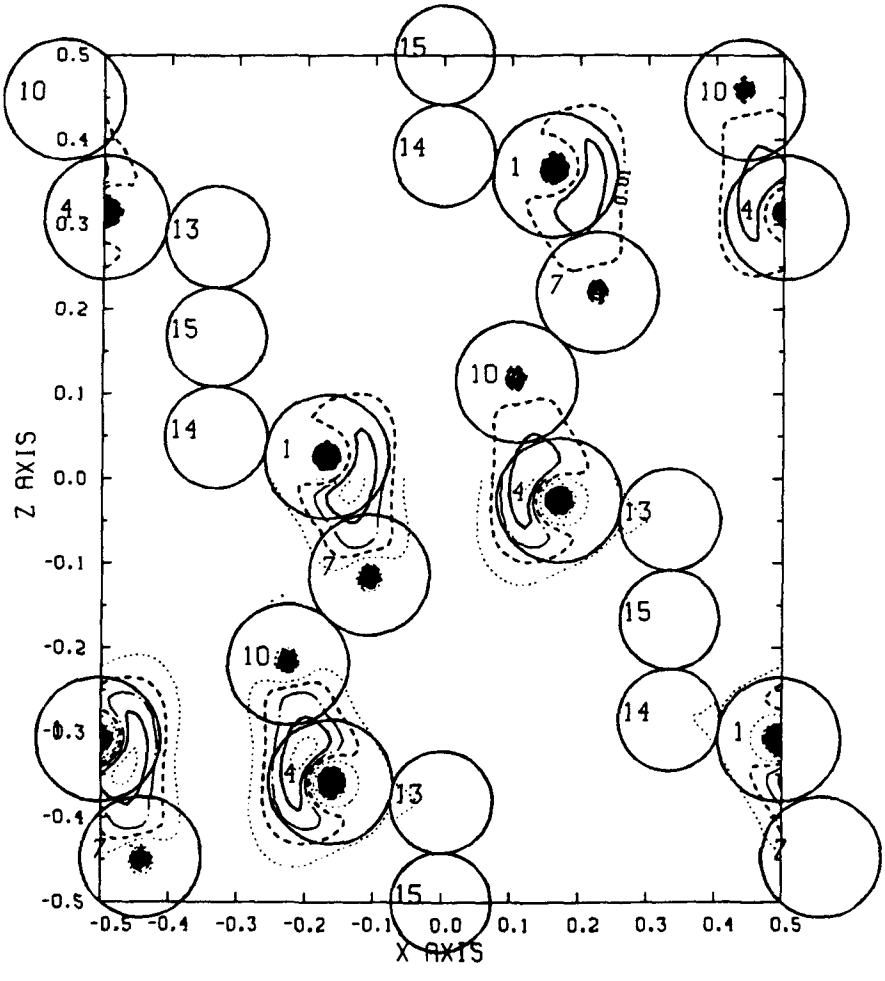

Figure 13. Valence charge density for L3', bands 4 and 5, of $B_{1,2}$ C-B-C. Contour interval: lower half, 0.005 e/(au)^3; upper half, 0.01 e/(au)^3.

Figure 14 shows the charge density associated with L3 state, bands 23 and 24, at the Fermi energy in boron carbide. This state was filled in the icosahedra(bands 16 and 17) and becomes partially occupied in boron carbide. It has a large B2 character and reflects polar bonds between the icosahedra, with lesser B1 and chain character.

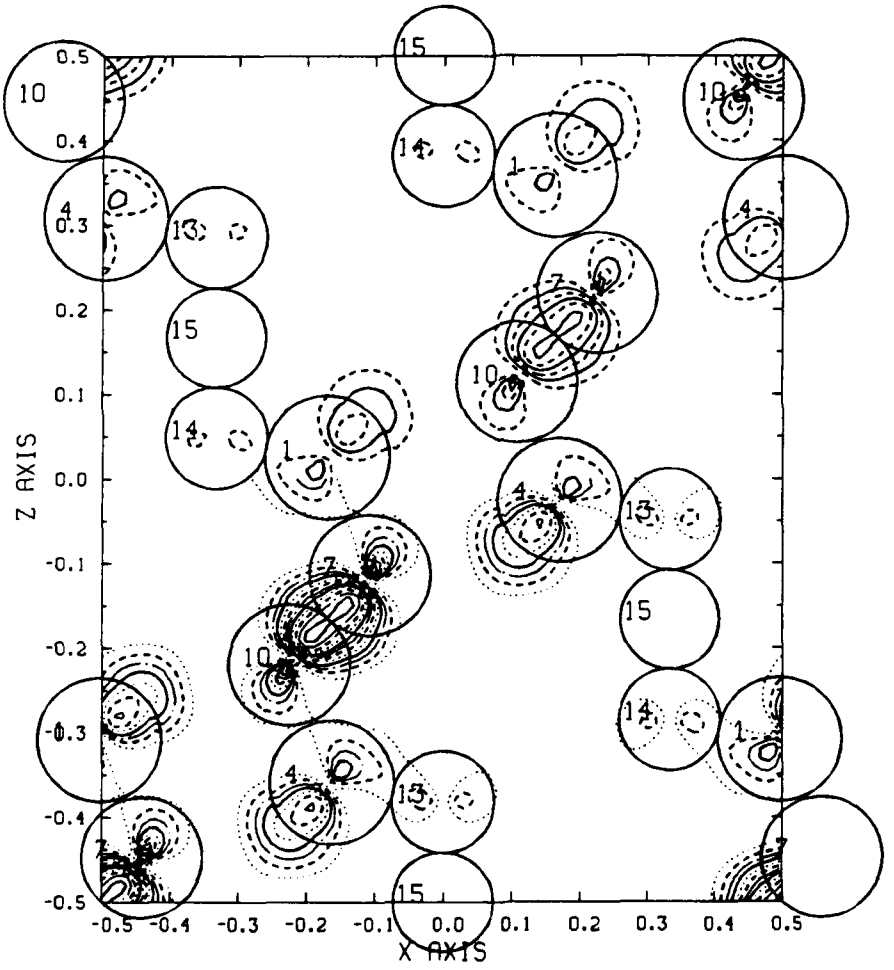

Figure 14. Valence charge density L3, bands 23 and 24, of $B_{12}C$-B-C. Contour interval: lower half, 0.005 e/(au)^3; upper half, 0.01 e/(au)^3.

The unoccupied states L3(22,23) of the icosahedron and (7,8) of the chain hybridized to form L3(21,22) of the carbide with somewhat less chain character than the original. This state is lowered (relative to the states of the icosahedra) because of its bonding interaction with the chains as is shown in Figure 15.

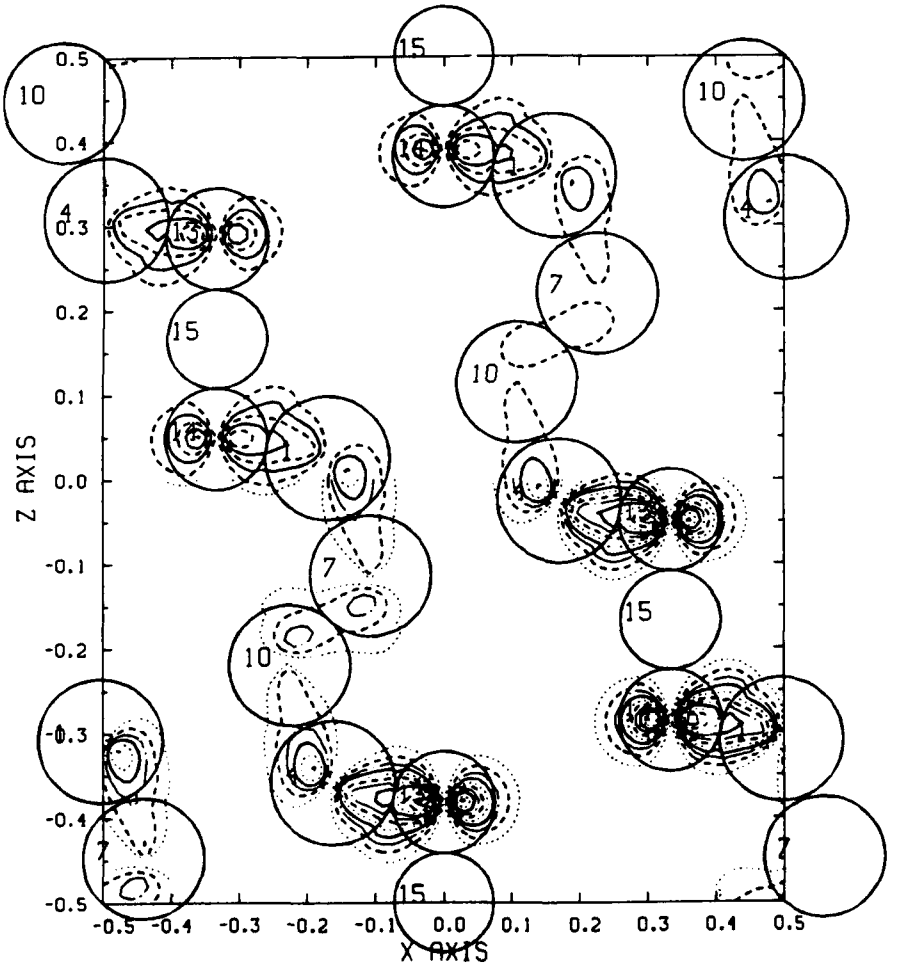

Figure 15. Valence charge density for L3, bands 21 and 22, of $B_{12}C$-B-C. Contour interval: lower half, 0.005 e/(au)^3; upper half, 0.01 e/(au)^3.

Figure 12 showed an L2' state in boron carbide which was largely chainlike. This state in the icosahedron(15) is largely localized on the equatorial borons, B1, with lobes pointing towards the ends of the missing chains. By symmetry and the conventional way of counting this would be considered an internal bonding orbital of the icosahedra. This is clearly not true. The internal bonding orbital is L2', band 27, which has large B2 character. This state is shown in Figure 15. It retains this character as the empty band 33 in boron carbide. Its nodal structure precludes a charge buildup between the B2s of different icosahedra.

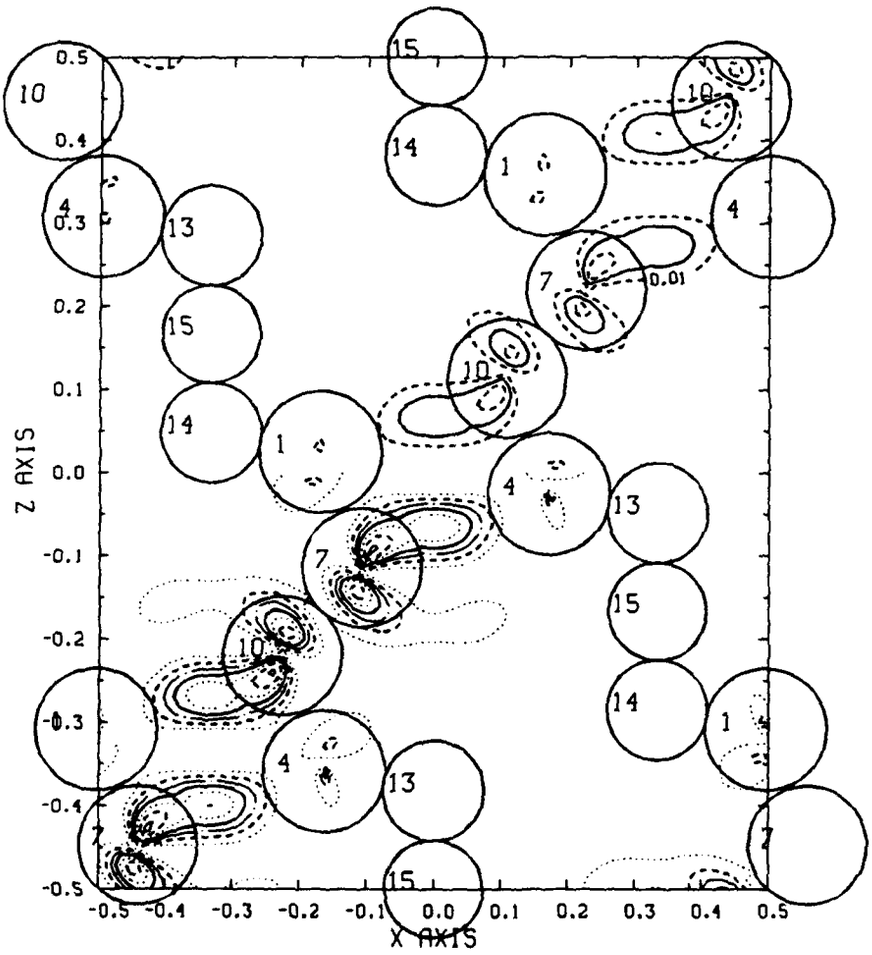

Figure 16. Valence charge density for L2', band 27, of $B_{12}Z$-Z-Z. Contour interval: lower half, 0.005 e/(au)^3; upper half, 0.01 e/(au)^3.

5. Conclusions

In this paper I have examined the nature of the states of $B_{12}C$-B-C in the context of boron icosahedra and C-B-C chains. There is evidence of strong interactions between the chains and the icosanedra as well as preservation of chainlike and icosahedral-like states. The largest accumulation of charge persists between the chain carbons and chain boron, although decreased from the isolated chain. Charge on the chain boron is lost to become involved in the bonds with the equatorial borons of the icosahedron via the chain end carbons. The bonding between the boron of the icosahedron and between the polar borons of the icosahedra is clearly shown. By and large the states associated with internal bonding in the icosahedra maintain their integrity in the center of the energy range. The mixing with the chain states occurs below and above this regime. Below this regime two low lying chain states are effectively added. The modification in the bonding occurs in the external orbitals which can interact with the chain, as might be expected. An excited state of the icosahedron and the chain is pulled down. This state is occupied by electrons which were in chain and icosahedral states which hybridized with the antibonding combination become elevated in energy and thus unoccupied.

6. Acknowledgements

I wish to acknowledge helpful discussions with T. A. Green and P. A. Schultz. This work was supported by the U. S. Department of Energy under Contract DE-AC-04-76-DP00789.

7. References

1. Koelling, D.D. and Arbman, G. O. (1975) 'Use of energy derivative in an augmented plane wave method: application to copper', J. Phys. F:Metal Phys. 5, 2041-54.

2. Hedin L. and Lundqvist, B. I. (1971) 'Explicit local exchange-correlation potentials', J. Physics C:Solid State 4, 2064-2083.

3. Mattheiss, L. F., Wood, J. H. and Switendick, A. C. (1968) 'A procedure for calculating electronic energy bands using symmetrized augmented plane waves', in B. Alder, S. Fernbach and M. Rotenberg (eds.), Methods in Computational Physics, Volume 8, Academic Press, New York, pp. 63-147.

4. Switendick, A. C. (1987) 'Electronic structure of boron and boron-rich borides' in D. Emin, T. L. Aselage and Charles Wood(eds.), Novel Refractory Semiconductors, Materials Research Society, Pittsburgh.

5. Jansen, H. J. F. and Freeman, A. J. 'Total-energy full-potential linearized-augmented -plane-wave method for bulk solids: electronic and structural properties of tungsten', Phys. Rev. B30, 561-9.

6. Weyrich, K. H., Brey, L. and Christensen, N. E. 'Full-potential linear-muffin-tin-orbital calculation of phonon frequencies in semiconductors', Phys. Rev. 38, 1392-1396.

7. Morosin, B., Mullendore, A. W., Emin, D. and Slack, G. A. (1986) 'Rhombohedral crystal structure of compounds containing boron-rich icosahedra' in D. E. Emin, T. Aselage, C. L. Beckel, I. A. Howard and C. Wood (eds.) Boron Rich Solids, American Institute of Physics, New York, pp. 70-86.

8. By a bond, we mean a simple geometrical connection as evidenced by the lines of Figure 1.

9. Yamazaki, Masatoshi (1957) 'Electronic band structure of boron carbide', J. Chem. Phys. 27, 746-751.

10. Bullett, D. W. (1982) 'Structure and bonding in crystalline boron and $B_{12}C_3$', J. Phys. C:Solid State Phys. 15, 415-426.

11. Armstrong, D. R., Bolland, J., Perkins, P. G., Will, G. and Kirfel, A. (1983) 'The nature of chemical bonding in boron carbide. IV. Electronic band structure of boron carbide, $B_{13}C_2$, and three models of the structure $B_{12}C_3$', Acta. Cryst. B39, 324-329.

12. Longuet-Higgins, H. C. and Roberts, M. de V. (1955) 'The electronic structure of an icosahedron of boron atoms', Proc. Roy. Soc. A230, 110-119.

13. Lipscomb, W. N. and Britton, D. (1960) 'Valence structure of higher borides', J. Chem. Phys. 33, 275-280.

14. Howard, I. A., Beckel, C. L. and Emin, D. (1987) 'Bipolarons in boron icosahedra', Phys. Rev. B35, 2929-33.

15. Howard, I. A., Beckel, C. L. and Emin, D. (1987) 'Bipolarons in boron-rich icosahedra: effects of carbon substitution', Phys. Rev. B35, 9265-70.

16. Green, T. A., Switendick, A. C. and Emin, D. (1988) 'Ab initio self-consistent field(SCF) calculations on borane icosahedra with zero, one, or two substituted carbon atoms', J. Chem Phys. 89, 6815-22.

17. Bouckaert, L. P., Smoluchowski, R. and Wigner, E. (1936) 'Theory of Brillouin zones and symmetry properties of wave functions in crystals', Phys. Rev. 50, 58-67.

18. Green, T. A. (1988) private communication

19. Domashevskaya, E. P., Solovjev, N. E., Terrekhov, V. A. and Ugai, Ya. A. (1976) 'On a study of the valence band structure of boron and some of its compounds by the X-ray soectral method', J. Less Common Met. 47, 189-193.

ELECTRONIC STRUCTURE OF LITHIUM BORIDE Li_3B_{14}

D.W. BULLETT
School of Physics
University of Bath
Claverton Down
Bath, BA2 7AY, UK

ABSTRACT. A number of binary lithium borides have been reported, but none of these phases had been well characterised until the recent single-crystal determinations by Mair, Nesper and von Schnering. We report here a calculation of the electron states in the novel Li_3B_{14} structure. This tetragonal crystal structure contains a covalently linked framework of B_8 and B_{10} clusters (in the ratio of 1:2), with Li atoms in the interstitial channels. The chemical formula $Li_6(B_8)(B_{10})_2$ supplies the boron framework with exactly the right number of electrons to fulfil the bonding requirements within and between the boron clusters, and the calculated energy gap of $\approx$ 2eV in the electron spectrum is consistent with the experimental properties of this transparent, red, diamagnetic semiconductor.

Until very recently, information about the binary compounds of the alkali metals with boron has been rather sparse. Three factors combine to create considerable experimental difficulties: (i) the extreme difference of the melting points of the components, and the lack of reactivity of alkali metals with boron at low temperatures, (ii) the high reactivity of the two components with the walls of the reactor, especially at high temperatures, and (iii) the thermal dissociation of the product borides at high temperatures. A review by Naslain, Etourneau and Hagenmuller [1] summarised the state of knowledge of these compounds in 1977. At that time only three binary phases had been clearly identified: NaB_6, KB_6, and NaB_{15}. The crystal structure of NaB_{15} contains icosahedral B_{12} units covalently bonded at each vertex to either a neighbouring icosahedron or to one of a triangle of isolated B atoms, with Na atoms in the interstitial sites of the covalent framework. The structure of KB_6 is that of CaB_6: a cubic array of B_6 octahedra, linked through each vertex, with the metal atom in the interstitial site at the centre of the cube, whereas the structure of NaB_6 remained elusive. Lithium is the alkali metal which reacts most readily with boron, and several different phases had been claimed in the 1970's [2-4] but none was well characterised.

R. Freer (ed.), The Physics and Chemistry of Carbides; Nitrides and Borides, 555–559.
© 1990 *Kluwer Academic Publishers. Printed in the Netherlands.*

The recent reinvestigation of the binary Li–B system by Mair, Nesper and von Schnering [5-7] identified three new boron–rich phases: Li_3B_{14}, LiB_6 and Li_6B_{19}, and found no evidence for any of the earlier suggestions. The key to their success lay in the choice of container materials: all compounds were prepared under inert conditions in inner crucibles of molybdenum, welded into niobium ampoules. Although the reaction begins at about 600K, synthesis of good single crystals required reaction temperatures of 1200–1700K for several days. All three are transparent, red, semiconductors with activation energies E_g = 1.4–1.6eV for electrical conduction in the temperature range 600–900K; at lower temperatures they show extrinsic conductivity via an impurity band, with activation energy 0.15eV. There is also an ionic component to the electrical conductivity arising from the mobile Li^+ species. The Li_2B_6 and Li_6B_{19} structures are each based on 3–dimensional networks of B_6 octahedra, the former in a tetragonal array reminiscent of CaB_6, and the latter in a hexagonal arrangement.

$Li_{13}B_{14}$ also contains a 3–dimensional covalently linked framework of boron clusters, but in this case they are B_8 and B_{10} clusters, which occur much less commonly in the solid borides (but are familiar in the chemistry of boron hydrides [8-10]). The crystal structure is tetragonal, with 112 boron atoms and 24 Li atoms in the body–centred unit cell (space group $I\bar{4}2d$). A very clear description of this novel structure can be found elsewhere [7]. Dodecahedral closo–B_8 and hexadecahedral closo–B_{10} cages are present in the ratio 1:2. Every boron atom is involved in one of these clusters, and forms one external bond to a neighbouring cluster: B_8 clusters are centred at the special positions 4b (0 0 $\frac{1}{2}$), and form eight B–B bonds to the eight neighbouring B_{10} clusters centred at the 8d positions (x $\frac{1}{4}$ $\frac{1}{8}$; x = -0.17), while external B–B bonds from the atoms of the B_{10} cluster connect to 6 other B_{10} clusters and 4 B_8 units. Between the cages there remain spiral–like channels in which the Li ions are statistically located, and along which they can diffuse relatively easily.

The electronic structure of this rather complex boron framework was calculated using an atomic–orbital based method, with no adjustable parameters, as detailed elsewhere [11-12]. Figure 1 shows the resulting distribution of electron states as a function of energy. The s and p valence levels of the boron atoms hybridise into a broad band of occupied states, extending over an energy range of about 20eV from the bottom-most bonding state to the highest filled state. This particular arrangement of boron atoms in the crystal structure leads to an energy gap, of about 1.9eV in this calculation, in the distribution of sp hybridised states. The ionised Li atoms at the composition Li_3B_{14} provide the boron framework with exactly the right number of extra electrons to fill all states below this gap in the spectrum, leading to the observed optical and electrical characteristics of this material.

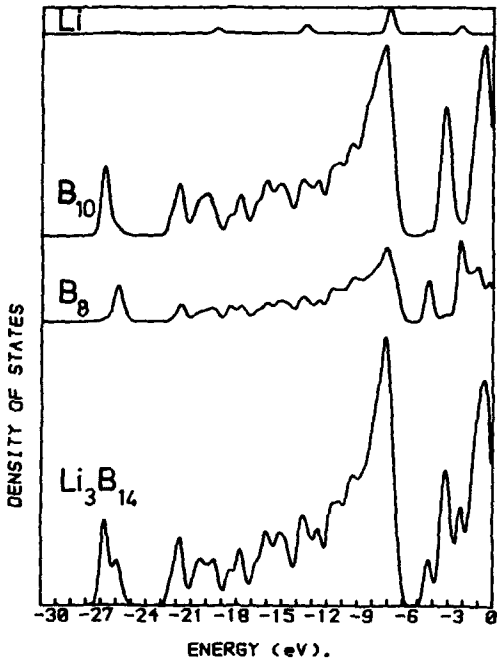

Figure 1. The calculated distribution of electron states in Li_3B_{14}, showing the relative contributions from B_8 and B_{10} clusters and from Li atoms. States are filled up to the valence band edge at $\approx$–6eV

We can seen how this energy distribution of electron states comes about by examining the molecular orbitals of the constituent clusters. The Li_3B_{14} framework contains closed B_8 dodecahedra and B_{10} hexadecahedra (in the ratio 1:2) from which every boron atom is linked by one external bond to a neighbouring cluster. The clearest way to model these two structural units is to tie each external bond to a hydrogen atom. The energy levels of the molecular orbitals for the resulting B_8H_8 and $B_{10}H_{10}$ model structures are shown in figure 2.

For convenience all terminal B–H bonds were here assumed to be the same length (1.21Å) and to be directed radially outward from the centre of the cluster. The results appear to be consistent with Wade's rules [13], that either of these clusters requires two extra electrons to fill the bonding cluster states, leading to $B_8H_8^{2-}$ and $B_{10}H_{10}^{2-}$. In the 3–dimensional framework where terminal B–H bonds become intercluster links, all bonding requirements will therefore be satisfied at the semiconducting composition $Li_3B_{14} = (Li^+)_6(B_8^{2-})(B_{10}^{2-})_2$.

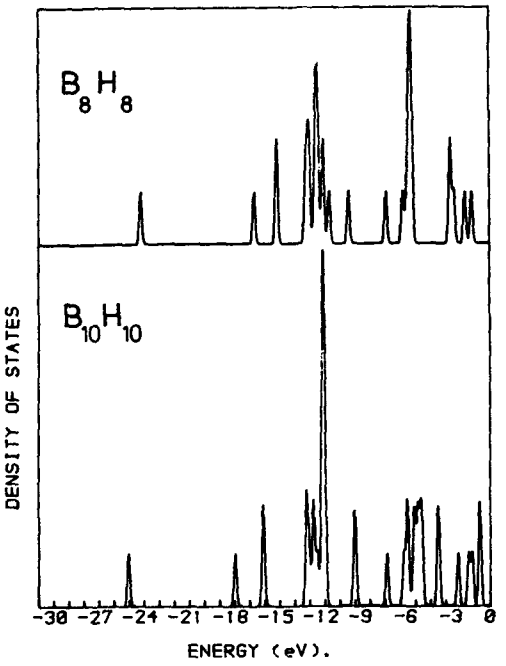

Figure 2. Energy levels calculated for the two isolated clusters B_8H_8 and $B_{10}H_{10}$. The highest occupied orbital for double-negatively charged states occurs at ≈-9 eV in each case.

References

1 Naslain, R., Etourneau, J. and Hagenmuller, P. (1977) "Alkali metal borides" in "Boron and Refractory Borides". V.J. Matkovich (Ed.), Springer, Berlin pp. 262-92.
2. James, S.D. and de Vries, L.E. (1976) J. Electrochem. Soc. **123**, 321.
3. Sorokin, V.P., Gavrilov, P.J. and Levakov, E.V. (1977) Russ. J. Inorg. Chem. (Eng. Edn.) **22**, 329.
4. Dallek, S., Ernst, D.W. and Larrik, B.F. (1979) J. Electrochem. Soc. **126** 866.
5. Mair, G., Nesper, R. and von Schnering, H.G. (1984) Annual report Max–Planck–Institut FKF, I–30.
6. Mair, G. (1984) Thesis, University of Stuttgart.
7. Mair, G., Nesper, R. and von Schnering, H.G. (1988) "Trilithium tetradecaboride Li_3B_{14}: synthesis structure, and properties", J. Solid-State Chemistry **75**, 30-40.
8. Muetterties, E.L. and Knoth, W.H. (1968) "Polyhedral Boranes" (Dekker, New York).
9. Hoffmann, R. and Lipscomb, W.N. (1962) "Boron hydrides: LCAO – MO and resonance studies" J. Chem. Phys. **37**, 2872–83.

10. Dobrott, R.D. and Lipscomb, W.N. (1962) "Structure of $Cu_2B_{10}H_{10}$" J. Chem. Phys. **37** 1779–84.
11. Bullett, D.W. (1982) "Structure and bonding in crystalline boron and $B_{12}C_3$" J. Phys. C: Solid State Phys. **15** 415-26.
12. Bullett, D.W. (1986) "Electronic structure studies of boron and boron–rich borides" in Boron–Rich Solids (AIP Conference Proceedings 140, eds. D. Emin, T. Aselage, C.L. Beckel, I.A. Howard and C. Wood, AIP, New York).
13. Wade, K. (1976) "Structural and bonding patterns in cluster chemistry" Adv. Inorg. Chem. Radiochem. **18**, 1–66.

VI. BULK MATERIALS and THIN FILMS -

ELECTRICAL, OPTICAL AND THERMAL PROPERTIES

OPTICAL AND ELECTRONIC PROPERTIES OF SiC

W.J. CHOYKE
Dept. of Physics
University of Pittsburgh
Pittsburgh, PA 15260
USA

ABSTRACT. This lecture is intended to be a short survey which highlights those aspects of the optical and electronic properties of SiC which are currently being studied on single crystal epitaxial films of SiC grown on Si or SiC. We touch on the following topics: optical constants, lattice bands, electronic band structure, low temperature photoluminescence, transport phenomena, defect states and wave-vector classification of SiC physical properties.

INTRODUCTION

In this Conference SiC is considered to be a member of the carbide family and is being discussed from a very broad materials viewpoint. We shall be very much more restrictive in this paper. SiC will be treated as a large band gap semiconductor. Furthermore, we restrict ourselves to a discussion of certain optical and electronic properties of single crystals of SiC. Why do we do this? This paper is meant as a preparation for a second paper which deals with current research on the optical and electronic properties of epitaxially single crystal films of SiC grown on crystals of Si or SiC. This is not an all inclusive review of this topic, and we have made a choice of discussing those phenomena which we believe will be helpful to the readers of our second paper. Some of our previous reviews [1-5] and the two issues of the Gmelin Handbook [6,7] may prove helpful in filling in the many gaps which our specialized review generates.

From a semiconductor point of view SiC first excited interest in the late fifties, a time when Germanium was the reigning semiconductor device material. One foresaw that the small band gap of Ge would make this material useless for applications much above room temperature. Si was just being developed, and it was not appreciated at the time that Si would become the wonder material of the second half of the twentieth century. It was known that SiC could be doped n- and p- type and that it had a a gap of the order of 2 to 3eV. This made it extremely attractive as a new high temperature semiconductor and many laboratories all over the world started to grow and measure crystals of SiC. By 1959 the first SiC semiconductor conference was convened in Boston and the Proceedings [8] from this meeting styill make interesting reading. Alas, Si technology develop[ed so rapidly shortly afterwards that by 1970 the industrial interest in SiC had totally dissipated. Of course, fundamental studies on single crystal and amorphous SiC continued all over the world, but at a very low key. What is different today and why is there so much renewed interest in SiC from the semiconductor industry? First of all, designers have pushed the temperature capabilities of Si almost to the limit. III-V and II-VI compounds do not look promising as high temperature and radiation resistant materials. SiC shows great promise now for good device performance up to and exceeding 500°C. We now have many applications that require high temperature, high speed and radiation resistant properties. Consequently there is presently an important economic drive to have a second look at SiC,

R. Freer (ed.), The Physics and Chemistry of Carbides; Nitrides and Borides, 563–587.
© 1990 *Kluwer Academic Publishers. Printed in the Netherlands.*

and we believe it will become the material of choice in this area during the next decade.

There are two technological developments which made possible today's enthusiasm over SiC as a high temperature, high speed and high power device material. In 1977 Tairov and Tsvetkov [9] showed how one might grow single polytype, single crystal boules from a seed by vapor transport. In 1983 Nishino, Powell and Will [10] grew large area single crystal films of 3C SiC on Si [001] wafers. Today, both these techniques have been greatly improved. Furthermore, the best epitaxial SiC is grown on substrates obtained from boule grown SiC. Other papers in this Conference will have more to say about these exciting developments. We shall now proceed to give a background of the optical and electronic properties of single crystal SiC which should be useful in reading the current literature.

EARLY OPTICAL, CRYSTALLOGRAPHIC AND ELECTRICAL EXPERIMENTS

Between 1906 and 1908 William W. Coblentz in Washington, D.C. published [11,12] the earliest infra-red transmission and reflection spectra of SiC. He saw the characteristic dip in the reflection near 10μm and 13μm. Polytypism was as yet unrecognized so the exact crystal modifications of his samples are not known, but they must surely have been hexagonal platelets. The transmission data was taken between 1.0μm and 4.0μm and was not very revealing. In 1907, H.J. Round, while working for Marconi in New York, published [13] the first known reference to light emitting diodes. He remarked, "On applying a potential of 10 volts between two points on a crystal of carborundum, the crystal gave out a yellowish light." In fact, he also saw SiC emitting green, orange and blue light. Round clearly recognized that this light emission was a junction phenomenon. The discovery of electroluminescence has been credited by many to Lossew's observations in SiC in Leningrad in 1923 [14], but that was 16 years after H.J. Round. At Marburg in 1915, O. Weigel did some remarkably detailed optical absorption measurements in the visible part of the spectrum [15]. He obtained the absorption coefficients of some hexagonal polytype (probably 6H SiC) over the temperature range from room temperature up to 985°C. In this way he really discovered the shift of the indirect band gap towards lower energy with increasing temperature, but he did not recognize this at the time. Since the crystals were hexagonal, he made careful measurements of the ordinary and extra-ordinary index of refraction. He also obtained the temperature variation of the index from 0° to~1000°C for wavelengths from 4554A to 6497A. In two important papers [16,17] condensed from his PhD dissertation at the University of Michigan (1944), Newman W. Thibault gives the morphological and structural crystallography as well as optical properties of six common polytypes of SiC. These papers pull together a lot of information on SiC known up to 1944. The final paper I wish to mention in this section is of great practical value. Richard S. Mitchell published a paper in 1953 [18] entitled, "Application of the Laue Photograph to the Study of Polytypism and Syntaxis Coalescence in Silicon Carbide." All workers currently involved in either SiC boule or epitaxial film growth and the study of the optical and electronic properties of these crystals, owe a debt of gratitude to Mitchell's publication.

OPTICAL CONSTANTS

The 6H polytype of SiC is the one that is found most frequently in growth runs from Acheson or Lely furnaces. Consequently, the vast majority of the older studies on the determination of the optical constants of SiC were made at room temperature on 6H platelets. Such a platelet is shown in the inset at the bottom left of Fig. 1 where the c axis is shown to be perpendicular to the basal plane. In a normal incidence transmission or reflection experiment one would then measure the ordinary (o) ray properties. If one cuts a prism out of a thick platelet in the manner shown in the inset at the bottom right of Fig. 1, one can determine both n_o and n_e where (e) stands for the extra-ordinary ray. A slice cut out of a thick platelet or a single polytype boule, parallel to the c-axis may be used to measure transmission and reflection of light polarized E parallel to c and E perpendicular to the c-axis.

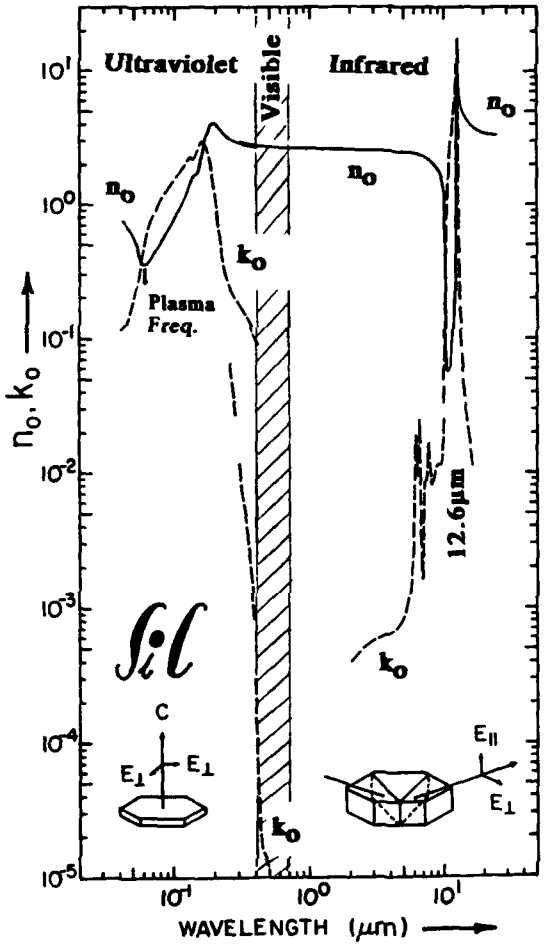

Fig. 1. A log-log plot of n and k for SiC at room temperature from 0.04 to 22μm

The data in the ultraviolet are a combination of the work of Rehn et al. [19] from 25 to 13eV and Leveque and Lynch [20] from 30 to 3eV. In Rehn *et al.* [19] the samples were single crystals of 6H SiC which were cleaned and heated to 700°C in air for 30 minutes before etching in concentrated hydrofluoric acid for ten minutes. Samples were then rinsed in distilled water and methanol before mounting with epoxy. The reflectometer was an ultraclean, all-metal sealed vacuum chamber with a base pressure of $1x10^{-10}$ torr or less. Reflectance was measured for five angles of incidence (15°, 30°, 45°, 60°, 75°) in the energy range 13 to 25eV. The absolute reflectances were used to deduce the optical constants and no correction for an "s" reflectance component was needed. These results are in good agreement with the results of Leveque and Lynch [20] who also utilized reflectivity of synchrotron radiation but used the Kramers Kronig analysis to obtain n and k. From the electron energy loss function Rehn et al. [19] also determined that the volume plasmon associated with the valence electrons appears near 22eV. This is the reason that SiC has such excellent normal incidence reflectivity in the ultraviolet until 22eV. This is the basis for using SiC for synchrotron radiation mirrors and diffraction gratings as well as UV optics in general [21-25].

At lower energy (4.75-3.2eV) the band-edge absorption has been measured by Choyke and Patrick [26], who used hexagonal platelets. Thus, they measured k_o. Samples of thickness 3.6-200μm were unsupported, while thinner ones were prepared by grinding and polishing samples glued to Suprasil II substrates. This work was undertaken to reveal direct and indirect transitions in the absorption edge that are not obvious from the data plotted in Fig. 1.

At lower energy the band-edge region has been studied by Groth and Kauer [27]. Values of k_o determined in the region 3.12 to 2.5eV are used in Fig. 1. It is interesting to point out that the values of Leveque and Lynch [20] near 3eV are too large by a factor of two. This is a caution to the reader that transmission measurements of k (where feasible) are generally more reliable than values of k derived from a Kramers Kronig analysis of the reflectivity.

In the transparent region just below the band-edge, measurements of n have typically been done with minimum-deviation prisms or plates exhibiting interference fringes. A typical prism (see insert of Fig. 1) is cut from a hexagonal plate so that the c axis is parallel to the prism apex edge. Then, both (*o*) (E *c*) and (*e*) (E *c*) polarization can be used. Thibault [16,17] measured n_o and n_e at several wavelengths of H, Na and Hg. Shaffer [28] fitted his data with the formulas

$$n_o = A' + (B'/\lambda_2), \qquad n_e = A + (B/\lambda_2),$$

with A' = 2.5531, B' = 0.0334 x 10^6, A = 2.5852, and B = 0.0368 x 10^6 and with wavelength in nanometers. The birefringence can, of course, be obtained from these results. Accuracy in n was limited by the estimated error of <1 min of angle to be <0.001.

Choyke and Patrick [29] measured n_o by utilizing interference fringes formed by their plates with the c axis perpendicular to the surface. They fitted their data with the formula

$$n^2_o - 1 = 5.52/[1 - (h\nu/7.53)^2],$$

with $h\nu$ given in electron volts for the range 4-0.5eV.

Spitzer et al. [30, 31] have measured the absorption coefficient α_o from 2 to 10μm using rather heavily doped platelets of SiC. Not surprisingly their results for several

samples showed free carrier absorption and the data from the weakest absorbing sample was used in Fig. 1. They measured both (o) amd (e) absorption but the difference is not significant here. The reflectivity was measured by Spitzer et al. [30,31] from 2-22μm for both (o) and (e) polarization. The 2-22μm region includes the very large restrahlen reflection (10 - 14μm). They fitted the reflection with an oscillator model

$$(n - ik)^2 = \varepsilon = \varepsilon_\infty [1 + \omega_L^2 - \omega_T^2] / [\omega_T^2 - \omega^2 + i\Gamma\omega]$$

with ω_L = 969 cm^{-1}, ω_T = 793 cm^{-1}, Γ = 4.76 cm^{-1} and ε_∞ = 6.7 for the ordinary ray (o).

The static dielectric constant has been measured at 20K to be 10.2 0.2 in the 1 - 100kHz. region [32].

From an analysis of published room-temperature data using the Lyddane-Sachs-Teller relation, $\varepsilon_o/\varepsilon_\infty = (\omega_L/\omega_T)^2$, Patrick and Choyke [33] obtained ε_∞ (⊥, O) = 6.52, ε_∞ (∥, e) = 6,70 and ε_S(⊥, O) = 9.66, ε_S(∥, e) = 10.03. A table of n_o and k_o from 30eV to 0.05eV and some additional details may be found in reference [34].

ELECTRONIC BAND STRUCTURE

In the mid fiftees the concept of indirect transitions was introduced for the group IV semiconductors [35, 36]. It was thus expected that 3C SiC would have its conduction band minima along [100] axes and have its valence band maximum at k=0 in the Brillouin zone. Optical absorption near the band edge should therefore be an indirect transition process with simultaneous absorption and emission of phonons. In the case of low temperature phototluminescence, the momentum conserving phonon side bands are due to emission of phonons only. For the non cubic (hexagonal or rhombohedral) polytypes of SiC there were no band structure calculations available, and one had little idea what to expect. The hexagonal and rhombohedral [alpha] SiC lattices (polytypes) have interatomic distances very nearly the same as 3C SiC, but differ in the ordering of the close packed planes. The issue was decided by experiment [37]. Indirect transitions were first observed for 6H SiC and subsequently for 15R, 3C, 4H, 21R, 33R, 2H and 24R SiC. In Fig. 2 the temperature dependence of the indirect exciton energy gaps E_{GX}, are given for these polytypes. Band structure calculations were soon to follow, primarily for the 3C modification. These calculations and comparison with experiment were discussed by Hemstreet and Fong in 1973 [38]. In Fig. 3 we show the theoretical band structure of 3C SiC determined by these authors as well as the result of Herman et al. [39]. The latter, in the same paper, also gave results for the hexagonal structures. Some recent theoretical work on the band structure of SiC may be found in a paper by Li and Lin-Chung [40]. A comparison of the important energy gaps in 3C SiC is given in Table IV of the paper by Li and Lin-Chung [40].

The mechanism of exciton recombination for an indirect semiconductor is illustrated schematically in Fig. 4. For a bound exciton, the hole at k=0 and the electron at $k=k_{CB}$ may recombine without phonon emission in some fraction of the transitions. This gives rise to very sharp lines termed "no-phonon lines." In SiC polytypes with multiple donor sites, the relative strength of a no-phonon line shows a direct correlation with the binding energy by which an exciton is bound to a neutral donor. In other transitions, crystal momentum is preserved by emission of a phonon which either scatters the electron to an

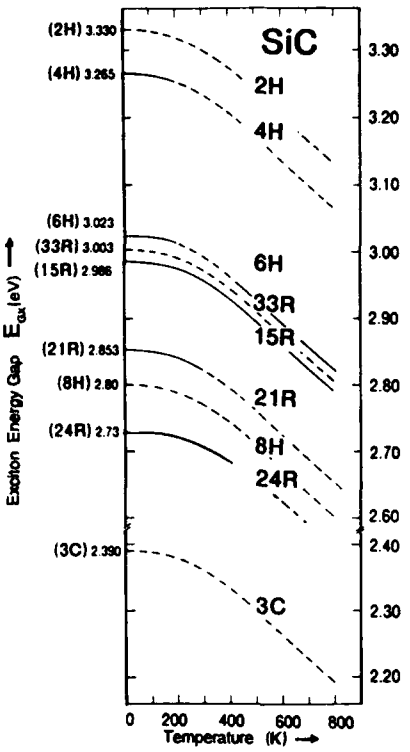

Fig. 2.

The temperature dependence of the 2H, 4H, 6H, 33R, 15R, 21R, 8H, 24R, and 3C exciton energy gap, E_{GX}. Solid lines indicate range of actual measurements. Dashed lines indicate a rough estimate of the temperature dependence. The more familiar energy gap E_G, is given by the expression $E_G = E_{GX} + E_X$, where E_X is the exciton binding energy. The exciton binding energy is still somewhat in doubt, the latest value of 27meV is deduced from wavelength modulated absorption experiments.

intermediate conduction-band state at k_0, or scatters the hole to an intermediate valence-band state at k_{CB}. Many recombination channels are available, because either the electron or the hole scattering may be to one of several bands of intermediate states. Those bands are favored which most nearly conserve energy in the intermediate state [41].

Humphrey, Bimberg and Choyke [42] used high resolution wavelength modulated absorption measurements in 6H, 15R and 3C SiC to obtain values for the spin-orbit splitting and to obtain a new estimate of the free exciton binding energy. They identified structure due to excitons derived from the top and spin-orbit split-off valence band. The spin-orbit splitting of the valence bands of the uniaxial (6H, 15R) and cubic (3C) polytypes are found to be 7 and 10meV, respectively. In the case of 3C SiC a new exciton binding energy of 27meV is obtained which is 15meV larger than the value proposed previously [43]. This gives a revised value of the fundamental energy band gap E_G=2.417eV at 2K. Another conclusion from this work is that the crystal field splitting in 6H and 15R SiC is large since the spin-orbit splitting in these uniaxial polytypes is 2/3 of the value in the cubic modification (3C SiC).

A final point of interest which is related to the band structure of the polytypes is their color when they are doped with nitrogen to levels above 10^{18} electrons / cm^3. Biederman [44] measured the optical absorption bands at room temperature and their anisotropy in 4H, 6H, 8H and 15R SiC. The results are shown in Fig. 5. The observed absorption bands are attributed to optical transitions from the lowest conduction band to other sites of

increased density of states in the higher, empty bands. This accounts for the fact that there are such large differences in the visible absorption among the n-type doped polytypes. We would not expect to see such differences if the absorption were due to transitions from impurity states in the gap to the bottom of the conduction band.

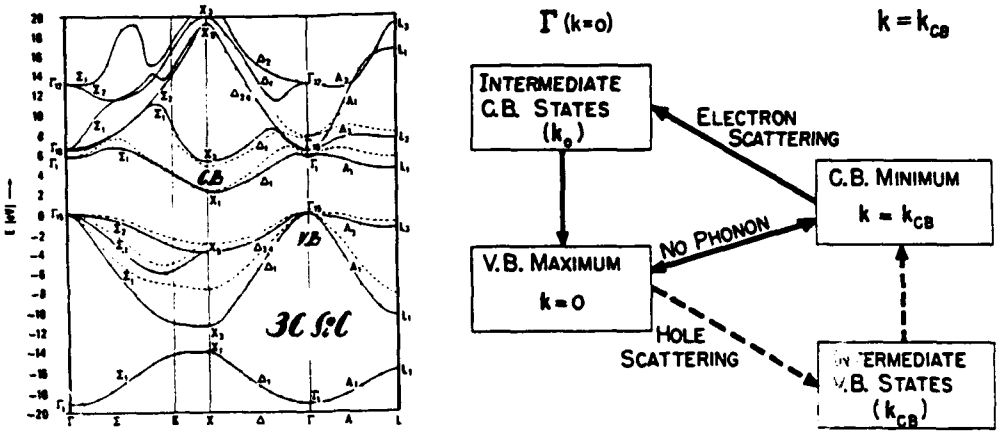

Fig. 3. On the left we have the energy band structure of 3C SiC after Hemstreet and Fong [38]. The dashed curves are the results of Herman,Van Dyke and Kortum [39].

Fig. 4. On the right we have a schematic of indirect exciton recombination for a semiconductor with valence band (V.B.) maximum at $\mathbf{k} = 0$ and (C.B.) minimum at $\mathbf{k} = \mathbf{k}_{CB}$. The no-phonon transition occurs only for the bound excitons. Other recombination modes require both an optical (vertical) transition and an electron or hole scattering, going through a number of intermediate states in which energy need not be conserved.

LOW TEMPERATURE PHOTOLUMINESCENCE

Photoluminescence spectroscopy at temperatures from 1.3K to 100K has been been extremely successful in studying free excitons, bound excitons, bound to bound impurity transitions and free to bound impurity transitions in high quality single crystals of the polytypes of SiC. In this section we touch on a few examples which may serve as a guide as we begin to study high quality single polytype films in the next few years.

In 1958 Murray Lampert [45] published a letter entitled, "Mobile and Immobile Effective-Mass-Particle Complexes on Nonmetallic Solids." His purpose was to outline a natural extension of the concept of the exciton, namely to consider bound aggregates of two or more charged particles in a nonmetallic solid, at least two of which are effective-mass particles (electrons in the conduction band or holes in the valence band). He termed such aggregates "effective-mass particle complexes." A complex which has as a constituent member an ion fixed in the lattice is localized about the ion and hence is called an immobile complex. An example would be an exciton bound to a neutral nitrogen atom in a polytype of SiC. In this case we would have a four-particle complex which we denote as (4). The free exciton is an example of a mobile complex. Lampert gave a table of some

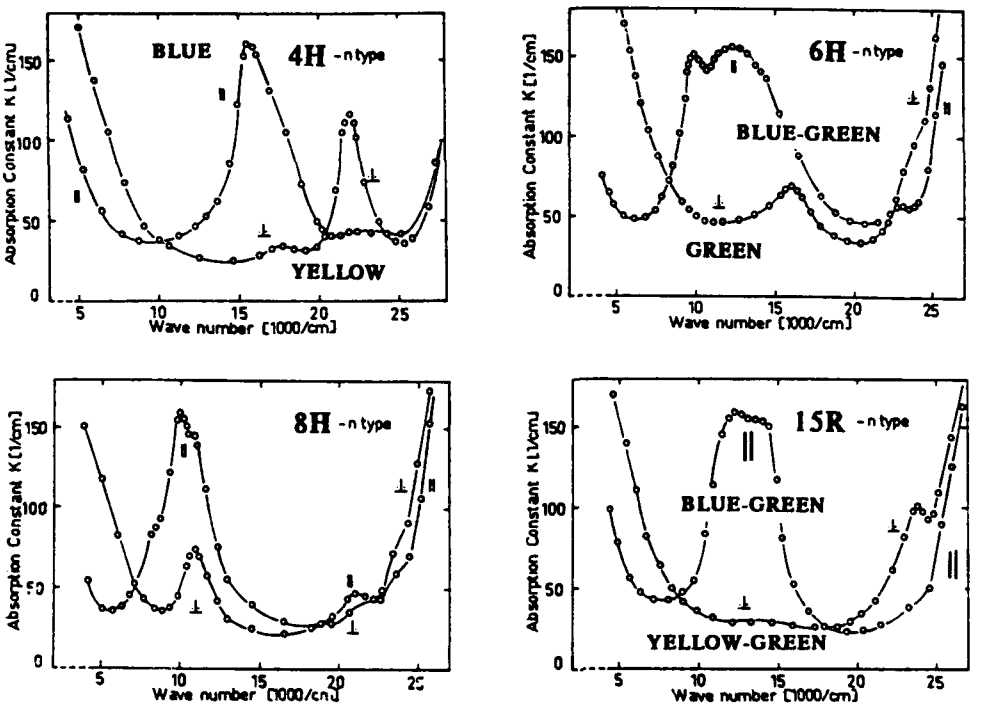

Fig. 5. Absorption curves of n-type 4H, 6H, 8H and 15R SiC crystals for polarization of light parallel and perpendicular to the c-axis of the crystals.

simple complexes which he thought might exist in semiconductors. Since that time most of these complexes have been found as well as many additional more complicated complexes.

Let us now consider some nitrogen four particle complexes in SiC since they have been extensively studied. The large unit cells of polytypes 4H, 6H, 8H, 15R, 21R and 33R have 2, 3, 4, 5, 7 and ll inequivalent sites in their respective unit cells. We would thus expect to see multiple no-phonon lines in the polytypes with large unit cells. In 2H SiC a very weak④particle no-phonon line was observed at 3.320eV giving a binding energy of the exciton to the neutral nitrogen donor of l0meV. In the case of 4H SiC we observe two no-phonon lines with binding energies of 7 and 20meV. The 7meV complex dissociates thermally near 20K. In 6H SiC we find three no-phonon lines with binding energies of 16, 31 and 33meV. At l5K, the 16meV line has been reduced by half and all three lines have dissociated by 77K. For the large unit cell of 33R SiC one expects ll no-phonon lines, but only ten have been observed. One might imagine that the missing line is associated with a binding energy which is very small or zero. The values of the binding energies of the observed lines range from 9.2 to 33.2meV. For 15R SiC we expect 5 lines, but see only four. Possibly the missing site is the same one that was not observed in 33R. The binding energy values are 7, 9, 19 and 20meV. The 21R SiC luminescence yields six instead of seven no-phonon lines. Again, the missing line may be due to a center which does not have a large enough binding energy. The bound lines in 21R SiC

have values ranging from 10 to 40meV. Finally, we have the single no-phonon line of 3C SiC which has been extensively studied in both bulk crystals and more recently in epitaxial single crystal films grown on Si or SiC by CVD. The binding energy of the exciton in cubic SiC is 10meV. We have summarized the observations in Fig. 6. For the phonon replicas (momentum conserving phonons) the situation becomes a little more complex.

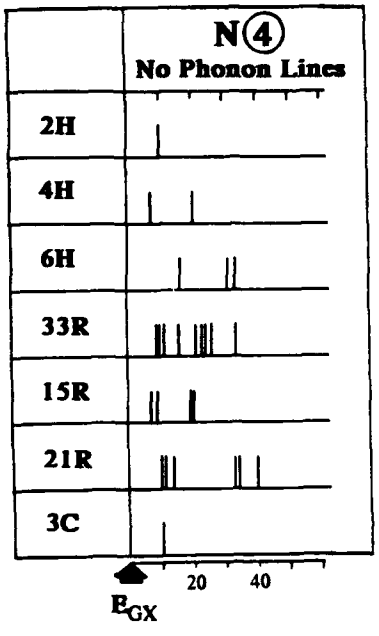

Fig. 6.

Observed no-phonon lines in the ④ particle nitrogen exciton spectrum of 2H, 4H, 6H, 33R, 15R, 21R and 3C SiC.

Neglecting degeneracy, the number of phonon branches for 2H, 4H, 6H, 33R, 15R, 21R and 3C are 12, 24, 36, 66, 30, 42 and 6 respectively. In low temperature luminescence we might then see the following number of one phonon bound exciton lines: 12 for 2H, 48 for 4H, 108 for 6H, 726 for 33R, 150 for 15R, 294 for 21R and 6 for 3C. For 3C SiC the conduction band minimum lies at the X point along [100]. Therefore, the TA and TO phonon modes are degenerate, and we see only four phonon replicas in this well known spectrum.

In the sixties many researchers reported a strong bright spectrum in 6H SiC whose no-phonon lines were bound by 162, 203 and 237meV. At first it was thought that this was an exciton bound to an ionized nitrogen donor. A similar spectrum was also found in polytypes 15R, 4H and 33R. The earliest doubts about the role of nitrogen for these deep levels followed the discovery of this spectrum in 4HSiC [46]. However, the most revealing experimental work was the magneto-optical study in 6H SiC of these three deep no-phonon lines by Dean and Hartman [47]. Patrick [48] re-interpreted their data to show that the luminescence could be attributed to a substitutional atom, although the center was not a donor, hence not nitrogen. Another observation by Dean and Hartman has proved valuable in identifying the center. Using very high resolution, they observed two satellite lines on either side of the 162, 203 and 237meV lines. They attributed these satellite lines to isotope shifts of the no-phonon line. Subsequently, Choyke and Patrick [2] attributed

this spectrum to Ti as an isoelectronic substituent for Si. In a further publication [49] these authors gave very high resolution spectra for 4H SiC showing the isotope structure of Ti. They gave a general discussion of the photoluminescence of Ti in 4H, 6H, 15R and 33R SiC. Van Kemenade and Hagen [50] confirmed the role of Ti by recording the luminescence spectrum of a 6H SiC sample that was intentionally doped with Ti enriched with the isotope ^{46}Ti. In 1985, K.M. Lee et al. [51] described optically detected magnetic resonance (ODMR) experiments carried out on the SiC Ti luminescence in 4H, 6H and 15R SiC polytypes. Spectral dependence studies of the ODMR signals allowed them to discuss the microscopic nature of the inequivalent sites for the Ti atom as well as to correctly assign the zero-phonon line and the accompanying characteristic phonons associated with each Ti site.

Donor-acceptor (D-A) pairs were observed in 3C SiC as early as 1963 [52], but it appeared impossible to give a satisfactory analysis at that time. By 1970 experimental techniques had improved so that the fine structure was well resolved [53], and the analytical techniques had improved so that the multipole splittings and the intensity cutoffs and enhancements could be interpreted [54]. A Type II spectrum was found and attributed to nitrogen on C sites and aluminum on Si sites. The lines were resolved up to shell m=80, and an extrapolation to infinite separation yielded an accurate value of the minimum photon energy, $h\nu_{\infty}$ = 2.0934ev. For the 3C energy gap a value E_G = 2.403eV at 4.2°K was used. This was obtained by Kiselev et al. [55]. At present there is still some doubt as to the precise value of E_G since the exciton binding energy [42] may be higher than what these authors [55] used. From the difference in these energies, one obtains

$$E_G - h\nu_{\infty} = E_D(N) + E_A(Al) = 310meV$$

where E_D and E_A are the donor and acceptor ionization energies. In any case, the division of the 310meV between E_D and E_A is open to two interpretations. In [53], two intensity anomalies were analyzed to obtain a value of E_D (N) = 118meV. However, in 1968 Zanmarchi [56] showed that above 77°K the DA spectrum is weak and the luminescence is largely due to what he called the A spectrum. This he attributed to free-to-bound transitions, i.e., free electrons recombining with holes bound to the deep Al acceptors. The A spectrum was also seen by Choyke and Patrick [53], with its no-phonon peak A_O at 2.153eV, but they thought at the time that Zanmarchi's interpretation was inconsistent with theirs. However, subsequent work has verified the free-to-bound mechanism in GaP, which, like 3C SiC, has the zincblende structure and conduction band minima at X. The variousluminescence mechansims in GaP and 3C SiC are very similar, and the temperature dependence of the free-to-bound transitions in GaP is like that observed for the A_O peak. Furthermore, a similar peak had by then been reported in 3C SiC containing nitrogen-boron DA pairs [58], apparently due to recombination of free electrons with holes bound to the deep B acceptors at 77°K. The N-B pair spectrum is discussed below. Because of these developments, Choyke and Patrick decided that the free-to-bound interpretation of peak A_O is correct, even though it leaves the intensity anomalies unexplained.

The energy of the A_O peak is expected to increase with temperature up to 100°K or more for

$$E(A_O) = E_G - E_A(Al) = ckT$$

and the kinetic energy of the electrons (ckT) increases with temperature faster than E_G decreases at low temperatures. The constant, c, is determined by the energy dependence of the capture cross-section. For an energy independent cross-section c = 1, and for the GaP example reported in [57] the Fig. 12 plot showed c = 1.37. With E_G = 2.402eV at 77°K for 3C SiC, the deduced value of E_A(Al) is 256 meV if c = 1, and 258meV if c = 1.37. Using an E_G of 2.402eV, one can obtain an average value of 257meV for E_A(Al), and by subtraction from 310meV one obtains E_D(N) = 53meV. However, if one believes that the revised energy gap for 3C SiC given in [42] is a better value, then one should use E_G = 2.416eV. This results in a value for E_A (Al) of 271meV instead of 257meV. We do not believe that the accuracy of E_D(N) = 53meV is in serious doubt since it is in good agreement with a value of E_D(N) = 53.6 $\pm$0.5meV obtained from a more accurate and independent experiment [59].

The DA spectrum also has a broad peak of unresolved lines due to distant pairs, which we called the "band" spectrum in [53]. The shell number at the maximum of this spectrum depends on excitation intensity, falling in the range 360 > m > 210 in our work. This band is often observed in samples in which the impurity density is too great for the appearance of well-resolved lines at small m. It was observed by Zanmarchi [56], and has since been studied by Long et al. [60], who showed how the band width and peak wavelength depend on the delay time of the measurement following excitation.

In the DA spectrum due to N-B pairs in 3C SiC [58] no resolved line structure was observed, but the band of unresolved lines was attributed to DA pairs because it shifted to higher energy with increased excitation intensity. A lower limit of 639meV was deduced for the ionization energy of the boron acceptor E_A(B). If Kuwabara et al. had used E_D(N)= 53meV instead of the earlier value of 118meV, they would have obtained a lower limit of more than 700meV for E_A(B). This value seems high, but an absorption experiment gave E_A(B) ~ 1 eV in 6H SiC [61].

In 6H SiC, DA spectra due to N-Al pairs have been observed and are frequently of good quality, with many lines. However, the reduced symmetry of 6H leads to additional shell splittings, and the presence of three inequivalent sites for each donor and acceptor leads to a multiplicity of nine in the number of DA spectra. A complete analysis of such a spectrum is a difficult tasks.

In a series of mangeto-optic experiments Dean et al. [59] measured the inter-bound state excitation spectrum of the N donor in 3C SiC through the "two electron" transition satellites observed in the low temperature luminescent recombination of excitons bound to the neutral N donors. Transitions are seen to p as well as s-like donor states although the transition oscillator strength is derived from the interaction with the impurity core since parity is conserved through inter-valley scattering by p-like, X phonons. The Zeeman splitting of a luminescence line involving the $2p_{\pm}$donor state yields the electron mass parameter $m_t = 0.24 \pm 0.01 m_0$. This and the direcly measured energy separations of the $2p_0$ and 2p states yields $m_t/m_l = 0.36 \pm 0.01$, with the static dielectric constant $\mathcal{E}_s$ = 9.92 $\pm$ 0.1. Mutually consistent central cell corections of 1.1 and 8.4 meV are observed for the $2s(A_1)$ and $1s(A_1)$ donor states. The ionization donor energy of the N donor, 53.6$\pm$0.5meV is consistent with the less accurate estimates from donor-acceptor and free-to-bound luminescence mentioned previously.

A direct method for determining the electron effective masses by means of cyclotron

resonance in epitaxial films of 3C SiC was reported by Kaplan et al. [62]. They obtained effective mass values of $0.247 \pm 0.011 m_0$ and $m_l = 0.677 \pm 0.015 m_0$ where m_t and m_l characterize orbits transverse to and aligned with the long axes of the conduction band constant energy ellipsoids. Additional measurements made by this group with the same sample tilted relative to the magnetic field direction yielded shifted absorption peaks. The shifts are consistent with a set of ellipsoids oriented along <100> directions in the crystal. These results are in very good agreement with those given in [59] on bulk crystals and discussed above. It is gratifying to note that in the band structure calculation of Li and Lin Chung [40] they obtained an electron effective mass associated with the conduction band minimum of $m_l = 0.7 m_0$. However, the calculated light-hole and heavy-hole mass along the <100> direction are found to be $m_{LH} = 0.17 m_0$ and $m_{HH} = 0.20 m_0$. This result appears to be contrary to our usual experience in semiconductors, i.e., that the hole masses are larger than the electron masses. Further work needs to be done to clarify this issue.

RAMAN SCATTERING

In pracrtice, sharp line spectra are only observed at very low temperatures. Many low temperature luminescence experiments are carried on below the lambda point of liquid helium (>2.2K). These experiments are a rich source of information on phonons especially in an indirect semiconductor like SiC. However, the phonons that are measured in this fashion are characteristic of very special positions in reciprocal space (**k** space). Since the availability of lasers, Raman scattering has become a very widely used technique for the study of the vibrational properties of SiC. When very large single crystal samples of a material are available, phonon dispersion curves may be obtained from neutron scattering. However, adequately large single crystal samples of SiC polytypes have never been grown for the neutron intensities presently available from research reactors. In 1968, Feldman, Parker, Choyke and Patrick [63,64] introduced a new method of obtaining dispersion curves based on the existence of polytypes. SiC polytypes differ in the stacking order of atomic planes, but are alike in many physical properties. Measurements on a polytype often yield results that are determined partly by the properties common to all polytypes, and partly by the unique structure of the polytype on which the measurements are made. An example is the first order Raman spectrum of 6H SiC [63]. The property assumed to be common to all polytypes is, in this case, the phonon spectrum in the axial direction [65]. Most of the lines in the Raman spectrum are, nevertheless, characteristic of the 6H structure, which determines the points of the common spectrum accessible to Raman measurements. The relationship of the Raman spectrum to the phonon spectrum is clear from a large zone [66] point of view, which permits the assignment of Raman frequencies to positions on dispersion curves, even though these modes have zero wave vector (approximately) in the Brillouin zone. The procedure is now termed "zone-folding" and is extensively used in the analysis of data obtained from semiconductor superlattices grown by means of MBE or MOCVD techniques. Fig. 7 illustrates the existenced of a common SiC phonon spectrum (within ~2%) for polytypes 4H, 6H, 15R and 21R. In a recent paper, Nakashima et al. [67] have added data for 8H and 27R SiC which fits extremely well on the curves depicted in Fig. 7. By this method, one is able to obtain dispersion curves comparable in completeness and accuracy, with those obtained for other materials by neutron diffraction (but for only one direction in momentum space).

Colwell and Klein [68] have investigated Raman scattering by electronic excitations in n-type SiC. The room-temperature Raman scattering of polytype 6H, reported earlier [63],

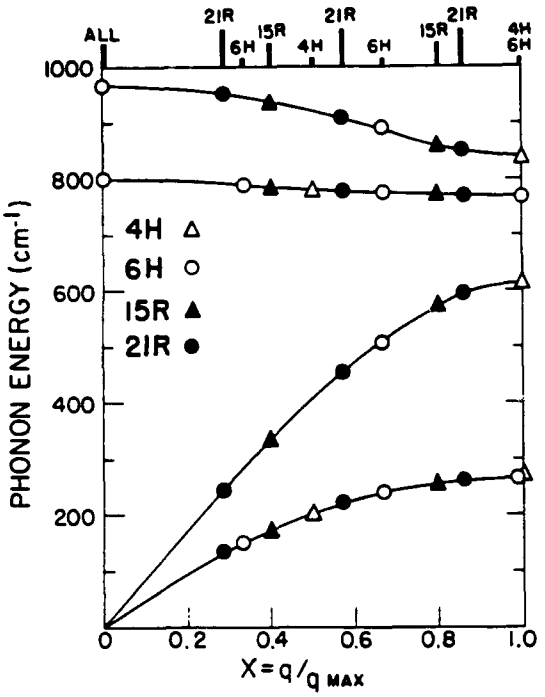

Fig. 7. Combined dispersion curves using data from 4H, 6H, 15R and 21R SiC polytypes. For each polytype, the Raman accessible values of $x = q/q_{max}$ are marked at the top of the figure.

was interpreted entirely in terms of lattice phonon scattering. However, at 6.4°K, as shown in Fig. 8, there are four new peaks in the 6H Raman data in N-doped crystals, and all have E_2 symmetry. Three of the peaks, at 13.0, 60.3 and 62.6meV are evidently due to the $1s(A_1)$ to 1s(E) valley-orbit excitations of the three inequivalent N donors. The fourth was attributed to scattering by a localized mode.

The set of $1s(A_1)$ to 1s(E) energy values, one small and two large, is analogous to the set of exciton binding energies at N-donor sites, which are 16, 31, and 33meV [69]. It suggests that there may be a similar set of N ionization energies, i.e., one small and two large. If so, the value of ~0.1eV usually found in electrical measurements [70] would be largely due to the N site with the small ionization energy. Although a simple classification of the three sites describes one as having hexagonal symmetry and two as having cubic symmetry, it is not clear that this has any relationship to the ionization energies. A different mechanism, the Kohn-Luttinger interference effect, seems to offer a better explanation of the differences [71]

The Raman results throw some light on the location of the 6H conduction-band minima, for the E_2 symmetry of the excitations is predicted only for minima on the M-L

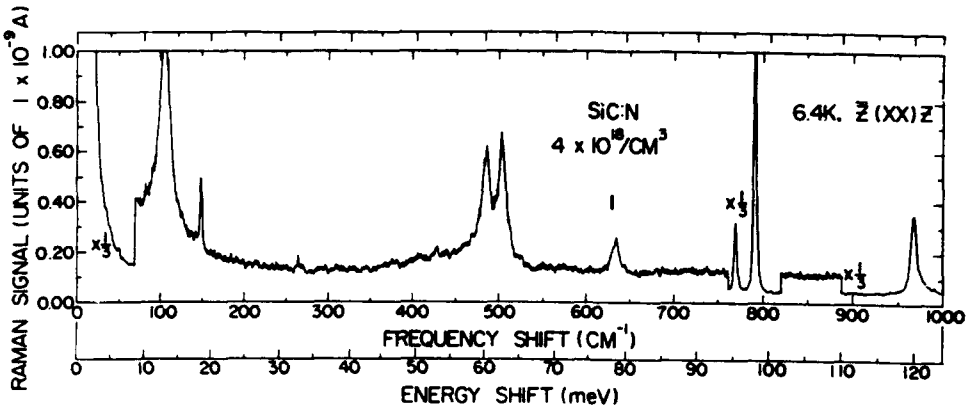

Fig. 8. Raman spectrum of 6H SiC:N at 6.4 K. Lines at 13.0, 60.3 and 62.6 meV are due to valley - orbit transitions of the N donor electron at the three inequivalent sites. From Colwell and Klein [68].

symmetry lines of the Brillouin zone. This is consistent with a suggestion of Herman et al. [39], and also with the calculations of Junginger and van Haeringen [72]. This placement on a line leaves one undetermined parameter k_z. It has been suggested [71] that k_z might be determined by ENDOR measurements, as a similar parameter was in Si, for the Kohn-Luttinger interference effect, in SiC as in Si, results in a complex donor-electron density pattern. Because good enough ENDOR results have not yet been reported, an interpretation of the exciton binding energies was used to suggest a position of the minima in [71]. The suggested k_z is one for which 6H SiC has six conduction-band minima.

Colwell and Klein [68] also observed an interference between the 13meV electronic transition and an E_2 lattice mode at 18.6meV. From a theory of the interference effect they calculated an electron-phonon coupling constant. In a sample with 6×10^{19} N/cm^3 they found plasmon coupling with the LO phonon. This phenomenon was the subject of a theoretical and experimental study in another paper [73].

An interesting PhD thesis was written by Philip Gaubis at Michigan State University in 1977 [74]. A detailed discussion of the two-phonon Raman spectra of 3C SiC is given and also the Raman scattering from nitrogen electronic impurity levels in 3C SiC.

In a series of three papers, Olego, Cardona and Vogl studied the pressure dependence and temperature dependence of the optical phonons and transverse effective charge in 3C SiC [75,76,77] using Raman scattering. The first order Raman spectra of 3C SiC were measured as a function of hydrostatic pressure up to 22.5 GPa in a diamond anvil. The mode-Gruneisen parameters of the LO and TO phonons at Γ were determined. An increase of the LO-TO splitting with pressure was observed from which an increase of the transverse effective charge upon compression results. The temperature dependence of the long-wavelength optical phonons has been measured up to 750°K. The LO-TO splitting diminishes with increasing temperature. From these data, a weak decrease of the transverse effective charge with increasing temperature is also derived.

DEFECT STATES

Currently, as semiconductor devices approach dimensions of 1000 Å and quantum-well devices regularly attain well widths of 10 Å, the understanding of defects in materials used for making these structures has become a major issue. It is a field that poses great challenges as we have seen in twenty-five years of discussions of the EL-2 center in GaAs, and more than a decade of discussions of the D-X center in AlGaAs.

In SiC the issue has currently become of great importance because of the stresses induced in epitaxially-grown films of 3C and 6H SiC, as well as the need for ion implantation for device preparation in both bulk material and single crystal films. It has been found that ion implantation of SiC at elevated temperatures, reduces the damage level sufficiently for present device preparation, but a thorough understanding of the nature of the defects and their role in controlling the electrical properties, is key to what has been termed "defect engineering." In bulk SiC, luminescence has been an effective way to study a variety of centers induced by room-temperature ion implantation, electron and neutron bombardment. In single crystal films [78] as well as plastically deformed crystals [79], similar centers and new ones have been seen in low temperature luminescence.

The severe lattice damage caused by the room temperature implantation of heavy ions ($Z > 1$) broadens the luminescence. Recovery of good line structure requires an anneal of at least 1000°C. A spectrum termed D_1 is already observed after a 1000°C anneal, but increases in intensity with annealing temperature to about 1300°C and persists even after a 1700°C anneal [80,81]. The growth of a spectrum at high temperature is evidence that it is not due to a simple lattice defect. Its independence of implanted ion and sample show that no impurity is involved. A plausible model for the D_1 center is some form of divacancy.

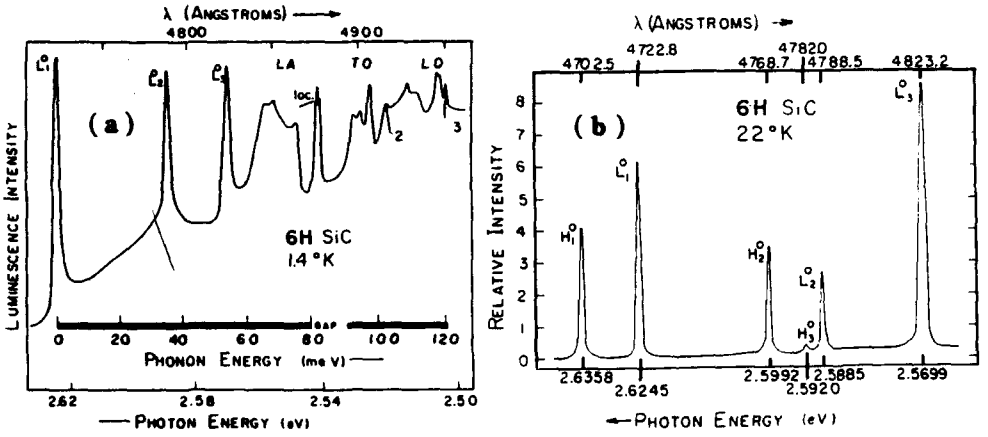

Fig.9. (a) A portion of the D_1 luminescence spectrum of an ion-bombarded 6H sample at 1.4K, after a 1300 °C anneal. The lines L^o_1, L^o_2 and L^o_3 are the three low temperature no-phonon lines. Most of the vibronic bands in this portion belong to the L^o_1 part of the spectrum. The gap in the phonon - energy scale is the gap between acoustic and optic lattice modes. (b) No phonon lines of the D_1 spectrum at an intermediate temperature (22K), showing both L^o_i and H^o_i , the low and high-temperature forms. The energy and wavelength are shown for each of the six lines.

The D_1 spectrum has an unusual temperature dependence, with two abrupt changes below 13°K in 3C SiC [80] and one change in 6H SiC [81]. Fig. 9a shows the no-phonon lines in implanted 6H SiC at 22°K, when both low temperature (L^o) and high temperature (H^o) forms appear. Since 6H SiC has three inequivalent sites there are three lines for the (L^o_i) and the (H^o_i) . They are indicated by the subscripts, 1 to 3. In both 3C and 6H polytypes the D_1 spectrum has a strong line due to an 83meV localized mode and much structure due to resonant modes, all of which appears to be independent of temperature. Some of these details are shown in Fig. 9b for the 1.4°K D_1 spectrum of 6H SiC.

In [82] it is argued that Zeeman splitting and lifetimes of the high energy H^o_i and low-energy L^o_i no-phonon lines in 6H SiC can be understood on a J-J coupling model for exciton binding at a defect with lattice symmetry. Components L^o_i from the three symmetry equivalent sites exhibit five magnetic subcomponents, while H^o_i remains unsplit; L^o_i involve forbidden transitions. The L^o_i states show a weak threefold crytal field splitting, while H^o_i are most probably split by energies that are large compared with the H^o_i - L^o_i, J - J splitting. These properties indicate exciton binding at an uncharged center behaving like an isoelectronic acceptor. The general consensus of optical properties suggests an associate center with axis parallel to the crystal C axis, perhaps a divacancy as has been mentioned earlier.

The high temperature form of the D_1 spectrum was observed in 3C SiC in electron-irradiated samples by Geiczy et al. [83]. This spectrum was also reported in proton-bombarded samples and in crystals that were quenched from 3000°C [84]. Makarov [85,86] reported the D_1 spectrum in 4H, 6H, 21R and 3C SiC after neutron irradiation, and he commented on the phonon structure. Makarov found only the high temperature, 80°K, form of the D_1 spectrum due to experimental limitations at the time. The absorption spectrum of the D_1 center in 3C SiC has been observed [87] in samples irradiated by neutrons. Excitation spectra were also obtained by these authors.

Another center induced by ion implantation is the D_2 center. The D_2 center was reported in 3C SiC [88] and in 15R SiC [89]. It is another intrinsic defect for, like D_1, it is independent of the implanted ion and sample. It is also a complex defect, for its intensity increased with annealing temperature to about 1550°C, and it persisted to the highest annealing temperature of 1700°C. It differs from D_1 in having a number of high-energy localized modes, ranging up to 164.7meV, and much higher than the lattice limit of 120.5meV.

High-energy localized modes are generated by light atoms, and require the lattice force constants to be stiffened by interstitial atoms rather than to be weakened by vacancies. Thus, a plausible model for the D_2 center is the carbon di-interstitial. The D_2 spectrum requires a higher annealing temperature than does D_1, and our model suggests that this is because its appearance depends on the diffusion of interstitial C atoms. The D_2 spectrum does not have a high-temperature form and is thermally quenched below 77°K. It was therefore not observed by those who investigated radiation damage only above 77°K [83-86].

Impurity-defect (ID) pairs are observed in implanted samples but are best examined in electron irradiated samples, where the minimal lattice damage allows the omission of the annealing operation. One then observes a number of lines that undergo progressive changes with annealing below 1000°C, where one has no interference from the D_1 and D_2 spectra. The original ID spectra anneal out at various temperatures while others grow with increasing annealing temperature or, in some cases, first appear only above a certain temperature. Very little remains of the ID spectra after annealing at 1200°C.

The ID spectra are sample dependent and are sometimes quite different in samples from different furnace runs. Both the original sample impurities and the electron-produced defects are needed to form the centers, hence the name impurity-defect pairs. The ID spectra can also be observed after proton bombardment, which does not damage the lattice enough to require an anneal.

An important problem is to identify the impurity in each ID spectrum. A possible solution is to introduce heavy ions by ion implantation, followed by high-temperature annealing to repair the lattice, and then to reintroduce the ID spectra by electron or proton bombardment. Thus, it may be possible to identify an impurity by its ID luminescence even though it does not produce a spectrum of its own.

An efficient photoluminescence spectrum in 4H, 6H and 15R SiC is produced by the implantation of protons or deuterons, followed by annealing at about 700°C, Choyke and Patrick [90, 91, 92]. In Fig. 10 we show the strong 1.3°K luminescence of H and D implanted 6H SiC. Annealing studies and the observation of C-H and C-D bond stretching vibrational modes of 370 and 274meV, respectively, suggest a model for the center, namely, an H (or D) atom bonded to a C atom at a Si vacancy. Note that in Fig. 10 we have only given the deuterium spectrum as an inset showing three C-D stretch modes since other features of the H- and D-spectra are very similar. In 6H SiC there are two kinds of spectra, called **primary** and **secondary** which are attributed to exciton recombination at two different charge states of the same center [93]. High resolution measurements show each no-phonon line, for example, H_1, H_2, H_3 of the primary spectrum in Fig. 10, to be

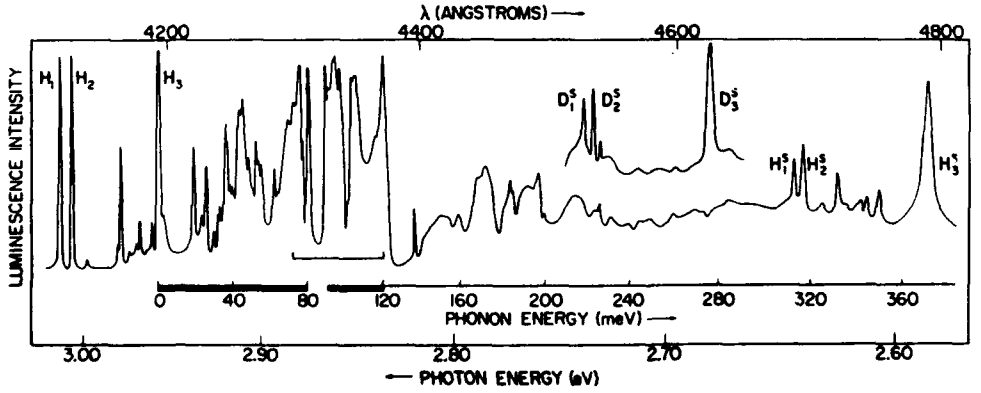

Fig. 10. Photoluminescence spectrum of H-implanted 6H SiC at 1.3K. Three inequivalent lattice sites result in three overlapping spectra whose no-phonon lines are marked H_1, H_2, and H_3. Energies of H_3 phonons may be read from the special phonon energy scale, H_3^S being at 368.8 meV. The inset shows the bond-stretching mode lines in the D - implanted 6H SiC.

an axial/non-axial doublet, as expected for a uniaxial crystal. The C-H bond direction is axial in one and non-axial in three of the four possible sites within a Si vacancy. The H atom at a Si vacancy lies within a tetrahedral cage of four C atoms, but it lies near only one of them, for the C-H bond length of 1.12 Å is small compared with the C-Si distance of 1.89 Å. Magneto-optical measurements were performed at 1.5°K, 4.2°K and 27°K on the primary and secondary spectra in 6H SiC. The primary spectrum is due to recombination of an exciton strongly bound to the center in a neutral state. Its magnetic splittings are explained by a strong-exchange model, with the singlet-exciton level 6.5meV above the triplet level. The triplet level has a zero field splitting of 0.2meV due to preferred spin alignment along axial directions. The secondary spectrum is due to recombination of an exciton weakly bound to a charged center. Its magnetic splittings are of the kind predicted by effective-mass theory, as developed by Thomas and Hopfield (1962), with $g_h = 2.8$ and $g_e = 1.8$.

TRANSPORT PROPERTIES

In this last section we shall very briefly touch on some of the considerations which enter into the determination of the electron mobilities of the polytypes of SiC, ionization energies and drift velocities in high fields. If one has large homogeneous crystals with superb doping control, as in Si, then the interpretation of the common transport measurements has become a fairly routine matter and of great importance to the device designers. In the case of SiC there is now hope on the horizon that in a few years large, very pure, uncompensated and homogeneous samples will become available. At present, transport measurements are routinely made on SiC, but their interpretation has to be done in a very careful manner, and there are subtle pitfalls.

Patrick gave a discussion of the electron mobilities in SiC polytypes in 1967 [44]. Two aspects of the electron mobility in n-type SiC are discussed in this paper:

a. Consideration of the clues to the electron-scattering mechanisms which are obtainable from observation, over a wide range of temperature, of the mobility ratio in two polytypes. This depends on the fact that electron effective masses are known to be significantly different in various SiC polytypes.

b. Experimental evidence indicating that in SiC intervalley scattering is the dominant mobility -limiting mechanism from 300° to 800°K.

The temperature dependence of the Hall mobility is usually the first and most important clue to scattering measurements in semiconductors. [95]. In the case of Ge and Si one is able to make independent measurements of the effective masses and the deformation potentials. This makes it possible to compare theoretical and experimental mobilities, and one is able to identify quantitatively the contributions of a number of scattering mechanisms [96,97]. Even today, the effective masses of SiC, with the exception of 3C SiC, are still unknown. Information on deformation potentials is equally sketchy. These quantities have at times been used as adjustable parameters in fitting mobility data, but such a procedure can lead to considerable ambiguity. In the very thorough monograph by van Daal [98], two different ways of fitting mobility are shown for an n-type sample, over the range 300° to 1000°K, without even considering intervalley scattering. Patrick points out that a polytype comparison introduces the mass dependence of the mobility into the problem, thus giving additional clues for the selection of an appropriate mechanism. The polytype comparison can only be used for n-type samples since the hole masses are

believed to be independent of polytype.

The structural differences of SiC polytypes are due to differences in the stacking order of close packed planes of atoms. This is disucssed at length in a book by Krishna [99]. These differences lead to only slight differences in many of the physical properties of SiC. On the other hand, properties which depend on the positions of the conduction band minima may experience considerable differences. In all the common polytypes of SiC, these conduction band minima lie at the Brillouin zone boundary, or more specifically, at the large zone boundary as discussed in [100]. The crystal structure determines the large zone boundaries which leads to unique positions of the conduction band minima for each of the SiC polytypes. Hence, the indirect energy gaps and the electronic properties should show a relatively strong dependence on polytype, whereas the hole mobility should not have such a dependence since for each polytype of SiC the valence band maximum is thought to be at the Brillouin zone center ($k = 0$). In p-type 3C SiC we may find an exception since there is no crystal field lifting the valence band degeneracy.

The SiC polytypes appear to have only insignificant differences in the lattice properties which are important for electron scattering, such as phonon spectrum, polaron coupling and dielectric constant. Mechanisms which are sensitive to a characteristic phonon frequency or lattice polarizability are likely to be important over the same temperature range in all the SiC polytypes. Again an exception may be 3C SiC where symmetry is high enough such that the group theoretical selection rules severely limit intervalley scattering [101]. Patrick concludes in [94] that the electron mobility ratio for two polytypes, over a temperature range dominated by a single scattering mechanism, should be a constant determined by the effective masses alone for some mechanisms and by a combination of masses and coupling constants for others. The ratio of Hall mobilities should be the same as the ratio of drift mobilities.

In Table I we list seven of the most probable scattering mechanisms in n-type SiC. The table gives the dependence of mobility on effective masses, deformation potentials (coupling constants) and temperature dependence [95]. Mechanisms for which the temperature dependence is primarily exponential are designated by X(T), where T is the characteristic temperature. Herring [102] showed that for intervalley scattering several branches of the phonon spectrum may contribute, each with a different characteristic temperature and coupling constant E_{1b}. Therefore, the acoustic branches may be active at

TABLE I. Dependence of mobility on effective mass (m), temperature (T) and deformation potential or coupling constant (E), for seven scattering mechanisms. When the temperature dependence is primarily exponential it is written X(T), where T is the energy in degrees of the pertinent phonon. More complete formulas for the mobility are given on the indicated page in Ziman's book [95].

Scattering Mechanism	Dependence on m, E and T	Page in Ref. [95]
1. Ionized Impurity	$m^{-1/2}T^{3/2}$	428
2. Neutral Impurity	mT^{0}	430
3. Piezoelectric	$m^{-3/2}T^{-1/2}$	Ref. [98] 76-78
4. Acoustic	$m^{-5/2}E_{1a}^{-2}T^{-3/2}$	433
5. Intervalley	$m^{-5/2}E_{1b}^{-2}X(540^{o}K$ and up)	443
6. Polar Optical	$m^{-3/2}X(1400^{o}K)$	438
7. Covalent Optical	$m^{-5/2}E_{3}^{-2}X(1140^{o}K)$	439

moderate temperatures in mechanism (5) of Table I, whereas mechanisms (6) and (7) are limited to higher temperatures because of the large optical phonon energies. Mechanisms (1) and (2) are limited to low temperatures because of their temperature dependence, but appear to be important up to 300°K in most samples. According to van Daal, mechanism (3) is probably not important in SiC. This leaves the acoustic (4) and intervalley (5) mechanisms as the most probable for the range 300°K and up. One might expect increasing contributions from polar optical (6) and covalent optical (7) scattering at higher temperatures.

The theory of intervalley scattering has been given by Herring [102] who showed how the $T^{-1.5}$ temperature dependence of mobility for acoustic scattering can be modified by the addition of intervalley scattering. In n-type Si ,one observes a $T^{-2.6}$ dependence, and it has been explained as a combination of acoustic and intervalley scattering by Long [97].

Over the temperature range 300°K to 800°K, n-type samples of both 6H and 15R SiC show a dependence of Hall mobility on temperature of about $T^{-2.4}$ to $T^{-2.6}$ [98,103]. By considering the possible scattering mechanisms and the observed $T^{-2.5}$ dependence of mobility, Patrick [94] concludes that acoustic and intervalley scattering combine to limit the mobility over a wide range of temperatures in n-type SiC in a similar way as they do in Si.

In a paper on electron mobility measurements in SiC polytypes Barrett and Campbell [103] found for their purest samples a mobility ratio for 15R SiC to 6H SiC of about 1.7. Both polytypes, in their experiments, were found to have a temperature dependence of mobility near $T^{-2.4}$ in the range 300°K to 800°K. For 6H SiC the room temperature mobility was $300cm^2V^{-1}sec^{-1}$ and $500cm^2V^{-1}sec^{-1}$ for 15R SiC. Polytype 4H showed higher mobilities than the 15R polytype samples.

Hagen and Kapteyns [70] using state of the art (1970) techniques produced SiC crystals which they had reason to believe were purer than any that had been produced up to that time. The purpose was to produce different polytypes doped under precisely the same experimental conditions. They then made careful measurements of carrier concentration and Hall mobility as a function of temperature and confirmed the measured Hall mobilities published by van Daal [98] and Barrett and Campbell [103]. A more important result is that they established that the ionization energy of nitrogen donor in 6H and 15R SiC are indeed different, as had been suggested earlier by photoluminescence measurements. For similarly nitrogen-doped 6H and 15R SiC donor ionizations of 81 and 40meV, respectively, were obtained. If the nitrogen donor, in the ground state, could be calculated from effective mass theory, then one would conclude that the effective mass of 15R SiC is smaller than that of 6H by a factor of two. However, there will be a considerable central cell correction required so that the the argument holds only qualitatively. At the time, these authors felt their results were out of line with luminescence data. This was before it was recognized by Choyke and Patrick [2] that the origin of the lines which led to the erroneously deep ionization energies for nitrogen were actually due to Ti. With the firm establishing of the nitrogen donor ionization energy in 3C SiC [59] at 53meV and assuming that Haynes rule applies, then the 81meV ionization energy for 6H and the 40meV ionization energy for 15R SiC appear reasonable.

Another transport property which is of importance today in the design of SiC devices is the drift velocity in high electric fields. Ferry [104] in 1975 gave a calculation of the drift velocity in high fields for SiC, diamond and GaN. He points out that the two physical properties which are important to the high frequency performance of semiconductor devices are: (a.) the "saturated" drift velocity of the carriers and (b.) the dielectric constant. In addition, power limitations are determined by the energy band gap since it is a determining factor on the critical field for avalanche breakdown and thermal conductivity. SiC polytypes have larger band gaps than most other semiconductors, a lower dielectric

constant, and a higher thermal conductivity. An early (1973) measurement [105] of the SiC carrier velocity, found a velocity of 8.2×10^6 cm / sec. with the curve still unsaturated. Si by comparison begins to saturate at 4×10^6 cm / sec.

The purpose of Ferry's paper was to calculate the expected high-field transport properties and to give an estimate of the "saturated" drift velocity of electrons in wide band gap semiconductors. The calculations were based upon a drifted Maxwellian distribution function. He concluded that the saturated drift velocity for SiC would be in the range $(2\text{-}3) \times 10^7$ cm / sec. At present, the quality of epitaxial single crystal films of SiC are such that in addition to the high saturated drift velocity, one is finding that one can impose higher than expected electric fields before breakdown occurs. Add to this the very high thermal conductivity of SiC it is apparent that SiC is now the material of choice for high-power, high-temperature and high-frequency devices.

SUMMARY

SiC is now becoming the material of choice for high-power, high-temperature, and high-frequency devices. This technology is based on the growth of excellent epitaxial films of single crystal polytypes on boule-grown substitutes of SiC. In this paper we have tried to sketch those optical and electronic properties of SiC which were studied in the past on bulk crystals grown by a number of techniques. We fully expect that optical techniques will continue to be of increasing importance as a diagnostic guide to the growers of SiC boule and single crystal film materials. The transport measurements are essential to the device designers, and we expect more reliable experimental results to be coming along as the boule and film quality improves in the near future.

Finally, I should like to close this review of the physical properties of SiC with a very succinct classification, by Lyle Patrick [106], of these properties according to the degree of their dependence on polytype. Table II gives examples of the three wave number dependent ($\mathbf{k}$) classes of properties (A), (B) and (C). These are defined as follows:

(A) Class A properties depend on wave vectors at the origin of the large zone ($\mathbf{k} = 0$), or along the zone axis ($k_z \neq 0$). Only **small** polytype differences are expected.

(B) Class B properties depend on a symmetrically-related set of wave vectors at the large zone boundary. Such properties may show **large** polytype differences.

(C) Class C properties depend on a weighted average over all wave vectors. These polytype differences are usually small, but occasionally the large weighting of a particular set of wave vectors leads to significant polytype differences.

TABLE II - Patrick's Wave-Vector Classification of SiC Physical Properties

A. Axial or zero wave vector

1. Direct energy gap at zone center
2. Hole masses and mobilities
3. X-ray coincidences
4. Axial phonon dispersion curves
5. Axial acoustic velocities

B. Zone-boundary wave vector

1. Indirect energy gaps
2. Electron masses and mobilities
3. Exciton luminescence
4. N-type dichroism
5. Crystal growth?

C. Weighted average over **k**

1. Dielectric function
2. Reflectivity
3. Birefringence
4. Thermal conductivity and expansion
5. Thermal expansion anomaly

The writing of this review paper was partially supported by ONR Grant N00014-89-J-1517.

REFERENCES

1. Choyke, W.J. (1969), ... Mat. Res. Bull. 4, 141.
2. Choyke, W.J. and Patrick, LA. (1974) in Silicon Carbide 1973, (University of South Carolina Press, Columbia, SC, USA), 261.
3. Choyke, W.J. (1977)... Inst. Phys. Conf. Ser. No. 31, 58.
4. Choyke, W.J. (1977)... XX Colloquium Spectroscopicum Internationale and 7th Int. Conf. on Atomic Spectr., Praha, 385.
5. Choyke, W.J. (1987... MRS Symposium Series, Vol. 97, 207, MRS Pittsburgh, PA.
6. Gmelin Handbook of Inorganic Chemistry, 8th ed., (1984)... Silicon-Supplement Vol B2, Springer-Verlag.
7. Gmelin Handbook of Inorganic Chemistry, 8th ed. (1986)... Silicon-Supplement Vol B3, Springer-Verlag.
8. O'Connor, J.R. and Smiltens, J. (eds.) (1960)... Silicon Carbide, Pergamon Press.
9. Tairov, Y.M. and Tsvetkov, V.F. (1978)... J. Cryst. Growth, Vol. 43, 209.
10. Nishino, S., Powell, J.A. and Will, H.A. (1983)... Appl. Phys. Lett., 42, 460.
11. Coblentz, W.W. (1906)... "Investigations of infra-red spectra," Part III and IV, Carnegie Institution of Washington, 94.
12. Coblentz, W.W. (1908)... "Supplementary investigations of infra-red spectra," Parts V, VI, VII Carnegie Institution of Washington, 36.
13. Round, H.J. (1907)... Electrical World, 309.
14. Lossew, O.W. (1923)... Telegr. Telef. 18, 61.
15. Weigle, O. (1915)... "Uber einege physikalische eigenschaften des carborunds," Nachr. Ges. Wiss., Gottingen, 264.
16. Thibault, N.W. (1944)... The American Minerologist, Vol. 29, 249.
17. Thibault, N.W. (1944)... The American Minerologist, Vol. 29, 327.
18. Mitchell, R.S. (1953)... The American Minerologist, Vol. 38, 60.
19. Rehn, V., Stanford, J.L., Jones, V.O., Choyke, W.J. (1976)... Proc. Int. Conf. Physics Semicond., 13th, Rome, 985.
20. Leveque, G. and Lynch, D.W. (1982)... Private communication.
21. Choyke, W.J., Farich, R.F., Hoffman, R.A. (1976)... Appl. Optics 15, 2006.
22. Rehn, V., Stanford, J.L., Baer, A.D., Jones, V.O., Choyke, W.J., (1977)... Appl. Optics 16, 111.
23. Choyke, W.J., Partlow, W.D., Supertzi, E.P., Venskytis, F.J., Brandt, G.B. (1977)... Appl. Optics 16, 2013.
24. Rehn, V., and Choyke, W.J. (1980)... Nucl. Inst. and Methods, 177, 173.
25. Mrowka, S., Jelinsky, P., Bowyer, S., Sanger, G., Choyke, W.J. (1986)... SPIE Proc., 597.
26. Choyke, W.J. and Patrick, L.A. (1968)... Phys. Rev., 172, 769.
27. Groth, R. and Kauer, E. (1961)... Phys. Status Solidi, 1, 445.
28. Shaffer, P.T.B. (1971)... Appl. Opt., 10, 1034.
29. Choyke, W.J. and Patrick, L.A. (1968)... Jour. Opt. Soc. Am., 58, 377.
30. Spitzer, W.G, Kleinman, D.A., Walsh, D. (1959)... Phys. Rev., 113, 127 .
31. Spitzer, W.G., Kleinman, D.A., Frosch, C.J. (1959)... Phys. Rev., 113, 133.
32. Hofman, D., Lely, J.A., Volger, J. (1959)... Physica, 23, 236.
33. Patrick, L.A. and Choyke, W.J. (1970)... Phys. Rev., B2, 2255.
34. Choyke, W.J. and Palik, E.D. (1985)..."Handbook of Optical Constants of solids," E.D. Palik (ed.), Academic Press, Inc., 587.
35. Bardeen, J. Blatt, F.J., Hall, L.H. (1954)... "Photoconductivity Conference," Atlantic City, Chapman and Hall, Ltd., 146.

36. Fan, H.Y., Shepherd, M.L., Spitzer, W. (1954)... "Photoconductivity Conference," Atlantic City, Chapman and Hall, Ltd., 184.
37. Choyke, W.J. and Patrick, L.A. (1957)... Phys. Rev., 105, 1721.
38. Hemstreet, L.A. and Fong, C.Y. (1974)... in Silicon Carbide 1973, University of South Carolina Press, Columbia, S.C., 284.
39. Herman, F., Van Dyke, J.P., Kortum, R.L. (1969)... Mat. Res. Bull. 4, 167.
40. Li, Y. and Lin-Chung, P.J. (1987)... Phys. Rev. B36, 1130.
41. McLean, T.P. (1960)... "Progress in semiconductors," 5, Heywood and Co., Ltd., London, 55.
42. Humphreys, R.G., Bimberg, D., Choyke, W.J. (1981)... Solid State Communications, 39, 163.
43. Nedzvetskii, D.S., Novikov, B.V., Prokofeva, N.K., Reifman, M.B. (1969)... Sov. Phys. Semicond., 2, 914.
44. Biederman, E. (1965)... Solid State Communications, 3, 343.
45. Lampert, M.A. (1958)... Phys. Rev. Lett., 1, 450.
46. Choyke, W.J., Patrick, L.A., Hamilton, D.R. (1964)... Proc. 7th Int. Conf. on Physics of Semic., Dunod, Paris, 75.
47. Dean, P.J. and Hartman, R.L. (1972)... Phys. Rev., B5, 4911.
48. Patrick, L.A. (1973)... Phys. Rev., B7, 1719.
49. Patrick, L.A. and Choyke, W.J. (1974)... Phys. Rev., B10, 5091.
50. van Kemenade, A.W.C. and Hagen, S.H. (1974)... Solid State Commun., 14, 1331.
51. Lee, K.M. Dang, Le Si., Watkins, G.D. and Choyke, W.J (1985)... Phys. Rev., B32, 2273.
52. Choyke,. W.J. Hamilton, D.R., Patrick, L.A. (1964)... Phys. Rev., 133, A1163.
53. Choyke, W. J. and Patrick, L.A. (1970)... Phys. Rev., B2, 4959.
54. Dean, P.J. (1973)... Progress in Solid State Chemistry, Pergamon, N.Y., 8, 1.
55. Kiselev, V.A., Novikov, B.V., Pimonenko, M.M., Shadrin, E.B.(1971)... Sov. Phys. Solid State, 13, 926.
56. Zanmarchi, G. (1968)... J. Phys. Chem. Solids, 29, 1727.
57. Bachrach, R.Z. and Lorimor, O.G. (1973)... Phys. Rev., B7, 700.
58. Kuwabara, H., Shiokawa, S., Yamaki S. (1973)... Phys. Stat. Solidi (a), 16, K67.
59. Dean, P.J., Choyke, W.J., Patrick, L.A. (1977)... J. of Lum., 15, 299.
60. Long, N.N., Nedzvetskii, D.S., Prokofeva, N.K., Reifman, M.B. (1971)... Opt. and Spectr., 30, 165.
61. Vakulenko, W.V. and Govorova, O.A. (1971)... Sov. Phys. Solid State, 13, 520.
62. Kaplan, R., Wagner, R.J., Kim, H.J., Davis, R.F. (1985)... Sol. State Comm., 55, 67.
63. Feldman, D.W., Parker, J.H., Choyke, W.J., Patrick, L.A. (1968)... Phys. Rev., 170, 698.
64. Feldman, D.W., Parker, J.H., Choyke, W.J., Patrick, L.A. (1968)... Phys. Rev., 173, 787.
65. Patrick, L.A. (1968)... Phys. Rev., 167, 809.
66. Jones, H. (1960)... "The theory of Brillouin zones and electronic states in crystals," North Holland Publishing Co., Amsterdam.
67. Nakashima, S., Katahama, Y., Nakakura, Y., Mitsuishi, A. (1986)... Phys. Rev., B33, 5721.
68. Colwell, P.J. and Klein, M.V. (1972)... Phys. Rev., B6, 498.
69. Choyke, W.J. and Patrick, L.A. (1962)... Phys. Rev., 127, 1868.
70. Hagen, S.H. and Kapteyns, C.J., (1970)... Philips Res. Repts., 25, 1.

71. Patrick, L.A. (1972)... Phys. Rev., B5, 2198.
72. Junginger, H.G. and van Haeringen, W. (1970)... Phys. Status Solidi, 37, 709.
73. Klein, M.V., Ganguly, B.N., Colwell, P.J. (1972)... Phys. Rev. , B6, 2380.
74. Gaubis, P.A. (1977)... "Raman scattering from two-phonon excitations and from electronic nitrogen impurity levels in cubic SiC," University Microfilms International, #78-10,053, Ann Arbor, Michigan 48106.
75. Olego, D. and Cardona, M. (1982)... Phys. Rev., B25, 1151.
76. Olego, D., Cardona, M., Vogl, P. (1982)... Phys. Rev., B25, 3878.
77. Olego, D. and Cardona, M. (1982)... Phys. Rev., B25, 3889.
78. Choyke, W.J., Feng, Z.C., Powell, J.A. (1988)... J. App. Phys., 64, 3163.
79. Gorban, I.S., Kravets, V.A., Mishinova, G.N., Nazarenko, K.V. (1977)... Sov. Phys. Semicond., 10, 1254.
80. Choyke, W.J. and Patrick, W.A. (1971)... Phys. Rev., B4, 1843.
81. Patrick, W.A. and Choyke, W.J. (1972)... Phys. Rev., B5, 3253
82. Dean, P.J., Bimberg, D., Choyke, W.J. (1979)... "Defects and radiation effects in semiconductors," Inst. of Phys. Conf. Ser. No. 46, 447.
83. Geiczy, I.I., Nesterov, A.A., Smirnov, L.S. (1971)... in "Radiation effects in semiconductors," Gordon and Breach, N.Y., 327.
84. Nesterov, A.A., Gurko, V.D., Smirnov, L.S. (1973)... Sov. Phys. Semicond., 6, 1130.
85. Makarov, V.V. (1967)... Sov. Phys. Solid State, 9, 457.
86. Makarov, V.V. (1972)... Sov. Phys. Solid State, 13, 1974.
87. Suleimanov, Y.M . Grekhov, V.M., Demakov, K.D. Plyuto, I.V. (1985)... Sov. Phys. Solid State, 27, 1910.
88. Patrick, L.A. and Choyke, W.J. (1973)... J. Phys. Chem. Solids, 34, 565.
89. Choyke, W.J. and Patrick, L.A. (1972)... in "Proc.Int. Conf. on Defects in Semicond.," Reading, UK, 218.
90. Choyke, W.J. and Patrick, L.A. (1972)... Phys. Rev. Lett., 29, 355.
91. Choyke, W.J. and Patrick, L.A.(1972)... in "Proc. IIth Int. Conf. in the Physics of Semicond., Warsaw, 177.
92. Choyke, W.J. and Patrick, L.A. (1974)... Phys. Rev., B9, 3214.
93. Choyke, W.J., Patrick, L.A., Dean, P.J. (1974)... Phys. Rev., B10, 2554.
94. Patrick, LA. (1967)... J. of Appl. Phys., 38, 50.
95. Ziman, J.M. (1960)... "Electrons and phonons," Oxford University Press, London.
96. Morin, F.J., Geballe, T.H., Herring, C. (1957)... Phys. Rev., 105, 525.
97. Long, D. (1960)... Phys. Rev. , 120, 2024.
98. van Daal, H.J. (1965)... Philips Res. Rept. Suppl., 3, 70.
99. Krishna, P. (ed.), (1983)... "Crystal growth and characterization of polytype structures," Pergamon Press, New York.
100. Patrick, L., Choyke, W.J., Hamilton, D.R. (1965)... Phys. Rev., 137, A1515.
101. Patrick, L.A. (1966)... J. Appl. Phys., 37, 4911.
102. Herring, C. (1955)... Bell System Tech. J., 34, 237.
103. Barrett, D.L. and Campbell, R.B. (1967)... J. Appl. Phys., 38, 53.
104. Ferry, D.K. (1975)... Phys. Rev., B12, 2361.
105. Berman, H.S., Heng, T.M., Nathenson, H.C., Campbell, R.B.(1974)... in "Silicon carbide 1973," University of South Carolina Press, Columbia, SC, USA.
106. Patrick, L.A. (1969)... Mat. Res. Bull., Pergamon Press, 4, 129.

RECENT ADVANCES REGARDING THE DEFINITION OF THE ATOMIC ENVIRONMENT, FILM GROWTH AND MICROELECTRONIC DEVICE DEVELOPMENT IN SILICON CARBIDE

Robert F. Davis
North Carolina State University
Department of Materials Science and Engineering
Box 7907
Raleigh, North Carolina 27695
United States of America

ABSTRACT. The extreme thermal and electronic properties of silicon carbide provide multiplicative combinations of attributes which lead to one of the highest figures of merit for any semiconductor material for use in high-power, -speed, -temperature, -frequency and radiation hard applications. Structurally, silicon carbide exists in a host of polytypes, the origins of which are incompletely understood. Recent magic angle spinning-NMR studies have provided considerable information regarding the positions of the inequivalent carbon sites in the simple polytypes. The continual development of the deposition of silicon carbide thin films and the associated technologies of impurity incorporation, etching, and electrical contacts have culminated in a host of solid state devices including field effect transistors capable of operation to 925K. The results of several research programs and the remaining challenges related to the development of silicon carbide vis' a' vis' microelectronics are presented and discussed in this review.

1. Introduction

In certain close-packed structures such as SiC, there exists a special one-dimensional type of polymorphism called polytypism. Polytypes are alike in the two dimensions of the close-packed planes but differ in the stacking sequence in the dimension perpendicular to these planes. In SiC, the stacking sequence of the close-packed planes of covalently bonded primary coordination tetrahedra (either SiC_4 or CSi_4) can be described by an ABC notation. If the pure ABC stacking is repetitive, one obtains the zinc blende structure. This is the only cubic SiC polytype and is referred to as 3C or β-SiC, where the 3 refers to the number of planes in the periodic sequence. The hexagonal (...ABAB...) sequence is also found in SiC. Furthermore, both can also occur in more complex, intermixed, forms yielding a wider range of ordered, larger period, stacked hexagonal or rhombohedral structures of which 6H is the most common. All of these noncubic structures are known collectively as α-SiC.

The extremes in the thermal, mechanical, chemical and electronic properties of all the common polytypes of silicon carbide (SiC) allow the types and the numbers of current and conceivable applications of this material to be substantial. However, the principal driving forces for the current resurgence in interest in this material are their potential as high power, high speed, high temperature, electronic and optoelectronic devices resistant to radiation damage.

R. Freer (ed.), The Physics and Chemistry of Carbides; Nitrides and Borides, 589–623.
© 1990 *Kluwer Academic Publishers. Printed in the Netherlands.*

The theory of the physical properties of semiconductors and of the relation of these properties to the operation of devices is well understood. Moreover, semiconductor device technology continues to advance so rapidly that it is important to inquire as to those factors which now limit progress toward maxima in packing densities, speeds and frequencies of operation and power handling capability. Further, the generalizations from the physical theory of devices can be applied to any semiconductor and provide a basis for comparison and ranking of the device potential of different materials. The results of these generalizations from theory can be expressed as "figures of merit" or as "physical limits."

Johnson[1] has considered the high frequency–high power capability of various semiconductors from the viewpoint of discrete devices. He argued that the basic limitation on various transistor characteristics is set by the product of the breakdown electric field*, E_B, and the saturated (limiting) electron velocity, V_S, i.e. the velocity at which an electron has enough energy to emit an optical phonon. Johnson's figures of merit, $(E_B V_S/p)^2$, and associated ratios to Si are presented in Table 1. The high breakdown fields of SiC (and diamond) are primarily responsible for their superior standing in this Table.

Keyes[2] has considered the switching speed of transistors in integrated circuits for computer logic applications. In this case a high limiting velocity allows high speed devices. Another problem of small, closely spaced devices is the very high density of power dissipation, i.e. the production of heat. The heat flows from the device by conduction through the semiconductor material, thereby encountering a thermal resistance that is inversely proportional to the size of the device. A lower limit is set on the device size by the maximum permissible thermal resistance, thus, a high thermal conductivity, σ_T, is greatly desired in the device material. An additional set of figures of merit which includes V_S, σ_T and the dielectric constant, K†, has been developed by Keyes[2] and is shown in Table 2. A perusal of the relative ratios of the Johnson and Keyes figures of merit in Tables 1 and 2, respectively, coupled with the present desire for devices for gigahertz logic, microwave communications, high temperature microprocessors and radiation hard applications makes obvious the present interest in the growth and characterization of and device development in SiC.

Finally, SiC is also of interest as light-emitting diodes. Although band-to-band transitions in SiC occur indirectly via intermediate energy levels in the conduction band and thus negate the possibility of laser applications, doping of the material with various donor and acceptor species allow electroluminescent devices to be produced; i.e., Be (red), Al (blue), B (yellow), and Sc (green). The creation of a sharp p(Al-doped)–n(N-doped) junction in the 6H a–SiC polytype also allows the fabrication of blue LEDs in this form of SiC.

The following sections present a brief perspective of the results and conclusions of recent crystallographic, thin film growth and electronic and optoelectronic device development as well as suggest directions for future study.

---

* Breakdown of a semiconductor occurs when carriers acquire enough energy to excite an electron across the bandgap, creating an electron-hole pair.

† The dielectric constant enters in the denomination in Keyes[2] calculation of the figure of merit, because the amount of charge stored in the device decreases with decreasing dielectric constant. Thus, since the speed with which charge can move through a semiconductor is inversely proportional to the ability of the material to store charge, the speed of a device is also proportional to 1/K.

TABLE 1 Johnson's figures of merit for a transistor's power and frequency performance for selected semiconductor materials

Material	E_B (V cm^{-1})	V_{SAT} (cm s^{-1})	$E_B V_{SAT}/\pi$ (V s^{-1})	$P_M F_L^2 Z_L = (E_B V_S/\pi)^2$ (W Ω s^{-2})	*Ratio to silicon* (Dimensionless)
Silicon	3×10^5	1.0×10^7	9.5×10^{11}	9.0×10^{23}	1.0
GaAs	4×10^5	2.0×10^7	25.0×10^{11}	62.5×10^{23}	6.9
InP	6×10^5	2.0×10^7	38.0×10^{11}	144.4×10^{23}	16.0
GaN	20×10^5	2.5×10^7	159.2×10^{11}	$2\,534\times10^{23}$	281.6
α-SiC(6H)	40×10^5	2.0×10^7	250.0×10^{11}	$6\,250\times10^{23}$	695.4
β-SiC	40×10^5	2.5×10^7	320.0×10^{11}	$10\,240\times10^{23}$	1137.8
Diamond	100×10^5	2.7×10^7	859.4×10^{11}	$73\,856\times10^{23}$	8206.0

TABLE 2 Keyes' figures of merit for the speed of a transistor for selected semiconductors

Material	σ_1 *(300 K)* (W cm^{-1})	V_{SAT} (cm s^{-1}	K (Dimensionless)	$\sigma_1(V_{SAT}/K)^{1/2}$ (W cm$^{-1/2}$ s$^{-1/2}$)	*Ratio to silicon* (Dimensionless)
Silicon	1.5	1.0×10^7	11.8	13.8×10^2	1
GaAs	0.5	2.0×10^7	12.8	6.2×10^2	0.456
InP	0.7	2.0×10^7	14.0	8.4×10^2	0.608
GaN	1.5	2.5×10^7	9.5	24.3×10^2	1.76
α-SiC(6H)	5.0	2.5×10^7	10.0	70.7×10^2	5.12
β-SiC	5.0	2.5×10^7	9.7	80.3×10^2	5.8
Diamond	20.0	2.7×10^7	5.5	444.0×10^2	32.2

Table 3. Percent hexagonality, band gap, lattice parameters *a* and *c*, average layer spacing *c/n*, and *c/na* ratios for several SiC polytypes (from Guth and Petuskey (1987(a)).

Polytype	%H	Bandgap (eV)	a (Å)	c (Å)	c/n	c/na	Ref.
3C	0	2.390	3.0827	7.5510	2.5170	0.8165	[1]
			3.08269	7.55124	2.51708	0.8165	[2]
8H	25		3.079	20.142	2.5177	0.8177	[3]
21R	29		3.08111	52.9034	2.51921	0.8176	[2]
6H	33	2.860	3.08086	15.1174	2.51955	0.8178	[2]
			3.08065	15.11738	2.5196	0.8179	[2]
15R	40		3.073	37.30	2.487	0.8092	[3]
			3.08043	37.8014	2.52009	0.8181	[2]
10H	40		3.08049	25.2011	2.52011	0.8181	[2
27R	44		3.08028	68.0495	2.52035	0.8182	[2]
4H	50	3.263	3.07997	10.0830	2.52076	0.8184	[2]
			3.076	10.046	2.5115	0.8165	[3]
2H	100	3.300	3.0763	5.0480	2.5240	0.8205	[4]

[1] Taylor and Jones, (1960); [2] Tairov and Tsvetkov (1983); [3] Donnay (1963); [4] Adamsky and Merz (1959).

2. Polytypism in Silicon Carbide

2.1. DESCRIPTION, ELEMENTARY STRUCTURAL CONSIDERATIONS AND NOMENCLATURE

As noted in the Introduction, the fundamental structural unit in all SiC polytypes is a covalently bonded tetrahedron of C atoms with a Si atom at the center. Each C is likewise tetrahedrally surrounded by Si atoms. The various polytypes have layers of these tetrahedra stacked to form polar structures in which all the tetrahedra have one apex out of the layer plane. The tetrahedra are linked through their corners, satisfying the four-fold coordination at any structural point and occupying an array of positions analogous to those occupied by spheres in close-packed structures. Both simple hexagonal and cubic stacking sequences of tetrahedra occur in SiC. These two sequences, however, also intermix to form the wide range of ordered, larger-period structures. Using Jagodzinski's suggested notation for stacking sequences[3], any one layer in these stacking sequences can be described as having a local cubic (*k*) or hexagonal (*h*) environment (at least with respect to the positions of the centroids of the immediate layer neighbors). The positions of the tetrahedra above and below a given layer are thus either different (*k*) or the same (*h*), respectively, as shown in Figure 1. In this particular method of describing SiC polytypes, each of the letters represents one tetrahedral layer. Furthermore, whereas the *ABC* (Ramsdell[4]) designation is arbitrary, the letters *h* and *k* cannot be assigned arbitrarily, since they denote not only a specific layer, but the relative orientations of the tetrahedra of the two adjacent layers.) Moreover, the acentricity of the tetrahedra requires that in sequences of the type *hhhh* the layers are not only offset but rotated by 180 degrees. Thus two stacking generations exist for SiC: (1) layer translation only, yielding (*kkkk*), and (2) layer translation and rotation, yielding (*hhhh*).

An alternative notations for identifying polytypes has been suggested by Zhadanov[5]. The letters *C*, *H* and *R* are used to represent cubic, hexagonal and rhombohedral structures, respectively (the only basic crystallographic structures found in SiC), combined with a numeral that represents the number of close-packed layers in the c direction before the sequence is repeated. Zhadanov's notation denotes the number of consecutive layers without rotation, shows the total stacking sequence, and uses a subscript to indicate the number of times a particular sequence is repeated without interruption in the crystal. Examining this notation for the long-period polytypes shows that the structures of these uncommon forms are mainly compound sequences of one or more of the common polytypes (see caption of Figure 1). The Ramsdell notation will be used extensively in this discussion because of its common use in SiC literature and its brevity. As an example of the three notations, the pure wurtzite form can be indicated by 2H, $(h)_2$, or (11). Additional comparative examples of the three notations and their associated structural diagrams are presented in Figure 1 for the four most common polytypes. An excellent discussion of these notations and polytypism in SiC has been presented by Jepps and Page[6].

2.2 STRUCTURAL REFINEMENTS AND RELATED MO AND MAS-NMR STUDIES ON SIC POLYTYPES

The crystallography and atomic environment surrounding a given atom in most polytypes of SiC are actually much more complex than the foregoing introductory remarks indicate. To describe and understand the idiosyncrasies of those structures, it is more convenient to visualize them as

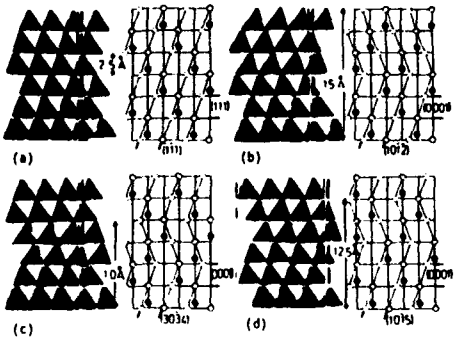

Figure 1. Models of four most common SiC polytype structures constructed with "solid" tetrahedra and tramline structure diagrams. Stacking sequences can be visualized by considering the zigzag sequence of nonbasal-plane tetrahedral faces. The respective Ramsdell, Jagodzinski, and Zhadanov symbols for these polytypes are (a), 3C, kkk, (∞); (b), 6H, $(hkk)_2$, (33); (c), 4H, hkhk, (22); (d) 15R, $(hkhkk)_3$, $(32)_3$ (from Ref. 6).

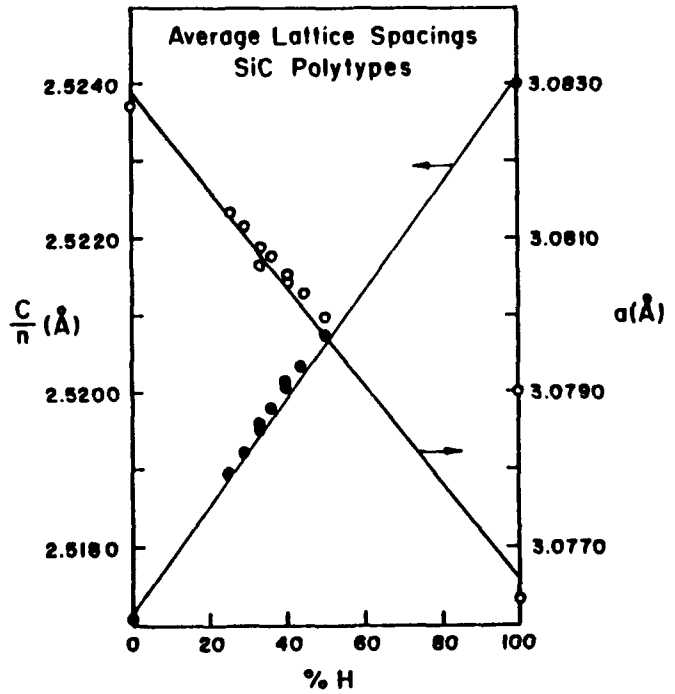

Figure 2. Hexagonal a and c/n lattice constants of a number of SiC polytypes from Table I vs. %H, the percentage of hexagonally coordinated layers in the structures. The average layer spacing c/n increases and decreases with increasing fraction of hexagonally coordinated layers (from Ref. 12).

composed of individual layers of Si atoms separated by layers of C atoms or of Si-C biplane layers stacked along the crystallographic C axis. The three notations described above for stacking of tetrahedra can be used with equal facility in these cases wherein they would now refer to individual layers of atoms of either Si or C or Si-C biplane layers. Ramsdell[4] noted that all atoms in the SiC polytypes lie on the $(11\bar{2}0)$ planes ((110) planes for 3C-SiC), and that on these planes the atoms lie in zigzag patterns characteristic of the stacking. In addition, each atom exhibits 3-fold rotational symmetry about the c-axis. Thus the lateral distances between adjacent vertical bonds in the $[\bar{1}10]$ direction are equal. This is also true for all other polytypes, however the distances have different magnitudes.

The percent hexagonality of a polytype may be determined by considering the coordination of the individual Si-C biplane in a manner similar to that used to derive Jagodzinski's notation for a particular structure. For example the 6 biplanes of the 6H polytype are composed of two biplanes with hexagonal coordination and four with cubic. Thus, it is 33% hexagonal in character. (No polytypes have been identified with greater than 50% hexagonality.) In this and all other intermediate polytypes, each hexagonal biplane is bounded by two cubic planes. As there is no mirror symmetry perpendicular to the (0001) planes, the orientation of the bonds in the hexagonal plane differs with respect to each cubic plane on opposite sides. This juxtaposition of biplanes with different coordination along the c-axis of the polytypes produces two different effects: (1) differences in the relative interplanar spacings, bond lengths and bond angles and (2) crystallographic nonequivalent Si and C sites. The latter is a consequence of the former. These effects are most readily observed as differences in lattice parameters. Figure 2 shows the experimentally determined (see Table 3) linear variation in the lattice parameter as a function of the percent hexagonal character of various polytypes. The c-axis parameter has been normalized with respect to the number (n) of biplane layers in the [0001] direction. These second (and higher) nearest neighbor (interplanar) interactions also affect the first coordination (Si-C) geometry.

The silicons (and carbons) in the cubic (3C) form have complete tetrahedral symmetry. This is the only structure from which reliable bond lengths can be obtained, since the c/a ratio (=2.4495) is equivalent to that of a regular tetrahedron. The bond angles are all 109.471° and the c and a parameters are known from X-ray data (see Table 3 and Refs. [7-10] cited in this Table); thus, the Si-C interatomic distances in each tetrahedron are everywhere equal to 1.8877Å. In all other polytypes, there must be one long (vertical) and three short (lateral) bonds, as a result of the c/a ratio being greater than ideal for close-packed spheres. DeMesquita[11] has shown that the three crystallographically independent Si atoms in 6H have identical nearest neighbor surroundings within experimental error. Each Si has one long (1.894Å) Si-C bond along the stacking axis and three shorter Si-C bonds of equal (1.886Å) length. All C-S-C angles are between 109.4 and 109.5°.

Guth and Petuskey[12] have extended the aforenoted research of DeMesquita[11] via *ab inito* molecular orbital calculations. The 3C, 6H, 4H and 2H polytypes as well as four general structures were modeled using $Si(CH_3)_4$ and $C(SiH_3)_4$. The external dimensions of these molecules were constrained to values equivalent to the lattice parameters of the polytypes. Differences due to hexagonal and cubic configurations originating from second order coordination effects around a central atom were determined for the various structures. The results of the calculations showed that as the percent hexagonality increased, the vertical bonds lengthen and the lateral bonds shorten relative to the regular tetrahedral (3C) structure. Moreover, the difference between their two bond lengths is greater for hexagonally than for

coordinated atoms; the opposite is true for the differences between the vertical and lateral bond angles. Finally, Mullikin population analysis revealed that the charge on the central atom is slightly greater for the hexagonal coordinated atoms and that Si and C atoms showed net positive and negative charges respectively.

From the viewpoints of an overall perspective and summary to this point, the very low stacking fault energy of SiC allows the apparently random generation of various polytypes even within the same single crystal as a result of thermal fluctuations, the presence and distribution of various impurities (see Ref. 6) and possibly different Si/C ratios (see discussion below on nonstoichiometry). Each polytype possesses a particular percentage of cubic and hexagonal sites (and layers) in separate planes. Second nearest neighbor interactions (as well those resulting from third and fourth order coordinations) with the atoms in these sites affect the Si-C distances and bond angles in this first neighbor coordination and the charge distribution of the central atom. These interactions are also responsible for the nonuniform interplanar spacings in the c direction and the nonequivalences in atomic sites observed in the polytypes. This last topic will be the principal focus of discussion in the remainder of this subsection.

In many previous reports regarding polytypism in SiC, it was tacitly assumed that in all polytypes there existed only two nonequivalent Si (and C) sites: the cubic site found in 3C and the hexagonal site extant in 2H. However, a detailed examination of the distributions of the atoms throughout the various polytype unit cells and the crystallographic movements necessary to uniquely define the positions of the Si and C atoms within their long range chemical environments reveals that all polytypes except 3C and 2H possess two or more nonequivalent lattice sites for both species, for reasons noted above. For example, 6H-SiC contains three crystallographically nonequivalent sites for both Si and C. Quantitative information regarding the crystallography of those sites in 6H has been obtained by very careful X-ray analyses and photo-optical studies by DeMesquita[11], and Choyke, Patrick and their coworkers[13-15], respectively. These results have been supplemented by MAS NMR research by Turner *et al* [16], Inkrott *et. al*[17], Hartman, and coworkers[18-19] and Guth and Petuskey[20]. These last studies are particularly interesting in that NMR is sensitive to local ordering, i.e., to the number and types of atoms around a particular nucleus. Thus, it can provide information regarding the distance over which the chemical environment influences an atom and thus affects the chemical shift. Silicon Carbide is ideal for MAS NMR research, since both elements have magnetically-dilute spin- 1/2 isotopes (^{29}Si, 4.7% and ^{13}C, 1.1%). All investigators have reported data for 3C-and 6H-SiC. Results for 15R were also reported in Refs. [19] and [20]; those of Guth and Petuskey[20] are shown in Figure 3, as they were the only investigators to resolve the two separate peaks in the center of this spectrum. The implications of this data are discussed below with particular emphasis on the 6H polytype.

Hartman *et al.*[19] have considered the chemical variations produced by additional layers surrounding a given layer (it is equally convenient to consider the coordination shells surrounding only one atom in the given layer, since all the atoms in this layer possess the same chemical environment) to explain MAS-NMR results. Using Figure 4, these authors have defined a central A layer containing Si atoms. On either side to a distance of 5.0Å, there are two layers of C atoms and one layer of Si atoms. The stacking sequence in this or any polytype define four unique environments for a given Si atom within the 10Å vertical diameter of Figure 4: bCcAaBb, cBbAaBb, aCcAaBb and aBbAaBb where the upper and lower case letters represent Si and C atoms, respectively and A is the central Si layer. These four distinct Si environments have been designated A, B, C and D, respectively, and are the basic geometrically nonequivalent Si sites for all SiC polytypes. Even if we consider only the first and second nearest neighbors to a Si atom

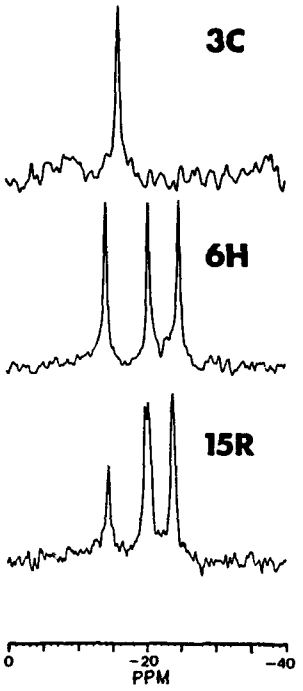

Figure 3. The ^{29}Si MAS-NMR spectra of (a), CVD grown 3C crystals 0.0255g, (b) SOHIO Co. 400–C5 6H powder).2450g, showing three peaks with area ratio 1:1:1 and (c) 15R crystal 0.0217g, showing three peaks with area ratio very near 1:2:2 (from Ref. 20).

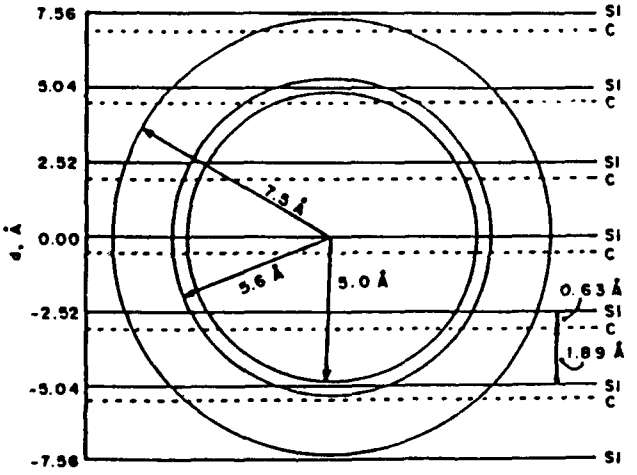

Figure 4. Layers surrounding an arbitrary central layer of silicon atoms. The 5-Å sphere does not quite reach the silicon layers at ±5.04 Å. The 5.6 Å sphere stops short of the carbon layer at ±5.67 Å, and the 7.5 Å sphere stops short of the silicon layers at ±7.56 Å (from Ref. 19).

in the A layer, the geometries of these shells are significantly different[19], as illustrated in Figure 5. Guth and Petuskey[20] have independently arrived at a similar conclusion regarding the existence of four second order Si coordinations by considering all possible orientations of neighboring atoms in the planes immediately above, below and containing a central Si atom.

A consequence of considering the chemical environment in the manner described above is that a method of determining the number of layers of Si atoms having each of the four environments (within a 10Å diameter) can be determined for any polytype by converting the ABC sequence of Hartman *et al.* [19] to Zhdanov symbols. The type A sequence can only be obtained if a Zhdanov number ≥ 3 occurs in the polytype symbol. Types B, C and D are found when the Zhdanov numbers are (≥2)(≥1), (≥1)(≥2) and (≥1)(1)(≥1), respectively. As illustrated by Hartman *et al.* [19] for the 15R polytype, having the Zhdanov symbol of /323232/3 (the slashes represent unit cell boundaries), the number "3" occurs three times thus indicating that there are three layers of type A Si. Moreover, the sequence (≥2)(≥1) occurs in six sequences (/32,23,32,23,32 and 2/3) indicating 6 type B Si. Similarly there are six type C Si. Table 4 provides a summary of the types and number of Si (and C) layers in several polytypes, with the caveat that the surroundings of a given layer (atom) have been limited to less than two layers away from the central layer. Since all SiC polytypes consist of two crystallographically equivalent interpenetrating C and Si sublattices, the above discussion also applies to the nonequivalencies in the C sites. Thus we have the unusual situation in which two elements from the same periodic group have essentially identical crystallographic environments in the same compound. Thus the factors which affect their chemical shifts in the NMR data may be compared

The peak position shown in Figure 3 for the 3C crystals is –16.1 ppm from tetramethylsilane (TMS); those for 6H and 15R are -14.3, -20.4 and -24.9 ppm and -14.6, -20.5 and –24.1ppm, respectively, from TMS. A comparison of the approximate 1:1:1 and 1:2:2 relative intensities for the 6H and 15R, respectively, with the relative numbers of the different types of chemical environments around a Si atom in these polytypes is given in Table 4. Both confirm the importance of non-nearest-neighbor geometry in determining chemical shifts and allow the assignment of the lowest field resonance to type A Si. Assignment of sites to the other peaks is not immediately obvious. Two different rationales have been used to assign them to a particular site and to explain the splitting in the middle 15R peak.

Both Hartman, *et al.* [19] and Guth and Petuskey [20] agree that next-nearest neighbors effects predominate in determining the chemical shift of a given peak. However, Hartman, *et al* [19] have reasoned that the chemical environment out to 4.75Å and that beyond 5Å from a central atom may also have a detectable effect on its chemical shift. The 15R polytype has five crystallographically nonequivalent sites, of which two are type B and two are type C. The chemical environment of the two type C sites become different if the two second layers of Si atoms on either side of the central layer is considered. Thus chemical differences begin to occur at 5.02Å (Figure 4). Differentiation of the B sites would occur only at approximately 6.0Å if another layer of carbon atoms is added. Thus a splitting of the type C peak would be more likely. Summarizing and extending this reasoning, there will be three peaks (in a 2:2:1 ratio) or four peaks (2:1:1:1) or five peaks (1:1:1:1:1) if surroundings to 5Å or 5.6Å or 7.5Å determine the chemical shift and the NMR resolution was sufficient to resolve the curves. Guth and Petuskey [20] have also associated the central and most negative 6H and 15R peaks with type C and B sites, respectively. However, they specifically neglect the effect of additional coordinations. Instead they postulate that both the splitting in the central 15R peak and the slight differences in chemical shift between the individual 6H and 15R peaks (same site types) are caused by the differences in the absolute vertical spacings within a polytype structure. However,

Table 4. Number and Types of Silicon (Carbon) Atoms in Different Polytypes of Silicon Carbide (from Hartman, et al (1987)).

Polytype	Zhdanov Symbol[a]	No. of Si (C) Atoms with surroundings of Type A	Type B	Type C	Type D
2H	(11)				2
3C		3			
4H	(22)		2	2	
6H	(33)	2	2	2	
8H	(44)	4	2	2	
9R	$(21)_3$		3	3	3
15R	$(32)_3$	3	6	6	
21R	$(34)_3$	9	6	6	
33R	$(3332)_3$	9	12	12	
45R	$(232233)_3$	9	18	18	
51R[b]	$(333332)_3$	15	18	18	
51R[c]	$(22222223)_3$	3	24	24	

[a]All Zhdanov sequences from Schaffer (1969) except 45R (Pandey and Krishna (1975) and 9R (Jepps, Smith and Page (1979)).
[b]More common 51R polytype.
[c]Less common 51R polytype.

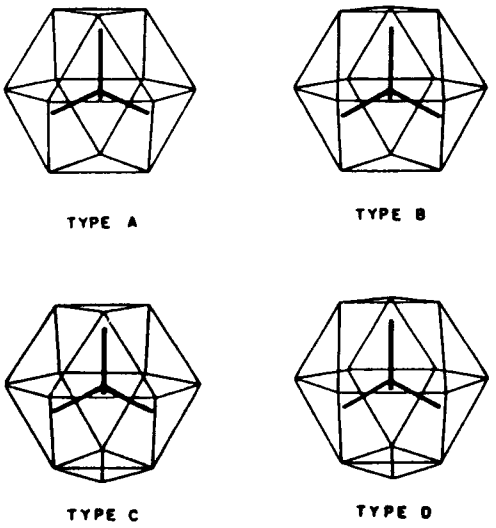

Figure 5. First and second neighbors for the four possible types of silicon (and carbon), surroundings in silicon carbide polytypes. In Type A, the 12 silicon second neighbors are located at the corners of a cuboctahedron, whereas in Type B, they are located at the corners of a twinned cuboctahedron (3:6:3 structure). Types C and D are characterized by having 13 second neighbors, 12 silicons and a carbon; in these, the carbon atom caps a trigonal face of the Types A and B polyhedra to give, respectively, a capped cuboctahedron and a capped twinned cuboctahedron (from Ref. 19).

since these differences in spacings are caused by the different hexagonal and cubic coordinations which, in turn, produce the nonequivalent sites and consequently the NMR peaks, this reasoning may be a distinction without a significant difference. Additional research on future higher resolution instruments with other polytypes such as 4H is desirable to determine the precise reason for the splitting. Finally, MAS-NMR of ^{13}C was also obtained,[19] however, extremely inefficient spin-lattice relaxation of this isotope did not allow an unambiguous assignment of the peaks.

The foregoing discussion has indicated very little regarding the kinetics and thermodynamics of polytype formation, growth and stability. Although a considerable body of literature exists which deals with these subjects, neither the physiochemical mechanism that produces the periodic sequences nor the forces leading to structures with very large unit cells are understood. Examining at least some of the recent knowledge in this and related areas is, nevertheless, a helpful guide to future research.

2.3. DISCUSSION REGARDING THE OCCURRENCE AND PROPAGATION OF POLYTYPES

In polytypic transitions in SiC, the thermodynamic arguments and governing laws associated with polymorphic transformations under varying temperatures and pressures do not explain many of the observations of numerous crystal-growth experiments from both the vapor and liquid states. This research has indicated that the principal resultant polytype depends on the growth rate, temperature, and degree of supersaturation of both Si and C in the surrounding medium, i.e., a mixture of thermodynamic and kinetic factors. Furthermore, many of the simple modifications of SiC apparently form under the same conditions of temperature and pressure, even within the same single crystal. If both phases are thermodynamically stable, their simultaneous existence in contact with the vapor phase appears to violate the Gibbs phase rule.

Many theories have been offered to account for the occurrence and propagation of polytypism. The theories generally involve (a) temperature and energy, (b) spiral growth around screw dislocations, (c) impurities, or (d) a combination of these factors. The four factors can be subdivided into two basic categories, kinetics and growth or thermodynamics. The growth theories are based principally on the spiral formation around a screw dislocation [24,25]. Major obstacles to this theory, however, are the apparent absence of both the dislocations associated with such spirals and formation of the growth polytype in the bulk of the SiC, as well as lack of a suitable explanation for the formation mechanism of the initial dislocation with a large enough Burgers vector for subsequent polytype growth.

From objections of the spiral-growth theory, Jagodzinski [26] proposed a thermodynamic theory based on the assumptions that (1) the cubic polytype was the most stable and the source of all other polytypes, (2) the internal energies of the polytype were similar, and (3) the vibrational entropy contribution to the free energy provided the driving force for the ordering of the stacking faults and the subsequent observation of the polytypes. Although initial X-ray studies by this author[27] showed good agreement with these predictions, transmission electron microscopy (TEM) by Jepps [28] and Gauther[29] and reflection high-energy electron diffraction (RHEED) [30] have established that the necessary density of faults is not distributed homogeneously.

The discrepancies between Jagodzinski's thermodynamic theory and the experimental results may be due, in part, to his assumption of similar internal energies. Indeed, as discussed above, measurements of bond lengths and lattice parameters as well as separate measurements of band gaps (see Table 3) (the larger the band gap, the larger the binding energy) of the common

polytypes are proof of their small but significant differences. These data alone would indicate that 2H and 3C are the most and least stable polytypes, respectively. The entropy contributions, however, must also be accounted for.

A partial list of polytype transformations, observed in SiC includes 2H→6H (including 2H→3C→6H), 3C→6H, 6H→4H, 15R→6H, 3C→4H, 3C→2H. An excellent review and discussion of these transformations can be found in Ref. [6]. Also important are the reverse transformations of 6H→3C and 4H (containing B)→6H which have been produced by heating (2073 to 2773 K) the first polytype under high pressure (up to 30 atm) in N_2[31,32]. At similar temperature and pressure but in Ar, these transformations were not observed. The latter transformation was also reported by Bootsma, Knippenberg and Verspui [33] who observed it in Al-rich 4H powders. Finally, the 6H→4H→2H transformations occur in SiC containing B or Al [34]. The data obtained in the kinetic studies of these transformations provide little information regarding the cause and mechanisms of the phenomenon. Indeed, the measured activation energies are associated with the growth kinetics, rather than the nucleation, of the new polytype. Moreover, impurities obviously play a role in both activating the nucleation of the transformation and controlling the kinetics of growth.

The existence of the most common polytypes may also be a manifestation of a narrow range of nonstoichiometry wherein the Si/C ratios are maximum for the 3C and minimum (possibly exactly 1:1) for the pure wurtzite 2H polytypes. In other words, the greater the degree of hexagonality, the smaller the Si/C ratio. Moreover, since Si preferentially evaporates from SiC at elevated temperatures, the transformations observed between polytypes containing very low levels of impurities may be caused solely by a gradual loss of Si. This would explain the 3C→6H, 6H→4H, 15R→6H, 3C–4H and 3C→2H transformations noted above. Arguments for and against the presence of this phenomenon in SiC are presented in the following paragraphs.

Early research by Lely [35] suggested that the deviations from stoichiometry in α-SiC crystals grown by sublimation at 2773 to 2873 K were less than 10^{-5} at.%. However, subsequent calculations from lattice-parameter measurements by Shaffer [36] revealed Si/C ratios of 1.049 and 1.032 for high-purity beta (3C) and alpha (6H) single crystals, respectively. A reformulation of these data gives Si concentrations (C_{Si}) of 71.04 and 70.7 wt%, respectively, for these materials (the stoichiometric C_{Si} = 70.05 wt%). Similar research on the same polytypes was conducted by Il'in *et al* [37] using an electron microprobe. The mean values of C_{Si} in the beta and alpha crystals were 71.06 and 70.60 wt%, respectively, which are close to those derived from Shaffer. Nagatome, Ishinara and Furukawa [38] reported a Si/C ratio of 1.04 (C_{Si} = 70.87) for a supposedly β-SiC thin film. However, this value falls in the middle of the values noted above for 3C and 6H crystals.

More recently, Tairov and Tsvetkov [39] succeeded in growing bulk single crystals of selected SiC polytypes using a special sublimation technique. Density measurements were conducted on each crystal with an identified polytype by hydrostatic weighing in a thermogradient tube filled with a liquid of a density near that of SiC. From the various Si/C ratios calculated from these density measurements, the concentration of Si and C vacancies were determined for each polytype. These results, as shown in Figure 6, indicate that the concentration of C vacancies decreases and that of Si vacancies increases when the degree of hexagonality, D, for the various polytypes increases. The Si/C ratios of 1.046 and 1.022 measured by these authors for their 3C and 6H crystals, respectively, are also in reasonable agreement with the values reported by Shaffer [36] and Il'in *et al* [37] these polytypes.

It is also plausible that the lattice parameter and density results are solely a consequence of the different numbers of cubic and hexagonal layers among the polytypes. As noted above, this results in different interplanar spacings and therefore different C/N ratios which would be manifest as quasi-continuous variations in lattice parameter and density. Nonstoichiometry would not exist. One may counter that the electron microprobe and ion backscattering data are valid regardless of crystallography, however these techniques are at present less accurate than the lattice parameter and density measurements. Moreover, standards are required to determine quantative values of C_{Si} from the electron microprobe data. And the most valid standard would be a SiC crystal (which would possess one of more of the polytype forms).

An example of the uncertainty regarding nonstoichiometry in SiC is derived from recent research of Birnie, *et al*[40]. These authors pursued two very different avenues of investigation: high temperature equilibration of SiC in the presence of excess Si and C and *ab inito* cluster calculations to evaluate the possibility of antisite defect formation. In their experiments these authors used powders of 3C SiC (average grain size, 0.25 mm) mixed with an excess (@15 wt%) of either Si or C (graphite) and equilibrated in a clean graphite crucible for 2 h at 2673 K to maximize the concentration of defects, then cooled at @40.0 K/s. Careful measurements of lattice parameters, densities, and the Si/C ratios of the SiC materials from these anneals revealed that the samples could not be distinguished, at a level of better than one part in one thousand, by their molecular weights per mole of crystal sites. It was thus concluded that the Si/C ratio in SiC is unaffected by differences in Si activity at high temperatures and that this phase is largely stoichiometric. The calculations yielded an energy of @870 kJ/mole (@9eV) for antisite-pair formation. An energy of this magnitude precludes large concentrations of the defects and virtually negates their contribution to nonstoichiometry in SiC.

With these last results, it would seem that the question on nonstoichiometry has now come full circle to the viewpoint postulated by Lely [35] more than 30 years ago. However, Wang, *et al* [41] have more recently completed calculations using the self-consistent pseudopotential method to determine the total energy of a supercell containing various native defects in 3C (b-) SiC. Their results showed that in a perfectly stoichiometric SiC, the dominant defect is the electrically inactive Si_C–C_{Si} antistructure pair (the same as that studied by Birnie *et al* [40]. However, the formation energy in these newer calculations was found to be only 6.4 eV. In Si-rich material (the purported state of 3C (see Figure 6)), the concentrations of the stoichiometry-comensating defects depend strongly on the Fermi level position, with the Si_C antisite (6.7 eV) and V_C (5.5 eV) being the dominant defects in n- and p-type material, respectively. However, high purity 3C SiC is invariably n-type, thus the Si_C antisite would be the primary defect.

This last result may also help to explain some of the self-diffusion data by Hong and Davis[42,43]. The investigators found that $^{14}C(^{30}Si)$ diffused more rapidly (slowly) in very pure 6H-SiC (although not 3C, this is also presumed to be a Si-rich polytype, as noted above) than in a similar material that had been N-doped (700 ppm). These differences can be explained by a decrease (increased) number of vacancies available for C (Si) diffusion caused by the essentially complete ionization of the donor-N impurity atoms and their subsequent interaction with the postulated donor-type C and acceptor-type Si vacancies.

These diffusion results also show very similar activation energies for a given species in pure or N-doped material. Furthermore, the ^{14}C diffusion coefficients in the N-doped and undoped SiC converge at high temperatures, which indicates that the intrinsic electron and hole generation and the concentration of thermal vacancies have surpassed those resulting from the presence of N donor species. In contrast, analogous data for Si diverge as temperature increases. Finally, the data for both species show low diffusion rates, high activation energies, and high preexponential

terms, indicating that a vacancy mechanism occurs in both cases. (These data also preclude a high concentration of C vacancies or Si interstitials.)

To explain the vacancy mechanism, Birnie [44] proposed, though later retracted[40], (that the diffusion of Si is coupled to and controlled by the diffusion of C vacancies and their subsequent occupation by Si atoms, which thus creates Si antisite defects. This antisite concept also indicates that any nonstoichiometry in SiC results from Si on C sites.

The question of nonstoichiometry in SiC remains in a state of uncertainty. As such, the importance of this chemical phenomenon to polytypism and mass transport in high purity and doped SiC are not fully understood. It is important that the theoretical and experimental research regarding these points continue, for antisite and other native defects, including the vacancies in a nonstoichiometric material, should play a significant role in the development of SiC as a semiconductor device material—the succeeding topic of discussion.

3. Silicon Carbide as a Semiconductor Material

3.1. INTRODUCTION

The successful employment of a material as a base into which active microelectronic devices can be fabricated requires that process conditions and methods be realized which allow the growth of this substance in high purity (or controlled purity) monocrystalline form. Early success was achieved in the growth and doping of small SiC single crystals predominantly of the hexagonal 6H polytype via the very high-temperature (@2900 K) Lely [45] sublimation process. However, the yield of usable crystals was frequently low, their size could not be increased and the energy required to operate the equipment was considerable. Much smaller beta-SiC crystals were also produced via reaction of molten Si with the walls of a high-purity graphite crucible. However, in this case the product was usually very highly faulted. Thus, as the technique of chemical vapor deposition (CVD) and the availability of very pure gases improved, investigators began to explore this process to achieve monocrystalline thin films of SiC (see Refs. [46-48] or an overview of the earlier efforts).

3.2 RECENT THIN FILM GROWTH AND CHARACTERIZATION STUDIES

Monocrystalline Si has been almost universally adopted as the substrate of choice for the growth of the β-SiC thin films because of the availability of the former in well characterized and reproducible forms of controlled purity. Amelioration of the mismatches in the coefficients of thermal expansion (~8%) and lattice parameters (~20%) via the initial reaction of the Si (100) surface with a C-containing gas followed by the successful CVD of relatively thick (up to 30 mm), epitaxial and crack-free β-SiC films on this converted layer using individual C- and Si-containing gases have been employed by Nishino, *et al* [49,50], and subsequently by Suzuki and co-workers[51], Addamiano and Klein[52], Sasaki *et al* [53], Liaw and Davis[54], Yoshida *et al* [55], Kim and Davis[56], Fujii *et al* [57], Kong *et al* [58] and Shinohara *et al.*[59] in this most recent SiC thrust. The studies in this regard described below draw primarily on the research in the present authors' laboratories. However, our studies were similar to those of other investigators with the exceptions of our use of C_2H_4 for growth and electron microscopy for characterization.

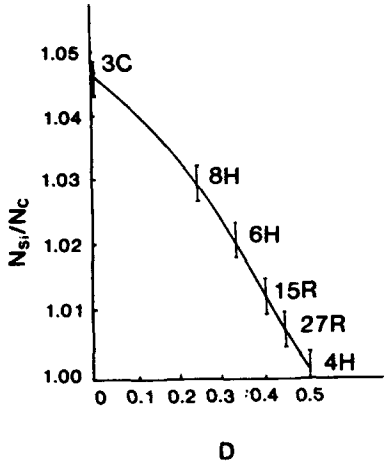

Figure 6. Si/C ratio as a function of the hexagonality proportion, D, for various SiC polytypes (from Ref. 39).

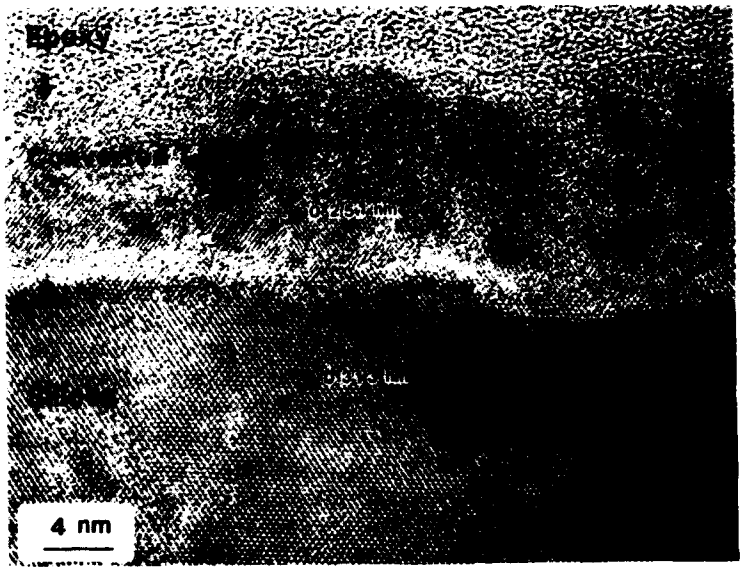

Figure 7. High-resolution XTEM micrograph of converted layer of monocrystalline β-SiC(100), on the Si(100), substrate prior to CVD deposition. The apparent amorphous interlayer between the Si substrate and the CVD grown film is an artifact of ion milling and not a residual oxide phase (from Ref. [62]). (Micrograph courtesy of S. Nutt, Brown University, Providence, RI).

For the chemical conversion process in our reactor, an experimentally determined optimum amount of 0.30 mole % of high purity C_2H_4 (1 sccm) entrained in purified (Pd/Ag cell) flowing H_2 (3000 sccm) is introduced into the cold wall, barrel-type reaction chamber at room temperature. The Si (100) substrates (and the associated SiC-coated graphite susceptor) is immediately and rapidly heated. The reaction is interrupted after an optimum growth period of 150 s. The maximum temperature obtained in this interval is ~1600 K.

An extensive study of the reaction of C_2H_4 with Si has been conducted by Mogab and Leamy[60] under conditions of molecular flow in both HV and UHV chambers in the pressure and temperature ranges of 1.3×10^{-5} Pa $\leq P(C_2H_4) \leq 6.5 \times 10^{-2}$ Pa and 1073 K $\leq T \leq$ 1373K, respectively. These investigators concluded that the occurrence of defects in the Si were intrinsic to the mechanism of film growth. This mechanism was presumed to be (1) the diffusion of Si through porous defects incorporated in the growing layer as a result of the concurrent formation of similar defects on the Si surface and (2) the subsequent reaction of this Si with the C in the C_2H_4. The resultant SiC assumes a porous polycrystalline morphology around these shallow (<200 nm) pits in the Si substrate which are also assumed to be the sources of Si for the reaction. The number and real density of the defects in the SiC layer were found to be proportional to the partial pressure of C_2H_4 and the SiC thickness. At $P(C_2H_4) > 1.3 \times 10^{-3}$ Pa, the defects in the SiC sealed at an early stage in the growth and further reaction was virtually arrested as a result of decreased diffusion rates. Scanning electron microscopy by Addaminano and Sprague[61] of layers produced at 1673K at 0.1 MPa revealed pyramidal-shaped pits bounded by {111} planes and $0.5–1.0 \times 10^{-6}$ m^2 in cross-section on the final growth surface. Our results[62] have been similar in that the Si and, subsequently, the converted layer continually develop pits which either become closed as a result of further growth or do not extend downward to the Si surface. Continued exposure beyond ≈180 s normally results in the occurrence of free C on the surface of our films, as shown by X-ray photoelectron spectroscopy (XPS) (see Ref. [62]).

Bozso *et al* [63] have conducted a study at 10^{-8} Pa of the reaction of Si(100) with C_2H_4 derived from a molecular beam source. Below 940 K, the rate of supply (r_S) of the C exceeded the bulk diffusion rate of this element. As a result, a Si-C alloy formed on the surface via reaction which was independent of gas phase excitation processes. At T≈940 K, $r_S = r_d$ and diffusion in the bulk began to dominate the kinetics of the surface reaction and crystalline SiC began to form. Furthermore, surface segregation of bulk Si was observed on the growing SiC layer indicating that the diffusion of Si through the growing layer and interaction with C from the C_2H_4 was the mechanism for the growth of this near surface region of SiC, in agreement with the results of Graul and Wagner[64]. At T>1000 K, C bulk diffusion was dominant, along with the continuation of the formation of the SiC and the Si overlayer.

The presence of the cubic (b)-SiC polytype was determined by high resolution cross-sectional transmission electron microscopy (XTEM) of the new layer[65]. This confirmed earlier reflection high energy electron diffraction analyses[66]. As revealed in Figure 7, this layer is monocrystalline and microscopically rough, varying in thickness from 5–12 nm. It also contains (a) a high density of planar defects that are primarily orthogonal sets of pure edge misfit dislocations with Burgers vectors a/2 <110> which form in the first monolayer at the semi-coherent interface as the nucleus extends laterally and which accommodate the strain with an interval of 5 times the spacing between (110) planes, (b) {111} microtwins and (c) intrinsic stacking faults. In addition, localized regions of the converted layer exhibit disorder. Pirouz and coworkers[67,68] have also conducted extensive TEM regarding the structural character of the

converted layer relative to the Si. The results are similar to ours, however, they have also considered mechanisms for the nucleation and growth of these defects as well as the dynamics of the occurrence of the aforenoted defects. The misfit dislocations occur immediately after the deposition begins. However, these authors postulate that the microtwins and stacking faults occur, in the main, in the cooling stage because of the mismatch in the coefficients of thermal expansion. For a complete review of the conversion process and the results of the analyses of the converted layers, the reader is referred to Ref. 62.

The subsequent CVD growth of the β-SiC(100) films on this layer was achieved by introducing SiH_4 into the H_2 gas stream at 1660 K and 1 atm total pressure. Growth rates of the films were typically 2μ m/hr.

Plan-view and cross-sectional transmission electron micrographs of a β-SiC thin film are shown in Figures 8(a) and 8(b), respectively. The micrographs show planar defects on {111} planes that intersect at 90° angles in the <100> projection (Figure 8(b)). As in the converted layer, these defects were identified as microtwins and intrinsic stacking faults. The density of defects is higher at the interface; it decreases over a distance of 3–4 μm form the interface and becomes approximately constant to the surface even for 20 μm thick films.

There are additional defects in Figure 8(a) that appear as bands of mottled contrast that extend from the Si-SiC interface to the growth surface (see arrows). These defects have been identified[68] as antiphase boundaries (APBs)and extensively studied via TEM[65-69]. For the (100) orientation, the APB problem can be avoided if the steps on Si are an even number of atomic layers high, and the nucleating species is of a single type (e.g., C). The vicinal (off-axis) Si (100) is particularly intriguing from this aspect in that it has a propensity to form primarily double steps when oriented 2°–4° from [100] toward [011]. Two structural models have been proposed[70,71] for these biatomic steps and Wierenga and coworkers[72] and Griffith, *et al* [73] have observed these steps directly with scanning tunneling microscopy (STM). The topography consists of straight double steps running along the $[1\bar{1}0]$ direction, separated by terraces of relatively uniform width. High temperature annealing greatly improves the initial surface condition in the vicinal Si (100) for APB-free growth. Sakamoto and Hashiguchi[74] have shown that annealing a two domain Si (100) 2×1 surface at 1273K for 1.2×10^3 s converts the surface to a single-domain 2×1 structure. This has been confirmed by STM results by Chadi (1987). Calculations by Aspnes and Ihm[70] show that there is an energetic preference for the type A double step over type B double steps and single steps.

To eliminate APBs in β-SiC, the Si (100) substrates were cut 1°–4° from [100] toward [011], chemically polished and annealed at 1300K, 1.8×10^3 s in flowing H_2. For the 1° substrates, the number of APBs is reduced, whereas for the 4° substrates, they are essentially eliminated. For all the substrates, APBs occurred near the cleaved edges as a result of residual strain. Annealing relieved this strain, and the APBs were no longer observed. Films grown on off-axis orientations greater than 2° were similar and also much smoother than those on the nonvicinal SiC films. This was verified by profilometry[69] and STM[75] results.

Choyke *et al.* have conducted low temperature photoluminescence[76] and Raman scattering [77] studies of the β-SiC films having a thickness range of 60 nm to 25 μm and grown on converted Si (100). In the former study, the "defect related" W band near 2.15eV and the G band near 1.90-1.92eV dominated the spectra for very thin film samples and are believed to be related to dislocations and extended defects. With an increase in thickness of the β-SiC layers beyond 3 μm, nitrogen-bound exiton (N-BE) emission increased relative to the other bands.

Figure 8. TEM micrographs showing the general microstructure of β-SiC films: (a), <100> plan view showing stacking faults and APBs (arrows); (b) <110> cross-sectional view showing interfacial strain contrast, dislocations, and stacking faults.

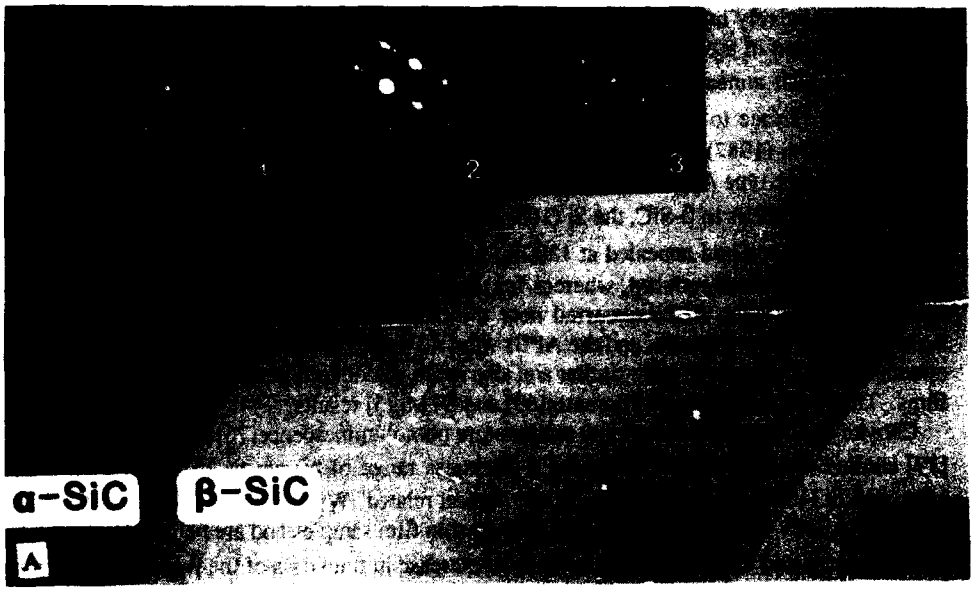

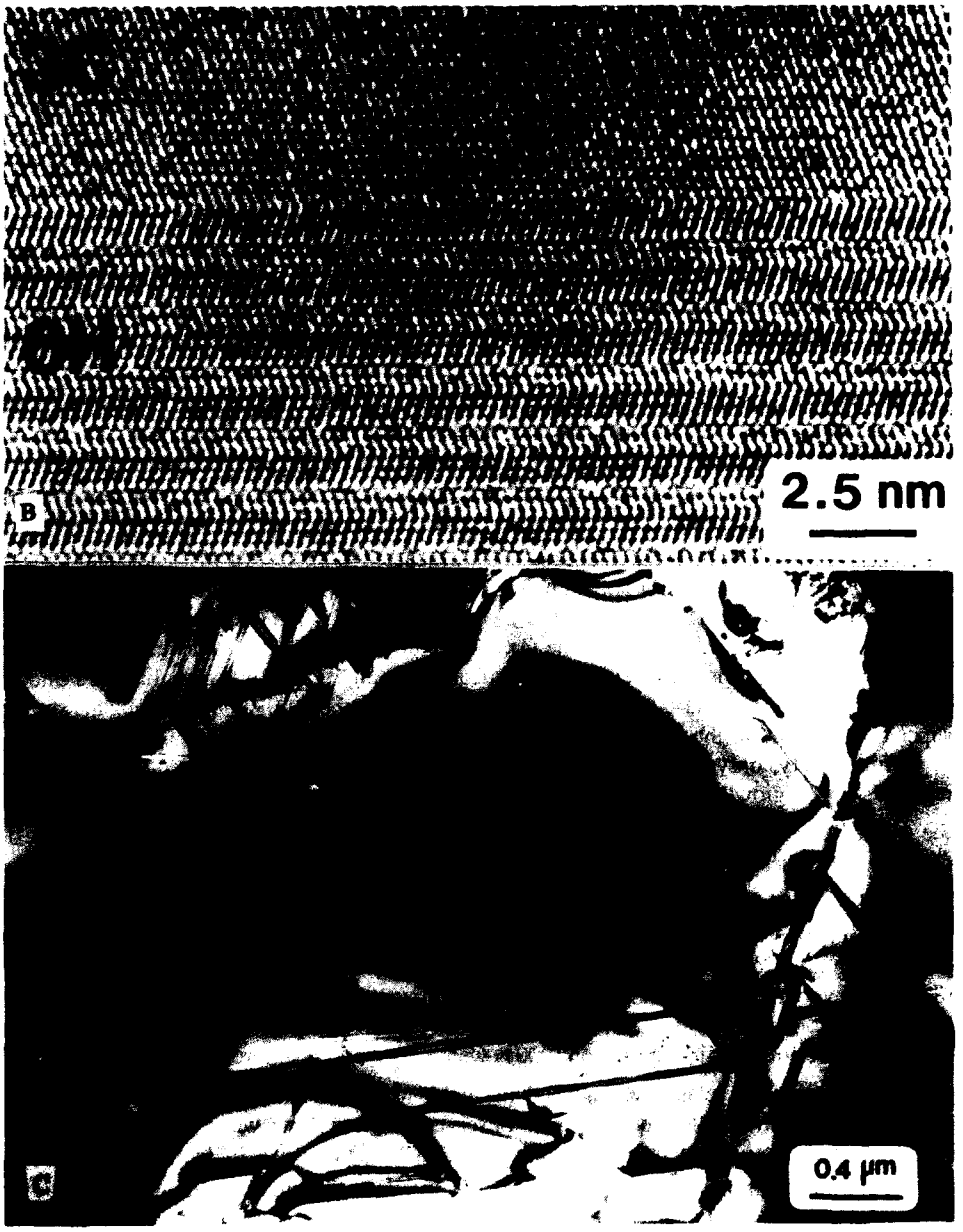

Figure 9. Cross-sectional TEM micrographs of the β-SiC/6H-SiC interface taken at (a), moderate and (b), high resolution. (Figure (b), is courtesy of Steve Nutt, Brown University, Providence, RI). (c), Plan view of same films showing double positioning boundaries and associated stacking faults.

The ratio of the intensities of the band and the N-BE line has been proposed[76] as a figure of merit for crystalline perfection in these types of films. Beyond a thickness of 16 μm, the spectra indicate that further improvement in film quality is dependent on the quality of the substrate and/or the initial nucleation conditions. It was also found that a 1-4 μm transition layer greatly reduces the interface misfit strain. For films thicker than 4 μm the film stress decreases only slightly within an increase of film thickness. This was supported by the Raman data which indicated an in-plane strain of 0.1%-0.2% in the thicker films. The biaxial stress state resulted in a reduction of the intensity in the phonon and no-phonon transitions.

The Raman study[77] also showed that the Si 522cm^{-1} phonon from a Si wafer is enhanced in intensity by a factor of 2-3 due to a CVD overlayer of cubic SiC. Furthermore, the 3C-SiC longitudinal optical phonon from the SiC/Si samples is enhanced by a factor of 2-3 following the removal of the Si substrate. The strict selection rules were no longer obeyed for this sample assembly.

The research regarding the deposition of β-SiC on Si(100) has now sufficiently matured such that new deposition technologies are now being used to address the problem of the high temperatures (T>1630K) of growth. Fuyuki *et al.*[78] have recently reported atomic layer-by-layer control using gas source molecular beam epitaxy of the deposition of β-SiC on Si(100) within the temperature range 1250-1320K. The source gases of Si_2H_6 and C_2H_2 were alternately introduced into a chamber previously evacuated to $3x10^{-10}$ Torr. The chamber was also equipped with a RHEED apparatus to follow the changes in the surface structure as a function of deposition. The RHEED pattern changed from (1x1) to (3x2) when the Si_2H_6 was introduced. However, it returned to the (1x1) structure when the C_2H_6 was introduced. The primary results of this process were (1) the fabrication of single crystalline films having a smooth and mirror-like surface and (2) the determination that the number of Si atoms forming the surface superstructure controls the growth rate of each layer.

Unfortunately, only the APBs are eliminated by the use of vicinal Si (100) substrates regardless of the growth technique. In an attempt to substantially reduce the concentrations of all the various defects simultaneously, growth on the nonvicinal Si (0001) and C (000$\bar{1}$) faces of commercial (Acheson-derived) 6H-SiC single crystals substrates has been investigated within the temperature range of 1683K–1823K at 1 atm. total pressure. The resulting films were β–SiC (111) at all temperatures studied. This SiC polytype was earlier grown α-SiC substrates in the temperature range of 1773K–1973K by Rai-Choudhury and Formigoni [79] and Berman, *et al* [80]. However, the growth conditions were not optimized, and the interface between the various SiC epilayers and their SiC substrates was not investigated.

The surfaces of our films grown on (0001) were very smooth and reflective; whereas, those grown on (000$\bar{1}$) were relatively rough and unsuitable for device fabrication. In contrast to films grown on Si substrates, few defects were observed in these films when examined by cross sectional transmission electron microscopy (XTEM) (Figure 9a). In fact, high resolution XTEM shows an abrupt and coherent β-SiC/α-SiC interface (Figure 9b). A single atomic layer runs completely across the interface which indicates that the growth direction of the β-SiC films was exactly [$\bar{1}\bar{1}\bar{1}$] in the region (for the growth of β-SiC on the α-SiC C face). However, examination in plan view revealed the presence of double positioning boundaries, (DPBs) on both the Si and C faces, as shown in plan view in Figure 9c[81,82]. In an FCC film, these defects, are caused by the existence of two equivalent sites (e.g., B and C on plane A in conventional crystal stacking notation in the [111] direction) on a (111) or (0001) surface. A

nucleus forming from an assembly of atoms on the A sites will be rotated 60° relative to a nucleus growing on the B sites. To release the internal energy many stacking faults were generated from the DPBs, as shown in Figure 9c. They either intersect another fault or stop at the partial dislocation which bounds them. When these nuclei grow and meet each other, DPBs are formed between them.

The elimination of the DPBs was achieved by using vicinal α-SiC (0001) crystals lapped such that [0001] was oriented 3° towards [11$\bar{2}$0][83]. The prepared substrates were oxidized prior to deposition to eliminate subsurface damage caused by the lapping. Deposition was conducted at 1773K at 1 atm. total pressure. In contrast with the results noted above, all films produced in this manner were a pure 6H polytype, as shown by the identical diffraction patterns shown as insets in the TEM lattice fringe imaging micrograph in Figure 10, taken from the substrate/film interface region. The horizontal fringes in Figure 10 are the traces of (0001) planes which can be seen to cross from the substrate into the epilayer without distortion. No line or planar defects were present in the area of this micrograph; in fact, few were observed in the entire XTEM sample. This low defect density was verified by extensive plan-view TEM[84]. More recently, Matsunami and co-workers have reported[85,86] similar off-axis growth studies, but without any associated microscopy.

A recent and very sophisticated attempt to deposit SiC films on α-SiC (0001) substrates held at 970K has been conducted by Withrow[87] using direct, low energy (40eV) ion beam deposition of alternating layers of $^{13}C^{+}$ and $^{30}Si^{+}$ from an ion implanter. Laser optical diffraction showed that the a(6H)-SiC substrate was oreinted such that <1$\bar{1}$20> was perpendicular to the plane of the image. The optical diffraction pattern obtained from the thin film was consistent with a β-SiC pattern, indicating that the film grew with <110>||<1120>. Thus, the film grew such that <10$\bar{1}$>||<1$\bar{1}$20> and the atoms were deposited such that (111)||(0001). The β-SiC overlayer was completely epitaxial with respect to the α-SiC. The most common defects were small areas or boundaries which appeared amorphous in nature. The atomic stacking was disrupted in these regions but the lattice was continuous on either side of the boundary and throughout the film. The stoichiometry of the film was not 1:1, but had an excess of ~30% carbon. Other defects observed in the film included dislocations and twins.

As a consequence of the recent use of α-SiC as a substrate, coupled with the availability of high quality monocrystalline Si wafers at reasonable cost, much of the research concerning device development and fabrication has been conducted using the latter substrate. The results of this research are described in the following subsections.

3.3. FABRICATION AND CHARACTERIZATION OF SIC ELECTRONIC DEVICES

3.3.1 *Schottky Barrier Diodes.* Diodes and more complex devices have recently been fabricated in β-SiC thin films. Yoshida, *et al* [88] have produced Schottky barrier diodes on unintentionally doped films grown on Si(100) using Ni and Au as the ohmic and rectifying contacts, respectively. The barrier heights, as determined by capacitance and photoresponse measurements, were 1.15 (±0.15) eV and 1.11 (±0.03) eV, respectively.

Gold–β-SiC Schottky diodes have been fabricated on films grown on 4° off-axis Si by Kong, *et al* [58]. Measurements of the C-V and I-V characteristics of these diodes indicate that

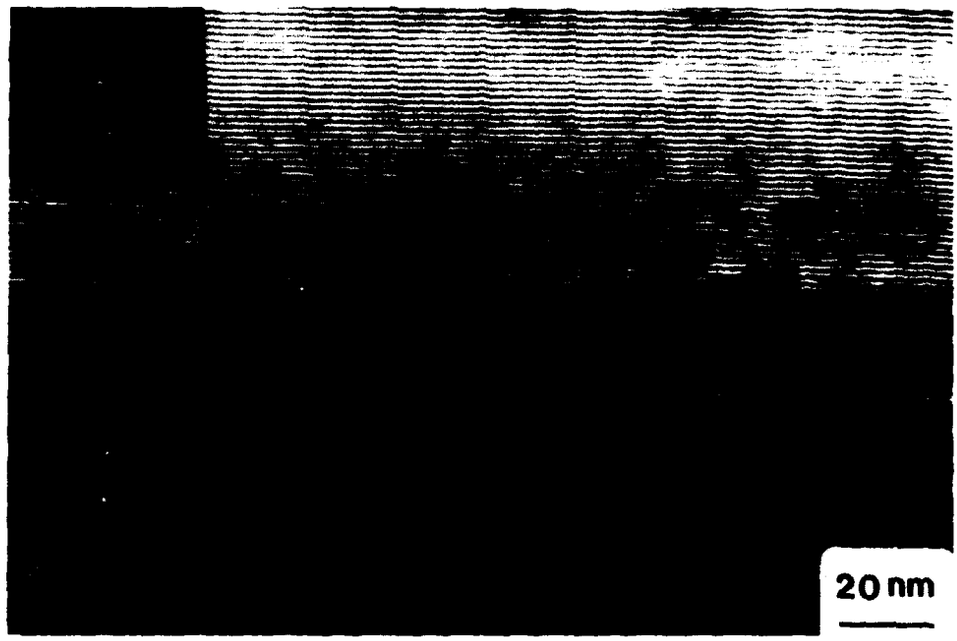

Figure 10. Cross-sectional TEM micrograph of the 6H-SiC/6H-SiC interface region. The two electron diffraction patterns taken from (1), epilayer and (2), substrate are identical and characteristic of the [11$\bar{2}$0] pole of 6H-SiC. Note the absence of line and planar defects in the bulk of the 6H-SiC epilayer and at the interface. The off-axis nature of the substrate is evident by comparing the angle between the interface and the lattice images.

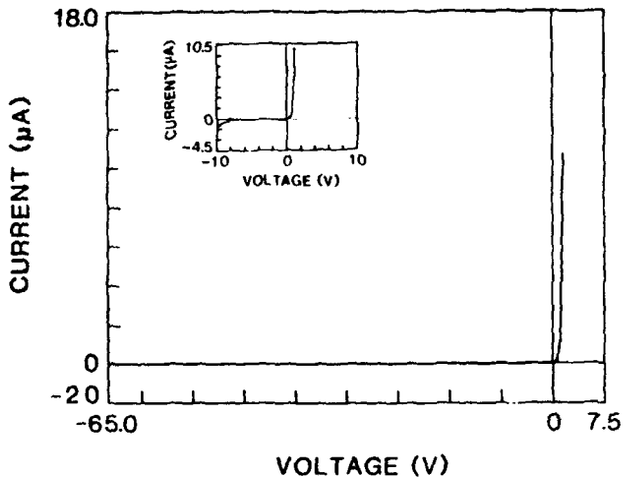

Figure 11. Current-voltage (I-V), characteristics of a Au Schottky diode fabricated on a 6H-SiC thin film grown on 6H-SiC C (000$\bar{1}$), face 3° off towards [11$\bar{2}$))0]. The area of the junction is 7.85×10^{-5} cm^2. Inset is an I-V curve of a Au-Schottky diode with a junction area of 1.4×10^{-4} mc^2 on a β-SiC thin film grown on 6H-SiC Si (0001), substrate (from Ref. [84]).

eliminating APBs significantly reduces the leakage current in the films. For example, the minimum leakage current density so far measured by these authors for a Schottky diode on a film on nonvicinal Si (100) is 0.89 A/cm^2 at a reverse bias of 18V. By contrast, leakage currents as low as 2.55×10^{-2}A/cm^2 at 18 V reverse bias have been achieved for similar diodes with the same junction area in films on off-axis Si. This decrease in leakage current when APBs are eliminated is attributed to the secondary defects associated with the APBs. As previously noted APBs contain numerous dislocations which may act as leakage channels during electrical measurements. Furthermore, many stacking faults intersect the APBs at various points, therefore, the APBs act as a connecting channel for these faults. Finally, local changes in electronic structure at the APBs which cause resistivity and/or carrier concentration changes are also possible. The ideality factor for these films was calculated from the I–V data to be approximately 1.4.

Fujii, *et al* [89] have also prepared Schottky diodes on β-SiC films grown on off-axis Si and studied the dependence of the Schottky characteristics on Si substrate orientation (n11) where the values of n=1,3,4,5, and 6. Data for nonvicinal Si(100) were also obtained. The diodes on Si(611), Si(411) and Si(111) showed lower reverse leakage currents (the lowest value at a bias voltage of 5 V was 6×10^{-4} A/cm^2 on (611)), ideality factors near unity and larger barrier heights than the films on Si(100). The respective barrier heights of 1.47 eV and 1.69 eV were determined for the Au- and Pt-diodes on Si(611) from plots of $1/C^2$ vs. V where C=capacitance and V=voltage.

Substantial improvement in these diodes has been achieved by Kong, *et al.*[84] as a result of their fabrication on a(6H)-SiC films grown on a(6H)-SiC (000$\bar{1}$) substrates oriented 3° off-axis towards [11$\bar{2}$0]. Figure 11 shows a typical current voltage plot from such diodes. Even at the much higher reverse bias of 55 V, the leakage current density was only 3.2×10^{-5}A/cm^2. When the reverse bias was increased to 65 V, the leakage current density increased to 3.8×10^{-4}A/cm^2. Compared with the Au Schottky barrier diodes made on β-SiC films grown on 6H-SiC (0001) substrates (see inset), the leakage current is greatly reduced. Likewise, it is much less than leakage currents measured in β-SiC films on Si. This data on the off-axis 6H-SiC films demonstrate the importance of eliminating both APBs and DBPs from the films.

3.3.2 *Blue light-emitting Diodes.* SiC has attracted much interest as a material for visible light-emitting diodes (LEDs), since different colors of photoluminescence may be produced depending on polytypes and impurities. Since red, orange, yellow and green LEDs are well developed using GaP, GaAsP and GaAlAs at present, much attention is being given to blue LEDs of 6H SiC. Blue LEDs of n-SiC with Al and N on p-SiC with Al have been prepared by Glasow and Ziegler[90] and Brander and Sutton[91] using liquid phase epitaxy with a Si melt in a graphite crucible. A brightness of 100 fL at room temperature was reported with no failure for longer than 15,000 h over the temperature range between room temperature and 400°C.

Extensive and more recent research on these devices has also been conducted by , Matsunami, and coworkers[92-95]. These investigators have prepared Al/N pn junctions in 6H-SiC using the combination of a Si solution, a rotating dipping method[92,93] and sequential double epitaxial growth. After the p-layer growth in the Si melt doped with Al, n-layer growth was carried out by introducing N_2 gas into the growth chamber.

Typical emission spectra of SiC blue LEDs at room temperature are shown in Figure 12[94]. For the measurement, pn junctions were driven with a current pulse of 3 ms in width and 2 kHz

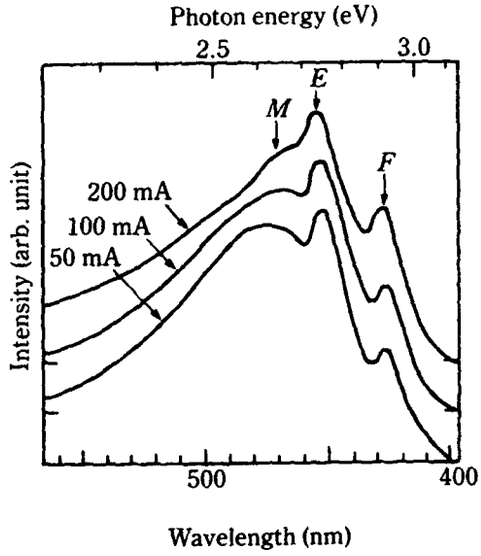

Figure 12. Typical emission spectra of a 6H-SiC blue LED at room temperature (from Ref. [94]).

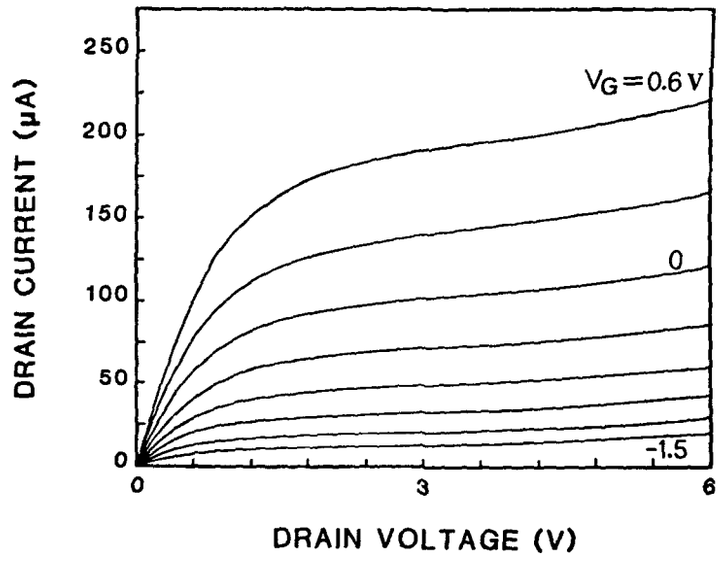

Figure 13. Drain Current-voltage characteristics at room temperature of a MESFET with a gate length of 3.5 μm at room temperature and fabricated in α β-SiC(100), monocrystalline film deposited on a Si(100), substrate (from Ref. [99]).

in repetition. The light-emission mechanism was investigated through the detailed analyses of temperature and excitation dependences of the spectra and time-resolved spectral change for various SiC LEDs emitting different colors. As shown by Ikeda, *et al* [93], the main mechanism is attributed to (i) donor-acceptor (D-A) pair recombination (M peak, ~480 nm), (ii) bound exciton recombination at localized centers related to Al impurities (E peak, ~455 nm) and (iii) free exciton recombination (F peak, ~425 nm). Since the intensity of the F peak increases with increases in current, the component of short-wavelength emission increases and hence the total brightness does not show saturation. If the content of N in n-type SiC is reduced, the main emission peak shifts to the short wavelength side (~460 nm) owing to the lower contribution of D-A pair recombination.

The external quantum efficiency of SiC blue LEDs prepared by LPE growth using 6H-SiC substrates grown by the Lely sublimation method has been reported by Matsunami, *et al* [94] to be in the range of 2×10^{-3}%. Recent increases in efficiency using transparent substrates by a modified Lely method have achieved a value of 2×10^{-2}% (7 mcd at 20 mA for 250×250 mm^2 diode area[96].

3.3.3 *Metal-Semiconductor Field-Effect Transistors (MESFETs).* Yoshida, *et al* [88,97] have also fabricated MESFETs by the successive CVD of Al-doped (1E17 cm^{-3}), p-type and undoped, n-type ((3–7)E16 cm^{-3}) β-SiC layers on p-type Si substrates. Gold and Al electrodes were used for the Schottky-barrier gate and the ohmic (source and drain) contacts, respectively, for the n-type SiC. Gate voltages from 1.0 to 0.6 V were applied. A high channel resistance and a small (10 mA) drain current indicated that the leakage current through both the SiC p-n junction used for isolation of the device region from the Si substrate and the isolation grooves was not negligible compared with the current through the n channel. A transconductance at saturation of ~0.09 mS/μm and a threshold voltage of ~1.4 V were reported. Finally, these researchers have investigated[98] the effect of heating to 573K on the operation of a MESFET similar to that just described but with the Al layer replaced with one containing B and a different configuration of electrodes. At 298K the leakage current was considerably reduced in this sample relative to the Al-doped material; the drain current was almost zero at negative gate voltage >1.6 V; and a transconductance of 0.5 mS/μm was reported. With increasing temperature, a considerable increase in leakage current was noted and the transconductance was reduced to 0.17 and 0.1 mS/μm in the saturation region at 473K and 573K, respectively. The cause of these changes were postulated to be related in that in the deep depletion mode, the current flow was through the B-doped layers wherein the resistivity was reduced by the increased thermal energy. Conversely, in the enhancement mode, the drain current was reduced by a decrease in the electron mobility with temperature. The drain I-V characteristics were not changed after heating to 573K in air.

Typical room temperature drain current vs. drain voltage (I_D - V_D) characteristics of the MESFETs produced by Kong, *et al* [99] in 60 nm thick, undoped, n-type β-SiC films epitaxially deposited on buried Al-doped, p-type β-SiC layers previously grown on p-type Si are shown in Figure 13. The Al-doped layer was used to (1) confine the current to a thin n-type active layer and (2) move this active layer away from the defect region which extended ~3 μm from the Si/SiC interface. The carrier concentrations of the n- and p-type layers were 5E16 cm^{-3}, respectively. A three level mask set employing a concentric ring geometry wherein the gate pattern completely enclosed the center, 100 μm (drain) contact, was used. The gate length and the source-to-drain distance were 3.5 μm and 10.5 mm, respectively. Sputtered $TaSi_2$ was

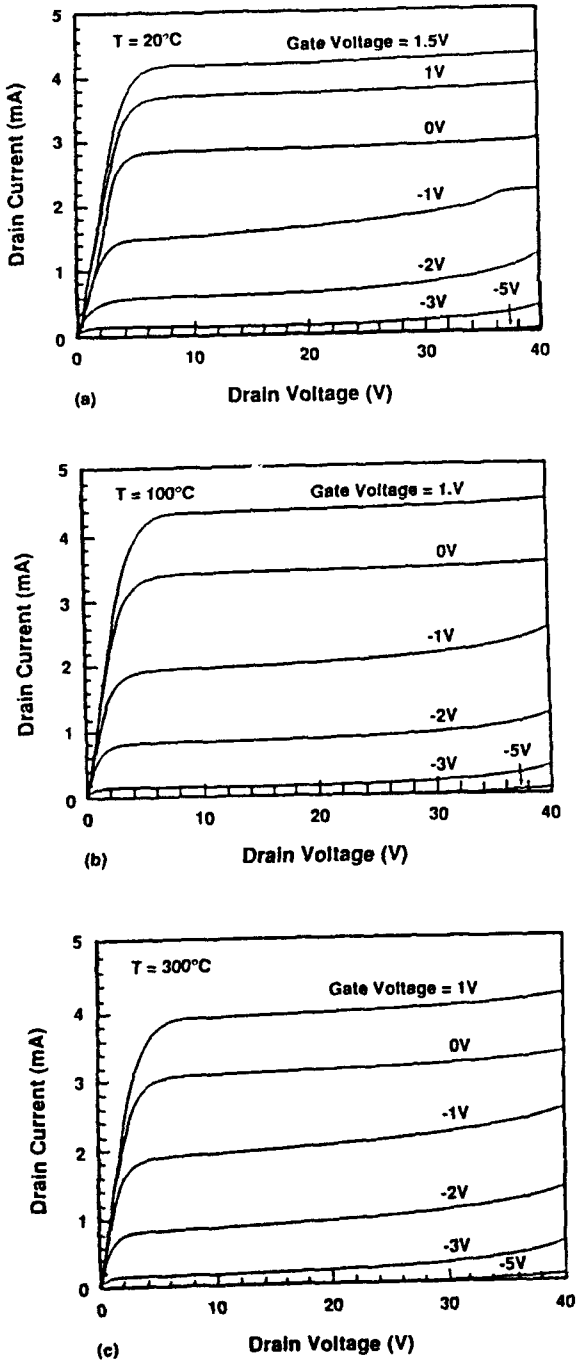

Figure 14. Drain current-voltage characteristics of α-SiC MESFET at (a), 293K, (b), 373K and (c), 573K.

used as the source and drain ohmic contacts. Thermally evaporated Au was used as the gate rectifying contact. The gate voltage (V_G) was varied from 0.6 V to 1.5 V in -0.3 V steps.

It can be seen from Figure 13 that very good drain current saturation is achieved as the drain voltage increases. The maximum transconductance in the saturated region for this device was 0.64 mS/mm, however, a maximum transconductance of 1.6 mS/μm was measured on other devices in this sample. The threshold voltage was -1.6 V, although after subtracting the leakage current, it is reduced to -1.4 V. It was observed that for V_G<-2 V the drain current was almost independent of the gate voltage, and thus the device could not be fully turned off. For example, in the device in Figure 13, the drain current was 2 mA at a drain voltage of 4 V and a gate voltage <-2.5 V. This indicates that there is some leakage current between the gate and drain. This leakage may be caused by the p-n junction underneath the thin n layer, by the leakage current between the gate and source and/or by the defects (e.g., APBs) in the β-SiC film.

Improvement in the performance of SiC MESFETs has been achieved in a manner analogous to that of the Schottky diodes, i.e., fabricating them in α-SiC substrates. Edmond and Palmour[100] of Cree Research, Inc. have produced devices having a gate length of 13 μm. The device shows(see Figure 14) moderately good current saturation to a drain voltage of 40V, however, there is some nonuniformity at the intermediate gate voltages. The maximum transconductance is 1.5mS/μm with a threshold voltage of 4.4 V. The subthreshold leakage is quite low, having a value of 44 μA at V_D=40V and a gate voltage (V_G of -6 V. The I-V characteristics of the MESFETs actually improved when heated to 100°C, as shown in Fig. 14(b). The maximum transconductance increased to 1.65 mS/mm, and the current saturation was very good to V_D = 30 V. Some leakage was present at higher drain voltages. The subthreshold leakage current was 52 μA at V_D = 40 V and V_G = -6 V. When heated to 200°C, the I-V characteristics were virtually identical to those shown at 100°C. The I-V characteristics at 300°C are shown in Fig. 14(c). The subthreshold leakage increased to 96 μA at V_D = 40 V and V_G = -6 V, and the maximum transconductance decreased to 1.26 mS/mm. However, overall these are still very good characteristics.

3.3.4 *Metal Oxide Semiconductor Field-Effect Transistors (MOSFETs).* Shibahara, *et al* [101] and Kondo, *et al* [102] have produced working metal oxide semiconductor transistors (MOSFETs) on β-SiC films. The MOSFET produced by the former group was fabricated in B doped, p-type SiC (thickness ~7 mm, n~E17 cm^{-3}) with source and drain formed by ion implantation of P^+ and subsequent annealing at 1353K for 3.6E3s. The leakage current between the source and gate was <1 mA for the gate bias of ±10 V. By contrast, Kondo, *et al* [102] produced their device on an undoped, n-type SiC layer grown on an Al-doped p-type layer previously deposited on p-type (40–60 ohm-cm) Si substrate. Poly-Si combined with Al metallization was used for the source and drain contacts with SiO_2 as the gate material. Their device also functioned in the enhancement or the depletion mode. However, considerable leakage current through the p-type layer was evident, as the drain current did not saturate even at drain voltages >-12 V.

Palmour *et al.*[103,104]] have also fabricated inversion mode MOSFETs in β-SiC grown on Si(100) and depletion mode devices on β-SiC grown on 6H-SiC(0001). In the former, a circular gate pattern similar to that used for the MESFETs was employed. A dual N implant 5E14/cm^{-2} at 70 keV and 3.35E14/cm^{-2} at 40 keV at 873K produced a dual peak concentration of 5E19/cm^{-3}. Poly-Si acted as an implant mask which also served as a self-aligned gate. The source and drain contacts were made of $TaSi_2$. The depletion mode devices were fabricated in

1.2 μm thick n-type layers (n=1.3E15 cm^{-3}). The source of p-type doping (p=1.6E16 cm^{-3}) was Al which diffused from the heavily Al doped 6H α-SiC substrate. This acceptor species also highly compensated the n-type layers, thus producing the unusually low carrier concentration. Windows for source and drain contacts, and the $TaSi_2$ contacts were similar to that described for the inversion devices.

Figure 15a shows the room temperature I_D vs. V_D characteristics for an inversion MOSFET having a 20 μm gate length over the gate voltage range of -4.0 to +8.0 V. The leakage currents at V_D=5 V and 10 V were <10 mA and were -2.4 V and 0.335 mS/mm, respectively. This device also showed good stability as a function of temperature to the highest measured point of 673K, as shown in Figure 15b. However, the leakage current increased steadily with temperature to a maximum of 85 mA at 5 V and 673K. The transconductance and threshold voltage range increased to 0.421 mS/μm and decreased to -5 to -6 V, respectively. This negative shift in threshold voltage with temperature was caused by a change in the barrier height between the metal and the semiconductor.

Decreasing the gate length to 3.5 μm also produced a stable device at 673K; however, the leakage current was markedly higher (760 mA at V_D=5 V) than for the 20 μm devices at this temperature and dominated the current at high drain voltages. The maximum transconductance at (V_D=3.0 V) again increased from 0.58 mS/μm at room temperature to 1.65 mS/μm at 673K. The threshold voltage decreased from 0 V to -2.5 V over the temperature range.

The drain current-voltage characteristics of a depletion MOSFET in β-SiC (111) at 296K are shown in Figure 16a. This particular device had a gate length and width of 7.2 μm and 390 mm, respectively. The source contact-to-drain contact distance was 24 mm. The device showed very stable drain current saturation out to a drain-source voltage of 25 V. (This trend actually continued to V_{DS}=30 V, at which point the oxide underwent breakdown.) The threshold voltage was determined to be at a gate voltage, V_G, of -12.9 V from a plot of $I_{DS(sat)}$ versus V_G. The leakage current at V_{DS}=25 V in the "off" state (V_G=15 V) in this device was 3.75 mA. The negative threshold voltage was due, in part, to the voltage required to deplete the n-channel, but it was made more negative by the presence of either fixed oxide charge or mobile ion charge in the range of 5–6¥10^{12} cm^{-2}, as obtained from MOS C-V curves of the gate oxide. The 723K anneal in forming gas did not change the threshold voltage. The maximum transconductance of this device at room temperature with V_{DS} fixed at 20 V was 5.32 mS/μm at V_G=2.5 V.

When this device was heated to 573K and allowed to stabilize for 15 mins., the transconductance actually increased to a maximum of 6.00 mS/μm at V_G=5.5 V and V_{DS}=20 V. This trend can also be observed by the increased current at V_G=0 V in the 573K drain characteristics shown in Figure 16b. The reason for this increase is currently under investigation. Despite the increase in temperature, the drain current saturation was still very stable to V_{DS}=25 V. The leakage current at V_{DS}=25 V and V_G=15 V increased to 22 mA, and the threshold voltage shifted negatively to V_G=13.3 V.

The drain characteristics of this depletion device were also determined at 673K and at every 50K interval to a maximum of 923K. Results for this last temperature are shown in Figure 16c. The transconductance remained unchanged at 673K; however, it decreased with further increases in temperature. The maximum transconductance measured was 11.9 mS/μm in a 2.4 μm gate length device at 673K. The lower transconductance of the device in Figure 16c at 923K is demonstrated by the lower current at V_G=0 V, as compared with the previous curves. Although the transconductance at this temperature became very erratic above V_G=1 V, it reached a

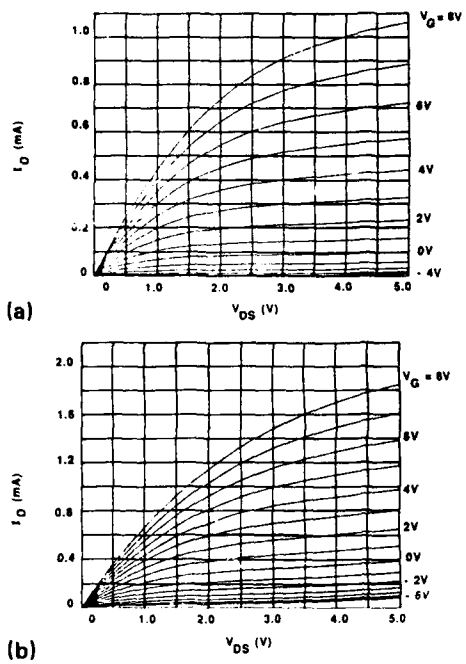

Figure 15. Current-voltage characteristics of a β-SiC n-channel inversion MOSFET with a channel width and channel length of 421 μm, respectively, at (a), 300K and (b) 673K.

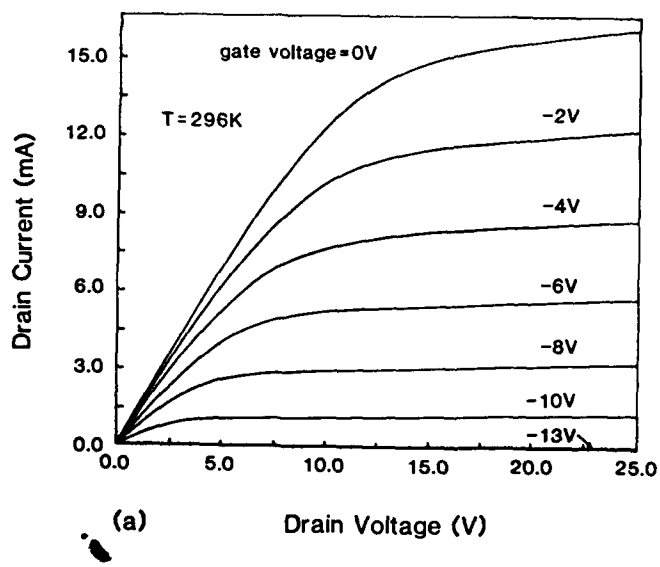

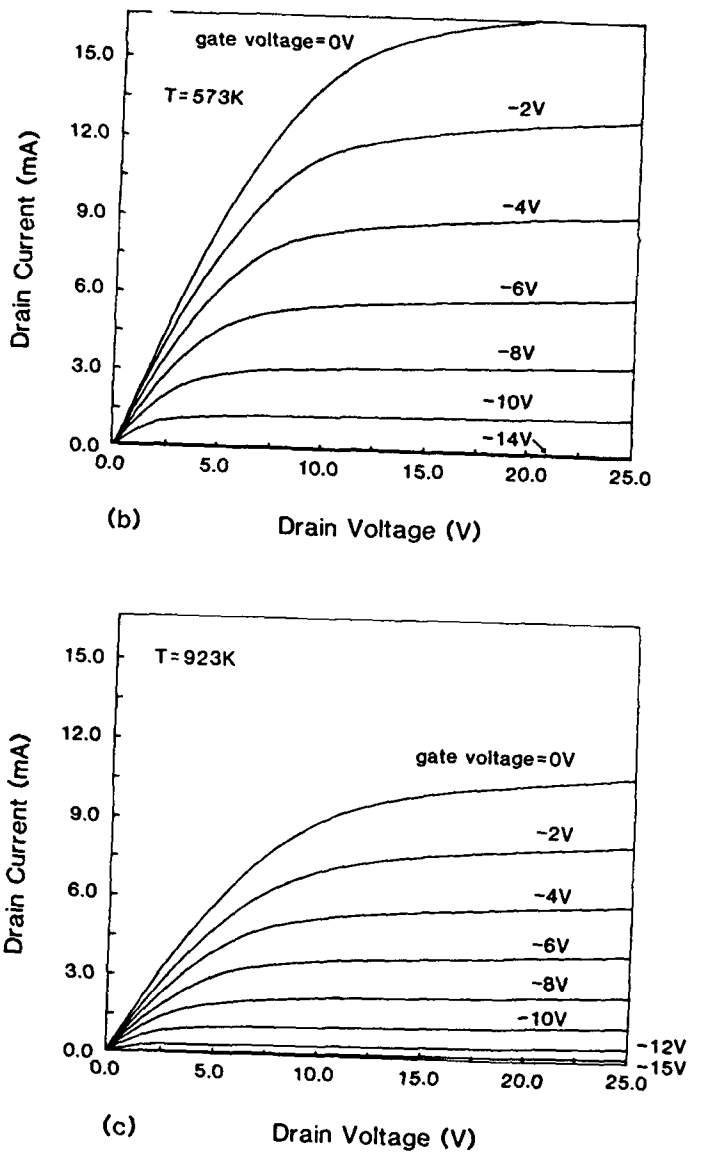

Figure 16. Drain characteristics of depletion mode n-channel MOSFET in β-SiC (111), thin film at (a) (see bottom figure, previous page) 296K, (b) 573K, (c) 923K. The gate length and width of this device was 7.2 μm and 390 μm, respectively.

maximum of about 4.8 mS/μm at V_G=8 V and V_{DS}=20 V. The decrease in transconductance above 673K is due to increasing lattice scattering with temperature. The threshold voltage again shifted negatively, to V_G=–14.8 V at 923K. The leakage current increased to 128 μA at V_G=-15 V and V_{DS}=25 V. When the temperature was raised to 973K, this device showed similar current saturation, but the gate oxide experienced breakdown. Thus, current was being injected at the gate and the device could not be cut off.

D. Summary

Because of its extreme properties and the variety of present and potential commercial applications, SiC is considered by many as the most important carbide. Despite the many fundamental-research programs conducted on SiC in one or more of its forms, however, we still do not understand why periodic stacking arrangements (polytypes) occur in this material or which polytypes are thermodynamically stable as a function of temperature, pressure, impurity introduction, and surrounding atmosphere or the nature of the transformation from one polytype to another. Furthermore, the questions of (1) nonstoichiometry among polytypes, (2) lattice-site location and ionization energies of most electronic dopants, and (3) the occurrence of antisite defects remain unanswered. This seemingly simple compound is actually profoundly complex. Nevertheless, from the viewpoint of microelectronics, much has been accomplished.

Monocrystalline thin films of high purity β-SiC have been grown directly on Si(100) and α-SiC(0001). Problems derived primarily from interface related defects and subboundaries in the material have prevented the optimization of the quality of the films. However, deposition on these materials oriented 2°–4° off-axis allows the elimination of the APBs in the material grown on Si(100) and the DPBs in the material deposited on SiC(0001); the latter resulting combination of α-SiC on α-SiC appears especially viable for device fabrication. Despite the defects, the existence of the films has allowed substantial progress in this research has shown that continued emphasis must be placed on improvement of the quality of the films.

Acknowledgements

The authors enthusiastically acknowledge the support of this program by the Office of Naval Research under contract N00014-82-K-0182F0009 and the National Science Foundation under grant number DMR–8512405 02. Appreciation is also expressed to Drs. C. H. Carter, Jr., H. Kong, J. E. Edmond, and J. W. Palmour now of Cree Research for the fabrication and characterization of the SiC films and devices, to K. L. More and Professor S. R. Nutt for the electron microscopy of the double positioning boundaries and the film substrate interfaces, respectively, and to Dr. G. Carver of the National Bureau of Standards and J. Wortman of NCSU for valuable discussions regarding device research.

References

1. Johnson, E.O. (1965), RCA Rev. **26**, 163-175.
2. Keyes, R.W. (1972), Proc. IEEE **60**, 225-236.

3. Jagodzinski, H. (1949), Acta. Crystallogr. **2**, 201-215.
4. Ramsdell, R.S. (1947), Am. Min. **32**, 64-88.
5. Zhadanov, G. R. (1945), C. R. Acad. Sci., SSSR,**48**, 39-55.
6. Jepps, N.W. (1983), and Page, T. F. in P. Krishna, (ed.), Progress in Crystal Growth and Characterization **7** Pergamon, New York, 1983, pp. 259–307.
7. Taylor, A. and Jones, R.M. (1980) in J. R. O'Connor and J. Smiltens, (eds.), Silicon Carbide, A High-Temperature Semiconductor Pergamon, New York, pp. 147–56.
8. Tairov, Y.M. and Tsvetkov,V. F., in Ref. 6, pp. 111–143.
9. Donnay, J.D.H. (1963), Crystal Data Determinative Tables, 2nd edn., American Crystallography Assoc. pp. 65-66.
10. Adamsky, R. F. and Merz, K. M. (1959), Zeit. Kristallogr.,**111**, 350-356.
11. DeMesquita, A. H. G. (1967), Acta. Cryst. **23**, 610-622.
12. Guth, J. and Petuskey, W. T. (1987), J. Phys. Chem. Solids,**48**, 541-550.
13. Choyke, W. J. and Patrick, L. (1962), Phy. Rev. **127**, 868-880.
14. Choyke, W. J. Hamilton D. R. and Patrick, L. (1962), Bull. Am. Phys. Soc. **7**, 185-195.
15. Patrick, L. (1962), Phys. Rev.,**127**, 1878-1892.
16. Turner, G.L., Kirkpatrick, R.J., Risbud, S.H. and Oldfield, E. (1987), Am. Ceram. Soc. Bull. **66**, 656-668.
17. Inkrott, K. I., Wharry, S. M., O'Donnell, D. J. (1986), in C. J. Brinker, D. E. Clark and D. R. Ulrich, (eds.), Better Ceramics Through Chemistry II," Materials Research Soc. Symp. **73**, Materials Research Society, Pittsburgh, pp. 165–171.
18. Findlay, G. R., Hartman, J. S., Richardson M. F. and Williams, B. L. (1985), J. Chem. Soc., Chem. Comm. **1985**, 159-164.
19. Hartman, J. S., Richardson, M. F., Sheriff B. L., and Winsborrow, B.G. (1987), J. Am. Chem. Soc. **1987**, 6059-6066.
20. Guth, J. R. and Petuskey, W. T. (1987), J. Phys. Chem. **91**, 5361-5370.
21. Schaffer, P.T.B. (1969), Acta. Crystallogr., Sec. B: Struct. Crystallogr. Cryst. Chem. **B25**, 477-485.
22. Pandey, D. and Krishna, P. (1975), Philos. Mag. **31**, 1133-1148.
23. Jepps, N. W., Smith D. J. and Page, T. F. (1979), Acta. Crystallogr., Sect. A: Cryst. Phys. Diff. Theory, Gen. Crystallogr.,**A35**, 916-930.
24. Frank, F. C. (1951), Phios. Mag. **42**, 1014-1025.
25. Amelincky, S. (1951), Nature **168**, 431-432.
26. Jagodzinski, H. (1954), N. J. Min. Monatsh. **3**, 209-212.
27. Jagodzinski, H. (1954), N. J. Min. Monatsh **3**, 49-55.
28. Jepps, N. W. (1979), Ph.D. Dissertation, Univ. Cambridge, UK.
29. Gauther, J.P. (1978), Ph.D. Thesis, Univ. Claude Bernard, Lyon, France.
30. Gauther, J.P. (1980), J. Microsc. (Oxford) **119**, 189-192.
31. Kieffer, P. Ettmayer, E. Gugel and Schmidt, A. (1969), Mater. Res. Bull. **4**, S153-S155.
32. Jepps, N. W. and Page, T. F. (1981), J. Am. Ceram. Soc. **64**, C177-C80.
33. Bootsma, G. A., Knippenberg, W. F.and Verspui, G. (1971), J. Cryst. Growth **8**, 341-351.
34. S. Shinozaki; personal communication.
35. Lely, J. A. (1955), Ber. Deut. Keram. Ger. **32**, 229-240.
36. Shaffer, P. T. B. (1969), Mater. Res. Bull. **4**, S97-S105.
37. Il'in, V. A., Piryutko, M. M., Sorokin, N. D., Yu. Tairov, M. and Tsvetkov, V. G. (1980), Inorg. Mater. (USSR) **16**, 699-708.

38. Nagatome, N., Ishinara, H. and Furukawa, S. (1979), Jpn. Jour. Appl. Phys. **8**, 765-777.
39. Tairov, Yu. M. and Tsvetkov, V. F. in Ref. 6, pp. 111–162.
40. Birnie, D. P. III, Mackrodt, W. C. and Kingery, W. D. (1987), in C. R. A. Catlow and W. C. Mackrodt, (eds.), Advances in Ceramics **23**, "Nonstoichiometric Compounds," American Ceramic Society, Westerville, OH, pp. 571–584.
41. Wang, C. Bernholc, J. and Davis, R. F. (1988), Phys. Rev. B **38**, 12752-12755.
42. Hong, J. D. and Davis, R. F. (1980), J. Am. Ceram. Soc. **63**, 546-556.
43. Hong, J. D. and Davis, R. F. (1981), J. Mater. Sci **16**, 2485-2495.
44. Birnie, D. P. III (1986), J. Am. Ceram. Soc. **69**, C33.
45. Lely, J. A. (1970), Ber. Deut. Keram. Ges. **32**, 229-251.
46. Rai-Choudhury, P. and Formigoni, N. P. (1969), J. Electrochem. Soc **116**, 1440-1448.
47. Harris, J. M.Gatos, H. C. and Witt, A. F. (1971), J. Electrochem. Soc.**118**, 335, 338-340.
48. Brander, R. W. (1974), in R. C. Marshall, J. W. Faust and C. E. Ryan (eds.),S licon Carbide, 1973, University of South Carolina Press, Columbia, pp. 124-136.
49. Nishino, S., Hazuki, Y., Matsunami, H. and Tanaka, T. (1980), J. Electrochem. Soc. **127**, 2674–2680.
50. Nishino, S., Powell, J. A. and Will, H. A. (1983), Appl. Phys. Lett., **42** 460–462.
51. Suzuki, A., Furukawa, K., Higashigaki, Y., Harada, S., Nakajima, S. and Inoguchi, T. (1984), J. Crystal Growth **70**, 287–290.
52. Addamiano, A. and Klein, P. H. (1984), J. Cryst. Growth **70**, 291–294.
53. Sasaki, K., Sakuma, E., Misana, S., Yoshida, S. and Gonda, S. (1984), Appl. Phys. Lett. **45**, 72–73.
54. Liaw, P.H. and Davis, R.F. (1985), J. Electrochem. Soc. **132**, 642-650.
55. Yoshida, S., Daiman, H., Yamanaka, M., Sakuma, E., Misana, S. and Endo, K. (1986), J. Appl. Phys. **60**, 2989-2910.
56. Kim, H.J. and Davis, R.F. (1986), J. Appl. Phys. **60**, 2897-2910.
57. Fujii, Y., Ogura, A., Furukawa, K., Shigeta, M., Suzuki, A. and Nakajima, S., presented at the 1987 Spring Meeting of the Materials Research Society, Reno, NV, to be published.
58. Kong, H. S., Wang, Y. C., Glass, J. T. and Davis, R. F. (1988), Jour. Mater. Res. **3**, 521-530.
59. Shinohara, M., Yamanaka, M., Daimon, H., Sakuma, E., Okumura, H., Misawa, S., Endo, K. and Yoshida, S. (1988), Jap. Jour. Appl. Phys. **27**, L434-L436.
60. Mogab, C. J. and Leamy, H. J. (1974), J. Appl. Phys **45**, 1075-1081.
61. Addamiano, A. and Sprague, J. A. (1984), Appl. Phys. Lett. **44**, 525.
62. Kim, H. J., Davis, R. F., Cox, X. B. and Linton, R. W. (1987), Jour. Electrochem. Soc. **134**, 2270-2278.
63. Bozso, F., Yates, J. T., Jr. (1985), W. J. Choyke and L. Muehlhoff, J. Appl. Phys. **57**, 2771-2777.
64. Graul, J. and Wagner, E. (1972), Appl. Phys. Lett. **21**, 67-68.
65. Carter, C. H., Jr., Davis, R. F. and Nutt, S. R. (1987), J. Mat. Res **1**, 811-817.
66. Pirouz, P., Chorey, C. M., Cheng, T. T. and Powell, J. A. (1987), in J.C.C. Fan, J. M. Phillips and B. Tsaur, (eds.), Heteroepitaxy on Silicon II, Mat. Res. Soc. Symp. **91**, Materials Research Society, Pittsburgh, PA, 399–404.

67. Chorey, C. M., Pirouz, P., Powell, J. A. and Mitchell, T. E. (1986), in Metallurgical Society of AIME, Semiconductor-based Heterostructures: Interfacial Structure and Stability, the Metallurgical Society of AIME, Philadelphia, PA, 115–125.
68. Shibahara, K., Nishino, S. and Matsunami, H. (1986), J. Cryst. Growth **78**, 538-546.
69. Kong, H. S., Wang, Y. C., Glass, J. T. and Davis, R. F. (1988), J. Mater. Res. **3**, 521-530.
70. Aspnes, D. E. and Ihm, J. (1986), Phys. Rev. Lett. **57**, 3054-3055.
71. Chadi, D. J. (1987), Phys. Rev. Lett. **59**, 1691-1693.
72. Wierenga, P. E., Kubby, J. A. and Griffith, J. E. (1987), Phys. Rev. Lett **59**, 2169-2171.
73. Griffith, J. E., Kubby, J. A., Wierenga, P. E., Becker, R. S. (1988), J. Vac. Sci. Technol. A**6**, 493-500.
74. Sakamoto, T. and Hashiguchi, G. (1986), Japan Jour. Appl. Phys. **25**, L57-L59.
75. Zheng, N. J., Knipping, U., Tsong, I. S. T., Petuskey, W. T., Kong, H.S. and Davis, R. F. (1988), J. Vac. Sci. Tech. **6**, 696-699.
76. Choyke, W.J., Fenz, Z.C. and Powell, J.A. (1988), J. Appl. Phys., **64**, 3163-3175.
77. Feng, Z.C., Mascarenhes, A.J., Choyke, W.J., and Powell, J.A.. (1988), Jour. Appl. Phys. **64**, 3176-3186.
78. Fuyuki, T., Nakayama, M., Yoshinobu, T. Shiomi, H. and Matsunami, H. (1989), Jour. Crystal. Growth **95**, 461-463.
79. Rai-Choudhury, P. and Formigoni, N. P. (1969), J. Electrochem. Soc. **116**, 1140.
80. Berman, I., Ryan, C. E., Marshall, R. C. and Littler, A. (1972), AFCRL Report #72-0737.
81. Kong, H. S., Jiang, B. L., Glass, J. T., Rozgonyi, G. A. and More, K. L. (1988), J. Appl. Phys. **63**, 2645.
82. Kong, H. S., Glass, J. T. and Davis, R. F. (1989), J. Mater. Res. **4**, 204-214.
83. Kong, H. S., Kim, H. J., Edmond, J. A., Palmour, J. W., Ryu, J., Carter, C. H., Jr., Glass, J. T. and Davis, R. F. (1987), in T. Aselage, E. Emin and C. Wood (eds.), Novel Refractory Semiconductors, Maters. Res. Soc. Sym. Proc. **97**, Materials Research Society, Pittsburgh, PA, pp. 233–245.
84. Kong, H. S., Glass, J. T. and Davis, R. F. (1988), Jour. Appl. Phys. **64**, 2672-2679.
85. Shibahara, K., Kuroda, N., Nishino, S. and Matsunami, H. (1987), Jpn. Jour. Appl. Phys., Part 2 **26**, 1815.
86. Kuroda, N., Shibahara, K., Yoo, W., Nishino, S. and Matsunami, H. (1987), Extended Abstract of the 19th Conf. on Solid State Devices and Materials, Tokyo, Japan, p. 227.
87. Withrow, S.P., private communication.
88. Yoshida, S., Sasaki, K., Sakuma, E., Misawa, S. and Gonda, S. (1985), Appl. Phys. Lett. **46**, 766.
89. Fujii, Y., Ogura, A., Furukawa, K., Shigeta, M., Suzuki, A. and Nakajima, S. (1987), in Novel Refractory Materials, Mater. Res. Soc. Symp. Proc. **97**, Materials Research Society, Pittsburgh, PA, pp. 233–45.
90. Glasow, P. and Ziegler, G. (1989), in M. Kukkonen (ed.), Optoelectronic Technologies and Remote Sensing from Space, SPIE Vol. 868, SPIE, Bellingham, WA, 40-45.
91. Brander, R. W. and Sutton, R. P. (1969), J. Phys. **D2**, 309.
92. Suzuki, A., Ikeda, M., Nagao, N., Matsumani, H. and Tanaka, T. (1976), J. Appl. Phys.**47**, 4546.

93. Ikeda, M., Hayakawa, T., Yamagiwa, S., Matsunami, H. and Tanaka, T. (1979), J. Appl. Phys. **50**, 8215.
94. Matsunami, H., Ikeda, M., Suzuki, A. and Kanaka, T. (1977), IEEE Trans. Electron Devices **ED-24**, 958.
95. Matsunami, H. (1987), Optoelectronics–Devices and Technologies **2**, 29.
96. Koga, K., Tanaka, T. and Niina, T. (1985), Ext. Abst. 17th Conf. SSDM, 249.
97. Yoshida, S., Daimon, H., Yamanaka, M., Sakuma, E., Misawa, S. and Endo, K. (1986), J. Appl. Phys. **60**, 2989.
98. Daimon, H., Yamanaka, M., Sakuma, E., Misawa, S., Endo K. and Yoshida, S. (1986), Jap. Jour. Appl. Phys., Part 2 **25**, L592.
99. Kong, H. S., Palmour, J. W., Glass, J. T. and Davis, R. F. (1987), Appl. Phys. Lett **51**, 442.
100. Edmond, J.A. and Palmour, J.W. private communication.
101. Shibahara, K., Saito, T., Nishino, S. and Matsunami, H., in Extended Abstracts of the 18th (1986 Internationa), Conference on Solid State Devices and Materials, p. 717.
102. Kondo, Y., Takahashi, T., Ishi, K., Hayashi, Y., Sakuma, E., Misawa, S., Daiman, H., Yamanaka, M. and Yoshido, S. (1986), IEEE Electron Device Letters **EDL-7**, 404.
103. Palmour, J. W., Kong, H. S. and Davis, R. F. (1987), Appl. Phys. Lett. **51**, 2028.
104. Palmour, J. W., Kong, H. S. and Davis, R. F. (1988), J.. Appl. Phys. **64**, pp. 2168-2177.

THERMAL CONDUCTIVITY OF TRANSITION METAL CARBIDES

WENDELL S. WILLIAMS
Department of Materials Science and Engineering
Case Western Reserve University
Cleveland
Ohio 44106, USA

ABSTRACT. Transition metal carbides, such as TiC, exhibit very low thermal conductivities (K) at low temperatures. The lattice conductivity at such temperatures is severely limited by phonon scattering by conduction electrons. At high temperatures, point-defect scattering of phonons by carbon vacancies in the non-stoichiometric compounds dominate K. Scattering of electrons by the vacancies limits the electronic contribution. Above ~1000°C the thermal conductivity of the carbides is increased by ambipolar diffusion.

The thermal conductivity of cemented carbides based on TiC (which is non-stoichiometric) is lower than that of cemented carbides based on WC (which is stoichiometric) at all temperatures. Increasing the content of the binder phase in cemented carbides reduces the thermal conductivity.

1. INTRODUCTION

The ability of the transition metal carbides (e.g. TiC) to transport heat is marked by unusual and interesting features. For example, even in the form of pure single crystals these materials have unexpectedly low thermal conductivity values [1]. In particular, the large peak found in the thermal conductivity versus temperature curve at very low temperatures for other crystalline solids is missing [2]. At high temperatures, instead of showing the temperature-independent thermal conductivity characteristic of pure metals, or the 1/T temperature dependence characteristic of pure dielectrics, the carbides show an increase in the value of the thermal conductivity as temperature increases [3] (Fig. 1).

These surprising properties of single-phase transition metal carbides inevitably affect the thermal and mechanical properties of more complex objects made from them, such as cemented carbide cutting tools and thermal barrier coatings.

The purpose of the present paper, thus, is four-fold: 1) to summarize measurements of the thermal conductivity of transition metal

R. Freer (ed.), The Physics and Chemistry of Carbides; Nitrides and Borides, 625–637.
© 1990 *Kluwer Academic Publishers. Printed in the Netherlands.*

carbides, 2) to interpret the single crystal results in terms of electron structure and defect properties from the perspective of solid state physics, 3) to apply the interpretation to the thermal properties of carbides as used in practice, and 4) to note the implications of these interpretations and measurements.

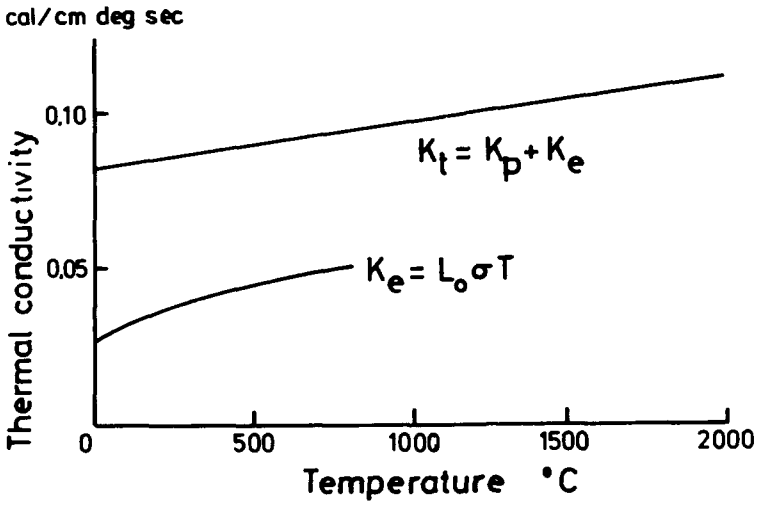

Figure 1. Thermal conductivity of polycrystalline titanium carbide. (From Taylor, ref. 3).

2. THERMAL CONDUCTIVITY

Thermal conductivity is a material property specifying the rate of heat flow through the material in response to a temperature gradient, taking into account the geometry of the specimen:

$$Q = - KA \frac{dT}{dx} \qquad (1)$$

where Q is the rate of heat flow, A is the cross-sectional area of a uniform specimen, dT/dx is the temperature gradient, and K is the coefficient of thermal conductivity. The negative sign expresses the fact that heat flows down a positive temperature gradient. The formula is analogous to the flux equation relating the rate of flow of electric charge (current) in a conductor to the potential gradient through the coefficient of electrical conductivity.

The rate of heat transport is determined by the ability of an excitation to absorb heat (the specific heat), the velocity of the excitation, which can also be expressed as the ratio of the mean free path to the velocity. An expression for the thermal conductivity incorporating these quantities is familiar from kinetic theory of gases, and was utilized first by Debye to describe heat transport in dielectric solids. However, the expression is general; the thermal

conductivity associated with any excitation carrying heat can be written as

$$K = 1/3\ C\ v\ \ell = 1/3\ C\ v^2/\tau \qquad (2)$$

where C is the specific heat, v is the velocity, ℓ is the mean free path of the excitation, and τ is the mean free time between scattering events.

Several different types of excitations that carry heat are found in solids. In a dielectric, the principal excitation can be described in terms of either elastic waves or their quanta, phonons. The discussion of thermal conductivity and its limitation by scattering mechanisms is facilitated by choosing the phonon description. The specific heat associated with phonons is given theoretically to a first approximation by Debye theory; the phonon velocity is taken as the velocity of sound; and the mean free path of the phonons is controlled by several scattering mechanisms, which include: 1) scattering of phonons at the boundaries of a specimen - a process which is important at extremely low temperatures, where the phonon mean free path can be of the same order as the dimensions of the specimen; 2) scattering of phonons by point defects, such as alloying atoms, impurity atoms, isotopes, vacancies and interstitials; 3) scattering of phonons by other phonons in three-phonon events made possible by the anharmonicity of the interatomic potential and which alter the direction of heat flow (Umklapp processes); 4) scattering of phonons by conduction electrons - a process that can be important in the case of alloys and metallic compounds, including those under discussion here; and 5) scattering of phonons by grain boundaries, dislocations and other crystalline defects. Given these several scattering mechanisms, our task here will be to determine which are critical in regulating heat flow in transition metal carbides, which, as indicated above, exhibit unusual thermal conductivities.

In the case of a metallic conductor, heat is also carried by the conduction electron gas. Indeed, for a pure, simple metal, this transport mechanism is the dominant one. The important electron scattering mechanisms are: 1) scattering of electrons by phonons; 2) scattering of electrons by point defects.

For more complex metallic materials, such as doped semiconductors, alloys and metallic compounds like transition metal carbides, the electronic contribution to the thermal conductivity is reduced by these scattering processes, so the phonon contribution (also called lattice contribution) to the total thermal, conductivity cannot be neglected. Then the contributions of these two heat transport processes are summed to give the total thermal conductivity:

$$K = K_p + K_e \qquad (3)$$

Unfortunately, there is no known experimental way of measuring these two contributions separately. It is necessary to find the phonon contribution indirectly by subtracting the electronic contribution from the measured total. The standard procedure for obtaining the electronicic contribution to the thermal conductivity is to measure the electrical conductivity directly and then to invoke the

well known relation between these two quantities, the Wiedemann-Franz law:

$$K_e = L_o \sigma T \qquad (4)$$

where L_o is a constant $= \left[\frac{\pi^2}{3}\right]\left[\frac{k_B}{e}\right]^2$, σ is the electrical conductivity and T is the absolute temperature. This relation follows from the assumption of identical scattering processes for charge transport and heat transport by the conduction electron gas, which is a fair assumption for simple metals. However, for the transition metal carbides it can be seriously in error, and some of the peculiarities of the observed thermal conductivity can be attributed to this breakdown, revealed most clearly through unexpected temperature dependence of the thermal conductivity [1,4], (Fig. 2).

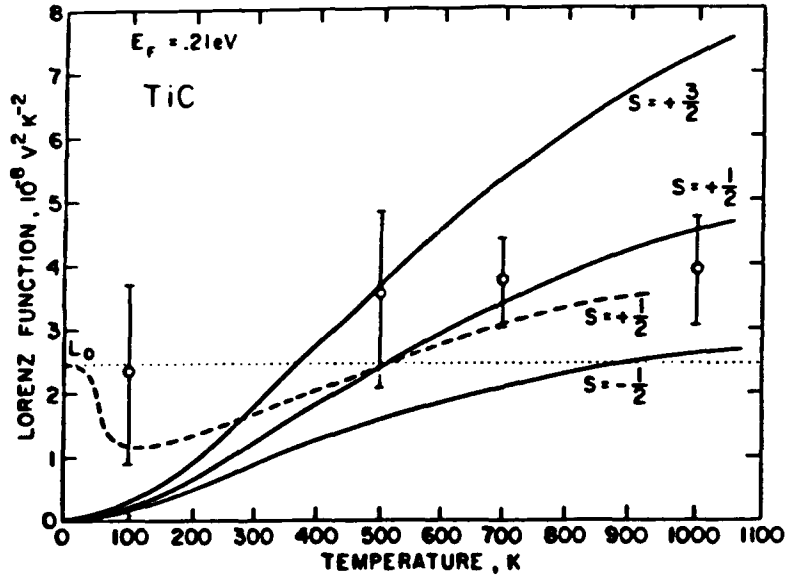

Figure 2. Calculated temperature dependence of the Lorenz function from 0-1100°C for titanium carbide (dashed curve) showing influence of scattering of electrons by optical phonons and by vacancies. Note factors of 2 difference at low and high temperatures relative to classical value, L_o (dotted line). (From Bethin and Williams, ref. 4).

In general, the way in which the thermal conductivity of a material depends on temperature reveals much about fundamental scattering and transport mechanisms. In the present case, we will see that studies of temperature-dependent effects in transition metal carbides at low temperatures have allowed us to identify scattering

mechanisms which operate also at high temperatures and to evaluate the strength of such scattering quantitatively.

3. TRANSITION METAL CARBIDES

The carbides under discussion in this paper are not silicon carbide or boron carbide but rather the *monocarbides* of the transition metals of groups IV, V and VI of the periodic table. (See Table I).

TABLE I. Transition metals of groups IV, V and VI of the periodic table.

IV	V	VI
Ti	V	Cr
Zr	Nb	Mo
Hf	Ta	W

The six metals in columns IV and V form cubic (NaCl-structure) non-stoichiometric compounds with carbon, while tungsten, from column VI, forms an hexagonal monocarbide which is essentially stoichiometric. This difference is critical to an understanding of the thermal and electrical properties of the transition metal carbides, as the non-stoichiometry in those formed from Ti, Zr, Hf, V, Nb and Ta is expressed in the carbon sublattice as atomic vacancies, which are potent scattering centres for both phonons and electrons. The transport properties, mechanical properties and bonding features of the transition metal carbides have been discussed from a solid state physics perspective by the author [5]. Structural and thermodynamic features have been emphasized in books by Toth [6] and by Storms [7].

The transition metal carbides have exceptionally high melting points - in the vicinity of 3,000°C. These high melting points and a tendency to vaporize rapidly and incongruently near the melting point have presented a challenge to investigators wishing to grow single crystals suitable for fundamental property measurement. This challenge was first met in the 1950's by the combination of inert gas welding technology and the Verneuil method for growing single crystals by dropping powders into a hot zone and slowly withdrawing the resulting boule. The crystals used in the thermal conductivity measurements described here were grown by this method. Later approaches to carbide crystal growth employed floating zone and strain annealing methods.

Some of the data discussed here, taken by other groups, are based on single-phase polycrystalline material, processed from powders of the compounds by hot pressing.

Although single-phase transition metal carbides are used in certain industrial applications (e.g. as coatings for cutting tools

applied by chemical vapour deposition) more material is manufactured in powder form and processed with a softer transition metal by liquid phase sintering to produce tough composites, called "refractory hard metals" or "cemented carbides", which serve as the bulk of the cutting tool [8]. Some of the specimens used by the author are representative of this class.

Scientific interest in the thermal conductivity of cemented carbides derives from curiosity about how heat transport in the composite is related to what is known about the constituents; engineering interest results from concern over how to drain heat from the tool/workpiece interface, where temperatures reach 1,000°C from frictional heating and the tool begins to soften.

4. THERMAL CONDUCTIVITY OF SINGLE-PHASE TRANSITION METAL CARBIDES

Measurements of the thermal conductivity of hot-pressed titanium carbide and zirconium carbide specimens at high temperatures, carried out in the 1960's by Taylor and his collaborators [3], showed a puzzling characteristic: the thermal conductivity increased with increasing temperature. As mentioned earlier, lattice thermal conductivity should decrease approximately as 1/T at high temperatures, and electronic thermal conductivity should be approximately independent of temperature in this range; the sum should thus decrease with increasing temperature. Evidently something unexpected occurs in these metallic ceramics.

Analysis of the data into electronic and lattice (phonon) contributions by Taylor, using the Wiedemann-Franz law with measured electrical resistivity values and subtraction, suggested that the electronic contribution constituted approximately half of the total thermal conductivity and increased somewhat with increasing temperature, leaving the lattice component approximately temperature independent and the puzzle unresolved (Fig. 1).

The author suggested that strong electron-vacancy scattering, leading to a large residual resistivity, could partially account for the strange temperature dependence of the electronic contribution [4]. In addition it was suggested that this effect would be further enhanced by electron scattering by optical phonons with polar character, expected for a compound [4]. Moreover, it was pointed out that at low temperatures, where phonons with long wavelengths (small wave vectors) predominate, electron-phonon scattering events which change the energy of an electron but have little influence on the direction of motion would affect heat transport more than charge transport. The basic assumption of the Wiedemann-Franz law (same scattering properties for electrical and thermal conductivity) would thus be violated, leading to a change in the simple relation between them. This change is incorporated into an altered value of the L in the Wiedemann-Franz law and helps to explain the strange temperature dependence of the thermal conductivity [4].

The importance of lattice vacancies, which are numerous in the non-stoichiometric cubic carbides, in affecting the electronic part of

the thermal conductivity is evident and has been discussed above, but lattice vacancies can also scatter lattice waves (or their quanta, phonons). This effect was suggested by the author [1] and by Taylor [3] as an important factor for TiC, ZrC and other cubic carbides.

To investigate the matter in more detail, Radosevich and the author in the 1970's studied single crystal specimens of these materials, having a range of vacancy concentrations, at low temperatures, between liquid helium and liquid nitrogen temperatures, where point defect scattering of phonons usually controls lattice thermal conductivity and the electronic contribution to thermal conductivity is negligible. Surprisingly enough, the thermal conductivity values measured scaled inversely from expectations: the crystals with the most vacancies had the highest thermal conductivities rather than the lowest [2]. This finding led to an intense search for another major scattering mechanism.

The approach was to model the lattice thermal conductivity after Callaway [9]: individual phonon scattering processes are identified and combined by summing their scattering rates, which have different dependencies on temperature and phonon frequency, coefficients are estimated from other data on the material, a Debye frequency spectrum is assumed, with cutoff frequency determined by the Debye temperature, and the general expression for thermal conductivity is used to generate a curve of lattice thermal conductivity versus temperature. This curve is compared against experiment and the coefficients adjusted as necessary for best fit. The relative importance of the various scattering processes can then be assessed.

The ingredients of the Callaway model are given below:

$$\frac{1}{\tau} = A + B\,\omega^4 + C\,\omega^2\,T\exp(-\theta_D/bkT) + D\,\omega \qquad (5)$$

The relevant phonon scattering processes are, from left to right: Boundary scattering, determined by the specimen size at low temperatures, for which the scattering rate is independent of the temperature and phonon frequency; point-defect scattering (Rayleigh scattering), which goes as the fourth power of the phonon frequency; Umklapp scattering, which is exponential in the temperature, reflecting the increasing probability of three-phonon processes as temperature increases from T=0 because more phonons are created; and finally, the one that turns out to be the most interesting and important in this case, phonon-electron scattering, which generally goes as the first power of the frequency [2].

The phonon velocity in this approximation is taken to be constant and equal to the sound velocity, and the specific heat is represented by the Debye (quantum mechanical) expression for elastic waves. The specific heat goes to zero (as T cubed) as T approaches zero because at low temperatures there is not enough energy to populate the higher energy states of the harmonic oscillators. This point is general and explains why the lattice thermal conductivity of even pure ceramics at low temperatures must approach zero - although the phonon mean free path may be long, and the velocity not much different from that at higher temperatures, the system cannot absorb much heat to transport.

The Callaway model described above was applied to TiC, ZrC and NbC by Radosevich and the author. A good fit was obtained to the single-crystal data, but only after a major change was made in the expression for the phonon-electron scattering rate: the first-power frequency dependence was changed to second-power, justified by Pippard's treatment of phonon-electron interactions when the phonon wavelength is greater than the electron mean free path - a condition met here because of the severe electron-vacancy scattering [10,11].

From the Callaway analysis of the experimental data, Radosevich and Williams [2] identified the major phonon scattering mechanism-interaction of the phonons with the conduction electron gas. Such scattering occurs to some degree in metal alloys and doped semiconductors but is evidently of paramount importance for this class of metallic ceramics - a term chosen to indicate that despite the strong covalent bonding and brittle behaviour of the transition metal carbides, they are electronic conductors and so constitute a mixed case.

As the above identification of the major scattering mechanism at low temperatures was based on an approximate theoretical model, it was important to put it to an experimental test. The ideal experiment would be one in which the phonon-electron scattering mechanism could be turned off, which, if the theory is correct, should lead to a large increase in thermal conductivity.

Fortunately, the opportunity for such an experiment was provided by the fact that one of the carbides under investigation (niobium carbide) becomes superconducting where the lattice thermal conductivity should be high but was found to be low for titanium carbide and zirconium carbide, which are not superconductors. In the superconducting state, the electron gas cannot scatter phonons, because to do so would require unfilled electron states at the Fermi energy for the electrons to be scattered into, and such do not exist because of the small energy gap that develops at the Fermi energy at temperatures below the superconducting transition.

The dramatic result of this experiment, carried out by Radosevich and Williams, [11], is shown in Figure 3. Below the superconducting transition temperature the thermal conductivity of nearly stoichiometric niobium carbide increased rapidly with decreasing temperature, reaching at its peak a value over two orders of magnitude higher than that found for a sub-stoichiometric specimen of niobium carbide for which the superconducting transition lay below the range of measurement and hence exhibited strong phonon-electron scattering.

The strong temperature dependence of the thermal conductivity below the transition results from the fact that the magnitude of the energy gap at the Fermi energy is temperature dependent, starting at zero and opening wider as the temperature falls. Hence the phonon-electron scattering probability decreases with decreasing temperature. The temperature dependence of the gap energy is described by the BCS theory of superconductivity, and in one of its developments, the increase of lattice thermal conductivity with decreasing temperature due to reduced phonon electron scattering is also calculated. Application of this theory to the niobium carbide

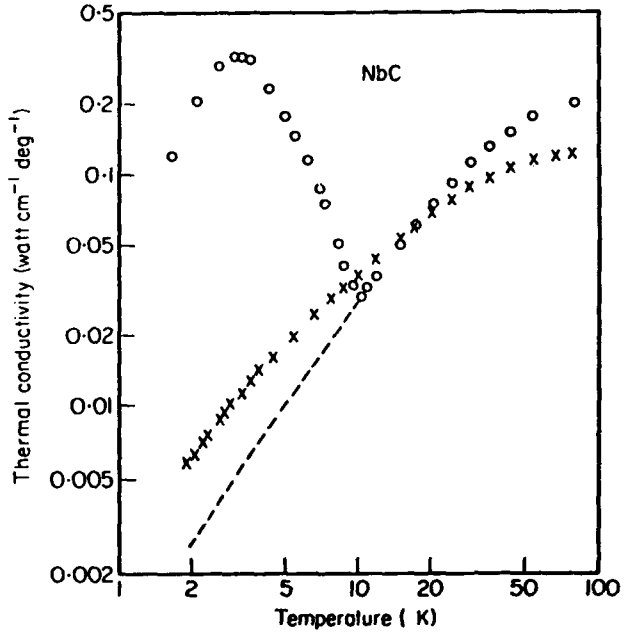

Figure 3. Log thermal conductivity versus log temperature for niobium carbide at low temperatures. Open circles show results for $NbC_{0.96}$, which becomes superconducting at 10K. Large increase in thermal conductivity is observed below this temperature. X's show thermal conductivity of $NbC_{0.76}$ which is not superconducting in this temperature range. Results demonstrate importance of phonon-electron scattering in suppressing the thermal conductivity of the transition metal carbides. (From Radosevich and Williams, ref. 11.)

results by Radosevich and Williams [11] led to the evaluation of the energy gap at zero K - a value later supported by direct tunnelling measurements by Shacklette and Williams.

This discussion has focussed on the lattice or phonon part of the thermal conductivity of the carbides in the superconducting state; what about the electronic contribution? Perhaps the large increase in total thermal conductivity measured below the transition results from a large amount of heat being transported, without scattering, by the electrons. Although the electrons constitute a supercurrent, this current cannot carry heat. Heat is disordered energy, and the superconducting electrons, which are in an ordered state, cannot carry disorder.

With confirmation of the importance of phonon-electron scattering in the carbides in suppressing heat transport, the issue of vacancy

scattering of phonons once more surfaced. The theoretical thermal conductivity curve calculated from the Callaway model for titanium carbide was extended to high temperatures by Radosevich and Williams (Fig. 4) and found to give a good fit to the earlier data of Taylor after some enhancement of the coefficient of the phonon-defect scattering rate. Additional data from Taylor, Wu and Storms [12] for non-stoichiometric zirconium carbide at room temperature and above demonstrated convincingly that vacancy scattering is important in this temperature range. The conclusion to be drawn is that the thermal conductivity of the carbides at low temperatures is governed by phonon-electron scattering, but at room temperature and above, carbon vacancies are controlling.

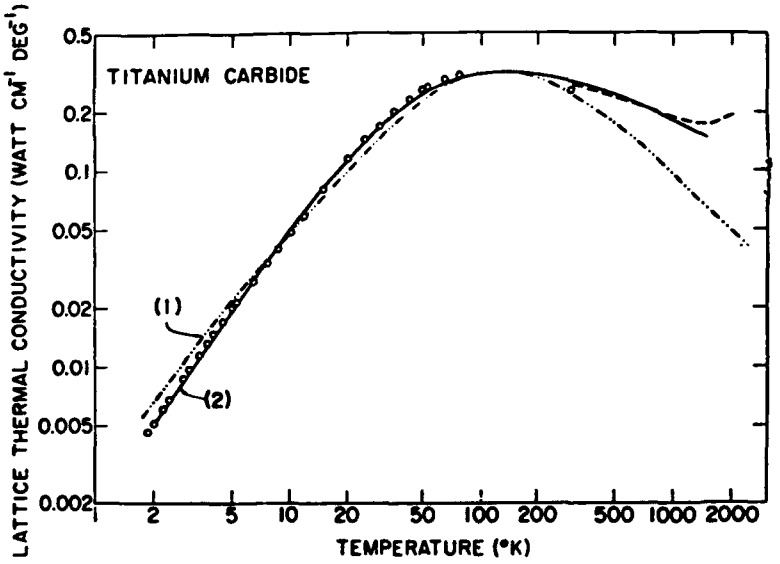

Figure 4. Lattice conductivity of titanium carbide. Theoretical model of summing scattering rates (Callaway) fits experimental data from 2K to 1000K. At highest temperatures, a divergence appears, attributed to ambipolar diffusion of electrons and holes. (From Radosevich and Williams, ref. 11a).

One part of the thermal conductivity puzzle still remains at this point: At the highest temperatures studied for single-phase carbides, beyond 1000°C, a divergency is seen in Figure 4 between the theoretical model and the experimental data. The model underestimates the data, and the error increases at higher temperatures. This divergency suggests that another heat conduction mechanism other than phonons and electrons is operating and that it becomes more important as temperature increases.

Several possible mechanisms were considered by Bethin and Williams [4]: radiation, excitons and ambipolar diffusion. Of these, ambipolar diffusion was found the most plausible. This heat transport mechanism, known to occur in semiconductors, is the migration down a temperature gradient of unbound electron-hole pairs and their recombination to deliver the gap energy. The theory had been modified to apply to semi-metals by Gallo et al [13], and it was then applied to titanium carbide, which can be described by that term, by Bethin and Williams. Although not confirmed experimentally, this mechanism appears to account for the upturn in thermal conductivity of TiC at very high temperatures.

5. THERMAL CONDUCTIVITY OF CEMENTED CARBIDES

Thermal conductivity measurements on a variety of cemented carbide compositions obtained from commercial suppliers of cutting tool inserts were conducted by Williams' group in three temperature ranges: low temperatures (10-100K), room temperature (300K) and high temperatures (up to 1200K). The techniques employed were longitudinal heat flow, thermal comparator, and a novel radiation-cooling method, respectively.

At low temperatures, Frandsen and Williams [14] found that the straight WC/Co composition had the highest thermal conductivity and showed the most pronounced maximum. As WC is essentially metallic and has few compositional vacancies to scatter electrons, this result is straightforward. Additions of grains of TiC, NbC and TaC during processing to improve mechanical properties in cutting operations was found to lower the thermal conductivity, in accord with expectations from the single-phase cubic carbide studies, which found low values for these materials.

The role of non-stoichiometric cubic carbides in reducing the lattice thermal conductivity of cemented carbide composites was shown by a Callaway analysis to result from strong scattering of phonons by carbon atom vacancies and by conduction electrons, while the reduction in electronic thermal conductivity results from scattering of electrons by carbon vacancies [14].

An additional scattering mechanism appears for the cemented carbides: point defect scattering of phonons and electrons by carbon and matrix metal dissolved in the binder phase reduces the total thermal conductivity as the amount of binder is increased [14].

Specimens made from a TiC-based cemented carbide having no WC grains, liquid-phase sintered with a Ni-Mo binder, showed even lower thermal conductivity values [14]. The carbon/metal ratio of this titanium carbide was 0.81, implying a vacancy concentration of 19% on the carbon sublattice, according to a microchemical analysis of an individual carbide grain using electron energy loss spectroscopy by Allison and Wil iams [15].

Measurements of the thermal conductivity of these same cemented carbide specimens at room temperature using a thermal comparator were carried out by Perecherla and Williams [16], who found the same

qualitative trends as described for low temperatures: the thermal conductivity of the composite is reduced by the addition of non-stoichiometric cubic carbide and binder phase alloy. These trends were also found in a high temperature study by Frandsen and Williams [17].

The thermal conductivity results on the cemented carbides - the materials of engineering interest - can thus be interpreted in terms of the conduction and scattering mechanisms established in earlier studies of the pure carbides in single crystal form and from general considerations of alloy properties.

6. IMPLICATIONS FOR ENGINEERING APPLICATIONS

From the point of view of engineering applications, we see that cutting tool insert compositions rich in non-stoichiometric carbides would not conduct heat away from a tool/workpiece interface as effectively as would straight WC/Co. This finding might influence the choice of composition for specific applications, as the hardness of the cemented carbides decreases exponentially with increasing temperature.

The low thermal conductivity of the cubic carbides might be exploited, however, in applications where thermal barrier coatings are desired, as in the "adiabatic" diesel engine.

The dramatic increase in the thermal conductivity of single-phase niobium carbide below the superconducting transition temperature might be utilized in a heat switch.

7. SUMMARY AND CONCLUSIONS

(1) The thermal conductivity of TiC, ZrC and NbC, measured in single crystals in the range from 2K to 100K, is surprisingly low.

(2) The lattice contribution at these temperatures, obtained by subtraction of the electronic contribution calculated from the electrical resistivity, is severely limited by phonon scattering by conduction electrons, according to a Callaway analysis.

(3) This point of view is confirmed by a two-hundred fold increase in the lattice conductivity of superconducting NbC several degrees below the superconducting transition since the BCS energy gap at the Fermi energy reduces the probability of phonons being scattered by electrons. The increase in thermal conductivity is not due to the electron supercurrent, since it cannot carry disorder, and heat is disordered energy.

(4) At high temperatures, point-defect scattering of phonons by carbon vacancies in these non-stoichiometric compounds dominates the thermal resistivity.

(5) Scattering of electrons by these vacancies limits the electronic contribution to the thermal conductivity at all temperatures and affects the details of the phonon scattering by electrons at low temperatures.

(6) Electron scattering by optical phonons with polar character and by scattering by long wavelength phonons which affects heat transport differently from charge transport alters the simple relation between the two conductivities but can be summarized in a temperature-dependent Lorenz function in the Wiedemann-Franz law.

(7) Above approximately 1,000°C, the thermal conductivity of the carbides appears to be increased by another heat conduction process: drifting of unbound electron/hole pairs down the temperature gradient, called ambipolar diffusion.

(8) The thermal conductivity of cemented carbides based on TiC, which is non-stoichiometric, is lower than that of cemented carbides based on WC, which is stoichiometric, in all temperature ranges. The difference is attributed to scattering of electrons and phonons by carbon vacancies in the former.

(9) The percent binder phase (Co or Ni/Mo) in cemented carbides also affects the thermal conductivity: more binder reduces the value.

8. REFERENCES

1. Williams, W.S. (1966) J. Am. Ceram. Soc., 49, 156-169.
2. Radosevich, L.G. and Williams, W.S. (1969) Phys. Rev., 181, 1110-1117.
3. Taylor, R.E. (1961) J. Am. Ceram. Soc., 44, 525-526.
4. Bethin, J. and Williams, W.S. (1977) J. Amer. Ceram. Soc., 60, 424-427.
5. Williams, W.S. (1971) Prog. Solid State Chem., 6, 57-118.
6. Toth, L.E. (1971) 'Transition Metal Carbides and Nitrides' (Academic Press, New York).
7. Storms, E.K. (1968) 'The Refractory Carbides', Vol. II, (Academic Press, New York).
8. Schwarzkopf, P. and Kieffer, R. (1960) 'Cemented Carbides' (Macmillan, New York) pp. 158-176.
9. Callaway, J. (1959) Phys. Rev., 113, 1048-1051.
10. Williams, W.S. (1964) Phys. Rev., 135, A505-A510.
11. Radosevich, L.G. and Williams, W.S. (1969) Phys. Rev., 188, 770-773.

11a. Radosevich, L.G. and Williams, W.S. (1970) J. Amer. Ceram. Soc. 53, 30.

12. Taylor, R.E., Wu and Storms, E.K. (1972) Thermal Conductivity Conference Proceedings.
13. Gallo, C.F., Miller, R.C., Sutter, P.H. and Ure, R.W. (1962) J. Appl. Phys., 33, 3144-3145.
14. Frandsen, M.V. and Williams, W.S., J. Amer. Ceram. Soc. (in press).
15. Allison, C. and Williams, W.S. (1984) Ultramicroscopy, 13, 253-264.
16. Perecherla, R. and Williams, W.S. (1988) J. Amer. Ceram. Soc., 71, 1130-1133.
17. Frandsen, M.V. (1987) Ph.D. Thesis, Department of Physics, University of Illinois at Urbana-Champaign, USA.

THE DIELECTRIC PROPERTIES OF NITRIDES

R. FREER and I.O. OWATE
Materials Science Centre
University of Manchester/UMIST
Grosvenor Street,
Manchester M1 7HS, U.K.

ABSTRACT. Most nitrides have a relative permittivity (ϵ_r) of ~10 at low frequencies and low temperature, but resistivities which vary from 10 to 10^{12} Ωcm at ambient conditions. The stability of many nitride ceramics at elevated temperature makes them attractive as dielectrics in harsh environments. The main trends in the published dielectric data are outlined, and discussed in detail for Si_3N_4-based ceramics. New data are presented for the electrical resistivity, relative permittivity, loss factor and breakdown strength of AlN and Si_3N_4 ceramics, and Si_3N_4-AlN ceramic composites. The effect of microstructural features on dielectric properties are discussed.

1. INTRODUCTION

Traditionally, nitrides have been primarily regarded as structural ceramics because of their high mechanical strength, corrosion resistance and stability at elevated temperatures [1]. In recent years there has been a growing interest in the use of nitrides for electrical and electronic applications. This arises in part because the materials can be employed at elevated temperature, but also because of their unique thermal, electrical and dielectric properties. For example, the mechanical and chemical stability, and high electrical resistivity of hexagonal boron nitride at high temperatures makes the compound a principal candidate for use as microwave windows in re-entry vehicle communication systems [2]. Silicon nitride-based ceramics are of interest as high temperature mm wave dielectric materials, since they combine low values of dielectric loss with exceptional mechanical strengths [3]. In thin film form the technological potential of Si_3N_4 has been identified and the material finds widespread use in semiconductor and integrated circuit technologies [4]. The high thermal conductivity of AlN makes it attractive as a substrate material [5], whilst GaN and InN are semiconductors. Sharif et al [6] noted that sialons could be used as solid electrolytes in high voltage cells.

In this paper we try to outline the typical dielectric and related

R. Freer (ed.), The Physics and Chemistry of Carbides; Nitrides and Borides, 639–651.
© 1990 Kluwer Academic Publishers. Printed in the Netherlands.

properties of the principal nitrides, and the factors controlling these parameters. In addition we present new dielectric and breakdown strength data for reaction bonded silicon nitride (RBSN), AlN and RBSN-AlN ceramic composites.

TABLE 1. Dielectric properties and electrical resistivity of some nitrides (temperature ~20°C except where stated).

	Frequency	ϵ_r	tanδ	ρ(Ωcm)	comment	ref.
AlN		9.14		$\geqslant 3\times10^{12}$		7
AlN		8.5		$\geqslant 3\times10^{12}$		8
BN		7.1		1×10^{10}		9
GaN		12.2		10		10
InN		9.3		1×10^{2}		11
Si_3N_4	100 kHz	9.58	0.005		HPSN	12
	0.5-7 GHz	5	0.00017		RBSN	13
	8-10 GHz	4.5-5.6			RBSN	14
	9.3 GHz	5.65	0.0040		HPSN	12
	9.3 GHz	4.85			Slip cast	15
		6.8			Flame sprayed	15
		8.3	0.007		HPSN	15
		5.5-5.9			Isopressed	15
	10 GHz	5.5-9.3	0.01-0.149		RBSN	16
	10 GHz	6.6	0.01-0.149		RB + MgO	16
	10 GHz	7.37			HPSN	16
	35 GHz	8-12	0.001-0.006		HP + MgO	3
Li-Sialon	1.6 kHz	9(20°C)	0.03	1.4×10^{6}	HP	6
		140(450°C)		6×10^{9}	HP	6
Y-Sialon	1.6 kHz	9(20°C)	0.52	6×10^{8}	HP	6
		14(450°C)	0.21	1.2×10^{9}	HP	6
Li-Sialon	9.3 GHz	4.4	0.005		HP	6
Y-Sialon	9.3 GHz	9.5	0.002		HP	6
β" Sialon glass ceramic	1-20 kHz	8-10	0.003			17
Oxynitride glass	1.6 kHz	7-10		$\sim10^{11}$		18

2. DIELECTRIC PROPERTIES OF NITRIDES

The dielectric properties of a range of nitrides are shown in Table 1. In general, the relative permittivity for all the materials listed is ~10 at low frequencies and low temperature, but the electrical and dielectric properties are sensitive to the method of manufacture,

composition, purity and measurement frequency.

Silicon nitride-based ceramics have been investigated more thoroughly than any other system. The two main manufacturing routes for bulk Si_3N_4 yield materials of widely different characteristics. Hot-pressed silicon nitride (HPSN) is usually compacted at temperatures ~1700°C to give maximum density, pore-free β-Si_3N_4 [19]. In contast for RBSN, the shaped component is usually heated in nitrogen (at 1 bar total pressure) at temperatures between 1250 and 1450°C (during which reaction bonding occurs) to give a product which is a mixture of α-Si_3N_4 and β-Si_3N_4 and contains a high degree of porosity, typically 20-25% [13].

Thorp et al [13] showed that for fully nitrided RBSN (weight gain 62%; porosity 19%) the relative permittivity was 4.60, almost independent of frequency for the range 0.5 to 7.0 GHz. Reducing the degree of nitridation caused a progressive increase in permittivity (to ~10) and loss factor (from $3x10^{-2}$ to 0.2) as the weight gain of ~40% was approached.

At lower frequencies (3 Hz to 300 kHz) Thorp et al [20] found that the permittivity of RBSN was sensitive to temperature over the range 20-900°C (Figure 1).

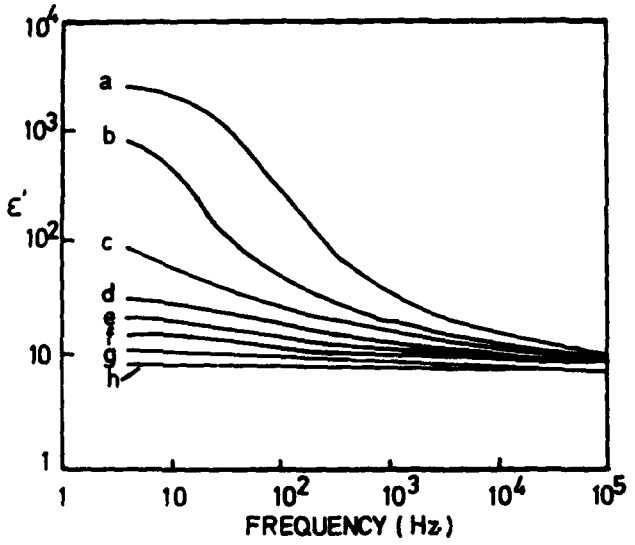

Figure 1. Variation of permittivity with frequency and temperature for RBSN (a = 900°C, d = 600°C, g = 300°C, h = 25°C; after [20]).

This behaviour is very similar to that observed for the temperature-frequency response of the permittivity of B_4C [21,22] and can be modelled in terms of RC networks. The increase in the permittivity at low frequency is due to a large capacitative component, which is effectively short- circuited at high frequencies. Usually, the capacitative component can be attributed to contact effects or internal barriers [23]. Thorp et al [20] found that the permittivity and loss

data could be fitted to a 'general description of dielectrics' proposed by Dissado and Hill [24] and Jonscher [25], and indeed loss peaks were observed at frequencies of 48 Hz and 8 Hz (at 900°C and 800°C respectively) as predicted.

As expected the permittivities for HPSN are higher than those for RBSN (Table 1) because of the lower porosity levels in the former. Although silicon nitrides are complex ceramics, ϵ_r data can be approximated to the simple volume-permittivity relationship:

$$\log K' = \sum_i V_i \log K_i \qquad (1)$$

where V_i is the volume fraction of component i, and K_i is the permittivity of that component. Rationalisation of loss data is more difficult because the loss factor depends upon a number of internal microstructural features (this will be examined in section 5).

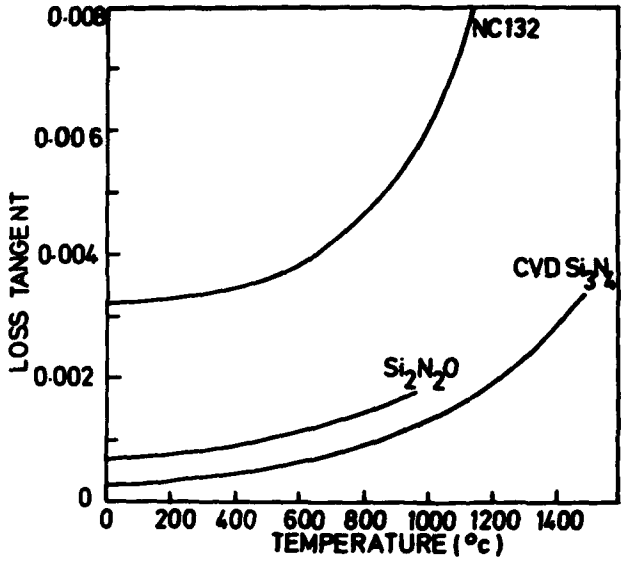

Figure 2. Temperature dependence of the loss tangent for HPSN (NC132), CVD Si_3N_4 and a silicon oxynitride measured at 35 GHz (after [3]).

Figure 2 illustrates the variation of loss tangent (at 35 GHz) as a function of temperature for different forms of Si_3N_4 and a Si_2N_2O. More recently Perera et al [17] noted that losses in sialon glasses and glass ceramics are more sensitive to the presence of trace impurities in the starting α silicon nitride powder (particularly Fe content), rather than cation ratios. However, their work confirmed the findings of Kenmuir et al [26] in that the dielectric constant of Mg sialon glasses increased almost linearly as oxygen was substituted by nitrogen (Figure 3).

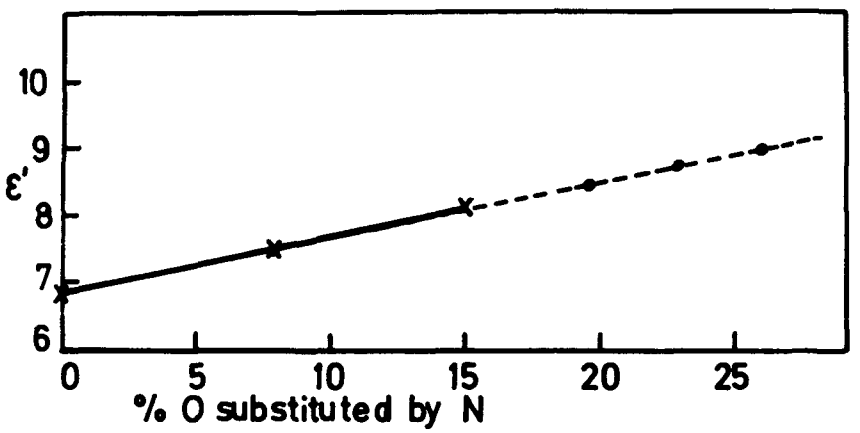

Figure 3. Permittivity of Mg sialon glasses (based on data of Kenmuir et al [26], solid line, and Perera et al [17], broken line).

Sharif et al [6] investigated the dielectric properties of hot pressed lithium and yttrium sialons. At 1.6 kHz the permittivity increased with temperature (20 to 450°C). At 20°C and 9.3 GHz, the permittivity for Li sialon had fallen to half its value at 1.6 kHz, whilst the permittivity of the Y sialon was almost unchanged from its low frequency value (Table 1). In contrast with the Si_3N_4 ceramics the dielectric data for the sialons are not compatible with the Kramers-Kronig relationship [27], and the anomalous behaviour does not support any particular type of conduction mechanism as proposed by Jonscher [27,28].

Whilst basic dielectric data are available for AlN, BN, GaN and InN (Table 1), there have been few detailed studies, and little information regarding the effect of temperature, frequency, purity or density. The electronic properties of these nitrides in thin film form are reviewed by Davis [29].

3. AlN AND Si_3N_4 CERAMICS

The main dielectric properties of AlN and Si_3N_4 hve been summarised in section 2. Here we consider the permittivity, loss factor, electrical resistivity at 20°C and 1 kHz, and the dielectric breakdown of typical commercial materials.

The aluminium nitride was obtained from Tokoyama Soda Ltd. From large sheets, planar disc shaped specimens, 26 mm diameter and thickness 0.2 to 10.0 mm, were prepared. The silicon nitride was reaction bonded (RBSN) in the form of planar disc shaped specimens of 10 mm diameter.

3.1. Electrical Resistivity and Dielectric Properties

For the determination of electrical resistivity, dielectric constant and loss tangent a standard a.c. bridge technique was used. Specimens were 1 mm thick in all cases, and the measuring frequency was 1 kHz. Details of the test cell and experimental procedures are reported elsewhere [30]. The results are summarised in Table 2.

TABLE 2. Dielectric properties and electrical resistivity at 1 kHz for AlN and Si_3N_4 ceramics.

	Density gm/cc	ϵ_r	tan δ	ρ Ωcm
AlN	2.43	8.89	0.0037	3.9×10^{12}
Si_3N_4	2.59	10.34	0.143	8.6×10^{7}

The results for ϵ_r and tan δ are broadly in agreement with published data (Table 1), but the low electrical resistivity for the RBSN reflects the relatively low density, which is a feature of RBSN.

3.2. Dielectric Breakdown

For dielectric breakdown tests the specimen discs were polished, cleaned and gold coated in the manner described elsewhere [30]. Standard a.c. breakdown tests were performed at 17°C and 50 Hz frequency. In all cases 8 mm diameter hemispherically-ended brass electrodes were clamped to the test specimen. The entire system was gradually immersed in an oil bath to prevent flashover effects and bubble formation. A continuous steady state voltage rise of 2 kV/sec was applied to all the specimens up to the breakdown point. Over 30 samples were tested for each set of experimental conditions. For AlN, sufficient tests were performed to assess the effect of thickness on breakdown strength, whilst for Si_3N_4, only specimens of 1 mm thickness were examined.

The average breakdown strength of AlN and Si_3N_4 for specimens of 1 mm thick were found to be 15 kV/mm and 5.2 kV/mm respectively. Figure 4 shows the breakdown strength of AlN as a function of specimen thickness.

The exponential decrease in breakdown strength with increasing specimen thickness is very similar to the behaviour observed for alumina ceramics [30], and this tends to suggest that defects in the bulk of the specimen are responsible for the initiation of breakdown in both Al_2O_3 and AlN. Frequently [31] such defects can be associated with gas trapped in pores. The present data are consistent with such ideas since the Si_3N_4, having a high degree of porosity, exhibits a much lower breakdown strength than the AlN. Hence an improvement in the electrical strength would be anticipated for hot pressed specimens, of near theoretical density.

For all samples, the breakdown process was associated with a single irregular puncture channel which terminated in a crater at the surface

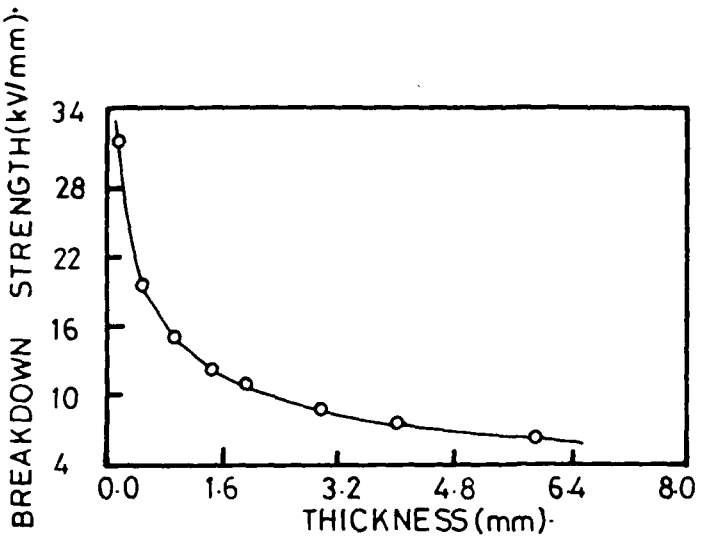

Figure 4. Breakdown strength of AlN ceramics as a function of specimen thickness (after [31]).

of the specimen. The crater surfaces of AlN and Si_3N_4 are shown in Figures 5 and 6. For both materials there is evidence of cracks and local melting. Within the craters of AlN two types of crystallization structures are observed: needle-like networks (Figure 5) and plate-like networks (Figure 7). In contrast, Si_3N_4 exhibited a particulate and smooth solidification pattern, with multiple cracks within the crater region (Figure 6).

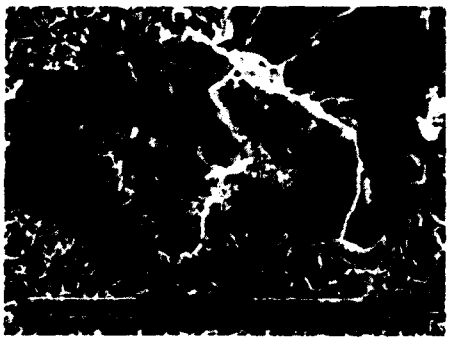

Figure 5. Crater surfaces of AlN ceramic showing needle-like crystallisation structures after breakdown.

Figure 6. Crater surface of Si_3N_4 ceramic after breakdown test.

Figure 7. Plate-like crystallisation structure in AlN specimen after breakdown test.

4. Si_3N_4-AlN CERAMIC COMPOSITES

A series of Si_3N_4 ceramics containing 10, 20, 30, 40, 50 mole% AlN were prepared commercially by a reaction bonding route. Appropriate amounts of Al and Si powder were mixed, milled, sieved, isopressed into billets and pre-sintered at 1000°C. After grinding to size and shape the slabs

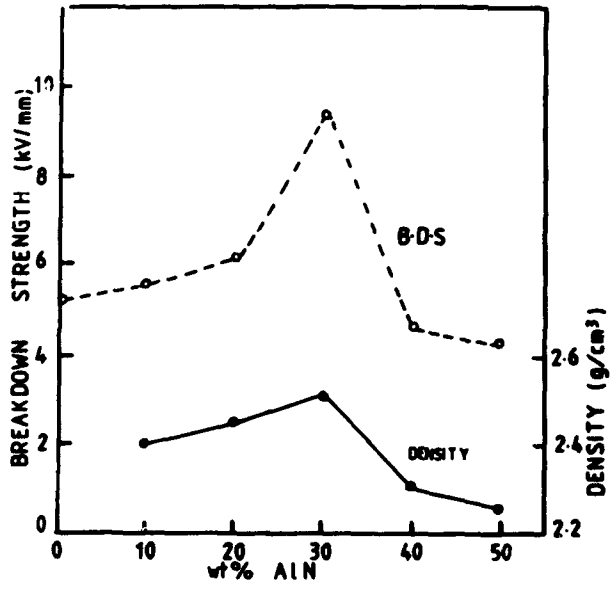

Figure 8. Density and breakdown strength of reaction bonded Si_3N_4-AlN ceramic composites.

were nitrided and sectioned. Planar disc shaped specimens (10 mm diameter, 1 mm thick) were examined for electrical resistivity, permittivity, tan δ, and breakdown strength using the procedures outlined in section 3.

The reaction bonding route produced Si_3N_4-AlN ceramic composites of densities in the range 2.27-2.51 gm/cc. The high porosities caused low electrical resistivities (~10^6 Ωcm), low ϵ_r (~8.9) and high tan δ (~0.40). The breakdown strengths increased in a non-linear manner from the value obtained for the pure Si_3N_4 end member (5.2 kV/mm) to a maximum of 9.5 kV/mm (for Si_3N_4 70%-AlN 30%) down to 4.4 kV/mm at the end of the series (Si_3N_4 50%-AlN 50%). Figure 8 summarises the density and breakdown strength data for the Si_3N_4-AlN composites.

Whilst electrical strength is undoubtedly sensitive to the density and grain boundary phases, it is of interest to note that the Si_3N_4 is present in both the α and β forms for composites containing up to 30% AlN, but only the β form is present in composites containing higher levels of AlN.

5. DISCUSSION

5.1. Permittivity and Loss Tangent

Most bulk ceramics contain a small fraction of pores (p) and so the measured permittivity corresponds to $\epsilon'(p)$. Walton [14] has given an expression relating the permittivities for porous and fully dense (p = 0) materials as

$$\epsilon'(p) = \epsilon'(0)^{(1-p)} \qquad (2)$$

and from this the permittivity of a fully dense ceramic can be evaluated. Published dielectric data for nitrides (Table 1) show that for a given composition the permittivities decrease with increasing frequency, but increase with increasing temperature. However, at ambient conditions and low frequencies, the permittivities of all materials considered are ~10.

In reality the majority of ceramics contain at least a small amount of glass, which has different permittivity and loss characteristics to that of the major phase (or phases). A description of the loss tangent must therefore include the role of the intergranular glass phase (IGF), and following Clark and Ho [3], tan δ may be approximated to

$$\tan \delta = \sum_i V_i \tan \delta_i$$

which is

$$\tan \delta = (V \tan \delta)_a + (V \tan \delta)_b + (V \tan \delta)_{IGF} \qquad (3)$$

for a ceramic containing 2 crystalline phases (a,b), a glass phase and no porosity.

In the case of HPSN Clark and Ho [3] noted that the intergranular glass phase determined, to a large extent, the overall loss tangent of the hot pressed material. Attempts to reduce the loss tangent therefore need to concentrate on the macroscopic properties of the glass phase, namely the viscosity and concentration of ions present. Clark and Ho [3] showed that for the glass phase

$$\tan \delta \propto \frac{nq^2}{\eta} \qquad (4)$$

where n is the number of mobile ions, q is the charge on a given ion, and η is the viscosity of the glass. The relationship in (4) has major implications for the design of high frequency, low loss Si_3N_4 (and a number of other) dielectrics. In addition to keeping the volume of the glass phase to a minimum, and minimising nq^2/η, sintering aids should be chosen to lead to the most refractory glass (i.e. highest viscosity) and ones having the smallest ionic concentration and ion charge. An alternative strategy could be to crystallise the glass phase, and this has already been attempted [32] to improve the high temperature mechanical properties of Si_3N_4 ceramics.

5.2. Dielectric Breakdown

Recent theories [5,33-35] of dielectric breakdown in solids support the role of electromechanical and thermal instabilities in the breakdown process. As the applied current rises there is an increase in the local stress at 'defects' (dislocations, impurities and trapped gas etc.), and once critical stress levels are exceeded microcracks and major cracks will start to form. In the final stages of breakdown the current flow begins to avalanche, the temperature rises rapidly and there is local melting and subsequent evaporation of material to form the breakdown channel. The low breakdown strengths recorded for Si_3N_4 and the Si_3N_4-AlN composites reflect the high porosities in these materials, but a reduction in the volume of the glass phase, or a significant increase in the viscosity of the glass should lead to some improvement in breakdown strength.

The solidification patterns observed after the breakdown process (Figures 5,6,7) only occur in the presence of both high temperatures and high electrical fields. The patterns vary with the applied stress, but the detailed mechanisms are not understood.

5.3. Nitrides as Substrates

Alumina is the traditional material for electronic circuit substrates, but as the packing density of components increase, or components of higher power are used, there is a need to dissipate more heat from the system. Aluminium nitride is attractive as a substrate material, because its thermal conductivity (K) is significantly higher than that of Al_2O_3 (Figure 9).

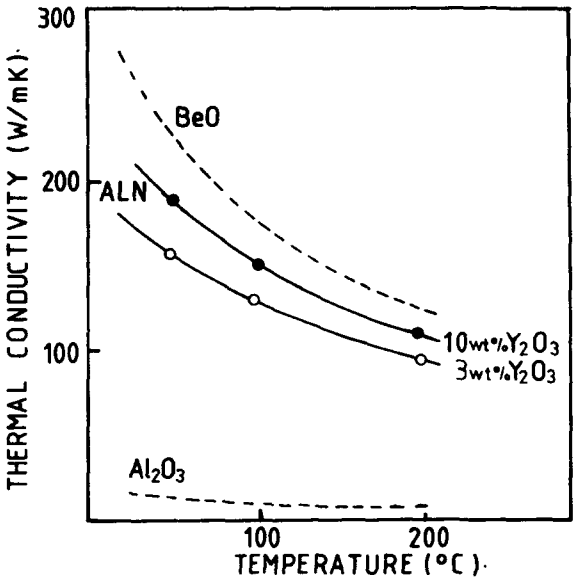

Figure 9. Thermal conductivity of AlN, BeO and Al_2O_3 ceramics as a function of temperature (after Braddeau et al [36]).

Unfortunately, a second requirement is a low ϵ_r since the capacitative propagation delay of signals is proportional to ϵ^2. The permittivity of AlN is not significantly lower than that of Al_2O_3, and indeed the cost of AlN is much higher. Amongst other nitrides, Si_3N_4 has a permittivity which is comparable with that of alumina but lower thermal conductivity. In contrast, cordierite glass ceramics and polymers (e.g. polyimide) have low ϵ and low K (Table 3).

TABLE 3. Relative permittivity, thermal conductivity, and thermal expansion of possible substrate materials.

	ϵ_r	K	α	ref.
AlN	9	140-170	2.7	37
Si_3N_4	10.4	20-35	2.5-3.9	38
Al_2O_3	9.5	10-33	6	39
Cordierite (glass ceramic)	5-8	4	0.2-0.8	40
Polyimide	2	0.8	14	37,40

Onn [41] therefore proposed that nitride-polymer composites may be worthy of investigation as they may exhibit high thermal conductivity and low ϵ_r.

6. SUMMARY

The nitrides are a family of materials exhibiting a wide range of electrical resistivities, but a compratively narrow range of permittivities. The stability of many nitrides at high temperatures and their favourable thermal properties makes them attractive for substrate, electromagnetic window and related applications. Whilst the value of Si_3N_4 thin films have already been recognised for microelectronic applications, ceramic-ceramic and ceramic-polymer composites may provide useful properties, which are not available in monolithic nitrides.

References

1. Riley, F.L. (1983) 'Progress in Nitrogen Ceramics (Nijhoff Publishers, The Hague) NATO ASI, Series E No. 65.
2. Frederiske, H.P.R., Kahn, A.H. and Dragoo, A.L. (1985) J. Amer. Ceram. Soc. 63, 131-135.
3. Clark, D.R. and Ho, W.W. (1983), Advances in Ceramics, 7, 246-252.
4. Morosanu, C.E. (1980) Thin Solid Films, 65, 171.
5. Buchanan, R.C. (1986) Ceramic Materials for Electronics (Marcel Dekker Inc., New York).
6. Sharif, R.I., Thorp, J.S. and Kavanagh, S.A. (1981) J. Mater. Sci., 16, 211-220.
7. Hagen, S.H. and Kapteyns, C.J. (1970) Philips Res. Repts., 25, 1.
8. Hudson, A.R. (1963) UPA patent 309087, May 21.
9. Phillips, J.C. (1973) Bonds and bands in semicondcutors, (Academic Press N.Y.).
10. Gladkii, V.V. and Zheludey, I.S. (1968) Soviet Phys. Crystal (Engl. Trans.) 12, 788.
11. Franz, I. and Langherinrich, W. (1971) Solid State Electron, 14, p. 499 and p. 835.
12. Thorp, J.S. and Sharif, R.I. (1977) J. Mater. Sci., 12, 2274.
13. Thorp, J.S., Ahmed, A.B., Kulesza, B.L.J. and Bushell, T.G. (1984) J. Mater. Sci., 19, 3680-3686.
14. Walton, J.D. (1974) Am. Ceram. Soc. Bu ., 53, 255.
15. Perry, G.S. and Moules, T.R. (1974) Proc. 12th Symposium on Electromagnetic Windows (Georgia Institute of Technology, Atlanta) Ed. J.N. Harris.
16. Messier, D.R. and Wong, P. (1976) Proc. 13th Symposium on Electromagnetic Windows (Georgia Institute of Technology, Atlanta) Ed. J.N. Harris.
17. Perera, D.S., Thompson, D.P. and Thorp, J.S. (1988) Br. Ceram. Proc., 41, 93-100.
18. Thorp, J.S. and Kenmuir, S.V.J. (1981) J. Mater. Sci., 16 Letters, 1407-9.
19. Jack, K. (1976) J. Mater. Sci., 11, 1135.
20. Thorp, J.S., Bushell, T.G., Evans, D. and Rad, N.E. (1987), J. Mater.Sci., 22, 2641-2644.

21. Korman, R. and Zuppiroli, L. (1985) Proc. Int. Conf. on Phys. and Chem. of Boron-rich Borides (Albuquerque, USA, 1985) AIP Conf. Proc. 140, 216.
22. Werheit, H. (1990) On the electronic transport properties of boron carbide - this volume.
23. Koops, G.C. (1951) Phys. Rev., 83, 121.
24. Dissado, L.A. and Hill, R.M. (1980) Philos. Mag. B41, 625.
25. Jonscher, A.K. (1981) J. Mater. Sci. 16, 2037.
26. Kenmuir, S.J.V., Thorp, J.S. and Kulesza, B.L.J. (1983) J. Mater. Sci., 18, 1725.
27. Jonscher, A.K. (1978) Philos. Mag., B38, 587.
28. Jonscher, A.K. (1977) Nature, 267, 673.
29. Davis, R.F. (1990) Current status of the research on III-V mononitride thin films for electronic and optoelectronic applications - this volume.
30. Owate, I.O. and Freer, R. (1988) Science of Ceramics, 14, 1013-1018.
31. Owate, I.O. and Freer, R. (1989) Silicate Industriels, 7-8, 123-127.
32. Sun, W.Y., Thompson, D.P.T. and Jack, K. (1986) Proceedings of seminar 'Tailoring Multiphase and Composite Ceramics', (Pennsylvania State University 1985) Eds. R.E. Tressler et al, Materials Science Research, 20, 93.
33. Zeller, H.P. (1987) IEEE Trans. on Elec. Insul. E1-22, 115.
34. Morse, C.T. and Hill, G.J. (1970), Proc. Br. Ceram. Soc., 18, 23.
35. Byoung-Chul, S. and Ho-Gi, K. (1988) Science of Ceramics, 14, 997.
36. Braddeau, P., Cales, B. and Torre, J.P. (1988) Science of Ceramics, 14, 413.
37. McCarthy, J.P., Pedder, D.J. and Brierly, C.J. (1984) Allen Clark Research Centre Annual Review, 105-112.
38. Morrell, R. Handbook of Properties of Technical and Engineering Ceramics, Data Review, Section on Si_3N_4 (unpublished).
39. Morrell, R. (1987) Handbook of Properties of Technical and Engineering Ceramics, Part 2, Data Reviews, Section 1 (NPL, UK).
40. Partridge, G., Elyard, C.A. and Budd, M.I. (1989) Glasses and Glass Ceramics (Chapman and Hall, UK) Ed. M.H. Lewis, p. 226.
41. Onn, D. (1987) personal communication.

CURRENT STATUS OF THE RESEARCH ON III-V MONONITRIDE THIN FILMS FOR ELECTRONIC AND OPTOELECTRONIC APPLICATIONS

Robert F. Davis
North Carolina State University
Department of Materials Science and Engineering
Box 7907
Raleigh, NC 27695
United States of America

ABSTRACT. Continued development and commercialization of optoelectronic devices, including light-emitting diodes and semiconductor lasers produced from III-V gallium arsenide-based materials, has also generated interest in the much wider bandgap semiconductor mononitride materials containing boron, aluminum, gallium and indium. The majority of the studies have been conducted on pure gallium nitride thin films having the wurtzite structure, and this emphasis continues to the present day. However, recent research has resulted in the fabrication of p-n junctions in cubic boron nitride, the deposition of cubic gallium nitride, as well as, the fabrication of multilayer heterostructures and the formation of thin film solid solutions. Chemical vapor deposition (CVD) has usually been the technique of choice for thin film fabrication. However, more recently these materials have also been deposited by plasma-assisted CVD, reactive ionized-cluster beam deposition, and reactive and ionized molecular beam epitaxy. The objective of this paper will be to review the recent developments in all the III-V nitride thin film materials vis' a' vis' electronic and optoelectronic applications.

1. Introduction

The commercial realization of light emitting diodes and semiconductor lasers in the previous decade generated much interest in thin films of the wider bandgap semiconductor III-V mononitrides, especially GaN. As noted in Table 1, the latter material, in the wurtzite form, has a bandgap of 3.45 eV (near UV region) at room temperature. It also forms a continuous range of solid solutions with AlN (6.28 eV) and InN (1.95 eV). Thus optoelectronic devices having specifically engineered bandgaps with energies from the visible to the deep UV region are theoretically possible with these materials. The wide bandgaps of these materials and their strong atomic bonding also makes them candidates for high power and high temperature devices, assuming appropriate doping impurities are available and can be incorporated on the crystal lattice sites.

By contrast, films of cubic(c) BN have been of interest primarily for wear and corrosion resistant, electrically insulating and passivating surfaces which can be used in high temperature and/or corrosive environments. Cubic BN also has considerable applications in the machining of steels where diamond tools cause problems as a result of the transfer of C into the metal following transformation to graphite at the hot interface. Moreover, electrically active, moderately shallow n- and p-type dopants exist for cBN, and considerable interest in this material for microelectronic applications has been stimulated by the recent creation of a pn junction diode having a portion of its emission spectra in the ultraviolet.

In the following subsections, reviews of the development of thin films of these materials and their current status are presented. The problems which are currently limiting the development of these materials and devices made from them are also discussed.

R. Freer (ed.), The Physics and Chemistry of Carbides; Nitrides and Borides, 653–669.
© 1990 *Kluwer Academic Publishers. Printed in the Netherlands.*

Table 1. Comparison of the Lattice Parameters and Bandgaps of the III-V Monon·trides

Material	Structure	a	c	Bandgap (eV)
BN	zincblende	3.615	3.615	6.4 ± 0.2 (I)*
AlN	wurtzite	3.11	4.98	6.28 (D)*
GaN	wurtzite	3.19	5.19	3.45 (D)*
	zincblende	4.54	4.54	3.26 (D)*
InN	wurtzite	3.54	5.70	1.95 (D)*

* I indicates indirect bandgap; D indicates direct bandgap

2. Review and Current Status of III-V Nitrides with an Emphasis on Electronic and Optoelectronic Applications

2.1 CUBIC BORON NITRIDE

Boron nitride has no counterpart in nature. By analogy to C, it exists as a soft, hexagonal, graphite-like material; as an extremely hard cubic form (zincblende structure); and as an equally hard hexagonal ((hBN) wurtzite) form[1]. The graphitic form of BN is used as a refractory material and a lubricant. The cubic form is produced under equilibrium conditions only at high temperatures and high pressures[2]. It is used primarily as an abrasive grain. But it is this material which is now attracting attention in terms of synthesis at lower temperatures and pressures in a manner recently developed for diamond. The applications would be for hard coatings and high power, high temperature electronics.

The first experimental evidence for the fabrication of either hBN or cBN under nonequilibrium conditions was reported by Sokolowski[3]. He used a reactive pulse plasma crystallization technique which involved an electric discharge between electrodes made of B and Cu contained in atmosphere of 3:1 N_2 and H_2. The plasma reaction products were thin layers containing B and N which were deposited on metal substrates held at 300K. The primary phase which occurred was hBN. This research was subsequently expanded by Weissmantel and coworkers[4-6] who formed hard films with characteristics of cBN using both ion beam plating of electron-beam evaporated B and N_2 ions and ion beam deposition using the precursor of borozine ($B_3N_3H_6$). The substrates were not heated. These investigators referred to this material as "i-BN" to indicate the critical role of ion bombardment in the growth process. The films were mostly amorphous, but contained 5-20nm cBN crystallites. Electron energy loss spectroscopy results confirmed the presence of this crystalline phase. These investigators also employed a dual ion beam technique involving (1) a sputtered beam from a B or BN target and (2) a N ion beam.

Weissmantel *et al.*[6] noted that the properties of the films were very dependent upon processing conditions, however, the relationships were never defined. They suggested that ionic species were essential to the process, although this was not confirmed experimentally. A criticism of the techniques is that they were not configured such as to provide a systematic identification of the species involved in the reaction, thus making improvements in the film quality difficult.

Shanfield and Wolfson[7] also extracted ions from a borozine plasma using a Kaufmann source and accelerated them to 100eV onto the substrate. X-ray spectra of the samples showed peaks of cBN. Auger analysis yielded a B/N ratio of 1:1. Almost simultaneous with this research was that

of Satou and Fujimoto[8] who employed a sophisticated combination of the electron beam evaporation of B and the production of N_2^+ ions. The latter species were derived from a Penning discharge source used for plasma generation and accelerated through a magnetic sector for mass and energy analysis. The N_2^+ ions also passed through a focusing magnetic lens system and a suppressor which controlled the secondary electron output from the Ta and NaCl substrates. The evaporation of the B and the N_2^+ bombardment of the substrates occurred simultaneously. Their deposition rates were controlled separately using a thickness monitor for B and by the beam current for N_2^+. The substrates were maintained at room temperature. Various N/B ratios were used. The resistivity of the films increased markedly at a ratio of ≈ 1.0. At a ratio of 1.8, N was incorporated in the form of bubbles, and the films were amorphous (or extremely fine grained). At a ratio of 2.5, fairly large grains of hBN (wurtzite) and cBN were observed by electron microscopy and selected area diffraction. No information regarding the better substrate for deposition was noted.

In research conducted by Chopra *et al.*[9] and more recently by Lin *et al.*[10] a modified activated reactive evaporation (ARE) process was used to prepare coatings containing cBN via evaporation of H_3BO_3 in an NH_3 plasma. ARE involves the electron beam or resistance heated evaporation of a metal or a compound in the presence of a reactive gas. In this case, the B_2O_3 formed by the decomposition of H_3BO_3 was reduced by atomic H to B which reacted with the atomic N produced in the plasma to form BN. Various substrates including steel and fused quartz as well as Si and NaCl single crystals were used. Microstructural (TEM and selected area diffraction), optical (UV-IR transmission spectra and optical band gap measurements) and hardness studies indicated the existence of the zincblende[9] or a simple cubic (a most unusual form)[10] structure of cBN in the polycrystalline films. No hexagonal phase was detected.

Inagawa and coworkers[11-14] have borrowed from the research of the previous investigators in their use of electron beam evaporated B (with either a standard 270° deflection type gun or a hollow cathode discharge gun) and plasma activated N to deposit cBN on substrates rf biased in the range of 0 to -600 volts. The schematics of this equipment are shown in Figure 1. The simultaneous addition of Ar into the N plasma considerably assisted the formation of cBN, as shown in Figures 2 and 3. At an Ar/N_2 ratio of 4:1, the films contained virtually 100% of the cubic phase.

The most recently published study of cBN deposition using electron beam evaporation and the use of an electrical arc to create a plasma (reactive ion plating technique) has been that of Ikeda *et al.*[15]. The Si substrate was held at 725K. An rf bias was also applied to the substrate. It was determined that the bias potential played an important role in the formation of the cBN films. Infrared spectra revealed the presence of cBN, and TEM showed that the microstructure consisted of 100Å average diameter grains of cBN deposited on an amorphous BN layer located on the substrate surface.

Wiggins *et al.*[16] and Seidel *et al.*[17] have used r.f. reactive sputtering. The structure of the film was not determined in the former study, however cBN was obtained in the latter research. Sharp diffraction rings were obtained in TEM when the bias potential was increased to a maximum of -33% in combination with an increase in the partial pressure of N_2 to a maximum of 1.3×10^{-2} mbar ($P_{total}=2 \times 10^{-2}$ mbar). This corresponded to nearly stoichiometric films. The films consisted of microcrystals with diameters in the range from 50-to-1000Å. Calculation of the lattice parameter from the diffraction patterns corresponded to the 3.61Å for cBN. It was estimated that nearly the whole film consisted of cBN microcrystals. Raising the substrate temperature from ambient to 573K did not markedly change the microstructure or the diffraction patterns of the films.

As noted in the first paragraph of this subsection, cBN is a nonequilibrium phase at the temperatures and pressures used in the experimental programs described above. As such, nonequilibrium routes which imparted additional internal energy to both the B and especially the N_2 were used to ensure that a high internal energy phase would be deposited. Successful deposition of cBN has been attained. However, the films have been polycrystalline and in most, if not all, cases mixed with other amorphous or hexagonal phases of BN. It is obvious that additional and very carefully controlled growth and in-situ analysis research must be conducted to ascertain the precursor species and the operating parameters such as the N/B ratio and ion energy under which the various forms of BN occur as a single phase. This research is continuing for the purpose of achieving hard, wear resistant coatings. The positive results of the research effort described in the following paragraphs should act as a catalyst for additional research with the objective of achieving

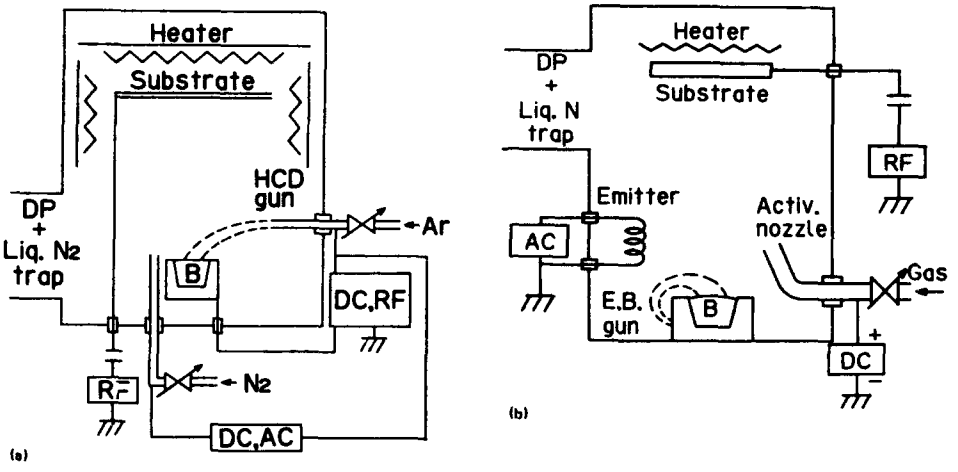

Figure 1. (a) Schematic diagram of a modified hollow cathode discharge-activated reactive (ARE) evaporation. (b) Schematic diagram of the modified ARE method using a conventional 270° electron beam gun. (From Ref. [14])

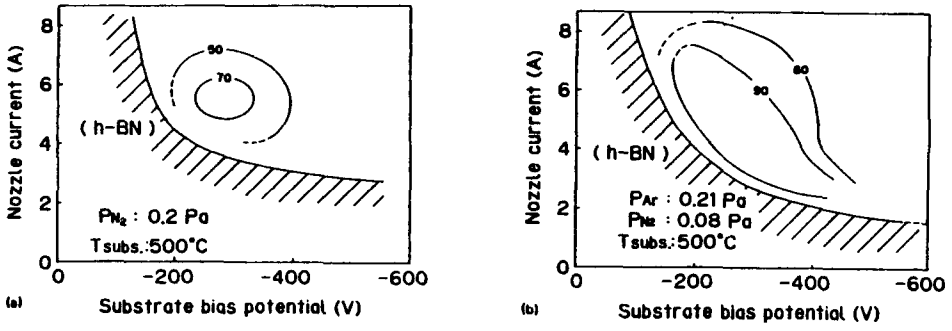

Figure 2. (a) Distribution topograph showing the percentage of cBN in the films deposited by conventional electron beam evaporation in pure N_2. (b) Distribution topograph showing the percentage of cubic phase in BN film obtained by conventional electron beam evaporation in a mixture of N_2+Ar. (From Ref. [14])

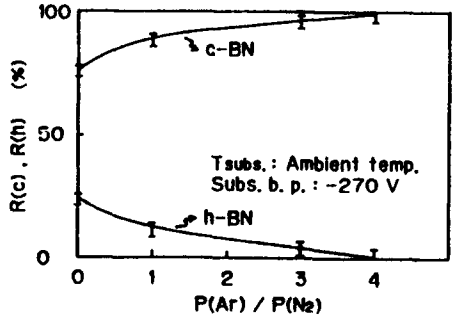

Figure 3. Percentages of cubic and hexagonal phases in the BN films obtained by the conventional EB evaporation in varying P(Ar)/P(N_2) ratios. (From Ref. [14])

monocrystalline cBN films containing selected dopants for microelectronic and optoelectronic applications.

The cBN single crystals grown by Mishima *et al.*[18] was obtained under the more standard conditions of ~55kbar and 2075K using $LiCaBN_2$ as a solvent. Under suitable growth conditions, crystals of ~3mm in size were obtained. In addition, pn junctions were produced[19] via two different growths of the same crystal but with the first in the presence of Si (n-type) and the second in a liquid containing Be (p-type). The diode was functional from room temperature to 923K[20] which is comparable to the highest operating temperature of a SiC transistor[21]. The resistivity ranges as an inverse function of temperature of the p- and n-type portions were $1\text{-}10^2$ and $10\text{-}10^3$, respectively. The activation energies of the conductivity of the p- and n-type areas were ~0.23 and ~0.24eV, respectively. Finally injection luminescence in the ultraviolet was observed for the first time in the forward-bias condition[22]. The total spectra extended from ~215nm to the red, having a few peaks in the ultraviolet. The principal roadblocks to the development of the high pressure technique is the resulting crystal size and the necessity to use the high pressure batch process. Thin films are much more ameable to continuous processing. In addition, good ohmic contacts to n- and p-type material must be found.

2.2 ALUMINUM NITRIDE

The properties of AlN indicate that it has great potential for several applications. The direct band gap of 6.28eV[23] suggests the possibility of windows which would transmit light in the ultraviolet region of the spectra and, if properly doped, optoelectronic devices which would emit light in the same spectral region. Second harmonic generators have also been proposed to make use of the high non-linear optical susceptibilities[24]. This material also possesses the highest reported surface acoustic wave velocity (Rayleigh V_R=6-6.2 km/s, longitudinal V_L=11-12 km/s[25-27]) reported for any material and a substantial electromechanical coupling coefficient (to 1%[27]). In addition, it is distinguished by high hardness (1800 on Knoop scale), chemical stability, transparency in the visible, infra-red (and ultra-violet) ranges, a melting point in excess of 2275K [28], high electrical resistivity ($\rho \geq 10^{13}\ \Omega$ cm) and excellent thermal conductivity. These last two properties coupled with a static dielectric constant of ≈ 9.0 have been commercially exploited in recent years in the manufacture of sintered polycrystalline ceramic heat sinks and substrates for semiconductor chips[29]. The material is also unaffected by electromagnetic radiation, electron and ion bombardment or shock waves (to 59 GPa)[30]. These properties (especially the acoustic) strongly indicate that superior surface acoustic wave devices, operational in aggressive media and under extreme conditions both as sensors for high temperatures and pressures and as acousto-optic devices[25-27,31] can be developed. However, progress regarding these (and other) applications is hampered by the lack of good single crystals. To this end, several studies have been directed toward the achievement of monocrystalline films of this material.

The research conducted prior to 1975 has been reviewed extensively by Duffy[32]. In brief, reactive sputtering, plasma discharge, sublimation and chemical vapor deposition (CVD) were used in this earlier period, with CVD being by far the most widely employed. Aluminum nitride films having single crystal character were deposited on Si, α-Al_2O_3 (sapphire), $MgAl_2O_4$ and α-SiC (33-42). Sapphire has been by far the most common substrate. In a majority of these studies, the deposition process involved a reaction at elevated temperatures between either $AlCl_3$ and NH_3 or $Al(CH_3)_3$ and NH_3. Yim and coworkers[37] and Callaghan *et al.*[40] noted that several orientations of AlN with varying degrees of crystalline perfection may be produced simultaneously on $(01\bar{1}2)$-oriented sapphire substrates by the chloride process. In contrast, AlN films grown by the metal-organic process are $(01\bar{1}2)$-oriented (R-plane) sapphire substrates by the chloride process. In contrast, AlN films grown by the metal-organic process are $(11\bar{2}0)$-oriented (A-plane)[36,38, 39,41,42]. This latter orientation is of greatest interest for surface acoustic wave applications. Unfortunately, essentially all the films grown on sapphire using either the chemistries or the crystallographic planes noted above resulted in highly faceted films (see Ref. 32 for a collection of micrographs on various sapphire planes).

Liu *et al.*[42] also deposited films on polished surfaces of previously grown AlN films. However, the microstructure of the original films and those deposited on AlN surfaces were similar

in appearance. Numerous morphological features including scale-like structures, ridge-like formations, and "bow-tie" shaped grains were evident. Preliminary results indicated that the interfacial strain extended approximately 1μ into the AlN film. Surface acoustic properties were also measured and found to strongly correlate with the quality of the AlN films.

Recent AlN deposition programs have used either past techniques with some modifications to the equipment and/or a change in the reactant species or a completely different approach. An example of the latter is the study by Harper and coworkers[43] who used a dual ion beam technique to supply a flux of Al from the Ar^+ ion beam (1500 eV, 37mA) sputtering of an Al target simultaneous with the low energy N_2^+ (100-500eV, 8mA) bombardment of the growing film. All films were deposited on graphite substrates at ambient temperature. In this reactive deposition of AlN, ion-assisted chemistry (i.e., collisionally-induced dissociative N_2 chemisorption), trapping and preferential sputtering all played strong roles in controlling the film composition. A wide range of arrival rate ratios ($0 \leq N/Al \leq 1.6$) was obtained in each deposition run, producing a composition range of ($0 \leq N/Al \leq 1.0$) across each film. The film composition varied linearly with N arrival flux and saturated at the composition of stoichiometric AlN with the rejection of excess N. For stoichiometric films, the texture and microstructure depended strongly on the N_2^+ flux and ion energy. For low ion energies (100eV) and flux, the films formed with the c-axis perpendicular to the film surface, whereas for high ion beam energies (500eV) the c-axis was close to the plane of the film All films were polycrystalline. The AlN grain size increased with N_2^+ energy. The microstructure was found to be determined primarily by chemical driving forces, but was assisted by ion-enhance diffusion and reaction.

Recently there has been a return to the use of CVD-related techniques but with new reactant materials or with the introduction of plasma. Matloubian and Gershenzan[44] used trimethylaluminum (TMA), NH_3, and (0001) sapphire and a substrate temperate range of 673-1473K. Monocrystalline AlN films were only obtained at 1473K. Itoh *et al.*[45] deposited AlN films on graphite using r-f (13.56 MHz) plasma-enhanced CVD (@50-500W) using mixtures of $AlBr_3$, N_2, H_2 and Ar and substrate temperatures in the range of 473-1073K. The deposition rate was strongly dependent on all these parameters as well as the linear flow velocity and the total pressure. Fine grained polycrystalline films were deposited at 973K under a total pressure of $\leq$ 10 Torr, as shown in Figure 4(a). Translucent polycrystalline AlN films having <0001> preferred orientation (Figure 4(b)) were deposited in the range 15-40 Torr at the same temperature. Finally, Dryburgh has obtained AlN via reaction between Al_2Se and N_2 in the temperature range 1815-1873K using a unique CVD reactor. The $1\bar{1}00$, $1\bar{2}10$ and $1\bar{1}02$ orientations of sapphire were used as the substrates. Reaction between sapphire and N_2 at T>1473K caused roughening of the surface of the former and partial replacement of Al_2O_3 by AlN.

Two major, related problems with the use of sapphire for the growth of AlN are (a) the significantly different expansion coefficients (α) and (b) the fact that the anisotropies in these coefficients for these two hexagonal crystals are in the opposite senses: for AlN, $\alpha_{\perp C} > \alpha_{\parallel C}$ while for Al_2O_3, $\alpha_{\perp C} < \alpha_{\parallel C}$. The poor results usually obtained in the attempts to grow smooth, monocrystalline layers of this material are thus explained. The same is true for GaN, the material under discussion in the next subsection.

2.3 GALLIUM NITRIDE

2.3.1. *Background.* Of all the III-V nitrides, GaN has been the most studied for optoelectronic applications. Films of GaN have been grown from the vapor phase by several techniques including low and high pressure CVD[47-83], plasma-enhanced CVD[84-85], reactive ionized-cluster beam deposition (RICB)[86,87], reactive and ionized molecular beam epitaxy (RMBE)[88-90], IMBE[85,91,92]. Reactive sputtering[94-98] of gallium in NH_3, N_2-NH_3 or N_2-Ar mixtures and solution growth[73,99,100] from gallium or Ga-Bi mixtures have also been used to grow crystalline or amorphous films and small bulk crystals respectively. Since these last two methods represent only a small fraction of the total research into GaN and their use did not result in better material, they will not be discussed further. Sapphire has been the most widely used substrate, although its lattice parameters and coefficients of thermal expansion are about 23% and about 25% greater, respectively, than those of GaN. A brief overview of the studies of deposition of this

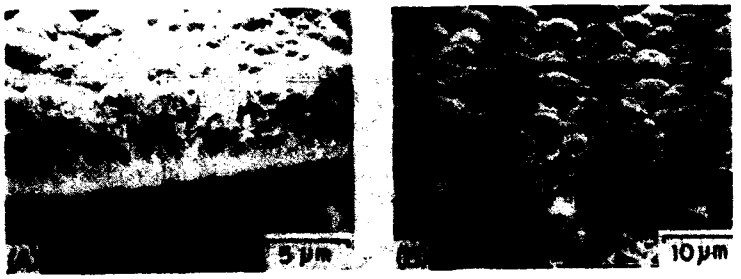

Figure 4. Scanning electron micrographs of AlN films deposited at 973K under total pressures of (a) 5 Torr and (b) 40 Torr. The latter films have a <0001> preferred orientation. (from Ref. [45])

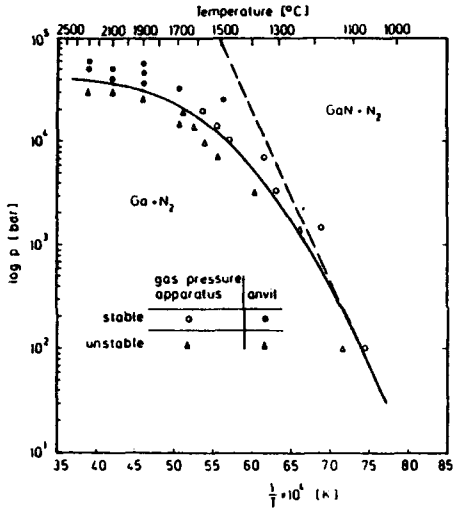

Figure 5. Equilibrium pressure of N_2 over GaN. The broken line was calculated for N_2 as an ideal gas. (from Ref. [72])

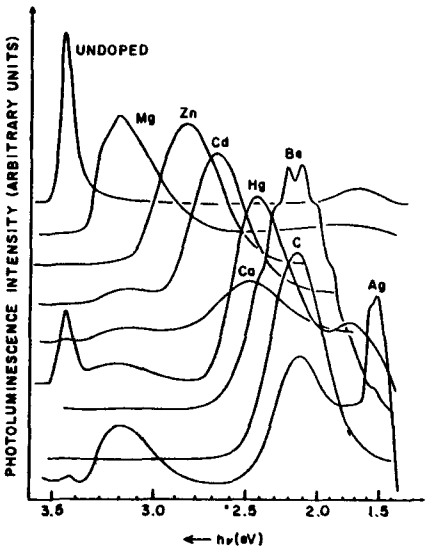

Figure 6. Characteristic emission spectra of an undoped sample of GaN as well as samples which have been implanted with different elements at 78 K. (from Ref. [101])

material from the vapor phase, including those currently in progress, is presented in the following subsections.

2.3.2. *Deposition of Intrinsic GaN from the Vapor Phase.* Chemical vapor deposition has been the most commonly used method to grow epitaxial GaN with GaCl (produced by passing dilute HCl vapor over molten gallium) and NH_3 being the most commonly used reactants. Maruska and Tietjen[47] were the first to use this technique but Pankove and coworkers[48-51] have achieved the greatest success. These researchers, as well as about 15 other groups[52-72] who have employed this technique, have all used substrate temperatures above 1173K and usually between 1273 and 1423K. The vapor pressure of nitrogen over GaN in the latter temperature range is from 10-50 MPa[73,74], as shown in Fig. 5. However, the equilibrium vapor pressure of NH_3 over GaN at 1323K is only 650 Pa[52] thus allowing GaN to form at these elevated temperatures. In this latter process, nitrogen is still lost to the atmosphere from the GaN (as it is with the use of N_2). However, in the presence of NH_3, when a nitrogen atom leaves the GaN, an NH_3 molecule decomposes and replaces it. Nevertheless, the rate of nitrogen replacement is apparently insufficient to maintain stoichiometry, or GaN is intrinsically non-stoichiometric, since no CVD-grown undoped GaN layers with carrier concentrations less than $1.4x10^{17}$ cm^{-3} have been reported, and free gallium is often found in films grown at slow rates.

Various other gallium sources have been used for CVD growth of GaN including trimethylgallium[74-77], triethylgallium[78], trimethylgallium-etherate[79], a gallium tribromide-ammonia complex[80-81], a triethylgallium-monamine complex[82], as well as gallium di- and trichloride and bromide[83]. Most of these were used in order to lower the temperature required for decomposition, with some being deposited at temperatures as low as 573K. However, all films deposited below 873K were polycrystalline. In addition, plasmas have been used to activate N_2 for use as the nitrogen source[84,85] but, since the partial pressure of nitrogen in the CVD reactor was always less than the equilibrium partial pressure of nitrogen over GaN at the substrate temperature, the samples universally contained very high n-type carrier concentrations. None of the latter CVD processes have been more successful at growing low carrier concentration, undoped, monocrystalline thin films of GaN than has been the GaCl and NH_3 system noted initially.

Almost all of the above studies were conducted using either basal- or R-plane-oriented sapphire as the substrate. In general, the basal-oriented films have been found to have a smoother surface than have the R-plane-oriented films, but the growth rate on the latter was usually greater. Wickenden *et al.*[54] used α-SiC(0001) substrates and obtained very smooth epilayers but the films had poor adherence and carrier concentrations lower than those of films grown on sapphire.

Several studies of the growth kinetics of GaN have been conducted[62,68,70,72] and agreement on several points has been achieved: (1) the growth rate on R-plane sapphire is higher than that on basal-plane sapphire at the same flow rates and temperatures; (2) the faster the growth at a given temperature, the lower the carrier concentration; (3) the higher the growth temperature at a given growth rate, the higher the n-type carrier concentration of the resulting film. These results (along with thermodynamic information and electrical data) have resulted in a nearly universal consensus that nitrogen vacancies are responsible for the n-type character of undoped GaN. However, Seifert *et al.*[53] claim that the temperature has no influence on the n-type carrier concentration. Moreover, Gillessen *et al.*[67] found that when they varied the N_2 pressure in their high pressure CVD system from 4 to 13 MPa, at temperatures from 933 to 1273K, there was virtually no change in the n-type carrier concentration (*e.g.* $2x10^{19}$-$1x10^{20}$ cm^{-3} was obtained regardless of pressure). According to the vapor pressure curves of Logan and Thurmond[73], and Madar *et al.*[74], GaN should be stable at the pressures employed by Gillessen *et al.* However, Gillessen *et al.* state that their results are in contrast with the results of Madar *et al.* who claim to have achieved p-type conduction by varying the growth conditions in the ranges 1373-1473K and 150-500 MPa. Nevertheless, Gillessen *et al.*[67] still believe that the n-type conductance is a result of nitrogen vacancies.

2.3.3. *Reactive Ionized-Cluster Beam Deposition.* Epitaxial GaN has been grown[76,87] on ZnO substrates using RICB at 573 and 723K. The ambient N_2 pressure was $5x10^{-4}$ Torr. In this technique, the gallium beam is introduced into a chamber by the adiabatic expansion of the vapor from a special nozzle. The beam is bombarded with electrons which causes ionization and the

division into many singly charged gallium clusters which are accelerated toward the substrate by a potential. Upon impact with the heated substrate, the clusters disintegrate into individual atoms which diffuse across the surface as well as react with the chosen gas to form the desired film. The GaN films grown by this process showed n-type conductivity with resistivities of 1-10 Ω cm. However, optical absorption measurements showed these films to be inferior to high quality CVD-grown samples.

2.3.4. *Molecular Beam Epitaxy.* Two modifications of this general technique have been used to grow GaN films: RMBE and IMBE. Both techniques are variations of gas source MBE. The former involves the use of a gallium Knudsen cell with NH_3 as the reactive gas whilst the latter uses ionized N_2 as the nitrogen source. Gotoh *et al.*[85] have grown GaN on sapphire using both methods. With RMBE the optimum substrate temperature and NH_3 pressure were 898K and $3x10^{-4}$ Torr respectively, which gave a growth rate of 100 nmh^{-1}. The films had smooth surfaces, a resistivity of $3.2x10^{-3}$ Ω•cm and a carrier concentration of $1.5x10^{19}$ cm^{-3}. Using IMBE, the optimum substrate temperature was lowered to 663K. The films produced by IMBE, as opposed to those produced by RMBE, had a more linear growth rate with time, a higher resistivity ($3.2x10^{-2}$ Ω•cm) and a lower carrier concentration (n=$5.8x10^{18}$ cm^{-3}). These investigators postulated that the liberated hydrogen in RMBE disturbs the growth process and causes defects.

Yoshida *et al.*[88,89] have used RMBE with an NH_3 flux of $2x10^{-4}$ Torr to grow GaN on AlN-coated sapphire substrates at 973K, but their success has been limited. This research is discussed more fully at the end of subsection 2.4.

Finally, Gershenzon[90] has described the preliminary results of his efforts to grow GaN on sapphire substrates at 973K by using RMBE. Four-point probe measurements showed the electrical resistivity to be no higher than for those films grown by the other vapor phase techniques noted above.

Very recent research using IMBE has been reported by Paisley *et al.*[91,92]. These investigators employed a microwave glow discharge plasma to dissociate/activate purified N_2, a Knudsen cell for the evaporation of Ga and substrates of β-SiC (cubic polytype), α(6H)-SiC (hexagonal polytype) and (0001) sapphire heated within the range of 500-700°C. The atomic arrangement of the substrate surface dictated the crystallography of the film: cubic (zincblende structure) GaN grew on the β-SiC while hexagonal (wurtzite structure) was deposited on the α-(6H)-SiC and (0001) sapphire. Electron diffraction via TEM confirmed the indications of RHEED patterns of four-fold symmetry and therefore the existence of cubic GaN. This research also supported the indications of cubic GaN grown on GaAs by Mizuta, *et al.*[93] using metalorganics and hydrazine. The lattice parameter and bandgap at 573K of the cubic phase were determined to be 0.454 nm and 3.26 eV, respectively. Cross-sectional TEM revealed that all the films contained numerous threading dislocations and microtwins. In the cubic material, these defects dropped rapidly after 25nm of growth. Auger analysis showed the film to be nominally stoichiometric and relatively free from contaminants. Unfortunately, the low values of the resistivities of resistivities of the films grown both on sapphire ($1.4x10^{-3}$ Ω•cm) and SiC (≈$3x10^{-3}$ Ω•cm) indicate that a phenomenon exists in these films which is similar to those which have plagued all previous GaN thin film research.

2.3.5. *Incorporation of Dopants into GaN.* Nearly all researchers who have grown GaN by any CVD process have also investigated *in situ* doping with zinc or magnesium. Both of these dopants have been found to compensate for the n-type character of GaN and to cause the GaN to become insulating, but neither has been used successfully in the making of p-type GaN. The dopants are usually introduced into the gas phase as organometallic compounds or by allowing the carrier gas to flow over a boat containing the heated metal; both methods are effective in achieving dopant introduction. However, there is a marked variation in the degree of linearity of the plots of the dopant concentration in the crystal vs. the concentration of a given species in the gas phase.

2.3.6. *Ion implantation.* Since GaN decomposes at the temperature required for diffusional doping, ion implantation is the most suitable method for the post-growth introduction of electrically active impurities. The first significant amount of research into implantation was conducted by

Pankove and Hutchby[101]. These researchers obtained the photoluminescence spectra from GaN implanted with 35 different elements. To achieve luminescence, all implanted samples were annealed for 1 h in flowing NH_3 at 323K. The resulting spectra are shown in Fig. 6. The most effecient emissions were obtained from zinc (2.88 eV), magnesium (3.2 eV) and cadmium (2.7 eV), when they were present at a level of $5x10^{18}$ atoms cm^{-3}.

In additional implantation research, Gershenzon *et al.*[52,78,90] found that silicon, germanium, tin and selenium are shallow donors whilst cadmium, zinc, berylium and magnesium are shallow acceptors. However, p-type GaN has never been produced under any circumstances.

Additional aspects of this research also introduced more evidence linking the metallic-like conductivity of intrinsic GaN and nitrogen vacancies. All unimplanted samples showed, via photoluminescence, the characteristic native shallow donor at 3.470 meV. This is believed to be caused by nitrogen vacancies, because Ga^+ implantation always increased this peak and N^+ implantation always decreased it. Moreover, the observed bound excition peak, appearing as a sharp line amid the normal shallow donor bound exciton lines, indicates that the native donor is a point defect. To be associated with an excess of gallium or a deficiency of nitrogen and to be a point defect it therefore must be either a gllium interstitial, a nitrogen vacancy, or an antisite gallium atom on a nitrogen site. If the defect were an antisite defect it should be an acceptor, which is in violation with their observations. Thermodynamically, a gallium interstitial should be much more difficult to form in GaN than a nitrogen vacancy. Thus, it is reasoned that the shallow donors are simple nitrogen vacancies.

2.4 AlN/GaN SOLID SOLUTIONS AND HETEROSTRUCTURES

Solid solutions of AlN and GaN have been produced by several methods to achieve bandgap engineering by analogy with the $Al_XGa_{1-X}X$ (X=Sb, As and P) systems. The $Al_XGa_{1-X}N$ solutions have the potential for optoelectronic devices operating in the ultraviolet as a result of the direct gaps between 3.45 and 6.28eV. Baranov *et al.*[102] and Hagen *et al.*[103] were the first to fabricate films of these materials via chloride vapor phase epitaxy. The former group produced films to x=0.45 at 1325K. The latter investigators showed the existence of complete solid solubility throughout the binary system. This research set in motion a semicontinuous exploration of these materials, primarily in Japan and the U.S.A. which is still ongoing.

Yoshida and coworkers[104], a collaborative effort between Khan *et al.* and Gershenzon[105] and the individual efforts of Gershenzon and his students[106] were the next research teams to produce and characterize these solid solutions. Yoshida *et al.* produced single crystal films over the entire composition range on (0001) sapphire and (111) Si at 973K by RMBE using evaporated Ga and Al and NH_3. The variations in lattice constant, electrical properties, energy gap and the energy of the intense peak in the cathodoluminescence spectra are shown in Figures 7-10. A persual of these figures show that the lattice constant exhibits a nonlinear dependence on composition. By contrast, the bandgap energy and the cathodoluminescence peaks vary smoothly throughout the compositional range. Similar but less extensive research has been conducted by Khan *et al.* using triethylgallium, trimethylaluminum (TMA), NH_3 and (0001) sapphire substrates held at a temperature of 1190K. In contrast to Yoshida, they found that the carrier mobility and the carrier concentration decreased with increasing X values. However, a linear dependence of the bandgap energy with composition was also found thus indicating (as did Yoshida's results) that the bowing parameter is small. This conclusion has been refuted by Koide *et al.*[107] who later reported that the energy gap in the range $0<X\leq0.4$ AlN does not change linearly but bows downward with increasing AlN. Samples with at% AlN>40% were highly resistive even at room temperature. Of particular interest was the implantation of pure GaN and $Al_{0.2}Ga_{0.18}N$ with Be^+ and N^+ implants on separate sample areas. Compensation of the n-type material was achieved and Cr/Au Schottky contacts were deposited onto the implanted regions. Rectifying characteristics for N^+ implants in the alloy were reported with moderate leakage current in reverse bias. Finally, in a related study, Sayyah *et al.*[106] using TMG, TMA and NH_3 in a H_2O-cooled reactor found that the incorporation rates of both Ga and Al in the growing film decreased rapidly with the substrate temperature above 1173K with the incorporation rates of Ga dropping faster than Al. These results

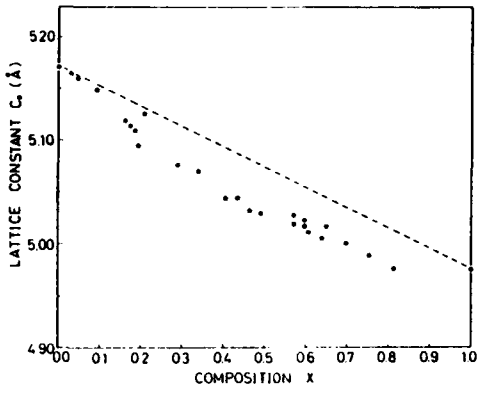

Figure 7. Variation of the lattice constant c_0 with the alloy composition x of $Al_xGa_{1-x}N$ films. (from Ref. [104])

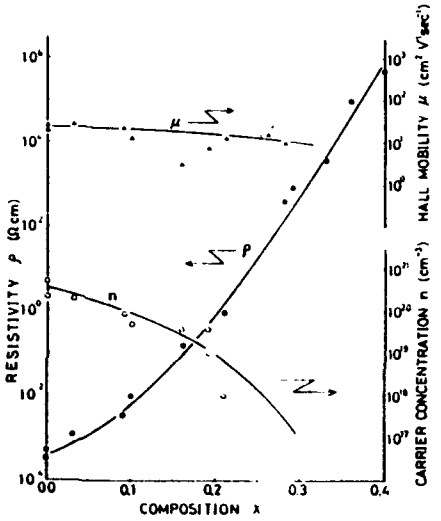

Figure 8. Composition dependence of the resistivity ρ, the carrier concentration n, and the Hall mobility μ at room temperature. (from Ref. [104])

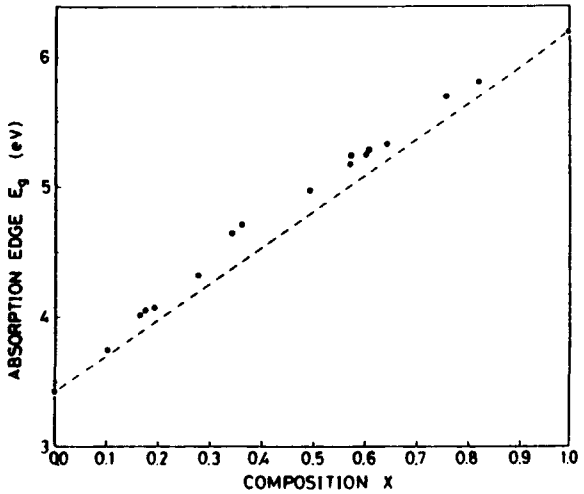

Figure 9. Composition dependence of the direct energy gap E_g of $Al_xGa_{1-x}N$ alloys. (from Ref. [104])

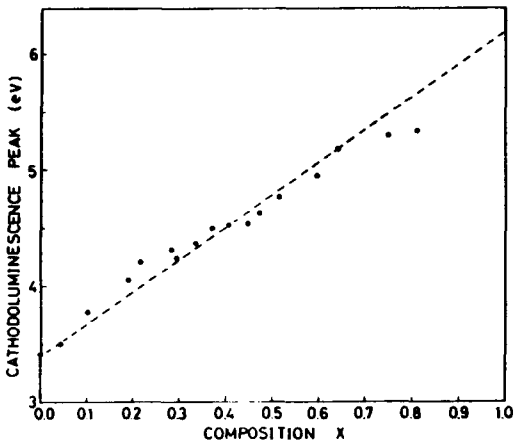

Figure 10. Composition dependence of the energy of the intense peak of cathoduluminescence spectra in the ultraviolet. (from Ref. [104])

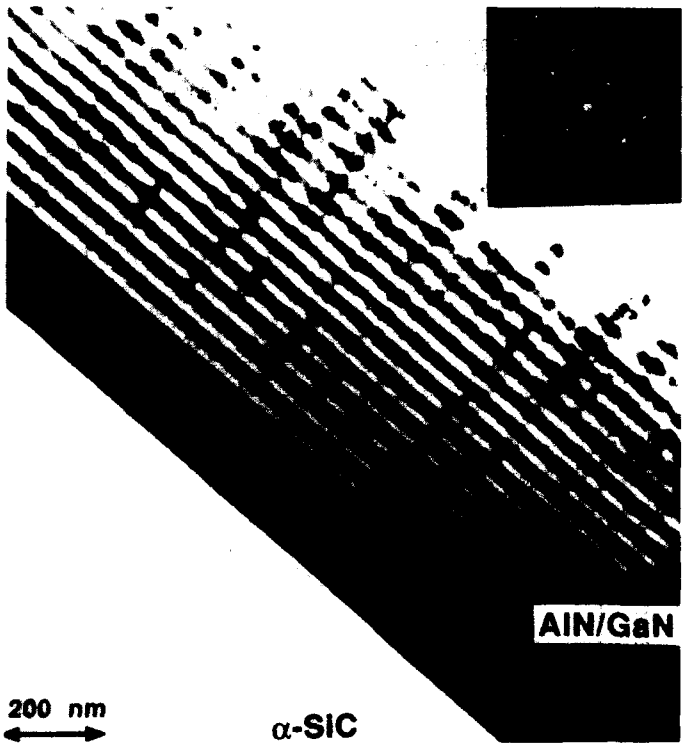

Figure 11. AlN (light)/GaN (dark) layered heterostructure grown on α(6H)-SiC. The thickness of the individual layers is 20 nm. (from Ref. [108[)

were postulated to be caused by the decrease in surface adsorption with the more rapid desorption of Ga relative to Al.

Heterostructures of AlN and GaN have been fabricated by Yosida *et al.*[88,89] and Sitar and coworkers[108]. In the research of the former group, (0001) GaN was deposited directly on (0001) sapphire or on ≈300nm of (0001) AlN previously deposited on sapphire. The substrate temperatures for all depositions of AlN and GaN were 1373K and 973K, respectively. The GaN deposited on the AlN showed a three-fold increase in Hall mobility to ≈34$cm^2/V \cdot sec$ which was independent of the film thickness. Moreover, the GaN cathodoluminesence peak at 360nm (valence band-to-conduction band transition) was sharper and much more intense for the material deposited on the AlN. This intensity increased with an increase in thickness of the GaN, especially beyond 0.2-0.4μm for all films due to the enhanced quality of the films. A decrease in the luminesence intensity was noted when the thickness of the AlN layer was less than 200 nm.

Multiple AlN/GaN bilayer heterostructures having individual periods of 1.5-40nm and total numbers of periods per deposition of 20-200 have been grown at NCSU on (0001)-oriented sapphire and α(6H)-SiC substrates containing a 140nm GaN buffer layer within the temperature range of 773-1025K using gas source MBE in the ionized mode [108]. Standard effusion cells were used as sources of Al and Ga. An MBE compatible, electron cyclotron resonance (ECR) plasma source produced activated/ionized nitrogen prior to deposition. Auger, X-ray diffractometry and TEM analyses showed the interfaces to be compositionally, structurally and microstructurally sharp. Figure 11 shows a TEM image of 5nm thick layers of each compound. The $(10\bar{1}1)$ diffraction pattern (inset), taken only from the layered structure confirms the monocrystalline nature of this assembly. Coherent interfaces (no relaxation by misfit dislocations) were observed for bilayer periods less than 6nm. By contrast, completely relaxed individual layers of GaN and AlN with respect to each other were present for bilayer periods above 20nm. Cathodoluminesence revealed a shift in the position of the principal emission peak from 3.42 eV for the sample with individual 10nm thick GaN layers to 4.11 eV for the sample having 1nm thick individual layers. These last results are tentatively interpreted to be caused by quantum size effects.

2.5 INDIUM NITRIDE

Of all the III-V nitride compounds, InN has been the least studied. All the aforementioned problems associated with GaN, i.e. high equilibrium N_2 vapor pressure, high electron carrier concentration and low mobility are found in InN[109]. As in the case of GaN, the poor semiconducting properties have been associated with the presence of N vacancies and therefore the high vapor pressure of this component. (The argument of self-compensation to explain the lack of p-type character in InN and GaN has never been used even though it apparently accounts for this phenomenon in ZnO and ZnSe.). As such, several low temperature film deposition methods have been employed over the years with varying results.

Hovel and Cuomo[110] were apparently the first to reactively rf sputter InN. They employed an In target, pure N_2 and (0001) sapphire and (111) Si heated in the range of 300-873K. The resulting films were polycrystalline, preferentially oriented and highly conducting n-type with an electron concentration of $7 \times 10^{18} cm^{-3}$ and a Hall mobility of 250 ± 50 $cm^3/V \cdot sec$. ($\rho = (3\text{-}5) \times 10^{-3}\ \Omega \cdot cm$). The achievement of InN films at T=873K is proof that although the equilibrium vapor pressure of N_2 is extreme, that of atomic nitrogen is much more moderate and can be used to successfully grow InN (and probably all other III-V nitrides) at higher than expected substrate temperatures. Extensive characterization of the reactive sputtering process of InN and related materials has been conducted by Natarajan *et al.*[111]. In additional reactive sputtering research, Tansley and Foley[112] have reported a direct correlation between fully nitrided targets and high electron mobilities (and low electron concentrations). These authors have reported the most favorable data to date for these parameters (μ=3000 $cm^2/V \cdot s$ and $n = (2\text{-}10) \times 10^{16}\ cm^{-3}$). However, sputtering from an incompletely nitrided target produced films with lower mobilities and higher n values ($> 10^{17}\ cm^{-3}$). This relationship between poorly nitrided targets and higher electron concentrations has been apparently confirmed in research by Sullivan *et al.*[113].

Electron beam evaporation of In, a pulsed nitrogen plasma and (0001) sapphire substrates at T=300-650K have been used by Trainor and Rose[114]. Typical growth rates ranged from 1.0-

1.2μm/hr. The best material had a Hall mobility at 300K of 20cm^2/V•s and a carrier concentration in the 10^{20} cm^{-3} range. These electronic results are similar to those of Marasina *et al.*[115] who employed the interaction of $InCl_3$ and NH_3 on (0001) sapphire. The former authors also found that annealing InN in N_2 at 773K caused rapid decomposition; however, this did not occur even within an hour at 10^{-3} Torr in the presence of atomic nitrogen. Similar research has more recently been conducted by Masaki *et al.*[116]. Their primary alteration was the use of an ion gun instead of a direct plasma to provide the reactive nitrogen species. Silicon and glass were additional substrate choices. The films were deposited at room temperature; however, In-N bonding was observed by infrared absorption only after heating the deposited film to 450K. Defects and/or impurities dominated the electrical characteristics, especially at and below room temperature.

3. Summary

The potential of III-V nitride thin films for applications in high power and high frequency electronic devices and optoelectronic devices over a broad range of wavelengths is considerable — but this has been recognized for many years without truly viable materials or devices being produced. The lack of a suitable substrate, with the possible exception of SiC for AlN, is a problem of considerable magnitude. This is compounded by the pressure of shallow donor bands in GaN and InN which are apparently caused by N vacancies. The question of whether these vacancies occur (if they do) as a result of intrinsic or extrinsic (as a result of deposition) nonstoichiometry has not been answered. Moreover, the inability to dope GaN and InN p-type may be due to the nitrogen vacancy problem arising from pure nonstoichiometry or vacancies produced by a self-compensation effect similar to that observed in ZnO and ZnSe. The present thrust toward lower temperature deposition in the presence of activated/ionized nitrogen species as are solution to these problems appears logically correct. However, the very small number of workers in this field may signal that commercial reality may be many years away.

Acknowledgments

The author acknowledges the support of the Office of Naval Research under Contract N00014-86-K-0686 P4. Deepest appreciation is expressed to Mr. Zlatko Sitar and Mr. Mike Paisley who contributed to this manuscript.

References

1. Wentorf, R.H. Jr., (1962), J-Chem. Phys. **36**, 1990-1998.
2. Devries, R.C. (1972), Report No. 72 CRD178, General Electric Company, Schenectady, N.Y. 12301, 17 pages.
3. Sokolowski, M. (1979), J. Cryst. Growth **46**, 136-138.
4. rler, H-J., Reisse, G. and Weissmantel, C. (1980) Thin Solid Films 65, 233-239.
5. Weissmantel, C. (1981), J. Vac. Sci. Technol. **18**, 179-185.
6. Weissmantel, C., Bewilgova, K., Bruer, K., Dietrich, D., Ebersbach, U., Erler, H-J., Rau, B., and Reisse, G., (1982), Thin Solid Films **96**, 31-38.
7. Shanfield, S. and Wolfson, R., (1983), J. Vac. Sci. Technol. A **1**, 323-332.
8. Satou, M. and Fujimoto, F., (1983), Jap. Jour. Appl. Phys. **22**, pp. L171-L172.
9. Chopra, K.L., Agrawal, V., Vankar, V.D., Deshpandey, C.V., and Bunshah, R.F., (1985) Thin Solid Films **126**, 307-315.
10. Lin, P., Deshpandey, C., Doerr, H.J., Bunshah, R.F., Chopra, K.L. and Vankar, V.D., (1987), Thin Solid Films **152**, 487-496.
11. Inagawa, K., Watanabe, K., Tanaka, I., Saitoh, S. and Itoh, A., (1985) in T. Takagi (ed.), Proc., Ninth Symp. Ion Sources and Ion-Assisted Tech., Published as a collection of papers by the Research Group on Ion Engineering, Kyoto University, Kyoto, pp. 467-470.

12. Inagawa, K. Watanabe, H., Ohsone, H., Saitoh, K. and Itoh, A. (1986), in T. Takagi (ed.) Proc. Tenth Symp. Ion Sources and Ion Assisted Tech., Published as a collection of papers by the Research Group on Ion Engineering, Kyoto University, Kyoto, pp. 381-384.
13. Watanabe, K., Saitoh, K. Yuchi, Y., Sekino, K., Inagawa, K. and Itoh, A. (1987), in T. Takagi (ed.), Proc. Eleventh Symp. Ion Sources and Ion-Assisted Tech., Published as a collection of papers by the Research Group on Ion Engineering, Kyoto University, Kyoto, pp. 347-350.
14. Inagawa, K. Watanabe, K. Ohsone, H., Saitoh, K. and Itoh, A. (1987), J. Vac. Sci. Technol. A **5**, 2696-2702.
15. Ikeda, T., Kawate, Y. and Hirai, Y. (1989), Kobelco Technology Review **6**, 1-4.
16. Wiggins, H.D., Aita, C.R. and Hickernell, F.S. (1984), J. Vac. Sci. and Technol. **A2**, 150-158.
17. Seidel, K.H., Reichelt, K., Schaal, W. and Dimigen, H. (1987), Thin Solid Films **156**, 215-230.
18. Mishima, O., Yamaoka, S. and Fukunaga, O. (1987), J. Appl. Phys. **61**, 2822-2827.
19. Mishima, O., Tanaka, J., Yamaoka, S. and Fukunaga, O. (1987), Science **238**, 181-186.
20. Mishima, O., private communication.
21. Palmour, J.W., Kong, H.S. and Davis, R.F., (1987), Appl. Phys. Lett. **51**, 2028-2030.
22. Mishima, O., Era, K., Tanaka, J. and Yamaoka, S. (1988), Appl. Phys. Lett. **53**, 962-964.
23. Yim, W.M., Stotko, E.J., Zanzucchi, P.J., Pankove, J.I., Ettenberg, M. and Gilbert, S.L. (1973), J. Appl. Phys. **44**, 292-295.
24. Fujii, Y., Yoshida, S., Misawa, S., Maekawa, S. and Sakudo, T. (1977), Appl. Phys. Lett. **31**, 815-817.
25. Kline, G.R. and Lakin, K.M. (1983), Proc. IEEE Symp. on Ultrasonics, pp. 495-453.
26. Kitayama, M., Fukui, T., Shiosaki, T. and Kawabata, A. (1982), Jap. J. Appl. Phys. **22 (Supplement)**, 139-143.
27. Tsubouchi, K., Sugai, K. and Mikoshiba in Ref. 25, pp. 340-346.
28. Sano, M. and Aoki, M. (1983), Oyo Butsuri **52**, 374-376 (in Japanese).
29. Norton, M.G., Steele, B.C.H. and Leach, C.A. (1988), Science of Ceramics **14**, 545-554.
30. Cartz, P. (1981), Rad. Effects **54**, 57-63.
31. Morita, M., Isogai, S. and Shimizu, N. (1981), Jap. Jour. Appl. Phys. **20**, 173-180.
32. Duffy, M.T. (1978) in G.W. Cullen and C.C. Wang, (eds.), Heteroepitaxial Semiconductors for Electronic Devices, Springer-Verlag, New York, pp. 150-181.
33. Cox, G.A., Cummins, D.O., Kawabe, K. and Tredgold, T. (1967), J. Phys. Chem. Solids **28**, 543-551.
34. Chu, T.L., Ing, D.W. and Noreika, A.J. (1967), Solid-State Electron. **10**, 1023-1026.
35. Noreika, A.J. and Ing, D.W. (1968), J. Appl. Phys. **39**, 5578-5584.
36. Mainasevit, H.M., Erdmann, F.M. and Simpson, W.I. (1971), J. Electrochem. Soc. **118**, 1864-1870.
37. Yim, W.M., Stofko, E.J. Zanzucchi, P.J. Pankove, J.I., Ettenberg, M. and Gilbert, S.M. (1973) J. Appl. Phys. **44**, 292-302.
38. Duffy, M.T., Wang, C.C., O'Clock, Jr., G.D., McFarlane III, S.H. and Zanzucchi, P.J. (1973), J. Electron. Mater. **2**, 359-370.
39. Lakin, K.M., Liu, L. and Wang, K. (1974) in Ultrasonics Symposium Proceed, IEEE Symp. #74 CHO 896-ISU, pp. 302-325.
40. Callaghan, M.P. Patterson, E., Richards, B.P. and Wallace, C.A. (1974), J. Cryst. Growth **22**, 85-95.
41. Pizzarello, F.A. and Coker, J.E. (1975), J. Electron. Mater. **4**, 25-32.
42. Liu, J.K., Lakin, K.M. and Wang, K.L. (1975), Jour. Appl. Phys. **46**, 3703-3706.
43. Harper, J.M.E., Cuomo, J.J. and Hentzell, H.T.G. (1985), J. Appl. Phys. **58**, 550-560.
44. Matloubian, M. and Gershenzon, M. (1985), J. Electron. Mater. **14**, 633-644.
45. Itoh, H., Kato, M. and Sugiyama, K. (1987), Thin Solid Films **146**, 255-264.
46. Dryburgh, P.M. (1989), Jour. Crystal Growth **94**, 23-33.
47. Maruska, H.P., and Tietjen (1969) J.J., Appl. Phys. Lett. **15**, 327-330.

48. Pankove, J.I., Miller, E.A., Richman, D., and Berkeyheiser, J.E. (1971), J. Lumin. **4**, 63-75.
49. Pankove, J.I., Miller, E.A. and Berkeyheiser, J.E. (1973) J. Lumin. **6**, 54-72.
50. Pankove, J.I. (1975), Phys. Rev. Lett. **34**, 809-812.
51. Maruska, H.P., Stevens, D.A., and Pankove, J.I. (1973), Appl. Phys. Lett. **22**, 303-305.
52. Gershenzon, M. (1980), Final Tech. Rep., (Contract N00014-75C-0295, NTIS No. Ad-A099544).
53. Seifet, W., Franzeld, R., Butter, E., Sobotta, H. and Riede, V. (1983), Cryst. Res. Technol. **18**, 383-395.
54. Wickenden, D.K., Faulkner, K.R., Brander, R.W. and Isherwood, B.J. (1971), J. Cryst. Growth **9**, 158-169.
55. Ilegems, M. and Montgomery, H.C. (1973), J. Phys. Chem. Solids **34**, 885-897.
56. Jacob, G., Boulou, M. and Furtado, M. (1977), J. Cryst. Growth **42**, 136-150.
57. Furtado, M. and Jacob, G. (1983), J. Cryst. Growth **64**, 257-272.
58. Andreev, V.M., Bykovskii, Yu. A., Vigdorovich, E.N., Oplesnin, A.V., Plavich, L.F., Smirnov, V.L. and Shmal'ko, A.V. (1978), Sov. J. Quantum Electron. **8**, 73-86.
59. Andreev, V.M., Oplesnin, V.L. and Petrov, M.N., (1978), Soc. Tech. Phys. Lett. **4**, 258-262.
60. Andreev, V.M., Petrov, M.N., and Pcichugin, I.V. (1983), Cryst. Res. Technol. **18**, 435.
61. Crouch, R.K., Debnam, W.J. and Fripp, A.L. (1978), J. Mater. Sci. **13**, 2358-2366.
62. Liu, S.S. and Stevenson, D.A., (1978), J. Electrochem. Soc. **135**, 1161-1168.
63. Monemar, B., Lagerstedt, O. and Gislason, H.P. (1980), J. Appl. Phys. **51**, 625-632..
64. Seifert, W. and Tempel, A. (1974), Phys. Status Solidi A **23**, K39.
65. Seifert, W., Bruhl, H.G., and Fitzl, G. (1980), Phys. Status Solidi A, **61**, 493.
66. Seifert, W., Fitzl, G. and Butter, E. (1981), J. Cryst. Growth, **52**, 257-266.
67. Gillesen, K., Schuller, K.H. and Struck, B. (1977), Mater. Res. Bull. **12**, 955-961.
68. Fremunt, R., Cerny, P., Kohout, J., Rosicka, V. and Burger, A. (1981), Cryst. Res. Technol. **16**, 1257-1266.
69. Ohki, Y., Toyoda, Y., Kobayashi, H. and Aksaki, I., (1981), Inst. Phys. Conf. Ser. **63**, 479-495.
70. Adomin, A.S., Evmenenko, V.A., Mikhailov, L.N. and Raybtsev, N.G. (1981), Inorg. Mater., USSR **17**, 1187-1193.
71. Kuznetson, A.V., Galstyan, V.G., Muratora, V.I. and Chaplygin, G.V. (1982), Sov. Microelectron. **11**, 214-217.
72. Karpinski, J., Jum, J. and Porowski, S. (1984), J. Cryst. Growth **66**, 1-7.
73. Logan, R.A. and Thurmond, C.D. (1972), J. Electrochem. Soc. **119**, 1727-1733.
74. Madar, R., Jacob, G., Hallais, J. and Fruchart, R. (1975), J. Cryst. Growth **31**, 197-209.
75. Knights, J.C. and Lujan, R.A. (1978), J. Appl. Phys. **49**, 1291-1299.
76. Kawabata, T., Matsuba, T. and Koike, S. (1984), J. Appl. Phys. **56**, 2367-2371..
77. Hashimoto, M., Amano, H., Sawaki, N. and Aksasoki, I (1984), J. Cryst. Growth **68**, 163-172.
78. Kahn, M.A., Skogman, R.A., Schulze, R.G. and Gershenzon, M. (1983), Appl. Phys. Lett. **42**, 430-433.
79. Dobrynin, A.V., Zorina, E.N., Popova, T.O., Neastroev, S.A. and Sokolov, E.B. (1979), Sokolov, Khim. Vys. Energ. **13**, 161-165.
80. Chu, T.L. (1971), J. Electrochem. Soc. **118**, 1200-1211.
81. Pankove, J.T. (1973), J. Lumin. **7**, 114-121.
82. Andrews, J.E. and Littlejohn, M.A. (1975), J. Electrochem. Soc. **122**, 1273-1278.
83. Born, P.J. and Robertson, D.S. (1980), J. Mater. Sci. **15**, 3003-3009.
84. Eremin, E.N., Nekrasov, L.I., Rubtsova, E.A., Belova, V.M., Ivanter, V.L., Zakharov, L.N. and Petukhov, V.P. (1982), Russ. J. Chem. **56**, 788-796.
85. Gotoh, H., Suga, T., Suzuki, H. and Kimata, M. (1981), Jpn. J. Appl. Phys. **20**, L545-L551.
86. Matsubara, K., Horibe, T., Takaoka, H. and Takagi, T. (1980), ISA Trans. **5**, 137-145.
87. Matsubara, K. and Takagi, T. (1983), Jpn. J. Appl. Phys. **22**, 511.

88. Yoshida, S., Misawa, S. and Gonda, S. (1983), Appl. Phys. Lett. **42**, 427-430.
89. Yoshida, S., Misawa, S. and Gonda, S. (1983), J. Vac. Sci. Technol. B **1**, 250-255.
90. Gershenzon, M. 1983, Final Tech. Rep., (Contract N00014-81K-0567, NTIS #AD/A-132988).
91. Paisley, M.J., Sitar, Z., Carter, C.H., Jr., and Davis, R.F. (1988), Proc. Soc. Photo-Opt. Instrum. Eng. **877**, 8-17.
92. Paisley, M.J., Sitar, Z., Posthill, J.B. and Davis, R.F. (1989), J. Vac. Sc. and Technology **7**, 701-705.
93. Mizuta, M., Fujieda, S., Matsumoto, Y. and Kawamura, T. (1986), Jap. Jour. Appl. Phys. **25**, L945-L948.
94. Shuskas, A.J., Quinn, D.J., Paradis, E.L., Berak, J.M., Cullen, D.E., Reeder, T.M. 1974, 5th Semi-Annu. Rep., (Contract N00014-72-C-0145, NTIS #AD/A-003005).
95. Lakshmi, E., Mathur, B., Bhattacharya, A.B. and Bhargara, V.P. (1980), Thin Solid Films **74**, 77-85.
96. Lakshmi, E. (1981), Thin Solid Films **83**, L137-L142.
97. Hariu, T., Usuba, T., Adchi, H. and Shibata, Y. (1978), Appl. Phys. Lett. **32**, 252-255.
98. Matsushita, K., Matsuro, Y., Hariu, T. and Shibata, Y. (1981) Thin Solid Films **80**, 243-250.
99. Karpinski, J., Jun., J. and Porowski, S. (1984), J. Cryst. Growth **66**, 1.
100. Elwell, D., Feigelson, R.S., Simkins, M.M. and Tiller, W.A. (1984), J. Cryst. Growth **66**, 45-55.
101. Pankove, J.I. and Hutchby, J.A. (1976), J. Appl. Phys. **47**, 5387-5394.
102. Baranov, B., Daweritz, L., Gutan, V.B., Jungk, G., Neumann, H. and Raidt, H. (1978) Phys. Status Solidi A **49**, 629-638.
103. Hagar, J., Metcalfe, R.D., Wickenden, D. and Clark, W. (1978), J. Phys. C **11**, L143-L148.
104. Yoshida, S., Misawa, S. and Gonda, S. (1982), J. Appl. Phys. **53**, 6844-6848.
105. Khan, M.A., Skogman, R.A., Schulze, R.G. and Gershenzon, M. (1983), Appl. Phys. Lett. **43**, 492-494.
106. Sayyah, K., Chung, B. and Gershenzon (1986), Journ. Crystal. Growth **77**, 424-429.
107. Koide, Y., Itoh, H., Khan, M.R.H., Hiramatu, K., Sawaki, N., Akasaki, I. (1987), J. Appl. Phys. **61**, 4540-4543.
108. Sitar, Z. Paisley, M.J., Yan, B., Ruan, J. and Choyke, J.W. and Davis, R.F. (1989), to be published in Jour. Vac. Sci. Tech.
109. MacChesney, J.B., Bridenbaugh, P.M. and O'Connor, P.B. (1970), Mat. Res. Bull. **5**, 783-792.
110. Hovel, H.J. and Cuomo, J.J. (1972), App. Phys. Lett. **20**, 71-73.
111. Natarajan, B.R., Eltoukhy, A.H., Greene, J.E. and Barr, T.L. (1979), Thin Solid Films **68**, 201-235.
112. Tansley, T.L. and Foley, C.P. (1986), J. Appl. Phys. **59**, 3241-3244.
113. Sullivan, B.T., Parsons, R.R., Westra, K.L. and Brett, M.J. (1988), J. Appl. Phys. **64**, 4144-4149.
114. Trainor, J.W. and Rose, K. (1974), Jour. Electronic Materials **3**, 821-828.
115. Marasina, L.A., Pichugin, I.G. and Tlaczala, M. (1977), Krist Tech. **12**, 541-545.
116. Masaki, S., Sudou, K., Kobayashi, H. and Morisaki, H. (1989), in T. Takagi (ed.), Proc., Twelfth Symp. Ion Sources and Ion-Assisted Tech., Published as a collection of papers by the Research Group on Ion Engineering, Kyoto University, Kyoto, pp. 391-394.

SHORT RANGE ORDER IN "AMORPHOUS" THIN FILMS OF TITANIUM DIBORIDE

WENDELL S. WILLIAMS
Case Western Reserve University
Cleveland,
Ohio 44106,
U.S.A.

ABSTRACT. Thin films of titanium diboride have been prepared by thermal vapourisation of crystalline specimens onto an unheated substrate. X-ray diffraction and electron diffraction studies confirmed that the films were "almost amorphous". EXAFS and EXELFS studies revealed that the films exhibited short range order, probably of the kind found in crystalline specimens, but lacked long-range periodicity.

1. INTRODUCTION

Titanium diboride in its crystalline form is a hard, high-melting refractory compound with metallic conductivity. It is of current interest in the microelectronics industry as a metallizing film.

The scientific questions motivating the present study were: (1) Can titanium diboride be prepared as an amorphous thin film? (2) If so, how are the atoms arranged? And (3) what are the properties of such a material?

It was found that thin films of TiB_2 amorphous to X-ray and electron diffraction could be produced by thermal vaporization from crystalline specimens onto an unheated substrate [1,2] or by chemical vapour deposition at moderate temperatures from an organometallic precursor [3]. Similar procedures were used by this group to make amorphous films of titanium carbide as well [4].

In the following sections, the former method of preparing the films will be described, analytical procedures for answering the first two questions will be outlined, and the results summarized. A brief comment on the third question will also be offered.

2. EXPERIMENTAL METHOD FOR PRODUCING THIN FILMS

A major problem in preparing stoichiometric films by the vaporization of compounds is unequal rates of vaporization of the different atomic species in the solid, leading in general to a condensate which is

R. Freer (ed.), The Physics and Chemistry of Carbides; Nitrides and Borides, 671–676.
© 1990 *Kluwer Academic Publishers. Printed in the Netherlands.*

different in composition from the source. However, in the case of titanium diboride this problem does not exist, as the compound is a constant boiling (or congruently vaporizing) material, thus ensuring that the film will be of the same composition as the starting material [5].

The starting material in this case consisted of fragments of single crystals of high purity, grown by the arc-Verneuil method. The fragments were placed in a water-cooled copper chamber and heated by an electron beam in a vacuum of 10^{-8} Torr to volatilize the material. Glass microscope slides served as substrates.

3. CHARACTERIZATION OF FILMS

The films produced were silver in colour, adherent to the substrates and approximately 1000 Å thick. They showed no X-ray diffraction peaks and only weak and diffuse electron diffraction rings [1,2]. Surface spectroscopies confirmed the chemical composition.

4. METHODS OF EXAFS AND EXELFS

To examine the films for evidence of short range order, the complementary methods of extended X-ray absorption fine structure (EXAFS) and extended electron energy loss fine structure (EXELFS) were used. Both methods exploit the fact that inner shell ionization yields an electron which is scattered by neighbouring atoms. Interference between the outgoing electron wave and the scattered electron wave produces modulation (fine structure) of the X-ray absorption coefficient or electron current on the high energy side of the absorption edge. After several stages of data filtering, background removal, Fourier transforming to k-space and back, the final result is a radial distribution function with peaks indicating the presence of shells of atoms at a given distance from the central atom. An advantage of the method is that a specific kind of atom can be selected for the central atom by choosing the energy range of the incident photons or electrons to match that atom's characteristic absorption edge.

5. APPLICATION TO TITANIUM DIBORIDE FILMS

In the present work, a rotating anode X-ray generator was used for the EXAFS study, with titanium as the central atom, and a transmission electron microscope with energy spectrometer for the transmitted electrons was used for the EXELFS study with boron as the central atom. Two different experiments were required because the X-ray intensity at long wavelengths is insufficient for detecting the boron fine-structure, but the energy loss method is particularly sensitive to light elements. With these two methods it was possible to generate the information needed without going to a synchrotron source.

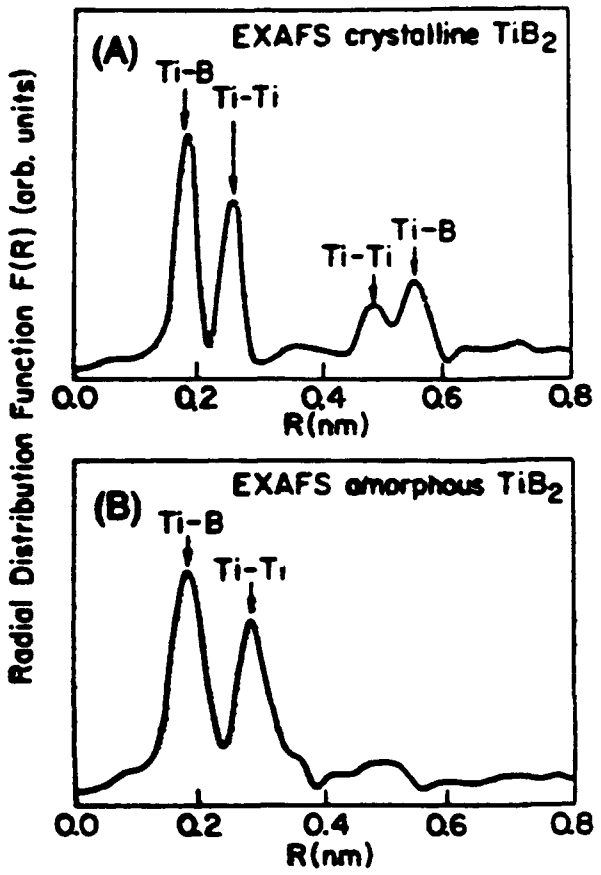

Figure 1. Comparison of radial distribution functions about Ti from EXAFS data on crystalline and amorphous films of titanium diboride at -195°C. Short-range order is apparent in the "amorphous" film, but only to the second shell of neighbours. (From Kaloyeros, et al, Ref. 2).

The radial distribution functions produced by both methods (Figure 1 and Figure 2) were mutually consistent in showing a major peak indicating short range order: a shell of Ti atoms around a B central atom, and a shell of B atoms around a Ti central atom. By contrast, crystalline titanium diboride produced several peaks, indicative of long-range order. A model of atomic positions

consistent with the radial distribution functions for the amorphous films was proposed: small clusters of atoms - which might be considered to be building blocks of the crystal - also exist in the amorphous film, but are rotated from each other to preclude long range order (Figure 3). More details can be found in publications [2,6] and theses [1,7] from these studies.

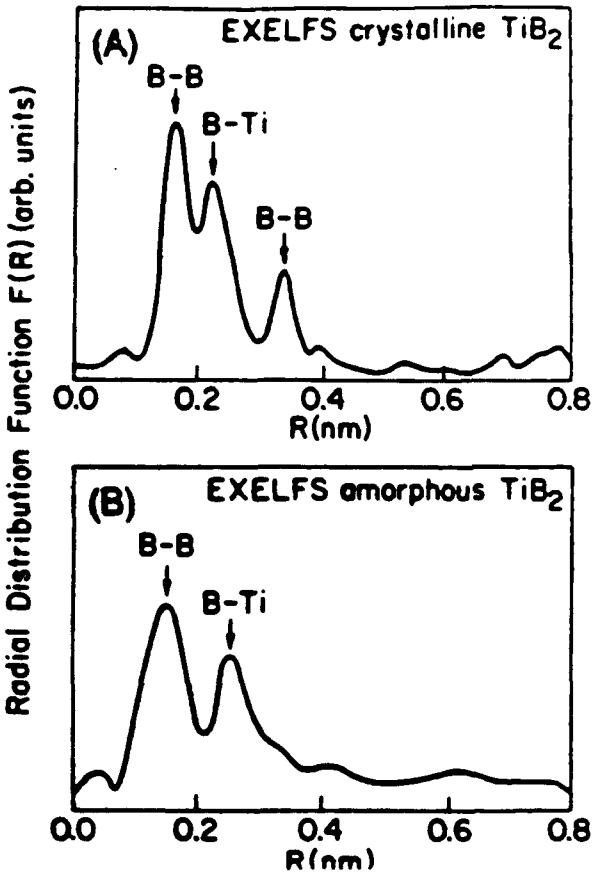

Figure 2. Comparison of radial distribution functions about B from EXELFS data on crystalline and amorphous films of titanium diboride at -195°C. Short range order is apparent in the "amorphous" film, but only to the second shell of neighbours. These results are complementary to and consistent with those of Fig. 1. (From Kaloyeros, et al, Ref. 2).

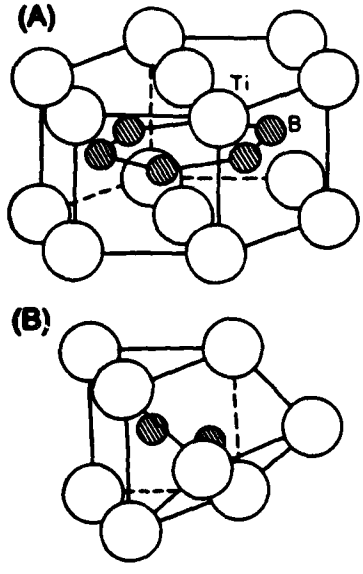

Figure 3. Proposed atomic model for short-range order in amorphous films of titanium diboride. (A) structure of crystalline titanium diboride; (B) two prismatic structural units from (A) rotated and repositioned to give only short-range order. (From Kaloyeros, et al, Ref. 2).

6. PROPERTIES OF AMORPHOUS FILMS

Preliminary scratch tests on the titanium diboride amorphous films indicated that they were softer than the bulk, crystalline material, which is noted for its hardness, though these results need to be confirmed by nanoindenter measurements.

Corrosion tests of similar films of titanium carbide prepared in this study showed an improvement relative to crystalline films, as would be expected for a material without grain boundaries. Corresponding tests of the titanium diboride films have yet to be performed.

7. SUMMARY AND CONCLUSIONS

The first two questions which motivated this study have been answered: (1) yes, amorphous films of titanium diboride can be prepared; (2) they exhibit short range order, probably of the kind found in the crystalline form but lacking long-range periodicity.

Acknowledgments

The work reported here was supervised by the author while on the faculty of the Physics Department of the University of Illinois at Urbana-Champaign and was carried out by Alain Kaloyeros and Mark Hoffman. The experimental facilities used are part of the Centre for the Analysis of Materials of the University of Illinois Materials Research Laboratory, supported by the US Department of Energy under Contract DE-AC0276ERO-1198. Dr. Kaloyeros was supported by NSF Grant MSM 8617318, as was the author, and Dr. Hoffman was supported by the DOE/MRL grant listed.

REFERENCES

1. M. Hoffman (1986) Ph.D. Thesis, Physics Department, University of Illinois at Urbana-Champaign, USA.
2. A.E. Kaloyeros, W.S. Williams, R.B. Rizk, F.C. Brown and A.E. Greene (1988) J. Amer. Ceramic Soc. 71, 948-955.
3. G. Girolami, J. Jensen, D.M. Pollina and J.E. Gozum (1988) Materials Research Society Program for 1988 Spring Meeting, Reno, Nevada, p. 133.
4. A.E. Kaloyeros, M.P. Hoffman and W.S. Williams (1986) Thin Solid Films, 141, 237-250.
5. A.W. Searcy, W.S. Williams and P.O. Schissel (1960) J. Chem. Phys. 32, 957-959.
6. A.E. Kaloyeros, W.S. Williams, F.C. Brown, A.E. Greene and J.B. Woodhouse (1988) Phys. Rev. B37, 771-784.
7. A.E. Kaloyeros (1986) Ph.D. Thesis, Physics Department, University of Illinois at Urbana-Champaign, USA.
8. C.M. Allocca, W.S. Williams and A.E. Kaloyeros (1987) J. Electrochem. Soc.: Solid State Sci. Technol. 134, 3170-3175.

ON THE ELECTRONIC TRANSPORT PROPERTIES OF BORON CARBIDE

HELMUT WERHEIT
Universität -Gesamthochschule- Duisburg
Solid State Physics Laboratory
Lotharstr. 1 - 21
D 4100 Duisburg 1
FRG

ABSTRACT: The problem of the electronic transport properties of boron carbide is generalized to the icosahedral boron-rich solids. It is shown that their semiconductor property, which is unique because of the odd electron number of the boron atoms, as well as other common structural and electronic properties can be attributed to the Jahn-Teller effect distorting the icosahedron, reducing its symmetry from I_h to D_{3d} thus explaining the preferred crystal symmetry R3m and leading to a separation of occupied and unoccupied electronic states. The electronic transport properties of boron carbide including several hitherto surprising results are qualitatively interpreted within this band structure model.

1. INTRODUCTION

The correct understanding of the electronic transport mechanism of boron carbide is important, because this semiconductor has very promising electronic properties e.g. for the direct thermoelectric energy conversion. But it must not be overlooked that boron carbide is only one representative of the boron-rich solids with icosahedral structure ranging from α-rhombohedral boron with 12 B atoms to YB_{66} and homologous borides with 1632 B atoms per unit cell.

In spite of this large variation in structure, essential characteristic properties of most of these materials are at least qualitatively related to one another (cp. e.g. [1,2,3,4]), and should be understood and interpreted in relation to the common structure properties.

Essentially the following properties are more or less common for the boron modifications and compounds with icosahedral structure:

A. Common Structure Properties:

(1) Besides the icosahedron being the fundamental structure element it is striking that crystal structures of the space group $R\bar{3}m$ are obviously preferred. This is not only found in all the representatives

R. Freer (ed.), The Physics and Chemistry of Carbides, Nitrides and Borides, 677–690.
© 1990 Kluwer Academic Publishers. Printed in the Netherlands.

of the α- and the ß-rhombohedral structure groups, but moreover in the majority of ion crystals based on the $[B_{12}H_{12}]^{--}$ ion, too, whose B_{12} icosahedral arrangement is assumed not to be disturbed by the small H atoms, covalently bonded to the B atoms [5].

(2) In all the reliable structure investigations, it was reported for all cases cited in section (1) and moreover for many other structures based on B_{12} icosahedra, too, that the icosahedron is distorted. In case of the ionic crystals, this distortion has been ascribed to a steric interaction with the cations [5], and in case of the covalently bonded crystals to the influence of the crystal field, but hitherto, this distortion has been assumed to be weak and negligible with respect to its influence on other properties as e.g. the electronic band structure and the electronic transport properties. Particularly, little attention has been paid to the fact that this distortion is almost the same in all these cases.

(3) Except for the ionic crystals, the IR active vibrations of solids with B_{12} structure elements are rather weak indicating a low ionic contribution to the bonding. Moreover the Raman effect is very weak, which results from a weak polarizability of the structural components.

B. Common Electronic Properties:

(1) Generally, atoms with odd numbers of electrons form metals in the crystalline state, because a highest energy band remains only partly filled with electrons. The only exception to this rule is boron, at least as far as it forms structures containing B_{12} icosahedra as the essential structure elements. The elementary modifications concerned, and moreover the compounds related in structure, too, are semiconductors or insulators.

(2) In spite of the large variety of structures, in most cases the band gaps vary only between about 1.3 and 2.4 eV.

(3) As far as the absorption edges of the semiconducting icosahedral boron structures have been investigated, in many cases a band of high density of states is found at about 0.2 eV above the valence band edge in the band gap.

(4) Generally the icosahedral boron modifications and compounds exhibit p-type conductivity up to high temperatures. As shown in ß-rhombohedral boron, an overcompensation demands electron densities of the order of 10^{20} cm^{-3} introduced by foreign atoms [6,7] to change the conductivity to n-type.

(5) The electronic transport is essentially determined by hopping processes often connected with an activation energy of about 0.2 eV.

To explain at least some of these structure overlapping properties, Golikova developed her "amorphous concept" [8]. She attributed to the

icosahedral structures a continuous variation from crystalline to amorphous semiconductor behaviour depending on the complexity of the structure to be determined in terms of the number of atoms per unit cell. But according to the careful investigation of the transport properties, especially of boron carbide (cp. e.g. [2]), ß-rhombohedral boron [9, 10] and YB_{66} [11], this model can be assumed to have been disproved.

Emin developed the bipolaron hopping model to explain the transport properties of boron carbide (see e.g. [12]). In spite of describing e.g. electrical conductivity and thermolelectric power of boron carbide at a wide range of higher temperatures successfully, this theory unfortunately does not take into account some essential properties of this material, as e.g. the low ionicity within the structure, the low polarizability, the band gap and the plasma edge. Therefore it seems doubtful, whether this model can be applied to other icosahedral structures and particularly to give a satisfactory explanation for the structure overlapping properties.

2. JAHN-TELLER EFFECT

When one searches for the fundamental reason for the common properties of the icosahedral boron-rich solids, it seems necessary to take into account the icosahedron as the general structure unit. It is especially noticable that the distortion of the icosahedron has not been considered with respect to its influence on the electronic properties.

Based on [13, 14] it will subsequently be shown that the icosahedron is distorted in consequence of the Jahn-Teller effect and that it is not admissible to neglect this irregularity, which yields the basis of a largely satisfactory explanation of the problems noted in the introduction.

The Jahn-Teller effect is a fundamental principle and acts in all cases, where in atomic arrangements of high symmetry the orbit-degenerated electronic states couple with asymmetrical vibrations. The only exceptions are twofold Kramer-degenerated states in arbitrary groupings and twofold orbit-degenerated states in linear arrangements of atoms. Both exceptions are not applicable in the case of the B_{12} icosahedron. The physical reason for this coupling, which leads to a distortion of the initially high-symmetrical arrangement and in consequence to a reduction of its symmetry, is the reduction of the total energy in the new equilibrium state in comparison with the initial one.

By group theoretical methods it was shown [9] that by this distortion the icosahedral point group I_h is reduced to the subgroup D_{3d}. But the group D_{3d} corresponds to the space group $R\bar{3}m$. Of course it must be expected that the Jahn-Teller distorted icosahedra crystallize preferably in such structures, where their symmetry remains unchanged, and therefore the formation energy of the crystal is minimized. Thus the Jahn-Teller effect of the icosahedron shows, why $R\bar{3}m$ is the preferred

symmetry of icosahedral boron crystal structures, or otherwise the preference of the space group $R\bar{3}m$ in the crystals can be taken as a confirmation that the Jahn-Teller effect is really the reason for the distortion of the B_{12} icosahedron.

3. JAHN-TELLER INDUCED MODIFICATIONS OF THE ELECTRONIC STRUCTURES

The influence of the Jahn-Teller effect on the electronic structures of the crystals will be especially effective, when the molecular orbitals of the intra-icosahedral bonding, which are expected to split in consequence of the Jahn-Teller distortion, form the uppermost part of the valence band, and this depends on the relative strengths of the different icosahedral bonds.

When we restrict ourselves to the α-rhombohedral and the ß-rhombohedral structure groups, two types of inter-icosahedral bonds are to be compared. In α-rhombohedral boron the polar atoms of the icosahedra are connected by covalent bonds, while the external bonds of the equatorial atoms are saturated by relatively weak three-center bonds. In the case of the other members of the α-rhombohedral structure group and of the members of the ß-rhombohedral structure group all the inter-icosahedral bonds are essentially covalent.

The clearest situation, which will be discussed in detail subsequently, is given in the case of exclusively covalent inter-icosahedral bonding. As can be obtained e.g. from the atomic distances, these bonds are distinctly stronger and therefore lowered in energy compared with the intra-icosahedral multiple-center bonds, which consequently form essentially the uppermost valence band region. Hence the influence of the Jahn-Teller effect on the internal bonds is important in this case.

In α-rhombohedral boron the inter-icosahedral three-center bonds of the equatorial atoms are the weakest ones, which therefore are responsible for the valence band edge. Here the influence of the Jahn-Teller effect on these external bonds becomes effective.

The new calculations of Bullet [15] confirm this previously qualitative estimation [9] of the relative contributions of the different bonds to the valence band edge. They show that the upper valence band edges of boron carbide and ß-rhombohedral boron are very similar but differ distinctly from that one of α-rhombohedral boron with respect to the density of states distribution.

It is known from previous calculations [16, 17] that in bonding the outer levels of the electronic ground state of the boron atom $1s^2\ 2s^2\ 2p^1$ are hybridized to $2s\ 2p_x\ 2p_y\ 2p_z$ with 3 electrons available. Hence for the regular B_{12} icosahedron result

48 orbitals	36 electrons

These are to be divided into

25 bonding orbitals	36 electrons
23 antibonding orbitals	0 electrons

for covalent inter-icosahedral bonds

12 orbitals	12 electrons

are to be considered and hence for the intra-icosahedral bonds remain

13 orbitals	24 electrons.

This electron deficient structure leads to the intra-icosahedral multiple-center bonds of the icosahedron, which, according to Howard et al. [18], is stable in this form in spite of lacking two electrons. Indeed, the low ionicity of the crystal structures, which can immediately be seen from the comparatively low oscillator strengths of the lattice vibrations [19, 20], indicates that these sites remain essentially unoccupied in the icosahedral crystal structures.

The qualitative influence of the Jahn-Teller effect on the electronic levels of the intra-icosahedral bonding orbitals was derived by group theoretical methods [13,14]. The comparison of the character tables of I_h and D_{3d} yields immediately that all the 3-, 4- and 5-fold degenerated irreducible representations of the icosahedral group split, because they are not comprised in the D_{3d} group. This holds also in the case of the highest partially occupied orbital of intra-icosahedral bonding in the regular icosahedron [17]. Thus its uppermost 4-fold degenerated G_u orbital, only partly occupied by six electrons, splits in consequence of the Jahn-Teller induced distortion of the icosahedron as qualitatively indicated in Fig. 1 leading to a separation of occupied and unoccupied levels. Hence the bond situation in the distorted B_{12} icosahedron is qualitatively different from that one considered e.g. by Weber and Thorpe [21], indicating a metal-like bonding condition in the regular icosahedron, because of its partly occupied 4-fold degenerated G_u orbital.

As discussed above, this situation can be transferred to the crystalline state, where, of course, in consequence of the long-range order the orbitals form energy bands. The situation for e.g. boron carbide and ß-rhombohedral boron, which are the hitherto best investigated boron-rich solids, is expected to be qualitatively the same, because in both cases the inter-icosahedral bonds are covalent. Of course they must be quantitatively different because of the different influence of the remaining structure elements.

Additionally the electron-electron interaction neglected in the above discussion must be considered. When the negative magnetoresistance of ß-rhombohedral boron is taken into acccount, a Hubbard splitting of the

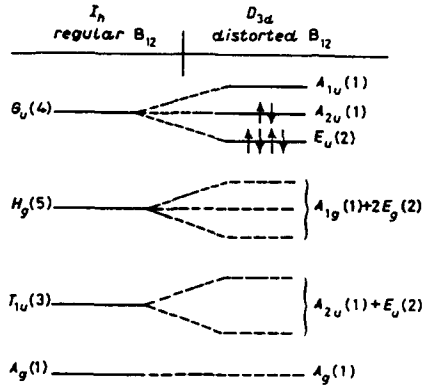

Figure 1. Qualitative Jahn-Teller induced splitting of the inter-icosahedral bonding orbitals of the B_{12} icosahedron [13]. Left: relative energetical position of the levels in the regular icosahedron (I_h symmetry) (obtained from [17]); right: indication of splitting of the levels in the distorted icosahedron (D_{3d} symmetry), degeneracy in brackets (the group theoretical results do not yield the absolute energetical positions). Inter-icosahedral bonds are omitted (see text).

uppermost level is expected in agreement with a previous discussion on the metal-insulator transition in boron carbide [22]. Hence the upper valence band structure shown in fig. 2 is qualitatively expected. Besides

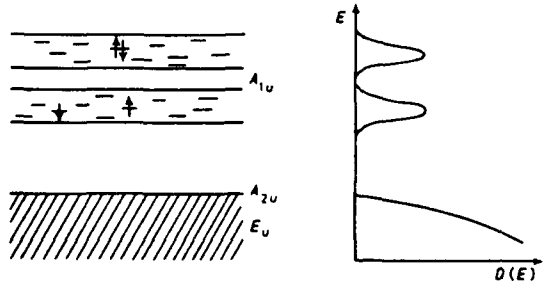

Figure 2. Expected qualitative contribution of the B_{12} icosahedra to the upper valence band structure range of icosahedral boron-rich solids with exclusively covalent external bondings of the icosahedra (e.g. boron carbide and ß-rhombohedral boron). Hubbard splitting of the split-off level is assumed according to the negative magnetoresistance in ß-rhombohedral boron.

the Hubbard splitting this band scheme is in close agreement with that one derived previously from experimental results for ß-rhombohedral boron [23].

The characteristic property is the split-off band at about 0.2 eV above the valence band edge. Its evidence is not only derived from the careful investigations of the absorption edge of ß-rhombohedral boron (see e.g. [1, 23, 24]), but additionally indicated in the case of boron carbide [22,24] and a number of other icosahedral boron-rich compounds (e.g. [25,26]).

This enables a qualitative explanation of the general electronic properties of icosahedral boron-rich solids listed in the introduction. Since, in consequence of the Jahn-Teller effect acting on the B_{12} icosahedra, occupied and unoccupied electronic states are separated, and therefore these materials are semiconductors or insulators in spite of the odd number of electron of the B atom. According to the experimental results this obviously holds not only in case of the boron modifications but moreover in case of the related borides, which leads to the conclusion that the additional structure elements cause only quantitative but no qualitative modifications. The reason is the high density of states of the split-off level at about 0.2 eV above the valence band edge; this level may be partly occupied by electrons originating from other structural units or foreign atoms. Nevertheless because of its high density (order of magnitude 10^{20} cm^{-3}) it acts like an intrinsic acceptor level determining p-type conductivity up to high temperatures. To change the conductivity character to n-type by overcompensating this intrinsic acceptor level, corresponding electron numbers are necessary [6,7]. Nevertheless the density of this split-off level is not sufficient for the formation of extended states, but leads to localization and hence to hopping conductivity.

4. CONSEQUENCES FOR THE ELECTRONIC TRANSPORT IN BORON CARBIDE

From optical investigations in the spectral range of the absorption edge and its low-energy tail, it can be concluded that the transition energies of ß-rhombohedral boron and boron carbide are very similar [24], in agreement with the discussion in the previous section. This means that boron carbide should be expected to behave essentially like a very strongly C doped ß-rhombohedral boron. Hence data obtained from this material can referred to for interpretation.

Contrary to the assumption in [22] it is now understood that the split-off band is not caused by the C atoms in the rhombohedral structure but at least largely by this structure itself. Otherwise the arguments discussed there remain essentially the same. This level seems to be superimposed by states introduced by the C atoms probably correlated with the optical absorption in the edge tail [24].

The Fermi edge is expected to be positioned within this level, which according to the sign of the Seebeck coefficient must be occupied more than half. At lower temperatures it is expected that hopping within this level is the prevailing conductivity process. The number of electrons within this level will increase by thermal activation from the valence band thus raising the density of occupied states and reducing the unoccupied destination sites of the hopping processes. These effects have to be taken into account in discussing the conductivity in the hopping range.

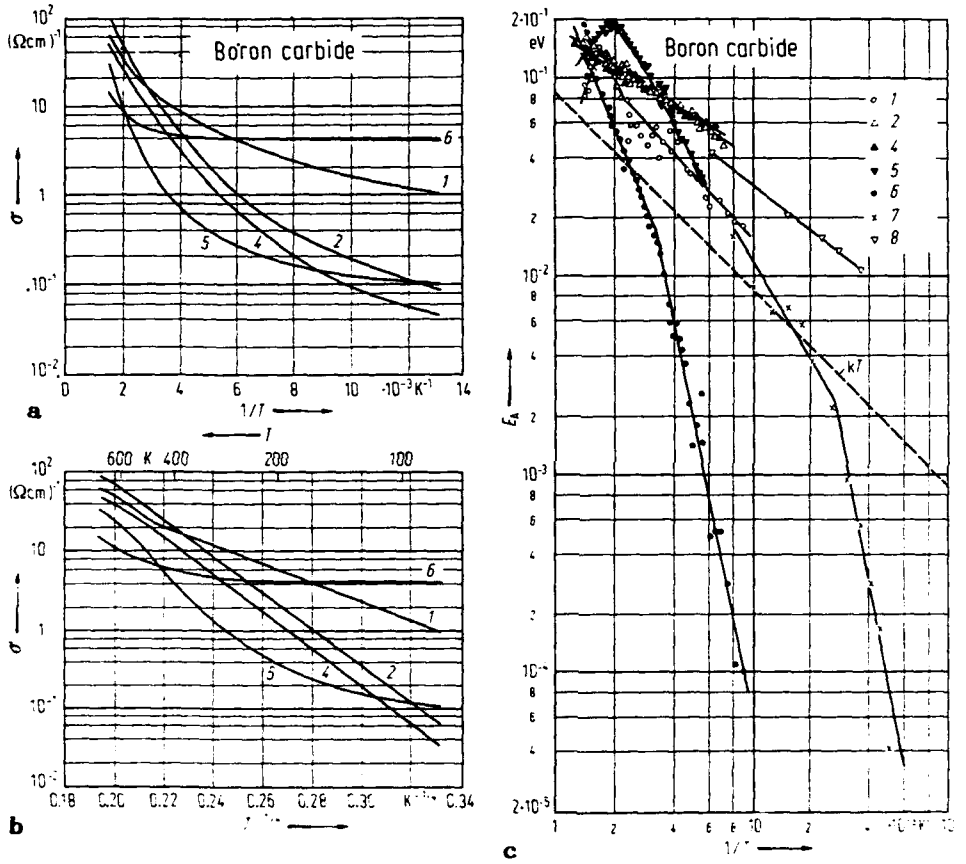

Figure 3. Electrical conductivity of coarse crystalline boron carbide (composition between $B_{12}C_3$ and B_4C) plotted vs. 1/T (**a**), and $T^{-1/4}$ (**b**). Activation energy E_A vs. 1/T (**c**) [22,2].

Simultaneously with increasing temperature an increasing stationary density of free holes in the valence band must be taken into account, whose mobility is distinctly higher than that of the hopping carriers in the split-off band. Both conductivity processes will be competitive, but depending on the type of experiment, one of them may be prevailing.

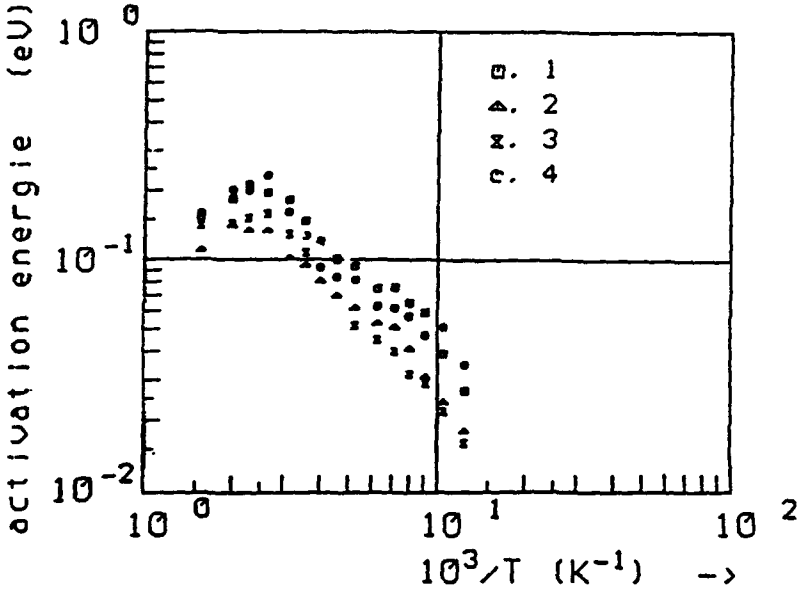

Figure 4. Activation energy of the electrical conductivity of boron carbide single crystals (composition approximately B_4C) [27].

From fig. 2 it can be inferred that electron pairs with antiparallel spins, denominated as "bipolarons" by Emin (see [12]), are sited in the upper Hubbard band and thus for energetical reasons are less probable in comparison with single electrons hopping in the lower Hubbard band.

5. DISCUSSION OF SOME EXPERIMENTAL RESULTS

Besides the general aspects of electronic transport in icosahedral boron-rich solids discussed in the previous section, it will be shown that a number of experimental results of transport properties of boron carbide, which have been ignored and can hardly be interpreted in the bipolaron transport model [12], can easily be explained, at least qualitatively, within the band scheme model presented above.

Regardless of the conductivity mechanism, from the temperature dependence of the electrical conductivity (fig. 3 a, b) the temperature dependence of the activation energy was formally derived (fig. 3 c) [22]. At higher temperatures, above about 500 K, the activation energy approaches a value between about 0.1 and 0.2 eV. This was confirmed later on by measurements on boron carbide single crystals (fig. 4) [27]. According to the above discussion this can be interpreted by the valence band conduction exceeding the hopping conduction in a temperature range, where the Fermi level is pinned in the split-off level.

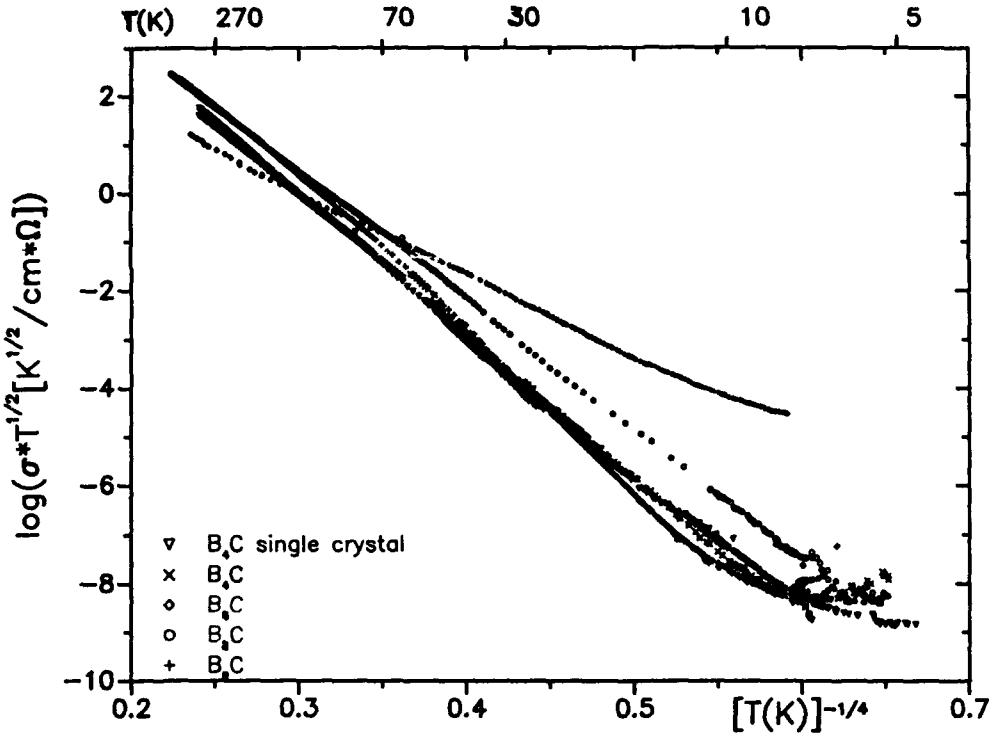

Figure 5. Low temperature electrical conductivity of hot pressed boron carbide of different compositions in comparison with a B_4C single crystal [28] plotted according to Mott's law.

At lower temperatures the conductivity obeys, more or less satisfactorily, Mott's law, indicating hopping to be the prevailing transport mechanism (fig. 5) [28]. But if one tries to evaluate quantitatively the hopping distances and the density of hopping centers according to the usual theories of hopping conductivity, one fails; the results are not reasonable. This may be caused by neglecting the temperature-dependent variation of the occupation density in the split-off level and the superimposed free hole conductivity in the valence band.

Hall effect and magnetoresistance at low temperatures behave as they are expected for the case of Bloch-type band conduction (fig. 6) [29]. The estimated activation energy of the carrier density corresponds to the split-off distance of the Jahn-Teller induced level in the band gap.

Free carriers with sufficiently high mobility and density as well as sufficiently low scattering frequency can be observed in the electromagnetic spectrum. Hence in this type of measurement the free holes in the valence band of boron carbide can obviously be observed separated from

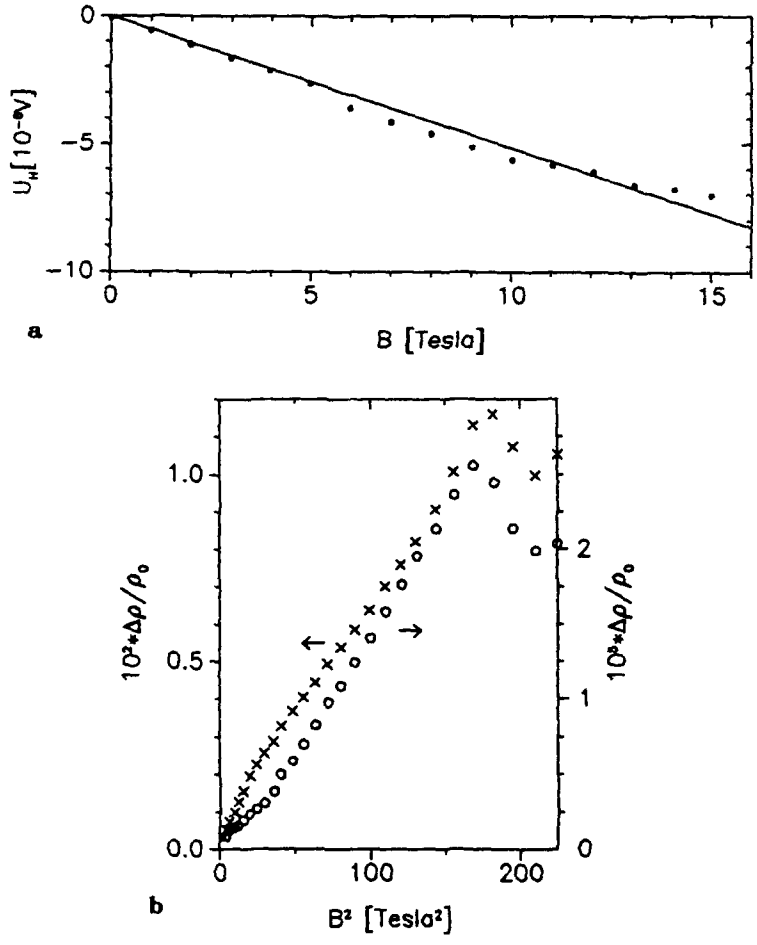

Figure 6. Hall voltage of a B_4C single crystal at 77 K (**a**) and magnetoresistance at 77 and 300 K in high magnetic fields (**b**) [29].

the hopping carriers in the split-off band. In the case of boron carbide it is known [2,19,20] that a strongly damped plasma edge influences the optical properties in the FIR region. Fig. 7 [30] shows the qualitative temperature dependence of this plasma edge in the FIR reflectivity spectrum of a boron carbide sample. As expected according to the previous discussion the estimated thermal activation energy of the carrier density corresponds to the energetical distance of the intrinsic acceptor-type level from the valence band.

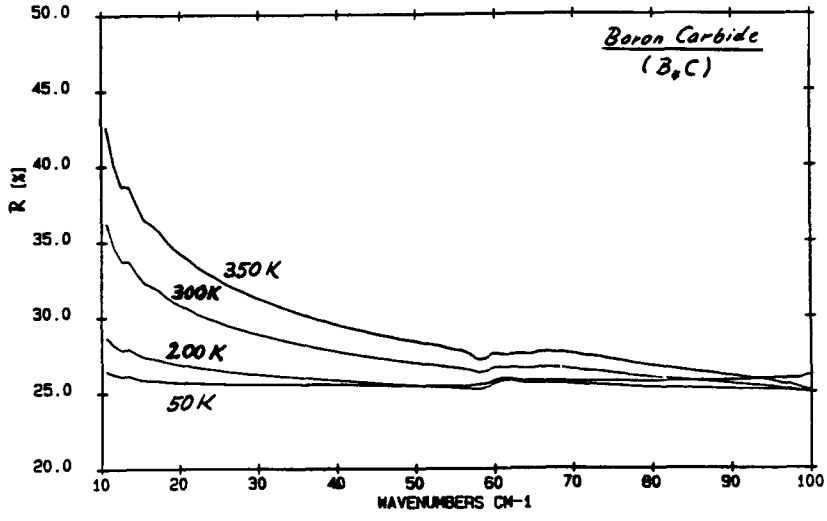

Figure 7. Temperature dependence of the plasma edge of B_4C. Optical reflectivity versus wave number [30].

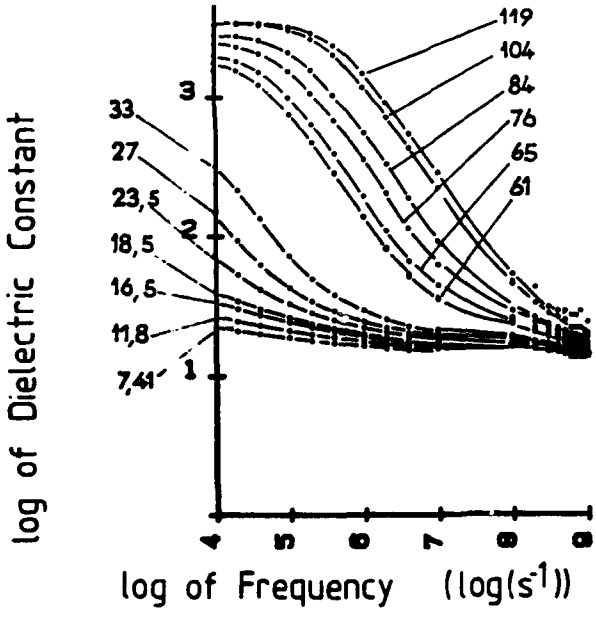

Figure 8. Real part of the dielectric function of boron carbide versus frequency (curve parameters: T [K]) [31].

The change of the reflectivity is essentially related to the change of the real part of the dielectric function. This was measured on boron carbide by Kormann and Zuppiroli (fig. 8) [31]. It is obvious that the spectral

and temperature dependence corresponds to the plasma vibrations seen in the FIR range and therefore a corresponding interpretation of the dielectric function of boron carbide seems to be much more appropriate than the Maxwell-Wagner effect assumed by the authors.

This discussion indicates that indeed the modification of the band structure induced by the Jahn-Teller effect acting on the B_{12} icosahedron and leading to an intrinsic acceptor-type level at about 0.2 eV above the valence band edge in the band gap yields the prerequisite to interprete the uncommon experimental results obtained on boron carbide at least qualitatively in a very satisfactory way.

Acknowledgements

With respect to the Jahn-Teller effect the scientific contribution of R. Franz, referring to the other new results reported in this paper the contributions of my other coworkers, especially U. Kuhlmann, H. Haupt, W. Winkelbauer and G. Gerlach, are gratefully acknowledged. - These investigations were supported by the Minister of Research and Technology of the FRG under contract number 317-4003-0328845A within a cooperation with Hermann C. Starck, Goslar and Laufenburg, FRG.

References

1. Werheit H. (1983). Boron, in Landoldt-Börnstein, New Series Vol. III/17e, Edts. O. Madelung, M. Schulz, and H. Weiss; Springer, Berlin, p. 9.
2. Werheit H. (1984). Boron Compounds, in: see [1] Vol. 17g, p. 9.
3. Golikova O.A. (1979). Phys. stat. sol. (a) 51, 11.
4. Werheit H., 1988. Prog. Crystal Growth and Charact. Vol. 16, 179.
5. Gmelin Handbook of Inorganic Chemistry, Vol. 54, Boron Compounds Part 20, Springer Berlin, Heidelberg, New York, p. 224.
6. Werheit H., de Groot K., Malkemper W., Lundström T. (1981). J. less-common Met. 82, 163.
7. Slack G.A., Rosolowski J.B., Hejna C., Garbauskas M., and Kasper J.S. (1987). Semiconducting Properties of Boron in Proc. 9th Intern. Symp. Boron, Borides and Related Compounds, Duisburg, FRG, Ed. H. Werheit, p. 132.
8. O.A. Golikova (1979). Phys. stat. sol. (a) 51, 11.
9. Franz R., Werheit H. (1987). See [7], p. 364.
10. Werheit H., Siejak V., Franz R. (1987). See [7] p. 366.
11. Werheit H., Kuhlmann U., Tanaka T. (1989). To be published.
12. Emin D. (1989). Theory of Electronic and Thermal Transport in Boron Carbides; this volume.
13. Franz R., Werheit H. (1989). Europhys. Lett. 9, 145.
14. Franz R., (1989). Thesis, University of Duisburg.
15. Bullet D. (1989). Electonic Structure and Charge Densities of Borides, this volume.

16. Longuet-Higgins H.C., de V. Roberts M. (1955). Proc. R. Soc. London, Ser. A, 230, 110.
17. Bambakidis G., Wagner R. (1981). J. Phys. Chem. Solids, 42, 1023.
18. Howard I.A., Beckel C.L., Emin D. (1985). In: Boron-Rich Solids, AIP Conference Proceedings 140, Edited by D. Emin, T. Aselage, C.L.Beckel, I.A. Howard, C. Wood; Albuquerque, p. 240.
19. Binnenbruck H., Werheit H. (1979). Z. Naturforsch. 34a, 787.
20. Werheit H. (1988). Prog. Crystal Growth and Charact. Vol. 16. Ed. V.N. Gurin, Pergamon Press, p. 179.
21. Weber W., Thorpe M.F. (1975). J. Phys. Chem. Solids 36, 967.
22. Werheit H., de Groot K. (1980). Phys. stat. sol. 97, 229. Werheit H., de Groot K., Malkemper W. (1981). J. less-common Met. 82, 153.
23. Werheit H. (1970). Die Halbleitereigenschaften des Bors in Festkörperprobleme X/Advances in Solid-State Physics, Pergamon-Vieweg, Braunschweig, p. 189.
24. Werheit H. (1989). Optical properties of icosahedral boron-rich solids; this volume.
25. Haupt H., Werheit H., Siejak V., Kannengießer U., Higashi I. (1987). See [7] p. 385.
26. Bullett D. (1989). Bandstructure calculations of Li-Boride, this volume.
27. Werheit H., Rospendowski S. (1985), see [18] p. 234.
28. Werheit H., Winkelbauer W., Kuhlmann U. (1989). To be published.
29. Werheit H. Franz R., Schneider D., Wolf M., Brann G. (1987). See [7], p. 381.
30. Werheit H., Gerlach G., Haupt H. (1989). To be published.
31. Kormann R., Zuppiroli L. (1985). See [18] p. 216.

THEORY OF ELECTRONIC AND THERMAL TRANSPORT IN BORON CARBIDES

DAVID EMIN
Sandia National Laboratories
Albuquerque, New Mexico 87185, USA

ABSTRACT. The boron carbides are refractory icosahedral boron-rich solids composed of twelve-atom boron rich icosahedral clusters directly linked by covalent bonds and indirectly linked through multiatom chains. The intericosahedral bonding is stronger and stiffer than that within icosahedra. The boron carbides exist as a single phase between about 9 atomic % and somewhat less that 20 atomic % carbon as boron and carbon substitute for one another within an essentially regular lattice structure. The electronic and thermal transport properties of the boron carbides are distinctive. The electronic carriers are small singlet bipolarons. Despite their exceptional hardness, these materials manifest very low thermal conductivities. These transport properties are explained in terms of distinctive features of these materials.

1. STRUCTURE AND BONDING OF ICOSAHEDRAL BORON-RICH SOLIDS

The icosahedral boron-rich solids are illustrated in Fig. 1. In each of these materials, twelve-atom icosahedral units reside at the vertices of the rhombohedral cell. Six atoms of each icosahedron are directly bonded to atoms of each of the six neighboring icosahedra. The six remaining icosahedral sites also participate in intericosahedral linkages. In the case of α-rhombohedral boron, Fig 1a, these linkages involve three-center bonds between atoms of three mutually adjacent icosahedra (depicted by solid triangles in Fig. 1a). A three-center bond is a bond formed between three atoms when a pair of electrons is centered within the triangle subtended by the three atoms. In the icosahedral boron-rich pnictides, $B_{12}P_2$ and $B_{12}As_2$, Fig. 1b, the indirect intericosahedral linkages are via a succession of two-center bonds through the two-pnictide-atom intericosahedral chains. In boron carbides, Fig. 1c, the indirect intericosahedral links are via three-atom intericosahedral chains.

The structures of Fig. 1 resemble molecular crystals based on icosahedral molecules. However, the bonding of these materials is unlike that of molecular solids. That is, in a molecular solid the bonding within molecules is much stronger and stiffer than that between molecules. Here, on the other hand, the intericosahedral bonding is stronger and stiffer than that within each icosahedron. In particular, in molecular solids intermolecular separations are adjusted so as to

R. Freer (ed.), The Physics and Chemistry of Carbides; Nitrides and Borides, 691–704.
© 1990 *Kluwer Academic Publishers. Printed in the Netherlands.*

accommodate different molecules. However, in the icosahedral boron rich solids the icosahedra deform so as to accommodate different intericosahedral structures. The relatively strong intericosahedral bonding results in the icosahedral boron-rich solids having very high melting temperatures, ≃ 2400 K, rather than the low melting temperatures characteristic of molecular solids. To distinguish the icosahedral boron-rich solids from molecular solids, I have termed these materials "inverted" molecular solids [1].

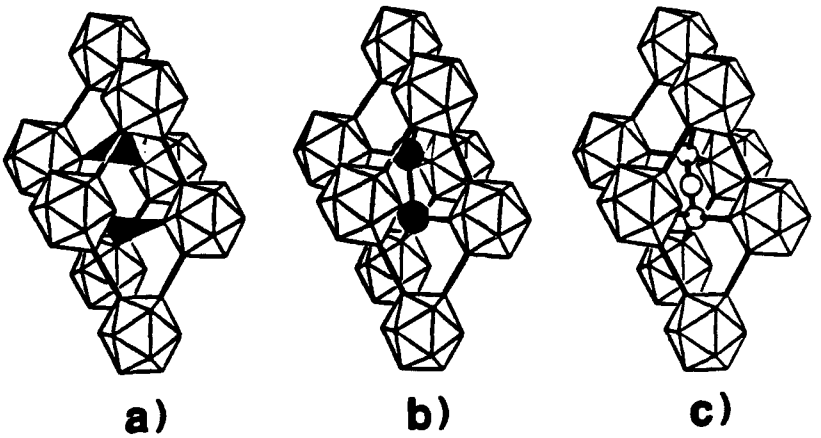

Fig. 1. The structures of a) α-rhombohedral boron, b) the icosahedral boron-rich pnictides, and c) the boron carbides described in the text.

The bonding within boron-rich icosahedra exemplifies "electron-deficient bonding" rather than two-center covalent bonding. "Electron-deficient bonding" is a molecular analogue of metallic bonding in solids [2]. Indicative of this situation, x-ray diffraction studies of these solids show peaks in the electron density above icosahedral faces rather than along icosahedral edges [3]. Thus, one may view the icosahedra in the icosahedral boron-rich solids as metallic spheroids with bonds that emanate outward from its atoms.

Electronic structure studies indicate that a boron icosahedron has thirteen molecular orbitals associated with its internal "metallic" bonding [4]. A neutral boron icosahedron possesses two fewer electrons than is required to fill (with two electrons each) these internal bonding orbitals once it has contributed an electron to each of twelve externally directed covalent bonding orbitals. Thus, in the boron-rich pnictides and boron carbides, a neutral boron icosahedron has an affinity for two additional electrons. This notion allows one to understand, in a purely ionic view, the insulating behavior of the boron-rich pnictides, such as $B_{12}P_2$. In particular, all bonding orbitals are filled as each boron icosahedron obtains an electron from each of two positively charged pnictide atoms.

2. STRUCTURE AND BONDING OF BORON CARBIDES

Distinctively, boron carbides exist as a single phase over a wide range of carbon concentrations, from about 9 atomic % to somewhat less than 20 atomic %. This situation occurs as boron and carbon atoms partially substitute for one another at various atomic locations. Thus, despite a regular arrangement of occupied sites, boron carbides are compositionally disordered.

The primary three-atom intericosahedral chains envisioned in the boron carbides are CBC and CBB chains [5]. In a CBC chain, each carbon atom at the end of a chain can provide the four second-shell electrons required for its covalent bonding to the four atoms adjacent to it. However, the central atom of the chain has one more electron than is required for covalent bonding in its two-fold coordination. This nonbonding electron is a prime candidate for donation to an icosahedral bonding orbital. In a CBB chain, the nonbonding electron of the boron atom at the center of the chain can be transferred toward the terminal boron atom of the chain so as to facilitate its four-fold covalent bonding.

One can also consider the chains that result when the central boron atom in a CBC or CBB chain is replaced by a carbon atom: a CCC or CCB chain, respectively. In these instances, since the second ionization potential of carbon is so large ($\simeq$ 25 eV), the central carbon atom retains a solitary nonbonding electron [5]. Electron-spin resonance measurements on boron carbides are consistent with about 1% of the intericosahedral chains possessing an unpaired p-electron [6,7]. Thus, the primary intericosahedral chains in the boron carbides appear to be CBC and CBB chains.

If each three-atom intericosahedral chain is a CBC chain and each icosahedron is composed of only boron atoms, one additional electron per icosahedron is required to fill all of the solid's bonding orbitals. The substitution of a carbon atom for a boron atom within an icosahedron provides this additional electron. Thus, a boron carbide with 20 atomic % carbon, composed of CBC chains and icosahedra that each contain a carbon atom, would have its bonding orbitals completely filled.

Rather than being electrical insulators, boron carbides are p-type conductors. This conducting behavior arises from having unfilled bonding orbitals due to boron carbides always containing less than 20 atomic % carbon. This carbon deficiency occurs because the cost in energy of reducing the carbon content by replacing a carbon atom with a boron atom (removing an icosahedral bonding electron) is offset by the lowering of the entropic contribution to the free energy caused by increased atomic disorder [8]. In this picture, entropy and energy both favor reducing the carbon concentration by replacing CBC chains with CBB chains rather than by replacing $B_{11}C$ icosahedra with B_{12} icosahedra. Icosahedral carbon is only replaced by boron if the carbon concentration is low enough that CBC chains are exhausted and only CBB chains remain, $<$ 13.3 atomic %.

Many experiments are consistent with this picture. First, x-ray studies indicate that the lattice constant in the direction of the three-atom intericosahedral chains increases as the carbon concentration

is reduced from near 20 atomic % to about 13 atomic % [9]. This behavior is consistent with replacing CBC chains with (less strongly bonded) CBB chains. Furthermore, this lattice constant remains unaffected by a further reduction of the carbon concentration. Second, Raman spectra lines associated with CBC chains are progressively replaced by lower-frequency lines associated with CBB chains as the carbon concentration is reduced from near 20 atomic % to near 13 atomic % [10,11]. Third, the weak composition dependence of the sound velocity between 20 atomic % and 13 atomic % carbon and the rapid decrease of the sound velocity when the carbon content is decreased below 13 atomic % carbon are consistent with this picture [12]. In particular, the sound velocity is a measure of the compressibility of the solid. Since a solid's compressibility is dominated by its most compressible component, in the icosahedral boron-rich solids the compressibility is determined by compressibility of the icosahedra. Thus, with the icosahedra's composition remaining unaltered as the carbon concentration is reduced from near 20 atomic % to about 13 atomic %, the sound velocity should also be essentially constant. However, when the carbon concentration falls below 13 atomic %, carbon is replaced by boron within $B_{11}C$ icosahedra: $B_{11}C \rightarrow B_{12}$. Since this replacement softens an icosahedron, this replacement is consistent with the rapid decrease of the sound velocity with decreasing carbon concentration once the carbon concentration is below 13 atomic %.

3. DISORDER AND ELECTRONIC TRANSPORT

Two qualitatively distinct approaches are applied to electronic transport in solids. In the high-mobility case ($\mu \gg 1$ cm^2/V-sec), a charge carrier is viewed as moving freely with its motion only occasionally disrupted by a scattering event. As the temperature is raised, the scattering of a carrier by displacements of atoms from their equilibrium position increases, and the carrier's mobility falls. For low-mobility transport ($\mu \lesssim 1$ cm^2/V-sec), a charge carrier is viewed as being localized. It then occasionally alters its location by making a phonon-assisted hop to another site. As the temperature is raised the rate of phonon-assisted hopping increases, and a carrier's mobility rises.

There are two distinct types of thermally activated hopping motion. At very low temperatures, < 10 K, hopping between shallow impurity states of a doped semiconductor can manifest a thermally activated mobility [13,14]. Each hop of this type only involves the emission or absorption of a single low energy acoustic phonon. Concomitantly, the activation energy for such motion is very small, < 0.001 eV. At higher temperatures, the rate for such hops (were this hopping conduction not generally dwarfed by itinerant electronic transport) rises linearly with temperature. Thermally activated hopping at higher temperatures arises from multiphonon small polaronic hopping between deep states [14-16]. The mobility for this type of hopping motion is characterized by activation energies that are much larger than those for impurity conduction, e.g., > 0.01 eV. In further contrast to the case of single-phonon

hopping, the elemental jump rate for multiphonon hopping loses its simple activated form as the temperature is lowered below a fraction of the phonon temperature [14,16,17].

Single-phonon hopping predominates between shallow electronic states because these states interact weakly with the atomic displacements. The weakness of the effective electron-lattice interaction arises because large radius states are only coupled to the small fraction of phonon states that have long wavelengths [13-17]. Multiphonon hopping dominates between deep states because their severe localization couples them to all phonon modes [14-17]. Thus, the presence of high temperature multiphonon hopping generally requires severely localized, small polaronic, states.

Small polaronic states form when a carrier resides on a site long enough for significant atomic displacements to occur [18,19]. This situation occurs in materials with especially narrow electronic bandwidths (e.g., some molecular solids and transition metal oxides) or in disordered materials. In the latter situation, the presence of disorder acts synergistically with the electron-lattice interaction to induce small-polaron formation [20-22].

This synergistic effect is caused by the self-trapping property of the electron-lattice interaction. That is, the greater the degree of localization of an electron, the greater the displacesive force that a carrier exerts on the atoms that it contacts. Increasing these atomic displacements deepens the potential well that localizes the carrier and thereby enhances the carrier's localization. It is because of this feedback effect that the electronic states of a covalent solid are dichotomous [18-24]. That is, a carrier may be sufficiently extended that the electron-lattice interaction has only a slight effect on its localization. Alternatively, a carrier may be severely localized in a potential well that arises to significant degree from the displacements of the atoms surrounding it (i.e., the localized state is small polaronic). The role of disorder is to produce sufficient localization so as to "trigger" the collapse of the electron into a small-polaronic state. This phenomenon is analogous to having a collision with a wave trigger the sinking of a pebble that is skimming over water.

α-rhombohedral boron and $B_{12}P_2$ are ordered materials. High-mobility transport of holes has been reported in these materials [25,26]. However, boron carbides are disordered because of carbon being distributed among different locations. In these materials, we find small-polaronic carriers [27]. Thus, it seems that boron carbides provide an example in which disorder impedes the motion of quasifree carriers sufficiently so as to trigger their collapse to small-polaronic carriers.

4. ELECTRONIC TRANSPORT IN BORON CARBIDES

4.1 Small-polaronic Carriers

The single-phase regime for hot-pressed boron carbides extends from about 9 atomic % carbon up to near 20 atomic % carbon [28]. Electronic

transport measurements have been performed on hot-pressed boron-carbide samples over this entire range of carbon concentrations [27]. These experiments imply that the electronic transport occurs via the hopping of small bipolaronic holes between $B_{11}C$ icosahedra. Here, I will review the arguments leading to this conclusion.

As illustrated in Fig. 2, the dc conductivity is thermally activated at and above room temperature. In particular, the conductivity above room temperature varies roughly as $T^{-m}\exp(-E/k_BT)$, where T is the temperature, k_B is the Boltzmann constant, $m \approx 1$ and E is the activation energy. In addition, the magnitude of this activation energy ($\simeq$0.16 eV) is essentially independent of carbon concentration. As shown in Fig. 2, at very high temperatures the temperature dependence of the preexponential factor produces a significant departure of the conductivity from a simple Arrhenius behavior. As the temperature is lowered below room temperature, the conductivity displays an ever weakening nonactivated temperature dependence. Finally, the magnitude of the prefactor of the electrical conductivity is found to depend nonmonotonically on carbon concentration. In particular, the temperature-independent prefactor of the conductivity peaks at a carbon concentration of about 13 atomic %, $B_{13}C_2$.

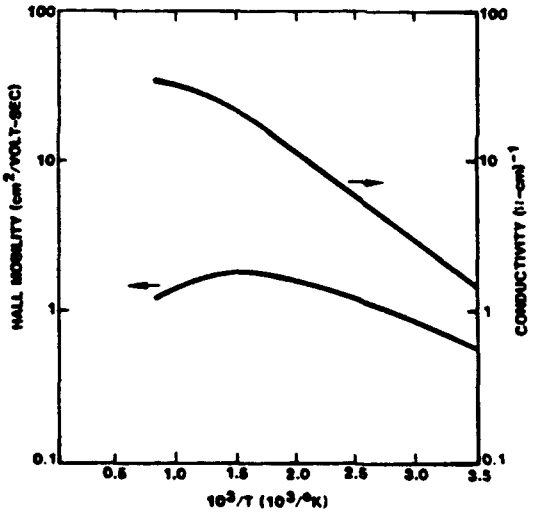

Fig. 2. The conductivity and Hall mobility of B_4C versus $10^3/T$.

To analyse these results, first recall that the electrical conductivity may be written as $\sigma = nq\mu$, where n is the density of carriers of charge q and μ is the carriers' mobility. In a traditional (itinerant type) semiconductor, the conductivity rises with increasing temperature because the increase of the carrier density overcomes the decrease of the carriers' mobility. The nonactivated prefactor of the conductivity

is the product of a "density of conducting states" factor, that increases with increasing temperature, and the carriers' mobility, that decreases with temperature. Typically, the net result of these competing effects is that the preexponential factor of the conductivity rises with temperature. However, as illustrated in Fig. 2, measurements of the boron carbides have the nonexponential prefactor of the conductivity falling with temperature as 1/T [27,29].

The observed electrical conductivities are in general accord with the small-polaronic hopping of a temperature-independent density of charge carriers [5]. In this situation, the carrier density is determined by the stoichiometry rather than the temperature. The temperature dependence of the conductivity then arises from the mobility. For the (adiabatic) hopping of small-polaronic carriers, the high-temperature mobility varies as $T^{-1}\exp(-E/k_BT)$, where the activation energy is associated with the carriers executing multiphonon hops [30]. As the temperature is lowered well below the phonon temperature, multiphonon hops are progressively frozen out and the small-polaronic mobility becomes increasingly less temperature dependent [14,18].

The independence of the activation energy for conduction, E, of carbon concentration implies that the nature of the sites between which the carrier hops does not vary with carbon concentration. The previously described view of boron carbide bonding suggests that the carriers occupy and move between icosahedra that contain a carbon atom since these are icosahedra with incompletely filled bonding orbitals that are common to all boron carbides with 10 to 20 atomic % carbon.

Measurements of the Hall mobility, illustrated in Fig. 2, provide confirmation of this picture [27,29]. In particular, the theory of adiabatic small-polaronic hopping predicts a low, $\lesssim 1$ cm^2/V-sec, thermally activated Hall mobility that has an activation energy that is less than (often about 1/3) that of the mobility that enters into the conductivity [30]. Thus, Hall mobility measurements are consistent with the expectations of small-polaronic hopping.

The carrier density can be estimated from the carbon concentration since it is the departure of the carbon concentration from 20 atomic % that results in the boron carbides having charge carriers. One may also use the measured conductivity along with the the expression for the conductivity mobility for adiabatic small-polaronic hopping to estimate the carrier density. In particular, the conductivity mobility is given by $\mu \approx (qa\,\nu/k_BT)\exp(-E/k_BT)$, where a is the jump distance and ν is the characteristic vibrational frequency [30]. Both procedures yield a carrier density of the order of 10^{21} cm^{-3}.

4.2 Small Bipolarons

Measurements of the magnetic susceptibility reveal a Curie-like paramagnetic susceptibility corresponding to a small temperature-independent density of localized spins, $\sim 10^{19}$ cm^{-3} [31]. Electron-spin resonance measurements on the same samples suggest that these spins are localized on the central atom of about 1% of the three-atom inter-icosahedral chains consistent with the formation of CCC and CCB chains [6,7]. Were these spins to arise from the charge carriers, the carrier

mobility deduced from the conductivity would be at least three orders of magnitude too high for the spins to be observed by ESR. Thus, the only observed spins appear to be associated with deep lying defects. This result implies that the carriers are spinless. In terms of small polaronic transport, this result implies that the charge carriers are small singlet bipolarons [18].

The mechanism by which carriers in solids form small polarons also enables carriers to pair as small bipolarons. In particular, the placing of two carriers at the same site in a solid increases the carrier-induced atomic displacements about the carriers. As a result of the increased atomic displacements, the potential well that self-traps the carriers is deeper when they occupy the same site than when they are apart. By itself, this effect produces an attraction between the carriers. However, there are also repulsive interactions between the carriers. In particular, it is only energetically favorable for two small polarons to merge to form a small bipolaron if the reduction in energy resulting from their sharing a common polaronic well overcomes their Coulombic repulsion energy [1,18].

Detailed knowledge of small bipolaron formation in the boron carbides is lacking. Nonetheless, several features favor the formation of hole-like small bipolarons on icosahedra in boron carbides. First, a strong electron-lattice interaction for holes (proportional to the bond strength) is implied by the refractory nature of boron carbides. Second, the least strongly bonded electrons appear to be internal to icosahedra (as evidenced by the relatively large interatomic separations on icosahedra). Therefore, icosahedra are the natural sites for holes. Third, the distribution of two carriers over (all or some portion of) the surface of an icosahedron reduces their Coulomb repulsion from what it would be if they jointly occupied a more compact structural unit.

Consider the formation of hole-like small bipolarons on $B_{11}C$ icosahedra. To begin, first recall that B_4C is envisioned as an insulator with $B_{11}C$ icosahedra linked by CBC chains [32]. As the carbon concentration of the boron carbides is reduced, carbon is replaced by boron within intericosahedral chains: CBC → CBB. While a neutral CBC chain in a boron carbide has a nonbonding electron to donate to the intraicosahedral bonding, a CBB chain (having one less electron) does not. Thus, replacing CBC chains by CBB chains introduces holes on the $B_{11}C$ icosahedra. It is these holes that pair to form small bipolarons.

Since filling the bonding orbitals of a $B_{11}C$ icosahedron in a boron carbide requires 38 [= 12 + 2(13)] second shell electrons and the icosahedron's atoms provide only 37 [= 3(11) + 4] second shell electrons, a $B_{11}C$ icosahedron with its bonding orbitals filled is represented as $(B_{11}C)^-$. Similarly, with the removal of a pair of bonding electrons from the icosahedron so as to form a hole-like small bipolaron, a $B_{11}C$ icosahedron is represented as $(B_{11}C)^+$. Then, bipolaronic hopping between $B_{11}C$ icosahedra is represented as

$$(B_{11}C)^- + (B_{11}C)^+ \rightarrow (B_{11}C)^+ + (B_{11}C)^- . \qquad (1)$$

The preexponential factor of the conductivity is proportional to the density of holelike bipolarons, $(B_{11}C)^+$ icosahedra. To determine

the density of bipolaronic carriers in boron carbides, first note that bipolaron formation on $B_{11}C$ icosahedra means that it is energetically favorable for two electrons to pair on a single icosahedra rather than remaining unpaired on separate icosahedra:

$$2(B_{11}C) \rightarrow (B_{11}C)^{+} + (B_{11}C)^{-}. \qquad (2)$$

In other words, a system containing only $B_{11}C$ icosahedra will, by itself, have half of the icosahedra occupied by bipolaronic holes, $(B_{11}C)^{+}$ icosahedra. However, CBC chains also donate electrons to these icosahedra. Therefore, fewer than half of the $B_{11}C$ are occupied by bipolaronic holes.

With the number of electron-donating (CBC) chains being reduced as the carbon concentration is reduced from 20 atomic %, the density of bipolaronic holes increases. This increase in the carrier density with decreasing carbon content continues until all of the electron-donating (CBC) intericosahedral chains are replaced by CBB chains, at about $B_{13}C_2$. With a further reduction in the carbon concentration, only the density of $B_{11}C$ icosahedra is reduced with a decrease in the carbon concentration: $B_{11}C \rightarrow B_{12}$. In this circumstance, the density of bipolaronic holes is about half the density of $B_{11}C$ icosahedra. Thus, at carbon concentrations lower than about 13 atomic %, $B_{13}C_2$, the carrier density will fall as the carbon density falls. This argument [5] provides an explanation of why the carrier density, as determined by the prefactor of the conductivity, varies nonmonotonically with carbon concentration with a peak at about 13 atomic % carbon [27,29,33].

4.3 Anomalous Seebeck Effect

Measurements of the Seebeck coefficient are also consistent with small-bipolaronic hopping. As indicated above, more than half of the $B_{11}C$ icosahedra have their bonding orbitals filled: are $(B_{11}C)^{-}$ icosahedra. As a result, bipolaronic hopping between $B_{11}C$ icosahedra always yields a p-type Seebeck coefficient. This is in accord with experimental observations over the entire range of carbon concentrations studied [27,29].

The Seebeck coefficient in the boron carbides is large, > 100 μV/K at 300 K, and increases with temperature. This behavior is at odds with the expectations of conventional semiconductors and metals. In particular, in a nondegenerate semiconductor, the Seebeck coefficient is typically large (> 100 μV/K) and decreases with increasing temperature. In a degenerate material (e.g. a metal), the Seebeck coefficient increases slowly with temperature but is very small (<< 100 μV/K).

The reported behavior of the Seebeck coefficient in boron carbides is, however, consistent with what was predicted [34,35] and subsequently observed [36] for polaronic hopping in degenerate disordered systems. In particular, the Seebeck coefficient is the entropy transported per unit charge by a charge carrier. For high-temperature (semiclassical) polaronic hopping, the Seebeck coefficient, S, may be written as [34,35]

$$S = (1/qT)\langle E - \mu\rangle - (1/qT)[(\partial \ell n\ \Gamma/\partial E)|_{\mu}\ (\langle E^2\rangle - \langle E\rangle^2)/2]. \qquad (3)$$

In Eq. (3), q is the charge of a carrier, μ is the chemical potential, E is the carrier's energy and Γ is the electron-lattice coupling strength. The averaging symbol indicates a thermal average over the occupied states of a carrier weighted by their partial conductivities, $\sigma(E)$. The distribution of carrier (bipolaronic) energies arises from the presence of disorder. Without disorder, the second term of Eq. (3) vanishes.

The first term in Eq. (3) is the change of the entropy of the system arising from the addition of a charge carrier. The second term of Eq. (3), proportional to $(\partial \ell n\ \Gamma/\partial E)|_{\mu}$, arises from the transfer of vibrational energy during a hop of a charge carrier [5,34,35]. That is, the first term depends only upon the presence of a carrier while the second term depends upon the mechanism of its transport. For jumps between sites with disparate energies and electron-lattice coupling strengths, vibrational energy is transferred during a hop. It is for this reason that the second term depends on the fractional variation of the electron-lattice coupling strength with carrier energy.

For bipolaronic hopping, the charge transport involves the motion of two electrons. Thus, the charge of a transported unit is twice the fundamental electronic charge, $-|e|$: $q = -2|e|$. Since any site can at most be occupied by a single bipolaron, these hopping singlet bipolarons obey Fermi statistics (rather than the Bose statistics that characterize free spinless particles). Thus, these hopping bipolarons are treated as spinless fermions.

For states near the bottom of an energy band, the density-of-states increases with carrier energy. Then, $\langle E - \mu\rangle > 0$. Furthermore, for states near the bottom of a band, the electron-lattice interaction decreases with increasing carrier energy as the carrier's state becomes less localized, $(\partial \ell n\ \Gamma/\partial E)|_{\mu} < 0$. As a result, electronic transport involving states at the bottom of a band yields a negative Seebeck coefficient, n-type conduction. Conversely, for states near the top of an energy band, the density of states decreases with carrier energy. Then $\langle E - \mu\rangle < 0$. Furthermore, for states near the top of an energy band, the electron-lattice interaction increases with carrier energy as the carrier's state becomes more localized, $(\partial \ell n\ \Gamma/\partial E)|_{\mu} > 0$. Thus, electronic transport involving states at the top of an energy band results in a positive Seebeck coefficient, p-type conduction. Since bipolaronic transport in the boron carbides is associated with a more-than-half-filled band of bipolaronic states, a p-type Seebeck coefficient is expected.

For a temperature-independent density of charge carriers the first contribution to the Seebeck coefficient in Eq. (3), $\langle E - \mu\rangle/qT$, generally rises with increasing temperature to the temperature independent limit $(k_B/q)\ \ell n[(1 - c)/c]$, where c is the fraction of $B_{11}C$ icosahedra that are negatively charged [34]. The second contribution to Eq. (3) rises linearly with temperature when the width of the carrier's energy band exceeds k_BT. Thus, Eq. (3) can account for the unusual magnitude and temperature dependence of the Seebeck coefficient that is observed in the boron carbides. In other words, measurements of the electrical conductivity, Hall mobility, and Seebeck coefficients of a

wide variety of boron carbides are consistent with a model that posits the hopping of a constant density of bipolarons between inequivalent $B_{11}C$ icosahedra.

4.4. Pressure dependence of the conductivity

The electrical conductivity of B_4C has been measured as a function of temperature under the application of hydrostatic pressure [37]. As is typical of hopping conduction, the prefactor of the electrical conductivity rises with pressure. This effect occurs because the solid's vibrational frequencies, carrier density, and electronic-overlap factors all generally rise upon compression. The activation energy for conduction also rises with the application of pressure. Unlike molecular systems, here the net effect of the pressure-dependent increases of the conductivity's preexponential factor and activation energy decreases the electrical conductivity with increasing pressure.

To understand this result, it should be noted that the activation energy for polaronic hopping is proportional to the square of the electron-lattice coupling strength associated with hopping [14-18]. The electron-lattice interaction strength for hopping between icosahedra is just the electron-lattice coupling strength of the icosahedra. Thus, the experiment indicates an increase of this electron-lattice coupling strength upon compression of the boron carbide. Since the electron-lattice coupling strength generally rises with compression, the experiment implies that the icosahedra are being compressed. This observation is consistent with the characterization of the icosahedral boron-rich solids as "inverted" molecular solids. That is, in the boron carbides, unlike molecular solids, the application of pressure produces significant compression of the "molecular-like" sites, the icosahedra, between which hopping occurs. Thus, while the hopping conductivity of the boron carbides decreases under hydrostatic pressure, in molecular systems, small polaronic hopping conductivity is observed to increase with hydrostatic pressure [38].

5. THERMAL TRANSPORT IN BORON CARBIDES

Boron carbides are exceptionally hard materials that, as expected, have very high sound velocities. For example, near B_4C the sound velocity is $\approx 1.4 \times 10^{6}$ cm/sec. However, as depicted in Fig. 3, the high-temperature thermal diffusivities of boron carbides are surprisingly small, $\approx 10^{-2}$ cm^2/sec [39,40].

These results are inconsistent with commonly employed approaches to thermal diffusivity. In particular, phonon mean-free-paths of only a few Angstroms are obtained from the thermal diffusivities of the boron carbides at 1000 C with the (acoustic) sound velocities. Furthermore, the thermal diffusivities are even below the product of the highest vibrational frequency and the square of the lattice constant, a proposed minimum of the thermal diffusivity, ≈ 0.1 cm^2/sec at 1000 C.

In an attempt to understand the experimental findings, the notion of "vibrational hopping" is being developed for application to the boron

carbides [41]. This approach complements treatments of thermal transport that associate thermal resistance with phonon scattering.

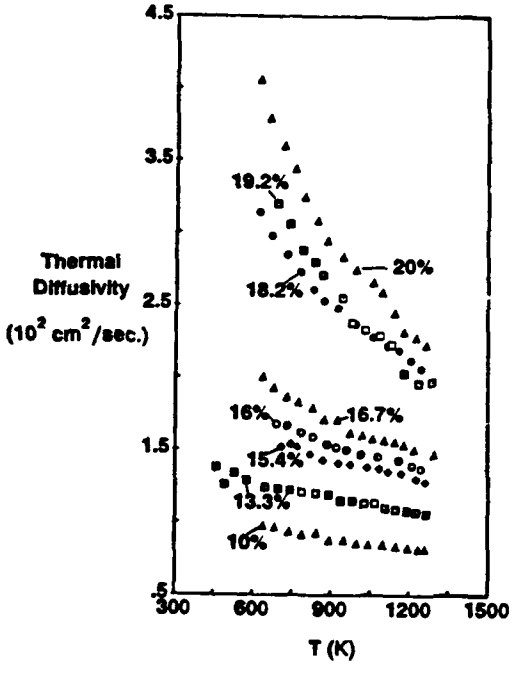

Fig. 3. The thermal diffusivity of boron carbides of various carbon concentrations plotted versus temperature.

The commonly employed treatment of thermal conduction envisions vibrational energy being transported coherently through a solid by phonons. With increasing temperature, the anharmonicity of the vibrations increases, thereby increasing phonon scattering and reducing the thermal diffusivity. Thus, transport of vibrational energy is treated in analogy with the transport of a quasifree electronic carrier.

In analogy with hopping-type electronic transport in solids, a hopping approach may be employed to describe the transport of vibrational energy in a vibrationally disordered material [41]. In this scheme, the transport of vibrational energy between individual oscillators with disparate frequencies is considered. One can begin by noting that little vibrational energy is transfered between two harmonic oscillators if the frequency difference between the two oscillators exceeds the (beat) frequency characterizing the coupling between them. This situation is altered if the oscillators are anharmonic. Specifically, an anharmonic oscillator is one for which the vibrational frequency is a function of its energy. Therefore, as energy is transfered amongst oscillators the frequencies of various pairs of oscillators may be brought into coincidence. Establishing a coincidence provides an opportunity for vibrational energy to be transferred between

the coincident oscillators. This description of vibrational hopping is analogous to that for the semiclassical hopping of small polarons [18].

In applying this model to boron carbides, it is recalled that these "inverted" molecular solids are characterized by intericosahedral bonding that is much stiffer than that within icosahedra. Thus, one may envision the transport of vibrational energy being dominated by transport through the relatively stiff intericosahedral chains rather than through (parallel paths through) the softer icosahedral units. In this situation, the disordering of the intericosahedral chains is the essential factor in limiting the high-temperature thermal diffusivity. In particular, reducing the carbon from near 20 atomic % results in CBC intericosahedral chains being replaced by CBB chains. Calculations indicate that the stiffness of portions of these intericosahedral chains are greatly altered by these atomic substitutions [42]. Specifically, the stiffness of a CB link of a CBC intericoahedral chain is much larger than (about twice) that of a BB link of a CBB chain. Thus, the rapid decline of the thermal diffusivity of boron carbides with decreasing carbon concentration can be qualitatively understood.

In summary, the low thermal diffusivities of the boron carbides are viewed as caused by the vibratory disorder that accompanies the compositional disorder of the boron carbides. The thermal transport appears to be inconsistent with conventional notions of thermal transport. However, the measurements are qualitatively consistent with the expectations of a "vibrational hopping" approach to thermal diffusion.

6. REFERENCES

* Work supported by the U.S. Dept. of Energy under Contract DE-AC04-76DP00789.

1. Emin, D. (Jan. 1987) Phys. Today, 40, p. 55.
2. Wannier, G. H. (1959) Elements of Solid State Theory (Cambridge, New York), pp. 245-256.
3. Morosin, B., Mullendore, A. W., Emin, D. and Slack, G. A. (1986) in Boron Rich Solids (AIP Conf. Proc. 140), D. Emin, T. L. Aselage, C. L. Beckel, I. A. Howard, C. Wood, eds., (AIP, New York) p. 70.
4. Longuet-Higgens, H. C. and Roberts, M. de V. (1955) Proc. R. Soc. London, Ser. A 230, 110.
5. Emin, D. (1986) in Boron Rich Solids (AIP Conf. Proc. 140), D. Emin, T. L. Aselage, C. L. Beckel, I. A. Howard, C. Wood, eds., (AIP, New York) p. 189.
6. Venturini, E. L., Azevedo, L. J., Emin, D. and Wood, C. (1986) in Boron Rich Solids (AIP Conf. Proc. 140), D. Emin, T. L. Aselage, C. L. Beckel, I. A. Howard, C. Wood, eds., (AIP, New York) p. 292.
7. Venturini, E. L., Emin, D. and Aselage, T. L. (1987) in Novel Refractory Semiconductors, D. Emin, T. L. Aselage and C. Wood, eds., (MRS, Pittsburgh) pp. 57-62.
8. Em n, D. (1988) Phys. Rev. B, 38, 6041.
9. Aselage, T. L. and Tissot, R. G. (to be published).
10. Tallant, D. R., Aselage, T. L., Campbell, A. N. and Emin, D. (1988) J. Noncrystalline Solids, 106, 370.

11. Tallant, D. R., Aselage, T. L., Campbell, A. N. and Emin, D. (1989) Phys. Rev. B, 40, 5649.
12. Gieske, J. H., Aselage, T. L. and Emin, D. (1990) Phys. Rev. B, (to be published).
13. Miller, A. and Abrahams, E. (1960) Phys. Rev., 120, 745.
14. Emin, D. (1974) Phys. Rev. Lett., 32, 303.
15. Emin, D. (1975) Adv. Phys., 24, 305.
16. Gorham-Bergeron, E. and Emin, D. (1977) Phys. Rev. B, 15, 3667.
17. Emin, D. (1976) in Physics of Structually Disordered Solids, S. S. Mitra, ed. (Plenum, New York). pp. 385-410.
18. Emin, D. (1982) Phys. Today, 35 (June), 34.
19. Emin, D. (1973) Adv. Phys., 22, 57.
20. Emin, D. (1983) Comments on Solid-State Physics, 11, 35.
21. Emin, D., Hillery, M. S. and Liu, N. L. (1987) Phys. Rev. B, 35, 641.
22. Emin, D. (1985) in Localization and Metal-Insulator Transitions, H. Fritzsche and D. Adler, eds. (Plenum, New York) pp. 323-335.
23. Toyozawa, Y. (1961) Prog. Theor. Phys., 26, 29.
24. Emin, D. and Holstein, T. (1976) Phys. Rev. Lett., 36, 323.
25. Golikova, O. A. (1984) Phys. Stat. Solidi A, 86, K51.
26. Golikova, O. A. (1987) in Novel Refractory Semiconductors, D. Emin, T. L. Aselage and C. Wood, eds., (MRS, Pittsburgh) pp. 17-26.
27. Wood, C. and Emin, D. (1985) Phys. Rev. B, 29, 4582.
28. Bouchacourt, M. and Thevenot, F. (1981) J. Less-Common Metals, 82, 219.
29. Wood, C. (1986) in Boron Rich Solids (AIP Conf. Proc. 140) D. Emin, T. L. Aselage, C. L. Beckel, I. A. Howard, C. Wood, eds., (AIP, New York) p. 206.
30. Emin, D. and Holstein, T. (1969) Ann. Physics (N.Y.), 53, 439.
31. Azevedo, L. J., Venturini, E. L., Emin, D. and Wood, C. (1985) Phys. Rev. B, 32, 7970.
32. Schilgaarde, M. Van and Harrison, W. A. (1985) Phys. Chem. Solids, 46, 1093.
33. Aselage, T. L., to be published.
34. Emin, D. (1975) Phys. Rev. Lett., 35, 882.
35. Emin, D. (1976) in Physics of Structually Disordered Solids, S. S. Mitra, ed. (Plenum, New York) pp. 461-506..
36. Weber, W. J., Griffin, C. W. and Bates, J. L. (1986) J. Mat. Res. 1, 675.
37. Samara, G. A., Emin, D. and Wood, C. (1985) Phys. Rev. B, 32, 2315.
38. Dolezalek, F. K. and Spear, W. E. (1970), J. Noncryst. Solids, 4, 97.
39. Wood, C., Emin, D., and Gray, P. E. (1985) Phys. Rev. B 31, 6811.
40. Wood, C., Aselage, T. L., and Emin, D. to be published.
41. Emin, D. (to be published).
42. Emin, D, Howard, I. A., Green, T. A., and Beckel, C. L. (1987) in Novel Refractory Semiconductors, D. Emin, T. L. Aselage and C. Wood, eds., (MRS, Pittsburgh) pp. 83-88.

OPTICAL PROPERTIES OF BORON-RICH SOLIDS WITH ICOSAHEDRAL STRUCTURE

HELMUT WERHEIT
Universität -Gesamthochschule- Duisburg
Solid State Physics Laboratory
Lotharstr. 1 - 21
D 4100 Duisburg 1
FRG

ABSTRACT: The solid state optical properties of selected representatives of the α-rhombohedral and the ß-rhombohedral structure group of boron are presented. Reliable previous optical absorption spectra are extended by new results e.g. on α-rhombohedral boron and boron carbide. The absorption edges, photoeffects related to gap states, IR-active lattice vibrations and plasma vibrations are discussed with respect to band structure models, band structure calculations, and structure conceptions.

1. INTRODUCTION

The optical properties of matter include all its direct and indirect interactions with electromagnetic waves as far as they can be investigated by the experimental methods of optics. The spectral range concerned depends on the state of physical and technical developement and extends at present essentially from synchrotron generated soft X-rays to mm-waves detectable by modern Fourier transform spectrometers.

One essential advantage of optical investigations is based on the fact that in most cases the electromagnetic waves are weakly coupled with the physical processes, thus closely approaching the ideal of a non-disturbing measuring method. Nevertheless since in large parts of the optical spectrum the wavelengths are small in comparison with the sample dimensions, the interactions are multiplied. Hence optical investigations of solids belong to the most sensitive ones and therefore also in case of the complex boron-rich solids they are a powerful tool to determine compositional and structural modifications and disorder and their influence on other properties.

At present this is important in two respects. Firstly, to detect the existance of deviations from the ideal structures at a time, when the boron materials usually available contain structural defects and are more or less impure in comparison with the classical semiconductors, and especi-

R. Freer (ed.), The Physics and Chemistry of Carbides; Nitrides and Borides, 705–725.
© 1990 Kluwer Academic Publishers. Printed in the Netherlands.

ally, because direct methods of structural determination fail or are not yet sufficiently developed for these complex structures. Secondly, systematical investigations of the influence of disorder and foreign atoms on electronic and other physical or technical properties are necessary at a time, when essential applications of boron-rich solids are in development, because it is necessary to generate the prerequisite for the purposive modification of such properties.

In this article selected examples of recently obtained results of optical investigations and their interpretation will be presented and discussed to demonstrate some of the progress in understanding or at least specifying problems in the field of boron-rich solids with icosahedral structures since previous articles on this topic [1,2].

2. ABSORPTION EDGE

In case of semiconductors, to whom the boron-rich solids are to be attributed, the range of fundamental optical absoption reflects the distribution of states in the valence and the conduction band. To specify this spectral range for the boron-rich materials at least roughly, in fig. 1 the fundamental absorption of amorphous boron is shown. In spite of inaccuracies e.g. due to unknown impurities, difficulties in the precise determination of the sample thicknesses and the unknown reflectivity at high energies, this result may be representative to a certain extent for other icosahedral boron-rich solids as well, because amorphous boron is assumed to consist essentially of randomly arranged B_{12} icosahedra.

The results at lower energies were obtained on evaporated films, while those at higher energies are derived from [3]. The authors attribute the absorption increasing towards high energies to 1s-2p transitions; hence the range of about 0.8 to 200 eV is due to optically excited interband transitions leading from the valence band into the conduction band.

With respect to the interpretation of optical and electrical properties of semiconductors and insulators the absorption in the range of the low energy limit of the fundamental absorption is especially important. This absorption edge reflects the distribution of states near the band edges, which are relevant for the transport properties. By extrapolation to zero absorption the band gap can be determined. Depending on the kind and position of the band extrema in the k space, different kinds of interband transitions can be distinguished according to the energy dependence of their absorption. Hence optical measurements in this spectral range are essential to check theoretical band structure calculations or to serve as their basis. This is especially important in case of the complex structures of boron-rich solids, where such calculations are very difficult and therefore hitherto performed only in a few cases.

The valence band edge of the icosahedral crystal structures must be expected to be formed by those molecular orbitals, which belong to the lowest bond strengths in the structure. These are, according to the

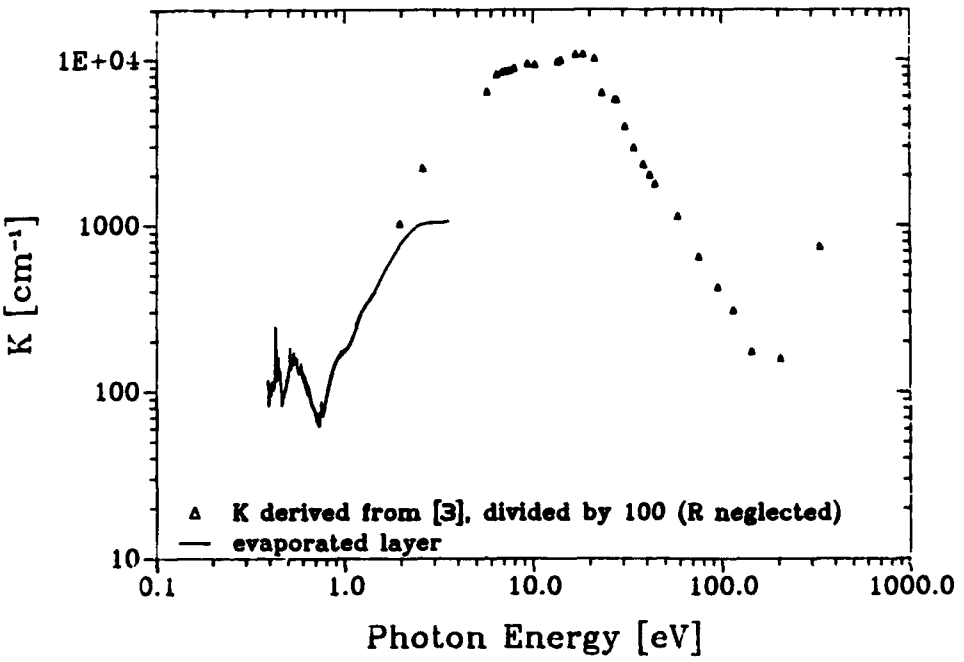

Figure 1. Fundamental absorption of amorphous boron films. Adapted absorption coefficient K plotted versus photon energy. Triangles derived from [3], reflectivity influence neglected.

bonding distances, in α-rhombohedral boron the inter-icosahedral three-center bonds connecting the equatorial atoms of the icosahedra. Therefore, as qualitatively discussed in [4] (see also [7]), the absorption edge of α-rhombohedral boron is expected to be distinctly different from e.g. boron carbide and ß-rhombohedral boron, the equatorial atoms of whose icosahedra are covalently bonded to neighbouring structure elements. Therefore in these materials the intra-icosahedral multiple-center bonds are expected to determine the upper valence band edge [4]. This qualitative estimation is quantitatively confirmed by Bullet's calculations [5,6]; unfortunately, the Jahn-Teller effect on the icosahedron [4,7] is not considered in these calculations.

2.1. α-Rhombohedal Boron

Fig. 2 shows the absorption edge of α-rhombohedral boron, which has the most simple structure of the materials to be discussed. The results were obtained on microcrystalline material (size 3 to 5 μm) [8] in a special optical arrangement. Using the theories of interband transitions (cp.

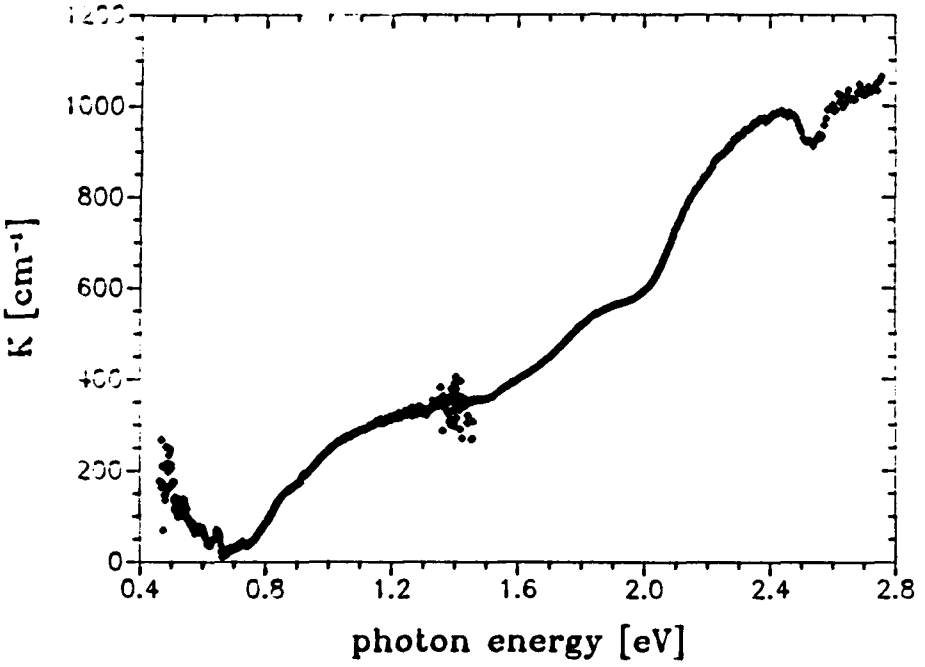

Figure 2. Absorption edge of α-rhombohedral boron. Absorption coefficient K plotted versus photon energy [7]. The results were obtained on crystals of about 3 to 5 μm size.

e ⁄. [9]) and the optical absorption to be attributed to deep levels [10] the edge can be decomposed into three transitions (table 1).

TABLE 1. Electronic transitions in α-rhombohedral boron derived from the optical absorption edge.

Nr.	energy [eV]	transition	density [cm^{-3}]	reduced mass $2m_r/m_e$
1	0.73(2)	deep level/band	$1.2 * 10^{19}$	
2a	1.49(2)	deep level/band	$1.25 * 10^{19}$	
	or			
2b	1.63(2)	interband/direct allowed		0.029
3.	2.055(2)	interband/direct allowed		0.034

Only the third transition was previously known, but with less precision [11, 12, 13]. In case of the second transition it was not possible to decide between the alternatives given in table 1, because the adaptation of both absorption theories was of the same quality. Also the derived

results on the density of states, in the case of the assumption of a deep level and on the reduced mass in the case of the direct transition, each, are acceptable in comparison with the other transitions.

Besides the quantitative results cited it is important that the theories of transitions, in which Bloch type states are involved, can be applied very well. This confirms the existance of this type of band states at least for α-rhombohedral boron. But moreover this conclusion seems to be transferable to the icosahedral boron-rich solids more or less in general.

The previous theoretically calculated band gaps of 2.4 eV [14], and 2.88 eV [15] are more or less satisfactory with respect to the quantitative result, but the theoretically determined kind of transition (indirect) is not confirmed by the experiment. Bullett's improved calculation [5] with a direct transition at 2.3 eV is quantatively better and qualitatively correct. Moreover his lowest gap agrees quantitatively well with the second version of the second transition in table 1. Unfortunately the type of this transition does not agree with the experimental result. Besides the comparison of transition energies it is important that the calculated density of states near the valence band edge of α-rhombohedral boron is distincly lower than e.g. in boron carbide and ß-rhombohe-

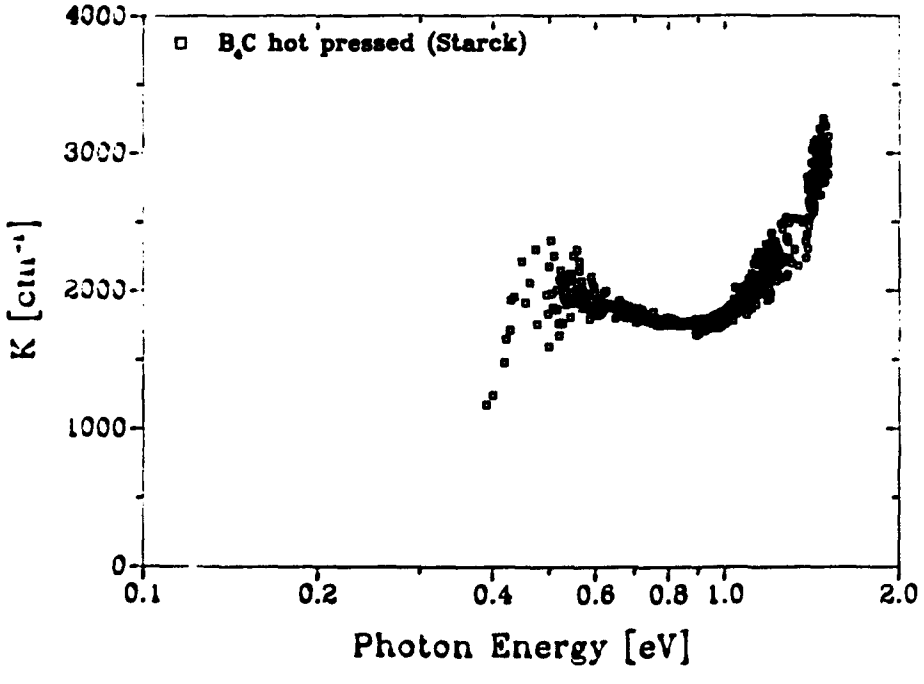

Figure 3. Absorption edge of B_4C (hot pressed material, provided by Hermann C. Starck, Laufenburg, FRG) [15].

dral boron [5]. This explains, why the absorption in fig. 2 is compatively low for direct transitions.

2.2 Boron Carbide

Boron carbide is another representative of the α-rhombohedral structure group. Additionally to the B_{12} icosahedra at the vertices of the unit cell a C-B-C chain is arranged along the main diagonal. This leads to the covalent saturation of the equatorial bonds. As expected, therefore the absorption edge (fig. 3) [16] differs distinctly from that one of the α-rhombohedral polymorph, but it exhibits close similarities with the ß-rhombohedral phase (as was discussed above and will be shown below by the experimental results) in spite of the different crystal structures. The transition 2 of table 2 is distinctly seen in fig. 3, and transition 3 was previously identified by differential reflectivity measurements [17]. To compare the results quantitatively it must be considered that the data in table 2 are already corrected by subtraction of the energies of the phonons involved.

Additionally at lower energies a deep level related absorption with inset at 0.26(3) eV is strongly marked. This will be further discussed in connection with ß-rhombohedral boron.

2.3. ß-Rhombohedral Boron

The analysis of the optical band gap of ß-rhombohedral boron obtained from previous results on the purest material available is listed in table 2. The energy of the phonons involved was taken from corresponding measurements on polycrystalline material, because temperature dependent measurements with polarized light on single crystals are not available. The anisotropy of both transitions amounts to some hundredth eV only [21] and is, according to new considerations, probably to be attributed essentially or even totally to the phonons involved [18].

TABLE. 2. Electronic interband transitions of ß-rhombohedral boron at 300 K obtained by optical absorption [19-21] (1 extrapolated from high temperatures)

Nr.	energy [eV]	polaris.	$k_B\Theta$ [meV]	transition
1	0.34(2)			deep level/band
2	1.39(3)	E ∥ c	32	interband/indirect allowed
	1.34(3)	E ⊥ c		with phonon emission
3	1.561(15)	E ∥ c	74	interband/indirect allowed
	1.541(15)	E ⊥ c		with phonon emission

It is well known that carbon is the most important hitherto not avoidable impurity in ß-rhombohedral boron. To assess its influence on the optical

properties, the absorption edges of a number of samples with different carbon contents, provided by different producers, are plotted in fig. 4 [16]. Characteristic pecularities of all these samples is the transition 2 (table 2), which hitherto has been assumed to be indirect allowed [19, 20, 21], but according to our new investigations it may rather be indirect forbidden or influenced by transitions into excitonic states, and transition 3, which is indirect allowed. The latter is attributed to the interband transition from the valence band into the conduction band, while the former is due to a partly occupied intrinsic acceptor level induced by the Jahn-Teller effect of the B_{12} icosahedron [4, 7].

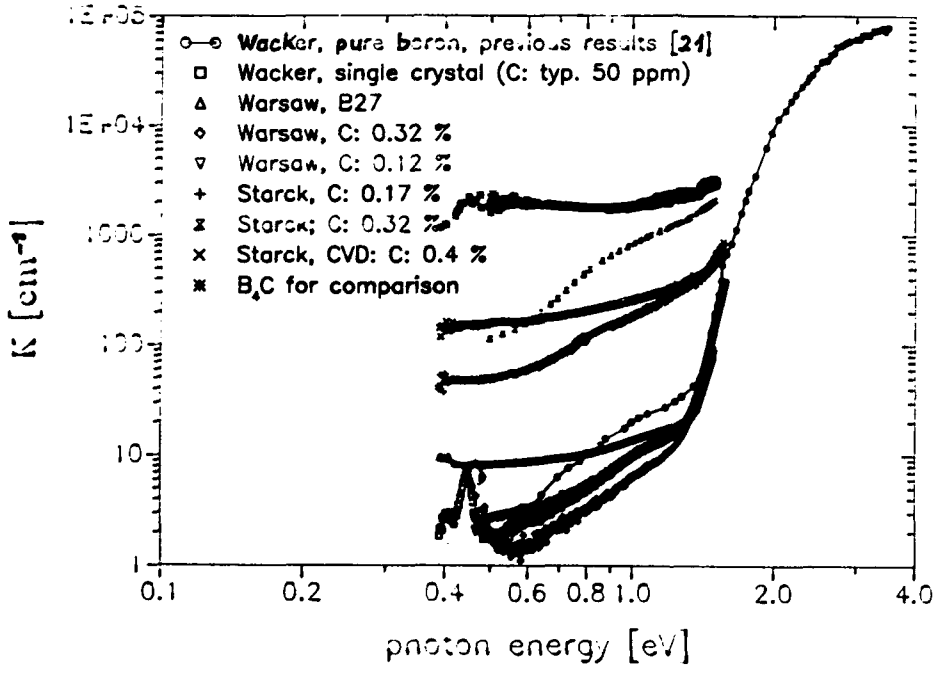

Figure 4. Absorption edge and edge tail of ß-rhombohedral boron, and of boron carbide (from fig. 3) for comparison. Absorption coefficient K plotted versus photon energy [15]. (Producer of the materials investigated: Wacker-Chemie, Munich, FRG; Hermann C. Starck, Goslar and Laufenburg, FRG; Research Center for Crystals, Warsaw).

Obviously the absorption at lower energies is essentially caused by the carbon content. Apart from the samples produced by the Research Center for Crystals, Warsaw, this absorption in all other cases can be described by the theory of deep levels [10] with an energy inset at 0.27(3) eV. The densities of states derived according to [10] are plotted in fig. 5 and are found to be proportional to the carbon content, even

when boron carbide is included, too. Indeed, the density of states is lower than the carbon content by a factor of about 100. This result agrees with spin density determinations by Gehrke and Siems [22] in the case of ß-rhombohedral boron and in the case of boron carbide by Venturini et al. [23]. The optical absorption shows that there is really a level in the band gap, whose density of states is lower than the carbon content by a factor of about 100, and which hence supersedes the assumption of bipolarons to explain this discrepancy (cp. e.g. [24]).

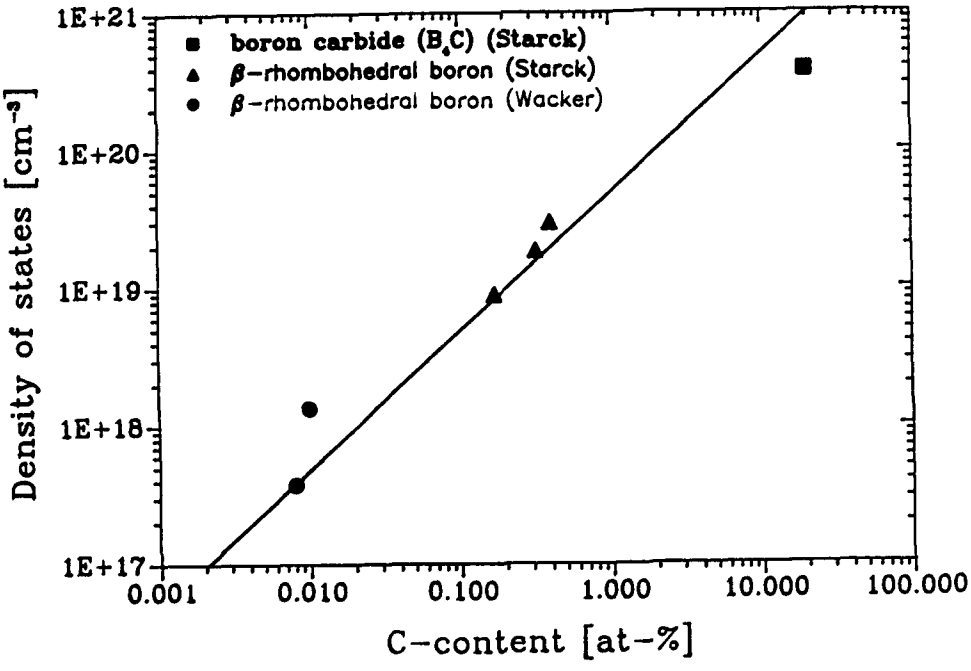

Figure 5. Density of states of a band gap level with 0.27(3) eV activation energy plotted versus C content. The density was derived according to the theory of deep levels [9] from the edge tail absorption in fig. 4.

The question, why Warsaw boron behaves differently from the others remains open. A possible explanation could be that in consequence of the preparation process different sites are occupied by the C atoms.

The results prove the narrow relationship between the electronic band structures of ß-rhombohedral boron and boron carbide with respect to the band edges and band gap states, as well as the qualitative difference of both to α-rhombohedral boron. This is discussed in [7] in more detail.

3. PHOTO EFFECTS

ß-rhombohedral boron is the only boron-rich solid, the photo effects of which have been investigated in some detail. The optical and electrical properties are strongly influenced by electronic states of high density in the band gap. It was shown [4] that there exists one intrinsic level induced by the Jahn-Teller effect and positioned at about 0.2 eV above the valence band. Moreover different thermal non-equilibrium states can be established at lower temperatures, when optically excited electrons occupy states at different distances from the conduction band [25]. Defined thermal conditions are to be obeyed for each of them.

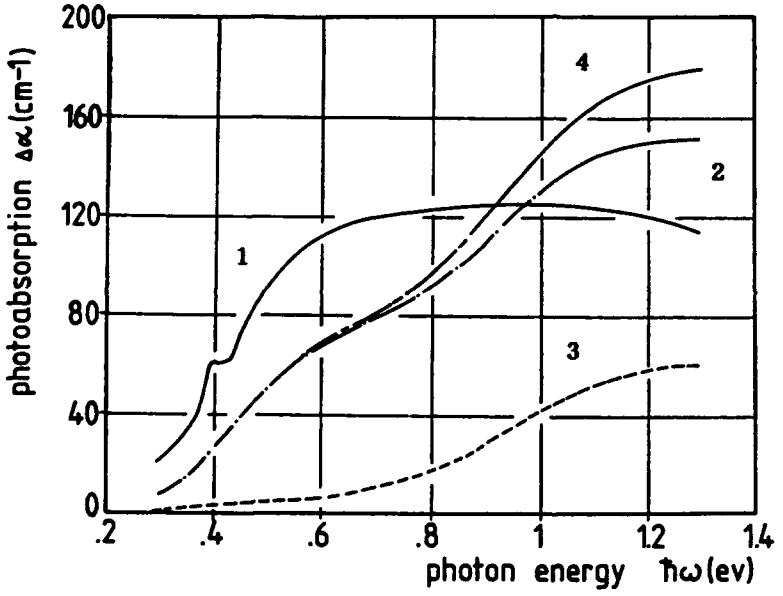

Figure 6. Optical absorption spectra of non-equilibrium states in ß-rhombohedral boron obtained by the same optical excitation (several hours optical excitation with a Xenon arc lamp) but at different thermal conditions (**1**: 90 K, **2**: 160 K, **3**: 240 K, **4**: at different temperatures) [25].

Fig. 6 shows the absorption spectra of such non-equilibrium states induced by optical excitation at different temperature conditions [25]. From these spectra and from temperature dependent glow curves three different levels in the band gap were determined (table 3). Obviously for the generation of these levels not only electrons excited into the conduction band are sufficient, but additionally the presence of specific phonons are necessary. This distinguishes these levels from usual polaronic states, which are assumed to be formed by electrons more or less statically polarizing their dielectric surrounding. Besides, the low ionicity of

TABLE. 3. Electronic states near the conduction band edge of ß-rhombohedral boron obtained by isothermal photoabsorption and glow technique measurements [25].

Level	Activation Energy [eV]		density
	isotherm.	glow	[cm^{-3}]
E_1	0.345	0.36	$4 * 10^{19}$
E_2	0.56	0.53	$1 * 10^{19}$
E_3	0.76	0.61	$9 * 10^{19}$

the icosahedral structures seems not to favour the formation of polarons. According to further results and considerations [18] we take the dynamical Jahn-Teller effect of the B_{12} icosahedron into consideration as the physical reason for this behaviour. Depending on the thermal excitation

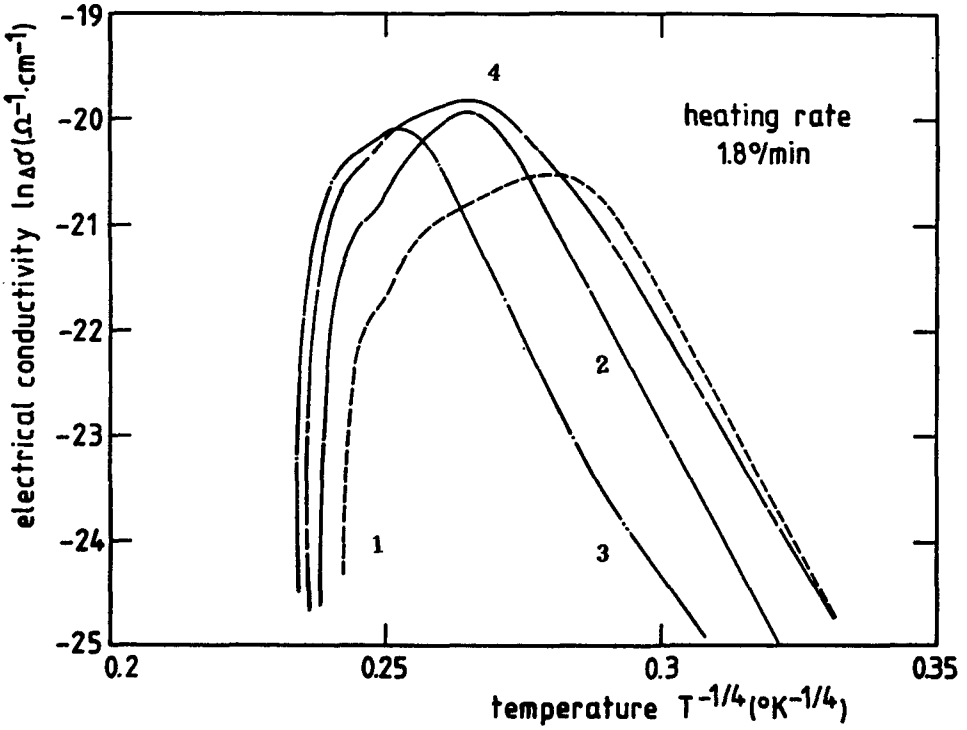

Figure 7. Temperature dependence of the electrical conductivity after optical excitation at defined temperatures (same conditions as in fig. 6); dark conductivity subtracted) [25].

of phonons at different temperatures the electron-phonon interaction leads to distinct states below the conduction band.

For the interpretation of the electronic transport properties in the boron-rich icosahedral structures simultaneous measurements of the occupation densities of these states by optical absorption and of the electrical conductivity are important. From fig. 7 it can be seen that in the thermal non-equilibrium state hopping conduction according to Mott's law is prevailing. The differential change of the absorption and the simultaneously measured conductivity with increasing temperature (fig. 8) [26,18] shows that at low temperatures thermally activated conductivity (phonon assisted hopping) in the intrinsic acceptor-like level near the valence band is prevailing, while the electron occupation density in this level remains unaltered. But when this is reduced by thermal activation of trapped electrons into the conduction band and subsequent

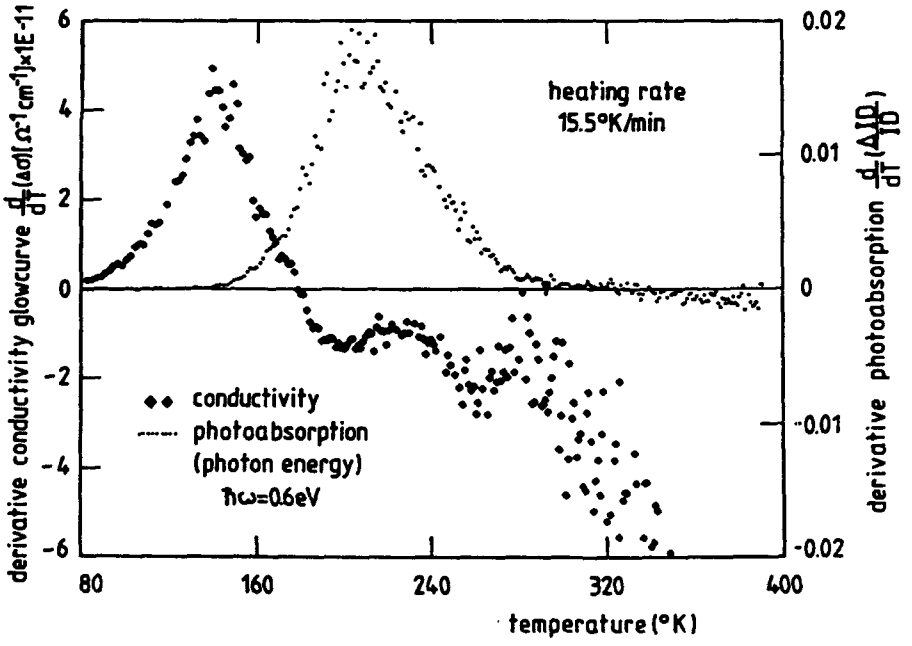

Figure 8. Typical derivatives of the simultaneously measured glow curves of the photoabsorption, which shows the occupation density of excited electrons trapped in a state near the conduction band, and the electrical conductivity, which indicates the electronic transport in the intrinsic acceptor-like level near the valence band after optical excitation [18, 26].

recombination into the intrinsic acceptor level, the conductivity decreases because of the reduced density of unoccupied hopping sites. The results yield the reliable conclusion that in ß-rhombohedral boron at lower temperatures the conductivity takes place essentially within the intrinsic acceptor-like level at about 0.2 eV above the valence band edge.

4. IR ACTIVE LATTICE VIBRATIONS

The lattice vibrations represent the most immediate relation between crystal structure and optical properties, because the phonon resonance frequencies are determined by the masses of vibrating atoms or atomic groups, bonding distances and angles, charge distribution and bond lengths.

TABLE 4: Group theoretical determination of the IR active and Raman active vibrations of several icosahedral B structures

System	Point/ Space group	Atoms per unit cell	IR modes theor.	IR modes exp.	Raman modes theor.	Raman modes exp.
isolated icosahedron						
B_{12}	I_h	12	1 F_{1u}		1 A_g 2 H_g	
isolated icosahedron						
B_{84}	I_h	84	8 F_{1u}		4 A_g 12 H_g	
α-rhomb. boron structure group						
B_{12}	3m	12	3 A_{2u} 5 E_u		4 A_{1g} 5 E_g	}9 }
$B_{12}X_2$ (chain)	3m	14	4 A_{2u} 6 E_u	}5 }	4 A_{1g} 6 E_g	
$B_{12}X_3$ (chain)	3m	15	5 A_{2u} 7 E_u	}9 + (3) }	5 A_{1g} 6 E_g	
$B_{12}B_4$ (plan.)	3m	16	4 A_{2u} 7 E_u		4 A_{1g} 7 E_g	
ß-rhombohedral structure group						
$B_{84}(B_{10})_2B$	3m	105	31 A_{2u} 52 E_u	24 25	31 A_{1g} 51 E_g	}10 }

In principle the number of vibrations depends on the number N of atoms per unit cell. The 3N-3 possible optical vibrations are only insignificantly reduced because of symmetry reasons. Therefore the lattice

vibration spectra of the complex boron-rich solids are very complicated. This is immediately indicated by table 4 showing the group theoretically determined numbers of possible vibrations. In many cases e.g. in ß-rhombohedral boron, the experimentally detected number of vibrations is distincly lower, which can hardly be explained by accidental degeneracy alone, but e.g. by assuming essentially different oscillator strengths [27].

In spite of this further complication it will be shown that also in such complicated structures the attribution of optical absorption bands to certain vibrations is possible and the bond parameters can be approximately determined by the application of a simple phenomenological theory.

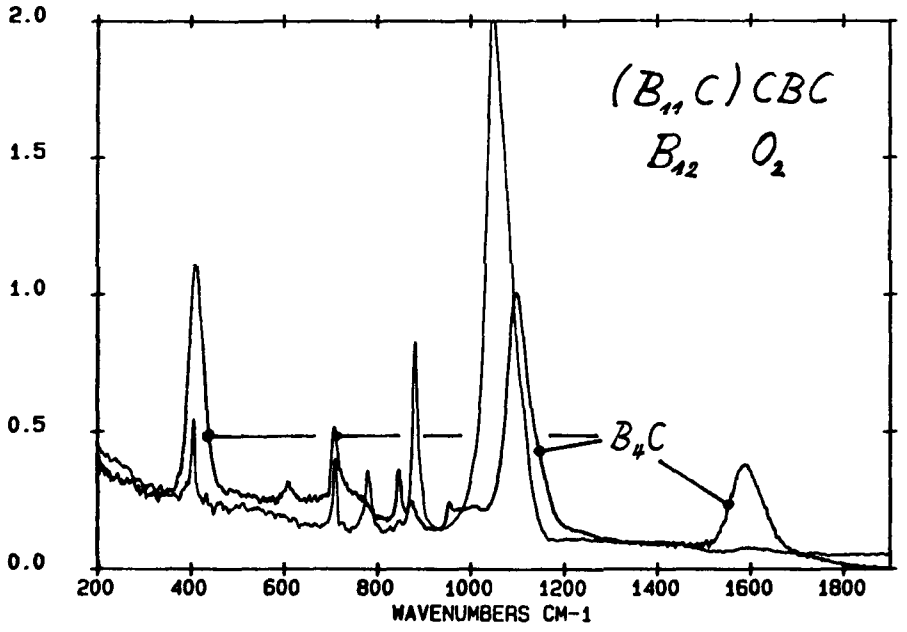

Figure 9. Comparison of the IR lattice vibration spectra of B_4C (structure formula $(B_{11}C)CBC$) and B_6O (structure formula $B_{12}O_2$) [28].
Absorption index k plotted versus wave number.

Fig. 9 compares the spectra of IR-active lattice vibrations of B_4C (structure formula $(B_{11}C)CBC$) and B_6O (structure formula $B_{12}O_2$), both representatives of the α-rhombohedral structure group. The spectra confirm that the essential difference in structure is the C-B-C and O-O chain on the main diagonal of the unit cell. Fig. 10 shows the corresponding spectrum of ß-rhombohedral boron [1,27].

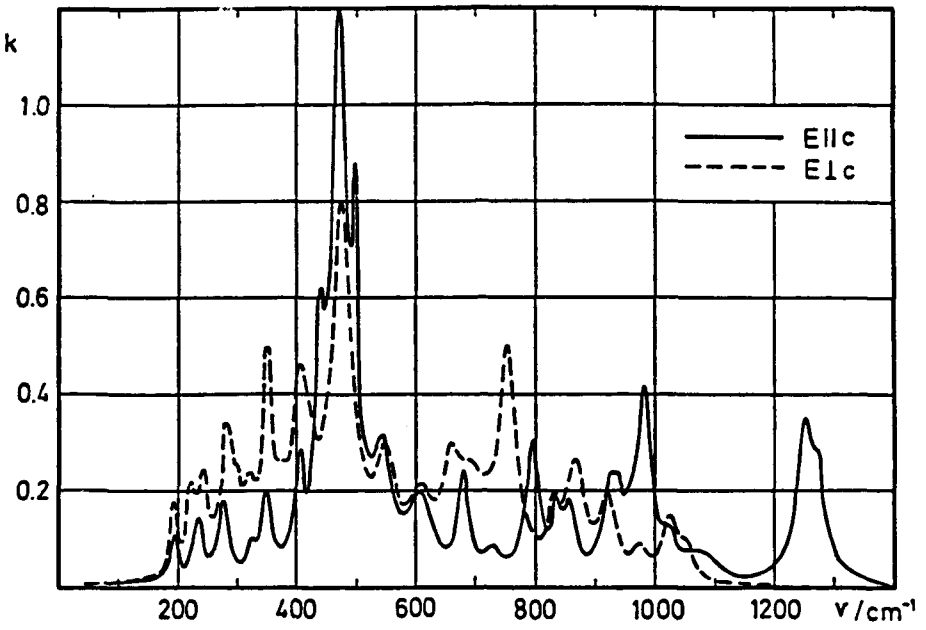

Figure 10. IR active lattice vibrations of ß-rhombohedral boron. Absorption index k plotted versus wave number [27].

The vibration, which is separated towards higher energies in boron carbide (1578 cm^{-1}) and in ß-rhombohedral boron (1.253/1307 cm^{-1}), is attributed to the central atom in the unit cell. This vibration is omitted in B_6O, because there is no dipole moment in the symmetrical O_2 chain [20,29]. The splitting of this band in ß-rhombohedral boron is caused by the different isotope masses. It cannot be resolved in boron carbide, because the band is broadened by damping.

The spectral position of these vibrations can be estimated by using a bond theoretical consideration analogous to 3-atomic molecules. After Waser and Pauling [30] the Badger rule of the relation between force constant and interatomic distance in molecules can also be applied in solids, and in the case of elements of the same row in the periodic table the same interaction constants can be applied [31].

The results for the central atom in the unit cell of boron carbide and of ß-rhombohedral boron are shown in table 5. In the case of boron carbide the agreement between calculated and real vibration frequency is very good in the case of the stretching vibration and the bending vibration as well. For ß-rhombohedral boron the situation is more difficult because the central atom is octahedrally surrounded by 6 atoms and not center of a three-atomic chain as assumed in the simple theory. This affects especially the bending mode. Therefore in this case also the agreement seems to be satisfactory.

TABLE 5. Comparison of calculated and measured vibration frequencies of the central atom in the unit cell of boron carbide and ß-rhombohedral boron at room temperature [31]

crystal	mode	wave number [cm^{-1}]	
		experimental	calculated
B_4C	A_{2u} (stretching)	1579	1503
	E_u (bending)	410	426
ß-rhomb. B	A_{2u} (stretching)	1253/1307	1063
	E_u (bending)	475	333

The frequency range from 400 to 1200 cm^{-1} in boron carbide and boron suboxide shows the inner vibrations of the icosahedron. The similarity is obvious. The large difference in the oscillator strengths of the vibration at 400 cm is assumed to be caused by the accidental degeneracy of the bending mode of the C-B-C chain with a special vibration of the icosahedron in boron carbide. The differences in the smaller vibrations are probably due to the occupation of icosahedral boron sites in boron carbide by carbon atoms. For the detailed investigation of the lattice vibrations of this structure group see [29].

It was mentioned previously that the numbers of experimentally determined vibrations in *ß-rhombohedral boron (fig.* 10) is much lower than the group theoretically predicted ones. An evident explanation seems to be that the oscillator strengths of the vibrations, which are originating from the F_{1u} mode, the only IR-active vibration of the free icosahedron, are distinctly stronger than those of the other ones [31]. To estimate the number of vibrations concerned for ß-rhombohedral boron, allowance must be made to the fact that several B_{12} icosahedra in the unit cell are coupled leading to a Davidov splitting of the vibration frequencies.

Starting from the simplified structure model of Runow [32], which describes the unit cell of ß-rhombohedral boron as approximately composed of eight unit cells of α-rhombohedral boron, then approximately eight split vibrations of eight coupled icosahedra are to be expected, which moreover underly an anisotropy splitting. This is in agreement with the result of group theory, when the vibrations of the B_{84} subunit (cp. e.g. [27, 31] are considered. Looking at the spectrum one finds approximately this number of vibrations in the frequency range between about 600 and 1100 cm^{-1}.

An other explanation could be that the eight vibrations of the Jahn-Teller distorted icosahedron in D_{3d} symmetry become IR active as A_{2u} and E_u modes, both, because of an additional reduction of the symmetry e.g. by the substitution of icosahedral boron sites by carbon atoms [18].

Following the assumption of Beckel and Vaughan [33] that the F_{1u} is a breathing mode of the icosahedron, this central vibration frequency can be estimated from the atomic spacing in the same way as described above. Fig. 11. shows the quite good agreement with the experimental result. Certain deviations are not surprising and to be accounted for inaccuracies in the oversimplified structure model.

At lower frequencies about eight absorption bands are found, which do not exhibit distinct anisotropy. According to group theoretical results [31] these vibrations can be attributed to the Davidov splitted vibrations of the rigid icosahedron. Because of the weak anisotropy of bonding in the structure the anisotropy of these vibrations is indeed expected to be very small. The calculated medium frequency of these vibrations is 436 cm^{-1} and agrees satisfactorily with the experimentally obtained center of the splitting range, which is positioned at about 400 cm^{-1}.

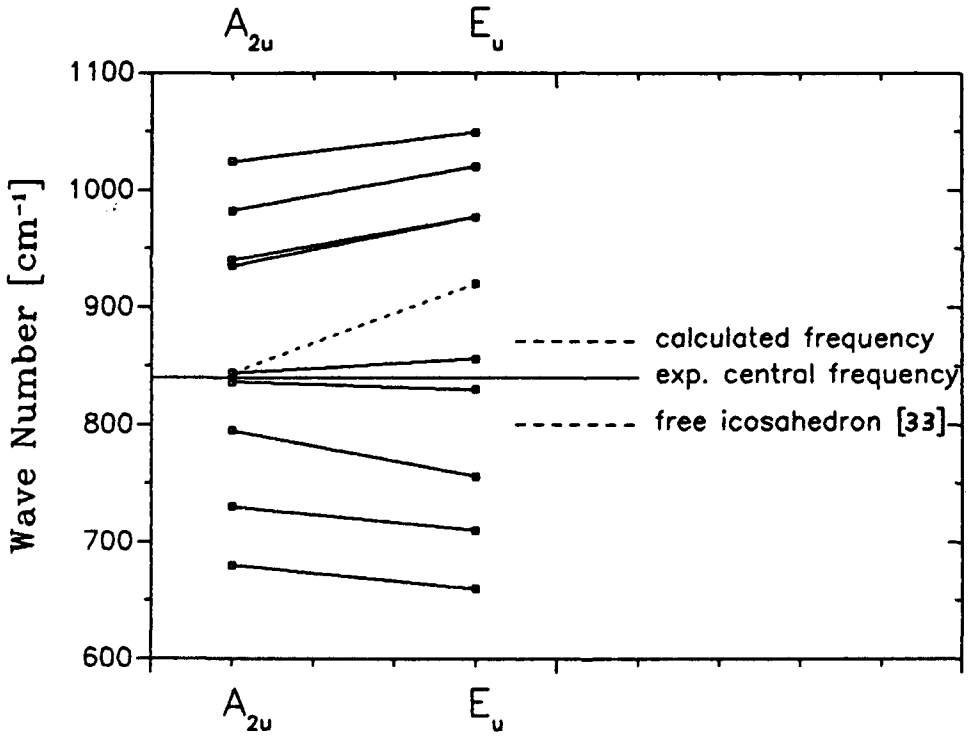

Figure 11. Splitted IR active inner vibrations of the B_{12} icosahedra in ß-rhombohedral boron [31]

By the considerations described at least a rough interpretation of the lattice vibration spectra of some important representatives of boron-rich solids is possible.

Boron carbide has a large homogeneity range, whose structural details are not yet precisely known. Fig. 12 shows that the optical lattice vibration spectrum enables sensitive details to be obtained. Fig. 12 contains the spectra of different boron carbide compounds within the homogeneity range and of boron carbide with excess carbon. When we restrict ourselves to the frequency range of the vibrations of the central atom, we see that with increasing boron content a frequency-shifted band is growing at a slightly lower frequency. Since the total oscillator strengths remains essentially unchanged, this can be interpreted by a change within the three-atomic chain, possibly from

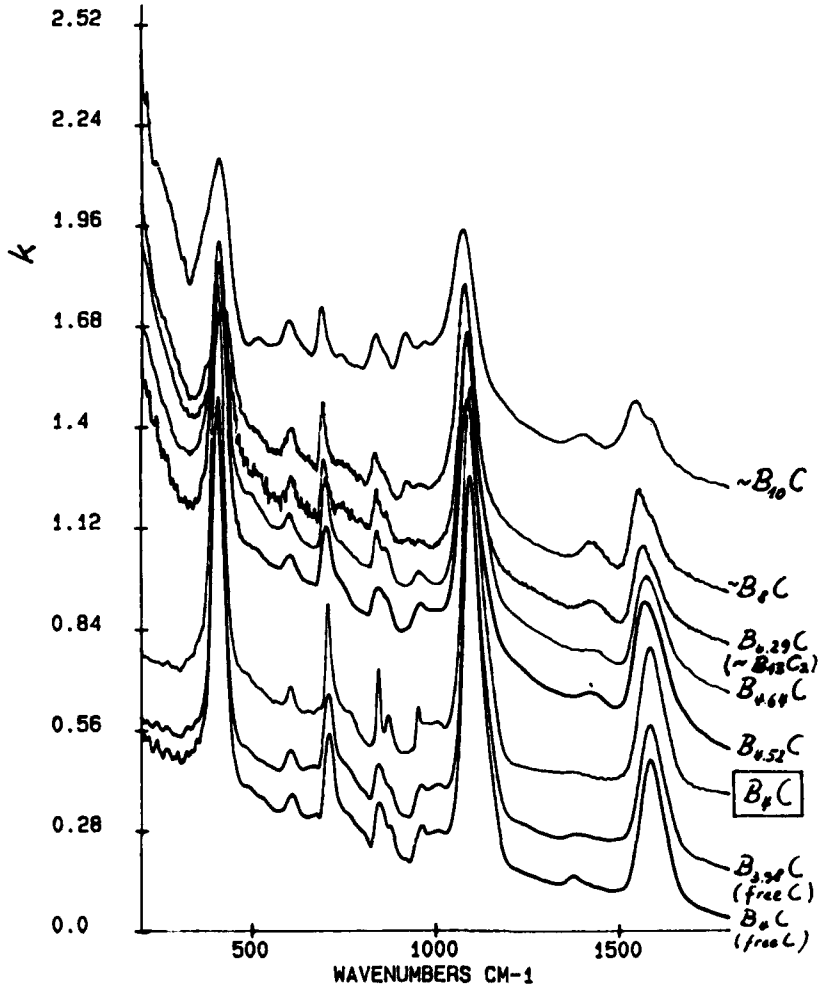

Figure 12. Variation of the IR active phonon spectrum of boron carbide depending on the chemical composition [28]. Absorption coefficient k plotted versus wave number. For clarity the single spectra are vertically shifted relative to one another.

C-B-C to C-B-B as proposed by Aselage [34] or simply by a change in the bonding force in consequence of the elongation of the chain. In any case it can be seen that the unit cells of boron carbide in the boron-rich range are not uniform.

Moreover an additional vibration probably due to a single vibrating atom is arising with maxima at 1432 cm^{-1} in the boron-rich, obviously correlated with a band at 180 cm^{-1} (fig. 13), and at 1379 cm^{-1} in the excess carbon range. Qualitatively the latter one indicates that C atoms in boron carbide beyond the carbon-rich limit of the homogeneity range are not only present in the form of graphitic free carbon, but additionally as single atoms in the structure. From the strong damping of this vibration it can be inferred that their bonding is not as precisely defined as in the case of the central atom of the chain, possibly this atom is at a less-defined interstitial position in the unit cell.

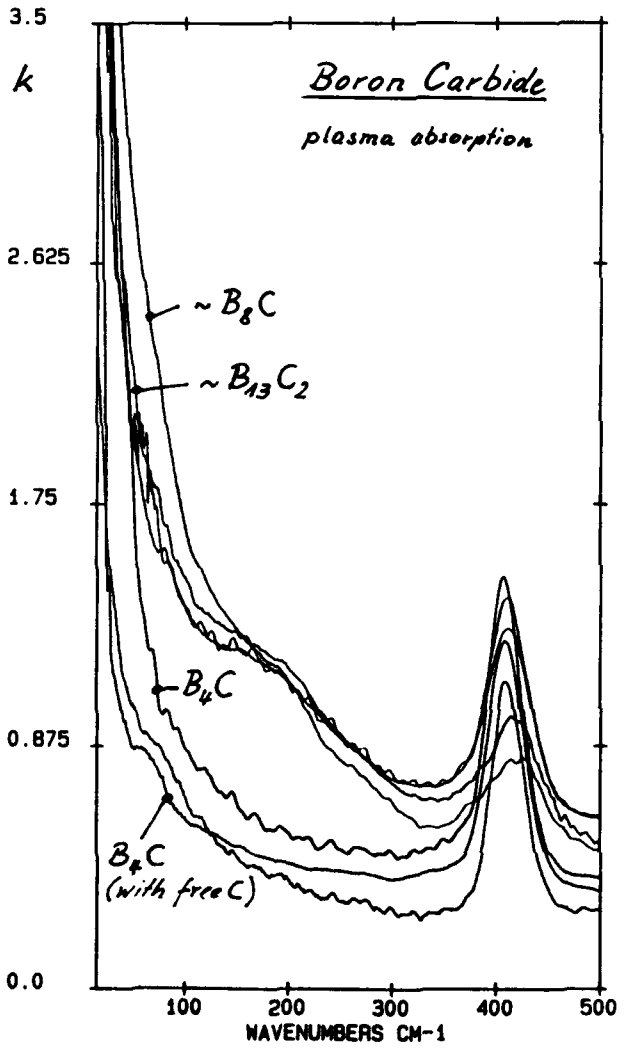

Figure 13. Plasma absorption of boron carbide and its variation depending on the chemical composition [28].

It seems that in the boron-rich part of the homogeneity range the corresponding vibration is due to single boron atoms in the structure, possibly at the same site as the C atom discussed above. The higher resonance frequency (1432 cm^{-1}) could be attributed to the stretching and the lower one (180 cm^{-1}) to the bending mode. Indeed, the experimentally derived relative frequency shift

$f_{C\text{-rich}}/f_{B\text{-rich}} = 0.963$ is only insignificantly smaller than that one estimated from the mass variation by calculating the simple relation

$$f_{C\text{-rich}}/f_{B\text{-rich}} = (m_B/m_C)^{1/2} = 0.949$$

The validity of the structure model of Yakel [35,36], who assumes planar B_4 arrangements statistically replacing the C-B-C chains in the boron-rich boron carbides, cannot be assessed. The group theory yields for this B_4 group two additional vibration frequencies in correspondence with the experimental results. Therefore Yakel's model remains as an alternative possiblity to explain the phonon spectra of boron-rich boron carbides.

The modifications of the vibrations between about 400 and 1100 cm^{-1}, which are to be attributed to the icosahedron, confirm that there are variations of the occupancy of sites in the icosahedron by C atoms within the homogeneity range.

5. PLASMA VIBRATIONS

In case of a sufficiently high carrier density and low effective mass the free carriers in a semiconductor can be excited to vibrate at frequencies in the optical range of the electromagnetic spectrum. It was previously shown [1,2,27] that in boron carbide the FIR spectral range is influenced by the absorption of free carriers. The reflectivity spectrum is determined by a strongly damped plasma edge, from which, in rough agreement with the evaluation of transport properties obtained on comparable material [37], for the effective can be estimated

$$m_h/m_0 \approx 0.2 \ldots 0.5$$

Fig. 13 shows the absorption coefficient of a series of boron carbide samples in the FIR spectral range. Presuming that the effective mass is not essentially influenced by changing the composition, the change of the carrier density can be estimated. The spectrum shows moreover a distinct plasmon-polariton interaction in the range of the 400 cm^{-1} phonon. As shown in [7] (fig. 8) the carrier density is thermally activated. The activation energy is of the order of magnitude 0.1 to 0.15 eV corresponding to the distance between the valence band and the Jahn-Teller induced split-off level (see [4,7]). A detailed investigation of the plasma edge in boron carbide promises a valuable insight into the transport mechanism of this material

Acknowledgements

With respect to the new results reported in this paper, the support of my coworkers R. Franz, H. Haupt, U. Kuhlmann, G. Gerlach, G. Krach and F.H. Werheit is gratefully acknowledged. These investigations were sup-

ported by the Minister of Research and Technology of the FRG under contract number 317-4003-0328845A within a cooperation with Hermann C. Starck, Goslar and Laufenburg, FRG, producer of the boron carbide material.

References

1. Werheit H. (1988). Optical properties of the crystalline modifications of boron and boron-rich solids. In: Progr. Crystal Growth and Charact., Ed. V.N. Gurin, Vol. 16, p. 179.
2. Werheit H. (1987). Optical Characterization of Icosahedral Boron Modifications and Compounds. In Proc. 9th Int. Symp. Boron, Borides and Related Compounds, Duisburg, Ed. H. Werheit, p. 142.
3. Labov S., Bowyer S., Steele G. (1985), Appl. Opt. 24, 576.
4. Franz R., Werheit H. (1989), Europhys. lett. 9, 145.
5. Bullett D.W. (1989). Further Electronic Structure Studies of Boron and Boron-Rich Borides, this volume.
6. Switendick A.C. (1989). The electronic Structure of Crystalline Boron Carbide II, this volume.
7. Werheit H. (1989). On the transport properties of boron carbide, this volume.
8. Werheit H., Werheit F.H., Franz R., Tsiskarishvili G.V., Krach G. (1989), to be published.
9. Smith R.A. (1961). Wave mechanics of crystalline solids; Chapman & Hall, London.
10. Lucovsky G. (1965). Solid State Comm. 3, 299.
11. Horn F.H., Taft E.A. and Oliver D.W. (1965). In Boron Vol. 2, Ed. G.K. Gaulé, Plenum Press, New York, p. 231.
12. Golikova O.A., Solov'ev N.E., Ugai Ya.A., Feigel'man V.A. (1979). Sov. Phys. Semicond. 13, 245.
13. Werheit H. (1983): Boron. In Landoldt-Börnstein, New Series, Group III Vol 17e, Ed. O. Madelung, M. Schulz and H. Weiss, Springer, Berlin, p. 9.
14. Armstrong D.R., Bolland J., and Perkins P.G. (1984). Theor. Chim Acta 64, 501.
15. Perrot F. (1981). Phys. Rev. B, 23, 2004.
16. Werheit H., Werheit F.H., Krach G. (1989). To be published.
17. Werheit H. (1979). J. Less-Common Met. 67, 143.
18. Franz R. (1989). Thesis, University of Duisburg.
19. Jaumann J., Werheit H. (1969). Phys. stat. sol. 33, 587.
20. Werheit H. (1970). Die Halbleitereigenschaften des Bors, in Festkörperprobleme X/Advances in Solid-State Physics X, Ed. O. Madelung, Vieweg, Braunschweig, p. 189.
21. Werheit H., Hausen A., Binnenbruck H., 1972. Phys. stat. sol. (b) 51, 115.
22. Gehrke U., Siems C.D. (1979). J. Less-Common Met. 67, 245.
23. Venturini E.L., Azevedo L.J., Emin D., Wood C. (1985). In Boron-Rich Solids, Eds.: D. Emin, T. Aselage, C.L.Beckel, I.A. Howard, C. Wood, AIP Conference Proceedings 140, Albuquerque, p. 292.

24. Emin D. (1989). Theory of Electronic ant Thermal Transport in Boron Carbides, this volume.
25. Franz R., Werheit H. (1987) Proc. 9th Int. Symp. Boron, Borides and Related Compounds, Duisburg, Ed. H. Werheit, p. 364.
26. Franz R., Werheit H. (1989). To be published.
27. Binnenbruck H., Werheit H. (1979). Z. Naturforsch. 34a, 787.
28. Haupt H., Werheit H. (1989). To be published.
29. Haupt H., Werheit H. (1987). Z. Naturforsch. 42a, 925.
30. Waser J., Pauling L. (1950). J. Chem Phys. 18, 747.
31. Haupt H., Werheit H., Lundström T., Higashi I. (1989). Z. Naturforsch. (in press).
32. Runow P. (1972). J. Mat. Sci. 7, 499.
33. Beckel C.L., Vaughan J.P. (1985). In: see [22] p. 305.
34. Aselage T., 1989. This volume.
35. Yakel H.L. (1975). Acta Crystallogr. Sect. B 31, 1797.
36. Yakel H.L. (1985). Recent Developements in the Structural Crystallography of Boron and Higher Borides. In: see [22] p. 97.
37. Geist D., Meyer J., and Peußner H., 1970. In Boron 3, Ed. T. Niemyski, PWN Warsaw, p. 207.

Subject Index

Actinide compounds
  melting temperatures, 359
  phase fields, 359
Actinoid metal boron carbides, structural chemistry 270–274
AES, diamond films, 175–176
Aluminium nitride, electronic devices, 657
Ambipolar diffusion, 634
Atomic hydrogen, 133–158
Atomic orbital-based method, 555–559
Augmented plane wave method, 485–511

Band gaps
  boron carbide, 677
  mono-nitrides, 654
Band structures, boron-rich solids, 705–725
Bipolarons, 677–690, 691–704
Boride ceramics
  fabrication, 115–117
  preparation, 113–115
Boride–carbide composites
  electrical properties, 475
  hot pressing, 463–465
  ternary diagrams, 462–481
Borides
  applications, 117–119
  powder synthesis, 97–102
  single crystal synthesis, 97–102
Boron carbide
  compressibility, 691–704
  crystal structures, 250–264
  DC conductivity, Hall mobility, 691–704
  dielectric properties, 688
  electrical conductivity, 683
  electronic structure, 525–553
  electronic transport, 677–690, 691–705
  magnetism, 276
  platelet synthesis, 87–96
  preparation, 87–96
  single crystal synthesis, 87–96
  sound velocities, 691–704
  thermal transport, 701–703
  thermodynamics, 274–275
  thin film synthesis, 87–96
Boron clusters, 555–559
Boron-rich pnictides, 691–704

Boron-rich solids
absorption edge, 706–712
band structure models, 705–725
optical properties, 705–725
photoeffects, 713–716
Breakdown strength, nitrides, 639–651

Carbides
defect structures, 329–355
diffusion data, 357–383
dislocations, 297–327
order–disorder, 329–355
ordering phenomena, 297–327
stabilities, 435–445
thermal conductivity, 625–637
Carburisation, 435–445
Ceramic powders, chemical synthesis, 3–11
Chemical bonding in carbides and nitrides, 485–511
Cluster variational methods, 329–355
Combustion chamber, corrosion, 387–401
Composites
boride–carbide, 457–481
reinforced with SiC, mechanical properties, 71
Si_3N_4–AlN, 639–651
Si_3N_4–SiC, 447–456
Crystal structure boron, boron compounds, 513–524

Defect data, carbides and nitrides, 357–383
Defect states, silicon carbide, 577
Defect structures, carbides and nitrides, 329–355
Density of states, carbides and nitrides, 485–511
Diamond
synthesis, 133–158
thin films, 133–158, 159–167, 169–181, 183–194
Dielectric properties
boron carbide, 688
nitrides, 639–651
Diffusion data, carbides and nitrides, 357–383
Discharge synthesis techniques, 139–144
Dislocations
in carbides, 297–327
in silicon carbide, 279–296

EACVD, diamond, 159–167
Electrical conductivity
borides, 108
boron carbide, 683
diamond films, 188–192
Electrical resistivity
composites, 475–481
silicon nitride, aluminium nitride, 639–651

Electronic structure
boron, boron carbide, boron compounds, 513–524
$B_{13}C_2$, 525–553
lithium boride, 555–559
silicon carbide, 567–587
TiC, TiN, 485–511
Electronic transport
boron carbide, 677–690, 691–704
EXAFS, TiB_2, 671–676
EXELFS, TiB_2, 671–676

Gallium nitride, electronic devices, 658
Gas phase reactions, 3–11

Hall effect in boron carbide, 687
Hemicarbides, 215–248
Heterostructures, AlN–GaN, 653–669
High resolution TEM, carbides, 297–327
Hot filament techniques, 135–139
Hydrothermal synthesis, 3–11

Icosahedral boron pnictides, 97–111
IR spectra, lanthanum silicon oxynitrides, 45–67
Irradiation studies, carbides, 297–327

Jahn–Teller effect, boron carbide, 679–683

Kinetic model
corrosion, 387–401
nitridation, 29–44

Lanthanum silicon oxynitrides
structures, 45–67
synthesis, 45–67
Laser ablation ICP MS, 121–130
Laser synthesis techniques, 90
Lattice parameters
mono-nitrides, 654
silicon carbide, 201
Lattice vibrations, borides, 716–724
Linearized APW method, 525–553
Liquid phase reactions, 3–11
Liquid phase sintering, nitrides, 423–433
Long range order, nitrides and carbides, 329–355

Magnetism, boron carbides, 276
MAS MNR, silicon carbide, 592–599
MBE, nitrides, 653–669
MESFETS, SiC, 613–615
Monte Carlo methods, 351
MOSFETS, SiC, 615–619

MPCVD, diamond, 159–167, 169–181, 183–194

Neutron diffusion studies
  carbides and nitrides, 329–355
Nitride solid solutions, 653–669
Nitrides
  defect structurs, 329–355
  densification, 423–433
  diffusion data, 357–383
  order–disorder, 329–355
Nitrogen ceramics, 423–433
Nitrogen glasses, 405–421

Optimal design methodology, 459–481
Order–disorder
  carbides, 215–248
  transformations, carbides and nitrides, 329–355
Ordering phenomena, carbides, 297–327
Oxygen in engineering ceramics, 423–433

Phase diagrams
  B–C–Si, 254–263
  carbides and nitrides, 349–350
Phase equilibria, boron carbides, 270–271
Photoluminescence, silicon carbide, 569–574
Plasma assisted CVD
  nitride film synthesis, 653–669
Plasma synthesis techniques, 90
Polymer pyrolysis, 3–11, 91
Powder handling, 423–433
Powder neutron diffraction, carbides, 215–248
Predominance area diagrams, 435–445

Quantitative analysis, 121–130

Raman scattering, silicon carbide, 574–576
Raman spectra
  borides, 104–106
  diamond, 165–166, 186
Rutherford backscattering–channelling, 362

Scattering of phonons, 625–637
Selective area deposition, 159–167
Selective nucleation, diamond, 159–167
Short range order
  carbides and nitrides, 329–355
  TiB_2, 671–676
  Si_3N_4–AlN composites, 639–651
Si_3N_4–SiC composites
  fabrication, 447–456
  mechanical properties, 447–456

Silicon, nitridation, 29–44
Silicon carbide
  bandgaps, 201
  corrosion, 387–401
  electronic properties, 563–587, 589–623
  fibre synthesis, 69–85
  grain boundary dislocations, 279–296
  hot pressing, 279–296
  interface faceting, 290
  lattice constants, 201
  light emitting diodes, 589–623
  optical properties, 563–587
  particle synthesis, 69–85
  platelet synthesis, 69–85
  polytypic transformations, 201
  Schottky barrier diodes, 589–623
  solid state devices, 589–623
  structure 198–209
  thermal shock, 387–401
  thin films, 563–587, 589–623
  tiles, 387–401
  whisker synthesis, 69–85
  whiskers and fibres, 209–211
Silicon nitride
  ceramic powders, 13–28
  corrosion, 402–404
  degradation, 403–404
  dielectric properties, 639–651
  electrical resistivity, 639–651
  mechanical properties, 21–23, 405–421
  oxidation, 403–404
  oxidation resistance, 405–421, 423–433
  sintering, 21–26
SIMS studies, diamond, 187
Single crystal, synthesis, borides, 97–102
Single crystals, boron carbide, 87–96
Sintering
  boron carbide – Si, 249–267
  silicon nitride, 21–26
Sol gel processing, 3–11
Solid sampling, 121–130
Sound velocities, borides, 106–108
Structural transformations, carbides, 215–248
Superstructures, carbides, 215–248

Transmission electron microscopy
  carbides, 297–327
  silicon carbide, 207, 279–296, 602–610

Thermal conductivity
AlN, 430–431
carbides, 625–637
cemented carbides, 625–637
Thermal diffusivity, boron carbide, 691–704
Thermal transport, boron carbide, 701–703
Thermochemical predictions, 435–445
Thermodynamics, boron carbides, 274–275
Thermoelectric energy conversion, 677–690
Thermogravimetry, 29–44
Thin films
boron carbide, 87–96
diamond, 133–158, 159–167, 169–181, 183–194
nitrides, III–V, 653–669
silicon carbide, 563–587, 589–623
titanium diboride, 671–676
Titanium diboride, thin films, 671–676
Trace element analysis, 121–130
Transition metal carbides, 297–327, 329–355, 625–637
Transition metal nitrides, 329–355

WC–Co powders, 435–445
Whiskers,
boron carbide, 87–96
silicon carbide, 69–85, 209–11

XPS, diamond silms, 174–176

Zeta, potentials, 448

Compound and System Index

AlB_{12}, 513–524
AlN, 3–11, 639–651, 653–669
AlN–GaN, 653–669

Boron, 97–111, 513–524, 677–690, 691–704, 705–725
B–C–(Th,U,Pu,Np), 269–277
B–C–Si, 249–267
$B_{10}Si_4$, 513–524
$B_{12}As_2$, 97–112, 513–524
$B_{12}C_3$, 677–690
$B_{12}P_2$, 97–111, 513–524, 691–704
$B_{13}C_2$, 97–111, 513–524, 525–553
B_4C, 3–11, 97–111, 113–120, 513–524, 677–690
Boron carbide, 677–690, 691–704
B_4C–$B_{10}C$, 87–96
BN, 3–11, 113–120, 639–651, 653–669
Boron-rich solids, 705–725

Co_7W_6, 435–445
$CoWO_4$, 435–445

Diamond, 133–158, 159–167, 169–181, 183–194

GaN, 639–651, 653–669

HfC, 357–383, 625–637

InN, 639–651, 653–669

$La_2Si_3N_4O_3$, 45–67
$La_4Si_2O_7N_2$, 45–67
$La_5Si_3O_{12}N$, 45–67
$LaSiO_2N$, 45–67
Li_3B_{14}, 555–559

Mo_2C, 215–248, 297–327

Nb_2C, 215–248, 297–327
Nb_6C_5, 297–327
NbC, 297–327, 329–355, 357–383, 625–637

Si–Al–O–N, 423–433, 639–651
Si_3N_4, 3–11, 13–28, 29–44, 121–130, 357–383, 403–404, 405–421, 423–433, 639–651
Si_3N_4–AlN, 639–651
Si_3N_4–SiC, 447–456
Si_3N_4–Y_2O_3–SiO_2, 405–421
SiC, 3–11, 69–85, 121–130, 197–214, 279–296, 357–383, 387–401, 423–433, 563–587, 589–623

SiC–TiB_2, 457–481
SiC–TiC, 457–481

Ta_2C, 215–248, 297–327
TaC, 297–327, 625–637
TiB_2, 3–11, 133–120, 671–676
TiB_2–TiC–SiC, 457–481
TiC, 297–327, 329–355, 357–383, 485–511, 625–637
TiC–TiB_2, 457–481
TiN, 329–355, 485–511

UC, 357–383
UN, 357–383
(U,Pu)N, 357–383

V_2C, 215–248, 297–327
V_8C_7, 297–327
VC, 297–327, 625–637

$W_{18}O_{49}$, 435–445
W_2C, 215–248, 297–327
WC, 357–383, 625–637
WC–Co, 435–445

ZrC, 297–327, 357–383, 625–637